F_5TeO–DERIVATIVES AND NgF_2 (Ng = Kr, Xe) COORDINATION COMPLEXES OF Hg(II), AND A Xe(II) OXIDE CATION

By

JOHN R.D. DE BACKERE, B.Sc. (Hons)

A Thesis Submitted to the School of Graduate Studies

in Partial Fulfillment of the Requirements for

the Degree Doctor of Philosophy

McMaster University

DOCTOR OF PHILOSOPHY (2018) McMaster University

(Chemistry) Hamilton, Ontario

TITLE: F_5TeO–Derivatives and NgF_2 (Ng = Kr, Xe) Coordination Complexes of Hg(II), and a Xe(II) Oxide Cation

AUTHOR: John R.D. De Backere, B.Sc. (Hons)

SUPERVISOR: Professor Gary J. Schrobilgen

NUMBER OF PAGES: 613, dcxiii

ABRIDGED ABSTRACT

The coordination chemistry of pentafluorooxotellurate(VI) (F_5TeO– or "teflate") derivatives, as well as $[PnF_6]^-$ (Pn = As, Sb) salts, of mercury(II), and the chemistry of Ng(II) (Ng = Kr, Xe), are the major focuses of this Thesis. The Lewis acid properties of $Hg(OTeF_5)_2$ were investigated using the nitrogen base, NSF_3, and $M[OTeF_5]$ salts (M = Cs^+, $N(CH_3)_4^+$, $N(CH_2CH_3)_4^+$) which resulted in a series of NSF_3 adducts, $F_2S(O)N$– derivatives, and several anions. Reactions of $Hg(OTeF_5)_2$ with NgF_2 also provided rare examples of bridging NgF_2 coordination complexes. Routes to $[Sb(OTeF_5)_6]^-$ salts containing weakly-solvated Hg^{2+} cations was developed, which provided an important synthetic precursor to explore further ligand substitution reactions at Hg^{2+}. The relatively unexplored chemistry of krypton was further advanced by synthesizing a series of coordination complexes of KrF_2 with $Hg(PnF_6)_2$ and $FHg(AsF_6)$ salts, providing rare examples of terminally coordinated and bridging KrF_2 ligands, and a new coordination mode for KrF_2 molecules. Advances in the chemistry of Xe(II) were also made through the synthesis and characterization of the second known, and simplest, xenon(II) oxide species. Characterization methods employed in this Thesis predominantly were single-crystal X-ray diffraction and Raman spectroscopy. Quantum-chemical calculations aided with Raman assignments, and were used to further investigate the nature of chemical bonding in the compounds that had been synthesized. The research described in this Thesis significantly contributes to and extends the chemistry of the pentafluorooxotellurate(VI) ligand, to our knowledge and understanding of the reactivity and bonding of krypton(II) and xenon(II) species, and most notably, the coordination chemistry of KrF_2.

ABSTRACT

The research described in this Thesis investigates the coordination chemistry of pentafluorooxotellurate(VI) (F_5TeO– or "teflate") and $[PnF_6]^-$ (Pn = As, F) derivatives of mercury(II), and expands the chemistry of Ng(II) (Ng = Kr, Xe) by characterizing several NgF_2 coordination complexes with mercury, and the synthesis of a new xenon(II) oxide cation. The compounds discussed herein were characterized predominately by low-temperature single-crystal X-ray diffraction and Raman spectroscopy, and were frequently complemented by quantum-chemical calculations.

The chemistry of the F_5TeO–group was developed for Hg(II) derivatives by investigating the Lewis acid properties of $Hg(OTeF_5)_2$. Initial efforts investigated interactions with the nitrogen base NSF_3, and resulted in the coordination complexes $[Hg(OTeF_5)_2{\cdot}N{\equiv}SF_3]_\infty$, $[Hg(OTeF_5)_2{\cdot}2N{\equiv}SF_3]_2$, and $Hg_3(OTeF_5)_6{\cdot}4N{\equiv}SF_3$ at 0^oC. Although the F_5TeO–group often bonds in a monodendate fashion, these less sterically saturated salts result in oxygen bridging in the solid state. In $Hg_3(OTeF_5)_6{\cdot}4N{\equiv}SF_3$, oxygen bridging between three metal centers by the pentafluorooxotellurate(VI) group is observed for the first time. The nature of this new bonding was further analysed computationally for $Hg_3(OTeF_5)_6{\cdot}4N{\equiv}SF_3$ by natural bond orbital analyses (NBO). At room temperature, reactions of $Hg(OTeF_5)_2$ with NSF_3 resulted in O/F metatheses to yield related F_2OSN–derivatives, namely $[Hg(OTeF_5)(N{=}SOF_2){\cdot}N{\equiv}SF_3]_\infty$ and $[Hg_3(OTeF_5)_5(N{=}SOF_2)\text{-}{\cdot}2N{\equiv}SF_3]_2$, accompanied by the elimination of TeF_6 as confirmed by ^{19}F NMR spectroscopy.

In related work, the acceptor properties of $Hg(OTeF_5)_2$ were further investigated in its reactions with $M[OTeF_5]$ ($M = [N(CH_3)_4]^+$, $[N(CH_2CH_3)_4]^+$, Cs^+) to form a series of teflate anion salts; $[N(CH_2CH_3)_4]_2[Hg(OTeF_5)_4]$, $[N(CH_3)_4]_3[Hg(OTeF_5)_5]$, $[N(CH_2CH_3)_4]_3[Hg(OTeF_5)_5]$, $[N(CH_3)_4]_2[Hg_2(OTeF_5)_6]$, $Cs_2[Hg(OTeF_5)_4]\cdot Hg(OTeF_5)_2$, and $\{Cs_3[Hg_2(OTeF_5)_7]\cdot Hg(OTeF_5)_2\}\cdot 4SO_2ClF$. In comparison to their halide counterparts, the less basic and more sterically demanding teflate ligands of the Hg(II) anions show less tendency to extensively bridge. The Raman spectra of the $[Hg(OTeF_5)_4]^{2-}$, $[Hg(OTeF_5)_5]^{3-}$, and $[Hg_2(OTeF_5)_6]^{2-}$ anions were fully assigned with the aid of their calculated gas-phase vibrational frequencies. NBO analyses further probed the bonding in the anions. The $[Hg(OTeF_5)_5]^{3-}$ anion provides an unusual square-pyramidal coordination sphere around mercury and the only presently known teflate-substituted anion with a net charge of 3–.

In related work, the weakly coordination anion (WCA) $[Sb(OTeF_5)_6]^-$ was substituted in Hg^{2+} salts using weakly coordinating SO_2ClF solvent to give the homoleptic solvent complex, $[Hg(SO_2ClF)_6][Sb(OTeF_5)_6]_2$. The ability of this salt to function as a precursor for other ligands was demonstrated by the reaction with the nitrogen bases NCR (R = $–CH_3$ or $–CH_2CH_3$) which resulted in the isolation and full characterization of the corresponding homoleptic nitrile complexes $[Hg(NCR)_5][Sb(OTeF_5)_6]_2\cdot 2SO_2ClF$. Gas-phase energy-minimized calculation of the cations aided in the vibrational assignment of the Raman spectra, whereas NBO and counterpoise corrected binding energies give insights into the strength of the metal-ligand bonds and resulting electronic effects of these interactions.

The established Lewis acidity of $Hg(OTeF_5)_2$, and known oxidative resistance of the F_5TeO–group, were exploited to form rare examples of noble-gas difluoride adducts, $Hg(OTeF_5)_2 \cdot 1.5NgF_2$ (Ng = Xe, Kr). The isostructural complexes were fully characterized, and the KrF_2 adduct provided only the second crystallographically characterized KrF_2 complex and the first example of bridge coordination by KrF_2.

The chemistry of krypton was significantly extended by further exploring the little studied coordination of KrF_2 with the salts $Hg(PnF_6)_2$ (Pn = As, Sb) and $FHg(AsF_6)$, leading to an important series of coordination complexes. The first homoleptic KrF_2 coordination complex, $[Hg(KrF_2)_8][AsF_6]_2 \cdot 2HF$, was thoroughly characterized by single-crystal X-ray diffraction, Raman spectroscopy, and quantum-chemical analyses. It provides the highest KrF_2-to-metal ratio that is currently known for a coordination complex. The bonding was extensively analysed by NBO, calculated binding energies, energy decomposition analyses (EDA), and Extended Transition State Natural Orbitals for Chemical Valence (ETS-NOCV) analyses. This computational work suggests that both orbital interactions, which incorporate covalent bonding, and electrostatic contributions are important stabilization factors and that the $8\sigma_g$ (HOMO–4) orbital and, to a lesser extent, a degenerate $4\pi_u$ (HOMO) orbital, derived from free KrF_2 ($D_{\infty h}$) are involved in adduct formation. This result helps to rationalize the observed M---F–Kr(F) coordination angles observed for most terminally coordinated NgF_2 complexes. A series of related complexes with one to five KrF_2 molecules per metal center were also characterized by single-crystal X-ray diffraction, namely $Hg(KrF_2)(HF)(AsF_6)_2$ (**1**), $Hg(KrF_2)_2(AsF_6)_2$ (**2**), $Hg(KrF_2)_3(HF)(SbF_6)_2$ (**3**), $[Hg(KrF_2)_4(HF)_2(SbF_6)]_2[SbF_6]_2$ (**4**), $Hg(KrF_2)_5(AsF_6)_2$ (**5**),

$Hg(KrF_2)_4(HF)_2(AsF_6)_2 \cdot HF$ (**6**), $FHg(\mu_3\text{-}FKrF)_{1.5}(KrF_2)_{0.5}(AsF_6)$ (**7**), and $FHg(\mu_3\text{-}FKrF)_{0.5}(KrF_2)_{1.5}(AsF_6)$ (**8**). These complexes were unambiguously characterized by single-crystal X-ray diffraction which showed that the structures became more extensively linked due to bridging between mercury and the $[PnF_6]^-$ anions as the number of coordinated KrF_2 ligands decreased. While compounds **(1)-(6)** solely contain terminally coordinated KrF_2 ligands, compound **(7)** also contains the second structurally characterized example of KrF_2 bridging two metal centers through each of its fluorine atoms. Replacement of $[AsF_6]^-$ by F^- in compounds **(7)** and **(8)** also resulted in the first examples of a new bonding modality of KrF_2, where only one of the fluorine atoms bridges two different metal centers. The Raman spectrum of (**5**) was assigned with the aid of calculated gas-phase vibrational frequencies. Natural bond orbital (NBO) analyses of $[Hg(KrF_2)_5][AsF_6]_2$ are consistent with coordinate covalent ligand-metal interactions. The nature of bonding for the unprecedented KrF_2 bonding modality was further probed computationally with EDA and ETS-NOCV analyses and corroborate an MO description where electron density is donated from both the $8\sigma_g$ (HOMO–4) and a degenerate $4\pi_u$ (HOMO) molecular orbital of KrF_2 to LUMOs involving the 6s and 6p orbitals of each mercury atom.

To further expand the chemistry of the noble-gases, the second known xenon(II) oxide, $[XeOXe]^{2+}$, was synthesized from the reaction of $[FXeOXe\text{---}FXeF][AsF_6]$ and acetonitrile at low-temperatures in anhydrous HF. The cation was isolated in macroscopic quantities as its well-isolated adduct-dication $[CH_3CN\text{---}XeOXe\text{---}NCCH_3][AsF_6]_2$ salt and was fully characterized by single-crystal X-ray diffraction and $^{16/18}O$ isotopic enrichment

Raman studies. The $[XeOXe]^{2+}$ adduct-cation provides an important example of σ-hole bonding by a nitrogen base to a Xe(II) atom. The nature and strength of the Xe–O and Xe–N bonds in the calculated gas-phase $[XeOXe]^{2+}$ and $[CH_3CN{-}{-}{-}XeOXe{-}{-}{-}NCCH_3]^{2+}$ cations were extensively explored using a range of quantum-chemical (QC) methods, namely, NBO, atoms in molecules (AIM), electron localization function (ELF), and molecular electrostatic potential surface (MEPS) analyses.

ACKNOWLEDGEMENTS

I wish to thank my supervisor, Prof. Gary J. Schrobilgen, for allowing me to pursue interesting and exciting avenues of research, as well as for his insight, guidance, and mentorship in the laboratory and in my scientific writing.

I would like to thank Dr. Hélène P. A. Mercier for imparting her invaluable expertise in X-ray crystallography, quantum-chemical calculations, and analyzing data, and for her many hours put towards our shared publications. Her encouragement, friendship, and support throughout the course of this work was unwavering.

I thank the members of my supervisory committee, Prof. Ignacio Vargas-Baca and Prof. David Emslie, for taking the time out from their busy schedules for meetings and examinations, and particularly for their continuous support, advice, guidance, and interest in my academic development.

I would also like to acknowledge Prof. Ignacio Vargas-Baca, as well as Jeffrey Price, for their support and guidance pertaining to EDA and ETS-NOCV calculations as implemented in ADF.

I thank Dr. Jim Britten (X-ray crystallographic facilities) for his expertise, helpful insights and suggestions on problematic data sets, and technical support at all hours of the day and night.

I would like to acknowledge members of the Schrobilgen group, both past and present, for their mentorship, support, and friendships. Thank you, Dr. James Goettel, Dr.

Matic Lozensek, Dr. David Brock, Dr. Maria Ivanova, Katherine Marczenko, Mark Bortolus, Jamie Haner, Daniel Stuart, and Ulf Breddemann.

I would like to acknowledge the National Science and Engineering Council of Canada (NSERC) for the Canada Graduate Scholarships. I also wish to acknowledge the Department of Chemistry at McMaster University for a Joy M. Cunningham Ontario Graduate Scholarship, as well as other financial support in the form of awards, bursaries, and travel scholarships over the years.

Most importantly and above all else, I am indebted to my wife, Aislin, for her never-ending love, support, encouragement, and patience during my graduate studies. You are my world. A heartfelt thank you goes out to my parents, Daniel and Roseanne, and to my sister, Lisa, for always being there to support me in every way possible. I would also like to thank my parents-in-law, Phil and Nadia, and sister-in-law, Rachel, for their encouragement throughout my post-secondary education. Finally, I thank all of my dear friends, you know who you are, as I could not have persevered without your support and all of our shared laughter.

TABLE OF CONTENTS

page

CHAPTER 4: Pentafluoro-oxotellurate(VI) Anions of Mercury(II); the Syntheses and Structures of $[Hg(OTeF_5)_4]^{2-}$, $[Hg(OTeF_5)_5]^{3-}$, $[Hg_2(OTeF_5)_6]^{2-}$, $[Hg(OTeF_5)_4]^{2-}\cdot Hg(OTeF_5)_2$, and $[Hg_2(OTeF_5)_7]^{3-}\cdot Hg(OTeF_5)_2$

CHAPTER 5: Syntheses and Characterization of Homoleptic Solvent Complexes of Hg^{2+} using the Weakly Coordinating $[Sb(OTeF_5)_6]^-$ Anion

CHAPTER 6: Noble-Gas Difluoride Complexes of Mercury(II); the Syntheses and Structures of $Hg(OTeF_5)_2 \cdot 1.5NgF_2$ (Ng = Xe, Kr) and $Hg(OTeF_5)_2$

CHAPTER 10: Conclusions and Directions for Future Work

LIST OF TABLES

LIST OF FIGURES

LIST OF SCHEMES

page

LIST OF ABBREVIATIONS AND SYMBOLS

General

ax	axial
eq	equatorial
b	bridging
t	terminal
CCD	charge-coupled device
FT	Fourier transform
FEP	perfluoroethylene/perfluoropropylene copolymer
IR	infrared
Kel-F	chlorotrifluoroethylene polymer
PTFE	tetrafluoroethylene polymer (Teflon)
VSEPR	valence shell electron pair repulsion
N.A.	natural (isotopic) abundance
aHF	anhydrous HF
WCA	weakly coordinating anion
AO	atomic orbital
MO	molecular orbital

Raman Spectroscopy

$\Delta\nu$	frequency (in Raman spectroscopy)
cm^{-1}	wavenumber
ν	stretching mode
δ	bending mode
ρ_w	wagging mode
ρ_r	rocking mode
ρ_t	twisting mode
o.o.p.	out-of-plane

i.p.	in-plane
– or OOP	out-of-phase
+ or IP	in-phase
br	broad
sh	shoulder
n.o.	not observed

Nuclear Magnetic Resonance Spectroscopy

NMR	nuclear magnetic resonance
ppm	parts per million
δ	chemical shift
I	nuclear spin quantum number
J	scalar coupling constant, in Hz
Hz	Hertz or cycles per second (cps)
FID	free induction decay
SF	spectral frequency
SW	sweep width
TD	time delay
PW	pulse width
$\Delta\nu_{1/2}$	line width at half height
WF	width factor

X-ray Crystallography

a, b, c	unit cell edge lengths
α, β, γ	unit cell angles
V	unit cell volume
λ	wavelength
Z	molecules per unit cell
mol. wt.	molecular weight

ρ	density
μ	absorption coefficient
R_1	conventional agreement index
wR_2	weighted agreement index
Å	Ångström

Quantum-chemical Calculations

DFT	density functional theory
B3LYP	Becke, 3-parameter, Lee-Yang-Parr hybrid functional
PBE	Perdew–Burke–Ernzerhof GGA functional
PBE0	Perdew–Burke–Ernzerhof hybrid functional
APFD	Austin-Frisch-Petersson hybrid functional with dispersion
GD3BJ	D3 version of Grimme's dispersion with Becke-Johnson damping
NBO	natural bond orbital
NPA	natural population analysis
BSSE	basis set superposition error
MEPS	molecular electrostatic potential surface
ELF	electron localization function
AIM	atoms in molecules
EDA	energy decomposition analysis
ETS–NOCV	extended transition state and natural orbitals for chemical valence
LUMO	lowest unoccupied molecular orbital
HOMO	highest occupied molecular orbital

DECLARATION OF ACADEMIC ACHIEVEMENT

Dr. Hélène P.A. Mercier, a research scientist in the Schrobilgen group, assisted in structure solutions and refinements of problematic single-crystal X-ray diffraction data sets and provided insights into the Raman interpretations for chapters on which she is co-author (Chapters 3–6). Jonathon Paxon, a former graduate student in the Schrobilgen group, initially identified the mercury teflate species $[Hg(OTeF_5)(N{=}SOF_2)\cdot N{\equiv}SF_3]_\infty$, $Cs[Hg(OTeF_5)_3]$, and $Hg(OTeF_5)_2{\cdot}1.5XeF_2$ (Chapters 3, 4, and 5, respectively) by preliminary X-ray structures. During his 4th year undergraduate thesis in the Schrobilgen group, Mark R. Bortolus assisted with experimental work leading to $[H_3CCN{---}XeOXe{---}NCCH_3][AsF_6]_2$ (Chapter 9) and is a co-author on the published paper. All other results were obtained by John R.D. De Backere.

PREFACE

The following Chapters have been published. All experimental and computational work was conducted by the author.

Chapter 3: DeBackere, J. R.; Mercier, H. P. A.; Schrobilgen, G. J. *Inorganic Chemistry*, **2015**, *54*, 9989–10000.

Chapter 4: DeBackere, J. R.; Mercier, H. P. A.; Schrobilgen, G. J. *Inorganic Chemistry*, **2015**, *54*, 1606–1626.

Chapter 6: DeBackere, J. R.; Mercier, H. P. A.; Schrobilgen, G. J. *Journal of the American Chemical Society*, **2014**, *136*, 3888–3903.

Chapter 7: DeBackere, J. R.; Schrobilgen, G. J. *Angewandte Chemie International Edition*, **2018**, *57*, 13167–13171.

Chapter 9: DeBackere, J. R.; Bortolus, M. R.; Schrobilgen, G. J. *Angewandte Chemie International Edition*, **2016**, *55*, 11917–11920.

CHAPTER 1

Introduction

The chapters of this Thesis have been published, or are being prepared for publication. Consequently, each Chapter possesses a self-contained introduction and references. The present Introduction provides a more general overview of the primary focuses of the Thesis, which includes the chemistry of the pentafluorooxotellurate(VI) group, coordination complexes of NgF_2 (Ng = Kr, Xe), and the chemistry of xenon(II) oxides.

1.1. The Pentafluorooxotellurate (VI) Group, $F_5TeO–$

The pentafluorooxotellurate(VI) group, also referred to as "teflate", was first synthesized in 1964 by Engelbrecht and Sladky[1] by the reaction of $BaTeO_4$ with FSO_3H (originally intended to form TeO_2F_2 by analogy with its selenium counterpart)[2] which resulted in the formation of $HOTeF_5$ ("teflic acid"). Further studies by Engelbrecht *et. al*,[3] demonstrated the strong Brønsted acid properties of $HOTeF_5$ (pKa = 9.2 in glacial acetic acid),[4] which is between that of HCl and HNO_3, enabled HCl displacements and the formation of a number of teflate salts; leading to a new class of compounds which incorporate this highly electronegative ligand. For example, displacement of HCl in the reaction of a threefold excess of $HOTeF_5$ with BCl_3 leads to the formation of $B(OTeF_5)_3$,[5] an important $F_5TeO–$group transfer reagent (*vide infra*).

Elements from every group of the periodic table, except the alkaline and rare earth metals, have been shown to form $F_5TeO–$derivatives (Table 1.1 and 1.2). All

Table 1.1. Known F_5TeO-Derivatives of the Main-Group Elements

Group 1	Group 13	Group 14	Group 15	Group 16	Group 17	Group 18
$HOTeF_5$ [1]	$B(OTeF_5)_3$ [5,7]	$\mathbf{R}(OTeF_5)$ [11–13]	$ON(OTeF_5)$ [17]	$F_5TeOOTeF_5$ [24–26]	$\mathbf{X}(OTeF_5)$ ($\mathbf{X}$ = F,[33,34] Cl,[25,33] Br,[35] I,[35])	$\mathbf{Ng}(OTeF_5)_2$ ($\mathbf{Ng}$ = Kr,[39,40] Xe,[24,25,41])
$\mathbf{A}[OTeF_5]$ ($\mathbf{A}$ = Li–Cs) [6]	$[B(OTeF_5)_4]^-$ [7]	$\mathbf{Y}(OTeF_5)_4$ ($\mathbf{Y}$ = C,[14] Si,[15])	$POF_2(OTeF_5)$ [8]	$HSO_3(OTeF_5)$ [27]	$[Br(OTeF_5)_2]^+$ [14]	$FXe(OTeF_5)$ [41–43]
	$[FB(OTeF_5)_3]^-$ [8]	$[C(OTeF_5)_3]^+$ [14]	$\mathbf{Pn}(OTeF_5)_3$ ($\mathbf{Pn}$ = P,[18] As,[15] Sb,[19])	$SO_2\mathbf{X}(OTeF_5)$ ($\mathbf{X}$ = F or Cl) [28]	$I(OTeF_5)_3$ [35, 65]	$[Xe(OTeF_5)]^+$ [43–45]
	$Al(OTeF_5)_3$ [9]	$[CBr_x(OTeF_5)_{(3-x)}]^+$ [14] (x = 1–2)	$F_2As(OTeF_5)$ [15]	$SO_2(OTeF_5)_2$ [27]	$ICl(OTeF_5)_2$ [36]	$[FXeFXe(OTeF_5)]^+$ [44]
	$[Al(OTeF_5)_4]^-$ [9]	$\mathbf{Y}(CH_3)_3(OTeF_5)$ ($\mathbf{Y}$ = Si, Ge, Sn) [15]	$O{=}P(OTeF_5)_3$ [18]	$NS(OTeF_5)$ [21]	$[I(OTeF_5)_4]^-$ [36]	$(F_5SeO)Xe(OTeF_5)_2$ [41]
	$Tl(OTeF_5)$ [10]	$Sn(CH_3)_2Cl(OTeF_5)$ [16]	$[AsF(OTeF_5)_5]^-$ [20]	$SeF_2(OTeF_5)_2$ [28]	$IF_{(5-x)}(OTeF_5)_x$ (x = 1–5) [8]	$XeF_{(4-x)}(OTeF_5)_x$ (x = 1–4) [46,47]
	$[Tl(mes)_2(OTeF_5)]_2$ [10]		$[AsF_5(OTeF_5)]^-$ [21]	$O{=}SeF_x(OTeF_5)_{(2-x)}$ (x = 0, 1) [28]	$O{=}I(OTeF_5)_3$ [8, 36]	$[XeF_x(OTeF_5)_{(3-x)}]^+$ (x = 0–2) [48]
			$\mathbf{Pn}(OTeF_5)_5$ ($\mathbf{Pn}$ = As,[18] Bi [22])	$F_5TeOTeF_5$ [24,29]	$[O{=}I(OTeF_5)_4]^-$ [36]	$XeF_{(6-x)}(OTeF_5)_x$ (x = 1–6) [39]
			$SbF_{(5-x)}(OTeF_5)_x$ (x = 1 or 2) [23]	$TeF_{(4-x)}(OTeF_5)_x$ (x = 1–4) [28, 30,31]	$O_2Br(OTeF_5)$ [37]	$[O{=}XeF_x(OTeF_5)_{(3-x)}]^+$ (x = 0–2) [48]
No Group 2 teflate derivatives are currently known			$[Sb(OTeF_5)_{(6-x)}Cl_{(x-2)}]^-$ ($x \geq 2$) [20]	$[TeF_x(OTeF_5)_{(3-x)}]^+$ (x = 0–3) [31]	$\mathbf{R^F}I(OTeF_5)_2$ [38]	$O{=}XeF_{(4-x)}(OTeF_5)_x$ (x = 1–4) [39, 47]
R = alkyl group R^F = fluoroalkyl group			$[\mathbf{Pn}(OTeF_5)_6]^-$ ($\mathbf{Pn}$ = As,[15,22] Sb,[22] Bi,[22])	$[TeF_x(OTeF_5)_{(5-x)}]^-$ (x = 0, 1) [32]		$[O_2Xe(OTeF_5)]^+$ [48]
				$TeF_{(6-x)}(OTeF_5)_x$ (x = 1–6) [28, 30]		$O_2XeF_{(2-x)}(OTeF_5)_{(2-x)}$ (x = 1–2) [47]

Table 1.2. Known F_5TeO-Derivatives of the Transition-Metal Elements

Group 4	Group 5	Group 6	Group 7	Group 8	Group 9	Group 10	Group 11	Group 12
$TiCl_{(4-x)}(OTeF_5)_x$ (x = 1–4) [49]	$O{=}V(OTeF_5)_3$ [53]	$O_2Cr(OTeF_5)_2$ [53]	**M**$(CO)_5(OTeF_5)$ (**M** = Mn, Re) [55,60]	$CpFe(CO)_2$-$(OTeF_5)$ [55]	$[Co(OTeF_5)_4]^2$ [67]	$[$**M**$(OTeF_5)_4]^{2-}$ (**M** = Ni,[67] Pd[68])	$[Cu(OTeF_5)_4]^2$ [67]	$Hg(CH_3)(OTeF)_5$ [6]
$[$**M**$(OTeF_5)_6]^{2-}$ (**M** = Ti,[49,50] Zr, Hf) [51]	**M**$(OTeF_5)_5$ (**M** = Nb, Ta) [53]	$[$**M**$(CO)_5(OTeF_5)]^-$ (**M** = Mo, W) [55]	**M**$(CO)_4L(OTeF_5)$ (**M** = Mn, Re) [61]	Fe(**Y**)$(OTeF_5)$ [65] (**Y** = TTP or OEP)		**M**$(L)_x(OTeF_5)_2$ (**M** = Pd, Pt; x = 1 or 2) [61,69]	$[Ag($**L**$)_x(OTeF_5)]_x$ (x = 1, 2)[6,70,71]	$Zn(PhNO_2)_x$-$(OTeF_5)_2$ (x = 2, 3) [73,74]
$[$**M**$(Cp)_2(OTeF_5)_2]$ (**M** = Ti, Zr, Hf) [52]	$[$**M**$(OTeF_5)_6]$ (**M** = Nb,[50,51] Ta) [54]	$[$**M**$(Cp)_2(OTeF_5)_2]$ (**M** = Mo or W) [52]	$O{=}Re(OTeF_5)_x$ (x = 4, 5) [62]	$Fe(OTeF_5)_3$ [66]			$[Au(OTeF_5)_3]_2$ [72]	$[Zn(OTeF_5)_4]^{2-}$ [75]
		$MoF_{(6-x)}(OTeF_5)_x$ (x = 1–6) [56,57]	$O_2Re(OTeF_5)_2$ [53]	$Ru(CO)_2$**L**$_2$-$(OTeF_5)$ [61]				**M**$(OTeF_5)_2$ (**M** = Zn,[74] Hg [6,25])
		$O{=}MoF_{(4-x)}(OTeF_5)_x$ (x = 1–4) [53,56,57]	$O_2Re(OTeF_5)_3$ [53,63]	$Os(CO)_4(CH_3)$-$(OTeF_5)$ [61]				
		$W(OTeF_5)_x$ (x = 5, 6 [53]) [56]	$[O_2Re(OTeF_5)_4]^-$ [63]	$O{=}Os(OTeF_5)_4$ [53]				
		$WCl(OTeF_5)_5$ [53]	$O_3Re(OTeF_5)$ [64]					
		$WF_{(6-x)}(OTeF_5)_x$ (x = 1–6) [53]						
		$O{=}W(OTeF_5)_4$ [56]						
		$UF_{(6-x)}(OTeF_5)_x$ (x = 1–6) [58, 59]						

No Group 3 teflate derivatives are currently known

L = Neutral Donor Ligand

F_5TeO–containing compounds, like most hypervalent fluorine compounds, are very moisture sensitive; with hydrolysis resulting in the formation of very corrosive hydrogen fluoride (HF) and $TeF_x(OH)_{(6-x)}$ (x = 1–6).[76,77]

Because F_5TeOH is the origin of the F_5TeO-group, the most direct route to introduce the F_5TeO-ligand is the reaction of F_5TeOH with a halide (usually a fluoride or chloride) derivative to give HX displacement as shown in eq 1.1. A number of other F_5TeO-ligand transfer reagents have also been employed, such as $Ag(OTeF_5)$,[6,70,71] $Hg(OTeF_5)_2$,[6,25] and $B(OTeF_5)_3$[5,7] (eq 1.2–1.4).[78]

$$n\ HOTeF_5 + MX_n \longrightarrow M(OTeF_5)_n + n\ HX\ (X = F \text{ or } Cl) \quad (1.1)$$

$$n\ AgOTeF_5 + MCl_n \longrightarrow M(OTeF_5)_n + n\ AgCl_{(s)} \quad (1.2)$$

$$^{n}/_{2}\ Hg(OTeF_5)_2 + MCl_n \longrightarrow M(OTeF_5)_n + {}^{n}/_{2}\ HgCl_{2(s)} \quad (1.3)$$

$$^{n}/_{3}\ B(OTeF_5)_3 + MF_n \longrightarrow M(OTeF_5)_n + {}^{n}/_{3}\ BF_{3(g)} \quad (1.4)$$

In addition to HX displacements, salt metatheses (eqs 1.2 and 1.3) are another means to form F_5TeO-derivatives from high-valent halides. These reactions are largely driven by the significant lattice energy associated with the formation of the insoluble halide salts (i.e., AgX and HgX_2). A third category of ligand transfer reagent is represented by $B(OTeF_5)_3$ (eq 1.4). The reaction is driven by the formation of very stable B–F bonds and the evolution, and removal, of volatile BF_3 under non-equilibrium conditions. A fourth class of reactions, which leads to F_5TeO-derivatization, are redox reactions involving $Xe(OTeF_5)_2$,[24,25,41] as both an oxidant and ligand transfer reagent as, exemplified by eq 1.5 and 1.6.[78]

$$Xe(OTeF_5)_2 + Te(OTeF_5)_4 \longrightarrow Te(OTeF_5)_6 + Xe_{(g)} \quad (1.5)$$

$$Xe(OTeF_5)_2 + [N(CH_3)_4][As(OTeF_5)_4] \longrightarrow [N(CH_3)_4][As(OTeF_5)_6] + Xe_{(g)} \quad (1.6)$$

The high electronegativity and oxidative resistance of the F_5TeO–group (*vide infra*) enable the stabilization of high-oxidation-state species and unusual coordination compounds for which there are few, if any, other examples outside of the fluorides. Some of the most striking examples of F_5TeO-derivatives are illustrated by it's noble-gas derivatives, e.g. $Xe(OTeF_5)_n$ (n = 2,[24,25,41] 4,[46,47] 6)[39] and $Kr(OTeF_5)_2$.[40]

Suflur and selenium analogues of the teflate group, F_5ChO– (Ch = S or Se), are also known. The selenium analogue was inadvertently first synthesized by Seppelt[79] as $HOSeF_5$ when attempting to form $OSeF_4$ by reaction of $SeOF_2$ with fluorine gas in anhydrous HF (eq 1.7). In the case of the sulfur analogue, the instability of $HOSF_5$ requires its synthesis by a different route (eq 1.8).[80,81]

$$SeOF_2 + F_2 + HF \longrightarrow HOSeF_5 \quad (1.7)$$

$$SOF_4 + ClF \xrightarrow{CsF} ClOSF_5 \xrightarrow[-Cl_2]{HCl} HOSF_5 \quad (1.8)$$

The use of the lighter analogues remains very limited, in large part due to their lower thermal stabilities and tendency to transfer a fluoride ion to strong electrophiles and form $OChF_4$.[78] For example, the compounds $Ti(OChF_5)_4$ and $W(OChF_5)_6$ (Ch = Se or Te) are very stable as their tellurium derivatives, but the selenium derivatives readily transfer fluoride to form mixtures of $F_xTi(OSeF_5)_{4-x}$ (x = 1–4) and $F_xW(OSeF_5)_{6-x}$ (x = 1–6) with the elimination of $OSeF_4$.[53,56,82] In the case of the F_5SO-group, fluoride

abstraction occurs so readily that very few derivatives are known.[78] The stability of teflate compounds towards fluoride abstraction is a discernible advantage,[5,78] even compared with other anions, such as $[BF_4]^-$ and $[PnF_6]^-$, which can also be susceptible to fluoride ion abstraction in the presence of strongly electrophilic cation species.[51]

The F_5TeO–group possesses pseudo-octahedral geometry (Te–O, 1.786(3) Å; Te–$F_{(av)}$, 1.853(3) Å; O–Te–$F_{eq(av)}$, 95.2(2)°),[83,84] and is nearly isostructural with $[SbF_6]^-$ (Sb–$F_{(av)}$, 1.844(3) Å[85]).[51] This results in a large ligand with an estimated ionic radius (~2.3–2.4 Å)[86], that is slightly greater than the effective ionic radii of iodide (2.2 Å)[87] and similar to that of $[SbF_6]^-$ (2.43 Å).[88] Computational support the largest concentration of negative charge of $[F_5TeO]^-$ is localized on the oxygen atom, with significantly less charge dispersed over its five fluorine atoms.[84] As a result of both its steric bulk and electronic properties, the F_5TeO-group σ-bonds through its oxygen atom and typically in a monodentate fashion. Structurally characterized teflate derivatives show a large variance in the M–O–Te angles (structure **I**), which has been attributed to both steric congestion around the central atom (M) and crystal packing.[22,56]

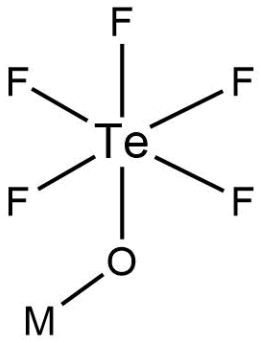

Structure I

There are also examples of oxygen-bridged F_5TeO-groups in the case of sterically noncongested Lewis acid centers such as in the crystal structures of $[Au(OTeF_5)_3]$,[72] $[Ag(L)_x(OTeF_5)]_2$ (L = solvent, x = 1 or 2),[6,70,71] and $[Zn(PhNO_2)_2\text{-}(OTeF_5)_2]_2$.[73,74]

With the charge on the F_5TeO-group predominantly concentrated on the oxygen atom and five peripheral fluorine atoms, the resulting ligand is typically of low nucleophilicity and high oxidative resistance. The low nucleophilicity of the group, which may for all intents and purposes be regarded as a sphere which only experiences weak intermolecular forces, is illustrated by $U(OTeF_5)_6$.[59] Even with its exceptionally high molecular weight (1670 g mol^{-1}), $U(OTeF_5)_6$ is a molecular compound which sublimes (60 ^oC) and melts (160 ^oC) at remarkably low temperatures. The high oxidative resistance of the F_5TeO-group is illustrated by the low-temperature synthesis of the only compound containing Kr–O bonds, namely $Kr(OTeF_5)_2$,[40] which is formed by the reaction of transfer reagent $B(OTeF_5)_3$ with the extremely aggressive oxidative fluorinator, KrF_2 (eq 1.9).

$$3\ KrF_2 + 2\ B(OTeF_5)_3 \xrightarrow[-110\ ^oC]{SO_2ClF} 3\ Kr(OTeF_5)_2 + 2\ BF_3 \qquad (1.9)$$

Characterization of $Kr(OTeF_5)_2$ has thus far been limited to ^{19}F and ^{17}O NMR spectroscopy because this species is very unstable, and readily decomposes in solution, even at temperatures as low as –100 ^oC, according to eq 1.10.[40]

$$Kr(OTeF_5)_2 \longrightarrow Kr + F_5TeOOTeF_5 \qquad (1.10)$$

The ability of the F_5TeO-group to stabilize high oxidation state species reflects its high group electronegativity, leading to its classification as a pseudohalide. Lentz and Seppelt[89] initially argued that the electronegativity of the teflate group exceeded that of fluorine based on the substitution behaviors of the mixed compounds, $F_xI(OSeF_5)_{(5-x)}$ and $F_xI(OTeF_5)_{(5-x)}$ (x = 1–5). The ^{19}F NMR spectra showed that the F_5ChO-groups only substituted at the equatorial positions of the square-pyramidal molecules, which was rationalized by extending VSEPR arguments used for trigonal bipyramidal geometries where occupancy of the axial positions favoured for the more electronegative ligand. Kinetic effects were dismissed because isomer distributions were neither time nor temperature dependent, and steric effects resulting from mutual hindrance of the bulky groups could be discounted on the basis of the crystal structures of the related *trans*-$F_2Te(OTeF_5)_4$,[90] and $Te(OTeF_5)_6$ [30] derivatives. Schrobilgen *et al.*[91] subsequently pointed out that for a pseudooctahedron, with which a square-based pyramid may be regarded, the ligand preferences can be more subtle and there are examples where the most electronegative ligands, in fact, occupy the axial position. This argument suggested that the conclusions based solely on stereochemical and VSEPR arguments may not be particularly reliable, especially when electronegativity differences are very small. Lentz and Seppelt [8] attempted to quantify the relative electronegativities by correlating P=O stretching frequencies, ^{31}P chemical shifts, and ^{31}P–^{19}F coupling constants for the series $O{=}PF_2X$ (X = F, $OTeF_5$, $OSeF_5$, Cl); all of which pointed to a group electronegativity approximately equal to that of fluorine. Subsequent comparisons of the $[FXeFXe(OTeF_5)]^+$ and $[FXeFXeF]^+$ cation behavior in solution using ^{129}Xe NMR

spectroscopy suggested the effective electronegativity of the F_5TeO-group to be lower than that of fluorine based on the relative lability of the Xe---F bonds and dominance of the valence-bond structure (**II**) below.[44]

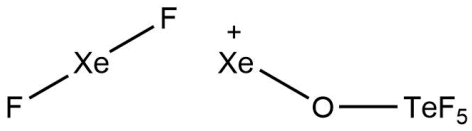

Structure II

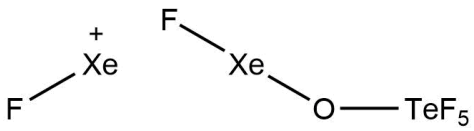

Structure III

To conclusively establish the relative electronegativity of the F_5TeO-group, Schrobilgen *et al.*[91] investigated a series of Xe, Te, and I derivatives using ^{129}Xe and ^{125}Te NMR, and ^{129}Xe and ^{127}I Mössbauer spectroscopy, because both techniques are extremely sensitive to electron density changes at the nuclei of atoms directly bonded to the ligand. The results consistently established that the electronegativity of $F_5TeO–$ is slightly less than that of fluorine (3.98,[92] Allred-Rochow scale), with an estimated electronegativity of 3.87 interpolated from Mössbauer quadrupole splittings.[91] This value is in good agreement with that determined using the Dailey and Shoolery equation[93] from ^1H chemical shifts differences between the methyl and methylene protons of CH_3CH_2X (X = I, Br, Cl, F, $OTeF_5$),[11] the latter providing a group electronegativity of 3.88.[91] The F_5TeO-group is therefore regarded as a bulky fluorine analogue, however, its low nucleophilicity and propensity to mainly bond through the oxygen atom in a monodentate fashion allows for the generation of coordinatively unsaturated, Lewis acidic centers that exhibit a diverse chemistry in close analogy with that of its fluorine analogues.

1.2. Weakly Coordinating Anions (WCAs)

One area of chemistry which has gained considerable interest over the last several decades is that of weakly coordinating anions (WCAs). This class of anions is of great significance to fundamental chemistry for stabilization, solid-state isolation, and structural characterization of highly electrophilic and oxidizing species such as reactive p-block cations,[94] and for exploring the structure and bonding of weakly bound or labile metal coordination complexes and polyatomic cations.[95,96] Weakly coordinating anions have also found potential in applied fields of chemistry,[95,97,98] including catalysis, ionic liquids, and battery electrolytes.

The optimal criteria for a WCA includes: (*i*) a single negative charge which is (*ii*) distributed and delocalized over a large number of atoms in order to minimize electrostatic cation-anion interactions, and (*iii*) must possess weakly polarizable peripheral ligand atoms that do not strongly coordinate, which is often accomplished by the use of fluorine atoms. Initial efforts in the field were directed towards replacement of halide anions in salts with larger, more complex anions such as $[BF_4]^-$, $[CF_3SO_3]^-$, $[ClO_4]^-$, and $[PnF_6]^-$ (Pn= P, As, Sb, Bi).[94–98] These classical anions continue to have widespread use today, however, X-ray crystallographic studies show that they have a strong tendency to coordinate to their counter-cation and, in a number of instances, the anion is susceptible to attack by extreme electrophiles, e.g. $[R_3Si]^+$ can abstract fluoride from $[AsF_6]^-$ to form R_3SiF.[94] By exchanging the fluorine atoms in these anions with much larger and more charge delocalized substituents such as the F_5TeO–group, weakly coordinating anions such as $[A(OTeF_5)_4]^-$ (A = B,[7] Al,[9]) and $[Pn(OTeF_5)_6]^-$,[15,22] have

become accessible. The F_5TeO–substituents in these anions create very weakly polarizable peripheral environments which protect the basic oxygen sites by means of the steric bulk of the F_5TeO–group. Other bulky and electronegative groups commonly employed to generate a variety of weakly coordinating anions include the $–C_6F_5$, perfluoro alkyl ($–R^{PF}$), and perfluoroalkoxyl ($–OR^{PF}$) substituents (Figure 1.1).[94–98] Efforts to achieve the penultimate "least coordinating anion" continue to motivate research in this field, leading to new WCAs such as carborane bases anions, e.g. $[CB_{11}(CF_3)_{12}]^–$,[99] and the even larger $[F(Al(OR^{PF})_3)_2]^–$ anion.[100]

Among the $[Pn(OTeF_5)_6]^–$ anions series, the $[Sb(OTeF_5)_6]^–$ salts have been shown to be the most stable.[51] From X-ray crystal structure data, the thermochemical volume of $[Sb(OTeF_5)_6]^–$ (724 $Å^3$)[101] is approximately six times greater than that of $[SbF_6]^–$ (121 $Å^3$);[102] with the negative charge dispersed over 30 peripheral fluorine atoms instead of six. Because the lattice energies of ionic compounds are inversely proportional to the sizes of the constituting ions, salts of very large WCAs can have solid-state environments with very weak coulombic interactions that almost mimic gas-phase conditions, leading to the description "pseudo gas-phase conditions" in the solid state.[95,97] Consequently, only minimal solvation energies are required to stabilize dissolved ions of WCAs in solution, and these salts generally have significant solubility in low-polarity solvents.

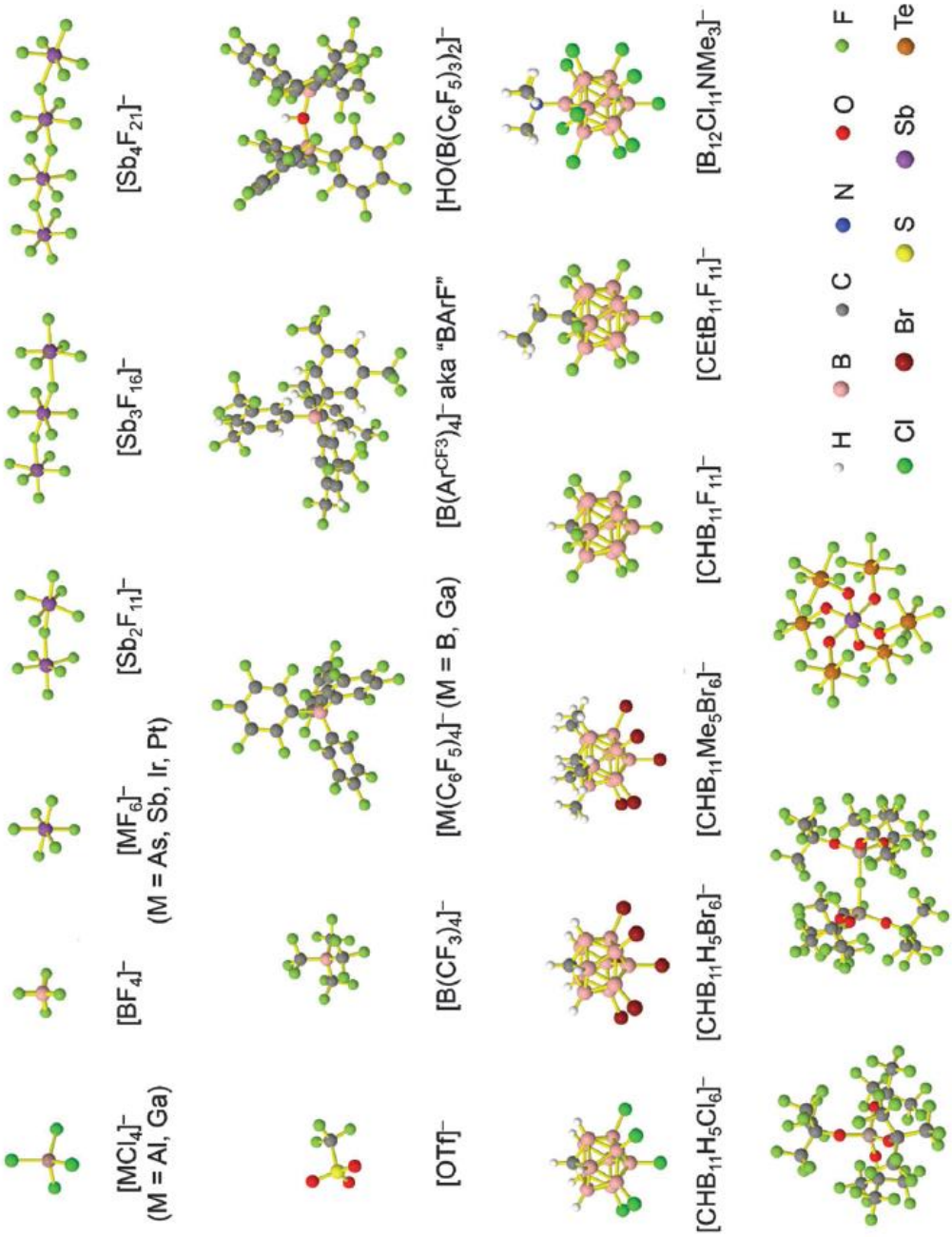

Figure 1.1. Some known weakly coordinating anions (WCA). Reproduced with permission from ref 94.

1.3. Noble-Gas Compounds

Among the earliest failed attempts to form compounds of the group 18 elements, or "noble-gases", was made by Henri Moissan in 1895 who tried to react the newly discovered element argon with fluorine gas at room temperature and under an induction spark.[103] Subsequent failed attempts to react krypton[104] and xenon[105] with halogen gases seemed to affirm the chemical inertness of these so called "inert gases" in the minds of chemists for following three decades,[106] and served to further entrench the so-called "octet rule".[107] It was not until 1962 that noble-gas reactivity was finally realized by Neil Bartlett by reaction of colorless xenon gas with deep red-brown PtF_6 vapor to yield the yellow-orange solid, $[XeF][PtF_6]$,[108,109] which was incorrectly formulated at the time as $[Xe][PtF_6]$.[110] There are several excellent review articles which discuss the events leading to the discovery of noble-gas reactivity, and which cover the now diverse chemistry thereof.[106,107, 111–116]

Many xenon compounds have been synthesized and well characterized which span the formal oxidation states 0, +½, +2, +4, +6, and +8; whereas krypton is confined to compounds in the +2 oxidation state. Numerous noble-gas inclusion compounds have also been synthesized and characterized, including Xe clathrates which are room temperature stable.[118–122] There are also isolable examples of Xe^0 functioning as a Lewis base, with several crystallographically characterized gold salts from the $Au^{x+}F_x/HF/SbF_5/Xe^0$ systems (x = 1–3), i.e., $[AuXe_4][Sb_2F_{11}]_2$,[123] $[AuXe_2](Sb_2F_{11})_2$ and $[AuXe_2](SbF_6)_2$,[124] $[(AuXe)_2F](SbF_6)_3$,[124] $[AuFXe_2](Sb_2F_{11})(SbF_6)$,[124] and $[(F_3As)AuXe](Sb_2F_{11})$,[125] and a related mercury salt, $[HgXe](Sb_2F_{11})(SbF_6)$ (Figure

1.2).[125] In the case of radon, compounds are also known to exist but they are only present at the radiotracer level with uncertain oxidation states,[126–128] whereas argon compounds such, as FArH,[129] have only been obtained in matrix-isolation studies.[129-133] For the most part, gas-phase and matrix-isolated noble-gas species have been excluded from the discussion herein.[113]

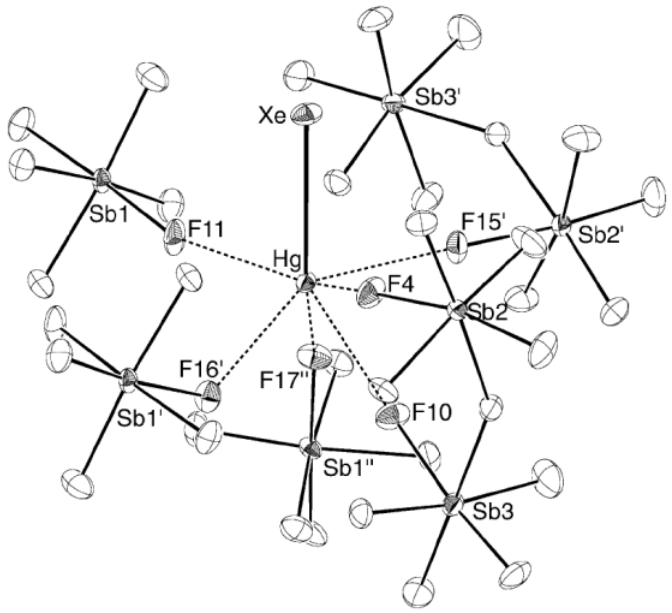

Figure 1.2. The crystal structure of $[HgXe](Sb_2F_{11})(SbF_6)$ showing the coordination sphere of Hg^{2+}. Thermal ellipsoids are shown at the 50% probability level. Reproduced with permission from ref 125. Copyright 2003 John Wiley and Sons.

1.3.1 Xenon Oxides

The chemistry of xenon is the most extensive. Among the compounds that have been characterized are examples containing Xe–X (X = F and Cl), Xe–O, Xe–C, and Xe–N bonds.[111–115,134] One particularly interesting area, which is further developed in this Thesis, is the chemistry of the xenon(II) oxides. Oxide species of every known xenon oxidation state (except 0 and +½) have been isolated,[111–115] i.e., $[Xe^{II}OXe^{II}OXe^{II}]^{2+}$,[135]

$Xe^{IV}O_2$,[136] $Xe^{VI}O_3$,[137,138] $Xe^{VIII}O_4$,[139,140] $(\eta^2\text{-}O_2)Xe^{VIII}O_3$,[141] and $[Xe^{VIII}O_6]^{4+}$.[142–147] In the case of Xe(VIII), the salt $Na_4[XeO_6]$ was first reported in 1963 and provided the first example of the very stable perxenate anion, $[XeO_6]^{4+}$.[142] While perxenate salts are typically quite thermally- and shock-resistant, e.g., $Na_4[XeO_6]$ is stable up to 375 °C,[145] the neutral Xe(VIII) oxide, XeO_4, is very shock- and temperature-sensitive, readily detonating to give Xe and O_2.[139] The neutral peroxo-compound, $\eta^2\text{-}O_2XeO_3$, has also been been obtained solely in a matrix-isolation study by low-temperature UV photolysis of XeO_4, but has not been isolated in macroscopic quantities.[141] The only known Xe(VI) oxide, XeO_3, is synthesized by either disproportionation of XeF_4 in H_2O,[137] or by hydrolysis of XeF_6;[138] however, like XeO_4 it is highly shock sensitive as a dry solid. The transient Xe(IV) oxide, XeO_2, was synthesized as an extended polymeric compound by reaction of XeF_4 with H_2O or 2.00 M $H_2SO_{4(aq)}$ but its characterization is limited to Raman spectroscopy.[136] Most recently, the first example of a Xe(II) oxide species, $[XeOXeOXe]^{2+}$, was obtained as the salt $[XeOXeOXe][\mu\text{-}F(ReO_2F_3)_2]_2$ (Figure 1.3).[135]

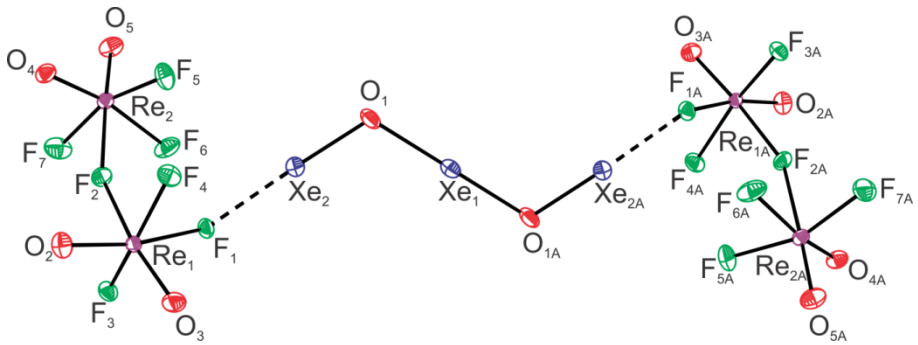

Figure 1.3. The crystal structure of $[XeOXeOXe][\mu\text{-}F(ReO_2F_3)_2]_2$. Thermal ellipsoids are shown at the 50% probability level. Reproduced with permission from ref 135. Copyright 2015 American Chemical Society.

It was characterized by low-temperature single-crystal X-ray diffraction and Raman spectroscopy, and the nature of bonding was further explored computationally. The salt was synthesized by the reaction of ReO_3F with XeF_2 in aHF at –30 ^oC according to eq 1.11. The crystal structure of $[XeOXeOXe][\mu\text{-}F\text{-}(ReO_2F_3)_2]_2$ shows a planar, zig-

$$5\ XeF_2 + 4ReO_3F \longrightarrow [XeOXeOXe][\mu\text{-}F\text{-}(ReO_2F_3)_2]_2 + 2Xe + O_2 \quad (1.11)$$

zag shaped $[XeOXeOXe]^{2+}$ cation with C_{2h} symmetry. The central Xe–O bond lengths (2.135(6) Å) are much longer than the terminal bonds (1.987(6) Å) which may be rationalized in terms of the dominant resonance contributors, **(1)** and **(2)**.[135] In

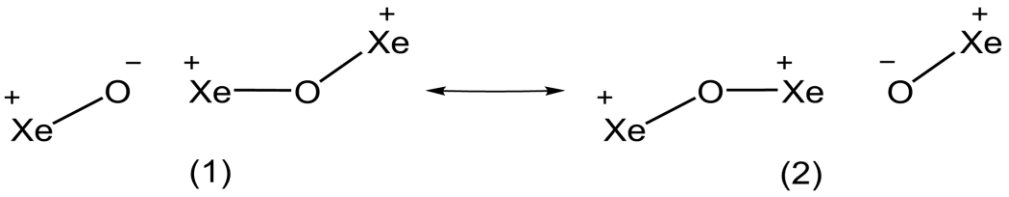

comparison, the central Xe–O bond lengths are equal within ±3σ to those of $Xe(OTeF_5)_2$ (2.119(11) Å),[148] whereas the terminal Xe–O bonds are equal within ±3σ to that of $[XeOTeF_5][Sb(OTeF_5)_6]\cdot SO_2ClF$ (1.969(4) Å).[45] The central O–Xe–O bond angle is linear by symmetry and consistent with an AX_2E_3 VSEPR arrangement at the xenon atoms, whereas the bent outer Xe–O–Xe angles (115.6(3)^o) are in accordance with an AX_2E_2 VSEPR arrangement at the oxygen atoms.[135] Each terminal Xe^{II} atom of $[XeOXeOXe]^{2+}$ interacts with a fluorine atom of a $[\mu\text{-}F(ReO_2F_3)_2]^-$ anion (2.392(4) Å),[135] however, these contacts are notably longer than the cation-anion contacts of $[XeF]^+$ salts, e.g., $[XeF][AsF_6]$ (2.208(3),[149] 2.212(5) Å),[150] $[XeF][SbF_6]$ (2.278(2) Å),[149] and

$[XeF][BiF_6]$ (2.204(7) Å).[149] The cation-anion interactions of $[XeOXeOXe][\mu\text{-}F\text{-}(ReO_2F_3)_2]_2$ were further investigated computationally and correspond to essentially electrostatic σ-hole type bonds.[135]

The proposed pathway leading to the formation of $[XeOXeOXe]^{2+}$ is rather complex, and invokes the formation of HOXeF as a key reaction intermediate. The HOXeF molecule has also been implicated to account for the formation of the related, and only crystallographically characterized xenon(II) oxide fluoride species, $[FXeOXeFXeF][PnF_6]$ (Pn = As, Sb) (Figure 1.4).[151] This oxide fluoride is formed by the

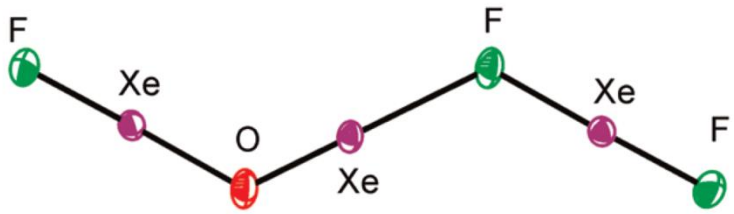

Figure 1.4. The $[FXeOXeFXeF]^+$ cation in the crystal structure of $[FXeOXeFXeF][PnF_6]$. Thermal ellipsoids are shown at the 50% probability level. Reproduced with permission from ref 151. Copyright 2009 American Chemical Society.

reaction of XeF_2 with $[H_3O][PnF_6]$ in HF (eq 1.12) and may be alternatively viewed as a $[FXeOXe]^+$ cation that is weakly coordinated to an XeF_2 molecule ($[FXeOXe\text{---}FXeF]^+$; Xe---F, 2.502(10)/2.513(6) Å).[151]

$$3XeF_2 + [H_3O][PnF_6] \longrightarrow [FXeOXeFXeF][PnF_6] + 3HF \qquad (1.12)$$

Previous work in the Schrobilgen research group has provided natural abundance and ^{18}O-enriched Raman spectroscopic evidence that XeF_2 can be displaced from the

$[FXeOXeFXeF]^+$ cation by neat $N{\equiv}SF_3$ at low-temperature to give $[FXeOXeN{\equiv}SF_3][AsF_6]$ (eq 1.13).[152]

$$[FXeOXeFXeF][AsF_6] + N{\equiv}SF_3 \longrightarrow [FXeOXeN{\equiv}SF_3][AsF_6] + XeF_2 \qquad (1.13)$$

The Schrobilgen group also obtained ^{19}F, ^{17}O, and ^{129}Xe NMR, as well as ^{16}O-, ^{17}O-, and ^{18}O-enriched Raman spectroscopic evidence that the reaction of the $[FXeOXeFXeF]^+$ cation with neat NOF results in the formation of $O(XeF)_2$ according to eq 1.14.[153,154] The gross structure of $O(XeF)_2$ was unambiguously determined by ^{19}F and

$$[FXeOXeFXeF][AsF_6] + NOF \longrightarrow FXeOXeF + NO[AsF_6] + XeF_2 \qquad (1.14)$$

^{129}Xe NMR spectroscopy based on detailed analyses of spin-spin coupling patterns which arise from the various xenon isotopologues of $O(XeF)_2$, which is analogous to that of isoelectronic $[Ng_2F_3]^+$ (*vide infra*).

1.3.2 Noble-Gas Difluorides, NgF_2 (Ng = Kr, Xe)

In contrast with the extensive chemistry of xenon, krypton is the only other noble-gas that forms compounds which are isolable in macroscopic amounts. Its compounds are solely found in the +2 oxidation state;[116] although there was a spurious report of KrF_4 in the early literature,[155] which was subsequently disproven.[156] Unlike XeF_2, KrF_2 is an endothermic compound (ΔH_f = 60.2 kJ mol^{-1})[157,158] which is thermodynamically unstable. Therefore, the high-temperature, high-pressure methods[159–161] which can be used to prepare XeF_2 (ΔH_f = –162.8 kJ mol^{-1}), XeF_4 (ΔH_f = –267.1 kJ mol^{-1}), and XeF_6

(ΔH_f = –338.2 kJ mol^{-1}),[162] cannot be employed. Instead, highly reactive fluorine radicals must be generated using either high-energy particle beams,[163,164] electric discharge,[156,165,166] UV irradiation,[167–171] or thermally by means of a hot wire-reactor,[171–173] which subsequently react with krypton to form KrF_2 at low temperatures.

Consistent with its thermodynamic instability, the very low mean thermochemical bond energy of KrF_2 (48.9 kJ mol^{-1})[157,158] makes it a potent oxidative fluorinating agent, with the relative oxidative strengths of the noble-gas fluorides increasing by $XeF_2 < XeF_4 < XeF_6 < KrF_2$.[116] Furthermore, the energy of atomization for KrF_2 (97.9 kJ mol^{-1}) [157,158] is significantly lower than even that of F_2 (157.7 ± 0.4 mol^{-1}),[174] resulting in a better source of fluorine atoms at low temperatures. The oxidizing/fluorinating strength of KrF_2 is well demonstrated by its ability to oxidize Xe to XeF_6,[175] I_2 to IF_7,[175] and Au to $[AuF_6]^-$.[176] Krypton cations, $[Kr_2F_3]^+$ and $[KrF]^+$ (*infra vide*),[116] are even more potent oxidants than KrF_2, with the latter cation among the strongest chemical oxidants currently known.[177] Their unparalleled oxidative potential has provided low-temperature synthetic routes towards a number of unusual high-oxidation state species, e.g., $[XF_6]^+$ (X = Cl, Br),[178,179] and $[NF_4]^+$.[179]

All krypton chemistry is derived from KrF_2,[116] and, other than $Kr(OTeF_5)_2$,[40] the few species that are known are limited to fluorine species and their derivatives. In the presence of sufficiently strong Lewis acid centers, such as the pnictogen pentafluorides, e.g. SbF_5, the noble-gas difluorides NgF_2 (Ng = Kr, Xe) form salts of the $[NgF]^+$ and $[Ng_2F_3]^+$ cations (Figures 1.5).[116] Xenon difluoride is a somewhat stronger donor than

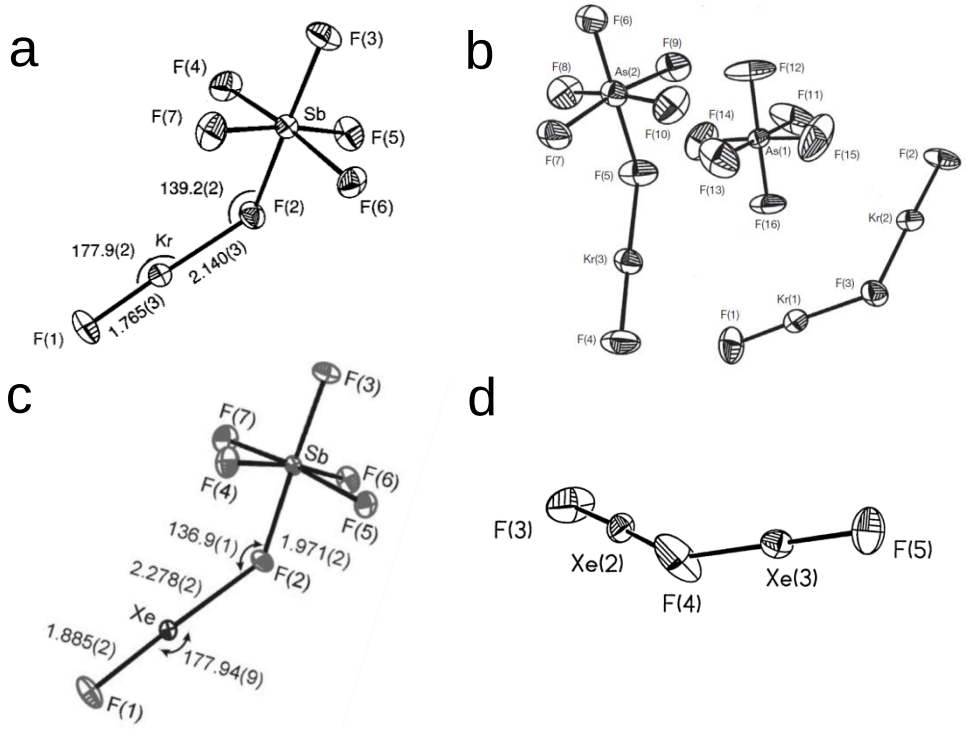

Figure 1.5. The structural units in the X-ray crystal structures of **(a)** $[KrF][SbF_6]$,[173] **(b)** $[Kr_2F_3][AsF_6]\cdot KrF_2$,[173] **(c)** $[XeF][SbF_6]$,[102] and **(d)** $[Xe_2F_3]^+$ in $[Xe_2F_3][AsF_6]$;[180] shown at the 50% probability level. Reproduced (adapted) with permission from refs 102, 173, and 180. Copyrights 2001 and 2010 American Chemical Society.

krypton difluoride, with the relative fluoride-ion donor strengths of all the noble-gas fluorides following the order $XeF_6 > XeF_2 \geq KrF_2 >> XeF_4$.[181] Although nearly all xenon fluoride salts are room-temperature stable, krypton fluoride salts are thermodynamically unstable but have appreciable kinetic stabilities.[116]

The crystal structures of $[NgF][SbF_6]$ salts show that the bond lengths of $[NgF]^+$ (Kr, 1.765(3) Å;[173] Xe, 1.885(2) Å)[102] are significantly shortened relative to solid NgF_2 ($D_{\infty h}$: Kr, 1.894(5) Å;[173] Xe, 1.999(4) Å),[102] whereas the Ng---F_b bond of the Ng---F_b–Sb

interaction (Kr, 2.140(3) Å;[173] Xe, 2.278(2) Å)[102] is significantly elongated. Correspondingly, the Sb–F_b(Kr) bond distance is slightly longer (Kr, 1.963(3) Å;[173] Xe, 1.971(2) Å)[102] than the terminal Sb–F_t bonds (Kr, 1.847(3)–1.861(3) Å;[173] Xe, 1.857(2)–1.868(2) Å).[102] An ion-pair description for these salts is further supported by the formation of coordination complexes of oxidatively resistant nitrile bases to Lewis acidic $[XeF]^+$, e.g., the nitrogen bonded $[RCN{-}{-}{-}XeF]^+$ (R = CF_3, C_2F_5, *n*-C_3F_7)[182,183] which have been characterized in anhydrous HF solution by low-temperature ^{19}F and ^{129}Xe NMR spectroscopy. In the case of krypton, only HCN and perfluorinated nitriles (i.e. R^{PF} = CF_3, C_2F_5, *n*-C_3F_7) have been identified by ^{19}F NMR,[183] but the complexes were not formed directly from the $[KrF]^+$ salts because the more electrophilic cation is too strong an oxidative fluorinator.[117] Instead, the salts must be generated *in situ* as outlined in eq 1.15–1.16.[183]

$$KrF_2 + R^{PF}CN{-}{-}{-}AsF_5 \xrightarrow[-60^{\circ}C]{BrF_5} [R^{PF}CN{-}{-}{-}KrF][AsF_6] \qquad (1.15)$$

$$KrF_2 + [HCNH][AsF_6] \xrightarrow[-60^{\circ}C]{HF} [HCN{-}{-}{-}KrF][AsF_6] + HF \qquad (1.16)$$

In the case of oxidatively resistant, weak to moderate strength Lewis acids, partial fluoride ion abstraction results in adduct formation, an important intermediate class of compounds. Formation of metal complexes of the type $M(XeF_2)_y^{n+}(PnF_6^-)_n$ (Pn = As, Sb, Bi) is largely favoured because the $[PnF_6]^-$ anions are relatively weak fluoro-bases and the room-temperature stable salts are readily soluble in anhydrous HF (eq 1.17).

$$M^{n+}(PnF_6^-)_n + x\,XeF_2 \xrightarrow{HF} M(XeF_2)_y^{n+}(PnF_6^-)_n + (x{-}y)\,XeF_2 \qquad (1.17)$$

Xenon difluoride coordination complexes show a great deal of structural diversity, with the number of molecules per Lewis acid center ranging from one to six.[184] A considerable number of XeF_2 coordination complexes with metals have been synthesized and structurally characterized by single-crystal X-ray diffraction (Table 1.3). Two modes of coordination have been observed for XeF_2. For terminal coordination, the XeF_2 ligand interacts with a single Lewis acid through one bridging fluorine atom (F_b), resulting in slightly elongated Xe–F_b bond lengths and shortened Xe–F_t terminal bonds; although the distortion is significantly less pronounced than observed for $[XeF]^+$ ion pairs. In the second coordination mode, XeF_2 bridges two different Lewis acids centers, each through one of its fluorine atoms. Because there are two possible coordination modes, the chemical formula of a complex may not always reflect the coordination sphere of the Lewis acid in the complex. For example, in the structures of $Hg(XeF_2)_5(PnF_6)_2$ (Pn = P, As, Sb),[184] the chemical formula suggests each mercury atom interacts with five XeF_2 molecules, however, the X-ray structure shows there are four terminal and two bridging XeF_2 molecules, resulting in six XeF2 molecules interacting with each mercury (Figure 1.6).

The compounds, $Cd(XeF_2)(HF)_2(AF_6)_2$ (A = Nb, Ta)[184] and $Mg(XeF_2)(XeF_4)(AsF_6)_2$,[185] are interesting examples where other neutral donor ligands are also present, with the latter providing the only example of the most weakly fluoro-basic noble-gas fluoride, XeF_4, functioning as a ligand. A number of other XeF_2 complexes have been identified mainly by ^{19}F NMR spectroscopy and/or Raman spectroscopy, or are yet to be published.[112]

Table 1.3. Crystallographically Characterized Metal XeF_2 Complexes. [a]

***n* = 1**
$Mg(XeF_2)(XeF_4)(AsF_6)_2$ [185]
$Cd(XeF_2)(BF_4)_2$ [186]
$WOF4 \cdot XeF_2$ [187]

***n* = 2**
$Li(XeF_2)_3(AsF_6)$ [196]
$Mg(XeF_2)_2(AsF_6)$ [191]
$Ag(XeF_2)_2(PnF_6)$ (Pn = As,[197] P) [198]
$Cu(XeF_2)_2(SbF_6)_2$ [194]

***n* = 2.5**
$Ca(XeF_2)_{2.5}(AsF_6)_2$ [188]
$La(XeF_2)_{2.5}(PnF_6)_3$ (Pn = As,[189] Sb[184])
$Nd(XeF_2)_{2.5}(AsF_6)_3$ [190]

***n* = 3**
$Sr(XeF_2)_3(PnF_6)_2$ (Pn = P,[199] As)[200]
$Pb(XeF_2)_3(PnF_6)_2$ (Pn = P,[199] As)[200]

***n* = 4**
$Mg(XeF_2)_4(AsF_6)_2$ [191]
$Ca(XeF_2)_4(AsF_6)_2$ [192]
$Ba(XeF_2)_4(PF_6)_2$ [193]
$Cu(XeF_2)_4(SbF_6)_2$ [194]
$Cd(XeF_2)_4(AsF_6)_2$ [188]

***n* = 5**
$Ca(XeF_2)_5(PF_6)_2$ [201]
$Ba(XeF_2)_5(AF_6)_2$ (A = As,[202] Sb,[203] Nb, Ru) [204]
$Cd(XeF_2)_5(PF_6)_2$ [201]
$Hg(XeF_2)_5(PnF_6)_2$ (Pn = P–Sb) [184]

***n* = 6**
$[Cu(XeF_2)_6][SbF_6]_2$ [195]
$[Zn(XeF_2)_6][SbF_6]_2$ [195]

n* = *other
$Ca_2(XeF_2)_9(AsF_6)_4$ [205]
$Pb_3(XeF_2)_{11}(PF_6)_6$ [199]
$Sr_3(XeF_2)_{10}(PF_6)_6$ [199]
$Cd_2(XeF_2)_{10}(SbF_6)_4$ [206]

[a] *n* is the ratio of XeF_2 molecules to Lewis acid centers.

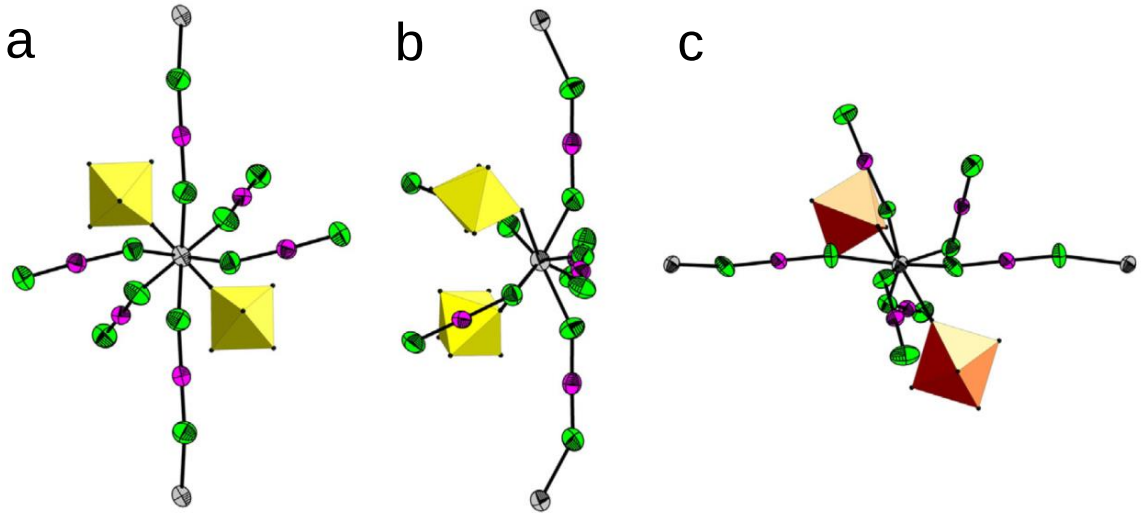

Figure 1.6. The X-ray crystal structures of **(a)** $Hg(XeF_2)_5(PF_6)_2$, **(b)** $Hg(XeF_2)_5(AsF_6)_2$, and **(c)** $Hg(XeF_2)_5(SbF_6)_2$; where the $[PnF_6]^-$ anions are denoted by an octahedron, mercury (grey), xenon (purple), and fluorine (green). Reproduced with permission from ref 184. Copyright 2014 Elsevier B.V.

At the onset of the present research, only one crystallographically characterized KrF_2 coordination complex was known, namely $[BrOF_2]$-$[AsF_6]\cdot 2KrF_2$ (Figure 1.7), in which two terminal KrF_2 molecules are coordinated to the $Br^{(V)}$ center of $[BrOF_2]^+$.[207] Its XeF_2 analogue was subsequently fully characterized.[208] Coordination of the two KrF_2 molecules results in slight contractions of the terminal Kr–F_t bond lengths (1.840(5), 1.847(4) Å) and slight elongations of the bridge Kr–F_t bonds (1.943(4), 1.933(4) Å) relative to free KrF_2 (1.894(5) Å).[173] The bond length distortions that occur upon coordination are significantly less than those of $[KrF][SbF_6]$ (vide supra); clearly supporting an adduct description of the ligand as opposed to $[KrF]^+$ salt formulation. A number of Lewis acid-base adducts with group 6 d^0 transition metal centers, namely $KrF_2\cdot nMOF_4$ (n = 1, M = W,[209] Mo,[209] Cr[210]); n = 2−3, M = Mo[209]), have also been

synthesized, but their characterization is limited to Raman spectroscopy and/or ^{19}F NMR spectroscopy. Similarly, adducts of $M(AuF_6)_2 \cdot nKrF_2$ (M = Ca, Sr, Ba; n=0–4) have been reported, but are structurally unsubstantiated with their characterization limited to Raman spectroscopy.[211]

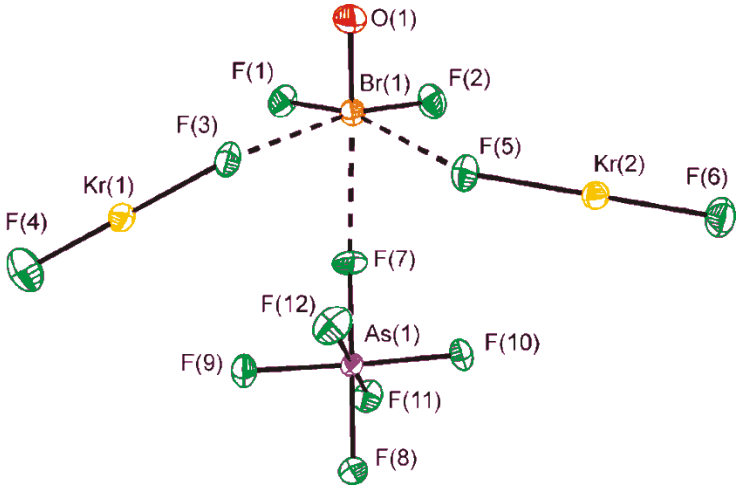

Figure 1.7. The structural unit in the X-ray crystal structure of $[BrOF_2][AsF_6] \cdot 2KrF_2$; thermal ellipsoids are shown at the 50% probability level. Reproduced with permission from ref 207. Copyright 2010 American Chemical Society.

1.4. Purpose and Scope of the Present Research

The overall goal of this Thesis is to advance and broaden our fundamental understanding of the chemistry of mercury as it relates to the pentafluorooxotellurate(VI) group, and to extend the chemistry of the noble-gas elements, xenon and krypton. The approach taken to accomplish these goals relies heavily on experimental/synthetic work using highly moisture-sensitive, and often temperature-sensitive, compounds. New compounds were structurally characterized predominantly by low-temperature single-

crystal X-ray diffraction and Raman spectroscopy using specialized techniques and equipment. Computational analyses aided in full Raman assignments, and were also used to gain new fundamentally important insights into novel bonding features.

A primary focus of this Thesis is to explore the coordination chemistry of the pentafluorooxotellurate(VI) group, more specifically with that of its Hg(II) derivatives. The high group electronegativity and steric bulk of the teflate groups of $Hg(OTeF_5)_2$ provides a coordinately unsaturated metal center having significant Lewis acidity. Chapters 3, 4, and 6 of this Thesis explore the Lewis acceptor properties of $Hg(OTeF_5)_2$, providing a number of novel derivatives. Initial work focuses on the neutral nitrogen Lewis basic NSF_3, resulting in rich coordination chemistry with interesting bonding features of the F_5TeO-group. Furthermore, the positively charged, coordinatively unsaturated sulfur(VI) atom of NSF_3 is susceptible to nucleophilic attack, resulting in a new and interesting mixed imidodifluorosulfate (F_2OSN-) derivative $Hg(OTeF_5)(NSOF_2)$, which was isolated as its NSF_3 complexes. The teflate anions of $Hg(OTeF_5)_2$ are also explored by reactions with the F_5TeO-group sources $Cs[OTeF_5]$ and the more "naked teflate" salts $M[OTeF_5]$ ($M = [N(CH_3)_4]^+$ or $[N(CH_2CH_3)_4]^+$), yielding a series of new $[Hg(OTeF_5)_{(2+n)}]^{n-}$ anions.

In Chapter 5, a weakly solvated Hg^{2+} cation, namely $[Hg(SO_2ClF)_6]^{2+}$, is formed using the weakly coordinating $[Sb(OTeF_5)_6]^-$ anion in the very weakly basic solvent SO_2ClF by extending a synthetic route used to form main-group carbocations.[212] The resulting homoleptic solvent complex provides a unique source of weakly solvated Hg^{2+} cations, that is shown to readily undergo ligand substitution reactions with stronger

nucleophiles than SO_2ClF. Sources of "naked" metal cations are desirable synthetic precursors for exploring the coordination chemistry of weak, unusual, and fundamentally important ligands.

Another focus of this Thesis is the advancement of the less studied krypton chemistry by further developing the coordination chemistry of KrF_2. In Chapter 6, the fluoride ion acceptor behavior of $Hg(OTeF_5)_2$ is initially investigated towards XeF_2, and then extended to the stronger oxidant KrF_2. Since metal salts of $[PnF_6]^-$ anions have been shown to form a diverse series of complexes with XeF_2, analogous chemistry of $Hg(PnF_6)_2$ (Pn = As, Sb) and $FHg(AsF_6)$ were investigated at low-temperatures with KrF_2 in Chapters 7 and 8 to further explore its ligand properties and expand the chemistry of krypton. These reactions provide a rare and unique series of KrF_2 coordination complexes featuring examples of both terminal and bridging coordination, as has been observed with XeF_2, but also a new bonding modality where one fluorine atom of a terminal KrF_2 molecule bridges two metals. Computational studies of the aforementioned systems also provide new fundamental insights into the structures of NgF_2 complexes and the nature of NgF_2 ligand bonding.

The final area of study in this Thesis advances xenon chemistry with the synthesis and characterization of a new xenon(II) oxide species. The only published xenon(II) oxide fluoride species, $[FXeOXeFXeF][AsF_6]$, has been shown in the Schrobilgen group to be a promising synthetic precursor for displacement of XeF_2. In Chapter 9, possible displacement reaction of $[FXeOXeFXeF][AsF_6]$ by the oxidatively resistant base CH_3CN were explored, which provided access to the $[XeOXe]^{2+}$ cation in aHF. This species

represents only the second, and simplest, xenon(II) oxide isolated in macroscopic amounts. In addition to obtaining the X-ray crystal structure, the Raman spectroscopic assignments were aided by ^{18}O-enrichment studies and the nature of bonding explored computationally. Similar to the only other known xenon(II) oxide, $[XeOXeOXe]^{2+}$, the aforementioned cation provides an example of σ-hole bonding and insight into the role of σ-hole bonds in stabilizing highly reactive electrophiles.

1.5. References

(1) Engelbrecht, A.; Sladky, F. *Angew. Chem. Int. Ed.*, **1964**, *3*, 383.

(2) Engelbrecht, A.; Stoll, B. *Z.* Anorg. Allg. Chem. **1957**, *292*, 20–24.

(3) Engelbrecht, A.; Sladky, F. *Inorg. Nucl. Chem. Lett.* **1965**, *1*, 15.

(4) Porcham, W.; Engelbrecht, A. *Monatsh. Chem.* **1971**, *102*, 333–349.

(5) Sladky, F.; Kropshofer, H.; Leitzke, O. *J. Chem. Soc. Chem. Comm.* **1973**, 134–135.

(6) Sladky, F.; Kropshofer, H.; Leitzke, O.; Peringer, P. *J. Inorg. Nucl. Chem.*, H. H. Hyman Memorial Volume, Supplement, **1976**, 69–71.

(7) Kropshofer, H.; Leitzke, O.; Peringer, P.; Sladky, F. *Chem. Ber.* **1981**, *114*, 2644–2648.

(8) Lentz, D.; Seppelt, K. *Z. Anorg. Allg. Chem.* **1980**, *460*, 5–16.

(9) Wisner, A.; Gries, T. W.; Steinhauer, S.; Beckers, H.; Riedel, S. *Angew. Chem. Int. Ed.***2017**, *56*, 8263–8266.

(10) Noirot, M. D.; Anderson, O. P.; Strauss, S. H. *Inorg. Chem.* **1987**, *26*, 2216–2223.

(11) Kropshofer, H.; Sladky, F.; *Inorg. Nucl. Chem. Lett.* **1972**, *8*, 195–197.

(12) Fraser, G. W.; Meikle, G. D.; *J. Chem. Soc., Dalton Trans.* **1975**, 1033–1036.

(13) Fraser, G. W.; Millar, J. B. *J. Chem. Soc., Dalton Trans.* **1974**, *19*, 2029–2031.

(14) Mercier, H. P. A.; Moran, M. D.; Schrobilgen, G. J.; Steinberg, C.; Suontamo, R. J. *J.Am. Chem. Soc.* **2004**, *126*, 5533–5548.

(15) Sladky, F.; Kropshofer, H. *J. Chem. Soc. Chem. Comm.* **1973**, 600–601.

(16) Vij, A.; Wilson, W. W.; Vij, V.; Corley, R. C.; Tham, F. S.; Gerken, M.; Haiges, R.; Schneider, S.; Schroer, T.; Wagner, R. I. *Inorg. Chem.* **2004**, *43*, 3189−3199.

(17) Thrasher, J. S.; Seppelt, K. *Z. Anorg. Allg. Chem.* **1985**, *529*, 85–88.

(18) Lentz, D.; Seppelt, K. *Z. Anorg. Allg. Chem.* **1983**, *50*, 83–88.

(19) Seppelt, K. *Chem. Ber.* **1977**, *110*, 1470–1476.

(20) Gerken, M.; Kolb, P.; Wegner, A.; Mercier, H. P. A.; Borrmann, H.; Dixon, D. A.; Schrobilgen, G. J. *Inorg. Chem.* **2000**, *39*, 2813–2824.

(21) Hoppenheit, R.; Mews, R. *Chem. Ber.* **1985**, *118*, 4276–4280.

(22) Mercier, H. P. A.; Sanders, J. C.; Schrobilgen, G. J. *J. Am. Chem. Soc.* **1994**, *116*, 2921–2937.

(23) Leitzke, O.; Sladky, F. *Z. Naturforsch.* **1981**, *36B*, 268–269.

(24) Sladky, F. *Monatsh. Chem.* **1970**, *101*, 1559–1570.

(25) Seppelt, K.; Nothe, D. *Inorg. Chem.* **1973**, *12*, 2727–2730.

(26) Zylka, P.; Oberhammer, H.; Seppelt, K. *J. Mol. Struct.* **1991**, *243*, 411–418.

(27) Engelbrecht, A.; Loreck, W.; Nehoda, W. *Z. Anorg. Allg. Chem.* **1968**, *50*, 88–96.

(28) Damerius, R.; Lentz, D.; Huppmann, P.; Seppelt, K. *J. Chem. Soc., Dalton Trans.* **1984**, 2821–2826.

(29) Oberhammer, H. Seppelt, K. *Inorg. Chem.* **1978**, *17*, 1435–1439.

(30) Lentz, D.; Pritzkow, H.; Seppelt, K. *Angew. Chem. Int. Ed.* **1977**, *16*, 729–730.

(31) Collins, M.; Schrobilgen, G. J. *Inorg. Chem.* **1985**, *24*, 2608–2614.

(32) Mercier, H. P. A.; Sanders, J. C.; Schrobilgen, G. J. *Inorg. Chem.* **1995**, *34*, 5261–5273.

(33) Schack, C. J.; Wilson, W. W.; Christe, K.O. *Inorg. Chem.* **1983**, *22*, 18–21.

(34) Schack, C. J.; Christe, K. O. *Inorg. Chem.* **1984**, *23*, 2922.

(35) Seppelt, K. *Chem. Ber.* **1973**, *106*, 1920–1926.

(36) Turowsky, L.; Seppelt, K. *Z. Anorg. Allg. Chem.* **1991**, *602*, 79–87.

(37) Hwang, I.; Kuschel, R.; Seppelt, K. *Z. Anorg. Allg. Chem.* **1997**, *623*, 379–383.

(38) Schack, C. J.; Christe, K. O. *J. Fluorine Chem.* **1990**, *47*, 79–87.

(39) Lentz, D.; Seppelt, K. *Angew. Chem. Int. Ed.* **1979**, *18*, 66–67.

(40) Sanders, J. C. P.; Schrobilgen, G. J. *J. Chem. Soc. Chem. Comm.* **1989**, 1576–1578.

(41) Seppelt, K.; Rupp, H. H. *Z. Anorg. Allg. Chem.* **1974**, *409*, 338–342.

(42) Sladky, F. *Monatsh. Chem.* **1970**, *101*, 1571–1577.

(43) Sladky, F. *Angew. Chem. Int. Ed.* **1969**, *8*, 373

(44) Keller, N.; Schrobilgen, G. J. *Inorg. Chem.* **1981**, *20*, 2118–2129.

(45) Mercier, H. P. A.; Moran, M. D.; Sanders, J. C. P.; Schrobilgen, G. J.; Suontamo, R. J. *Inorg. Chem.* **2005**, *44*, 49–60.

(46) Lentz, D.; Seppelt, K. *Angew. Chem. Int. Ed.* **1978**, *17*, 356–357.

(47) Schumacher, G. A.; Schrobilgen, G. J. *Inorg. Chem.* **1984**, *23*, 2923–2929.

(48) Syvret, R. G.; Mitchell, K. M.; Sanders, J. C. P.; Schrobilgen, G. J. *Inorg. Chem.* **1992**, *31*, 3381–3385.

(49) Schröder, K.; Sladky, F. *Chem. Ber.* **1980**, *113*, 1414–1419.

(50) Seggen, D. M.; Hurlburt, P. K.; Anderson, O. P.; Strauss, S. H. *J. Am. Chem. Soc.* **1992**, *114*, 10995–10997.

(51) Seggen, D. M.; Hurlburt, P. K.; Anderson, O. P.; Strauss, S. H. *Inorg. Chem.* **1995**, *34*, 3453–3464.

(52) Crossman, M. C.; Hope, E. G.; Saunders, G. C. *J. Chem. Soc., Dalton Trans.* **1996**, 509–511.

(53) Huppmann, P.; Labischinski, H.; Lentz, D.; Pritzkow, H.; Seppelt, K. *Z. Anorg. Allg. Chem.* **1982**, *487*, 7–25.

(54) Moock, K.; Seppelt, K. *Z. Anorg. Allg. Chem.* **1988**, *561*, 132–138.

(55) Abney, K. D.; Long, K. M.; Anderson, O. P.; Strauss, S. H. *Inorg. Chem.* **1987**, *26*, 2638–2643.

(56) Turowsky, L.; Seppelt, K. *Z. Anorg. Allg. Chem.* **1990**, *590*, 23–36.

(57) Schröder, K.; Sladky, F. *Chem. Ber.* **1981**, *447*, 95–100.

(58) Seppelt, K. *Chem. Ber.* **1976**, *109*, 1046–1052.

(59) Templeton, L. K.; Templeton, D. H.; Bartlett, N.; Seppelt, K. *Inorg. Chem.* **1976**, *15*, 2720–2722.

(60) Crossman, M. C.; Hope, E. G.; Wootton, L. J. *J. Chem. Soc., Dalton Trans.* **1998**, 1813–1817.

(61) Buggey, L. A. Ph. D. Thesis, University of Liecester, Leicester, England, UK, **1993**.

(62) Turowsky, L.; Seppelt, K. *Z. Anorg. Allg. Chem.* **1990**, *590*, 37–47.

(63) Casteel, W. J.; MacLeod, D. M.; Mercier, H. P. A.; Schrobilgen, G. J. *Inorg. Chem.* **1996**, *35*, 7279–7288.

(64) Huppmann, P. Ph.D. Thesis, Free University of Berlin, Berlin, Germany, 1983.

(65) Kellet, P. J.; Pawlik, M. J.; Taylor, L. F.; Thompson, R. G.; Levstik, M. A.; Anderson, O.P.; Strauss, S. H. *Inorg. Chem.* **1989**, *28*, 440–447.

(66) Drews, T.; Seppelt, K. *Z. Anorg. Allg. Chem.* **1991** *606*, 201–207.

(67) Strauss, S. H. *Chem. Rev.* **1993**, *93*, 927–942.

(68) Colsman, M. R.; Newbound, T. D.; Marshall, L. J.; Noirot, M. D.; Miller, M. M.; Wulfsberg, G. P.; Frye, J. S.; Anderson, O. P.; Strauss, S. H. *J. Am. Chem. Soc.* **1990**, *112*, 2349–2362.

(69) Colsman, M. R.; Manning, M. C.; Anderson, O. P.; Strauss, S. H. *Inorg. Chem.* **1987**, *26*, 3958–3960.

(70) Strauss, S. H.; Noirot, M. D.; Anderson, O.P. *Inorg. Chem.* **1985**, *24*, 4307–4311.

(71) Mayer, E.; Sladky, F. *Inorg. Chem.* **1975**, *14*, 589–592.

(72) Huppmann, P.; Hartl, H.; Seppelt, K. *Z. Anorg. Allg. Chem.* **1985**, *524*, 26–32.

(73) Hurlburt, P. K.; Kellet, P. K.; Anderson, O. P.; Strauss, S. H. *J. Chem. Soc. Chem. Comm.* **1990**, 576–578.

(74) Rack, J. J.; Hurlburt, P. K.; Kellet, P. K.; Luck, J. D.; Anderson, O. P.; Strauss, S. H. *Inorg. Chem. Acta.* **1996**, *242*, 71–79.

(75) Hurlburt, P. K.; Rack, J. J.; Dec, S. F.; Anderson, O. P.; Strauss, S. H. *Inorg. Chem.***1993**, *32*, 373–374.
(76) Fraser, G. W.; Meikle, G. D. *J. Chem. Soc. Chem. Comm.* **1974**, 624–625.
(77) Elgad, U.; Selig, H. *Inorg. Chem.* **1975**, *14*, 140–145.
(78) Seppelt, K. *Angew. Chem. Int. Ed.* **1982**, *21*, 877–888.
(79) Seppelt, K. *Angew. Chem. Int. Ed.* **1972**, *11*, 630.
(80) Seppelt, K. *Angew. Chem. Int. Ed.* **1976**, *15*, 44–45.
(81) Seppelt, K. *Z. Anorg. Allg. Chem.* **1977**, *428*, 35–42.
(82) Seppelt, K. *Chem. Ber.* **1975**, *108*, 1823–1829.
(83) Kellet, P. J.; Anderson, O. P.; Strauss, S. H. *Can. J. Chem.* **1989**, *67*, 2023–2029.
(84) Miller, P. K.; Abney, K. D.; Rappé, A. K.; Anderson, O. P.; Strauss, S. H. *Inorg. Chem.* **1988**, *27*, 2255–2261.
(85) Kruger, G. J.; Pistorius, C. W. F. T. *Acta Cryst.* **1976**, *B32*, 2916–2918.
(86) Crossman, M. C. Ph. D. Thesis, University of Liecester, Leicester, England, UK, **1995**.
(87) Shannon, R. D. *Acta Cryst.* **1976**, *A32*, 751–767.
(88) Simoes, M. C.; Hughes, K. J.; Ingham, D. B.; Ma, L.; Pourkashanian, M. *Inorg. Chem.* **2017**, *56*, 7566−7573.
(89) Lentz, D.; Seppelt, K. *Angew. Chem. Int. Ed.* **1978**, *17*, 355–356.
(90) Pritzkow, H.; Seppelt, K. *Inorg. Chem.* **1977**, *16*, 2685–2687.
(91) Birchall, T.; Myers, R.; Waard, H.; Schrobilgen, G. J. *Inorg. Chem.* **1982**, *21*, 1068–1073.
(92) Allred, A. L. L *Inorg. Nucl. Chem.* **1961**, *17*, 215–221.
(93) Dailey, B. P.; Shoolery, J. N. *J. Am. Chem. Soc.* **1955**, *77*, 3977–3981.
(94) Engesser, T. A.; Lichtenthaler, M. R.; Schleep, M.; Krossing, I. *Chem. Soc. Rev.* **2016**, *45*, 789–899.
(95) Riddlestone, I. M.; Kraft, A.; Schaefer, J.; Krossing, I. *Angew. Chem. Int. Ed.* DOI:10.1002/anie.201710782
(96) Aris, D.; Beck, J.; Decken, A.; Dionne, I. Günne, J. S.; Hoffbauer, W.; Köchner, T.; Krossing, I.; Passmore, J.; Rivard, E.; Steden, F.; Wang, X. *Dalton Trans.* **2011**, *40*, 5865–5880.
(97) Krossing, I.; Raabe, I. *Angew. Chem. Int. Ed.* **2004**, *43*, 2066–2090.
(98) Strauss, S. H. *Chem. Rev.* **1993**, *93*, 927–942.
(99) King, B. T.; Michl, J. *J. Am. Chem. Soc.* **2000**, *122*, 10255–10256.

(100) Bihlmeier, A.; Gonsior, M.; Raabe, I.; Trapp, N.; Krossing, I. *Chem. Eur. J.* **2004**, *10*, 5041–5051.

(101) Cameron, T. S.; Krossing, I.; Passmore, J. *Inorg. Chem.* **2001**, *40*, 4488–4490.

(102) Elliot, H. A.; Legmann, J. F.; Mercier, H. P. A.; Jenkins, D. B.; Schrobilgen, G. J. *Inorg. Chem.* **2010**, *49*, 8504–8523.

(103) a) Moissan, H. Compt. Rend. **1895**, *120*, 966; b) Moissan, H. Ann. Chim. Phys. **1896**, *8*, 141–144.

(104) Antropoff, A.; Frauenhof, H.; Krüger, K. H. *Naturwissenschaften* **1933**, *21*, 315.

(105) Yost, D. M.; Kaye, A. L. *J. Am. Chem. Soc.* **1933**, *55*, 3890−3892.

(106) Laszlo, P.; Schrobilgen, G. J. *Angew. Chem. Int. Ed. Engl.* **1988**, *27*, 479−489.

(107) Ball, P., "Not So Noble", In *Elegant Solutions: Ten Beautiful Experiments in Chemistry*, The Royal Society of Chemistry, Cambridge, UK, 2005, Chapter 7, pp. 139−150.

(108) Sladky, F. O.; Bulliner, P. A.; Bartlett, N. *J. Chem. Soc. A* **1969**, 2179–2188.

(109) Graham, L.; Graudejus, O.; Jha, N. K.; Bartlett, N. *Coord. Chem. Rev.* **2000**, *197*, 321–334.

(110) Bartlett, N. *Proc. Chem. Soc.*, **1962,** 218.

(111) Schrobilgen, G. J.; Moran, M. D. "Noble Gas Compounds" in *Kirk-Othmer Encyclopedia of Chemical Technology*, 5th Ed., John Wiley & Sons, Inc., Hoboken, NJ, **2006**, Chapter 17, pp 323−343.

(112) Brock D. S.; Schrobilgen G. J.; Žemva B. "Noble-Gas Chemistry" in *Comprehensive Inorganic Chemistry II*, vol. 1, Ed., J. Reedijk and K. Poepplemeier, Elsevier, Oxford, UK, **2013**, pp 755−822.

(113) Grochala, W. *Chem. Soc. Rev.* **2007**, *36*, 1632–1655.

(114) Gerken, M.; Schrobilgen, G. J. *Coord. Chem. Rev.* **2000**, *197*, 335−395.

(115) Haner, J.; Schrobilgen, G. J. *Chem. Rev.* **2015**, *115*, 1255–1295.

(116) Lehmann, J. F.; Mercier, H. P. A.; Schrobilgen, G. J. *Coord. Chem. Rev.* **2002**, *233-234*, 1−39.

(118) Lahr, P. H.; Williams, H. L. *J. Phys. Chem.***1959**, *63*, 1432–1434.

(119) Mock, J. E.; Myers, J. E.; Trabant, E. A. *Indust. Eng. Chem.* **1961**, *53*, 1007–1010.

(120) Birchall, T.; Frampton, C. S.; Schrobilgen, G. J.; Valsdóttir, J. *Acta Cryst. C* **1989**, *45*, 944–946.

(121) Ripmeester, J. A.; Ratcliffe, C. I. *J. Phys. Chem.* **1990**, *94*, 8773–8776.

(122) Dyadin, Y. A.; Larionov, E. G.; Manakov, A. Y.; Zhurko, F. V.; Aladko, E. Y.; Mikina, T. V.; Komarov, V. Y. *Mendeleev Commun.* **1999**, *9*, 209–210.

(123) Seidel, S.; Seppelt, K. *Science*, **2000**, *290*, 117–118.

(124) Drews, T.; Seidel, S.; Seppelt, K. *Angew. Chem. Int. Ed.* **2002**, *41*, 454–456.

(125) Hwang, I. C.; Seidel, S.; Seppelt, K. *Angew. Chem. Int. Ed.* **2003**, *42*, 4392–4395.

(126) Fields, P. R.; Stein, L.; Ziran, M. H. *J. Am. Chem. Soc.* **1962**, *84*, 4164−4165.

(127) Stein, L. *J. Am. Chem. Soc.* **1969**, *91*, 5396−5397.

(128) Stein, L. *Radiochim. Acta* **1983**, *32*, 163−171.

(129) Khriachtchev, L.; Pettersson, M.; Runeberg, N.; Lundell, J.; Räsänen, M. *Nature*, **2000**, *406*, 874−876.

(130) Berkowitz, J.; Chupka, W. A.; *Chem. Phys. Lett.* **1970**, *7*, 447−450.

(131) Runeberg, N.; Petterson, M.; Khriachtchev, L.; Lundell, J.; Räsänen, M. *J. Chem. Phys.* **2001**, *114*, 836−841.

(132) Khriachtchev, L.; Lignell, A.; Tanskanen, H.; Lundell, J.; Kiljunen, H.; Räsänen, M. *J. Phys. Chem. A* **2006**, *110*, 11876.

(133) Khriachtchev, L.; Domanskaya, A.; Lundell, J.; Akimov, A.; Räsänen, M.; Misochko, E. *J. Phys. Chem. A* **2010**, *114*, 4181−4187.

(134) Frohn, H. *Organometallics* **2001**, *20*, 4750−4762.

(135) Ivanova, M. V.; Mercier, H. P. A.; Schrobilgen, G. J. *J. Am. Chem. Soc.* **2015**, *137*, 13398−13413.

(136) Brock, D. S.; Schrobilgen, G. J. *J. Am. Chem. Soc.* **2011**, *133*, 6265–6269.

(137) Templeton, D. H.; Zalkin, A.; Forrester, J.D.; Williamson, S. M. *J. Am. Chem. Soc.* **1963**, *85*, 817.

(138) Smith, D. F. *J. Am. Chem. Soc.* **1963**, *85*, 816−817.

(139) Selig, H.; Claassen, H. H.; Chernick, C. L.; Malm, J. G.; Huston, J. L. *Science* **1964**, *143*, 1322−1323.

(140) Gunn, S. R. *J. Am. Chem. Soc*. **1965**, *87*, 2290.

(141) Vent-Schmidt, T.; Goettel, J. T.; Schrobilgen, G. J.; Riedel, S. *Chem. Eur. J.* **2015**, *21*, 11244–11252.

(142) Malm, J. G.; Holt, B. D.; Bane, R. W. In *Noble Gas Compounds*; Hyman, H. H., Ed.; University of Chicago Press: Chicago, IL, 1963; p 167.

(143) Appelman, E. H.; Malm, J. G. *J. Am. Chem. Soc.* **1964**, *86*, 2141–2148.

(144) Marcus, Y.; Cohen, D. *Inorg. Chem.* **1966**, *5*, 1740–1743.

(145) Aleinikov, N. N.; Isupov, V. K.; Kirin, I. S.; Korsunskii, B. L.; Dubovitskii, F. I.; *Chem. Russ. Bull.* **1974**, *23*, 250–253.

(146) Isupov, V. K.; Kirin, I. S.; Alejnikov, N. N.; Korsunskij, B. L. *Zh. Neorg. Khim.* **1977**, *22*, 1297–1300.

(147) Shustov, L. D.; Tolmacheva, N. S.; Nabiev, S.; Il'in, E. K.; Klimov, V. D.; Ushakov, V. P. *Zh. Neorg. Khim.* **1989**, *34*, 1673–1676.

(148) Fir, B. A.; Mercier, H. P. A.; Sanders, J. C. P.; Dixon, D. A.; Schrobilgen, G. J. *J. Fluorine Chem.* **2001**, *110*, 89–107.

(149) Elliot, H. A.; Lehmann, J. F.; Mercier, H. P. A.; Jenkins, H. D. B.; Schrobilgen, G. J. *Inorg. Chem.* **2010**, *49*, 8504−8523.

(150) Zalkin, A.; Ward, D. L.; Biagioni, R. N.; Templeton, D. H.; Bartlett, N. *Inorg. Chem.* **1978**, *17*, 1318−1322.

(151) Gerken, M.; Moran, M. D.; Mercier, H. P. A.; Pointner, B. E.; Schrobilgen, G. J.; Hoge, B.; Christe, K. O.; Boatz, J. A. *J. Am. Chem. Soc.* **2009**, *131*, 13474−13489.

(152) Smith, G. L. Ph. D. Thesis, McMaster University, Hamilton, ON, Canada, **2010**.

(153) Moran, M. D. Ph. D. Thesis, McMaster University, Hamilton, ON, Canada, **2007**.

(154) Brock, D. S. Ph. D. Thesis, McMaster University, Hamilton, ON, Canada, **2011**.

(155) Grosse, A. V.; Kirshenbaum, A. D; Streng, A. G.; Streng, L. V. *Science*, **1963**, *139*, 1047−1048.

(156) Schreiner, F.; Malm, J.G.; Hindman, J.C. *J. Am. Chem. Soc.* **1965**, *87*, 25−28.

(157) Gunn, S. R. *J. Am. Chem. Soc.* **1966**, *88*, 5924.

(158) Gunn, S. R. *J. Phys. Chem.* **1967**, *71*, 2934−2937.

(159) Mercier, H. P. A.; Sanders, J. C. P.; Schrobilgen, G. J.; Tsai, S. S. *Inorg. Chem.* **1993**, *32*, 386−393.

(160) Malm, J. G.; Chernick, C. L. *Inorg. Synth.* **1966**, *8*, 254−258.

(161) Chernick, C. L.; Malm, J. G. *Inorg. Synth.* **1966**, *8*, 258−260.

(162) Johnson, G. K.; Malm, J. G.; Hubbard, W. N. *J. Chem. Thermodyn.***1972**, *4*, 879−891.

(163) MacKenzie, D. R. *Science* **1963**, *141*, 1171.

(164) MacKenzie, D. R.; Fajer, J. *Inorg. Chem.* **1966**, *5*, 699−700.

(165) Prusakov, V. N.; Sokolov, V. B. *At. Energ.* **1971**, *31*, 259−268; *Sov. At. Energ.* **1971**, *31*, 990−999.

(166) Sessa, P. A.; McGee Jr, H. A. *J. Phys. Chem.* **1969**, *73*, 2078−2080.

(167) Turner, J. J.; Pimentel, G. C. *Science* **1963**, *140*, 974–975.

(168) Streng, L. V.; Streng, A. G. *Inorg. Chem.* **1966**, *5*, 328−329.

(169) Slivnik, J.; Šmalc, A.; Lutar, K.; Žemva, B.; Frlec, B. *J. Fluorine Chem.* **1975**, *5*, 273−274.

(170) Šmalc, A.; Lutar, K.; Žemva, B. *Inorg. Synth.* **1992**, *29*, 11−15.

(171) Kinkead, S. A.; FitzPatrick, J. R.; Foropoulos, Jr, J.; Kissane, R. J.; Purson, J. D. *ACS Symp. Ser.* **1994**, *555*, 40−55.

(172) Bezmel'nitsyn, V. N.; Legasov, V. A.; Chaivanov, B.B. *Dokl. Akad. Nauk. SSSR* **1977**, *235*, 96−98; *Dokl. Chem.* **1977**, *235*, 365−367.

(173) Lehmann, J. F.; Dixon, D. A.; Schrobilgen, G. J. *Inorg. Chem.* **2001**, *40*, 3002−3017.

(174) Stamper, J. G.; Barrow, R. F. *Trans. Faraday Soc.* **1958**, *54*, 1592−1594.

(175) Frlec, B.; Holloway, J. H. *J. Chem. Soc. Chem. Commun.* **1973**, 370−371.

(176) Holloway, J. H.; Schrobilgen, G. J. *J. Chem. Soc. Chem. Commun.* **1975**, 623−624.

(177) Christe, K. O.; Dixon, D. A. *J. Am. Chem. Soc.* **1992**, *114*, 2978−2985.

(178) Gillespie, R.; Schrobilgen, G. J. *Inorg. Chem.* **1974**, *13*, 1230−1235.

(179) Christe, K. O.; Wilson, W. W.; Wilson, R. D. *Inorg. Chem.* **1984**, *23*, 2058−2063.

(180) Fir, B. A.; Gerken, M.; Pointner, B. E.; Mercier, H. P. A.; Dixon, D. A.; Schrobilgen, G. J. *J. Fluorine Chem.* **2000**, *105*, 159−167.

(181) Lozinšek, M.; Mercier, H. P. A.; Brock, D. S.; Žemva, B.; Schrobilgen, G. J. *Angew. Chem. Int. Ed.* **2017**, *129*, 6347−6350.

(182) Emara, A. A. A.; Schrobilgen, G. J. *J. Chem. Soc., Chem. Commun.* **1987**, 1644−1646.

(183) Schrobilgen, G. J. *J. Chem. Soc., Chem. Commun.* **1988**, 1506−1508.

(184) Tavčar, G.; Tramšek, M. *J. Fluorine Chem.* **2015**, *174*, 14−21.

(185) Tavčar, G.; Žemva, B. *Angew. Chem. Int. Ed.* **2009**, *48*, 1432–1434.

(186) Tavčar, G.; Žemva, B. *Inorg. Chem.* **2005**, *44*, 1525−1529.

(187) Tucker, P. A.; Taylor, P. A.; Holloway, J. H.; Russell, D. R. *Acta Crystallogr.* **1975**, *B31*, 906−908.

(188) Benkič, P.; Tramšek, M.; Žemva, B. *Solid State Sciences* **2002**, *4*, 1425–1434.

(189) Lutar, K.; Borrmann, H.; Mazej, Z.; Tramšek, M.; Benkič, P.; Žemva, B. *J. Fluorine Chem.* **2000**, *101*, 155–160.

(190) Tramšek, M.; Lork, E.; Mews, R.; Žemva, B. *J. Solid State Chem.* **2001**, *162*, 243–249.

(191) Tramšek, M.; Benkič, P.; Žemva, B. *Inorg. Chem.* **2004**, *43*, 699–703.

(192) Tavčar, G.; Benkič, P.; Žemva, B. *Inorg. Chem.* **2004**, *43*, 1452−1457.

(193) Benkič, P.; Tramšek, M.; Goreshnik, E.; Žemva, B. *Solid State Sciences*, **2008**, *10*, 1511−1516.

(194) Mazej, Z.; Goreshnik, E. *Inorg. Chem.* **2008**, *47*, 4209−4214.

(195) Tavčar, G.; Goreshnik, E.; Mazej, Z. *J. Fluorine Chem.* **2006**, *127*, 1368−1373.

(196) Tavčar, G.; Žemva, B. *Inorg. Chem.* **2013**, *52*, 4319−4323.

(197) Hagiwara, R.; Hollander, F.; Maines, C.; Bartlett, N. *Eur. J. Solid State Inorg. Chem.* **1991**, *28*, 855−866.

(198) Matsumoto, K.; Hagiwara, R.; Ito, Y.; Tamada, O. *Solid State Sciences*, **2002**, *4*, 1465−1469.

(199) Bunič, T.; Tramšek, M.; Goreshnik, E.; Tavčar, G.; Žemva, B. *Inorg. Chem.* **2007**, *46*, 5276−5282

(200) Tramšek, M.; Benkič, P.; Žemva, B. *Solid State Sciences*, **2002**, *4*, 9−14.

(201) Bunič, T.; Tavčar, G.; Tramšek, M.; Žemva, B. *Inorg. Chem.* **2006**, *45*, 1038−1042.

(202) Gerken, M.; Hazendonk, P.; Iuga, A.; Nieboer, J.; Tramšek, M.; Goreshnik, E.; Žemva, B.; Zheng, S.; Autschbach, J. *Inorg. Chem.* **2007**, *46*, 6069−6077.

(203) Turičnik, A.; Benkič, P.; Žemva, B. *Inorg. Chem.* **2002**, *41*, 5521−5524.

(204) Bunič, T.; Tramšek, M.; Goreshnik, E.; Žemva, B. *Collect. Czech. Chem. Commun.* **2008**, *73*, 1645−1654.

(205) Tramšek, M.; Benkič, P.; Žemva, B. *Angew. Chem. Int. Ed.* **2004**, *43*, 3456–3458.

(206) Tavčar, G.; Tramšek, M.; Bunič, T.; Benkič, P.; Žemva, B. *J. Fluorine Chem.* **2004**, *125*, 1579−1584.

(207) Brock, D. S.; Casalis de Pury, J. J.; Mercier, H. P. A.; Schrobilgen, G. J.; Silvi, B. *J. Am. Chem. Soc.* **2010**, *132*, 3533−3542.

(208) Brock, D. S.; Casalis de Pury, J. J.; Mercier, H. P. A.; Schrobilgen, G. J.; Silvi, B. *Inorg. Chem.* **2010**, *49*, 6673–6689.

(209) Holloway, J. H.; Schrobilgen, G. J. *Inorg. Chem.* **1981**, *20*, 3363−3368.

(210) Christe, K. O.; Wilson, W. W.; Bougon, R. A. *Inorg. Chem.* **1986**, *13*, 2163−2169.

(211) Nabiev, Sh. Sh.; Sokolov, V. B.; Spirin, S. N.; Chaivanov, B. B. *Russ. J. Phys. Chem. A* **2011**, *85*, 1931–1941.

(212) Mercier, H. P. A.; Moran, M. D.; Schrobilgen, G. J.; Steinberg, C.; Suontamo, R. J. *J. Am. Chem. Soc.* **2004**, *126*, 5533−5548.

CHAPTER 2

General Experimental Section

2.1. Standard Techniques

2.1.1. Drybox and Vacuum Line Techniques

The compounds used and prepared during the course of this work were typically moisture- and temperature-sensitive, and were handled under rigorously anhydrous conditions on glass and metal vacuum line systems or in an inert atmosphere (N_2 gas) drybox (Vacuum Atmospheres Model DLX, oxygen and moisture <0.1 ppm) equipped with a glass cryowell for low-temperature work. Preparative work inside the drybox requiring low temperatures was accomplished using a metal Dewar filled with 4.5 mm copper-plated spheres (air rifle BBs) that had been previously cooled using liquid nitrogen to at least –140 ^{o}C inside the glass cryowell (–196 ^{o}C) of the drybox.

Preparative work involving volatile fluorides that could attack glass (e.g., HF) were carried out on a metal vacuum line that was constructed primarily from 316 stainless steel and nickel, and fitted with 316 stainless steel valves (Autoclave Engineers, Inc., Figure 2.1). Pressures were measured at ambient temperatures using MKS Model PDR-5B pressure transducers with wetted surfaces constructed of Inconel. The pressure transducer possessed a range of 0–1150 Torr, which was accurate to ±0.5 Torr.

Transfer of non-corrosive reagents were carried out using Pyrex glass vacuum lines equipped with grease-free 6-mm J. Young glass stopcocks outfitted with PTFE barrels (Figure 2.2). Pressures inside the glass manifold were monitored using a

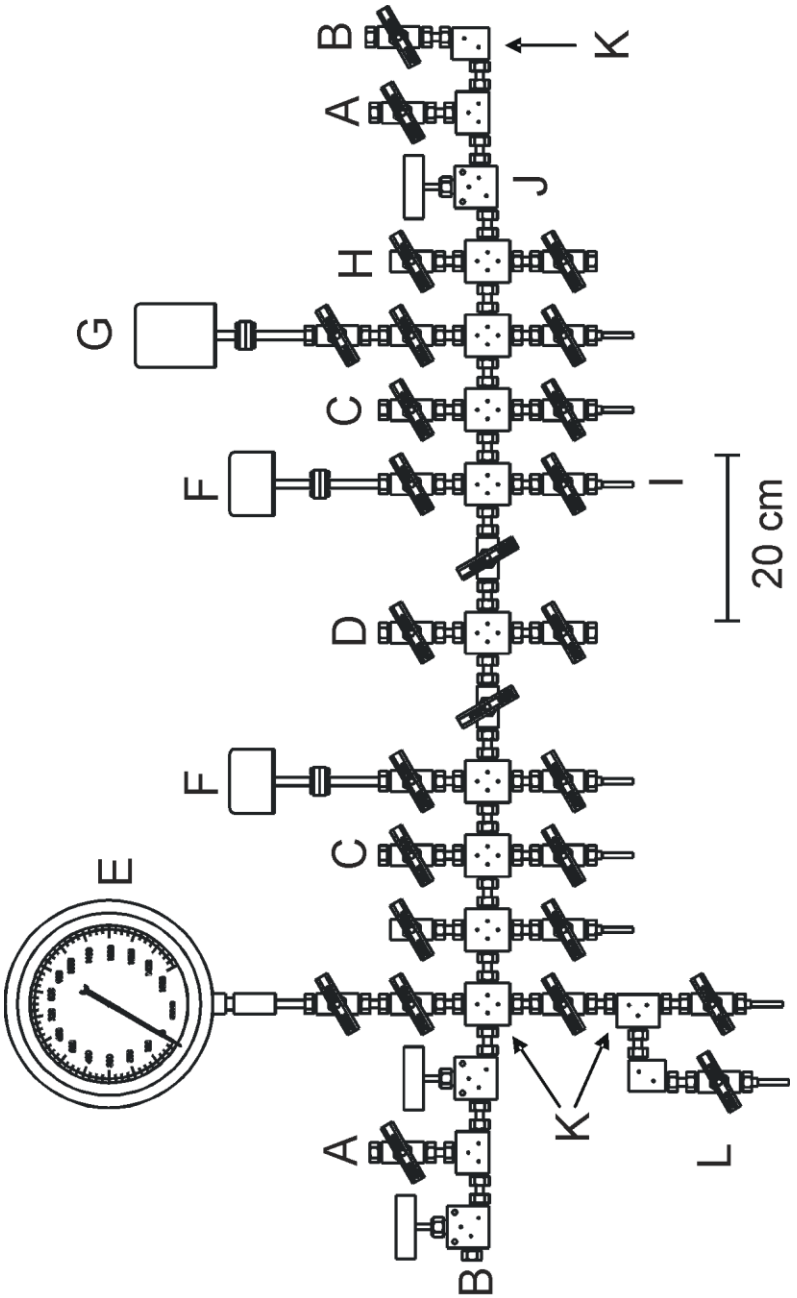

Figure 2.1. The metal vacuum line used for the manipulation of corrosive materials. (A) Outlet to liquid nitrogen and soda lime traps followed by a two-stage direct-drive rotary vacuum pump (Edwards E2M8) – roughing vacuum. (B) Outlet to soda lime and liquid nitrogen traps followed by a two-stage direct-drive rotary vacuum pump (Edwards E2M8) – high vacuum. (C) Dry N_2 inlets. (D) F_2 inlet. (E) Bourdon pressure gauge (0–1500 Torr). (F) MKS Model PDR-5B pressure transducers (0–1000 Torr). (G) MKS Model PDR-5B pressure transducer (0–10 Torr). (H) Ultra-high purity argon inlet. (I) ¼-in. o.d. ($^1/_8$-in. i.d.) nickel reaction vessel port. (J) High-pressure stainless steel valve (Autoclave Engineers). (K) 316 stainless steel X-, T-, and L-connections employing $^3/_8$-in. o.d. ($^1/_8$-in. i.d.) threaded nickel tubing. (L) Submanifold. Reproduced with permission from ref. 1.

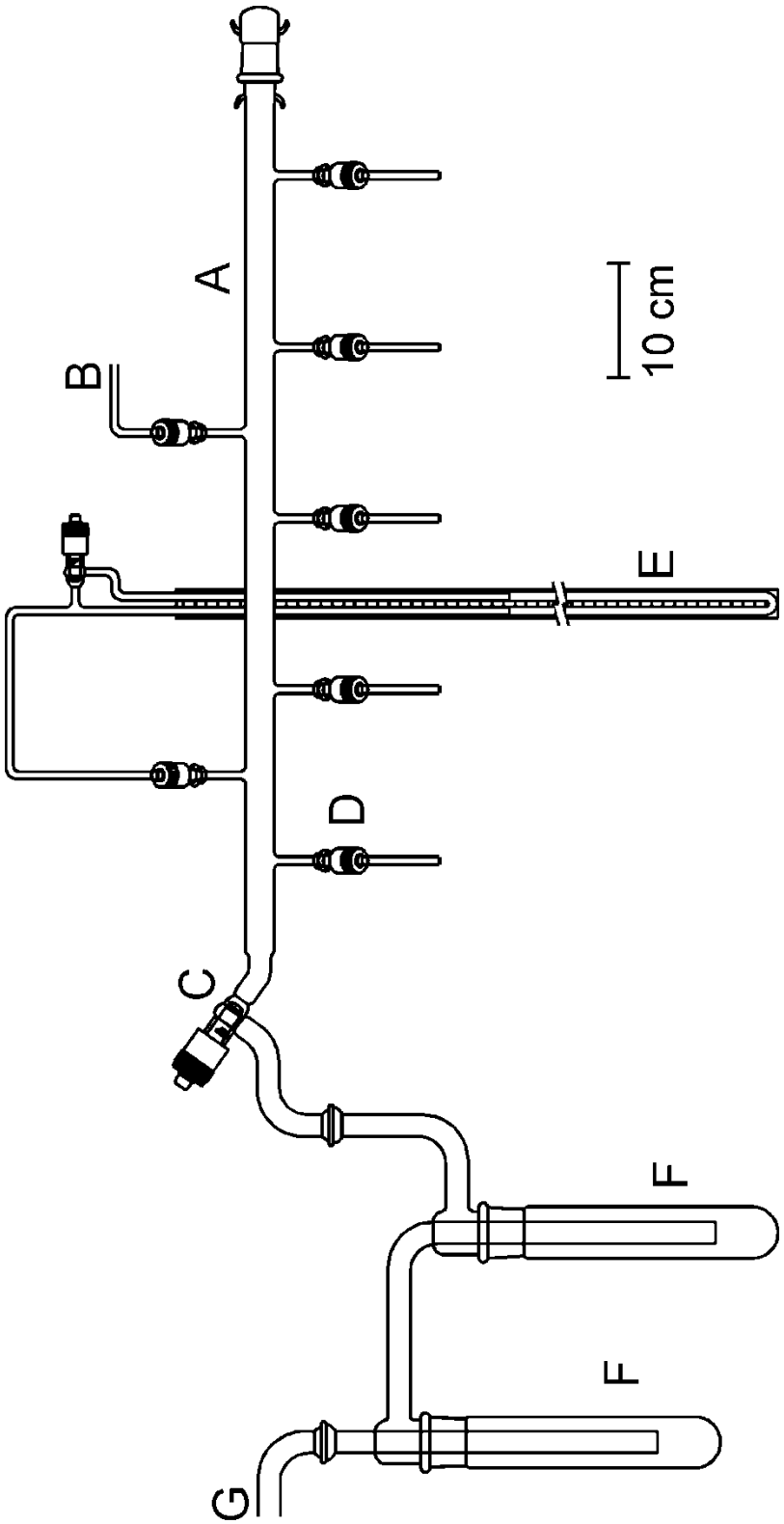

Figure 2.2. Glass vacuum line used for the manipulation of non-corrosive volatile materials. (A) Main vacuum manifold. (B) Dry N_2 inlet. (C) 15-mm greaseless glass J. Young stopcock with PTFE barrel. (D) 6-mm greaseless J. Young stopcock with PTFE barrel. (E) Mercury manometer. (F) Liquid N_2 cold trap. (G) Outlet to vacuum pump. Reproduced with permission from ref. 1.

mercury manometer. Vacuum on the glass vacuum lines (ca. 10^{-3}–10^{-4} Torr) was accomplished using Edwards two-stage internal vane E2M8 direct-drive vacuum pumps. Vacuum was maintained on the metal line using three E2M8 vacuum pumps. The first, referred to as the "rough pump", was used primarily for the removal of volatile fluoride and oxide fluoride compounds and first passed through a fluoride/fluorine trap consisting of a stainless steel tube (ca. 60 cm, 15 cm dia.) packed with soda lime absorbent (Fisher Scientific, 4–8 mesh), followed by a final trapping procedure, utilizing a glass liquid nitrogen trap to remove CO_2 and water formed by reaction of fluoride materials with soda lime and other volatile materials that were unreactive towards soda lime. The other two pumps, referred to as "fine pumps" provided high vacuum (ca. 10^{-4} Torr) to each half of the manifold and were fitted with glass liquid nitrogen traps to protect the pumps and trap any potential volatile materials.

2.1.2. Synthetic Apparatus and Sample Vessels

All synthetic work was carried out in reactors made from ¼-in. o.d. FEP tubing, which was heat-joined for T-shaped vessels, heat-sealed closed at the ends, and heat-flared (45^{o} SAE) at one end to connect the tube to a Kel-F valve, encased in aluminum housing, using a brass flare fitting. All vessels were then connected to a glass vacuum line using ¼-in. stainless steel Swagelok Ultratorr unions, and were rigorously dried by pumping (a minimum of 6 h) under dynamic vacuum. Vessels were then connected to the metal vacuum line using ¼-in. stainless steel Swagelok Ultratorr unions and passivated with ca. 1000 Torr of F_2 for ca. 12 h. Once passivated, vessels were evacuated under

dynamic vacuum to remove all volatile impurities and back-filled with dry N_2 (ca. 1000 Torr) prior to use. Similarly, connections made to a metal vacuum line were dried under dynamic vacuum and passivated with F_2 gas overnight. Connections made to a glass vacuum line were dried under dynamic vacuum overnight. Glass vessels used were dried under dynamic vacuum for a minimum of 8 h and were periodically heated using a Bunsen burner.

Nuclear magnetic resonance spectra were acquired using sample tubes prepared from lengths of 4-mm o.d. FEP tubing which were heat-sealed closed at one end and fused to ca. 5 cm of ¼-in. o.d. thick wall tubing at the other. The open end of the ¼-in. o.d. thick wall tubing was heat-flared (45^o SAE) to make a connection to a Kel-F valve as previously described. Prior to acquisition of the NMR data, the ¼-in. o.d. FEP sample tube and its contents were heat-sealed closed under dynamic vacuum using a nichrome wire resistance furnace of appropriate diameter. The FEP NMR same tube was inserted into a 5-mm o.d. thin wall precision glass NMR tube (Wilmad) in order to be placed in the NMR instrument.

2.1.3. Disposal of Compounds

Extreme caution is required when disposing of samples containing KrF_2 to avoid violent detonations. Routine disposal of HF and KrF_2 was carried out by dynamic pumping through a stainless steel column packed with soda lime or were carried out by freezing the sample in liquid nitrogen, cutting the FEP vessel open near the valve and

inverting it into a cold solution of aqueous base solution. The latter procedure was carried out inside a fumehood and appropriate personal protective equipment was worn.

2.2. Syntheses of SO_2ClF and Purification of Starting Materials

2.2.1. Sources and Purification of Gasses; N_2, F_2, Xe, and Kr

House nitrogen gas was either generated by boiling off liquid nitrogen (Air Liquide) with further drying through a freshly regenerated bed of type 4Å molecular sieves or industrial grade N_2 gas (99.995%, Praxair) was used without further purification. Technical grade fluorine gas (Air Products) and ultra-high purity Xe (Air Products, 99.995%) and Kr (Air Products, 99.995%) were used without further purification.

2.2.2. Synthesis and Purification of Solvents

Anhydrous HF. Hydrogen fluoride, HF (Harshaw Chemical Co.), was purified by addition of ca. 5 atm of fluorine gas to a commercial HF sample contained in a nickel can for a period of approximately one month prior to use, converting residual water to HF and O_2. The HF was then distilled into a Kel-F storage vessel equipped with a Kel-F valve and stored at room temperature for future use. Transfer of HF was accomplished by vacuum distillation from the Kel-F storage vessel, on a metal vacuum line, through connections constructed from FEP, as shown in Figure 2.3. ***Note:*** *Hydrogen fluoride cylinders should be safely vented or returned to the vendor at least every two years in*

order to release possible pressure build-up due to H_2 gas generated by the reaction of HF with the iron in carbon steel cylinders.

SO_2ClF. Sulfurylchlorofluoride, was either synthesized according to the literature method,[2] or SO_2ClF (Allied Chemical, Baker Adamson Division) was purified as previously described.[3] This purification involves condensing the SO_2ClF into an FEP U-tube containing ca. 80 g of SbF_5 at –78 ^oC and slowly warming to room temperature with vigorous mixing to convert any unreacted SO_2Cl_2 and complex any SO_2. The SO_2ClF was then transferred to an FEP U-tube cooled to –78 ^oC which contained dried KF. Again, the mixture was slowly warmed to room temperature with vigorous mixing and allowed to stand at room temperature for ca. 2 h with periodic mixing in order to remove any residual HF. The solvent was transferred into a 1.25-in. FEP reaction vessel containing XeF_2 (1.7 g) for 24 h to ensure all impurities with reducing properties (i.e., SO_2) were removed. Finally, the liquid was distilled by dynamic pumping at –78 ^oC into a glass vessel, outfitted with a 6-mm J. Young all glass stopcock, over a bed of dry KF. Transfers were performed using a glass vacuum line by vacuum distillation of SO_2ClF through a sub-manifold comprised of a Y-shaped glass connection to the reaction vessel (Figure 2.4). The sample was stored at room temperature until used.

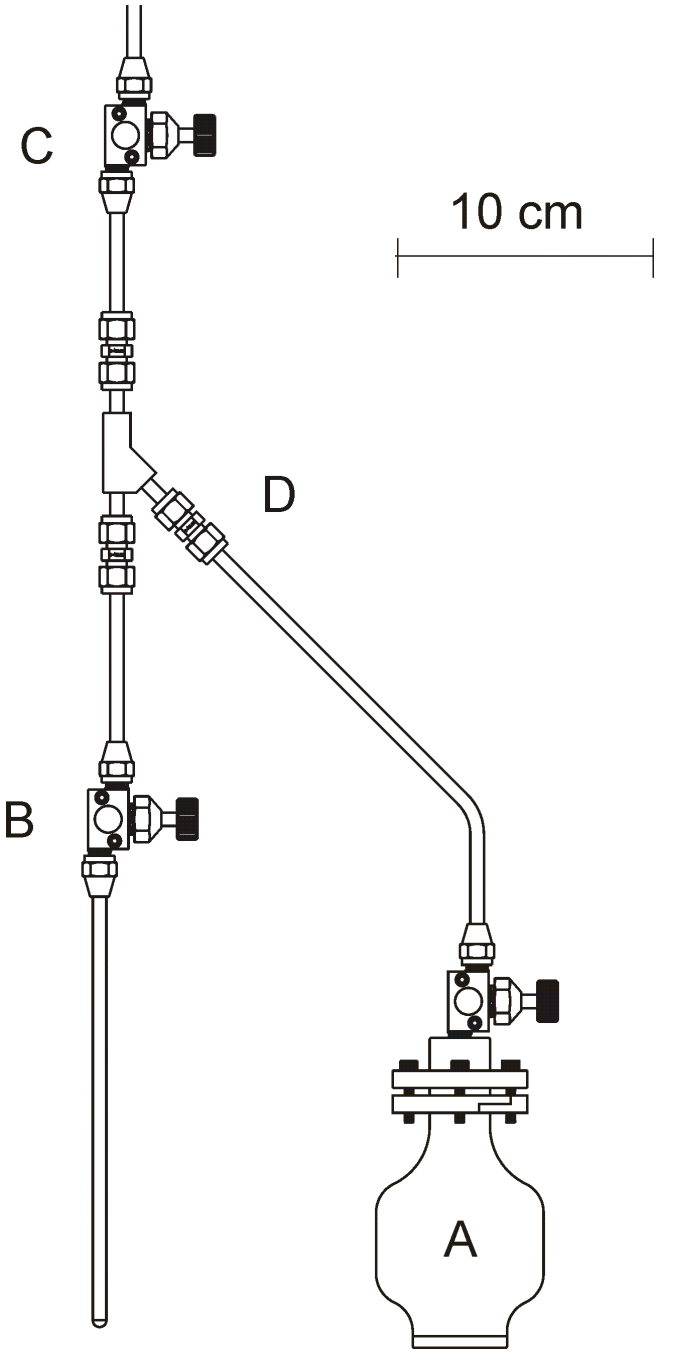

Figure 2.3. Hydrogen fluoride distillation apparatus. (A) Kel-F storage vessel containing HF. (B) FEP reaction vessel fitted with a Kel-F valve. (C) Kel-F valve connected to vacuum manifold. (D) Kel-F Y-connection with ¼-in. PTFE Swagelok unions. Reproduced with permission from ref. 1.

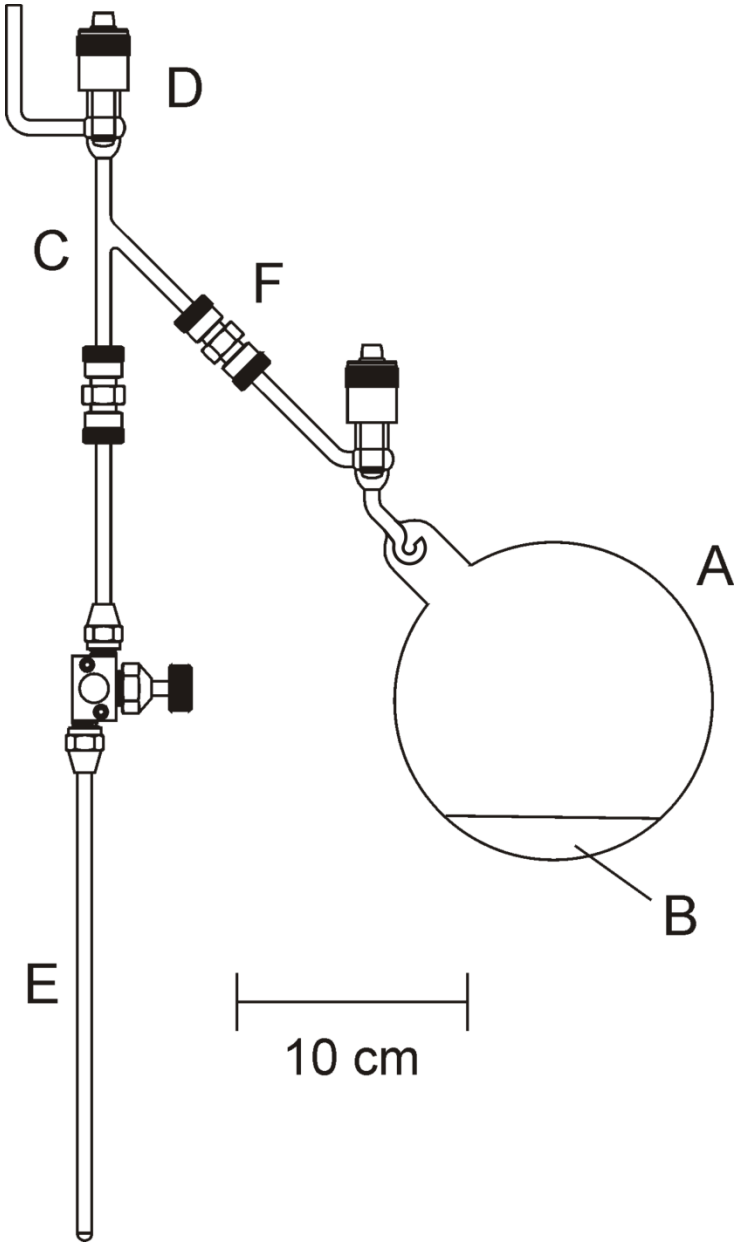

Figure 2.4. Apparatus used for the vacuum transfer of SO_2ClF solvent. (A) 250-mL glass vessel equipped with a grease-free 6-mm J. Young PTFE/glass stopcock outfitted with PTFE barrel. (B) Bed of dry, powdered KF. (C) Glass Y-connector. (D) 6-mm J. Young PTFE/glass valve. (E) FEP reaction vessel fitted with a Kel-F valve. (F) Stainless steel Swagelok Ultratorr Union. Reproduced with permission from ref. 1.

CH_3CN. Acetonitrile (Caledon, HPLC Grade) was purified according to the literature method,[4] and was stored over Davison type 3 Å molecular sieves (Fisher Scientific) in a glass vessel outfitted with a grease-free 6-mm J. Young glass/PTFE stopcock. The molecular sieves were dried under dynamic vacuum for 24 h at 120 ^{o}C prior to use as a drying agent. Acetonitrile was then dispensed into individual reaction vessels under static vacuum using a glass Y-connector (Figure 2.5).

SO_2. Sulfur dioxide (Aldrich) was stored over P_4O_{10} in a glass vessel, outfitted with a grease-free 6-mm J. Young PTFE/glass stopcock. Transfers were carried out under static vacuum using a glass vacuum line and a glass Y-connector (Figure 2.5).

Freon-114. 1,2-Dichlorotetrafluoroethane or "Freon-114" (Aldrich) was dried over P_4O_{10} for several days before being distilled into glass vessels fitted with 4-mm J. Young PTFE/glass stopcock for storage. Transfers were performed under vacuum using a glass vacuum line and a glass Y-connector (Figure 2.5).

Methylene chloride (CH_2Cl_2) and Methylene chloride-*d_2* (CD_2Cl_2).

Methylene chloride (Caledon, reagent grade) was dried over previously vacuum-dried (250 °C) Davison type 3 Å molecular sieves (Fisher Scientific) for 3 days followed by vacuum distillation into a dry glass bulb equipped with a 4-mm J. Young PTFE/glass stopcock for storage. Methylene chloride-d_2 (D, 99.5%; BDH Chemicals) was transferred into a dry glass bulb and dried over CaH_2 powder (99.5%, BDH Chemicals).

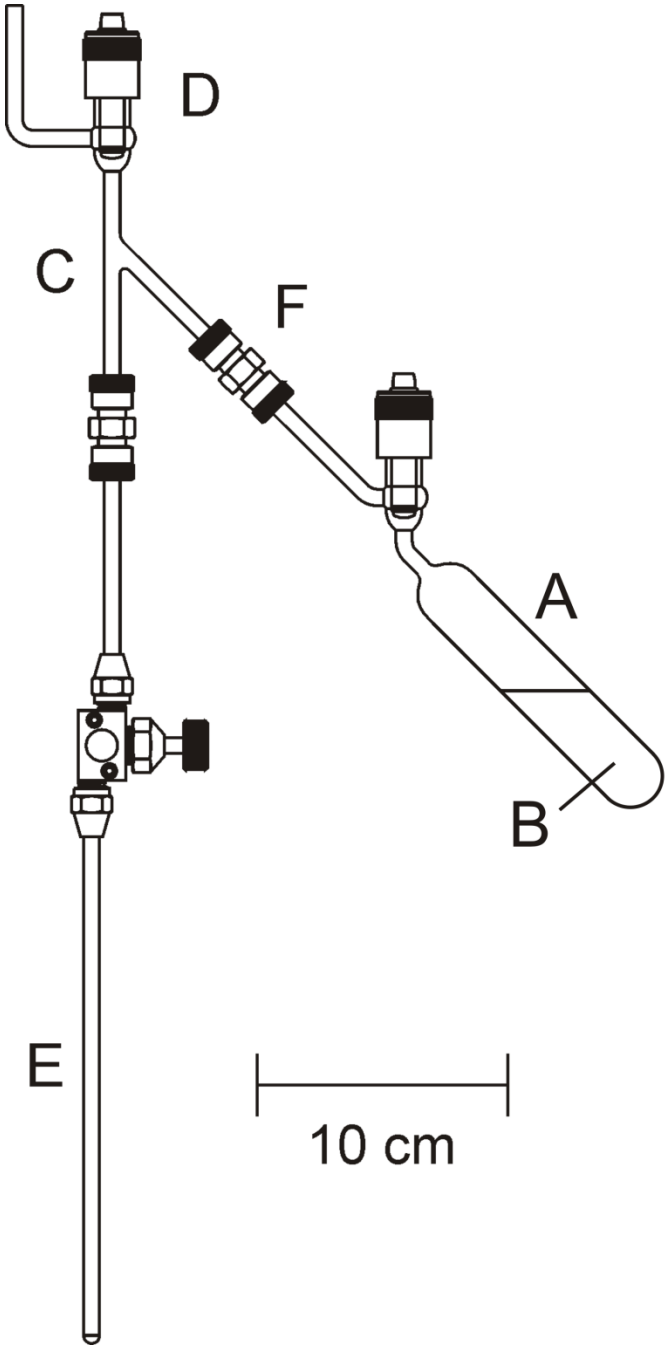

Figure 2.5. Apparatus used for the vacuum transfer of solvent. (A) 200-mL glass vessel equipped with a grease-free 6-mm J. Young PTFE/glass stopcock outfitted with PTFE barrel. (B) solvent. (C) Glass Y-connector. (D) 6-mm J. Young PTFE/glass valve. (E) FEP reaction vessel fitted with a Kel-F valve. (F) Stainless steel Swagelok Ultratorr Union. Reproduced with permission from ref. 1.

2.2.3. Syntheses and Purification of Reagents

AsF_3. Arsenic trifluoride was prepared according to the literature method.[5]

AsF_5. Arsenic pentafluoride was prepared as previously described,[6,7] by direct fluorination of AsF_3 with purified F_2 in a nickel can. The AsF_5 was used from the reaction can without further purification.

SbF_3. Antimony trifluoride (Aldrich, 98%) was purified as previously described,[8] by sublimation under dynamic vacuum and treatment with HF, and stored in the drybox.

SbF_5. Antimony pentafluoride was either purified (Ozark-Mahoning Co.) by the literature method,[9] or synthesized in situ by the direct fluorination of SbF_3 in aHF.

$Cs[OTeF_5]$. Cesium pentafluorooxotellurate(VI) was synthesized by the reaction of ca. tenfold excess of $HOTeF_5$ with dry, powdered CsCl (Fluka) according to the literature method.[10]

$[N(R)_4]Cl$ ($R = CH_3$ or CH_2CH_3). Literature methods were used for the purification of $[N(CH_3)_4]Cl$ (Fluka) and $[N(CH_2CH_3)_4]Cl$ (Fluka),[11] which were stored in FEP sample tubes inside a drybox until used.

$[N(R)_4][OTeF_5]$ ($R = CH_3$ or CH_2CH_3). The tetramethylammonium- and tetraethylammonium pentafluorooxotellurate(VI) salts were both synthesized in a similar

fashion by the reaction of their respective chloride salts and $HOTeF_5$ as outlined in the literature.[12,13]

XeF_2. Xenon difluoride[6] was prepared according to the literature method and stored in a Kel-F sample tube inside a drybox until needed.

$Hg(PnF_6)_2$ (Pn = As, Sb). The starting material, $Hg(AsF_6)_2$, was prepared according to the literature method from HgF_2 and AsF_5,[14,15] wheras $Hg(SbF_6)_2$ was synthesized using a similar procedure but with SbF_5 that had been generated in situ by the direct fluorination of SbF_3 in aHF.

$FHg(AsF_6)$. As outlined in the literature,[14] the direct 1:1 molar ratio reaction between HgF_2 and AsF_5 in aHF only leads to mixtures of $Hg(AsF_6)_2$ and HgF_2 rather than the desired compound, $FHg(AsF_6)$. Instead, a modified literature route[14] was employed which began with the formation of $Hg_2(AsF_6)_2$ by oxidation of dry elemental mercury (1.2041 g, 6.003 mmol) with a stoichimetric excess of AsF_5 (1.537 g, 9.046 mmol) in liquid SO_2 at room temperature. The $Hg_2(AsF_6)_2$ was then dissolved in anhydrous HF and a large excess of elemental fluorine (0.5691 g, 14.979 mmol) was condensed into the vessel at –196 ^oC. The reactor was slowly warmed to –78 ^oC, and then to room temperature where it was allowed to react for 2 days while being agitated on wrist-action shaker. Removal of all volatiles at room temperature yielded a colorless product (2.0969 g), which consisted mainly of $FHg(AsF_6)$, contaminated with a small amount of $Hg(AsF_6)_2$ by-product as shown by low-temperature Raman spectroscopy. In order to obtain pure $FHg(AsF_6)$, the sequential decomposition pathway of $Hg(AsF_6)_2$ outlined in

the literature[16] was exploited (eq 2.1) by heating the product mixture to 70 °C under dynamic vacuum for several hours to give pure $FHg(AsF_6)_2$. Weighing before and after purification suggested ~4 mol% of $Hg(AsF_6)_2$ contaminant was present.

$$Hg(AsF_6)_{2\,(s)} \xrightarrow{65\text{–}95\ ^oC} FHg(AsF_6)_{(s)} + \uparrow AsF_{5\,(g)} \xrightarrow{95\text{–}430\ ^oC} HgF_{2\,(s)} + \uparrow AsF_{5\,(g)} \quad (2.1)$$

$B(OTeF_5)_3$. Boron tris(bis(pentafluoro-orthotellurate(VI)) was prepared from the stoichiometric reaction of BCl_3 and $HOTeF_5$ as previously described,[17] and was stored in an FEP sample tube inside a drybox until needed.

$Xe(OTeF_5)_2$. Xenon(II) bis(pentafluoro-orthotellurate(VI)) was prepared by the stoichiometric reaction of XeF_2 and $B(OTeF_5)_3$ in Freon-114 as previously described,[12] and was stored in an FEP sample tube inside a drybox until needed.

$Sb(OTeF_5)_3$. Antimony(III) tris(pentafluoro-orthotellurate(VI)) was prepared according to the literature method[18] by the stoichiometric reaction of purified SbF_3 with $B(OTeF_5)_3$ in SO_2ClF and was stored in an FEP sample tube inside a drybox until needed.

$N{\equiv}SF_3$. Liquid $N{\equiv}SF_3$ was synthesized and purified using a modification of a previously described method[19,20] which involves the reaction of $FC(O)N{=}SF_2$ with AgF_2.

$[XeOTeF_5][Sb(OTeF_5)_6]{\cdot}SO_2ClF$. The salt, $[XeOTeF_5][Sb(OTeF_5)_6]{\cdot}SO_2ClF$, was synthesized according to the literature method[21] by the stoichiometric reaction of $Xe(OTeF_5)_2$ and $Sb(OTeF_5)_3$ in SO_2ClF solvent at –20 °C.

$[H_3{}^{16}O][AsF_6]$ and $[H_3{}^{18}O][AsF_6]$. Literature methods were used for the syntheses of $[H_3O][AsF_6]$,[22] by the reaction of $H_2{}^{16}O$ or $H_2{}^{18}O$ (MSD Isotopes, 97.8 atom% ^{18}O) with AsF_5 in HF solvent.

$[Xe_3O^{16/18}F_3][AsF_6]$. The optimized literature route was used to synthesize $[Xe_3O^{16/18}F_3][AsF_6]$ in amounts <0.100 g.[23] This procedure involved the reaction of near-equimolar amounts of $[H_3{}^{16/18}O][AsF_6]$ and XeF_2 (no more than 20 mol% excess of XeF_2) in HF at a concentration of ca. 0.2–3 M $[H_3{}^{16/18}O][AsF_6]$. The solution was rapidly warmed from –50 °C to –30 °C for ca. 30 s to completely dissolve the reactants and initiate the reaction before being immediately cooled back to –50 °C. The reaction miture was maintained at –50 °C for ca. 30 min during which time a deep red-orange precipitate of $[Xe_3O^{16/18}F_3][AsF_6]$ formed which was subsequently isolated by decanting the supernatant and drying it under dynamic vacuum at –78 °C

2.2.4. Synthesis of KrF_2.

Krypton difluoride was prepared using a 316 stainless steel hot-wire reactor (Figure 2.6) equipped with a nickel filament, similar to that originally described[24] and subsequently modified.[25] The filament was fabricated from a $^1/_{16}$-in. diameter nickel wire tightly wound about a second length of $^1/_{16}$-in. diameter nickel wire that was, in turn, coiled and stretched into a helix. In a typical preparation, the hot-wire reactor was pressurized with 1000 Torr (50 mmol) of krypton and then cooled to –196 ^oC in a 20-L Dewar. After reaching thermal equilibrium, the reactor was pressurized with 25 Torr of F_2 and the DC power supply for the nickel filament was adjusted to ca. 6 V and 30 A (the

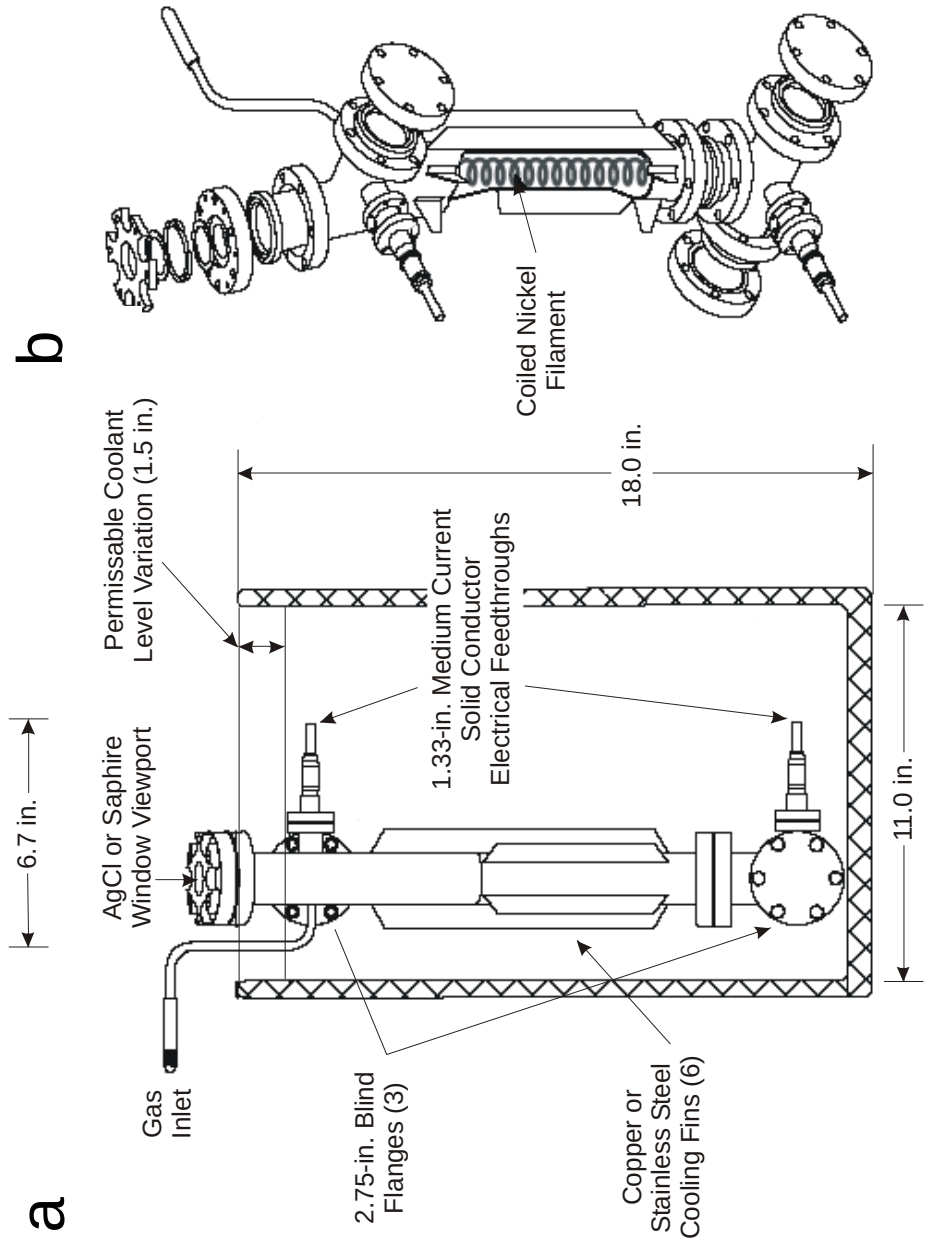

Figure 2.6. The stainless steel hot-wire reactor used for the synthesis of KrF_2. (a) External view and dimensions of a hot-wire reactor submerged in a liquid nitrogen coolant bath. (b) A perspective drawing of the hot-wire reactor showing the flange assembly and nickel filament (cut away region). Reproduced with permission from ref. 26.

filament was dull red in color under these conditions). The F_2 pressure was increased to ca. 45 Torr after the power supply had been turned on and was regulated between 25 and 45 Torr by the periodic addition of F_2 throughout the synthesis. The decrease in F_2 pressure was used to monitor the production of KrF_2, and additional Kr (1.0 to 2.0 mmol) was periodically condensed into the reactor when the rate of KrF_2 production slowed to prevent serious decline of the KrF_2 production rate. Upon completion of the reaction (*ca.* 10–12 h), excess F_2 was removed under dynamic vacuum at –196 ^oC. The excess Kr and crude KrF_2 were recovered as a slightly pink solid (the coloration presumably arises from CrO_2F_2 contamination) by allowing the reactor to slowly warm to room temperature while dynamically pumping the volatile contents into a ½-in. o.d. FEP U-trap (–196 ^oC). The Kr/KrF_2 mixture was then warmed to –78 ^oC while under dynamic vacuum to remove unreacted Kr. The crude KrF_2 was purified by briefly warming the sample to 0 ^oC and flash distilling off the more volatile CrO_2F_2 contaminant. The remaining colorless KrF_2 was finally warmed to room temperature and rapidly sublimed into a $^3/_8$-in. o.d. FEP tube equipped with a Kel-F valve, where it was stored under 1000 Torr of N_2 or Ar at –78 ^oC until used. This synthesis is highly reproducible and typically yields 2.5 to 3.0 g of purified KrF_2.

2.2.5. Synthesis of High-Purity HgF_2.

In a typical synthesis, triply distilled mercury (Johnson Matthey Ltd.), was transferred into a ¼-in. o.d. glass vessel and connected to a grease-free 4-mm J. Young Teflon stopcock by means of a ¼-in. stainless steel Swagelok Ultratorr union outfitted with Viton O-rings. The mercury and glass vessel were dried overnight under dynamic

vacuum. A ½-in. o.d. FEP reaction vessel which had been fused to a length of ¼-in. o.d. thick-wall FEP tubing and equipped with a Kel-F valve was dried and passivated with F_2 and transferred to a drybox. Dry mercury (2.3049 g, 11.491 mmol) was transferred into the ½-in. o.d. FEP reaction vessel. The reaction vessel was cooled using copper plated steel spheres (air rifle shot) that had been previously cooled to ca. –140 ^{o}C inside the cryowell of the drybox, and 2.0339 g (12.0143 mmol) of XeF_2 was transferred into the reactor. The reactor was removed cold from the drybox and attached to a metal vacuum line while maintaining the temperature at –78 ^{o}C. Approximately 2 mL of anhydrous HF was condensed onto the solid mixture at –196 ^{o}C. The reactor was slowly warmed to room temperature while maintaining a back pressure of N_2 (1 atm) within the reaction vessel which remained open to the metal vacuum line manifold to allow the combined xenon and HF pressures to be monitored. ***Caution:*** *Initial gas evolution was rapid and was followed by a rapid temperature increase, producing high pressures within the reaction vessel and manifold. The pressures were controlled by quenching the reaction with liquid N_2 followed by pumping the reactor and manifold to ca. 1 atm after cooling the reactor and contents to –78 ^{o}C.* Once the reaction rate had subsided, the reactor and contents were again warmed to room temperature and the reaction was allowed to proceed while monitoring and adjusting the pressure. This procedure was repeated until no pressure increase was observed (over a period of three days). Hydrogen fluoride and residual XeF_2 were removed by pumping on the sample at –78 ^{o}C, followed by pumping the product at room temperature for 0.5 h to give HgF_2 (2.7196 g, 11.399 mmol) as a friable white powder in near quantitative yield (99.2%). The purity was verified by

recording the Raman spectrum of the solid at −155 °C. The spectrum consisted of a single strong vibrational band at 255 cm^{-1}.

2.2.6. Synthesis of Pentafluoroorthotelluric Acid ($HOTeF_5$).

Pentafluoroorthotelluric ("teflic") acid was synthesized using a procedure similar to a previously reported one.[27,28] The present procedure avoids the direct use of HSO_3F and was carried out in two steps. Initially, a solution of HSO_3F was prepared according to eqs 2.2 and 2.3.

$$H_2SO_4 + NaF \longrightarrow HF + NaHSO_4 \qquad (2.2)$$

$$SO_3 + HF \longrightarrow HSO_3F \qquad (2.3)$$

A 1L (94-mm o.d., 17 cm) FEP bottle (Nalgene®) equipped with a modified screw cap (Tefzel®) with two ¼ in-holes drilled through it, was loaded with 152.52 g (3.63 mol) of NaF (Fischer Scientific) inside a drybox that had been previously dried at 250 °C for 3 days under dynamic vacuum. Upon removal of the FEP bottle from the drybox, a ¼ in-FEP N_2 by-pass tube was inserted through one hole in the screw cap and a pressure-equalized glass separatory funnel equipped with a N_2 by-pass and containing 500 g of 27–33% oleum (Baker Chemical; 1.69−2.06 mol SO_3 and 3.42−3.72 mol H_2SO_4) was inserted through the remaining hole. In this way, both the FEP bottle and the separatory funnel were blanketed with dry N_2 gas by maintaining a slow flow of N_2. The FEP vessel was slowly cooled to –78 °C and oleum was added in three equal portions. With each addition, the mixture was allowed to slowly warm to room temperature, whereupon dissolution of solid NaF and some HF gas evolution occurred. ***Caution***: *The*

exothermicity of this reaction causes the temperature of the reaction mixture to rise rapidly. It should not be allowed to exceed ca. 40 °C and thus requires periodic quenching at –78 °C to control the temperature and reaction rate. Once all of the oleum had been added, the mixture was maintained at room temperature for several days and allowed to react, with periodic sonications at 40 °C to aid in the dissolution of NaF. The reaction produces fluorosulfuric acid, HSO_3F, excess HF, and $NaHSO_4$, which is incompletely soluble and yields a white suspension.

In the second step, $HOTeF_5$ was prepared according to eq 2.4. The overall reaction is given by eq 2.5.

$$5HSO_3F + Te(OH)_6 \longrightarrow F_5TeOH + 5H_2SO_4 \qquad (2.4)$$

$$5H_2SO_4{\cdot}SO_3 + 5NaF + Te(OH)_6 \longrightarrow 5NaHSO_4 + F_5TeOH + 5H_2SO_4 \qquad (2.5)$$

The $H_2SO_4/HSO_3F/NaHSO_4$ mixture was transferred, as a slurry, into the round-bottom flask (1 L) of a one-piece, grease-free glass distillation apparatus inside a dry N_2-flushed polyethylene glove bag. The distillation apparatus was equipped with a Vigreux distillation column, an air-cooled distillation bridge, and a silicon oil gas bubbler connected to the top of the distillation column (also consult ref. 27 where a similar distillation apparatus was used to synthesize $HOTeF_5$ directly from HSO_3F and $Te(OH)_6$). Telluric acid, $Te(OH)_6$, (BDH Chemicals Ltd.; 69.29 g, 0.302 mol) was then added at room temperature using a FEP powder funnel. The estimated HSO_3F:$Te(OH)_6$ molar ratio employed in eq 2.4 is 5.6−6.8.

The suspension was heated to ca. 160 °C and vigorously stirred for ca. 1 h using a Teflon-coated magnetic stir bar. The mixture was then refluxed for ca. 2 h (190–200 °C). After reflux, the cooling water in the Vigreux column was turned off and crude $HOTeF_5$ was distilled into a ¾-in. o.d. FEP receiving tube equipped with a Kel-F valve. Crude $HOTeF_5$ (57.21 g, 0.239 mol; 79.1% yield) was obtained as a colorless crystalline solid in admixture with impure, premelted $HOTeF_5$.

For purification of the crude product, concentrated H_2SO_4 (Caledon) (95–97%, 200 mL) was added to the larger chamber of a double-chambered (ca. 300 and 650 mL) purification vessel equipped with 6-mm Teflon/glass stopcocks. Crude $HOTeF_5$ was then vacuum distilled onto the surface of frozen H_2SO_4 at –78 ^{o}C. The mixture was warmed to room temperature and mixed using a magnetic stir bar. The solution was frozen at –78 ^{o}C and evacuated for 15 min to remove dissolved nitrogen. The vessel was closed and allowed to warm to room temperature and the reaction mixture was then heated in an oil bath to 100 °C with vigorous stirring and refluxed under static vacuum for 12 h. After refluxing, the temperature of the mixture was maintained at 100 °C and $HOTeF_5$ was distilled under static vacuum into the second, smaller chamber where it condensed at –78 °C. The purified $HOTeF_5$ was then distilled from the second chamber at room temperature into a ¾-in. o.d. FEP vessel at –78 °C. Pure $HOTeF_5$ (56.1803 g; 0.234 mol) was isolated as a colorless solid in 77.5% yield. The purity of $HOTeF_5$ was verified by Raman spectroscopy and ^{19}F NMR spectroscopy.

2.2.7. Synthesis of High-Purity $Hg(OTeF_5)_2$.

In a typical synthesis, a passivated FEP reaction vessel equipped with a Kel-F valve was loaded with high-purity HgF_2 (0.4938 g, 2.069 mmol) inside a drybox. The reaction vessel was then transferred to a metal vacuum line where aliquots of $HOTeF_5$ were distilled into it. The contents of the reaction vessel were allowed to react at 50 °C for several hours with periodic agitation. The progress of the reaction was monitored by Raman spectroscopy, and was deemed complete upon observation of persistent residual unreacted $HOTeF_5$ in the spectrum. The residual $HOTeF_5$ and minor amounts of HF formed in the reaction (eq 2.6) were removed by pumping under dynamic vacuum for 3 h at room temperature, resulting in a friable, white solid in essentially quantitative yield (99.1%).

$$HgF_2 + 2\,HOTeF_5 \longrightarrow Hg(OTeF_5)_2 + 2HF \qquad (2.6)$$

2.3. X-ray Crystallography

2.3.1. Crystal Growth Apparatus

The low-temperature crystal growing apparatus depicted in Figure 2.7 was used to observe and isolate a number of crystalline samples. The temperature inside the glass-jacketed dewar was controlled by use of a Variac which heated a coil inside a dewar of liquid nitrogen, resulting in a nitrogen cold flow around the sample which was monitored with a thermocouple.

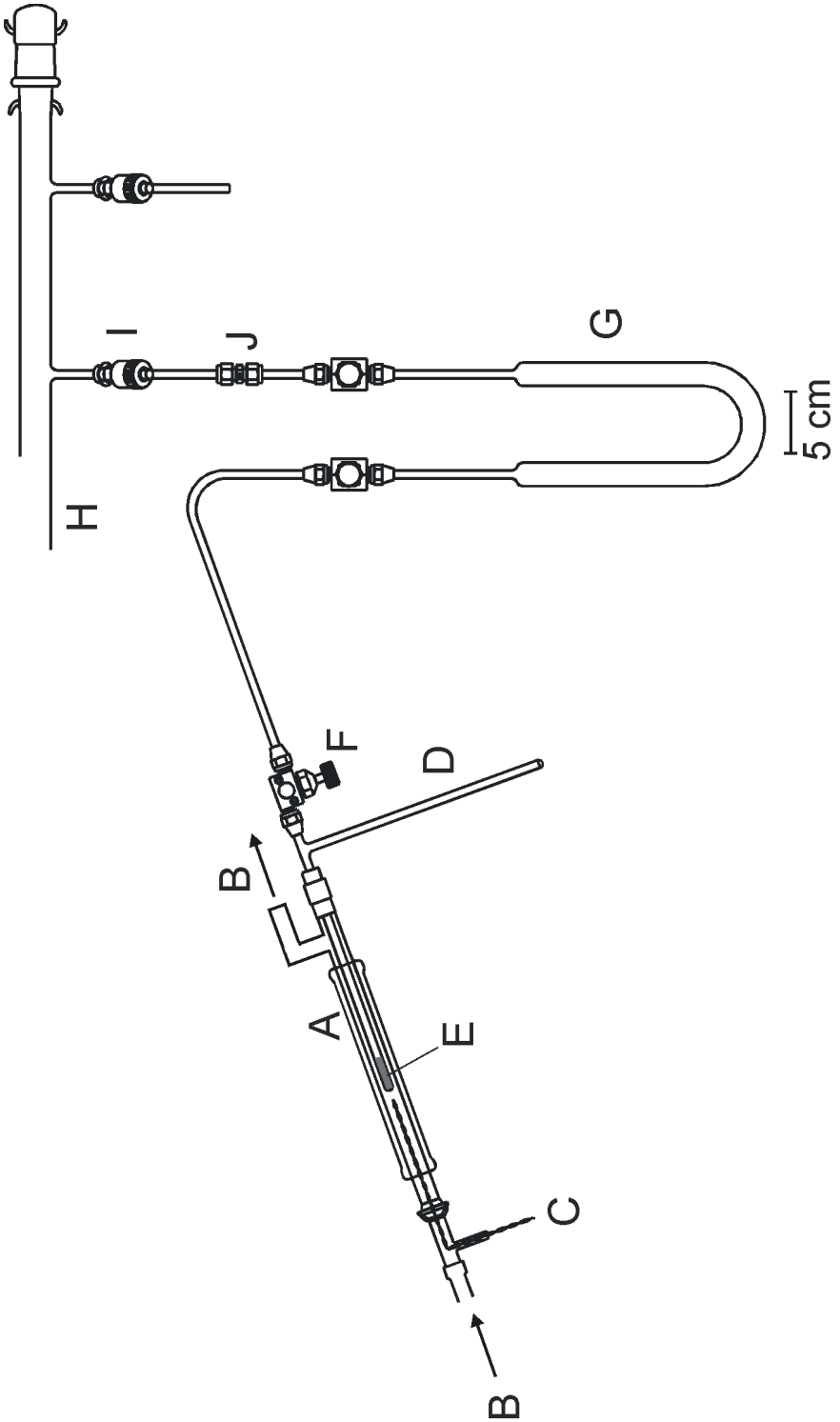

Figure 2.7. Low-temperature crystal growing apparatus. (A) Glass-jacketed dewar. (B) Nitrogen cold flow. (C) Thermocouple lead. (D) T-shaped FEP reaction vessel with side arm. (E) Sample region. (F) Kel-F valve. (G) FEP U-trap. (H) Vacuum manifold. (I) Greaseless J-Young valve with PTFE barrel. (J) ¼-in o.d. PTFE Swagelok or ¼-in. stainless steel Swagelok Ultra-Torr connector. Reproduced with permission from ref. 1.

2.3.2. Low-Temperature Crystal Mounting

Because the samples investigated in this work were thermally unstable and/or moisture sensitive, all crystals were mounted at low temperatures using the apparatus depicted in Figures 2.8 and 2.9. While maintaining the sample at –78 ^{o}C, the reaction vessels were first cut open below the Kel-F valve and then quickly dumped into to the 10-mm o.d. aluminum trough of the crystal mounting apparatus (Figure 2.8) which had been precooled (–104 $\pm$2 ^{o}C) by a regulated flow of dry nitrogen gas through a 5-L dewar filled with liquid N_2. In some instances, an analogous setup was used which instead had a larger, 25-mm o.d. FEP trough instead of the aluminum trough. The temperature inside the trough was measured using a copper-constantan thermocouple positioned in the sample region of the trough. Using an additional glass sleeve, which was concentrically fitted around the silvered cold-flow dewar, an ambient nitrogen gas was slowly passed through the sleeve in order to maintain a laminar flow, thereby inhibiting the formation of frost accumulation inside the trough. Crystals were then selected using a stereo-zoom microscope and mounted on either a glass fibre (0.05 to 0.1-mm o.d.) or nylon cryoloop (MiTeGen MicroMounts^{TM}), outfitted with a magnetic base, using perfluorinated polyether oil (Ausimont Inc., Fomblin Z15 or Z25) which served as an adhesive upon freezing at low temperature. The magnetic wand (Hampton Research) served as the magnetic base to which the encapsulated frozen crystal was attached on the adjustable support stag. This permitted inspection of mounted individual crystals under the stereo-zoom microscope prior to transfer to the goniometer head. Following inspection, the mounted crystal and magnetic pin were quickly (ca. 5 s) transferred from

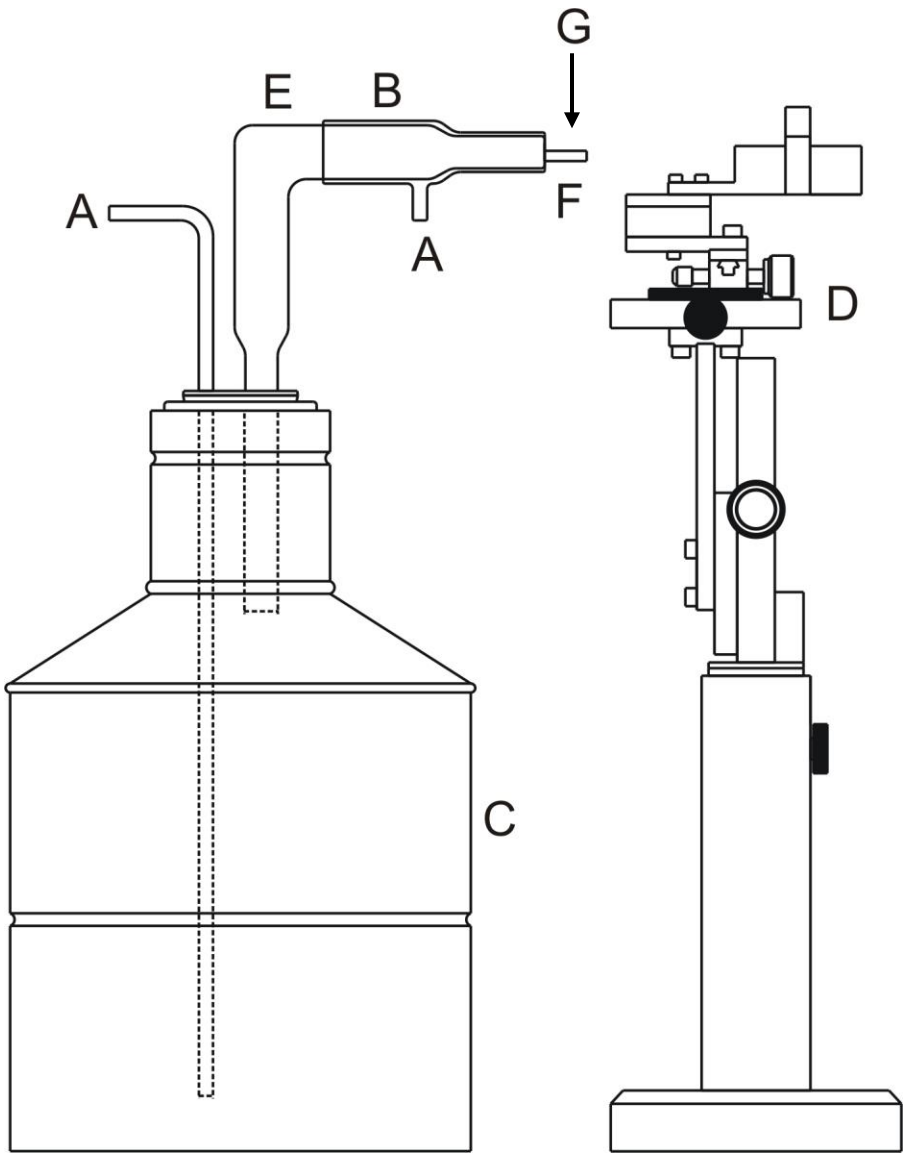

Figure 2.8. Low-temperature crystal mounting apparatus. (A) Nitrogen inlet. (B) Glass sleeve for ambient nitrogen flow. (C) Liquid N_2 dewar. (D) Adjustable support stage. (E) Silvered dewar (glass). (F) Aluminum trough. (G) Stereo-zoom microscope. Reproduced with permission from ref. 1.

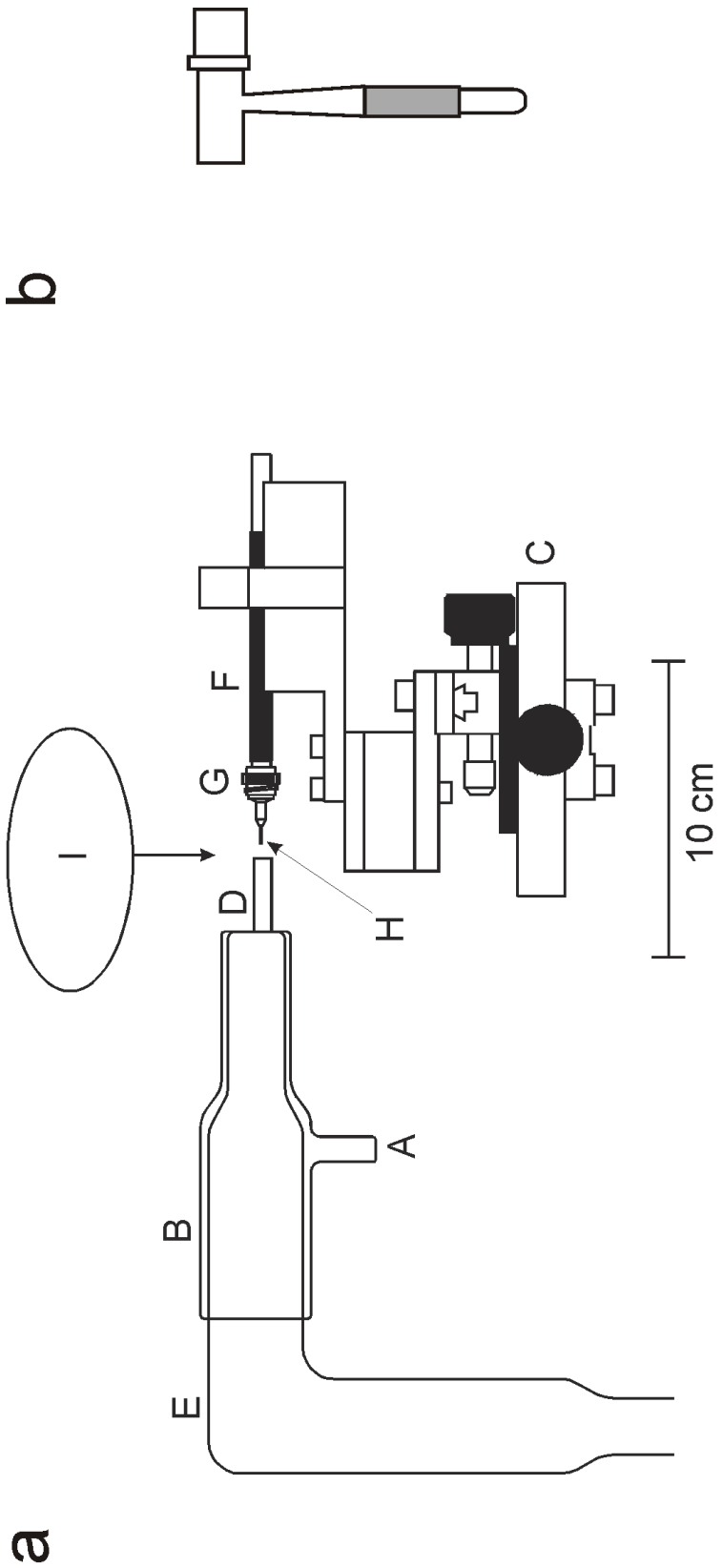

Figure 2.9. (a) Enlarged view of a portion of the apparatus used to mount single crystals; (A) Ambient nitrogen gas flow inlet. (B) Glass sleeve for ambient nitrogen gas flow. (C) Adjustable support stage. (D) Aluminum trough. (E) Silvered glass jacketed dewar. (F) Magnetic-tipped wand affixed to (G) the magnetic-based copper pin-fibre assembly. (H) Glass fibre. (I) Stereo-zoom microscope. (b) A set of cryotongs employed in the transfer of the copper pin-fibre assembly with attached crystal from the support stage to the goniometer head. Reproduced with permission from ref 1.

the crystal mounting apparatus to the magnetic mount of the goniometer head by means of a cryotong (Hampton Research) which was precooled in liquid N_2 prior to use. The crystals were maintained at low temperature on the goniometer head by a cold N_2 gas flow provided by an Oxford Cryosystems low-temperature cryostream accessory.

2.3.3. Data Collections

The crystallographic data were acquired using a Bruker SMART APEX II diffractometer that was equipped with an APEX II 4K CCD (charge-coupled device) area detector and a triple-axis goniometer controlled by either the APEX2 or APEX3 Graphical Use Interface (GUI) software.[29] Graphite-monochromated Mo Kα radiation (λ = 0.71073 Å) was used in the case of $Hg(OTeF_5)_2$ and $Hg(OTeF_5)_2 \cdot 1.5XeF_2$, whereas a Bruker Triumph curved crystal monochromator with a Mo Kα (λ = 0.71073 Å) radiation source was used for all remaining compounds. Diffraction data collections were carried out at –173 ^{o}C and consisted of a ω scans and sometimes ϕ-rotations which were fixed at $\chi = 54.74^{o}$ and collected at 0.5° intervals. The crystal-to-detector distance was between 4.946–4.960 cm, and the data collections were carried out in a 512 × 512 pixel mode using 2 × 2 pixel binning. Processing of the raw data was completed using the APEX GUI software,[29] which applied Lorentz and polarization corrections to three-dimensionally integrated diffraction spots.

2.3.4. General Solutions and Data Refinements

Specific solutions and refinements are discussed in each Chapter of the thesis. For non-twinned data, the program SADABS[30] was used for the scaling of diffraction data,

the application of a decay correction, and an empirical absorption correction based on the intensity ratios of redundant reflections. The XPREP[31] program was used to confirm the unit cell dimensions and the crystal lattices. Cell Now[32] was used to find unit cells for non-merohedrally twinned or multiple crystals, and the program TWINABS[33] was used to scale and process the resulting data. Structure solutions were obtained by intrinsic phasing or direct methods. The final refinements were obtained by introducing anisotropic parameters for all atoms (except hydrogen), any suggested extinction parameter, and the recommended weight factor. The maximum electron densities in the final difference Fourier maps were located around the heavy atoms. All calculations were performed using the SHELXTL package for the structure determination, refinement, and molecular graphics.[34]. The PLATON[35] program was used to ensure no additional or alternative symmetries were present. The Olex2[36] and Mercury[37] programs were also used to visualize structures.

2.4. Raman Spectroscopy

All Raman spectra were recorded on a Bruker RFS 100 Fourier transform Raman spectrometer employing a quartz beam splitter and a liquid-nitrogen cooled Ge diode detector. The 1064-nm line of a Nd-YAG laser was used for excitation with a laser spot of < 0.1 mm at the sample and configured such that only the 180^{o}-backscattered radiation was detected. The scanner velocity was 5 kHz and the wavelength range was 5894 to 10394 cm^{-1} relative to the laser line at 9394 cm^{-1}, resulting in a spectral range of 3501 to –999 cm^{-1}. Fourier transformations were processed using a Blackman Harris 4-term

apodization and a zero-filling factor of 2. Typical acquisitions used 1.0 cm^{-1} resolution, 500 mW power, and ~1000–1200 scans. Low-temperature spectra were acquired using a Bruker I0121 low-temperature accessory which provided temperatures ranging from −40 to –160 ^{o}C for routine samples, with an estimated error of $\pm$0.5 ^{o}C.

2.5. Nuclear Magnetic Resonance Spectroscopy

The ^{19}F NMR spectra were recorded on a Bruker AVANCE DRX-500 spectrometer equipped with an 11.744-T cryomagnet. Low-temperature spectra were obtained by cooling the NMR probe using a nitrogen flow and variable temperature controller (BVT-3000). The chemical shift convention used is a positive (negative) sign indicates a chemical shift to high (low) frequency of the reference compound.

To confirm that the formation of TeF_6 resulted from oxygen/fluorine metatheses to yield $[Hg(OTeF_5)(NSOF_2)\cdot NSF_3]_\infty$ and $[Hg_3(OTeF_5)_5(NSOF_2)\cdot 2NSF_3]_2$ in Chapter 3, ^{19}F spectra were recorded unlocked (field drift < 0.1 Hz h^{-1}) at –35 ^{o}C using a 5-mm broad band reverse (BBR) probe operating at 470.631 MHz. Spectra were recorded in 65 K memory, with a spectral width setting of 47 kHz, yielding data-point resolutions of 0.72 Hz/data point and acquisition times of 1.43 s. The pulse width, corresponding to a bulk magnetization tip angle of approximately 90^{o}, was 10 μs. A relaxation delay of 2.00 s was used, and 128 transients were accumulated. A line broadening of 0.50 Hz was used in the exponential multiplication of the free induction decays prior to Fourier transformation. Fluorine-19 spectra were referenced externally at –35 ^{o}C to samples of neat $CFCl_3$.

In Chapter 4. the spectrum of $Hg(OTeF_5)_2$ was recorded at 25 ^oC using a 5-mm combination $^1H/^{19}F$ probe operating at 470.568 MHz. The ^{19}F spectrum was recorded in 32 K memory, using a spectral width setting of 24 kHz, yielding a data-point resolution of 0.73 Hz/data point and an acquisition time of 0.68 s. The pulse width, corresponding to bulk magnetization tip angles of approximately 90° was 7.7 μs. A relaxation delay of 2 s was used, and 1200 transients were accumulated. A line broadening of 0.3 Hz was used in the exponential multiplication of the free induction decay prior to Fourier transformation. The ^{19}F spectrum was referenced externally at room temperature (25 °C) to a sample of neat $CFCl_3$.

2.6. References

(1) Leblond, N. Ph. D. Thesis, McMaster University, Hamilton, ON, Canada, 1998.

(2) Reddy, V. P; Bellew, D. R.; Prakash, G. K. S. *J. Fluorine Chem.* **1992**, *56*, 195–197.

(3) Brock, D. S. Ph. D. Thesis, McMaster University, Hamilton, ON, Canada, 2011.

(4) Winfield, J. M. *J. Fluorine Chem.* **1984**, *25*, 91−98.

(5) Breuer, G. *Handbuch der Präparafiven Anorgansichen Chemie*, vol. 1, Ed. F. Enke, Verlag, Stuttgart, Germany, **1960**, pp. 189.

(6) Mercier, H. P. A.; Sanders, J. C. P.; Schrobilgen, G. J.; Tsai, S. S. *Inorg. Chem.* **1993**, *32*, 386−393.

(7) Emara, A. A. A.; Lehmann, J. F.; Schrobilgen, G. J. *J. Fluorine Chem.* **2005**, *126*, 1373–1376.

(8) Mercier, H. P. A.; Sanders, J. C. P.; Schrobilgen, G. J.; Tsai, S. S. *Inorg. Chem*. 1993, *32*, 386−393.

(9) Kinkead, S. A; FitzPatrick, J. R.; Foropoulos, J. J.; Kissane, R. J.; Purson, J. D. *In Fluorine Chemistry Toward the 21st Century*; Thrasher, J. S., Strauss, S. H., Eds.; ACS Symposium Series 555; American Chemical Society: Washington, DC, 1994; Chapter 3, pp 40−55.

(10) Mayer, E.; Sladky, F. *Inorg. Chem.* **1975**, *14*, 589−592.

(11) Dillon, K. B.; Platt, A. W. G. *J. Chem. Soc., Dalton Trans.* **1982**, 1199−1204.

(12) Mercier, H. P. A.; Sanders, J. C. P.; Schrobilgen, G. J. *J. Am. Chem. Soc.* **1994**, *116*, 2921−2937.

(13) Moock, K.; Seppelt, K. *Z. Anorg. Allg. Chem.* **1988**, *561*, 132−138.

(14) Mazej, Z.; Goreshnik, E. A. *J. Solid State Chem.* **2015**, *228*, 59–59.

(15) Frlec, B.; Gantar, D.; Holloway, J. H. *J. Fluorine Chem.* **1982**, *19*, 485–500.

(16) Frlec, B.; Gantar, D.; Holloway, J. H. *J. Fluorine Chem.* **1982**, *20*, 217–226.

(17) Kropshofer, H.; Leitzke, O.; Peringer, P.; Sladky, F. *Chem. Ber.* **1981**, *114*, 2644–2648.

(18) Lentz, D.; Seppelt, K. Z. *Anorg. Allg. Chem.* **1983,** *502*, 83–88.

(19) Mews, R.; Keller, K.; Glemser, O. *Inorg. Synth.* **1986,** *24*, 12–17.

(20) Smith, G. L. Ph. D. Thesis, McMaster University, Hamilton, ON, Canada, 2010.

(21) Mercier, H. P. A.; Moran, M. D.; Sanders, J. C. P.; Schrobilgen G. J. S.; Suontamo, R. J. *Inorg. Chem.* **2005**, *44*, 49–60

(22) Christe, K. O.; Schack, C. J.; Wilson, R. D. *Inorg. Chem.* **1975**, *14*, 2224–2230.

(23) Gerken, M.; Moran, M. D.; Mercier, H. P. A.; Pointner, B. E.; Schrobilgen, G. J.; Hoge, B.; Christe, K. O.; Boatz, J. A. *J. Am. Chem. Soc.* **2009**, *131*, 13474–13489.

(24) Bezmel'nitsyn, V. N.; Legasov, V. A.; Chaivanov, B.B. *Dokl. Akad. Nauk. SSSR* **1977**, *235*, 96−98; *Dokl. Chem.* **1977**, *235*, 365−367.

(25) Kinkead, S. A.; FitzPatrick, J. R.; Foropoulos, Jr, J.; Kissane, R. J.; Purson, J. D. *ACS Symp. Ser.* **1994**, *555*, 40−55.

(26) Lehmann, J. F.; Mercier, H. P. A.; Schrobilgen, G. J. *Coord. Chem. Rev*. **2002**, *233-234*, 1−39.

(27) Seppelt, K.; Nothe, D. *Inorg. Chem.* **1973**, *11*, 2727 −2730.

(28) DeBackere, J. R.; Mercier, H. P. A.; Schrobilgen, G. J. *J. Am. Chem. Soc*. **2014**, *136*, 3888−3903.

(29) a) *APEX2*, release v2011.6-1; Bruker AXS, Inc.: Madison, WI, **1995**; b) *APEX3*, release v2017.3-0; Bruker AXS, Inc.: Madison, WI, **2017**.

(30) Sheldrick, G. M. *SADABS* (Siemens Area Detector Absorption Corrections), version 2.10; Siemens Analytical X-ray Instruments, Inc.: Madison, WI, **2004**.

(31) Bruker. XPREP v2008/2. Bruker AXS Inc.: Madison, WI, **2014**.

(32) Sheldrick, G. M. *CELL_NOW*, 2008/4, University of Göttingen: Göttingen, Germany.

(33) Sheldrick, G. M. *TWINABS*, 2008/4, University of Göttingen: Göttingen, Germany.

(34) Sheldrick, G. M. SHELXTL-plus, release 6.14; Siemens Analytical Xray Instruments, Inc.: Madison, WI, 1993−2014.

(35) a) Spek, A. L. *Acta Crystallogr. D* **2009**, *65*, 148; b) Spek, A. L. *PLATON* - A Multipurpose Crystallographic Tool; Utrecht University, Utrecht, The Netherlands, **2011**.

(36) Dolomanov, O. V.; Bourhis, L. J.; Gildea, R. J.; Howard, J. A. K.; Puschmann, H., *J. Appl. Cryst.* **2009**, *42*, 339−341.

(37) Macrae, C. F.; Bruno, I. J.; Chisholm, J. A.; Edgington, P. R.; McCabe, P.; Pidcock, E.; Rodriguez-Monge, L.; Taylor, R.; van de Streek, J.; Wood, P. A. *J. Appl. Cryst.* **2008**, *41*, 466−470.

CHAPTER 3

Thiazyl Trifluoride (NSF_3) Adducts and Imidodifluorosulfate (F_2OSN-) Derivatives of $Hg(OTeF_5)_2$

Adapted with permission from: DeBackere, J.R., Mercier, H.P.A., and Schrobilgen, G.J. *Inorganic Chemistry*, **2015**, *54*, 9989–1000.

3.1. Introduction

Thiazyl trifluoride, NSF_3, has been of importance as a synthetic precursor and in the development of sulfur-nitrogen-fluorine chemistry.[1-4] The distorted tetrahedral geometry of NSF_3 has been thoroughly studied by ^{19}F NMR,[5] IR,[5-7] Raman,[8] and microwave spectroscopy[9] and, more recently, by low-temperature single-crystal X-ray diffraction.[10] The reactivity of NSF_3 may be generally described in terms of three reaction types: (1) addition to the π-system of the N≡S bond, (2) nucleophilic attack at the positively charged and coordinatively unsaturated sulfur(VI) atom, and (3) donation of the nitrogen electron lone pair to a Lewis acidic center.

The Lewis basicity of NSF_3 is illustrated by its reactions with the Lewis acids AsF_5, SbF_5, and BF_3, which yield the Lewis acid-base adducts $F_3S{\equiv}NAsF_5$,[3,11] $F_3S{\equiv}NSbF_5$,[11] and $F_3S{\equiv}NBF_3$.[6,12] Other NSF_3 adducts with main-group atom centers include $[(CF_3)_nSF_{3-n}N{\equiv}SF_3][AsF_6]$ (n = 0–2),[13] $[F_3S(N{\equiv}SF_3)_2][AsF_6]$,[14] $[F_4SNXeN{\equiv}SF_3][AsF_6]$,[14] and $[F_3S{\equiv}NXeF][AsF_6]$,[15] with the latter three adduct-cations and $F_3S{\equiv}NAsF_5$,[3] having been characterized by single-crystal X-ray diffraction. The reactions of NSF_3 with Lewis acidic metal centers have also been studied and provide a series of transition metal adducts $[M(N{\equiv}SF_3)_4(AsF_6)_2]$ (M = Mn, Fe, Co, Ni, Cu, Zn),[16–18]

$[CpFe(CO)_2N{\equiv}SF_3][AsF_6]$,[19] $[M(CO)_5N{\equiv}SF_3][AsF_6]$ (M = Mn, Re),[19,20] and $[Ag(N{\equiv}SF_3)_n][AsF_6]$ (n = 1, 2),[16] which have been structurally characterized by methods such as IR and/or Raman spectroscopy, NMR spectroscopy, and mass spectrometry. The only transition metal complexes of NSF_3 that have been characterized by single-crystal X-ray diffraction are $[M(N{\equiv}SF_3)_4(AsF_6)_2]$ (M = Mn,[17] Zn[18]), $[Re(CO)_5N{\equiv}SF_3][AsF_6]$,[19] and $[CpFe(CO)_2N{\equiv}SF_3][AsF_6]$[19] in which the NSF_3 ligands are terminally N-coordinated to the metal.

A considerable number of covalently bonded main-group derivatives of the F_2OSN-ligand are known as exemplified by $XNSOF_2$ (X = H, F, Cl, Br, I, $(Me)_3Si$, $CH_3OS(O)$, CF_3CO, CF_3S, $OCNSO_2$, Cl_3PNSO_2, OCNCO, $(C_6H_5)_4As$, $(C_6H_5)_4P$, $O{=}PF_2$, O=PFCl, $O{=}PCl_2$, $S{=}PCl_2$, $(CH_3)_2SnCl$, $(CH_3)_2SnBr$),[21-25] $X(NSOF_2)_2$ (X = $(CH_3)_2Si$, $(C_6H_5)CH_3Si$, OS, OSe, O_2S, O=PF, O=PCl, S=PCl, S=PF, $M(CH_3)_2Sn$),[22-25] and $X(NSOF_2)_3$ (X = B, P, As, Sb, CH_3Si, O=P, S=P),[22-25] $(N{=}CNSOF_2)_3$,[26] $[B(NSOF_2)_4]^-$,[27] $Si(NSOF_2)_4$,[22] $Sb(NSOF_2)_5$.[22,24] Examples of transition metal derivatives include $Hg(NSOF_2)_2$,[21] $AgNSOF_2$,[25] $Re(CO)_5[NSOF_2]$,[28] $[(CO)_4M(NSOF_2)]_2$ (M = Re,[28] Mn[28-30]), $M(NSOF_2)_2$ (M = Ni, Co, Cu),[31] $[Cu(NSOF_2)(AsF_5NSOF_2)]$,[31] $[Ni(SO_2)_2\{AsF_4(NSOF_2)_2\}_2]$,[31] as well as the $[Ag(NSOF_2)_2]^-$ [32] and $[M(NSOF_2)_4]^{2-}$ anions (M = Zn, Hg, Mn, Co, Pd, Cu).[32,33] Their structural characterizations have been limited to IR and/or Raman spectroscopy, NMR spectroscopy, electron diffraction, and mass spectrometry. The only F_2OSN-derivatives that have been characterized by single-crystal X-ray diffraction are $(NCNSOF_2)_3$,[26] $[Ni(SO_2)_2\{AsF_4(NSOF_2)_2\}_2]$,[31] and $[(CO)_4Mn(NSOF_2)]_2$.[29,30] In the case of $(NCNSOF_2)_3$, the trimeric structure is comprised

of an *s*-C_3N_3 ring in which the F_2OSN-groups are bonded to carbon.[26] The F_2OSN-ligands of the transition metal derivatives bridge two metal centers.

The X-ray crystal structure of $Hg(OTeF_5)_2$ consists of discrete $Hg(OTeF_5)_2$ units that interact through long Hg---O and Hg---F intermolecular contacts.[34] The Lewis acidity of $Hg(OTeF_5)_2$ was recently demonstrated by the formation of the noble-gas difluoride adducts, $Hg(OTeF_5)_2 \cdot 1.5NgF_2$ (Ng = Kr, Xe)[34] and a series of mercury(II) pentafluoro-oxotellurate(VI) anions.[35] The bulky, highly electronegative F_5TeO- (teflate) group is terminally bonded in the majority of its compounds. However, several examples of μ-oxygen bonded F_5TeO-groups are known, e.g., $Au(OTeF_5)_3$,[36] $[AgOTeF_5(C_6H_5Cl)_3)_2]_2$,[37] $[AgOTeF_5(1,2\text{-}C_2H_4Cl_2)]_2$,[38,39] $[Zn(OTeF_5)_2(C_6H_5NO_2)_2]_2$,[40] $[Ag(CO)][B(OTeF_5)_4]$,[41] and $Ag(CH_2C1_2)Pd(OTeF_5)_4$.[39,42] Oxygen-bridged F_5TeO-ligands have also been observed for several Hg(II) teflate salts, $[N(CH_3)_4]_2[Hg_2(OTeF_5)_6]$, $Cs_2[Hg(OTeF_5)_4] \cdot Hg(OTeF_5)_2$, and $\{Cs_3[Hg_2(OTeF_5)_7] \cdot Hg(OTeF_5)_2\} \cdot 4SO_2ClF$.

In view of the limited number of metal NSF_3 adducts that have been structurally characterized, and the absence of NSF_3 coordination complexes of mercury, the possible formation of NSF_3 adducts with $Hg(OTeF_5)_2$ and their structures were of interest. Prior to this study, the known transition metal complexes of NSF_3 had been limited to cations that were stabilized by the weakly fluoro-basic $[AsF_6]^-$ anion. The present study describes the reactivity of $Hg(OTeF_5)_2$ with NSF_3 and the formation and structural characterization of several neutral NSF_3 adducts and structurally related compounds that contain F_2OSN-groups.

3.2. Results and Discussion

3.2.1. Syntheses of $[Hg(OTeF_5)_2{\cdot}N{\equiv}SF_3]_\infty$, $[Hg(OTeF_5)_2{\cdot}2N{\equiv}SF_3]_2$, $Hg_3(OTeF_5)_6{\cdot}4N{\equiv}SF_3$, $[Hg(OTeF_5)(N{=}SOF_2){\cdot}N{\equiv}SF_3]_\infty$ and $[Hg_3(OTeF_5)_5(N{=}SOF_2){\cdot}2N{\equiv}SF_3]_2$

The compounds $[Hg(OTeF_5)_2{\cdot}N{\equiv}SF_3]_\infty$, $[Hg(OTeF_5)_2{\cdot}2N{\equiv}SF_3]_2$, and $Hg_3(OTeF_5)_6{\cdot}4N{\equiv}SF_3$ were synthesized by the reaction of $Hg(OTeF_5)_2$ with excess NSF_3 at 0 °C in their respective solvents (see Experimental Section), and were found to form mixtures of NSF_3 adducts. However, reactions carried out at room temperature over periods of several hours resulted in the mixed NSF_3/F_2OSN-derivatives, namely $[Hg(OTeF_5)(N{=}SOF_2){\cdot}N{\equiv}SF_3]_\infty$ and $[Hg_3(OTeF_5)_5(N{=}SOF_2){\cdot}2N{\equiv}SF_3]_2$. These observations were supported by Raman spectroscopy which showed the absence of F_2OSN-ligand stretching bands when reaction mixtures were not warmed above 0 °C for extended periods of time. However, when these reactions were carried out at room temperature in Freon-114® (1, 2-dichloromethane), and rapidly crystallized (within ca. 3 h), only $Hg_3(OTeF_5)_6{\cdot}4N{\equiv}SF_3$ was isolated. Low-temperature Raman spectra were recorded on the colorless crystalline products that were obtained by slow solvent evaporation. The Raman spectra, in conjunction with X-ray crystallographic unit cell determinations, were used to speciate the reaction mixtures.

3.2.2. Proposed Reaction Pathway for F_2OSN-group Formation

A proposed reaction pathway for the formation of the F_2OSN-group is provided in Scheme 3.1. The stable coordination compounds, $[Hg(OTeF_5)_2{\cdot}N{\equiv}SF_3]_\infty$, $[Hg(OTeF_5)_2{\cdot}2N{\equiv}SF_3]_2$, and $[Hg_3(OTeF_5)_6{\cdot}4N{\equiv}SF_3]$ are initially formed at 0 °C. At room temperature, nucleophilic attack by a F_5TeO-group occurs at sulfur (eq 2) to form the

Scheme 3.1. Proposed Reaction Pathway for the O/F Metatheses of $Hg(OTeF_5)_2$ Adducts of NSF_3.

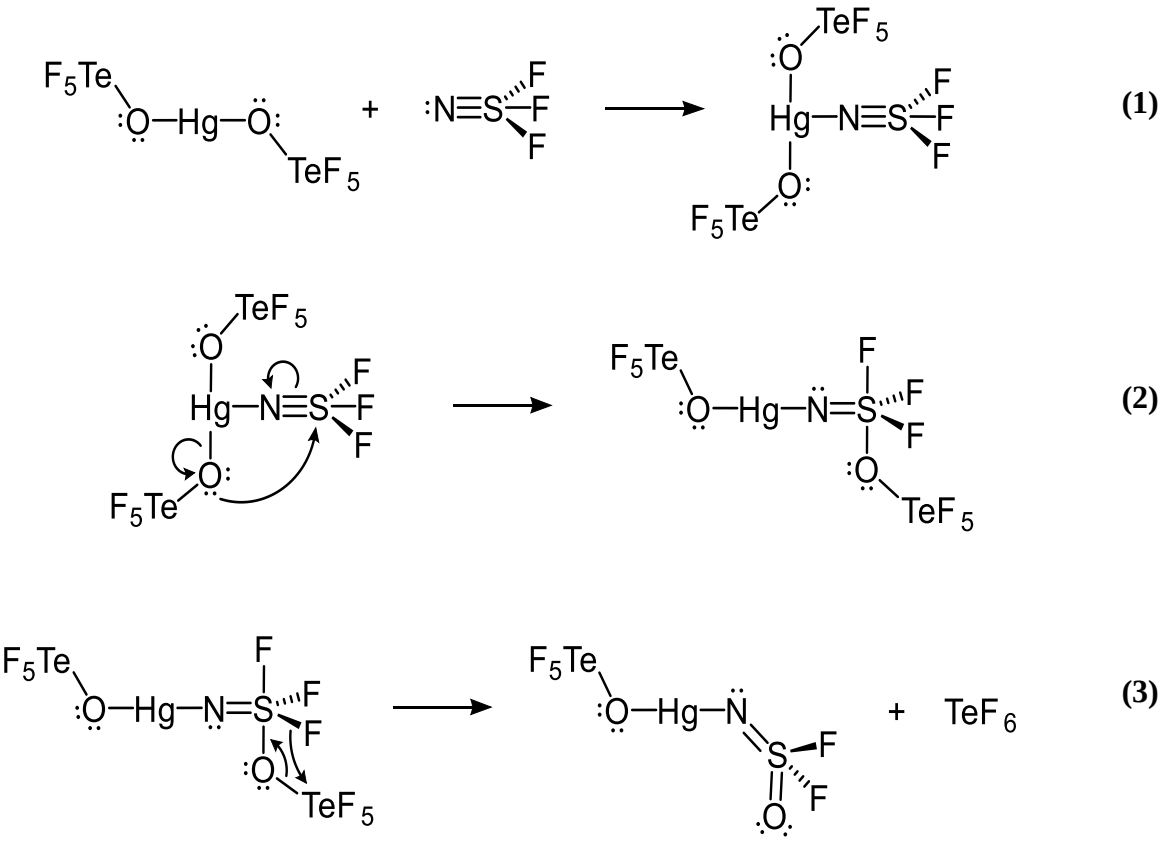

$(F_5TeO)F_3S{=}N$-ligand as an intermediate. The related $F_4S{=}N$-group was recently characterized by single-crystal X-ray diffraction in $[F_4S{=}NXe][AsF_6]$.[43] Subsequent F/O metathesis results in the elimination of gaseous TeF_6 from the intermediate, $(F_5TeO)Hg\{N{=}SF_3(OTeF_5)\}$, at room temperature leading to F_2OSN-group formation (eq 3). The formation of TeF_6 was confirmed by VT-^{19}F NMR spectroscopy for the reaction of $Hg(OTeF_5)_2$ with excess NSF_3 in Freon-114® solvent. After reaction at room temperature for 24 h, the volatile components of the reaction mixture were isolated by vacuum distillation and their ^{19}F NMR spectrum was recorded. The spectrum consisted of

intense resonances due to TeF_6 [–53.7 ppm, $^1J(^{125}Te–^{19}F)$ = 3738 Hz, $^1J(^{123}Te–^{19}F)$ = 3100 Hz], unreacted NSF_3 [67.9 ppm, $^2J(^{19}F–^{14}N)$ = 25.9 Hz], and Freon-114® (–72.4 ppm). The NMR parameters of TeF_6 are in good agreement with previously reported values.[44] Several very low-intensity AB_4 patterns assigned to F_5TeO-groups were also observed between –33 and –54 ppm.

The reaction of $Hg(OTeF_5)_2$ with NSF_3 at room temperature for 11 days in Freon-114® only yielded $[Hg(OTeF_5)(N{=}SOF_2){\cdot}N{\equiv}SF_3]_\infty$, with no sign of nucleophilic attack of NSF_3 by the remaining F_5TeO-group.

3.2.3. X-ray Crystallography

Summaries of the data collection parameters and other crystallographic information for $[Hg(OTeF_5)_2{\cdot}N{\equiv}SF_3]_\infty$ (**1**), $[Hg(OTeF_5)_2{\cdot}2N{\equiv}SF_3]_2$ (**2**), $Hg_3(OTeF_5)_6{\cdot}4N{\equiv}SF_3$ (**3**), $[Hg(OTeF_5)(N{=}SOF_2){\cdot}N{\equiv}SF_3]_\infty$ (**4**), and $[Hg_3(OTeF_5)_5(N{=}SOF_2){\cdot}2N{\equiv}SF_3]_2$ (**5**) are provided in Table 3.1. Selected bond lengths and bond angles are provided in Tables 3.2–3.6 and full lists of geometrical parameters are given in Tables S3.1–S3.6. In cases where NSF_3 and F_5TeO-groups are affected by disorder (see X-ray Crystallography), only the geometrical parameters of the ordered groups are discussed. The geometrical parameters associated with the F_5TeO-groups are in good agreement with previously published values[34,35] and do not require further commentary.

Table 3.1. Summaries of Crystal Data and Refinement Results for $[Hg(OTeF_5)_2 \cdot N{\equiv}SF_3]_\infty$ (**1**), $[Hg(OTeF_5)_2 \cdot 2N{\equiv}SF_3]_2$ (**2**), $Hg_3(OTeF_5)_6 \cdot 4N{\equiv}SF_3$ (**3**), $[Hg(OTeF_5)(N{=}SOF_2) \cdot N{\equiv}SF_3]_\infty$ (**4**), and $[Hg_3(OTeF_5)_5(N{=}SOF_2) \cdot 2N{\equiv}SF_3]_2$ (**5**)

compound	**(1)**	**(2)**	**(3)**	**(4)**	**(5)**
space group	$P2_1/n$	$P2_1/c$	$Pna2_1$	$P2_1/c$	$P\bar{1}$
a (Å)	6.6574(2)	8.295(2)	24.1661(15)	9.4117(6)	10.2252(11)
b (Å)	11.7945(4)	10.489(2)	13.7016(10)	21.6140(15)	10.9529(11)
c (Å)	15.5201(5)	17.853(4)	12.8714(8)	17.3578(12)	17.5285(19)
α (deg)	90.0	90.0	90.0	90.0	103.114(6)
β (deg)	94.305(2)	95.887(4)	90.0	104.116(1)	93.788(6)
γ (deg)	90.0	90.0	90.0	90.0	116.496(5)
V (Å^3)	1215.21(7)	1545.2(6)	4261.9(5)	3424.4(4)	1679.3(3)
molecules/ unit cell	4	2	4	12	1
mol wt (g mol^{-1})	780.86	883.93	2445.65	642.33	2100.98
calcd density (g cm^{-3})	4.268	3.800	3.812	3.738	4.155
T (^{o}C)	–173	–173	–173	–173	–173
μ (mm^{-1})	17.71	14.112	15.22	16.49	18.34
$R_1{}^a$	0.0307	0.0568	0.0387	0.0250	0.0502
$wR_2{}^b$	0.0563	0.1093	0.0849	0.0519	0.1140

$^a R_1$ is defined as $\Sigma \| F_o | - | F_c \| / \Sigma | F_o |$ for $I > 2\sigma(I)$. $^b wR_2$ is defined as $[\Sigma[w(F_o^2 - F_c^2)^2]/\Sigma w(F_o^2)^2]^{½}$ for $I > 2\sigma(I)$.

3.2.3.1. X-ray Crystal Structure of $[Hg(OTeF_5)_2 \cdot N{\equiv}SF_3]_\infty$.

The crystal structure of $[Hg(OTeF_5)_2 \cdot N{\equiv}SF_3]_\infty$ (Figure 3.1) consists of well-isolated chains which run parallel to the *a*-axis of the crystallographic unit cell. The chains interact with one another through weak F---F intermolecular contacts (2.75(6)–2.94(8) Å) that are close to twice the F van der Waals radius (2 x 1.47 Å).[45] The repeat unit of the chain consists of a $Hg(OTeF_5)_2$ molecule that is N-coordinated to an NSF_3 molecule. The coordination sphere of each mercury atom is comprised of four bridging

Table 3.2. Selected Experimental Geometrical Parameters for $[Hg(OTeF_5)_2 \cdot N{\equiv}SF_3]_\infty$

Bond Lengths (Å)			
$Hg_1–O_1$	2.241(4)	Te–O	1.811(5)–1.812(4)
$Hg_1–O_2$	2.227(5)	Te–F	1.823(6)–1.871(5)
$Hg_1–O_{1A}$	2.502(4)		
$Hg_1–O_{2B}$	2.470(4)	N–S	1.398(5)
$Hg_1–N_1$	2.112(5)	S–F	1.489(6)–1.516(7)
Bond Angles (deg)			
$O_1–Hg_1–O_2$	84.5(2)	$O_1–Hg_1–O_{1A}$	76.5(2)
$N_1–Hg_1–O_1$	134.5(2)	$O_1–Hg_1–O_{2B}$	108.0(2)
$N_1–Hg_1–O_2$	140.9(2)	$O_2–Hg_1–O_{1A}$	99.6(2)
$N_1–Hg_1–O_{1A}$	92.1(2)	$O_2–Hg_1–O_{2B}$	75.4(2)
$N_1–Hg_1–O_{2B}$	88.7(2)	$O_{1A}–Hg_1–O_{2B}$	172.6(2)
$Hg_1–N_1–S_1$	160.5(4)		
N–S–F	119.3(6)–128(3)	F–S–F	95.4(8)–96.5(7)

The atom labeling scheme corresponds to that used in Figure 3.1. See Table S3.1 for a complete list of geometrical parameters.

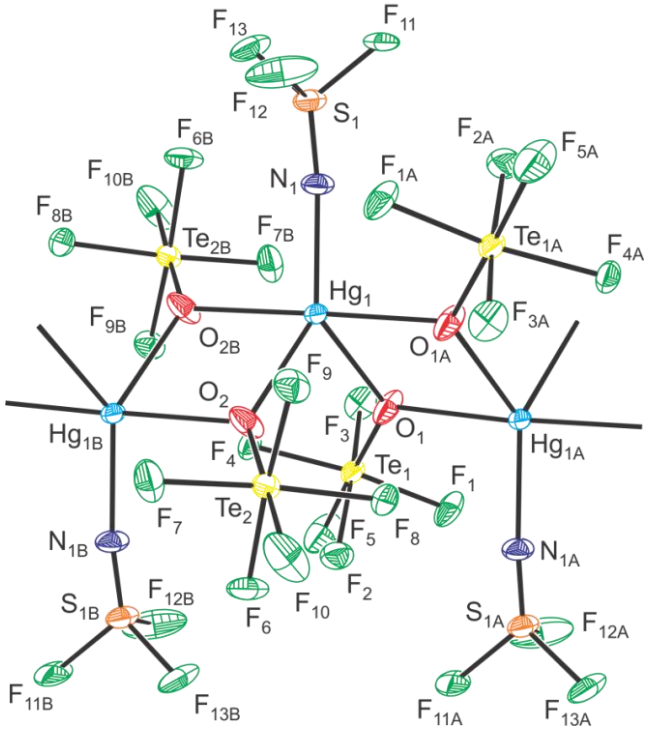

Figure 3.1. The X-ray crystal structure of $[Hg(OTeF_5)_2 \cdot N{\equiv}SF_3]_\infty$ showing the bonding to symmetry equivalent atoms in the chain structure and the orientations of the coordinated NSF_3 molecules along the *a*-axis of the unt cell. Thermal ellipsoids are shown at the 50% probability level.

F_5TeO-groups ($Hg_{(1)}$–$O_{(2)}$, 2.227(5) Å; $Hg_{(1)}$–$O_{(1)}$, 2.241(4) Å; $Hg_{(1)}$–$O_{(1A)}$, 2.470(4) Å; $Hg_{(1)}$–$O_{(2B)}$, 2.502(4) Å), two of them being symmetry related, and a terminal NSF_3 group (Hg–N, 2.122(5) Å). The ligand atom arrangements around each five-coordinate mercury atom lie between a square pyramid and a trigonal bipyramid as indicated by the τ-parameter,[46] 0.548, where $\tau = |\beta - \alpha|/60$ and β and α are the two largest coordination angles involving different ligand atoms in the mercury coordination sphere. The ideal values for a square pyramid and a trigonal bipyramid are 0 and 1, respectively. The Hg–O bond lengths are longer than those of $Hg(OTeF_5)_2$ (2.016(6) Å). Bond elongations presumably result from electron density donated to the Lewis-acidic mercury center by the nitrogen lone pair of NSF_3 which, in turn, diminishes the covalent characters of the Hg–O bonds. This is also reflected in the Te–O bond lengths, which are shorter (1.798(2)–1.802(2) Å) than the Te–O bonds of $Hg(OTeF_5)_2$ (1.842(7) Å), and is consistent with enhancement of the π characters of their Te–O bonds.[35] The Te–O bond lengths of $[Hg(OTeF_5)_2{\cdot}N{\equiv}SF_3]_\infty$ are comparable to the Te–O_μ bond lengths of $[Hg_2(OTeF_5)_6]^{2-}$ (1.790(4) and 1.802(4) Å).[35] The $O_{(1A)}$–$Hg_{(1)}$–$O_{(2B)}$ angle (172.6(2)°) is comparable to that of $Hg(OTeF_5)_2$ (170.5(4)°) in its crystal structure,[34] which also exhibits a *gauche* conformation. The Hg–N bond length (2.122(5) Å) is similar to those of $Hg(NSF_2)_2$ (2.050(13) Å),[47] and $[Hg(N_3)_3]^-$ (2.077(4)–2.113(2) Å).[48] The Hg–N–S angle is bent (160.5(4)°), as previously observed in $[Mn(N{\equiv}SF_3)_4][AsF_6]_2$ (162.0(3)°),[17] and is significantly less than the ideal 180° angle observed in $F_5AsN{\equiv}SF_3$,[3] suggesting that intra- and/or intermolecular contacts within the crystal lattice may be responsible for the bent angle. An even more severely bent angle occurs in $[F_3S{\equiv}NXeF][AsF_6]$ (∠Xe–N–S,

142.6(3)°), whereas quantum-chemical calculations predict a linear structure, thus supporting the influence of crystal packing on the Xe–N–S angle,[15] and by inference, on the Hg–N–S angle.

The S–F (1.489(6)–1.516(7) Å) bond lengths are comparable to those of $[M(N{\equiv}SF_3)_4(AsF_6)_2]$ (Mn, 1.501(5)–1.511(4) Å; Zn, 1.423(9)–1.515(5) Å),[17,18] $[Re(CO)_5N{\equiv}SF_3][AsF_6]$ (1.499(10) Å),[19] and $[CpFe(CO)_2N{\equiv}SF_3][AsF_6]$ (1.512(3)–1.519(3) Å).[19] The shorter S–F bond lengths of adducted NSF_3 relative to those of free NSF_3 (1.531(1)–1.534(2) Å) are consistent with adduct formation.[10] The N–S bond lengths (1.398(5) Å) are also comparable to those of $[M(N{\equiv}SF_3)_4(AsF_6)_2]$ (Mn, 1.357(6)–1.373(5) Å; Zn, 1.350(7)–1.387(6) Å), $[Re(CO)_5N{\equiv}SF_3][AsF_6]$ (1.384(14) Å), $[CpFe(CO)_2N{\equiv}SF_3][AsF_6]$ (1.376(3) Å), and free NSF_3 (1.400(3) Å). The N–S–F (119.3(6)–121.8(6)°) and F–S–F (95.6(5)–96.5(4)°) bond angles are similar to those of the metal complexes and free NSF_3 and require no further commentary.

3.2.3.2. X-ray Crystal Structure of $[Hg(OTeF_5)_2{\cdot}2N{\equiv}SF_3]_2$

The crystal structure of $[Hg(OTeF_5)_2{\cdot}2N{\equiv}SF_3]_2$ (Figure 3.2) consists of well-isolated dimers with the shortest intermolecular F---F distances (2.732(11)–2.930(12) Å) being close to the sum of twice the F van der Waals radius (2.94 Å). The mercury coordination spheres are comprised of a terminal F_5TeO-group (Hg–O, 2.154(8) Å), two bridging F_5TeO_μ-groups (Hg–O_μ, 2.348(7), 2.467(8) Å), and two N-coordinated NSF_3 molecules (Hg–N, 2.164(10), 2.377(10) Å). Aspects of this structure are similar to those of the dimeric $[Hg_2(OTeF_5)_6]^{2-}$ anion, which has slightly shorter Hg–O (2.040(4)–2.104(5) Å) and comparable Hg–O_μ (2.350(4)–2.508(4) Å) bond lengths.[35]

Table 3.3. Selected Experimental Geometrical Parameters for $[Hg(OTeF_5)_2 \cdot 2N{\equiv}SF_3]_2$

Bond Lengths (Å)			
$Hg_1–O_1$	2.154(8)	Te–O	1.798(7)–1.820(8)
$Hg_1–O_2$	2.348(7)	Te–F	1.820(8)–1.858(7)
$Hg_1–O_{2A}$	2.467(8)		
$Hg_1–N_1$	2.164(10)	N–S	1.388(10)–1.394(10)
$Hg_1–N_2$	2.377(10)	S–F	1.498(7)–1.544(7)
Bond Angles (deg)			
$O_1–Hg_1–O_2$	94.0(3)	$Hg_1–O_2–Hg_{1A}$	100.8(3)
$O_1–Hg_1–O_{2A}$	86.4(3)	$Hg_1–N_1–S_1$	154.7(7)
$O_1–Hg_1–N_1$	169.3(4)	$Hg_1–N_2–S_2$	150.8(6)
$O_1–Hg_1–N_2$	94.4(3)	$N_1–Hg_1–N_2$	93.3(4)
$O_2–Hg_1–O_{2A}$	79.2(3)	$N_1–Hg_1–O_{2A}$	85.4(3)
$O_2–Hg_1–N_1$	91.2(3)	$N_2–Hg_1–O_{2A}$	174.8(3)
$O_2–Hg_1–N_2$	105.9(3)		
N–S–F	119.3(6)–123.1(6)	F–S–F	94.3(4)–96.6(4)

The atom labeling scheme corresponds to that used in Figure 3.2. See Table S3.2 for a complete list of geometrical parameters.

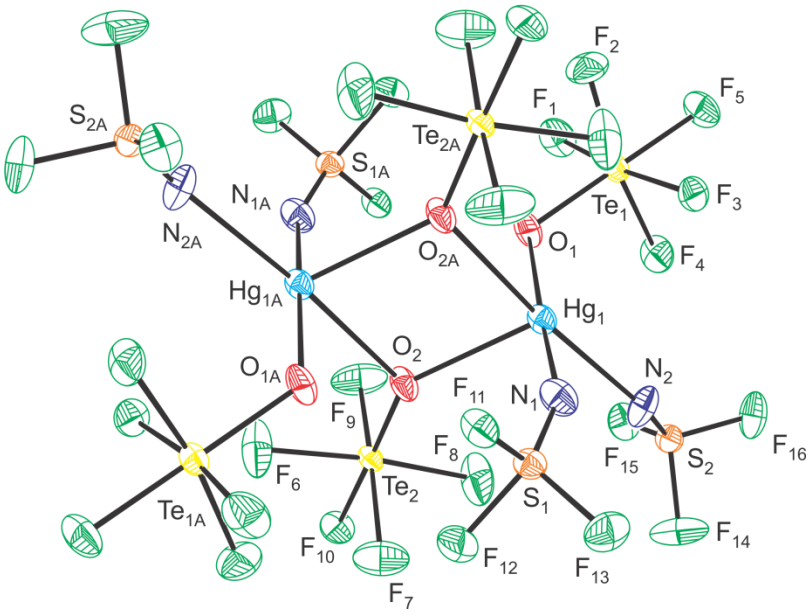

Figure 3.2. The X-ray crystal structure of dimeric $[Hg(OTeF_5)_2 \cdot 2N{\equiv}SF_3]_2$ showing the $(HgO_\mu)_2$ ring. Thermal ellipsoids are shown at the 50% probability level.

In the present instance, the dimeric structure is generated through an inversion center, i.e., the adduct is comprised of two crystallographically equivalent $Hg(OTeF_5)_2(N{\equiv}SF_3)_2$ moieties that are coordinated to one another through two bridging F_5TeO_μ-groups. As observed in $[Hg_2(OTeF_5)_6]^{2-}$, the O_μ atoms and the two Hg atoms form a $(HgO_\mu)_2$ ring. The Hg−O_μ−Hg (100.8(3)°) and O_μ−Hg−O_μ (79.2(3)°) bridge angles are comparable to those of $[Hg_2(OTeF_5)_6]^{2-}$ (∠Hg−O_μ−Hg, 102.1(1)°, 104.6(1)°; ∠O_μ−Hg−O_μ, 70.1(1)°, 73.9(1)°).[35] The τ-parameter, 0.092, associated with the Hg coordination sphere is close to that of a square pyramid (see above). The $O_{(2)}$ atom occupies the axial position whereas the remaining ligand atoms ($O_{(2A)}$, $O_{(1)}$, $N_{(1)}$, and $N_{(2)}$) occupy the equatorial positions of the square pyramid.

The coordinated NSF_3 molecules possess N–S (1.388(10), 1.394(10) Å) and S–F (1.498(7)–1.544(7) Å) bond lengths, as well as ∠N–S–F (119.3(6)–123.1(6)°) and ∠F–S–F (94.3(4)–96.6(4)°) bond angles that are comparable to those of $[Hg(OTeF_5)_2{\cdot}N{\equiv}SF_3]_\infty$ (see above). The more weakly coordinated NSF_3 ligands (Hg_1−N_2, 2.377(10) Å) lie in the plane of the $(HgO_\mu)_2$ ring, whereas the more strongly bonded NSF_3 ligands (Hg_1−N_1, 2.164(10) Å) are perpendicular to the $(HgO_\mu)_2$ ring and lie on either side of the ring. The Hg–N–S angles (150.8(6), 154.7(7)°) are more closed than those of $[Hg(OTeF_5)_2{\cdot}N{\equiv}SF_3]_\infty$.

3.2.3.3. X-ray Crystal Structure of $Hg_3(OTeF_5)_6{\cdot}4N{\equiv}SF_3$

The crystal structure of $Hg_3(OTeF_5)_6{\cdot}4N{\equiv}SF_3$ (Figure 3.3) consists of a well-isolated structural unit, with the shortest intermolecular F---F distances ranging from 2.68(3) to 2.94(2) Å, close to twice the sum of the fluorine van der Waals radii. The

Table 3.4. Selected Experimental Geometrical Parameters for $Hg_3(OTeF_5)_6 \cdot 4N{\equiv}SF_3$

Bond Lengths (Å)			
$Hg_1–O_1$	2.327(8)	$Hg_3–O_1$	2.644(7)
Hg_1---O_2	2.781(11)	Hg_3---O_2	2.723(11)
$Hg_1–O_5$	2.307(10)	$Hg_3–O_3$	2.192(9)
$Hg_1–O_4$	2.301(8)	$Hg_3–O_4$	2.292(8)
$Hg_1–N_1$	2.265(11)	$Hg_3–N_2$	2.234(11)
$Hg_1–N_4$	2.223(10)	$Hg_3–N_3$	2.240(11)
$Hg_2–O_1$	2.501(8)	Te–O	1.787(8)–1.836(7)
$Hg_2–O_2$	2.143(7)	Te–F	1.806(10)−1.860(10)
$Hg_2–O_3$	2.501(8)		
$Hg_2–O_5$	2.557(9)	N–S	1.371(11)−1.398 (11)
$Hg_2–O_6$	2.051(9)	S–F	1.506(5)−1.536(7)
Bond Angles (deg)			
$Hg_1–O_1–Hg_2$	96.2(4)	$O_5–Hg_2–O_3$	136.3(4)
$Hg_1–O_1–Hg_3$	95.7(4)	$O_5–Hg_2–O_1$	70.2(4)
$Hg_2–O_1–Hg_3$	90.0(3)	$O_5–Hg_2–O_2$	75.8(4)
$Hg_1–O_2–Hg_2$	92.9(4)	$O_3–Hg_2–O_1$	70.0(4)
$Hg_1–O_2–Hg_3$	84.2(3)	$O_3–Hg_2–O_2$	76.0(4)
$Hg_2–O_2–Hg_3$	96.0(4)	$O_1–Hg_2–O_2$	73.1(4)
$Hg_1–O_4–Hg_3$	107.0(4)	$O_2–Hg_3–O_3$	70.6(4)
$Hg_3–O_3–Hg_2$	101.4(5)	$O_2–Hg_3–O_4$	73.2(4)
$Hg_2–O_5–Hg_1$	95.1(4)	$O_2–Hg_3–O_1$	62.4(3)
$N_1–Hg_1–N_4$	94.3(7)	$O_3–Hg_3–O_4$	136.6(4)
$N_2–Hg_3–N_3$	108.7(6)	$O_3–Hg_3–O_1$	72.1(4)
$O_5–Hg_1–O_1$	77.8(4)	$O_4–Hg_3–O_1$	70.4(4)
$O_5–Hg_1–O_2$	69.0(4)	$O_1–Hg_1–O_4$	76.3(4)
$O_5–Hg_1–O_4$	139.4(4)	$O_2–Hg_1–O_4$	71.9(3)
$O_1–Hg_1–O_2$	65.2(3)		
$Hg_1–N_1–S_1$	151(1)	$Hg_3–N_3–S_3$	166(1)
$Hg_1–N_4–S_4$	176(1)	$Hg_3–N_2–S_2$	161(1)
N–S–F	116.3(12)–126.4(12)	F–S–F	93.5(8)–98.0(8)
Dihedral Angles (deg)			
$Te_6–O_6–Hg_2–O_2–Te_2$	5.8 (8)		

The atom labeling scheme corresponds to that used in Figure 3.3. See Table S3.3 for a complete list of geometrical parameters.

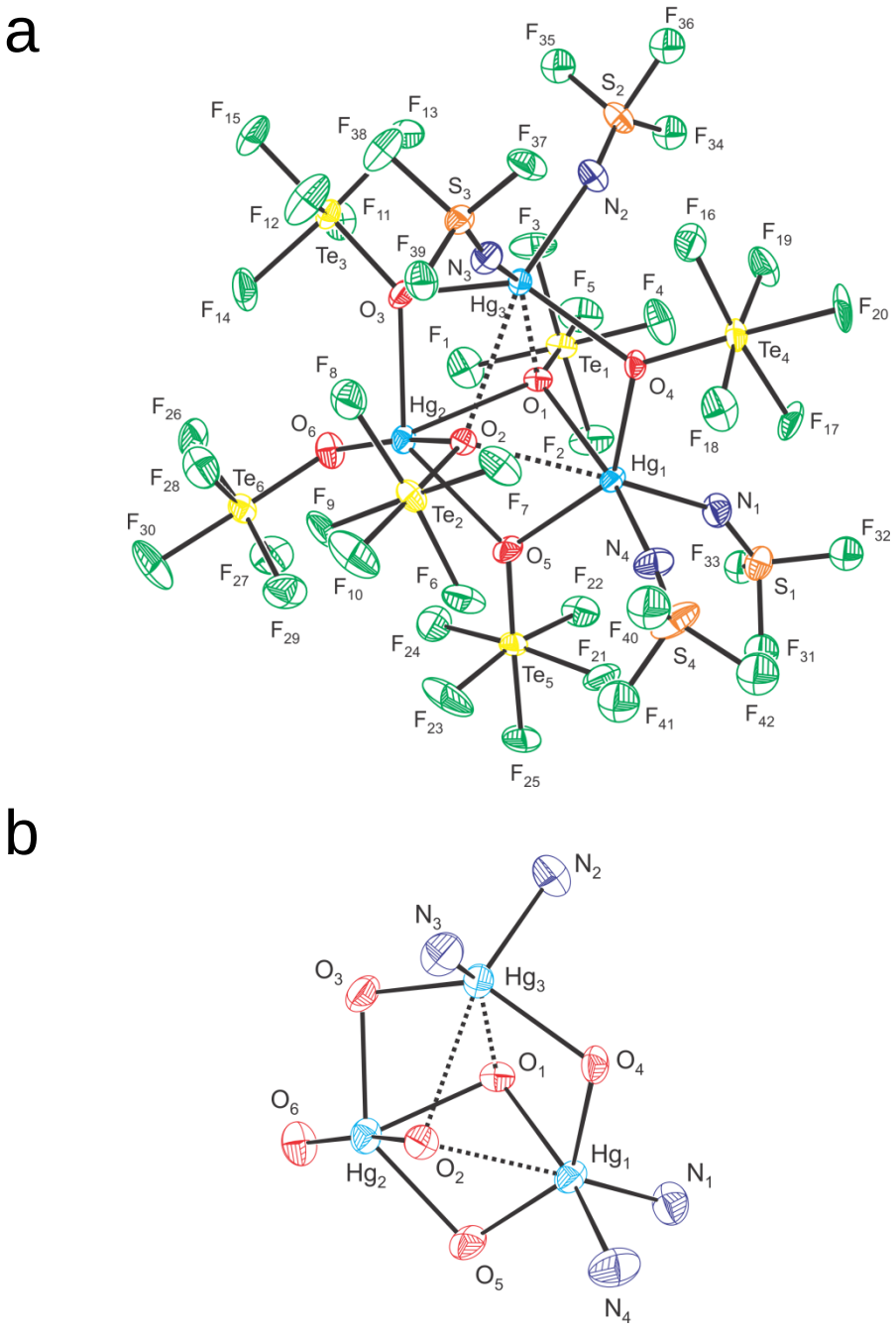

Figure 3.3. (**a**) The X-ray crystal structure of $[Hg_3(OTeF_5)_6 \cdot 4N{\equiv}SF_3]$ showing the $(HgO_\mu)_3$ ring and its capping F_5TeO-groups and (**b**) the coordination environments around the mercury atoms, where dashed lines indicate secondary bonding interactions. Thermal ellipsoids are shown at the (**a**) 30% probability level for greater clarity and (**b**) 50% probability level.

structure may be formally described as the interaction of a $Hg_{(2)}(OTeF_5)_2$ molecule with $[Hg(OTeF_5)_2{\cdot}2N{\equiv}SF_3]_2$. The oxygen atoms of the $F_5TeO_{(3,5)}$-groups of $[Hg(OTeF_5)_2{\cdot}2N{\equiv}SF_3]_2$ behave as pincers in their coordination to $Hg_{(2)}$ ($Hg_{(2)}{-}O_{(3)}$, 2.501(8) Å; $Hg_{(2)}{-}O_{(5)}$, 2.557(9) Å), whereas the $F_5TeO_{(1)}$-group of $[Hg(OTeF_5)_2{\cdot}2N{\equiv}SF_3]_2$ interacts with $Hg_{(2)}(OTeF_5)_2$ through a short $Hg_{(2)}{-}O_{(1)}$ contact (2.501(8) Å) to give a μ_3-oxygen bridged teflate group. The core of the structure is a distorted six-membered $(HgO_\mu)_3$ ring in which the Hg atoms are linked to one another through a μ-oxygen bridged teflate group. In addition, a μ_3-oxygen bridged teflate group caps each face of the $(HgO_\mu)_3$ ring. The μ_3-coordination descriptions for $O_{(1)}$ and $O_{(2)}$ are supported by the $O_{(1)}{-}Hg$ and $O_{(2)}{-}Hg$ bond orders (see Computational Results and Tables S3.6 and S3.7). The Hg and O_μ atoms of the $(HgO_\mu)_3$ ring are almost coplanar, with the ring atoms lying between 0.145 Å above and 0.191 Å below the average $(HgO_\mu)_3$ plane. The $Hg{-}O_\mu{-}Hg$ ring angles (95.1(4)–107.0(4)°) are similar to those of $[Hg(OTeF_5)_2{\cdot}2N{\equiv}SF_3]_2$ (100.8(3)°), whereas the $O_\mu{-}Hg{-}O_\mu$ angles (136.3(4)–139.4(4)°) are significantly more open than those of $[Hg(OTeF_5)_2{\cdot}2N{\equiv}SF_3]_2$ (79.2(3)°) to accommodate the larger ring size. The capping $Hg{-}O_{\mu_3}{-}Hg$ angles (84.2(3)°–96.2(4)°) are smaller than the $Hg{-}O_\mu{-}Hg$ ring angles, and their $Hg{-}O_{\mu_3}$ bond lengths, $Hg{-}O_{(1)}$ (2.327(8), 2.501(8), 2.644(7) Å) and $Hg{-}O_{(2)}$ (2.143(7), 2.723(11), 2.781(11) Å), are significantly less than the sum of the F and Hg van der Waals radii (3.02 Å).[45,49] Although asymmetric, this appears to represent the first example of a μ^3-oxygen bridged F_5TeO-group. In addition, each $Hg_{(1)}$ and $Hg_{(3)}$ atom is coordinated to two NSF_3 molecules, which are positioned above and below the $(HgO_\mu)_3$ ring, whereas the $Hg_{(2)}$ atom is

coordinated to one terminal F_5TeO-group. The $Hg_{(2)}{-}O_{(6)}$ bond length of the terminal F_5TeO-group (2.051(9) Å) is comparable to those of $Hg(OTeF_5)_2$ (2.016(6) Å),[34] whereas the $Hg_{(2)}{-}O_{(2)}$ bond length is significantly elongated (2.143(7) Å). The $O_{(2)}{-}Hg_{(2)}{-}O_{(6)}$ bond angle (166.3(5)°) is close to that of free $Hg(OTeF_5)_2$ (170.5(4)°); however, the F_5TeO-groups adopt an essentially *syn*-conformation (dihedral $Te_{(2)}{-}O_{(2)}{-}Hg_{(2)}{-}O_{(6)}{-}Te_{(6)}$ angle, 5.8(8)°), contrasting with the *gauche*-conformation of the uncoordinated molecule (dihedral Te–O–Hg–O–Te angle, 53.7(3)°).[34] The asymmetric $Hg_{(2)}(OTeF_5)_2$ moiety results from the additional short $Hg_{(2)}{-}O_{(1)}$ contact (2.501(8) Å) and longer contacts with $O_{(2)}$ ($O_{(2)}$---$Hg_{(1)}$, 2.781(11) Å; $O_{(2)}$---$Hg_{(3)}$, 2.723(11) Å). The Hg–N bond lengths (2.223(10)–2.265(11) Å) are intermediate with respect to those of $[Hg(OTeF_5)_2{\cdot}2N{\equiv}SF_3]_2$ (2.164(10), 2.377(10) Å). The geometrical parameters of the coordinated NSF_3 molecules (Table 3.4) are comparable to those of $[Hg(OTeF_5)_2{\cdot}2N{\equiv}SF_3]_2$ (see above) and do not require further commentary.

3.2.3.4. X-ray Crystal Structure of $[Hg(OTeF_5)(N{=}SOF_2){\cdot}N{\equiv}SF_3]_\infty$

The crystal structure of $[Hg(OTeF_5)(N{=}SOF_2){\cdot}N{\equiv}SF_3]_\infty$ (Figure 3.4) consists of well-isolated chains which run along the *a*-axis of the crystallographic unit cell, with the shortest F---F (2.707(3)–2.935(3) Å) and F---O (2.841(3)–2.921(3) Å) distances being near the sum of the F and O van der Waals radii, 2.99 Å.[45] The infinite chains are comprised of three crystallographically unique Hg atoms which are bonded through bridging F_2OSN- and F_5TeO-groups. Each Hg atom is also coordinated to an NSF_3 molecule.

Table 3.5. Selected Experimental Geometrical Parameters for $[Hg(OTeF_5)(N{=}SOF_2)\text{-}\cdot N{\equiv}SF_3]_\infty$

Bond Lengths (Å)			
$Hg_1{-}O_1$	2.537(2)	$Hg_3{-}O_3$	2.483(2)
$Hg_1{-}O_{3A}$	2.408(2)	$Hg_3{-}O_2$	2.425(2)
$Hg_1{-}N_1$	2.130(2)	$Hg_3{-}N_5$	2.130(2)
$Hg_1{-}N_{5A}$	2.146(2)	$Hg_3{-}N_4$	2.156(2)
$Hg_1{-}N_2$	2.496(3)	$Hg_3{---}N_6$	2.538(3)
$Hg_2{-}O_1$	2.415(2)	$Hg_2{---}N_3$	2.573(3)
$Hg_2{-}N_1$	2.127(2)	$Hg_2{-}N_4$	2.109(2)
Te−O	1.798(2)–1.802(2)	$Hg_2{-}O_2$	2.506(2)
Te−F	1.838(2)−1.864(2)		
F_2OSN-group		*NSF_3*	
N−S	1.484(2)–1.487(2)	N−S	1.399(3)–1.407(3)
S−O	1.403(3)–1.407(2)	S−F	1.519(3)–1.533(2)
S−F	1.525(2)–1.540(2)		
Bond Angles (deg)			
$Hg_1{-}O_1{-}Hg_2$	91.8(1)	$N_1{-}Hg_2{-}O_1$	78.5(1)
$Hg_1{-}N_1{-}Hg_2$	113.4(1)	$O_2{-}Hg_2{-}N_4$	77.8(1)
$Hg_2{-}O_2{-}Hg_3$	91.6(1)	$N_4{-}Hg_3{-}O_2$	78.7(1)
$Hg_2{-}N_4{-}Hg_3$	111.9(1)	$N_5{-}Hg_3{-}O_3$	76.1(1)
$Hg_3{-}O_3{-}Hg_{1A}$	56.7(1)	$N_{5A}{-}Hg_1{-}O_{3A}$	77.4(1)
$Hg_3{-}N_5{-}Hg_{1A}$	89.6(1)	$N_1{-}Hg_1{-}O_1$	75.7(1)
$S_1{-}N_1{-}Hg_1$	122.2(1)	$S_4{-}N_4{-}Hg_2$	126.8(1)
$S_1{-}N_1{-}Hg_2$	124.4(1)	$S_4{-}N_4{-}Hg_3$	121.3(1)
$S_5{-}N_5{-}Hg_3$	124.5(1)	$S_5{-}N_5{-}Hg_{1A}$	123.6(1)
F_2OSN-group		*NSF_3*	
N−S−O	122.1(2)–123.2(1)	N−S−F	120.0(2)–122.8(2)
N−S−F	108.5(1)–110.6(1)	F−S−F	94.9(1)–95.9(1)
O−S−F	107.1(2)–109.1(1)		
F−S−F	93.7(1)–94.7(1)		

The atom labeling scheme corresponds to that used in Figure 3.4. See Table S3.4 for a complete list of geometrical parameters.

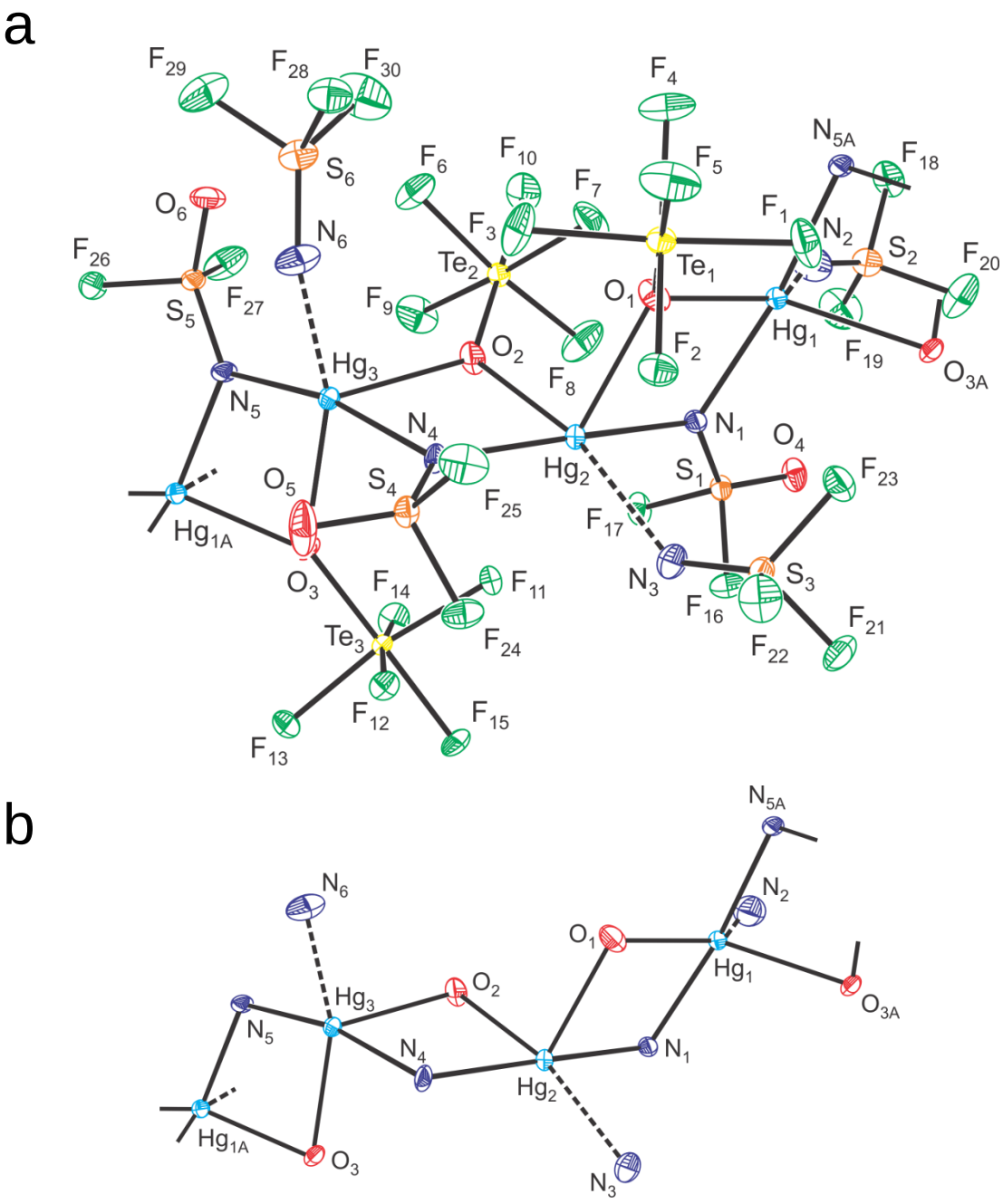

Figure 3.4. The X-ray crystal structure of $[Hg(OTeF_5)(N{=}SOF_2)\cdot N{\equiv}SF_3]_\infty$ showing (**a**) the repetitive unit of the chain and (**b**) the coordination environments of the mercury atoms. The dashed lines indicate secondary bonding interactions; thermal ellipsoids are shown at the 50% probability level.

The coordination spheres of the Hg atoms are similar to that of $[Hg(OTeF_5)_2{\cdot}N{\equiv}SF_3]_\infty$, except a F_5TeO-ligand has been replaced by a μ-N bridged F_2OSN-ligand. Each Hg coordination sphere consists of two Hg–N bonds (2.109(2)–2.156(2) Å) with bridging F_2OSN-ligands, two longer Hg–O bonds (2.408(2)–2.537(2) Å) with bridging F_5TeO-ligands, and one longer Hg–N bond (2.496(3)–2.573(3) Å) with NSF_3. The Hg–N bridge bonds are much shorter than those of $[Hg(N_3)_3]^-$ (2.452(2), 2.485(4) Å),[48] whereas the Hg–N terminal bonds are much longer than the Hg–N terminal bonds of the aforementioned adducts and $Hg(NSF_2)_2$ (2.050(13) Å).[47]

The NSF_3 molecules are more weakly coordinated than those of $[Hg(OTeF_5)_2{\cdot}N{\equiv}SF_3]_\infty$ (see above), consequently, the N–S (1.399(3)–1.407(3) Å) and S–F (1.520(2)–1.533(2) Å) bond lengths are equal, within ±3σ, to those of free NSF_3 (1.400(3) and 1.531(1)–1.534(2) Å, respectively).[10] The F_2OSN-ligands are readily distinguished from coordinated NSF_3 molecules by their substantially shorter S–O bonds (1.403(3)–1.407(2) Å) when compared with their S–F bonds (1.525(2)–1.540(2) Å). Furthermore, the N–S bonds (1.484(2)–1.488(3) Å) are significantly longer than the N≡S bond of NSF_3 (see above), indicative of the N=S character of the imido group. The bond lengths of the F_2OSN-groups are in good agreement with those of $[Mn(CO)_4NSOF_2]_2$ (N–S, 1.434(6) Å; S–O, 1.402(8) Å; S–F, 1.535(6), 1.556(6) Å),[29,30] and $[Ni(SO_2)_2\{AsF_4(NSOF_2)_2\}_2]$ (N–S, 1.477(3), 1.476(4) Å; S–O, 1.389(3), 1.420(3)Å; S–F, 1.509(4)–1.528(5) Å).[31] The F_2OSN-ligands are also distinguished by their bond angles. The Hg–N–S angles involving the F_2OSN-groups are significantly more closed (124.4(1)–124.5(1)^o) than those associated with the terminal NSF_3 groups (141.5(2)–

152.8(2)^{o}). The coordination environments of the bridging N atoms are essentially planar, showing that the nitrogen atoms do not possess stereochemically active lone pairs and that they are formally sp^2-hybridized. Planar F_2OSN-groups have also been observed in $[Mn(CO)_4NSOF_2]_2$.[29,30]

3.2.3.5. X-ray Crystal Structure of $[Hg_3(OTeF_5)_5(N{=}SOF_2){\cdot}2N{\equiv}SF_3]_2$

The structure (Figures 3.5 and S3.1) is related to that of $Hg_3(OTeF_5)_6{\cdot}4N{\equiv}SF_3$, with structural differences arising from the replacement a μ-oxygen bridged $F_5TeO_{(2,4)}$-group by a μ-nitrogen bridged F_2OSN-group. Furthermore, $Hg_{(1)}$ is no longer coordinated to two NSF_3 molecules, instead, two asymmetric $Hg_3(OTeF_5)_5(N{=}SOF_2){\cdot}2N{\equiv}SF_3$ units interact through $Hg_{(1)}$---$O_{\mu(1A)}$ and $Hg_{(1A)}$---$O_{\mu(1)}$ contacts (2 x 2.658(7) Å) to form a dimer. The dimers are well-isolated from one another in their crystal lattice, with the shortest F···F intermolecular contacts ranging from 2.676(10) to 2.937(11) Å. The structure of the asymmetric unit may be formally described as the interaction of a $Hg_{(2)}(OTeF_5)_2$ molecule with a $Hg_2(OTeF_5)_3(NSOF_2)(N{\equiv}SF_3)_2$ moiety to form a distorted (Hg_3O_2N) ring. The $Hg_{(2)}(OTeF_5)_2$ unit (dihedral Te−O−$Hg_{(2)}$−O−Te angle, 40.7(6)°) retains the *gauche*-conformation observed in the crystal structure of $Hg(OTeF_5)_2$ (∠Te−O−Hg−O−Te, 53.7(3)°) and, correspondingly, the $Hg_{(2)}$–O bond lengths ($O_{(4)}$, 2.027(8); $O_{(3)}$, 2.077(6) Å) and $O_{(3)}$−$Hg_{(2)}$−$O_{(4)}$ bond angle (169.3(2)°) are comparable to those of $Hg(OTeF_5)_2$ (2.016(6) Å; 170.5(4)°).[34] The $Hg_{(2)}(OTeF_5)_2$ unit also interacts with two bridging F_5TeO-groups ($Hg_{(2)}$−O, 2.506(7), 2.501(7) Å). The $Hg_{(3)}$ atom is coordinated to two NSF_3 molecules ($Hg_{(3)}$–N, 2.260(8), 2.284(8) Å), one bridging F_5TeO-

Table 3.6. Selected Experimental Geometrical Parameters for $[Hg_3(OTeF_5)_5(N{=}SOF_2)\cdot 2N{\equiv}SF_3]_2$

Bond Lengths (Å)			
$Hg_1{-}O_1$	2.053(6)	$Hg_3{-}N_1$	2.185(8)
$Hg_1{---}O_{1A}$	2.658(7)	$Hg_3{-}N_2$	2.340(12)
$Hg_1{-}O_2$	2.462(7)	$Hg_3{-}N_3$	2.284(8)
$Hg_1{---}O_3$	2.711(7)	$Hg_1{-}N_1$	2.065(7)
$Hg_2{-}O_3$	2.077(6)	$Hg_3{-}O_5$	2.126(7)
$Hg_2{-}O_4$	2.027(8)		
$Hg_2{-}O_2$	2.506(7)	Te−O	1.806(8)–1.840(7)
$Hg_2{-}O_5$	2.501(7)	Te−F	1.800(8)–1.867(8)
F_2OSN-group		**NSF_3**	
$N_1{-}S_1$	1.483(8)	N−S	1.399(8)
$S_1{-}O_6$	1.415(8)	S−F	1.495(7)–1.509(7)
S−F	1.516(8), 1.526(8)		
Bond Angles (deg)			
$Hg_1{-}O_2{-}Hg_2$	104.7(3)	$O_1{-}Hg_1{-}O_2$	92.2(3)
$Hg_2{-}O_5{-}Hg_3$	109.8(3)	$O_3{-}Hg_2{-}O_4$	169.3(3)
$Hg_3{-}N_1{-}Hg_1$	112.5(3)	$O_2{-}Hg_2{-}O_5$	72.7(3)
$N_1{-}Hg_1{-}O_2$	89.6(3)	$O_5{-}Hg_2{-}O_2$	69.1(3)
$N_1{-}Hg_1{-}O_1$	176.9(3)	$O_5{-}Hg_3{-}N_1$	132.1(3)
$O_1{-}Hg_1{-}O_{1A}$	75.2(3)	$Hg_1{-}O_1{---}Hg_{1A}$	104.8(3)
$Hg_2{-}N_3{-}S_3$	152.0(6)	$Hg_1{-}N_1{-}S_1$	119.8(5)
$Hg_2{-}N_2{-}S_2$	155(1)	$Hg_3{-}N_1{-}S_1$	127.2(4)
$[NSOF_2]^-$		**NSF_3**	
N−S−O	122.9(4)	N−S−F	118.9(6)–123.4(7)
N−S−F	108.6(4), 109.0(5)	F−S−F	92.6(6)–98.1(6)
O−S−F	109.0(5), 109.1(4)		
F−S−F	94.3(5)		
Dihedral Angles (deg)			
$Te_4{-}O_4{-}Hg_2{-}O_3{-}Te_3$	40.7(6)		

The atom labeling scheme corresponds to that used in Figures 3.5 and S3.1. See Table S3.5 for a complete list of geometrical parameters.

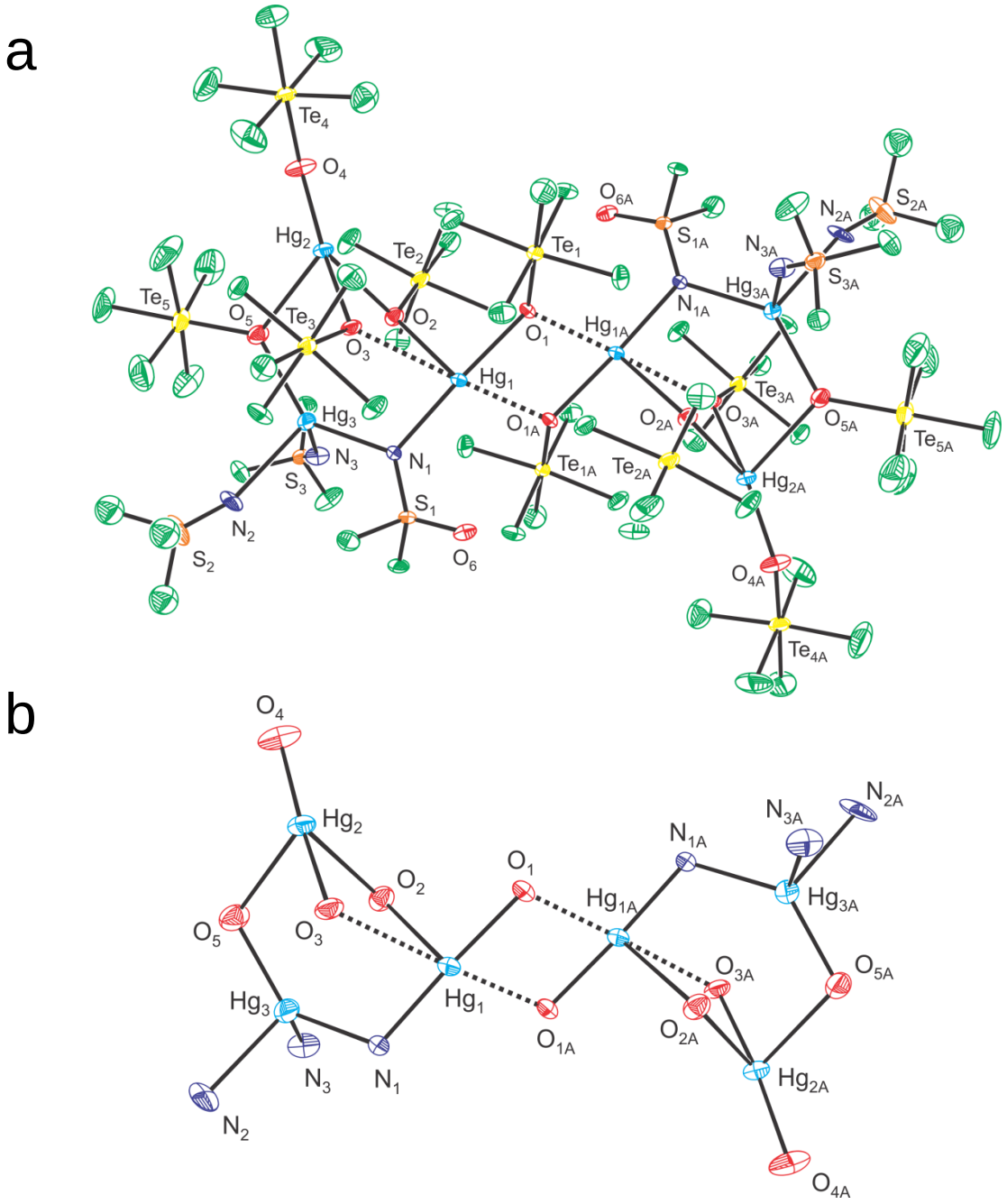

Figure 3.5. (**a**) The X-ray crystal structure of dimeric $[Hg_3(OTeF_5)_5(N{=}SOF_2)\cdot 2N{\equiv}SF_3]_2$ where the F atoms (green) are not labeled for clarity (see Figure S3.1 for the fully labeled structure) and (**b**) the coordination environments of mercury. The dashed lines indicate secondary bonding interactions. Thermal ellipsoids are shown at the (**a**) 30% probability level for clarity and (**b**) 50% probability level.

group ($Hg_{(3)}$–$O_{(5)}$, 2.126(7) Å), and a bridging F_2OSN-group ($Hg_{(3)}$–$N_{(1)}$, 2.185(8) Å). The $Hg_{(1)}$ coordination environment consists of a bridging F_5TeO-group ($Hg_{(1)}$–$O_{(2)}$, 2.462(7) Å), a bridging $NSOF_2$-group ($Hg_{(1)}$–$N_{(1)}$, 2.065(5) Å), and a terminal $F_5TeO_{(1)}$-group ($Hg_{(1)}$–$O_{(1)}$, 2.053(6) Å). Additionally, $Hg_{(1)}$ and $Hg_{(1A)}$ have long contacts with $O_{(1A)}$ and $O_{(1)}$, respectively, of the symmetry-related $F_5TeO_{(1,1A)}$-groups (Figure 3.5). These contacts result in dimer formation and a $(HgO)_2$ ring as found in $[Hg(OTeF_5)_2 \cdot 2N{\equiv}SF_3]_2$. The structural parameters of the coordinated NSF_3 molecules and F_2OSN-ligand, including the Hg–N bond lengths and Hg–N–S bond angles, are similar to those of $[Hg(OTeF_5)(NSOF_2) \cdot N{\equiv}SF_3]_\infty$ and do not require further commentary.

3.2.4. Raman Spectroscopy

The Raman spectra of $[Hg(OTeF_5)_2 \cdot 2N{\equiv}SF_3]_2$ (**2**), $Hg_3(OTeF_5)_6 \cdot 4N{\equiv}SF_3$ (**3**), $[Hg(OTeF_5)(N{=}SOF_2) \cdot N{\equiv}SF_3]_\infty$ (**4**), and $[Hg_3(OTeF_5)_5(N{=}SOF_2) \cdot 2N{\equiv}SF_3]_2$ (**5**) were recorded at –150 °C (Table 3.7 and Figures 3.6–3.9). The spectra are complex due to the presence of several crystallographically distinct F_5TeO-groups, whose Raman bands overlap with those of NSF_3 and the $NSOF_2$-group, preventing their unambiguous assignments. However, a significant number of non-overlapping bands could be assigned by comparison with the literature.

Raman bands centered at approximately 1190 cm^{-1} ((**4**), 1191, 1196 cm^{-1}; (**5**), 1187, 1199 cm^{-1}), were assigned to S–N stretching modes of F_2OSN-ligands by comparison with those reported for $Hg(NSOF_2)_2$ (1191 cm^{-1}),[21] $(CH_3)_3SiNSOF_2$ (1191 cm^{-1}),[21] $[Hg(NSOF_2)_4]^{2-}$ (1180 cm^{-1}),[33] $[Ni(SO_2)_2\{AsF_4(NSOF_2)_2\}_2]$ (1190 cm^{-1}),[31] and

Table 3.7. Experimental Raman Frequencies[a] and Intensities[b] for $[Hg(OTeF_5)_2{\cdot}2N{\equiv}SF_3]_2$ (**2**), $[Hg_3(OTeF_5)_6{\cdot}4N{\equiv}SF_3]$ (**3**), $[Hg(OTeF_5)(N{=}SOF_2){\cdot}N{\equiv}SF_3]_\infty$ (**4**), and $[Hg_3(OTeF_5)_5(N{=}SOF_2){\cdot}2N{\equiv}SF_3]_2$ (**5**)[c]

(**2**)	(**3**)	(**4**)	(**5**)	assgnts
1622(5) 1597(13) 1583(11) 1559(18) 1553(16)	1597(32) 1572(13)	1545(24) 1533(27) 1530(32) 1517(2) 1514(2)	1578(44) 1566(32)	$\nu(S{\equiv}N)_{NSF_3}$
		1391(4)		$\nu(S{=}O)_{NSOF_2}$
		1196(44) 1191(15)	1199(8) 1187(48)	$\nu(S{\equiv}N)_{NSOF_2}$
906(6) 880(9) 858(27)	909(10) 902(9) 899(8) 897(8) 890(5) 848(44)	883(7) 874(2) 863(10) 852(9) 844(4)	909(16) 901(12) 897(8) 871(4) 844(84)	$\nu_{as}(SF_3)_{NSF_3}$ / $\nu_{as}(SF_2)_{NSOF_2}$
831(79) 819(100) 797(15)	833(100) 820(10) 815(10) 812(9) 808(9) 792(5) 767(13)	825(sh) 822(29) 818(33) 811(70) 808(100) 802(42)	838(40) 821(100) 798(12) 777(4) 748(16)	[ν(Hg–O) – ν(Te–O)] / $\nu_s(SF_3)_{NSF_3}$ / $\nu_s(SF_2)_{NSOF_2}$
688(sh) 681(71) 674(61) 643(6) 622(40) 613(sh)	702(83) 695(38) 684(32) 675(29) 640(69) 632(19) 627(18) 619(9)	699(2) 687(27) 679(76) 625(8) 616(sh) 614(17) 608(10) 603(17)	719(76) 711(sh) 708(68) 703(sh) 695(44) 683(32) 677(28) 644(100) 633(sh) 631(40) 620(12) 610(20)	ν(Te–F)
579(2) 569(2) 552(2) 541(13)	547(12)	569(12) 565(7) 535(10)	575(8) 567(20) 553(4) 548(sh) 546(12)	$\delta_s(SF_3)_{NSF_3}$ / $\delta_s(NSF_2)_{NSOF_2}$

Table 3.7. continued …

	479(5) 472(4)	497(5) 494(6)	514(8) 501(36) 496(24) 486(sh) 484(24)	[ν(Hg–O) + ν(Te–O)]
449(36)	450(35) 436(8)	456(sh) 451(17) 446(20)	457(sh) 453(44) 442(8)	$\delta_s(NSF_2)_{NSF_3}$ / $\delta_s(NSF_2)_{NSOF_2}$
394(16) 381(12) 359(28) 354(34) 340(16) 331(11)	412(4) 359(27) 336(14)	381(30) 366(15) 361(16) 356(17) 342(6) 333(8) 329(7)	363(sh) 359(32) 342(16) 336(20) 332(sh) 326(12)	$\delta_{as}(NSF_3)_{NSF_3}$ / $\delta_s(NSF_2)_{NSOF_2}$
315(7) 295(9) 232(2)	295(11) 240(3)	294(2) 291(4) 289(4) 278(2) 263(2) 260(3) 217(2) 199(5) 188(5)	319(8) 316(8) 268(4) 242(8) 240(8) 236(8) 228(4) 204(4) 186(16)	F_5TeO-group bends
139(8)	124(14)	159(32) 116(2) 112(2) 106(2)	142(28) 132(28)	F_5TeO- and NSF_3-groups deformation modes

[a] Frequencies are given in cm^{-1}. [b] Values in parentheses denote relative Raman intensities. The Raman spectra of (**2**), (**3**), and (**5**) were recorded in ¼-in. o.d. FEP sample tubes; the Raman spectrum of (**4**) was recorded in a ¼-in. o.d. Pyrex glass tube. All Raman spectra were recorded at –150 to –155 °C using 1064-nm excitation. [c] Abbreviations denote shoulder (sh), stretch (ν), bend (δ), symmetric (s), and asymmetric (as).

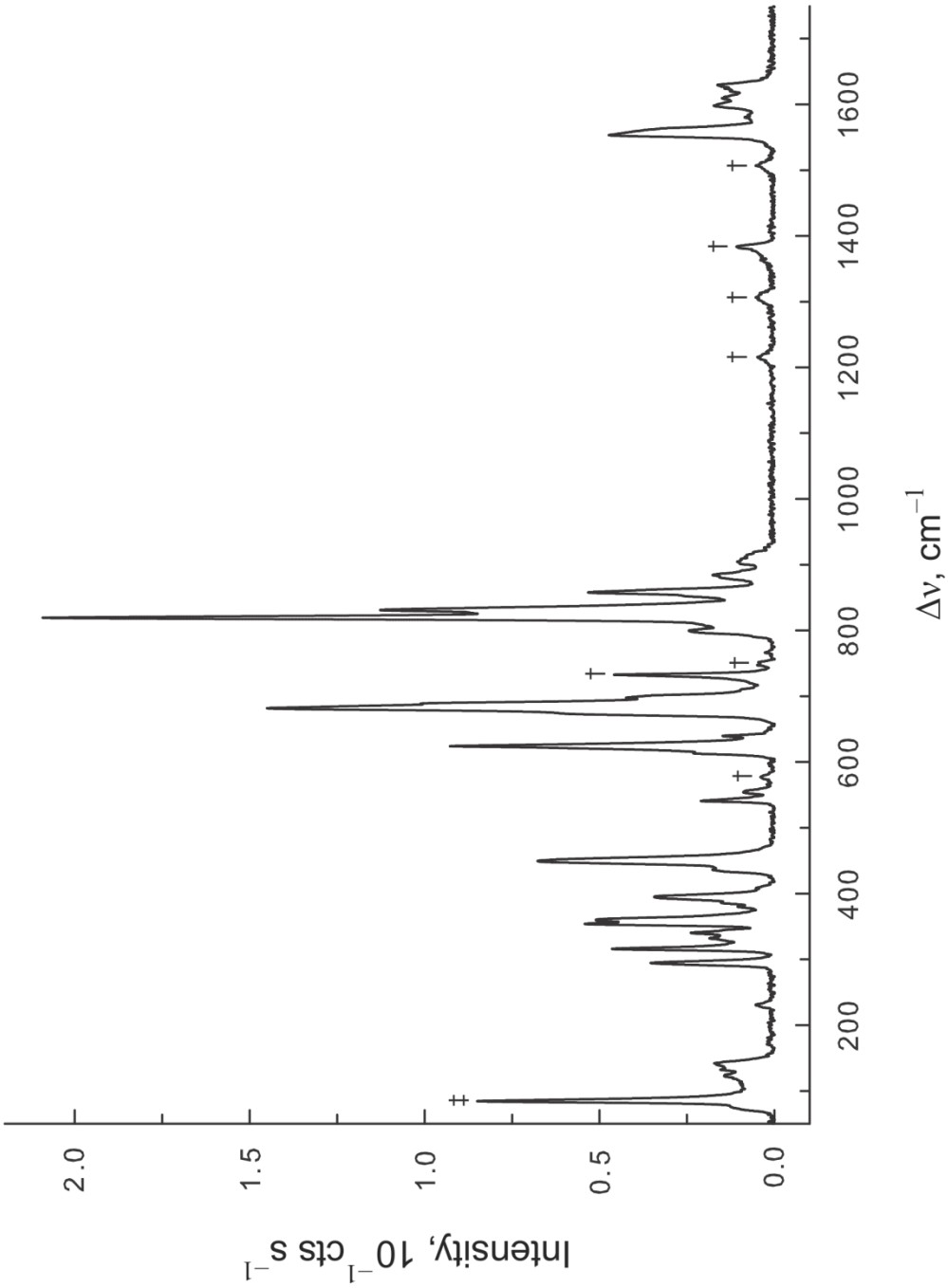

Figure 3.6. The Raman spectrum of $[Hg(OTeF_5)_2{\cdot}2N{\equiv}SF_3]_2$ (**2**) between 50–1750 cm^{-1} recorded at −155 °C using 1064-nm excitation. Symbols denote FEP sample tube bands (†) and an instrumental artifact (‡).

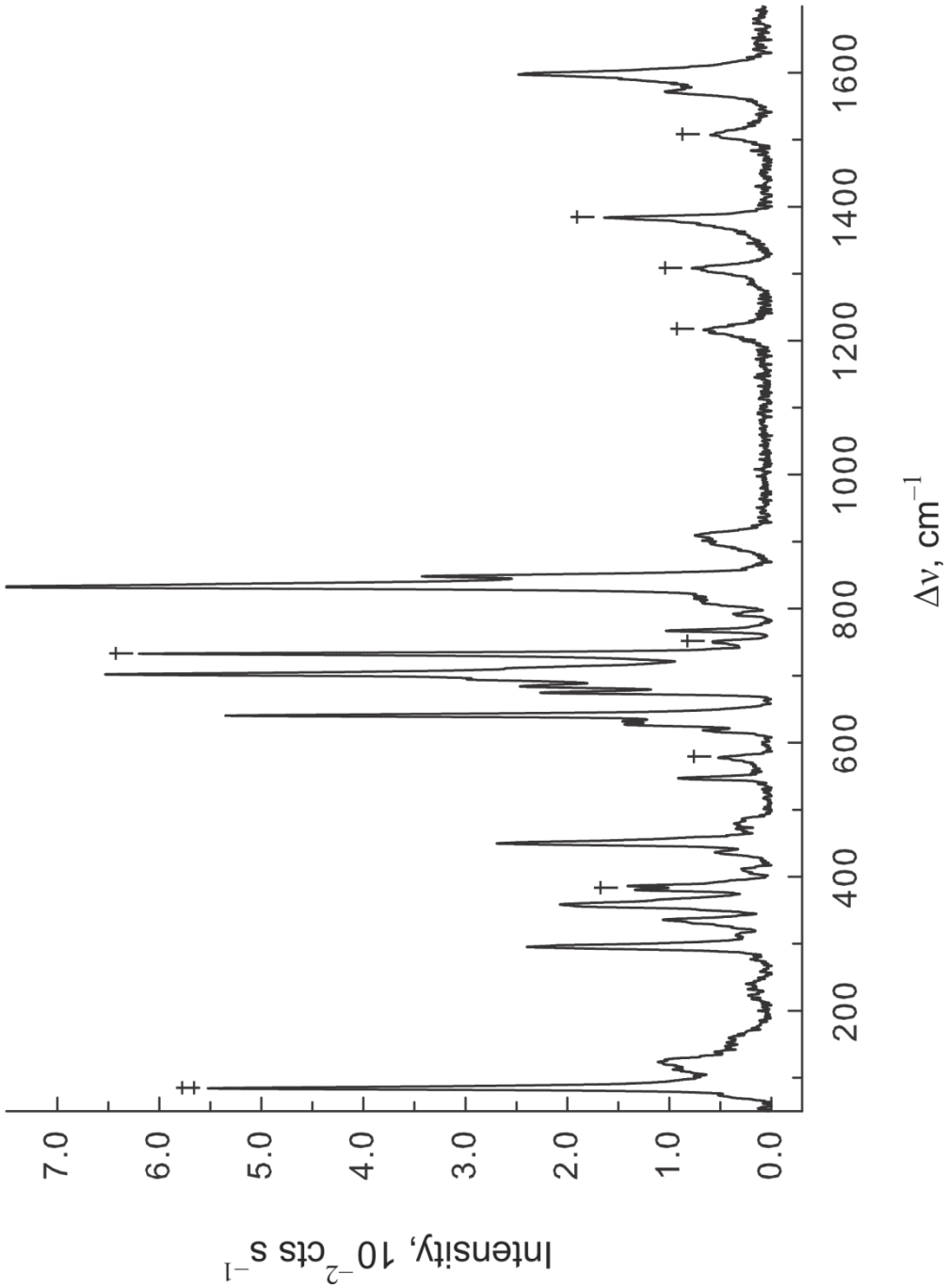

Figure 3.7. The Raman spectrum of $[Hg_3(OTeF_5)_6{\cdot}4N{\equiv}SF_3]$ (**3**) between 50–1650 cm^{-1} recorded at −150 °C using 1064-nm excitation. Symbols denote FEP sample tube bands (†) and an instrumental artifact (‡).

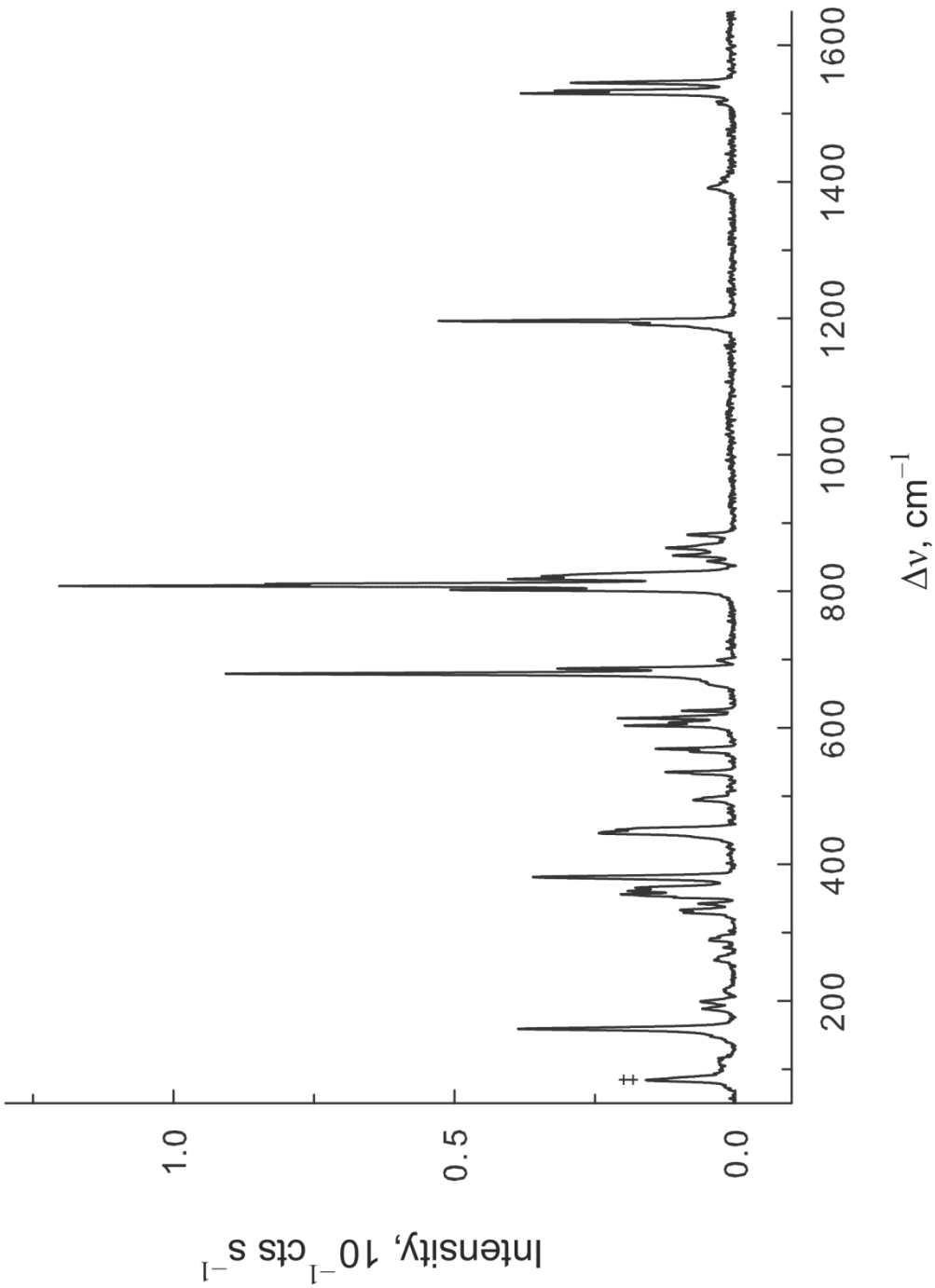

Figure 3.8. The Raman spectrum of $[Hg(OTeF_5)(N{=}SOF_2){\cdot}N{\equiv}SF_3]_\infty$ (**4**) between 50–1650 cm^{-1} recorded in a Pyrex glass sample tube at −150 °C using 1064-nm excitation. The symbol (‡) denotes an instrumental artifact.

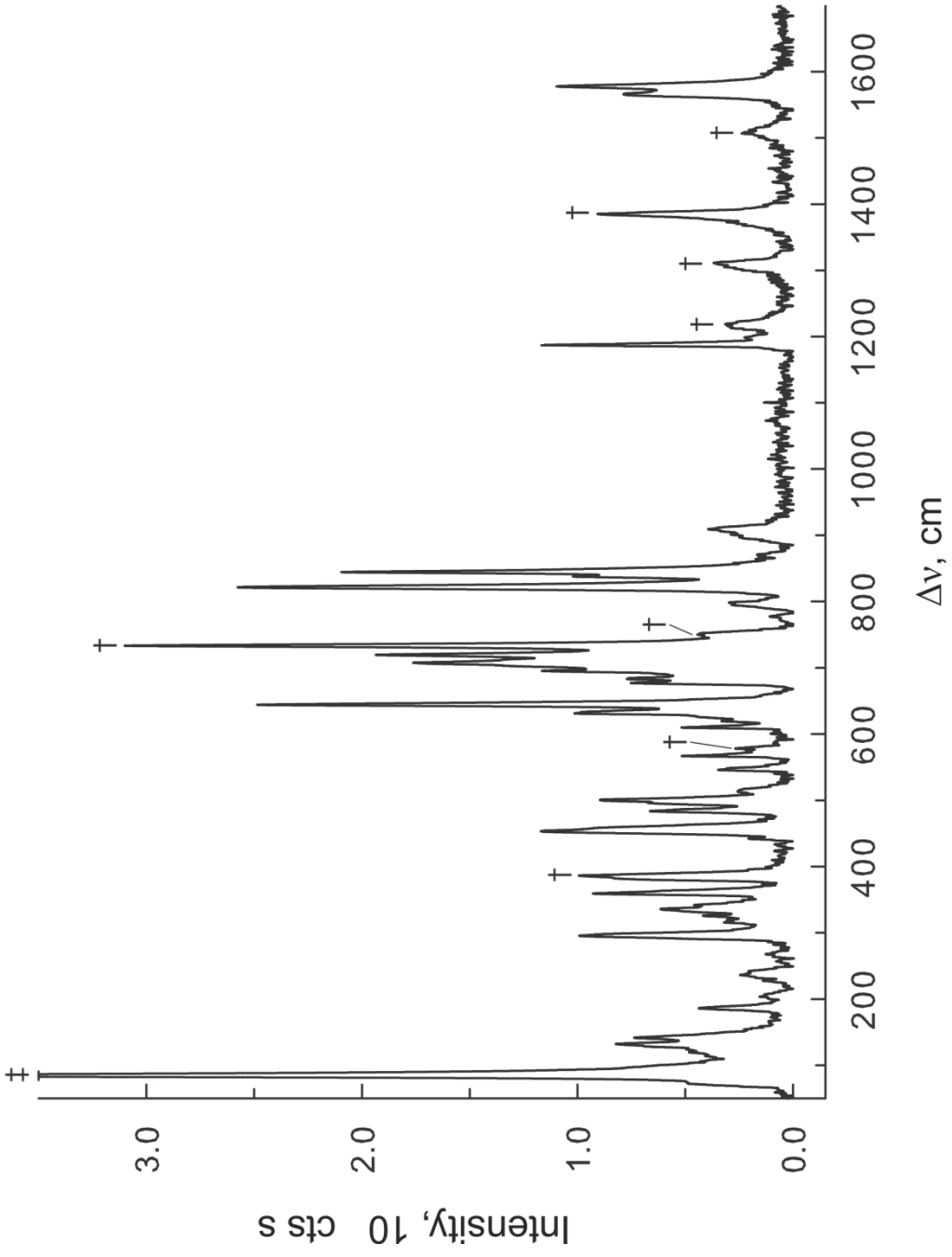

Figure 3.9. The Raman spectrum of $[Hg_3(OTeF_5)_5(N{=}SOF_2){\cdot}2N{\equiv}SF_3]_2$ (**5**) between 50–1650 cm^{-1} recorded at –150 °C using 1064-nm excitation. Symbols denote FEP sample tube bands (†) and an instrumental artifact (‡)

$[Cu(SO_2)_2\{AsF_4(NSOF_2)_2\}_2]$ (1173, 1198 cm^{-1}).[31] A weak band at 1391 cm^{-1} (**4**) was assigned to $\nu_{as}(SO)$ of the F_2OSN-ligand by comparison with $Hg(NSOF_2)_2$ (1396 cm^{-1}), $(CH_3)_3SiNSOF_2$ (1365, 1396 cm^{-1}), $[Ni(SO_2)_2\{AsF_4(NSOF_2)_2\}_2]$ (1409 cm^{-1}), and $[Cu(SO_2)_2\{AsF_4(NSOF_2)_2\}_2]$ (1398, 1410 cm^{-1}). It is noteworthy that the Raman spectra of (**2**) and (**3**) are devoid of vibrational bands within this frequency range, in accordance with the observation that the F_2OSN-derivatives, (**4**) and (**5**), do not form at significant rates below 0 °C (see Syntheses).

Bands in the 1514–1622 cm^{-1} region of the spectrum were assigned to ν(SN) of coordinated NSF_3 by comparison with those of $[F_3S{\equiv}NXeF]^+$ (1527–1548 cm^{-1}),[15] $[Mn(N{\equiv}SF_3)_4][AsF_6]_2$ (1580 cm^{-1}),[16] $F_5AsN{\equiv}SF_3$ (1610 cm^{-1}),[3] and $[Re(CO)_5N{\equiv}SF_3][AsF_6]$ (1643 cm^{-1}).[20] Overall, S–N stretching bands are shifted to high-frequency relative to those of free NSF_3 (1503–1524 cm^{-1}).[8] The lowest frequency bands (1514–1545 cm^{-1}) observed for (**4**) correlate with the weakest Hg–NSF_3 bonds (Hg–N, 2.496(3)–2.573(3) Å), whereas the highest frequency bands (1553–1622 cm^{-1}) were observed for (**2**), and correlate with the shortest Hg–NSF_3 bonds (2.164(10) Å). The remaining ν(SN) frequencies and Hg–N bond lengths fall between the aforementioned extremes. In this instance, X-ray crystallography fails to reliably differentiate among S–N bond lengths, whereas the S–N stretching frequencies clearly show increases upon adduct formation.

In contrast with S–N bond lengths, the S–F bond lengths are more sensitive to donor-acceptor interactions, displaying shorter S–F bonds upon NSF_3 coordination. Correspondingly, the S–F stretching frequencies shift to higher frequencies, as observed

for $[F_3S{\equiv}NXeF]^+$ (869–952 cm^{-1}).[15] The bands between 844 and 909 cm^{-1} in the Raman spectra of (**2**) and (**3**) can be confidently assigned to $\nu_{as}(SF_3)$ stretches by comparison with those of $[Mn(CO)_5N{\equiv}SF_3][AsF_6]$ (882 cm^{-1}), $[CpFe(CO)_2N{\equiv}SF_3][AsF_6]$ (876, 888 cm^{-1}), and $[Re(CO)_5N{\equiv}SF_3][AsF_6]$ (889, 900 cm^{-1}).[20] In the cases of (**4**) and (**5**), the $\nu_{as}(SF_2)$ bands of their F_2OSN-groups overlap with this region of the spectrum. For comparison, the $\nu_{as}(SF_2)$ bands of $(CH_3)_3SiNSOF_2$,[21] occur at 810 and 853 cm^{-1}. The spectral region between 748 and 838 cm^{-1} in (**2**)–(**5**) is associated with the symmetric counterparts, $\nu_s(SF_3)$ and $\nu_s(SF_2)$, but is also complicated by overlap with [ν(Hg-O) – ν(Te-O)]-type stretching modes. The most intense band is found in this range and is assigned to $\nu_s(SF_3)$ ((**2**), 833 cm^{-1}, (**3**), 819 cm^{-1}, (**4**), 808 cm^{-1}, (**5**), 821 cm^{-1}). The bands lying between 603 and 719 cm^{-1} are characteristic of $\nu(Te–F_{eq})$ and $\nu(Te–F_{ax})$ stretching modes, and are comparable to those of $Hg(OTeF_5)_2$ (624–735 cm^{-1}),[34] $Hg(OTeF_5)_2{\cdot}1.5XeF_2$ (623–753 cm^{-1}),[34] and $[Hg_2(OTeF_5)_6]^{2-}$ (604–707 cm^{-1}).[35] Bands appearing between 472 and 514 cm^{-1} are assigned to [ν(Hg-O) + ν(Te-O)]-type stretching modes by comparison with $Hg(OTeF_5)_2$ (472–511 cm^{-1}) and its derivatives.[34,35]

The bands lying between 541 and 579 cm^{-1} in the Raman spectra of (**2**) and (**3**) are assigned to $\delta_s(SF_3)_{NSF_3}$ by comparison with NSF_3 (526 and 530 cm^{-1})[8] and $[F_3S{\equiv}NXeF]^+$ (556–570 cm^{-1}).[15] The bands between 535 and 575 cm^{-1} in the spectra of (**4**) and (**5**) may also be assigned to $\delta_s(NSF_2)_{NSOF_2}$ as observed in $[Hg(NSOF_2)_4]^{2-}$ (555 cm^{-1}).[33] Bands at 436–450 cm^{-1} and 331–412 cm^{-1} in the spectra of (**2**) and (**3**) are assigned to $\delta_s(NSF_2)_{NSF_3}$

and $\delta_{as}(NSF_2)_{NSF_3}$, respectively, by comparison with those of NSF_3 (438, 445; 349, 355 cm^{-1})[8] and $[F_3S{\equiv}NXeF]^+$ (448, 471; 357, 369(6) cm^{-1}).[15]

3.2.5. Computational Results

Quantum-chemical calculations were carried out to gain insight into the bonding of the μ_3-oxygen bridged teflate groups observed in structure (**3**) (see X-ray Crystallography). The electronic structure of $Hg_3(OTeF_5)_6{\cdot}4N{\equiv}SF_3$ (C_1) was optimized, with all frequencies real, at the PBE0/def2-SVP level of theory (Table S3.6 and Figure 3.10). The experimental geometry is well reproduced by the calculations, in particular its bicapped $(HgO_\mu)_3$ ring and capping F_5TeO-groups. The Hg–N bond lengths are all overestimated by 0.08-0.1 Å. All the Hg–O bond lengths are well reproduced except for Hg_3–O_2, which is underestimated by 0.21 Å. The calculated geometry reproduces the three types of $Hg–O_{(TeF_5)}$ bonds encountered in the experimental structure of (**3**), i.e., those involving terminal F_5TeO-groups and μ- and μ_3-O bridging F_5TeO-groups. As observed in the experimental structure, the μ_3-O atoms are asymmetrically coordinated to the mercury centers. Although the NBO valencies and charges (Table S3.7) remain nearly constant for all oxygen atoms, ranging from 0.80 to 0.85 and –1.110 to –1.215, respectively, the bond orders vary significantly and correlate with their experimental and calculated Hg–O bond lengths. The Hg–O bond order is greatest for the terminal F_5TeO-group (O_6, 0.240), and decreases significantly for the μ-O bridged F_5TeO-groups (O_3, 0.08 and 0.13; O_4, 0.10 and 0.11; O_5, 0.07 and 0.13) and the μ_3-O bridged F_5TeO-groups (O_1, 0.06, 0.07 and 0.10; O_2, 0.04, 0.07 and 0.15). It is noteworthy that the $Hg–O_{\mu3}$ bond

orders are comparable to the Hg–O_μ bond orders. The calculated Te–O bond lengths do not vary significantly, nor do the Te–O bond orders (Table S3.7).

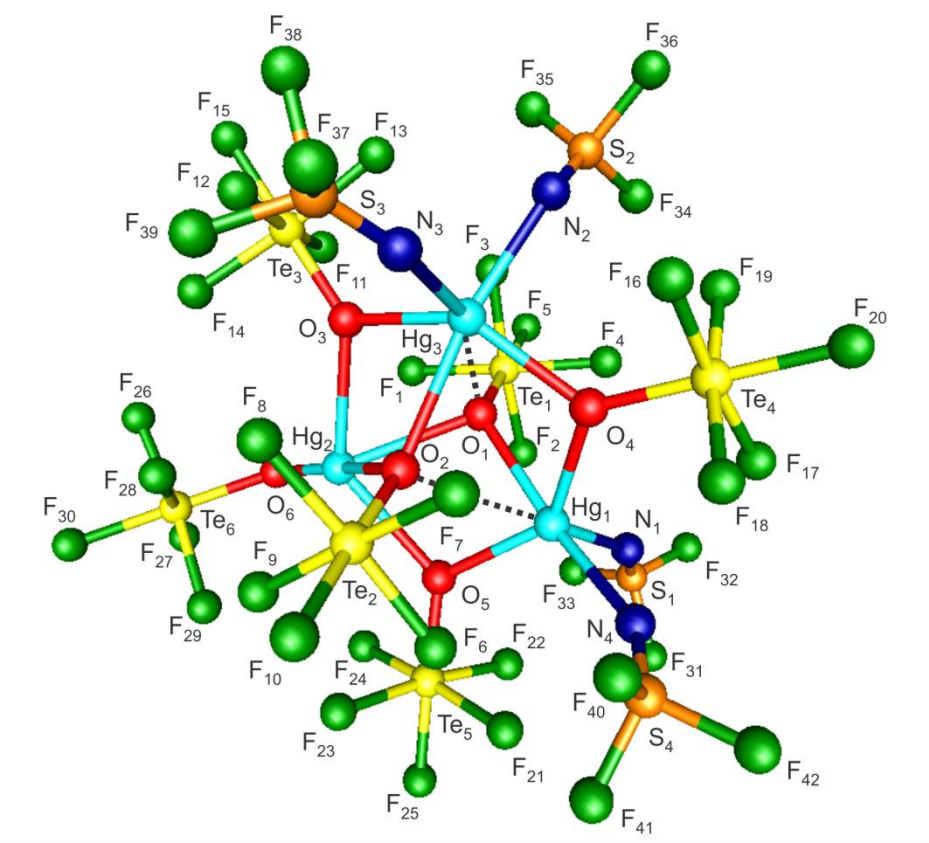

Figure 3.10. The gas-phase, energy-minimized geometry of $Hg_3(OTeF_5)_6{\cdot}4N{\equiv}SF_3$ (C_1) calculated at the PBE0/def2-SVP level of theory. The longest bonding interactions are denoted by dashed lines.

3.3. Conclusions

Donor-acceptor adducts form between the Lewis acidic Hg(II) center of $Hg(OTeF_5)_2$ and the nitrogen base, NSF_3, at 0 °C, yielding $[Hg(OTeF_5)_2{\cdot}N{\equiv}SF_3]_\infty$ (**1**), $[Hg(OTeF_5)_2{\cdot}2N{\equiv}SF_3]_2$ (**2**), and $Hg_3(OTeF_5)_6{\cdot}4N{\equiv}SF_3$ (**3**). When these reactions are carried out at room temperature, nucleophilc attack by a F_5TeO-group at the sulfur(VI)

atom of NSF_3 occurs, followed by O/F metathesis between Hg-coordinated NSF_3 molecules and F_5TeO-ligands, and TeF_6 elimination to yield the structurally related F_2OSN-derivatives, $[Hg(OTeF_5)(N{=}SOF_2){\cdot}N{\equiv}SF_3]_\infty$ (**4**) and $[Hg_3(OTeF_5)_5(N{=}SOF_2){\cdot}2N{\equiv}SF_3]_2$ (**5**). The Raman bands associated with the coordinated NSF_3 molecules and F_2OSN-ligands were tentatively assigned for compounds (**2**)–(**5**) by comparison with other NSF_3 adducts and F_2OSN-derivatives, confirming that the F_2OSN-group is only formed at a significant rate above 0 ^oC. The X-ray crystal structures exhibit a variety of structural motifs, including the infinite chain structures of (**1**) and (**4**); a dimeric structure, (**2**), based on a $(HgO_\mu)_2$ ring at its core; (**3**), a cage structure comprised of an $(HgO_\mu)_3$ ring that is capped on either side by two μ_3-oxygen bridged F_5TeO- groups; and (**5**), a dimeric structure that possesses two distorted (Hg_3O_2N) rings. The description of the capping F_5TeO-groups of (**3**) as μ_3-oxygen bridged is supported by the calculated gas-phase geometry and Mayer bond orders. Teflate groups that form μ-oxygen bridges between mercury centers are encountered in all five structures, a recurrent structural feature in group 11 and 12 metal teflate species.[35-42] Compounds (**1**)–(**5**) represent a novel class of neutral transition metal complexes with NSF_3, providing the first examples of NSF_3 coordination to mercury. Compounds (**4**) and (**5**) also provide the only examples of F_2OSN-derivatives of mercury that have been characterized by single-crystal X-ray diffraction.

3.4. Experimental

General experimental techniques, procedures, and equipment, as well as the preparation and purification of all starting materials are described in Chapter 2.

3.4.1. Syntheses and Crystal Growth.

In a drybox, $Hg(OTeF_5)_2$ was weighed into an FEP reaction vessel at room temperature. The vessel was transferred to a metal vacuum line, connected to an FEP vessel (–78 °C) containing NSF_3 and all connections were thoroughly passivated with F_2. The NSF_3 storage vessel was warmed to 0 °C prior to condensing NSF_3 into the reaction vessel at −78 °C. Sufficient NSF_3 was used to cover the solid $Hg(OTeF_5)_2$ with liquid NSF_3 when the reaction mixture was warmed to –50 °C. The appropriate solvent was then condensed onto the frozen reaction mixture at −78 °C and warmed to either 0 °C or to room temperature to effect dissolution and reaction. Crystals suitable for X-ray structure determinations were grown by cooling the side arm of the reaction vessel to −78 °C to establish a thermal gradient for the slow distillation of the solvent from the reaction mixture into the side arm of the reaction vessel. The side arm containing the condensed solvent was then cooled to −196 °C and heat-sealed off under dynamic vacuum. Low-temperature Raman spectra (–150 °C) were recorded directly on the crystalline sample.

(i) $[Hg(OTeF_5)_2{\cdot}N{\equiv}SF_3]_\infty$. The reagents, $Hg(OTeF_5)_2$ (0.0937 g, 0.1382 mmol) and excess NSF_3, were combined in an FEP reaction vessel followed by condensation of ~0.5 mL of SO_2ClF at –78 °C. The sample was maintained at −78 °C under 400 Torr of dry N_2. The solution was then warmed to 0 °C and a thermal gradient was established for crystal growth by cooling the reactor side arm to –78 °C. Colorless needles grew over a

period of ca. 2 days. A crystal having the dimensions 0.03 x 0.03 x 0.22 mm^3 was selected for a low-temperature X-ray crystal structure determination. Unit cell determinations on several crystals and Raman spectroscopy established that $[Hg(OTeF_5)_2{\cdot}N{\equiv}SF_3]_\infty$ was a minor product and that the sample was mostly comprised of $[Hg(OTeF_5)_2{\cdot}2N{\equiv}SF_3]_2$.

(ii) $[Hg(OTeF_5)_2{\cdot}2N{\equiv}SF_3]_2$. The reagents, $Hg(OTeF_5)_2$ (0.1139 g, 0.1681 mmol) and excess $N{\equiv}SF_3$, were combined in an FEP reaction vessel. Freon-114® (~0.4 mL) was condensed onto the reaction mixture at −78 °C and the reactor was backfilled to 400 Torr with dry N_2 and warmed to 0 °C to dissolve the reactants. Colorless, plate-shaped crystals were grown by slow solvent evaporation over a 5 h period by cooling the side arm to −78 °C. A crystal having the dimensions 0.05 x 0.11 x 0.13 mm^3 was selected for a low-temperature X-ray structure determination.

(iii) $Hg_3(OTeF_5)_6{\cdot}4N{\equiv}SF_3$. The reactants, $Hg(OTeF_5)_2$ (0.1298 g, 0.1914 mmol) and excess NSF_3, were combined in an FEP reaction vessel with ~0.3 mL of Freon-114® solvent and warmed to 0 °C. The reactor and contents were backfilled to 400 Torr with dry N_2 and crystals were grown over a 12 h period by cooling the side arm of the reactor to −78 °C. Colorless needles remained after all of the solvent had transferred. A crystal having the dimensions 0.07 x 0.26 x 0.04 mm^3 was selected for a low-temperature X-ray structure determination. The crystalline sample was primarily composed of $[Hg(OTeF_5)_2{\cdot}2N{\equiv}SF_3]_2$, which was identified by unit cell determinations on several crystals and by Raman spectroscopy. A second reaction was carried out under similar conditions using 0.0718 g of $Hg(OTeF_5)_2$ (0.1059 mmol) in SO_2ClF solvent at room

temperature (under 400 Torr N_2). This sample was rapidly crystallized over a 3 h period and resulted in only $Hg_3(OTeF_5)_6 \cdot 4N{\equiv}SF_3$, which was identified by unit cell determinations on several crystals and by the Raman spectrum of the bulk sample. No vibrational bands attributable to the F_2OSN-group were observed.

(iv) $[Hg(OTeF_5)(N{=}SOF_2) \cdot N{\equiv}SF_3]_\infty$. A reaction vessel was loaded with $Hg(OTeF_5)_2$ (0.0905 g, 0.1335 mmol) and excess NSF_3 was condensed onto the solid at –78 °C followed by ~0.3 mL of SO_2ClF solvent which was also condensed onto the mixture at –78 °C. The void above the solution was backfilled with 800 Torr of dry N_2 at –78 °C, and the mixture was warmed to room temperature to dissolve the reactants. The side arm was cooled to –78 °C in order to create a temperature gradient. Colorless needles formed after 3 days. The remaining solution was decanted into the side arm of the reaction vessel and removed by heat-sealing off the side arm and contents under vacuum at –196 °C. A crystal having the dimensions 0.57 x 0.05 x 0.05 mm^3 was selected for a low-temperature X-ray structure determination. The crystalline product was transferred into a dry ¼-in. o.d. Pyrex glass tube, sealed using a Swagelok Ultratorr plug, and the Raman spectrum was recorded. The reaction was repeated in Freon-114 and was allowed to react at room temperature for 11 days. Based on the Raman spectrum and multiple unit cell determinations, only $[Hg(OTeF_5)(N{=}SOF_2) \cdot N{\equiv}SF_3]_\infty$ had formed.

(v) $[Hg_3(OTeF_5)_5(N{=}SOF_2) \cdot 2N{\equiv}SF_3]_2$. The reagents, $Hg(OTeF_5)_2$ (0.1406 g, 0.2074 mmol) and excess NSF_3, were combined in an FEP reaction vessel and SO_2 (~0.3 mL) was condensed onto the reagents at −78 °C. The reactor and contents were backfilled to 800 Torr with dry N_2 at −78 °C and warmed to room temperature to dissolve the

reactants. Crystals were grown at room temperature by solvent evaporation over a 12 h period by cooling the side arm of the vessel to −78 °C, resulting in colorless plates. A crystal having the dimensions 0.05 x 0.08 x 0.14 mm^3 was selected for a low-temperature X-ray structure determination.

3.4.2. Structure Solution and Refinement

The XPREP[56] program was used to confirm the crystal system, and the space group. The structures were solved in their respective space groups by use of direct methods using SHELXS[56] or SIR92,[57] and the solutions yielded the positions of all the heavy atoms as well as some of the lighter atoms. Successive difference Fourier syntheses revealed the positions of the remaining light atoms. The final refinements were obtained by introducing anisotropic parameters for all the atoms, an extinction parameter, and the recommended weighting factor. The maximum electron densities in the final difference Fourier maps were located around the heavy atoms. The PLATON program[57] could not suggest additional or alternative symmetries .

Structure refinements of $[Hg(OTeF_5)_2{\cdot}2N{\equiv}SF_3]_2$ and $[Hg(OTeF_5)(N{=}SOF_2){\cdot}N{\equiv}SF_3]_\infty$ were straightforward. In the structure of $[Hg_3(OTeF_5)_5(N{=}SOF_2){\cdot}2N{\equiv}SF_3]_2$, one $N{\equiv}SF_3$ molecule was disordered among three equally populated orientations. Two NSF_3 molecules were two-fold (50/50) in the structure of $Hg_3(OTeF_5)_6{\cdot}4N{\equiv}SF_3$. The $N{\equiv}SF_3$ molecule of $[Hg(OTeF_5)_2{\cdot}N{\equiv}SF_3]_\infty$ was disordered among three equally occupied orientations, and both terminal teflate groups were found to be two-fold disordered (50/50). The disorders were dealt with by using the command SAME.[56] The disordered groups shared a common central sulfur or tellurium

atom; as a consequence, the fluorine atoms of the disordered entities were refined isotropically. X-ray crystallographic files are available in CIF format for the structure determinations of (**1**), (**2**), (**3**), (**4**), and (**5**); this material is available free of charge via the Internet at http://pubs.acs.org.

3.4.3. NMR Sample Preparation

A ^{19}F NMR sample was prepared to support the postulated reaction pathway given in Scheme 1. A T-shaped reaction vessel was constructed from a ¼-in. o.d length of FEP tubing and was fused to 4-mm o.d. length of FEP tubing, which served as a side arm and NMR sample tube. To the ¼-in. section of the reaction vessel, 0.1027 g (0.1515 mmol) of $Hg(OTeF_5)_2$ was added in a drybox followed by condensation of excess NSF_3 and ~0.3 mL of Freon-114® solvent at –196 ^oC. The reaction vessel was warmed to –78 ^oC, backfilled to 400 Torr with dry N_2, and was allowed to react at room temperature, with periodic agitation, for 24 h. The 4-mm o.d. side arm/NMR tube was cooled to –78 ^oC to establish a thermal gradient for the distillation of volatiles from the reaction mixture. When distillation appeared to be complete, both arms of the reaction vessel were cooled to –196 ^oC, and N_2 was removed under dynamic vacuum. The ¼-in. section of the reaction vessel was warmed to room temperature under static vacuum to ensure all volatiles had condensed into the side arm/NMR tube immediately before it was heat-sealed at –196 ^oC under dynamic vacuum. The colorless solution was stored at –78 ^oC until the ^{19}F NMR spectrum could be obtained. The 4-mm FEP sample tube was inserted into a 5-mm o.d. thin wall precision glass NMR tube (Wilmad) prior to recording the ^{19}F

NMR spectrum.

3.4.4. Computational Details.

The optimized gas-phase geometry of $Hg_3(OTeF_5)_6 \cdot 4N{\equiv}SF_3$ was obtained at the PBE0 level of theory using the def2-SVP basis sets. The basis sets were obtained online from the EMSL Basis Set Exchange.[58] Quantum-chemical calculations were carried out using the program Gaussian 09[59] for geometry optimizations and vibrational frequencies and intensities. Natural bond orbital analyses were performed using PBE0 densities with the NBO program (version 6.0).[60]

3.5. Supporting Information Contents - Appendix A

Complete experimental geometrical parameters of (**1**) (Table S3.1), (**2**) (Table S3.2), (**3**) (Table S3.3), (**4**) (Table S3.4), and (**5**) (Table S3.5), Fully labeled X-ray crystal structure of dimeric $[Hg_3(OTeF_5)_5(N{=}SOF_2) \cdot 2N{\equiv}SF_3]_2$ (Figure S3.1), calculated geometrical parameters (Table S3.6) and NBO Analyses of (**3**) (Table S3.7).

3.5. References

(1) Glemser, O.; Mews, R. *Adv. Inorg. Chem. Radiochem.* **1972**, *14*, 333–390.

(2) Mews, R. Adv. *Inorg. Chem. Radiochem.* **1976**, *19*, 185–237.

(3) Glemser, O.; Mews, R. *Angew. Chem., Int. Ed. Engl.* **1980**, *19*, 883–899.

(4) Roesky, H. W. *J. Fluorine Chem.* **1999**, *100*, 217–226.

(5) Richert, H.;Glemser, O. *Z. Anorg. Allg. Chem.* **1961**, *307*, 328–344.

(6) Glemser, O.; Richert, H. *Z. Anorg. Allg. Chem.* **1961**, *307*, 313–327.

(7) Koeniger, F.; Müller, A.; Glemser, O. *J. Mol. Struct.* **1978**, *46*, 29–34.

(8) Müller, A.; Ruoff, A.; Krebs, B.; Glemser, O.; Koch, W. *Spectrochim. Acta, Part A* **1969**, *25*, 199–205.

(9) Kirchhoff, W. H.; Wilson, E. B., Jr. *J. Am. Chem. Soc.* **1962**, *84*, 334–336.

(10) Borrmann, T.; Lork, E.; Mews, R.; Parsons, S.; Petersen, J.; Stohrer, W.-D.; Watson, P. G. *Inorg. Chim. Acta* **2008**, *361*, 479–486.

(11) Glemser, O.; Koch,W. *An. Asoc. Quim. Argent.* **1971**, *59*, 143–148.

(12) Müller, A.; Glemser, O.; Scherf, K. *Chem. Ber.* **1966**, *99*, 3568–3571.

(13) Erhart, M.; Mews, R. *Z. Anorg. Allg. Chem.* **1992**, *615*, 117–122.

(14) Smith, G.L.; Schrobilgen, G.J. *Inorg. Chem.* **2009**, *48*, 7714–7728.

(15) Smith, G.L.; Mercier, H.P.A.; Schrobilgen, G.J. *Inorg. Chem.* **2007**, *46*, 1369–1378.

(16) Mews, R. *J. Chem. Soc., Chem. Commun.* **1979**, *6*, 278–279

(17) Buss, B.; Clegg, W.; Hartmann, G.; Jones, P.G.; Mews, R.; Noltemeyer, M.; Sheldrick, G. *J. Chem. Soc., Dalton Trans.* **1981**, *1*, 61–63.

(18) Behrens, U.; Hoppenheit, R.; Isenberg, W.; Lork, E.; Petersen, J.; Mews, R. *Z. Naturforsch., B: Chem. Sci.* **1994**, *49*, 238–242.

(19) Behrens, U.; Lork, E.; Petersen, J.; Waterfeld, A.; Mews, R. *Z. Anorg. Allg. Chem.* **1997**, *623*, 1518–1524.

(20) Mews, R.; Glemser, O.; *Angew. Chem.* **1975**, *87*, 205.

(21) Seppelt, K.; Sundermeyer, W. *Angew. Chem., Int. Ed. Engl.* **1970**, *9*, 905.

(22) Jäckh, C.; Roland, A.; Sundermeyer, W. *Chem. Ber.* **1975**, *108*, 2580–2588.

(23) Feser, M.; Höfer, R.; Glemser, *Z. Naturforsch., B: Chem. Sci.* **1974**, *29*, 716–718.

(24) Feser, M.; Höfer, R.; Glemser, O. *Z. Naturforsch., B: Chem. Sci.* **1975**, *30*, 327–329.

(25) Roland, A.; Sundermeyer, W. *Z. Naturforsch., B: Chem. Sci.* **1972**, *27*, 1102–1103.

(26) Höfs, H.; Mews, R.; Noltemeyer, M.; Sheldrick, G.M.; Schmidt, M. *Z. Naturforsch., B: Chem. Sci.* **1983**, *38*, 454–459.

(27) Eisenbarth, R.; Sundermeyer, W. *Angew. Chem.* **1978**, *90*, 226.

(28) Mews, R.; Glemser, O. *J. Chem. Soc., Chem. Commun.* **1973**, *21*, 823–824.

(29) Buss, B.; Altena, D. *Z. Anorg. Allg. Chem.* **1978**, *440*, 65–73.

(30) Buss, B.; Altena, D. *Z.*; Mews, R.; Glemser, O. *Angew. Chem.* **1978**, *90*, 287–288.

(31) Hoppenheit, R.; Mews, R.; Noltemeyer, M.; Sheldrick, G.M. *Chem. Ber.* **1983**, *116*, 874–881.

(32) Eisenbarth, R.; Sundermeyer, W. *Z. Naturforsch., B: Chem. Sci.* **1981**, *36*, 1343–1344.

(33) Eisenbarth, R.; Sundermeyer, W. *Z. Naturforsch., B: Chem. Sci.* **1978**, *33*, 1194–1195.

(34) DeBackere, J. R.; Mercier, H. P. A.; Schrobilgen, G. J. *J. Am. Chem. Soc.* **2014**, *136*, 3888−3903.

(35) DeBackere, J. R.; Mercier, H. P. A.; Schrobilgen, G. J. *Inorg. Chem.* **2015**, *54*, 1606−1626.

(36) Huppmann, P.; Hartl, H.; Seppelt, K. *Z. Anorg. Allg. Chem.* **1985**, *524*, 26−32.

(37) Strauss, S. H.; Noirot, M. D.; Anderson, O. P. *Inorg. Chem.* **1985**, *24*, 4307−4311.

(38) Colsman, M. R.; Noirot, M. D.; Miller, M. M.; Anderson, O. P.; Strauss, S. H. *J. Am. Chem. Soc.* **1988**, *110*, 6886−6888.

(39) Colsman, M. R.; Newbound, T. D.; Marshall, L. J.; Noirot, M. D.; Miller, M. M.; Wulfsberg, G. P.; Frye, J. S.; Anderson, O. P.; Strauss, S. H. *J. Am. Chem. Soc.* **1990**, *112*, 2349−2362.

(40) Rack, J. J.; Hurlburt, P. K.; Kellett, P. J.; Luck, J. S.; Anderson, O. P.; Strauss, S. H. *Inorg. Chim. Acta* **1996**, *242*, 71−79.

(41) Hurlburt, P. K.; Anderson, O. P.; Strauss, S. H. *J. Am. Chem. Soc.* **1991**, *113*, 6277−6278.

(42) Newbound, T. D.; Colsman, M. R.; Miller, M. M.; Wulfsberg, G. P.; Anderson, O. P.; Strauss, S. H. *J. Am. Chem. Soc.* **1989**, *111*, 3762−3764.

(43) Smith, G. L.; Mercier, H. P. A.; Schrobilgen, G. J. *J. Am. Chem. Soc.* **2009**, *131*, 7272–7286.

(44) Elgad, U.; Selig, H. *Inorg. Chem.* **1975**, *14*, 140−145.

(45) Bondi, A. *J. Phys. Chem.* **1964**, *68*, 441−451.

(46) Addison, A. W.; Rao, T. N. *J. Chem. Soc., Dalton Trans.* **1984**, *7*, 1349−1356.

(47) Krebs, B.; Meyer-Hussein, E.; Glemser, O.; Mews, R. *Chem. Commun.* **1968**, *24*, 1578–1579.

(48) Schulz, A.; Villinger, A. *Chem.–Eur. J.* **2015**, *21*, 3649–3663.

(49) Bondi, A. *J. Phys. Chem.* **1966**, *70*, 3006−3007.

(50) Casteel, W. J., Jr.; Dixon, D. A.; Mercier, H. P. A.; Schrobilgen, G. J. *Inorg. Chem.* **1996**, *35*, 4310−4322.

(51) Mews, R.; Keller, K.; Glemser, O. *Inorg. Synth.* **1986**, *24*, 12–17.

(52) Schack, C.; Wilson, R. D. *Inorg. Chem.* **1970**, *9*, 311−314.

(53) Gerken, M.; Dixon, D. A.; Schrobilgen, G. J. *Inorg. Chem.* **2000**, *39*, 4244−4255.

(54) APEX2, release v2011.6−1; Bruker AXS, Inc.: Madison, WI, 1995.

(55) Sheldrick, G. M. SADABS (Siemens Area Detector Absorption Corrections), version 2.10; Siemens Analytical X-ray Instruments, Inc.: Madison, WI, 2004.

(56) Sheldrick, G. M., SHELXTL, release 6.14; Siemens Analytical X-ray Instruments, Inc.; Madison, WI, 1993−2014.

(57) Spek, A. L. *J. Appl. Crystallogr.* **2003**, *36*, 7−13.

(58) Basis sets were obtained from the Extensible Computational Chemistry Environment Basis set Database, version 2/25/04, as developed and distributed by the Molecular Science Computing Facility, Environmental and Molecular Science Laboratory, which is part of the Pacific Northwest Laboratory, P.O. Box 999, Richland, WA 99352. https://bse.pnl.gov/bse/portal

(59) Frisch, M. J.; Trucks, G. W.; Schlegel, H. B.; Scuseria, G. E.; Robb, M. A.; Cheeseman, J. R.; Scalmani, G.; Barone, V.; Mennucci, B.; Petersson, G. A.; Nakatsuji, H.; Caricato, M.; Li, X.; Hratchian, H. P.; Izmaylov, A. F.; Bloino, J.; Zheng, G.; Sonnenberg, J. L.; Hada, M.; Ehara, M.; Toyota, K.; Fukuda, R.; Hasegawa, J.; Ishida, M.; Nakajima, T.; Honda, Y.; Kitao, O.; Nakai, H.; Vreven, T.; Montgomery, J. A., Jr.; Peralta, J. E.; Ogliaro, F.; Bearpark, M.; Heyd, J. J.; Brothers, E.; Kudin, K. N.; Staroverov, V. N.; Kobayashi, R.; Normand, J.; Raghavachari, K.; Rendell, A.; Burant, J. C.; Iyengar, S. S.; Tomasi, J.; Cossi, M.; Rega, N.; Millam, N. J.; Klene, M.; Knox, J. E.; Cross, J. B.; Bakken, V.; Adamo, C.; Jaramillo, J.; Gomperts, R.; Stratmann, R. E.; Yazyev, O.; Austin, A. J.; Cammi, R.; Pomelli, C.; Ochterski, J. W.; Martin, R. L.; Morokuma, K.; Zakrzewski, V. G.; Voth, G. A.; Salvador, P.; Dannenberg, J. J.; Dapprich, S.; Daniels, A. D.; Farkas, Ö.; Foresman, J. B.; Ortiz, J. V.; Cioslowski, J.; Fox, D. J. Gaussian 09, Revision D.01; Gaussian, Inc: Wallingford, CT, 2009.

(60) NBO 6.0. Glendening, E. D.; Badenhoop, J. K.; Reed, A. E.; Carpenter, J. E.; Bohmann, J. A.; Morales, C. M.; Landis, C. R.; Weinhold, F. Theoretical Chemistry Institute, University of Wisconsin, Madison (2013).

CHAPTER 4

Pentafluoro-oxotellurate(VI) Anions of Mercury(II); the Syntheses and Structures of $[Hg(OTeF_5)_4]^{2-}$, $[Hg(OTeF_5)_5]^{3-}$, $[Hg_2(OTeF_5)_6]^{2-}$, $[Hg(OTeF_5)_4]^{2-}\cdot Hg(OTeF_5)_2$, and $[Hg_2(OTeF_5)_7]^{3-}\cdot Hg(OTeF_5)_2$

Adapted with permission from: DeBackere, J.R., Mercier, H.P.A., and Schrobilgen, G.J. *Inorganic Chemistry*, **2015**, *54*, 1606–1626.

4.1. Introduction

Mercury(II) halogeno-anions have been extensively studied, revealing a considerable structural diversity in the solid state. From the large number of chloro-, bromo-, and iodomercury(II) anions that have been synthesized and structurally characterized by single-crystal X-ray diffraction, it is evident that the solid-state anion structures often do not reflect the empirical formula.[1] For example, over 30 chloromercury(II) anions have been reported with structures ranging from isolated mononuclear $[HgCl_3]^-$ and dinuclear $[Hg_2Cl_6]^{2-}$ to infinite chain $[HgCl_3^-]_\infty$ anions.[1] The mononuclear halogenomercury(II) anions, $[HgX_3]^-$ (X = Cl,[1] I[2]) and $[HgX_4]^{2-}$ (X = Cl,[1] Br[3], I[4]) are well known, but examples of $[HgX_5]^{3-}$ and $[HgX_6]^{4-}$ are limited to the trigonal bipyramidal anions of $[Cr(NH_3)_6][HgCl_5]$,[5] $[Co(NH_3)_6][HgBr_5]$,[6] and $[H_3N(CH_2)_2NH_2(CH_2)_2NH_3]_2[HgCl_5]$,[7] and the octahedral anions of $[Tl]_4[HgX_6]$ (X = Br,[8] I[9]) and $[NH_4]_4[HgBr_6]$.[10] Halogen-bridging between mercury(II) atoms results in the formation of polynuclear anions. Among those which have been structurally characterized are the halogen-bridged dinuclear $[Hg_2X_6]^{2-}$ and $[Hg_2X_7]^{3-}$ (X = Cl,[1] I[11,12]) anions, trinuclear $[Hg_3Cl_7]^-$ [1] and $[Hg_3X_8]^{2-}$ (X = Cl,[1] I[13]) anions; higher polynuclear anions such as $[Hg_4Cl_{14}]^{6-}$, $[Hg_5Cl_{11}]^-$, and $[Hg_6Cl_{13}]^-$; and examples of extensively halogen-bridged

polymeric and network structures.[1] Although not comprehensive, these examples illustrate considerable structural diversity that exists among the heaver halogenomercury(II) anions. In the case of fluoromercury(II) anions, the greater propensity for fluorine to bridge has limited the number of structurally characterized examples to the extended three-dimensional network solids, $MHgF_3$ (M = K, Rb, Cs)[14] and M_2HgF_4 (M = Rb, Cs).[15] The geometries of the $[HgF_3]^-$ (D_{3h}) and $[HgF_4]^{2-}$ (T_d) anions have been calculated in the gas phase.[16]

The pentafluoro-orthotellurate group, F_5TeO– (teflate), is a bulky pseudohalide with a group electronegativity (3.88[17] and 3.87[18]) that is comparable to that of fluorine (3.98, Allred-Rochow scale). The binding strength of the teflate ligand has been shown to follow the order Cl^- > $[F_5TeO]^-$ > $[ClO_4^-]$ for Fe(TTP)(L) ($[TTP]^{2-}$ = *meso*-tetraphenylporphinate and L = Cl^-, $[F_5TeO]^-$, $[ClO_4]^-$).[19] The F_5TeO–group is terminally bonded in the majority of its compounds, with only a few examples of μ–oxygen bonding. The latter bonding modality has been predominantly found in neutral metal compounds, e.g., $[TlOTeF_5(mes)_2]_2$·mes (mes = 1,3,5-trimethylbenzene),[20] $Au(OTeF_5)_3$,[21] $[AgOTeF_5(C_6H_5CH_3)_2]_2$,[22] $[AgOTeF_5(1,2\text{-}C_2H_4Cl_2)]_2$,[23] and $[Zn(OTeF_5)_2(C_6H_5NO_2)_2]_2$,[24] as well as in the salts, $[Ag(CO)][B(OTeF_5)_4]$[25] and $Ag(CH_2C1_2)Pd(OTeF_5)_4$.[26] Unlike HgF_2 (Hg coordination number = 8), which possesses an extended three-dimensional solid-state structure similar to $[HgF_3]^-$ and $[HgF_4]^{2-}$ (Hg coordination number = 6), the crystal structure of $Hg(OTeF_5)_2$ consists of discrete molecular units that only interact through long Hg---O and Hg---F intermolecular contacts.[27] Consequently, mercury teflate anions are not expected to form extensively teflate-bridged lattices. Considering the

notable differences between the solid-state structures of HgF_2 and $Hg(OTeF_5)_2$, it was of interest to determine if teflate analogues of halogenomercury(II) anions could be formed and to establish their structural diversity.

Anions derived from the teflate group are known for their weakly coordinating properties and their ability to stabilize strong electrophiles and high oxidation states.[28] The $[M(OTeF_5)_n]^{m-}$ anions that have been characterized in the solid state are limited to tetrahedral $[B(OTeF_5)_4]^-$,[29,30] square-planar $[I(OTeF_5)_4]^-$ [31] and $[Pd(OTeF_5)_4]^{2-}$,[26] square-pyramidal $[Te(OTeF_5)_5]^-$,[32] and octahedral $[M(OTeF_5)_6]^-$ (M = As,[33] Sb,[32,34] Bi,[33] Nb,[34] Ta[34]) and $M(OTeF_5)_6^{2-}$ (M = Ti, Zr, Hf)[34]. Among the group 12 elements, three salts containing the $[Zn(OTeF_5)_4]^{2-}$ anion have been briefly mentioned in the literature.[35] The salt, $Ag_2[Zn(OTeF_5)_4]$, was characterized by infrared and ^{19}F NMR spectroscopy, whereas $[Ag(CO)]_2[Zn(OTeF_5)_4]$ and $[Ag(CO)_2]_2[Zn(OTeF_5)_4]$ were characterized by infrared and ^{13}C MAS NMR spectroscopy.[36]

The present study describes the syntheses of a series of Hg(II) teflate anions and their characterizations by low-temperature single-crystal X-ray diffraction; Raman spectroscopy; and quantum-chemical calculations. The anions series represents the first examples of mercury(II) teflate anions that have been synthesized and structurally characterized.

4.2. Results and Discussion

4.2.1. Syntheses

Low-temperature Raman spectra were recorded on colorless crystalline samples obtained by slow solvent evaporation at 0 °C unless otherwise stated. Single crystals suitable for X-ray structure determinations were obtained from the Raman samples. The compounds showed high solubility in SO_2 and CH_2Cl_2, whereas SO_2ClF provided low to moderate solubility.

4.2.1.1. Syntheses of $[NR_4]_2[Hg(OTeF_5)_4]$ and $[NR_4]_3[Hg(OTeF_5)_5]$ (R = $-CH_2CH_3$)

The $[N(CH_2CH_3)_4]_2[Hg(OTeF_5)_4]$ salt was synthesized by the reaction of $Hg(OTeF_5)_2$ with $[N(CH_2CH_3)_4][OTeF_5]$ (ca. 1:2 molar ratio) in SO_2ClF solvent at room temperature (eq 4.1).

$$Hg(OTeF_5)_2 + 2\,[N(CH_2CH_3)_4][OTeF_5] \longrightarrow [N(CH_2CH_3)_4]_2[Hg(OTeF_5)_4] \qquad (4.1)$$

The salt, $[N(CH_2CH_3)_4]_3[Hg(OTeF_5)_5]$, was synthesized by combining $Hg(OTeF_5)_2$ with $[N(CH_2CH_3)_4][OTeF_5]$ (ca. 1:4 molar ratio) in SO_2ClF solvent at room temperature (eq 4.2).

$$Hg(OTeF_5)_2 + 3\,[N(CH_2CH_3)_4][OTeF_5] \longrightarrow [N(CH_2CH_3)_4]_3[Hg(OTeF_5)_5] \qquad (4.2)$$

4.2.1.2. Syntheses of $[NR_4]_2[Hg_2(OTeF_5)_6]$ (R = $-CH_3$ or $-CH_2CH_3$)

The synthesis of $[N(CH_3)_4]_3[Hg(OTeF_5)_5]$ was carried out in liquid SO_2 by combining $[N(CH_3)_4][OTeF_5]$ with $Hg(OTeF_5)_2$ (2.2:1 molar ratio) at 0 ^oC (eq 4.3).

$$Hg(OTeF_5)_2 + 3\,[N(CH_3)_4][OTeF_5] \longrightarrow [N(CH_3)_4]_3[Hg(OTeF_5)_5] \qquad (4.3)$$

The salt, $[N(CH_3)_4]_2[Hg_2(OTeF_5)_6]$, was synthesized at room temperature by the reaction of $Hg(OTeF_5)_2$ with $[N(CH_3)_4][OTeF_5]$ in a 1:1 molar ratio using CH_2Cl_2 as the solvent (eq 4.4).

$$2\ Hg(OTeF_5)_2 + 2\ [N(CH_3)_4][OTeF_5] \longrightarrow [N(CH_3)_4]_2[Hg_2(OTeF_5)_6] \quad (4.4)$$

4.2.1.3. $Cs_2[Hg(OTeF_5)_4]\cdot Hg(OTeF_5)_2$ and $\{Cs_3[Hg_2(OTeF_5)_7]\cdot Hg(OTeF_5)_2\}\cdot 4SO_2ClF$

The reaction of $Hg(OTeF_5)_2$ with a stoichiometric excess of $Cs[OTeF_5]$ (ca. 1:4 molar ratio) in SO_2ClF solvent at room temperature resulted in the formation of $Cs_2[Hg(OTeF_5)_4]\cdot Hg(OTeF_5)_2$ according to eq 4.5.

$$2\ Hg(OTeF_5)_2 + 2\ Cs[OTeF_5] \longrightarrow Cs_2[Hg(OTeF_5)_4]\cdot Hg(OTeF_5)_2 \quad (4.5)$$

At a 1:2 molar ratio of $Hg(OTeF_5)_2$: $Cs[OTeF_5]$, crystalline $\{Cs_3[Hg_2(OTeF_5)_7]\cdot Hg(OTeF_5)_2\}\cdot 4SO_2ClF$ was obtained from SO_2ClF and characterized by single-crystal X-ray diffraction. Regardless of the stoichiometric excess of $Cs[OTeF_5]$ that was used, no other species were isolated or identified by Raman spectroscopy.

4.2.1.4. Attempted Syntheses of $[NR_4][Hg(OTeF_5)_3]$ and $[NR_4]_4[Hg(OTeF_5)_6]$ ($R = CH_2CH_3$)

Reactions employing high molar ratios of $[N(CH_2CH_3)_4][OTeF_5]$ to $Hg(OTeF_5)_2$ only resulted in $[N(CH_2CH_3)_4]_2[Hg(OTeF_5)_4]$ and $[N(CH_2CH_3)_4]_3[Hg(OTeF_5)_5]$. Attempts to synthesize the mononuclear $[Hg(OTeF_5)_3]^-$ anion using 1:1 molar ratios of $[N(CH_2CH_3)_4][OTeF_5]$ to $Hg(OTeF_5)_2$ resulted in a colorless vitrous solid which failed to

diffract in a X-ray beam. The Raman spectrum of the material showed bands similar to those identified for the anion of $[N(CH_3)_4]_2[Hg_2(OTeF_5)_6]$, suggesting that the $[N(CH_2CH_3)_4]^+$ salt of $[Hg_2(OTeF_5)_6]^{2-}$ had been synthesized.

4.2.2. X-ray Crystallography

Details of the data collection parameters and other crystallographic information for $[N(CH_2CH_3)_4]_2[Hg(OTeF_5)_4]$, $[N(CH_3)_4]_3[Hg(OTeF_5)_5]$, $[N(CH_2CH_3)_4]_3[Hg(OTeF_5)_5]$, $[N(CH_3)_4]_2[Hg_2(OTeF_5)_6]$, $Cs_2[Hg(OTeF_5)_4]\cdot Hg(OTeF_5)_2$, and $\{Cs_3[Hg_2(OTeF_5)_7]\cdot Hg(OTeF_5)_2\}\cdot 4SO_2ClF$ are provided in Table 4.1. Selected bond lengths and angles for the title anions are listed in Tables 4.2–4.6, and a full list of their geometrical parameters along with the structural parameters of the $[N(CH_3)_4]^+$ and $[N(CH_2CH_3)_4]^+$ cations and SO_2ClF are given in Tables S4.1–S4.6. The cations and SO_2ClF parameters are in good agreement with previously published values[37–41] and do not require further comment.

Table 4.1. Summary of Crystal Data and Refinement Results for $[N(CH_2CH_3)_4]_2[Hg(OTeF_5)_4]$, $[N(CH_3)_4]_3[Hg(OTeF_5)_5]$, $[N(CH_2CH_3)_4]_3[Hg(OTeF_5)_5]$, $[N(CH_3)_4]_2[Hg_2(OTeF_5)_6]$, $Cs_2[Hg(OTeF_5)_4]\cdot Hg(OTeF_5)_2$, and $\{Cs_3[Hg_2(OTeF_5)_7]\cdot Hg(OTeF_5)_2\}\cdot 4SO_2ClF$

	$[N(CH_2CH_3)_4]_2[Hg(OTeF_5)_4]$	$[N(CH_3)_4]_3[Hg(OTeF_5)_5]$	$[N(CH_2CH_3)_4]_3[Hg(OTeF_5)_5]$	$[N(CH_3)_4]_2[Hg_2(OTeF_5)_6]$	$Cs_2[Hg(OTeF_5)_4]\cdot Hg(OTeF_5)_2$	$\{Cs_3[Hg_2(OTeF_5)_7]\cdot Hg(OTeF_5)_2\}\cdot 4SO_2ClF$
space group	*Pc*	*Cc*	$P2_1$	$P2_1/c$	$C2/c$	$P2_1/c$
a (Å)	10.4748(6)	16.2076(19)	14.5473(2)	19.7463 (3)	22.6115(3)	20.5000(4)
b (Å)	13.4264(7)	14.4552(11)	17.9914(2)	11.4754 (2)	10.9340(2)	13.8017(3)
c (Å)	16.2322(7)	16.2482(12)	18.7584(2)	18.0628(3)	15.2294(4)	22.1592(4)
β (deg)	127.345(2)	90.172(3)	95.265(1)	109.147(1)	125.797(1)	107.729(1)
V (Å^3)	1814.9(2)	3806.7(6)	4888.9(1)	3866.6(1)	3053.8(1)	5971.8(2)
molecules/unit cell	2	4	4	8	8	4
mol wt (g mol^{-1})	1415.49	1616.03	1784.34	990.54	1049.30	3621.94
calcd density (g cm^{-3})	2.590	2.820	2.424	3.403	4.564	4.028
T (°C)	–173	–173	–173	–173	–173	–173
μ (mm^{-1})	7.52	7.95	6.20	12.54	18.21	14.33
R_1[a]	0.0285	0.0196	0.0282	0.0194	0.0216	0.0514
wR_2[b]	0.0632	0.0423	0.0465	0.0403	0.0436	0.1122

[a] R_1 is defined as $\Sigma \| F_o | - | F_c \| / \Sigma | F_o |$ for $I > 2\sigma(I)$. [b] wR_2 is defined as $[\Sigma[w(F_o^2 - F_c^2)^2]/\Sigma w(F_o^2)^2]^{1/2}$ for $I > 2\sigma(I)$.

4.2.2.1. $[N(CH_2CH_3)_4]_2[Hg(OTeF_5)_4]$

The crystal structure of $[N(CH_2CH_3)_4]_2[Hg(OTeF_5)_4]$ (Figure 4.1 and S4.1) consists of well-isolated $[Hg(OTeF_5)_4]^{2-}$ anions and $[N(CH_2CH_3)_4]^+$ cations, with the shortest F---CH_3 distances (3.178(12) – 3.398(11) Å) being near the sum of the F[42] and CH_3[43] van der Waals radii (3.47 Å) and equally distributed among the four F_5TeO-groups. The anion geometry closely approximates the calculated gas-phase structure (see Computational Section), which is consistent with minimal and well-dispersed cation-anion interactions.

The Hg(II) coordination sphere is a distorted tetrahedron with O–Hg–O bond angles ranging from 86.3(2) to 125.9(3)°. The $[B(OTeF_5)_4]^-$ anion[29] is the only other tetrahedrally coordinated teflate anion that has been structurally characterized by single-crystal X-ray diffraction; however, $[Hg(OTeF_5)_4]^{2-}$ is more distorted than $[B(OTeF_5)_4]^-$ (∠O–B–O, 106.8(3)–113.8(3)°)[30] or $C(OTeF_5)_4$ (∠O–C–O, 105(1)–116(1)°).[30] Although the isovalent $[Zn(OTeF_5)_4]^{2-}$ anion has been referred to in the literature,[35,36] its crystal structure has not been reported. The $[Pd(OTeF_5)_4]^{2-}$ anion has been characterized by single-crystal X-ray diffraction, but the anion is not isolated in the crystal structure. Instead, the square-planar PdO_4 moiety is O-bridged to two $[Ag(C_nH_{2n}Cl_2)_2]^+$ (n = 1, 2) cations.[44] The Hg–O bond lengths of $[Hg(OTeF_5)_4]^{2-}$ (2.146(7)–2.275(7) Å) are slightly longer than those of $Hg(OTeF_5)_2$ (2.016(6) Å).[27] Because of its negative charge, the Hg–O bonds of $[Hg(OTeF_5)_4]^{2-}$ are expected to be longer and more polar than those of neutral $Hg(OTeF_5)_2$ (see Computational Results, NBO section). Increases in the Hg–O bond lengths are paralleled by decreases in the Te–O bond lengths ($[Hg(OTeF_5)_4]^{2-}$, 1.788(6)–1.805(7) Å; $Hg(OTeF_5)_2$, 1.842(7) Å),[27] which have more π character and are comparable

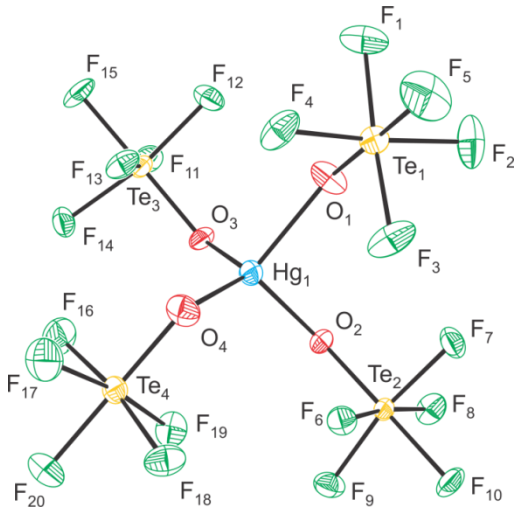

Figure 4.1. The $[Hg(OTeF_5)_4]^{2-}$ anion in the X-ray crystal structure of $[N(CH_2CH_3)_4]_2[Hg(OTeF_5)_4]$ with thermal ellipsoids drawn at the 50% probability level.

Table 4.2. Selected Experimental Geometrical Parameters for the $[Hg(OTeF_5)_4]^{2-}$ Anion in $[N(CH_2CH_3)_4]_2[Hg(OTeF_5)_4]$ and Selected Calculated Geometrical Parameters for $[Hg(OTeF_5)_4]^{2-}$

exptl (C_1) [a]		**calcd (S_4)** [b]	
Bond Lengths (Å)			
$Hg_{(1)}–O_{(1)}$	2.214(6)	$Hg_1–O_8$	2.226
$Hg_{(1)}–O_{(2)}$	2.229(7)	$Hg_1–O_{14}$	2.226
$Hg_{(1)}–O_{(3)}$	2.275(7)	$Hg_1–O_{18}$	2.226
$Hg_{(1)}–O_{(4)}$	2.146(7)	$Hg_1–O_{28}$	2.226
Te–O	1.788(6)–1.805(7)	Te–O	1.799
Te–F	1.816(6)–1.861(6)	Te–F	1.864–1.871
Bond Angles (deg)			
$O_{(1)}–Hg_{(1)}–O_{(2)}$	96.8(3)	$O_8–Hg_1–O_{14}$	108.0
$O_{(1)}–Hg_{(1)}–O_{(3)}$	96.6(2)	$O_8–Hg_1–O_{18}$	112.4
$O_{(1)}–Hg_{(1)}–O_{(4)}$	120.1(3)	$O_8–Hg_1–O_{28}$	108.0
$O_{(2)}–Hg_{(1)}–O_{(3)}$	86.3(2)	$O_{14}–Hg_1–O_{18}$	108.0
$O_{(2)}–Hg_{(1)}–O_{(4)}$	125.9(3)	$O_{14}–Hg_1–O_{28}$	112.4
$O_{(3)}–Hg_{(1)}–O_{(4)}$	122.8(3)	$O_{18}–Hg_1–O_{28}$	108.0

[a] The atom labeling scheme corresponds to that used in Figures 4.1 and S4.1. [b] Calculated at the PBE0/def2-TVZPP level of theory; The atom labeling scheme corresponds to that used in Figure 4.10a.

to those of $[C_{14}H_{19}N_2][OTeF_5]$ (1.803 Å). The Te–O bond lengths are shorter than in any other anion containing terminally bonded F_5TeO-groups, i.e., $[Nb(OTeF_5)_6]^-$ (1.806(9)–1.824(7) Å),[34] $[Ti(OTeF_5)_6]^{2-}$, 1.812(9)–1.822(7) Å),[34] $[B(OTeF_5)_4]^-$ (1.828(2)–1.834(2) Å),[30] and $[Pn(OTeF_5)_6]^-$ (Sb, 1.832(7)–1.849(7) Å,[34] and Bi, 1.846(6)–1.860(6) Å[33]). The Te–F bond lengths (Te–F_{ax}, 1.816(6)–1.832(6) Å; Te–F_{eq}, 1.832(6)– 1.861(6) Å) are slightly longer than those of $Hg(OTeF_5)_2$ (Te–F_{ax}, 1.819(6) Å; Te–F_{eq}, 1.824(6)–1.839(6) Å),[27] which is consistent with the increased negative charge on the oxygen atoms and shorter Te–O bond lengths. These trends are reproduced by the calculated geometries and are reflected in the NBO analyses (see Computational Results).

4.2.2.2. $[NR_4]_3[Hg(OTeF_5)_5]$ (R = $-CH_3$ or $-CH_2CH_3$)

The crystal structure of $[N(CH_3)_4]_3[Hg(OTeF_5)_5]$ (Figures 4.2 and S4.2) consists of well-isolated $[Hg(OTeF_5)_5]^{3-}$ anions and $[N(CH_3)_4]^+$ cations, where the shortest F---CH_3 cation-anion distances (3.094(9) – 3.406(9) Å) are near the sum of the F[42] and CH_3[43] van der Waals radii. In contrast with $[N(CH_2CH_3)_4]_2[Hg(OTeF_5)_4]$, the long F---$CH_3$ cation-anion interactions are not equally distributed among the teflate groups, with the largest number of long F---CH_3 interactions occuring between three F_5TeO-groups ($F_5Te_{(1)}O$, $F_5Te_{(4)}O$, and $F_5Te_{(3)}O$), causing the bond pair arrangement around the central Hg atom to deviate significantly from that of the ideal trigonal bipyramidal geometry that is predicted by the VSEPR rules[45] for the gas-phase anion (see Computational Section). The $O_{(1)}$–Hg–$O_{(4)}$ angle (156.3(2)^o), which should be equal to the $O_{(1)}$–Hg–$O_{(3)}$ (96.4(1)^o) and $O_{(4)}$–Hg–$O_{(3)}$ (107.3(2)^o) angles in a trigonal bipyramid, is splayed open such that $O_{(1)}$

Table 4.3. Selected Experimental Geometrical Parameters for the $[Hg(OTeF_5)_5]^{3-}$ Anion in $[N(CH_3)_4]_3[Hg(OTeF_5)_5]$ and $[N(CH_2H_3)_4]_3[Hg(OTeF_5)_5]$, as well as Selected Calculated Geometrical Parameters for $[Hg(OTeF_5)_5]^{3-}$

	exptl (C_1)					calcd (C_1) [c]	
Bond Lengths (Å)							
	$[N(CH_3)_4]^+$ [a]			$[N(CH_2H_3)_4]^+$ [b]			
$Hg_{(1)}–O_{(1)}$	2.318(5)	$Hg_{(1)}–O_{(2)}$	2.317(3)	$Hg_{(2)}–O_{(6)}$	2.297(3)	$Hg_1–O_8$	2.481
$Hg_{(1)}–O_{(3)}$	2.301(5)	$Hg_{(1)}–O_{(3)}$	2.313(3)	$Hg_{(2)}–O_{(9)}$	2.319(3)	$Hg_1–O_{12}$	2.510
$Hg_{(1)}–O_{(4)}$	2.323(4)	$Hg_{(1)}–O_{(5)}$	2.276(3)	$Hg_{(2)}–O_{(10)}$	2.290(3)	$Hg_1–O_{25}$	2.482
$Hg_{(1)}–O_{(2)}$	2.227(5)	$Hg_{(1)}–O_{(1)}$	2.265(3)	$Hg_{(2)}–O_{(7)}$	2.262(3)	$Hg_1–O_{34}$	2.111
$Hg_{(1)}–O_{(5)}$	2.230(5)	$Hg_{(1)}–O_{(4)}$	2.259(3)	$Hg_{(2)}–O_{(8)}$	2.266(3)	$Hg_1–O_{22}$	2.110
$Hg_{(1)}$---$F_{(17)}$	3.008(4)	$Hg_{(1)}$---$F_{(17)}$	3.141(3)	$Hg_{(2)}$---$F_{(46)}$	3.133(3)		
Te–O	1.772(5)–1.801(4)	Te–O	1.782(3)–1.795(3)	Te–O	1.777(3)–1.795(3)	Te–O	1.777–1.779
Te–F	1.837(5)–1.863(4)	Te–F	1.844(3)–1.860(3)	Te–F	1.832(4)–1.865(3)	Te–F	1.854–1.891
Bond Angles (deg)							
$O_{(1)}–Hg_{(1)}–O_{(2)}$	95.7(2)	$O_{(1)}–Hg_{(1)}–O_{(2)}$	116.4(1)	$O_{(6)}–Hg_{(2)}–O_{(7)}$	86.5(1)	$O_8–Hg_1–O_{12}$	122.1
$O_{(1)}–Hg_{(1)}–O_{(3)}$	96.4(1)	$O_{(1)}–Hg_{(1)}–O_{(3)}$	104.6(1)	$O_{(6)}–Hg_{(2)}–O_{(8)}$	108.9(1)	$O_8–Hg_1–O_{22}$	88.2
$O_{(1)}–Hg_{(1)}–O_{(4)}$	156.3(2)	$O_{(1)}–Hg_{(1)}–O_{(4)}$	102.3(1)	$O_{(6)}–Hg_{(2)}–O_{(9)}$	145.9(1)	$O_8–Hg_1–O_{25}$	115.8
$O_{(1)}–Hg_{(1)}–O_{(5)}$	84.3(2)	$O_{(1)}–Hg_{(1)}–O_{(5)}$	88.1(1)	$O_{(6)}–Hg_{(2)}–O_{(10)}$	87.6(1)	$O_8–Hg_1–O_{34}$	89.9
$O_{(2)}–Hg_{(1)}–O_{(3)}$	94.8(2)	$O_{(2)}–Hg_{(1)}–O_{(3)}$	138.6(1)	$O_{(7)}–Hg_{(2)}–O_{(8)}$	107.5(1)	$O_{12}–Hg_1–O_{22}$	91.8
$O_{(2)}–Hg_{(1)}–O_{(4)}$	83.5(2)	$O_{(2)}–Hg_{(1)}–O_{(4)}$	88.3(1)	$O_{(7)}–Hg_{(2)}–O_{(9)}$	87.8(1)	$O_{12}–Hg_1–O_{25}$	122.1
$O_{(2)}–Hg_{(1)}–O_{(5)}$	161.6(2)	$O_{(2)}–Hg_{(1)}–O_{(5)}$	88.0(1)	$O_{(7)}–Hg_{(2)}–O_{(10)}$	161.5(1)	$O_{12}–Hg_1–O_{34}$	91.8
$O_{(3)}–Hg_{(1)}–O_{(4)}$	107.3(2)	$O_{(3)}–Hg_{(1)}–O_{(4)}$	88.3(1)	$O_{(8)}–Hg_{(2)}–O_{(9)}$	104.9(1)	$O_{22}–Hg_1–O_{25}$	89.9
$O_{(3)}–Hg_{(1)}–O_{(5)}$	103.5(2)	$O_{(3)}–Hg_{(1)}–O_{(5)}$	88.1(1)	$O_{(8)}–Hg_{(2)}–O_{(10)}$	91.0(1)	$O_{22}–Hg_1–O_{34}$	176.4
$O_{(4)}–Hg_{(1)}–O_{(5)}$	89.2(2)	$O_{(4)}–Hg_{(1)}–O_{(5)}$	169.5(1)	$O_{(9)}–Hg_{(2)}–O_{(10)}$	87.4(1)	$O_{25}–Hg_1–O_{34}$	88.3

[a] The atom labeling scheme corresponds to that used in Figures 4.2 and S4.2 of the Appendix B. [b] The atom labeling scheme corresponds to that used in Figure S4.3 of the Appendix B [c] Calculated at the PBE0/def2-TVZPP level of theory. The atom labeling scheme corresponds to that used in Figure 4.10b.

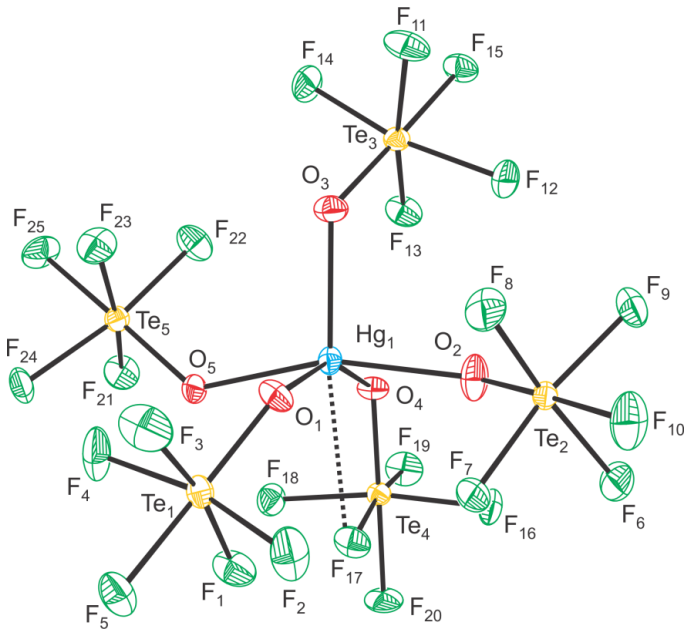

Figure 4.2. The $[Hg(OTeF_5)_5]^{3-}$ anion in the X-ray crystal structure of $[N(CH_3)_4]_3[Hg(OTeF_5)_5]$, where the Hg_1---F_{17} contact is indicated by a dashed line; thermal ellipsoids are shown at the 50% probability level.

and $O_{(4)}$ become essentially coplanar with $O_{(2)}$ and $O_{(5)}$ (with $O_{(1)}$ and $O_{(4)}$ positioned –0.062 Å below the average $O_{(1)}O_{(4)}O_{(2)}O_{(5)}$-plane, and $O_{(2)}$ and $O_{(5)}$ positioned +0.061 Å above this plane), giving rise to a Hg(II) coordination sphere that is best described as a distorted square pyramid. This description is supported by the anions τ-parameter ($\tau = |\beta - \alpha|/60$), where β and α are the two largest angles involving different oxygen ligand atoms,[46] i.e., $O_{(1)}$–Hg–$O_{(4)}$ (156.3(2)°) and $O_{(2)}$–Hg–$O_{(5)}$ (161.6(2)°). The τ-parameter can range from 0 to 1 and can be used as a quantitative measure of how closely the geometry approximates either a trigonal bipyramid (ideal value, 1) or a square pyramid (ideal value, 0). In the present case, $\tau = 0.088$ where the $O_{(3)}$ atom is in the axial position and the remaining oxygen atoms ($O_{(1)}$, $O_{(2)}$, $O_{(4)}$, and $O_{(5)}$) form the equatorial plane of the square

pyramid. The Hg(II) atom is +0.411 Å above the average $O_{(1)}O_{(4)}O_{(2)}O_{(5)}$-plane and the Hg−$O_{eq}$ bonds in the equatorial plane are bent away from the axial oxygen, $O_{(3)}$; consequently, the O_{eq}–Hg–$O_{(3)}$ bond angles (94.8(2)−107.3(2)^o) are larger than 90^o. The *cis*-O_{eq}–Hg–O_{eq} bond angles range from 83.5(2) to 95.7(2)^o. There are two groups of Hg−O_{eq} bonds, two shorter *trans*-bonds (2.227(5) and 2.230(5) Å), and two longer *trans*-bonds (2.318(5) and 2.323(4) Å); the axial Hg−$O_{(3)}$ bond length is intermediate (2.301(5) Å). The two equatorial *trans*-$OTeF_5$ groups, $F_5Te_{(1)}O$− and $F_5Te_{(4)}O$−, point away from the axial $F_5Te_{(3)}O$-group, adopting a *trans, syn*-conformation relative to one another. The $F_5Te_{(5)}O$-group adopts a *cis, anti*-conformation relative to the $F_5Te_{(1)}O$- and $F_5Te_{(4)}O$-groups, whereas the $F_5Te_{(2)}O$-group adopts a *cis, gauche*-conformation in order to avoid the apical $F_5Te_{(3)}O$-group which points towards the midpoint of a line drawn between $O_{(2)}$ and $O_{(4)}$ of the $F_5Te_{(2)}O$- and $F_5Te_{(4)}O$-groups. The Hg−O bonds are slightly longer than those in $[Hg(OTeF_5)_4]^{2-}$ (see above). The Hg−O bond lengths elongate and the Hg−O valencies decrease with increasing negative charge and number of F_5TeO-groups, i.e., 2.016(6) Å ($Hg(OTeF_5)_2$) < 2.146(7)–2.275(7) Å ($[Hg(OTeF_5)_4]^{2-}$) < 2.227(5)–2.323(4) Å ($[Hg(OTeF_5)_5]^{3-}$) (see Computational Results and NBO section). The Te–O (1.772(5)–1.801(4) Å) and Te–F (1.837(5)–1.863 (4) Å) bond lengths are comparable to those in $[Hg(OTeF_5)_4]^{2-}$ (Te–O, 1.788(6)–1.805(7) Å; Te–F, 1.819(6)–1.839(6) Å). An additional long $Hg_{(1)}$---$F_{(17)}$ (3.008(9) Å) intra-ionic contact occurs *trans* to Hg---$O_{(3)}$, which may favor the observed square-pyramidal geometry. In the crystal structure of $[N(CH_2CH_3)_4]_3[Hg(OTeF_5)_5]$ (Figure S4.1, Appendix B), the τ parameters for the two crystallographycally distinct $[Hg(OTeF_5)_5]^{3-}$ anions are 0.28 and 0.50, indicating that the

anion geometries are intermediate with respect to the square-pyramidal anion geometry in the $[N(CH_3)_4]^+$ salt and the trigonal-bipyramidal gas-phase geometry. Long $Hg_{(1)}$---$F_{(1)}$ (3.142(8) Å) and $Hg_{(2)}$---$F_{(26)}$ (3.157(10) Å) intra-ionic contacts analogous to the $Hg_{(1)}$---$F_{(17)}$ contacts in the $[N(CH_3)_4]^+$ salt also occur for each anion.

The only other known pentacoordinate teflate anion is $[Te(OTeF_5)_5]^-$.[32] In this instance, the geometry of the Te(IV) coordination sphere is dictated by the presence of a tellurium valence electron lone pair that results in a distorted octahedral arrangement of five bond pairs and one electron lone pair in the Te(IV) valence shell. The geometry around Te(IV) is also a distorted square pyramid, but differs from that of $[Hg(OTeF_5)_5]^{3-}$, with O_{ax}–Te–O_{eq} bond angles that are less than 90° and equatorial oxygen atoms that are displaced toward the axial oxygen so that the central Te atom is positioned below the equatorial plane of oxygen atoms. The displacement is caused by electron lone pair – equatorial electron bond pair interactions in the Te(IV) valence shell.

4.2.2.3. $[N(CH_3)_4]_2[Hg_2(OTeF_5)_6]$

The crystal structure of $[N(CH_3)_4]_2[Hg_2(OTeF_5)_6]$ consists of $[N(CH_3)_4]^+$ cations and dimeric $[Hg_2(OTeF_5)_6]^{2-}$ anions (Figures 4.3 and S4.4, Appendix B). The anions pack along the *c*-axis and interact which each other through long Hg---F contacts ($Hg_{(1)}$---$F_{(4A)}$, 2.850(3) Å; $Hg_{(2)}$---$F_{(18B)}$, 2.812(4) Å). Two additional long $Hg_{(1)}$---$F_{(11)}$ (3.093(4) Å) and $Hg_{(2)}$---$F_{(3)}$ (3.214(4) Å) intra-ionic contacts contribute to the distorted octahedral coordination spheres of $Hg_{(1)}$ and $Hg_{(2)}$.

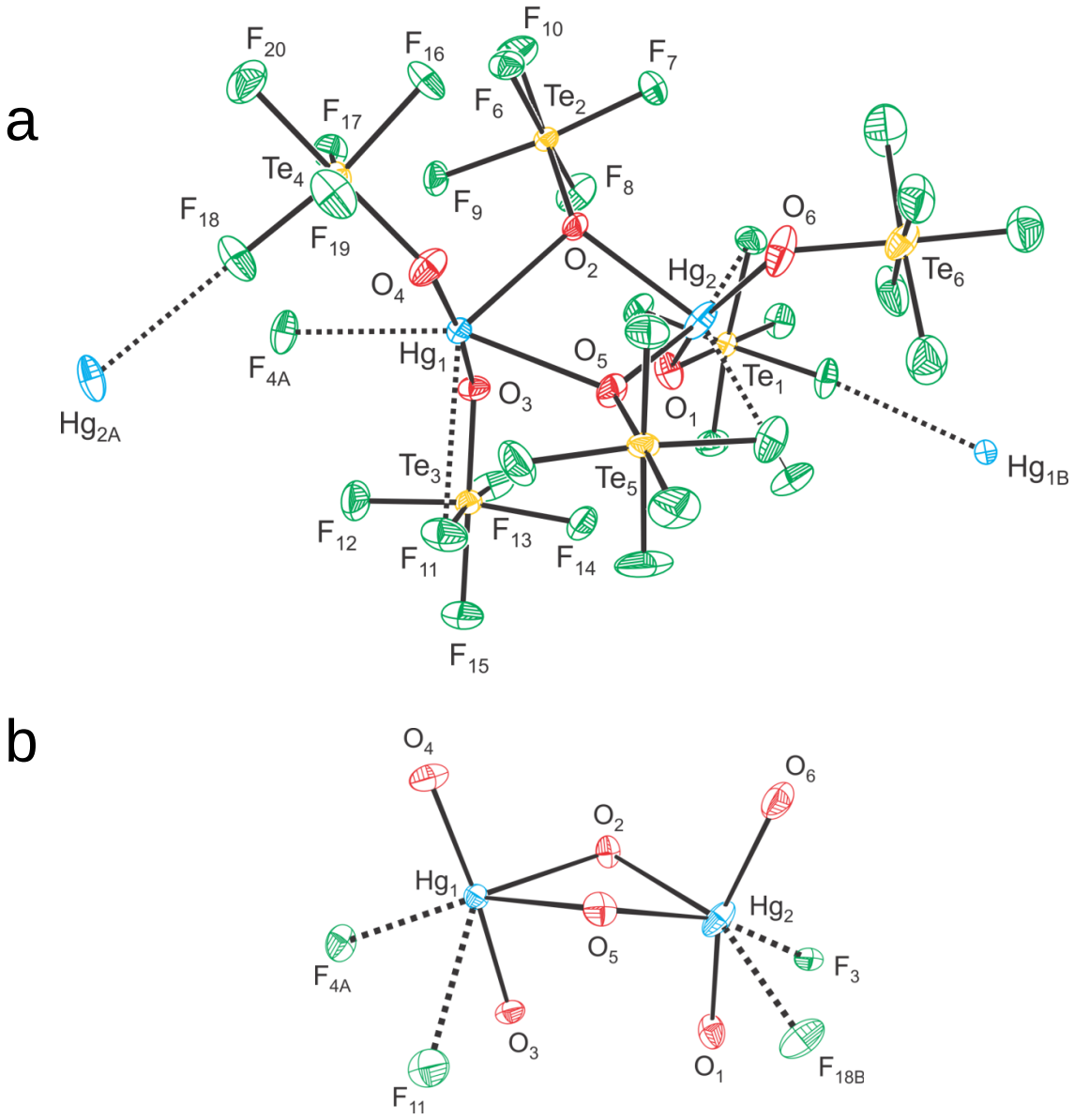

Figure 4.3. (**a**) The $[Hg_2(OTeF_5)_6]^{2-}$ anion in the X-ray crystal structure of $[N(CH_3)_4]_2[Hg_2(OTeF_5)_6]$ showing the the immediate coordination environments around Hg_1 and Hg_2 in the structural unit. The F_5Te– groups have been omitted for clarity in panel (**b**). Secondary bonding interactions are indicated by dashed lines; thermal ellipsoids are shown at the 50% probability level.

Table 4.4. Selected Experimental Geometrical Parameters for $[Hg_2(OTeF_5)_6]^{2-}$ in $[N(CH_3)_4]_2[Hg_2(OTeF_5)_6]$ and Selected Calculated Geometrical Parameters for $[Hg_2(OTeF_5)_6]^{2-}$

	exptl (C_1) [a]		**calcd (D_2)** [b]
Bond Lengths (Å)			
$Hg_{(1)}–O_{(4)}$	2.040(4)	$Hg_1–O_{37}$	2.081
$Hg_{(1)}–O_{(3)}$	2.062(4)	$Hg_1–O_{22}$	2.081
$Hg_{(1)}–O_{(5)}$	2.486(4)	$Hg_1–O_{34}$	2.441
$Hg_{(1)}–O_{(2)}$	2.508(4)	$Hg_1–O_{24}$	2.441
$Hg_{(1)}$---$F_{(4A)}$	2.850(3)		
$Hg_{(1)}$---$F_{(11)}$	3.093(4)		
$Hg_{(2)}–O_{(1)}$	2.075(4)	$Hg_2–O_{36}$	2.081
$Hg_{(2)}–O_{(6)}$	2.104(5)	$Hg_2–O_{39}$	2.081
$Hg_{(2)}–O_{(5)}$	2.350(4)	$Hg_2–O_{34}$	2.441
$Hg_{(2)}–O_{(2)}$	2.416(4)	$Hg_2–O_{24}$	2.441
$Hg_{(2)}$---$F_{(18)}$	2.813(4)		
$Hg_{(2)}$---$F_{(3)}$	3.214(4)		
$Te_{(1)}–O_{(1)}$	1.816(4)	$Te_3–O_{36}$	1.821
$Te_{(2)}–O_{(2)}$	1.790(4)	$Te_5–O_{24}$	1.810
$Te_{(3)}–O_{(3)}$	1.821(4)	$Te_6–O_{22}$	1.821
$Te_{(4)}–O_{(4)}$	1.812(4)	$Te_4–O_{37}$	1.821
$Te_{(5)}–O_{(5)}$	1.802(4)	$Te_7–O_{34}$	1.810
$Te_{(6)}–O_{(6)}$	1.809(5)	$Te_8–O_{39}$	1.821
Te–F [c]	1.825(3)–1.858(3)	Te–F	1.853–1.865
Bond Angles (deg)			
$Hg_{(1)}–O_{(2)}–Hg_{(2)}$	102.1(1)	$Hg_1–O_{24}–Hg_2$	107.2
$Hg_{(1)}–O_{(5)}–Hg_{(2)}$	104.7(1)	$Hg_1–O_{34}–Hg_2$	107.2
$O_{(2)}–Hg_{(1)}–O_{(5)}$	70.0(1)	$O_{24}–Hg_1–O_{34}$	72.8
$O_{(3)}–Hg_{(1)}–O_{(4)}$	174.1(2)	$O_{22}–Hg_1–O_{37}$	162.5
$O_{(3)}–Hg_{(1)}–O_{(2)}$	85.4(2)	$O_{22}–Hg_1–O_{24}$	96.5
$O_{(3)}–Hg_{(1)}–O_{(5)}$	87.2(2)	$O_{22}–Hg_1–O_{34}$	97.6
$O_{(4)}–Hg_{(1)}–O_{(2)}$	98.3(2)	$O_{37}–Hg_1–O_{24}$	97.6
$O_{(4)}–Hg_{(1)}–O_{(5)}$	98.4(2)	$O_{37}–Hg_1–O_{34}$	72.8
$O_{(2)}–Hg_{(2)}–O_{(5)}$	73.9(1)	$O_{24}–Hg_2–O_{34}$	72.80
$O_{(1)}–Hg_{(2)}–O_{(6)}$	157.0(2)	$O_{36}–Hg_2–O_{39}$	162.5
$O_{(1)}–Hg_{(2)}–O_{(2)}$	99.2(2)	$O_{36}–Hg_2–O_{24}$	97.6
$O_{(1)}–Hg_{(2)}–O_{(5)}$	108.6(2)	$O_{36}–Hg_2–O_{34}$	96.5
$O_{(6)}–Hg_{(2)}–O_{(2)}$	93.7(2)	$O_{39}–Hg_2–O_{24}$	96.5
$O_{(6)}–Hg_{(2)}–O_{(5)}$	93.2(2)	$O_{39}–Hg_2–O_{34}$	97.6

Table 4.4. continued …

Dihedral Angles (deg)			
$Te_{(3)}–O_{(3)}–Hg_{(1)}–O_{(4)}–Te_{(4)}$	122.3(3)	$Te_6–O_{22}–Hg_1–O_{37}–Te_4$	12.1
$Te_{(1)}–O_{(1)}–Hg_{(2)}–O_{(6)}–Te_{(6)}$	34.7(5)	$Te_3–O_{36}–Hg_2–O_{39}–Te_8$	12.1

[a] The atom labeling scheme corresponds to that used in Figures 4.3 and S4.4. [b] Calculated at the PBE0/def2-TVZPP level of theory; The atom labeling scheme corresponds to that used in Figure 4.10c. [c] Bond lengths associated to the disordered F_5TeO-group are not included.

Each anion is comprised of two crystallographically inequivalent $Hg(OTeF_5)_2$ molecules that are linked to two crystallographically inequivalent bridging bidentate F_5TeO_μ-groups to form a $[HgO_\mu]_2$ core. The $[N(CH_3)_4]^+$ cations weakly interact with the anions; the shortest F---CH_3 (2.949(8) – 3.394(7) Å) distances being less than or near the sum of the F[42] and CH_3[43] van der Waals radii (Table S4.3, Appendix B).

The Hg and O_μ atoms are not co-planar, with the two Hg atoms positioned +0.24 Å above the average $HgO_\mu HgO_\mu$ plane, and the two O_μ atoms positioned –0.24 Å below this plane. The result is a butterfly-shaped $[HgO_\mu]_2$ geometry having Hg–O_μ–Hg angles of 102.1(1) and 104.6(1)^o and O_μ–Hg–O_μ angles of 70.1(1) and 73.9(1)^o. Similar dimeric $[MO_\mu]_2$ core structures have been observed in other teflate derivatives, e.g., $[AgOTeF_5(1,2\text{-}C_2H_4Cl_2)]$,[21] $[TlOTeF_5(mes)_2]_2\cdot mes$,[19] $[Zn(OTeF_5)_2(C_6H_5NO_2)_2]_2$;[23] however, $[Hg_2(OTeF_5)_6]^{2-}$ is the first anionic example. Each Hg(II) atom is coordinated to two terminal F_5TeO_t-groups and two bridging F_5TeO_μ-groups. The $Hg_{(1)}$–O_t bond lengths that involve terminal F_5TeO_t-groups ($O_{(3)}$, 2.064(4) and $O_{(4)}$, 2.044(4) Å) are comparable to those of $Hg(OTeF_5)_2$ (2.016(6) Å), whereas the $Hg_{(2)}$–O_t bond lengths ($O_{(1)}$, 2.074(4)

and $O_{(6),}$ 2.103(4) Å) are slightly elongated. As expected, the Hg–O_μ bonds are longer than the Hg–O_t bonds, with the bridging $Hg_{(1)}$–O_μ bonds ($O_{(2)}$, 2.507(4) and $O_{(5)}$, 2.486(4) Å) being slightly elongated with respect to the $Hg_{(2)}$–O_μ bridge bonds ($O_{(2)}$, 2.417(4) and $O_{(5)}$, 2.353(4) Å). Analogous Zn–O bond length trends have been observed in $[Zn(OTeF_5)_2(C_6H_5NO_2)_2]_2$ (Zn–O_t (1.928(7) Å) < Zn–O_μ (2.012(5) Å).[23] The $O_{(3)}$–$Hg_{(1)}$–$O_{(4)}$ bond angle (174.1(2)^o) is comparable to that in $Hg(OTeF_5)_2$ (170.5(4)^o),[26] whereas the $O_{(1)}$–$Hg_{(2)}$–$O_{(6)}$ bond angle (157.0(2)^o) is significantly smaller. In both cases, and as observed in $Hg(OTeF_5)_2$, the Hg–O_t bonds are *trans* to one another, but the Te–O_t–Hg–O_t–Te dihedral angles are remarkably different. The terminal teflate groups of $Hg_{(2)}$ adopt a *gauche*-conformation (dihedral $Te_{(1)}$–$O_{(1)}$–$Hg_{(2)}$–$O_{(6)}$–$Te_{(6)}$ angle, 34.7(5)^o) similar to that observed in $Hg(OTeF_5)_2$ (53.7(3)^o),[26] whereas the $Hg_{(1)}(OTeF_5)_2$ moiety possesses an *anti*-conformation (dihedral $Te_{(3)}$–$O_{(3)}$–$Hg_{(1)}$–$O_{(4)}$–$Te_{(4)}$ angle, 122.3(3)^o) close to that calculated for gas-phase $Hg(OTeF_5)_2$ (dihedral Te–O_t–Hg–O_t–Te angle, 139.1^o). As expected, the Te–O_μ bonds (1.788(4) and 1.800(4) Å) are shorter than the Te–O_t bonds (1.811(4), 1.817(4), 1.821(4) Å), consistent with Te–O_μ having more π character than Te–O_t. Interestingly, the opposite trend is observed in $[Zn(OTeF_5)_2(C_6H_5NO_2)_2]_2$ (Te–O_μ (1.837(5) Å > Te–O_t (1.782(6) Å).[23] There are no significant differences among the Te–F bond lengths for all F_5TeO-groups, which are comparable to those of $Hg(OTeF_5)_2$[26] and other teflate derivatives.

4.2.2.4. $Cs_2[Hg(OTeF_5)_4]\cdot Hg(OTeF_5)_2$

The interaction of $Hg(OTeF_5)_2$ with $Cs[OTeF_5]$ affords a chain-type structure (Figures 4.4 and S4.5). The chains result from the interaction of two unique Hg atoms through long Hg---O and Hg---F contacts (vide infra). The Hg environments consist of $Hg(OTeF_5)_2$ molecules that alternate with $[Hg(OTeF_5)_4]^{2-}$ anions along the *c*-axis. Adjacent chains form isolated layers along the *a*- and *b*-axes with no F---F contacts between them that are less than twice the fluorine van der Waals radius (2.94 Å).[37] Columns of Cs^+ cations run parallel to these chains such that each Cs^+ column interacts with three anion chains. The $Cs_{(1)}^+$ cation has nine short Cs---F contacts, six with the $[Hg(OTeF_5)_4]^{2-}$ anions (3.076(1)–3.360(1) Å) and three with the $Hg(OTeF_5)_2$ molecules (3.128(1)–3.347(1) Å).

The $Hg_{(1)}$ coordination sphere (Figure 4.4a) is a distorted pseudo-octahedron with two primary $Hg_{(1)}-O_{(2)}$ bonds (2.058(2) Å), two shorter $Hg_{(1)}$---$O_{(3)}$ (2.555(1) Å), and two slightly longer $Hg_{(1)}$---$O_{(1)}$ contacts (2.737(1) Å). The secondary $Hg_{(1)}$---O contacts involve oxygen atoms from two adjacent $[Hg(OTeF_5)_4]^{2-}$ anions and are significantly less than the sums of the van der Waals radii (3.05 Å for Hg···O),[37] indicating significant covalent interactions between $Hg_{(1)}$ and the oxygen atoms of the $[Hg(OTeF_5)_4]^{2-}$ anions. The oxygen bonding with $Hg_{(1)}$ is reminiscent of that observed for $Hg(OTeF_5)_2$, which also possesses a distorted octahedral coordination sphere consisting of primary Hg−O bonds (2 x 2.016(6) Å) and long Hg_1---O_2 (2 x 2.641(7) Å) and Hg---F (2 x 2.810(7) Å) contacts.[26] The $Hg_{(1)}$–$O_{(2)}$ bonds are slightly longer than in $Hg(OTeF_5)_2$. The corresponding $Te_{(2)}$–$O_{(2)}$ (1.808(2) Å) and $Te_{(2)}$–F (Te–F_a, 1.838(1)–1.863(1) Å and

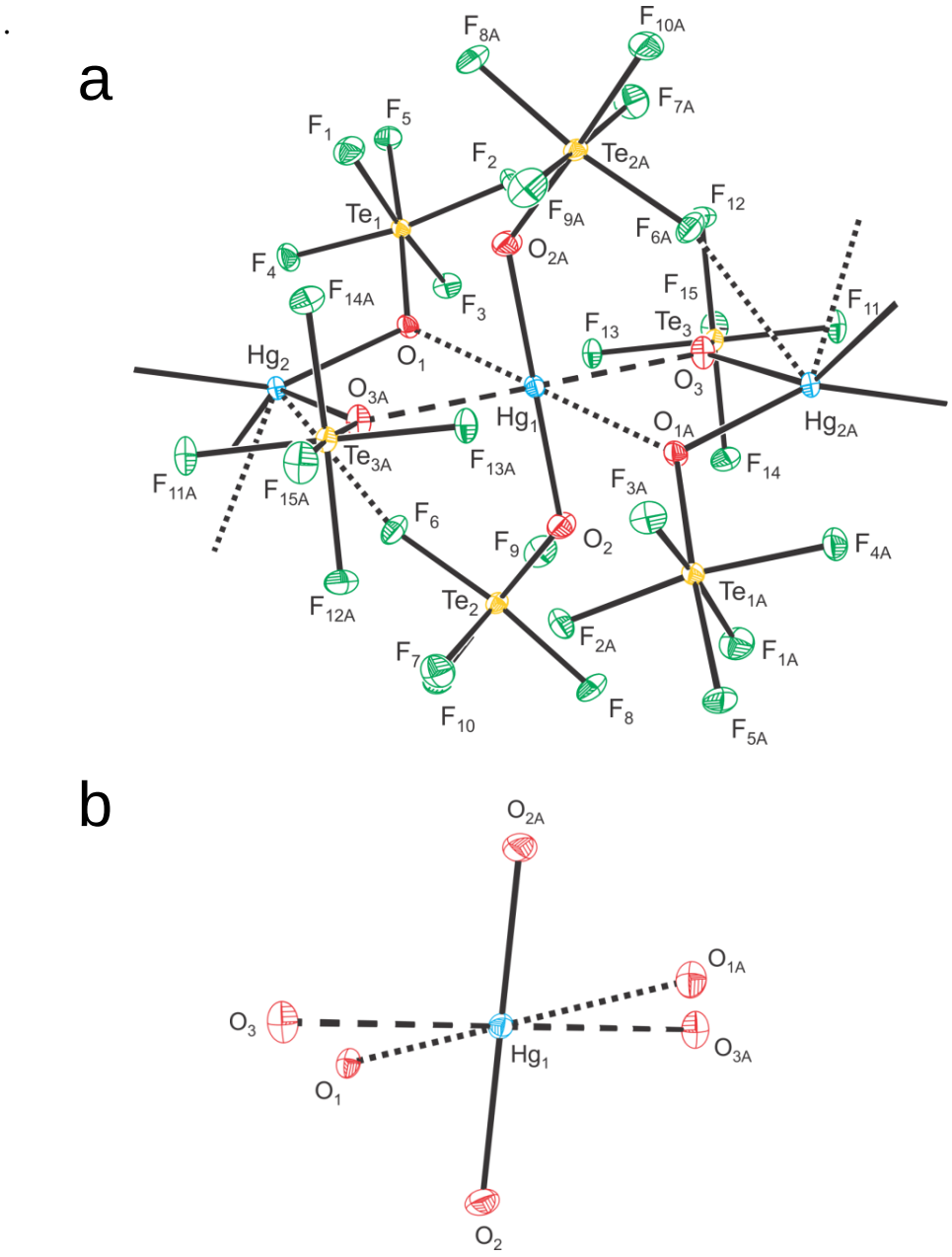

Figure 4.4a. The X-ray crystal structure of $Cs_2[Hg(OTeF_5)_4]\cdot Hg(OTeF_5)_2$ showing the primary coordination sphere (**a**) of Hg_1 in the "$Hg(OTeF_5)_2$" unit and (**b**) for clarity, the F_5Te–groups have been omitted. Long contacts are indicated by dashed lines, and thermal ellipsoids are shown at the 50% probability level.

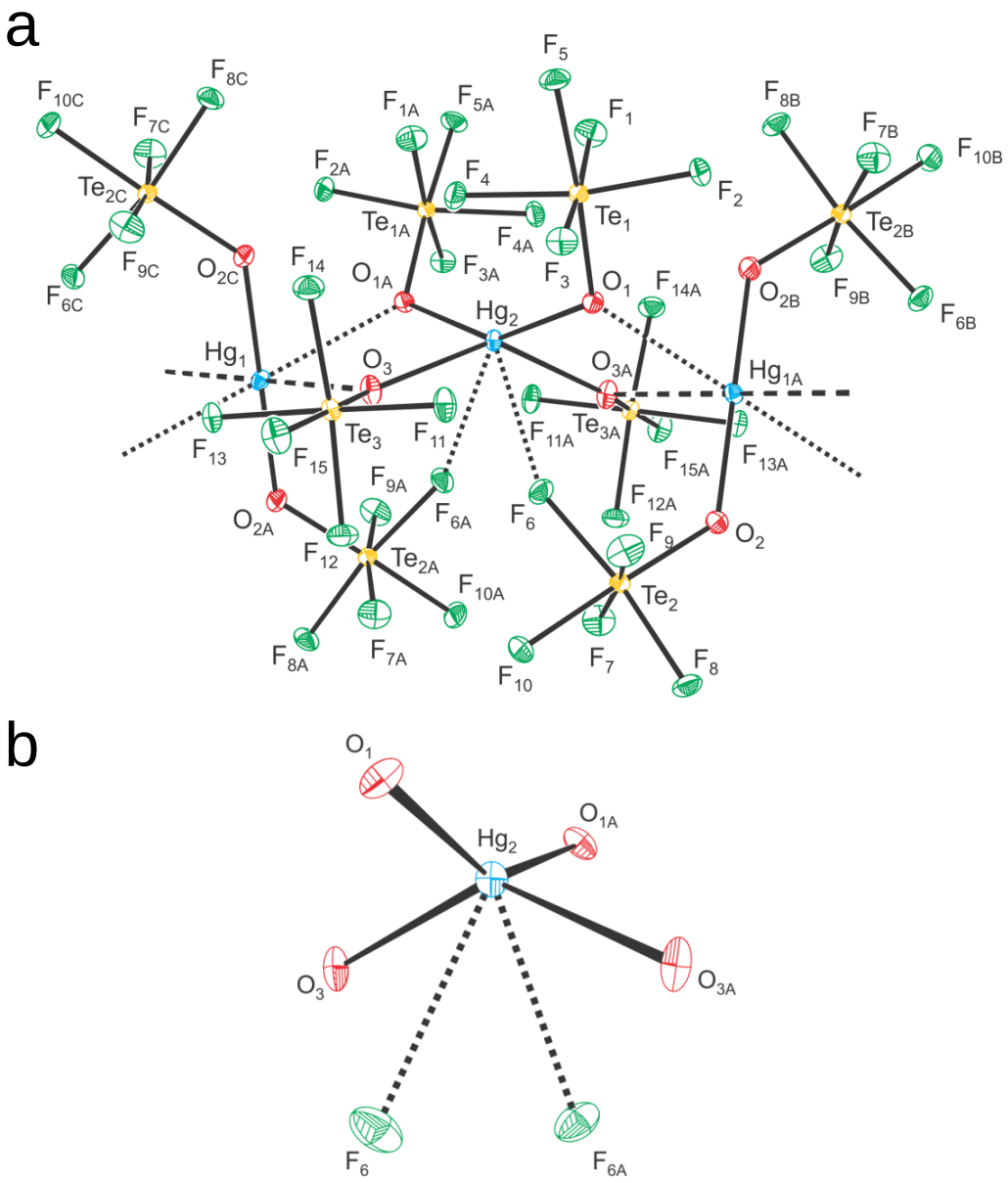

Figure 4.4b. The X-ray crystal structure of $Cs_2[Hg(OTeF_5)_4]\cdot Hg(OTeF_5)_2$ showing the primary coordination sphere (**a**) of Hg_2 in the "$[Hg(OTeF_5)_4]^{2-}$" unit and (**b**) for clarity, the F_5Te–groups have been omitted. Long contacts are indicated by dashed lines, and thermal ellipsoids are shown at the 50% probability level.

Table 4.5. Selected Experimental Geometrical Parameters for $Cs_2[Hg(OTeF_5)_4]\cdot Hg(OTeF_5)_2$ and Selected Calculated Geometrical Parameters for $[Hg_3(OTeF_5)_8]^{2-}$

exptl $Cs_2[Hg(OTeF_5)_4]\cdot Hg(OTeF_5)_2$ (C_1) [a]		calcd $[Hg_3(OTeF_5)_8]^{2-}$ (C_1) [b]	
Bond Lengths (Å)			
$Hg_{(1)}-O_{(2)}$	2.058(2)	Hg_2-O_{24}	2.040
		Hg_2-O_{23}	2.040
		$Hg_{45}-O_{46}$	2.040
		$Hg_{45}-O_{47}$	2.041
$Hg_{(1)}\cdots O_{(3)}$	2.555(1)	$Hg_2\cdots O_{31}$	2.560
		$Hg_2\cdots O_{17}$	2.558
$Hg_{(1)}\cdots O_{(1)}$	2.737(1)	$Hg_{45}\cdots O_{16}$	2.564
		$Hg_{45}\cdots O_{32}$	2.554
$Hg_{(2)}-O_{(1)}$	2.186(1)	Hg_1-O_{16}	2.228
		Hg_1-O_{17}	2.238
$Hg_{(2)}-O_{(3)}$	2.287(1)	Hg_1-O_{31}	2.231
		Hg_1-O_{32}	2.241
$Hg_{(2)}\cdots F_{(6)}$	2.731(1)		
Te–O	1.798(1)–1.816(1)	Te–O	1.823–1.824
Te–F	1.841(1)–1.863(1)	Te–F	1.823–1.866
Bond Angles (deg)			
$O_{(2)}-Hg_{(1)}-O_{(2A)}$	180.0	$O_{23}-Hg_2-O_{24}$	172.2
		$O_{46}-Hg_{45}-O_{47}$	172.0
$O_{(2)}-Hg_{(1)}\cdots O_{(3)}$	86.7(1)	$O_{23}-Hg_2\cdots O_{31}$	92.4
		$O_{24}-Hg_2\cdots O_{31}$	94.2
$O_{(2)}-Hg_{(1)}\cdots O_{(3A)}$	93.2(1)	$O_{23}-Hg_2\cdots O_{17}$	96.3
$O_{(2)}-Hg_{(1)}\cdots O_{(1)}$	106.6(1)	$O_{24}-Hg_2\cdots O_{17}$	90.1
$O_{(2)}-Hg_{(1)}\cdots O_{(1A)}$	73.4(1)	$O_{46}-Hg_{45}\cdots O_{16}$	90.9
		$O_{47}-Hg_{45}\cdots O_{32}$	92.5
$O_{(2)}-Hg_{(1)}\cdots O_{(3A)}$	93.2(1)	$O_{46}-Hg_{45}\cdots O_{32}$	93.9
		$O_{47}-Hg_{45}\cdots O_{16}$	96.1
$O_{(1)}-Hg_{(2)}-O_{(3)}$	110.4(1)	$O_{16}-Hg_1-O_{17}$	126.8
		$O_{16}-Hg_1-O_{31}$	128.7
$O_{(1)}-Hg_{(2)}-O_{(3A)}$	81.4(1)	$O_{16}-Hg_1-O_{32}$	77.8
$O_{(1)}-Hg_{(2)}-O_{(1A)}$	147.8(1)	$O_{17}-Hg_1-O_{31}$	77.8
$O_{(3)}-Hg_{(2)}-O_{(3A)}$	137.9(1)	$O_{17}-Hg_1-O_{32}$	127.0
		$O_{31}-Hg_1-O_{32}$	126.6
Dihedral Angles (deg)			
$Te_{(2)}-O_{(2)}-Hg_{(1)}-O_{(2A)}-Te_{(2A)}$	0.0	$Te_5-O_{23}-Hg_2-O_{24}-Te_{25}$	2.2
		$Te_{48}-O_{46}-Hg_{45}-O_{47}-Te_{49}$	15.0

[a] The atom labeling scheme corresponds to that used in Figures 4.4 and S4.5.
[b] Calculated at the PBE0/def2-TVZPP level of theory; The atom labeling scheme corresponds to that used in Figure 4.10d.

Te–F_e, 1.843(1)–1.856(1) Å) bonds are shortened and elongated with respect to those in $Hg(OTeF_5)_2$ (Te–O, 1.842(7) Å; Te–F_a, 1.819(6) and Te–F_e, 1.824(6)–1.839(6) Å).[26] The Te–F bond elongations and Te–O bond contractions are consistent with the occurrence of interactions between the $[Hg_2(OTeF_5)_4]^{2-}$ anions and neutral $Hg_{(1)}(OTeF_5)_2$ (vide infra), contrasting with the interactions among $Hg(OTeF_5)_2$ molecules in the crystal structure of $Hg(OTeF_5)_2$. The symmetry-imposed *trans-anti*-conformation observed for the $Hg_{(1)}(OTeF_5)_2$ unit (dihedral $Te_{(2)}$–$O_{(2)}$–$Hg_{(1)}$–$O_{(2A)}$–$Te_{(2A)}$ angle, 180°) contrasts with the symmetry-imposed *trans-gauche*-conformation in the crystal structure of $Hg(OTeF_5)_2$ (dihedral Te–O–Hg–O–Te angle, 53.7(3)°), which was attributed to crystal packing.[26] However, the *trans-anti*-conformation is in accordance with that calculated for gas-phase $Hg(OTeF_5)_2$. The $O_{(2)}$–$Hg_{(1)}$–$O_{(2A)}$ bond angle (180°) is imposed by symmetry, whereas it is bent in the crystal structure of $Hg(OTeF_5)_2$ ($O_{(1)}$–$Hg_{(1)}$–$O_{(1B)}$, 170.5(4)°).[26]

A second mercury environment ($Hg_{(2)}$, Figure 4.4b) has a coordination sphere consisting of two $Hg_{(2)}$–$O_{(1,1A)}$ (2.186(1) Å), two $Hg_{(2}$–$O_{(3,3A)}$ (2.287(1) Å) primary bonds, and two long $Hg_{(2)}$---$F_{(6,6A)}$ contacts (2.731(1) Å). The Hg---F contacts are significantly less than the sum of the mercury and fluorine van der Waals radii (3.02 Å)[37] and are indicative of significant covalent bonding interactions between $Hg_{(2)}$ and the $F_{(6)}$ and $F_{(6A)}$ atoms. The latter belong to two symmetry related $Hg_{(1,1A)}(OTeF_5)_2$ groups. The $Hg_{(2)}$–O bonds form a flattened tetrahedron having O–$Hg_{(2)}$–O angles that are larger ($O_{(3A)}$–$Hg_{(2)}$–$O_{(3)}$, 137.9(1)° and $O_{(1)}$–$Hg_{(2)}$–$O_{(1A)}$, 147.8(1)°) and smaller ($O_{(1)}$–$Hg_{(2)}$–$O_{(3A)}$, 81.4(1)°) than the ideal tetrahedral angle (109.5°); however, the $O_{(1)}$–$Hg_{(2)}$–$O_{(3)}$ angle (110.4(1)°) is very close to the ideal angle. Flattening of the tetrahedron results from additional $Hg_{(2)}$---$F_{(6,6A)}$

contacts. Interestingly, a twist between the $O_{(3A)}Hg_{(2)}O_{(3)}$- and $O_{(1)}Hg_{(2)}O_{(1A)}$-planes is introduced, producing a spiral along the backbone of the chain. The $Hg_{(2)}$–O bonds (2.186(1) and 2.287(1) Å) of $[Hg(OTeF_5)_4]^{2-}$ are equal, within ±3σ, to those in $[N(CH_2CH_3)_4]_2[Hg(OTeF_5)_4]$ (2.146(7)–2.275(7) Å) and are longer than the $Hg_{(1)}$–O bonds (2.058(2) Å) of $Hg_{(1)}(OTeF_5)_2$. The Te–O (1.798(1) and 1.816(1) Å), Te–F_{ax} (1.842(1) and 1.843(1) Å), and Te–F_{eq} (1.841(1)–1.863(1) Å) bond lengths are comparable to those of $[N(CH_2CH_3)_4]_2[Hg(OTeF_5)_4]^{2-}$ (vide supra).

4.2.2.5. $\{Cs_3[Hg_2(OTeF_5)_7]\cdot Hg(OTeF_5)_2\}\cdot 4SO_2ClF$

The co-crystallization of SO_2ClF afforded another chain structure that is comprised of three crystallographically distinct Hg environments interacting through long Hg---O and Hg---F contacts (vide infra). The chain consists of $Hg(OTeF_5)_2$ molecules that alternate with $[Hg_2(OTeF_5)_7]^{3-}$ anions along the *c*-axis (Figures 4.5 and S4.6). The Cs^+ cations and SO_2ClF molecules form columns which run parallel to the chains. The chains and the SO_2ClF columns stack and alternate along the *a*- and *b*-axes, forming layers; one chain alternates with two SO_2ClF columns (Figure S4.6). The SO_2ClF molecules weakly interact with each other and with the $[Hg_2(OTeF_5)_7]^{3-}$ anions through long Cl---F and F---F contacts (Table S4.5). Columns of Cs^+ cations stack inbetween the above layers. Each Cs^+ cation has eight short contacts with the $Hg(OTeF_5)_2$ molecules, $[Hg_2(OTeF_5)_7]^{3-}$ anions, and SO_2ClF molecules (Table S4.5).

The $Hg_{(1)}$ environment of $\{Cs_3[Hg_2(OTeF_5)_7]\cdot Hg(OTeF_5)_2\}\cdot 4SO_2ClF$ (Figure 4.5a) is similar to the $Hg_{(1)}$ environment of $Cs_2[Hg(OTeF_5)_4]\cdot Hg(OTeF_5)_2$, with two

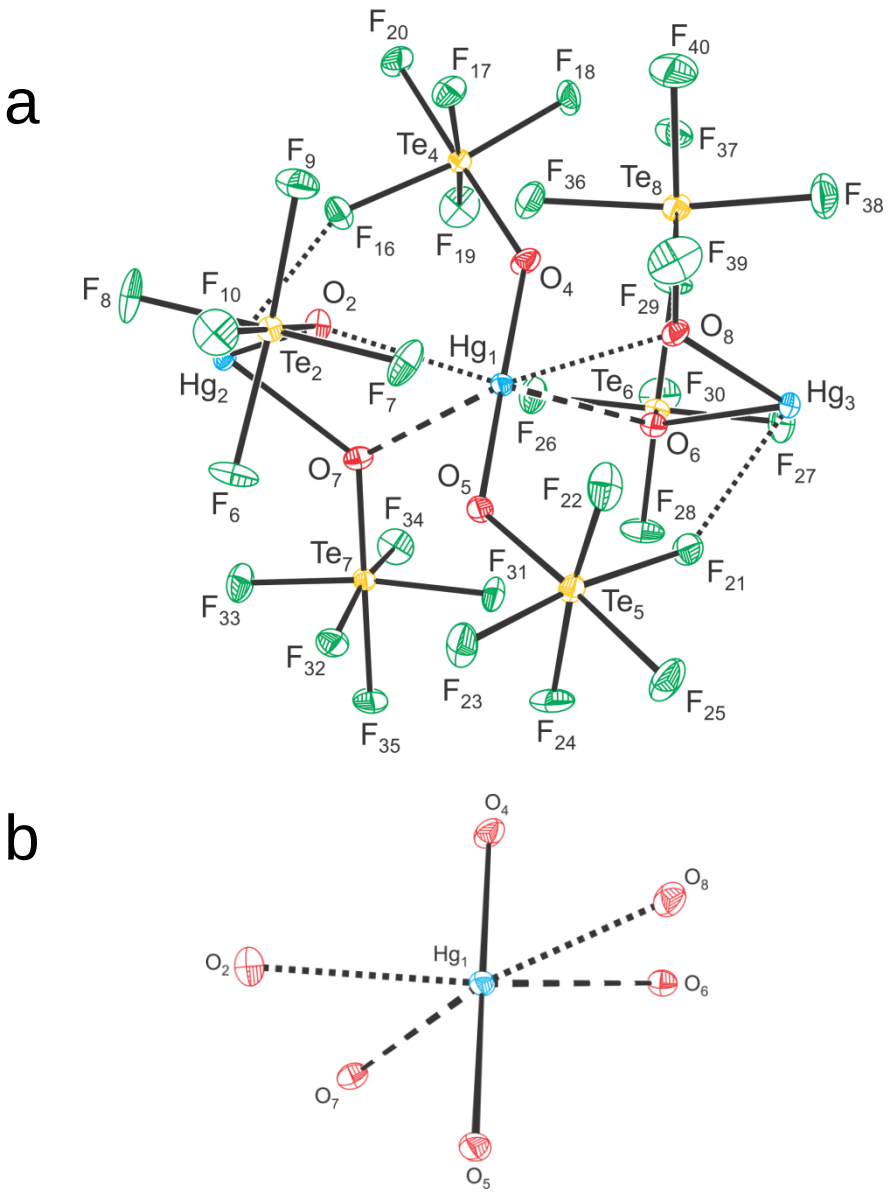

Figure 4.5a. The X-ray crystal structure of $\{Cs_3[Hg_2(OTeF_5)_7]\cdot Hg(OTeF_5)_2\}\cdot 4SO_2ClF$ showing (**a**) the primary coordination sphere of Hg_1 in the "$Hg(OTeF_5)_2$" unit and (**b**) for clarity, the F_5Te–groups have been omitted. Long contacts are indicated by dashed lines, and thermal ellipsoids are shown at the 50% probability level.

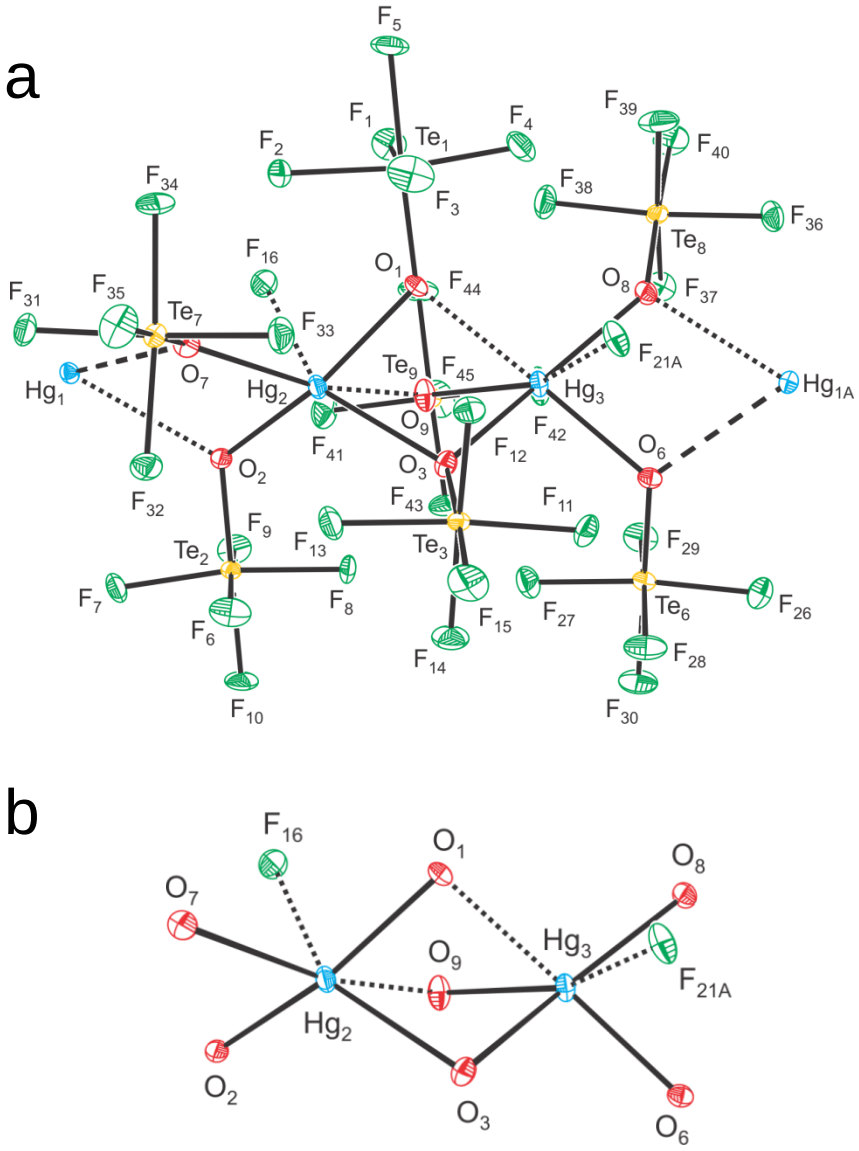

Figure 4.5b. The X-ray crystal structure of $\{Cs_3[Hg_2(OTeF_5)_7]\cdot Hg(OTeF_5)_2\}\cdot 4SO_2ClF$ showing (**a**) the primary coordination sphere of Hg_2 and Hg_3 in the "$[Hg_2(OTeF_5)_7]^{2-}$" unit in the anion chain structure and (**b**) for clarity, the F_5Te–groups have been omitted. Long contacts are indicated by dashed lines, and thermal ellipsoids are shown at the 50% probability level.

Table 4.6. Selected Experimental Geometrical Parameters for $\{Cs_3[Hg_2(OTeF_5)_7]\cdot Hg(OTeF_5)_2\}\cdot 4SO_2ClF$ [a]

Bond Lengths (Å)			
$Hg_{(1)}-O_{(4)}$	2.059(5)	$Hg_{(3)}-O_{(9)}$	2.211(5)
$Hg_{(1)}-O_{(5)}$	2.073(5)	$Hg_{(3)}-O_{(8)}$	2.234(5)
$Hg_{(1)}---O_{(6)}$	2.605(5)	$Hg_{(3)}-O_{(6)}$	2.266(5)
$Hg_{(1)}---O_{(7)}$	2.529(5)	$Hg_{(3)}-O_{(3)}$	2.369(5)
$Hg_{(1)}---O_{(8)}$	2.653(5)	$Hg_{(3)}---O_{(1}$	2.631(5)
$Hg_{(1)}---O_{(2)}$	2.737(5)	$Hg_{(3)}---F_{(21)}$	2.675(5)
$Hg_{(2)}-O_{(1)}$	2.169(5)		
$Hg_{(2)}-O_{(2)}$	2.156(5)	Te–O	1.801(5)–1.816(5)
$Hg_{(2)}-O_{(3)}$	2.356(5)		
$Hg_{(2)}-O_{(7)}$	2.359(5)	Te–F	1.830(5)–1.860(5)
$Hg_{(2)}---O_{(9)}$	2.680(5)		
$Hg_{(2)}---F_{(16)}$	2.668(5)		
Bond Angles (deg)			
$O_{(4)}-Hg_{(1)}-O_{(5)}$	174.7(2)	$Hg_{(2)}-O_{(1)}---Hg_{(3)}$	134.0(2)
$Hg_{(2)}-O_{(3)}-Hg_{(3)}$	96.(2)	$Hg_{(2)}---O_{(9)}-Hg_{(3)}$	91.7(2)
$O_{(1)}-Hg_{(2)}-O_{(2)}$	156.4(2)	$O_{(9)}-Hg_{(3)}-O_{(8)}$	127.2(2)
$O_{(1)}-Hg_{(2)}-O_{(3)}$	75.0(2)	$O_{(9)}-Hg_{(3)}-O_{(6)}$	127.2(2)
$O_{(1)}-Hg_{(2)}-O_{(7)}$	108.4(2)	$O_{(9)}-Hg_{(3)}-O_{(3)}$	79.1(2)
$O_{(2)}-Hg_{(2)}-O_{(3)}$	117.4(2)	$O_{(8)}-Hg_{(3)}-O_{(6)}$	81.2(2)
$O_{(2)}-Hg_{(2)}-O_{(7)}$	79.4(2)	$O_{(8)}-Hg_{(3)}-O_{(3)}$	149.2(2)
$O_{(3)}-Hg_{(2)}-O_{(7)}$	130.8(2)	$O_{(6)}-Hg_{(3)}-O_{(3)}$	95.3(2)
Dihedral Angles (deg)			
$Te_{(4)}-O_{(4)}-Hg_{(1)}-O_{(5)}-Te_{(5)}$		150.9 (4)	

[a] The atom labeling scheme corresponds to those used in Figures 4.5 and S4.6 of the Appendix B.

primary $Hg_{(1)}$−O bonds ($O_{(4)}$, 2.059(5) Å; $O_{(5)}$, 2.059(5) Å), and two shorter contacts, $Hg_{(1)}$---O ($O_{(7)}$, 2.529(5) Å; $O_{(6)}$, 2.605(5) Å), and two slightly longer $Hg_{(1)}$---O contacts ($O_{(8)}$, 2.653(5) Å; $O_{(2)}$, 2.737(5) Å). The $O_{(4)}$–$Hg_{(1)}$–$O_{(5)}$ bond angle (174.7(2)°) is intermediate with respect to that calculated for gas-phase $Hg(OTeF_5)_2$ (180°) and that determined in the solid state for $Hg(OTeF_5)_2$ (170.5(4)°). A *trans-anti*-conformation similar to that observed in $Cs_2[Hg(OTeF_5)_4]\cdot Hg(OTeF_5)_2$ is observed, with a dihedral $Te_{(4)}$–$O_{(4)}$–$Hg_{(1)}$–$O_{(5)}$–$Te_{(5)}$ angle of 150.9(4)^o that is comparable to that calculated for gas-phase $Hg(OTeF_5)_2$ (139.1^o).[26]

The $Hg_{(2)}$ and $Hg_{(3)}$ atoms (Figure 4.5b) have coordination spheres similar to that of $Hg_{(2)}$ in $Cs_2[Hg(OTeF_5)_4]\cdot Hg(OTeF_5)_2$, with two groups of $Hg_{(2)}$–O (2.156(5) and 2.169(5) Å; 2.356(5) and 2.359(5) Å) and $Hg_{(3)}$–O (2.211(5) and 2.234(5) Å; 2.266(5) and 2.369(5) Å) bonds. The $F_5TeO_{(3)}$-group, which is equally shared between $Hg_{(2)}$ and $Hg_{(3)}$ ($Hg_{(2)}$–$O_{(3)}$, 2.356(5) Å; $Hg_{(3)}$–$O_{(3)}$, 2.369(5) Å) is best described as a bridging F_5TeO_{μ}-group. The $Hg_{(2)}$ and $Hg_{(3)}$ atoms are also asymmetrically linked to each other through long Hg---O contacts ($Hg_{(2)}$–$O_{(9)}$, 2.680(5) Å; $Hg_{(3)}$–$O_{(1)}$, 2.631(5) Å) and to the $Hg_{(1)}$ atom through long Hg---F contacts ($Hg_{(2)}$–$F_{(16)}$, 2.668(5) Å; $Hg_{(3)}$–$F_{(21A)}$, 2.675(5) Å). The four short Hg–O bonds form distorted tetrahedral environments around $Hg_{(2)}$ and $Hg_{(3)}$ having large O–Hg–O bond angles ($Hg_{(2)}$, 130.8(2) and 156.4(2)°; $Hg_{(3)}$, 127.2(2) and 149.2(2)°) as observed in $Cs_2[Hg(OTeF_5)_4]\cdot Hg(OTeF_5)_2$. The Te–O and Te–F bond lengths are also comparable to those in $Cs_2[Hg(OTeF_5)_4]\cdot Hg(OTeF_5)_2$.

4.2.3. Raman Spectroscopy

The low-temperature, solid-state Raman spectra of $[N(CH_2CH_3)_4]_2[Hg(OTeF_5)_4]$, $[N(CH_3)_4]_3[Hg(OTeF_5)_5]$, $[N(CH_3)_4][Hg_2(OTeF_5)_6]$, and $Cs_2[Hg(OTeF_5)_4]\cdot Hg(OTeF_5)_2$ are shown in Figures 4.6–4.9 and S4.7–S4.9. Vibrational frequencies and mode descriptions are listed in abbreviated form in Tables 4.7–4.10, and detailed mode descriptions are provided in Tables S4.7–S4.10. Spectral assignments were made by comparison with the calculated frequencies and Raman intensities obtained for the energy-minimized, gas-phase geometries of the $[Hg(OTeF_5)_4]^{2-}$ (S_4), $[Hg(OTeF_5)_5]^{3-}$ (C_1), $[Hg_2(OTeF_5)_6]^{2-}$ (D_2), and $[OTeF_5]^-$ (C_{4v}) anions, and the presently unknown $[Hg_3(OTeF_5)_8]^{2-}$ (C_1) anion. The vibrational assignments were also aided by comparison with the recently published experimental and calculated frequencies of $Hg(OTeF_5)_2$.[26] The low-temperature Raman spectra of $[N(CH_2CH_3)_4][OTeF_5]$, $[N(CH_3)_4][OTeF_5]$, and $Cs[OTeF_5]$ were also recorded for comparison with mode assignments for the F_5TeO-ligands (Table S4.11, Figure S4.10). The vibrational bands of the $[N(CH_3)_4]^+$ [42] and $[N(CH_2CH_3)_4]^+$ [43,44] cations have been previously assigned, and are not discussed in the ensuing section.

4.2.3.1 $[N(CH_2CH_3)_4]_2[Hg(OTeF_5)_4]$ and $[N(CH_3)_4]_3[Hg(OTeF_5)_5]$

Values in square brackets refer to the $[Hg(OTeF_5)_5]^{3-}$ anion. Overall, the trends in vibrational frequencies and intensities for the calculated $[Hg(OTeF_5)_4]^{2-}$ and $[Hg(OTeF_5)_5]^{3-}$ anions agree well with the experimental values. In the case of $[Hg(OTeF_5)_4]^{2-}$, the "asymmetric" [ν(Hg–O) – ν(Te–O)]-type stretching modes were

overestimated by 31–32 cm^{-1}, whereas the "symmetric" [ν(Hg–O) + ν(Te–O)]-type stretching modes were underestimated by 18–30 cm^{-1}. In the case of $[Hg(OTeF_5)_5]^{3-}$, the "asymmetric"-type modes were overestimated by 23–26 cm^{-1}, whereas the "symmetric"-type were in good agreement with the experimental values.

As observed for $Hg(OTeF_5)_2$, the ν(Hg–O) and ν(Te–O) anion stretches couple, but to a lesser extent. Four [five] modes are derived from coupled "asymmetric" [ν(Hg–O) – ν(Te–O)]-type stretches. The totally in-phase coupled mode (calcd, 880 [893] cm^{-1}) was observed at 848 [867] cm^{-1}, and the two [four] out-of-phase coupled modes (calcd, 839/839 [832/849/872/877] cm^{-1}) appear as one [three] band (exptl, 807 [809/827/853] cm^{-1}). In each case, the experimental in-phase and out-of-phase coupled modes are shifted to higher frequency relative to the corresponding modes in $Hg(OTeF_5)_2$ (825 and 801 cm^{-1}, respectively);[26] the high-frequency shifts are also reproduced by their calculated vibrational frequencies ($Hg(OTeF_5)_2$, 824 and 787/793 cm^{-1}, respectively).

The totally in-phase coupled modes, 848 [867] cm^{-1}, occur at frequencies that approach those of the ν(Te–O) stretches of the $[OTeF_5]^-$ anions ($[N(CH_2CH_3)_4]^+$ salt, 866 cm^{-1}; $[N(CH_3)_4]^+$ salt, 854 cm^{-1}; see Table S4.11). This suggests that the major contributors to these coupled modes are the *ν*(Te–O) stretches. The Hg–O bonds are somewhat elongated when compared with those of $Hg(OTeF_5)_2$ as a result of the 2– and 3– charges of the anions. Accordingly, the Te–O bonds are somewhat shorter (see X-ray crystallography), having acquired more π character, resulting in the observed and calculated high-frequency shifts.

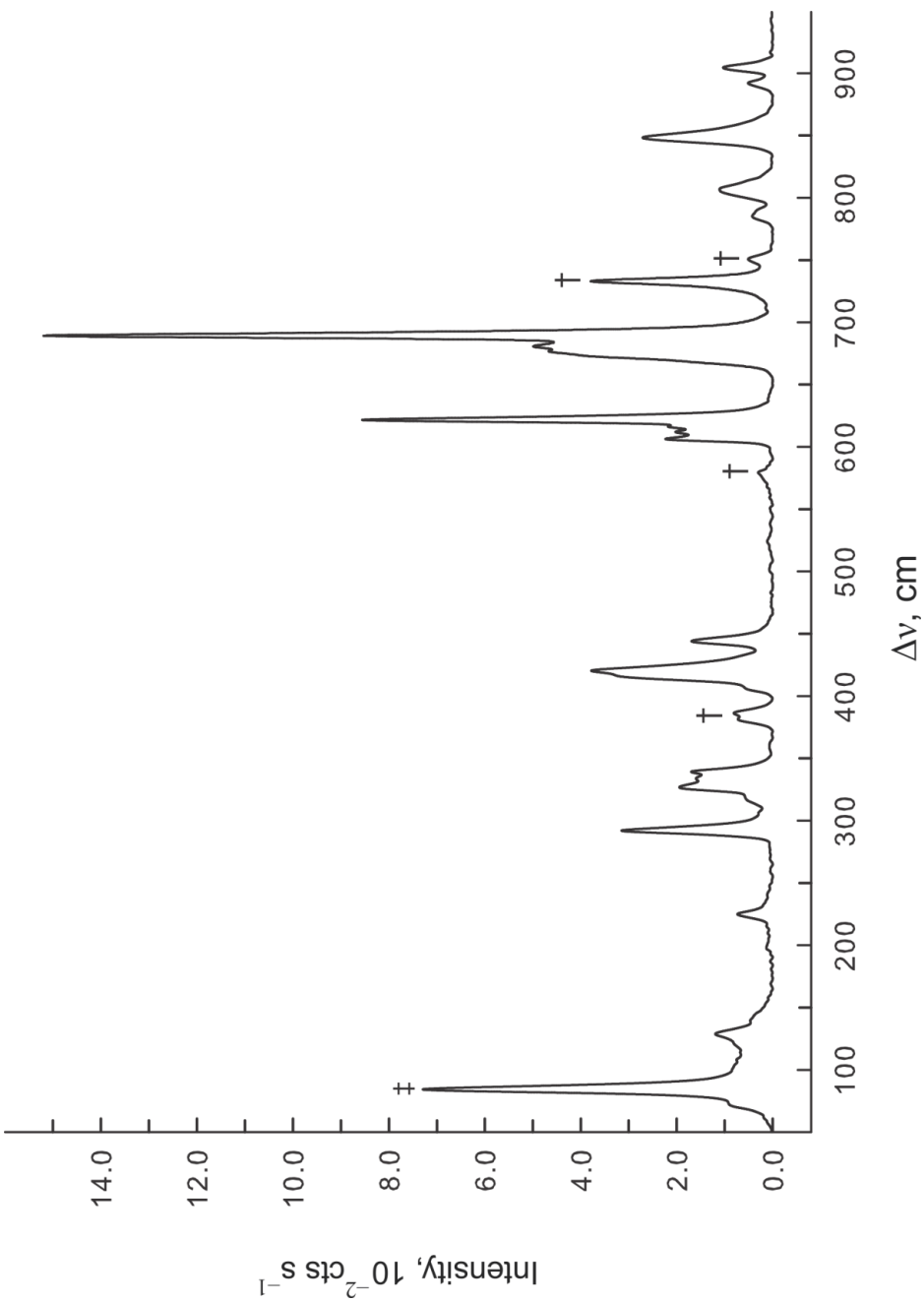

Figure 4.6. The Raman spectrum of $[N(CH_3)_4]_2[Hg(OTeF_5)_4]$ recorded at −155 °C using 1064-nm excitation. The full spectrum, including the cation bands, is shown in Figure S4.7 of the Appendix B. Symbols denote FEP (†) bands and an instrumental artifact (‡).

Table 4.7. Experimental Raman Frequencies and Intensities for $[Hg(OTeF_5)_4]^{2-}$ in $[N(CH_2CH_3)_4]_2[Hg(OTeF_5)_4]$ and Calculated Vibrational Frequencies and Intensities for $[Hg(OTeF_5)_4]^{2-}$

exptl $[Hg(OTeF_5)_4]^{2-}$ in $[N(CH_2CH_3)_4]_2[Hg(OTeF_5)_4]$ [a,b]	calcd $[Hg(OTeF_5)_4]^{2-}$ (S_4) [a,c,d,e,f]		assgnts
848(18)	879(98)[0]	A	
807(7)	839(36)[375]	E	ν(Hg-O) – ν(Te-O)
	839(27)[439]	B	
681(33)	683(2)[372]	B	
	681(2)[404]	E	
	679(5)[0]	A	
677(31)	677(6)[59]	B	ν(Te-F_e)
	675(19)[0]	A	
	673(<1)[17]	E	
689(100)	660(117)[0]	A	
	656(5)[122]	E	ν(Te-F_a) + ν(Te-F_{4e})$_{small}$
	656(5)[132]	B	
	609(5)[<0.1]	B	
622(57)	608(2)[2]	E	ν(Te-F_e)
616(14)	608(4)[0]	A	
612(13)	604(14)[0]	A	
606(14)	600(2)[<1]	B	ν(Te-F_a) – ν(Te-F_{4e})
	599(1)[6]	E	
420(25) [f]	390(<1)[90]	E	
417, sh	390(3)[7]	B	ν(Hg-O) + ν(Te-O)
406, sh	388(4)[0]	A	
	340(<1)[0]	A	δ(TeF_{4e})$_{umb}$
	338(<1)[75]	B	
	338(2)[0]	A	
339(11)	337(<1)[14]	E	δ(F-Te-F)
334(11)	335(<1)[20]	B	
327(13)	334(<1)[58]	E	
	332(<0.1)[0]	A	
	329(3)[65]	B	δ(TeF_{4e})$_{umb}$
	328(<1)[90]	E	
	320(1)[109]	B	δ(O-Hg-O)$_{o.o.p.}$
317, sh, br	318(4)[0]	A	
	313(<1)[25]	E	ρ_t(O-Hg-O)
	286(2)[<0.1]	B	
292(15)	286(2)[<0.1]	E	δ(F-Te-F)
	286(<0.1)[0]	A	

Table 4.7. continued …

225(5)	216(1)[0]	A	ρ_w(F-Te-F)
	215(<0.1)[<1]	B	
	214(<0.1)[<1]	E	
	213(<1)[0]	A	
	211(<1)[7]	E	ρ_w(F-Te-F) / ρ_w(F-Te-O)
	211(<1)[5]	B	ρ_w(F-Te-F)
129(8)	113(2)[0]	A	ρ_r(Te-$F_{4e}F_a$)

[a] Frequencies are given in cm^{-1}. [b] Values in parentheses denote relative Raman intensities. The Raman spectrum was recorded in an FEP sample tube at −150 °C using 1064-nm excitation. The abbreviations denote shoulder (sh), broad (br), and not observed (n.o.). [c] Values in parentheses denote calculated Raman intensities ($Å^4$ amu^{-1}), whereas values in square brackets denote calculated infrared intensities (km mol^{-1}). Assignments are for the energy-minimized geometry calculated at the PBE0/def2-TZVPP level; only general descriptions of the vibrational modes are listed. The abbreviations denote umbrella (umb), equatorial (4e, where the four F_e atoms are in-phase), axial (a), stretch (ν), bend (δ), twist (ρ_t), wag (ρ_w), and rock (ρ_r). [d] See Table S4.7 for a complete listing of frequencies and detailed descriptions of the assignments. [e] Calculated band intensity corresponds to one component of the doubly degenerate E mode. [f] Overlaps with a cation band.

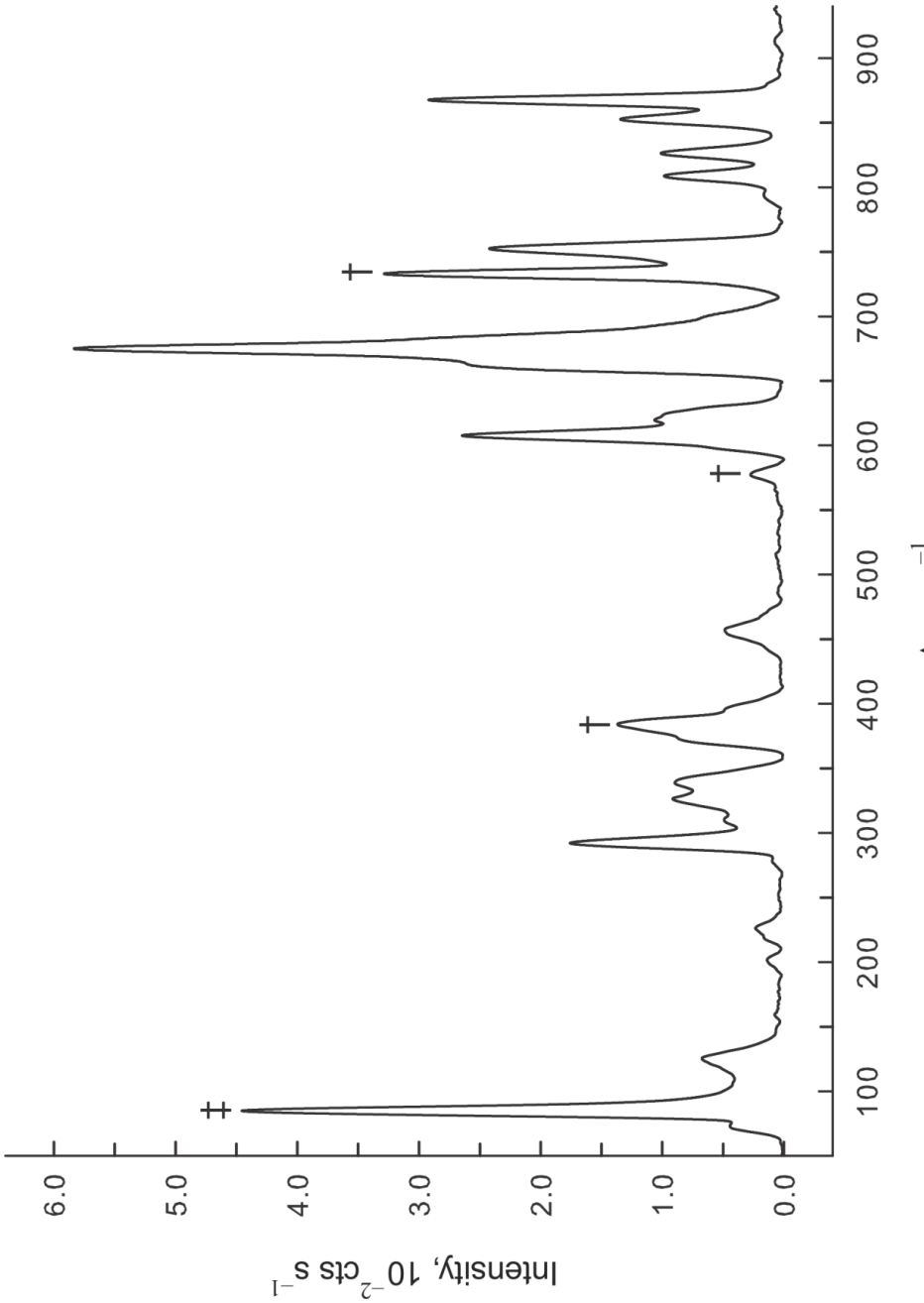

Figure 4.7. The Raman spectrum of $[N(CH_3)_4]_3[Hg(OTeF_5)_5]$ recorded at −155 °C using 1064-nm excitation. The full spectrum, including the cation bands, is shown in Figure S4.8 of the Appendix B. Symbols denote FEP (†) bands and an instrumental artifact (‡).

Table 4.8. Experimental Raman Frequencies and Intensities for $[Hg(OTeF_5)_5]^{3-}$ in $[N(CH_3)_4]_3[Hg(OTeF_5)_5]$ and Calculated Vibrational Frequencies and Intensities

exptl $[Hg(OTeF_5)_5]^{3-}$ in $[N(CH_3)_4]_3[Hg(OTeF_5)_5]$ [a,b]	calcd $[Hg(OTeF_5)_5]^{3-}$ (C_1) [a,c,d]	assgnts
867(52)	893(222)[10]	
853(22)	877(54)[315]	
	872(71)[322]	ν(Hg-O) – ν(Te-O)
827(16)	849(4)[528]	
809(16)	832(46)[25]	
690, sh	688(<1)[357]	
	688(<1)[336]	
682, sh	687(3)[22]	ν(Te-F_e)
	686(4)[1]	
675(100)	657(112)[13]	ν(Te-F_a) + ν(Te-F_{4e})
670, sh	657(<1)[560]	
	655(6)[173]	ν(Te-F_e)
	654(2)[125]	
661(42)	653(2)[60]	ν(Te-F_e) / ν(Te-F_a) + ν(Te-F_{4e})
	652(10)[10]	
	652(<1)[<1]	ν(Te-F_e)
	649(1)[9]	
627(15)	637(74)[16]	
	635(7)[152]	
622(18)	634(9)[152]	ν(Te-F_a) + ν(Te-F_{4e})
619(15)	613(3)[3]	
	613(3)[15]	ν(Te-F_e)
608(42)	597(1)[19]	
	597(4)[7]	ν(Te-F_a) – ν(Te-F_{4e})
600. sh	587(4)[<1]	
	586(5)[1]	
	586(1)[1]	ν(Te-F_e)
578(3)	570(3)[1]	
	569(1)[10]	
	568(2)[8]	ν(Te-F_a) – ν(Te-F_{4e})
396(7)	428(<1)[60]	
	401(10)[10]	ν(Hg-O) + ν(Te-O)
341(13)	344(1)[42]	
	344(1)[35]	
	343(1)[28]	
339(13)	343(1)[13]	
	343(<1)[53]	
337(13)	342(<1)[2]	δ(F-Te-F) / ρ_w(F-Te-F)
	342(<1)[7]	
	340(<1)[2]	
328(15)	340(<1)[9]	δ(F-Te-F) / δ(F-Te-O)
	338(1)[27]	
326(13)	336(1)[96]	δ(F-Te-F) / δ(TeF_{4e})$_{umb}$
	335(<1)[140]	δ(F-Te-F) / ρ_w(F-Te-F) / δ(TeF_{4e})$_{umb}$
	333(1)[13]	δ(F-Te-F) / ρ_w(F-Te-F)

Table 4.8. continued …

324(13)	328(<0.1)[1] 327(<0.1)[49]	$\delta(TeF_{4e})_{umb}$
320(10)	324(3)[121] 322(6)[35]	δ(F-Te-F) / δ(F-Te-O)
316(7)	319(3)[50] 319(1)[83] 316(2)[30]	δ(O-Hg-O)
312(7)	312(<1)[<1]	$\rho_r(Hg_1\text{-}O_8O_{12}O_{25})$
308(7)	311(2)[21] 303(<1)[12]	ρ_w(O-Hg-O) $\rho_r(Hg_1\text{-}O_{12}O_{22}O_{34})$
292(15)	290(1)[3] 288(1)[2]	δ(F-Te-F)
	281(3)[<0.1] 280(<1)[<1] 280(1)[<1]	δ(F-Te-F)
n.o.	229(<0.1)[9]	δ(F-Te-F) / ρ_w(F-Te-F)
226(4)	219(<1)[<0.1] 218(<0.1)[<0.1] 218(<0.1)[<0.1]	ρ_w(F-Te-F)
	217(1)[<1]	ρ_w(F-Te-F) / ρ_w(F-Te-O)
	213(<0.1)[<0.1] 213(<1)[<0.1]	ρ_w(F-Te-F)
201(3)	198(<0.1)[<0.1] 196(<0.1)[<0.1] 192(<1)[<1] 191(<1)[<1] 189(<0.1)[<1] 189(<0.1)[<1] 188(<0.1)[<0.1] 186(<0.1)[<1]	δ(F-Te-F) / ρ_w(F-Te-O)
n.o. 124(10)	153(<0.1)[19] 112(2)[<0.1]	coupled deformation and torsion modes

[a] Frequencies are given in cm^{-1}. [b] Values in parentheses denote relative Raman intensities. The Raman spectrum was recorded in an FEP sample tube at −150 °C using 1064-nm excitation. The abbreviations denote shoulder (sh), broad (br), and not observed (n.o.). [c] Values in parentheses denote calculated Raman intensities ($Å^4$ amu^{-1}), whereas values in square brackets denote calculated infrared intensities (km mol^{-1}). Assignments are for the energy-minimized geometry calculated at the PBE0/def2-TZVPP level; only general descriptions of the vibrational modes are listed. The abbreviations denote umbrella (umb), equatorial (4e, where the four F_e atoms are in-phase), axial (a), stretch (ν), bend (δ), twist (ρ_t), wag (ρ_w), and rock (ρ_r). [d] See Table S4.8 for a complete listing of frequencies and detailed descriptions of the assignments.

The three [two] modes associated with the coupled ″symmetric″ [ν(Hg–O) + ν(Te–O)]-type stretching modes of $[Hg(OTeF_5)_4]^{2-}$ and $[Hg(OTeF_5)_5]^{3-}$ (calcd, 388/390/390 [401/428] cm^{-1}) were observed as three [one] bands at 406/417/420 [396] cm^{-1}. In contrast to their "asymmetric" counterparts, these modes are shifted to lower frequencies relative to the corresponding $Hg(OTeF_5)_2$ modes (exptl, 472/481/511 cm^{-1}; calcd, 506/516/528/530). The greater low-frequency shift observed for $[Hg(OTeF_5)_5]^{3-}$ relative to that of $[Hg(OTeF_5)_4]^{2-}$ is consistent with its higher negative charge, resulting in more ionic Hg–O bonds. The observed low-frequency shifts suggest that the ν(Hg–O) stretches are significant contributors to the coupled ″symmetric″ [ν(Hg–O) + ν(Te–O)]-type stretching modes.

The bands between 689 [690] and 606 [578] cm^{-1} are assigned to ν(Te–F) stretches which are shifted to lower frequency relative to those of $Hg(OTeF_5)_2$ (735–624 cm^{-1}),[26] in accordance with the Te–F bond lengths, which are slightly longer in both anions than in $Hg(OTeF_5)_2$ (see X-ray Crystallography). These shifts are reproduced by the calculations ($[Hg(OTeF_5)_4]^{2-}$, 683–599 cm^{-1}; $[Hg(OTeF_5)_5]^{3-}$, 688–568 cm^{-1}; $Hg(OTeF_5)_2$, 726–640 cm^{-1}). The in-phase coupled axial $\nu_s(Te–F_a)$ modes are the strongest bands in both Raman spectra ($[Hg(OTeF_5)_4]^{2-}$, 689 cm^{-1}; $[Hg(OTeF_5)_5]^{3-}$, 675 cm^{-1}) as was observed for $Hg(OTeF_5)_2$ (709 cm^{-1}). The $\nu_s(Te–F_a)$ stretches occur at higher frequencies than those of their respective $[OTeF_5]^-$ salts ($[N(CH_2CH_3)_4]^+$, 643–579 cm^{-1}; $[N(CH_3)_4]^+$, 650–590 cm^{-1}; see Table S4.11), which is presumably the result of lower negative charges on the F_5TeO-groups of the mercury teflate anions (see Computational Results, NBO section).

The bands at 317 and 316 cm^{-1} are assigned to the O–Hg–O bending modes of $[Hg(OTeF_5)_4]^{2-}$ and $[Hg(OTeF_5)_5]^{3-}$, respectively, by analogy with the weak band observed at 331 cm^{-1} in $Hg(OTeF_5)_2$ (calcd; 313–320, 316–319, and 332 cm^{-1}, respectively).

4.2.3.2. $[N(CH_3)_4][Hg_2(OTeF_5)_6]$

Overall, the trends in vibrational frequencies and intensities for the calculated $[Hg_2(OTeF_5)_6]^{2-}$ anion are in very good agreement with the experimental values for $[N(CH_3)_4][Hg_2(OTeF_5)_6]$. Discrepancies between the calculated and experimental frequencies may arise from failure to reproduce the *anti*- and *gauche*-conformations observed around $Hg_{(1)}$ and $Hg_{(2)}$ in the solid state (see Computational Results).

As determined from the atomic displacements of the gas-phase anion, the highest frequency bands (805–853 cm^{-1}) of $[Hg_2(OTeF_5)_6]^{2-}$ are derived from ″asymmetric″ [ν(Hg–O) – ν(Te–O)]-type stretching modes. The intense band at 853 cm^{-1} (calcd, 856 cm^{-1}) is assigned to the totally in-phase coupled mode, $[\nu(Hg–O_\mu) – \nu(Te–O_\mu)] + [\nu(Hg–O_t) – \nu(Te–O_t)]$. The latter frequency is comparable to that observed for the corresponding mode in $[Hg(OTeF_5)_4]^{2-}$ (848 cm^{-1}) and the ν(Te–O) stretch of the $[OTeF_5]^-$ anion in its $[N(CH_3)_4]^+$ salt, 854 cm^{-1}. The broad band at 826 cm^{-1} is assigned to an out-of-phase $[\nu(Hg–O_t) – \nu(Te–O_t)]$-type stretch (calcd, 822 cm^{-1}). The calculated frequencies, 819 and 823 cm^{-1}, are predicted to be weak in the Raman spectrum and were not observed. These frequencies are essentially the same as that of the corresponding mode in $Hg(OTeF_5)_2$ (exptl, 825 cm^{-1}; calcd, 824 cm^{-1}). The bands at 805 and 808 cm^{-1} are assigned to an out-of-phase mode involving both the bridging and terminal teflate

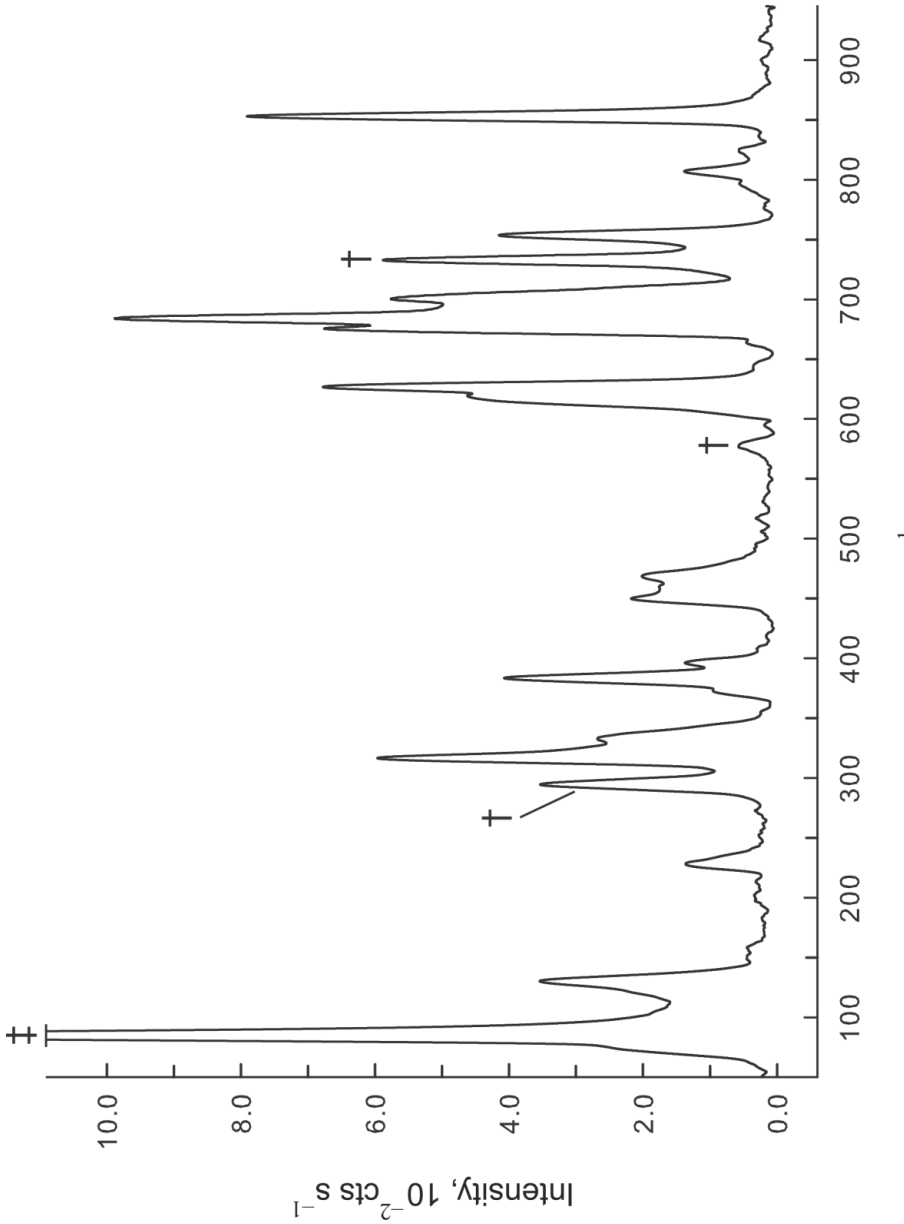

Figure 4.8. The Raman spectrum of $[N(CH_3)_4]_2[Hg_2(OTeF_5)_6]$ recorded at −155 °C using 1064-nm excitation. The full spectrum, including the cation bands, is shown in Figure S4.9 of the Appendix B. Symbols denote FEP (†) bands and an instrumental artifact (‡).

Table 4.9. Experimental Raman Frequencies and Intensities for $[Hg_2(OTeF_5)_6]^{2-}$ in $[N(CH_3)_4]_2[Hg_2(OTeF_5)_6]$ and Calculated Vibrational Frequencies and Intensities for $[Hg_2(OTeF_5)_6]^{2-}$

exptl $[Hg_2(OTeF_5)_6]^{2-}$ in $[N(CH_3)_4]_2[Hg_2(OTeF_5)_6]$ [a,b]	calcd $[Hg_2(OTeF_5)_6]^{2-}$ (D_2) [a,c,d]		
			assgnts
853(77)	856(127)[0]	A	
826(5), br	823(<1)[665]	B_2	ν(Hg-O) – ν(Te-O)
	822(47)[6]	B_1	
	819(<1)[593]	B_3	
808(12)	812(<0.1)[543]	B_1	
805(12), br	806(18)[0]	A	
707(30)	699(1)[138]	B_3	
	699(21)[0]	A	
	698(4)[164]	B_2	
	698(<0.1)[525]	B_1	
703(52) 699(47) 689(49)	696(1)[539]	B_2	ν(Te-F_e)
	695(5)[17]	B_3	
	691(3)[0]	A	
	689(3)[5]	B_1	
	688(<0.1)[59]	B_2	
	687(<0.1)[1]	B_3	
	679(<0.1)[216]	B_3	
	675(2)[2]	B_2	
684(100)	673(155)[0]	A	ν(Te-F_a) + ν(Te-F_{4e})
678(51) 674(62)	670(<1)[309]	B_3	ν(Te-F_a)
	669(<0.1)[51]	B_2	
	669(11)[3]	B_1	
	666(15)[0]	A	ν(Te-F_a) + ν(Te-F_{4e})
	665(<0.1)[136]	B_1	
627(72) 621(41) 618(41) 613(34) 604(12)	624(<1)[<1]	B_1	ν(Te-F_e) / ν(Te-F_a)
	623(2)[<1]	B_2	
	622(17)[0]	A	
	621(4)[2]	B_3	
	621(12)[0]	A	
	619(<1)[5]	B_3	
	617(5)[0]	A	
	617(<0.1)[<0.1]	B_1	
	617(<0.1)[<1]	B_2	
	616(<1)[<1]	B_1	
	610(2)[0]	A	
	609(<0.1)[<1]	B_1	
479(8) 470(17)	469(<0.1)[116]	B_2	ν(Hg-O) + ν(Te-O)
	465(<0.1)[<1]	B_1	
	464(<0.1)[45]	B_3	
	463(24)[0]	A	
397(13)	407(<0.1)[183]	B_3	ν(Hg-O)
	392(17)[<0.1]	B_2	
341(14)	343(<1)[0]	A	δ(TeF_{4e})$_{umb}$
	337(1)[<0.1]	B_3	δ(F-Te-F) / ρ_w(F-Te-F)
	337(<0.1)[53]	B_2	

Table 4.9 continued …

334(23) 330(22)	334(<0.1)[203]	B_1	δ(F-Te-F) / ρ_w(F-Te-F) / $\delta(TeF_{4e})_{umb}$
	334(<0.1)[53]	B_3	ν(Te-F)
	334(1)[0]	A	
	334(2)[32]	B_2	
	333(<0.1)[205]	B_3	
327(22)	332(<0.1)[28]	B_1	$\delta(TeF_{4e})_{umb}$ / δ(F-Te-F)
	331(<1)[0]	A	$\delta(TeF_{4e})_{umb}$
	331(<0.1)[41]	B_2	δ(F-Te-O)
	329(<1)[26]	B_3	δ(F-Te-O) / δ(F-Te-F)
	329(11)[111]	B_2	
	329(<1)[17]	B_1	δ(F-Te-F) / ρ_w(F-Te-F)
	329(1)[0]	A	δ(F-Te-F)
322(32)	327(4)[4]	B_3	δ(F-Te-O)
	326(1)[9]	B_1	δ(F-Te-F) / ρ_w(F-Te-F)
	326(<1)[38]	B_2	
	325(<0.1)[27]	B_3	
	324(<0.1)[71]	B_2	δ(F-Te-F)
316(57)	320(<0.1)[80]	B_1	$\delta(O\text{-}Hg\text{-}O)_{o.o.p.}$
	316(3)[<0.1]	B_2	
	312(<1)[0]	A	ρ_t(O-Hg-O)
	309(<1)[3]	B_3	
296(31)	290(3)[0]	A	δ(F-Te-F_e)
	290(2)[<0.1]	B_3	
	289(1)[<1]	B_1	
	289(<1)[<1]	B_2	
	286(2)[<0.1]	B_1	
	286(<0.1)[0]	A	
233(9)	233(<0.1)[<1]	B_2	δ(F-Te-F) / ρ_w(F-Te-F)
	233(1)[<1]	B_1	
	228(<0.1)[12]	B_3	
	228(4)[0]	A	
226(12)	212(<0.1)[<1]	B_1	ρ_w(F-Te-F)
	212(<0.1)[0]	A	
	212(<0.1)[<0.1]	B_3	
	212(<0.1)[<0.1]	B_2	
	212(<0.1)[0]	A	
	211(<0.1)[<1]	B_1	
130(31)	121(<0.1)[2]	B_3	$\rho_r(TeF_{2e}F_a)$
	121(3)[0]	A	

[a] Frequencies are given in cm^{-1}. [b] Values in parentheses denote relative Raman intensities. The Raman spectrum was recorded in an FEP sample tube at −150 °C using 1064-nm excitation. The abbreviations denote shoulder (sh), broad (br), and not observed (n.o.). [c] Values in parentheses denote calculated Raman intensities ($Å^4$ amu^{-1}), whereas values in square brackets denote calculated infrared intensities (km mol^{-1}). Assignments are for the energy-minimized geometry calculated at the PBE0/def2-TZVPP level; only general descriptions of the vibrational modes are listed. The abbreviations denote umbrella (umb), equatorial (4e, where the four F_e atoms are in-phase), axial (a), stretch (ν), bend (δ), twist (ρ_t), wag (ρ_w), and rock (ρ_r). [d] See Table S4.9 for a complete listing of frequencies and detailed descriptions of the assignments.

groups (calcd, 806 cm^{-1}). The frequencies are comparable to that observed for the corresponding mode in $[Hg(OTeF_5)_4]^{2-}$ (exptl, 807 cm^{-1}; calcd, 839/839/839 cm^{-1}) and $Hg(OTeF_5)_2$ (exptl, 801 cm^{-1}; calcd, 787/793 cm^{-1}). An additional low-intensity, out-of-phase [$\nu(Hg–O_\mu)$ – $\nu(Te–O_\mu)$]-type stretching band was calculated (812 cm^{-1}), but was too weak to be observed.

The bands observed at 470 and 479 cm^{-1} in the Raman spectrum of $[Hg_2(OTeF_5)_6]^{2-}$ are associated with the ″symmetric″ in-phase coupled [$\nu(Hg–O_t)$ + $\nu(Te–O_t)$]-type stretching mode (calcd, 463 cm^{-1}). The out-of-phase coupled counterparts (calcd, 464/469/465 cm^{-1}) are predicted to be weak and were not observed. The above bands at 470 and 479 cm^{-1} are reminiscent of the corresponding bands in $Hg(OTeF_5)_2$ (exptl, 472/481/511 cm^{-1}; calcd, 504 cm^{-1}). The band at 397 cm^{-1} was assigned to a mode involving only $\nu(Hg–O_\mu)$ stretches, [$\nu(Hg_1–O_{24})$ + $\nu(Hg_2–O_{34})$] – [$\nu(Hg_2–O_{24})$ + $\nu(Hg_1–O_{34})$]. The experimental frequency is in excellent agreement with the calculated value (392 cm^{-1}). A similar weak mode is predicted, [$\nu(Hg_1–O_{24})$ + $\nu(Hg_1–O_{34})$] – [$\nu(Hg_2–O_{24})$ + $\nu(Hg_2–O_{34})$], at 407 cm^{-1} but was not observed.

The above results suggest that the terminal teflate groups of $[Hg_2(OTeF_5)_6]^{2-}$ interact in a fashion similar to that in $Hg(OTeF_5)_2$, and that the majority of the charge remains on the bridging teflate groups, resulting in $Hg–O_\mu$ bonds that are overall more ionic and $Te–O_\mu$ bonds with greater π character (see Computational Results, NBO section).

The band at 316 cm^{-1} (calcd, 316/320 cm^{-1}) is tentatively assigned to O–Hg–O bending modes by analogy with those observed and calculated for $[Hg(OTeF_5)_4]^{2-}$ (exptl, 317 cm^{-1}; calcd, 318/320 cm^{-1}) and $Hg(OTeF_5)_2$ (exptl, 331 cm^{-1}; calcd, 332 cm^{-1}).

The bands between 604 and 707 cm^{-1} (calcd, 609–699 cm^{-1}) are assigned to ν(Te–F) stretches and are intermediate with respect to those observed for $[Hg(OTeF_5)_4]^{2-}$ (exptl, 606–689 cm^{-1}; calcd, 599–683 cm^{-1}) and $Hg(OTeF_5)_2$ (exptl, 624–735 cm^{-1}; calcd, 640–726 cm^{-1}). The bands between 674 and 684 cm^{-1} (calcd, 665–673 cm^{-1}) involve axial ν(Te–F) stretching modes, with the totally symmetric stretching mode at 684 cm^{-1} being the strongest band in the Raman spectrum (calcd, 673 cm^{-1}).

4.2.3.3. $Cs_2[Hg(OTeF_5)_4]\cdot Hg(OTeF_5)_2$

The use of two calculated models, the hypothetical $[Hg_3(OTeF_5)_8]^{2-}$ anion and the known $Hg(OTeF_5)_2$ monomer, allowed the assignment of the experimental spectrum of $Cs_2[Hg(OTeF_5)_4]\cdot Hg(OTeF_5)_2$. The approach allowed modes involving only the $[Hg(OTeF_5)_4]^{2-}$ anion or $Hg(OTeF_5)_2$ moieties, as well as coupled modes of the anion and $Hg(OTeF_5)_2$, to be distinguished. There is very good agreement between the experimental and calculated frequencies.

The bands occuring between 776 and 866 cm^{-1} are assigned to ″asymmetric″ [ν(Hg–O) – ν(Te–O)]-type stretches. The strong band at 866 cm^{-1} (calcd, 853 cm^{-1}) is assigned to the totally in-phase coupled mode. Both $[Hg(OTeF_5)_4]^{2-}$ and $Hg(OTeF_5)_2$ contribute to this mode which occurs at higher frequency than the analogous mode in $[N(CH_2CH_3)_4]_2[Hg(OTeF_5)_4]$ (848 cm^{-1}). The bands at 776/780/790/795, 816, and 826

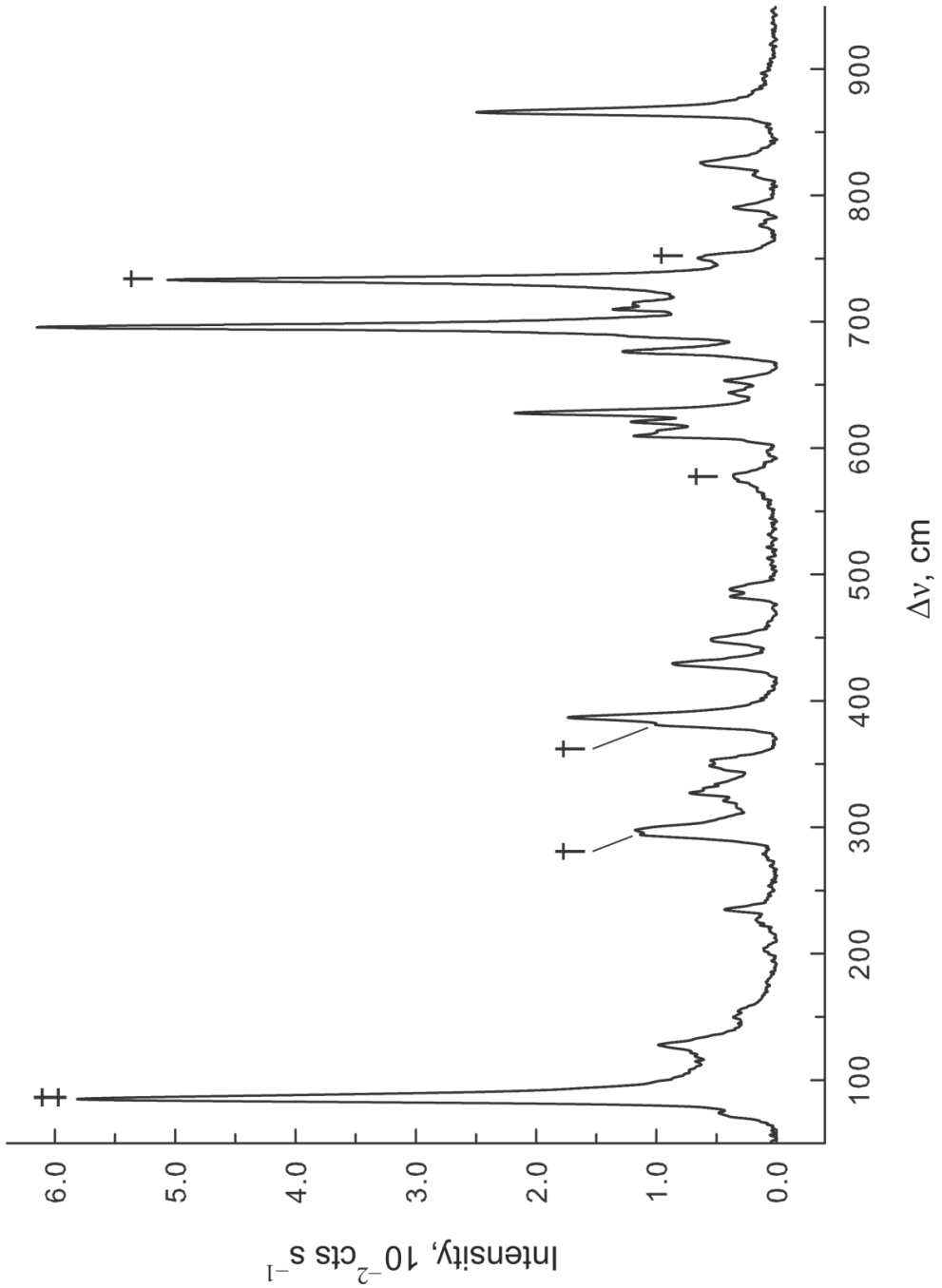

Figure 4.9. The Raman spectrum of $Cs_2[Hg(OTeF_5)_4]\cdot Hg(OTeF_5)_2$ recorded in a FEP tube at −155 °C using 1064-nm excitation. Symbols denote FEP (†) bands and an instrumental artifact (‡).

Table 4.10. Experimental Raman Frequencies and Intensities for $Cs_2[Hg(OTeF_5)_4]\cdot Hg(OTeF_5)_2$ and Calculated Vibrational Frequencies and Intensities for $[Hg_3(OTeF_5)_8]^{2-}$

exptl [a,b] **$Cs_2[Hg(OTeF_5)_4]\cdot Hg(OTeF_5)_2$**	**calcd** [a,c,d] **$[Hg_3(OTeF_5)_8]^{2-}$ (C_1)**	assgnts
866(40)	853(120)[8]	$[\nu(Hg\text{-}O) - \nu(Te\text{-}O)]_t$ + $[\nu(Hg\text{-}O) - \nu(Te\text{-}O)]_c$
826(10), br	834(8)[382] 826(14)[398] 823(20)[310]	$[\nu(Hg\text{-}O) - \nu(Te\text{-}O)]_t$ / $[\nu(Hg\text{-}O) - \nu(Te\text{-}O)]_c$
816(3)	814(5)[69] 812(18)[205]	
795(sh) 790(6) 780(2) 776(2)	792(1)[583] 791(1)[558]	$[\nu(Hg\text{-}O) - \nu(Te\text{-}O)]_c$
721(15)	707(13)[37] 706(3)[202] 702(2)[10] 697(<1)[82]	$[\nu(Te\text{-}F)]_t$
715(19) 713(19) 710(23)	708(7)[107] 706(4)[155] 705(1)[363] 705(6)[151] 704(1)[424]	$[\nu(Te\text{-}F)]_t$ / $[\nu(Te\text{-}F)]_c$
696(100)	681(167)[<1]	
691(sh)	699(<1)[29] 699(1)[21] 696(<1)[387] 695(1)[45]	
688(sh)	692(9)[3] 689(1)[4] 688(1)[5]	$[\nu(Te\text{-}F)]_c$
676(21) 671(sh)	678(3)[245] 678(8)[9] 677(5)[61] 677(2)[73] 677(2)[121] 676(7)[80]	$[\nu(Te\text{-}F)]_t$ / $[\nu(Te\text{-}F)]_c$
653(6)	674(10)[102]	
644(6)	631(<0.1)[1] 630(1)[2] 629(2)[1] 629(3)[<1]	$[\nu(Te\text{-}F)]_t$
628(35)	633(34)[<0.1] 628(4)[<1]	$[\nu(Te\text{-}F)]_t$ / $[\nu(Te\text{-}F)]_c$
621(19)	627(6)[<1]	
613(16)	627(<1)[<1] 626(8)[2] 624(3)[4]	

Table 4.10 continued …

610(19) 604(sh)	623(8)[<1]	$[\nu(Te\text{-}F)]_t$ / $[\nu(Te\text{-}F)]_c$
n.o.	624(1)[1] 623(<1)[1]	$[\nu(Te\text{-}F)]_t$
n.o.	627(<1)[<1] 620(<1)[<1] 620(<1)[<1]	$[\nu(Te\text{-}F)]_c$
492(sh)	499(<1)[40] 498(<1)[40]	$[\nu(Hg\text{-}O) + \nu(Te\text{-}O)]_t$
488(6) 483(6)	488(18)[24] 487(14)[32]	
448(8)	444(24)[<1] 435(<1)[393]	$[\nu(Hg\text{-}O)]_c$ / $[\nu(Hg\text{-}O)]_t$
430(15)	419(9)[3] 419(9)[<1]	
353(10)	345(1)[<1]	$[\delta(TeF_{4e})_{umb}]_t$ / $[\delta(TeF_{4e})_{umb}]_c$
349(10)	338(<1)[2] 336(<0.1)[155] 336(<1)[127]	$[\delta(TeF_{4e})_{umb}]_c$
	336(<1)[159]	$[\delta(F\text{-}Te\text{-}F)]_c$
334(8)	334(<1)[156] 334(<0.1)[154]	$[\delta(TeF_{4e})_{umb}]_c$ / $[\delta(F\text{-}Te\text{-}F)]_t$
	334(<0.1)[41] 334(<1)[27]	$[\delta(F\text{-}Te\text{-}F)]_t$ / $[\delta(F\text{-}Te\text{-}F)]_c$ / $[\rho_w(F\text{-}Te\text{-}F)]_c$
330(10)	333(<1)[24] 333(<1)[8]	$[\delta(TeF_{4e})_{umb}]_t$
327(11)	332(1)[5]	$[\delta(F\text{-}Te\text{-}F)]_t$ / $[\delta(F\text{-}Te\text{-}F)]_c$
321(6)	332(<1)[1] 332(<1)[13] 331(<1)[24] 330(<1)[25]	$[\delta(F\text{-}Te\text{-}F)]_t$ / $[\delta(F\text{-}Te\text{-}O)]_t$
317(5)	329(1)[12] 328(2)[21] 328(3)[65] 327(1)[63] 327(3)[42] 326(<1)[32] 325(<1)[18] 323(<1)[11]	$[\delta(F\text{-}Te\text{-}F)]_t$ / $[\delta(F\text{-}Te\text{-}O)]_t$ / $[\delta(F\text{-}Te\text{-}F)]_c$ / $[\delta(F\text{-}Te\text{-}O)]_c$
n.o.	323(<1)[10]	$[\delta(F\text{-}Te\text{-}F)]_c$ / $[\rho_w(O\text{-}Hg\text{-}O)]_t$
	322(<0.1)[12]	$[\delta(O\text{-}Te\text{-}F)]_t$ / $[\rho_t(O\text{-}Hg\text{-}O)]_c$
	321(<0.1)[76]	$[\delta(F\text{-}Te\text{-}F)]_c$
	319(2)[3] 319(2)[4]	$[\delta(F\text{-}Te\text{-}F)_c$ / $[\rho_w(O\text{-}Hg\text{-}O)]t$
305(sh)	313(<1)[6] 312(<0.1)[2] 293(1)[<1] 293(1)[<1] 292(1)[<1] 291(1)[<1]	$[\delta(F\text{-}Te\text{-}F)]_t$

Table 4.10 continued …

298(19)	321(<0.1)[9] 290(<1)[<1] 290(2)[<0.1] 290(2)[<0.1] 289(<0.1)[<0.1]	$[\delta(F\text{-}Te\text{-}F)]_c$
235(6)	242(<1)[<0.1] 241(<1)[<1] 233(2)[6] 231(2)[6]	$[\delta(F\text{-}Te\text{-}F)]_t$ / $[\rho_w(F\text{-}Te\text{-}F)]_t$
204(2)	216(2)[<0.1] 214(<0.1)[1]	$[\delta(F\text{-}Te\text{-}F)]_c$
	213(<0.1)[<0.1] 212(<0.1)[<1] 212(<0.1)[<1] 212(<0.1)[<1] 212(<0.1)[<1] 212(<0.1)[<1] 211(<1)[<0.1] 211(<0.1)[<0.1]	$[\rho_w(F\text{-}Te\text{-}F)]_t$ / $[\rho_w(F\text{-}Te\text{-}F)]_c$
n.o.	209(<0.1)[1] 209(<0.1)[1] 202(<0.1)[<1] 202(<0.1)[<1] 202(<0.1)[<0.1] 201(<0.1)[<0.1]	$[\rho_w(O\text{-}Te\text{-}F)]_t$ / $[\rho_w(O\text{-}Te\text{-}F)]_c$
n.o.	201(<0.1)[<0.1] 200(<1)[<1] 193(<0.1)[<1] 190(<0.1)[<0.1]	$[\rho_w(O\text{-}Te\text{-}F)]_t$ / $[\rho_w(F\text{-}Te\text{-}F)]_t$
150(6)	159(<1)[5] 158(<1)[5]	
n.o.	142(<0.1)[4]	
128(16)	126(2)[<1] 126(<1)[3]	$[\rho_r(TeF_{2e}F_a)]_t$

[a] Frequencies are given in cm^{-1}. [b] Values in parentheses denote relative Raman intensities. The Raman spectrum was recorded in an FEP sample tube at −150 °C using 1064-nm excitation. The abbreviations denote shoulder (sh), broad (br), and not observed (n.o.). [c] Values in parentheses denote calculated Raman intensities ($Å^4$ amu^{-1}), whereas values in square brackets denote calculated infrared intensities (km mol^{-1}). Assignments are for the energy-minimized geometry calculated at the PBE0/def2-TZVPP level; only general descriptions of the vibrational modes are listed. The abbreviations denote umbrella (umb), equatorial (4e, where the four F_e atoms are in-phase), axial (a), stretch (ν), bend (δ), twist (ρ_t), wag (ρ_w), and rock (ρ_r). [d] See Table S4.10 for a complete listing of frequencies and detailed descriptions of the assignments.

cm^{-1} are assigned to out-of-phase coupled modes, by comparison with their calculated modes (791/792, 812/814, and 823/826/834, respectively). The three modes observed at 483,488, and 492 cm^{-1} (calcd, 487/488,498/499 cm^{-1}) are associated with the coupled ″symmetric″ [ν(Hg–O) + ν(Te–O)]-type stretching modes of the $Hg(OTeF_5)_2$ moieties and occur at frequencies similar to the corresponding modes in solid $Hg(OTeF_5)_2$ (exptl, 472/481/511 cm^{-1}; calcd, 506/516/528/530 cm^{-1}). The bands calculated at 419/419 and 435/444 cm^{-1} only involve ν(Hg–O) stretches, and were observed at 430 and 448 cm^{-1}, respectively.

The bands between 604 and 721 cm^{-1} (calcd, 620–707 cm^{-1}) are assigned to ν(Te–F) stretching modes of the F_5Te-groups and are comparable to those in both $[Hg(OTeF_5)_4]^{2-}$ (exptl, 606–689 cm^{-1}; calcd, 599–683 cm^{-1}) and $Hg(OTeF_5)_2$ (exptl, 624–735 cm^{-1}; calcd, 640–726 cm^{-1}).

4.3. Computational Results

The electronic structures of the $[Hg(OTeF_5)_4]^{2-}$ (S_4), $[Hg(OTeF_5)_5]^{3-}$ (C_1), $[OTeF_5]^-$ (C_{4v}), $[Hg_2(OTeF_5)_6]^{2-}$ (D_2), and $[Hg_3(OTeF_5)_8]^{2-}$ (C_1) anions were calculated using PBE0 functionals and def2-TVZPP basis sets starting from the crystallographic coordinates (C_1 symmetry). The PBE0/def2-TVZPP method was previously shown to be reliable for related systems, i.e., $Hg(OTeF_5)_2$ and $[Hg(OTeF_5)_2]_3{\cdot}2NgF_2$ (Ng = Kr, Xe).[26] All calculations resulted in stationary points with all frequencies real. Calculated vibrational frequencies, intensities, and geometrical parameters are reported in Tables 4.2–4.5, 4.7–4.10 and S4.7–S4.16 and energy-minimized structures are shown in Figures

4.10–4.13 and S4.10. NBO analyses for all species were carried out with NBO 6.0[45] at the same level of theory (Tables S4.17–S4.21).

4.3.1. Calculated Geometries

4.3.1.1. Calculated Geometry of $[Hg(OTeF_5)_4]^{2-}$

The $[Hg(OTeF_5)_4]^{2-}$ anion was optimized to S_4 symmetry (Figure 4.10), giving a local environment around Hg(II) that is close to tetrahedral (∠O–Hg–O: 4 x 108.0° and 2 x 112.4°), in contrast with the more distorted tetrahedral environment observed in the solid state (∠O–Hg–O: 86.3(2)–125.9(3)°) (Figure 4.1). This strongly suggests that the solid-state distortion is likely the result of crystal packing, i.e., weak anion-cation interactions. The calculated Hg–O (2.226 Å) and Te–O (1.799 Å) bond lengths are in

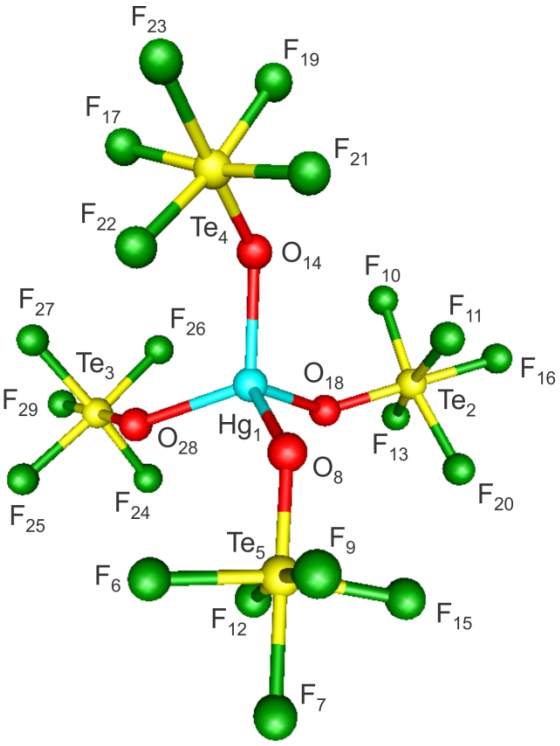

Figure 4.10. Gas-phase, energy-minimized geometry of $[Hg(OTeF_5)_4]^{2-}$ (S_4)

very good agreement with the experimental values (2.216(7) and 1.797(6) Å, respectively) and are elongated and shortened in comparison to those calculated for $Hg(OTeF_5)_2$ (2.008 and 1.865 Å, respectively),[26] in agreement with the observed trend (Table 4.2). The calculated Te–F_{ax} and Te–F_{eq} bond lengths (1.864–1.871 Å) are, on average, slightly longer when compared with the experimental bond lengths (1.816(6)–1.861(6) Å) and the calculated Hg–O–Te angles (132.4°) are somewhat more open than the experimental angles (118.2(3)–124.1(3)°) It is noteworthy that the geometries of the related $C(OTeF_5)_4$ molecule and $[B(OTeF_5)_4]^-$ anion also optimized to S_4 symmetry[29] and that the calculated O–Hg–O angles are almost equal to those of $C(OTeF_5)_4$ (∠O–C–O: 4 x 107.8° and 2 x 113.0°), whereas the O–B–O angles are equal to the ideal tetrahedral angle (∠O–B–O: 4 x 109.4° and 2 x 109.5°).

4.3.1.2. Calculated Geometry of $[Hg(OTeF_5)_5]^{3-}$

The $[Hg(OTeF_5)_5]^{3-}$ anion optimized (Figure 4.11) to a slightly distorted trigonal bipyramidal environment around Hg(II) (τ = 0.905),[41] in contrast to the distorted square pyramidal geometries observed in the solid state. Attempts to optimize the square pyramidal structure resulted in the more energetically favorable trigonal bipyramidal geometry, supporting the influence of the cation-anion interactions on the solid-state geometry (see X-ray Crystallography). In the gas-phase, the two axial Hg–O_{ax} bond lengths (2.110 and 2.111 Å) are significantly shorter than the three equatorial Hg–O_{eq} bond lengths (2.481–2.510 Å). Although more pronounced in the gas-phase calculation, these bond length differences are also present in the solid state, with two shorter Hg–O

bonds (2.227(5) and 2.230(5) Å) and three slightly longer Hg–O bonds (2.318(5), 2.323(4) and 2.301(5) Å). The relative $Hg–O_{ax}$ and $Hg–O_{eq}$ bond lengths of the trigonal bipyramidal $[Hg(OTeF_5)_5]^{3-}$ anion are opposite to those normally encountered for trigonal bipyramidal main-group species, i.e., $E–X_{eq} < E–X_{ax}$.[40] The difference presumably results from greater steric interactions among the F_5TeO_{eq}-groups in the equatorial plane and with the F_5TeO_{ax}-groups. The calculated $Te–O_{eq}$ bonds (1.777–1.779 Å) are shorter than the calculated $Te–O_{ax}$ bonds (1.806–1.808 Å), consistent with $Hg–O_{eq} > Hg–O_{ax}$. Correspondingly, the $Te–F_{ax}$ and $Te–F_{eq}$ bond lengths of both axial groups are shorter than those of the equatorial groups.

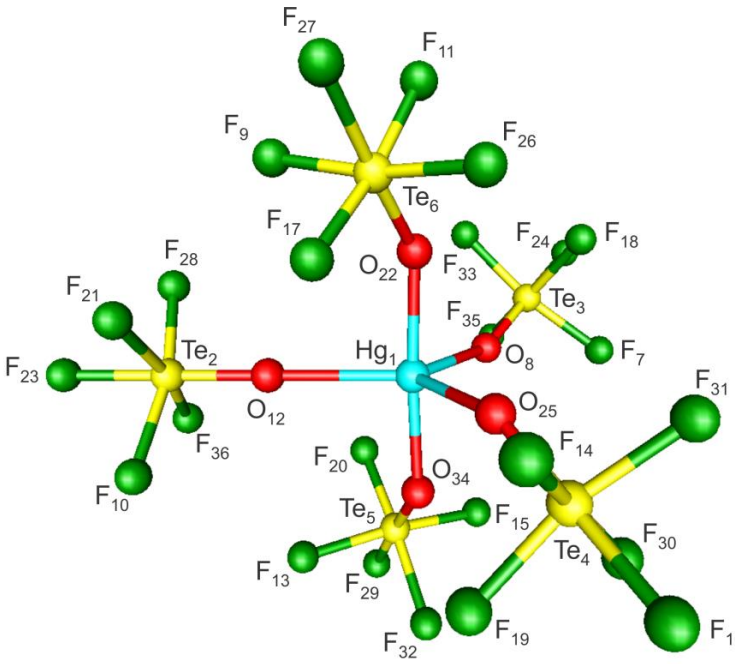

Figure 4.11. Gas-phase, energy-minimized geometry of $[Hg(OTeF_5)_5]^{3-}$ (C_1) calculated at the PBE0/def2-TZVPP level of theory.

Although the calculated gas-phase geometry of $[Hg(OTeF_5)_5]^{3-}$ differs from that observed in the solid state, the calculated vibrational frequencies and intensities can be

used to aid in the assignment of the experimental spectrum. However, it is not possible to discriminate between the vibrational bands arising from the axial or equatorial modes of the F_5TeO-groups.

4.3.1.3. Calculated Geometry of $[Hg_2(OTeF_5)_6]^{2-}$

The calculated structure of the $[Hg_2(OTeF_5)_6]^{2-}$ anion optimizes to D_2 symmetry (Figure 4.12) and provides a valid model for the dimeric $[Hg_2(OTeF_5)_6]^{2-}$ anion observed in the crystal structure. The main features observed in the solid-state structure were reproduced, except for the conformations of the $Hg(OTeF_5)_2$ groups which both optimized to a *syn*-

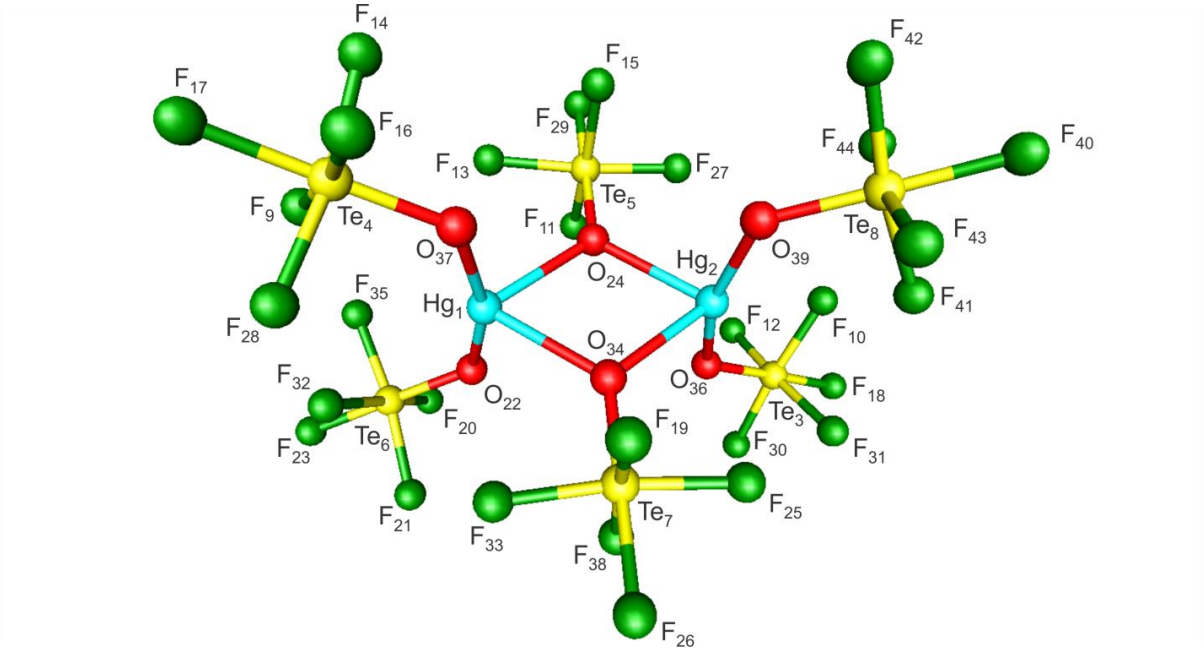

Figure 4.12. Gas-phase, energy-minimized geometry of $[Hg_2(OTeF_5)_6]^{2-}$ (D_2) calculated at the PBE0/def2-TZVPP level of theory.

conformation (dihedral $Te–O_t–Hg–O_t–Te$ angle, 12.1°), instead of the observed *anti*- (122.3(3)°) and *gauche*- (34.7(5)°) conformations.[26] Discrepancies between the calculated

and observed conformations are likely the result of the secondary interionic Hg---F contacts between dimers in the solid state, which are absent in the model anion.

The Hg and O_μ atoms of the calculated $[HgO_\mu]_2$ core are coplanar by symmetry. The core has geometrical parameters that are in excellent agreement with the experimental values (calcd: $\angle O_\mu$–Hg–O_μ, 72.8°, $\angle$Hg–O_μ–Hg, 107.2°, Hg–O_μ, 2.441 Å; exptl: $\angle O_\mu$–Hg–O_μ, 70.1(1) and 73.9(1)°, $\angle$Hg–O_μ–Hg, 102.1(1) and 104.6(1)°, Hg–O_μ, 2.353(4)–2.507(4) Å). The Hg–O_t bond lengths (2.081 Å) are significantly shorter than the Hg–O_μ bond lengths but are only slightly elongated with respect to those of neutral $Hg(OTeF_5)_2$ (2.008 Å).[26] Both Hg–O_μ bonds are elongated compared to the calculated Hg–O bond lengths of $[Hg(OTeF_5)_4]^{2-}$ (2.226 Å), but are slightly less elongated than the three equatorial Hg–O bonds (2.481–2.510 Å) in the optimized gas-phase geometry of $[Hg(OTeF_5)_5]^{3-}$ (vide supra). The calculated O_t–Hg–O_t bond angles (162.5°) are intermediate with respect to those subtended at $Hg_{(2)}$ (157.0(2)°) and $Hg_{(1)}$ (174.1(2)°) in the crystal structure. The calculated Te–O_μ bond lengths (1.810 Å) are slightly shorter than the Te–O_t bond lengths (1.821 Å), a trend that is also observed in the crystal structure (Te–O_μ, 1.788(4)–1.800(4) Å; Te–O_t, 1.811(4)–1.821(4) Å). There are no significant differences among the calculated Te–F bond lengths and angles for F_5TeO- groups in either the calculated or experimental structures.

4.3.1.4. Calculated Geometry of $[Hg_3(OTeF_5)_8]^{2-}$

The calculated structure of the unknown $[Hg_3(OTeF_5)_8]^{2-}$ anion (Figure 4.13) was used to model the Hg environments present in the crystal structure of $Cs_2[Hg(OTeF_5)_4]\cdot Hg(OTeF_5)_2$.

The environment around the central Hg atom is very well reproduced. The Hg–O bond lengths (2.231–2.241 Å) of the central $[Hg(OTeF_5)_4]^{2-}$ unit are intermediate with respect to the experimental values (2 x 2.186(1) Å and 2 x 2.287(1) Å). The environment around the central Hg atom is a distorted tetrahedron with O–Hg–O bond angles that are significantly larger (calcd, 126.6 and 128.7°; exptl, 137.9(1) and 147.8(1)°) and smaller (calcd, 77.8 and 77.8°; exptl, 110.4(1) and 81.4(1)°) than the ideal tetrahedral angle,

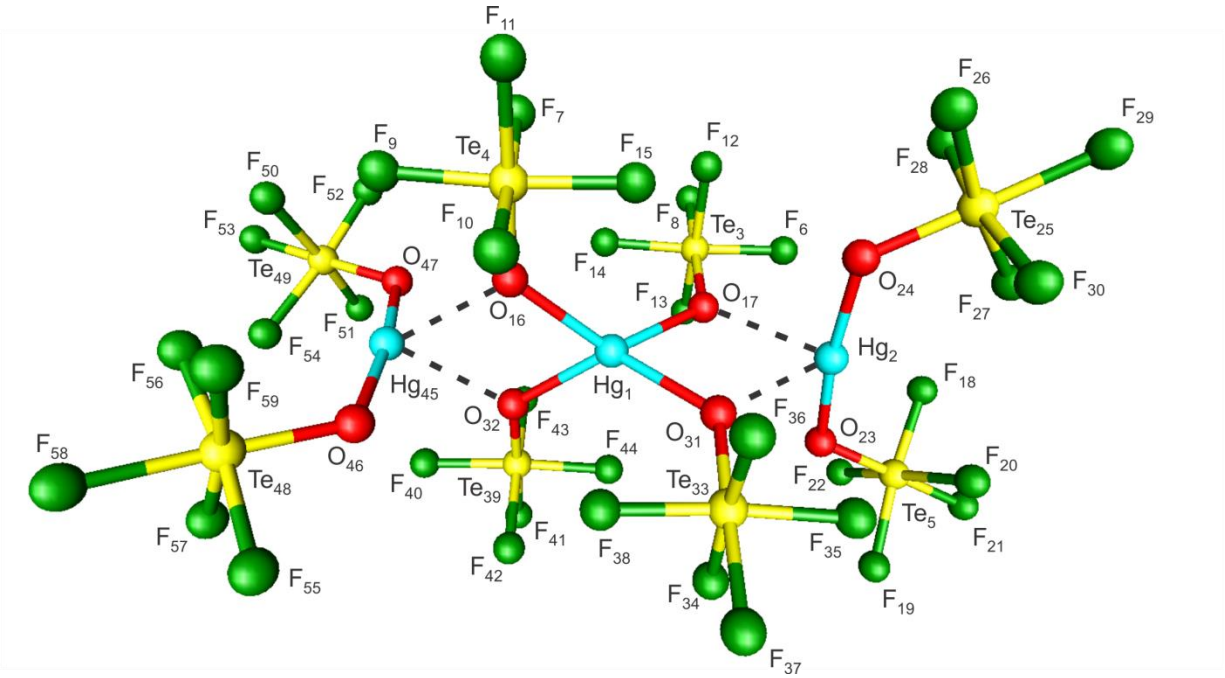

Figure 4.13. Gas-phase, energy-minimized geometries of $[Hg_3(OTeF_5)_8]^{2-}$ (C_1) calculated at the PBE0/def2-TZVPP level of theory. Long contacts between the central "$[Hg(OTeF_5)_4]^{2-}$ unit" and terminal "$Hg(OTeF_5)_2$ units" are indicated by dashed lines.

109.5°. As observed in the crystal structure, the four oxygen atoms of the central $[Hg(OTeF_5)_4]^{2-}$ unit interact with two $Hg(OTeF_5)_2$ units through Hg---O contacts (2.554–2.564 Å), in good agreement with the experimental values (2 x 2.555(1) and 2 x 2.737(1) Å). The Hg---F contacts to fluorine atoms of adjacent $Hg(OTeF_5)_2$ units are not present in the gas-phase structure because both terminal $Hg(OTeF_5)_2$ units adopt *syn*-conformations.

The calculated Te–O (1.823–1.824 Å) bond lengths are slightly elongated when compared to the observed bond lengths of the $[Hg(OTeF_5)_4]^{2-}$ unit (1.798(1) and 1.816(1) Å), and those of the isolated $[Hg(OTeF_5)_4]^{2-}$ anion (calcd, 1.799 Å; exptl, 1.797(6) Å). The Te–F bond lengths (1.852–1.866 Å) are in good agreement with the experimental values (1.838(1)–1.865(1) Å) with no significant differences between the axial and equatorial bond lengths.

In the calculated $[Hg_3(OTeF_5)_8]^{2-}$ anion, both terminal $Hg(OTeF_5)_2$ units adopt *syn*-conformations (dihedral Te_5–O_{23}–Hg_2–O_{24}–Te_{25} angle, 15.0°; dihedral Te_{49}–O_{47}–Hg_{45}–O_{46}–Te_{48} angle, 2.2°), in contrast with the *anti*-conformation (dihedral Te–O–Hg–O–Te angle, 139.1°) that is present in the solid-state (Figure 4.4). Despite this conformational difference, and because the model takes into account some interactions with the $[Hg(OTeF_5)_4]^{2-}$ unit, the overall trends in geometrical parameters and vibrational frequencies are very well reproduced.

The calculated Hg–O bond lengths (2.039–2.041 Å) are elongated compared to monomeric $Hg(OTeF_5)_2$ (1.976 Å).[26] As observed experimentally, the elongations of the Hg–O bonds are attributable to additional Hg---O contacts. Correspondingly, the calculated Te–O bond lengths (1.829–1.830 Å) are shorter than in $Hg(OTeF_5)_2$ (1.856 Å).

The calculated Te–F bond lengths (1.847–1.864 Å) do not differ significantly from those of $Hg(OTeF_5)_2$ (1.835–1.866 Å). The calculated O–Hg–O bond angles (172.0 and 172.2°) are very close to the corresponding bond angle in $Hg(OTeF_5)_2$ (177.0°).

4.3.2. Natural Bond Orbital (NBO) Analyses; Charges, Valencies, and Bond Orders

4.3.2.1. NBO Analyses of $[Hg(OTeF_5)_4]^{2-}$ and $[Hg(OTeF_5)_5]^{3-}$

The Hg charges are significantly more positive in the anions (1.689 and 1.675, respectively) than in neutral $Hg(OTeF_5)_2$ (1.422) (Tables S4.17 and S4.18). The highest negative charges reside on the O atoms, and are more negative for the 2– anion (4 x –1.235) compared to those of the 3– anion (ax: 2 x –1.202; eq: –1.202, –1.203, –1.210). The most negative charge in the equatorial HgO_3-plane corresponds to the longest, most ionic, Hg–O bond. The Hg–O bond orders are significantly less in $[Hg(OTeF_5)_4]^{2-}$ (4 x 0.115) and $[Hg(OTeF_5)_5]^{3-}$ (ax: 2 x 0.170; eq: 2 x 0.036 and 0.034) than in $Hg(OTeF_5)_2$ (0.291), consistent with more polar Hg–O bonds in the anions than in neutral $Hg(OTeF_5)_2$. Correspondingly, the Te–O bond orders are greater in $[Hg(OTeF_5)_4]^{2-}$ (4 x 0.784) and $[Hg(OTeF_5)_5]^{3-}$ (ax: 2 x 0.766; eq: 2 x 0.841 and 0.846) anions than in $Hg(OTeF_5)_2$ (0.672). Overall, the teflate groups of the anions accommodate significantly more negative charge than those of $Hg(OTeF_5)_2$, as reflected by the average total F_5TeO-group charges ($Hg(OTeF_5)_2$, –0.711; $[Hg(OTeF_5)_4]^{2-}$, –0.922; $[Hg(OTeF_5)_5]^{3-}$, –0.934). In $[Hg(OTeF_5)_5]^{3-}$, most of the negative charge is located on the F_5TeO_{eq}-groups (F_5TeO_{eq}-, –0.981; F_5TeO_{ax}-, –0.863). The charge difference is consistent with the calculated Te–O_{eq} bond lengths where Te–O_{eq} > Te–O_{ax} (see Table S4.14). The Hg valencies of

$[Hg(OTeF_5)_4]^{2-}$ (0.455) and $[Hg(OTeF_5)_5]^{3-}$ (0.444) compared to that of $Hg(OTeF_5)_2$ (0.602) are also consistent with the enhanced polarities of the Hg–O bonds of the anions.

4.3.2.2. NBO Analyses of $[Hg_2(OTeF_5)_6]^{2-}$

The charges on the terminal Hg_1 and Hg_2 atoms (1.470) (Table S4.19, Figure 4.13) are little affected by contacts with $[OTeF_5]^-$ when compared with gas-phase $Hg(OTeF_5)_2$ (1.422). The highest negative charges reside on the O atoms, with charges on the terminal O_t atoms (–1.197) that are slightly more negative than in $Hg(OTeF_5)_2$ (–1.176). This is accompanied by a decrease in the Hg–O_t bond orders (0.183) with respect to those of $Hg(OTeF_5)_2$ (0.291) and an increase in the Te–O_t bond orders (0.741) with respect to those of $Hg(OTeF_5)_2$ (0.672). The charges on the bridging O_μ atoms (–1.297) are even more negative than for O_t (–1.197) and more negative than for the $[OTeF_5]^-$ anion (–1.127). The Te–O_μ bond orders (0.754) decrease with respect to that of the $[OTeF_5]^-$ anion (0.866), consistent with coordination of $Hg(OTeF_5)_2$ to $[OTeF_5]^-$. The small Hg_1–O_μ bridge bond orders (0.020) are consistent with rather weak covalent interactions between the $Hg(OTeF_5)_2$ acceptor and the F_5TeO-ligand.

4.4. Conclusions

The coordination behavior of Hg(II) towards the $[OTeF_5]^-$ anion was investigated by reactions of $Hg(OTeF_5)_2$ with $[M][OTeF_5]$ ($M^+ = [N(CH_3)_4]^+$, $[N(CH_2CH_3)_4]^+$, Cs^+). The resulting salts, $[N(CH_2CH_3)_4]_2[Hg(OTeF_5)_4]$, $[N(CH_3)_4]_3[Hg(OTeF_5)_5]$, $[N(CH_2CH_3)_4]_3[Hg(OTeF_5)_5]$, $[N(CH_3)_4]_2[Hg_2(OTeF_5)_6]$, $Cs_2[Hg(OTeF_5)_4]\cdot Hg(OTeF_5)_2$,

and $\{Cs_3[Hg_2(OTeF_5)_7]\cdot Hg(OTeF_5)_2\}\cdot 4SO_2ClF$ were characterized in the solid state by single-crystal X-ray diffraction. The $[Hg(OTeF_5)_4]^{2-}$ anion of the $[N(CH_2CH_3)_4]^+$ salt is well-isolated, having nearly ideal tetrahedral coordination at Hg(II). In contrast, the $[Hg(OTeF_5)_4]^{2-}$ anion of $Cs_2[Hg(OTeF_5)_4]\cdot Hg(OTeF_5)_2$ comprises part of a chain structure in which it weakly interacts with $Hg(OTeF_5)_2$, resulting in a flattened $[Hg(OTeF_5)_4]^{2-}$ tetrahedron. The $[N(CH_3)_4]_3[Hg(OTeF_5)_5]$ and $[N(CH_2CH_3)_4]_3[Hg(OTeF_5)_5]$ salts contain well-isolated $[Hg(OTeF_5)_5]^{3-}$ anions having distorted square-pyramidal geometries that contrast with the energy-minimized trigonal bipyramidal geometry calculated for the gas-phase anion. The occurrence of significant cation-anion contacts and an intra-ionic Hg---F interaction likely accounts for the square-pyramidal geometry in the solid state. Although attempts to form the $[Hg(OTeF_5)_3]^-$ anion failed, its dimer, $[Hg_2(OTeF_5)_6]^{2-}$, has been isolated as the $[N(CH_3)_4]^+$ salt in which two $Hg(OTeF_5)_2$ moieties are linked to each other through two bridging F_5TeO-groups. The structure of the $[Hg_2(OTeF_5)_7]^{3-}$ anion may be formulated as two $[Hg(OTeF_5)_3]^-$ anions bridged by a $[OTeF_5]^-$ anion. This anion also participates in a chain structure in which it alternates and interacts with $Hg(OTeF_5)_2$ molecules. Attempts to synthesize salts of the $[Hg(OTeF_5)_6]^{4-}$ anion only yielded $[Hg(OTeF_5)_4]^{2-}$ and $[Hg(OTeF_5)_5]^{3-}$.

Quantum-chemical calculations have been used to model the gas-phase geometries of the $[Hg(OTeF_5)_4]^{2-}$, $[Hg(OTeF_5)_5]^{3-}$, $[Hg_2(OTeF_5)_6]^{2-}$, and the hypothetical $[Hg_3(OTeF_5)_8]^{2-}$ anion. Their calculated vibrational frequencies and intensities aided in the assignment of the Raman spectra of $[N(CH_2CH_3)_4]_2[Hg(OTeF_5)_4]$,

$[N(CH_3)_4]_3[Hg(OTeF_5)_5]$, $[N(CH_2CH_3)_4]_3[Hg(OTeF_5)_5]$, and $Cs_2[Hg(OTeF_5)_4]\cdot Hg(OTeF_5)_2$. The NBO analyses show that the Hg–O bonds of the gas-phase $[Hg(OTeF_5)_4]^{2-}$ and $[Hg(OTeF_5)_5]^{3-}$ anions are similar, and significantly more polar than the Hg–O bonds in $Hg(OTeF_5)_2$.

The $[Hg(OTeF_5)_4]^{2-}$, $[Hg_2(OTeF_5)_6]^{2-}$, and $[Hg_2(OTeF_5)_7]^{3-}$ anions exhibit structural features that are in common with their chlorine, bromine, and iodine analogues and are rare examples of teflate derivatives that contain bridging F_5TeO-groups. The square-pyramidal $[Hg(OTeF_5)_5]^{3-}$ anion geometry contrasts with the trigonal bipyramidal geometries of the $[HgX_5]^{3-}$ (X = Cl, Br) anions in the solid state and is the first teflate anion to be isolated that bares a 3– charge.

4.5. Experimental

General experimental techniques, procedures, and equipment, as well as the preparation and purification of all starting materials are described in Chapter 2.

4.5.1. ***Syntheses and Crystal Growth.*** Reagents were combined in ¼-in. o.d. T-shaped FEP reaction vessels at room temperature inside of a drybox. The vessels were then transferred onto a glass vacuum line where the solvent was vacuum distilled and condensed onto the reactants. All crystal growing was carried out under reduced N_2 pressure by slow evaporation of the solvent at 0 °C into the side arm of the reaction vessel, which was cooled to −78 ^{o}C using a dry ice/acetone bath. The side arm containing the condensed solvent was then cooled to −196 ^{o}C and heat-sealed off under dynamic

vacuum. Unless otherwise stated, the low-temperature Raman spectra (–150 °C) were recorded directly on the freshly crystallized sample.

(i) $[N(CH_2CH_3)_4]_2[Hg(OTeF_5)_4]$. The reaction vessel was loaded with $Hg(OTeF_5)_2$ (0.0476 g, 0.0702 mmol) and $[N(CH_2CH_3)_4][OTeF_5]$ (0.0510, 0.1382 mmol) followed by condensation of ~ 0.4 mL of SO_2ClF solvent onto the reagents at −78 ^oC. The void above the solution was backfilled with 300 Torr of dry N_2, and warmed to room temperature for 1 h to solubilize and allow the reagents to fully react. Slow evaporation of the solvent into the side arm of the reaction vessel was complete after 16 h, leaving a deposit of colorless, plate-shaped crystals on the walls of the FEP reactor. A $[N(CH_2CH_3)_4]_2[Hg(OTeF_5)_4]$ crystal having the dimensions 0.06 x 0.10 x 0.14 mm^3 was selected for a low-temperature X-ray structure determination.

(ii) $[N(CH_3)_4]_3[Hg(OTeF_5)_5]$. The reagents, $Hg(OTeF_5)_2$ (0.0937 g, 0.1383 mmol) and $[N(CH_3)_4][OTeF_5]$ (0.0970, 0.3103 mmol), were combined in an FEP reaction vessel, and SO_2 (~ 0.3 mL) was condensed onto the reagents at −78 ^oC. The reactor and contents were backfilled to 760 Torr with dry N_2 . When warmed to 0 ^oC, the reagents completely dissolved. Crystals were grown by evaporation over a 7 h period and resulted in colorless, plate-shaped crystals. A $[N(CH_3)_4]_3[Hg(OTeF_5)_5]$ crystal having the dimensions 0.10 x 0.15 x 0.26 mm^3 was selected for a low-temperature X-ray structure determination.

(iii) $[N(CH_2CH_3)_4]_3[Hg(OTeF_5)_5]$. The starting materials, $Hg(OTeF_5)_2$ (0.0322 g, 0.0475 mmol) and $[N(CH_2CH_3)_4][OTeF_5]$ (0.0761 g, 0.2062 mmol), were combined inside an FEP reaction vessel, and SO_2ClF (~ 0.3 mL) was condensed onto the reagents at −78 ^oC. The reaction vessel and contents were backfilled with 350 Torr of dry N_2. The

reaction mixture was allowed to stand at room temperature for 8 h to solubilize and react. Crystal growth by slow evaporation was complete after 16 h, leaving a deposit of colorless, plate-shaped crystals on the walls of the FEP reactor. The Raman spectrum was not obtained for this salt. A crystal of $[N(CH_2CH_3)_4]_3[Hg(OTeF_5)_5]$ having the dimensions 0.04 x 0.07 x 0.09 mm^3 was selected for a low-temperature X-ray structure determination.

(iv) $[N(CH_3)_4]_2[Hg_2(OTeF_5)_6]$. In a typical synthesis, $Hg(OTeF_5)_2$ (0.0485, 0.0715 mmol) and $[N(CH_3)_4][OTeF_5]$ (0.0204, 0.0651 mmol) were weighed out and added to a FEP reaction vessel. Approximately 0.25 mL of CH_2Cl_2 was condensed onto the reagents and the reactor and contents were backfilled to 100 Torr with dry N_2. The reaction vessel was warmed to room temperature for 5 h to allow complete dissolution and reaction. Crystal growth was induced by slow evaporation of the solvent over 16 h which resulted in the formation of colorless, tetragonal prisms. A $[N(CH_3)_4]_2[Hg_2(OTeF_5)_6]$ crystal having the dimensions 0.05 x 0.05 x 0.16 mm^3 was selected for a low-temperature X-ray structure determination.

(v) $Cs_2[Hg(OTeF_5)_4]\cdot Hg(OTeF_5)_2$ and $\{Cs_3[Hg_2(OTeF_5)_7]\cdot Hg(OTeF_5)_2\}\cdot 4SO_2ClF$. In the ensuing description, parentheses denote quantities/conditions used for the synthesis of $Cs_2[Hg(OTeF_5)_4]\cdot Hg(OTeF_5)_2$ and square brackets denote quantities used for the synthesis of $\{Cs_3[Hg_2(OTeF_5)_7]\cdot Hg(OTeF_5)_2\}\cdot 4SO_2ClF$. Although a wide range of molar ratios were investigated, no other salts were isolated.

In a typical synthesis, the reaction vessel was loaded with $Hg(OTeF_5)_2$ (0.0639 g, 0.0439 mmol) [0.0765 g, 0.1129 mmol] and $Cs[OTeF_5]$ (0.0297g, 0.1719 mmol) [0.0858 g, 0.2308 mmol] followed by condensation of ~ 0.3 mL of SO_2ClF solvent onto the reagents at −78 °C. The voids above the solutions were backfilled with 400 Torr of dry N_2 and the reaction mixtures were warmed to room temperature for 3 h. Solvent evaporation was complete after 16 h, and resulted in the formation of colorless, plate-shaped crystals. The Raman spectrum was not obtained for the SO_2ClF solvate. A crystals having the dimensions 0.06 x 0.15 x 0.18 mm^3 [0.11 x 0.11 x 0.40 mm^3] were selected for a low-temperature X-ray structure determination.

(vi) Attempted Syntheses of $[N(CH_2CH_3)_4][Hg(OTeF_5)_3]$ and $[N(CH_2CH_3)_4]_4[Hg(OTeF_5)_6]$. Several reactions between $Hg(OTeF_5)_2$ and $[N(CH_2CH_3)_4][OTeF_5]$ were attempted with the view to isolate and characterize the $[Hg(OTeF_5)_3]^-$ and $[Hg(OTeF_5)_6]^{4-}$ anions. A range of molar ratios spanning 1:1 to 1:5 for $Hg(OTeF_5)_2$: $[N(CH_2CH_3)_4][OTeF_5]$ were used at scales similar to those described above. A variety of solvents (SO_2ClF, SO_2, and CH_2Cl_2) were used for crystal growth. Reactions using high molar ratios of $[N(CH_2CH_3)_4][OTeF_5]$ only resulted in $[N(CH_2CH_3)_4]_2[Hg(OTeF_5)_4]$ and $[N(CH_2CH_3)_4]_3[Hg(OTeF_5)_5]$ (vide supra). At low molar ratios, a colorless and vitreous material formed that failed to crystallize. Raman spectra showed bands similar to $[N(CH_3)_4]_2[Hg_2(OTeF_5)_6]$, suggesting that the $[N(CH_2CH_3)_4]_2[Hg_2(OTeF_5)_6]$ salt may have formed.

4.5.2. Structure Solution and Refinement

The XPREP[54] program was used to confirm the unit cell dimensions, the crystal system and space group. The structures were solved in their respective space groups by use of direct methods using SHELXS[54] or SIR92[55], and the solutions yielded the positions of all the heavy atoms as well as some of the lighter atoms. Successive difference Fourier syntheses revealed the positions of the remaining light atoms. The final refinements were obtained by introducing anisotropic parameters for all the atoms, an extinction parameter, and the recommended weighting factor. The positions of the hydrogen atoms in the $[N(CH_3)_4]^+$ and $[N(CH_2CH_3)_4]^+$ cations were calculated. The maximum electron densities in the final difference Fourier maps were located around the heavy atoms. The PLATON program[55] could not suggest additional or alternative symmetries.

The refinement of the structure of $Cs_2[Hg(OTeF_5)_4]\cdot Hg(OTeF_5)_2]$ was straight forward. In the structure of $\{Cs_3[Hg_2(OTeF_5)_7]\cdot Hg(OTeF_5)_2\}\cdot 4SO_2ClF$, one SO_2ClF molecule ($S_{(3)}$) was found to be disordered between two orientations (72/28) sharing a common central sulfur atom. In the structure of $[N(CH_3)_4]_2[Hg_2(OTeF_5)_6]$, one of the two $[N(CH_3)_4]^+$ cations ($N_{(2)}$) as well as one of the terminal teflate groups ($Te_{(6)}$) were found to be disordered between two orientations (50/50), sharing a common central nitrogen or tellurium atom. For both disordered structures, the disorder was dealt with by using the command SAME.[54] As a consequence, the light atoms of the disordered entities were refined isotropically. The structure of $[N(CH_2CH_3)_4]_2[Hg(OTeF_5)_4]$ was solved in the *Pc* space group and was refined as a racemic twin. For $[N(CH_3)_4]_3[Hg(OTeF_5)_5]$, a satisfactory model could be obtained in the *Cc* space group, however, the refinement as a

single crystal remained at an overall agreement factor of about 33%, with unsatisfactory behavior for several parameters. With the introduction of the twin matrix ($\bar{1}$ 0 0 0 $\bar{1}$ 0 0 0 1) characteristic of a pseudo-merohedral twin, the refinement converged. A refinement was carried out using this law, giving rise to a drastic drop in R_1 to 0.15, indicating the correct law had been selected. At this stage, the possibility of a racemic twin or wrong absolute structure was suggested by the program. Although the absolute structure was checked, it was shown that the contribution of a racemic twin had to be taken into consideration. The final twin law used was ($\bar{1}$ 0 0 0 $\bar{1}$ 0 0 0 1 $\bar{4}$), which resulted in a R_1-value of 0.0196. Attempts were made to solve the structure in the *C*2/c space group, but were unsuccessful. For $[N(CH_2CH_3)_4]_3[Hg(OTeF_5)_5]$, a preliminary solution was obtained in the $P2_1$ space group as a racemic twin. Attempts were made to solve the structure in the $P2_1$/m space group, but were unsuccessful. X-ray crystallographic files in CIF format for the structure determinations of $[N(CH_2CH_3)_4]_2[Hg(OTeF_5)_4]$, $[N(CH_3)_4]_3[Hg(OTeF_5)_5]$, $[N(CH_2CH_3)_4]_3[Hg(OTeF_5)_5]$, $[N(CH_3)_4]_2[Hg_2(OTeF_5)_6]$, $Cs_2[Hg(OTeF_5)_4]\cdot Hg(OTeF_5)_2$, $\{Cs_3[Hg_2(OTeF_5)_7]\cdot Hg(OTeF_5)_2\}\cdot 4SO_2ClF$ are available free of charge via the Internet at http://pubs.acs.org/.

4.5.3. Computational Details.

The optimized gas-phase geometries and vibrational frequencies of $[Hg(OTeF_5)_4]^{2-}$, $[Hg(OTeF_5)_5]^{3-}$, $[Hg_2(OTeF_5)_6]^{2-}$ and $[Hg_3(OTeF_5)_8]^{2-}$ were obtained at the PBE0 level of theory using the def2-TZVPP basis set. The PBE0/def2-TZVPP method was chosen because it has proven reliable for $Hg(OTeF_5)_2$ and $Hg(OTeF_5)_2\cdot 1.5NgF_2$ (Ng = Kr, Xe).[26] All basis sets were obtained online from the EMSL

Basis Set Exchange (https://bse.pnl.gov/bse/portal).[59-64] Quantum-chemical calculations were carried out using the program Gaussian 09[65] for geometry optimizations, vibrational frequencies, and their intensities. All geometries were fully optimized using analytical gradient methods. The program GaussView[66] was used to visualize the vibrational displacements that form the basis for the vibrational mode descriptions given in Tables 4.7–4.10 and S4.7–S4.10. Natural bond orbital analyses were performed using the PBE0 densities with the NBO program (version 6.0).[45]

4.6. Supporting Information Contents - Appendix B

Complete list of experimental geometrical parameters of $[N(CH_2CH_3)_4]_2[Hg(OTeF_5)_4]$ (Table S4.1), $N(CH_3)_4]_3[Hg(OTeF_5)_5]$ (Table S4.2), $N(CH_3)_4]_2[Hg_2(OTeF_5)_6]$ (Table S4.3), $Cs_2[Hg(OTeF_5)_4]\cdot Hg(OTeF_5)_2$ (Table S4.4), $\{Cs_3[Hg_2(OTeF_5)_7]\cdot Hg(OTeF_5)_2\}\cdot 4SO_2ClF$ (Table S4.5); $[N(CH_2CH_3)_4]_3[Hg(OTeF_5)_5]$ (Table S4.6), the $[Hg(OTeF_5)_5]^{3-}$ anions in the $[N(CH_2CH_3)_4]_3[Hg(OTeF_5)_5]$ salt (Figure S4.1), the asymmetric unit of $[N(CH_2CH_3)_4]_2[Hg(OTeF_5)_4]$ (Figure S4.2), $[N(CH_3)_4]_3[Hg(OTeF_5)_5]$ (Figure S4.3), $[N(CH_3)_4]_2[Hg_2(OTeF_5)_6]$ (Figure S4.4), packing of $Cs_2[Hg(OTeF_5)_4]\cdot Hg(OTeF_5)_2$ (Figure S4.5), packing of $\{Cs_3[Hg_2(OTeF_5)_7]\cdot Hg(OTeF_5)_2\}\cdot 4SO_2ClF$ (Figure S4.6); the full Raman spectra of $[N(CH_2CH_3)_4]_2[Hg(OTeF_5)_4]$ (Figure S4.7), $[N(CH_3)_4]_3[Hg(OTeF_5)_5]$ (Figure S4.8), $[N(CH_3)_4]_2[Hg_2(OTeF_5)_6]$ (Figure S4.9); full list of calculated vibrational frequencies and intensities and assignments for $[Hg(OTeF_5)_4]^{2-}$ (Table S4.7); $[Hg(OTeF_5)_5]^{3-}$ (Table S4.8), $[Hg_2(OTeF_5)_6]^{2-}$ (Table S4.9), and $[Hg_3(OTeF_5)_8]^{2-}$ (Table S4.10); experimental and calculated vibrational data for $[OTeF_5]^-$ (Table S4.11); calculated geometry of $[OTeF_5]^-$ (Figure S4.10); calculated geometrical parameters of $[OTeF_5]^-$ (Table S4.12); complete list of calculated geometrical parameters of $[Hg(OTeF_5)_4]^{2-}$ (Table S4.13); $[Hg(OTeF_5)_5]^{3-}$ (Table S4.14), $[Hg_2(OTeF_5)_6]^{2-}$ (Table S4.15), and $[Hg_3(OTeF_5)_8]^{2-}$

(Table S4.16); NBO Analyses of $[Hg(OTeF_5)_4]^{2-}$ (Table S4.17); $[Hg(OTeF_5)_5]^{3-}$ (Table S4.18), $[Hg_2(OTeF_5)_6]^{2-}$ (Table S4.19), $Hg(OTeF_5)_2$ (Table S4.20), $[OTeF_5]^-$ (Table S4.21).

4.7. References

(1) House, D. A.; Robinson, W. T.; McKee, V. *Coord. Chem. Rev. 135/136*, **1994**, 533–586.

(2) Svensson, P. H.; Kloo, L. *Inorg. Chem.* **1999**, *38*, 3390–3393.

(3) Pabst, I.; Bats, J. W.; Fuess, H. *Acta Cryst.* **1990**, *B46*, 503–508.

(4) Pickardt, J.; Wischlinsky, P. *Z. Anorg. Allg. Chem.* **1996**, *622*, 1125–1128.

(5) Clegg, W.; Greenhalgh, D. A.; Straughan, B. P. *J. Chem. Soc., Dalton Trans.* **1975**, *23*, 2591–2593.

(6) Sharma, R. P.; Sharma, R.; Kumar, A.; Venugopalan, P.; Brando, P.; Felix, V. *Inorg. Chem. Commun.* **2009**, *12*, 945–947.

(7) Battaglia, L. P.; Corradi, A. B. *J. Chem. Soc., Dalton Trans.* **1986**, *12*, 2529–2533.

(8) Brodersen, K.; Thiele, G.; Görz, G. *Z. Anorg. Allg. Chem.* **1973**, *401*, 217–314.

(9) Berthold, H. J.; Haas, D.; Tamme, R.; Brodersen, K.; Jensen, K.esser, D.; Thiele, G. *Z. Anorg Allg Chem*, **1979**, *456*, 29–40.

(10) Loukil, M.; Kabadou, A.; Svoboda, I. *J. Chem. Crystallogr.* **2008**, *38*, 85–9.

(11) Pickardt, J.; Wischlinski, P. *Z. Anorg. Allg. Chem.* **1999**, *625*, 1527–1531.

(12) House, D. A.; McKee, V.; Robinson, W. T. *Inorg. Chim. Acta.* **1989**, 160, 71–76.

(13) Pickardt, J.; Kuhn, B. *J. Chem. Soc., Chem. Commun.*, **1995**, *4*, 451–452.

(14) Hoppe, R.; Homann, R. *Z. Anorg. Allg. Chem.* **1969**, *369*, 212–216.

(15) Schrötter, F.; Müller, B. G. *Z. Anorg. Allg. Chem.* **1992**, *618*, 53–58.

(16) Riedel, S.; Kaupp, M.; Pyykkö, P. *Inorg. Chem.* **2008**, *47*, 3379−3383.

(17) Sladky, F.; Kropshofer, H. *Inorg. Nucl. Chem. Lett.* **1972**, *8*, 195–197.

(18) Birchall, T.; Myers, R. D.; de Waard, H.; Schrobilgen, G. J. *Inorg. Chem.* **1982**, *21*, 1068–1073.

(19) Kellet, P. J.; Pawlik, M. J.; Taylor, L. F.; Thompson, R. G.; Levstik, M. A.; Anderson, O. P.; Strauss, S. H. *Inorg. Chem.* **1989**, *28*, 440–441.

(20) Strauss, S. H.; Noirot, M. D.; Anderson, O. P. *Inorg. Chem.* **1986**, *25*, 3850–3851.

(21) Huppmann, P.; Hartl, H.; Seppelt, K. *Z. Anorg. Allg. Chem.* **1985**, *524*, 26–32.

(22) Strauss, S. H.; Noirot, M. D.; Anderson, O. P. *Inorg. Chem.* **1985**, *24*, 4307–4311.

(23) Colsman, M. R.; Noirot, M. D.; Miller, M. M.; Anderson, O. P.; Strauss, S. H. *J. Am. Chem. Soc.* **1988**, *110*, 6886–6888.

(24) Rack, J. J.; Hurlburt, P. K.; Kellett, P. J.; Luck, J. S.; Anderson, O. P.; Strauss, S. H. *Inorg. Chim. Acta.* **1996**, *242*, 71–79.

(25) Hurlburt, P. K.; Anderson, O. P.; Strauss, S. H. *J. Am. Chem.* Soc. **1991**, *113*, 6277–6278.

(26) Newbound, T. D.; Colsman, M. R.; Miller, M. M.; Wulfsberg, G. P.; Anderson, O.P.; Strauss, S. H. *J. Am. Chem. Soc.* **1989**, *111*, 3762–3764.

(27) DeBackere, J. R.; Mercier, H. P. A.; Schrobilgen, G. J. *J. Am. Chem. Soc*. **2014**, *136*, 3888−3903.

(28) Mercier, H. P. A.; Moran, M. D.; Schrobilgen, G. J.; Steinberg, C.; Suontamo, R. J. *J. Am. Chem. Soc.* **2004**, *126*, 5533–5548.

(29) Noirot, M. D.; Anderson, O. P.; Strauss, S. H. *Inorg. Chem.* **1987,** *26*, 2216–2223.

(30) Moran, M. D.; Mercier, H. P. A.; Schrobilgen, G. J. *Inorg. Chem.* **2007**, *46*, 5034−5045.

(31) Turowsky, L.; Seppelt, K. *Z. Anorg. Allg. Chem.* **1991**, *602*, 79–87.

(32) Mercier, H. P. A.; Sanders, J. C. P.; Schrobilgen, G. J. *Inorg. Chem.* **1995**, *34*, 5261–5273.

(33) Mercier, H. P. A.; Sanders, J. C. P.; Schrobilgen, G. J. *J. Am. Chem. Soc.* **1994**, *116*, 2921–2937.

(34) Van Seggen, D. M.; Hurlburt, P. K.; Anderson, O. P.; Strauss, S. H. *Inorg. Chem.* **1995**, *34*, 3453–3464.

(35) Hurlburt, P. K.; Rack, J. J.; Dec, S. F.; Anderson, O. P.; Strauss, S. H. *Inorg. Chem.* **1993**, *32*, 373–374.

(36) Hurlburt, P. K. PhD. Dissertation, Colorado State University, **1993**.

(37) Mercier, H. P. A.; Moran, M. D.; Sanders, J. C. P.; Schrobilgen, G. J. *Inorg. Chem.* **2005**, *44*, 49–60.

(37) Gerken, M.; Hazendonk, P.; Iuga, A.; Mack, J. P.; Mercier, H. P. A.; Schrobilgen, G. J. *J. Fluorine Chem.* **2006**, *127*, 1328−1338.

(38) Ivanova, M. V.; Köchner, T.; Mercier, H. P. A.; Schrobilgen, G. J. *Inorg. Chem.* **2013**, *52*, 6806−6819.

(39) Einstein, F. W. B.; Jones, R. D. G. *J. Chem. Soc. A* **1971**, 2762−2766.

(40) Casey, C. P.; Meszaros, M. W.; Neumann, S.; Genick Cesa, I.; Haller, K. J. *Organomet.* **1985**, *4*, 143−149.

(41) Mercier, H. P. A.; Moran, M. D.; Sanders, J. C. P.; Schrobilgen, G. J. *Inorg. Chem.* **2005**, *44*, 49−60.

(42) Bondi, A. *J. Phys. Chem.* **1964**, *68*, 441−451.

(43) Pauling, L. *The Nature of the Chemical Bond*, 3rd ed.; Cornell University: Ithaca, NY, 1960; p 260.

(44) Colsman, M. R.; Newbound, T. D.; Marshall, L. J.; Noirot, M. D.; Miller, M. M.; Wulfsberg, G. P.; Frye, J. S.; Anderson, O. P.; Strauss, S. H. **1990**, *112*, 2349−2362.

(45) Gillespie, R. J.; Hargittai, I. In *The VSEPR Model of Molecular Geometry*; Allyn and Bacon: Boston, MA, 1991.

(46) Addison, A. W.; Rao, T. N. *J. Chem. Soc., Dalton Trans.* **1984**, *7*, 1349−1356.

(47) Kabisch, G. *J. Raman Spectrosc.* **1980**, *9*, 279−285.

(48) Herstedt, M.; Henderson, W. A.; Smirnov, M.; Ducasse, L.; Servant, L.; Talaga, D.; Lassègues, J. C. *J. Mol. Struct.* **2006**, *783*, 145−156.

(49) Glaucio B.; Ferreira, G. B.; Comerlato, N. M.; Wardell, J. L.; Hollauer, E. *J. Braz. Chem. Soc.* **2004**, *15*, 951−963.

(50) *NBO 6.0*. Glendening, E. D.; Badenhoop, J. K.; Reed, A. E.; Carpenter, J. E.; Bohmann, J. A.; Morales, C. M.; Landis, C. R.; Weinhold, F. Theoretical Chemistry Institute, University of Wisconsin, Madison (2013).

(51) Casteel, W. J., Jr.; Dixon, D. A.; Mercier, H. P. A.; Schrobilgen, G. J. *Inorg. Chem.* **1996**, *35*, 4310–4322.

(52) Sladky, F.; Kropshofer, H.; Leitzke, O.; Peringer, P. *J. Inorg. Nucl. Chem.*, H. H. Hyman Memorial Volume, Supplement **1976**, 69–71.

(53) Mercier, H. P. A.; Sanders, J. C. P.; Schrobilgen, G. J. *J. Am. Chem. Soc.* **1994**, *116*, 2921–2937.

(54) Moock, *K.;* Seppelt, K. *Z. Anorg. Allg. Chem.* **1988**, *561*, 132–138.

(55) Schack, C.; Wilson, R. D. *Inorg. Chem.* **1970**, *9*, 311−314.

(56) Gerken, M.; Dixon, D. A.; Schrobilgen, G. J. *Inorg. Chem.* **2000**, *39*, 4244−4255.

(57) APEX2, release v2011.6-1; Bruker AXS Inc.: Madison, WI, 1995.

(58) Sheldrick, G. M. SADABS (Siemens Area Detector Absorption Corrections), version 2.03; Madison, WI, 1999.

(59) Sheldrick, G. M. SHELXTL-Plus, release 5.1; Siemens Analytical X-ray Instruments, Inc.: Madison, WI, 1998.

(60) Spek, A. L. *J. Appl. Crystallogr.* **2003**, *36*, 7–13.

(61) Weigend, F.; Ahlrichs, R. *Phys. Chem. Chem. Phys.* **2005**, *7*, 3297−3305.

(62) Peterson, K.A.; Figgen, D.; Goll, E.; Stoll, H.; Dolg, M. *J. Chem. Phys.* **2003**, *119*, 11113−11123.

(63) Andrae, D.; Haeussermann, U.; Dolg, M.; Stoll, H.; Preuss, H. *Theor. Chim. Acta* **1990**, *77*, 123−141.

(64) Basis sets and pseudo-potentials were obtained from the Extensible Computational Chemistry Environment Basis set Database, version 2/25/04, as developed and distributed by the Molecular Science Computing Facility, Environmental and Molecular Science Laboratory, which is part of the Pacific Northwest Laboratory, P.O. Box 999, Richland, WA 99352.

(65) Frisch, M. J.; Trucks, G. W.; Schlegel, H. B.; Scuseria, G. E.; Robb, M. A.; Cheeseman, J. R.; Scalmani, G.; Barone, V.; Mennucci, B.; Petersson, G. A.; Nakatsuji, H.; Caricato, M.; Li, X.; Hratchian, H. P.; Izmaylov, A. F.; Bloino, J.; Zheng, G.; Sonnenberg, J. L.; Hada, M.; Ehara, M.; Toyota, K.; Fukuda, R.; Hasegawa, J.; Ishida, M.; Nakajima, T.; Honda, Y.; Kitao, O.; Nakai, H.; Vreven, T.; Montgomery, Jr., J. A.; Peralta, J. E.; Ogliaro, F.; Bearpark, M.; Heyd, J. J.; Brothers, E.; Kudin, K. N.; Staroverov, V. N.; Kobayashi, R.; Normand, J.; Raghavachari, K.; Rendell, A.; Burant, J. C.; Iyengar, S. S.; Tomasi, J.; Cossi, M.; Rega, N.; Millam, N. J.; Klene, M.; Knox, J. E.; Cross, J. B.; Bakken, V.; Adamo, C.; Jaramillo, J.; Gomperts, R.; Stratmann, R. E.; Yazyev, O.; Austin, A. J.; Cammi, R.; Pomelli, C.; Ochterski, J. W.; Martin, R. L.; Morokuma, K.; Zakrzewski, V. G.; Voth, G. A.; Salvador, P.; Dannenberg, J. J.; Dapprich, S.; Daniels, A. D.; Farkas, Ö.; Foresman, J. B.; Ortiz, J. V.; Cioslowski, J.; Fox, D. J. Gaussian 09, Revision D.01, Gaussian, Inc., Wallingford CT, 2009.

(66) G*aussView*, release 3.0; Gaussian Inc.: Pittsburgh, PA, 2003.

CHAPTER 5

Syntheses and Characterization of Homoleptic Solvent Complexes of Hg^{2+} using the Weakly Coordinating $[Sb(OTeF_5)_6]^-$ Anion

Prepared for Publication: DeBackere, J.R., Mercier, H.P.A., and Schrobilgen, G.J.

5.1. Introduction

In the past few decades, the field of weakly coordinating anions (WCAs) has significantly advanced the design and syntheses of anions which provide only weak electrostatic and dispersive interactions.[1–3] Some of the most effective anions, e.g., $[Sb(OTeF_5)_6]^-$,[4,5] $[Al(OC(R_F)_3)_4]^-$,[6] and $[F\{Al(O(R_F)_3\}_2]$ (R_F = perfluoroalkyl),[7,8] and $[HCB_{11}(CF_3)_{11}]^-$,[9] are so weakly coordinating that the resulting environments can be referred to as "pseudo-gas-phase conditions" in the solid state.[1–3] Consequently, interesting coordination complexes with cations having weak and unusual ligands that were initially identified in the gas-phase can now be synthesized and characterized in the condensed state. For example, $[Ag(L)]_n]^+$ (L = S_8 or S_{16})[10,11] were initially observed by advanced mass spectrometric (MS) methods and subsequently characterized in the solid state when partnered with a suitable WCA.[12] Solid-state methods of characterization have provided definitive structural and geometric information which is otherwise unavailable from MS methods.

Among the known WCAs, the large perfluorinated $[Sb(OTeF_5)_6]^-$ anion offers considerable promise for the stabilization of novel electrophilic and highly reactive cations because it is both chemically robust and redox-stable.[1–3,13] However, its chemistry remains relatively unexplored and therefore its full synthetic potential likely has not been realized. Its

use is currently limited to the stabilization of the main-group cations $[CX_3]^+$ (X = Cl, Br),[14,15] $[CBr_x(OTeF_5)_{(3-x)}]^+$ (x = 1–3),[14,15] $[CFX_2]^+$ (X = Cl, Br),[15] $[C(C_6H_5)_3]^+$,[5] $[XeOTeF_5]^+$,[16] $[SbX_4]^+$ (X = Cl, Br),[17] $[F(TeCl_3)_2]^+$,[18] Cs^+,[19] NR_4^+ (R = Me,[20] Et,[20] *n*-Bu)[5], and several $[Ag(L)]_n^+$ complexes (L = S_8,[12] Se_6,[21,22] SO_2,[21,22] CH_2Br_2,[5] and $C_2H_4Br_2$)[5].

Beyond exploring the coordination chemistry of unusual, weak, and fundamentally significant ligands such as nonclassical $[M(CO)_x]^{n+}$ and $[M(Ch_x)_y]^{n+}$ cations (Ch = S, Se, Te; M = metal cation), coordinately and electronically unsaturated metal complexes are also of importance to several areas of chemistry, e.g., preparative organometallic chemistry, catalysis, battery technologies, and electrolytes.[1–3,13] Although "naked" metal cations would provide ideal starting materials, solvated metal species are the precursors for metal complexes that are synthesized in both aqueous and non-aqueous media. In these instances, the choice of an appropriate solvent is of paramount importance and may be challenging to accommodate. The general characteristics of the ideal solvent for include: oxidative resistance, adequate polarity to enable dissolution, and low enough Lewis basicity to facilitate desired ligand substitutions. Some representative solvents that have been used with WCAs include CH_3CN, SO_2, and CH_2Cl_2. The influence of the solvent is well illustrated by $Ag[Sb(OTeF_5)_6]$ where its synthesis in less oxidatively resistant CH_2Cl_2 resulted in the solvent coordinated Ag^+ cation that can react to give undesirable product(s).[19] In contrast, attempts to synthesize $Ag[Sb(OTeF_5)_6]$ from $SbCl_5$ and $Ag[OTeF_5]$ using the very weakly basic solvent sulfuryl chlorofluoride (SO_2ClF) resulted in incomplete substitution and a mixture of products according to eq 5.1.[23]

$$6\ Ag[OTeF_5] + SbCl_5 \xrightarrow{SO_2ClF} Ag[SbCl_n(OTeF_5)_{6-n}] + (6-n)\ AgCl + n\ Ag[OTeF_5] \quad (n = 0–6) \quad (5.1)$$

Overall, the properties of weakly basic SO_2ClF make it an attractive solvent in this area of chemistry, i.e., low nucleophilicity and polarity, very high chemical stability towards strong electrophiles and strongly oxidizing species, and a useful liquid range (m.p., –124.7 ^oC; b.p., 7.1 ^oC). Furthermore, salts of the $[Sb(OTeF_5)_6]^-$ anion are typically quite soluble in SO_2ClF. Therefore, viable synthetic routes to the formation of metal cations in SO_2ClF solvent are highly desirable. The potential synthetic utility of the strong oxidant $[Xe(OTeF_5)][Sb(OTeF_5)_6]$ in SO_2ClF solution to generate of main-group cations stabilized by the pre-formed WCA has been demonstrated by the isolation of the extremely electrophilic $[CX_3]^+$ (X = Cl, Br),[14,15] $[CBr_x(OTeF_5)_{(3-x)}]^+$ (x = 1–3),[14,15] and $[CFX_2]^+$ (X = Cl, Br)[15] cations. The present Chapter details a synthetic route to very weakly solvated Hg^{2+} salts in anhydrous SO_2ClF using $[XeOTeF_5][Sb(OTeF_5)_6]$ as a source of the preformed $[Sb(OTeF_5)_6]^-$ anion by extension of the aforementioned approach. The solid-state homoleptic, solvated salt, $[Hg(SO_2ClF)_6][Sb(OTeF_5)_6]$, was fully characterized by single-crystal X-ray diffraction, Raman spectroscopy, and quantum-chemical calculations. To demonstrate the potential use of $[Hg(SO_2ClF)_6][Sb(OTeF_5)_6]$ as a suitable precursor for substitution reactions, the salts, $[Hg(NCR)_5][Sb(OTeF_5)_6]$ (R = CH_3 or CH_2CH_3), were synthesized by reaction with the respective nitriles, and were also structurally characterized. To the best of the authors knowledge, these salts represent the first divalent metal salts of the $[Sb(OTeF_5)_6]^-$ anion

that have been characterized and provide the first example of a homoleptic complex of the very weakly basic SO_2ClF molecule.

5.2. Results and Discussion

Low-temperature Raman spectra were recorded on the colorless crystalline samples in FEP reaction vessels. Single crystals suitable for X-ray structure determinations were obtained from the Raman samples.

5.2.1. Syntheses

5.2.1.1. Synthesis of $[Hg(SO_2ClF)_6][Sb(OTeF_5)_6]_2$.

The salt, $[Hg(SO_2ClF)_6][Sb(OTeF_5)_6]_2$, was synthesized by the low-temperature reaction of $[XeOTeF_5][Sb(OTeF_5)_6]$ with half a molar equivalent of either $Hg(OTeF_5)_2$ (eq 5.2) or $HgCl_2$ (eq 5.3) at –78 °C followed by slow warming under dynamic vacuum

$$Hg(OTeF_5)_2 + 2\,[XeOTeF_5][Sb(OTeF_5)_6] \xrightarrow[-78\ ^oC\ to\ 22\ ^oC]{SO_2ClF} [Hg(SO_2ClF)_6][Sb(OTeF_5)_6]_2 + 2\,Xe(OTeF_5)_2 \qquad (5.2)$$

$$HgCl_2 + 2\,[XeOTeF_5][Sb(OTeF_5)_6] \xrightarrow[-78\ ^oC\ to\ 0\ ^oC]{SO_2ClF} [Hg(SO_2ClF)_6][Sb(OTeF_5)_6]_2 + 2\,Xe_{(g)} + 2\,ClOTeF_5 \qquad (5.3)$$

to 0 °C. The strong oxidant, $[XeOTeF_5][Sb(OTeF_5)_6]$, has been shown to be very soluble in SO_2ClF (> 2 M at –78 °C) and is only stable up to –20 °C.[16] The latter approach (eq 5.3) was preferred because both Xe and $ClOTeF_5$ are volatile and can be removed under dynamic vacuum.[24] However, when the reaction mixture is warmed too quickly or under static vacuum, some $Hg(OTeF_5)_2$ was also detected in the Raman spectrum of the reaction

product. This is likely attributable to unwanted side reactions involving $ClOTeF_5$ at higher temperatures. The solid salt was isolated as the colorless, homoleptic-solvated complex, $[Hg(SO_2ClF)_6][Sb(OTeF_5)_6]_2$, which is stable under dynamic vacuum at 0 °C for several hours. Monitoring by low-temperature Raman spectroscopy showed that pumping at room temperature for 1 h resulted in complete removal of coordinated solvent molecules, however, addition of SO_2ClF solvent at –78 ^oC followed by pumping up to 0 °C reformed $[Hg(SO_2ClF)_6][Sb(OTeF_5)_6]_2$.

5.2.1.2. Synthesis of $[Hg(NCR)_5][Sb(OTeF_5)_6]_2 \cdot 2SO_2ClF$ (R = CH_3 or CH_2CH_3).

Addition of a small amount of nitrile RCN (R = CH_3 or CH_2CH_3), to a SO_2ClF solution of the $[Hg][Sb(OTeF_5)_6]_2$ salt resulted in the solid state isolation of the salts $[Hg(NCR)_5][Sb(OTeF_5)_6]_2 \cdot 2SO_2ClF$ (R = CH_3 or CH_2CH_3) (eq 5.4).

$$[Hg(SO_2ClF)_6][Sb(OTeF_5)_6] + 5\ RCN \xrightarrow{SO_2ClF} [Hg(NCR)_5][Sb(OTeF_5)_6]_2 \qquad (5.4)$$

The CH_3CN adduct was stable for several weeks are room temperature and when placed under dynamic vacuum according to Raman spectroscopy.

5.2.2. X-ray Crystallography

Details of the data collection parameters and other crystallographic information for $[Hg(SO_2ClF)_6][Sb(OTeF_5)_6]_2$ and $[Hg(NCR)_5][Sb(OTeF_5)_6]_2 \cdot 2SO_2ClF$ (R = CH_3, CH_2CH_3) are provided in Table 5.1. The bond lengths and angles for the cations are listed in Tables 5.2−5.4. A preliminary structure solution for the $[Hg(NCCH_3)_5]^{2+}$ salt has been obtained, but only the cation is discussed. A better disorder model for the anions and co-crystallized SO_2ClF molecules is still required which will likely improve the refinement

Table 5.1. Summary of Crystal Data and Refinement Results for $[Hg(SO_2ClF)_6][Sb(OTeF_5)_6]_2$, $[Hg(NCCH_3)_5][Sb(OTeF_5)_6]_2 \cdot 2SO_2ClF$, and $[Hg(NCCH_2CH_3)_5][Sb(OTeF_5)_6]_2 \cdot 2SO_2ClF$

	$[Hg(SO_2ClF)_6][Sb(OTeF_5)_6]_2$	**$[Hg(NCCH_3)_5][Sb(OTeF_5)_6]_2 \cdot 2SO_2ClF$** [a]	**$[Hg(NCCH_2CH_3)_5][Sb(OTeF_5)_6]_2 \cdot 2SO_2ClF$**
space group	$R\bar{3}$	$P\bar{1}$	$P\bar{1}$
a (Å)	15.0455(4)	11.6477(4)	11.8021(4)
b (Å)	15.0455(4)	14.1217(4)	14.1684(5)
c (Å)	28.2583(7)	23.2583(7)	24.0737(8)
α(deg)	90.0	87.770(2)	89.126(2)
β (deg)	90.0	84.772(2)	84.789(2)
γ (deg)	120.0	81.236(2)	83.140(2)
V (Å^3)	5539.7(3)	3764.0(2)	3980.1(2)
Z	3	2	2
F_w (g mol^{-1})	4018.4	3749.6	3819.7
ρ_{calcd} (g cm^{-3})	3.614	3.308	3.187
T (^{o}C)	–173	–173	–173
μ (mm^{-1})	8.058	7.636	7.225
R_1 [b]	0.0374	0.0589	0.0350
wR_2 [c]	0.0938	0.1529	0.0825

[a] Preliminary solution. [b] R_1 is defined as $\Sigma||F_o| - |F_c|/\Sigma|F_o|$ for $I > 2\sigma(I)$. [c] wR_2 is defined as $[\Sigma[w(F_o^2 - F_c^2)^2]/\Sigma w(F_o^2)^2]^{1/2}$ for $I > 2\sigma(I)$.

for this salt. The geometric parameters of the co-crystallized SO_2ClF molecules and $[Sb(OTeF_5)_6]^-$ anions for the nitrile adduct salts are provided in the Appendix C (Tables S5.1−S5.2). The geometric parameters of $[Sb(OTeF_5)_6]^-$ anion are in good agreement with previously published values[14–22] and do not require further comment.

5.2.2.1. $[Hg(SO_2ClF)_6][Sb(OTeF_5)_6]_2$.

The crystal structure of $[Hg(SO_2ClF)_6][Sb(OTeF_5)_6]_2$ consists of well-separated $[Hg(SO_2ClF)_6]^{2+}$ cations (Figure 5.1a and S5.1) and $[Sb(OTeF_5)_6]^-$ anions (Figure S5.2), where the shortest Cl---F, O---F, and F---F cation-anion contacts are only slightly shorter than the sum of the corresponding van der Waals radii (Table S5.1). The Hg^{2+} atom is oxygen-coordinated to six SO_2ClF solvent molecules (Hg–O_b, 2.342(4) Å), resulting in a slightly distorted octahedral mercury coordination sphere (Table 5.2). Only one crystallographically unique SO_2ClF ligand is defined, with the remaining ligand atom positions generated by crystal symmetry to give S_6-symmetry of the dication. The Hg–O_b–S angles (122.7(2)^o) in $[Hg(SO_2ClF)_6]^{2+}$ are smaller than those of the only other crystallographically characterized examples of SO_2ClF coordinated complexes: $[Xe(OTeF_5)][Sb(OTeF_5)_6]\cdot SO_2ClF$ (∠Xe–O_b–S, 139.6(3)^o),[16] $Fe(OTeF_5)_3\cdot 3SO_2ClF$ (∠Fe–O_b–S, 132.6(3)–145.2(4)^o),[24] and $[C(OTeF_5)_3][Sb(OTeF_5)_6]\cdot 3SO_2ClF$ (∠C–O_b–S, 160.3(7)^o).[14] The bent coordination angles can be rationalized by a VSEPR description of the lone pairs on oxygen; however, the smaller angle in $[Hg(SO_2ClF)_6]^{2+}$ suggests a greater degree of coordinate-covalent character for the Hg–O_b bonds (see Computational Results, NBO section), whereas significantly more open aforementioned angles,

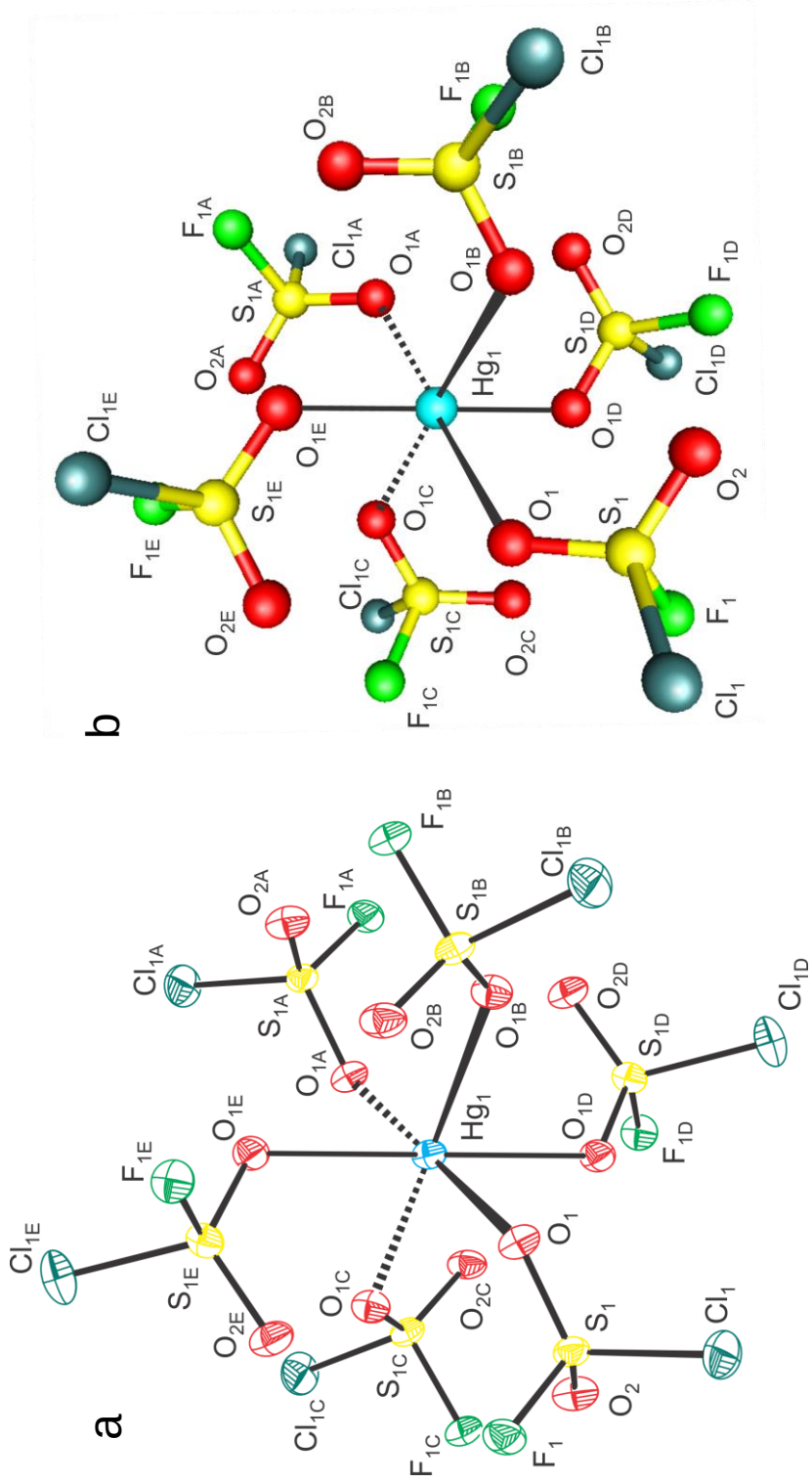

Figure 5.1. The $[Hg(SO_2ClF)_6]^{2+}$ cation **(a)** in the single-crystal X-ray structure of $[Hg(SO_2ClF)_6][Sb(OTeF_5)_6]_2$ with thermal ellipsoids shown at the 50% probability level and **(b)** calculated (S_6) at the PBE0/def2-TZVPD(GD3BJ) level of theory.

Table 5.2. Geometric Parameters for the $[Hg(SO_2ClF)_6]^{2+}$ Dication[a] in the X-ray Crystal Structure of $[Hg(SO_2ClF)_6][Sb(OTeF_5)_6]_2$ (S_6) and in the Calculated Gas-phase Structure (S_6)

	exptl	**calcd** [b]
Bond Lengths (Å)		
$Hg_1–O_1$	2.342(4)	2.363
$S_1–O_1$	1.442(4)	1.444
$S_1–O_2$	1.409(4)	1.406
$S_1–F_1$	1.524(3)	1.529
$S_1–Cl_1$	1.917(2)	1.947
Bond Angles (deg)		
$O_1–Hg_1–O_{1A}$	180.0	180.0
$O_1–Hg_1–O_{1B}$	82.9(2)	89.3
$O_1–Hg_1–O_{1C}$	97.1(2)	90.7
$O_1–Hg_1–O_{1D}$	82.9(2)	89.3
$O_1–Hg_1–O_{1E}$	97.1(2)	90.7
$Hg_1–O_1–S_1$	122.7(2)	128.9
$F_1–S_1–O_1$	105.1(3)	105.4
$F_1–S_1–O_2$	109.1(3)	109.2
$Cl_1–S_1–O_1$	109.0(2)	107.9
$Cl_1–S_1–O_2$	112.3(2)	112.4
$Cl_1–S_1–F_1$	100.6(2)	100.2
$O_2–S_1–O_1$	119.0(3)	119.8

[a] The atom labeling scheme corresponds to that used in Figure 5.1.
[b] Calculated at the PBE0/def2-TZPD(GD3BJ) level of theory.

particularly for the coordinated SO_2ClF molecules in $[C(OTeF_5)_3][Sb(OTeF_5)_6]\cdot 3SO_2ClF$,[14] are most likely the result of predominantly electrostatic interactions.

The S–O_b bridge bonds (1.442(4) Å) of the SO_2ClF ligands are slightly elongated relative to their terminal S–O_t bonds (1.409(4) Å). The S–O_t bonds are equal within ±3σ to those of solid SO_2ClF (av. S–O, 1.408(4) Å).[26] The coordinated molecules also have S–Cl (1.917(2) Å) and S–F (1.524(3) Å) bonds that are somewhat shorter than those of solid SO_2ClF (av. S–Cl, 1.9638(11) Å; av. S–F, 1.538(2) Å).[26] The Cl–S–F (100.6(2)^o) and O–S–O (119.0(3)^o) bond angles are also slightly larger and smaller, respectively, than those of solid SO_2ClF (av. ∠Cl–S–F, 98.70(8)^o; av. ∠O–S–O, 122.5(14)^o).[26] Similar bond length and bond angle differences have been observed for the other SO_2ClF complexes that have been referred to above, which result from inductive effects due to electron density donation from the bridging oxygen to the Lewis acid site. These subtle structural differences are well reproduced by the calculated gas-phase $[Hg(SO_2ClF)_6]^{2+}$ cation and SO_2ClF, and the electronic effects are reflected in the NBO analyses (see Computational Results).

5.2.2.2. $[Hg(NCR)_5][Sb(OTeF_5)_6]_2\cdot 2SO_2ClF$ (R = CH_3 or CH_2CH_3).

The ability of $[Hg(SO_2ClF)_6][Sb(OTeF_5)_6]_2$ to function as a precursor for substitution reactions at Hg^{2+} was probed by the addition of nitriles RCN (R = CH_3 or CH_2CH_3) to SO_2ClF solutions of $[Hg(SO_2ClF)_6]^{2+}$. The X-ray crystal structures of the resulting $[Hg(NCR)_5][Sb(OTeF_5)_6]_2\cdot 2SO_2ClF$ complex salts are similar and consist of well-separated $[Hg(NCR)_5]^{2+}$ cations and $[Sb(OTeF_5)_6]^-$ anions, in addition to two co-

crystallized SO_2ClF molecules. There are only long contacts with the anions in $[Hg(NCCH_2CH_3)_5][Sb(OTeF_5)_6]_2 \cdot 2SO_2ClF$ (Table S5.2). The $[Hg(NCR)_5]^{2+}$ cations (Figures 5.2 and 5.3; Tables 5.3 and 5.4) possess five crystallographically independent nitrile molecules that are coordinated to the Hg^{2+} cation through the valence electron lone pair of their formally *sp*-hybridized nitrogen atoms, resulting in slightly distorted trigonal bipyramidal coordination spheres (CH_3CN: $\angle N_{eq}–Hg–N_{eq}$, 115.5(3)–127.6(4)^o; $\angle N_{ax}–Hg–N_{eq}$, 82.3(4)–96.2(4)^o; $\angle N_{ax}–Hg–N_{ax}$, 178.8(4)^o; CH_3CH_2CN; $\angle N_{eq}–Hg–N_{eq}$, 116.5(2)–122.7(2)^o; $\angle N_{ax}–Hg–N_{eq}$, 84.6(2)–94.8(2)^o; $\angle N_{ax}–Hg–N_{ax}$, 173.5(2)^o). The axial $Hg–N_{ax}$ bond lengths are elongated (CH_3CN: 2.381(11), 2.455(10) Å; CH_3CH_2CN: 2.393(5),2.402(5) Å) relative to the equatorial $Hg–N_{eq}$ bonds (CH_3CN: 2.217(9), 2.231(10), 2.235(8) Å; CH_3CH_2CN: 2.216(4), 2.220(5), 2.240(4) Å). This can be attributed to increased steric congestion at the axial positions in accordance with VSEPR arguments.[27] The Hg–N–C angles are 164.4(10)–178.8(13)^o for CH_3CN and 164.9(4)–179.6(4)^o for CH_3CH_2CN, with deviations from linearity likely resulting from crystal packing. This is supported by the calculated gas-phase structure which have linear Hg–N–C angles (vide infra). The geometric parameters of the coordinated CH_3CN molecules are equal within $\pm 3\sigma$ to those of solid CH_3CN.[28] Although the crystal structure of CH_3CH_2CN has not been published, the geometrical parameters of the CH_3CH_2CN ligands of the $[Hg(NCCH_2CH_3)_5]^{2+}$ cation are also similar to those of other structurally characterized adducts[29] and co-crystals of CH_3CH_2CN.[30] The three equatorial ligands of the propionitrile adduct-cation have their H_3C-groups ($\angle C–C–C$, 110.2–110.7^o) oriented essentially in line with the $N_{ax}–Hg–N_{ax}$ axis. This interesting structural feature is also

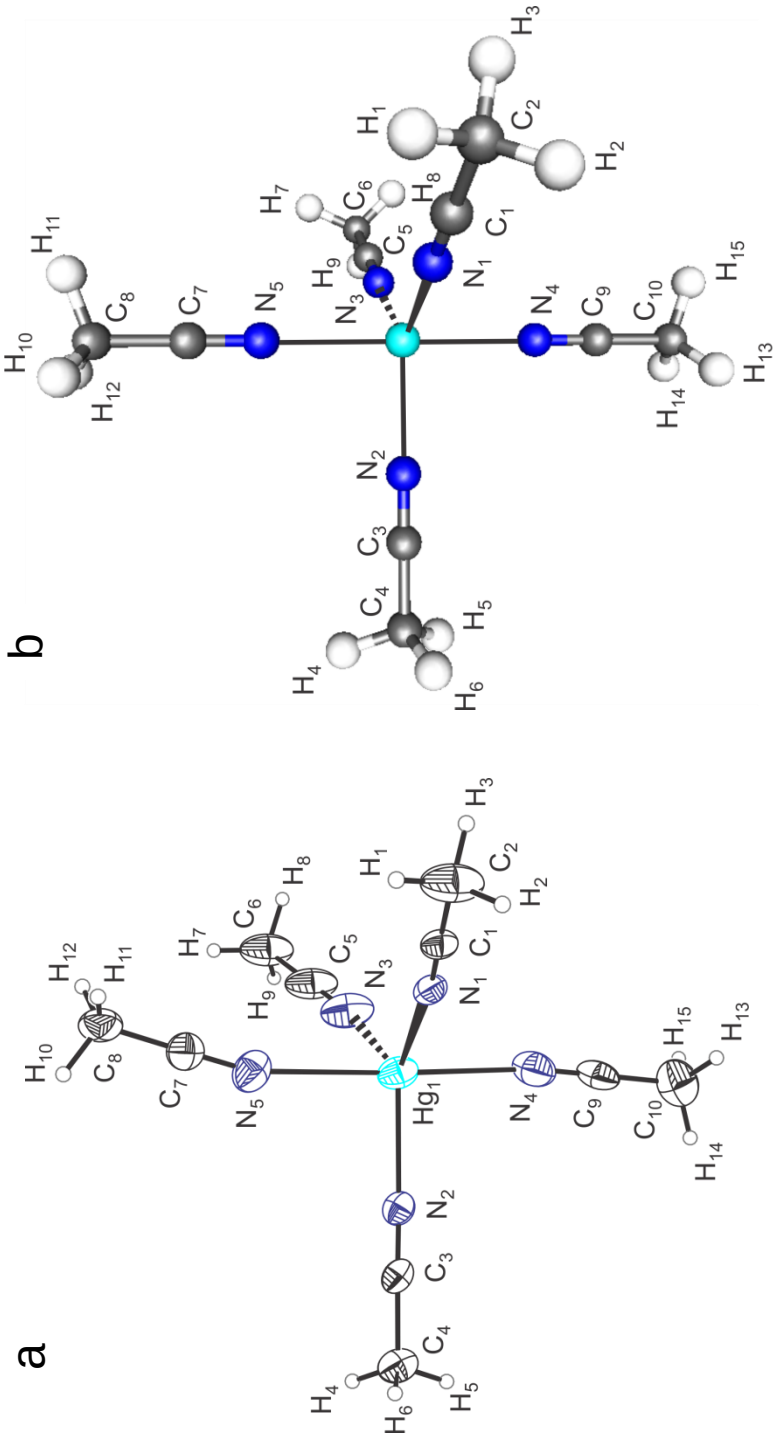

Figure 5.2. The $[Hg(NCCH_3)_5]^{2+}$ cation in **(a)** the preliminary X-ray crystal structure of $[Hg(NCCH_3)_5][Sb(OTeF_5)_6]_2 \cdot 2SO_2ClF$ with thermal ellipsoids shown at the 50% probability level and **(b)** calculated (C_3) at the PBE0/def2-TZVPD(GD3BJ) level of theory.

Table 5.3. Geometrical Parameters for the $[Hg(NCCH_3)_5]^{2+}$ Dication[a] in the Preliminary X-ray Crystal Structure of $[Hg(NCCH_3)_5]$-$[Sb(OTeF_5)_6]_2 \cdot 2SO_2ClF$ (C_1) and in the Calcualted Gas-phase Structure (C_3)

	exptl	**calcd** [b]
Bond Lengths (Å)		
$Hg_1–N_1$	2.217(9)	2.251
$Hg_1–N_2$	2.231(10)	2.251
$Hg_1–N_3$	2.235(8)	2.251
$Hg_1–N_4$	2.381(11)	2.401
$Hg_1–N_5$	2.455(10)	2.401
$N_1–C_1$	1.125(13)	1.145
$N_2–C_3$	1.129(16)	1.145
$N_3–C_5$	1.123(18)	1.145
$N_4–C_7$	1.147(16)	1.147
$N_5–C_9$	1.138(15)	1.147
$C_1–C_2$	1.465(14)	1.440
$C_3–C_4$	1.447(22)	1.440
$C_5–C_6$	1.455(14)	1.440
$C_7–C_8$	1.444(20)	1.442
$C_9–C_{10}$	1.141(17)	1.442
Bond Angles (deg)		
$N_1–Hg_1–N_2$	127.6(4)	120.0
$N_1–Hg_1–N_3$	116.4(3)	120.0
$N_2–Hg_1–N_3$	115.5(3)	90.1
$N_1–Hg_1–N_5$	90.7(3)	89.9
$N_1–Hg_1–N_4$	91.4(3)	120.0
$N_2–Hg_1–N_4$	90.8(5)	90.1
$N_2–Hg_1–N_5$	88.5(4)	89.9
$N_3–Hg_1–N_4$	96.2(4)	90.1
$N_3–Hg_1–N_5$	82.3(3)	89.9
$N_4–Hg_1–N_5$	178.84)	180.0
$Hg_1–N_1–C_1$	178.4(9)	179.9
$Hg_1–N_2–C_3$	167.7(14)	179.9
$Hg_1–N_3–C_5$	172.7(9)	179.9
$Hg_1–N_4–C_7$	164.4(10)	180.0
$Hg_1–N_5–C_9$	178.8(13)	180.0

Table 5.3. continued….

	exptl	**calcd** [b]
$N_1–C_1–C_2$	178.8(11)	180.0
$N_2–C_3–C_4$	179.2(16)	180.0
$N_3–C_5–C_6$	179.3(12)	180.0
$N_4–C_7–C_8$	179.4(15)	180.0
$N_5–C_9–C_{10}$	179.0(13)	180.0

[a] The atom labeling scheme corresponds to that used in Figure 5.2. [b] Calculated at the PBE0/def2-TZPD(GD3BJ) level of theory.

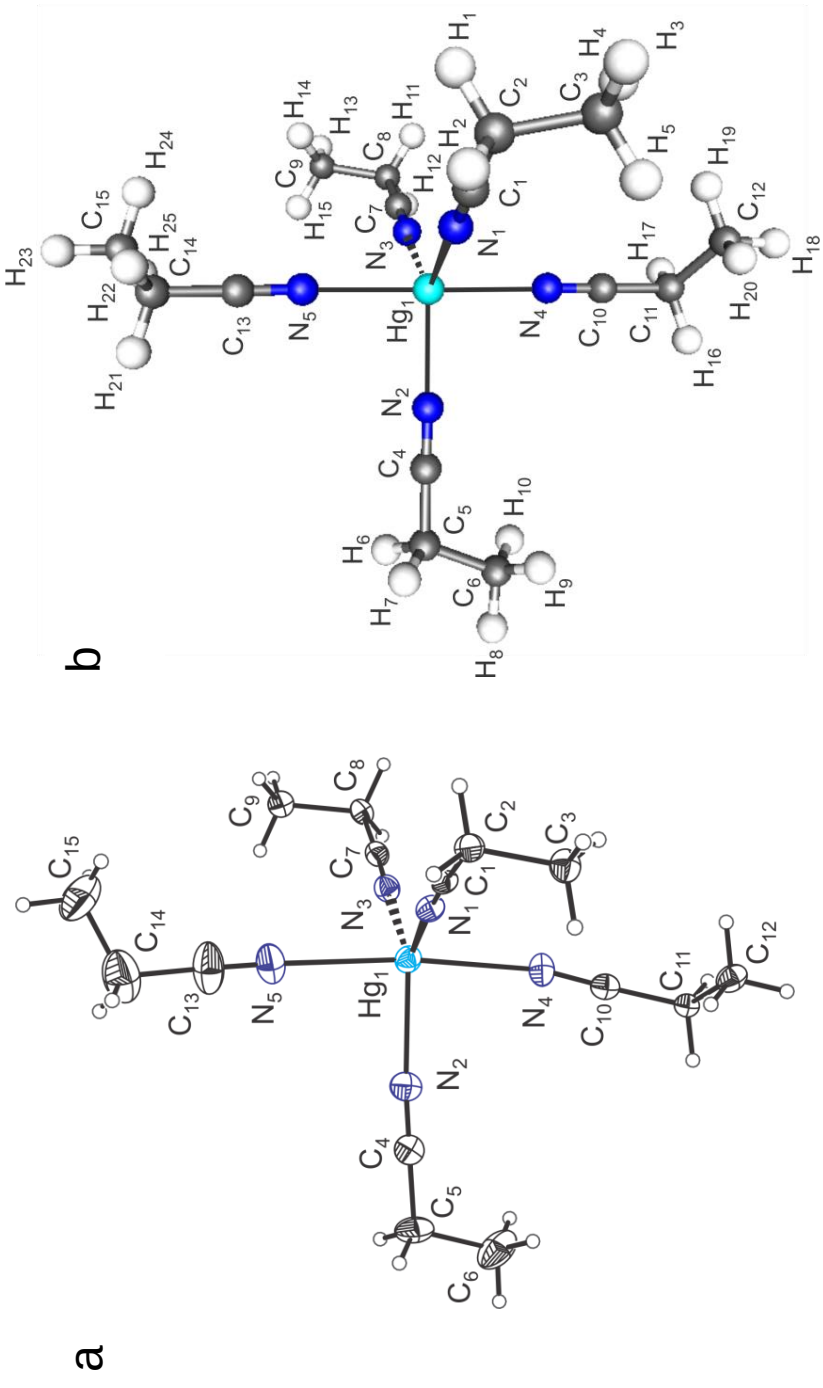

Figure 5.3. The $[Hg(NCCH_2CH_3)_5]^{2+}$ cation **(a)** in the single-crystal X-ray structure of $[Hg(NCCH_2CH_3)_5][Sb(OTeF_5)_6]_2 \cdot 2SO_2ClF$ with thermal ellipsoids shown at the 50% probability level and **(b)** calculated (C_1) at the PBE0/def2-TZVPD(GD3BJ) level of theory.

Table 5.4. Geometric Parameters[a] for the $[Hg(NCCH_2CH_3)_5]^{2+}$ Dication in the Crystal Structure of $[Hg(NCCH_2CH_3)_5][Sb(OTeF_5)_6]_2 \cdot 2SO_2ClF$ (C_1) and the Calculated Gas-phase (C_1) Structure.

	exptl	**calcd** [b]
Bond Lengths (Å)		
$Hg_1–N_1$	2.216(4)	2.248
$Hg_1–N_2$	2.240(4)	2.248
$Hg_1–N_3$	2.220(5)	2.248
$Hg_1–N_4$	2.402(5)	2.403
$Hg_1–N_5$	2.393(5)	2.403
$N_1–C_1$	1.136(6)	1.146
$N_2–C_4$	1.138(6)	1.146
$N_3–C_7$	1.132(6)	1.146
$N_4–C_{10}$	1.143(6)	1.148
$N_5–C_{13}$	1.088(9)	1.147
$C_1–C_2$	1.472(6)	1.447
$C_4–C_5$	1.451(7)	1.447
$C_7–C_8$	1.466(6)	1.447
$C_{10}–C_{11}$	1.465(6)	1.449
$C_{13}–C_{14}$	1.480(1)	1.449
$C_2–C_3$	1.534(7)	1.529
$C_5–C_6$	1.561(9)	1.529
$C_8–C_9$	1.534(6)	1.529
$C_{11}–C_{12}$	1.527(6)	1.529
$C_{14}–C_{15}$	1.490(1)	1.529
Bond Angles (deg)		
$N_1–Hg_1–N_2$	120.8(2)	119.9
$N_1–Hg_1–N_3$	122.7(2)	120.2
$N_1–Hg_1–N_4$	94.8(2)	90.0
$N_1–Hg_1–N_5$	89.4(2)	89.9
$N_2–Hg_1–N_3$	116.5(2)	119.9
$N_2–Hg_1–N_4$	84.6(2)	90.2
$N_2–Hg_1–N_5$	89.0(2)	90.0
$N_3–Hg_1–N_4$	91.4(2)	89.9
$N_3–Hg_1–N_5$	90.4(2)	89.9
$N_4–Hg_1–N_5$	173.5(2)	179.7

Table 5.4. continued….

	exptl	**calcd** [b]
$Hg_1–N_1–C_1$	177.2(4)	179.0
$Hg_1–N_2–C_4$	175.7(4)	178.8
$Hg_1–N_3–C_7$	179.6(4)	179.3
$Hg_1–N_4–C_{10}$	164.9(4)	178.9
$Hg_1–N_5–C_{13}$	174.7(5)	178.6
$N_1–C_1–C_2$	177.5(5)	179.1
$N_2–C_4–C_5$	179.2(5)	179.1
$N_3–C_7–C_8$	178.0(5)	179.1
$N_4–C_{10}–C_{11}$	176.2(5)	179.1
$N_5–C_{13}–C_{14}$	178.1(8)	179.1
$C_1–C_2–C_3$	110.7(4)	112.4
$C_4–C_5–C_6$	110.8(5)	112.4
$C_7–C_8–C_9$	110.2(4)	112.4
$C_{10}–C_{11}–C_{12}$	110.2(4)	112.5
$C_{13}–C_{14}–C_{15}$	111.5(7)	112.5

[a] The atom labeling scheme corresponds to that used in Figure 5.3. [b] Calculated at the PBE0/def2-TZVPD(GD3BJ) level of theory.

reproduced in the calculated gas-phase structure of the $[Hg(NCCH_2CH_3)_5]^{2+}$ cation (see Computational Results).

5.2.3. Raman Spectroscopy

The low-temperature, solid-state Raman spectra of $[Hg(SO_2ClF)_6][Sb(OTeF_5)_6]_2$, and $[Hg(NCR)_5][Sb(OTeF_5)_6]_2 \cdot 2SO_2ClF$ (R = CH_3, CH_2CH_3) are shown in Figures 5.4−5.6. Bands assigned to the cations are listed in Tables 5.5−5.7. The low-temperature Raman spectra of SO_2ClF, CH_3CN, CH_3CH_2CN were also acquired (–150 ^oC) for comparison (Tables 5.5−5.7). The $[Sb(OTeF_5)_6]^-$ anion bands are listed in Table S5.3 and were assigned by comparison with the literature values,[16,19] and aided by comparison with the calculated frequencies of the gas-phase optimized $[Sb(OTeF_5)_6]^-$ anion (S_6). In the case of the nitrile adduct-cations, the vibrational bands of the co-crystallized SO_2ClF molecules were assigned by comparison with those of solid SO_2ClF.

5.2.3.1. $[Hg(SO_2ClF)_6][Sb(OTeF_5)_6]_2$

The Raman bands of the $[Hg(SO_2ClF)_6]^{2+}$ cation (Table 5.5) were fully assigned with the aid of the calculated frequencies and Raman intensities obtained for the energy-minimized gas-phase $[Hg(SO_2ClF)_6]^{2+}$ cation (S_6, Figure 5.1b) and free SO_2ClF (C_s) (Figure S5.4). The calculated gas-phase vibrational frequencies well reproduce the observed frequencies and show that significant intermolecular coupling among the vibrational modes of the SO_2ClF ligands occurs. The band at 1401 cm^{-1} (calcd, 1442, 1444 cm^{-1}) is assigned to in-phase and out-of-phase coupled $\nu(S{=}O_t)$ stretches whereas

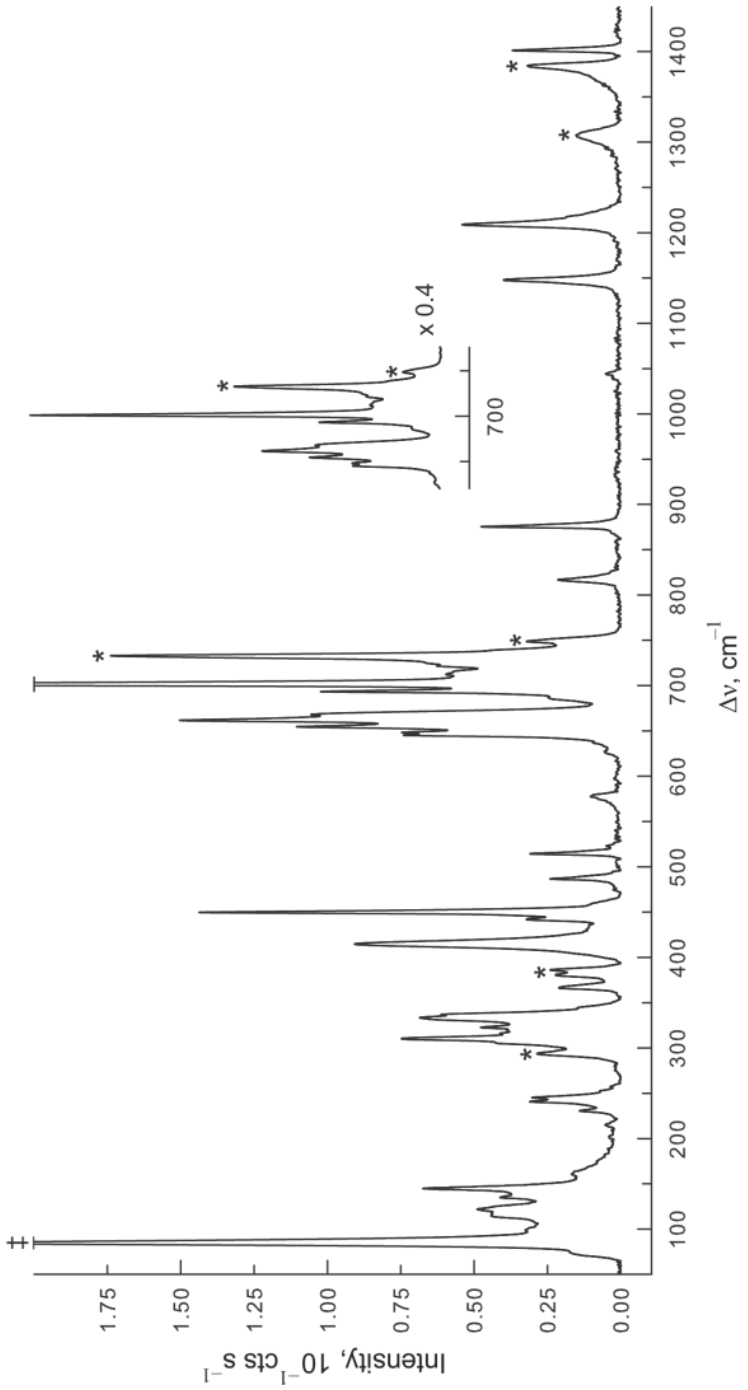

Figure 5.4. Raman spectrum of crystalline $[Hg(SO_2ClF)_6][Sb(OTeF_5)_6]_2$ recorded at –150 °C using 1064-nm excitation. Symbols denote FEP sample tube lines (*) and an instrumental artifact (‡).

Table 5.5. Experimental Raman frequencies and intensities, and Calculated Gas-phase frequencies and intensities of the $[Hg(SO_2ClF)_6]^{2+}$ cation, and SO_2ClF.

$[Hg(SO_2ClF)_6]^{2+}$			SO_2ClF (C_s)		
exptl [a, b]	calcd [c]	assgnt [d]	exptl [b, e]	calcd [c]	assgnt [d]
1401(11)	1444(0)[595] 1442(30)[0] 1442(0)[22]	$\nu(S{=}O_t)_{o.o.p.}$	1441(6) 1437(4) 1431(17) 1416(sh)	1503(8)[218]	$\nu_{as}(SO_2)$
	1444(3)[0]	$\nu(S{=}O_t)_{i.p.}$			
1209(16)	1235(69)[0]	$\nu(S{=}O_b)_{i.p.}$	1258(1)		
1148(12)	1194(0)[1054] 1192(0)[643] 1178(53)[0]	$\nu(S{=}O_b)_{o.o.p.}$	1218(sh) 1214(19) 1208(69) 1205(5)	1262(22)[157]	$\nu_s(SO_2)$
	903(0)[689] 896(2)[0] 896(0)[90]	$\nu(S{-}F)_{o.o.p.}$	849(2) 844(3) 825(10)	839(7)[187]	$\nu(S{-}F)$
875(14)	898(26)[0]	$\nu(S{-}F)_{i.p.}$	818(32)		
655(32) [f]	675(80)[0]	$\delta_{umb}(SO_2F)_{i.p.}$			
627(2)	663(0)[147] 662(0)[873] 658(4)[0]	$\delta_{umb}(SO_2F)_{o.o.p.}$	611(53)	635(7)[211]	$\delta_{umb}(SO_2F)$
523(2) 514(9)	511(0)[70] 511(0)[2] 509(5)[0]	$\delta(O_tSO_b)_{o.o.p.}$	538(2) 507(26)	503(2)[14]	$\delta(O_{(1)}SO_{(2)})$
	511(<1)[0]	$\delta(O_tSO_b)_{i.p.}$			
487(7)	492(0)[4] 491(0)[20] 489(5)[0]	$\delta(O_tSF)_{o.o.p.}$	480(21)	474(1)[13]	$\delta(FSO_{(1)}) - \delta(FSO_{(2)})$
	492(<1)[0]	$\delta(O_tSF)_{i.p.}$			
450(42)	450(34)[0]	$\nu(S{-}Cl)_{i.p.}$			
442(9) 430(sh)	448(0)[3] 447(0)[33] 447(10)[0]	$\nu(S{-}Cl)_{o.o.p.}$	432(100) [g] 424(40) [g]	423(13)[<1]	$\nu(S{-}Cl)$
316(12)	332(11)[0]	$\rho_t(O_tSO_b)_{i.p.}$			
310(22)	328(0)[5] 327(0)[7] 321(3)[0]	$\rho_t(O_tSO_b)_{o.o.p.}$/ $\rho_t(O_bSF)_{small}$	312(27) 309(12)	301(2)[<1]	$\rho_t(O_{(1)}SO_{(2)})$

Table 5.5. continued…

$[Hg(SO_2ClF)_6]^{2+}$			SO_2ClF (C_s)		
exptl [a, b]	calcd [c]	assgnt [d]	exptl [b, e]	calcd [c]	assgnt [d]
306(sh)	304(0)[<1] 303(3)[0] 300(0)[<1] 299(2)[0]	δ(FSCl) / $\rho_t(O_tSF)$	295(15)	289(1)[<0.1]	δ(FSCl)
161(5)	134(0)[15]	$\rho_r(S\text{-}O_bFCl)_{o.o.p.}$ / $\nu(Hg\text{–}O_b)_{o.o.p.}$			
	133(6)[0]	$\rho_r(S\text{-}O_bFCl)_{i.p.}$ / $\nu(Hg\text{–}O_b)_{i.p.}$			
	130(0)[10]	$\rho_r(S\text{-}O_bFCl)_{o.o.p.}$			
	86(<1)[0] 72(0)[<1] 70(<1)[0] 69(0)[20] 64(0)[8] 62(<0.1)[0] 60(<1)[0] 59(0)[5] 50(1)[0] 36(0)[<1] 32(<1)[0] 31(<1)[0] 27(0)[<1] 19(0)[1] 18(0)[1] 15(<1)[0] 11(0)[<1] 5(1)[0] 3(0)[<1]	deformation modes			

[a] The Raman spectrum was obtained at −150 °C on a crystalline sample of $[Hg(SO_2ClF)_6][Sb(OTeF_5)_6]_2$ contained in an FEP sample tube using 1064-nm excitation. The $[Sb(OTeF_5)_6]^-$ anion bands are provided in Table S5.3. [b] Values in parentheses denote relative experimental Raman intensities. [c] Calculated using the PBE0/def2-TZVPD(GD3BJ) level of theory. Values in parentheses denote calculated Raman intensities ($Å^4$ amu^{-1}). Values in square brackets denote calculated infrared intensities (km mol^{-1}). [d] Bond elongations and angle openings are denoted by plus (+) signs and bond contractions and angle compressions are denoted by minus (–) signs. Symbols and abbreviations denote stretch (ν), bend (δ), rock (ρ_r), twist (ρ_t), in-phase (i.p.), out-of-phase (o.o.p.), bridging (b), terminal (t), shoulder (sh), and not observed (n.o.). [e] This work. [f] Possible overlap between cation and anion bands. [g] The ν(S–Cl) mode of SO_2ClF displays $^{35}Cl/^{37}Cl$ isotope splitting.

the in-phase and out-of-phase coupled ν(S=O_b) stretches (exptl, 1148 and 1209 cm^{-1}; calcd, 1178–1194 cm^{-1} and 1235 cm^{-1}) occur at lower frequency; consistent with S–O_b bond elongation upon adduct formation. Similar frequency values were observed for the adduct-cation $[F_5TeOXe(SO_2ClF)]^+$ (1415,1423 cm^{-1} and 1147–1177 cm^{-1}),[16] which lie between the $\nu_{as}(SO_2)$ (1416–1441 cm^{-1}) and $\nu_s(SO_2)$ (1205–1218 cm^{-1}) stretching frequencies of solid SO_2ClF. The band at 875 cm^{-1} in the Raman spectrum of $[Hg(SO_2ClF)_6]^{2+}$ is assigned to the in-phase coupled ν(S–F) stretching mode (calcd, 898 cm^{-1}). The out-of-phase coupled ν(S–F) modes (calcd, 896, 903 cm^{-1}) are expected to be very weak. Both modes are significantly shifted to higher frequencies relative to the ν(S–F) mode of solid SO_2ClF (exptl, 818–849 cm^{-1}; calcd, 839 cm^{-1}), in agreement with S–F bond contraction upon formation of the adduct-cation. For added comparison, the ν(S–F) stretching mode of $[F_5TeOXe(SO_2ClF)]^+$ occurs at 860 cm^{-1}.[16] The in-phase and out-of-phase coupled ν(S–Cl) stretching modes of $[Hg(SO_2ClF)_6]^{2+}$ (exptl, 450 cm^{-1} and 442, 430 cm^{-1}; calcd, 450 cm^{-1} and 447, 448 cm^{-1}, respectively) occur at higher frequencies than the ν(S–Cl) mode of solid SO_2ClF (426/431 cm^{-1}), also reflecting the shorter S–Cl bond lengths in the adduct-cation. These bands are comparable to those observed for $[F_5TeOXe(SO_2ClF)]^+$ (442 and 436 cm^{-1}, respectively).[16] The in-phase umbrella bend, $\delta_{umb}(SO_2F)$, of $Hg(SO_2ClF)_6]^{2+}$ occurs at 655 cm^{-1} (calcd, 675 cm^{-1}) which is shifted to higher frequency than the corresponding mode of solid SO_2ClF (exptl, 611 cm^{-1}; calcd, 635 cm^{-1}). The in-phase and out-of-phase ν(Hg–O_b) stretches are coupled to the ρ_r(S–O_bFCl) deformation modes and are assigned to a band at 161 cm^{-1} (calcd, 130, 133, 134 cm^{-1}). Several other bending modes were also assigned which appear to be less strongly

influenced by bond length distortions. Their frequencies are in good agreement with the calculated values and the corresponding vibrational bands of solid SO_2ClF and $[F_5TeOXe(SO_2ClF)]^+$.[16]

5.2.3.2. $[Hg(NCR)_5][Sb(OTeF_5)_6]_2 \cdot 2SO_2ClF$ (R = CH_3 or CH_2CH_3).

The Raman bands of the $[Hg(NCCH_3)_5]^{2+}$ (Figure 5.5, Table 5.6) and $[Hg(NCCH_2CH_3)_5]^{2+}$ (Figure 5.6, Table 5.7) cations were assigned with the aid of their calculated frequencies and Raman intensities of the energy-minimized gas-phase structures, in addition to the experimental frequencies of solid CH_3CN and CH_3CH_2CN which were also fully assigned using the calculated frequencies of free CH_3CN (C_{3v}) (Figure S5.5) and CH_3CH_2CN (C_s) (Figure S5.6), which are generally in good agreement with their experimental values. Although vibrational frequency shifts occur upon adduct formation, the calculated structural parameters of the adducted nitrile molecules change only marginally upon coordination to Hg^{2+} (see Computational Results). The calculated vibrational modes of the cations show interligand coupling predominantly between the equatorial ligands and between the axial ligands, with minimal coupling between the two positions.

(i) $[Hg(NCCH_3)_5]^{2+}$. The highest frequency bands were observed at 2950 and 3015 cm^{-1} and are assigned to coupled $\nu(CH_3)$ stretches (calcd, 3067, 3068, 3154 cm^{-1}) of $[Hg(NCCH_3)_5]^{2+}$ which occur at frequencies that are similar to those of solid CH_3CN (exptl; 2938, 2999 cm^{-1}: calcd; 3070, 3151 cm^{-1}). The out-of-phase and in-phase coupled $\nu(C{\equiv}N)_{eq}$ stretches occur at 2307 (calcd, 2417 cm^{-1}) and 2324 cm^{-1} (calcd, 2420 cm^{-1}),

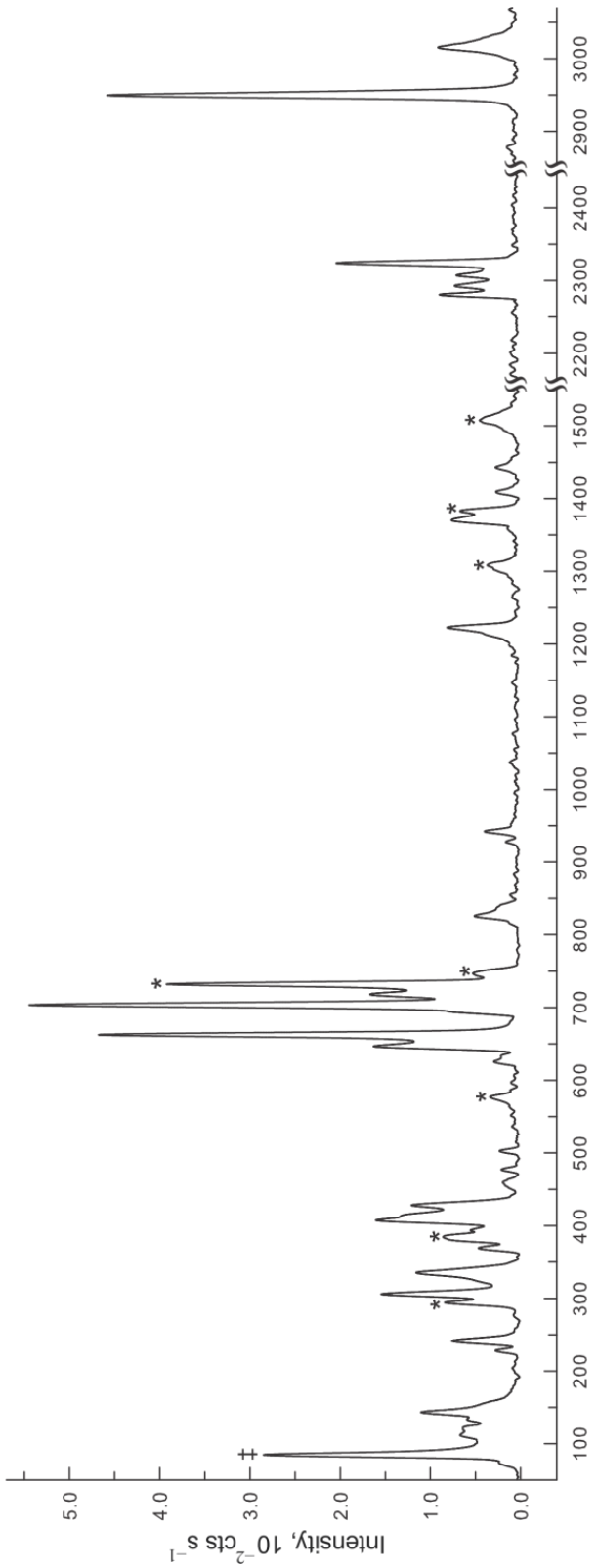

Figure 5.5. Raman spectrum of crystalline $[Hg(NCCH_3)_5][Sb(OTeF_5)_6]_2 \cdot 2SO_2ClF$; recorded at –150 °C using 1064-nm excitation. Symbols denote FEP sample tube lines (*) and an instrumental artifact (‡).

Table 5.6. Experimental Raman frequencies and intensities, and Calculated Gas-phase frequencies and intensities of the $[Hg(NCCH_3)_5]^{2+}$ cation and $NCCH_3$.

$[Hg(NCCH_3)_5]^{2+}$			$NCCH_3$ (C_{3v})		
exptl [a, b]	calcd [c, d]	assgnt [e]	exptl [b, f, g]	calcd [c]	assgnt [e]
3015(17)	3154(100)[16] 3154(1)[<1] 3154(32)[25] 3154(70)[<1] 3154(63)[5] 3154(54)[6]	$[\nu(CH_3)_{eq}]_{o.o.p.}$ $[\nu(CH_3)_{eq}]_{i.p.}$ $[\nu(CH_3)_{ax}]_{o.o.p.}$	2999(54)	3151(56)[<1]	$\nu_{as}(CH_3)$
2950(85)	3068(420)[12] 3067(459)[18] 3067(284)[1] 3067(24)[34]	$[\nu(CH_3)_{ax}]_{i.p.}$ $[\nu(CH_3)_{eq}]_{i.p.}$ $[\nu(CH_3)_{eq}]_{o.o.p.}$	2938(97)	3070(191)[2]	$\nu_s(CH_3)$
2324(37) 2307(13) 2293(13) 2281(17)	2420(459)[<0.1] 2417(116)[282] 2405(19)[289] 2404(292)[18]	$[\nu(C\equiv N)_{eq}]_{i.p.}$ $[\nu(C\equiv N)_{eq}]_{o.o.p.}$ $[\nu(C\equiv N)_{ax}]_{o.o.p.}$ $[\nu(C\equiv N)_{ax}]_{i.p.}$	2295(3) 2248(100) 2200(1)	2392(77)[12]	$\nu(C\equiv N)$
1443(6) [h]	1446(4)[20] 1446(8)[12] 1442(11)[25] 1442(2)[48] 1442(<0.1)[1] 1441(5)[<1]	$\delta(CH_3)_{ax}$ $\delta(CH_3)_{eq}$	1457(11) 1454(7) 1425(4) 1421(4)	1463(5)[12]	$\delta(CH_3)$
1370(15)	1397(26)[<1] 1396(1)[14] 1394(22)[<0.1] 1394(10)[13]	$[\delta_{umb}(CH_3)_{ax}]_{i.p.}$ $[\delta_{umb}(CH_3)_{ax}]_{o.o.p.}$ $[\delta_{umb}(CH_3)_{eq}]_{i.p.}$ $[\delta_{umb}(CH_3)_{eq}]_{o.o.p.}$	1376(15) 1371(3) 1368(2)	1400(6)[3]	$\delta_{umb}(CH_3)$
	1045(<1)[6] 1045(<1)[5] 1042(<0.1)[18] 1042(<1)[2] 1042(<1)[6] 1042(0)[0]	$\rho_w(CH_3)_{ax}$ $\rho_w(CH_3)_{eq}$	1042(1)	1052(<1)[2]	$\rho_w(CH_3)$
942(7) 928(4)	972(13)[0] 969(1)[13] 961(<0.1)[18] 958(5)[<0.1]	$[\nu(C–C)_{ax} + \nu(C–C)_{eq}]_{i.p.}$ $[\nu(C–C)_{eq}]_{o.o.p.}$ $[\nu(C–C)_{ax}]_{o.o.p.}$ $[\nu(C–C)_{ax}]_{i.p.}$	922(20)	950(5)[1]	$\nu(C–C)$

Table 5.6. continued…

$[Hg(NCCH_3)_5]^{2+}$			$NCCH_3$ (C_{3v})		
exptl [a, b]	calcd [c, d]	assgnt [e]	exptl [b, f, g]	calcd [c]	assgnt [e]
407(30) 394(11)	419(<0.1)[8]	$[\delta(C–C\equiv N)_{eq,OOP}]_{i.p.}$			
	419(3)[<0.1]	$[\delta(C–C\equiv N)_{eq,OOP}]_{o.o.p.}$			
	416(<1)[3]	$[\delta(C–C\equiv N)_{eq,IP}]_{o.o.p.}$	400(4) 395(12) 392(9) 387(15)	388(1)[<1]	$\delta(C–C\equiv N)$
	414(0)[0]	$[\delta(C–C\equiv N)_{eq,IP}]_{i.p.}$			
	413(<1)[2]	$[\delta(C–C\equiv N)_{ax,OOP}]_{i.p.}$			
	413(<1)[2]	$[\delta(C–C\equiv N)_{ax,IP}]_{i.p.}$			
	412(<1)[<0.1]	$[\delta(C–C\equiv N)_{ax,OOP}]_{o.o.p.}$			
	412(<1)[<0.1]	$[\delta(C–C\equiv N)_{ax,IP}]_{o.o.p.}$			
204(2), br	220(4)[0]	$[\nu(Hg–N)_{eq}]_{i.p.}$			
	209(<0.1)[9]	$[\nu(Hg–N)_{eq}]_{o.o.p.}$			
	178(<0.1)[2]	$[\nu(Hg–N)_{ax}]_{o.o.p}$			
155(sh)	140(3)[<0.1]	$[\delta(Hg–N–C)_{eq,OOP}]_{o.o.p.}$ / $[\delta(Hg–N–C)_{ax,IP}]_{o.o.p.}$			
	125(0)[66]	$[\delta(Hg–N–C)_{eq,OOP}]_{i.p.}$			
	114(<1)[44]	$[\delta(Hg–N–C)_{ax,IP}]_{i.p.}$ / $[\delta(Hg–N–C)_{eq,IP}]_{o.o.p.}$			
	91(<1)[<0.1]	$[\nu(Hg–N)_{ax}]_{i.p.}$			
	91(<1)[4]	$[\delta(N–Hg–N)_{eq}$ + $\rho_w(N–Hg–N)_{ax}]$			
	84(<0.1)[0]	$[\delta(Hg–N–C)_{eq,IP}]_{i.p.}$			
	74(<1)[<0.1] 44(0)[0] 39(8)[<0.1] 31(0)[<0.1] 29(2)[7] 28(2)[16] 16(<0.1)[<1] 4(<0.1)[<0.1] 3(0)[0]	deformation modes			
			116(17) 108(11) 102(13) 96(31)		lattice modes

[a] The Raman spectrum was obtained at −150 °C on a crystalline sample of $[Hg(NCCH_3)_5][Sb(OTeF_5)_6]_2 \cdot 2SO_2ClF$ contained in an FEP sample tube using 1064-nm excitation. A combination band was also observed at 1409(6) cm^{-1} (703 cm^{-1} x 2). Bands associated with co-crystallized SO_2ClF molecules are assigned to 1223(15), 1213(sh), 835(sh),

Table 5.6. continued…

826(9), 626(6), 503(4), 477(4), 459(4), 428(22), and 306(28) cm^{-1}. The $[Sb(OTeF_5)_6]^-$ anion bands are provided in Table S5.3. [b] Values in parentheses denote relative experimental Raman intensities. [c] Calculated using the PBE0/def2-TZVPD(GD3BJ) level of theory. Values in parentheses denote calculated Raman intensities ($Å^4$ amu^{-1}). Values in square brackets denote calculated infrared intensities (km mol^{-1}). [d] Bond elongations and angle openings are denoted by plus (+) signs and bond contractions and angle compressions are denoted by minus (–) signs. Symbols and abbreviations denote stretch (ν), bend (δ), rock (ρ_r), twist (ρ_t), wag (ρ_w), in-phase (i.p.), in-plane (IP), out-of-phase (o.o.p.), out-of-plane (OOP), shoulder (sh), and broad (br). [f] From this work. [g] Combination bands of H_3CCN were also observed at 2884(1) cm^{-1} (1442 cm^{-1} x 2), 2849(1) cm^{-1} (1426 cm^{-1} x 2), and 2736(6) cm^{-1} (1368 cm^{-1} x 2). [h] Possible overlap with $\nu_{as}(SO_2)$ of co-crystallized SO_2ClF.

respectively, whereas the corresponding $\nu(C{\equiv}N)_{ax}$ stretches occur at slightly lower frequencies (exptl; 2293, 2281 cm^{-1} and calcd; 2405, 2404 cm^{-1}). Overall, they are shifted to slightly higher frequencies than the ν(C≡N) stretch of solid CH_3CN (exptl; 2200, 2248, 2295 cm^{-1} and calcd, 2392 cm^{-1}). The bands at 1443 (calcd, 1441, 1442, 1446 cm^{-1}) and 1370 (calcd, 1394, 1396, 1397 cm^{-1}) are assigned to coupled $\delta(CH_3)$ and $\delta_{umb}(CH_3)$ bending modes, respectively, and are comparable to those of CH_3CN (exptl; 1421–1457, 1368–1376 cm^{-1} and calcd; 1463, 1400 cm^{-1}). The ν(C–C) stretches occur at 928 and 947 cm^{-1} (calcd, 958–972 cm^{-1}) and are also shifted to higher frequencies relative to CH_3CN (exptl, 922 cm^{-1}; calcd, 950 cm^{-1}). Two bands at 394 and 407 (calcd, 412–419) cm^{-1} are assigned to coupled δ(C–C≡N) bending modes which occur at slightly higher frequency than that of CH_3CN (exptl, 387–400 cm^{-1}; calcd, 388 cm^{-1}). The high-frequency shifts of the ν(C≡N), ν(C–C), and δ(C–C≡N) modes relative to those of free CH_3CN are consistent with adduct formation, as has been observed in prior studies.[29,31,32]

The calculated ν(Hg–N) stretches are coupled to one another and are predicted to occur between 178 and 220 cm^{-1}; a broad band observed at 204 cm^{-1} is assigned to ν(Hg–N) stretching modes. The band at 155 cm^{-1} is tentatively assigned to the coupled deformation mode, δ(Hg–C–C) (calcd, 140 cm^{-1}).

(ii) $[Hg(NCCH_2CH_3)_5]^{2+}$. As is the case for the $[Hg(NCCH_3)_5]^{2+}$ cation, the ν(C≡N), ν(C–C), and δ(C–C≡N) modes of $[Hg(NCCH_2CH_3)_5]^{2+}$ are generally shifted to higher frequencies relative to those of the solid CH_3CH_2CN which is consistent with adduct formation.[29,31,32] The highest frequency bands at 3032 (calcd, 3164, 3165, 3169 cm^{-1}), 3016 and 3005 cm^{-1} (calcd, 3162, 3168 cm^{-1}) are assigned to the coupled out-of-phase ν(CH_3) stretches of the equatorial and axial ligands, respectively. These bands occur at slightly higher frequencies than the $\nu_{as}(CH_3)$ stretches of CH_3CH_2CN (exptl; 2991, 2967 cm^{-1} and calcd; 3153, 3150 cm^{-1}). A similar trend is observed for the out-of-phase coupled $\nu(CH_2)_{ax}$ (exptl, 2981 cm^{-1}; calcd, 3110 cm^{-1}) and $\nu(CH_2)_{eq}$ (exptl, 2966 cm^{-1}; calcd, 3108, 3109 cm^{-1}) modes, whose frequencies occur at slightly higher frequency than $\nu_{as}(CH_2)$ of CH_3CH_2CN (exptl, 2942 cm^{-1}; calcd, 3105 cm^{-1}). Predominately in-phase coupled ν(CH_3) and ν(CH_2) stretches result in bands at 2900, 2942, and 2954 cm^{-1} (calcd, 3066–3079 cm^{-1}), whereas similarly coupled stretches of solid CH_3CH_2CN occur at 2892 and 2920 cm^{-1} (calcd, 3066 and 3069 cm^{-1}). The coupled ν(C≡N) stretching bands of the adduct-cation at 2247–2312 cm^{-1} (calcd, 2390–2407 cm^{-1}) occur at higher frequencies than those of solid CH_3CH_2CN at 2244/2261 cm^{-1} (calcd, 2283 cm^{-1}). The coupled δ(C–C≡N) modes of the cation-adduct are assigned to distinct spectral regions for both

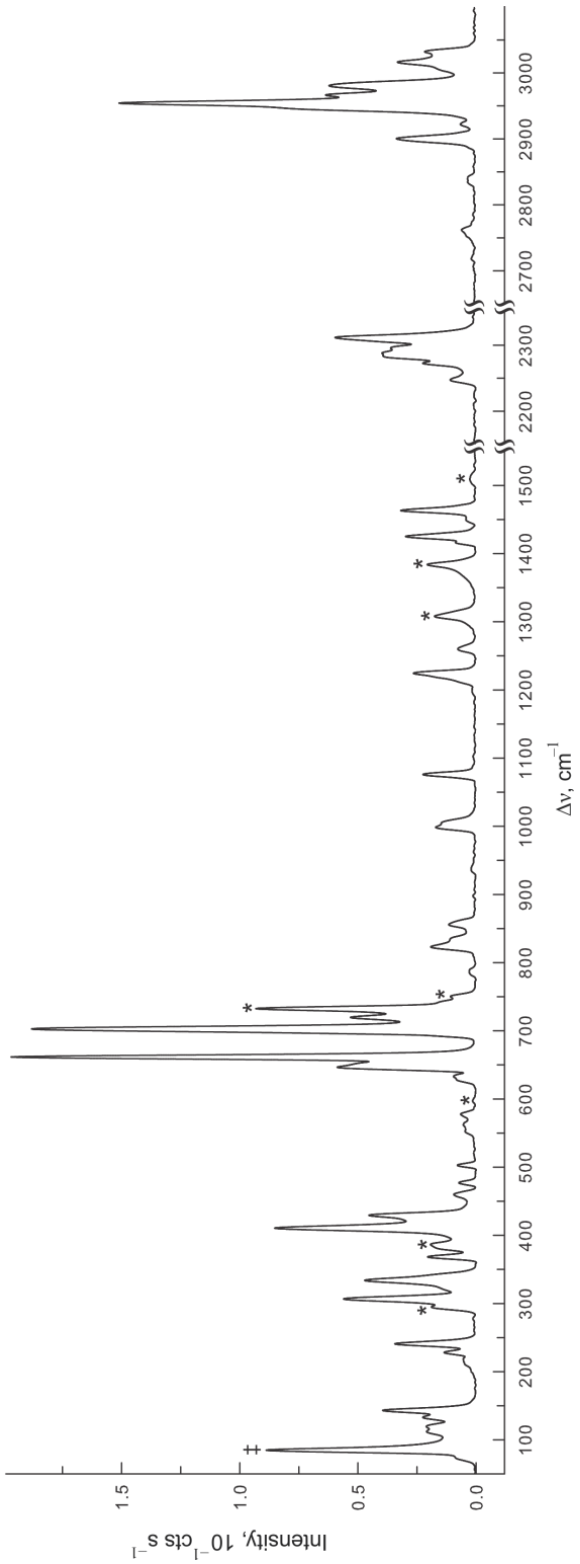

Figure 5.6. Raman spectrum of crystalline $[Hg(NCCH_2CH_3)_5][Sb(OTeF_5)_6]_2 \cdot 2SO_2ClF$; recorded at –150 °C using 1064-nm excitation. Symbols denote FEP sample tube lines (*) and an instrumental artifact (‡).

Table 5.7. Experimental Raman frequencies and intensities, and Calculated Gas-phase frequencies and intensities of the $[Hg(NCCH_2CH_3)_5]^{2+}$ cation and $NCCH_2CH_3$.

$[Hg(NCCH_2CH_3)_5]^{2+}$					$NCCH_2CH_3$ (C_s)				
[illegible]	[illegible]	[illegible]	[illegible]	[illegible]	[illegible]	[illegible]	[illegible]	[illegible]	[illegible]
			δ	δ				δ	

Table 5.7. continued…

$[Hg(NCCH_2CH_3)_5]^{2+}$			$NCCH_2CH_3$ (C_s)		
exptl [a, b]	**calcd** [c]	**assgnt** [d]	**exptl** [b, e, f]	**calcd** [c]	**assgnt** [d]
1450(2) [g]	1448(10)[11] 1448(10)[11]	$\delta(CH_2)_{ax}$	1461(4)	1463(8)[6]	$\delta(CH_2)$
	1445(14)[1] 1445(5)[29] 1445(11)[7]	$\delta(CH_2)_{eq}$			
1416(5) 1390(sh)	1417(1)[<1]	$\{[\delta_{umb}(CH_3)_{ax}]_{i.p.} + [\delta_{umb}(CH_3)_{eq}]_{i.p.}\}$	1425(10) 1421(13)	1411(<1)[2]	$\delta_{umb}(CH_3)$
	1417(<1)[2] 1417(1)[<1] 1416(<1)[6] 1416(3)[2]	$\{[\delta_{umb}(CH_3)_{ax}]_{o.o.p.} - [\delta_{umb}(CH_3)_{eq}]_{o.o.p.}\}$			
1312(sh) 1308(6) [g]	1332(13)[2] 1332(1)[8]	$[\rho_w(CH_2)_{ax}]$	1315(5)	1347(3)[3]	$\rho_w(CH_2)$
	1329(10)[<1] 1328(4)[8] 1328(6)[5]	$[\rho_w(CH_2)_{eq}]$			
1260(4)	1281(2)[<0.1] 1281(2)[<0.1] 1280(2)[<0.1] 1280(2)[<0.1] 1280(<1)[<0.1]	$\rho_t(CH_2)_{ax}$ $\rho_t(CH_2)_{eq}$	1264(9)	1286(2)[<0.1]	$\rho_t(CH_2)$
	1108(<0.1)[<1] 1108(<0.1)[<1]	$\rho_t(CH_2)_{ax}$ / $\rho_t(CH_3)_{ax}$		1110(<1)[<1]	$\rho_t(CH_2)$ / $\rho_t(CH_3)$
	1107(<0.1)[<0.1] 1107(<0.1)[<0.1] 1107(<0.1)[<1]	$\rho_t(CH_2)_{eq} + \rho_t(CH_3)_{eq}$			
1076(11) 1072(sh)	1090(23)[<0.1] 1090(2)[22]	$\rho_w(CH_3)_{ax}$	1074(9)	1097(6)[4]	$\rho_w(CH_3)$
	1089(6)[5] 1089(4)[15] 1088(3)[15]	$\rho_w(CH_3)_{eq}$			
1004(sh) 999(9)	1031(14)[<0.1] 1030(3)[1] 1029(1)[<1] 1029(<1)[<1] 1028(3)[<0.1]	$[\nu(H_2C–CH_3)_{ax} - \nu(H_2C–CH_3)_{eq}]$	1010(7)	1038(3)[<1]	$\nu(H_2C–CH_3)$
856(6)	874(14)[<0.1] 872(<1)[5] 871(1)[4] 865(<1)[6] 862(1)[<1]	$\nu(NC–CH_2)_{ax}$ / $\nu(NC–CH_2)_{eq}$	840(15)	857(6)[<0.1]	$\nu(NC–CH_2)$

Table 5.7. continued…

$[Hg(NCCH_2CH_3)_5]^{2+}$			$NCCH_2CH_3$ (C_s)		
exptl [a, b]	**calcd** [c]	**assgnt** [d]	**exptl** [b, e, f]	**calcd** [c]	**assgnt** [d]
787(2)	784(<1)[8] 784(<1)[8]	$[\rho_t(CH_2)_{ax} - \rho_t(CH_3)_{ax}]$	781(5)	788(<1)[4]	$[\rho_r(CH_2) + \rho_t(CH_3)]$
	783(<1)[7] 783(<1)[6] 783(<1)[2]	$[\rho_r(CH_2)_{eq} - \rho_t(CH_3)_{eq}]$			
562(3) 552(sh)	582(6)[<1] 582(1)[6] 581(1)[7]	$[\delta(C–C\equiv N)_{eq}]_{IP}$	545(2)	558(1)[<1]	$\delta(C–C\equiv N)_{IP}$
553(3)	577(<1)[12] 577(3)[<1]	$[\delta(C–C\equiv N)_{ax}]_{IP}$			
411(43)	420(1)[2] 420(<1)[2] 418(<0.1)[<0.1]	$[\delta(C–C\equiv N)_{eq}]_{OOP}$	390(5)	398(1)[<1]	$\delta(C–C\equiv N)_{OOP}$
	418(1)[<1] 418(<1)[<1]	$[\delta(C–C\equiv N)_{ax}]_{OOP}$			
241(17) [h]	265(2)[4] 260(1)[9] 256(2)[7]	$\delta(C–C–C)_{eq}$	229(8) 223(9)	213(2)[4]	$\delta(C–C–C)$
228(7) [h]	235(1)[23] 226(1)[13]	$\delta(C–C–C)_{ax}$			
218(3) 214(sh)	218(<1)[4] 218(<0.1)[6] 217(<1)[<1] 217(<1)[<1] 216(<0.1)[<0.1]	$\rho_t(CH_3)_{ax}$ / $\rho_t(CH_3)_{eq}$		220(<1)[1]	$\rho_r(CH_3)$
	186(<1)[7] 176(1)[11]	$[\nu(Hg–N)_{eq}]_{o.o.p.}$			
	184(3)[<1]	$[\nu(Hg–N)_{eq}]_{i.p.}$			
	144(<0.1)[24]	$[\nu(Hg–N)_{ax}]_{o.o.p.}$			
	111(<1)[6] 108(<1)[17] 102(<1)[13] 101(<1)[15]	$\delta(Hg–N–C)_{ax}$ / $\delta(Hg–N–C)_{eq}$			
	96(<1)[21]	$[\nu(Hg–N)_{ax}]_{i.p.}$			

Table 5.7. continued…

$[Hg(NCCH_2CH_3)_5]^{2+}$			$NCCH_2CH_3$ (C_s)		
exptl [a, b]	calcd [c]	assgnt [d]	exptl [b, e, f]	calcd [c]	assgnt [d]
	83(<1)[1]	deformation modes			
	77(<1)[3]				
	76(<1)[3]				
	76(<1)[<0.1]				
	55(<1)[<0.1]				
	52(<1)[<0.1]				
	24(1)[4]				
	24(1)[3]				
	21(1)[2]				
	19(2)[1]				
	18(<1)[2]				
	14(<1)[<0.1]				
	13(<1)[<0.1]				
	9(<1)[<0.1]				
	7(<1)[<0.1]				
	6(<1)[<0.1]				
	6(<1)[<0.1]				
	4(<1)[<0.1]				
			103(12)		lattice mode

[a] The Raman spectrum was obtained at −150 °C on a crystalline sample of $[Hg(NCCH_2CH_3)_5][Sb(OTeF_5)_6]_2 \cdot 2SO_2ClF$ contained in an FEP sample tube using 1064-nm excitation. Combination bands were also observed at 2922(4) cm^{-1} (1463 cm^{-1} x 2), 2839(2) cm^{-1} (1416 cm^{-1} x 2), 2762(3) (1390 cm^{-1} x 2). Bands associated with co-crystallized SO_2ClF molecules are observed at 1450(2), 1425(15), 1224(14), 834(sh), 823(10), 635(5), 627(sh), 503(4), 477(4), 460(5), 429(23), 307(28) cm^{-1}. The $[Sb(OTeF_5)_6]^-$ anion bands are provided in Table S5.3. [b] Values in parentheses denote relative experimental Raman intensities. [c] Calculated at the PBE0/def2-TZPD(GD3BJ) level of theory. Values in parentheses denote calculated Raman intensities ($Å^4$ amu^{-1}). Values in square brackets denote calculated infrared intensities (km mol^{-1}). [d] Bond elongations and angle openings are denoted by plus (+) signs and bond contractions and angle compressions are denoted by minus (–) signs. Symbols/abbreviations denote stretch (ν), bend (δ), rock (ρ_r), twist (ρ_t), wag (ρ_w), in-phase (i.p.), in-plane (IP), out-of-phase (o.o.p.), out-of-plane (OOP), and shoulder (sh). [e] From this work [f] Combination bands were also observed at 2838(4) cm^{-1} (1421 cm^{-1} x 2), 2750(5) cm^{-1} (1390(sh) cm^{-1} x 2), 2619(1) cm^{-1} (1315 cm^{-1} x 2), and 2195(1) (1074 cm^{-1} x 2). [g] Overlaps with FEP band. [h] Overlaps with a band which is predominantly an anion band. [h] Possible overlap with $\nu_{as}(SO_2)$ of co-crystallized SO_2ClF

in-the-plane (exptl, 553, 552, 562 cm^{-1}; calcd, 577–582 cm^{-1}) and out-of-plane (exptl, 411 cm^{-1}; calcd, 418–420 cm^{-1}) modes. The corresponding bending modes occur at 545 cm^{-1} (calcd, 558 cm^{-1}) and 390 cm^{-1} (calcd, 398 cm^{-1}) for solid CH_3CH_2CN. The δ(C–C–C) bends of the equatorial (exptl, 241 cm^{-1}; calcd, 256–265 cm^{-1}) and axial (exptl, 228 cm^{-1}; calcd, 226, 235 cm^{-1}) ligands are shifted to high-frequency relative to that of solid CH_3CH_2CN (exptl, 223/229 cm^{-1}; calcd, 213 cm^{-1}), in accordance with the more strongly bound equatorial ligands. The ν(Hg–N) stretches (calcd, 144–186 cm^{-1}) are expected at lower frequencies than in the CH_3CN adduct-cation but are predicted to be weak, and could not be observed.

5.2.4. Computational Results

The geometries of the $[Hg(SO_2ClF)_6]^{2+}$ (S_6), $[Hg(NCCH_3)_5]^{2+}$ (C_3), and $[Hg(NCCH_2CH_3)_5]^{2+}$ (C_1) dications were optimized using the B3LYP, APFD, and PBE0 functionals and the def2-TZVPD basis set (Tables S5.4–S5.6) starting from the crystallographic coordinates. The optimized structures obtained by use of the PBE0 functional included the GD3BJ empirical dispersion correction and overall most closely reproduced the experimental results; the energy-minimized structures are shown in Figures 5.1b, 5.2b, and 5.3b. The geometries and vibrational frequencies of the free molecules SO_2ClF (C_s), CH_3CN (C_{3v}), and CH_3CH_2CN (C_s) were also calculated at the PBE0/def2-TZVPD(GD3BJ) level of theory (Figures S5.4−S5.6 and Tables S5.7−S5.9).

5.2.4.1. Calculated Geometries.

(i) $[Hg(SO_2ClF)_6]^{2+}$. The experimental geometric parameters of $[Hg(SO_2ClF)_6]^{2+}$ are well reproduced by the calculated gas-phase structure. The coordination environment around Hg^{2+} in the calculated gas-phase cation is only slightly distorted from ideal octahedral symmetry (*cis*-O_b–Hg–O_b, 89.3 and 90.7°), with calculated Hg–O_b bond lengths (calcd, 2.363 Å) that are only slightly longer than the experimental values (2.342(4) Å). The calculated bond lengths and angles of the coordinated SO_2ClF molecules are in very good agreement with their experimental values, although the S–Cl bond lengths are slightly overestimated (Table 5.2). The calculated trends in geometric parameter changes are characteristic of adduct formation and reproduce that observed experimentally, i.e., the calculated S–Cl and S–F bond lengths are shortened ($[Hg(SO_2ClF)_6]^{2+}$: 1.947 and 1.529 Å: free SO_2ClF; 1.990 and 1.552 Å), the S–O_b bond length is elongated ($[Hg(SO_2ClF)_6]^{2+}$: 1.444 Å; free SO_2ClF: 1.410 Å), whereas the S–O_t bond length remains essentially unchanged ($[Hg(SO_2ClF)_6]^{2+}$, 1.406 Å; free SO_2ClF, 1.410 Å). The increase of the Cl–S–F bond angle (100.2°), and corresponding decrease of the O–S–O bond angle (119.8°) upon coordination to Hg^{2+} is also reproduced by the gas-phase calculations (free SO_2ClF, 97.8 and 123.8°, respectively).

(ii) $[Hg(NCCH_3)_5]^{2+}$. The calculated gas-phase structure of $[Hg(NCCH_3)_5]^{2+}$ reproduces the experimental trigonal bipyramidal coordination sphere of Hg^{2+} (Table 5.3). The calculated Hg–N bond lengths are also in good agreement with the experimental values, where the axial Hg–N_{ax} bonds (calcd, 2 x 2.401 Å; exptl, 2.381(11) and 2.455(10) Å) are elongated relative to the equatorial Hg–N_{eq} bonds (calcd, 3 x 2.251 Å; exptl, 2.217(9)–

2.235(8) Å). The structural parameters of the coordinated CH_3CN molecules are well reproduced and change very little relative to those calculated for the free CH_3CN molecule (Table S5.5).

(iii) $[Hg(NCCH_2CH_3)_5]^{2+}$. The calculated gas-phase structure of $[Hg(NCCH_2CH_3)_5]^{2+}$ also well reproduces the slightly distorted trigonal bipyramidal geometry of the experimental structure. The axial Hg–N_{ax} bonds (2 x 2.406 Å) are significantly longer than the equatorial Hg–N_{eq} bonds (3 x 2.248 Å) as observed in the crystal structure (Table S5.4). The CH_3 groups of the equatorial CH_3CH_2CN ligands are also approximately orientated along the N_{ax}–Hg–N_{ax} axis, as observed in the crystal structure.

5.2.4.2. Natural Bond Orbital (NBO) Analyses

Natural bond orbital (NBO) analyses were carried out for all three calculated adduct-cations and free ligands at the PBE0/def2-TZVPD(GD3BJ) level of theory using both NBO versions 3.1 and 6.0 (Tables S5.10−S5.15).[33–35] Version 3.1 includes the 6p AOs of Hg as valence orbitals whereas version 6.0 suppresses the *n*p AOs for groups 1-12 by treating them as polarization functions.[36] This results in overestimated charges on Hg and underestimated charges on O_b and N_b with the latter. For this reason, only values obtained by use of version 3.1 are discussed below.

(i) $[Hg(SO_2ClF)_6]^{2+}$. The NPA charge on Hg (+1.346) is considerably less than that expected for the purely ionic, naked cation (+2); with significantly less positive charge

when the 6p orbitals are included as valence orbitals as has been observed for other complexes.[37] The charges are consistent with a significant degree of charge transfer from each coordinated SO_2ClF molecule to mercury (0.109 e). The Hg^{2+} cation of $[Hg(SO_2ClF)_6]^{2+}$ is, however, more "naked" than in the $[Hg(NCR)_5]^{2+}$ cations, as indicated by the calculated NPA charge on mercury which is much more positive than those of $[Hg(NCR)_5]^{2+}$ (*vide infra*). The corresponding Hg–O_b Wiberg bond indices (6 x 0.166) further corroborate the covalent character of this interaction. Interestingly, upon coordination of SO_2ClF, the calculated charge on the bridging oxygen atom becomes more negative (–0.937) relative to that of the free molecule (–0.842). In contrast, the charges of the remaining atoms of the ligand acquire more positive charge, with the largest increase occurring on the Cl atom, which increases from –0.152 in the free molecule to –0.027 in the complex. These charge shifts are also reflected by the Wiberg bond indices of the SO_2ClF ligands, where S–O_b bond weakening decreases the bond order from 1.422 to 1.200, whereas the S–O_t bond is little affected (increased from 1.422 to 1.448). In contrast, the S–Cl bond order showed the largest increase from 0.844 to 0.953, and the S–F bond order is also significantly increased from 0.683 to 0.730. These bond order differences reflect the observed bond length changes that occur upon SO_2ClF coordination.

(ii) $[Hg(NCR)_5]^{2+}$ Cations (R = CH_3, CH_3CH_2). The NBO results for the nitrile complexes are very similar, and show features analogous to those discussed for the gas-phase $[Hg(SO_2ClF)_6]^{2+}$ cation, including a large influence from the 6p orbitals on mercury. The NPA charges of Hg (+1.204 and +1.205) are even less positive for the

nitrile complexes, which is indicative of even greater charge transfer from the more basic nitrile ligands to Hg^{2+}. The three equatorial nitrile ligands of both complexes transfer more charge (0.173 e) than the two axial ligands (0.137 and 0.138 e), reflecting stronger bonding interactions with the equatorial ligands and correspondingly shorter Hg–N bonds. The resulting Hg–N Wiberg bond indices of the equatorial (0.323 and 0.322) and axial (0.246 and 0.248) nitrile ligands are consistent with more covalent character for these interactions than for SO_2ClF, particularly for the equatorial ligands.

Coordination of CH_3CN in $[Hg(NCCH_3)_5]^{2+}$ results in more negative charge on the nitrogen atoms of the equatorial (–0.460) and axial (–0.444 and –0.445) ligands than for the nitrogen atom in the free CH_3CN (–0.320). This charge is more positive when the Hg 6p valence orbitals are included, reflecting the increased charge transfer to mercury. The triply bonded carbon atom also shows a very large charge increase from +0.278 in free CH_3CN to +0.504 for the equatorial and +0.465 or +0.467 for the axial ligands of the adduct-cation.

The Wiberg bond indices indicate weakening of the C≡N bond with reduction of the Wiberg bond indices from 2.908 in free CH_3CN to 2.756 for the more strongly bound equatorial ligands and 2.789 and 2.790 for the axial ligands. The methyl group charges also become more positive upon complex formation (+0.116 or +0.129) relative to the free ligand (+0.043) due to inductive effects.

A very similar situation occurs for the CH_3CH_2CN ligands of $[Hg(NCCH_2CH_3)_5]^{2+}$, where coordination results in increased negative charge localization

on the nitrogen atom whereas the carbon of the triple bond becomes more positively charged upon coordination (Table S5.15). Coordination of the CH_3CH_2CN ligands to the Hg^{2+} cation results in inductive effects and a slight increase of the charges on the H_2C-groups from –0.023 to +0.016/0.024, and the charges on the H_3C-groups from +0.064 to +0.104/0.109.

5.2.4.3. Binding Energies

The gas-phase, Basis Set Superposition Error (BSSE) corrected total binding energies were also calculated for the $[Hg(SO_2ClF)_6]^{2+}$ and $[Hg(NCR)_5]^{2+}$ at the PBE0/def2-TZVPD(GD3BJ) level of theory (eqs 5.5–5.7).

$$[Hg(SO_2ClF)_6]_{(g)}^{2+} \longrightarrow Hg_{(g)}^{2+} + 6\ SO_2ClF_{(g)} \qquad -1380.8\ kJ\ mol^{-1} \qquad (5.5)$$

$$[Hg(NCCH_3)_5]_{(g)}^{2+} \longrightarrow Hg_{(g)}^{2+} + 5\ NCCH_{3(g)} \qquad -2093.0\ kJ\ mol^{-1} \qquad (5.6)$$

$$[Hg(NCCH_2CH_3)_5]_{(g)}^{2+} \longrightarrow Hg_{(g)}^{2+} + 5\ NCCH_2CH_{3\ (g)} \qquad -2506.8\ kJ\ mol^{-1} \qquad (5.7)$$

The average binding energies per SO_2ClF (–230.1 kJ mol^{-1}), CH_3CN (–418.6 kJ mol^{-1}), and CH_3CH_2CN (–501.4 kJ mol^{-1}) ligand correlate well with their expected relative basicity following the order $SO_2ClF << CH_3CN < CH_3CH_2CN$. These values provide a measure of the metal-ligand interaction strength and support the SO_2ClF ligands as being significantly less strongly coordinated to Hg^{2+}, thus allowing their displacement by the stronger nitrile bases and the $[Hg(SO_2ClF)_6]^{2+}$ salt as an effective source of naked Hg^{2+} cations.

5.3. Conclusions

The strong oxidant $[XeOTeF_5][Sb(OTeF_5)_6]$ was used to prepare a salt of a very weakly coordinated Hg^{2+} cation in the solvent SO_2ClF. In the solid state, the homoleptic complex $[Hg(SO_2ClF)_6][Sb(OTeF_5)_6]_2$ possesses only weakly adducted SO_2ClF molecules that coordinate to the Hg^{2+} cation through their oxygen atoms. The ability of the weakly coordinated Hg^{2+} cation to undergo substitution reactions in SO_2ClF solvent was demonstrated by the reaction of $[Hg(SO_2ClF)_6]^{2+}$ with CH_3CN and CH_3CCH_2N, which resulted in SO_2ClF ligand displacement and the formation and isolation of the $[Hg(NCCH_3)_5][Sb(OTeF_5)_6]_2{\cdot}2SO_2ClF$ and $[Hg(NCCH_2CH_3)_5]$-$[Sb(OTeF_5)_6]_2{\cdot}2SO_2ClF$. The salts were characterized in the solid-state by low-temperature single-crystal X-ray diffraction and Raman spectroscopy, and by use of quantum-chemical calculations. The crystal structure of the solvated Hg^{2+} cation salts provide models for the inner sphere coordination environments in solution. Calculations showed that the SO_2ClF ligands were significantly less strongly coordinated than the nitriles, and are therefore easily displaced by nitriles to give the $[Hg(NCR)_5]^{2+}$ cations described in this study. Thus, the weakly coordinated $[Hg(SO_2ClF)_6]^{2+}$ adduct-cation provides an accessible source of the Hg^{2+} dication. The methodology developed during the course of this work is likely to be transferable to the syntheses of other metal cations. These systems should be useful for exploring the chemistry of ligands which are very weak donors, thermally labile, and/or highly reactive. With the trivalent lanthanide salts, $[Ln(NCCH_3)_n][Al(ptfb)_4]_3$ (n = 9, Ln = Nd, Eu, Gd, Dy; n = 8, Ln = Tm), having been recently synthesized and characterized,[38] the question of how highly charged a solvated metal cation can be is an open question that

is of particular interest. Furthermore, whether or not even less nucleophilic solvents, such as SO_2F_2,[39,40] could be used in this area of chemistry should be further investigated.

5.4. Experimental

General experimental techniques, procedures, and equipment, as well as the preparation and purification of all starting materials are described in Chapter 2.

5.4.1. Syntheses and Crystal Growth

(i) $[Hg(SO_2ClF)_6][Sb(OTeF_5)_6]_2$. The compound, $[Hg(SO_2ClF)_6][Sb(OTeF_5)_6]_2$, was synthesized by the reaction of two molar equivalents of $[XeOTeF_5][Sb(OTeF_5)_6]$ with either half a molar equivalent of $Hg(OTeF_5)_2$ or $HgCl_2$.

In a typical synthesis, $[XeOTeF_5][Sb(OTeF_5)_6]$ (0.06955 g; 0.341 mmol) was synthesized as previously described[16] by the reaction of $Xe(OTeF_5)_2$ with $Sb(OTeF_5)_3$ in ~0.5 mL of SO_2ClF (eq 5.8). To the resulting solution of $[XeOTeF_5][Sb(OTeF_5)_6]$, half a

$$2\ Xe(OTeF_5)_2 + Sb(OTeF_5)_3 \longrightarrow [XeOTeF_5][Sb(OTeF_5)_6] + Xe \qquad (5.8)$$

molar equivalent of $Hg(OTeF_5)_2$ (0.015g; 0.22 mmol) was added at –140 ^oC in a drybox. The solution was slowly warmed to room temperature to give a pale yellow solution. To obtain crystalline $[Hg(SO_2ClF)_6][Sb(OTeF_5)_6]_2$, the side arm of the T-shaped reaction vessel was positioned horizontally and cooled to –78 ^oC. The solvent slowly distilled at room temperature into the –78 ^oC side arm over a 10 h period resuling in colorless crystals immersed in the remaining supernatant. The residual solvent was decanted into the side arm of the reaction vessel at –78 ^oC and isolated by heat sealing the side arm

under dynamic vacuum at –196 ^{o}C. The crystalline solid was pumped at –78 ^{o}C for 1 h to remove residual SO_2ClF.

In order to avoid the direct formation of $Xe(OTeF_5)_2$, a second synthetic approach was used which is analogous to route used to synthesize $[CCl_3][Sb(OTeF_5)_6]$ and its related carbocations.[14] In a typical synthesis, $[XeOTeF_5][Sb(OTeF_5)_6]$ (ca. 0.100 g; 0.0515 mmol) in ~0.5 mL of SO_2ClF was transferred into a drybox at –196 ^{o}C, and half a molar equivalent of $HgCl_2$ (ca. 0.007 g; 0.0258 mmol) was transferred onto the frozen solution. The reactor was removed from the drybox, and after standing at –78 ^{o}C overnight, the solution was slowly warmed to 0 ^{o}C under dynamic vacuum to effect complete reaction and to simultaneously remove $ClOTeF_5$ and residual solvent.

(ii) $[Hg(NCCH_3)_5][Sb(OTeF_5)_6]_2 \cdot 2SO_2ClF$. The salt, $[Hg(SO_2ClF)_6]$-$[Sb(OTeF_5)_6]_2$ (0.0883 g; 0.0267 mmol), was synthesized from $HgCl_2$ as outlined above and all volatile components were removed under dynamic vacuum at 0 ^{o}C. Sulfuryl chloride fluoride (~0.33 mL) was added back onto the product and a small quantity of CH_3CN (~0.1 mL) was condensed onto the frozen solution at –196 ^{o}C and warmed to room temperature. The solution was decanted into the side arm of the reactor and slowly cooled to –78 ^{o}C which resulted in the formation of colorless crystals over several hours. The solvent was removed under dynamic vacuum at –78 ^{o}C and a low-temperature Raman spectrum was obtained directly on the crystalline material inside the FEP reaction vessel.

(iii) $[Hg(NCCH_2CH_3)_5][Sb(OTeF_5)_6]_2 \cdot 2SO_2ClF$. The salt, $[Hg(SO_2ClF)_6]$-$[Sb(OTeF_5)_6]_2$ (0.1220 g; 0.0369 mmol), was synthesized from $Hg(OTeF_5)_2$ as previously described (*vide supra*). Proprionitrile (~0.1 mL) was condensed onto the frozen SO_2ClF solution at –196 ^oC. The solvent mixture was warmed to –50 ^oC and then slowly cooled to –65 ^oC over a 4h period whereupon colorless crystals formed. The crystals were initially dried under dynamic vacuum at –65 ^oC for 3 h, and then at –40 ^oC for an additional 2 h to remove residual solvent. The low-temperature Raman spectrum was obtained directly on the crystalline material inside its FEP reaction vessel.

5.4.2. Structure Solution and Refinement

The XPREP[41,42] program was used to confirm the unit cell dimensions, the crystal system and space group. The structures were solved in their respective space groups and refined using SHELXTL programs,[43] and the solutions yielded the positions of all heavy atoms as well as some lighter atoms. Successive difference Fourier syntheses revealed the positions of the remaining light atoms. The final refinements were obtained by introducing anisotropic parameters for all non-hydrogen atoms, and the recommended weighting factor. The hydrogen atom positions of the CH_3CN and CH_3CH_2CN ligands were calculated. The maximum electron densities in the final difference Fourier maps were located around the heavy atoms. The PLATON program[44] could not suggest additional or alternative symmetries.

The final refinement of the structure of $[Hg(SO_2ClF)_6][Sb(OTeF_5)_6]_2$ included the twin matrix ($0\ \bar{1}\ 0\ \bar{1}\ 0\ 0\ 0\ 0\ \bar{1}$) characteristic of a mirror + inversion twin, using a BASF of 0.151. For the preliminary solution of $[Hg(NCCH_3)_5][Sb(OTeF_5)_6]_2 \cdot 2SO_2ClF$, one of

the crystallographically unique anions has each of its F_5TeO-groups disordered between two orientations, as well as both co-crystallized SO_2ClF molecules possessing highly elongated ellipsoids indicative of positional disorder which at this point could not be improved. Additional refinement to appropriately model this disorder should greatly improve the solution. In the structure of $[Hg(NCCH_2CH_3)_5][Sb(OTeF_5)_6]_2 \cdot 2SO_2ClF$, the three crystallographically unique F_5TeO-groups of the $Sb_{(3)}$ anion environment were found to be disordered between two orientations, sharing a common central tellurium atom. The co-crystallized SO_2ClF molecule of $S_{(2)}$ was also disordered between two positions. The disorder was dealt with by using the command SAME.[43]

5.4.4. Computational Details

The hybrid density functionals B3LYP,[45] APFD,[46] and PBE0[47] were evaluated for the cations using the def2-TZVPD basis set[48] and effective core potentials for Sb[49] and Hg.[50] For the PBE0-def2-TZVPD level of theory, the empirical dispersion correction of Grimme[51] with Becke-Johnson damping (GD3BJ) was also included and is denoted PBE0/def2-TZVPD(GD3BJ). The free solvent molecules were only calculated at the PBE0/def2-TZVPD(GD3BJ) level of theory. The basis sets were obtained online from the EMSL Basis Set Exchange.[52] The gas-phase geometries of the cations were optimized starting from crystallographic coordinates and all optimized geometries resulted in stationary points with all frequencies real. The vibrational mode descriptions were obtained by visualization of the vibrational displacements of the calculated models with the *GaussView* program.[53] Natural bond orbital analyses were carried out at the PBE0/def2-TZVPD(GD3BJ) level of theory with the NBO program (versions 3.1 and

6.0).[33,34] In order to obtain more accurate total computed binding energies for the cations, the Basis Set Superposition Error (BSSE) was corrected for using the counterpoise method.[54] Quantum-chemical calculations were carried out using the program Gaussian 09.[55]

5.5. Supporting Information Contents - Appendix C

Complete list of experimental geometrical parameters for the $[Sb(OTeF_5)_6]^-$ anion in $[Hg(SO_2ClF)_6][Sb(OTeF_5)_6]_2$ (Table S5.1); Crystal packing diagram for $[Hg(SO_2ClF)_6][Sb(OTeF_5)_6]_2$ (Figure S5.1); $[Sb(OTeF_5)_6]^-$ anion in the single-crystal X-ray structure of $[Hg(SO_2ClF)_6][Sb(OTeF_5)_6]_2$ (Figure S5.2); Complete list of experimental geometrical parameters for the $[Sb(OTeF_5)_6]^-$ anion and co-crystallized SO_2ClF molecules in $[Hg(NCCH_2CH_3)_5][Sb(OTeF_5)_6]_2 \cdot 2SO_2ClF$ (Table S5.2); Asymmetric unit in the single-crystal X-ray structure of $[Hg(NCCH_2CH_3)_5][Sb(OTeF_5)_6]_2 \cdot 2SO_2ClF$ (Figure S5.3); Experimental Raman frequencies and intensities, and calculated gas-phase frequencies and intensities of the $[Sb(OTeF_5)_6]^-$ anions (Table S5.3); Experimental and calculated geometrical parameters of $[Hg(SO_2ClF)_6]^{2+}$ (Table S5.4); Experimental and calculated geometrical parameters of $[Hg(NCCH_3)_5]^{2+}$ (Table S5.5); Experimental and calculated geometrical parameters of $[Hg(NCCH_2CH_3)_5]^{2+}$ (Table S5.6); Calculated geometrical parameters for SO_2ClF (Table S5.7); Calculated SO_2ClF molecule (Figure S5.4); Calculated geometrical parameters for CH_3CN (Table S5.8); Calculated CH_3CN molecule (Figure S5.5); Calculated geometrical parameters for CH_3CH_2CN (Table S5.9); Calculated CH_3CH_2CN molecule (Figure S5.6); NBO analyses of $[Hg(SO_2ClF)_6]^{2+}$ (Table S5.10); NBO analyses of SO_2ClF (Table S5.11); NBO analyses of $[Hg(NCCH_3)_5]^{2+}$ (Table S5.12); NBO analyses of CH_3CN (Table S5.13); NBO analyses of $[Hg(NCCH_2CH_3)_5]^{2+}$ (Table S5.14); NBO analyses of CH_3CH_2CN (Table S5.15).

5.6. References

(1) Strauss, S. H. *Chem. Rev.* **1993**, *93*, 927–942.

(2) Krossing, I.; Raabe, I. *Angew. Chem. Int. Ed.* **2004**, *43*, 2066–2090.

(3) Riddleston, I. M.; Kraft, A.; Schaefer, J.; Krossing, I. *Angew. Chem. Int. Ed.* Accepted Author Manuscript, doi:10.1002/anie.201710782

(4) Mercier, H. P. A.; Sanders, J. C. P.; Schrobilgen, G. J. *J. Am. Chem. Soc.* **1994**, *116*, 2921–2937.

(5) Van Seggen, D. M.; Hurlburt, P. K.; Anderson, O. P.; Strauss, S. H. *Inorg. Chem.* **1995**, *34*, 3453–3464.

(6) Krossing, I. *Chem. Eur. J.* **2001**, *7*, 490–502.

(7) Gonsior, M.; Krossing, I.; Müller, L.; Raabe, I.; Jansen, M.; van Wüllen, L. *Chem. Eur. J.* **2002**, *8*, 4475–4492.

(8) Martens, A.; Weis, P.; Christian Krummer, M.; Kreuzer, M.; Meierhöfer, A.; Meier, S. C.; Bohnenberger, J.; Scherer, H.; Riddlestone, I.; Krossing, I. *Chem. Sci.* **2018**, *Advance Article*, doi:10.1039/C8SC02591F

(9) King, B. T.; Michl, J. *J. Am. Chem. Soc.* **2000**, *122*, 10255–10256.

(10) Dance, I. G.; Fisher, K. J.; Willet, G. D. *Inorg. Chem.* **1996**, *35*, 4177–4184.

(11) Liu, P.; Han, C.; Gao, Z.; Kong, F.; Zhu, Q. *J. Phys. Chem. B* **1999**, *103*, 3337–3339.

(12) Cameron, T. S.; Decken, A.; Dionne, I.; Fang, M.; Krossing, I.; Passmore, J. *Chem. Eur. J.* **2002**, *8*, 3386–3401.

(13) Engesser, T. A.; Lichtenthaler, M. R.; Schleep, M.; Krossing, I. *Chem. Soc. Rev.* **2016**, *45*, 789–899.

(14) Mercier, H. P. A.; Moran, M. D.; Schrobilgen, G. J.; Steinberg, C.; Suontamo, R. *J. Am. Chem. Soc.* **2004**, *126*, 5533–5548.

(15) Mercier, H. P. A.; Moran, M. D.; Schrobilgen, "Syntheses of the CFY_2^+ (Y = Cl, Br) and CX_3^+ (X = Cl, Br, $OTeF_5$) Cations Employing the Noble-Gas Oxidant, $XeOTeF_5^+Sb(OTeF_5)_6^-$" in *Recent Developments in Carbocation and Onium Ion Chemistry*, K. Laali, Ed.,Vol. 965, ACS Symposium Series, **2007**, pp. 394–427.

(16) Mercier, H. P. A.; Moran, M. D.; Sanders, J. C. P.; Schrobilgen, G. J.; Suontamo, R. J. *Inorg. Chem.* **2005**, *44*, 49–60.

(17) Casteel, W. J.; Kolb, P.; LeBlond, N.; Mercier, H. P. A.; Schrobilgen, G. J. *Inorg. Chem.* **1996**, *35*, 929–942.

(18) Cameron, T. S.; Dionne, I.; Krossing, I.; Passmore, J. *Solid State Sciences* **2002**, *4*, 1435–1441.

(19) Cameron, T. S.; Krossing, I.; Passmore, J. *Inorg. Chem.* **2001**, *40*, 4488–4490.

(20) Mercier, H. P. A.; Sanders, J. C. P.; Schrobilgen, G. J. *J. Am. Chem. Soc.* **1994**,*116*, 2921–2937.

(21) Aris, D.; Beck, J.; Decken, A.; Dionne, I.; Krossing, I.; Passmore, J.; Rivard, E.; Steden, F.; Wang, X. *Phosphorus, Sulfur, and Silicon*, **2004**, *179*, 859–863.

(22) Aris, D.; Beck, J.; Decken, A.; Dionne, I.; Schmedt auf der Günne, J.; Hoffbauer, W.; Köchner, T.; Krossing, I.; Passmore, J.; Rivard, E.; Steden, F.; Wang, X. *Dalton Trans.* **2011**, *40*, 5865–5880.

(23) Gerken, M.; Kolb, P.; Wegner, A.; Mercier, H. P. A.; Borrmann, H.; Dixon, D. A.; Schrobilgen, G. J. *Inorg. Chem.* **2000**, *39*, 2813–2824.

(24) Schack, C. J.; Christe, K. O. *J. Fluorine Chem.* **1982**, *21*, 393–396.

(25) Drews, T.; Seppelt, K. *Z. Anorg. Allg. Chem.* **1991**, *606*, 201–207.

(26) Mootz, D.; Merschenz-Quack, A. *Acta Cryst.* **1988**, *C44*, 924–925.

(27) Gillespie, R. J.; Hargittai, I. In The VSEPR Model of Molecular Geometry; Allyn and Bacon: Boston, MA, **1991**; pp 127−130.

(28) Brackemeyer, T.; Erker, G.; Fröhlich, R.; Prigge, J.; Peuchert, U. *Chem. Ber.* **1997**, *130*, 899–902.

(29) a) Abdelhalim-Ahmed, I.; Blachnik, R.; Reuter, H.; Stumpf, K. *Z. Kristallogr. NCS*, **1999**, *214*, 119–120; b) Goettel, J. T.; Matsumoto, K.; Mercier, H. P. A.; Schrobilgen, G. J. *Angew. Chem. Int. Ed.* **2016**, *55*, 13780–13783; c) Vierle, M.; Zhang, Y.; Santos, A. M.; Köhler, K.; Haeßner, C.; Herdtweck, E.; Bohnenpoll, M.; Nuyken, O.; Kühn, F. E. *Chem. Eur. J.* **2004**, *10*, 6323–6332; Cotton, F. A.; Poli, R. *J. Am. Chem. Soc.* **1988**, *110*, 830–841.

(30) a) Koutsantonis, G. A.; Morien, T. S.; Skelton, B. W.; White, A. H. *Acta Cryst.* **2003**, *C59*, m361–m365; b) Boorman, M. P.; Gao, X.; Freeman, G. K. W.; Fait, J. F. *J. Chem. Soc., Dalton. Trans.* **1991**, 115–120; c) Fritz, S.; Ehm, C.; Lentz, D. *Inorg. Chem.* **2015**, *54*, 5220−5231.

(31) Matsumoto, K.; Haner, J.; Mercier, H. P. A.; Schrobilgen, G. J. *Angew. Chem. Int. Ed.* **2015**, *54*, 14169–14173.

(32) Brock, D. S.; Bilir, V.; Mercier, H.P. A.; Schrobilgen, G. J. *J. Am. Chem. Soc.* **2007**, *129*, 3598–3611.

(33) NBO Version 3.1, E. D. Glendening, A. E. Reed, J. E. Carpenter, F. Weinhold, Theoretical Chemistry Institute, University of Wisconsin, Madison, **1998**.

(34) NBO Version 6.0, E. D. Glendening, J. K. Badenhoop, A. E. Reed, J. E. Carpenter, J. A. Bohmann, C. M. Morales, C. R. Landis, F. Weinhold, Theoretical Chemistry Institute, University of Wisconsin, Madison, **2013**.

(35) Reed, A. E.; Curtiss, L. A.; Weinhold, F. *Chem. Rev.* **1988**, *88*, 899–926.

(36) Grabowski, S. J.; Ugalde, J. M.; Andrada, D. M.; Frenking, G. *Chem. Eur. J.* **2016**, *22*, 11317–11328.

(37) DeBackere, J. R.; Schrobilgen, G. J. *Angew. Chem. Int. Ed.* **2018**, *57*, *13167–13171*.

(38) Bodizs, G.; Raabe, I.; Scopelliti, R.; Krossing, I.; Helm, L. *Dalton Trans.* **2009**, 5137–5147.

(39) Olah, G. A.; Donovan, D. J.; Lin, H. C. *J. Am. Chem. Soc.* **1976**, *98*, 2661–2663.

(40) Calves, Y.; Gillespie, R. J. *J. Am. Chem. Soc.* **1977**, *98*, 1788–1792.

(41) Bruker. XPREP v2008/2. Bruker AXS Inc.: Madison, WI, **2014**.

(42) Sheldrick, G. M. SHELXTL-plus, release 6.14; Siemens Analytical Xray Instruments, Inc.: Madison, WI, 1993−2014.

(43) Sheldrick, G. M. SHELXTL-plus, release 6.14; Siemens Analytical Xray Instruments, Inc.: Madison, WI, 1993−2014.

(44) (a) Spek, A. L. *Acta Crystallogr. D* **2009**, *65*, 148.; (b) A. L. Spek, (**2011**) *PLATON* - A Multipurpose Crystallographic Tool; Utrecht University, Utrecht, The Netherlands.

(45) (a) Becke, A.D. *J. Chem. Phys.* **1993**, 98, 5648–5652.; (b) Lee, C.; Yang, W.; Parr, R.G. *Phys. Rev. B* **1988**, *37*, 785–789.

(46) Austin, A.; Petersson, G. A.; Frisch, M. J.; Dobek, F. J.; Scalmani, G.; Throssell, K. *J. Chem. Theory Comput.* **2012**, *8*, 4989–5007.

(47) a) Perdew, J. P.; Burke, K.; Ernzerhof, M. *Phys. Rev. Lett.* **1996**, *77*, 3865–3868; b) Adamo, C.; Barone, V. *J. Chem. Phys.* **1999**, *110*, 6158–6169.

(48) Rappoport, D.; Furche, F. *J. Chem. Phys.* **2010**, *133*, 134105.

(49) Metz, B.; Stoll, H.; Dolg, M. *J. Chem. Phys.* **2000**, *113*, 2563–2569.

(50) Andrae, D.; Haeussermann, U.; Dolg, M.; Stoll, H.; Preuss, H. *Theor. Chim. Acta.* **1990**, *77*, 123–141.

(51) Grimme, S.; Ehrlich, S.; Goerigk, L. *J. Comput. Chem*. **2011**, *32*, 1456.

(52) (a) Feller, D. *J. Comput. Chem.* **1996**, *17*, 1571–1586.; (b) Schuchardt, K. L.; Didier, B. T.; Elsethagen, T.; Sun, L.; Gurumoorthi, V.; Chase, J.; Li, J.; Windus, T. L. *J. Chem. Inf. Model.* **2007**, *47*, 1045–1052.

(53) G*aussView*, release 3.0; Gaussian Inc.: Pittsburgh, PA, **2003**.

(54) S. F. Boys, F. Bernardi, *Mol. Phys.* **1970**, *19*, 553.

(55) Gaussian 09, revision E.01; M. J. Frisch, G. W. Trucks, H. B. Schlegel, G. E. Scuseria, M. A. Robb, J. R. Cheeseman, G. Scalmani, V. Barone, B. Mennucci, G. A. Petersson, H. Nakatsuji, M. Caricato, X. Li, H. P. Hratchian, A. F. Izmaylov, J. Bloino, G. Zheng, J. L Sonnenberg, M. Hada, M. Ehara, K. Toyota, R. Fukuda, J. Hasegawa, M. Ishida, T. Nakajima, Y. Honda, O. Kitao, H. Nakai, T. Vreven, J. A., Jr. Montgomery, J. E. Peralta, F. Ogliaro, M. Bearpark, J. J. Heyd, E. Brothers, K. N. Kudin, V. N. Staroverov, R. Kobayashi, J. Normand, K.

Raghavachari, A. Rendell, J. C. Burant, S. S. Iyengar, J. Tomasi, M. Cossi, N. Rega, N. J. Millam, M. Klene, J. E. Knox, J. B. Cross, V. Bakken, C. Adamo, J. Jaramillo, R. Gomperts, R. E. Stratmann, O. Yazyev, A. J. Austin, R. Cammi, C. Pomelli, J. W. Ochterski, R. L. Martin, K. Morokuma, V. G. Zakrzewski, G. A. Voth, P. Salvador, J. J. Dannenberg, S. Dapprich, A. D. Daniels, Ö. Farkas, J. B. Foresman, J. V. Ortiz, J. Cioslowski, D. J., Gaussian, Inc.: Wallingford, CT, **2013**.

CHAPTER 6

Noble-Gas Difluoride Complexes of Mercury(II); the Syntheses and Structures of $Hg(OTeF_5)_2 \cdot 1.5NgF_2$ (Ng = Xe, Kr) and $Hg(OTeF_5)_2$

Adapted with permission from: DeBackere, J.R., Mercier, H.P.A., and Schrobilgen, G.J. *Journal of the American Chemical Society*, **2014**, *136*, 3888–3903.

6.1. Introduction

The fluoride-ion donor behavior of noble-gas difluorides towards strong fluoride ion acceptors such as AsF_5 and SbF_5 are well established, with several examples of NgF^+ and $Ng_2F_3^+$ (Ng = Xe, Kr) salts having been characterized in the solid state and in solution.[1,2,3] Avoidance of "complete" fluoride transfer requires the corresponding Lewis acid center to be weak to moderate in strength and oxidatively resistant. In the case of XeF_2, two coordination modalities, terminal and bridging, have been observed.[1] Both fluorine atoms of XeF_2 may coordinate to two Lewis acid centers to give a bridging XeF_2 ligand, or a single fluorine atom of XeF_2 may coordinate to give a terminal XeF_2 ligand. Examples of both coordination modalities are known with XeF_2 coordinated to a non-metal ($[BrOF_2][AsF_6]\cdot 2XeF_2$)[4] and to metal cation centers (Li^+, Mg^{2+}, Ca^{2+}, Cu^{2+}, Zn^{2+}, Sr^{2+}, Ag^+, Cd^{2+}, Ba^{2+}, La^{3+}, Nd^{3+}, and Pb^{2+}).[5-9] The majority of these complexes have been structurally characterized by single-crystal X-ray diffraction. Among the group 12 metal cation complexes of XeF_2 that have been structurally characterized are $Cd(XeF_2)(BF_4)_2$,[7] $Cd_2(XeF_2)_{10}(SbF_6)_4$,[9] $Cd(XeF_2)_4(AsF_6)_2$,[10] $Cd(XeF_2)_5(PF_6)_2$,[11] and $Zn(XeF_2)_6(SbF_6)_2$,[12] Preliminary X-ray crystal structures and Raman studies of the Hg^{2+} cation complexes, $Hg(XeF_2)_5(AsF_6)_2$[13] and $Hg(XeF_2)_5(SbF_6)_2$[14] have also been reported.

In contrast, examples of KrF_2 coordination complexes are very rare. The complex, $[BrOF_2][AsF_6]\cdot 2KrF_2$, represents the first KrF_2 coordination complex to have been structurally characterized by X-ray crystallography and contains two terminally coordinated KrF_2 molecules.[15] Several NgF_2 complexes of group 6 d^0 transition metals, i.e., $XeF_2\cdot n MOF_4$ (n = 1–3, M = W,[16,17] Mo;[17] n = 4, M = Mo[17]) and $KrF_2\cdot n MOF_4$ (n = 1, M = W,[18] Mo,[18] Cr[19]); n = 2–3, M = Mo[18]) have also been synthesized and characterized in the solid state by Raman spectroscopy and/or in solution by ^{19}F and ^{129}Xe multi-NMR spectroscopy. A low-precision, room-temperature X-ray crystal structure of $XeF_2\cdot WOF_4$ has also been reported.[20]

The pentafluoro-orthotellurate group, $-OTeF_5$, may be regarded as a bulky fluorine analogue having a group electronegativity (3.88[21] and 3.87[22]) comparable to that of fluorine (3.98, Allred-Rochow scale). Negative charge dispersal over its five fluorine and an oxygen atom results in a ligand group of low nucleophilicity and high oxidative resistance.[23] The steric bulk and propensity of the $-OTeF_5$ group not to extensively oxygen bridge, but to bond in a monodentate fashion,[24-26] is expected to result in molecular species that have smaller mercury coordination numbers in the solid state than its fluorine analogue, HgF_2, which possesses a three-dimensional, networked structure (CN= 8, fluorite structure).[27] Overall, the less crowded coordination environment of Hg(II) in $Hg(OTeF_5)_2$ provides more space for donor ligand molecules such as NgF_2 to coordinate to Hg(II).

In the present study, $Hg(OTeF_5)_2$ has been synthesized in high purity and yield, along with its isostructural noble-gas difluoride coordination complexes,

$Hg(OTeF_5)_2 \cdot 1.5NgF_2$ (Ng = Xe, Kr), and structurally characterized by low-temperature single-crystal X-ray diffraction, Raman spectroscopy, and quantum-chemical calculations. Mercury(II) bis(pentafluoro-orthotellurate(VI)) was also characterized in solution by ^{19}F NMR spectroscopy in the present and past[28,29] studies. The present work provides a significant extension of the little studied coordination chemistry of KrF_2 by providing the only example of a bridging KrF_2 molecule that is currently known, and insight into the coordination behavior and Lewis acidity of Hg(II) in the neutral $Hg(OTeF_5)_2$ molecule.

6.2. Results and Discussion

6.2.1. Syntheses

The purities of all products and progress of all reactions were routinely monitored by periodically quenching the reactions at −196 °C and recording the low-temperature Raman spectra (–150 ºC) of the reaction mixtures in the solid state or in frozen solutions.

6.2.1.1. Synthesis of $Hg(OTeF_5)_2$. The synthesis of $Hg(OTeF_5)_2$ is based on a modification of prior synthetic procedures,[28,29] and was accomplished by the reaction of high-purity HgF_2 with a small molar excess of $HOTeF_5$ (1:2.05) at 50 °C for several hours (eq 6.1; see Chapter 2). The Raman spectrum of pure $Hg(OTeF_5)_2$ is provided in Figure S6.1.

$$HgF_2 + 2\ HOTeF_5 \longrightarrow Hg(OTeF_5)_2 + 2HF \qquad (6.1)$$

The literature procedures for the synthesis of $Hg(OTeF_5)_2$ call for purification of the product by sublimation at 180[28] or 200 ^oC.[29] In the present work, the Raman spectrum of sublimed $Hg(OTeF_5)_2$ (135–165 ^oC) showed several additional weak bands (Figure S6.2) that do not appear in the Raman spectrum of unsublimed $Hg(OTeF_5)_2$ (Figure S6.1), indicating that some decomposition had occurred during sublimation; however, the decomposition products have not been identified. The Raman bands associated with the decomposition products may have been too broad and weak at room temperature to be observed in the prior studies. The main bands observed in the presently reported low-temperature Raman spectrum of the product are in agreement with those previously obtained for $Hg(OTeF_5)_2$ by room-temperature Raman spectroscopy (CH_2Cl_2 solution)[28] and room-temperature infrared spectroscopy (solid in a CsBr pellet[28] or in a nujol mull[29]).

The current synthetic procedure produces $Hg(OTeF_5)_2$ in high yield and purity without the need for further purification, and has allowed its full characterization in the solid state by low-temperature single-crystal X-ray diffraction, Raman spectroscopy, and in solution by ^{19}F NMR spectroscopy.

The ^{19}F (470.568 MHz) NMR spectrum of $Hg(OTeF_5)_2$ was obtained in CD_2Cl_2 at 25 ^oC. The spectrum was second order and consisted of an AB_4 pattern with the A resonance (δ_A = –38.4 ppm; $^2J(^{19}F_A–^{19}F_B)$ = 185 Hz; $^1J(^{125}Te–^{19}F_A)$ = 3363 Hz; $^1J(^{123}Te–^{19}F_A)$ = 2794 Hz) occuring to high frequency of the B_4 resonance (δ_B = –42.1 ppm; $^1J(^{125}Te–^{19}F_B)$ = 3603 Hz; $^1J(^{123}Te–^{19}F_B)$ = 2982 Hz). The δ_A and δ_B chemical shifts and $^2J(^{19}F_A\text{-}^{19}F_B)$ coupling constant are in good agreement with the previously reported values: –38.2[28] [–38.1],[29] –40.1[28] [–40.2][29] ppm and 186[28] [185][29] Hz in CH_2Cl_2, –27.8[28]

[–27.4],[29] –40.4[28] [–40.3][29] ppm and 180[28] [180][29] Hz in CH_3CN. Accurate $^1J(^{123,125}Te–^{19}F_{A,B})$ couplings are reported here for the first time; only one coupling was previously reported (3560 Hz in CH_2Cl_2 and 3580 Hz in CH_3CN) which was described as a $J(^{125}Te–^{19}F)$ coupling but was not specifically assigned to F_A or F_B.[28]

6.2.1.2. Syntheses of $Hg(OTeF_5)_2 \cdot 1.5XeF_2$

The $Hg(OTeF_5)_2 \cdot 1.5XeF_2$ complex was synthesized by adding a 1:1.7 molar excess of XeF_2 to $Hg(OTeF_5)_2$ at –140 ºC. Sulfuryl chloride fluoride was condensed onto the mixture at –78 ºC, followed by warming to 0 ºC for 5 min, whereupon the solid dissolved. The mixture was maintained at –78 ºC for 5 days prior to removing the solvent under dynamic vacuum at –78 ºC, leaving behind a white solid corresponding to $Hg(OTeF_5)_2 \cdot 1.5XeF_2$. When the solid complex was warmed to room temperature under 1 atm of dry N_2, slow dissociation into $Hg(OTeF_5)_2$ and XeF_2 occurred and was complete within 6 days (eq 6.2).

$$Hg(OTeF_5)_2 \cdot 1.5XeF_2 \longrightarrow Hg(OTeF_5)_2 + 1.5XeF_2 \qquad (6.2)$$

6.2.1.3. Syntheses of $Hg(OTeF_5)_2 \cdot 1.5KrF_2$

The $Hg(OTeF_5)_2 \cdot 1.5KrF_2$ complex was synthesized by the reaction of $Hg(OTeF_5)_2$ and KrF_2 (1:2.2 molar ratio) in SO_2ClF solvent. The mixture was warmed to –20 ºC for 2 min and then maintained at –78 ºC for 3 h. Removal of the solvent at –78 ºC resulted in $Hg(OTeF_5)_2 \cdot 1.5KrF_2$ as a white solid. When warmed to 0 ºC under 1 atm of dry N_2 for 3 h, the $Hg(OTeF_5)_2 \cdot 1.5KrF_2$ complex underwent a redox decomposition to form HgF_2,

$F_5TeOOTeF_5$, KrF_2, and Kr according to eq 6.3. The formation of HgF_2 and $F_5TeOOTeF_5$ was confirmed by quenching the decomposition reaction in the Raman spectrometer, and recording its spectrum at –150 ºC. The Raman spectrum showed two strong bands at 254 (HgF_2) and 464 cm^{-1} (KrF_2), as well as bands characteristic of $F_5TeOOTeF_5$, in particular, a strong band corresponding to the O–O stretch of $F_5TeOOTeF_5$ appeared at 899 cm^{-1}.

$$Hg(OTeF_5)_2 \cdot 1.5KrF_2 \longrightarrow HgF_2 + F_5TeOOTeF_5 + Kr + \tfrac{1}{2}KrF_2 \qquad (6.3)$$

The absence of $Hg(OTeF_5)_2$ as a decomposition product indicates that fluorination of $Hg(OTeF_5)_2$ by KrF_2 rather than dissociation of the complex occurs at elevated temperatures. A previous computational study predicted that HgF_2 and $F_5TeOOTeF_5$ will be the dominant products resulting from the decomposition of $F_2Hg(OTeF_5)_2$ (eq 6.4).[30] Thus, the formation of $F_2Hg(OTeF_5)_2$ as an intermediate in the decomposition pathway of the complex (eqs 6.4 and 6.5) cannot be ruled out.

$$Hg(OTeF_5)_2 \cdot 1.5KrF_2 \longrightarrow F_2Hg(OTeF_5)_2 + Kr + \tfrac{1}{2}KrF_2 \qquad (6.4)$$

$$F_2Hg(OTeF_5)_2 \longrightarrow F_5TeOOTeF_5 + HgF_2 \qquad (6.5)$$

6.2.2. X-ray Crystallography.

Details of the data collection parameters and other crystallographic information for $Hg(OTeF_5)_2$ and $Hg(OTeF_5)_2 \cdot 1.5NgF_2$ (Ng = Xe, Kr) are provided in Table 6.1 and the bond lengths and angles are listed in Tables 6.2 and 6.3.

Table 6.1. Summary of Crystal Data and Refinement Results for $Hg(OTeF_5)_2$ and $Hg(OTeF_5)_2 \cdot 1.5NgF_2$ (Ng = Xe, Kr)

chem formula	**$Hg(OTeF_5)_2$**	**$Hg(OTeF_5)_2 \cdot 1.5XeF_2$**	**$Hg(OTeF_5)_2 \cdot 1.5KrF_2$**
space group	*C*2/*c*	$P2_1/n$	$P2_1/n$
a (Å)	18.681(1)	9.0574(2)	8.7981(4)
b (Å)	8.6489(4)	17.8943(3)	17.4153(9)
c (Å)	5.8008(3)	9.1285(2)	9.2243(4)
β (deg)	96.215(3)	114.548(1)	113.788(3)
V (Å^3)	931.74(1)	1345.78(6)	1293.3(2)
Z (molecules/unit cell)	4	2	2
M (g mol^{-1})	677.79	931.74	860.49
ρ_{calcd} (g cm^{-3})	4.832	4.599	4.419
T (^{o}C)	–173	–173	–173
μ (mm^{-1})	22.80	19.55	21.57
R_1[a]	0.0461	0.0282	0.0284
wR_2[b]	0.1232	0.0595	0.0716

[a] R_1 is defined as $\Sigma \| F_o | - | F_c \| / \Sigma | F_o |$ for $I > 2\sigma(I)$.
[b] wR_2 is defined as $[\Sigma[w(F_o^2 - F_c^2)^2]/\Sigma w(F_o^2)^2]^{½}$ for $I > 2\sigma(I)$.

6.2.2.1. $Hg(OTeF_5)_2$.

Unlike the three-dimensional network structure of HgF_2, the structure of $Hg(OTeF_5)_2$ consists of discrete $Hg(OTeF_5)_2$ units that interact through long Hg---O and Hg---F intramolecular contacts, resulting in chains that run parallel to the *c*-axis of its crystallographic unit cell (Figure 6.1a and S6.3). The adjacent chains form isolated layers along the *a*- and *b*-axes with no F---F distances between them that are less than the sum of twice the fluorine van der Waals radii (2.94 Å, Figure S6.3b).

The Hg(II) coordination sphere is a distorted octahedron consisting of secondary Hg---O (2 x 2.641(7) Å) and slightly longer Hg---F contacts (2 x 2.810(7) Å) in addition to the primary Hg–O bonds (2 x 2.016(6) Å), as illustrated in Figure 6.1b. The Hg–O bonds are trans to one another whereas the Hg---O and Hg---F contacts are cis to one another and to the primary Hg–O bonds. The secondary contacts are significantly less than the sums of the van der Waals radii (3.05 Å for Hg---O and 3.06 Å for Hg---F),[31] indicating significant covalent interactions between Hg(II) and the $–OTeF_5$ groups of neighbouring $Hg(OTeF_5)_2$ molecules. Among the secondary contacts, the Hg---O contacts are the strongest. The Te–O (1.842(7) Å) and Te–F (1.819(6)–1.839(6) Å) bond lengths are comparable to those of $Xe(OTeF_5)_2$ (1.842(11) and 1.843(11) Å; 1.823(9)–1.855(11) Å).[32] An interesting feature of the $Hg(OTeF_5)_2$ structure is the *gauche*-conformation adopted by the two $–OTeF_5$ groups in the solid state, with a dihedral Te–O–Hg–O–Te angle of 53.7(3)°. The *gauche*-conformation is attributed to crystal packing and to the aforementioned Hg---O and Hg---F secondary contacts with adjacent $–OTeF_5$ groups. This was supported computationally by showing that the calculated gas-phase geometry

Table 6.2. Experimental Geometrical Parameters for $Hg(OTeF_5)_2$ and Calculated Geometrical Parameters for $[Hg(OTeF_5)_2]_3$

exptl $Hg(OTeF_5)_2$ [a]		**calcd $[Hg(OTeF_5)_2]_3$** [b]	
Bond Lengths (Å)			
$Hg_1–O_1$	2.016(6)	$Hg_{16}–O_{22}$	2.008
$Te_1–O_1$	1.842(7)	$Te_{17}–O_{22}$	1.865
$Te_1–F_1$	1.819(6)	$Te_{17}–F_{18}$	1.832
$Te_1–F_2$	1.824(6)	$Te_{17}–F_{21}$	1.839
$Te_1–F_3$	1.830(6)	$Te_{17}–F_{23}$	1.848
$Te_1–F_4$	1.833(6)	$Te_{17}–F_{19}$	1.837
$Te_1–F_5$	1.839(6)	$Te_{17}–F_{20}$	1.855
Hg_1---O_{1A}	2.641(7)	$Hg_{16}---O_{14}$	2.737
Hg_1---O_{1C}	2.641(7)	$Hg_{16}---O_{30}$	2.737
Hg_1---F_{4D}	2.810(7)		
Hg_1---F_{4H}	2.810(7)		
Bond Angles (deg)			
$O_1–Hg_1–O_{1B}$	170.5(4)	$O_{22}–Hg_{16}–O_{37}$	176.0
$Hg_1–O_1–Te_1$	124.1(3)	$Hg_{16}–O_{22}–Te_{17}$	122.0
$O_1–Te_1–F_1$	178.3(3)	$O_{22}–Te_{17}–F_{18}$	179.6
$O_1–Te_1–F_2$	91.0(3)	$O_{22}–Te_{17}–F_{21}$	90.2
$O_1–Te_1–F_3$	92.9(3)	$O_{22}–Te_{17}–F_{23}$	91.7
$O_1–Te_1–F_4$	90.7(3)	$O_{22}–Te_{17}–F_{19}$	91.6
$O_1–Te_1–F_5$	91.8(3)	$O_{22}–Te_{17}–F_{20}$	91.6
$F_1–Te_1–F_2$	89.0(3)	$F_{18}–Te_{17}–F_{21}$	89.4
$F_1–Te_1–F_3$	88.8(3)	$F_{18}–Te_{17}–F_{23}$	88.2
$F_1–Te_1–F_4$	87.6(3)	$F_{18}–Te_{17}–F_{19}$	88.5
$F_1–Te_1–F_5$	88.2(3)	$F_{18}–Te_{17}–F_{20}$	88.8
$F_2–Te_1–F_4$	89.7(3)	$F_{21}–Te_{17}–F_{19}$	90.2
$F_4–Te_1–F_5$	89.1(3)	$F_{19}–Te_{17}–F_{20}$	90.5
$F_5–Te_1–F_3$	89.5(3)	$F_{20}–Te_{17}–F_{23}$	88.7
$F_3–Te_1–F_2$	91.5(3)	$F_{23}–Te_{17}–F_{21}$	90.5
$F_2–Te_1–F_5$	177.0(3)	$F_{21}–Te_{17}–F_{20}$	178.0
$F_3–Te_1–F_4$	176.2(3)	$F_{23}–Te_{17}–F_{19}$	176.6
$O_1–Hg_1---F_{4D}$	105.9(3)		
$O_1–Hg_1---F_{4H}$	78.3(3)		
$O_1–Hg_1---O_{1A}$	78.7(3)	$O_{22}–Hg_{16}---O_{14}$	73.0
$O_1–Hg_1---O_{1C}$	93.8(3)	$O_{22}–Hg_{16}---O_{30}$	103.8
$O_{1A}---Hg_1---F_{4D}$	78.3(3)		

Table 6.2 continued….

O_{1A}---Hg_1---F_{4H}	105.9(3)		
O_{1C}---Hg_1---F_{4H}	155.7(3)		
O_{1A}---Hg_1---O_{1C}	81.3(3)	O_{14}---Hg_{16}---O_{30}	79.7
F_{4D}---Hg_1---F_{4H}	129.6(3)		
Dihedral Angles (deg)			
Te_1–O_1–Hg_1–O_{1B}–Te_{1B}	53.7(3)	Te_{17}–O_{22}–Hg_{16}–O_{37}–Te_{32}	55.8

[a] The atom labeling scheme corresponds to that used in Figure 6.1b. [b] Calculated at the PBE0/def2-TVZPP level of theory. The atom labeling scheme corresponds to that used in Figure 6.6b. Only the parameters associated with the central $Hg(OTeF_5)_2$ unit are reported.

of the unknown trimeric $[Hg(OTeF_5)_2]_3$ molecule, which possesses two long Hg---O contacts (2.737 Å), retains the experimental *gauche*-conformation (Te–O–Hg–O–Te, 55.8°; see Computational Results). In contrast, gas-phase monomeric $Hg(OTeF_5)_2$ optimizes to an *anti*-conformation (dihedral Te–O–Hg–O–Te angle, 139.1°).

Another interesting structural feature is the O–Hg–O angle, which deviates significantly from linearity (170.5(4)°) in the crystal structure. The deformation, albeit smaller, is reproduced in the calculated gas-phase structure of $[Hg(OTeF_5)_2]_3$ (176.0°) which also reproduced the Hg---O secondary contacts. It is therefore likely that this feature predominantly results from crystal packing in addition to the steric demands of the $–OTeF_5$ ligands. Moreover, the experimental structure contains additional Hg---F(Te) contacts that further contribute to a decrease in the O–Hg–O angle owing to their steric demands. These contacts originate from Hg---F(Te) interactions between adjacent $Hg(OTeF_5)_2$ units within a chain, and approach the Hg(II) atom in a direction opposite to the direction toward which the O–Hg–O angle is bent.

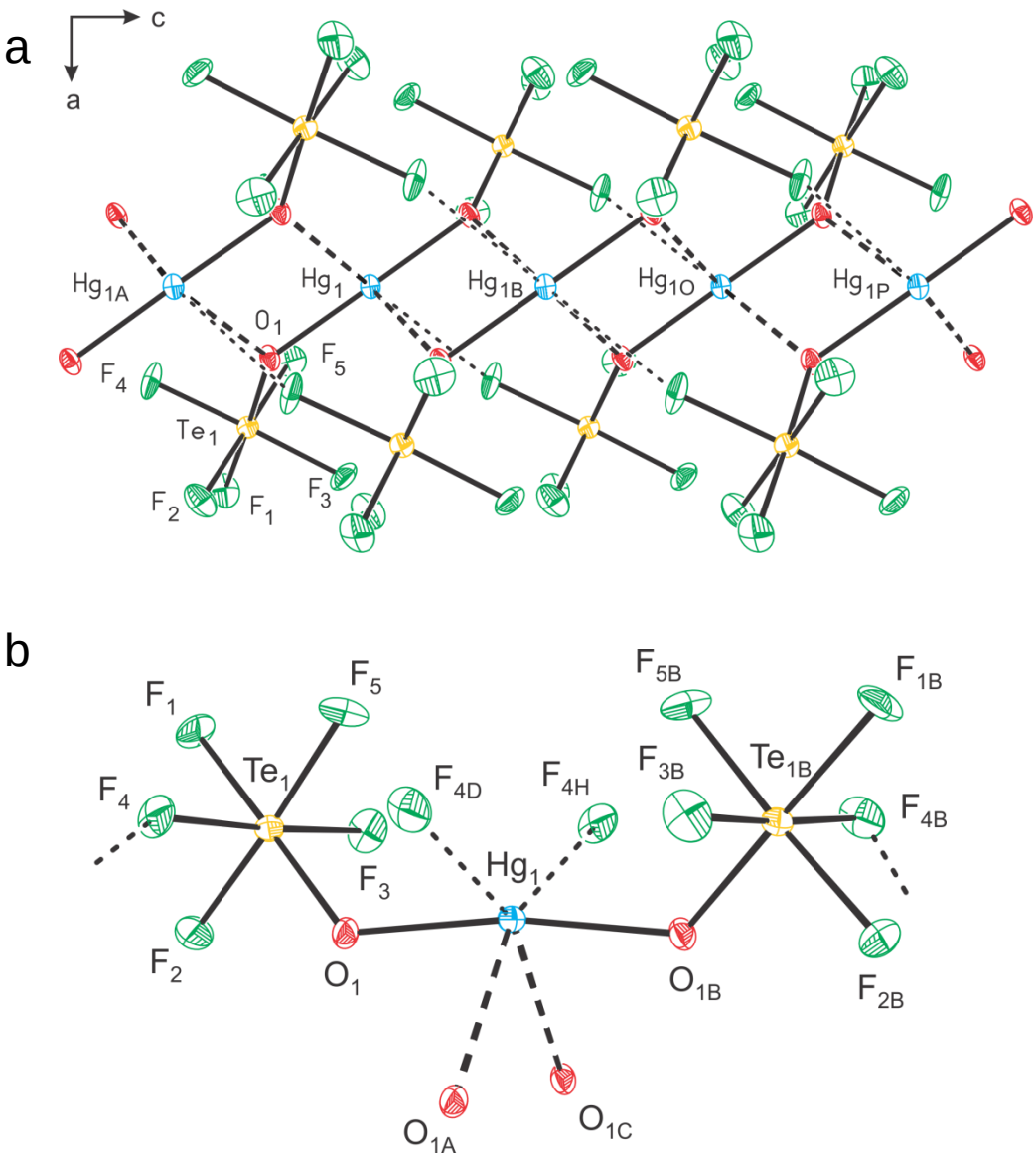

Figure 6.1. The X-ray crystal structure of $Hg(OTeF_5)_2$ showing (**a**) its chain structure viewed along the *b*-axis and running parallel to the *c*-axis, and (**b**) the pseudo-octahedral coordination around Hg(II) resulting from the secondary bonding interactions (indicated by dashed lines) between Hg(II) and the F and O atoms of $–OTeF_5$ groups in adjacent $Hg(OTeF_5)_2$ units; thermal ellipsoids are shown at the 50% probability level.

6.2.2.1. $Hg(OTeF_5)_2 \cdot 1.5NgF_2$ (Ng = Xe, Kr). The coordination complexes, $Hg(OTeF_5)_2 \cdot 1.5NgF_2$, are isostructural and belong to the $P2_1/n$ space group. The crystal structures of $Hg(OTeF_5)_2 \cdot 1.5NgF_2$ are analogous, containing $Hg(OTeF_5)_2$ units that are linked to one another through bridging NgF_2 molecules (Figures 6.2). As expected, the $Hg(OTeF_5)_2 \cdot 1.5XeF_2$ complex has a slightly larger unit cell (Table 6.1), reflecting the larger covalent radius of xenon (1.40 Å) relative to that of krypton (1.16 Å).[33]

The mercury coordination spheres of $Hg(OTeF_5)_2 \cdot 1.5NgF_2$ are comparable to that of $Hg(OTeF_5)_2$ (vide supra), consisting of very distorted pseudo-octahedra (Figure 6.3 and Table 6.3). The $Hg(OTeF_5)_2$ units likewise have *gauche*-conformations with Hg–O bonds *trans* to one another. The contacts with mercury include two shorter Hg---F contacts (Xe, 2.606(5) and 2.623(4) Å; Kr, 2.664(3) and 2.675(3) Å) that are *trans* to one another and two slightly longer Hg---F and Hg---O contacts (Xe, 2.701(5) and 2.749(4) Å; Kr, 2.741(3) and 2.725(3) Å, respectively) that are *trans* to one another. The Hg---F contacts originate from the fluorine ligands of three non-equivalent NgF_2 molecules and the Hg---O contact from an oxygen atom of an adjacent $Hg(OTeF_5)_2$ group. These contacts are significantly less than the sums of their respective van der Waals radii and indicate significant covalent interactions. The Hg---F and Hg---O contacts within the NgF_2 complexes are shorter and longer, respectively, than those within the chain networks of $Hg(OTeF_5)_2$ (Hg---F, 2.810(7) and Hg---O, 2.641(7) Å). These secondary bonding interactions, which are similar to the secondary bonding interactions found in the crystal structure of $Hg(OTeF_5)_2$, presumably favor the observed *gauche*–conformation of

Table 6.3. Experimental Geometrical Parameters for $Hg(OTeF_5)_2 \cdot 1.5NgF_2$ (Ng = Xe, Kr)

	Ng = Xe	**Ng = Kr**		**Ng = Xe**	**Ng = Kr**
Bond Lengths (Å)					
$Hg_1–O_1$	2.015(5)	2.017(3)	$Te_2–F_8$	1.828(5)	1.836(3)
$Hg_1–O_2$	2.037(5)	2.029(3)	$Te_2–F_9$	1.827(5)	1.836(3)
$O_1–Te_1$	1.815(5)	1.819(3)	$Te_2–F_{10}$	1.814(5)	1.824(3)
$O_2–Te_2$	1.811(6)	1.836(3)	Hg_1---O_{2B}	2.749(4)	2.725(3)
$Te_1–F_1$	1.827(5)	1.837(3)	Hg_1---F_{11}	2.606(5)	2.664(3)
$Te_1–F_2$	1.831(4)	1.839(3)	Hg_1---F_{12}	2.623(4)	2.675(3)
$Te_1–F_3$	1.837(4)	1.844(3)	Hg_1---F_{13B}	2.701(5)	2.741(3)
$Te_1–F_4$	1.841(4)	1.848(3)	$Ng_2–F_{11}$	1.981(4)	1.883(3)
$Te_1–F_5$	1.845(4)	1.835(3)	$Ng_2–F_{11A}$	1.981(4)	1.883(3)
$Te_2–F_6$	1.835(5)	1.838(3)	$Ng_1–F_{12}$	2.012(4)	1.897(3)
$Te_2–F_7$	1.822(4)	1.829(3)	$Ng_1–F_{13}$	1.991(4)	1.885(3)
Bond Angles (deg)					
$O_1–Hg_1–O_2$	173.0(2)	173.3(1)	$F_8–Te_2–F_7$	87.0(2)	87.7(1)
$Hg_1–O_1–Te_1$	132.8(3)	129.6(2)	$F_8–Te_2–F_{10}$	86.6(3)	87.1(2)
$Hg_1–O_2–Te_2$	127.2(3)	126.5(1)	$F_9–Te_2–F_7$	90.2(2)	90.1(1)
$O_1–Te_1–F_1$	93.2(2)	93.0(1)	$F_7–Te_2–F_{10}$	91.8(2)	91.3(2)
$O_1–Te_1–F_2$	94.7(2)	94.4(1)	$F_{10}–Te_2–F_6$	90.0(2)	90.1(1)
$O_1–Te_1–F_3$	95.3(2)	95.0(1)	$F_6–Te_2–F_9$	87.5(2)	88.0(1)
$O_1–Te_1–F_4$	91.1(2)	90.6(1)	$F_9–Te_2–F_{10}$	173.6(3)	174.2(2)
$O_1–Te_1–F_5$	176.7(2)	176.8(1)	$F_6–Te_2–F_7$	173.5(2)	174.2(1)
$O_2–Te_2–F_6$	95.0(2)	94.8(1)	$F_{11A}–Ng_2–F_{11}$	180.0	180.0
$O_2–Te_2–F_7$	91.2(2)	90.8(1)	$F_{12}–Ng_1–F_{13}$	179.4(2)	178.9(1)
$O_2–Te_2–F_8$	178.0(2)	178.5(1)	$Ng_2–F_{11}---Hg_1$	158.3(3)	150.6(2)
$O_2–Te_2–F_9$	93.4(2)	92.7(1)	$Ng_1–F_{12}---Hg_1$	119.3(2)	119.5(1)
$O_2–Te_2–F_{10}$	92.7(3)	92.8(2)	$O_1–Hg_1---F_{13B}$	79.7(2)	78.5(1)
$F_5–Te_1–F_2$	86.6(2)	86.4(1)	$O_1–Hg_1---F_{11}$	99.2(2)	99.4(1)
$F_5–Te_1–F_3$	87.7(2)	88.1(1)	$O_1–Hg_1---F_{12}$	77.2(2)	75.9(1)
$F_5–Te_1–F_4$	86.0(2)	86.3(1)	$O_2–Hg_1---F_{13B}$	101.1(2)	103.0(1)
$F_5–Te_1–F_1$	85.5(2)	86.2(2)	$O_2–Hg_1---F_{11}$	84.4(2)	83.0(2)
$F_2–Te_1–F_4$	89.5(2)	90.5(1)	$O_2–Hg_1---F_{12}$	96.4(3)	98.2(2)
$F_4–Te_1–F_1$	89.8(2)	89.4(1)	$O_1–Hg_1---O_{2B}$	103.3(2)	103.4(1)
$F_1–Te_1–F_3$	89.4(2)	89.1(1)	$O_{2B}---Hg_1---F_{13B}$	139.9(2)	139.6(1)
$F_3–Te_1–F_2$	90.4(2)	90.2(1)	$O_{2B}---Hg_1---F_{11}$	77.2(2)	74.2(1)
$F_3–Te_1–F_4$	173.6(2)	174.3(1)	$O_{2B}---Hg_1---F_{12}$	69.8(2)	69.4(1)
$F_1–Te_1–F_2$	172.1(2)	172.5(1)	$F_{12}---Hg_1---F_{11}$	144.7(2)	140.8(1)
$F_8–Te_2–F_9$	87.4(2)	87.4(2)	$F_{13B}---Hg_1---F_{11}$	142.5(2)	146.0(1)
$F_8–Te_2–F_6$	86.9(2)	86.7(1)	$F_{13B}---Hg_1---F_{12}$	77.2(2)	72.2(1)
Dihedral Angle (deg)					
$Te_1–O_1–Hg_1–O_2–Te_2$	45.2(5)	50.3(3)			

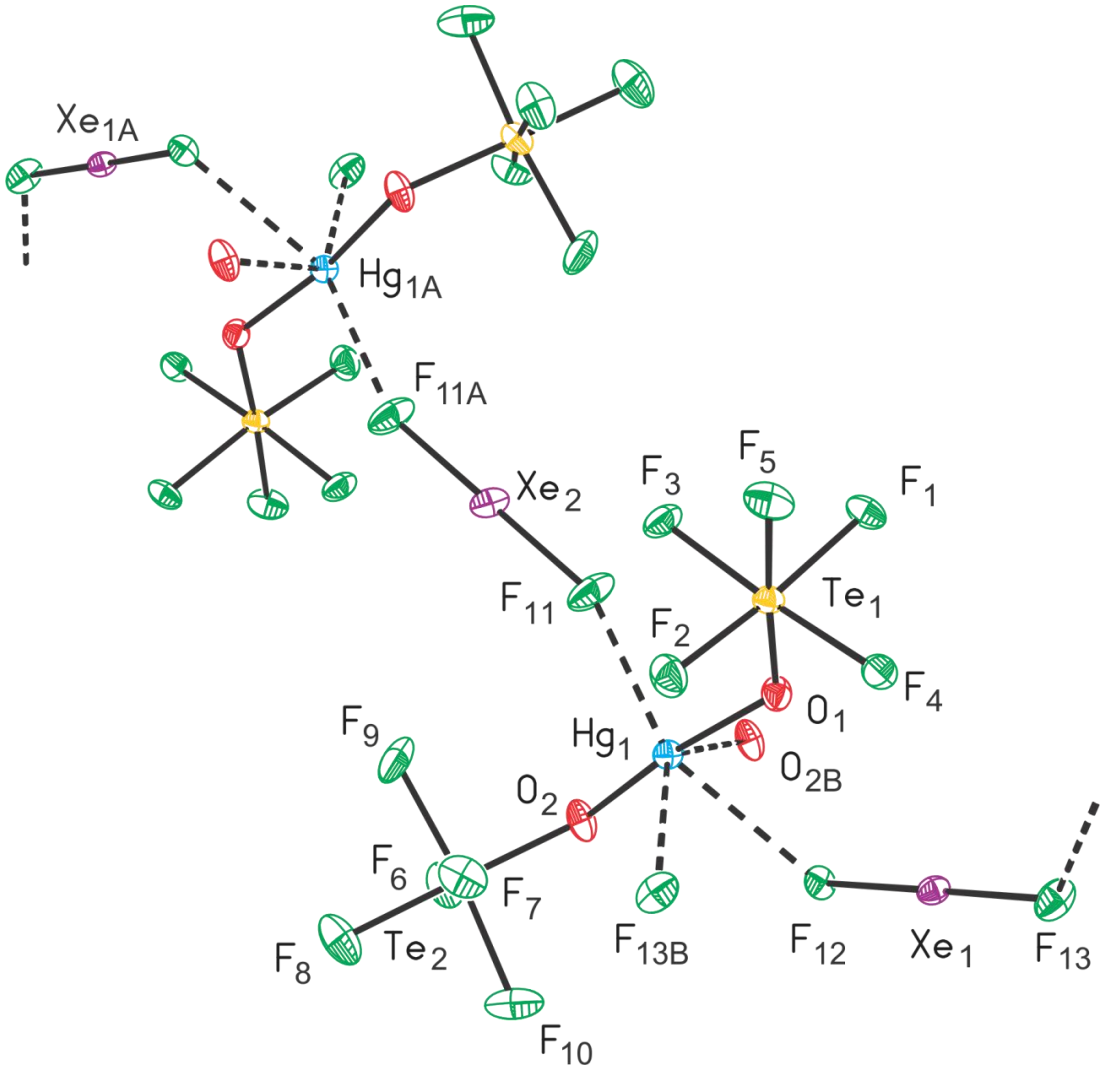

Figure 6.2a. The chain structure in the X-ray crystal structure of $Hg(OTeF_5)_2 \cdot 1.5XeF_2$; thermal ellipsoids are shown at the 50% probability level. Secondary bonding interactions from the F and O atoms of adjacent XeF_2 and $–OTeF_5$ groups to Hg(II) are indicated by dashed lines.

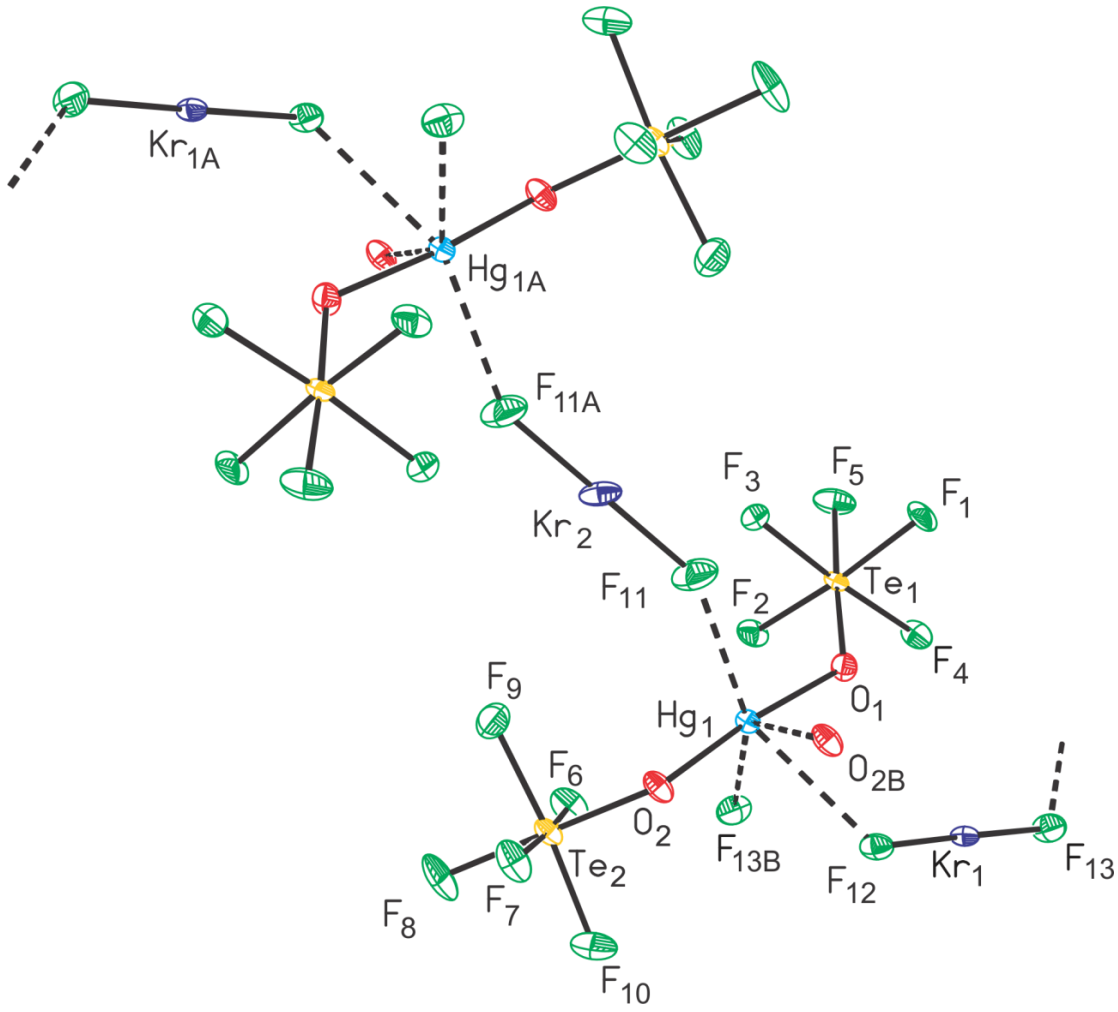

Figure 6.2b. The chain structure in the X-ray crystal structure of $Hg(OTeF_5)_2 \cdot 1.5KrF_2$; thermal ellipsoids are shown at the 50% probability level. Secondary bonding interactions from the F and O atoms of adjacent KrF_2 and $-OTeF_5$ groups to Hg(II) are indicated by dashed lines.

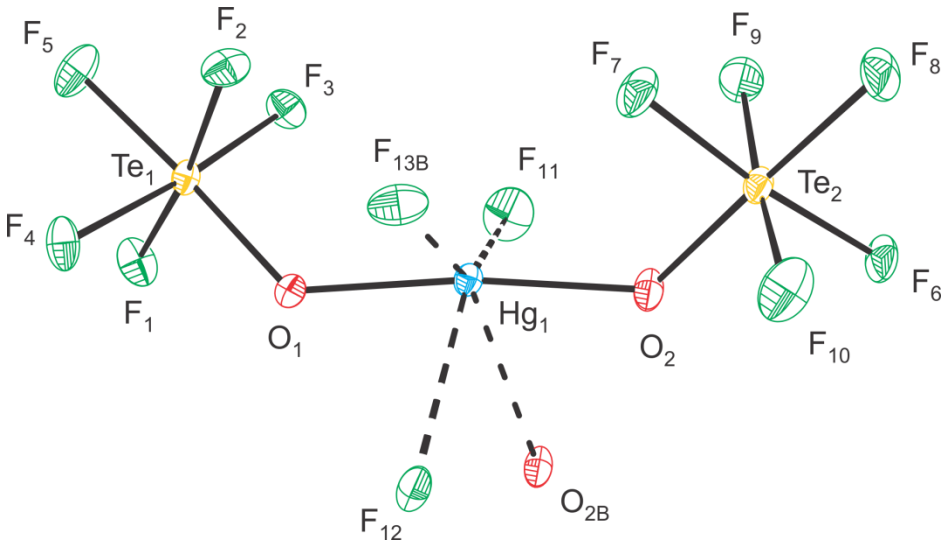

Figure 6.3. The the pseudo-octahedral coordination around Hg(II) in the X-ray crystal structure of $Hg(OTeF_5)_2 \cdot 1.5KrF_2$ (see Figure 6.2b) with thermal ellipsoids drawn at the 50% probability level. Secondary bonding interactions are indicated by dashed lines drawn from the F and O atoms of adjacent KrF_2 and $–OTeF_5$ groups to Hg(II).

the $Hg(OTeF_5)_2$ unit. Although both structures are similar, the secondary bond distances between mercury and the fluorine atoms of NgF_2 are somewhat shorter in $Hg(OTeF_5)_2 \cdot 1.5XeF_2$ than in the KrF_2 analogue (Table 6.3), which is consistent with the more polar characters of the Xe–F bonds.[3]

The Te−F bond lengths (Xe, 1.814(5)−1.845(4) Å; Kr, 1.824(3)−1.848(3) Å) and F−Te−F angles (Xe, 85.5(2)−91.8(2)^o and 172.1(2)−173.6(3)^o; Kr, 86.2(2)−91.3(2)^o and 172.5(1)−174.3(1)^o) are comparable in the krypton and xenon analogues and to those of $Hg(OTeF_5)_2$ (vide supra). The Hg−O (Xe, 2.015(5) and 2.037(5) Å; Kr, 2.017(3) and

2.029(3) Å) and Te−O (Xe, 1.811(6) and 1.815(5) Å; Kr, 1.819(3) and 1.836(3) Å) bond lengths are all equal (within ±3σ) to those of $Hg(OTeF_5)_2$. The effects of NgF_2 coordination to mercury are reflected in the O−Hg−O (Xe, 173.0(2)°; Kr, 173.3(1)°) and Hg−Te−O (Xe, 132.8(3) and 127.2(3)°; Kr, 129.6(2) and 126.5(1)°) angles, which are slightly larger (within ±3σ) than those of $Hg(OTeF_5)_2$ and in the dihedral Te−O−Hg−O–Te angles (Xe, 45.2(5)°; Kr, 50.3(3)°), which are smaller than in $Hg(OTeF_5)_2$ (53.7(3)°).

There are two crystallographically inequivalent bridging NgF_2 molecules within the asymmetric units of $Hg(OTeF_5)_2 \cdot 1.5NgF_2$; one Ng atom is positioned on an inversion center, providing two symmetry-equivalent Ng–F bonds (Xe, 1.981(4) Å; Kr, 1.883(3) Å), whereas the other Ng atom is on a general position, giving rise to two symmetry-inequivalent Ng–F bonds (Xe, 1.991(4) and 2.012(4) Å; Kr, 1.897(3) and 1.885(3) Å). The Ng–F bond lengths are equal within ±3σ to those observed in free NgF_2 (XeF_2, 1.999(4) Å;[3] KrF_2, 1.894(5) Å [2]). The Xe–F bond lengths are comparable to those observed for the bridging XeF_2 molecule in $Cd(XeF_2)_4(AsF_6)_2$ (Xe–F_b, 1.995(5) and 2.017(5) Å)[10] and in $Cd(XeF_2)_5(PF_6)_2$ (Xe–F_b, 1.999(6) and 2.016(6) Å).[11] The structure of $Hg(OTeF_5)_2 \cdot 1.5KrF_2$ currently represents the only example of KrF_2 coordinated to a neutral metal center and of a bridging KrF_2 molecule. The $[BrOF_2][AsF_6] \cdot 2KrF_2$ complex is the only other KrF_2 complex reported to date that has been characterized by X-ray crystallography. The Kr–F bridge bonds of the present complex are shorter than the Kr–F bridge bonds of the terminally coordinated KrF_2 molecules in $[BrOF_2][AsF_6] \cdot 2KrF_2$ (1.943(4) and 1.933(4) Å),[15] indicating that they are more covalent and more weakly coordinated than those of $[BrOF_2][AsF_6] \cdot 2KrF_2$.

6.2.3. Raman Spectroscopy

The low-temperature, solid-state Raman spectra of $Hg(OTeF_5)_2$, and $Hg(OTeF_5)_2 \cdot 1.5NgF_2$ (Ng = Xe, Kr) are shown in Figures S6.1, 6.4, and 6.5. Their assignments are listed in abbreviated form in Tables 6.4–6.6 and in more detail in Tables S6.1–S6.4; along with their experimental and calculated frequencies and intensities.

Spectral assignments for $Hg(OTeF_5)_2$ were made by comparison with the calculated frequencies and Raman intensities (Tables 6.4, S6.1, and S6.2) obtained for the energy-minimized, gas-phase geometries of $Hg(OTeF_5)_2$ (C_2) monomer and the presently unknown trimer, $[Hg(OTeF_5)_2]_3$ (C_1) (Figure 6.6b). The central $Hg(OTeF_5)_2$ unit of the trimeric model provides a good approximation of the repeat unit in the chain structure (Figure 6.1). A similar approach has been successfully used to assign the Raman spectra of the polymeric open chain structures OsO_3F_2[34] and $MoSF_4$[35]. In another related structure, $XeOF_4 \cdot XeF_2$, the model compounds, $2XeOF_4 \cdot XeF_2$ and $XeOF_4 \cdot 4XeF_2$, have provided good approximations for the local environments of XeF_2 and $XeOF_4$ and their vibrational assignments.[36]

The $-OTeF_5$ ligands of the central $Hg(OTeF_5)_2$ unit of $[Hg(OTeF_5)_2]_3$ have a *gauche*-conformation and two *cis*-Hg---O secondary contacts to the Hg(II) atoms from the terminal $Hg(OTeF_5)_2$ units. The Raman spectrum of $Hg(OTeF_5)_2$ is also compared with that of $Xe(OTeF_5)_2$.[32] The vibrational assignments for $Hg(OTeF_5)_2 \cdot 1.5NgF_2$ were made by comparison with the experimental frequencies of $Hg(OTeF_5)_2$ (Table 6.4) and NgF_2 (Tables S6.5 and S6.6), and the calculated frequencies and assignments of NgF_2 and the $[Hg(OTeF_5)_2]_3 \cdot 2NgF_2$ model compounds. These models also enabled the assignments

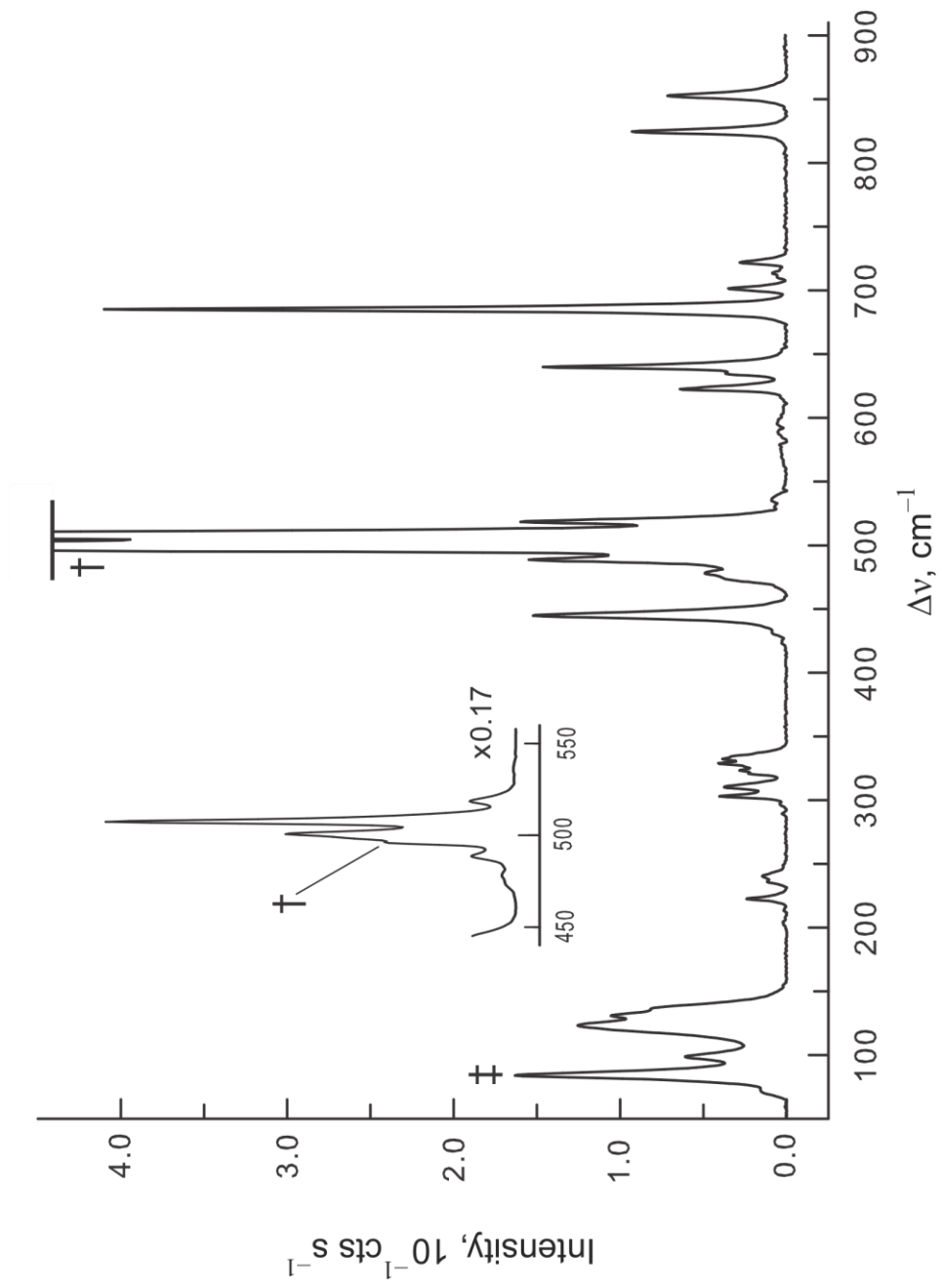

Figure 6.4. The Raman spectrum of $Hg(OTeF_5)_2 \cdot 1.5XeF_2$ recorded in a quartz tube at −155 °C using 1064-nm excitation. Symbols denote unreacted XeF_2 at 496 cm^{-1} (†) and an instrumental artifact (‡).

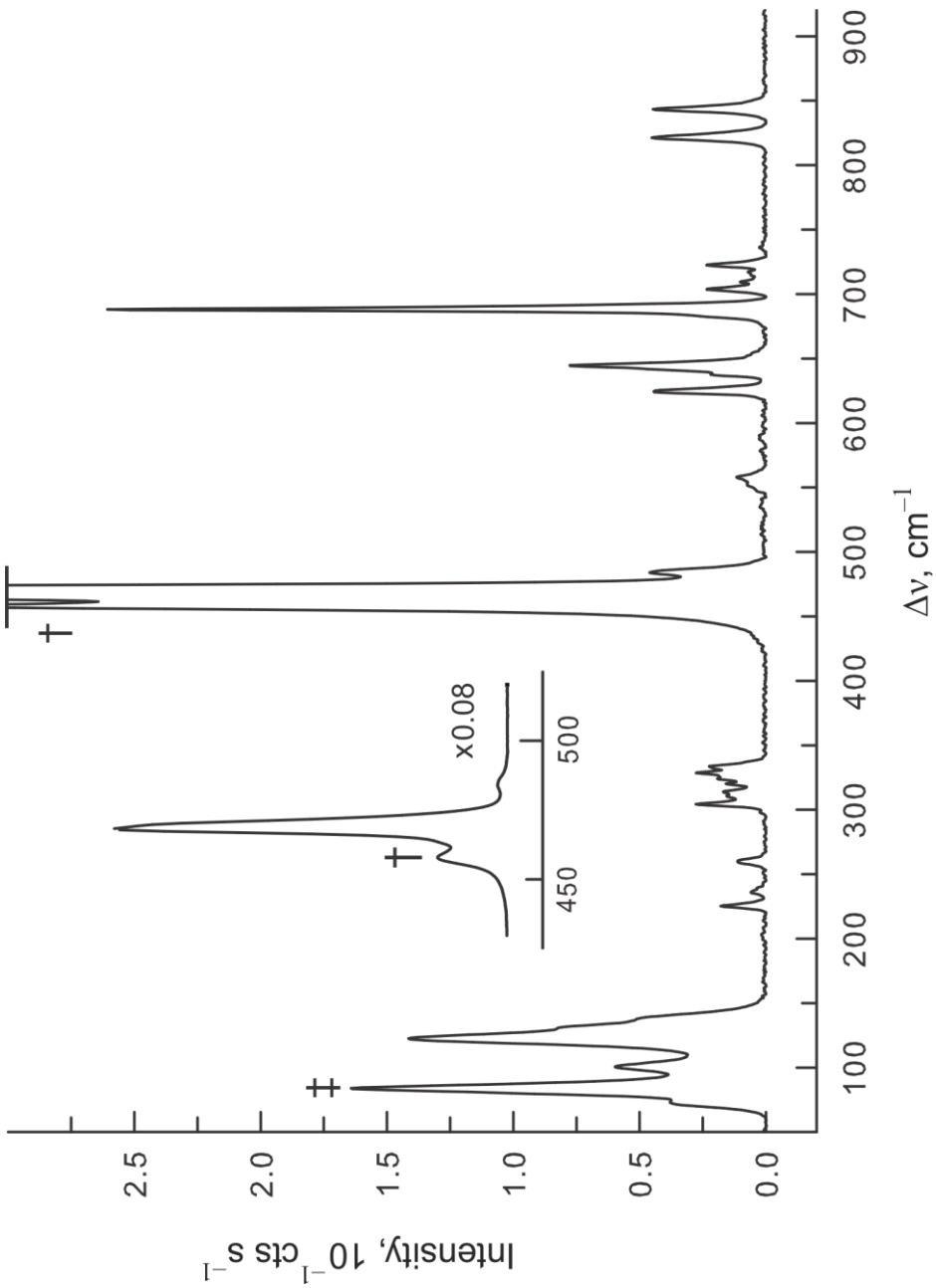

Figure 6.5. The Raman spectrum of $Hg(OTeF_5)_2 \cdot 1.5KrF_2$ recorded in a quartz tube at −155 °C using 1064-nm excitation. Symbols denote unreacted KrF_2 at 464 cm^{-1} (†) and an instrumental artifact (‡).

Table 6.4. Experimental Raman Frequencies and Intensities for $Hg(OTeF_5)_2$ and Calculated Vibrational Frequencies and Intensities for $[Hg(OTeF_5)_2]_3$

exptl [a,b,c] **$Hg(OTeF_5)_2$**	**calcd** [a,d] **$[Hg(OTeF_5)_2]_3$**	*assgnts* [e]
825(19)	824(27)[76]	[ν(Hg-O) – ν(Te-O)]
n.o.	806(4)[112]	
801(8)	793(3)[663]	
	787(1)[314]	
735(25)	726(11)[2]	[ν(Te-F_e)]
	725(<0.1)[218]	
	724(<0.1)[235]	
709(100)	709(6)[45]	[ν(Te-F_a)]
	707(28)[61]	
699(3)	719(15)[<1]	[ν(Te-F_e)]
	719(<1)[392]	
	717(<1)[17]	
	716(<1)[249]	
	714(2)[18]	
652(46)	654(50)[1]	
647, sh	649(1)[10]	
	649(<1)[10]	
630, sh	641(2)[8]	
624(45)	640(6)[<1]	
511(7)	530(2)[81]	[ν(Hg-O) + ν(Te-O)]
	528(6)[11]	
481(52)	506(75)[3]	
472, sh	516(3)[138]	
349(2)	341(<1)[5]	$\delta(TeF_{4e})_{umb}$
331(9)	332(<0.1)[137]	δ(O-Hg-O)$_{o.o.p.}$
	331(<0.1)[219]	$\delta(TeF_{4e})_{umb}$
327(20)	328(<0.1)[364]	$\delta(TeF_{4e})_{umb}$
	327(<1)[22]	
324, sh	324(<0.1)[52]	δ(O-Hg-O)$_{o.o.p.}$ / δ(O-Te-F) / ρ_w(F-Te-F)
	323(<1)[15]	ρ_t(O-Hg-O)
318(5)	320(2)[17]	δ(F-Te-F) / δ(F-Te-O)
	320(<0.1)[11]	
312(1)	315(6)[1]	δ(F-Te-F) / ρ_w(F-Te-F) / ρ_w(F-Te-O)
	315(<1)[<0.1]	δ(F-Te-F) / ρ_w(F-Te-F)
298(9)	295(2)[<1]	δ(F-Te-F)
	295(1) [<0.1]	
n.o.	245(<1)[<1]	ρ_w(F-Te-F)
	244(<0.1)[4]	
	234(<0.1[7])	δ(F-Te-F) / ρ_w(O-Te-F)
233(12)	232(6)[1]	δ(F-Te-F) / ρ_w(F-Te-F)
n.o.	207(<0.1)[<1]	ρ_w(F-Te-F)
	206(<0.1)[<0.1]	
	195(<0.1)[<0.1]	ρ_w(F-Te-F) / δ(O-Hg-O)$_{o.o.p.}$

Table 6.4 continued …

194(2)	191(<0.1)[<0.1] 190(<1)[<0.1]	ρ_w(F-Te-F) / ρ_t(O-Hg-O) / ρ_w(O-Te-F)
173(<1)	167(<0.1)[<1]	ρ_w(O-Te-F) / ρ_w(F-Te-F)
127(16)	129(<1)[2] 127(4) [<0.1]	$\rho_r(TeF_{4e}F_a)$
92(9)	97(<1)[17] 94(<0.1)[3] 93(2)[1]	δ(O-Hg-O)$_{i.p.}$ δ(O-Hg-O)$_{o.o.p.}$ δ(O-Hg-O)$_{i.p.}$

[a] Frequencies are given in cm^{-1}. [b] Values in parentheses denote relative Raman intensities. The Raman spectrum was recorded in an FEP sample tube at −150 °C using 1064-nm excitation. [c] The abbreviations denote shoulder (sh) and not observed (n.o.). [d] Values in parentheses denote calculated Raman intensities ($Å^4$ amu^{-1}) whereas values in square brackets denote calculated infrared intensities (km mol^{-1}). [e] Assignments are for the energy-minimized geometry calculated at the PBE0/def2-TZVPP level; only simplified mode assignments (separated by the symbol "/") that involve the central $Hg(OTeF_5)_2$ unit are listed. See Table S6.2 for a complete listing of frequencies and detailed descriptions of the assignments. The abbreviations denote out-of-plane (o.o.p.) and in-plane (i.p.) where the planes contain the (Te–O–Hg–O–Te) groups, umbrella (umb), equatorial (e), axial (a), stretch (ν), bend (δ), twist (ρ_t), wag (ρ_w), and rock (ρ_r). The atom labeling scheme is given in Figure 6.6.

Table 6.5. Experimental Raman Frequencies and Intensities for $Hg(OTeF_5)_2 \cdot 1.5XeF_2$ and Calculated Vibrational Frequencies and Intensities for $[Hg(OTeF_5)_2]_3 \cdot 2XeF_2$

exptl[a,b,c] **$Hg(OTeF_5)_2$-$\cdot 1.5XeF_2$**	**calcd**[a,d] **$[Hg(OTeF_5)_2]_3 \cdot 2XeF_2$**	*assgnts*[e]
853(5)	828(9)[155]	[ν(Hg-O) – ν(Te-O)]
825(7)	817(2)[547]	[ν(Hg-O) – ν(Te-O)]
	815(2)[346]	[ν(Hg-O) – ν(Te-O)]
753(<1)$_{broad}$	721(16)[10]	[ν(Te-F_e)]
	717(4)[102]	[ν(Te-F_e)]
	716(5)[291]	[ν(Te-F_e)]
	715(9)[278]	[ν(Te-F_e)]
722(2)	714(2)[135]	[ν(Te-F_e)]
711(<1)	713(2)[13]	[ν(Te-F_e)]
	713(2)[243]	[ν(Te-F_e)]
	711(<1)[21]	[ν(Te-F_e)]
702(3)	695(<1)[205]	[ν(Te-F_e)]
685(29)	705(13)[8]	[ν(Te-F_a)]
	699(18)[18]	[ν(Te-F_a)]
	644(38)[4]	[ν(Te-F_e)]
640(10)	643(2)[11]	[ν(Te-F_e)]
635(2)	640(3)[8]	[ν(Te-F_e)]
	639(3)[7]	[ν(Te-F_e)]
623(4)	628(9)[14]	[ν(Te-F_e)]
	622(3)[14]	[ν(Te-F_e)]
518(10)	534(3)[178]	[ν(Xe_{13}-F_{17}) – ν(Xe_{13}-F_{20})] / [ν(Hg-O) + ν(Te-O)]
	528(5)[167]	[ν(Xe_{13}-F_{17}) – ν(Xe_{13}-F_{20})] + [ν(Xe_{16}-F_{23}) – ν(Xe_{16}-F_{40})] / [ν(Hg-O) + ν(Te-O)]
508(100)	524(9)[67]	[ν(Hg-O) + ν(Te-O)]
	521(54)[90]	[ν(Xe_{13}-F_{20})] – [ν(Xe_{16}-F_{40})]
501(56)	516(38)[11]	[ν(Xe_{13}-F_{17}) + ν(Xe_{13}-F_{20})] + [ν(Xe_{16}-F_{23}) + ν(Xe_{16}-F_{40})]$_{small}$
489(10)	510(35)[80]	[ν(Xe_{13}-F_{17})] – [ν(Xe_{16}-F_{23})]
478(3)	502(73)[3]	[ν(Hg-O) + ν(Te-O)]
474, sh	502(73)[3]	[ν(Hg-O) + ν(Te-O)]
445(11)	499(6)[230]	[ν(Hg-O) + ν(Te-O)] / ν(Xe_{16}-F_{23})
	337(<1)[34]	δ(TeF_{4e})$_{umb}$
334, sh	334(<1)[10]	δ(TeF_{4e})$_{umb}$
	334(<1)[99]	δ(TeF_{4e})$_{umb}$
332(3)	331(<1)[95]	δ(O-Hg-O)$_{o.o.p.}$ / δ(TeF_{4e})$_{umb}$
	330(<1)[83]	δ(TeF_{4e})$_{umb}$ / ρ_w(O-Te-F) / ρ_w(F-Te-F)
329(3)	328(1)[145]	δ(O-Te-F) / δ(F-Te-F) / ρ_w(F-Te-F)
	326(<1)[54]	δ(O-Te-F) / δ(F-Te-F)] / ρ_w(F-Te-F)
326, sh	326(<1)[34]	δ(O-Hg-O)$_{o.o.p.}$ / δ(O-Te-F) / δ(F-Te-F) / ρ_w(O-Te-F) / ρ_w(F-Te-F)
	326(1)[21]	δ(F-Te-F) / ρ_w(F-Te-F) / δ(F-Te-F)
324(2)	324(<1)[13]	ρ_w(O-Te-F) / ρ_w(F-Te-F) / δ(F-Te-F)
	322(<1)[28]	δ(F-Te-F) / δ(O-Te-F) / ρ_w(F-Te-F)
321(1)	321(<1)[8]	δ(F-Te-F) / ρ_w(F-Te-F)
	320(<1)[26]	δ(F-Te-F) / ρ_w(F-Te-F)

Table 6.5 continued…

311(2)	317(<1)[12]		δ(F-Te-F) / ρ_w(F-Te-F) / ρ_t(O-Hg-O)
	316(1)[16]		ρ_t(O-Hg-O) / δ(F-Te-O) / δ(F-Te-F)
	316(<1)[15]		δ(F-Te-F) / ρ_w(F-Te-F) / ρ_t(O-Hg-O)
303(3)	293(2)[<1]	}	δ(F-Te-F)
	291(1)[<1]		
248, sh	244(<1)[<1]		δ(F-Te-O) /ρ_w(F-Te-F)
241(1)	236(<1)[22]		$\delta(F_{17}\text{-}Xe_{13}\text{-}F_{20})_{o.o.p.}$
236(1)	231(3)[3]		ρ_w(F-Te-F) / δ(F-Te-O)
223(2)	221(<1)[21]		$[\delta(F_{17}\text{-}Xe_{13}\text{-}F_{20})_{i.p.}]_{small} + \delta(F_{23}\text{-}Xe_{16}\text{-}F_{40})_{o.o.p.}$
	219(<1)[21]		$\delta(F_{23}\text{-}Xe_{16}\text{-}F_{40})_{i.p.}$
	218(<0.1)[12]		$\delta(F_{17}\text{-}Xe_{13}\text{-}F_{20})_{i.p.} + [\delta(F_{23}\text{-}Xe_{16}\text{-}F_{40})_{o.o.p.}]_{small}$
n.o.	210(<0.1)[<1]		ρ_w(F-Te-F)
	209(<0.1)[<1]		ρ_w(F-Te-F)
	202(<0.1)[<1]		ρ_w(O-Te-F) / ρ_w(F-Te-F)
	191(<0.1)[<0.1		ρ_w(O-Te-F) / ρ_w(F-Te-F)
	162(<0.1)[6]		ρ_r(F-Te-F) / ρ_w(F-Te-F)
137(5)	129(1)[<1]	}	$\rho_r(TeF_{2e}F_a)$
131(7)	128(2)[<1]		
124(8)	106(4)[9]		$\rho_t(F_{17}\text{-}Xe_{13}\text{-}F_{20})$
	100(<1)[3]		$\rho_t(F_{17}\text{-}Xe_{13}\text{-}F_{20})$ / $\delta(O\text{-}Hg\text{-}O)_{i.p.}$
99(3)	96(1)[3]		$\delta(O\text{-}Hg\text{-}O)_{i.p.}$ / $\rho_r(F_{20}\text{-}Xe_{13}\text{-}F_{17})_{small}$
	91(<1)[5]		$\delta(O\text{-}Hg\text{-}O)_{o.o.p.}$ / $\rho_r(F_{20}\text{-}Xe_{13}\text{-}F_{17})_{small}$
	83(2)[<1]		$\rho_t(F_{40}\text{-}Xe_{16}\text{-}F_{23})$
	78(3)[<1]		$\rho_t(F_{40}\text{-}Xe_{16}\text{-}F_{23})$
	72(2)[<1]		$\rho_r(F_{17}\text{-}Xe_{13}\text{-}F_{20})$

[a] Frequencies are given in cm^{-1}. [b] Values in parentheses denote relative Raman intensities. The Raman spectrum was recorded in a quartz sample tube at −155 °C using 1064-nm excitation. A band at 496(27) cm^{-1} (not listed, see Figure 6.4) is assigned to excess XeF_2. [c] The abbreviations denote shoulder (sh) and not observed (n.o.). [d] Values in parentheses denote calculated Raman intensities ($Å^4$ amu^{-1}), whereas values in square brackets denote calculated infrared intensities (km mol^{-1}). [e] Assignments are for the energy-minimized geometry calculated at the PBE0/def2-TZVPP level. Only simplified mode assignments (separated by the symbol "/") that involve the central $Hg(OTeF_5)_2$ unit are listed; the modes involving XeF_2 are fully described. See Table S6.3 for a complete listing of frequencies and more detailed descriptions of the assignments. The abbreviations denote out-of-plane (o.o.p.) and in-plane (i.p.) where the planes may contain the (Te–O–Hg–O–Te) groups or the two XeF_2 molecules, umbrella (umb), equatorial (e), axial (a), stretch (ν), bend (δ), twist (ρ_t), wag (ρ_w), and rock (ρ_r). The subscript "small" denotes that the bracketed vibrational mode makes a small contribution relative to the other coupled vibrations. The atom labeling scheme is given in Figure 6.7.

Table 6.6. Experimental Raman Frequencies and Intensities for $Hg(OTeF_5)_2 \cdot 1.5KrF_2$ and Calculated Vibrational Frequencies and Intensities for $[Hg(OTeF_5)_2]_3 \cdot 2KrF_2$

exptl[a,b,c] **$Hg(OTeF_5)_2$-$\cdot 1.5KrF_2$**	**calcd**[a,d] **$[Hg(OTeF_5)_2]_3[KrF_2]_2$**	*assgnts*[e]
844(3)	826(9)[165]	$[\nu(Hg\text{-}O) - \nu(Te\text{-}O)]$
821(2)	812(2)[358]	
723(1)	723(16)[15]	$[\nu(Te\text{-}F_e)]$
	718(4)[92]	
	717(5)[294]	
717(<1)	715(13)[215]	
715(<1)	715(2)[186]	
709(1)	714(1)[32]	
704(1)	713(2)[195]	
	712(<1)[49]	
	693(1)[231]	
688(14)	706(12)[7]	$[\nu(Te\text{-}F_a)]$
683, sh	700(2)[223]	
	699(20)[4]	
	646(24)[12]	$[\nu(Te\text{-}F_e)]$
645(4)	642(3)[8]	
642, sh	641(2)[9]	
638(1)	627(11)[22]	
624(2)	624(2)[32]	
	623(4)[3]	
558(1)	574(2)[342]	$[\nu(Kr_{13}\text{-}F_{17}) - \nu(Kr_{13}\text{-}F_{20})] + [\nu(Kr_{16}\text{-}F_{23}) - \nu(Kr_{16}\text{-}F_{40})]$
553(<1)	560(6)[339]	$[\nu(Kr_{13}\text{-}F_{17}) - \nu(Kr_{13}\text{-}F_{20})] - [\nu(Kr_{16}\text{-}F_{23}) - \nu(Kr_{16}\text{-}F_{40})]$
484(3)	527(2)[34]	$[\nu(Hg\text{-}O) + \nu(Te\text{-}O)]$
	513(61)[5]	$[\nu(Kr_{13}\text{-}F_{17}) + \nu(Kr_{13}\text{-}F_{20})] + [\nu(Kr_{16}\text{-}F_{23}) + \nu(Kr_{16}\text{-}F_{40})]$
468(100)	512(100)[5]	$[\nu(Kr_{13}\text{-}F_{17}) + \nu(Kr_{13}\text{-}F_{20})] - [\nu(Kr_{16}\text{-}F_{23}) + \nu(Kr_{16}\text{-}F_{40})]$
458(17)	505(69)[37]	$[\nu(Hg\text{-}O) + \nu(Te\text{-}O)]$
	337(<1)[35]	
334(1)	335(<1)[14]	$\delta(TeF_{4e})_{umb}$
	334(<1)[102]	
329(1)	331(<1)[62]	$\delta(O\text{-}Hg\text{-}O)_{o.o.p}$ / $\delta(TeF_{4e})_{umb}$
	330(<1)[102]	$\delta(TeF_{4e})_{umb}$ / $\rho_w(O\text{-}Te\text{-}F)$ / $\rho_w(F\text{-}Te\text{-}F)$ / $\delta(O\text{-}Hg\text{-}O)_{o.o.p}$
	328(1)[133]	$\delta(O\text{-}Te\text{-}F)$ / $\delta(F\text{-}Te\text{-}F)$ / $\rho_w(F\text{-}Te\text{-}F)$
	326(<1)[70]	$\delta(O\text{-}Te\text{-}F)$ / $\delta(F\text{-}Te\text{-}F)$ / $\rho_w(F\text{-}Te\text{-}F)$ / $\rho_w(O\text{-}Hg\text{-}O)$
324(1)	326(<1)[22]	$\delta(O\text{-}Hg\text{-}O)_{o.o.p.}$ / $\delta(O\text{-}Te\text{-}F)$ / $\delta(F\text{-}Te\text{-}F)$ /
	326(1)[62]	$\rho_w(O\text{-}Te\text{-}F)$ / $\rho_w(F\text{-}Te\text{-}F)$
		$\delta(O\text{-}Te\text{-}F)$ / $\delta(F\text{-}Te\text{-}F)$ / $\rho_w(F\text{-}Te\text{-}F)$
	322(<1)[25]	$\delta(O\text{-}Te\text{-}F)$ / $\delta(F\text{-}Te\text{-}F)$ / $\rho_w(F\text{-}Te\text{-}F)$
320(1)	321(<1)[19]	$\delta(F\text{-}Te\text{-}F)$ / $\rho_w(F\text{-}Te\text{-}F)$
	320(<1)[22]	$\delta(F\text{-}Te\text{-}F)$ / $\rho_w(F\text{-}Te\text{-}F)$ / $\delta(O\text{-}Te\text{-}F)$
	320(2)[21]	$\delta(F\text{-}Te\text{-}F)$ / $\delta(O\text{-}Te\text{-}F) + \rho_w(F\text{-}Te\text{-}F)$
314(1)	316(1)[20]	$\rho_t(O\text{-}Hg\text{-}O)$ / $\delta(F\text{-}Te\text{-}F)$ / $\delta(F\text{-}Te\text{-}O)$
311(1)	316(<1)[18]	$\delta(F\text{-}Te\text{-}F)$ / $\rho_w(F\text{-}Te\text{-}F)$ / $\rho_t(O\text{-}Hg\text{-}O)$
304(2)	293(2)[<1]	$\delta(F\text{-}Te\text{-}F)$
291, sh	291(1)[<1]	

Table 6.6 continued …

260(1)		266(<1)[25]	$\delta(F_{17}\text{-}Kr_{13}\text{-}F_{20})_{o.o.p.}$
237(<1)	{	254(<1)[18]	$\delta(F_{17}\text{-}Kr_{13}\text{-}F_{20})_{i.p.} + \delta(F_{23}\text{-}Kr_{16}\text{-}F_{40})_{o.o.p.}$
		252(1)[22]	$\delta(F_{17}\text{-}Kr_{13}\text{-}F_{20})_{i.p.} + \delta(F_{23}\text{-}Kr_{16}\text{-}F_{40})_{o.o.p.}$
		252(<1)[10]	$\delta(F_{17}\text{-}Kr_{13}\text{-}F_{20})_{i.p.} - \delta(F_{23}\text{-}Kr_{16}\text{-}F_{40})_{o.o.p}$
n.o.	{	244(<1)[5]	$\delta(F_{17}\text{-}Kr_{13}\text{-}F_{20})_{i.p.}$ / δ(F-Te-F) / ρ_w(F-Te-F)
		243(<1)[3]	ρ_t(F-Te-F) / ρ_r(F-Te-F) / ρ_w(F-Te-F)
225(1)		231(3)[4]	δ(F-Te-F) / ρ_w(F-Te-F)
n.o.	{	211(<0.1)[<1]	} ρ_w(F-Te-F)
		209(<0.1)[<1]	
n.o.		202(<0.1)[<1]	ρ_w(O-Te-F) / ρ_w(F-Te-F)
n.o.		192(<1)[<1]	ρ_w(O-Te-F) / ρ_w(F-Te-F)
		161(<0.1)[6]	ρ_r(F-Te-F) / ρ_w(F-Te-F)
138, sh 130, sh		129(2)[<1]	$\rho_r(TeF_{2e}F_a)$ / ρ_w(F-Te-F)
123(7)		102(2)[7]	$\rho_t(F_{20}\text{-}Kr_{13}\text{-}F_{17}) + \rho_r(Te_{33}\text{-}F_3,F_4,F_5) - \rho_r(Te_6\text{-}F_9,F_{10},F_{11})$
		98(2)[3]	$\rho_t(F_{20}\text{-}Kr_{13}\text{-}F_{17})$ / $\rho_r(TeF_{2e}F_a)$ / $\delta(O\text{-}Hg\text{-}O)_{i.p.}$
101(3)		95(4)[4]	$\rho_t(F_{20}\text{-}Kr_{13}\text{-}F_{17})$ / $\rho_r(TeF_{2e}F_a)$
n.o.	{	94(1)[2]	$\rho_r(F_{20}\text{-}Kr_{13}\text{-}F_{17})$ / $\delta(O\text{-}Hg\text{-}O)_{i.p.}$ / $\rho_r(F_{23}\text{-}Kr_{16}\text{-}F_{40})$
		91(1)[5]	$\delta(O\text{-}Hg\text{-}O)_{o.o.p.}$ / $\rho_r(F_{20}\text{-}Kr_{13}\text{-}F_{17})_{small}$
		78(3)[2]	$\rho_t(F_{40}\text{-}Kr_{16}\text{-}F_{23})$
		77(7)[<1]	$\rho_r(F_{40}\text{-}Kr_{16}\text{-}F_{23})$
		70(2)[1]	$\rho_r(F_{17}\text{-}Kr_{13}\text{-}F_{20})$
		67(<1)[1]	δ(Te-O-Hg)

[a] Frequencies are given in cm^{-1}. [b] Values in parentheses denote relative Raman intensities. The Raman spectrum was recorded in a quartz sample tube at −155 °C using 1064-nm excitation. A band at 464(21) cm^{-1} (not listed, see Figure 6.5) is assigned to excess KrF_2. [c] The abbreviations denote shoulder (sh) and not observed (n.o.). [d] Values in parentheses denote calculated Raman intensities ($Å^4$ amu^{-1}), whereas values in square brackets denote calculated infrared intensities (km mol^{-1}). [e] Assignments are for the energy-minimized geometry calculated at the PBE0/def2-TZVPP level. Only simplified mode assignments (separated by the symbol "/") that involve the central $Hg(OTeF_5)_2$ unit are listed; the modes involving KrF_2 are fully described. See Table S6.4 for a complete listing of frequencies and more detailed descriptions of the assignments. The abbreviations denote out-of-plane (o.o.p.) and in-plane (i.p.) where the planes may contain the (Te–O–Hg–O–Te) groups or the two KrF_2 molecules, umbrella (umb), equatorial (e), axial (a), stretch (ν), bend (δ), twist (ρ_t), wag (ρ_w) and rock (ρ_r) modes. The subscript "small" denotes that the bracketed vibrational mode makes a small contribution relative to the other coupled vibrations. The atom labeling scheme is given in Figures 6.7.

of the intra-molecular coupled modes that occur among $Hg(OTeF_5)_2$ units and/or NgF_2 units. The following frequency assignments and related discussions exclusively refer to the modes associated with the central $Hg(OTeF_5)_2$ units of gas-phase $[Hg(OTeF_5)_2]_3$ and $[Hg(OTeF_5)_2]_3 \cdot 2NgF_2$ and with the NgF_2 ligands. The calculated frequencies of $\nu_{as}(NgF_2)$, $\nu_s(NgF_2)$, and $\delta(KrF_2)$ of the free NgF_2 molecules were overestimated, whereas that of $\delta(XeF_2)$ was close to the experimental value (Tables S6.5 and S6.6). This pattern aided in the assignment of the corresponding calculated frequencies of the $[Hg(OTeF_5)_2]_3 \cdot 2NgF_2$ complexes.

6.2.3.1. $Hg(OTeF_5)_2$. The vibrational assignments of $Hg(OTeF_5)_2$ were initially based on a gas-phase monomeric model (C_2 symmetry, Table S6.1, and Figure 6.6a). The 39 vibrations of monomeric $Hg(OTeF_5)_2$ span the irreducible representations $\Gamma_{vib} = 20A + 19B$, which are Raman and infrared active.

The calculated vibrational frequencies and intensities at the B3LYP and PBE0 levels of theory using the def2-TZVPP and aug-cc-PTVZ basis sets reproduce the experimental trends, but the $Hg(OTeF_5)_2$ frequencies obtained at the B3LYP level (Table S6.1) were significantly underestimated when compared with the frequencies calculated at the PBE0 level. Consequently, calculations for $[Hg(OTeF_5)_2]_3$ and $[Hg(OTeF_5)_2]_3 \cdot 2NgF_2$ were carried out at the PBE0 level using only the def2-TZVPP basis set due to the large sizes of these molecules. Although most of the observed frequencies and intensities could be accounted for using the gas-phase monomeric model, the observation of additional bands that are not accounted for by the monomeric model suggested that this model was too limited. Moreover, the *anti*-conformation of the

F_5TeO–groups in the gas-phase monomer differs from that of the solid-state *gauche*-conformation.

The use of the trimeric model, $[Hg(OTeF_5)_2]_3$, (Figure 6.6b) addresses these differences by reproducing the *gauche*-conformation and reveals the additional bands that were not accounted for in the monomeric model arise from intermolecular couplings among the $Hg(OTeF_5)_2$ units (see above and Tables 6.4 and S6.2).

The *ν*(Hg-O) and *ν*(Te-O) stretches couple, giving rise to eight vibrational modes. Four of these modes are derived from "symmetric" [ν(Hg-O) + ν(Te-O)]-type stretching modes. The [$\nu(Hg_{16}\text{-}O_{22}) + \nu(Te_{17}\text{-}O_{22})$] mode is in-phase coupled to [$\nu(Hg_{16}\text{-}O_{37}) + \nu(Te_{32}\text{-}O_{37})$] and is also coupled in-phase (481 cm^{-1}) and out-of-phase (472 cm^{-1}) with the analogous modes of the two outer $Hg(OTeF_5)_2$ units of the trimer. The totally in-phase coupled mode at 481 cm^{-1} is the second most intense band in the spectrum. The calculated frequencies (506 and 516 cm^{-1}, respectively) are in good agreement with the observed values. As in the experimental spectrum, the calculated Raman intensity of the 506 cm^{-1} band is also very intense. The [$\nu(Hg_{16}\text{-}O_{22}) + \nu(Te_{17}\text{-}O_{22})$] mode is also out-of-phase coupled to the [$\nu(Hg_{16}\text{-}O_{37}) + \nu(Te_{32}\text{-}O_{37})$] mode (511 cm^{-1}). The [$\nu(Hg_{16}\text{-}O_{22}) + \nu(Te_{17}\text{-}O_{22})$] mode is further coupled in-phase and out-of-phase (530 cm^{-1}) and out-of-phase and in-phase (528 cm^{-1}) to the analogous modes of the two terminal $Hg(OTeF_5)_2$ units. The agreement between the observed (511 cm^{-1}) and calculated values (530 and 528 cm^{-1}) is again very good. Four modes are predicted which involve the "asymmetric" [$\nu(Hg_{16}\text{-}O_{22}) - \nu(Te_{17}\text{-}O_{22})$] and [$\nu(Hg_{16}\text{-}O_{37}) - \nu(Te_{32}\text{-}O_{37})$] stretching modes and are expected to be out-of-phase (793 cm^{-1}) and in-phase (787, 806 and 824 cm^{-1}) coupled.

The latter three modes arise from additional coupling with the analogous modes of the terminal $Hg(OTeF_5)_2$ units. The calculated band at 824 cm^{-1} is expected to be relatively intense and is observed as a medium-intensity band at 825 cm^{-1}. The weak Raman band at 801 cm^{-1} has been assigned to the weak modes calculated at 793 and 787 cm^{-1}. The calculated mode at 806 cm^{-1} was not observed and is predicted to be weak in the Raman spectrum.

The above frequencies and relative intensities are reminiscent of, but are at higher frequency than those observed for the coupled *ν*(Xe-O) and *ν*(Te-O) stretches in $Xe(OTeF_5)_2$ (440/445 cm^{-1}, 796/788 cm^{-1}, and 730 cm^{-1}).[32] The band analogous to the low-intensity band of $Hg(OTeF_5)_2$ at 511 cm^{-1}, is predicted at 547 cm^{-1} in $Xe(OTeF_5)_2$, i.e., $[\nu(Xe\text{-}O) + \nu(Te\text{-}O)] - [\nu(Xe\text{-}O') - \nu(Te'\text{-}O')] + \delta(OXeO')$, but was not observed.[32] The O_{22}-Hg_{16}-O_{37} bending mode of $Hg(OTeF_5)_2$ is observed as a weak band at 331 cm^{-1} (calcd, 332 cm^{-1}) and its frequency is very similar to that of δ(O-Xe-O) (328 cm^{-1}) in $Xe(OTeF_5)_2$.[32]

The bands between 624 and 735 cm^{-1} are assigned to stretching modes of the TeF_5 groups and are in good agreement with the calculated values (640–726 cm^{-1}) and with those observed in $Xe(OTeF_5)_2$ (635–710 cm^{-1}).[32] In both cases, the coupled axial ν_s(Te-F_a) modes occur as strong bands in the Raman spectrum ($Hg(OTeF_5)_2$, 709 cm^{-1}; $Xe(OTeF_5)_2$, 690 cm^{-1}). The coupled umbrella mode, $[\delta(Te_{17}F_{4e})_{umb} + \delta(Te_{32}F_{4e'})_{umb}]$, is observed as a weak band at 349 cm^{-1} (calcd, 341 cm^{-1}) that also in-phase couples with the analogous modes of the two outer $Hg(OTeF_5)_2$ units. This mode was not observed for $Xe(OTeF_5)_2$ (calcd, 360 cm^{-1}).[32]

6.2.3.2. $Hg(OTeF_5)_2 \cdot 1.5NgF_2$. Spectral assignments were aided by obtaining the energy-minimized geometries of the unknown model complexes, $[Hg(OTeF_5)_2]_3 \cdot 2NgF_2$, and their vibrational frequencies at the PBE0 level using the def2-TZVPP basis set (Tables 6.5, 6.6, S6.3 and S6.4). These approximations reliably reproduced the experimental trends. Overall, couplings among the vibrational modes of the XeF_2 complex are more extensive than among the vibrational modes of the KrF_2 complex.

As observed for $[Hg(OTeF_5)_3]$, the two highest frequency bands (Xe, 853 and 825 cm^{-1}; Kr, 844 and 821 cm^{-1}) involve "asymmetric" $[\nu(Hg_{12}\text{-}O_{28}) - \nu(Te_{14}\text{-}O_{28})]$ and $[\nu(Hg_{12}\text{-}O_{31}) - \nu(Te_{15}\text{-}O_{31})]$ stretches which are in-phase and out-of-phase coupled. These bands are shifted to higher frequencies relative to the analogous Raman bands of solid $Hg(OTeF_5)_2$ (825 and 801 cm^{-1}), a trend that is also observed for the calculated frequencies (Xe, 828 and 817/815 cm^{-1}; Kr, 826 and 812 cm^{-1}; $[Hg(OTeF_5)_2]_3$: 824/806 and 787/793 cm^{-1}). These shifts are noteworthy because the experimental Hg–O and Te–O bond lengths are equal within $\pm 3\sigma$ in the crystal structures of $Hg(OTeF_5)_2$ and $Hg(OTeF_5)_2 \cdot 1.5NgF_2$. As observed in earlier studies, the present studies also illustrate that Raman spectroscopy can be a more sensitive probe than X-ray crystallography for the detection of small bond strength/bond length differences. The high-frequency shifts of the XeF_2 adduct are anticipated because the Hg---F(NgF) contacts are shorter in the XeF_2 complex (2.606(5) and 2.623(4) Å) than in the KrF_2 complex (2.664(3) and 2.675(3) Å) (see X-ray Crystallography). The experimental stretching frequencies of the axial fluorine atoms are also affected, shifting to lower frequency (Xe, 685 cm^{-1}; Kr, 683 and 688 cm^{-1}) relative to $Hg(OTeF_5)_2$ (709 cm^{-1}). The corresponding calculated frequencies also follow

the same trend (Xe: 699, 705 cm^{-1}; Kr: 699, 700, 706 cm^{-1}; $[Hg(OTeF_5)_2]_3$: 707, 709 cm^{-1}). Bands involving ν(Te-F_e) stretches are not predicted to be significantly affected by complex formation (see X-ray Crystallography); moreover, the Te–F_e bond lengths are equal within ±3σ among all crystal structures. In practice, these bands show very little, if any, change among the complexes and $Hg(OTeF_5)_2$ (Xe: 702–753, 623–640 cm^{-1}; Kr: 704–723, 624–645 cm^{-1}; $Hg(OTeF_5)_2$: 735, 624–699 cm^{-1}). The calculated frequencies also remain within the same ranges (Xe: 695–721, 622–644 cm^{-1}; Kr: 693–723, 623–646 cm^{-1}; $[Hg(OTeF_5)_2]_3$: 724–726, 640–719 cm^{-1}). The frequencies of the $\delta(TeF_{4e})_{umb}$ umbrella modes also remain essentially unchanged. The bands below 332 (Xe) and 329 cm^{-1} (Kr) are assigned to coupled deformation and torsional modes and are well reproduced by the calculations (Tables 6.5 and 6.6). Modes that are exclusively of the "symmetric" [ν(Hg-O) + ν(Te-O)]-type occur in a frequency range similar to that of $Hg(OTeF_5)_2$. As observed for the "asymmetric" [ν(Hg-O) – ν(Te-O)]-type modes, the "symmetric" modes occur at higher frequencies for the XeF_2 complex (exptl, 474/478 and 508 cm^{-1}) than those of the KrF_2 complex (exptl, 458 and 484 cm^{-1}). In the case of the XeF_2 complex, a third band occurs at 445 cm^{-1} which has an additional coupling with $\nu(Xe_{16}\text{-}F_{23})$ in the theoretical model. In the KrF_2 complex, only two [$\nu(Hg\text{-}O) + \nu(Te\text{-}O)$]-type modes are predicted where [$\nu(Hg_{12}\text{-}O_{28}) + \nu(Te_{14}\text{-}O_{28})$] is only coupled in-phase (exptl, 458 cm^{-1}; calcd, 505 cm^{-1}) or out-of-phase (exptl, 484 cm^{-1}; calcd, 527 cm^{-1}) with [$\nu(Hg_{12}\text{-}O_{31}) + \nu(Te_{15}\text{-}O_{31})$]. In the XeF_2 complex, only one mode is predicted in which [$\nu(Hg_{12}\text{-}O_{28}) + \nu(Te_{14}\text{-}O_{28})$] is out-of-phase coupled with [$\nu(Hg_{12}\text{-}O_{31}) + \nu(Te_{15}\text{-}O_{31})$] (exptl, 508 cm^{-1}; calcd, 524 cm^{-1}). Two modes are predicted where [$\nu(Hg_{12}\text{-}O_{28})$ +

$\nu(Te_{14}\text{-}O_{28})]$ is in-phase coupled with $[\nu(Hg_{12}\text{-}O_{31}) + \nu(Te_{15}\text{-}O_{31})]$ (exptl, 478/474 and 445 cm^{-1}; calcd, 502 and 499 cm^{-1}) because, in both cases, there is additional coupling with $\nu(Xe_{16}{-}F_{23})$ and/or analogous modes of the terminal $Hg(OTeF_5)_2$ units.

The calculated vibrational displacements show that the stretching modes of the bridging KrF_2 and XeF_2 units are extensively coupled, and reveal differences between their inter- and intra-ligand couplings in their respective complexes. The four coupled modes of the KrF_2 complex are each comprised of inter- and intra-ligand coupling components whereas there is less intra-ligand coupling in the XeF_2 complex. Instead, some coupling with the terminal $Hg(OTeF_5)_2$ units occurs. Coupling among the stretching modes of the NgF_2 units in the $[BrOF_2][AsF_6]\cdot 2XeF_2$[4] and $[BrOF_2][AsF_6]\cdot 2KrF_2$[15] complexes have also been observed.

The modes derived from the symmetric (Raman-active and infrared-inactive) stretches of the free NgF_2 molecules, i.e., $[\nu(Ng_{13}\text{-}F_{17}) + \nu(Ng_{13}\text{-}F_{20})]$ and $[\nu(Ng_{16}\text{-}F_{23}) + \nu(Ng_{16}\text{-}F_{40})]$, are expected to occur at lower frequency than those derived from the asymmetric stretching mode of free NgF_2, i.e., $[\nu(Ng_{13}\text{-}F_{17}) - \nu(Ng_{13}\text{-}F_{20})]$ and $[\nu(Ng_{16}\text{-}F_{23}) - \nu(Ng_{16}\text{-}F_{40})]$. The "symmetric" modes in the KrF_2 complex are expected to in-phase couple, $[\nu(Kr_{13}\text{-}F_{17}) + \nu(Kr_{13}\text{-}F_{20})] + [\nu(Kr_{16}\text{-}F_{23}) + \nu(Kr_{16}\text{-}F_{40})]$, and out-of-phase couple, $[\nu(Kr_{13}\text{-}F_{17}) + \nu(Kr_{13}\text{-}F_{20})] - [\nu(Kr_{16}\text{-}F_{23}) + \nu(Kr_{16}\text{-}F_{40})]$. The latter modes were calculated at 512 and 513 cm^{-1}, and are assigned to a single band at 468 cm^{-1}, the most intense band in the Raman spectrum. In the XeF_2 complex, the totally in-phase analogue, $[\nu(Xe_{13}\text{-}F_{17}) + \nu(Xe_{13}\text{-}F_{20})] + [\nu(Xe_{16}\text{-}F_{23}) + \nu(Xe_{16}\text{-}F_{40})]$, is observed at 501 cm^{-1} and is also a strong band. In addition, there are two bands corresponding to the out-of-phase

stretching mode, [ν(Xe_{13}-F_{17})] − [ν(Xe_{16}-F_{23})] (489 cm^{-1}) and [ν(Xe_{13}-F_{20})] − [ν(Xe_{16}-F_{40})] (508 cm^{-1}). These frequencies are comparable to the Raman-active ν_s(Ng-F_2) mode of free NgF_2 (Xe, 494 cm^{-1};[37] Kr, 464 cm^{-1})[38] and are in accordance with the observed Ng–F bond lengths (Xe, 1.981(4) – 2.012(4) Å and Kr, 1.883(3) – 1.897(3) Å in the complexes; Xe, 1.999(4) Å,[3] and Kr, 1.894(5) Å,[2] for free NgF_2). The corresponding calculated NgF_2 frequencies and Ng–F bond lengths of the complexes and free NgF_2 follow the same trend (Xe: 516, 521, 510 cm^{-1}, 1.991–2.003 Å and Kr: 513, 512 cm^{-1}, 1.868–1.878 Å; free XeF_2: 530 cm^{-1}, 1.980 Å and free KrF_2: 519 cm^{-1}, 1.865 Å). In both complexes, the "symmetric" stretching mode appears at slightly higher frequency than the symmetric stretching mode of free NgF_2. The "symmetric" stretch of the XeF_2 complex appears at lower frequency than other "symmetric" stretching modes of the bridging XeF_2 molecules in the Cd^{2+} coordination complexes, $Cd(XeF_2)_4(AsF_6)_2$ (521 cm^{-1})[10] and $Cd(XeF_2)_5(PF_6)_2$ (521 cm^{-1}).[11]

The bands at 558 and 553 (Kr) cm^{-1} and 518 (Xe) cm^{-1} are assigned to NgF_2 stretching modes that are derived from the asymmetric (infrared-active and Raman-inactive) stretches of the free NgF_2 molecules. In order to understand why the formally Raman inactive bands in free NgF_2 are observed in the Raman spectra of both NgF_2 complexes, the positioning of the two crystallographically inequivalent NgF_2 molecules in the crystal structures must be taken into account. One NgF_2 molecule is positioned on an inversion center, so that the vibrational activities of the corresponding stretching modes will be the same as those of free NgF_2, i.e., the symmetric stretch will be Raman active and the asymmetric stretch will be infrared active. The second NgF_2 molecule is on

a general position, resulting in two crystallographically inequivalent Ng–F bonds. As a result, both coupled modes derived from the asymmetric stretch of free NgF_2 will be Raman and infrared active. The $[Hg(OTeF_5)_2]_3 \cdot 2NgF_2$ models (C_1 symmetry) display this behavior.

The "asymmetric" NgF_2 stretches are coupled in-phase, $[\nu(Ng_{13}\text{-}F_{17}) - \nu(Ng_{13}\text{-}F_{20})] + [\nu(Ng_{16}\text{-}F_{23}) - \nu(Ng_{16}\text{-}F_{40})]$ (Xe, 518 cm^{-1}; Kr, 558 cm^{-1}), and out-of-phase, $[\nu(Ng_{13}\text{-}F_{17}) - \nu(Ng_{13}\text{-}F_{20})] - [\nu(Ng_{16}\text{-}F_{23}) - \nu(Ng_{16}\text{-}F_{40})]$ (Xe, 518 cm^{-1}; Kr, 553 cm^{-1}). These "asymmetric" modes occur at lower frequencies than their infrared-active asymmetric counterparts in free XeF_2 (555 cm^{-1})[37] and KrF_2 (580 cm^{-1}).[39] This trend is reproduced by the calculations (Xe, 521/524 and 538/534 cm^{-1}; Kr, 574 and 560 cm^{-1} for NgF_2 in the complexes; Xe, 568 cm^{-1}; Kr, 607 cm^{-1} for free NgF_2). It is noteworthy that, although the XeF_2 bridging molecules in $Cd(XeF_2)_4(AsF_6)_2$,[10] $Cd(XeF_2)_5(PF_6)_2$,[11] $Ca(XeF_2)_n(AsF_6)_2$ (n = 4, 2.5),[40] $Ca_2(XeF_2)_9(AsF_6)_4$,[41] $Ca(XeF_2)_5(PF_6)_2$,[11] $Sr_3(XeF_2)_{10}(PF_6)_6$,[8] and $Pb_3(XeF_2)_{11}(PF_6)_6$[8] also have two crystallographically inequivalent Xe–F bonds, their "asymmetric" XeF_2 stretches were not identified.

As previously observed for $[BrOF_2][AsF_6] \cdot 2NgF_2$,[4,15] the double degeneracy of the NgF_2 bending modes of free NgF_2 (ν_2, Π_u) is removed when NgF_2 is asymmetrically fluorine bridged to mercury, resulting in splitting into out-of-plane, $\delta(NgF_2)_{o.o.p.}$ and in-plane, $\delta(NgF_2)_{i.p.}$ modes with respect to the plane containing both NgF_2 ligands. The bending modes are observed at 223 and 241 cm^{-1} (Xe) and at 237 and 260 cm^{-1} (Kr) and are slightly shifted to higher frequencies relative to those of free XeF_2 (213 cm^{-1})[37] and free KrF_2 (236 cm^{-1}).[39] The calculated and experimental frequencies are also in good

agreement (Xe: 218, 219, 221, and 236 cm^{-1}; Kr: 252, 252, 254, and 266 cm^{-1} for NgF_2 in the complexes; cf., Xe, 215 cm^{-1}; Kr, 250 cm^{-1} in free NgF_2).

6.2.4. Computational Results

Unless otherwise noted, the following discussion refers to the central units of the gas-phase model compounds, $[Hg(OTeF_5)_2]_3$ and $[Hg(OTeF_5)_2]_3 \cdot 2NgF_2$.

6.2.4.1. Calculated Geometries

(i) $Hg(OTeF_5)_2$ and $[Hg(OTeF_5)_2]_3$. The gas-phase geometry of monomeric $Hg(OTeF_5)_2$ (C_2) (Figure 6.6a) was optimized at the B3LYP and PBE0 levels of theory using the def2-TZVPP and aug-cc-PTVZ basis sets, resulting in stationary points with all frequencies real (Table S6.1). The calculated bond lengths and angles are provided in Table S6.7. Although both levels of theory well reproduced the observed trends (see Raman Spectroscopy), better agreement was obtained at the PBE0 level. All attempts to optimize the monomeric $Hg(OTeF_5)_2$ unit, regardless of the starting geometry, resulted in an *anti*-conformation (C_2 symmetry) resembling that observed (C_{2h} in the crystal structure) and calculated (C_2) for $Xe(OTeF_5)_2$.[32] The authors were unable to reproduce the previously reported[30] calculated C_{2h} geometry for $Hg(OTeF_5)_2$. However, the *anti*-conformation of the gas-phase $Hg(OTeF_5)_2$ monomer contrasts with the *gauche*-conformation observed in the crystal structure. The optimization of the presently unknown trimer, $[Hg(OTeF_5)_2]_3$ (Figures 6.6b), using the PBE0/def2-TZVPP method also resulted in a stationary point with all frequencies real (Table S6.2). This model reproduced the observed *gauche*-conformation of the central $Hg(OTeF_5)_2$ molecule

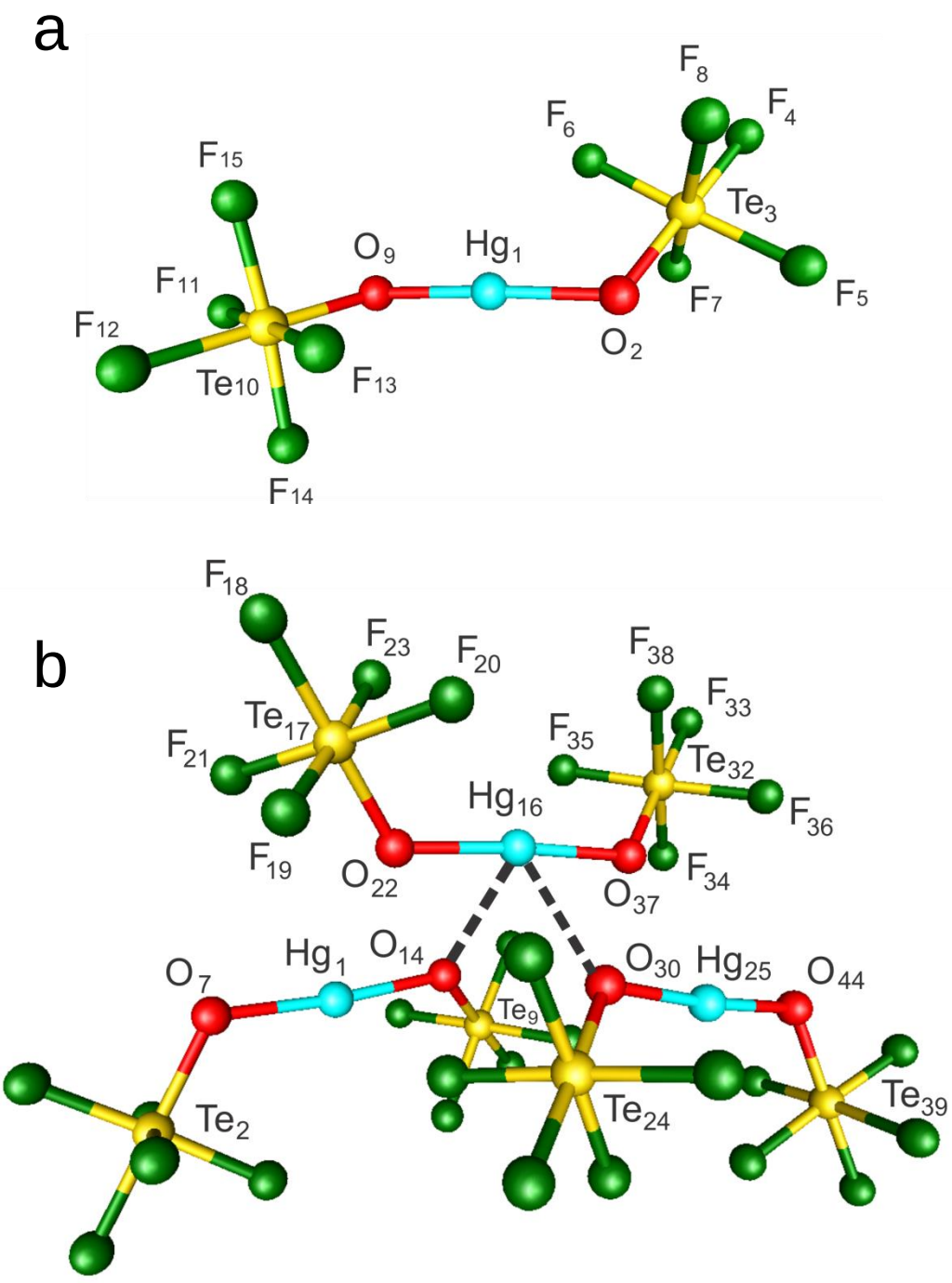

Figure 6.6. The gas-phase, energy-minimized geometries of (**a**) monomeric $Hg(OTeF_5)_2$ (C_2) and (**b**) trimeric $[Hg(OTeF_5)_2]_3$ (C_1) calculated at the PBE0/def2-TZVPP level of theory. The long contacts (dashed lines) between the Hg(II) atom of the central $Hg(OTeF_5)_2$ unit and two oxygen atoms of two adjacent terminal $Hg(OTeF_5)_2$ units are shown in (**b**).

showing that crystal packing and accompanying Hg---O contacts (2.737 Å) with neighboring terminal $Hg(OTeF_5)_2$ molecules are likely major factors in stabilizing the solid-state *gauche*-conformation. This is supported by the fact that the two terminal $Hg(OTeF_5)_2$ units also retain the *gauche*-conformation with similar Hg---O contacts (2.775 Å). Because of its size, the hypothetical trimeric model was only calculated with the smaller basis set, def2-TZVPP.

In the trimer, the largest discrepancies from that observed are for the $Hg\text{---}O_{(1A,1C)}$ secondary bonding interactions (calcd, 2.737 Å; exptl, 2.641(7) Å) and the $O_{(1)}\text{–}Hg\text{---}O_{(1A,1C)}$ bond angles (calcd, 73.0 and 103.8º; exptl, 78.7 and 93.8(3)º). These differences are likely attributable to the model itself, where the Hg---F secondary contacts are absent for the central $Hg(OTeF_5)_2$ unit. Ideally, a total of five $Hg(OTeF_5)_2$ molecules would be required to reproduce all secondary contacts observed in the crystal structure. The calculated O–Hg–O bond angle (176.0º) is more open than the observed angle in $Hg(OTeF_5)_2$ (170.5(4)º) (see X-ray Crystallography), but is in close agreement with the O–Hg–O bond angle calculated for the $Hg(OTeF_5)_2$ monomer (calcd, 176.8º).

The Hg–O bond lengths of the calculated gas-phase $[Hg(OTeF_5)_2]_3$ molecule (2.008 Å) are in better agreement with the experimental bond length (2.016(6) Å) than the calculated Hg–O bond lengths of $Hg(OTeF_5)_2$ (1.976 Å). The Te–F and Te–O bond lengths are overall slightly shorter for the calculated structure of $[Hg(OTeF_5)_2]_3$ (1.832–1.855 Å, and 1.865 Å, respectively) when compared with those calculated for monomeric $Hg(OTeF_5)_2$ (1.835–1.866 Å, and 1.856 Å, respectively), but are also in better agreement with those observed for solid $Hg(OTeF_5)_2$ (Table 6.2).

(ii) $[Hg(OTeF_5)_2]_3 \cdot 2NgF_2$ (Ng = Xe, Kr). The calculated gas-phase geometries of the model complexes, $[Hg(OTeF_5)_2]_3 \cdot 2NgF_2$ (Ng = Xe, Kr) (Figures 6.7 and Table 6.7), were optimized at the PBE0 level of theory using the def2-TZVPP basis set, resulting in stationary points with all frequencies real (Tables S6.3 and S6.4). These systems were too large and demanding of CPU time to be optimized using the larger aug-cc-PTVZ basis set. The calculated structures of $[Hg(OTeF_5)_2]_3 \cdot 2NgF_2$ mimic the local environments of both $Hg(OTeF_5)_2$ and NgF_2 in the crystal structures of $Hg(OTeF_5)_2 \cdot 1.5NgF_2$. The central $Hg(OTeF_5)_2$ unit of the starting models take into account the two shorter Hg---F(NgF) contacts that are *trans* to one another. In the optimized geometries, the central $Hg(OTeF_5)_2$ units retained the *gauche*-conformation observed in the crystal structures, as was calculated for the central $Hg(OTeF_5)_2$ unit of $[Hg(OTeF_5)_2]_3$. The calculated models retained the two Hg---F(NgF) contacts to the central Hg atom (Xe, 2.724 and 2.723 Å; Kr, 2.762 and 2.754 Å), but optimized so that the Hg---F(NgF) secondary bonds are *cis* to one another with contact distances that better reproduce the longer Hg---F(NgF) contacts observed in the crystal structures (Xe, 2.701(5) Å ; Kr, 2.741(3) Å). In both the Kr and Xe models, one of the outer $Hg(OTeF_5)_2$ units optimized to a *syn*-conformation (Te–O–Hg–O–Te dihedral angles of 126.5º for Xe and 122.8º for Kr), when only a single, long secondary Hg---F(NgF) bond is present (Xe, 2.746 Å; Kr, 2.816 Å). In contrast, the other terminal $Hg(OTeF_5)_2$ unit optimized to a *gauche*-conformation presumably because the secondary Hg---F(NgF) contacts (Xe, 2.694 Å; Kr, 2.739 Å) are somewhat shorter and more covalent. These differences are reminiscent of those observed for the $[Hg(OTeF_5)_2]_3$ model (vide supra) and may also result from the model's inability to take into account the

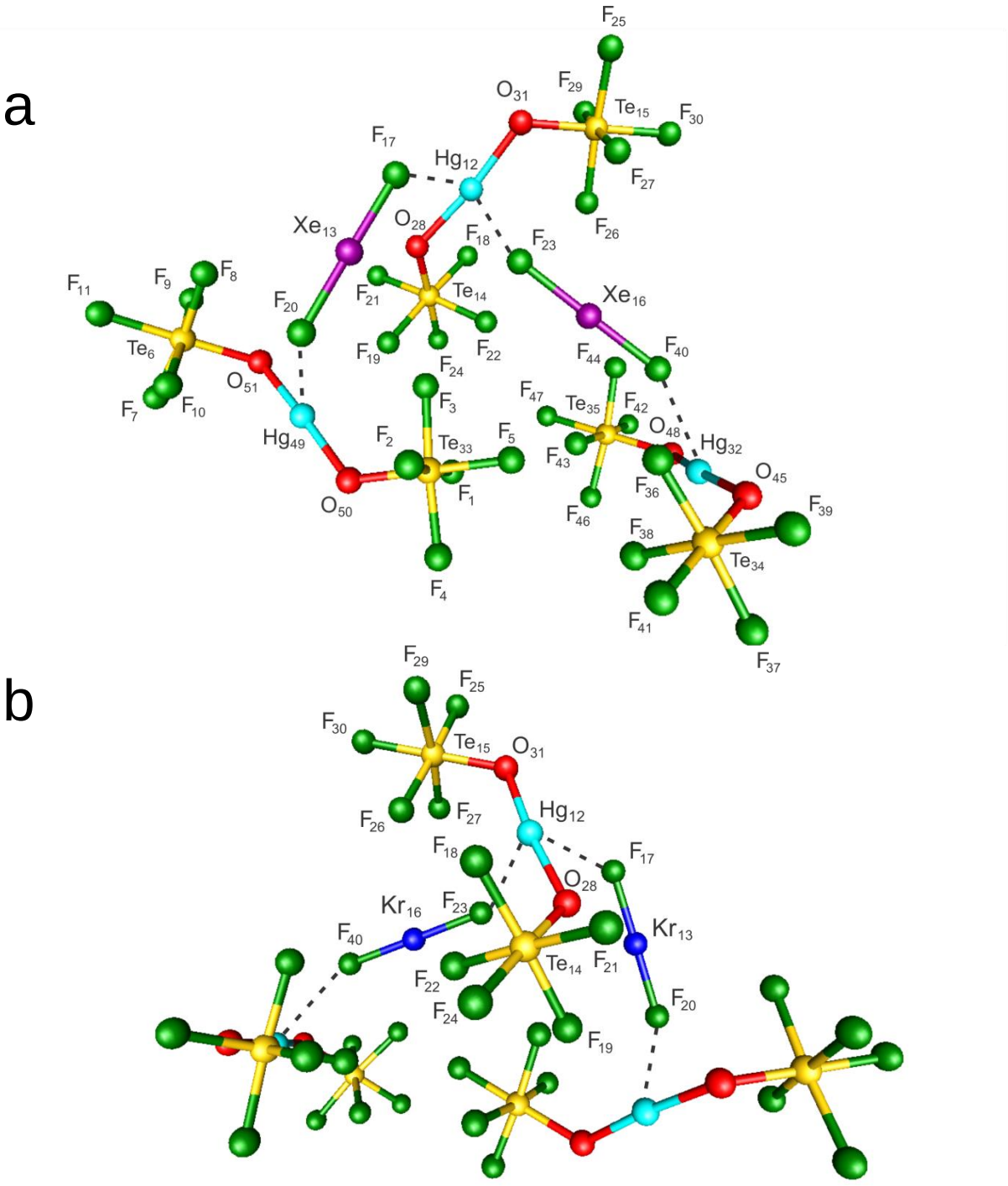

Figure 6.7. The gas-phase, energy-minimized geometry of **a)** $[Hg(OTeF_5)_2]_3 \cdot 1.5XeF_2$ and **b)** $[Hg(OTeF_5)_2]_3 \cdot 1.5KrF_2$; calculated at the PBE0/def2-TZVPP level of theory. The dashed lines show the contacts between the Hg(II) atom of the central $Hg(OTeF_5)_2$ unit and two fluorine atoms of two adjacent NgF_2 molecules.

Table 6.7. Calculated Geometrical Parameters[a] for $Hg(OTeF_5)_2 \cdot 1.5NgF_2$ (Ng = Xe, Kr)

	Xe	Kr		Xe	Kr
Bond Lengths (Å)					
$Hg_{12}–O_{31}$	1.991	1.988	$Te_{14}–F_{18}$	1.854	1.855
$Hg_{12}–O_{28}$	2.002	2.000	$Te_{14}–F_{24}$	1.834	1.833
$O_{31}–Te_{15}$	1.847	1.849	$Te_{14}–F_{22}$	1.854	1.851
$O_{28}–Te_{14}$	1.847	1.849	$Te_{14}–F_{21}$	1.839	1.840
$Te_{15}–F_{27}$	1.852	1.851	$Hg_{12}---F_{23}$	2.723	2.754
$Te_{15}–F_{29}$	1.843	1.843	$Hg_{12}---F_{17}$	2.724	2.762
$Te_{15}–F_{26}$	1.870	1.869	$Ng_{16}–F_{23}$	2.003	1.878
$Te_{15}–F_{25}$	1.836	1.835	$Ng_{16}–F_{40}$	1.991	1.869
$Te_{15}–F_{30}$	1.838	1.838	$Ng_{13}–F_{17}$	1.997	1.877
$Te_{14}–F_{19}$	1.855	1.855	$Ng_{13}–F_{20}$	1.993	1.868
Bond Angles (deg)					
$O_{31}–Hg_{12}–O_{28}$	173.6	173.7	$F_{26}–Te_{15}–F_{25}$	176.4	176.6
$Hg_{12}–O_{31}–Te_{15}$	122.4	122.4	$F_{27}–Te_{15}–F_{29}$	173.8	173.9
$Hg_{12}–O_{28}–Te_{14}$	123.6	122.4	$F_{24}–Te_{14}–F_{22}$	87.3	87.4
$O_{31}–Te_{15}–F_{27}$	93.1	93.0	$F_{24}–Te_{14}–F_{19}$	88.0	88.0
$O_{31}–Te_{15}–F_{29}$	92.9	92.8	$F_{24}–Te_{14}–F_{18}$	88.6	88.7
$O_{31}–Te_{15}–F_{26}$	92.5	92.5	$F_{24}–Te_{14}–F_{21}$	87.7	87.7
$O_{31}–Te_{15}–F_{25}$	91.0	90.9	$F_{22}–Te_{14}–F_{18}$	89.2	89.3
$O_{31}–Te_{15}–F_{30}$	179.8	179.8	$F_{18}–Te_{14}–F_{21}$	90.8	90.6
$O_{28}–Te_{14}–F_{19}$	90.3	90.4	$F_{21}–Te_{14}–F_{19}$	89.8	89.7
$O_{28}–Te_{14}–F_{18}$	93.0	92.9	$F_{19}–Te_{14}–F_{22}$	90.0	90.1
$O_{28}–Te_{14}–F_{24}$	178.3	178.4	$F_{22}–Te_{14}–F_{21}$	175.0	175.2
$O_{28}–Te_{14}–F_{22}$	92.9	92.7	$F_{19}–Te_{14}–F_{18}$	176.6	176.7
$O_{28}–Te_{14}–F_{21}$	92.1	92.1	$F_{40}–Ng_{16}–F_{23}$	179.2	179.3
$F_{30}–Te_{15}–F_{29}$	87.3	87.3	$F_{17}–Ng_{13}–F_{20}$	179.1	179.5
$F_{30}–Te_{15}–F_{26}$	87.6	87.7	$Ng_{16}–F_{23}---Hg_{12}$	138.4	136.9
$F_{30}–Te_{15}–F_{25}$	88.9	88.9	$Ng_{13}–F_{17}---Hg_{12}$	118.3	117.7
$F_{30}–Te_{15}–F_{27}$	86.8	86.9	$O_{31}–Hg_{12}---F_{23}$	97.3	96.5
$F_{29}–Te_{15}–F_{25}$	91.0	91.0	$O_{31}–Hg_{12}---F_{17}$	99.7	98.7
$F_{25}–Te_{15}–F_{27}$	90.7	90.7	$O_{28}–Hg_{12}---F_{23}$	87.1	87.3
$F_{27}–Te_{15}–F_{26}$	88.3	88.3	$O_{28}–Hg_{12}---F_{17}$	76.8	77.1
$F_{26}–Te_{15}–F_{29}$	89.6	89.6	$F_{17}---Hg_{12}---F_{23}$	75.8	77.6
Dihedral Angle (deg)					
$Te_{15}–O_{31}–Hg_{12}–O_{28}–Te_{14}$				31.0	34.0

[a] The atom labeling scheme corresponds to that used in Figures 6.7. All bond lengths and angles refer to the central $Hg(OTeF_5)_2$ unit and to the coordinated NgF_2 molecules of the unknown $[Hg(OTeF_5)_2]_3 \cdot 2NgF_2$ molecules calculated at the PBE0/def2-TZVPP level of theory.

additional Hg---F and Hg---O secondary contacts which are also present in the crystal structures (see X-ray Crystallography).

The complexed NgF_2 molecules are essentially linear with F–Ng–F angles (Xe, 179.2 and 179.1º; Kr, 179.5 and 179.3º) and Ng–F bond lengths (Xe, 1.991–2.003 Å; Kr, 1.868–1.878 Å) that well reproduce those observed in the crystal structures (Xe: 180 and 179.4(2)º, 1.981(4)–2.012(4) Å; Kr: 180 and 178.9(1)º, 1.883(3)–1.897(3) Å). The calculated Ng–F bond lengths are slightly underestimated for free NgF_2 (calcd: Xe, 1.980 Å and Kr, 1.865 Å; exptl: Xe, 1.999(4) Å [3] and Kr, 1.894(5) Å [2]).

The Hg–O (Xe: 1.991, 2.002 Å; Kr: 1.998, 2.000 Å) and Te–O (Xe: 1.847 Å; Kr: 1.849 Å) bond lengths are slightly under- and overestimated, respectively, compared to the Hg–O (Xe: 2.015(5), 2.037(5) Å; Kr: 2.017(3), 2.029(3) Å) and Te–O (Xe: 1.815(5), 1.811(6) Å; Kr: 1.819(3), 1.836(3) Å) bond lengths in the crystal structures of $Hg(OTeF_5)_2 \cdot 1.5NgF_2$. The calculated O–Hg–O bond angles (Xe, 173.6º; Kr, 173.7º) accurately reproduce the observed O–Hg–O bond angles (Xe, 173.0(2)º; Kr, 173.3(1)º) of the complexes whereas the Hg–O–Te bond angles (Xe: 122.4, 123.6º; Kr: 122.4º) are smaller than observed (Xe: 132.8(3), 127.2(3)º; Kr: 129.6(2), 126.5(1)º). This may reflect the elongation of the secondary bonding interactions and the absence of the two additional Hg---F and Hg---O contacts that are present in the crystal structure. This limitation in the model may contribute to the calculated Te−O−Hg−O−Te dihedral angles (Xe, 31.0º; Kr, 34.0º) which give a central $Hg(OTeF_5)_2$ unit that more closely approximates a *syn*-conformation than those observed in the solid state (Xe, 45.2(5)º; Kr, 50.3(3)º). All Te–F bond lengths (Xe, 1.834–1.870 Å; Kr, 1.833–1.869 Å) are in the same

ranges as those observed in the crystal structures (Xe, 1.814(5)–1.845(4) Å; Kr, 1.824(3)–1.848(3) Å) with the exception of the Te_{15}–F_{26} bond lengths (Xe, 1.870 Å; Kr, 1.869 Å), which are slightly longer.

6.2.4.2. Natural Bond Orbital (NBO) Analyses.

The NBO analyses reported in this section (Table S6.8) refer to the central $Hg(OTeF_5)_2$ units of $[Hg(OTeF_5)_2]_3$ and $[Hg(OTeF_5)_2]_3 \cdot 2NgF_2$ (Figures 6.6 and 6.7) unless noted otherwise.

When compared with gas-phase $Hg(OTeF_5)_2$, the charge on Hg is little affected by contacts with adjacent units within $[Hg(OTeF_5)_2]_3$. The situation is essentially the same when NgF_2 coordinates to $[Hg(OTeF_5)_2]_3$, providing the model complexes, $[Hg(OTeF_5)_2]_3 \cdot 2NgF_2$. The highest negative charges reside on the O atoms of $[Hg(OTeF_5)_2]_3$ (−1.208), with their charges becoming more positive upon NgF_2 coordination (Kr and Xe, −1.137). This is reflected by small increases in the Hg–O bond orders from 0.320 to 0.419/0.439 for KrF_2 and to 0.413/0.434 for XeF_2, and in the oxygen atom valencies from 0.948 to 1.025/1.015 for KrF_2 and to 1.023/1.011 for XeF_2. Little change in the Te–O bond orders and Te valencies occur upon NgF_2 coordination.

In each NgF_2 complex, there are small negative charge transfers from both NgF_2 ligands (Kr, 0.033/0.045; Xe, 0.040/0.052) to the central $Hg(OTeF_5)_2$ units (Kr, –0.038; Xe, –0.046) and combined charge transfers to the two terminal $Hg(OTeF_5)_2$ units (Kr, –0.040 ; Xe, –0.046). The small Hg---F(Ng) bridge bond orders (~0.06) and small degrees of NgF_2 polarization by the central $Hg(OTeF_5)_2$ unit of $[Hg(OTeF_5)_2]_3$ are

consistent with weak covalent interactions between the Hg(II) acceptor sites and the σ-donor fluorine ligands of NgF_2.

6.3. Conclusions

The -$OTeF_5$ analogue of HgF_2, $Hg(OTeF_5)_2$, was structurally characterized by single-crystal X-ray diffraction and the low-temperature Raman spectrum was assigned using quantum-chemical calculations. The crystal structure of $Hg(OTeF_5)_2$ showed that the $Hg(OTeF_5)_2$ molecules are not isolated but participate in a chain structure that results from long Hg---O and Hg---F secondary bonding interactions with Hg(II) centers of adjacent $Hg(OTeF_5)_2$ molecules. The Raman spectrum was assigned using the calculated vibrational frequencies and intensities of the hypothetical trimer, $[Hg(OTeF_5)_2]_3$, which reproduced the solid-state *gauche*-conformation and the shortest Hg---O contacts observed in the crystal structure. The *gauche*-conformation was rationalized based on the occurrence of secondary Hg---F and Hg---O bonding interactions with the Hg(II) center. In contrast, the optimized gas-phase structure of monomeric $Hg(OTeF_5)_2$ provided a geometry having its –$OTeF_5$ groups in an *anti*-conformation similar to that observed in $Xe(OTeF_5)_2$. The coordination complexes, $Hg(OTeF_5)_2 \cdot 1.5NgF_2$ (Ng = Xe, Kr), were also synthesized and structurally characterized by single-crystal X-ray diffraction and low-temperature Raman spectroscopy. In both chain structures, the NgF_2 molecules form bridges between mercury centers by coordination to the metal through their fluorine ligands. The contact distances between Hg(II) and the F atoms of XeF_2 are shorter than those of the KrF_2 analogue, consistent with the greater ionic character of the Xe–F bonds

in XeF_2. NBO analyses are consistent with weak covalent interactions between the $Hg(OTeF_5)_2$ acceptor and the NgF_2 σ-donor ligands. The calculated frequencies and intensities of $[Hg(OTeF_5)_2]_3 \cdot 2NgF_2$ aided in the assignment of the experimental Raman spectra of $Hg(OTeF_5)_2 \cdot 1.5NgF_2$. The $Hg(OTeF_5)_2 \cdot 1.5NgF_2$ complexes are currently the only examples of coordination complexes in which KrF_2 and XeF_2 are coordinated to mercury in a neutral compound and provide the only example of a bridging KrF_2 ligand.

6.4. Experimental Section

General experimental techniques, procedures, and equipment, as well as the preparation and purification of all starting materials are described in Chapter 2.

6.4.1. Synthesis and Crystal Growth.

(i) $Hg(OTeF_5)_2$ A passivated FEP reaction vessel equipped with a Kel-F valve was loaded with HgF_2 (0.4938 g, 2.069 mmol) inside a drybox. The reaction vessel was then transferred to a metal vacuum line where $HOTeF_5$ was distilled into it. The contents of the reaction vessel were allowed to react at 50 °C for several hours with periodic agitation. Residual $HOTeF_5$, observed by Raman spectroscopy, and HF formed in the reaction (eq 6.1) were removed by pumping under dynamic vacuum for 3 h at room temperature, resulting in a friable, white solid in essentially quantitative yield (99.1%). The Raman spectrum of the product was recorded at −150 ^{o}C.

Crystals of $Hg(OTeF_5)_2$ were grown by slow evaporation of a CH_2Cl_2 solution. The solution was prepared in a ¼-in. o.d. FEP T-shaped reaction vessel by dissolving

$Hg(OTeF_5)_2$ (0.0314 g, 0.0463 mmol) in ca. 0.3 mL of CH_2Cl_2 at room temperature under anhydrous conditions. The void above the solution was backfilled with 0.5 atm of dry N_2 at −78 °C. A temperature gradient was established by cooling the empty side arm of the vessel to −78 °C in a dry ice/acetone bath while maintaining the solution at 0 °C. This temperature gradient resulted in slow evaporation of the CH_2Cl_2 solvent and growth of colorless crystals over the course of 11 days. The side arm containing the evaporated supernatant was then cooled to −196 °C and heat-sealed off under dynamic vacuum. The crystalline material was further dried at −78 °C under dynamic vacuum. A $Hg(OTeF_5)_2$ crystal having the dimensions of 0.22 x 0.10 x 0.04 mm^3 was selected for a low-temperature X-ray structure determination.

(ii) Synthesis of $Hg(OTeF_5)_2 \cdot 1.5XeF_2$ and Crystal Growth.

In the section that follow, square brackets denote quantities/conditions used for crystal growth and unbracketed quantities/conditions denote Raman sample preparations.

In a typical synthesis, 0.1816 g (0.2679 mmol) [0.0879 g (0.1298 mmol)] of $Hg(OTeF_5)_2$ was weighed, inside a drybox, into a ¼-in. o.d. quartz [T-shaped FEP] reaction vessel equipped with a 4-mm J. Young [Kel-F] valve. Xenon difluoride, 0.0750 g (0.443 mmol) [0.0267 g (0.1578 mmol)], was added to the reactor at –140 °C inside the drybox. The reactor was removed from the drybox at –196 °C and attached to a glass vacuum line while maintaining the reagents at –78 °C. Sulfuryl chloride fluoride (~0.2 mL) was condensed onto the reagents and the temperature was increased to 0 °C for 5 min and continuously agitated to dissolve the reactants. The solvent was removed from the

Raman sample under dynamic vacuum at −78 °C leaving behind a white solid. The Raman spectrum of the product was recorded at −155 °C. The solution used for crystallization was pale yellow and was cooled to –78 °C. Over the course of 5 days, colorless crystals formed. The supernatant was decanted into the side arm of the T-shaped FEP vessel at −78 °C. Once the majority of the supernatant had been transferred, the contents of the side arm were cooled to −196 °C, and the supernatant was isolated and removed by heat sealing off this portion of the reaction vessel under dynamic vacuum at −196 °C. This was followed by removal of the residual solvent from the crystalline sample under dynamic vacuum at –78 °C. A $Hg(OTeF_5)_2 \cdot 1.5XeF_2$ crystal having the dimensions 0.25 x 0.04 x 0.04 mm^3 was selected for a low-temperature X-ray structure determination.

(iii) Synthesis of $Hg(OTeF_5)_2 \cdot 1.5KrF_2$ and Crystal Growth.

In the section that follow, square brackets denote quantities/conditions used for crystal growth and unbracketed quantities/conditions denote Raman sample preparations.

In a typical synthesis, KrF_2 was sublimed under static vacuum from a FEP storage container at room temperature into a pre-weighed, fluorine-passivated 4-mm o.d FEP vessel cooled to −196 °C. Krypton difluoride, 0.0161 g (0.132 mmol) [0.0538 g (0.4417 mmol)] was condensed under static vacuum through a FEP connection into a fluorine-passivated ¼-in. o.d. quartz [T-shaped FEP] reaction vessel cooled to −196 °C, that had been previously loaded with $Hg(OTeF_5)_2$, 0.0404 g (0.0596 mmol) [0.1152 g (0.1610 mmol)] inside a drybox. Sulfuryl chloride fluoride was condensed onto the reagents (ca.

0.3 mL) [ca. 0.5 mL] and upon warming the reaction vessel to −20 °C for 2 min, the solid mixture partially dissolved to give a pale yellow solution plus a suspension of white solid. The reaction mixture used for preparation of the Raman sample was allowed to react at −78 °C for 3 h followed by removal of SO_2ClF under dynamic vacuum at −78 °C. The Raman spectrum of the product was recorded at −155 °C. The FEP reaction vessel and solution used for crystal growth were maintained at −78 °C for two weeks. Crystals were isolated as described in section (c) above. A $Hg(OTeF_5)_2 \cdot 1.5KrF_2$ crystal having the dimensions 0.18 x 0.08 x 0.05 mm^3 was selected for a low-temperature X-ray structure determination.

6.4.2. Structure Solution and Refinement

The XPREP[54] program was used to confirm the unit cell dimensions and the crystal system and space group. The structures were solved in their respective space groups by use of direct methods, and the solutions yielded the positions of all the heavy atoms as well as some of the lighter atoms. Successive difference Fourier syntheses revealed the positions of the remaining light atoms. The final refinement was obtained by introducing anisotropic parameters for all the atoms, an extinction parameter, and the recommended weighting factor. The maximum electron densities in the final difference Fourier maps were located around the heavy atoms. The PLATON program[55] could not suggest additional or alternative symmetries. X-ray crystallographic files in CIF format for the structure determinations of $Hg(OTeF_5)_2$ and $Hg(OTeF_5)_2 \cdot 1.5NgF_2$ (Ng = Xe, Kr) is available free of charge via the Internet at http://pubs.acs.org/.

6.4.3. NMR Sample Preparation.

A $Hg(OTeF_5)_2$ sample was prepared in a precision thin-wall Pyrex glass NMR sample tube (Wilmad) as previously described.[25] The NMR sample tube was fused to a ¼-in. Pyrex glass tube which was connected to a grease-free 6-mm J. Young glass stopcock outfitted with a Teflon barrel using a ¼-in. stainless steel Swagelok Ultratorr union fitted with Viton elastomer O-rings and was rigorously dried under dynamic vacuum. The CD_2Cl_2 solvent was distilled into the vessel at −78 °C before the sample was transfered into a drybox where $Hg(OTeF_5)_2$ was added to the frozen solvent at −140 °C. The union and valve assembly were replaced and the reactor was attached to a vacuum manifold where the NMR sample tube was cooled to −196 °C and heat-sealed under dynamic vacuum and stored at –78 °C until the ^{19}F NMR spectrum could be obtained. The sample was dissolved at 25 °C just prior to data acquisition.

6.4.4. Computational Details.

The optimized gas-phase geometry and vibrational frequencies of $Hg(OTeF_5)_2$ were calculated at the B3LYP and PBE0 levels of theory using two different basis sets. The aug-cc-pVTZ basis sets where used for H, O, and F whereas aug-cc-pVTZ-(PP) basis sets having pseudo-potentials were used for Hg and Te, and the def2-TZVPP basis sets for H, O, F, Hg, and Te. The optimized gas-phase geometries and vibrational frequencies of $[Hg(OTeF_5)_2]_3$ and $[Hg(OTeF_5)_2]_3 \cdot 2NgF_2$ (Ng = Xe, Kr) were only calculated using the PBE0/def2-TZVPP (H, O, F, Kr, Te, Xe, and Hg) method due to the large sizes of these molecules. The noble-gas difluorides, NgF_2 (Ng = Xe, Kr), were also calculated for comparison using the PBE0/def2-TZVPP method. All basis sets were obtained online

from the EMSL Basis Set Exchange.[56-61] The NBO analyses[62-65] were performed for the PBE0–optimized local minima. Quantum-chemical calculations were carried out using the program Gaussian 09[66] for geometry optimizations, vibrational frequencies, and their intensities. All geometries were fully optimized using analytical gradient methods. The program GaussView[67] was used to visualize the vibrational displacements that form the basis for the vibrational mode descriptions given in Tables 6.4-6.6 and S6.1-S6.6.

6.5. Supporting Information Contents - Appendix D

Raman spectrum of $Hg(OTeF_5)_2$ (Figure S6.1); Raman spectrum of sublimed $Hg(OTeF_5)_2$ (Figure S6.2); crystal packing of $Hg(OTeF_5)_2$ along the *c*- and *a*-axes (Figure S6.3); experimental Raman frequencies and intensities, calculated vibrational frequencies and infrared and Raman intensities, and detailed assignments of the Raman spectra for $Hg(OTeF_5)_2$ (exptl and calcd) (Table S6.1), $Hg(OTeF_5)_2$ (exptl) and $[Hg(OTeF_5)_2]_3$ (calcd) (Table S6.2), $Hg(OTeF_5)_2 \cdot 1.5XeF_2$ (exptl) and $[Hg(OTeF_5)_2]_3 \cdot 2XeF_2$ (calcd) (Table S6.3), $Hg(OTeF_5)_2 \cdot 1.5KrF_2$ (exptl) and $[Hg(OTeF_5)_2]_3 \cdot 2KrF_2$ (calcd) (Table S6.4); experimental and calculated Raman frequencies for XeF_2 (Table S6.5) and KrF_2 (Table S6.6); experimental ($Hg(OTeF_5)_2$) and calculated (monomer $Hg(OTeF_5)_2$) bond lengths and bond angles (Table S6.7); NBO valencies, bond orders, and NPA charges for $Hg(OTeF_5)_2$, $[Hg(OTeF_5)_2]_3$, and $[Hg(OTeF_5)_2]_3 \cdot 2NgF_2$ (Table S6.8).

6.6. References

(1) Brock, D. S.; Schrobilgen, G.J.; Žemva B. *Noble-Gas Chemistry*. In *Comprehensive Inorganic Chemistry*; Reedijk J. and Poeppelmeier K., eds.; II, Vol 1. Oxford: Elsevier; **2013**, Chapter 1.25, p. 755−822.

(2) Lehmann, J. F.; Dixon, D. A.; Schrobilgen, G. J. *Inorg. Chem.* **2001**, *40*, 3002−3017.

(3) Elliott, H. St. A.; Lehmann, J.; Mercier, H. P. A.; Jenkins, H. D.; Schrobilgen, G. J. *Inorg. Chem.* **2010**, 49, 8504−8523.

(4) Brock, D. S.; Casalis de Pury, J. J.; Mercier, H. P. A.; Schrobilgen, G. J.; Silvi, B. *Inorg. Chem.* **2010**, 49, 6673−6689.

(5) Tavčar, G.; Tramšek, M.; Bunič, T.; Benkič, P.; Žemva, B. *J. Fluorine Chem.* **2004**, *125*, 1579–1584.

(6) Tramšek, M.; Žemva, B. *J. Fluorine Chem.* **2006**, *127*, 1275–1284.

(7) Tavčar, G.; Žemva, B. *Inorg. Chem.* **2005**, *44*, 1525–1529.

(8) Bunič, T.; Tramšek, M.; Goreshnik, E.; Tavčar, G.; Žemva, B. *Inorg. Chem.* **2007**, *46*, 5276–5282.

(9) Bunič, T.; Tramšek, M.; Goreshnik, E.; Žemva, B. *Solid State Sci.* **2008**, *10*, 1511–1516.

(10) Tavčar, G.; Benkič, P.; Žemva, B. *Inorg. Chem.* **2004**, *43*, 1452–1457.

(11) Bunič, T.; Tavčar, G.; Tramšek, M.; Žemva, B. *Inorg. Chem.* **2006**, *45*, 1038–1042.

(12) Tavčar, G.; Goreshnik, E.; Mazej, Z. *J. Fluorine Chem.* **2006**, *127*, 1368–1373.

(13) Tavčar, G.; Goreshnik, E.; Mazej, Z. *Abstracts of Papers*. Group 12 Coordination Chemistry with Fluoride Ligands. Presented at the 2011 National Meeting of the Slovenian Chemical Society; Slovenian Chemistry Days (Slovenski Kemijski Dnevi), Portorož, Slovenia, September 14–16, 2011; Paper, Anorganska Kemija in Structurna Kemija ter Gradiva, p 69.

(14) Tavčar, G.; Goreshnik, E. *Abstracts of Papers*. Mercury Ion as a Center for Coordination of the XeF_2 Ligand. Presented at the 17th European Symposium on Fluorine Chemistry, Paris, France, July 21–25, 2013; Poster P2.46.

(15) Brock, D. S.; Casalis de Pury, J. J.; Mercier, H. P. A.; Schrobilgen, G. J.; Silvi, B. *J. Am. Chem. Soc.* **2010**, *132*, 3533–3542.

(16) Holloway, J. H.; Schrobilgen, G. J.; Taylor, P. *J. Chem. Soc., Chem. Commun.***1975**, *2*, 40–41**.**

(17) Holloway, J. H.; Schrobilgen, G. J. *Inorg. Chem.* **1980**, *19*, 2632–2640.

(18) Holloway, J. H.; Schrobilgen, G. J. *Inorg. Chem.* **1981**, *20*, 3363–3368.

(19) Christe, K. O.; Wilson, W. W.; Bougon, R. A. *Inorg. Chem.* **1986**, *13*, 2163–2169.

(20) Tucker, P. A.; Taylor, P. A.; Holloway, J. H.; Russell, D. R. *Acta Crystallogr.* **1975**, *B31*, 906–908.

(21) Sladky, F.; Kropshofer, H. *Inorg. Nucl. Chem. Lett.* **1972**, *8*, 195–197.

(22) Birchall, T.; Myers, R. D.; de Waard, H.; Schrobilgen, G. J. *Inorg. Chem.* **1982**, *21*, 1068–1073.

(23) Riedel, S.; Kaupp, M. *Coord. Chem. Rev.* **2009**, *253*, 606–624.

(24) Mercier, H. P. A.; Sanders, J. C. P.; Schrobilgen, *J. Am. Chem. Soc.* **1994**, *116*, 2921−2937.

(25) Mercier, H. P. A.; Moran, M. D.; Schrobilgen, G. J.; Steinberg, C.; Suontamo, R. J. *J. Am. Chem. Soc.* **2004**, *126*, 5533−5548.

(26) Mercier, H. P. A.; Moran, M. D.; Sanders, J. C. P.; Schrobilgen, G. J.; Suontamo, R. J. *Inorg. Chem.* **2005**, *44*, 49−60.

(27) Ebert, F.; Woitinek, H. *Z. Anorg. Allg. Chem.* **1933**, *210*, 269−272.

(28) Seppelt, K.; Nothe, D. *Inorg. Chem.* **1973**, *11*, 2727 −2730.

(29) Sladky, F.; Kropshofer, H.; Leitzke, O.; Peringer, P. *J. Inorg. Nucl. Chem., H. H. Hyman Memorial Volume* **1976**, 69–71.

(30) Riedel, S.; Straka, M.; Kaupp , M. *Chem. Eur. J.* **2005**, *11*, 2743–2755.

(31) Bondi, A. *J. Phys. Chem.* **1964**, *68*, 441−451.

(32) Fir, B. A.; Mercier, H. P. A.; Sanders, J. C. P.; Dixon, D. A.; Schrobilgen, G. J. *J. Fluorine Chem.* **2001**, *110*, 89–107.

(33) Cordero, B.; Gómez, V.; Platero-Prats, A.E.; Revés, M.; Echeverría, J.; Cremades, E.; Barragán, F.; Alvarez, S. *Dalton Trans.* **2008**, 2832–2838.

(34) Hughes, M. J.; Mercier, H. P. A.; Schrobilgen, G. J. *Inorg. Chem.* **2009**, *48*, 4478–4490.

(35) Nieboer, J.; Mack, J. P.; Mercier, H. P. A.; Gerken, M. *Inorg. Chem.* **2010**, *49*, 6153–6159.

(36) Hughes, M. J.; Brock, D. S.; Mercier, H. P. A.; Schrobilgen, G. J. *J. Fluorine Chem.* **2011**, *132*, 660–668.

(37) Agron, P. A.; Begun, G. M.; Levy, H. A.; Mason, A. A.; Jones, C. G.; Smith, D. F. *Science* **1963**, *139*, 842–844.

(38) Al-Mukhtar, M.; Holloway, J. H.; Hope, E. G.; Schrobilgen, G. J. *J. Chem. Soc., Dalton Trans.* **1991**, 2831–2834.

(39) Turner, J. J.; Pimentel, G. C. *Science* **1963**, *140*, 974–975.

(40) Benkič, P.; Tramšek, M.; Žemva, B. *Solid State Sci.* **2002**, *4*, 1425–1434.

(41) Tramšek, M.; Benkič, P.; Žemva, B. *Angew. Chem. Int. Ed.* **2004**, *43*, 3456–3458.

(42) Bertolini, J. C. *J. Emerg. Med.* **1992**, *10*, 163−168.

(43) Peters, D.; Mietchen, R. *J. Fluorine Chem.* **1996**, *79*, 161−165.

(44) Segal, E. B. *Chem. Health Saf.* **2000**, 18−23.

(45) Casteel, W. J., Jr.; Dixon, D. A.; Mercier, H. P. A.; Schrobilgen, G. J. *Inorg. Chem.* **1996**, *35*, 4310–4322.

(46) Mercier, H. P. A.; Sanders, J. C. P.; Schrobilgen, G. J.; Tsai, S. S. *Inorg. Chem.* **1993**, *32*, 386−393.

(47) Kinkead, S. A.; FitzPatrick, J. R.; Foropoulos, J., Jr.; Kissane, R. J.; Purson, J. D. In *Fluorine Chemistry Toward the 21st Century*; Thrasher, J. S., Strauss, S. H., Eds.; ACS Symposium Series 555; American Chemical Society: Washington, DC, 1994; Chapter 3, pp 40-55.

(48) Lehmann, J. F.; Mercier, H. P. A.; Schrobilgen, G. J. *Coord. Chem. Rev.*, **2002**, *233-234*, 1−39.

(49) Emara, A. A. A.; Schrobilgen, G. J. *Inorg. Chem.* **1992**, *31*, 1323−1332.

(50) Schack, C.; Wilson, R. D. *Inorg. Chem.* **1970**, *9*, 311−314.

(51) Gerken, M.; Dixon, D. A.; Schrobilgen, G. J. *Inorg. Chem.* **2000**, *39*, 4244−4255.

(52) APEX2, release v2011.6-1; Bruker AXS Inc.: Madison, WI, 1995.

(53) Sheldrick, G. M. SADABS (Siemens Area Detector Absorption Corrections), version 2.03; Madison, WI, 1999.

(54) Sheldrick, G. M. SHELXTL-Plus, release 5.1; Siemens Analytical X-ray Instruments, Inc.: Madison, WI, 1998.

(55) Spek, A. L. *J. Appl. Crystallogr.* **2003**, *36*, 7–13.

(56) Basis sets and pseudo-potentials were obtained from the Extensible Computational Chemistry Environment Basis set Database, version 2/25/04, as developed and distributed by the Molecular Science Computing Facility, Environmental and Molecular Science Laboratory, which is part of the Pacific Northwest Laboratory, P.O. Box 999, Richland, WA 99352. https://bse.pnl.gov/bse/portal

(57) Dunning, T. H., Jr. *J. Chem. Phys.* **1989**, *90*, 1007−1023.

(58) Kendall, R. A.; Dunning, T. H. Jr.; Harrison, R. J. *J. Chem. Phys.* **1992**, *96*, 6796−6806.

(59) Peterson, K.A.; Figgen, D.; Goll, E.; Stoll, H.; Dolg, M. *J. Chem. Phys.* **2003**, *119*, 11113−11123.

(60) Peterson, K.A.; Puzzarini, C.; *Theor. Chem. Acc.* **2005**, *114*, 283−296.

(61) Weigend, F.; Ahlrichs, R. Balanced basis sets of split valence, triple zeta valence and quadruple zeta valence quality for H to Rn: Design and assessment of accuracy. *Phys. Chem. Chem. Phys.* **2005**, *7*, 3297−3305.

(62) Reed, A. E.; Weinstock, R.B.; Weinhold, F. *J. Chem. Phys.* **1985**, *83*, 735−746.

(63) Reed, A. E.; Curtiss, L. A.; Weinhold, F. *Chem. Rev.* **1998**, *88*, 899−926.

(64) Glendening, E. D.; Reed, A. E.; Carpenter, J. E.; Weinhold, F. *NBO Version 3.1*; Gaussian Inc.: Pittsburgh, PA, 1990.

(65) Glendening, E. D.; Badenhoop, J. K.; Reed, A. E.; Carpenter, J. E.; Bohmann, C. M.; Morales, C. M.; Weinhold, F. *NBO Version 5.0*; Theoretical Chemistry Institute, University of Wisconsin: Madison, WI, 2001.

(66) Gaussian 09, Revision D.01, Frisch, M. J.; Trucks, G. W.; Schlegel, H. B.; Scuseria, G. E.; Robb, M. A.; Cheeseman, J. R.; Scalmani, G.; Barone, V.; Mennucci, B.; Petersson, G. A.; Nakatsuji, H.; Caricato, M.; Li, X.; Hratchian, H. P.; Izmaylov, A. F.; Bloino, J.; Zheng, G.; Sonnenberg, J. L.; Hada, M.; Ehara, M.; Toyota, K.; Fukuda, R.; Hasegawa, J.; Ishida, M.; Nakajima, T.; Honda, Y.; Kitao, O.; Nakai, H.; Vreven, T.; Montgomery, Jr., J. A.; Peralta, J. E.; Ogliaro, F.; Bearpark, M.; Heyd, J. J.; Brothers, E.; Kudin, K. N.; Staroverov, V. N.; Kobayashi, R.; Normand, J.; Raghavachari, K.; Rendell, A.; Burant, J. C.; Iyengar, S. S.; Tomasi, J.; Cossi, M.; Rega, N.; Millam, N. J.; Klene, M.; Knox, J. E.; Cross, J. B.; Bakken, V.; Adamo, C.; Jaramillo, J.; Gomperts, R.; Stratmann, R. E.; Yazyev, O.; Austin, A. J.; Cammi, R.; Pomelli, C.; Ochterski, J. W.; Martin, R. L.; Morokuma, K.; Zakrzewski, V. G.; Voth, G. A.; Salvador, P.; Dannenberg, J. J.; Dapprich, S.; Daniels, A. D.; Farkas, Ö.; Foresman, J. B.; Ortiz, J. V.; Cioslowski, J.; Fox, D. J. Gaussian, Inc., Wallingford CT, 2009.

(67) *GaussView*, release 3.0; Gaussian Inc.: Pittsburgh, PA, 2003.

CHAPTER 7

A Homoleptic KrF_2 Complex, $[Hg(KrF_2)_8][AsF_6]_2 \cdot 2HF$

Adapted with permission from: DeBackere, J.R., and Schrobilgen, G.J. *Angew. Chem. Int. Ed.* **2018**, *57*, 13167–13171.

7.1. Introduction

The ligand behavior of a noble-gas difluoride, namely XeF_2, and its ability to coordinate to a metal cation was discovered in 1991 by Bartlett *et al.*,[1] who reported the synthesis and X-ray crystal structure of $Ag(XeF_2)_2(AsF_6)$. In the ensuing years, XeF_2 was shown to function as a ligand towards a variety of main-group, *d*-block, and *f*-block metal cations, e.g., $M^{n+}(XeF_2)_p(AF_x)^-_n$ (M = Li, Ag, Mg–Ba, Cu, Zn–Hg, Pb, La, Pr, Nd; A = B, P, As, Sb, Bi, V, Nb, Ta, Ru)[2,3]. Two coordination modes have been observed for XeF_2; terminal coordination, where one fluorine atom of XeF_2 is coordinated to a Lewis acid center, and bridge coordination, where each fluorine atom of the XeF_2 molecule is coordinated to a different Lewis acid center. The metal-ligand polyhedra of these complexes are often linked through bridging XeF_2 molecules and/or $[AF_x]^-$ anions. Consequently, such XeF_2-metal cation complexes exhibit considerable structural diversity.

The relatively low fluoro-basicity of an $[PnF_6]^-$ (Pn = P, As, Sb) anion may result in its displacement from the metal coordination sphere by XeF_2. Consequently, only a few complexes are known in which the metal cation is exclusively (homoleptically) coordinated to XeF_2 molecules.[4–6] Both $Pb_3(XeF_2)_{11}(PF_6)_6$,[4] and $Ca_2(XeF_2)_9(AsF_6)_4$,[5]

possess one metal cation which is homoleptically coordinated to bridging and, in the latter complex, terminal and bridging XeF_2 molecules. In both instances, the remaining metal cations are heteroleptically coordinated to bridging XeF_2 molecules and the $[PnF_6]^-$ anions. The isostructural $[M(XeF_2)_6][SbF_6]_2$ (M = Zn and Cu)[6] complexes are currently the only structurally documented examples in which XeF_2 is homoleptically coordinated to a cation in an exclusively terminal fashion. The $[M(XeF_2)_6]^{2+}$ cations are well-isolated and only interact with $[SbF_6]^-$ through weak electrostatic forces.

Studies related to the coordination chemistry of KrF_2 have, no doubt, been impeded by the technical challenges presented by the synthesis of KrF_2, its thermodynamic instability, and its exceptionally strong oxidative fluorinating properties.[7] It is only recently that compounds in which KrF_2 functions as a ligand towards Lewis acid centers have been synthesized and structurally characterized by single-crystal X-ray diffraction; namely $F_2OBr(KrF_2)_2(AsF_6)$, in which two KrF_2 molecules are terminally coordinated through fluorine to the Br^v atom of $[F_2OBr]^+$,[8] $Hg(KrF_2)_{1.5}(OTeF_5)_2$, where KrF_2 molecules bridge two mercury atoms,[9] and $Mg(KrF_2)_4(AsF_6)_2$, which provides the first example of KrF_2 terminally coordinated to an *s*-block element.[10]

The synthesis and structural characterization of the first homoleptic coordination complex of KrF_2 is described in the present study.

7.2. Results and Discussion

7.2.1. Synthesis of $[Hg(KrF_2)_8][AsF_6]_2 \cdot 2HF$

The HF-solvated complex salt, $[Hg(KrF_2)_8][AsF_6]_2 \cdot 2HF$, was synthesized by

reaction of $Hg(AsF_6)_2$ and a tenfold molar excess of KrF_2 in anhydrous HF (eq 7.1).

$$Hg(AsF_6)_2 + 8\ KrF_2 \xrightarrow{HF} [Hg(KrF_2)_8][AsF_6]_2 \cdot 2HF \qquad (7.1)$$

The compound was characterized by low-temperature single-crystal X-ray diffraction and Raman spectroscopy.

7.2.2. X-ray Crystallography

A summary of crystal data and refinement results for $[Hg(KrF_2)_8][AsF_6]_2 \cdot 2HF$ (Figure 7.1) is given in Table 7.1. A complete list of bond lengths and bond angles for are provided in Tables 7.2 and 7.3. The crystal structure of $[Hg(KrF_2)_8][AsF_6]_2 \cdot 2HF$ consists of well-separated $[Hg(KrF_2)_8]^{2+}$ cations (C_2-symmetry, Figure 7.2a) in which eight KrF_2 molecules are terminally coordinated to Hg^{2+}, and is the highest KrF_2-to-metal cation ratio that has been realized thus far for a KrF_2 coordination complex. The Hg^{2+} atom is located on a twofold rotation axis so that four of the eight coordinated KrF_2 molecules are crystallographically unique, and the resulting coordination sphere around mercury is a slightly distorted square antiprism. (Figure S7.1a). The distorted cation geometry is well reproduced by the gas-phase calculations (Figures 7.2b and S7.1**,** Table 7.2; see *Appendix E*).

The Hg–F_b bond lengths (2.300(1)–2.412(1) Å) of $[Hg(KrF_2)_8]^{2+}$ are significantly shorter than those of $Hg(KrF_2)_{1.5}(OTeF_5)_2$ (2.664(3) Å).[9] This interaction results in polarization of the ligand Kr–F bonds, giving shorter terminal bonds (Kr–F_t, 1.822(1)–1.852(1) Å) and correspondingly longer bridge bonds (Kr–F_b, 1.933(1)–1.957(1) Å). Similar bond polarizations occur for the terminally coordinated KrF_2 molecules of $Mg(KrF_2)_4(AsF_6)_2$ (Kr–F_t, 1.817(2)–1.821(2) Å; Kr–F_b, 1.965(1)–1.979(1) Å)[10] and

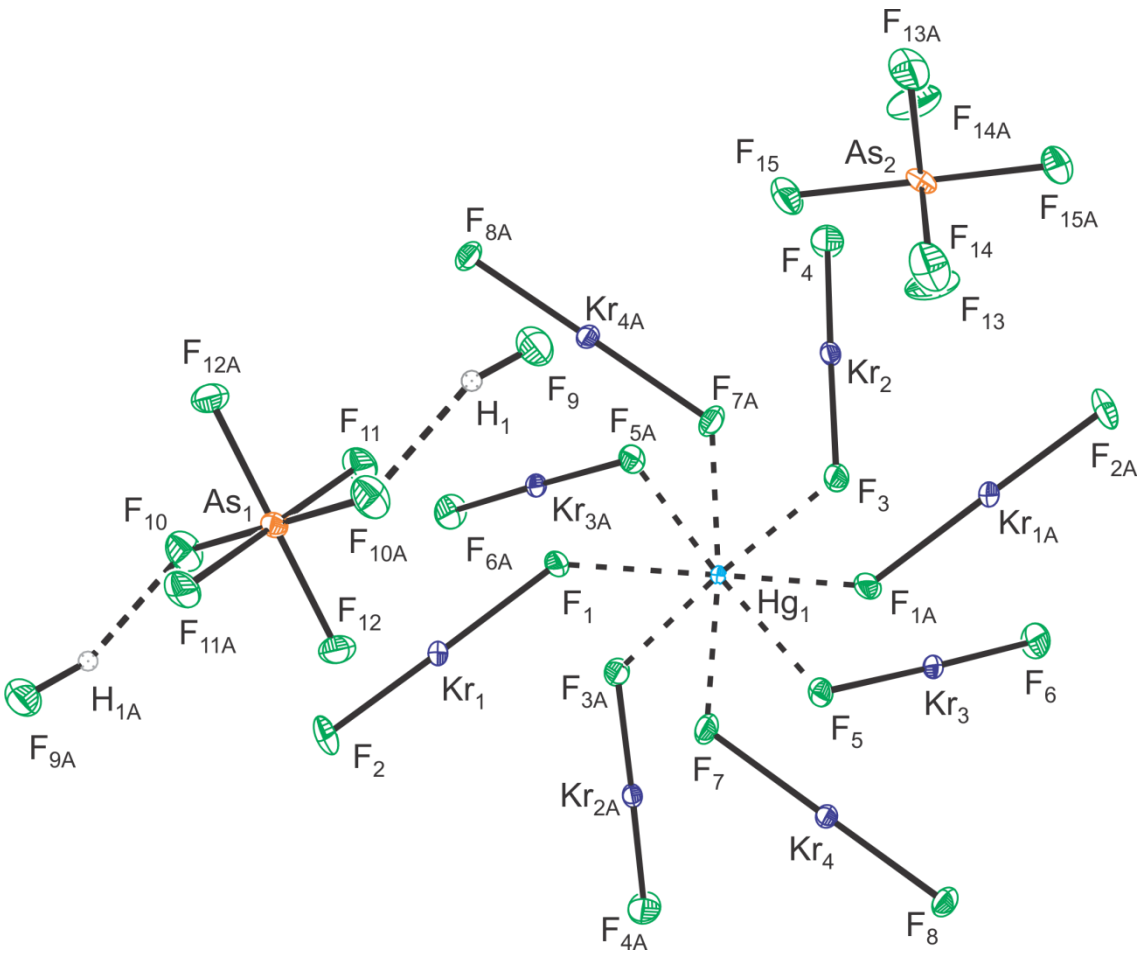

Figure 7.1. The X-ray crystal structure of $[Hg(KrF_2)_8][AsF_6]_2 \cdot 2HF$; the atom labeling corresponds to that used in Tables 7.2 and 7.3.

Table 7.1. Summary of crystal data and refinement results for $[Hg(KrF_2)_8][AsF_6]_2 \cdot 2HF$

crystal system	monoclinic
space group	*C*2/c (No. 15)
a (Å)	11.4367(4)
b (Å)	13.4517(5)
c (Å)	18.9927(7)
β	102.177(2)
V (Å^3)	2856.15(18)
Z (molecules/unit cell)	4
mol wt (g mol^{-1})	1592.85
calcd density (g cm^{-3})	3.704
T (^{o}C)	–173.0
μ (mm^{-1})	20.193
R_1[a]	0.0218
wR_2[b]	0.0423

[a] R_1 is defined as $\Sigma \| F_o \| - | F_c \| / \Sigma | F_o |$ for $I > 2\sigma(I)$.
[b] wR_2 is defined as $[\Sigma[w(F_o^2 - F_c^2)^2]/\Sigma w(F_o^2)^2]^{½}$ for $I > 2\sigma(I)$.

Table 7.2. Experimental geometrical parameters of $[Hg(KrF_2)_8]^{2+}$ in $[Hg(KrF_2)_8][AsF_6]_2 \cdot 2HF$ and the calculated gas-phase geometrical parameters of $[Hg(KrF_2)_8]^{2+}$

	exptl [a]	**calcd APFD (S_8)** [b]	**calcd B3LYP (S_8)** [b]	**calcd PBE (C_4)** [c]
Bond Lengths (Å)				
$Hg_1–F_1(Kr_1)$	2.300(1)	2.346	2.432	2.438
$Hg_1–F_3(Kr_2)$	2.381(1)			2.439
$Hg_1–F_5(Kr_3)$	2.375(1)			
$Hg_1–F_7(Kr_4)$	2.412(1)			
$Kr_1–F_2$	1.822(1)	1.806	1.832	1.868
$Kr_2–F_4$	1.840(2)			
$Kr_3–F_6$	1.844(1)			
$Kr_4–F_8$	1.852(1)			
$Kr_1–F_1$	1.957(1)	1.980	2.002	2.032
$Kr_2–F_3$	1.949(1)			
$Kr_3–F_5$	1.933(1)			
$Kr_4–F_7$	1.939(1)			
$Kr---F(AsF_5)$	≥ 2.969(2)			
Kr---F(H)	≥ 3.199(1)			
Kr---F(KrF) [d]	≥ 3.085(1)			
Bond Angles (deg)				
$Hg_1–F_3–Kr_2$	133.6(1)	127.8	134.6	127.6
$Hg_1–F_5–Kr_3$	127.7(1)			127.5
$Hg_1–F_1–Kr_1$	134.3(1)			
$Hg_1–F_7–Kr_4$	124.0(1)			
$F_5–Kr_3–F_6$	178.8(1)	179.7	179.6	179.4
$F_3–Kr_2–F_4$	178.9(1)			179.3
$F_8–Kr_4–F_7$	179.3(1)			
$F_1–Kr_1–F_2$	178.8(1)			
$F_5–Hg_1–F_1$	139.1(1)	141.7	142.3	141.8
$F_3–Hg_1–F_7$	140.4(1)			
$F_7–Hg_1–F_{5A}$	145.9(1)			
$F_3–Hg_1–F_1$	140.6(1)			
$F_7–Hg_1–F_{7A}$	111.1(1)	117.9	115.2	117.5
$F_3–Hg_1–F_{3\,A}$	116.8(1)			117.6
$F_5–Hg_1–F_{5\,A}$	121.1(1)			
$F_1–Hg_1–F_{1A}$	124.5(1)			
$F_5–Hg_1–F_{1A}$	72.7(1)	74.6 75.4	73.3 77.4	74.4 74.5
$F_5–Hg_1–F_{3A}$	73.2(1)			
$F_1–Hg_1–F_{3A}$	73.5(1)			
$F_5–Hg_1–F_7$	74.2(1)			
$F_1–Hg_1–F_{7A}$	72.4(1)			
$F_3–Hg_1–F_{7A}$	79.8(1)			
$F_3–Hg_1–F_5$	76.9(1)			
$F_1–Hg_1–F_7$	77.1(1)			

[a] The atom labeling scheme corresponds to that used in Figure 7.1 and 7.2a. [b] Calculated using the def2-TZVPD basis set. KrF_2 ($D_{\infty h}$) was also calculated: d(Kr– F) = 1.867 (APFD) and 1.896

Table 7.2 continued…

(B3LYP) Å. [c] Calculated using the TZ2P basis set. KrF_2 ($D_{\infty h}$) was also calculated: d(Kr–F) = 1.928 Å (PBE). [d] The contacts are between different $[Hg(KrF_2)_8]^{2+}$ cations.

Table 7.3. Experimental geometrical parameters for the $[AsF_6]^-$ anions in $[Hg(KrF_2)_8][AsF_6]_2 \cdot 2HF$ [a]

Bond Lengths (Å)			
$As_1–F_{10}$	1.733(1)	$As_2–F_{13}$	1.721(1)
$As_1–F_{11}$	1.715(1)	$As_2–F_{14}$	1.712(1)
$As_1–F_{12}$	1.721(1)	$As_2–F_{15}$	1.717(1)
F_9---F_{10}	2.669(1)		
Bond Angles (deg)			
$F_{12}–As_1–F_{12A}$	180	$F_{13}–As_2–F_{14A}$	179.4(1)
$F_{11}–As_1–F_{11A}$	180	$F_{13A}–As_2–F_{14}$	179.4(1)
$F_{10}–As_1–F_{10A}$	180	$F_{15}–As_2–F_{15A}$	177.7(1)
$F_{12}–As_1–F_{11}$	90.1(1)	$F_{13}–As_2–F_{14}$	89.6(1)
$F_{11}–As_1–F_{12A}$	89.9(1)	$F_{13}–As_2–F_{15A}$	89.0(1)
$F_{12}–As_1–F_{10}$	89.8(1)	$F_{13}–As_2–F_{15}$	89.4(1)
$F_{12}–As_1–F_{10A}$	90.2(1)	$F_{13}–As_2–F_{13A}$	91.0(1)
$F_{11}–As_1–F_{10}$	90.0(1)	$F_{14}–As_2–F_{14A}$	89.8(1)
$F_{11}–As_1–F_{10A}$	90.0(1)	$F_{14}–As_2–F_{15}$	90.8(1)

[a] The atom labeling scheme corresponds to that used in Figure 7.1.

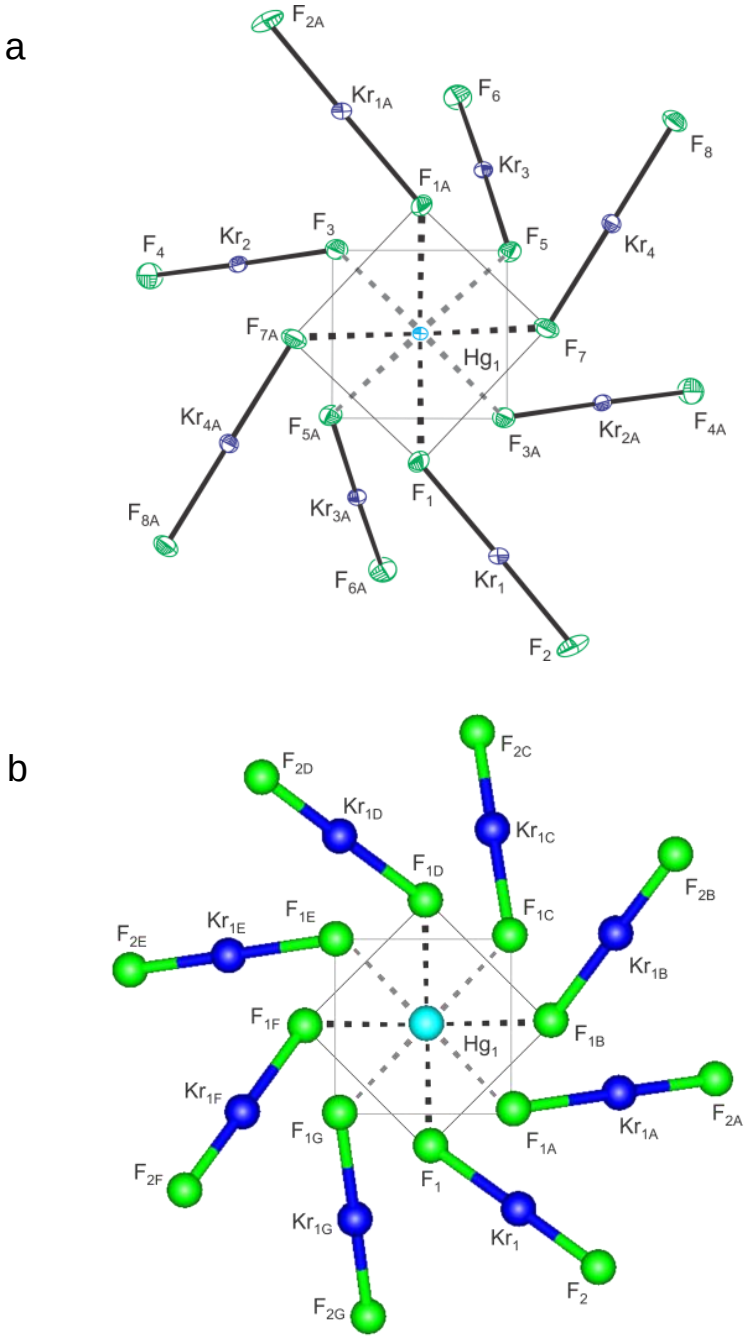

Figure 7.2. The $[Hg(KrF_2)_8]^{2+}$ cation **a**) in the single-crystal X-ray structure of $[Hg(KrF_2)_8][AsF_6]_2 \cdot 2HF$ viewed down the C_2-axis with thermal ellipsoids shown at the 50% probability level and **b**) calculated (S_8) at the B3LYP/def2-TZVPD level of theory viewed down the S_8-axis. Dotted lines indicate bonds coming out of (black) and going into (grey) the plane of the paper. Square faces of square-antiprism polyhedron are indicated by thin lines.

$F_2OBr(KrF_2)_2(AsF_6)$ (Kr–F_t, 1.840(5),1.847(4) Å; Kr–F_b, 1.933(4), 1.943(4) Å).[8] These bond length differences are significantly less than those observed for the ion-paired salts of $[KrF]^+$, e.g., $[KrF][AsF_6]$, which has much shorter Kr–F_t (1.765(3) Å) and much longer Kr–F_b (2.131(2) Å) bonds.[11] In contrast, the Kr–F bond lengths of the bridging KrF_2 ligands of $Hg(KrF_2)_{1.5}(OTeF_5)_2$ (1.883(3)–1.897(3) Å) are equal, within ±3σ, to those of free KrF_2 (1.894(5) Å). The F–Kr–F bond angles in $[Hg(KrF_2)_8]^{2+}$ are nearly linear (178.3(1)–178.9(1)^o) and are comparable to those of other KrF_2 adducts.[8-10] The Hg–F–Kr bond angles lie between 124.0(1) and 134.3(1)^o (calcd: 127.8^o, APFD; 134.6^o, B3LYP), and are comparable to the Br–F–Kr and Mg–F–Kr angles of $F_2OBr(KrF_2)_2(AsF_6)$ (132.1(2), 139.9(2)^o) and $Mg(KrF_2)_4(AsF_6)_2$ (121.84(7)–144.43(8)^o).[8,10]

The $[AsF_6]^-$ anions are slightly distorted from O_h symmetry, with one anion lying on a twofold rotation axis and the other located on an inversion center (Figure 7.1). Two co-crystallized HF molecules are H-bonded to the $[As_{(1)}F_6]^-$ anion with $F_{(9/A9)}(H)$---$F_{(10A/10)}$ distances of 2.669(1) Å. This is corroborated by the $As_{(1)}$–$F_{(10/10A)}$ bond lengths (1.733(1) Å), which are slightly elongated relative to the other $As_{(1)}$–F_t bonds (1.715(1), 1.721(1) Å).

7.2.3. Raman Spectroscopy

The Raman spectrum of $[Hg(KrF_2)_8][AsF_6]_2 \cdot 2HF$ is shown in Figure 7.3 and a list of vibrational frequencies and assignments is provided in Table 7.4. Raman spectral assignments for $[Hg(KrF_2)_8]^{2+}$ were aided by quantum-chemical calculations of its frequencies and intensities, and by comparison with the vibrational spectra of other KrF_2

adducts,[8-10] and KrF_2.[12,13] Factor-group analyses account for the experimental Raman activities and additional vibrational band splittings (Figures S7.2–S7.4). Overall, the assigned frequencies and their trends are well reproduced by the calculations.

The calculated vibrational displacements reveal no significant intra-ligand coupling between the Kr–F_t and Kr–F_b stretching modes, significant inter-ligand coupling does occur, as in the cases of $Mg(KrF_2)_4(AsF_6)_2$[10] and $F_2OBr(KrF_2)_2(AsF_6)$.[8] The coupled Kr–F_t stretching modes are assigned to bands at 540, 543, 554, and 603 cm^{-1} (calcd; 584–614 cm^{-1} (B3LYP), 616–645 cm^{-1} (APFD)). Their frequencies are similar to those of $Mg(KrF_2)_4(AsF_6)_2$ (558, 569, 578, 589 cm^{-1}),[10] $F_2OBr(KrF_2)_2(AsF_6)$ (533, 549 cm^{-1}),[8] and the IR-active asymmetric stretching mode of gas-phase KrF_2 (ν_3, $\sum_u^+$), which is centered at 580 cm^{-1}.[12] The coupled Kr–F_b stretching modes are assigned to overlapping bands between 449 and 508 cm^{-1} (calcd; 413–467 cm^{-1} (B3LYP), 438–492 cm^{-1} (APFD)) which are also similar to those of $Mg(KrF_2)_4(AsF_6)_2$ (449/460, 467/475, 486, 495 cm^{-1}),[10] $F_2OBr(KrF_2)_2(AsF_6)$ (443, 472 cm^{-1}),[8] and the Raman-active symmetric stretching mode (ν_1, $\sum_g^+$) of solid KrF_2 at 466.5 cm^{-1}.[13] The F–Kr–F bending modes are assigned to bands at 238, 262, and 282 cm^{-1} (calcd; 219–255 cm^{-1} (B3LYP), 231–286 cm^{-1} (APFD)) and are also in accordance with those of $Mg(KrF_2)_4(AsF_6)_2$ (227, 293 cm^{-1}),[10] $F_2OBr(KrF_2)_2(AsF_6)$ (254, 266, 301 cm^{-1}),[8] and the doubly-degenerate IR-active bending mode of gas-phase KrF_2 (232.6 cm^{-1}).[12]

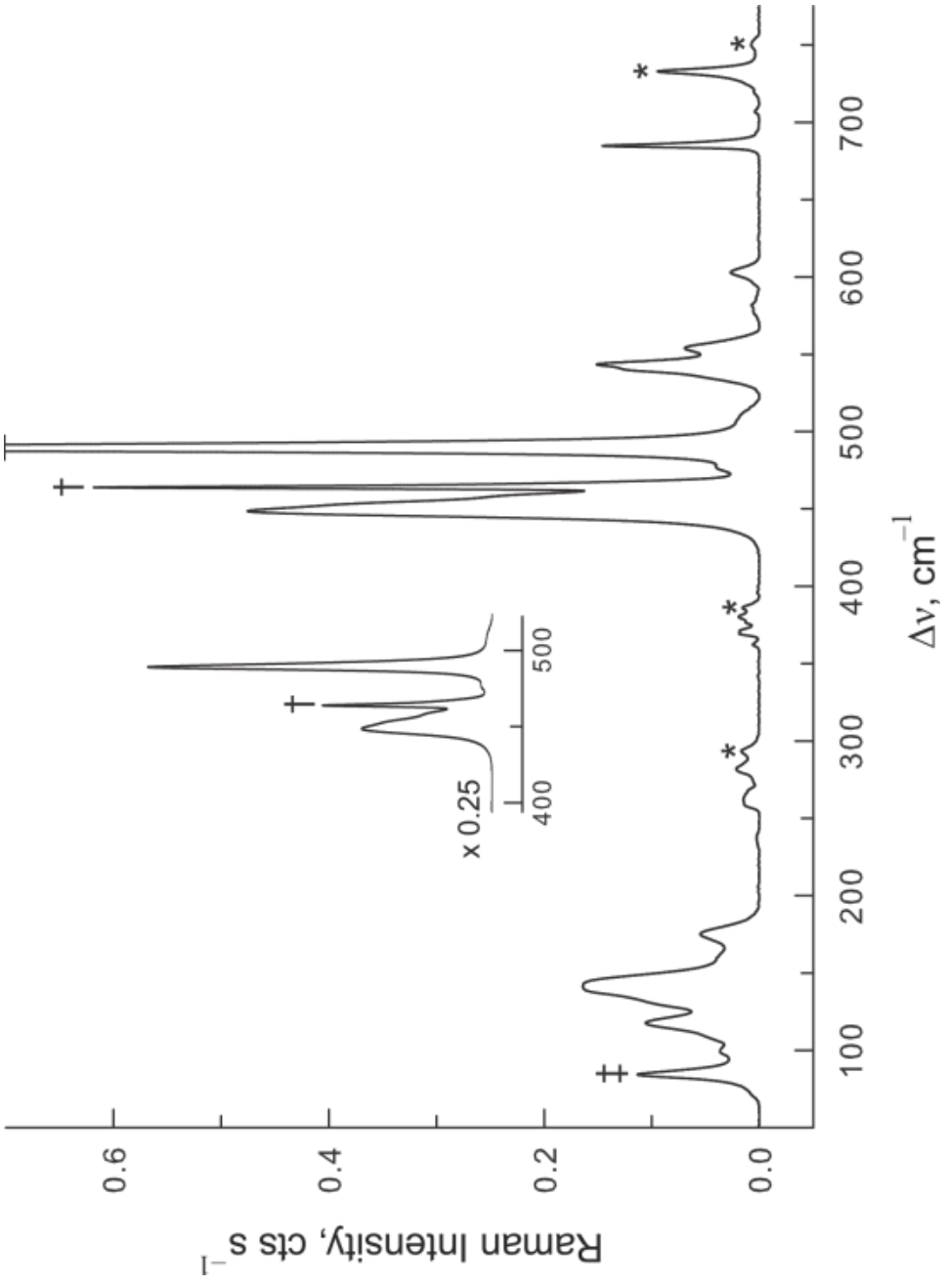

Figure 7.3. Raman spectrum of $[Hg(KrF_2)_8][AsF_6I_2 \cdot 2HF$ recorded at –150 °C using 1064-nm. Symbols denote FEP sample tube lines/overlap (*), instrumental artifact (‡), and unreacted KrF_2 (†).

Table 7.4. Experimental Raman frequencies and intensities of $[Hg(KrF_2)_8][AsF_6]_2 \cdot 2HF$ and the calculated gas-phase vibrational frequencies and intensities of $[Hg(KrF_2)_8]^{2+}$

exptl [a, b]	calcd $[Hg(KrF_2)_8]^{2+}$ (S_8)		
	calcd APFD[c]	calcd B3LYP[c]	assgnts [d,e]
707(<1)			$\nu_3(T_{1u})$ $[AsF_6]^-$
685(12)			$\nu_1(A_{1g})$ $[AsF_6]^-$
	645(104)[0]	614(124)[0]	$[\nu(Kr_1\text{-}F_2) + \nu(Kr_{1B}\text{-}F_{2B}) + \nu(Kr_{1G}\text{-}F_{2G}) + \nu(Kr_{1E}\text{-}F_{2E}) + \nu(Kr_{1D}\text{-}F_{2D}) + \nu(Kr_{1F}\text{-}F_{2F}) + \nu(Kr_{1C}\text{-}F_{2C}) + \nu(Kr_{1A}\text{-}F_{2A})]$
	624(0)[635]	591(0)[596]	$[\nu(Kr_1\text{-}F_2) + \nu(Kr_{1G}\text{-}F_{2G}) + \nu(Kr_{1F}\text{-}F_{2F})] - [\nu(Kr_{1B}\text{-}F_{2B}) + \nu(Kr_{1D}\text{-}F_{2D}) + \nu(Kr_{1C}\text{-}F_{2C})]$
603(2)	624(0)[635]	591(0)[596]	$[\nu(Kr_1\text{-}F_2) + \nu(Kr_{1B}\text{-}F2_B) + \nu(Kr_{1A}\text{-}F_{2A})] - [\nu(Kr_{1E}\text{-}F_{2E}) + \nu(Kr_{1D}\text{-}F_{2D}) + \nu(Kr_{1F}\text{-}F_{2F})]$
554(6)	618(0)[249]	588(0)[361]	$[\nu(Kr_1\text{-}F_2) + \nu(Kr_{1B}\text{-}F2_B) + \nu(Kr_{1D}\text{-}F_{2D}) + \nu(Kr_{1F}\text{-}F_{2F})] - [\nu(Kr_{1G}\text{-}F_{2G}) + \nu(Kr_{1E}\text{-}F_{2E}) + \nu(Kr_{1C}\text{-}F_{2C}) + \nu(Kr_{1A}\text{-}F_{2A})]$
543(12)	616(55)[0]	584(59)[0]	$[\nu(Kr_1\text{-}F_2) + \nu(Kr_{1D}\text{-}F_{2D})] - [\nu(Kr_{1B}\text{-}F_{2B}) + \nu(Kr_{1F}\text{-}F_{2F})]$
540(sh)	616(55)[0]	584(59)[0]	$[\nu(Kr_{1G}\text{-}F_{2G}) + \nu(Kr_{1C}\text{-}F_{2C})] - [\nu(Kr_{1E}\text{-}F_{2E}) + \nu(Kr_{1A}\text{-}F_{2A})]$
	616(45)[0]	584(52)[0]	$[\nu(Kr_1\text{-}F_2) + \nu(Kr_{1F}\text{-}F_{2F}) + \nu(Kr_{1C}\text{-}F_{2C})] - [\nu(Kr_{1B}\text{-}F_{2B}) + \nu(Kr_{1G}\text{-}F_{2G}) + \nu(Kr_{1D}\text{-}F_{2D})]$
	616(45)[0]	584(52)[0]	$[\nu(Kr_1\text{-}F_2) + \nu(Kr_{1B}\text{-}F_{2B}) + \nu(Kr_{1E}\text{-}F_{2E})] - [\nu(Kr_{1D}\text{-}F_{2D}) + \nu(Kr_{1F}\text{-}F_{2F}) + \nu(Kr_{1A}\text{-}F_{2A})]$
582(<1), br			$\nu_2(E_g)$ $[AsF_6]^-$
	492(220)[0]	467(246)[0]	$[\nu(Kr_1\text{-}F_1) + \nu(Kr_{1B}\text{-}F_{1B}) + \nu(Kr_{1G}\text{-}F_{1G}) + \nu(Kr_{1E}\text{-}F_{1E}) + \nu(Kr_{1D}\text{-}F_{1D}) + \nu(Kr_{1F}\text{-}F_{1F}) + \nu(Kr_{1C}\text{-}F_{1C}) + \nu(Kr_{1A}\text{-}F_{2A})]$
508(sh)	462(0)[532]	436(0)[482]	$[\nu(Kr_1\text{-}F_1) + \nu(Kr_{1G}\text{-}F_{1G}) + \nu(Kr_{1F}\text{-}F_{1F}) + \nu(Kr_{1E}\text{-}F_{1E})_{small}] - [\nu(Kr_{1B}\text{-}F_{1B}) + \nu(Kr_{1D}\text{-}F_{1D}) + \nu(Kr_{1C}\text{-}F_{1C}) + \nu(Kr_{1A}\text{-}F_{2A})_{small}]$
489(100)	462(0)[532]	436(0)[482]	$[\nu(Kr_1\text{-}F_1) + \nu(Kr_{1B}\text{-}F_{1B}) + \nu(Kr_{1A}\text{-}F_{2A}) + \nu(Kr_{1G}\text{-}F_{1G})_{small}] - [\nu(Kr_{1E}\text{-}F_{1E}) + \nu(Kr_{1D}\text{-}F_{1D}) + \nu(Kr_{1F}\text{-}F_{1F}) + \nu(Kr_{1C}\text{-}F_{1C})_{small}]$
476(3)	447(0)[286]	426(0)[376]	$[\nu(Kr_1\text{-}F_1) + \nu(Kr_{1B}\text{-}F_{1B}) + \nu(Kr_{1D}\text{-}F_{1D}) + \nu(Kr_{1F}\text{-}F_{1F})] - [\nu(Kr_{1G}\text{-}F_{1G}) + \nu(Kr_{1E}\text{-}F_{1E}) + \nu(Kr_{1C}\text{-}F_{1C}) + \nu(Kr_{1A}\text{-}F_{2A})]$
464(49)[f]	445(31)[0]	417(37)[0]	$[\nu(Kr_1\text{-}F_1) + \nu(Kr_{1D}\text{-}F_{1D})] - [\nu(Kr_{1B}\text{-}F_{1B}) + \nu(Kr_{1F}\text{-}F_{1F})]$
456(sh)	445(31)[0]	417(37)[0]	$[\nu(Kr_{1G}\text{-}F_{1G}) + \nu(Kr_{1C}\text{-}F_{1C})] - [\nu(Kr_{1E}\text{-}F_{1E}) + \nu(Kr_{1A}\text{-}F_{2A})]$
451(sh)	438(35)[0]	413(62)[0]	$[\nu(Kr_1\text{-}F_1) + \nu(Kr_{1F}\text{-}F_{1F}) + \nu(Kr_{1C}\text{-}F_{1C})] - [\nu(Kr_{1B}\text{-}F_{1B}) + \nu(Kr_{1G}\text{-}F_{1G}) + \nu(Kr_{1D}\text{-}F_{1D})]$
449(38)	438(35)[0]	413(62)[0]	$[\nu(Kr_1\text{-}F_1) + \nu(Kr_{1B}\text{-}F_{1B}) + \nu(Kr_{1E}\text{-}F_{1E})] - [\nu(Kr_{1D}\text{-}F_{1D}) + \nu(Kr_{1F}\text{-}F_{1F}) + \nu(Kr_{1A}\text{-}F_{2A})]$
375(sh)			
371(2)			$\nu_5(T_{2g})$ $[AsF_6]^-$
369(2)			
362(<1)			
	286(0)[121]	255(0)[112]	$\{\delta(F_2\text{-}Kr_1\text{-}F_1) + \delta(F_{2B}\text{-}Kr_{1B}\text{-}F_{1B}) + \delta(F_{2G}\text{-}Kr_{1G}\text{-}F_{1G}) + \delta(F_{2D}\text{-}Kr_{1D}\text{-}F_{1D}) + \delta(F_{2F}\text{-}Kr_{1F}\text{-}F_{1F}) + \delta(F_{2C}\text{-}Kr_{1C}\text{-}F_{1C})\}_{i.p.}$
	286(0)[121]	255(0)[112]	$\{\delta(F_2\text{-}Kr_1\text{-}F_1) + \delta(F_{2B}\text{-}Kr1B\text{-}F_{1B}) + \delta(F_{2E}\text{-}Kr_{1E}\text{-}F_{1E}) + \delta(F_{2D}\text{-}Kr_{1D}\text{-}F_{1D}) + \delta(F_{2F}\text{-}Kr_{1F}\text{-}F_{1F}) + \delta(F_{2A}\text{-}Kr_{1A}\text{-}F_{1A})\}_{i.p.}$
	281(2)[0]	250(1)[0]	$\{\delta(F_2\text{-}Kr_1\text{-}F_1) + \delta(F_{2B}\text{-}Kr_{1B}\text{-}F_{1B}) + \delta(F_{2G}\text{-}Kr_{1G}\text{-}F_{1G}) + \delta(F_{2E}\text{-}Kr_{1E}\text{-}F_{1E}) + \delta(F_{2D}\text{-}Kr_{1D}\text{-}F_{1D}) + \delta(F_{2F}\text{-}Kr_{1F}\text{-}F_{1F}) + \delta(F_{2C}\text{-}Kr_{1C}\text{-}F_{1C}) + \delta(F_{2A}\text{-}Kr_{1A}\text{-}F_{1A})\}_{i.p.}$
282(2)	277(0)[49]	249(0)[27]	$\{[\delta(F_2\text{-}Kr_1\text{-}F_1) + \delta(F_{2B}\text{-}Kr_{1B}\text{-}F_{1B}) + \delta(F_{2D}\text{-}Kr_{1D}\text{-}F_{1D}) + \delta(F_{2F}\text{-}Kr_{1F}\text{-}F_{1F})] - [\delta(F_{2G}\text{-}Kr_{1G}\text{-}F_{1G}) + \delta(F_{2E}\text{-}Kr_{1E}\text{-}F_{1E}) + \delta(F_{2C}\text{-}Kr_{1C}\text{-}F_{1C}) + \delta(F_{2A}\text{-}Kr_{1A}\text{-}F_{1A})]\}_{i.p.}$
262(1)			
	265(4)[0]	246(3)[0]	$\{[\delta(F_{2B}\text{-}Kr_{1B}\text{-}F_{1B}) + \delta(F_{2F}\text{-}Kr_{1F}\text{-}F_{1F})] - [\delta(F_2\text{-}Kr_1\text{-}F_1) + \delta(F_{2D}\text{-}Kr_{1D}\text{-}F_{1D})]\}_{i.p.}$
	265(4)[0]	246(3)[0]	$\{[\delta(F_{2G}\text{-}Kr_{1G}\text{-}F_{1G}) + \delta(F_{2C}\text{-}Kr_{1C}\text{-}F_{1C})] - [\delta(F_{2E}\text{-}Kr_{1E}\text{-}F_{1E}) + \delta(F_{2A}\text{-}Kr_{1A}\text{-}F_{1A})]\}_{i.p.}$
	264(4)[0]	244(4)[0]	$\{[\delta(F_{2B}\text{-}Kr_{1B}\text{-}F_{1B}) + \delta(F_{2G}\text{-}Kr_{1G}\text{-}F_{1G}) + \delta(F_{2E}\text{-}Kr_{1E}\text{-}F_{1E})] - [\delta(F_{2F}\text{-}Kr_{1F}\text{-}F_{1F}) + \delta(F_{2C}\text{-}Kr_{1C}\text{-}F_{1C}) + \delta(F_{2A}\text{-}Kr_{1A}\text{-}F_{1A})]\}_{i.p.}$
	264(4)[0]	244(4)[0]	$\{[\delta(F_2\text{-}Kr_1\text{-}F_1) + \delta(F_{2E}\text{-}Kr_{1E}\text{-}F_{1E}) + \delta(F_{2C}\text{-}Kr_{1C}\text{-}F_{1C})] - [\delta(F_{2G}\text{-}Kr_{1G}\text{-}F_{1G}) + \delta(F_{2D}\text{-}Kr_{1D}\text{-}F_{1D}) + \delta(F_{2A}\text{-}Kr_{1A}\text{-}F_{1A})]\}_{i.p.}$

Table 7.4. continued…

238(<1)	245(<0.1)[0]	230(<0.1)[0]	$\{[\delta(F_2\text{-}Kr_1\text{-}F_1) + \delta(F_{2B}\text{-}Kr_{1B}\text{-}F_{1B}) + \delta(F_{2G}\text{-}Kr_{1G}\text{-}F_{1G}) + \delta(F_{2E}\text{-}Kr_{1E}\text{-}F_{1E}) + \delta(F_{2D}\text{-}Kr_{1D}\text{-}F_{1D}) + \delta(F_{2F}\text{-}Kr_{1F}\text{-}F_{1F}) + \delta(F_{2C}\text{-}Kr_{1C}\text{-}F_{1C}) + \delta(F_{2A}\text{-}Kr_{1A}\text{-}F_{1A})\}_{o.o.p.}$
	240(0)[95]	227(0)[83]	$\{[\delta(F_2\text{-}Kr_1\text{-}F_1) + \delta(F_{2B}\text{-}Kr_{1B}\text{-}F_{1B}) + \delta(F_{2D}\text{-}Kr_{1D}\text{-}F_{1D}) + \delta(F_{2F}\text{-}Kr_{1F}\text{-}F_{1F})] - [\delta(F_{2G}\text{-}Kr_{1G}\text{-}F_{1G}) + \delta(F_{2E}\text{-}Kr_{1E}\text{-}F_{1E}) + \delta(F_{2C}\text{-}Kr_{1C}\text{-}F_{1C}) + \delta(F_{2A}\text{-}Kr_{1A}\text{-}F_{1A})\}_{o.o.p.}$
	239(0)[15]	225(0)[14]	$\{[\delta(F_{2G}\text{-}Kr_{1G}\text{-}F_{1G}) + \delta(F_{2E}\text{-}Kr_{1E}\text{-}F_{1E}) + \delta(F_{2F}\text{-}Kr_{1F}\text{-}F_{1F})] - [\delta(F_{2B}\text{-}Kr_{1B}\text{-}F_{1B}) + \delta(F_{2C}\text{-}Kr_{1C}\text{-}F_{1C}) + \delta(F_{2A}\text{-}Kr_{1A}\text{-}F_{1A})]\}_{o.o.p.}$
	239(0)[15]	225(0)[14]	$\{[\delta(F_2\text{-}Kr_1\text{-}F_1) + \delta(F_{2G}\text{-}Kr_{1G}\text{-}F_{1G}) + \delta(F_{2A}\text{-}Kr_{1A}\text{-}F_{1A})] - [\delta(F_{2E}\text{-}Kr_{1E}\text{-}F_{1E}) + \delta(F_{2D}\text{-}Kr_{1D}\text{-}F_{1D}) + \delta(F_{2C}\text{-}Kr_{1C}\text{-}F_{1C})]\}_{o.o.p.}$
	232(<1)[0]	219(<1)[0]	$\{[\delta(F_2\text{-}Kr_1\text{-}F_1) + \delta(F_{2D}\text{-}Kr_{1D}\text{-}F_{1D})] - [\delta(F_{2B}\text{-}Kr_{1B}\text{-}F_{1B}) + \delta(F_{2F}\text{-}Kr_{1F}\text{-}F_{1F})]\}_{o.o.p.}$
	232(<1)[0]	219(<1)[0]	$\{[\delta(F_{2G}\text{-}Kr_{1G}\text{-}F_{1G}) + \delta(F_{2C}\text{-}Kr_{1C}\text{-}F_{1C})] - [\delta(F_{2E}\text{-}Kr_{1E}\text{-}F_{1E}) + \delta(F_{2A}\text{-}Kr_{1A}\text{-}F_{1A})]\}_{o.o.p.}$
	231(<1)[0]	219(<1)[0]	$\{[\delta(F_{2B}\text{-}Kr_{1B}\text{-}F_{1B}) + \delta(F_{2E}\text{-}Kr_{1E}\text{-}F_{1E})] - [\delta(F_{2F}\text{-}Kr_{1F}\text{-}F_{1F}) + \delta(F_{2A}\text{-}Kr_{1A}\text{-}F_{1A})]\}_{o.o.p.}$
	231(<1)[0]	219(<1)[0]	$\{[\delta(F_2\text{-}Kr_1\text{-}F_1) + \delta(F_{2C}\text{-}Kr_{1C}\text{-}F_{1C})] - [\delta(F_{2G}\text{-}Kr_{1G}\text{-}F_{1G}) + \delta(F_{2D}\text{-}Kr_{1D}\text{-}F_{1D})]\}_{o.o.p.}$
141(13) 118(8)	164(0)[10]	136(0)[19]	$\{[\rho_t(F_{2B}\text{-}Kr_{1B}\text{-}F_{1B}) + \rho_t(F_{2G}\text{-}Kr_{1G}\text{-}F_{1G}) + \rho_t(F_{2D}\text{-}Kr_{1D}\text{-}F_{1D}) + \rho_t(F_{2F}\text{-}Kr_{1F}\text{-}F_{1F}) + \rho_t(F_{2C}\text{-}Kr_{1C}\text{-}F_{1C}) + \rho_t(F_{2A}\text{-}Kr_{1A}\text{-}F_{1A})]\}_{i.p.}$
	164(0)[10]	136(0)[19]	$\{[\rho_t(F_2\text{-}Kr_1\text{-}F_1) + \rho_t(F_{2G}\text{-}Kr_{1G}\text{-}F_{1G}) + \rho_t(F_{2E}\text{-}Kr_{1E}\text{-}F_{1E}) + \rho_t(F_{2D}\text{-}Kr_{1D}\text{-}F_{1D}) + \rho_t(F_{2C}\text{-}Kr_{1C}\text{-}F_{1C}) + \rho_t(F_{2A}\text{-}Kr_{1A}\text{-}F_{1A})]\}_{i.p.}$
	155(1)[0]	135(2)[0]	$\{[\rho_t(F_2\text{-}Kr_1\text{-}F_1) + \rho_t(F_{2B}\text{-}Kr_{1B}\text{-}F_{1B}) + \rho_t(F_{2G}\text{-}Kr_{1G}\text{-}F_{1G}) + \rho_t(F_{2E}\text{-}Kr_{1E}\text{-}F_{1E}) + \rho_t(F_{2D}\text{-}Kr_{1D}\text{-}F_{1D}) + \rho_t(F_{2F}\text{-}Kr_{1F}\text{-}F_{1F}) + \rho_t(F_{2C}\text{-}Kr_{1C}\text{-}F_{1C}) + \rho_t(F_{2A}\text{-}Kr_{1A}\text{-}F_{1A})]\}_{i.p.}$
	153(0)[8]	131(0)[17]	$\{[\rho_t(F_2\text{-}Kr_1\text{-}F_1) + \rho_t(F_{2B}\text{-}Kr_{1B}\text{-}F_{1B}) + \rho_t(F_{2D}\text{-}Kr_{1D}\text{-}F_{1D}) + \rho_t(F_{2F}\text{-}Kr_{1F}\text{-}F_{1F})] - [\rho_t(F_{2G}\text{-}Kr_{1G}\text{-}F_{1G}) + \rho_t(F_{2E}\text{-}Kr_{1E}\text{-}F_{1E}) + \rho_t(F_{2C}\text{-}Kr_{1C}\text{-}F_{1C}) + \rho_t(F_{2A}\text{-}Kr_{1A}\text{-}F_{1A})]\}_{i.p.}$
	120(13)[0]	99(12)[0]	$\{[\rho_t(F_2\text{-}Kr_1\text{-}F_1) + \rho_t(F_{2D}\text{-}Kr_{1D}\text{-}F_{1D})] - [\rho_t(F_{2B}\text{-}Kr_{1B}\text{-}F_{1B}) + \rho_t(F_{2F}\text{-}Kr_{1F}\text{-}F_{1F})]\}_{i.p.}$
	120(13)[0]	99(12)[0]	$\{[\rho_t(F_{2G}\text{-}Kr_{1G}\text{-}F_{1G}) + \rho_t(F_{2C}\text{-}Kr_{1C}\text{-}F_{1C})] - [\rho_t(F_{2E}\text{-}Kr_{1E}\text{-}F_{1E}) + \rho_t(F_{2A}\text{-}Kr_{1A}\text{-}F_{1A})]\}_{i.p.}$
	118(9)[0]	99(15)[0]	$\{[\rho_t(F_{2B}\text{-}Kr_{1B}\text{-}F_{1B}) + \rho_t(F_{2E}\text{-}Kr_{1E}\text{-}F_{1E})] - [\rho_t(F_{2F}\text{-}Kr_{1F}\text{-}F_{1F}) + \rho_t(F_{2A}\text{-}Kr_{1A}\text{-}F_{1A})]\}_{i.p.}$
	118(9)[0]	99(15)[0]	$\{[\rho_t(F_2\text{-}Kr_1\text{-}F_1) + \rho_t(F_{2C}\text{-}Kr_{1C}\text{-}F_{1C})] - [\rho_t(F_{2G}\text{-}Kr_{1G}\text{-}F_{1G}) + \rho_t(F_{2D}\text{-}Kr_{1D}\text{-}F_{1D})]\}_{i.p.}$
99(3)	97(0)[9]	85(12)[0]	$\{[\rho_t(F_2\text{-}Kr_1\text{-}F_1) + \rho_t(F_{2G}\text{-}Kr_{1G}\text{-}F_{1G}) + \rho_t(F_{2F}\text{-}Kr_{1F}\text{-}F_{1F})] - [\rho_t(F_{2B}\text{-}Kr_{1B}\text{-}F_{1B}) + \rho_t(F_{2D}\text{-}Kr_{1D}\text{-}F_{1D}) + \rho_t(F_{2C}\text{-}Kr_{1C}\text{-}F_{1C})]\}_{o.o.p.}$
	97(0)[9]	84(0)[16]	$\{[\rho_t(F_2\text{-}Kr_1\text{-}F_1) + \rho_t(F_{2B}\text{-}Kr_{1B}\text{-}F_{1B}) + \rho_t(F_{2A}\text{-}Kr_{1A}\text{-}F_{1A})] - [\rho_t(F_{2E}\text{-}Kr_{1E}\text{-}F_{1E}) + \rho_t(F_{2D}\text{-}Kr_{1D}\text{-}F_{1D}) + \rho_t(F_{2F}\text{-}Kr_{1F}\text{-}F_{1F})]\}_{o.o.p.}$
	97(8)[0]	84(0)[11]	$\{[\rho_t(F_2\text{-}Kr_1\text{-}F_1) + \rho_t(F_{2B}\text{-}Kr_{1B}\text{-}F_{1B}) + \rho_t(F_{2G}\text{-}Kr_{1G}\text{-}F_{1G}) + \rho_t(F_{2E}\text{-}Kr_{1E}\text{-}F_{1E}) + \rho_t(F_{2D}\text{-}Kr_{1D}\text{-}F_{1D}) + \rho_t(F_{2F}\text{-}Kr_{1F}\text{-}F_{1F}) + \rho_t(F_{2C}\text{-}Kr_{1C}\text{-}F_{1C}) + \rho_t(F_{2A}\text{-}Kr_{1A}\text{-}F_{1A})]\}_{o.o.p.}$
	89(0)[12]	84(0)[11]	$\{[\rho_t(F_2\text{-}Kr_1\text{-}F_1) + \rho_t(F_{2B}\text{-}Kr_{1B}\text{-}F_{1B}) + \rho_t(F_{2D}\text{-}Kr_{1D}\text{-}F_{1D}) + \rho_t(F_{2F}\text{-}Kr_{1F}\text{-}F_{1F})] - [\rho_t(F_{2G}\text{-}Kr_{1G}\text{-}F_{1G}) + \rho_t(F_{2E}\text{-}Kr_{1E}\text{-}F_{1E}) + \rho_t(F_{2C}\text{-}Kr_{1C}\text{-}F_{1C}) + \rho_t(F_{2A}\text{-}Kr_{1A}\text{-}F_{1A})]\}_{o.o.p.}$

Table 7.4. continued…

	76(2)[0]	67(0)[1]	
	76(2)[0]	67(0)[1]	
	74(0)[2]	63(1)[0]	
	74(0)[2]	63(1)[0]	
	71(1)[0]	59(<1)[0]	
	71(1)[0]	59(<1)[0]	
	69(0)[2]	55(0)[1]	
	53(2)[0]	42(4)[0]	
	42(4)[0]	34(4)[0]	
	42(4)[0]	34(4)[0]	
	38(<1)[0]	29(2)[0]	
	38(<1)[0]	29(<1)[0]	
n.o.	29(0)[<1]	22(0)[<1]	deformation modes
	29(0)[<1]	22(0)[<1]	
	26(1)[0]	19(1)[0]	
	26(1)[0]	19(1)[0]	
	21(0)[<0.1]	18(0)[<0.1]	
	17(0)[<1]	17(4)[0]	
	17(3)[0]	15(3)[0]	
	17(3)[0]	15(3)[0]	
	16(3)[0]	13(0)[<0.1]	
	12(0)[<1]	13(0)[<0.1]	
	12(0)[<1]	13(0)[<0.1]	
	5(<1)[0]	3(<1)[0]	
	5(<1)[0]	3(<1)[0]	

[a] The Raman spectrum was obtained at −150 °C on a crystalline sample of $[Hg(KrF_2)_8][AsF_6]_2 \cdot 2HF$ contained in an FEP sample tube using 1064-nm excitation. [b] Values in parentheses denote relative experimental Raman intensities. [c] Calculated using the def2-TZVPD basis set. Values in parentheses denote calculated Raman intensities ($Å^4$ amu^{-1}). Values in square brackets denote calculated infrared intensities (km mol^{-1}). [d] The atom labeling scheme corresponds to that used in Figures 7.1, 7.2, and S7.1. Assignments were made by visual inspection of the vibrational displacements obtained at the B3LYP level of theory. Bond elongations and angle openings are denoted by plus (+) signs and bond contractions and angle compressions are denoted by minus (–) signs. Symbols/abbreviations denote stretch (ν), bend (δ), rock (ρ_r), twist (ρ_t), in-plane (i.p.), out-of-plane (o.o.p.), and shoulder (sh). [e] The $[AsF_6]^-$ anion bands were assigned under O_h symmetry by comparison with the literature values.[14] [f] The band is assigned to the Raman active (ν_1, $\sum_g^+$) stretching mode of free KrF_2.

Raman bands arising from the $[AsF_6]^-$ anions were assigned by comparison with the literature values[14] of its $\nu_3(T_{1u})$, 707 cm^{-1}; $\nu_1(A_{1g})$, 685 cm^{-1}; $\nu_2(E_g)$, 574 cm^{-1}, and $\nu_5(T_{2g})$, 362, 369, 371, 375 cm^{-1} vibrational modes. Lowering of the anion symmetry from O_h to C_i- and C_2-site symmetries and vibrational mode coupling within the crystallographic unit cell (factor-group splitting, see Figures S7.3 and S7.4) result in the observation of the formally Raman-inactive (IR-active) $\nu_3(T_{1u})$ band. Although the $[AsF_6]^-$ anion is fluorine-coordinated to Mg^{2+} similar frequencies were also observed for the $[AsF_6]^-$ anion of $Mg(KrF_2)_4(AsF_6)_2$ (712, 687, 364, 374, 383, 386 cm^{-1}).[10]

7.2.4. Computational Results

The fully optimized gas-phase geometries and vibrational frequencies and intensities of $[Hg(KrF_2)_8]^{2+}$ (S_8; Figure 7.2b and S7.1b), Hg^{2+} and KrF_2 ($D_{\infty h}$) were calculated with the hybrid functionals APFD and B3LYP using the def2-TZVPD basis set. Overall, the APFD functional better reproduced the Hg–F_b bond lengths (calcd., 2.346 Å; av. exptl., 2.367(2) Å) when compared with the B3LYP functional, which overestimated these bond lengths (2.432 Å). The APFD functional also gave Kr–F_b bond lengths that were in better agreement with the experimental values (calcd., 1.980 Å; av. Exptl., 1.945(2) Å); however, the Kr–F_t bond lengths were slightly underestimated (calcd., 1.805 Å; av. exptl., 1.840(3) Å) when compared with those calculated at the B3LYP level (calcd., 1.832 Å). Both calculations well reproduced the observed experimental geometry including the square antiprismatic mercury coordination sphere.

Fundamental vibrations were calculated for the optimized structures with all frequencies real. The calculation at the B3LYP level (*vide supra*) resulted in better

agreement with experiment for the Kr–F_t stretching frequencies, whereas the APFD level gave better agreement for the Kr–F_b stretching frequencies.

The gas-phase geometries of $[Hg(KrF_2)_8]^{2+}$ and KrF_2 used for EDA and ETS-NOCV analyses were optimized using the program ADF at the DFT level using the Perdew-Burke-Ernzerhof (PBE) density functional[15] with the triple-ζ double-polarization all-electron basis set (TZ2P). Relativistic effects were taken into account by use of the zero-order regular approximation (ZORA)[16] and Grimme's DFT-D3-BJ correction was used to account for dispersion effects.[17] Although the $[Hg(KrF_2)_8]^{2+}$ cation could only be optimized to C_4-symmetry (the highest symmetry subgroup available in ADF is C_2), it is very close to S_8-symmetry and well reproduces the structural features (Table 7.2).

Analytical frequency calculations[18] were carried out for the ADF-optimized structures and fragments to ensure the geometry optimizations led to minima on their potential energy surfaces. The vibrational frequencies were real in all cases. The atomic partial charges were calculated by use of the Hirshfeld partitioning scheme.[19]

7.2.4.1. Natural Bond Orbital (NBO) Analyses

The NBO analyses of $[Hg(KrF_2)_8]^{2+}$ (Table 7.5) were carried out using NBO versions 3.1 and 6.0 [values given in square brackets] and are discussed for values calculated at the B3LYP level of theory.[20] The *n*p AOs of groups 1–12 are treated as polarization functions in NBO version 6.0, whereas version 3.1 includes the *n*p AOs as valence orbitals.[21] The NPA charge of Hg (+1.451 [+1.713]) is less than the formal charge expected for a purely ionic compound (+2). Inclusion of the mercury 6p AOs results in significantly more charge transfer from predominantly the bridging F-atom of

Table 7.5. Calculated Natural Population Analysis (NPA) charges, Wiberg bond indices, and Wiberg valences for $[Hg(KrF_2)_8]^{2+}$ [a]

B3LYP/def2-TZVPD				
Atom[b]	**NPA Charges**	**Valences**	**Bond**	**Bond Indices**
Hg_1	1.451 [1.713]	1.115 [0.615]	Hg_1–F_1	0.122 [0.064]
Kr_1	1.051 [1.046]	1.087 [1.084]	Kr_1–F_1	0.388 [0.388]
F_1	–0.593 [–0.623]	0.719 [0.652]	Kr_1–F_2	0.677 [0.682]
F_2	–0.389 [–0.387]	0.874 [0.870]		
$\sum KrF_2$	**0.069 [0.036]**			
$\sum Hg(KrF_2)_8$	**2.000 [2.000]**			

APFD/def2-TZVPD				
Atom[b]	**NPA Charges**	**Valences**	**Bond**	**Bond Indices**
Hg_1	1.395 [1.717]	1.227 [0.619]	Hg_1–F_1	0.132 [0.064]
Kr_1	1.066 [1.058]	1.097 [1.091]	Kr_1–F_1	0.382 [0.382]
F_1	–0.599 [–0.634]	0.718 [0.642]	Kr_1–F_2	0.686 [0.690]
F_2	–0.391 [–0.389]	0.875 [0.870]		
$\sum KrF_2$	**0.076 [0.035]**			
$\sum Hg(KrF_2)_8$	**2.000 [2.000]**			

[a] Values were calculated using NBO versions 3.1 and 6.0 [in square brackets].[20] [b] The atom labeling scheme corresponds to that used in Figures 7.2b and S7.1b.

each KrF_2 ligand bonded to Hg (0.069 [0.036] e) (*vide infra*). The Hg–F_b(KrF) Wiberg bond indices (0.122 [0.064]) involving the mercury 6p AOs are in accordance with the coordinate-covalent character of the Hg–F_b bonds. The NPA charges of the KrF_2 ligands are consistent with their asymmetric bond lengths, where polarization by Hg^{2+} results in significantly more negative charge on F_b (–0.593 [–0.623]) than on F_t (–0.389 [–0.387]).

7.2.4.2. Binding Energies of $[Hg(KrF_2)_8]^{2+}$

The gas-phase counterpoise-corrected binding energies were calculated for $[Hg(KrF_2)_8]^{2+}$ at the B3LYP and APFD methods. The total energy change for coordination of the eight KrF_2 ligands to Hg^{2+} is –1373.5 (APFD) and –1221.6 kJ mol^{-1} (B3LYP), giving average binding energies of –171.7 (APFD) and –152.7 kJ mol^{-1} (B3LYP) per KrF_2 ligand.

7.2.4.3. Energy Decomposition Analysis (EDA)

The metal-ligand bonding of $[Hg(KrF_2)_8]^{2+}$ was further analyzed using the energy decomposition analysis (EDA) of Ziegler and Rauk[22] at the PBE/TZ2P level of theory (see *Appendix E*). The major contributions to the total interaction energy (–1209.0 kJ mol^{-1}; inclusive of the preparation energy) are the attractive orbital (ΔE_{orb} = –940.1 kJ mol^{-1}) and electrostatic (ΔE_{elstat} = –651.0 kJ mol^{-1}) interactions, and the repulsive Pauli interaction (ΔE_{Pauli} = 331.4 kJ mol^{-1}) (Table S7.1). The EDA calculation indicates both orbital interactions, which incorporate covalent bonding, and electrostatic contributions are important stabilization factors for $[Hg(KrF_2)_8]^{2+}$. The calculated Hirshfeld charges of Hg (+1.521) and the $(KrF_2)_8$ fragment (+0.478) are similar to those obtained from the

NBO analysis when the Hg 6p AOs are treated as valence orbitals (*vide supra*), and are in accordance with significant electron donation to the metal center.

7.2.4.4. Extended Transition State Natural Orbitals for Chemical Valence (ETS-NOCV) Analysis

The orbital interaction energy (ΔE_{orb}) was further partitioned into contributions from the Hg^{2+} atomic orbitals and the $(KrF_2)_8$ ligand group MOs using the Extended Transition State Natural Orbitals for Chemical Valence (ETS-NOCV) approach[23] (see *Appendix E*). In this work, the MOs of the $(KrF_2)_8$ fragment are described in terms of their constituent KrF_2 ligand MOs which are designated by the MO symmetries of the free KrF_2 ($D_{\infty h}$) molecule (Figure 7.4). The analysis shows two different MOs from each KrF_2 ligand which donate electron density from F_b to Hg^{2+} through predominantly the $8\sigma_g$ (HOMO–4) orbital and, to a lesser extent, a degenerate $4\pi_u$ (HOMO) orbital (Figure 7.5a). The most significant metal-ligand orbital contribution (–275.5 kJ mol^{-1}) arises from in-phase combinations of the ligand donor orbitals with the empty 6s orbital of Hg^{2+} (Figures 7.6a and S7.6a). Three other contributions involve interactions of the empty mercury 6p orbitals with ligand donor MO combinations which provide significant stabilization (–231 kJ mol^{-1}). The square antiprismatic geometry of the cation results in degenerate ligand orbital interactions with the $6p_x$ and $6p_y$ orbitals of Hg^{2+} (2 x –78.8 kJ mol^{-1}; Figures 7.6b and 7.6c, Figures S7.6b and S7.6c) that are slightly more stabilizing than those with the $6p_z$ orbital of Hg^{2+} (–72.8 kJ mol^{-1}, Figures 7.6c and S7.6d). Electron donation from the occupied $8\sigma_g$ and $4\pi_u$ MOs of KrF_2 to the 6s and 6p acceptor orbitals of Hg^{2+} also accounts for the bent Hg–F–Kr bond angles (124.0(1)–134.3(1)^o), which are

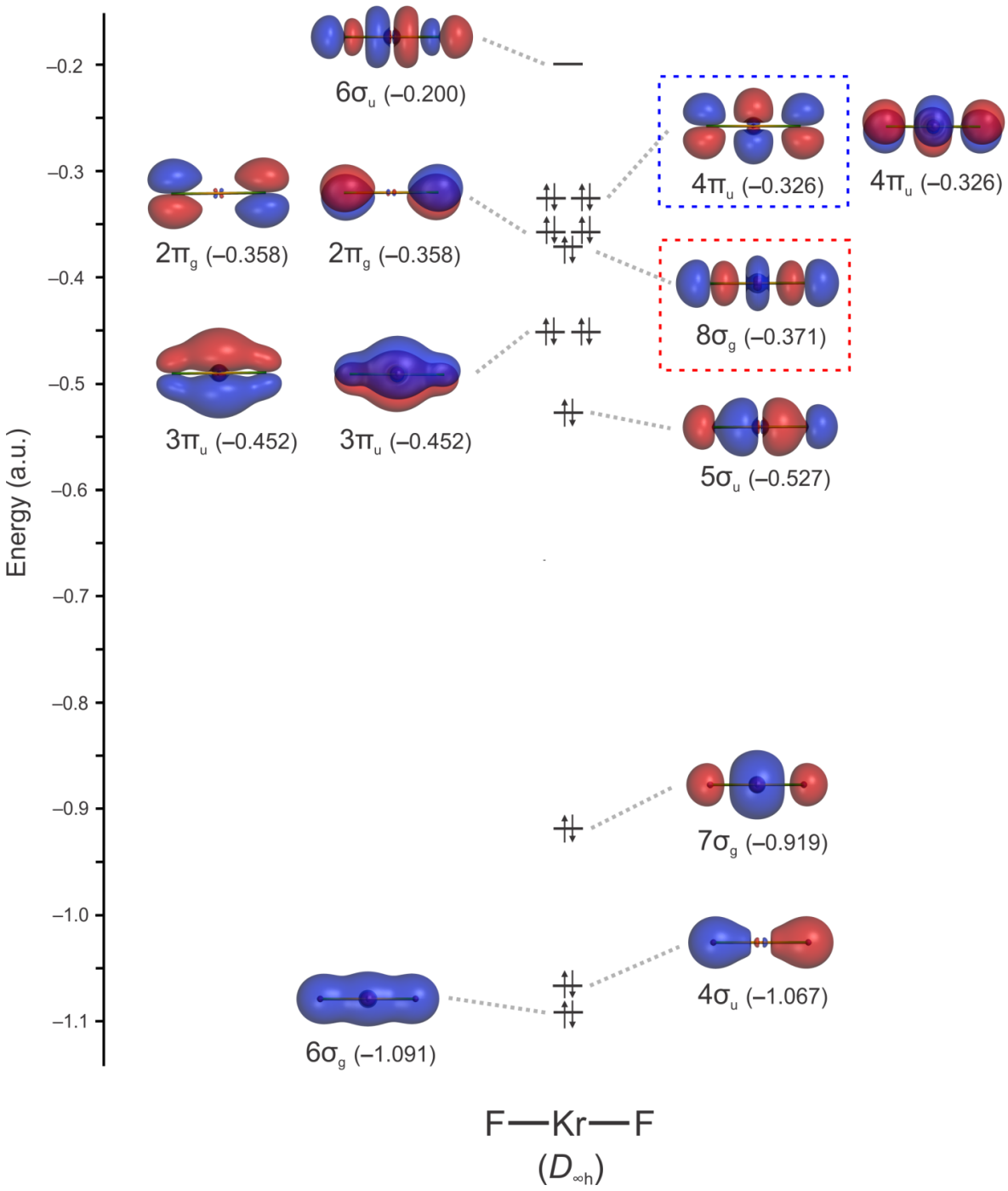

Figure 7.4. The MO energy level diagram of KrF_2 ($D_{\infty h}$, PBE/TZ2P) for the $6\sigma_g$ (HOMO−10) – $6\sigma_u$ (LUMO) orbitals are shown for 0.03 a.u. isosurfaces. The $8\sigma_g$ (HOMO–4) and degenerate $4\pi_u$ (HOMO) orbitals that are involved in bonding with Hg^{2+} are enclosed in red and blue dashed boxes, respectively.

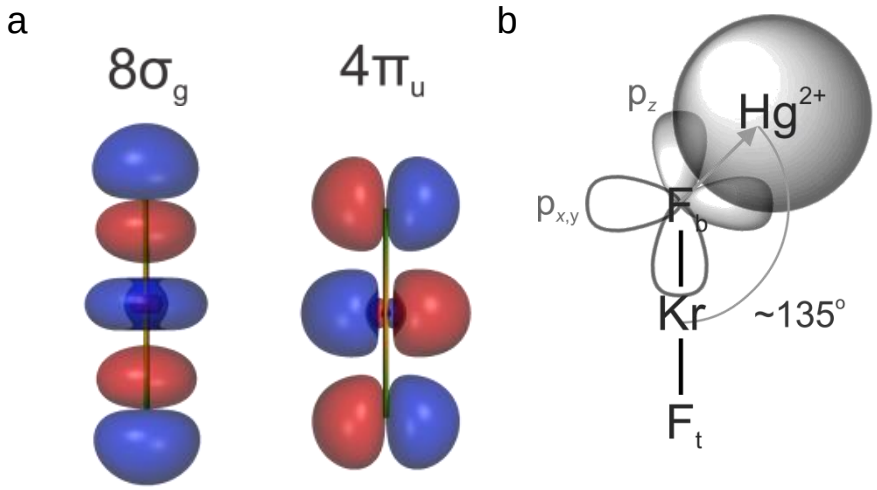

Figure 7.5. (**a**) The occupied Kohn-Sham $8\sigma_g$ and $4\pi_u$ MOs of KrF_2 ($D_{\infty h}$, Figure 7.4). (**b**) A simplified diagram showing the interaction of the unoccupied 6s AO of Hg^{2+} with the F_b "$2p_z$" and "$2p_{x,y}$" AO-components of the $8\sigma_g$ and $4\pi_u$ MOs, respectively. These interactions, along with those involving the 6p AOs of Hg^{2+} (not shown), account for the nonlinear Hg–F–Kr contact angle (~135°).

well reproduced by the calculations (127.5, 127.6°). In a simplified description, two "2p" orbitals of F_b serve as σ-electron donors to Hg^{2+} (Figure 7.5b). Similar orbital interactions likely account for the bent E–F–Ng angles of other terminally coordinated NgF_2 adducts (Ng = Xe or Kr) and the bent fluorine bridge angles that occur between the cations and anions of $[NgF]^+$ salts.[2,8–10]

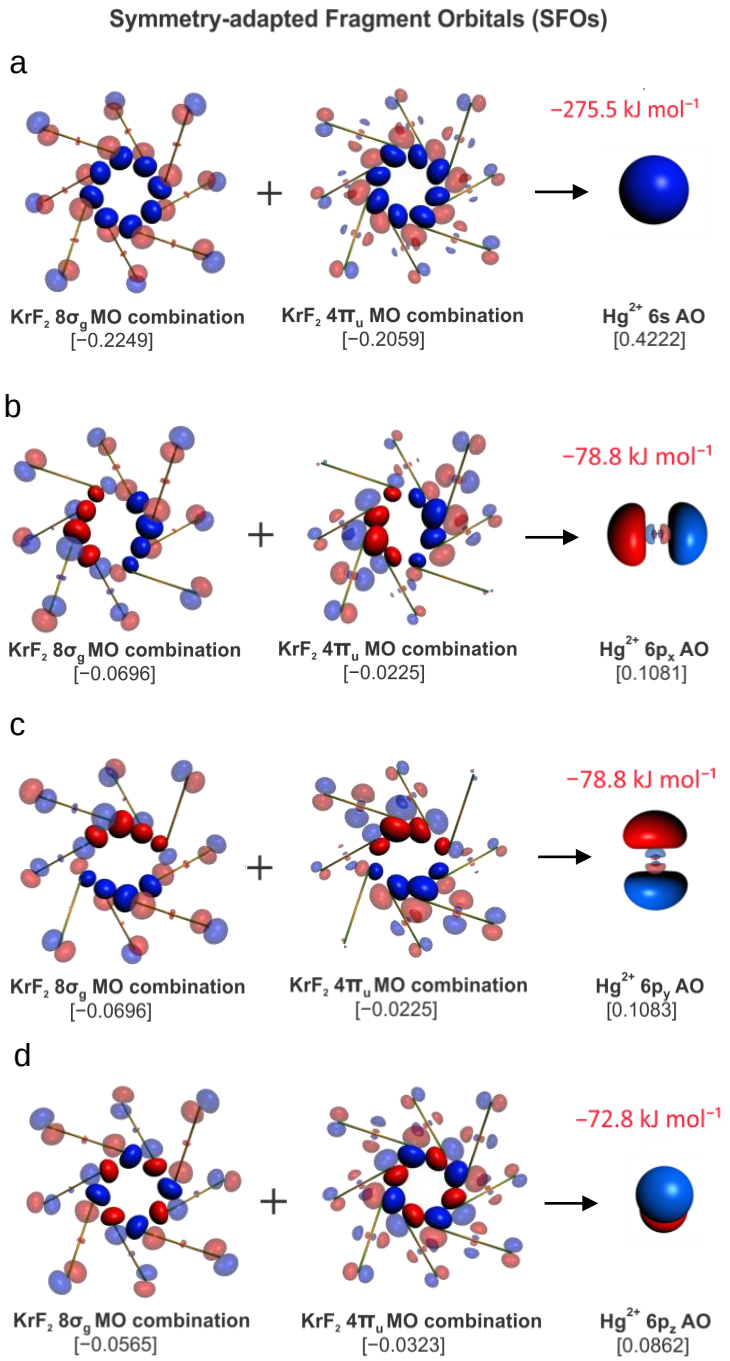

Figure 7.6. The most significant fragment orbitals derived from the ETS-NOCV analysis of $[Hg(KrF_2)_8]^{2+}$ are shown (isosurface values: ligands (0.03 a.u.) and Hg^{2+} (0.06 a.u.)) for combinations of the $(KrF_2)_8$ ligand group orbitals with unoccupied Hg^{2+} orbitals **a**) 6s, **b**) $6p_x$, **c**) $6p_y$, and **d**) $6p_z$ viewed along the $C_2(z)$-axis of the square antiprismatic cation. Labels correspond to MOs derived from free KrF_2 (see Figure 7.4 and 7.5a) and the atomic orbitals of Hg^{2+}. Fractional SFO contributions to the ETS-NOCVs are given in square brackets. Relative orbital phases are indicated by red and blue colors. Solid colors denote orbital lobes of the metal and ligand fragments that constructively interact.

7.3. Conclusions

The synthesis and isolation of $[Hg(KrF_2)_8][AsF_6]_2 \cdot 2HF$ provides the first structurally characterized example of a homoleptic KrF_2 complex and of KrF_2 terminally coordinated to a transition-metal element. It is also the highest KrF_2-to-metal ratio that is currently known for a KrF_2 coordination complex. The EDA calculations indicate both electrostatic and orbital interactions are important for the stabilization of $[Hg(KrF_2)_8]^{2+}$. The NBO analyses corraborate the coordinate-covalent character of the metal-ligand bonds and illustrate the importance of including both the 6s and 6p AOs of Hg^{2+} in the bonding description. The ETS-NOCV analyses show the $8\sigma_g$ and $4\pi_u$ MOs of the KrF_2 molecule are the dominant ligand donor orbitals and also account for the bent $Hg–F_b–Kr$ bond angles of the complex.

7.4. Experimental

General experimental techniques, procedures, and equipment, as well as the preparation and purification of all starting materials are described in Chapter 2.

7.4.1. Synthesis and Crystal Growth of $[Hg(KrF_2)_8][AsF_6]_2 \cdot 2HF$

In a typical synthesis, $Hg(AsF_6)_2$ (0.0117 g, 0.020 mmol) was placed in a dry, fluorine-passivated T-shaped reactor constructed from ¼″-in. o.d. FEP tubing and equipped with a Kel-F valve. Anhydrous HF (ca. 0.5 mL) was condensed, under static vacuum, onto the starting material at –78 ^oC. The mixture was cooled to –196 ^oC and KrF_2 (0.0296 g, 0.243 mmol) was sublimed into the reaction vessel under static vacuum. The vessel was backfilled with dry N_2 and warmed to and maintained at –78 ^oC until the

HF melted. The reactor and contents were warmed to room temperature for ca. 1 min whereupon the reactants dissolved to give a colorless solution. The reaction mixture was cooled to and maintained at –78 ^{o}C for several days over which time colorless, block-shaped crystals grew. The crystalline material was isolated by decanting the supernatant into the side arm of the reaction vessel at –78 ^{o}C which was subsequently cooled to –196 ^{o}C and heat sealed off under dynamic vacuum. The HF-wetted crystals remaining in the reactor were pumped on at –78 ^{o}C for 1 h which resulted in dry, colorless crystals that were suitable for an X-ray crystal structure determination.

7.4.2. Solution and Refinement of $[Hg(KrF_2)_8][AsF_6]_2 \cdot 2HF$

The XPREP[24] program (as part of the APEX3 v2017.3–0 software) was used to confirm the crystal lattice as well as the space group. The structure was solved in the centrosymmetric space group, *C*2/c, using SHELXT[25] which located the positions of all atoms in the crystal structures except the H-atoms, which were placed at calculated positions using the SHELXTL-Plus package[25] and their positions were restrained using the DFIX command. Refinement of the crystal structure using SHELXL[25] was straightforward. The final refinement was obtained by introducing anisotropic thermal parameters and the recommended weightings for all non-hydrogen atoms. The maximum electron densities in the final difference Fourier maps were located near the mercury atoms. Molecular graphics calculations were carried out using the SHELXTL-Plus package. The space group choice was confirmed using the PLATON program.[26] A very small second crystal phase contribution was also present, resulting in some weak

systematic absences (I>3σ(I)). However, this had little impact on the high quality of the final refinement and was therefore ignored.

7.4.3. Computational Details.

The fully optimized gas-phase geometries and vibrational frequencies and intensities of $[Hg(KrF_2)_8]^{2+}$ (S_8), Hg^{2+} and KrF_2 ($D_{\infty h}$) were calculated with density functional theory using the Gaussian 09 software package.[27] The hybrid functionals APFD and B3LYP were evaluated for these systems using the def2-TZVPD basis set which was obtained online from the EMSL Basis Set Exchange. [28] Overall, the APFD functional better reproduced the Hg–F_b bond lengths (calcd., 2.346 Å; av. exptl., 2.367(2) Å) when compared with the B3LYP functional, which overestimated these bond lengths (2.432 Å). The APFD functional also gave Kr–F_b bond lengths that were in better agreement with the experimental values (calcd., 1.980 Å; av. Exptl., 1.945(2) Å); however, the Kr–F_t bond lengths were slightly underestimated (calcd., 1.805 Å; av. exptl., 1.840(3) Å) when compared with those calculated at the B3LYP level (calcd., 1.832 Å). Both calculations well reproduced the observed experimental geometry including the square antiprismatic mercury coordination sphere.

Fundamental vibrations were calculated for the optimized structures with all frequencies real. The calculation at the B3LYP level (*vide supra*) resulted in better agreement with experiment for the Kr–F_t stretching frequencies, whereas the APFD level gave better agreement for the Kr–F_b stretching frequencies. The GaussView[29] program was used to visualize the vibrational displacements for $[Hg(KrF_2)_8]^{2+}$ which form the

basis for the vibrational mode descriptions given in Table S3. NBO analyses were carried out using the NBO program (versions 3.1and 6.0).[20] In order to obtain more accurate total computed binding energies for eight coordinated KrF_2 molecules, the Basis Set Superposition Error (BSSE) was corrected for $[Hg(KrF_2)_8]^{2+}$ using the counterpoise method.[30]

The gas-phase geometries of $[Hg(KrF_2)_8]^{2+}$ and KrF_2 used for EDA and ETS-NOCV analyses were optimized using the ADF (Amsterdam Density Functionals) package, Software for Chemistry and Materials (SCM, version 2016.106).[31] Although the $[Hg(KrF_2)_8]^{2+}$ cation could only be optimized to C_4-symmetry (the highest symmetry subgroup available in ADF is C_2), it is very close to S_8-symmetry and well reproduces the structural features (Table 7.2).The computational results were visualized using the ADF Graphical User Interface (SCM).[31]

7.5. Supporting Information Contents - Appendix E

Side view of experimental and calculated $[Hg(KrF_2)_8]^{2+}$ cation (Figure S7.1); factor-group analysis for $[Hg(KrF_2)_8]^{2+}$ (Figure S7.2); factor-group analysis for $[As_{(1)}F_6]^-$ (Figure S7.3); factor-group analysis for $[As_{(2)}F_6]^-$ (Figure S7.4); SCF deformation density isosurface for $[Hg(KrF_2)_8]^{2+}$(Figure S7.5); ETS-NOCV analysis for Hg^{2+} and the $(KrF_2)_8$ ligand group (Figure S7.6); description of the EDA and ETS-NOCV analyses; EDA analysis for $[Hg(KrF_2)_8]^{2+}$ (Table S7.1); Supplementary crystallographic data can be obtained free of charge from FIZ Karlsruhe by quoting deposition number CSD-434664.

7.6. References

(1) R. Hagiwara, F. Hollander, C. Maines, N. Bartlett, *Eur. J. Solid State Inorg. Chem.* **1991**, *28*, 855.

(2) D. S. Brock, G. J. Schrobilgen, B. Žemva, in; J. Reedijk, K. Poeppelmeier, Eds., Comprehensive Inorganic Chemistry II, Elsevier Ltd., Amsterdam, **2013**, pp. 755–822 and references therein.

(3) G. Tavčar, M. Tramšek, *J. Fluorine Chem.* **2015**, *174*, 14 and references therein.

(4) T. Bunič, M. Tramšek, E. Goreshnik, G. Tavčar, B. Žemva, *Inorg. Chem.* **2007**, *46*, 5276.

(5) M. Tramšek, P. Benkič, B. Žemva, *Angew. Chem. Int. Ed.* **2004**, *43*, 3456.

(6) G. Tavčar, E. Goreshnik, Z. Mazej, *J. Fluorine Chem.* **2006**, *127*, 1368.

(7) J. F. Lehmann, H. P. A. Mercier, G. J. Schrobilgen, *Coord. Chem. Rev.* **2002**, *233*, 1 and references therein.

(8) D. S. Brock, J. J. Casalis de Pury, H. P. A. Mercier, G. J. Schrobilgen, B. Silvi, *J. Am. Chem. Soc.* **2010**, *132*, 3533.

(9) J. R. DeBackere, H. P. A. Mercier, G. J. Schrobilgen, *J. Am. Chem. Soc.* **2014**, *136*, 3888.

(10) M. Lozinšek, H. P. A. Mercier, D. S. Brock, B. Žemva, G. J. Schrobilgen, *Angew. Chem. Int. Ed.* **2017**, *56*, 6251.

(11) J. F. Lehmann, D. A. Dixon, G. J. Schrobilgen, *Inorg. Chem.* **2001**, *40*, 3002.

(12) H. H. Claassen, G. L. Goodman, J. G. Malm, F. Schreiner, *J. Chem. Phys.* **1965**, *42*, 1229.

(13) M. Al-Mukhtar, J. H. Holloway, E. G. Hope, G. J. Schrobilgen, *J. Chem. Soc., Dalton Trans.* **1991**, 2831.

(14) a) C. Naulin, R. Bougon, *J. Chem. Phys.* **1976**, *64*, 4155; b) A. I. Popov, A. V. Scharabarin, V. F. Sukhoverkhov, N. A. Tchumaevsky, *Z. Anorg. Allg. Chem.* **1989**,*576*, 242.

(15) J. P. Perdew, K. Burke, M. Ernzerhof, *Phys. Rev. Lett.* **1996**, *77*, 3865.

(16) a) E. van Lenthe, E. J. Baerends, J. G. Snijders, *J. Chem. Phys.* **1993**, *99*, 4597; b) E. van Lenthe, E. J. Baerends, J. G. Snijders, *J. Chem. Phys.* **1994**, *101*, 9783; c) E. van Lenthe, A. Ehlers, E. Baerends, *J. Chem. Phys.* **1999**, *110*, 8943; d) E. van Lenthe, J. G. Snijders, E. J. Baerends, *J. Chem. Phys.* **1996**, *105*, 6505; e) E. van Lenthe, R. van Leeuwen, E. J. Baerends, J. G. Snijders, *Int. J. Quantum Chem.* **1996**, *57*, 281.

(17) S. Grimme, S. Ehrlich, L. Goerigk, *J. Comput. Chem*. **2011**, *32*, 1456.

(18) a) A. Bérces, R. M. Dickson, L. Fan, H. Jacobsen, D. Swerhone, T. Ziegler, *Comput. Phys. Commun.* **1997**, *100*, 247; b) H. Jacobsen, A. Bérces, D. Swerhone,

T. Ziegler, *Comput. Phys. Commun.* **1997**, *100*, 263; c) S. K. Wolff, *Int. J. Quantum Chem.* **2005**, *104*, 645.

(19) a) F. L. Hirshfeld, *Theoret. Chim. Acta*, **1977**, *44*, 129; b) K. B. Wiberg, R. B. Rablen, *J. Comput. Chem.* **1993**, *14*, 1504.

(20) a) NBO Version 6.0, E. D. Glendening, J. K. Badenhoop, A. E. Reed, J. E. Carpenter, J. A. Bohmann, C. M. Morales, C. R. Landis, F. Weinhold, Theoretical Chemistry Institute, University of Wisconsin, Madison, **2013**; b) NBO Version 3.1, E. D. Glendening, A. E. Reed, J. E. Carpenter, and F. Weinhold, Theoretical Chemistry Institute, University of Wisconsin, Madison, **1998**.

(21) S. J. Grabowski, J. M. Ugalde, D. M. Andrada, G. Frenking, *Chem. Eur. J.* **2016**, *22*, 11317.

(22) a) T. Ziegler, A. Rauk, *Theor. Chim. Acta* **1977**, *46*, 1. b) T. Ziegler, A. Rauk, *Inorg. Chem.***1979**, *18*, 1755; c) T. Ziegler, A. Rauk, *Inorg. Chem.* **1979**, *18*, 1558.

(23) a) A. Michalak, R. L. De Kock, T. Ziegler, *J. Phys. Chem. A* **2008**, *112*, 7256; b) R. F. Nalewajski, J. Mrozek, A. Michalak, *Int. J. Quantum Chem.* **1997**, *61*, 589; c) M. Mitoraj, A. Michalak, T. Ziegler, *J. Chem. Theory Comput.* **2009**, *5*, 962; d) M. Mitoraj, A. Michalak, T. Ziegler, *Organometallics* **2009**, *28*, 3727.

(24) Bruker (**2014**). XPREP v2008/2. Bruker AXS Inc., Madison, Wisconsin, USA

(25) a) G. M. Sheldrick, *Acta Crystallogr. A*, **2008,** *64*, 112; b) G. M. Sheldrick, *Acta Crystallogr. A*, **2015,** *71*, 3; c) G. M. Sheldrick, *Acta Crystallogr. C*, **2015,** *71*, 3.

(26) a) A. L. Spek, *J. Appl. Crystallogr.* **2003**, *36*, 7; b) A. L. Spek, *Acta Crystallogr. D* **2009**, *65*, 148.

(27) Gaussian 09, revision E.01; M. J. Frisch, G. W. Trucks, H. B. Schlegel, G. E. Scuseria, M. A. Robb, J. R. Cheeseman, G. Scalmani, V. Barone, B. Mennucci, G. A. Petersson, H. Nakatsuji, M. Caricato, X. Li, H. P. Hratchian, A. F. Izmaylov, J. Bloino, G. Zheng, J. L Sonnenberg, M. Hada, M. Ehara, K. Toyota, R. Fukuda, J. Hasegawa, M. Ishida, T. Nakajima, Y. Honda, O. Kitao, H. Nakai, T. Vreven, J. A., Jr. Montgomery, J. E. Peralta, F. Ogliaro, M. Bearpark, J. J. Heyd, E. Brothers, K. N. Kudin, V. N. Staroverov, R. Kobayashi, J. Normand, K. Raghavachari, A. Rendell, J. C. Burant, S. S. Iyengar, J. Tomasi, M. Cossi, N. Rega, N. J. Millam, M. Klene, J. E. Knox, J. B. Cross, V. Bakken, C. Adamo, J. Jaramillo, R. Gomperts, R. E. Stratmann, O. Yazyev, A. J. Austin, R. Cammi, C. Pomelli, J. W. Ochterski, R. L. Martin, K. Morokuma, V. G. Zakrzewski, G. A. Voth, P. Salvador, J. J. Dannenberg, S. Dapprich, A. D. Daniels, Ö. Farkas, J. B. Foresman, J. V. Ortiz, J. Cioslowski, D. J., Gaussian, Inc.: Wallingford, CT, **2013**.

(28) a) D. Feller, *J. Comput. Chem.* **1996**, *17*, 1571; b) K. L. Schuchardt, B. T. Didier, T. Elsethagen, L. Sun, V. Gurumoorthi, J. Chase, J. Li, T. L. Windus, *J. Chem. Inf. Model.* **2007**, *47*, 1045.

(29) *GaussView*, release 3.0; Gaussian Inc.: Pittsburgh, PA, 2003.

(30) S. F. Boys, F. Bernardi, *Mol. Phys.* **1970**, *19*, 553.

(31) a) ADF2016, SCM, Theoretical Chemistry, Vrije Universiteit, Amsterdam, The Netherlands, http://www.scm.com; b) C. Fonseca Guerra, J. G. Snijders, G. te Velde, E. J. Baerends, *Theor. Chem. Acc.* **1998**, *99*, 391; c) G. te Velde, F. M. Bickelhaupt, E. J. Baerends, C. Fonseca Guerra, S. J. A. van Gisbergen, J. G. Snijders, T. Ziegler, *J. Comput. Chem.* **2001**, *22*, *931*.

CHAPTER 8

Syntheses and Structures of a Series of Krypton Difluoride Coordination Complexes of $Hg(PnF_6)_2$ (Pn = As or Sb) and $FHg(AsF_6)$

Prepared for Publication: DeBackere, J.R., and Schrobilgen, G.J.

8.1. Introduction

The noble-gas difluorides, NgF_2 (Ng = Kr, Xe), undergo fluoride ion abstraction by suitably strong Lewis acids, such as AsF_5 and SbF_5, to form strongly ion-paired salts of the $[NgF]^+$ cations as well as salts of the $[Ng_2F_3]^+$ cations which are not ion-paired.[1–3] In the case of weak to moderate-strength Lewis acids, XeF_2 and KrF_2 may act as ligands and coordinate to the Lewis acid site through a fluorine bridge interaction without undergoing fluoride ion abstraction. Known modes of coordination include a single fluorine atom of the NgF_2 molecule interacting with one Lewis acid site to give a terminally coordinated NgF_2 molecule, or both fluorine atoms coordinating to two Lewis acid sites to give a bridging NgF_2 molecule. Many examples of both coordination types have been synthesized and structurally characterized for XeF_2 complexes.[5-14] Among the structurally characterized complexes that have been reported are less common examples in which XeF_2 is coordinated to nonmetals, i.e., $F_2OBr(XeF_2)_2(AsF_6)$,[4] and more common examples in which a variety of metal cations are coordinated to XeF_2 (Li^+, Mg^{2+}, Ca^{2+}, Cu^{2+}, Zn^{2+}, Sr^{2+}, Ag^+, Cd^{2+}, Ba^{2+}, La^{3+}, Nd^{3+}, and Pb^{2+}).[5-10] Structurally characterized examples of group 12 metal cation complexes include $Cd(XeF_2)(BF_4)_2$,[7] $Cd(XeF_2)(HF)_2(MF_6)_2$ (M = Nb, Ta),[10] $Cd_2(XeF_2)_{10}(SbF_6)_4$,[9] $Cd(XeF_2)_4(AsF_6)_2$,[11] $Cd(XeF_2)_5(PF_6)_2$,[12] $[Zn(XeF_2)_6][SbF_6]_2$,[13] and $Hg(XeF_2)_5(PnF_6)_2$ (Pn = P, As, Sb).[10] The

$Cd(XeF_2)(HF)_2(MF_6)_2$ (M = Nb, Ta)[10] and $Mg(XeF_2)(XeF_4)(AsF_6)_2$[14] complexes are the only examples in which other neutral ligands are also coordinated to the metal. The complexes $XeF_2 \cdot nMOF_4$ (M = W[15,16] or Mo[16]; n = 1–4) have also been characterized by ^{19}F and ^{129}Xe NMR,[16] and $XeF_2 \cdot nMOF_4$ (n = 1, 2) by Raman spectroscopy.[15] A low-precision, room-temperature X-ray crystal structure of $XeF_2 \cdot WOF_4$ has also been reported.[17]

Like XeF_2, KrF_2 is capable of forming coordination complexes, however, examples are limited due to its thermodynamic instability and exceptionally strong oxidative fluorinating properties. Raman and NMR spectroscopic studies have provided evidence for the formation of $KrF_2 \cdot MOF_4$ (M = W,[18] Mo,[18] Cr[19]) and $KrF_2 \cdot nMoOF_4$ (*n* = 2–3),[18] and also Raman evidence suggesting the formation of $M(AuF_6)_2 \cdot nKrF_2$ (M = Ca, Sr, Ba; *n* = 0–4);[20] however, their crystal structures have not been reported. Examples of terminally coordinated KrF_2, which have been structurally characterized by single-crystal X-ray diffraction, are currently limited to $F_2OBr(KrF_2)_2(AsF_6)$,[21] $Mg(KrF_2)_4(AsF_6)_2$,[22] and most recently, $[Hg(KrF_2)_8][AsF_6]_2 \cdot 2HF$.[23] The crystal structure of $Hg(KrF_2)_{1.5}(OTeF_5)_2$ is the only example of bridging coordination for KrF_2.[24]

The $[Hg(KrF_2)_8][AsF_6]_2 \cdot 2HF$ complex has provided the first homoleptic KrF_2 complex and is the highest KrF_2-to-metal ratio complex that has been observed and structurally characterized.[23] In the present study, a series of KrF_2 adducts with $Hg(PnF_6)_2$ (Pn = As or Sb) and $FHg(AsF_6)$ has been isolated and structurally characterized by single-crystal X-ray diffraction and Raman spectroscopy. Interestingly, the complex $Hg(KrF_2)_5(AsF_6)_2$ **(5)** complex is not isostructural with $Hg(XeF_2)_5(AsF_6)_2$;[10] whereas

XeF_2 analogues of the remaining KrF_2 complexes described in the present study are currently unknown. This study provides several rare examples of known coordination modes of KrF_2 and the first examples of a new bonding modality in which KrF_2 interacts with two metals through a single fluorine atom.

8.2. Results and Discussion

8.2.1. Syntheses

Reactions were carried out for $Hg(PnF_6)_2$ (Pn = As, Sb) to KrF_2 ratios between 2:1 and 1:5 in anhydrous hydrogen fluoride (aHF) solvent and have provided routes to a series of coordination complexes in which one to five KrF_2 molecules are coordinated to Hg^{2+}. The initial reaction stoichiometries did not always reflect the resulting complexes formed, which often produced a mixture of products (*vide infra*). Low KrF_2 to $Hg(AsF_6)_2$ ratios generally favored $Hg(KrF_2)(HF)(AsF_6)_2$ **(1)** and $Hg(KrF_2)_2(AsF_6)_2$ **(2)** formation, whereas use of KrF_2 in stoichiometric excess allowed for the isolation of the higher ratio complexes, i.e., $Hg(KrF_2)_3(HF)(SbF_6)_2$ **(3),** $[Hg(KrF_2)_4(HF)_2(SbF_6)]_2[SbF_6]_2$ **(4)**, $Hg(KrF_2)_5(AsF_6)_2$ **(5)**, and $Hg(KrF_2)_4(HF)_2(AsF_6)_2 \cdot HF$ **(6)**. The low-temperature Raman spectra of the aforementioned salts were recorded on colorless crystalline samples that had been obtained by slow cooling of the reaction mixtures from –20 to –78 ^{o}C over several hours, which also yielded crystals that were suitable for X-ray structure determinations. The Raman spectra of the bulk crystalline samples and crystallographic unit cell determinations of selected crystals showed that the products were usually mixtures in which one species dominated. Although Raman spectra of each individual compound could not be obtained, the vibrational bands of $Hg(KrF_2)_5(AsF_6)_2$ were

assigned with confidence.

Crystalline $FHg(\mu_3\text{-}FKrF)_{1.5}(KrF_2)_{0.5}(AsF_6)$ **(7)** was also unexpectedly obtained as a minor component from the reaction of $Hg(AsF_6)_2$ with a threefold excess of KrF_2 in aHF solvent, and was characterized by single-crystal X-ray diffraction. Its formation may have resulted from the presence of a small amount of $FHg(AsF_6)$ in the starting material and/or the *in situ* formation of some $FHg(AsF_6)$. Attempts to further investigate **(7)** were made by low-temperature reactions $FHg(AsF_6)$ with KrF_2 in aHF solvent. Although previous work had shown $FHg(AsF_6)$ is stable indefinitely in aHF at room temperature,[25] the presence of KrF_2, even at low-temperatures such as –50 ^oC, favors the formation of $Hg(AsF_6)_2$. This primarily resulted in the crystallization of the KrF_2 complexes, namely $Hg(KrF_2)_2(AsF_6)_2$ **(2)**, $Hg(KrF_2)_5(AsF_6)_2$ **(5)**, and $[Hg(KrF_2)_8][AsF_6]_2 \cdot HF$,[23] and the new salt, $Hg_4F_5(AsF_6)_3 \cdot HF$ **(9)** (see Appendix F); as indicated by unit cell determinations for crystals obtained from the product mixtures and supported by Raman Spectroscopy. Despite the propensity of $FHg(AsF_6)$ to form $Hg(AsF_6)_2$ in the presence of KrF_2, suitable single crystals of $FHg(\mu_3\text{-}FKrF)_{0.5}(KrF_2)_{1.5}(AsF_6)$ **(8)** were obtained, in admixture with the aforementioned $Hg(AsF_6)_2$ complexes and $Hg_4F_5(AsF_6)_3 \cdot HF$, by very briefly warming a solution to –30 ^oC to effect dissolution of some material, followed by immediate cooling to –78 ^oC. No other complexes of $FHg(AsF_6)$, including $FHg(\mu_3\text{-}FKrF)_{1.5}(KrF_2)_{0.5}(AsF_6)$ **(7)**, were isolated in this manner.

8.2.2. X-ray Crystallography

Details of the data collection parameters and other crystallographic information are provided in Table 8.1. Selected bond lengths and angles for **(1)**-**(8)** are listed in Table 8.2,

Table 8.1. Summary of Crystal Data and Refinement Results for $Hg(KrF_2)(HF)[AsF_6]_2$ **(1)**, $Hg(KrF_2)_2[AsF_6]_2$ **(2)**, $Hg(KrF_2)_3(HF)[SbF_6]_2$ **(3)**, $[Hg(KrF_2)_4(HF)_2(SbF_6)]_2[SbF_6]_2$ **(4)**, $Hg(KrF_2)_5[AsF_6]_2$ **(5)**, $Hg(KrF_2)_4(HF)_2[AsF_6]_2 \cdot HF$ **(6)**, $FHg(\mu_3\text{-}FKrF)_{1.5}(KrF_2)_{0.5}(AsF_6)$ **(7)**, $FHg(\mu_3\text{-}FKrF)_{0.5}(KrF_2)_{1.5}(AsF_6)$ **(8)**, and $Hg_4F_5(AsF_6)_3 \cdot HF$ **(9)**

	(1)	(2)	(3)	(4)	(5)	(6)	(7)	(8)	(9)
formula	$As_2F_{15}HKrHg$	$As_2F_{16}Kr_2Hg$	$F_{19}HKr_3HgSb_2$	$F_{44}H_4Kr_{16}Hg_2Sb_4$	$As_2F_{22}Kr_5Hg$	$As_2F_{23}H_3Kr_4Hg$	$AsF_{11}Kr_2Hg$	$AsF_{11}Kr_2Hg$	$As_3F_{15}HHg$
space group	$P2_1/c$	$P2_1/c$	$P2_1/c$	$P\bar{1}$	$Pna2_1$	$P\bar{1}$	$C2/c$	$P\bar{1}$	$P\bar{1}$
a (Å)	10.2658(13)	16.711(4)	5.7154(1)	8.9530(2)	14.4582(13)	8.2067(4)	18.181(2)	8.1507(4)	7.2969(3)
b (Å)	10.0192(12)	7.953(2)	28.0215(6)	8.9948(2)	8.3122(8)	9.0263(5)	11.8986(14)	11.5762(5)	9.3497(4)
c (Å)	10.9533(14)	9.923(2)	10.6182(3)	14.5134(3)	16.5589(15)	15.1395(8)	18.509(2)	11.8003(6)	13.6580(5)
α (deg)	90.0	90.0	90.0	94.722(1)	90.0	82.727(3)	90.0	116.819(1)	80.866(2)
β (deg)	92.343(3)	101.644(3)	90.190(1)	96.087(1)	90.0	82.457(2)	103.082(2)	90.424(2)	74.959(2)
γ (deg)	90.0	90.0	90.0	118.190(1)	90.0	65.061(2)	90.0	102.557(2)	72.130(2)
V (Å^3)	1125.7(2)	1291.7(5)	1700.54(7)	1012.57(4)	1990.0(3)	1004.9(1)	3900.2(8)	962.74(8)	853.29(6)
Z	4	4	4	1	4	4	16	4	2
mol. wt. (g mol^{-1})	720.24	822.03	1056.49	1199.31	1187.43	562.83	652.11	652.11	1484.12
ρ_{calcd} (g cm^{-3})	4.250	4.227	4.127	3.934	3.963	3.720	4.442	4.499	5.776
T (°C)	–173	–173	–173	–173	–173	–173	–173	–173	–173
μ (mm^{-1})	23.600	23.989	20.092	19.075	22.265	19.867	28.301	28.663	41.884
R_1[a]	0.0310	0.0322	0.0250	0.0213	0.0235	0.0265	0.0397	0.0278	0.0292
wR_2[b]	0.0693	0.0722	0.0569	0.0498	0.0515	0.0672	0.0991	0.0616	0.0714

[a] R_1 is defined as $\Sigma||F_o| - |F_c|/\Sigma|F_o|$ for $I > 2\sigma(I)$. [b] wR_2 is defined as $[\Sigma[w(F_o^2 - F_c^2)^2]/\Sigma w(F_o^2)^2]^{1/2}$ for $I > 2\sigma(I)$.

Table 8.2. Selected Bond Lengths (Å) and Bond Angles (°) for Compounds (1)–(8) [a]

	(1)	(2)	(3)	(4)	(5)	(6)	(7)	(8)
Hg−F(Kr)								
Hg_1–F_1	2.205(5)	2.136(3)	2.289(3)	2.361(2)	2.317(4)	2.574(3)	2.542(6)	2.345(2)
Hg_1–F_3		2.141(3)	2.366(3)	2.345(2)	2.332(5)	2.639(3)	2.757(6)	2.455(2)
Hg_1–F_5			2.317(3)	2.383(2)	2.307(5)	2.529(3)	2.458(5)	
Hg_1–F_7				2.309(2)	2.381(4)	2.929(3)	2.290(6)	
Hg_1–F_9					2.324(5)			
Hg_2–F_1							2.691(6)	
Hg_2–F_3							2.635(6)	2.883(3)
Hg_2–F_5								2.445(4)
Hg_2–F_6							2.620(6)	
Hg_2–F_7							2.907(5)	2.421(4)
Hg−F(H)	2.285(4)		2.366(3)	2.369(2)		2.086(3)		
				2.400(2)		2.079(3)		
Kr−F_b								
Kr_1–F_1	1.956(5)	1.995(3)	1.950(3)	1.938(2)	1.948(4)	1.909(3)	1.955(6)	1.937(2)
Kr_2–F_3		2.004(2)	1.956(3)	1.932(2)	1.938(4)	1.927(3)	1.969(6)	1.958(2)
Kr_3–F_5			1.956(3)	1.934(2)	1.932(5)	1.923(3)	1.912(6)	1.932(3)
Kr_3–F_6							1.854(6)	
Kr_4–F_7				1.945(1)	1.932(5)	1.895(3)	1.999(6)	1.952(3)
Kr_5–F_9					1.948(5)			
Kr−F_t								
Kr_1–F_2	1.809(5)	1.805(3)	1.835(3)	1.844(2)	1.842(4)	1.872(3)	1.836(9)	1.856(3)
Kr_2–F_4		1.811(3)	1.826(3)	1.843(2)	1.850(5)	1.858(3)	1.846(8)	1.831(3)
Kr_3–F_6			1.828(4)	1.841(2)	1.843(5)	1.859(4)		1.849(3)
Kr_4–F_8				1.840(2)	1.851(5)	1.871(3)	1.820(6)	1.832(4)
Kr_5–F_{10}					1.847(5)			
Hg−F−Kr								
Hg_1–F_1–Kr_1	168.5(3)	148.6(2)	138.4(1)	130.6(1)	128.9(2)	140.4(1)	134.4(3)	125.7(1)
Hg_1–F_3–Kr_2		135.1(1)	137.8(2)	135.6(1)	138.6(2)	128.4(1)	128.6(3)	130.5(1)
Hg_1–F_5–Kr_3			134.3(1)	136.9(1)	133.5(2)	143.1(1)	136.6(3)	
Hg_1–F_7–Kr_4				127.3(1)	139.1(2)	145.9(2)	135.4(3)	
Hg_1–F_9–Kr_5					124.6(2)			
Hg_2–F_1–Kr_1							125.3(3)	
Hg_2–F_3–Kr_2							124.8(3)	121.9(1)
Hg_2–F_5–Kr_3								127.1(2)
Hg_2–F_6–Kr_3							168.4(3)	
Hg_2–F_7–Kr_4							127.8(2)	127.3(1)
$Hg_{(1)}$−μ_3-F(Kr)−$Hg_{(2)}$							86.5(2)	96.4(1)
							83.3(2)	
							94.9(2)	

[a] Labeling schemes correspond to the structures depicted in Figures 8.1–8.8.

and complete listings of geometric parameters are provided in the Appendix F (Tables S8.1−S8.9). The geometrical parameters of the $[PnF_6]^-$ anions are in good agreement with previously published values in which the anion interacts with a metal cation or is hydrogen bonded to HF.[10,25] The complexes reported in this work display a preference for a primary mercury coordination number of eight which usually result in distorted square antiprismatic mercury coordination spheres, similar to that of $[Hg(KrF_2)_8][AsF_6]_2 \cdot 2HF$.[23]

8.2.2.1. $Hg(KrF_2)_5(AsF_6)_2$ (5)

The crystal structure of **(5)** (Figure 8.1a and S8.1) consists of well-separated structural units in which the Hg^{2+} cations are terminally coordinated to five KrF_2 ligands and to one monodentate and one bidentate $[AsF_6]^-$ anion. The Hg---F_b(As) interactions of bidendate $[AsF_6]^-$ (2.558(5) and 2.591(5) Å) are considerably longer than those of the monodendate anion (2.392(5) Å). These interactions result in shorter terminal As−F_t bonds (1.697(5)−1.717(5) Å) relative to the As−F_b bonds which bridge to mercury (1.752(4)−1.759(4) Å), a characteristic of coordinated $[PnF_6]^-$ anions.[10]

The Hg–F_b(Kr) bond distances (2.307(5)−2.381(4) Å) are comparable to those of $[Hg(KrF_2)_8]^{2+}$ (2.300(1)–2.412(1) Å),[23] which are significantly shorter than those of the bridging KrF_2 ligands of $Hg(KrF_2)_{1.5}(OTeF_5)_2$ (2.664(3), 2.675(3), 2.741(3) Å).[24] The KrF_2 molecules are nearly linear (177.6(2)–179.1(2)^o) with Hg–F–Kr coordination angles (124.6(2)–139.1(2)^o) that are comparable to those of the other terminally coordinated KrF_2 adducts $[Hg(KrF_2)_8][AsF_6]_2 \cdot 2HF$ (Hg–F–Kr, 124.0(1)–134.3(1)^o),[23] $F_2OBr(KrF_2)_2(AsF_6)$ (Br–F–Kr, 132.1(2), 139.9(2)^o),[21] and $Mg(KrF_2)_4(AsF_6)_2$ (Mg–F–Kr, 121.84(7)–144.43(8)^o).[22]

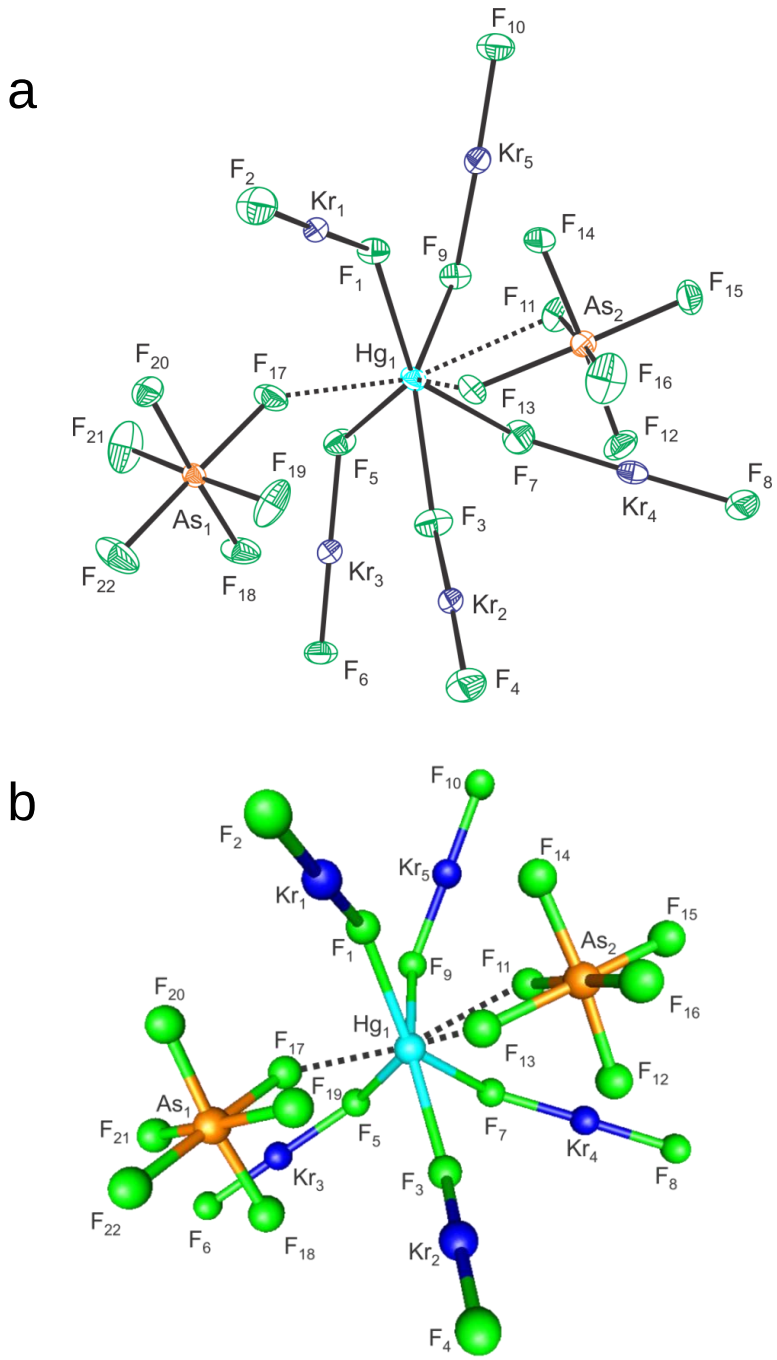

Figure 8.1. **(a)** The X-ray crystal structure of $Hg(KrF_2)_5(AsF_6)_2$ **(5)**; thermal ellipsoids shown at the 50% probability level. **(b)** The gas-phase, energy-minimized geometry of $Hg(KrF_2)_5(AsF_6)_2$ (C_1) calculated at the B3LYP/def2-TZVPP level of theory. Dashed lines indicate contacts with the $[AsF_6]^-$ anions.

Orbital interactions between the occupied $8\sigma_g$ (HOMO–4) and a $4\pi_u$ (HOMO) molecular orbital of the KrF_2 ligands and unoccupied valence 6s and 6p orbitals of Hg^{2+} in $[Hg(KrF_2)_8]^{2+}$ were shown to result in a significant degree of σ-donation which accounts for the bent Hg–F–Kr angles of this cation.[23] Similar Hg–F–Kr angles are observed throughout the Hg^{2+} series of KrF_2 coordination complexes described in this study and are also attributed to similar orbital interactions. This structural feature is not mentioned further in the ensuing discussions of related Hg^{2+} coordination complexes of KrF_2.

As previously noted,[21–23] the Kr–F bond lengths of terminally coordinated KrF_2 are significantly distorted with respect to its centrosymmetric, gas-phase and solid state geometries. The Kr–F_b bridge bonds are elongated (1.932(5)−1.948(4) Å), whereas the terminal Kr–F_t bonds are contracted (1.842(4)−1.851(5) Å) relative to the Kr–F bonds of free KrF_2 (1.894(5) Å).[26] Similar Kr–F bond polarizations have been observed in other terminally coordinated species, $[Hg(KrF_2)_8]^{2+}$ (Kr–F_b, 1.933(1)–1.957(1) Å; Kr–F_t, 1.822(1)–1.852(1) Å),[23] $Mg(KrF_2)_4(AsF_6)_2$ (Kr–F_b, 1.965(1)–1.979(1) Å; Kr–F_t, 1.817(2)–1.821(2) Å),[22] and $F_2OBr(KrF_2)_2(AsF_6)$ (Kr–F_b, 1.933(4), 1.943(4) Å; Kr–F_t, 1.840(5),1.847(4) Å).[21] The structure of $Hg(KrF_2)_5(AsF_6)_2$ differs significantly from those of its $Hg(XeF_2)_5(PnF_6)_2$ (Pn = P, As, Sb) analogues,[10] in which the Hg^{2+} cations interact with four terminally coordinated XeF_2 and two XeF_2 molecules which bridge between two mercury atoms, giving rise to chains rather than the nonbridged structure observed for the KrF_2 analogue in this study.

8.2.2.2. $[Hg(KrF_2)_4(HF)_2(SbF_6)]_2[SbF_6]_2$ (4)

The crystal structure of **(4)** (Figures 8.2 and S8.2) consists of a dimeric cation that is comprised of two $[Hg(KrF_2)_4(HF)_2(SbF_6)]^+$ cations which are symmetry-related through an inversion center with the Hg^{2+} cations linked by two *cis*-bridged $[Sb_{(1)}F_6]^-$ anions (Hg---$F_b(Sb_{(1/1A)})$; 2.384(2), 2.410(2) Å). The Sb–F_b bond lengths (1.908(2), 1.913(2) Å) are elongated relative to the terminal Sb–F_t bonds (1.858(2)–1.868(2) Å). The $[Sb_{(2)}F_6]^-$ anions are not directly coordinated to mercury, however, short F---F contact distances between two of its fluorine atoms and two HF molecules (F_9(H)---$F_{20}(Sb_{(2)})$, 2.526(2); F_{10B}(H)---$F_{22}(Sb_{(2)})$, 2.553(2) Å) of different dimeric cations are consistent with H-bonding interactions (Figure S8.3). This is corroborated by slightly elongated $Sb_{(2)}$–$F_{20/22}$ bond lengths (1.899(2) and 1.896(2) Å) relative to the other Sb–F bonds (1.864(2)–1.874(2) Å). In addition to the $[Sb_{(1/1A)}F_6]^-$ anions, each Hg^{2+} cation is coordinated to four terminal KrF_2 molecules (Hg−F_b(Kr), 2.309(2)−2.383(2) Å) and two HF molecules (Hg−F(H), 2.369(2) and 2.400(2) Å), resulting in eight-coordinated Hg^{2+} cations. The Kr−F_b (1.932(2)−1.945(1) Å) and Kr−F_t (1.841(2)−1.844(2) Å) bond lengths, and Hg−F−Kr bond angles (127.3(1)−136.9(1)^o) are comparable to those of $Hg(KrF_2)_5(AsF_6)_2$. The Hg−F(H) interactions in **(4)** are much longer than those of $Hg(HF)_2(AsF_6)_2$ (Hg–F(H), 2.055(5) Å; CN = 6) and are slightly shorter than those of $Hg(HF)(AsF_6)_2$ (Hg–F(H), 2.458(8) Å; CN = 9).[25] Other than **(1)** and **(3)** (*vide infra*), these are the only examples of KrF_2 coordination complexes in which other neutral ligands (HF) are coordinated to a common metal center.

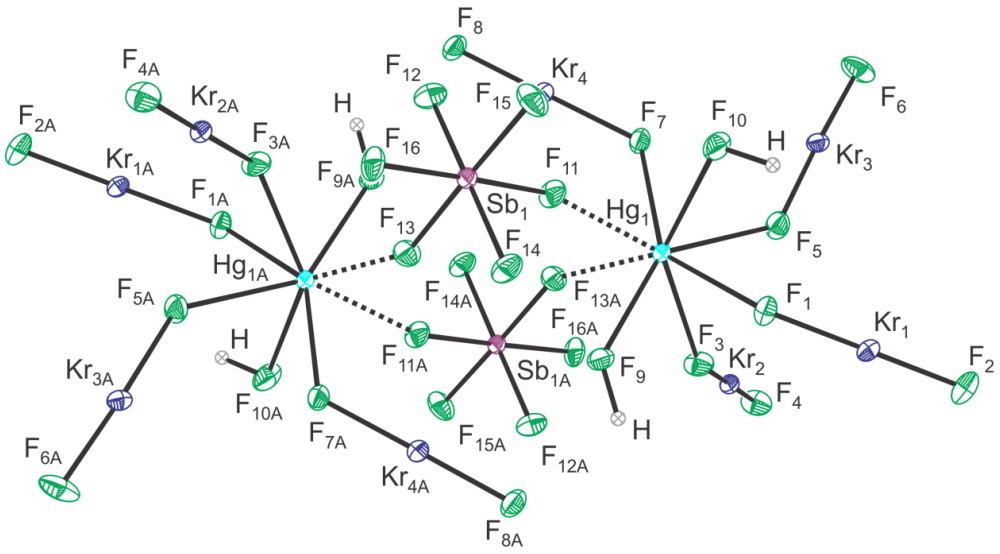

Figure 8.2. The X-ray crystal structure of the $[Hg(KrF_2)_4(HF)_2(SbF_6)]_2^{2+}$ dimeric cation of **(4)** showing the coordination environments of the Hg^{2+} atoms, where dashed lines indicate bonds with the bridging $[SbF_6]^-$ anions. Thermal ellipsoids are shown at the 50% probability level. The coordination environments of the $[Sb_{(2)}F_6]^-$ anion is shown in Figure S8.3.

The dimeric $[Hg(KrF_2)_4(HF)_2(SbF_6)]_2[SbF_6]_2$ complex is structurally distinct from the only other known dimeric NgF_2 complex, $[Cd_2(XeF_2)_{10}][SbF_6]_4$,[9] where the Cd^{2+} cations are bridged through a single XeF_2 molecule and are coordinated to two $[SbF_6]^-$ anions and either four or five terminal XeF_2 ligands .

8.2.2.3. $Hg(KrF_2)_3(HF)(SbF_6)_2$ (3).

Coordination of the Hg^{2+} cation to only three KrF_2 molecules and a HF molecule in **(3)** results in increased interconnectivity among the Hg^{2+} cations and $[SbF_6]^-$ anions (Figure 8.3), giving chains that run parallel to the *a*-axis of the unit cell (Figure S8.4) in which each Hg^{2+} cation interacts with four bridging $[SbF_6]^-$ anions. The $[Sb_{(1)}F_6]^-$ anion

bridges two mercury atoms through *cis*-fluorine atoms, whereas the $[Sb_{(2)}F_6]^-$ anion lies on an inversion center and bridges four Hg^{2+} cations through four coplanar bridging fluorine atoms. The Hg---$F_b(Sb_{(1/1A)})$ bonds (2.388(3), 2.404(3) Å) are slightly shorter than the Hg---$F_b(Sb_{(2/2A)})$ bonds (2.424(3), 2.448(2) Å), and are comparable to those of

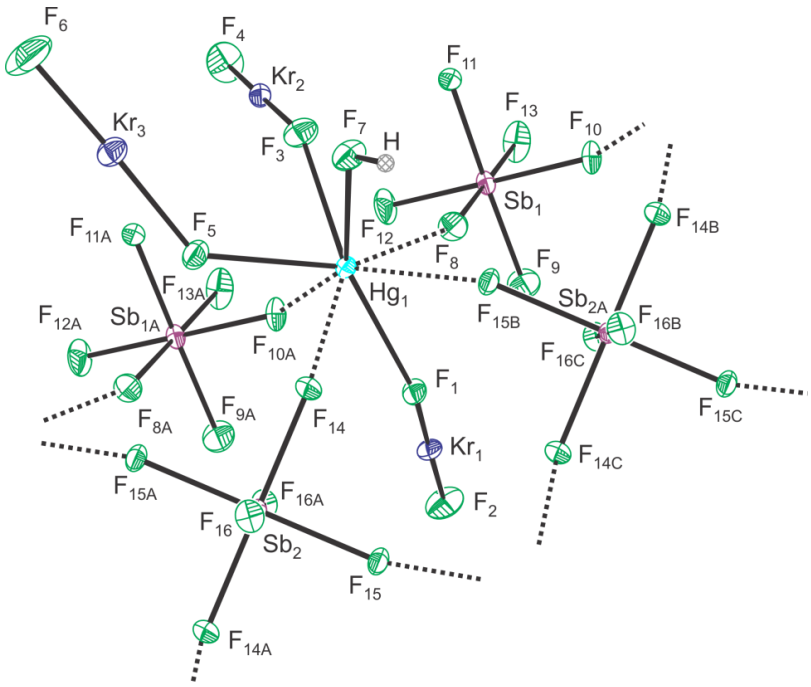

Figure 8.3. The X-ray crystal structure of $Hg(KrF_2)_3(HF)(SbF_6)_2$ **(3)** showing the coordination environment of the Hg^{2+} cation, where dashed lines indicate contacts with the bridging $[SbF_6]^-$ anions. Thermal ellipsoids are shown at the 50% probability level. The coordination environment of the $[Sb_{(3)}F_6]^-$ anion is shown in Figure S8.5.

compound **(4)**. Another anion, $[Sb_{(3)}F_6]^-$, also lies on an inversion center but does not directly interact with Hg^{2+} (Figure S8.5). Similar to **(4)**, each $[Sb_{(3)}F_6]^-$ anion of **(3)** interacts with two HF molecules from neighboring chains (F(H)---$F_b(Sb_{(3)}$, 2.483(3) Å). Consequently, the $Sb_{(3)}$–F_b bonds (1.908(3) Å) are elongated relative to those not

involved in hydrogen bonding (1.864(3), 1.866(3) Å). The Hg–F(H) bond distance (2.367(3) Å) is comparable to those of compound **(4).** The three terminally coordinated KrF_2 molecules (Hg−F_b(Kr), 2.289(3), 2.366(3), 2.317(3) Å) have Kr−F_b (1.950(3), 1.956(3), 1.956(3) Å) and Kr−F_t (1.835(3), 1.826(3), 1.828(4) Å) bond lengths which are more polarized than those of **(4)** and **(5)**, but generally comparable to those of $[Hg(KrF_2)_8]^{2+}$.[23]

8.2.2.4. $Hg(KrF_2)_2(AsF_6)_2$ (2)

Each Hg^{2+} cation of **(2)** is terminally *trans*-coordinated by two KrF_2 molecules that are oriented anti to one another with a $Kr_{(1)}$–$F_{(1)}$–$F_{(3)}$–$Kr_{(2)}$ dihedral angle of 174.5(2) (Figure 8.4). The Hg^{2+} cations are also coordinated to two bridging $[AsF_6]^-$ anions (Hg---$F_b(As_{(1)})$, 2.408(3); Hg---$F_b(As_{(2)})$, 2.423(3) Å) and to two symmetry-related, asymmetrically coordinated bidendate $[AsF_6]^-$ anions (Hg---$F_b(As_{(1A)})$; 2.594(3), 2.679(3) Å and Hg---$F_b(As_{(2A)})$; 2.547(3), 2.875(3) Å). The increased number of Hg---F_b(As) contacts results in a layered structure in which the layers pack along the *b*-axis (Figure S8.6). The mercury atoms are eight coordinate, however unlike compounds **(3)**–**(5),** which clearly possess square antiprismatic geometries, the mercury coordination sphere of (**2**) is not square antiprismatic.

The two terminally coordinated KrF_2 molecules have the shortest and strongest Hg−F_b(Kr) bonds (2.136(3), 2.141(3) Å) of all mercury coordination compounds reported in this study. This is also reflected by significantly longer Kr−F_b (1.995(3), 2.004(2) Å) and shorter Kr−F_t (1.805(3), 1.811(3) Å) bond lengths, giving the largest mean Kr−F

bond differences ($\Delta_{av.}$Kr−F, 0.192(6) Å) observed in this study. The Hg−F−Kr bond angles are 135.1(1) and 148.6(2)^{o}, with the latter angle being considerably more open than those of **(3)**–**(5)**. The structurally related complexes, $Mg(XeF_2)_2(AsF_6)_2$[27] and $Cu(XeF_2)_2(SbF_6)_2$,[28] have two terminal XeF_2 molecules which are also *trans*-coordinated, however, because the cations of both complexes only attain a coordination number of six, they form chains rather than layered structures.

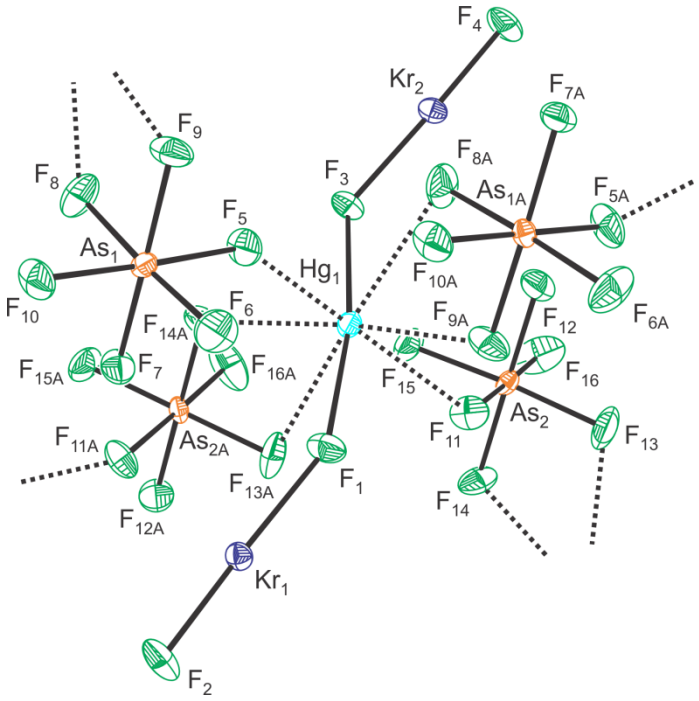

Figure 8.4. The X-ray crystal structure of $Hg(KrF_2)_2(AsF_6)_2$ **(2)** showing the coordination environment of the Hg^{2+} cation, where dashed lines indicate short contacts with the bridging $[AsF_6]^-$ anions. Thermal ellipsoids are shown at the 50% probability level.

8.2.2.5. $Hg(KrF_2)(HF)(AsF_6)_2$ (1).

The crystal structure of **(1)** (Figure 8.5) provides the lowest metal-to-KrF_2 molar ratio complex that has thus been structurally characterized. The Hg^{2+} cation of **(1)** interacts with only one KrF_2 and one HF molecule, allowing a greater number of cation interactions with bridging $[AsF_6]^-$ anions than in other complexes described in this study; resulting in an extended, three-dimensional network. Each Hg^{2+} cation is coordinated to five $[AsF_6]^-$ anions, four are monodendate (Hg---F_b(As), 2.376(4), 2.437(4), 2.428(4), 2.482(4) Å) and one is bidentate with assymetric Hg---F_b(As) bonds (2.470(4), 2.610(4) Å). One monodendate anion also has a long secondary contact to

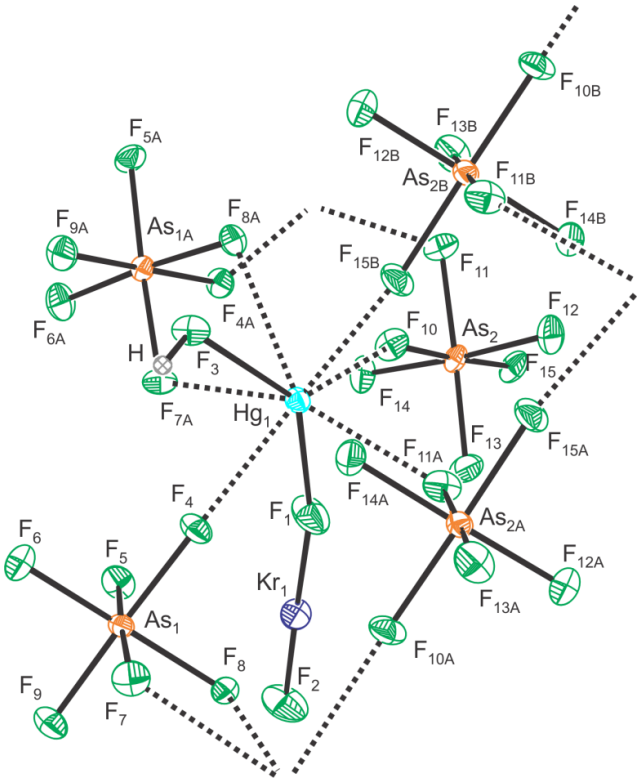

Figure 8.5. The X-ray crystal structure of $Hg(KrF_2)(HF)(AsF_6)_2$ **(1)** showing the coordination environment of the Hg^{2+} cation, where dashed lines indicate short contacts between Hg^{2+} cation and bridging $[AsF_6]^-$ anions. Thermal ellipsoids are shown at the 50% probability level.

Hg^{2+} (2.838(4) Å), which is equal to that of $Hg(HF)(AsF_6)_2$ (2.838(8) Å).[25] The $[As_{(1)}F_6]^-$ anions are facially coordinated to two symmetry-related Hg^{2+} cations whereas the $[As_{(2)}F_6]^-$ anions are merohedrally coordinated to three symmetry-related Hg^{2+} cations. The coordinated HF molecule is more strongly bound to Hg^{2+} (Hg–F(H), 2.285(4) Å) than in compounds **(3)** and **(4)**. Although not shown in Figure 8.5, each $[As_{(1)}F_6]^-$ anion is also H-bonded to a HF molecule with a $F_{(3)}(H)$---$F_{(9B)}(As_{(1B)})$ distance (2.512(4) Å) that is intermediate with respect to the F(H)---F_b(Sb) distances of **(3)** and **(4)**.

The terminally coordinated KrF_2 molecule has a Hg–F_b(Kr) bond (2.205(5) Å) that is significantly longer than those of compound **(2)** but much shorter than those of **(3)–(6)**. As such, the Kr–F bond lengths (Kr–F_b, 1.956(5); Kr–F_t, 1.809(5) Å) of **(1)** are more polarized than those of **(3)–(6)** but less so than in **(2)**. The Hg–F–Kr bond angle (168.5(3)^o) is significantly more open than for any other terminally coordinated KrF_2 complex encountered in this study or elsewhere (121.8(1)–144.4(1)^o),[21-23] and may arise from crystal packing and/or long interactions between the krypton atom and fluorine atoms of the $[AsF_6]^-$ anions (Kr–F(As), 3.103–3.530(5) Å). This is corroborated by the calculated monomeric gas-phase model of $Hg(KrF_2)(HF)(AsF_6)_2$ **(1')** (see *Computational Section*), where these solid-state interactions are absent and the observed coordination angle is not reproduced (calcd, Hg–F–Kr, 139.0^o). The resulting primary coordination sphere of mercury is a very distorted square antiprism with an additional long secondary fluorine contact with an $[AsF_6]^-$ anion (2.838(4) Å) that caps one of its square faces.

8.2.2.6. $Hg(KrF_2)_4(HF)_2(AsF_6)_2 \cdot HF$ (6)

Complex **(6)** (Figure 8.6) possesses two HF molecules that are *trans*-coordinated to mercury with nearly equal Hg–F(H) bond lengths (2.086(3), 2.079(3) Å) that are significantly shorter than those of **(1)**, **(3)**, and **(4),** but are only slightly longer than those of $Hg(HF)_2(AsF_6)_2$ (Hg–F(H), 2.055(5) Å), where the HF molecules are also *trans*-coordinated.[25] The Hg^{2+} cation also interacts with two $[AsF_6]^-$ anions through Hg---F_b(As) bonds ($As_{(1)}$, 2.626(3) Å; $As_{(2)}$, 2.844(3) Å) that are significantly longer than

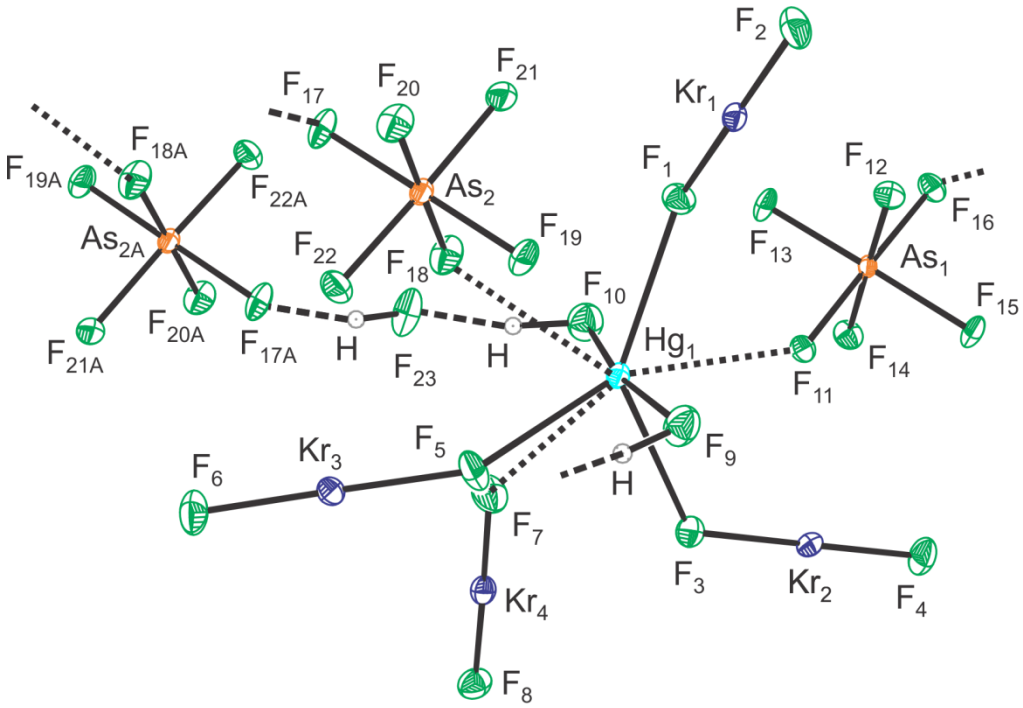

Figure 8.6. The X-ray crystal structure of $Hg(KrF_2)_4(HF)_2(AsF_6)_2 \cdot HF$ **(6)** showing the environment around the Hg^{2+} cations, where dotted lines indicate short contacts with the bridging $[AsF_6]^-$ anions and the long contact to $Kr_{(3)}F_2$. Thermal ellipsoids are shown at the 50% probability level.

those of **(1)**, **(2)**, and **(5)**. The coordinated $HF_{(9)}$ molecule hydrogen bonds to a fluorine atom of a neighboring $[As_{(1A)}F_6]^-$ anion ($F_{(9)}(H)$---$F_{(16A)}(As_{(1A)})$, 2.682(5) Å). The other coordinated hydrogen fluoride molecule, $HF_{(10)}$, hydrogen bonds to the fluorine atom of a co-crystallized $HF_{(23)}$ molecule ($F_{(10)}(H)$---$F_{(23)}(H)$, 2.655(5) Å) which, in turn, hydrogen bonds to the fluorine atom of a neighboring $[As_{(2A)}F_6]^-$ anion ($F_{(23)}(H)$---$F_{(17A)}(As_{(2A)})$, 2.562(4) Å). This interaction is corroborated by the $As_{(2)}$–$F_{(17)}$ bond (1.743(3) Å) being elongated relative to the terminal $As_{(2)}$–F_t bonds (1.709(4)–1.733(3) Å).

Three of the four KrF_2 molecules that are terminally coordinated to the Hg^{2+} cation of **(6)** have Hg−F_b(Kr) bond lengths (2.574(3), 2.529(3), 2.639(3) Å) that are significantly longer than those of compounds **(1)**–**(5)**, but are shorter than those of the bridging KrF_2 molecules in $Hg(KrF_2)_{1.5}(OTeF_5)_2$ (2.664(3), 2.675(3), 2.741(3) Å).[24] The corresponding Kr−F_b (1.909(3), 1.923(3), 1.927(3) Å) and Kr−F_t (1.858(3), 1.859(4), 1.872(3) Å) bonds are only weakly polarized, resulting in a smaller average bond length difference ($\Delta_{av.}$Kr−F, 0.057(6) Å) relative to those of **(1)**–**(5)**. The remaining KrF_2 molecule in **(6)** is even more weakly coordinated to Hg^{2+} with a much longer bond distance (Hg−$F_{(7)}(Kr_{(4)})$, 2.929(3) Å), with correspondingly smaller, but significant, Kr–F bond length difference (Kr−F_b, 1.895(3) Å and Kr−F_t, 1.871(3) Å; ΔKr−F, 0.024(4) Å). The resulting eight-coordinate mercury coordination sphere is highly distorted with respect to a square antiprism.

8.2.2.7. $FHg(\mu_3\text{-}FKrF)_{1.5}(KrF_2)_{0.5}(AsF_6)$ (7).

The substitution of $[AsF_6]^-$ for F^- in **(7)** results in structural features which do not occur in compounds **(1)**–**(6)**. The crystal structure of **(7)** (Figures 8.7 and S8.8) consists of an extended three-dimensional network formed from complex layers that are parallel to the diagonal of the *ac*-plane of the unit cell, and are linked through bridging $[AsF_6]^-$ anions. The Hg---F_b(As) bond distances (2.484(7)–2.575(9) Å) are comparable to those of other $[AsF_6]^-$ salts described in this study and also possess As–F_b (1.735(5)–1.741(6) Å) bonds that are slightly elongated relative to their As–F_t bonds (1.690(7)–1.719(6) Å). The layers contain parallel, zig-zag chains comprised of ($–F_{(10)}–Hg_{(2)}–F_{(9)}–Hg_{(1)}–$) units containing two crystallographically unique Hg sites and two unique μ–F bridges. The $Hg_{(1)}–F_{(9/10)}–Hg_{(2)}$ and $F_{(9)}–Hg_{(1/2)}–F_{(10)}$ bond angles are 116.9(2)/130.7(3)^o and 139.6(2)/177.5^o, respectively. The $Hg_{(2)}–F_{(9/10)}$ (2.032(5)/2.053(5) Å) bridge bonds are significantly shorter than the $Hg_{(1)}–F_{(9/10)}$ (2.155(5)/2.203(5) Å) bridge bonds. These chains are reminiscent of those observed in the crystal structure of $FHg(AsF_6)$ (Hg–μ-F, 2.058(6), 2.088(7) Å; Hg–μ-F–Hg, 143.2(4)^o; μ-F–Hg–μ-F, 163.0(3) ^{o}).[25]

The (–F–Hg–) chains of **(7)** are also linked to one another through an asymmetrically bridged KrF_2 molecule ($Hg_1–F_5(Kr_{(3)})$, 2.458(5) Å; $Hg_2–F_{6A}(Kr_{(3A)})$, 2.620(6) Å) to form the aforementioned layers. The Hg–F_b(Kr) bond lengths are shorter than in $Hg(KrF_2)_{1.5}(OTeF_5)_2$ (2.664(3), 2.675(3), 2.741(3) Å).[24] Other than $Hg(KrF_2)_{1.5}(OTeF_5)_2$, compound (**7**) provides the only other crystallographically characterized example of a bridging KrF_2 molecule. The $Hg_{(1)}–F_b$ interaction with the bridging KrF_2 molecule is much stronger than the $Hg_{(2)}–F_b$ interaction, resulting in

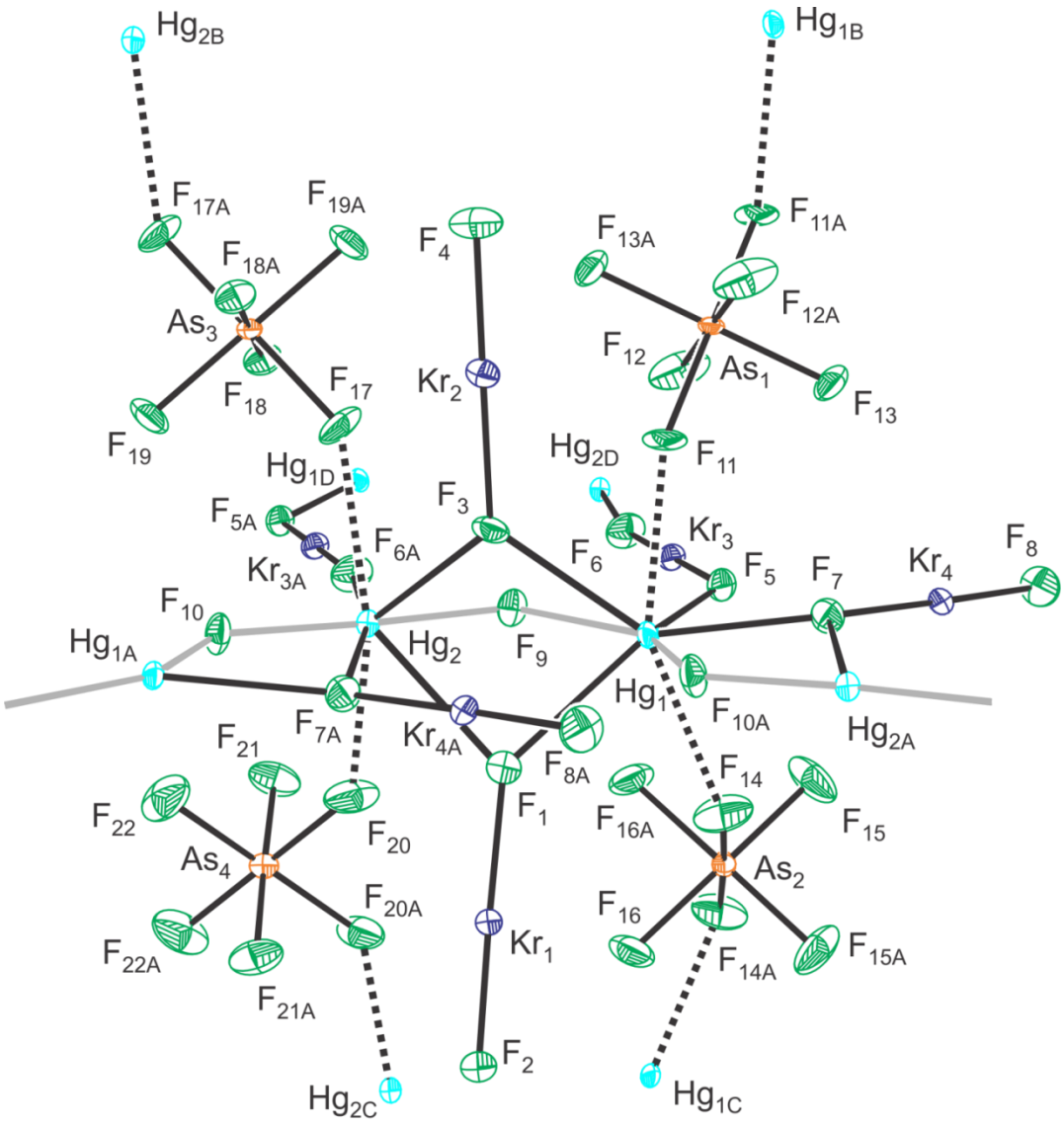

Figure 8.7. The X-ray crystal structure of $FHg(\mu_3\text{-}FKrF)_{1.5}(KrF_2)_{0.5}(AsF_6)$ **(7)** showing its extended interconnectivity with the interactions between the Hg^{2+} cations and $[AsF_6]^-$ anions shown as dashed lines. Grey colored bonds are used to emphasize the zig-zag $(-Hg-F-)_n^{n+}$ chain that is parallel to the *b*-axis. Thermal ellipsoids are shown at the 50% probability level.

asymmetric Kr–F bonds (1.912(6), 1.854(6) Å), whereas the Kr–F bonds of $Hg(KrF_2)_{1.5}(OTeF_5)_2$ (1.883(3), 1.885(3), 1.897(3) Å) are equal within ±3σ.[24]

Both Hg^{2+} environments in the ($–F_{(10)}–Hg_{(2)}–F_{(9)}–Hg_{(1)}–$) units are also linked to one another through terminally coordinated KrF_2 molecules that bridge the two Hg^{2+} cations through a single μ_3-flourine atoms, denoted as μ_3-FKrF. This represents a new KrF_2 bonding modality for NgF_2 ligands, and has yet to be observed for a XeF_2 coordination complex. There are two types of μ_3-FKrF ligands present in **(7)** which alternate between lying in the layers and above/below the layer of the extended structure. The interactions of the μ_3-FKrF ligands with the Hg^{2+} cations, in all cases, are asymmetric, however the asymmetry is less pronounced for the μ_3-FKrF ligands that are situated above and below the layers ($Hg_{(1)}–\mu_3$-$F(Kr_{(1)})$, 2.542(6) Å and $Hg_{(2)}–\mu_3$-$F(Kr_{(1)})$, 2.691(6) Å; $Hg_{(1)}–\mu_3$-$F(Kr_{(2)})$, 2.757(6) Å and $Hg_{(2)}–\mu_3$-$F(Kr_{(2)})$, 2.635(6) Å) relative to the μ_3-FKrF ligand within the layers ($Hg_{(1)}–\mu_3$-$F(Kr_{(4)})$, 2.290(6) Å and $Hg_{(2)}–\mu_3$-$F(Kr_{(4)})$, 2.907(5) Å). Although the Hg–μ_3-F(Kr) bonds of **(7)** are significantly longer than the Hg–F_b(Kr) bonds of the terminally coordinated KrF_2 ligands in **(1)**–**(5)**, their Hg–F_b(Kr) bond lengths are comparable to those of the terminal KrF_2 ligands of **(6)** and the bridging KrF_2 molecules of $Hg(KrF_2)_{1.5}(OTeF_5)_2$.[24] Even the longest interaction with a μ_3-FKrF ligand (2.907(5) Å) of **(7)** is shorter than the weakly terminally coordinated KrF_2 ligand of **(6)** (Hg−F_7(Kr), 2.929(3) Å). The μ_3-F bridged KrF_2 ligands have elongated μ_3-F_b–Kr (1.955(6), 1.969(6), 1.999(6) Å) and contracted Kr–F_t (1.836(9), 1.846(8), 1.820(6) Å) bonds similar to those encountered for other terminally coordinated KrF_2 complexes. The degree of Kr–F bond polarization is consistent with μ_3-F interactions involving two Hg^{2+}

cations. For example, in complex **(6)** one of the terminally coordinated KrF_2 ligands (Hg–F_b(Kr), 2.529(3) Å) has a ΔKr–F value (0.064(5) Å) that is approximatly half that of μ_3-$F_bKr_{(1)}F_t$ (ΔKr–F, 0.119(8) Å) in **(7)** for which the shortest Hg–μ_3-$F_b(Kr_{(1)})$ interaction is comparable (2.542(6), 2.691(6) Å). The μ_3-FKrF ligands have Hg–μ_3-F_b–Kr coordination angles ($Hg_{(1)}$; 134.4(3), 128.6(3)^o and $Hg_{(2)}$; 125.3(3), 124.8(3)^o) that are comparable to those of the terminally coordinated ligands of **(2)**–**(6)**. The Hg^{2+} cations of **(7)** are eight-coordinated, however, the coordination sphere of $Hg_{(2)}$ is highly distorted relative to a square antiprism.

8.2.2.7. $FHg(\mu_3\text{-}FKrF)_{0.5}(KrF_2)_{1.5}(AsF_6)$ (8)

Although compound **(8)** has the same chemical formula as **(7)**, their structures are markedly different. The crystal structure of **(8)** (Figure 8.8) also contains $(–Hg–F–)_n^{n+}$ chains, however, in this case, two parallel chains interact to form ribbons that are parallel to the *a*-axis of the unit cell (Figure S8.9a). The two crystallographically unique Hg^{2+} environments are linked by μ_3-F bridges through shorter Hg–μ_3-F bonds ($Hg_{(1)}$–$F_{(9/10C)}$, 2.222(2)/2.229(2) Å; $Hg_{(2)}$–$F_{(9/10)}$, 2.241(2)/2.167(2) Å) which form chains and one longer bond ($Hg_{(1)}$–$F_{(10A)}$, 2.387(2) Å; $Hg_{(2)}$–$F_{(9A)}$, 2.452(2) Å) which cross-links these chains to form the ribbons. The shorter Hg–μ_3-F bonds within the chains are, on average, longer than corresponding bonds in compound **(7)** and those of $FHg(AsF_6)$.[25]

The ribbons interact with $[AsF_6]^-$ anions (Hg---F_b(As), 2.376(2)–2.605(3) Å) and KrF_2 molecules to form parallel columns which run parallel to the *a*-axis. The columns are well isolated with no significant intermolecular contacts between adjacent columns

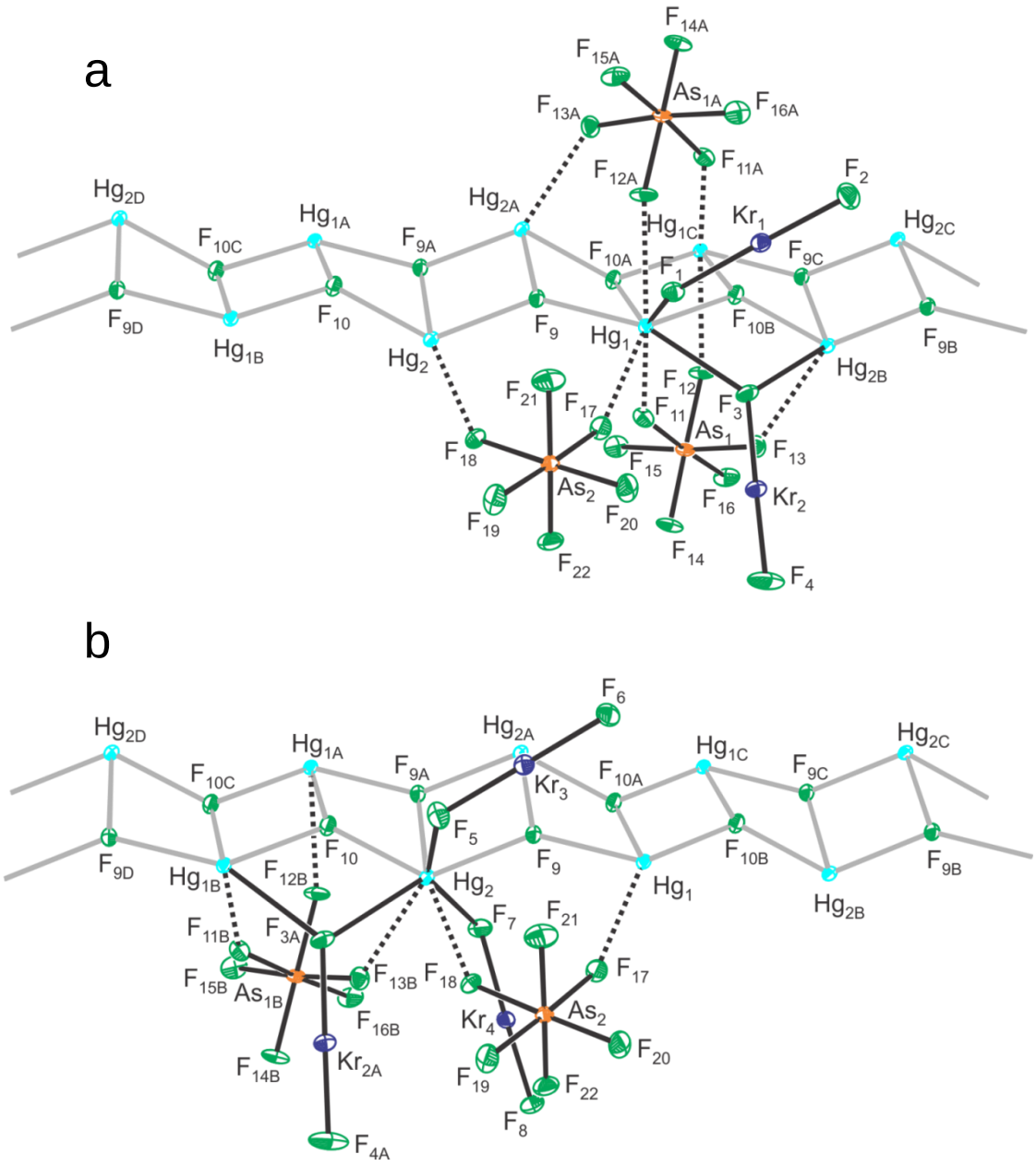

Figure 8.8. The X-ray crystal structure of $FHg(\mu_3\text{-}FKrF)_{0.5}(KrF_2)_{1.5}(AsF_6)$ **(8)** showing the environments of **(a)** $Hg_{(1)}$ and **(b)** Hg_2. The ribbon backbone parallel the *a*-axis are denoted by gray-colored Hg–F bonds. Interactions between the Hg^{2+} cations and $[AsF_6]^-$ anions are indicated by dashed lines. Thermal ellipsoids are shown at the 50% probability level.

(Figure S8.9b). There are two types of KrF_2 ligands present; the $Hg_{(1)}$ atom is coordinated to one terminal KrF_2 ligand ($Hg_{(1)}$–F_b(Kr), 2.345(2) Å) whereas $Hg_{(2)}$ is coordinated to two terminal KrF_2 ligands ($Hg_{(2)}$–F_b(Kr), 2.445(4) and 2.421(4) Å). There is also one μ_3-FKrF ligand which asymmetrically bridges $Hg_{(1)}$ and $Hg_{(2)}$, with a shorter $Hg_{(1)}$–μ_3-$F_{(1)}$(Kr) bond (2.445(2)Å) and a much longer $Hg_{(2)}$–μ_3-$F_{(1)}$(Kr) bond (2.883(3) Å). The asymmetry of these bonds is intermediate with respect to those observed in **(7)**. Since the $Hg_{(2)}$–F_b bond length of the terminal $Kr_{(3)}F_2$ ligand (2.445(4) Å) is experimentally equal to the shorter $Hg_{(2)}$–μ_3-F_b bond length (2.455(2) Å), comparison of the corresponding Kr–F bond length polarizations (ΔKr–F, 0.083(4) vs 0.127(4) Å) further corroborates a second interaction through the longer Hg-μ_3-F($Kr_{(2)}$) bond (2.883(3) Å). The Hg–F–Kr (125.7(1)-127.3(1)^o) and Hg–μ_3-F–Kr (121.9(1), 130.5(1)^o) bond angles are comparable to those observed in compounds **(2)–(6)** and **(7)**.

8.2.3 Raman Spectroscopy

The Raman spectra of the crystalline reaction products were recorded at –150 ^{o}C (Figure S8.11 and Table S8.10). Because the reactions often resulted in product mixtures (*vide supra*), it was not possible to fully assign vibrational bands of most complexes. The only complex that could be confidently assigned was $Hg(KrF_2)_5(AsF_6)_2$ **(5)** because it was the major product in several reactions and, in one instance, a spectrum of the nearly pure complex was obtained. The vibrational assignments for **(5)** were made with the aid of the gas-phase calculated frequencies of $Hg(KrF_2)_5(AsF_6)_2$ **(5′)** (Figure 8.1b) and by comparison with the experimental and calculated frequencies of $[Hg(KrF_2)_8]^{2+}$.[23] For the

remaining complexes, the gas-phase structures of the simplified model compounds, denoted by **(1′)**–**(4′)** and **(6′)**, (Figure 8.9) were also calculated to aid in the general assignments of the Raman spectra and to provide insights into inter-ligand vibrational couplings. In the case of **(7)** and **(8)**, these complexes were minor products and their corresponding bands were not identified in the Raman spectra. Raman bands arising from the $[AsF_6]^-$ and $[SbF_6]^-$ anions (Table S8.10) were assigned by comparison with the literature values,[29,30] and by comparison with $[Hg(KrF_2)_8][AsF_6]_2 \cdot 2HF$ (see Appendix F).[23]

The KrF_2 molecule loses its center of symmetry when terminally coordinated, resulting in Raman-active $\nu(Kr–F_b)$ and $\nu(Kr–F_t)$ stretching modes. The calculated gas-phase models of **(1′)–(6′)** indicate there is no significant intra-ligand coupling between $\nu(Kr–F_b)$ and $\nu(Kr–F_t)$. However, significant KrF_2 inter-ligand coupling occurs among the $\nu(Kr–F_b)$ stretching modes, and similarly among the $\nu(Kr–F_t)$ stretching modes of the KrF_2 ligands. The same behavior was observed for $[Hg(KrF_2)_8][AsF_6]_2 \cdot 2HF$,[23] $Mg(KrF_2)_4(AsF_6)_2$,[22] and $F_2OBr(KrF_2)_2(AsF_6)$.[21] The calculated vibrational modes of **(1′)**, which contains only one KrF_2 ligand, also show that $\nu(Kr–F_b)$ and $\nu(Kr–F_t)$ are not coupled. The resulting bands are observed within distinct ranges, such that the coupled $\nu(Kr–F_b)$ modes occur close to the Raman-active symmetric stretching mode of free KrF_2 ($\nu_1(\sum_g^+)$, 464 cm^{-1})[31] whereas the coupled $\nu(Kr–F_t)$ modes occur close to the formally infrared-active asymmetric stretching mode of free KrF_2 ($\nu_3(\sum_u^+)$, 588 cm^{-1}).[32] The calculated models **(1′)–(6′)** also indicate that weak couplings also occur between the $\nu(Kr–F)$ and $\nu(Pn–F)$ stretches for some modes (Table S8.10).

The Raman bands of **(5)**, which occur at 449, 456 and 488 cm^{-1} are assigned to coupled $\nu(Kr–F_b)$ stretching modes (calcd, 436, 439, 444, 453, 465, 481, 493 cm^{-1}), where the 488 cm^{-1} band is the most intense band in the Raman spectrum. These frequencies are comparable to those of $[Hg(KrF_2)_8][AsF_6]_2 \cdot 2HF$ (449–508 cm^{-1}),[23] $Mg(KrF_2)_4(AsF_6)_2$ (449–495 cm^{-1}),[22] and $F_2OBr(KrF_2)_2(AsF_6)$ (443, 472 cm^{-1}).[21] In the case of the Raman spectra of **(1)**–**(4)** and **(6)**, the vibrational bands occur in a similar frequency range, 439–492 cm^{-1} (calcd, 413–481 cm^{-1}). In the spectra of product mixtures containing predominantly higher KrF_2-to-Hg^{2+} ratio complexes, i.e., **(4)**–**(6)**, bands in this region are the most intense in the spectra.

The Raman spectrum of **(5)** has medium-intensity bands at 537, 546, and 554 cm^{-1} that are assigned to coupled $\nu(Kr–F_t)$ modes (calcd, 565, 568, 572, 574, 576, 597 cm^{-1}). The bands are in good agreement with those observed for $[Hg(KrF_2)_8][AsF_6]_2 \cdot 2HF$ (540, 543, 554, 603 cm^{-1}),[23] $Mg(KrF_2)_4(AsF_6)_2$ (558–589 cm^{-1}),[22] and $F_2OBr(KrF_2)_2(AsF_6)$ (533, 549 cm^{-1}).[21] The coupled $\nu(Kr–F_t)$ modes of **(1)**–**(4)** and **(6)** are assigned to bands at 540–603 cm^{-1} (calcd, 552–608 cm^{-1}). For mixed samples comprised predominantly of the lower KrF_2-to-Hg^{2+} ratio complexes, **(1)**–**(3)**, the most intense bands in the Raman spectra occur in the latter region.

The Raman bands of **(5)** that occur at 264 and 274 cm^{-1} are assigned to KrF_2 bending modes (calcd, 225–268 cm^{-1}). The analogous $\delta(KrF_2)$ modes of $[Hg(KrF_2)_8][AsF_6]_2 \cdot 2HF$ are observed at similar frequencies (238, 262, 282 cm^{-1}).[23] The $\delta(KrF_2)$ bands of the remaining complexes in this series are assigned to bands which lie within a similar frequency range, 237–292 cm^{-1} (calcd, 196–270 cm^{-1}). By comparison,

the formally Raman-inactive, doubly-degenerate bending mode of free KrF_2 (ν_2, Π_u) occurs at 233 cm^{-1}.[31]

8.2.4. Computational Results

8.2.4.1. Calculated Geometries

The gas-phase geometry of $Hg(KrF_2)_5(AsF_6)_2$ **(5′)** (C_1, Figure 8.1b) was optimized at the B3LYP/def2-TZPP level of theory which resulted in a stationary point with all frequencies real. The calculated bond lengths and angles are provided in Table S8.1. The optimized geometry of **(5′)** well reproduces the distorted square antiprismatic mercury coordination sphere observed experimentally. Similarly, one $[AsF_6]^-$ anion is monodentate coordinated to Hg^{2+} (calcd. Hg–F_b(As), 2.316 Å), whereas the other $[AsF_6]^-$ anion is bidentate-coordinated with longer Hg–F_b(As) bond distances (calcd. 2.438 and 2.615 Å). The calculated As–F_b bridge bond lengths (1.793–1.856 Å) are significantly elongated relative to the terminal As–F_t bonds (1.711–1.751 Å), which is also observed in the structure of **(5)** (exptl As−F_b, 1.752(4)−1.759(4) Å; As−F_t, 1.697(5)−1.717(5) Å). The five terminally coordinated KrF_2 ligands of the calculated gas-phase structure have Hg–F–Kr coordination angles (124.4°–131.9°) that are in good agreement with the experimental values for of **(5)** (124.6(2)–139.1(2)°). Overall, the calculated Hg–F_b(Kr) bond distances are slightly overestimated (calcd. av., 2.420 Å; exptl. av., 2.332(10) Å), but the Kr–F_b (calcd. av., 1.967 Å; exptl. av., 1.940(10) Å) and Kr–F_t (calcd. av., 1.852 Å; exptl. av., 1.857(11) Å) bond lengths are in better agreement. The corresponding gas-phase model complexes of **(1)**–**(4)**, and **(6)** were also calculated at the B3LYP/ def2-TZPP level of theory (Figure 8.9) These gas-phase models optimized to C_1 symmetry for

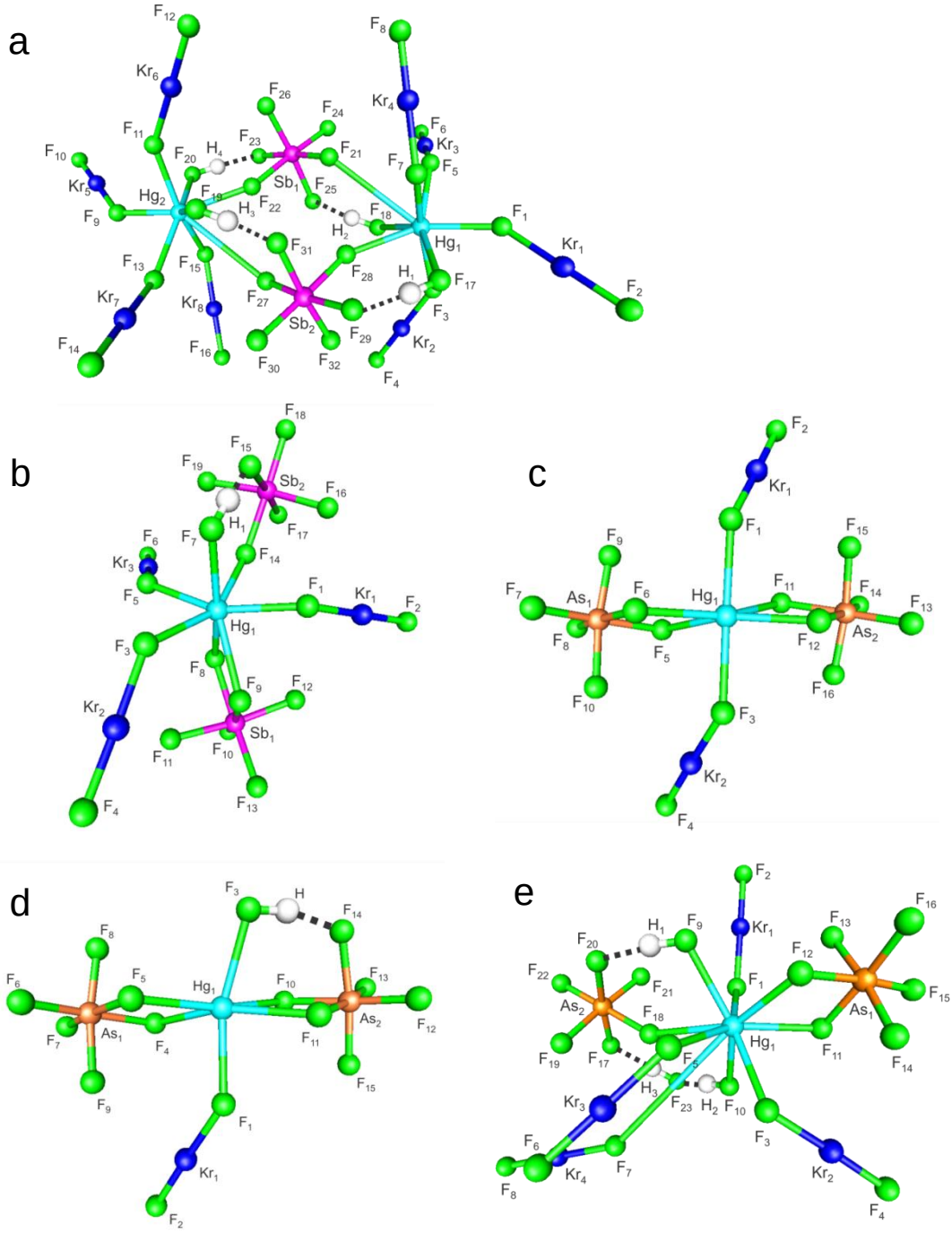

Figure 8.9. The gas-phase, energy–minimized geometries of isolated **a)** $Hg(KrF_2)_4(HF)_2(SbF_6)_2$ **(4′)**, **b)** $Hg(KrF_2)_3(HF)(SbF_6)_2$ **(3′)**, **c)** $Hg(KrF_2)_2(AsF_6)_2$ **(2′)**, **d)** $Hg(KrF_2)(HF)(AsF_6)_2$ **(1′)** and **e)** $Hg(KrF_2)_4(HF)_2(AsF_6)_2 \cdot HF$ ion pairs; calculated at the B3LYP/def2–TZVPP level of theory. Dashed lines indicate intramolecular hydrogen bonds.

(1′), **(3′), (4′),** and **(6′)**, and C_2 symmetry for **(2′)**, and in all cases resulted in stationary points with all frequencies real (Table S8.10). The calculated bond lengths and angles are provided in Tables S8.2–S8.6. Because the extended interactions for these structures are not taken into account by the calculated gas-phase models, they neither fully reproduce the experimental geometries nor the coordination environments of mercury. Calculations which attempted to optimize larger, more extended models for **(1)-(4)** failed. A common feature of **(1′)**, **(3′)**, **(4′)** and **(6′)** are HF molecules which are hydrogen bonded to a fluorine atom of one of the coordinated $[PnF_6]^-$ anions; this imitates the hydrogen bonding that is experimentally observed. The corresponding As–F_b bonds (interacting with either Hg or H atoms) are also elongated relative to non-interacting As–F_t bond. Two important experimental features are reproduced in the case of **(6')**, one of the KrF_2 molecules is very weakly coordinated and a coordinated HF molecule hydrogen bonds to a second HF molecule that, in turn, interacts with an $[AsF_6]^-$ anion. Even with the geometrical limitations, the models still reasonably reproduce the core features of the experimental structures and are useful for the assignment of the vibrational modes and frequencies of the KrF_2 ligands.

To further investigate the nature of μ_3-FKrF ligand bonding, the hypothetical $[F(HgF)_2(\mu_3\text{-}FKrF)_2]^+$ cation (Figure 8.10), was optimized using the PBE/TZVP level of theory (dispersion corrected) which resulted in a stationary point with all frequencies real and a structure having C_{2v} symmetry. This level of theory was chosen because it was used for $[Hg(KrF_2)_8]^{2+}$,[23] and allowed for energy decomposition (EDA)[33–36] and extended transition state natural orbitals of chemical valence (ETS-NOCV)[37,38] analyses to be

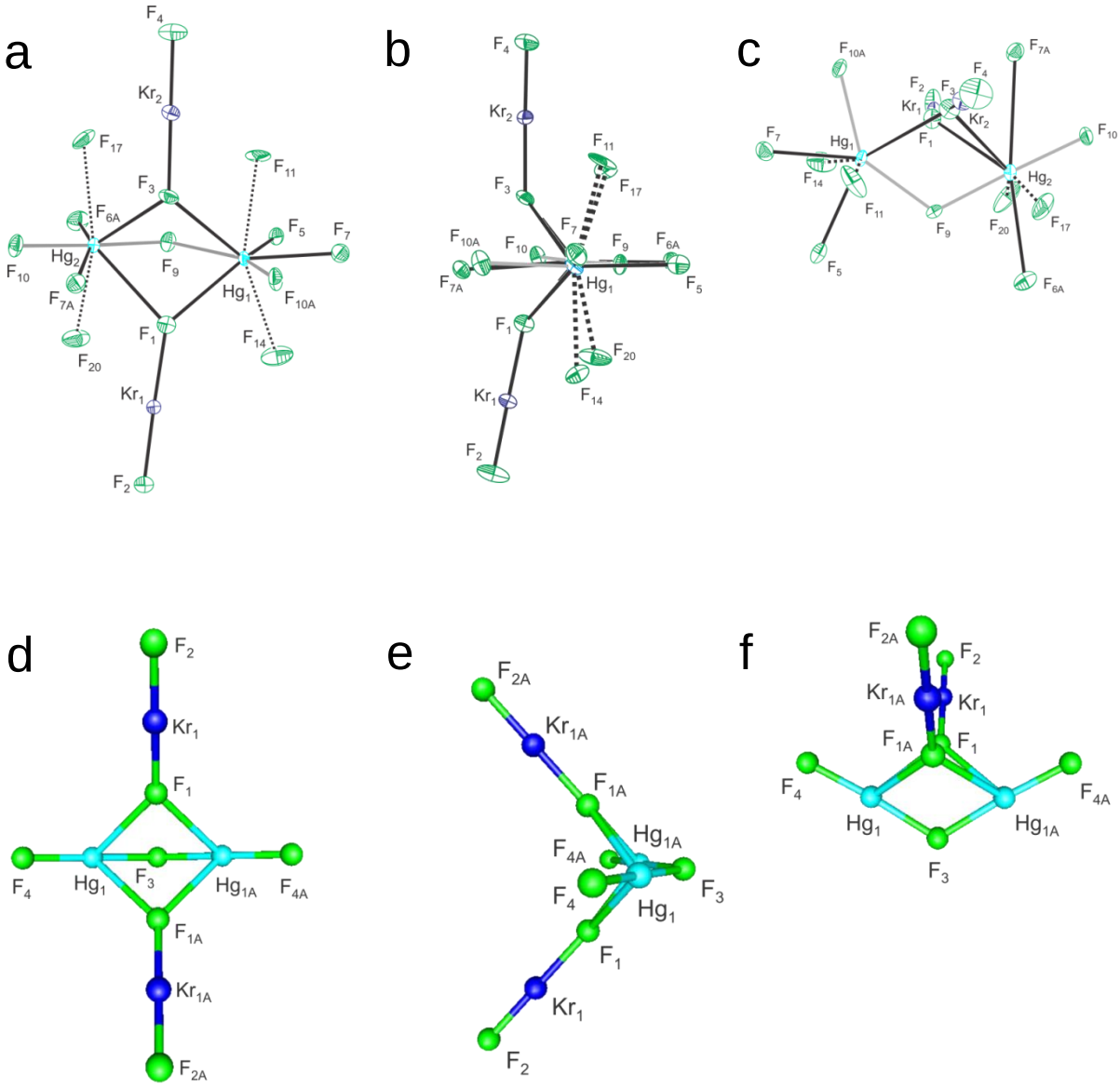

Figure 8.10. The X-ray crystal structure of $FHg(\mu_3\text{-}FKrF)_{1.5}(KrF_2)_{0.5}(AsF_6)$ **(7)** showing the μ_3-FKrF and coordination environments of the mercury atoms viewed **(a)** from above the (–F–Hg–) chain, **(b)** along the (–F–Hg–) chain and **(c)** perpendicular to the (–F–Hg–) chain. Grey-colored bonds are used to emphasize the (–F–Hg–) chain that is parallel to the *b*-axis of the unit cell. Thermal ellipsoids are shown at the 50% probability level. The gas-phase, energy-minimized geometry of $[F(HgF)_2(\mu_3\text{-}FKrF)_2]^+$ (C_{2v}) calculated at the PBE/TZ2P level of theory is shown viewed **(d)** down the C_2-axis, **(e)** along the $[F(HgF)_2]^+$ fragment bonds, and **(f)** perpendicular to the $[F(HgF)_2]^+$.

carried out. The calculated bond lengths and angles are provided in Table S8.7. The $[F(HgF)_2(\mu_3\text{-}FKrF)_2]^+$ cation models the most important structural features pertaining to the least asymmetrically bridging μ_3-FKrF molecules in $FHg(\mu_3\text{-}FKrF)_{1.5}(KrF_2)_{0.5}(AsF_6)$ **(7)** (Figure 8.10). The $[F(HgF)_2]^+$ fragment has a central Hg–F–Hg angle (116.5°) that is nearly identical to that of $FHg(\mu_3\text{-}FKrF)_{1.5}(KrF_2)_{0.5}(AsF_6)$ (116.9(2)°). The calculated Hg–F_t bond lengths (2 x 1.935 Å) are much shorter than the calculated Hg–μ-F_b bond lengths (2 x 2.083 Å), with the latter being intermediate with respect to the $Hg_{(1/2)}$–μ-$F_{(9)}$ bond lengths of **(7)** ($Hg_{(1)}$–μ-$F_{(9)}$, 2.155(5) Å; $Hg_{(2)}$–μ-$F_{(9)}$, 2.053 (5) Å). The mercury atoms of the $[F(HgF)_2]^+$ fragment are also bridged by two μ_3-FKrF ligands with Hg–μ_3-F(Kr) bond lengths (4 x 2.699 Å) which are overall slightly longer than the bonds of **(7)** (exptl, 2.542(6), 2.635(6), 2.691(6), 2.757(6) Å; av. μ_3-F−Kr, 2.656(6) Å). The Hg–μ_3-F_b(Kr)–Hg (2 x 82.0°) and Hg–μ_3-F_b–Kr (4 x 138.9°) angles calculated for $[F(HgF)_2(\mu_3\text{-}FKrF)_2]^+$ are also in good agreement with those of **(7)** (86.5° and 83.3(2)°; 128.6(3)–136.6(3)°), although the μ_3-FKrF ligands of the calculated structure coordinate at an angle of 39.1° relative to the plane formed by the Hg/F backbone (Figure 8.10c and 8.10e) that is more acute than that of **(7)** (78.4(3) and 86.4(3)°). The difference may be attributed to crystal packing. The calculated μ_3-FKrF ligand Kr–F_b bond lengths (2 x 2.027 Å) are elongated relative to the Kr–F_t bond lengths (2 x 1.871 Å), reproducing the experimental trend but are slightly overestimated relative to those of **(7)** (Kr–F_b, 1.955(6) and 1.969(6) Å; Kr–F_t, 1.836(9) and 1.846(8) Å).

8.2.4.2. Natural Bond Orbital (NBO) Analyses of $Hg(KrF_2)_5(AsF_6)_2$ (5′)

The NBO analyses (Table S8.11) were carried out for $Hg(KrF_2)_5(AsF_6)_2$ **(5′)** using both NBO versions 3.1 and 6.0 [values given in square brackets],[39–41] because the former includes the 6p AOs of Hg as valence orbitals whereas the later version suppresses the *n*p AOs for groups 1-12 by treating them as polarization functions.[42] The calculated NPA charge on Hg (+1.448 [+1.702]) is significantly less than the formal charge expected for a purely ionic compound (+2) and is comparable to that calculated of $[Hg(KrF_2)_8]^{2+}$ (+1.451 [+1.713]).[23] As previously noted for $[Hg(KrF_2)_8]^{2+}$, inclusion of the 6p AOs of Hg results in significantly more charge transfer from predominantly the bridging F-atom of each KrF_2 ligand to Hg (0.062–0.074 [0.032–0.040] e). The charge transferred from each ligand is also comparable to that of $[Hg(KrF_2)_8]^{2+}$ (0.069 [0.036] e).[23] The Hg–F_b(Kr) Wiberg bond indices (0.108-0.134 [0.058-0.076]) are also similar to those of $[Hg(KrF_2)_8]^{2+}$ (0.122 [0.064]) and corroborate the coordinate-covalent character of the metal-ligand interactions and involvement of the 6s and 6p AOs in bonding. The charge distributions on the KrF_2 ligands are consistent with the asymmetric bond lengths of coordinated KrF_2, where polarization by Hg^{2+} results in significantly more negative charge on F_b than on F_t.

The overall charges of the $[AsF_6]^-$ anions ($As_{(1)}$, –0.881 [–0.936]; $As_{(2)}$, –0.909 [–0.948]) are slightly more positive than expected (–1) for a purely ionic bonding model, suggesting some charge transfer onto the cation. The resulting Hg–F_b(As) Wiberg bond indices (0.079-0.142 [0.039-0.084]) are similar to those calculated for the KrF_2 ligands.

8.2.4.3. Energy Decomposition Analyses (EDA) of $[F(HgF)_2(\mu_3\text{-}FKrF)_2]^+$

Compound **(7)** provides the prototype for the new KrF_2 ligand coordination modality. It is of interest to probe the nature of these metal-ligand bonding interactions by use of the calculated model. The nature μ_3-FKrF bridges in the hypothetical, energy-minimized $[F(HgF)_2(\mu_3\text{-}FKrF)_2]^+$ cation (C_{2v}, Figure 8.10) was evaluated using the energy decomposition analysis of Ziegler and Rauk[33–37] at the PBE/TZ2P level of theory. The bonding was analyzed in terms of the interaction between $[F(HgF)_2]^+$ and two symmetry-related neutral μ_3-FKrF ligands (Table 8.3). Treatment of the two μ_3-FKrF ligands as one single fragment resulted in the same overall bonding description with negligible energy differences (Table S8.12). An instantaneous Kohn-Sham interaction energy ($\Delta E_{int} = \Delta E_{elstat} + \Delta E_{orb} + \Delta E_{disp} + \Delta E_{Pauli}$) of –166.5 kJ mol^{-1} was calculated having relative contributions of ΔE_{elstat} = –173.4 kJ mol^{-1} (corresponding to the quasi-classical electrostatic interaction energy, calculated using unperturbed charge distributions of both fragments), ΔE_{orb} = –125.8 kJ mol^{-1} (orbital interaction energy; includes contributions from intrafragment polarization), ΔE_{Pauli} = 146.2 kJ mol^{-1} (Pauli repulsion), and a minor contribution from ΔE_{disp} = –13.5 kJ mol^{-1} (dispersion interactions). The preparation energy (ΔE_{prep} = 29.6 kJ mol^{-1}) is the energy needed to bring each fragment from their optimized geometries to their geometries in the complex. From these values, the total interaction energy ($\Delta E_{int} + \Delta E_{prep}$ = –136.9 kJ mol^{-1}) corresponds to average metal-ligand interaction energies of –34.2 kJ mol^{-1} for each Hg–μ_3-F_b(Kr) bond. These interactions are much weaker than the average calculated interaction energies of the terminally coordinated KrF_2 molecule in

$[Hg(KrF_2)_8]^{2+}$ (–151.1 kJ mol^{-1}).[23] Like $[Hg(KrF_2)_8]^{2+}$, both electrostatic interaction and orbital interaction terms are important stabilizing factors in $[F(HgF)_2(\mu_3\text{-}FKrF)_2]^+$.

Table 8.3. Energy Decomposition Analysis (EDA) of $[F(HgF)_2(\mu_3\text{-}FKrF)_2]^+$ (C_{2v}) [a]

	$[F(HgF)_2]^+ + 2\ \mu_3$-FKrF
ΔE_{int}	–166.5
ΔE_{orb} [b]	–125.8 (40.2%)
ΔE_{elstat} [b]	–173.4 (55.4%)
ΔE_{disp} [b]	–13.5 (4.3%)
ΔE_{Pauli}	146.2
Total ΔE_{prep} [c]	29.6
ΔE_{prep} $[F(HgF)_2]^+$	11.6
ΔE_{prep} *per* KrF_2	9.0
$-D_E$	–136.9

[a] Calculated using the PBE density functional with TZ2P all-electron basis set. Values given in kJ mol^{-1}. [b] Values in parentheses denote the percentages of totally attractive interactions. [c] Total $\Delta E_{prep} = (\Delta E_{prep}[F(HgF)_2]^+) + 2(\Delta E_{prep}KrF_2)$

8.2.4.4. ETS-NOCV Analysis of $[F(HgF)_2(\mu_3\text{-}FKrF)_2]^+$

The ETS-NOCV approach further partitions the orbital interaction energy (E_{orb}), suggesting five dominant bonding contributions. The MO labels for the μ_3-FKrF fragments are based on those of the free KrF_2 molecule under $D_{\infty h}$ symmetry (see Chapter 7, Figure 7.4). The analysis shows two dominant MOs for each μ_3-FKrF ligand, namely the $8\sigma_g$ (HOMO–4) and a degenerate $4\pi_u$ (HOMO) orbital, that σ-donate electron density through the F_b atom to both Hg atoms. In free KrF_2, these orbitals are essentially non-bonding and can be assigned as lone pairs, with the $8\sigma_g$ predominately composed from the both fluorines p_z AOs (91%) whereas the degenerate $4\pi_u$ orbitals are comprised mostly of both fluorines p_x or p_y AOs (81%) although the Kr $p_{x/y}$ AOs (18%) are also involved.

The most significant metal-ligand orbital interaction in $[F(HgF)_2(\mu_3\text{-}FKrF)_2]^+$ (–40.6 kJ mol^{-1}; A_1 symmetry) involves electron donation by in-phase combinations of the $8\sigma_g$ MO of each μ_3-FKrF molecule which predominantly donate electron density into the $[F(HgF)_2]^+$ fragment LUMO and, to a lesser extent, LUMO+2 (Figure 8.11a and S8.13a). These $[F(HgF)_2]^+$ fragment MOs are largely comprised of in-phase combinations of the 6s (57%), and the 6p (89%) valence orbitals, respectively, of both Hg^{2+} cations. The second most important contribution (–26.5 kJ mol^{-1}; B_2 symmetry) also involves the $8\sigma_g$ MOs of each μ_3-FKrF molecule, which are out of phase and σ-donate electron density to LUMO+3 of the $[F(HgF)_2]^+$ fragment. This unoccupied acceptor MO is essentially comprised of in-phase combination of the Hg 6p orbitals (94%) that are perpendicular to the plane formed by the fragment atoms (Figure 8.11b and S8.13c). The third most important contribution (–18.9 kJ mol^{-1}); B_1 symmetry) σ-donates from the in-phase $4\pi_u$ MOs of each μ_3-FKrF molecule to the LUMO+1 and LUMO+5 of the $[F(HgF)_2]^+$ fragment, with the latter acceptor MOs predominantly comprised of out-of-phase combinations of the mercury atoms 6s (62%) orbitals and the in-plane 6p (75%) valence orbitals with respect to the plane formed by the $[F(HgF)_2]^+$ atoms, respectively (Figures 8.11c and S813b). The out-of-phase combination of the $4\pi_u$ MOs of both μ_3-FKrF ligands also donates electron density to LUMO+4 of $[F(HgF)_2]^+$ (–9.5 kJ mol^{-1}; A_2 symmetry). This $[F(HgF)_2]^+$ fragment MO accepts electron density using the out-of-phase combination of the Hg 6p orbitals (98%) perpendicular to the plane formed by the $[F(HgF)_2]^+$ atoms (Figure 8.11e and S8.13e). Interestingly, there is also a contribution (–11.3 kJ mol^{-1}; A_1 symmetry) which suggests donation of electron density from the

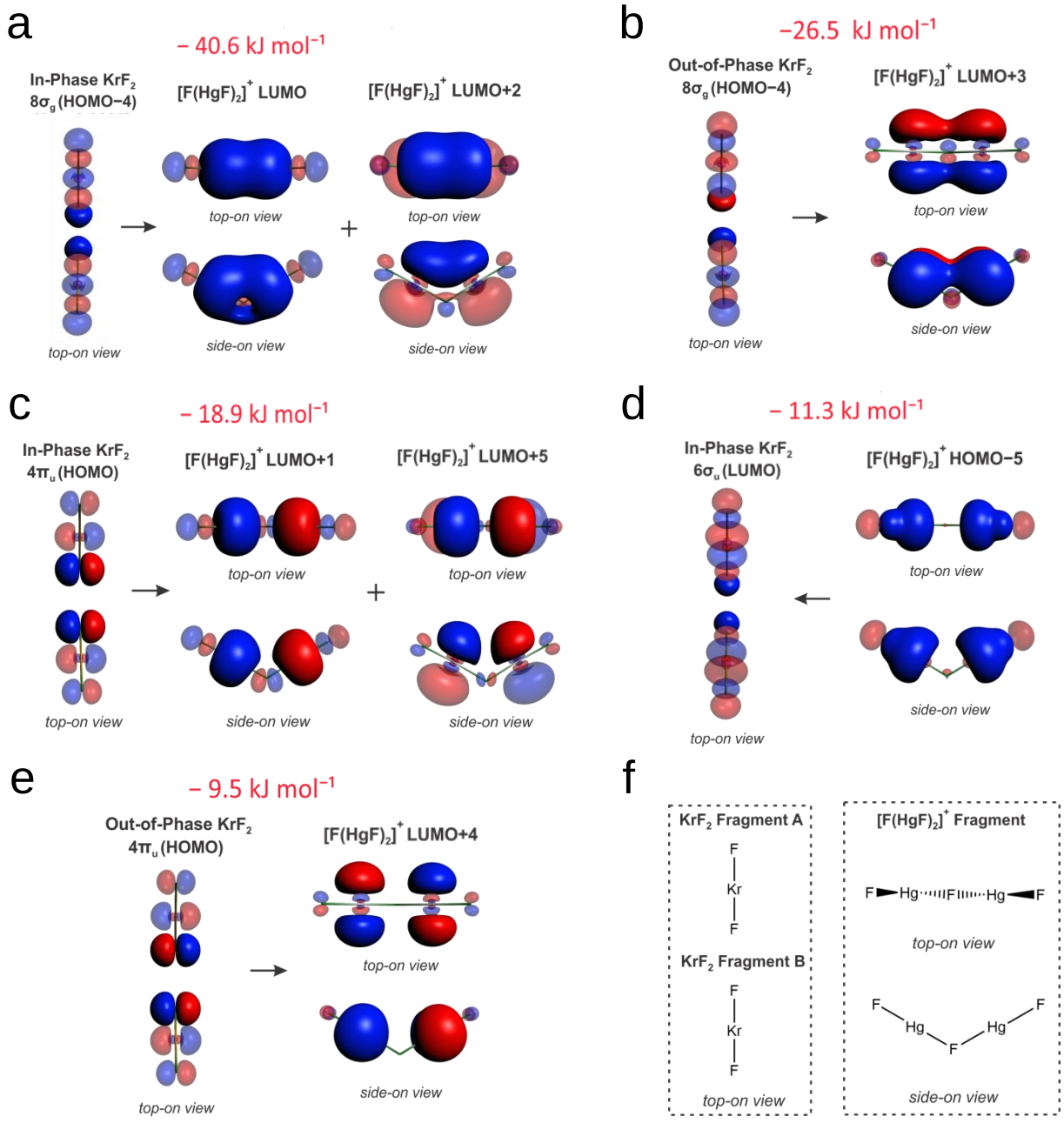

Figure 8.11. The most significant Symmetry-adapted Fragment Orbitals (SFOs) derived from the ETS-NOCV analysis of the hypothetical $[F(HgF)_2(\mu_3\text{-}FKrF)_2]^+$ cation, shown at isosurface values of 0.03 and 0.06 a.u. for μ_3-FKrF and $[F(HgF)_2]^+$, respectively, for fragment orbital combinations having (**a**) A_1, (**b**) B_2, (**c**) B_1, (**d**) A_1, and (**e**) A_2 symmetries. (**f**) A simplified drawing showing the fragments and their relative orientations. Labels correspond to MOs derived from free KrF_2 (see Chapter 7, Figure 7.4) and the MOs of $[F(HgF)_2]^+$. Relative orbital phases are denoted by red and blue colors. More intense colors denote orbital lobes of the metal and ligand fragments that constructively interact.

HOMO–5 of the $[F(HgF)_2]^+$ fragment into the unoccupied $6\sigma_u$ LUMOs of the μ_3-FKrF ligands (Figure 8.11d). The $[F(HgF)_2]^+$ MO is comprised of large contributions from the Hg 6s (36%) valence orbitals and 2p orbitals (36%) of the terminal fluorine atoms. The corresponding deformation density isosurface (Figure S8.13d) shows depleted electron density between the fragments, suggesting the interactions are likely electrostatic, due to polarization upon bond formation, rather than covalent in character.

The ETS-NOCV analysis reveals that both the $8\sigma_g$ and $4\pi_u$ MOs of the μ_3-FKrF ligands are involved in bonding, which are the same orbitals that account for the terminal bonding in $[Hg(KrF_2)_8]^{2+}$,[23] and result in the bent Hg–F–Kr coordination angles (121.9(1)–134.4(3)^o) in the experimental crystal structures. The latter are ~135^o to accommodate interactions involving two mutually perpendicular p-orbitals on the bridging ligands fluorine atom. In the case of μ_3-FKrF coordination, a second Hg atom is appropriately positioned so that the ligand MOs can interact with orbital combinations from both mercury atoms. As is the case for $[Hg(KrF_2)_8]^{2+}$, both the 6s and 6p valence orbitals of mercury are considered in this bonding description.

8.2.4.5. Hirshfeld Charge Analysis of $[F(HgF)_2(\mu_3\text{-}FKrF)_2]^+$

In accordance with some covalent character of the Hg–μ_3-F(Kr) bonds, the Hirshfeld charge analysis of $[F(HgF)_2(\mu_3\text{-}FKrF)_2]^+$ shows that the charge on $[F(HgF)_2]$ fragment (+0.828 e) is reduced due to electron donation from the μ_3-FKrF ligands (+0.086 e each). The average calculated Hirshfeld charge on the terminal KrF_2 ligands in $[Hg(KrF_2)_8]^{2+}$ was slightly less at +0.060 e.

8.3. Conclusions

A series of KrF_2 adducts of $Hg(PnF_6)_2$ and $FHg(AsF_6)$ were synthesized and characterized by single-crystal X-ray diffraction. The structures exhibit considerable diversity, ranging from a well-separated structural unit **(5),** extensively hydrogen-bonded structure **(6)**, a dimeric structure **(4)**, chain structures **(3)** and **(8)**, layered structure **(2)**, and three-dimensional network structures **(1)** and **(7)**. Interestingly, compound **(5)** is not isostructural with a known XeF_2 analogue having the same formulation. Furthermore, the XeF_2 analogues of the remaining complexes of Hg^{2+} reported in this study are currently unknown. The KrF_2 ligands in complexes **(1)**–**(6)** are all terminally coordinated, whereas compound **(7)** also contains an asymmetrically bridged KrF_2 molecule which is only the second crystallographically characterized example of a bridging KrF_2 ligand other than $Hg(KrF_2)_{1.5}(OTeF_5)_2$.[24] Furthermore, **(7)** and **(8)** also exhibit a new μ_3-FKrF bridge-bonding modality not previously encountered in noble-gas difluoride coordination chemistry, where one fluorine atom of a terminal KrF_2 molecule bridges two Hg^{2+} cations. The Raman spectrum of **(5)** was confidently assigned with the aid of vibrational frequencies calculated by quantum-chemical methods, whereas more general assignments were made for complexes **(1)**–**(4)** and **(6)** using calculated gas-phase models. The results of the NBO analyses of $Hg(KrF_2)_5(AsF_6)_2$ are consistent with coordinate covalent ligand-metal interactions. The nature of bonding associated with the μ_3-FKrF ligand was probed computationally. The EDA of the $[F(HgF)_2(\mu_3\text{-}FKrF)_2]^+$ cation model suggests orbital and electrostatic interactions are important stabilizing factors, similar to that for $[Hg(KrF_2)_8]^{2+}$.[23] The ETS-NOCV analyses indicate the $8\sigma_g$ and $4\pi_u$ MOs of KrF_2 are

predominantly involved in bonding and donate electron density into the 6s and 6p valence orbitals of the Hg^{2+} cations.

This work represents a significant extension of KrF_2 coordination chemistry by providing a comprehensive series of adducts which includes the lowest KrF_2-to-metal ratio coordination complex that is currently known, namely $Hg(KrF_2)(HF)(AsF_6)_2$, and compounds **(7)** and **(8)** offer a new class of coordination complexes in which the first examples of μ_3-FKrF bonded ligands have been characterized.

8.4. Experimental

General experimental techniques, procedures, and equipment, as well as the preparation and purification of all starting materials are described in Chapter 2.

8.4.1. Syntheses and Crystal Growth

In a typical reaction, $Hg(PnF_6)_2$ (< 0.100 g) was weighed out inside a drybox and loaded into a ¼-in o.d. FEP reaction vessel. Anhydrous hydrogen fluoride (~0.5 mL) was distilled on a metal vacuum line through an FEP submanifold onto the sample at –78 ^oC; however with the starting material showing very little solubility even when warmed to room temperature. The reaction mixture was then frozen at –196 ^oC and KrF_2 was sublimed under static vacuum from a preweighed FEP storage vessel that had been temporarily warmed to room temperature. The reaction vessel was backfilled with 1 atm of N_2 gas and subsequent reweighing of the KrF_2 storage vessel provided the reaction stoichiometry. The reaction vessel and contents were then warmed to –20 ^oC which resulted in the dissolution of most of the starting material with only a small amount of undissolved powder remaining. The solution was then slowly cooled to –78 ^oC over

several hours, during which time colorless crystals deposited. The solvent was removed under dynamic vacuum at –78 ^{o}C and a Raman spectrum (–150 ^{o}C) of the crystalline material was obtained followed by single-crystal X-ray structure determinations. Colorless, plate-shaped crystals of $Hg(KrF_2)_5(AsF_6)_2$ (**5**) were readily obtained from a reaction mixture which contained excess KrF_2 ($Hg(AsF_6)_2$:KrF_2 molar ratio, ~1:3). Minor formation of $Hg(KrF_2)_2(AsF_6)_2$ **(2)** was also present in the product based on unit cell determinations and Raman spectroscopy. No coordination complexes having a Hg^{2+}:KrF_2 ration higher than 1:5 could be isolated under the outlined reaction conditions even when a large excess of KrF_2 was used (~1:10 molar ratio). In a similar reaction with a ~1:7 molar excess of KrF_2, colorless plate-shaped crystals of $Hg(KrF_2)_4(HF)_2(AsF_6)_2{\cdot}HF$ **(6)** were obtained. Use of a small excess of $Hg(AsF_6)_2$ (~1:0.8 molar ratio) afforded colorless block-shaped crystals of both $Hg(KrF_2)(HF)(AsF_6)_2$ **(1)** and $Hg(KrF_2)_2(AsF_6)_2$ **(2)**, as well as **(5)**, in the same reaction mixture which were confirmed by a series of unit cell determinations. Reaction of $Hg(SbF_6)_2$ with a ~2.4 molar excess of KrF_2 afforded colorless plates of $Hg(KrF_2)_3(HF)_2(SbF_6)_2$ **(3)** whereas a larger excess of KrF_2 ($Hg(SbF_6)_2$:KrF_2 ~1:5) resulted in colorless plates of $[Hg(KrF_2)_4(HF)_2(SbF_6)]_2[SbF_6]_2$ **(4)**.

The reaction of $Hg(AsF_6)_2$ with a threefold molar excess of KrF_2 also unexpectedly yielded a colorless plate of $FHg(\mu_3\text{-}FKrF)_{1.5}(KrF_2)_{0.5}(AsF_6)$ **(7)** which was characterized by an X-ray structure determination. To further investigate the formation of compound **(7)**, several reactions of $FHg(AsF_6)$ (< 0.100 g) with KrF_2 at different molar ratios ($FHg(AsF_6)$:KrF_2 ~1:1 to ~1:4) were explored in HF (~0.5 mL). However, even when the reaction temperature was as low as –50 ^{o}C, the KrF_2 complexes isolated

correspond to those of the $Hg(AsF_6)_2$ complexes (as indicated by Raman spectroscopy and unit cell determinations) of **(2)**, **(5)** and $[Hg(KrF_2)_8][AsF_6]_2 \cdot 2HF$,[23] as well as the compound $Hg_4F_5(AsF_6)_3 \cdot HF$ **(9)** as colorless plates. When a twofold molar excess of KrF_2 was used, a solution that had been momentarily warmed from –78 °C to –30 °C for ca. 2 min. resulted in only slight dissolution of the starting reagents, and upon rapid re-cooling to –78 °C afforded some colorless needles corresponding to $FHg(\mu_3\text{-}FKrF)_{0.5}(KrF_2)_{1.5}(AsF_6)$ **(8)**. The Raman spectrum and numerous unit cell determinations for this sample suggest that compounds **(5)** and **(9)** were still the dominant products.

8.4.2. Structure Solution and Refinement

The XPREP[43,44] program was used to confirm the unit cell dimensions, the crystal systems and space groups. The structures were solved in their respective space groups and refined using SHELXTL programs.[44] The crystal structure of $Hg(KrF_2)_5(AsF_6)_2$ (**5**) was refined as a two-component inversion twin (BASF, 0.347). The analysis of $Hg(KrF_2)(HF)(AsF_6)_2$ (**1**) with CELL_NOW[45] suggested non-merohedral twinning with two major components, the second being rotated by 179.9° about the reciprocal axis –0.998 0.000 1.000. The raw data were processed using the multi-component version of SAINT[46] under control of the two-component orientation file generated by CELL_NOW. The program, TWINABS,[47] was then used to generate the hkl files; the best R_{int} was obtained by fitting the single reflections of both domains as well as the composite reflections (BASF, 0.361). The crystal structure of $FHg(\mu_3\text{-}FKrF)_{1.5}(KrF_2)_{0.5}(AsF_6)$ **(7)** was also analyzed using CELL_NOW which suggested non-merohedral twinning with two major components, the second being rotated by 179.9° about the reciprocal axis 0.968

0.000 1.000. The data was processing was similar to that for compound (**1**), using a BASF of 0.423. The hydrogen atom positions in the crystal structures of **(1)**, **(3)**, **(4)**, and **(6)** could not be localized from the difference Fourier maps and instead were placed at calculated positions using the SHELXTL-Plus software package[44] and their geometrical parameters restrained using the DFIX command. In the case of $Hg_4F_5(AsF_6)_3 \cdot HF$, the hydrogen atom was also placed at a calculated position and its coordinates set using the AFIX command. The final refinement was obtained by introducing anisotropic thermal parameters and the recommended weightings for all non-hydrogen atoms. The PLATON program[48] could not suggest additional or alternative symmetries.

8.4.3. Computational Details

The optimized gas-phase geometries of (**1'**)–(**6'**) were obtained at the B3LYP/def2-TZVPP level of theory[49,50] with effective core potentials for Sb[51] and Hg,[52] using the program Gaussian 09.[53] The basis sets were obtained online from the EMSL Basis Set Exchange (https://bse.pnl.gov/bse/portal).[54] Natural bond orbital analyses of (**5**) were performed at the same level of theory with the NBO program (versions 3.1 and 6.0).[39,40] The vibrational mode descriptions given in Table S8.10 were constructed by visualizing the vibrational displacements of the calculated models by use of the program *GaussView*.[55]

The hypothetical model cation, $[F(HgF)_2(\mu_3\text{-}KrF_2)_2]^+$, and the $[F(HgF)_2]^+$ and KrF_2 fragments, were optimized at the PBE/TZ2P level of theory[56,57] using the ADF (Amsterdam density functionals) package (SCM, version 2016.106).[58] Relativistic effects were taken into account by use of the zero-order regular approximation (ZORA)[59] and

dispersion effects were considered using Grimme's DFT-D3-BJ correction.[60] Analytical frequency calculations[61] were carried out for the ADF-optimized structures and fragments to ensure the geometry optimizations led to minima on their potential energy surfaces. The vibrational frequencies were real in all cases. The atomic partial charges were calculated by use of the Hirshfeld partitioning scheme.[62] The computational results were visualized by use of the ADF Graphical User Interface (SCM).[58]

8.5. Supporting Information Contents - Appendix F

Experimental and Calculated Geometrical Parameters of (**5**) and (**5′**) (Table S8.1), (**4**) and (**4′**) (Table S8.2), (**3**) and (**3′**) (Table S8.3), (**2**) and (**2′**) (Table S8.4), (**1**) and (**1′**) (Table S8.5), (**6**) and (**6′**) (Table S8.6), (**7**) and $[F(HgF)_2(\mu_3–FKrF)_2]^+$ (Table S8.7), Experimental Geometrical Parameters of (**8**) (Table S8.8); Experimental Geometrical Parameters of (**9**) (Table S8.9); Crystallographic packing of (**5**) (Figure S8.1); Crystallographic packing of (**4**) (Figure S8.2); Hydrogen Bonding in the crystal structure of (**4**) (Figure S8.3); Crystallographic packing of (**3**) (Figure S8.4); Hydrogen Bonding in the crystal structure of (**3**) (Figure S8.5); Crystallographic packing of (**2**) (Figure S8.6); Crystallographic packing of (**6**) (Figure S8.7); Crystallographic packing of (**7**) (Figure S8.8); Crystallographic packing of (**8**) (Figure S8.9); Crystal structure of $Hg_4F_5(AsF_6)_3 \cdot HF$ (**9**) (Figure S8.10); Raman Spectra of crystalline reaction products (Figure S8.11); Experimental and Calculated Raman frequencies and intensities comprised of (**1**)–(**6**) (Table S8.10); NBO analyses of (**5'**) (Table S8.11); Energy Decomposition Analysis (EDA) & ETS-NOCV additional discussion; EDA of $[F(HgF)_2(\mu_3\text{-}FKrF)_2]^+$ (Table S8.12); SCF deformation density isosurface of $[F(HgF)_2(\mu_3\text{-}FKrF)_2]^+$ (Figure S8.12); ETS-NOCV analysis for $[F(HgF)_2]^+$ and two KrF_2 ligands (Figure S8.13).

8.6. References

(1) Brock, D. S.; Schrobilgen, G. J.; Žemva, B. Noble-Gas Chemistry. In *Comprehensive Inorganic Chemistry*; Reedijk, J., Poeppelmeier, K., Eds.; Elsevier: Oxford, 2013; Vol 1, Chapter 1.25, pp 755−822.

(2) Lehmann, J. F.; Dixon, D. A.; Schrobilgen, G. J. *Inorg. Chem.* **2001**, *40*, 3002−3017.

(3) Elliott, H. St. A.; Lehmann, J.; Mercier, H. P. A.; Jenkins, H. D.; Schrobilgen, G. J. *Inorg. Chem.* **2010**, *49*, 8504−8523.

(4) Brock, D. S.; Casalis de Pury, J. J.; Mercier, H. P. A.; Schrobilgen, G. J.; Silvi, B. *Inorg. Chem.* **2010**, *49*, 6673−6689.

(5) Tavčar, G.; Tramšek, M.; Bunič, T.; Benkič, P.; Žemva, B. *J. Fluorine Chem.* **2004**, *125*, 1579−1584.

(6) Tramšek, M.; Žemva, B. *J. Fluorine Chem.* **2006**, *127*, 1275−1284.

(7) Tavčar, G.; Žemva, B. *Inorg. Chem.* **2005**, *44*, 1525−1529.

(8) Bunič, T.; Tramšek, M.; Goreshnik, E.; Tavčar, G.; Žemva, B. *Inorg. Chem.* **2007**, *46*, 5276−5282.

(9) Bunič, T.; Tramšek, M.; Goreshnik, E.; Žemva, B. *Solid State Sci.* **2008**, *10*, 1511−1516.

(10) Tavčar, G.; Tramšek, M. *J. Fluorine Chem.* **2015**, *174*, 14−21 and references therein.

(11) Tavčar, G.; Benkič, P.; Žemva, B. *Inorg. Chem.* **2004**, *43*, 1452−1457.

(12) Bunič, T.; Tavčar, G.; Tramšek, M.; Žemva, B. *Inorg. Chem.* **2006**, *45*, 1038−1042.

(13) Tavčar, G.; Goreshnik, E.; Mazej, Z. *J. Fluorine Chem.* **2006**, *127*, 1368−1373.

(14) Tavčar, G.; Žemva, B. *Angew. Chem. Int. Ed.* **2009**, *48*, 1432–1434.

(15) Holloway, J. H.; Schrobilgen, G. J.; Taylor, P. *J. Chem. Soc., Chem. Commun.* **1975**, *2*, 40−41.

(16) Holloway, J. H.; Schrobilgen, G. J. *Inorg. Chem.* **1980**, *19*, 2632−2640.

(17) Tucker, P. A.; Taylor, P. A.; Holloway, J. H.; Russell, D. R. *Acta Crystallogr.* **1975**, *B31*, 906−908.

(18) Holloway, J. H.; Schrobilgen, G. J. *Inorg. Chem.* **1981**, *20*, 3363−3368.

(19) Christe, K. O.; Wilson, W. W.; Bougon, R. A. *Inorg. Chem.* **1986**, *13*, 2163−2169.

(20) Nabiev, Sh. Sh.; Sokolov, V. B.; Spirin, S. N.; Chaivanov, B. B. *Russ. J. Phys. Chem. A* **2011**, *85*, 1931–1941.

(21) Brock, D. S.; Casalis de Pury, J. J.; Mercier, H. P. A.; Schrobilgen, G. J.; Silvi, B. *J. Am. Chem. Soc.* **2010**, *132*, 3533−3542.

(22) Lozinšek, M.; Mercier, H. P. A.; Brock, D. S.; Žemva, B.; Schrobilgen, G. J. *Angew. Chem. Int. Ed.* **2017**, *56*, 6251–6350.

(23) DeBackere, J. R.; Schrobilgen, G. J. *Angew. Chem. Int. Ed.* **2018**, *57*, 13167–13171.

(24) DeBackere, J. R.; Mercier, H. P. A.; Schrobilgen, G. J. *J. Am. Chem. Soc.* **2014**, *136*, 3888–3903.

(25) Mazej, Z.; Goreshnik, E. A. *J. Solid State Chem.* **2015**, *228*, 59–59.

(26) Lehmann, J. F.; Dixon, D. A.; Schrobilgen, G. J. *Inorg. Chem.* **2001**, *40*, 3002–3017.

(27) Tramšek, M.; Benkič, P.; Žemva, B. *Inorg. Chem.* **2004**, *43*, 699−703.

(28) Mazej, Z.; Goreshnik, E. A. *Inorg. Chem.* **2008**, *47*, 4209–4214.

(29) a) Naulin, C.; Bougon, R. *J. Chem. Phys.* **1976**, *64*, 4155–4158; b) Popov, A. I.; Scharabarin, A. V.; Sukhoverkhov, V. F.; Tchumaevsky, N. A.; *Z. Anorg. Allg. Chem.* **1989**, *576*, 242–254.

(30) a) Carter, H. A.; Aubke, F. *Can. J. Chem.* **1970**, *48*, 3456–3459; b) Christe, K. O.; Schack, C. J.; Wilson, R. D. *Inorg. Chem.* **1975**, *14*, 2224–2230.

(31) Al-Mukhtar, M.; Holloway, J. H.; Hope, E. G.; Schrobilgen, G. J. *J. Chem. Soc., Dalton Trans.* **1991**, 2831–2834.

(32) Claassen, H. H.; Goodman, G. L.; Malm, J. G.; Schreiner, F. *J. Chem. Phys.* **1965**, *42*, 1229–1232.

(33) Ziegler, T.; Rauk, A. *Theor. Chim. Acta* **1977**, *46*, 1–10.

(34) Ziegler, T.; Rauk, A. *Inorg. Chem.* **1979**, *18*, 1558–1565.

(35) Ziegler, T.; Rauk, A. *Inorg. Chem.***1979**, *18*, 1755–1759.

(36) Bickelhaupt, F.M.; Baerends, E.J. In: *Rev. Comput. Chem*.; K.B. Lipkowitz and D.B. Boyd, Eds.; Wiley, New York, **2000**, Vol. 15, pp1-86.

(37) Mitoraj, M.; Michalak, A.; Ziegler, T. *J. Chem. Theory Comput.* **2009**, *5*, 962–975.

(38) Mitoraj, M.; Michalak, A.; Ziegler, T. *Organometallics* **2009**, *28*, 3727–3733.

(39) NBO Version 3.1, E. D. Glendening, A. E. Reed, J. E. Carpenter, F. Weinhold, Theoretical Chemistry Institute, University of Wisconsin, Madison, **1998**.

(40) NBO Version 6.0, E. D. Glendening, J. K. Badenhoop, A. E. Reed, J. E. Carpenter, J. A. Bohmann, C. M. Morales, C. R. Landis, F. Weinhold, Theoretical Chemistry Institute, University of Wisconsin, Madison, **2013**.

(41) Reed, A. E.; Curtiss, L. A.; Weinhold, F. *Chem. Rev.* **1988**, *88*, 899–926.

(42) Grabowski, S. J.; Ugalde, J. M.; Andrada, D. M.; Frenking, G. *Chem. Eur. J.* **2016**, *22*, 11317–11328.

(43) Bruker. XPREP v2008/2. Bruker AXS Inc.: Madison, WI, **2014**.

(44) Sheldrick, G. M. SHELXTL-plus, release 6.14; Siemens Analytical Xray Instruments, Inc.: Madison, WI, 1993−2014.

(45) Sheldrick, G. M. *CELL_NOW*, 2008/4, University of Göttingen: Göttingen, Germany.

(46) *SAINT+*, Version 6.02 ed., Siemens Energy and Automation Inc.; Madison, WI, 1999.

(47) Sheldrick, G. M. *TWINABS*, 2008/4, University of Göttingen: Göttingen, Germany.

(48) (a) Spek, A. L. *Acta Crystallogr. D* **2009**, *65*, 148.; (b) A. L. Spek, (**2011**) *PLATON* - A Multipurpose Crystallographic Tool; Utrecht University, Utrecht, The Netherlands.

(49) (a) Becke, A.D. *J. Chem. Phys.* **1993**, 98, 5648–5652.; (b) Lee, C.; Yang, W.; Parr, R.G. *Phys. Rev. B* **1988**, *37*, 785–789.

(50) Weigend, F.; Ahlrichs, R. *Phys. Chem. Chem. Phys.*, **2005**, *7*, 3297–305.

(51) Metz, B.; Stoll, H.; Dolg, M. *J. Chem. Phys.* **2000**, *113*, 2563–2569.

(52) Andrae, D.; Haeussermann, U.; Dolg, M.; Stoll, H.; Preuss, H. *Theor. Chim. Acta.* **1990**, *77*, 123–141.

(53) Gaussian 09, Revision E.01; Frisch, M. J.; Trucks, G. W.; Schlegel, H. B.; Scuseria, G. E.; Robb, M. A.; Cheeseman, J. R.; Scalmani, G.; Barone, V.; Mennucci, B.; Petersson, G. A.; Nakatsuji, H.; Caricato, M.; Li, X.; Hratchian, H. P.; Izmaylov, A. F.; Bloino, J.; Zheng, G.; Sonnenberg, J. L.; Hada, M.; Ehara, M.; Toyota, K.; Fukuda, R.; Hasegawa, J.; Ishida, M.; Nakajima, T.; Honda, Y.; Kitao, O.; Nakai, H.; Vreven, T.; Montgomery, J. A., Jr.; Peralta, J. E.; Ogliaro, F.; Bearpark, M.; Heyd, J. J.; Brothers, E.; Kudin, K. N.; Staroverov, V. N.; Kobayashi, R.; Normand, J.; Raghavachari, K.; Rendell, A.; Burant, J. C.; Iyengar, S. S.; Tomasi, J.; Cossi, M.; Rega, N.; Millam, N. J.; Klene, M.; Knox, J. E.; Cross, J. B.; Bakken, V.; Adamo, C.; Jaramillo, J.; Gomperts, R.; Stratmann, R. E.; Yazyev, O.; Austin, A. J.; Cammi, R.; Pomelli, C.; Ochterski, J. W.; Martin, R. L.; Morokuma, K.; Zakrzewski, V. G.; Voth, G. A.; Salvador, P.; Dannenberg, J. J.; Dapprich, S.; Daniels, A. D.; Farkas, Ö.; Foresman, J. B.; Ortiz, J. V.; Cioslowski, J.; Fox, D. J. Gaussian, Inc: Wallingford, CT, 2009.

(54) (a) Feller, D. *J. Comput. Chem.* **1996**, *17*, 1571–1586.; (b) Schuchardt, K. L.; Didier, B. T.; Elsethagen, T.; Sun, L.; Gurumoorthi, V.; Chase, J.; Li, J.; Windus, T. L. *J. Chem. Inf. Model.* **2007**, *47*, 1045–1052.

(55) G*aussView*, release 3.0; Gaussian Inc.: Pittsburgh, PA, **2003**.

(56) Perdew, J. P.; Burke, K.; Ernzerhof, M. *Phys. Rev. Lett.* **1996**, *77*, 3865–3868.

(57) van Lenthe, E.; Baerends, E.J. *J. Comput. Chem.* **2003**, *24*, 1142–1156.

(58) (a) ADF2016, SCM, Theoretical Chemistry, Vrije Universiteit, Amsterdam, The Netherlands, http://www.scm.com.; (b) Fonseca Guerra, C.; Snijders, J. G.; Velde, G.; Baerends, E. J. *Theor. Chem. Acc.* **1998**, *99*, 391–403; (c) Velde, G.; Bickelhaupt, F. M.; Baerends, E. J.; Fonseca Guerra, C.; Gisbergen, S. J. A.; Snijders, J. G.; Ziegler, T. *J. Comput. Chem.* **2001**, *22*, 931–967.

(59) (a) Lenthe, E.; Baerends, J.; Snijders, J. G. *J. Chem. Phys.* **1993**, *99*, 4597–4610; (b) Lenthe, E.; Baerends, J.; Snijders, J. G. *J. Chem. Phys.* **1994**, *101*, 9783–9792; (c) Lenthe, E.; Ehlers, A.; Baerends, E. *J. Chem. Phys.* **1999**, *110*, 8943–8953; (d) Lenthe, E.; Snijders, J. G.; Baerends, J. *J. Chem. Phys.* **1996**, *105*, 6505–6516.

(60) Grimme, S.; Ehrlich, S.; Goerigk, L. *J. Comput. Chem.* **2011**, *32*, 1456–1465.

(61) (a) Bérces, A.; Dickson, R. M.; Fan, L.; Jacobsen, H.; Swerhone, D.; Ziegler, T. *Comput. Phys. Commun.* **1997**, *100*, 247–262; (b) Jacobsen, H.; Bérces, A.; Swerhone, D.; Ziegler, T. *Comput. Phys. Commun.* **1997**, *100*, 263–276; (c) Wolff, S. K. *Int. J. Quantum Chem.* **2005**, *104*, 645–659.

(62) (a) Hirshfeld, F. L. *Theoret. Chim. Acta*, **1977**, *44*, 129–138.; (b) Wiberg, K. B.; Rablen, R. B. *J. Comput. Chem.* **1993**, *14*, 1504–1518.

CHAPTER 9

A New Xenon(II) Oxide; Synthesis and Characterization of $[XeOXe]^{2+}$ in the Adduct-Cation Salt, $[CH_3CN{-}{-}{-}XeOXe{-}{-}{-}NCCH_3][AsF_6]_2$

Adapted with permission from: DeBackere, J.R., Bortolus, M.R., and Schrobilgen, G.J. *Angew. Chem. Int. Ed.* **2016**, *55,* 11917–11920.

9.1. Introduction

Although thermodynamically unstable with respect to their elements, oxides of every known xenon oxidation state except +½ have been isolated and characterized in macroscopic quantities.[1] In the case of Xe(II), the simplest oxide, XeO, has been observed in the gas-phase by UV and vacuum UV emission spectroscopy where the emission spectrum was attributed to Xe^+O^- ion pair states.[2] Monomeric XeO has only been characterized in an argon matrix by UV spectroscopy which suggested that the ground state is essentially a van der Waals molecule.[3] Subsequent gas-phase quantum-chemical calculations showed XeO to have an unbound $^3\Pi$ ground state with the only bound state being the excited $1^1\Sigma^+$ state.[4]

The first Xe(II) oxide to be synthesized in isolable amounts was recently reported as a salt of the planar zig-zag shaped $[XeOXeOXe]^{2+}$ cation. The salt, $[XeOXeOXe][\mu\text{-}F(ReO_2F_3)_2]_2$, was synthesized in aHF at −30 °C by O/F metathesis between ReO_3F and XeF_2 (eq. 9.1) and was characterized by low-temperature single-crystal X-ray diffraction and Raman spectroscopy.[5]

$$4[ReO_3F]\cdot 2HF + 3XeF_2 \xrightarrow{HF} [XeOXeOXe][\mu\text{-}F(ReO_2F_3)_2]_2 + 2[H_3O][HF_2] \qquad (9.1)$$

The related [FXeOXe---FXeF][AsF_6] salt is presently the only known Xe(II) oxide fluoride.[6] It can be viewed as a fluorine derivative of the $[XeOXe]^{2+}$ cation in which one xenon atom is strongly bound to a terminal fluorine atom (Xe–F, 1.992(6) Å) and the remaining xenon atom is weakly coordinated to a XeF_2 molecule through a long Xe---F contact (2.502(10) Å). The reaction of [FXeOXe---FXeF][AsF_6] with excess CH_3CN in HF at –60 ^oC resulted in the formation of the Xe(II) oxide cation, $[XeOXe]^{2+}$, as the CH_3CN adduct-cation salt.

9.2. Results and Discussion

9.2.1. Synthesis of $[CH_3CN---XeOXe---NCCH_3][AsF_6]_2$

The deep red-orange to magenta [FXeOXe---FXeF][AsF_6] was allowed to react with excess CH_3CN in HF at –60 ^oC. Over a 2h period, some slow gas evolution was observed and pale yellow, plate-shaped crystals formed on top of the starting material as it reduced in quantity. The majority of the solvent mixture was decanted and heat sealed off, and the crystalline material mounted wet using a modified procedure to give the Xe(II) oxide cation, $[XeOXe]^{2+}$, as the CH_3CN adduct-cation salt, $[CH_3CN---XeOXe---NCCH_3][AsF_6]_2$ (eq. 9.2).

$$2[FXeOXe---FXeF][AsF_6] + 2CH_3CN \longrightarrow CH_3CN---XeOXe---NCCH_3][AsF_6]_2 + XeF_2 + \tfrac{1}{2}O_2 + Xe \quad (9.2)$$

The crystals were mounted wet with HF/CH_3CN because this solvent mixture could not be completely removed by dynamic pumping below –50 ^oC, at which temperature $[CH_3CN---XeOXe---NCCH_3][AsF_6]_2$ completely decomposed; one of the

products being $[FXe{---}NCCH_3][AsF_6]$ according to Raman Spectroscopy and X-ray diffraction.

The proposed reaction pathway (Scheme 9.1) that leads to the formation of $[CH_3CN{---}XeOXe{---}NCCH_3][AsF_6]_2$ is premised on the initial displacement of XeF_2 from $[FXeOXe{---}FXeF][AsF_6]$ by CH_3CN to form $[FXeOXe{---}NCCH_3][AsF_6]$ as an intermediate. Protonation of excess CH_3CN by HF to give $[CH_3CNH][F]\cdot(HF)_x$ is postulated to lead to a double displacement reaction with $[FXeOXe{---}NCCH_3][AsF_6]$ to form $[CH_3CNH][AsF_6]$ and $O(XeF)_2$. Gas evolution was observed as the reaction proceeded which is attributed to the rapid low-temperature redox decomposition of $O(XeF)_2$ in HF to form XeF_2, Xe, and O_2. Salt metathesis between $[CH_3CNH][AsF_6]$ and $[FXeOXe{---}NCCH_3][AsF_6]$ forms $[CH_3CNH][F]\cdot(HF)_x$ and $[XeOXe{---}NCCH_3][AsF_6]_2$, with the latter intermediate subsequently coordinating a second CH_3CN molecule to give the title compound. Bands in the Raman spectra of $[CH_3CN{---}XeOXe{---}NCCH_3][AsF_6]_2$ that are attributed to $[CH_3CNH][F]\cdot(HF)_x$ were assigned by comparison with its previously published frequencies (Table 9.3).[7]

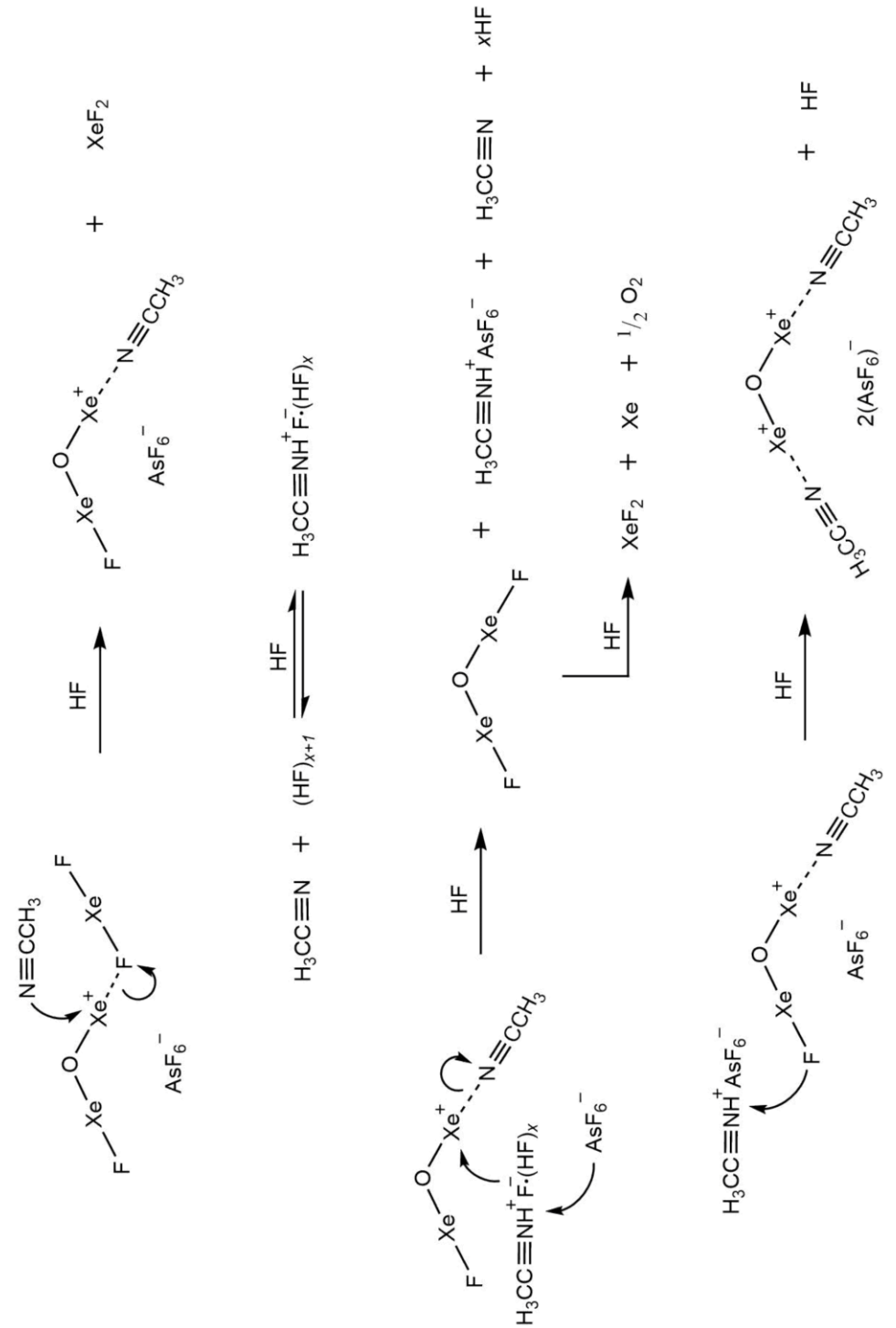

Scheme 9.1. The proposed reaction pathway leading to the formation of $[H_3CCN{-}{-}{-}XeOXe{-}{-}{-}NCCH_3][AsF_6]_2$.

9.2.2. X-ray Crystallography

A summary of crystal data and refinement results for $[CH_3CN{-}{-}{-}XeOXe{-}{-}{-}NCCH_3][AsF_6]_2$ is given in Table 9.1.

The compound $[CH_3CN{-}{-}{-}XeOXe{-}{-}{-}NCCH_3][AsF_6]_2$ (Figure 9.1) crystallized in the *C2/c* space group. The $[CH_3CN{-}{-}{-}XeOXe{-}{-}{-}NCCH_3]^{2+}$ cation lies on a general position (C_1 symmetry). The $[AsF_6]^-$ anions are slightly distorted from O_h symmetry, with two anions located on a C_2-axis and the remaining anion on a general position. The Xe–O bond lengths (2.032(2), 2.033(2) Å) are well reproduced by gas-phase calculations (2.049 Å) (see Figure 9.3 and Table 9.2). These values are intermediate with respect to those of the terminal (1.987(6) Å) and central (2.135(6) Å) Xe–O bonds of $[XeOXeOXe]^{2+}$,[5] and those of $[FXeOXe{-}{-}{-}FXeF]^+$ (1.938(8) and 2.101(8) Å).[6] The Xe–N distances (2.293(2), 2.304(2) Å) are in excellent agreement with their calculated values (2.306 Å). These bonds are significantly shorter than those of related Xe(II)–N adducts: $[C_6F_5Xe{-}{-}{-}NCCH_3][BY_4]$ (Y = CF_3, 2.640(6); Y = C_6F_5, 2.610(11) Å);[8] $[C_6F_5Xe{-}{-}{-}NCCH_3][(C_6F_5)_2BF_2]$ (2.681(8) Å);[9] $[C_6F_5Xe{-}{-}{-}NC_5H_3F_2][AsF_6]$ (2.694(5) Å);[10] and $[F_4S{=}N\text{-}Xe{-}{-}{-}N{\equiv}SF_3][AsF_6]$ (2.583(3) Å).[11] In contrast, the Xe–N distances of $[CH_3CN{-}{-}{-}XeOXe{-}{-}{-}NCCH_3]^{2+}$ are very similar to that of $[F_3S{\equiv}N{-}{-}{-}XeF][AsF_6]$ (2.236(4) Å).[12]

The Xe–O–Xe bond angle (113.0(1)°) of $[CH_3CN{-}{-}{-}XeOXe{-}{-}{-}NCCH_3]^{2+}$ is similar to those of $[XeOXeOXe]^{2+}$ (115.6(3)°)[5] but is more closed than in its precursor, $[FXeOXe{-}{-}{-}FXeF]^+$ (122.8(5)°).[6] This angle is substantially less than the calculated gas-

Table 9.1. Summary of Crystal Data and Refinement Results for $[H_3CCN{-}{-}{-}XeOXe{-}{-}{-}NCCH_3][AsF_6]_2$

crystal system	monoclinic
space group	*C*2/c (No. 15)
a (Å)	23.8785(8)
b (Å)	11.4645(4)
c (Å)	12.5440(4)
β	109.064(2)
V (Å^3)	3245.6(2)
Z (molecules/unit cell)	8
mol wt (g mol^{-1})	738.55
calcd density (g cm^{-3})	3.023
T (^{o}C)	–173.0
μ (mm^{-1})	8.35
R_1 [a]	0.0292
wR_2 [b]	0.0714

[a] R_1 is defined as $\Sigma \| F_o \| - | F_c \| / \Sigma | F_o |$ for $I > 2\sigma(I)$.
[b] wR_2 is defined as $[\Sigma[w(F_o^2 - F_c^2)^2] / \Sigma w(F_o^2)^2]^{1/2}$ for $I > 2\sigma(I)$.

Table 9.2. Experimental Geometrical Parameters of $[H_3CCN{---}XeOXe{---}NCCH_3]^{2+}$ in $[H_3CCN{---}XeOXe{---}NCCH_3][AsF_6]_2$ and the Calculated Gas-Phase Geometrical Parameters of $[H_3CCN{---}XeOXe{---}NCCH_3]^{2+}$ (C_{2v}) and $[XeOXe]^{2+}$ (C_{2v})[a]

	$[H_3CCN{---}XeOXe{---}NCCH_3]^{2+}$		*$[XeOXe]^{2+}$*
	exptl	**calcd**[b]	**calcd**[b]
Bond Lengths (Å)			
$Xe_1–O_1$	2.033(2)	2.049	2.039
$Xe_2–O_1$	2.032(2)		
$Xe_1{---}N_1$	2.304(2)	2.310	
$Xe_2{---}N_2$	2.294(2)		
$N_1–C_1$	1.140(4)	1.148	
$N_2–C_3$	1.132(4)		
$C_1–C_2$	1.436(4)	1.442	
$C_3–C_4$	1.441(4)		
$C_2–H$	0.98 [c]	1.091	
$C_4–H$	0.98 [c]		
Bond Angles (deg)			
$Xe_1–O_1–Xe_2$	113.0(1)	125.3	123.3
$N_1–Xe_1–O_1$	177.0(1)	174.2	
$N_2–Xe_2–O_1$	178.1(1)		
$C_1–N_1–Xe_1$	156.0(2)	175.8	
$C_3–N_2–Xe_2$	155.8(2)		
$C_2–C_1–N_1$	179.0(3)	179.8	
$C_4–C_3–N_2$	179.6(3)		

[a] The atom labels correspond to those given in Figures 9.1, 9.3 and 9.4. [b] B3LYP/aug-cc-pVTZ-(PP). [c] The hydrogen atom positions were calculated with the C–H bond lengths fixed at 0.98 Å.

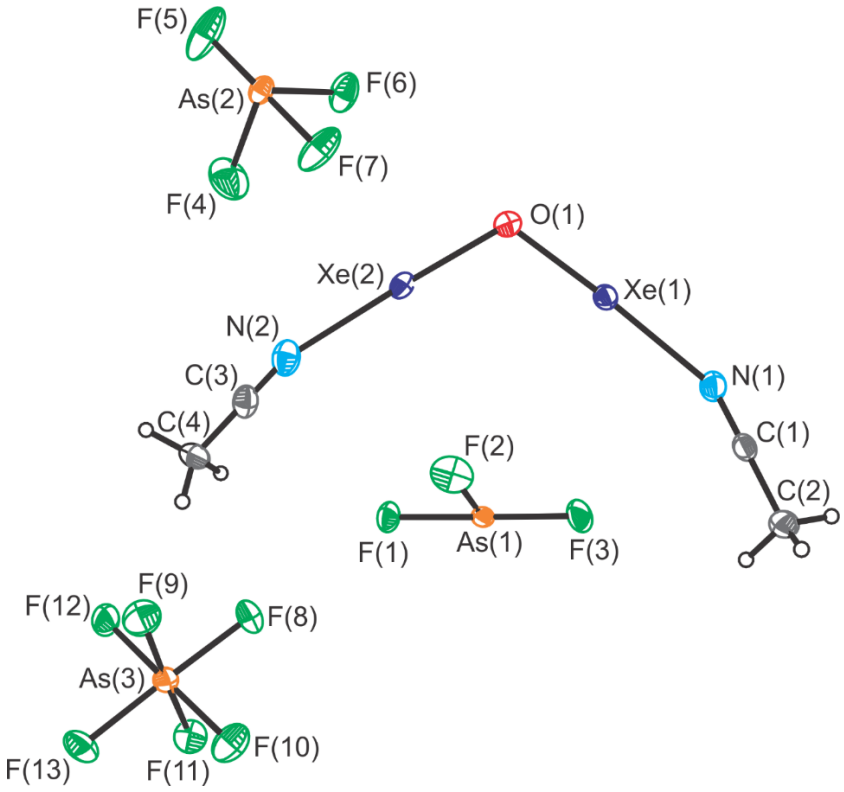

Figure 9.1. The asymmetric unit in the crystal structure of $[H_3CCN{---}XeOXe{---}NCCH_3][AsF_6]_2$ (also see Figure 9.3). Thermal ellipsoids are shown at the 50% probability level.

phase values of $[CH_3CN{---}XeOXe{---}NCCH_3]^{2+}$ (125.2°) and $[XeOXe]^{2+}$ (123.3 °) (Figure 9.4).

The Xe–N–C angles (Figures 9.1 and 9.3) are deformed both in and out of the Xe–O–Xe plane relative to the optimized gas-phase dication (C_{2v}, 175.8°). The angle distortions likely result from crystal packing, where long Xe---F cation-anion contacts (3.247(2)–3.563(2) Å) that are close to the sum of the van der Waals radii of xenon and fluorine (3.63 Å)[13] likely contribute to compression of the Xe–O–Xe and Xe–N–C angles and to the torsional angles about the Xe–N bonds.

9.2.3. Raman Spectroscopy

The Raman spectra of natural abundance and ^{18}O-enriched [CH_3CN---XeOXe---$NCCH_3$][AsF_6]$_2$ are shown in Figure 9.2. Experimental and calculated gas-phase frequencies and assignments are provided in Table 9.3.

Vibrational frequencies and isotopic shifts were well reproduced by quantum-chemical calculations. Bands associated with $[AsF_6]^-$ were assigned by comparison with their previously published frequencies.[6] In the ensuing discussion, the Raman frequencies of the ^{18}O-enriched compounds are given in square brackets following their natural abundance ^{16}O- values. In accordance with adduct formation, high-frequency ligand complexation shifts relative to free CH_3CN occur for ν(CN) (Δν(CN), 36 and 42 cm^{-1}) and ν(CC) (Δν(CC), 19 cm^{-1}).[14]

The asymmetric Xe–O stretching mode, ν(Xe_1O) – ν(Xe_2O), occurs at 599.9 [566.4] cm^{-1} and is well reproduced by the calculated value 586.0 [554.9] cm^{-1}. The experimental (–33.5 cm^{-1}) and calculated (–31.1 cm^{-1}) isotope shifts, $\Delta\nu^{16/18}$, are in excellent agreement. This frequency is comparable to that of the symmetric out-of-phase stretching mode (ν_1, A_g) of the $[XeOXeOXe]^{2+}$ cation, which occurs at 581.6 [549.3] cm^{-1} and possesses a similar $^{16}O/^{18}O$ isotope shift (–32.3 cm^{-1}).[5]

The symmetric stretching mode, ν(Xe_1O) + ν(Xe_2O), is weakly coupled to the $\delta(CCN)_{ip}$ deformation modes of the CH_3CN ligands. The band occurs at 452.0 [431.0] cm^{-1} and is well reproduced by the calculated values (443.8 [428.6] cm^{-1}). The experimental (–21.0 cm^{-1}) and calculated (–15.2 cm^{-1}) $^{16/18}O$ isotope shifts are in good

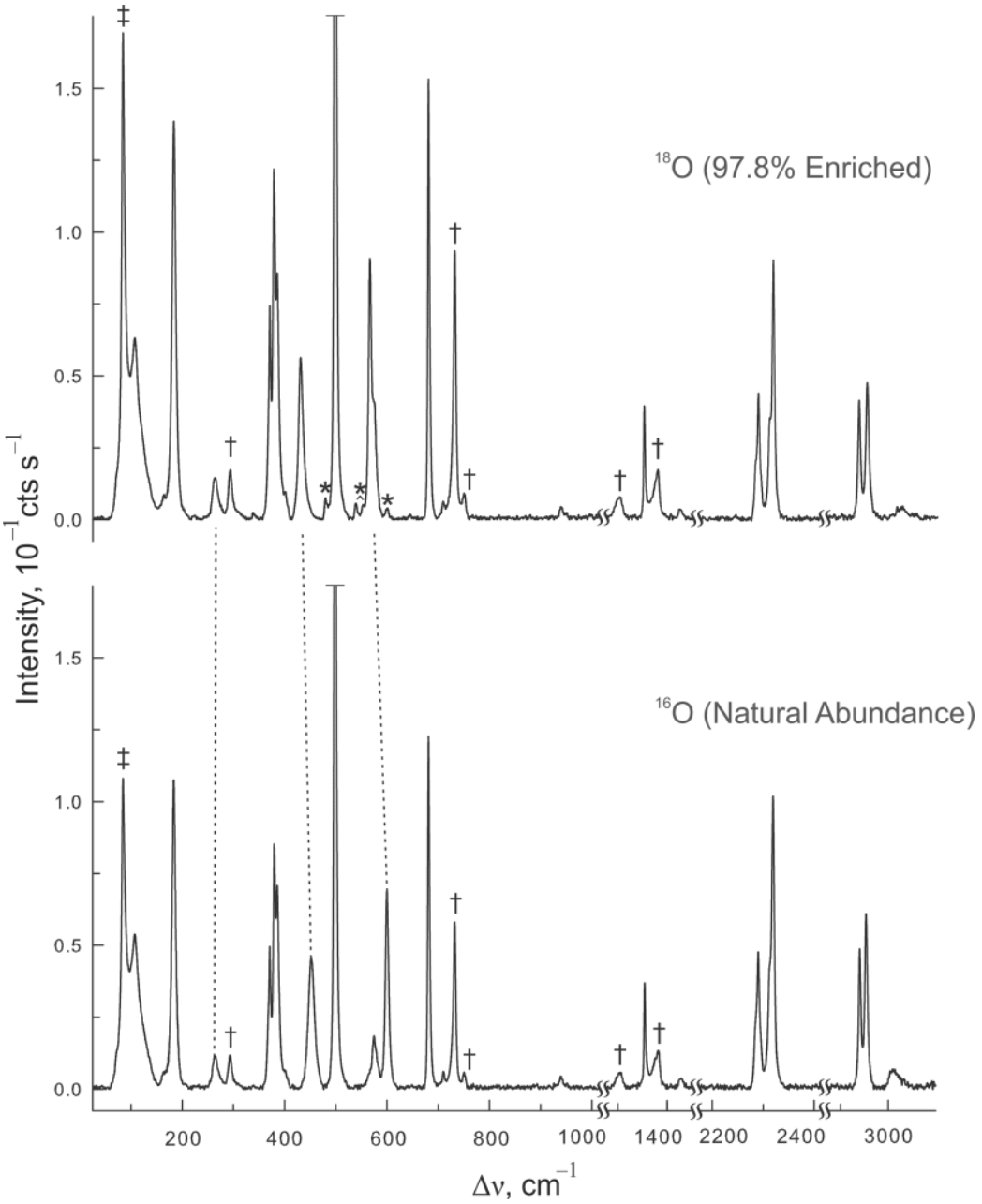

Figure 9.2. Raman spectra of $[CH_3CN{-}{-}{-}XeOXe{-}{-}{-}NCCH_3][AsF_6]_2$ recorded at –140 °C using 1064-nm excitation for natural abundance (lower trace) and 97.8% ^{18}O-enriched (upper trace) salts. Symbols denote FEP sample tube lines (†), instrumental artifact (‡), and unreacted $[FXeOXe{-}{-}{-}FXeF][AsF_6]$ (*). The Σ_g^+ band of free XeF_2 (498 cm^{-1}) is the most intense feature in both spectra (see eq. 9.2). The three vibrational bands of $[XeOXe]^{2+}$ are denoted by dashed lines drawn between the spectra of the ^{16}O- and ^{18}O-isotopologues.

Table 9.3. Experimental and Calculated (Gas-Phase) Vibrational Frequencies, Intensities, $^{16/18}$O Isotopic Shifts, and Assignments for the $[H_3CCN{-}{-}{-}XeOXe{-}{-}{-}NCCH_3]^{2+}$ Cation in $[H_3CCN{-}{-}{-}XeOXe{-}{-}{-}NCCH_3][AsF_6]_2$

exptl[a],[b]			calcd[a],[c]			assgnts[d]
^{16}O[e]	^{18}O[f]	$\Delta\nu^{16/18}$	^{16}O	^{18}O	$\Delta\nu^{16/18}$	
3009.6(6)	3009.1(3)	--	3114.3(74)[32]	3114.3(74)[32]	0.0	B_1, $\nu_{as}(CH_3)_{A+B}$
			3114.3(114)[0]	3114.3(114)[0]	0.0	A_2, $\nu_{as}(CH_3)_{A-B}$
			3113.3(60)[29]	3113.3(61)[29]	0.0	A_1, $\nu_{as}(CH_3)_{A+B}$
			3113.3(153)[4]	3113.3(153)[4]	0.0	B_2, $\nu_{as}(CH_3)_{A-B}$
2940.2(40)	2940.3(25)	0.1	3036.5(924)[8]	3036.5(924)[8]	0.0	A_1, $\nu_s(CH_3)_{A+B}$
			3036.3(27)[122]	3036.3(27)[122]	0.0	B_2, $\nu_s(CH_3)_{A-B}$
2290.3(40)	2290.2(26)	–0.1	2368.0(984)[70]	2368.0(984)[70]	0.0	A_1, $\nu(CN)_{A+B}$
2284.2(sh)[g]	2284.1(12)[g]	–0.1	2363.4(103)[1154]	2363.1(103)[1155]	0.0	B_2, $\nu(CN)_{A-B}$
1428.5(3)	1426.1(2)	–2.4	1439.8(7)[32]	1439.8(7)[32]	0.0	A_1, $\delta_{as}(CH_3)_{A+B}$
			1439.8(8)[2]	1439.8(8)[2]	0.0	B_2, $\delta_{as}(CH_3)_{A-B}$
			1439.2(<1)[35]	1439.2(<1)[35]	0.0	B_1, $\delta_{as}(CH_3)_{A+B}$
			1439.2(15)[0]	1439.2(15)[0]	0.0	A_2, $\delta_{as}(CH_3)_{A-B}$
1354.5(29)	1354.6(24)	0.1	1397.7(42)[1]	1397.7(42)[1]	0.0	A_1, $\delta_s(CH_3)_{A+B}$
			1397.5(6)[7]	1397.5(6)[7]	0.0	B_2, $\delta_s(CH_3)_{A-B}$
1024.2(4)	1024.2(3)	0.0	1045.8(<1)[16]	1045.8(<1)[16]	0.0	B_1, $\rho_r(CH_3)_{A+B}$
			1045.8(5)[0]	1045.8(5)[0]	0.0	A_2, $\rho_r(CH_3)_{A-B}$
			1044.5(10)[14]	1044.5(10)[14]	0.0	A_1, $\rho_r(CH_3)_{A+B}$
			1044.5(3)[3]	1044.5(3)[3]	0.0	B_2, $\rho_r(CH_3)_{A-B}$
940.2(3)	939.5(3)	–0.5	943.7(2)[6]	943.7(2)[6]	0.0	A_1, $\nu(CC)_{A+B}$
			940.8(<0.1)[111]	940.8(<0.1)[112]	0.0	B_2, $\nu(CC)_{A-B}$
599.9(55)	566.4(54)	–33.5	586.0(32)[377]	554.9(29)[347]	–31.1	B_2, $\nu(Xe_1O) - \nu(Xe_2O)$
452.0(37)	431.0(33)	–21.0	443.8(34)[17]	428.6(15)[17]	–15.2	A_1, $\nu(Xe_1O) + \nu(Xe_2O) + [(\delta(CCN)_{A+B})_{ip}]_{small}$

Table 9.3 continued …

401.4(6)	401.4(6)	0.0	410.6(3)[0]	410.6(3)[0]	0.0	A_2, $(\delta(CCN)_{A-B})_{oop}$
			410.5(<1)[4]	410.5(<1)[4]	0.0	B_1, $(\delta(CCN)_{A+B})_{oop}$
			410.0(1)[<1]	410.0(1)[<1]	0.0	B_2, $(\delta(CCN)_{A-B})_{ip}$
385.9(45)	385.4(51)	–0.5	403.3(35)[<0.01]	398.6(47)[1]	–4.7	A_1, $(\delta(CCN)_{A+B})_{ip} + [\nu(Xe_1O) + \nu(Xe_2O)]_{small}$
263.9(9)	263.7(8)	–0.2	243.0(15)[5]	243.1(16)[4]	0.1	A_1, $\delta(Xe_1OXe_2)_{ip} - \nu(XeN)_{A+B}$
n.o.	n.o.		208.7(<1)[236]	209.2(<1)[237]	–0.5	B_2, $\nu(XeN)_{A-B}$
n.o.	n.o.		196.0(<1)[15]	191.9(<1)[15]	–4.1	B_1, $\delta(Xe_1OXe_2)_{oop} + (\delta(XeNC)_{A+B})_{oop}$
183.6(88)	183.6(82)	0.0	167.4(35)[4]	168.0(36)[4]	0.6	A_1, $(\delta(XeNC)_{A+B})_{ip}$
			162.0(<1)[0]	162.4(<1)[0]	0.4	A_2, $(\delta(XeNC)_{A-B})_{oop}$
164.0(5)	164.5(5)	0.5	155.9(<1)[<0.1]	156.4(<1)[<1]	0.5	B_2, $(\delta(XeNC)_{A-B})_{ip}$
107.2(44)	107.4(37)	0.2	86.8(7)[6]	86.9(7)[6]	0.1	A_1, $(\delta(XeNC)_{A+B})_{ip} - \delta(Xe_1OXe_2)_{ip}$
n.o.	n.o.		60.2(<0.1)[4]	59.2(<0.1)[4]	–1.0	B_1, $\delta(Xe_1OXe_2)_{oop} - (\delta(XeNC)_{A-B})_{oop}$
			44.6(<1)[1]	44.8(<1)[1]	0.2	B_2, $\rho_t(CH_3)_{A-B}$
			44.4(2)[0]	44.7(2)[0]	0.3	A_2, $\rho_r(Xe_1OXe_2) + (\delta(XeNC)_{A+B})_{oop}$
			24.7(6)[10]	24.7(6)[10]	0.0	A_1, $\rho_w(NCC)_{A+B}$
			16.7(<0.1)[0]	16.7(<0.1)[0]	0.0	A_2, $\rho_t(CH_3)_{A+B}$
			15.9(<0.1)[<1]	15.9(<0.1)[<1]	0.0	B_1, $\rho_t(CH_3)_{A-B}$

Table 9.3 continued …

[a] Vibrational frequencies and isotopic shifts are given in cm^{-1}; $\Delta\nu^{16/18} = \nu(^{18}O) - \nu(^{16}O)$. [b] The Raman spectra of the $[AsF_6]^-$ salts were recorded in FEP sample tubes at −140 °C using 1064-nm excitation. Values in parentheses denote relative experimental Raman intensities. Abbreviation denotes not observed (n.o.). [c] Calculated at the B3LYP/aug-cc-pVTZ(-PP) level of theory. Values in parentheses denote calculated Raman intensities ($Å^4$ amu^{-1}). Values in square brackets denote calculated infrared intensities (km mol^{-1}). [d] Bond elongations and angle openings are denoted by plus (+) signs, and bond contractions and angle compressions are denoted by minus (–) signs. Abbreviations denote stretch (ν), bend (δ), rock (ρ_r), twist (ρ_t), in-plane (ip), out-of-plane (oop). The two CH_3CN ligands in the calculated molecule are distinguished as A (containing atoms N_1,C_1 and C_2) and B (containing atoms N_2,C_3 and C_4), and the subscripts, A+B and A–B, denote in-phase and out-of-phase modes, respectively. The atom labels correspond to those given in Figure 9.3. [e] Frequencies associated with the $[AsF_6]^-$ anion were observed at 710(5) [$\nu_3(T_{1u})$], 681(100) [$\nu_1(A_{1g})$], 575(14) [$\nu_2(E_g)$], and 371(41)/380(69) [$\nu_5(T_{2g})$] cm^{-1}. A band arising from XeF_2 was also observed at 498(311) cm^{-1}. Bands were also observed at 2954(50), 2319(83), 2312(35), and 1376(9) cm^{-1} which were assigned to $[CH_3CNH][F]\cdot(HF)_x$ (see ref. 7). [f] Frequencies associated with the $[AsF_6]^-$ anion were observed at 710(4) [$\nu_3(T_{1u})$], 681(91) [$\nu_1(A_{1g})$], 575sh [$\nu_2(E_g)$], and 371(44)/379(72) [$\nu_5(T_{2g})$] cm^{-1}. A band arising from XeF_2 was also observed at 498(285) cm^{-1}. Bands arising from unreacted $[FXeOXe{-}{-}{-}FXeF]^+$ were also observed at 553(3), 539(4) and 479(5) cm^{-1}. A band at 2302(4) cm^{-1} was observed and was assigned to a combination mode (1355 + 940 cm^{-1}). Bands observed at 2954(28), 2319(54), and 2313(21) cm^{-1} are assigned to $[CH_3CNH][F]\cdot(HF)_x$ (see ref. 7). [g] Overlaps with a $[CH_3CNH][F]\cdot(HF)_x$ band (see ref. 7).

agreement but are much smaller in magnitude than those of the asymmetric stretching mode. The $^{16/18}$O isotope shift of the in-phase symmetric stretching mode (ν_2, A_g) of $[XeOXeOXe]^{2+}$ (exptl, –17.8 cm^{-1}; calcd, –18.9 cm^{-1}) is comparable to that of the adducted $[XeOXe]^{2+}$ cation. However, the symmetric stretching frequency of $[CH_3CN{-}{-}{-}XeOXe{-}{-}{-}NCCH_3]^{2+}$ is considerably higher than the experimental value of $[XeOXeOXe]^{2+}$ (358.7 [340.9] cm^{-1}). The calculated gas-phase frequency of $[XeOXe]^{2+}$ (424.6 [404.1] cm^{-1}) is only slightly shifted to lower frequency relative to that of the CH_3CN adduct-cation, suggesting that coupling with CH_3CN has a relatively small effect on the observed frequency. The band at 263.9 [263.7] cm^{-1} is assigned to the $\delta(Xe_1OXe_2)_{ip}$ bending mode which is strongly coupled with the in-phase xenon-nitrogen stretching mode, $\nu(XeN)_{A+B}$. The calculated frequency (243.0 [243.1] cm^{-1}) is in good agreement with the experimental value and also does not exhibit an $^{16/18}$O isotope shift. The corresponding bending mode of $[XeOXeOXe]^{2+}$ also did not exhibit an isotope shift.[5] The $\delta(Xe_1OXe_2)_{ip}$ bend of $[CH_3CN{-}{-}{-}XeOXe{-}{-}{-}NCCH_3]^{2+}$ occurs at a much higher frequency than that of $[XeOXeOXe]^{2+}$ (92.8 [90.3] cm^{-1}), highlighting the effect of strong coupling with the Xe–N stretching modes. This interpretation is supported by the calculated gas-phase $\delta(Xe_1OXe_2)_{ip}$ bending frequencies of $[XeOXe]^{2+}$ (123.9 [124.6] cm^{-1}), which occur at significantly lower frequencies than its CH_3CN adduct.

9.2.4. Computational Results

The fully optimized gas-phase geometries and vibrational frequencies including ^{18}O-isotopic shifts and intensities of $[H_3CCN{-}{-}{-}XeOXe{-}{-}{-}NCCH_3]^{2+}$, $[XeOXe]^{2+}$ and

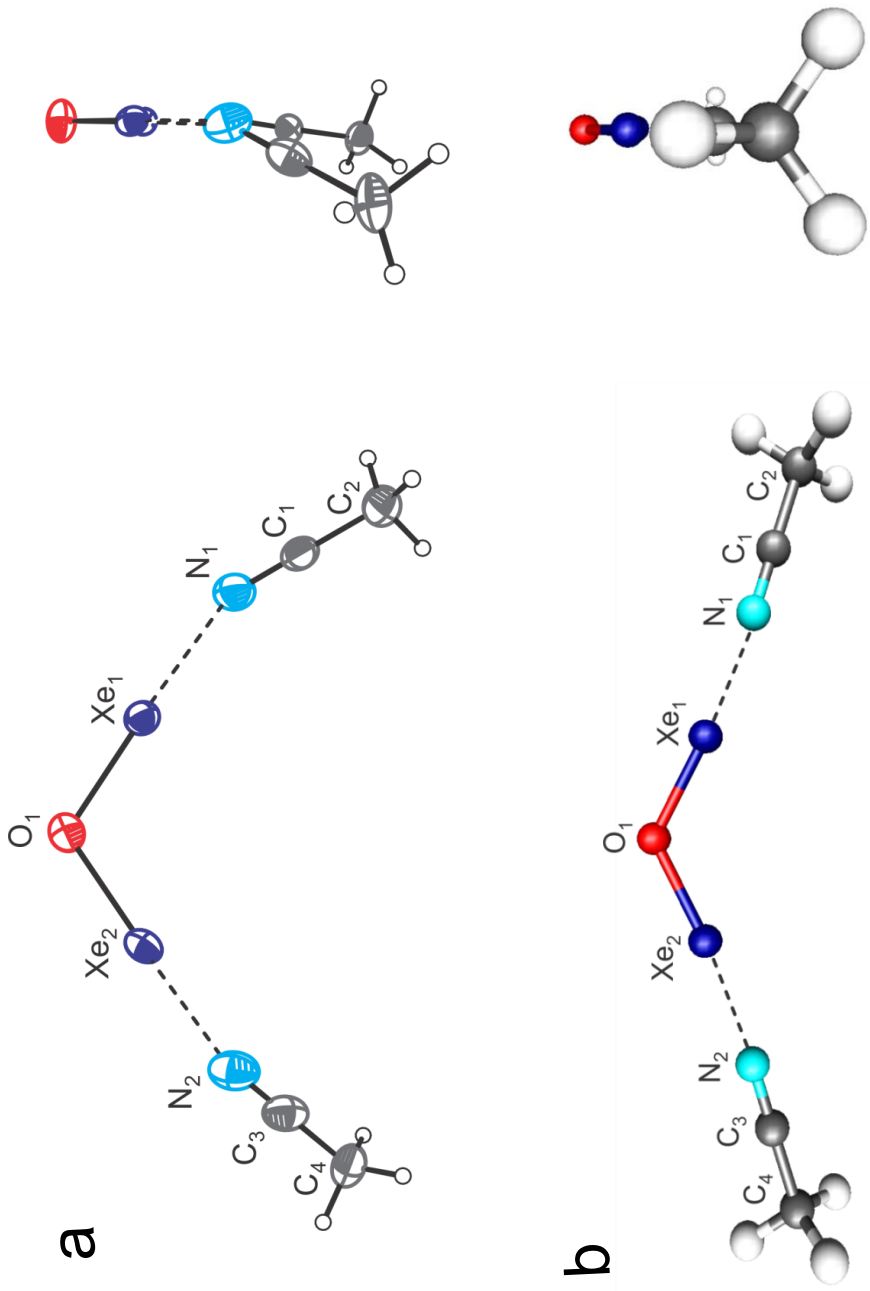

Figure 9.3. (**a**) The crystal structure of the $[H_3CCN{-}{-}XeOXe{-}{-}NCCH_3]^{2+}$ cation in its $[AsF_6]^-$ salt shown lying within and perpendicular to the N_2, Xe_2, O_1, Xe_1, N_1-plane. Thermal ellipsoids are shown at the 50% probability level. (**b**) The calculated gas-phase structure of $[H_3CCN{-}{-}XeOXe{-}{-}NCCH_3]^{2+}$ (C_{2v}, B3LYP/aug-cc-pVTZ(-PP)) is displayed with the same relative orientations as in (**a**).

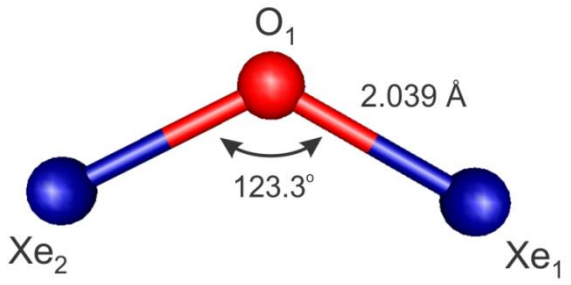

Figure 9.4. Calculated gas-phase structure of the $[XeOXe]^{2+}$ cation (C_{2v}, B3LYP/aug-cc-pVTZ(-PP)).

Table 9.4. Calculated[a] Vibrational Frequencies, $^{16/18}O$ Isotopic Shifts, and Assignments for the Gas-Phase $[XeOXe]^{2+}$ Cation (C_{2v})

^{16}O[b]	^{18}O[b]	$\Delta\nu^{16/18}$	assgnts[c]
505.4(4)[22]	479.0(3)[19]	–26.4	$\nu(Xe_1O) - \nu(Xe_2O)$
424.6(8)[<1]	404.1(7)[<1]	–20.5	$\nu(Xe_1O) + \nu(Xe_2O)$
123.9(11)[<1]	124.6(11)[<1]	–0.7	$\delta(Xe_1OXe_2)_{ip}$

[a] Calculated at the B3LYP/aug-cc-pVTZ(-PP) level of theory. [b] Vibrational frequencies and isotopic shifts, $\Delta\nu^{16/18} = \nu(^{18}O) - \nu(^{16}O)$, are given in cm^{-1}. Values in parentheses denote calculated Raman intensities (Å amu^{-1}) and values in square brackets denote calculated infrared intensities (km mol^{-1}). [c] Bond elongations and angle openings are denoted by plus (+) signs, and bond contractions and angle compressions are denoted by minus (–) signs. Abbreviations denote stretch (ν), bend (δ), and in-plane (ip). The atom labeling scheme is given in Figure 9.4.

CH_3CN were calculated using density functional theory (B3LYP). Three combinations of basis sets were evaluated for $[H_3CCN{-}{-}{-}XeOXe{-}{-}{-}NCCH_3]^{2+}$: Def2-SVPD (H, C, N, O)/aug-cc-pVDZ(-PP) (Xe), Def2-TSVPD (H, C, N, O)/aug-cc-pVDZ(-PP) (Xe), and aug-cc-pVTZ (H, C, N, O)/aug-cc-pVTZ-PP (Xe) (see Tables S9.2 and S9.3). All combinations provided comparable results. The aug-cc-pVTZ(-PP) basis sets were used for further analyses and discussions.

9.2.4.1. Natural Bond Orbital (NBO) Analyses

The NBO analysis[15] (Table S9.4) shows that the O and Xe atom charges of $[CH_3CN{-}{-}{-}XeOXe{-}{-}{-}NCCH_3]^{2+}$ (O, –0.865; Xe, 1.190) and $[XeOXe]^{2+}$ (O, –0.575; Xe, 1.288) are considerably less than the formal charges expected for a purely ionic compound (O, −2; Xe, +2) and are consistent with semi-ionic bonding. The greater charge difference between Xe and O in $[CH_3CN{-}{-}{-}XeOXe{-}{-}{-}NCCH_3]^{2+}$ (2.06) relative to that of $[XeOXe]^{2+}$ (1.863) also suggests slightly more ionic Xe–O bonds in the adduct-cation. Furthermore, there is significant negative charge transfer from the CH_3CN ligands onto the $[XeOXe]^{2+}$ cation, resulting in an overall +1.515 charge on the XeOXe-moiety and +0.242 charge on each CH_3CN ligand. Charge transfer results in Xe–N (0.330) and Xe–O (0.676) Wiberg bond indices that are significantly smaller than those of the gas-phase $[XeOXe]^{2+}$ cation (0.929). The NLMO analysis also shows that the nitrogen valence electron lone pair (VELP) of CH_3CN is mostly localized (86.1%) in an sp-hybridized orbital (s, 50.3%; p, 49.6%) with 12.9% delocalized into the σ^*_{Xe-O} LUMO which is primarily p in character (Xe: 1.1% s, 98.4% p; O: 8.8% s, 90.6% p). The second-order perturbation analysis shows each $n_N \rightarrow \sigma^*_{Xe-O}$ interaction contributes 208.1 kJ mol^{-1} of stabilization.

The gas-phase binding energies (B3LYP level) were also calculated for the Xe–N interactions. Single coordination of a CH_3CN ligand (eq. 9.3) to $[XeOXe]^{2+}$ gave a larger energy change than coordination of a second CH_3CN ligand (eq. 9.4).

$$[XeOXe]^{2+} + CH_3CN \longrightarrow [CH_3CN\text{---}XeOXe]^{2+} \quad -454.0 \text{ kJ mol}^{-1} \qquad (9.3)$$

$$[CH_3CN\text{---}XeOXe]^{2+} + CH_3CN \longrightarrow [CH_3CN\text{---}XeOXe\text{---}NCCH_3]^{2+} \quad -329.6 \text{ kJ mol}^{-1} \qquad (9.4)$$

These binding energies are substantially greater than those calculated for $F_6XeNCCH_3$ (–157.1 kJ mol^{-1}) and $F_6Xe(NCCH_3)_2$ (–129.5 kJ mol^{-1}) at the MP2 level.[16] Although different levels of theory do not allow a precise comparison to be made, it is apparent that $[XeOXe]^{2+}$ is a much stronger Lewis acid toward CH_3CN than XeF_6.

9.2.4.2. Molecular Electrostatic Potential Surface (MEPS) Analyses

The exposed core region maxima of +1126 kJ mol^{-1} on the Xe atoms in the MEPS of $[XeOXe]^{2+}$ (Figure 9.5) correspond to σ-holes into which the N VELPs coordinate. The MEPS of $[XeOXe]^{2+}$ also show that the minimum electrostatic potential (EP), +849 kJ mol^{-1}, resides on the oxygen atom. These EPs are considerably more positive than the corresponding maximum and minimum of $[XeOXeOXe]^{2+}$ (+895 and +635 kJ mol^{-1}).[5] The MEPs also show EP maxima between the Xe atoms of $[XeOXe]^{2+}$ (+1116 kJ mol^{-1})

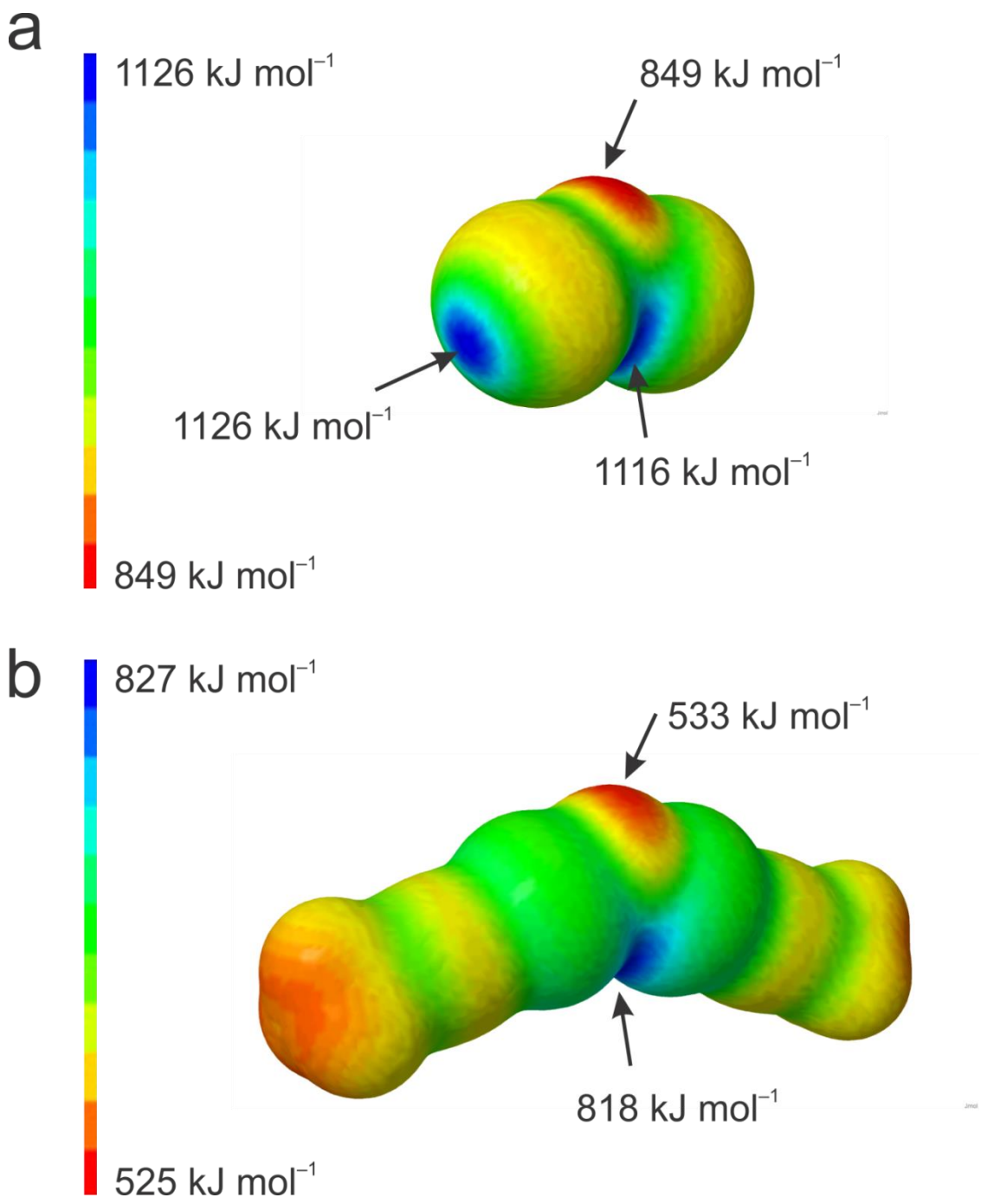

Figure 9.5. Calculated molecular electrostatic potential surfaces (MEPS) are shown at the 0.001 e bohr^{-3} isosurface for (a) $[XeOXe]^{2+}$ (C_{2v}) and (b) $[H_3CCN{-}{-}{-}XeOXe{-}{-}{-}NCCH_3]^{2+}$ (C_{2v}); calculated from the gas-phase geometries that have been optimized at the B3LYP/aug-cc-pVTZ(-PP) level of theory.

and the adduct-cation (+818 kJ mol^{-1}) and EP minima on the O atoms (+849 and +533 kJ mol^{-1}, respectively). The O atom and inter-Xe atom EPs both decrease by ca. +300 kJ mol^{-1} upon adduct formation, indicative of significant negative charge transfer onto the cation.

9.2.4.3. Electron Localization Function (ELF) Analyses

ELF analyses were carried out for $[H_3CCN{---}XeOXe{---}NCCH_3]^{2+}$ (C_{2v}), $[XeOXe]^{2+}$ (C_{2v}), and CH_3CN (C_{3v}) at the B3LYP/aug-cc-pVTZ(-PP) level of theory to visualize and compare the behavior of the Xe VELPs and bonding in these species. In the ensuing discussion, the following abbreviations denote atomic basin populations (N(A)), electron localization function (η(r)), core basin (C(A)), monosynaptic valence basin (V(A)), disynaptic valence basin (V(A, B)), and closed isosurface (η(r) = f, where f is defined as the isosurface contour). The ELF isosurface plots are shown for each species in Figures 9.6–9.8 (see Table 9.5 and Figure 9.9 for ELF parameters).

The ELF basin populations of the Xe_1 and Xe_2 cores are nearly identical for $[H_3CCN{---}XeOXe{---}NCCH_3]^{2+}$ (45.71) and $[XeOXe]^{2+}$ (45.72), and are close to the ideal core population of the Xe atom, [Kr] $4d^{10}$ = 46 e. The ELF valence population analyses show slightly higher electron densities for the valence shells of Xe (6.92) and O (7.00) in the adduct relative to those of the gas-phase $[XeOXe]^{2+}$ cation (Xe, 6.84/6.85; O, 6.76). This is in accordance with the NBO analysis in which some negative charge is delocalized from the CH_3CN ligands onto the [XeOXe]-moiety. The valence electron populations of both Xe and O are intermediate with respect to the valence octet expected for pure covalent (8 and 6, respectively) and ionic (6 and 8, respectively) bonds,

consistent with the semi-ionic nature of the Xe–O bonds. The localization domain reduction tree diagrams[17,18] (Figure 9.9) provide the hierarchies of the ELF basins and the corresponding basin separation values (f_{sep}) for $[H_3CCN{-}{-}{-}XeOXe{-}{-}{-}NCCH_3]^{2+}$ (C_{2v}), $[XeOXe]^{2+}$ (C_{2v}), and CH_3CN (C_{3v}). As previously observed,[19] the CH_3CN bonds are shown as disynaptic basins having the largest f_{sep}-values in both the adduct and isolated CH_3CN molecule, in accordance with the strong covalent bonding of the CH_3CN ligand. The greatest differences occur between the separation values of $V(N_{1,2},C_{1,3})$ which are slightly higher in the adduct (f_{sep} = 0.79) than in isolated CH_3CN (f_{sep} = 0.74), reflecting slight weakening of the N–C triple bond upon adduct formation and are in accordance with their smaller bond orders (2.678 versus 2.901, respectively). The $V(Xe_{1,2})$ and $V(O_1)$ valence basins separate at much lower values than the strong covalent bonds of CH_3CN, which is consistent with the semi-ionic nature of the Xe–O bonds. In $[H_3CCN{-}{-}{-}XeOXe{-}{-}{-}NCCH_3]^{2+}$, $V(Xe_{1,2},O_1)$ separates at lower values (f_{sep} = 0.44) than those of $[XeOXe]^{2+}$ (f_{sep} = 0.49) and is consistent with more ionic bonding character in the former, as shown by the NBO analysis.

The Xe valence basins have toroidal-shapes, which result from the combination of the three nonbonding VELP domains of Xe. The Xe core basins are exposed at the centers of these tori. Toroidal valence basins have been calculated for other Xe(II) compounds such as XeF_2,[20,21] $[XeF_3]^-$,[21] $[XeOTeF_5]^+{\cdot}SO_2ClF$,[22] the NgF_2 (Ng = Kr or Xe) ligands in $[BrOF_2][AsF_6]{\cdot}2NgF_2$,[20,23] and most notably for $[XeOXeOXe][\mu\text{-}F(ReO_2F_3)_2]_2$ and the $[XeOXeOXe]^{2+}$ cation.[5] In the latter cases, the Xe(II) valence tori are noticeably contracted at the extremities of the terminal Xe VELP basins, giving somewhat conical-

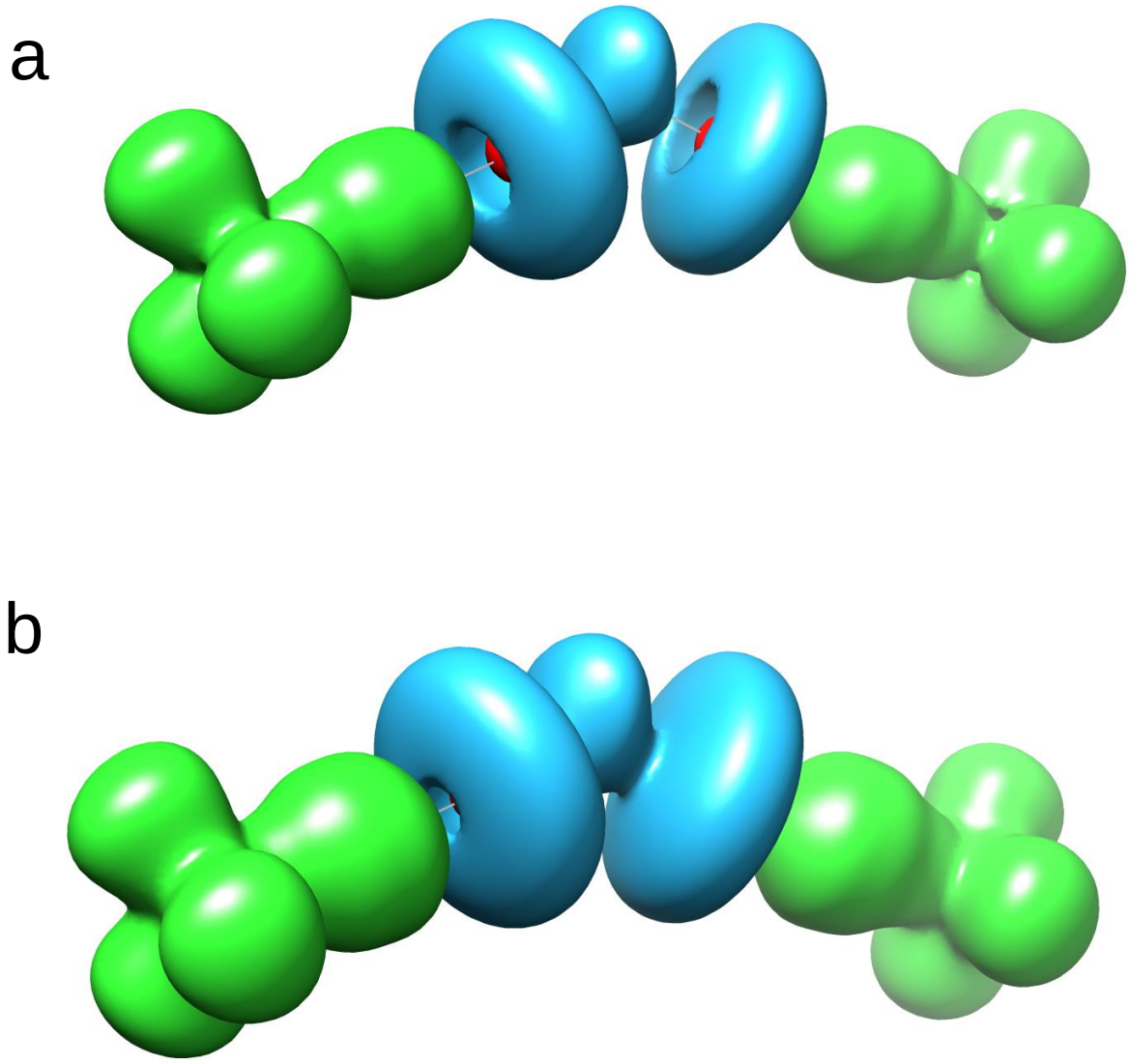

Figure 9.6. ELF isosurface plots of $[H_3CCN\text{---}XeOXe\text{---}NCCH_3]^{2+}$ (C_{2v}) at (a) $\eta(r)$ = 0.54 and (b) $\eta(r)$ = 0.37 (B3LYP/aug-cc-pVTZ(-PP)). Color code: red = xenon core basin, blue = monosynaptic basins (oxygen and Xe VELP), and green = disynaptic basins.

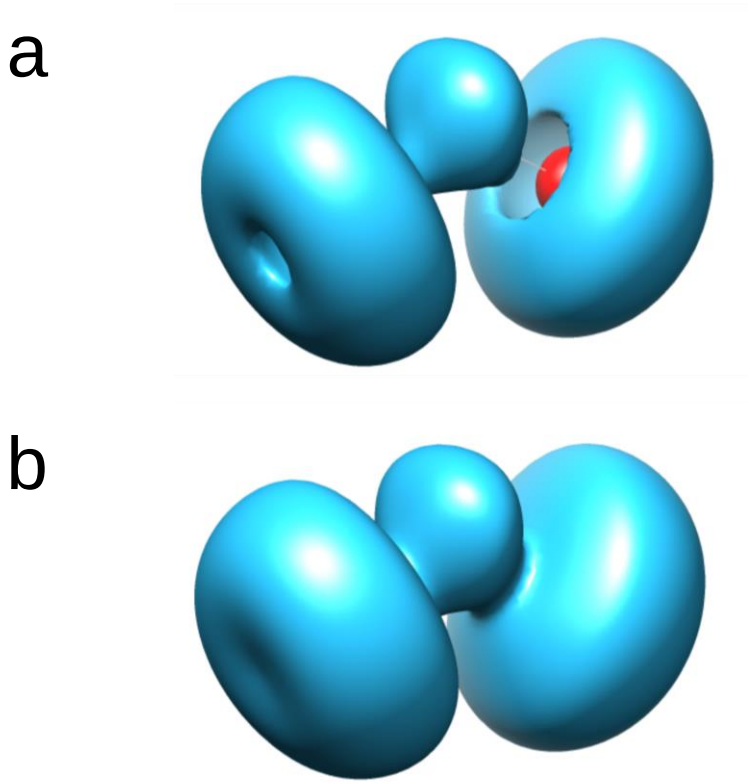

Figure 9.7. ELF isosurface plots of $[XeOXe]^{2+}$ (C_{2v}) at (a) $\eta(r) = 0.54$ and (b) $\eta(r) = 0.37$ (B3LYP/aug-cc-pVTZ(-PP)). Color code: red = xenon core basin, blue = monosynaptic basins (oxygen and Xe VELP).

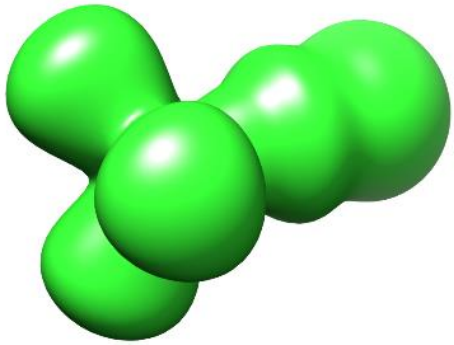

Figure 9.8. ELF isosurface plot of CH_3CN (C_{3v}) at $\eta(r) = 0.54$ (B3LYP/aug-cc-pVTZ(-PP)) Color code: green = disynaptic basins.

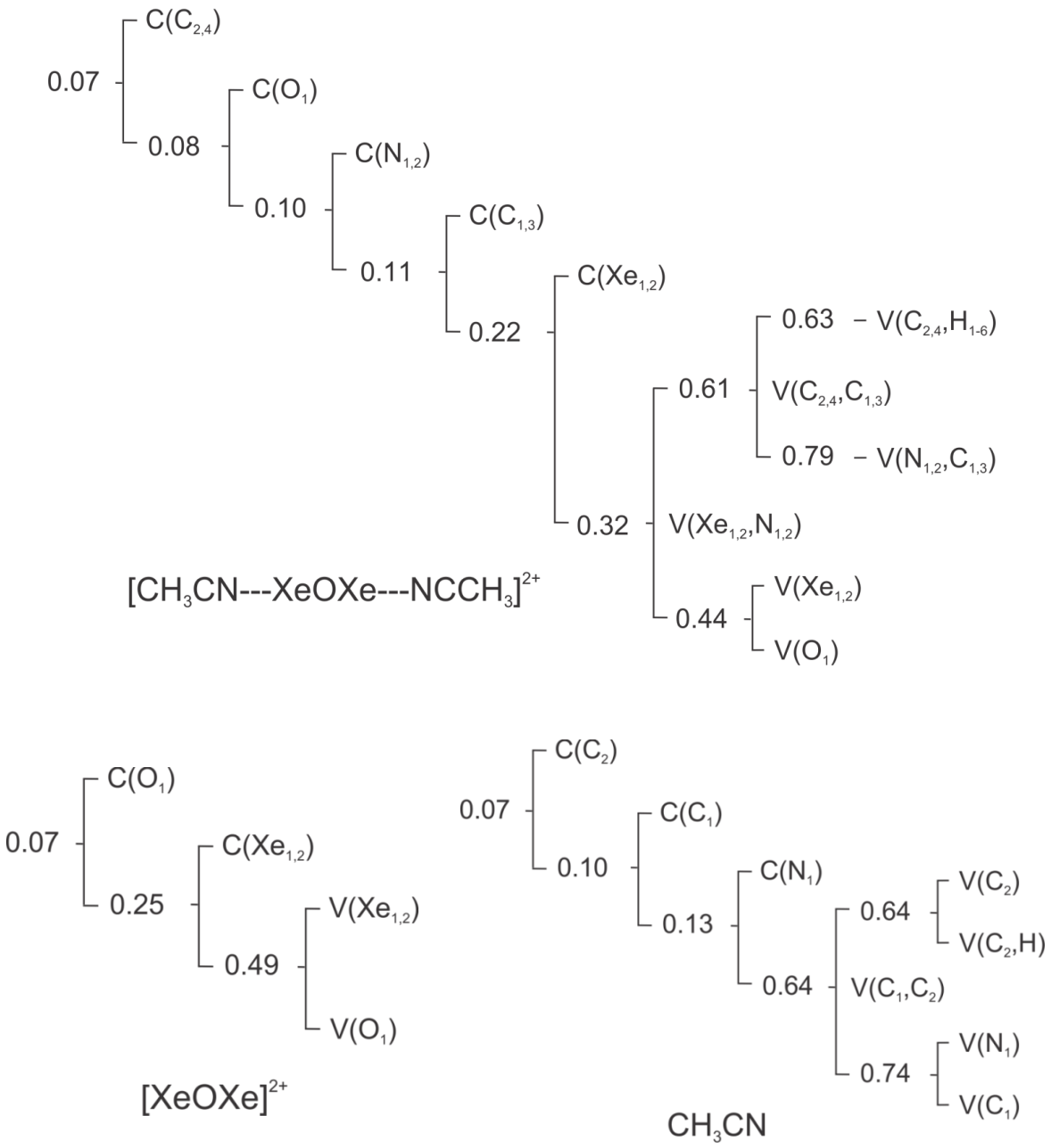

Figure 9.9. Reduction of the localization diagrams for $[H_3CCN\text{---}XeOXe\text{---}NCCH_3]^{2+}$ (C_{2v}), $[XeOXe]^{2+}$ (C_{2v}), and CH_3CN (C_{3v}) showing the ordering of localization nodes and the boundary isosurface values, $\eta(r)$, at which the reducible domains separate. The atom numbering scheme corresponds to that used in Figures 9.3 and 9.4.

shaped tori and narrowed toroidal σ-holes. In the case of $[H_3CCN{---}XeOXe{---}NCCH_3]^{2+}$, the N VELP interacts with the xenon cores by means of electrostatic interactions at the σ-holes. A very similar situation is found in $[XeOXeOXe]^{2+}$ except these electrostatic interactions occur through fluorine bridging with the counter anion, $[\mu\text{-}F(ReO_2F_3)_2]$. The σ-hole bonding description for $[H_3CCN{---}XeOXe{---}NCCH_3]^{2+}$ is in accordance with the charge transfer description of the N VELP to the $\sigma^*_{Xe–O}$ LUMO as deduced from the NBO analysis. As recently noted by Politzer *et al.*[24] *"*… there is no real physical distinction between charge transfer and polarization…" and "the difference is more semantics and definition than reality. Overlapping an occupied orbital of the negative site with a σ* antibonding orbital involving the atom with the σ-hole is simply a mathematical technique for describing the physical phenomenon, the polarization of the negative site and of the atom with the σ-hole." The relative strength of the σ-hole interaction is also reflected in the ELF reduction of localization diagram (Figure 9.9) which shows that the adduct separates (f_{sep} = 0.32) into $[XeOXe]^{2+}$ and two CH_3CN molecules at a significantly greater separation value than the Xe core basins (f_{sep} = 0.22), approaching those of the semi-ionic Xe–O bonds (f_{sep} = 0.44). This is consistent with a relatively strong Xe–N bonding interaction. In contrast, the Xe(VI) adducts, $F_6XeNCCH_3$ and $F_6Xe(NCCH_3)_2$, separate into CH_3CN and XeF_6 *f*-localization domains significantly before the separation of the Xe core basin which is indicative of considerably weaker Xe–N bonding interactions.[19]

9.2.4.4. Quantum Theory of Atoms in Molecules (QTAIM) Analyses

For two atoms to be bonded to one another, it is necessary that they be linked by a bond path which indicates that some electronic charge is accumulated between the two nuclei. The presence of a bond path implies the existence of a bond critical point along it, at which the charge density (ρ) is at its minimum value but is a maximum with respect to lines perpendicular to its bond path. Several AIM properties (Table 9.5) evaluated at the bond critical points (denoted by subscript b in the ensuing discussion) can be used to assess the nature of a bond. For example, significantly negative values for the Laplacian of electron density ($\nabla^2\rho_b$) and a density of all electrons (ρ_b) greater than 0.2 au are, associated with covalent bonding. Significantly negative values for the total energy density of Cremer and Kraka (H_b) are also consistent with strong covalent bonds. The energy (H_b) is defined as the sum of G_b and V_b, in which G_b is the Lagrangian kinetic energy and V_b is the potential energy density. In covalent bonds, G_b is dominated by V_b which gives a negative value for H_b. The aforementioned trends are clearly observed for the covalent C–N, C–C, and C–H bonds of $[H_3CCN\text{---}XeOXe\text{---}NCCH_3]^{2+}$ and free CH_3CN (Table 9.5) and overall follow that observed in $F_6XeNCCH_3$ and $F_6Xe(NCCH_3)_2$.[19] Upon adduct formation, the largest bond property changes occur for the C–N bond, which displays significant decreases in ρ_b and $\nabla^2\rho_b$, reflecting weakening of the N–C triple bond upon adduct formation (see ELF and NBO Analyses). When dealing with semi-ionic bonds, the signs or the small absolute values of the above properties can be ambiguous, and it is necessary to look at the combined properties to characterize the nature of the bond. In the present case, the delocalization indices (δ) were also

Table 9.5. QTAIM Density of all Electrons (ρ_b), Laplacian of Electron Density ($\nabla^2\rho_b$), Energy Density (H_b), QTAIM Delocalization Indices (δ), QTAIM Atomic Populations ($\bar{N}$), and ELF Basin Populations ($\bar{N}$[A]) in $[H_3CCN{---}XeOXe{---}NCCH_3]^{2+}$, $[XeOXe]^{2+}$ and CH_3CN [a]

Bond[b]	ρ_b[c]	$\nabla^2\rho_b$[d]	H_b[e]	δ	$\bar{N}$		$\bar{N}$[A]	
				$[H_3CCN{---}XeOXe{---}NCCH_3]^{2+}$ (C_{2v})				
$Xe_{1,2}$–O_1	0.125	0.110	−0.065	1.02	$\bar{N}(Xe_{1,2})$	52.84	$\bar{N}$[C($Xe_{1,2}$)][f]	45.71
$Xe_{1,2}$---$N_{1,2}$	0.074	0.124	−0.022	0.58	$\bar{N}(O_1)$	8.80	$\bar{N}$[V($Xe_{1,2}$)]	6.92
$N_{1,2}$–$C_{1,3}$	0.486	−0.199	−0.918	2.08	$\bar{N}(N_{1,2})$	8.30	$\bar{N}$[C(O_1)]	2.12
$C_{1,3}$–$C_{2,4}$	0.272	−0.793	−0.324	1.05	$\bar{N}(C_{1,3})$	4.98	$\bar{N}$[V(O_1)]	7.00
$C_{2,4}$–H_{1-6}	0.286	−1.121	−0.318	0.90	$\bar{N}(C_{2,4})$	5.88	$\bar{N}$[C($N_{1,2}$)]	2.11
					$\bar{N}(H_{1-6})$	0.86	$\bar{N}$[V($N_{1,2}$)]	3.04
							N [V($N_{1,2}$,$C_{1,3}$)]	4.32
							$\bar{N}$[C($C_{1,3}$)]	2.11
							$\bar{N}$[C($C_{2,4}$)]	2.09
							N [V($C_{1,3}$,$C_{2,4}$)]	2.32
							$\bar{N}$[V($C_{2,4}$,H_{1-6})]	1.94
				$[XeOXe]^{2+}$ (C_{2v})				
$Xe_{1,2}$–O_1	0.128	0.080	−0.067	1.20	$\bar{N}(Xe_{1,2})$	52.74	$\bar{N}$[C($Xe_{1,2}$)][g]	45.72
					$\bar{N}(O_1)$	8.51	$\bar{N}$[V(Xe_1)]	6.84
							$\bar{N}$[V(Xe_2)]	6.85
							$\bar{N}$[C(O_1)]	2.12
							$\bar{N}$[V(O_1)]	6.76

Table 9.5 continued …

Bond[b]	ρ_b[c]	$\nabla^2\rho_b$[d]	H_b[e]	δ	$\bar{N}$		$\bar{N}$[A]	
				CH_3CN (C_{3v})				
N_1–C_1	0.498	−0.236	−0.948	2.39	$\bar{N}(N_1)$	8.18	$\bar{N}$[C(N_1)]	2.11
C_2–C_2	0.272	−0.810	−0.288	1.05	$\bar{N}(C_1)$	5.11	$\bar{N}$[V(N_1)]	3.21
C_2–H_{1-3}	0.287	−1.115	−0.321	0.94	$\bar{N}(C_2)$	5.88	N [V(N_1,C_1)]	4.41
					$\bar{N}(H_{1-3})$	0.94	$\bar{N}$[C(C_1)]	2.10
							$\bar{N}$[C(C_2)]	2.10
							N [V(C_1,C_2)]	2.20
							$\bar{N}$[V(C_2,H_{1-3})]	1.96

[a] The geometry was optimized at the B3LYP/aug-cc-pVTZ(-PP) level of theory. [b] For the atom labeling scheme see Figures 9.3 and 9.4. [c] The au for ρ_b is e/a_0^3 (1 au = 6.748 e Å^{-3}, a_0 = Bohr radius = 0.52918 Å, e = charge on an electron). [d] The atomic unit (au) for $\nabla^2\rho_b$ is e/a_0^5 (1 au = 24.098 e Å^{-5}). [e] The au for H_b is e^2/a_0^4 (1 au = E_h/a_0^3 = 6.748 E_h/Å^3, E_h = hartree = e^2/a_0). [f] $\bar{N}$[C(Xe_1)] = $\bar{N}$[C(Xe_2)] = ½{158 – ($\bar{N}$[C(O_1)] + $\bar{N}$[C(N_1)] + $\bar{N}$[C(N_2)] + $\bar{N}$[C(C_1)] + $\bar{N}$[C(C_2)] + $\bar{N}$[C(C_3)] + $\bar{N}$[C(C_4)] + $\bar{N}$[V(Xe_1)] + $\bar{N}$[V(Xe_2)] + $\bar{N}$[V(O_1)] + $\bar{N}$[V(N_1)] + $\bar{N}$[V(N_2)] + $\bar{N}$[V(N_1,C_1)] + $\bar{N}$[V(N_2,C_3)] + (6 x $\bar{N}$[V($C_{2,4}$,H)]) + $\bar{N}$[V(C_1,C_2)] + $\bar{N}$[V(C_3,C_4)])}. [g] $\bar{N}$[C(Xe_1)] = $\bar{N}$[C(Xe_2)] = ½{114 – ($\bar{N}$[C(O_1)] + $\bar{N}$[V(O_1)] + $\bar{N}$[V(Xe_1)] + $\bar{N}$[V(Xe_2)])}.

considered. The charge density contour maps showing bond critical points are shown for $[H_3CCN{---}XeOXe{---}NCCH_3]^{2+}$ and $[XeOXe]^{2+}$ in Figure 9.10 where the bond critical points are indicated by black dots.

The Xe–O bond properties of $[H_3CCN{---}XeOXe{---}NCCH_3]^{2+}$ and $[XeOXe]^{2+}$ (Table 9.5) both possess small positive ρ_b values (0.125 and 0.128 au, respectively) and $\nabla^2\rho_b$ values (0.110 and 0.080 au, respectively), consistent with semi-ionic Xe–O bonds. The electron delocalization indices ($\delta_{Xe–O}$, 1.02 and 1.20 au, respectively) and very small negative values for the total energy densities (H_b, –0.065 and –0.067 au, respectively) lend further support to this description. Overall, the Xe–N bond properties of $[H_3CCN{---}XeOXe{---}NCCH_3]^{2+}$ are consistent with significantly less covalent character than the Xe–O bonds. The small positive ρ_b (0.074 au) and $\nabla^2\rho_b$ (0.124 au) values are in accordance with closed-shell Xe–N interactions that are predominantly electrostatic in nature (σ-hole bonds). The delocalization indices ($\delta_{Xe–N}$, 0.58 au) and total energy density (H_b, –0.022 au) also provide measures of the degree of electron sharing between these atoms and are consistent with the description provided by the NBO and ELF analyses.

The charge density contour maps of the Laplacian distribution ($\nabla^2\rho$) (Figure 9.10) and valence shells of charge concentration (VSCC) relief maps ($-\nabla^2\rho$) (Figure 9.11) are provided for $[H_3CCN{---}XeOXe{---}NCCH_3]^{2+}$ and $[XeOXe]^{2+}$. The $\nabla^2\rho$ contour maps depict positive (blue solid lines) and negative (red dashed lines) values of $\nabla^2\rho$. The most prominent features of the VSCC relief maps are the Xe regions of charge concentration. When the inner spike-like feature at the Xe nucleus is counted, the Xe atom exhibits five alternating regions of charge concentration and depletions corresponding to five quantum

shells. The Laplacian distributions show that $[H_3CCN{---}XeOXe{---}NCCH_3]^{2+}$ and $[XeOXe]^{2+}$ are surrounded by continuous valence shell concentrations. In contrast, the weaker Xe–N interactions in $F_6XeNCCH_3$ have charge density contours that are significantly constricted between the Xe and N atoms. In the case of $F_6Xe(NCCH_3)_2$, the XeF_6 and CH_3CN interactions are much weaker and the charge density contours are not conjoined.[19]

The Xe VELP densities of the $[XeOXe]^{2+}$ cation and its CH_3CN adduct, which combine to form tori around each Xe atom (see ELF Analyses), are readily discernable in the charge density contour maps. The Xe valence tori lie in planes that are perpendicular to the planes of $[XeOXe]^{2+}$ and $[H_3CCN{---}XeOXe{---}NCCH_3]^{2+}$ cations, so that the plane of the charge density contour map depicted in Figure 9.10 passes through each torus to give two concentrations of VELP charge density that lie on either side of each Xe core in the $\nabla^2\rho$ contour map. Small bonded densities appear to occur between Xe and O of $[XeOXe]^{2+}$.

In the VSCC relief maps the Xe valence concentrations (VELPS) appear as two cusps on either side of the Xe cores showing the presence of a hole in its outer sphere of charge concentration (Figure 9.11). The O VELPS are not apparent in the $\nabla^2\rho$ maps or the VSCC relief maps in the ion planes and in the perpendicular planes passing through the O atoms. There are small VSCCs between the Xe and O atoms, which correspond to bonded charge concentrations. Figure 9.11 shows that the charge densities and VSCCs for all six atoms of the CH_3CN fragment are linked to give one continuous valence shell of charge concentration. This contrasts with the localized, atom-like nature of the O and Xe atoms

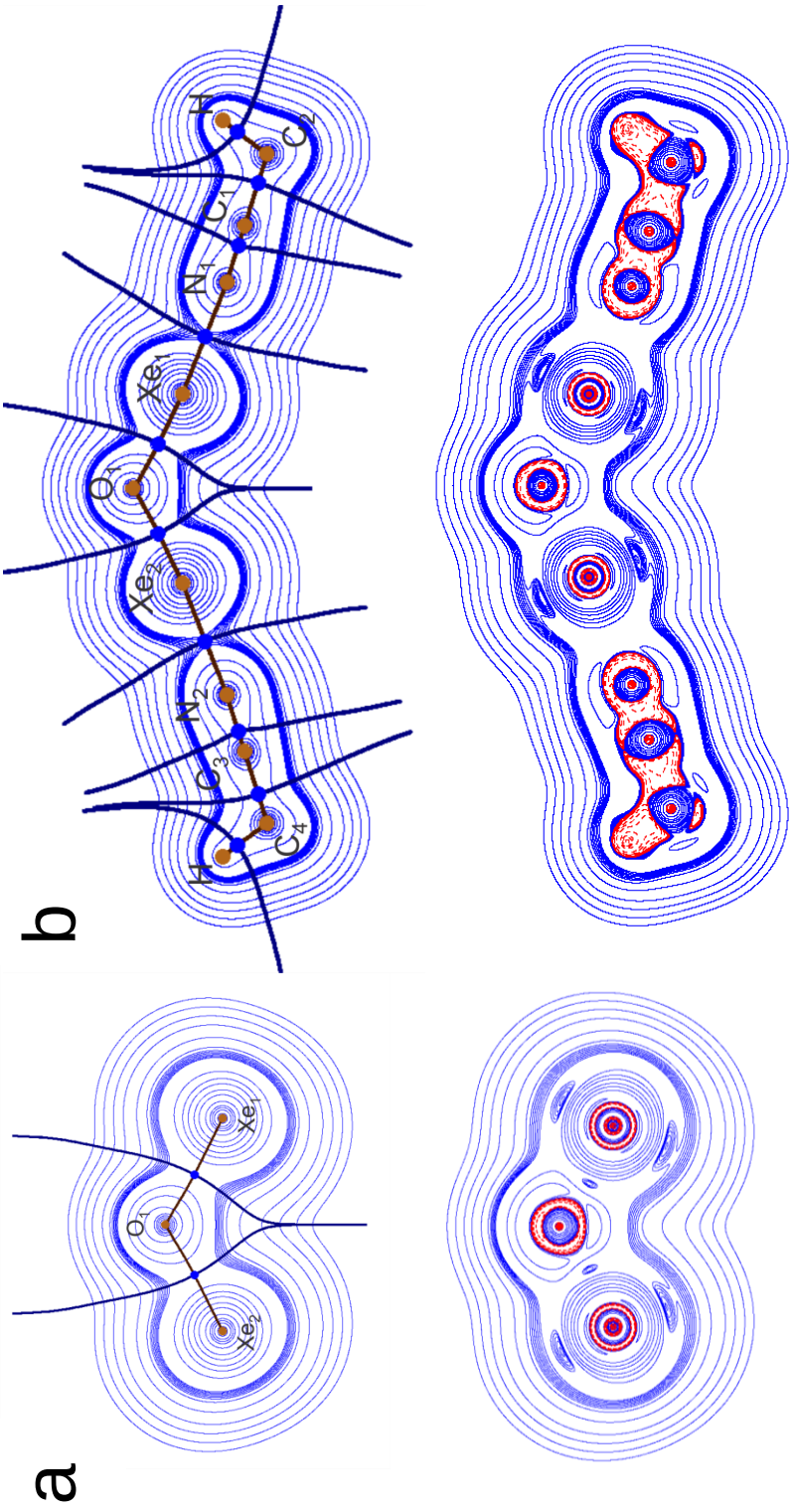

Figure 9.10. Contour maps of the charge density, showing the bond paths and the intersections of the interatomic surfaces (top) and charge-density contour maps of the Laplacian distributions (bottom) for (**a**) $[XeOXe]^{2+}$ and (**b**) $[CH_3CN{-}{-}XeOXe{-}{-}NCCH_3]^{2+}$. The nuclear positions are identical in both cases. The contour maps lie in the Xe_1–O_1–Xe_2 planes. The contour values start at ±0.001 au and increase in the order $\pm 2x10^n$, $\pm 4x10^n$, and $\pm 8x10^n$ with n starting at −3 and increasing in steps of 1 to give a maximum contour value of $8x10^6$ with several additional contour values (±0.05, ±0.055, ±0.060, ±0.065, ±0.070, and ±0.075au). Bond critical points are denoted by blue dots. Solid blue contours denote positive, and dashed red lines denote negative values of $\nabla^2\rho$.

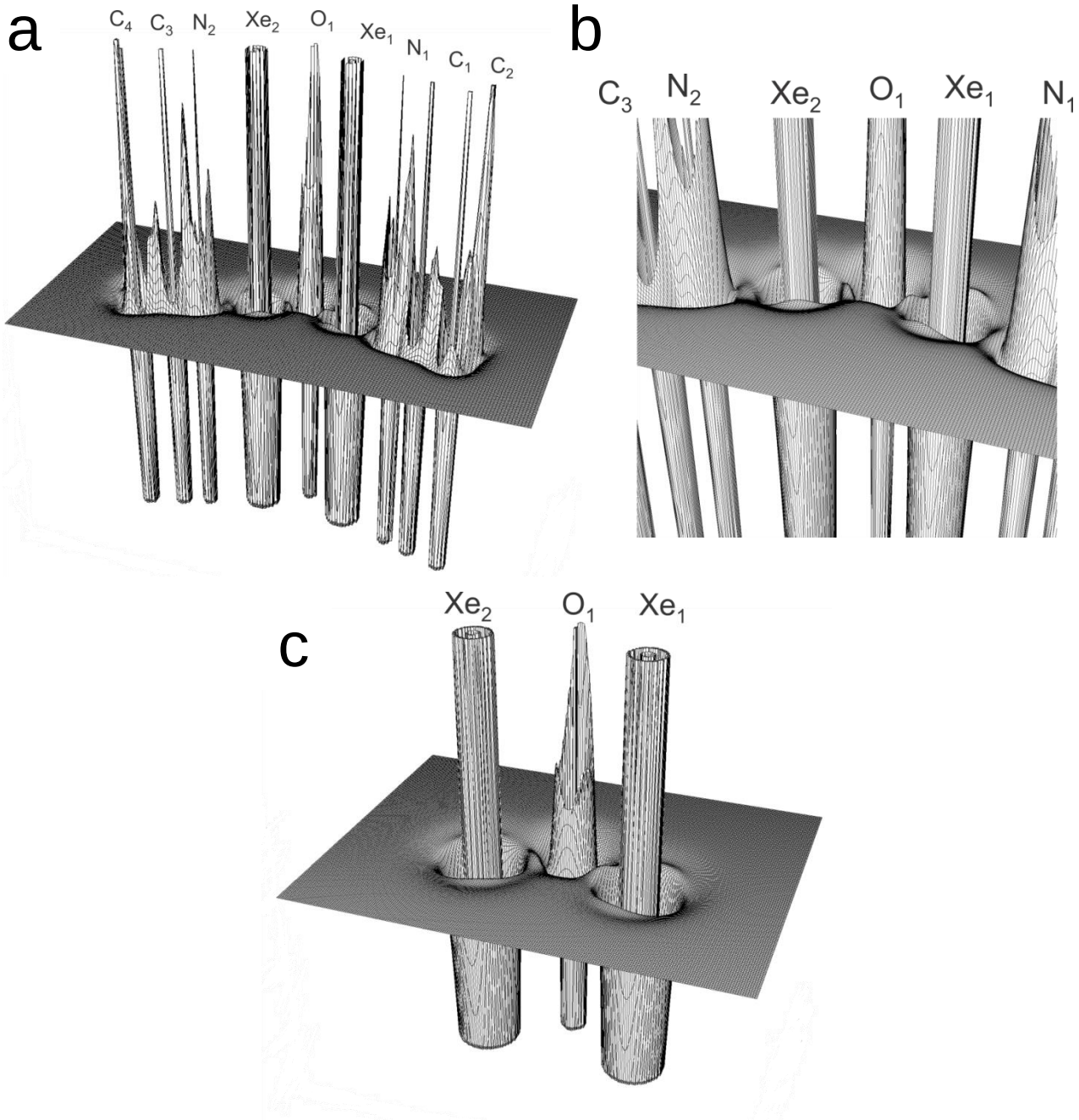

Figure 9.11. Relief maps of $-\nabla^2\rho_b$ for (**a**) $[CH_3CN\text{---}XeOXe\text{---}NCCH_3]^{2+}$, (**b**) the enlarged central regions of $[CH_3CN\text{---}XeOXe\text{---}NCCH_3]^{2+}$, and (**c**) $[XeOXe]^{2+}$. A maximum in the relief map is a maximum in charge concentration.

in the $\nabla^2\rho$ VSCC maps of $[H_3CCN{---}XeOXe{---}NCCH_3]^{2+}$ and $[XeOXe]^{2+}$. There are small cusps on the N sides of the Xe atoms. These densities may be associated with the N VELPs and with weak Xe–N bonded charge densities.

9.3. Conclusions

Acetonitrile and $[FXeOXe{---}FXeF][AsF_6]$ react at –60 ^{o}C in anhydrous HF (aHF) to form the CH_3CN adduct of the previously unknown $[XeOXe]^{2+}$ cation. The low-temperature X-ray structure of $[CH_3CN{---}XeOXe{---}NCCH_3][AsF_6]_2$ exhibits a well-isolated adduct-cation that has among the shortest Xe–N distances obtained for an sp-hybridized nitrogen base adducted to xenon. The Raman spectrum was fully assigned by comparison with the calculated vibrational frequencies and with the aid of ^{18}O-enrichment studies. Natural bond orbital (NBO), atoms in molecules (AIM), electron localization function (ELF), and molecular electrostatic potential surface (MEPS) analyses show that the Xe–O bonds are semi-ionic whereas the Xe–N bonds may be described as strong electrostatic (σ-hole) interactions.

9.4. Experimental

General experimental techniques, procedures, and equipment, as well as the preparation and purification of all starting materials are described in Chapter 2.

9.4.1. Synthesis and Crystal Growth.

In a typical synthesis, the starting material, $[FXeOXeFXeF][AsF_6]$, was prepared from $[H_3O][AsF_6]$ (0.124 g, 0.597 mmol) and XeF_2 (0.118 g, 0.611 mmol) in aHF solvent (ca. 0.5 to 0.7 mL) in a T-shaped ¼“-in. o.d. FEP reaction vessel equipped with a Kel-F

valve. Dry CH_3CN (ca. 0.2 mL) was then condensed under static vacuum at –196 ^oC onto the frozen [FXeOXeFXeF][AsF_6] and HF mixture. The reaction mixture was warmed to –78 ^oC to allow HF to melt and dissolve CH_3CN. After 2 h at –78 ^oC, the mixture was warmed to –60 ^oC for 2 h over which time slow gas evolution occurred and pale yellow crystals formed as the starting material dissolved and reacted. The reaction mixture was then cooled to –78 ^oC for 12 h and the supernatant was decanted into the side arm of the reactor and heat sealed off, leaving behind pale yellow plate-shaped crystals that were wetted with HF. The low-temperature Raman spectra (–140 ^oC) were obtained on the wetted crystalline compound.

9.4.2. Decomposition of $[CH_3CN{-}{-}{-}XeOXe{-}{-}{-}NCCH_3][AsF_6]_2$

When the typical synthesis outlined above was attempted with warming to –50 ^oC, only the decomposition product [FXe---$NCCH_3$][AsF_6] was observed by X-ray diffraction.

9.4.3. Modified Crystal Mounting

Crystals were mounted at low temperature under a stream of dry cold nitrogen using a minor modification[25] of the original procedure.[26] In the present work, the lower portion of the FEP reaction tube was severed from the remainder of the reactor leaving the sample tube end contained inside a larger diameter FEP cooling trough that had been cooled to –80 °C. At this temperature, the residual HF solvent which wetted the crystalline material remained liquid. A wet crystal was then removed from the open FEP

tube inside the cold trough using the tip of a pre-cooled glass pipet. While still inside the cold trough, the crystal was affixed to a nylon cryoloop (MiTeGen MicroMounts^{TM}) that had been dipped in an inert perfluorinated polyether. Crystal dimensions could not be accurately obtained because the crystal was encased in a frozen aHF/CH_3CN/ perfluorinated polyether mixture when mounted on the diffractometer at −173 °C.

9.4.4. Structure Solution and Refinement

The XPREP[27] program was used to confirm the crystal lattice as well as the space group. The structure was solved in the centrosymmetric space group, *C*2/c, using intrinsic phasing which located the positions of all atoms in the crystal structures except the H atoms, which were added later using the SHELXTL-Plus package.[27] Refinement of the crystal structure was straightforward. The final refinement was obtained by introducing anisotropic thermal parameters and the recommended weightings for all of the atoms. The maximum electron densities in the final difference Fourier maps were located near the heavy atoms and near one carbon atom, C3. The latter residual density may be due to the presence of very small crystallites. All calculations were performed using the SHELXTL-Plus package[27] for the structure determination, solution refinement, and molecular graphics. The space group choice was confirmed using Platon from the WinGX software package.[28] Supplementary crystallographic data can be obtained free of charge from The Cambridge Crystallographic Data Centre by quoting deposition number CCDC-1496589.

9.4.5. Computational Details.

The fully optimized gas-phase geometries and vibrational frequencies and intensities of $[H_3CCN{---}XeOXe{---}NCCH_3]^{2+}$, $[XeOXe]^{2+}$ and CH_3CN were calculated

using density functional theory (B3LYP). All calculations were performed using the Gaussian 09[29] software package. Three combinations of basis sets were evaluated for $[H_3CCN{---}XeOXe{---}NCCH_3]^{2+}$: Def2-SVPD (H, C, N, O)/aug-cc-pVDZ(-PP) (Xe), Def2-TSVPD (H, C, N, O)/aug-cc-pVDZ(-PP) (Xe), and aug-cc-pVTZ (H, C, N, O)/aug-cc-pVTZ-PP (Xe) (see Tables S9.2 and S9.3). All basis sets were obtained online from the EMSL Basis Set Exchange.[30] Fundamental vibrations were calculated for the optimized structures. NBO analyses were performed with the NBO program (version 6.0).[15] The MEPS were calculated using the cubegen utility as implemented in G09 and formatted Gaussian 09 checkpoint files as input. The G09 checkpoint files were created upon optimization of the geometries at the B3LYP/aug-cc-pVTZ(-PP) level. AIM and ELF analyses were performed as implemented in the Multiwfn package,[31] using formatted Gaussian 09 wave function files as input. The G09 wave function files were created by performing single-point calculations at the B3LYP/aug-cc-pVTZ(-PP) levels of theory on the optimized geometries. The GaussView[32] program was used to visualize the vibrational displacements that form the basis for the vibrational mode descriptions given in Tables 9.3 and 9.4. The MEPS and NBO diagrams were drawn with Jmol[33] and Chimera,[34] respectively.

9.5. Supporting Information Contents - Appendix G

Experimental Geometrical Parameters of the $[AsF_6]^-$ Anions (Table S9.1**)**; Calculated Vibrational Frequencies of $[H_3CCN{---}XeOXe{---}NCCH_3]^{2+}$ (Table S9.2**)**; Calculated Geometrical Parameters of $[H_3CCN{---}XeOXe{---}NCCH_3]^{2+}$ (Table S9.3**)**; NBO analyses for $[H_3CCN{---}XeOXe{---}NCCH_3]^{2+}$, $[XeOXe]^{2+}$, and CH_3CN (Table S9.4**)**.

9.6. References

(1) a) D. S. Brock, G. J. Schrobilgen, *J. Am. Chem. Soc.* **2011**, *133*, 6265−6269; b) D. F. Smith, *J. Am. Chem. Soc.* **1963**, *85*, 816−817; c) D. H. Templeton, A. Zalkin, J. D. Forrester, S. M. Williamson, *J. Am. Chem. Soc*. **1963**, *85*, 817; d) W. C. Hamilton, J. A. Ibers, D. R. Mackenzie, *Science* **1963**, *141*, 532−534. e) H. Selig, H. H. Claassen, C. L. Chernick, J. G. Malm, J. L. Huston, *Science* **1964**, *143*, 1322−1323; f) M. Gerken, G. J. Schrobilgen, *Inorg. Chem.* **2002**, *41*, 198−204 and references therein; g) T. Vent-Schmidt, J. T. Goettel, G. J. Schrobilgen, S. Riedel, *Chem. – Eur. J.* **2015**, *21*, 11244−11252.

(2) a) M. F. Golde, B. A. Trush, *Chem. Phys. Lett.* **1974**, *29*, 486−490; b) J. Xu, D. W. Setser, J. K. Ku, *Chem. Phys. Lett.* **1986**, *132*, 427−436; c) A. Kvaran, A. Ludviksson, W. S. Hartree, J. P. Simons, *Chem. Phys. Lett.* **1987**, *137*, 209−218; d) D. E. Johnson, *Chem. Phys. Lett.* **1995**, *238*, 71−76.

(3) B. S. Ault, L. Andrews, *Chem Phys. Lett.* **1976**, *43*, 350−352.

(4) a) T. H. Dunning, P. J. Hay, *J. Chem. Phys.* **1977**, *66*, 3767−3777; b) S. R. Langhoff, *J. Chem. Phys.* **1980**, *73*, 2379−2386; c) M. Yamanishi, K. Hirao, K. J. Yamashita, *J. Chem. Phys.* **1998**, *108*, 1514−1521.

(5) M. V. Ivanova, H. P. A. Mercier, G. J. Schrobilgen, *J. Am. Chem. Soc.* **2015**, *137*, 13398−13413.

(6) M. Gerken, M. D. Moran, H. P. A. Mercier, B.E. Pointner, G. J. Schrobilgen, B. Hoge, K. O. Christe, J. A, Boatz, *J. Am. Chem. Soc.* **2009**, *131*, 13474−13489.

(7) D. S. Brock, V. Bilir, H. P. A. Mercier, G. J. Schrobilgen, *J. Am. Chem. Soc.* **2007**, *129*, 3598–3611.

(8) K. Koppe, H. J. Frohn, H. P. A. Mercier, G. J. Schrobilgen, *Inorg. Chem.* **2008**, *47*, 3205–3217.

(9) H. J. Frohn, S. Jakobs, G. Henkel, *Angew. Chem. Int. Ed.* **1989**, *28*, 1506–1507.

(10) H. J. Frohn, T. Schroer, G. Henkel, *Z. Naturforsch.* **1995**, *50b*, 1799–1810.

(11) G. L. Smith, G. J. Schrobilgen, *Inorg. Chem.* **2009**, *48*, 7714–7728.

(12) G. L. Smith, H. P. A. Mercier, G. J. Schrobilgen, *Inorg. Chem.* **2007**, *46*, 1369–1378.

(13) A. Bondi, *J. Phys. Chem.* **1964**, *68*, 441–451.

(14) D. S. Brock, V. Bilir, H. P. A. Mercier, G. J. Schrobilgen, *J. Am. Chem. Soc.* **2007**, *129*, 3598–3611.

(15) NBO 6.0. E. D. Glendening, J. K. Badenhoop, A. E. Reed, J. E. Carpenter, J. A. Bohmann, C. M. Morales, C. R. Landis, F. Weinhold, Theoretical Chemistry Institute, University of Wisconsin, Madison, **2013**.

(16) K. Matsumoto, J. Haner, H. P. A. Mercier, G. J. Schrobilgen, *Angew. Chem. Int. Ed.* **2015**, *54*, 14169 –14173.

(17) A. Savin, B. Silvi, F. Colonna, *Can. J. Chem.* **1996**, *74*, 1088–1096.

(18) M. Calatayud, J. Andrés, A. Beltrán, B. Silvi, *Theor. Chem. Acc.* **2001**, *105*, 299–308.

(19) J. Haner, K. Matsumoto, H. P. A. Mercier, G. J. Schrobilgen, *Chem. Eur. J.* **2016**, *22*, 4833–4842.

(20) D. S. Brock, J.J. Casalis de Pury, H. P. A. Mercier, G. J. Schrobilgen, B. Silvi, *Inorg. Chem*. **2010**, *49*, 6673−6689.

(21) N. Vasdev, M. D. Moran, H. M. Tuononen, R. Chirakal, R. J. Suontamo, A. D. Bain, G. J. Schrobilgen, *Inorg. Chem*. **2010**, *49*, 8997−9004.

(22) H. P. A. Mercier, M. D. Moran, J. C. P. Sanders, G. J. Schrobilgen, *Inorg. Chem*. **2005**, *44*, 49−60.

(23) D. S. Brock, J. J. Casalis de Pury, H. P. A. Mercier, G. J. Schrobilgen, B. Silvi, *J. Am. Chem. Soc*. **2010**, *132*, 3533−3542.

(24) P. Politzer, J. S. Murray, T. Clark, *Phys. Chem. Chem. Phys.* **2013**, *15*, 11178−11189.

(25) J. T. Goettel, N. Kostiuk, M. Gerken, *Inorg. Chem*. **2016**, *55*, 7126−7134.

(26) M. Gerken, D. A. Dixon, G. J. Schrobilgen, *Inorg. Chem*. **2000**, *39*, 4244−4255.

(27) Sheldrick, G. M. SHELXTL-Plus, release 5.1; Siemens Analytical X-ray Instruments, Inc.: Madison, WI, **1998**.

(28) A. L. Spek, *J. Appl. Crystallogr.* **2003**, *36*, 7−13.

(29) Gaussian 09, revision D.01; M. J. Frisch, G. W. Trucks, H. B. Schlegel, G. E. Scuseria, M. A. Robb, J. R. Cheeseman, G. Scalmani, V. Barone, B. Mennucci, G. A. Petersson, H. Nakatsuji, M. Caricato, X. Li, H. P. Hratchian, A. F. Izmaylov, J. Bloino, G. Zheng, J. L. Sonnenberg, M. Hada, M. Ehara, K. Toyota, R. Fukuda, J. Hasegawa, M. Ishida, T. Nakajima, Y. Honda, O. Kitao, H. Nakai, T. Vreven, J. A., Jr. Montgomery, J. E. Peralta, F. Ogliaro, M. Bearpark, J. J. Heyd, E. Brothers, K. N. Kudin, V. N. Staroverov, R. Kobayashi, J. Normand, K. Raghavachari, A. Rendell, J. C. Burant, S. S. Iyengar, J. Tomasi, M. Cossi, N. Rega, N. J. Millam, M. Klene, J. E. Knox, J. B. Cross, V. Bakken, C. Adamo, J. Jaramillo, R. Gomperts, R. E. Stratmann, O. Yazyev, A. J. Austin, R. Cammi, C. Pomelli, J. W. Ochterski, R. L. Martin, K. Morokuma, V. G. Zakrzewski, G. A. Voth, P. Salvador, J. J. Dannenberg, S. Dapprich, A. D. Daniels, Ö. Farkas, J. B. Foresman, J. V. Ortiz, J. Cioslowski, D. J., Gaussian, Inc.: Wallingford, CT, **2013**.

(30) Basis sets and pseudopotentials were obtained from the Extensible Computational Chemistry Environment Basis Set Database, version 2/25/04, as developed and distributed by the Molecular Science Computing Facility, Environmental and Molecular Science Laboratory, which is part of the Pacific Northwest Laboratory, P.O. Box 999, Richland, WA 99352. https://bse.pnl.gov/bse/portal

(31) Multiwfn, version 3.3.8; T. Lu, F. Chen, *J. Comput. Chem.* **2012**, *33*, 580−592.

(32) GaussView, version 3.0; Gaussian Inc.: Pittsburgh, PA, **2003**.

(33) Jmol, an open-source Java viewer for chemical structures in 3D (http://www.jmol.org/).

(34) E. F. Pettersen, T. D. Goddard, C. C. Huang, G. S. Couch, D. M. Greenblatt, E. C. Meng, T. E. Ferrin, *J. Comput. Chem.* **2004**, *25*, 1605−1612.

CHAPTER 10

Conclusions and Directions for Future Work

10.1. Conclusions

The acceptor properties of $Hg(OTeF_5)_2$ were initially investigated using the nitrogen Lewis base NSF_3, which resulted in the coordination complexes $[Hg(OTeF_5)_2{\cdot}N{\equiv}SF_3]_\infty$, $[Hg(OTeF_5)_2{\cdot}2N{\equiv}SF_3]_2$, and $Hg_3(OTeF_5)_6{\cdot}4N{\equiv}SF_3$. The latter complex contains a unique $(HgO_\mu)_3$ ring which is capped on each side by F_5TeO-groups that oxygen bridge three mercury atoms, and provide the first examples of this bonding behaviour for a F_5ChO-group (Ch = S, Se, Te). Interestingly, room-temperature reactions of $Hg(OTeF_5)_2$ with NSF_3 underwent O/F metathesis between NSF_3 and the teflate ligand with the elimination of TeF_6. This resulted in the formation of the new imidodifluorosulfate (F_2OSN-) derivative, $Hg(OTeF_5)(NSOF_2)$, which also acted as a Lewis acid towards NSF_3 to give $[Hg(OTeF_5)(N{=}SOF_2){\cdot}N{\equiv}SF_3]_\infty$ and $[Hg_3(OTeF_5)_5(N{=}SOF_2){\cdot}2N{\equiv}SF_3]_2$.

In related work, the acceptor properties of $Hg(OTeF_5)_2$ were further investigated in its reactions with teflate anion sources, $M[OTeF_5]$ (M = $[N(CH_3)_4]^+$, $[N(CH_2CH_3)_4]^+$, Cs^+), resulting in several new anions including $[Hg(OTeF_5)_4]^{2-}$, $[Hg_2(OTeF_5)_6]^{2-}$, $[Hg_2(OTeF_5)_7]^{3-}$ and $[Hg(OTeF_5)_5]^{3-}$. The $[Hg(OTeF_5)_5]^{3-}$ anion provides an unusual square-pyramidal coordination sphere around mercury and the only presently known teflate-substituted anion with a net charge of 3–.

A synthetic route was explored for the formation of only very weakly coordinated Hg^{2+} cations using the weakly coordinating $[Sb(OTeF_5)_6]^-$ anion in the very weakly basic solvent SO_2ClF. The salt, $[Hg(SO_2ClF)_6][Sb(OTeF_5)_6]_2$, was synthesized starting from either $Hg(OTeF_5)_2$ or $HgCl_2$, and was characterized by X-ray crystallography and Raman spectroscopy. This salt provided the first example of a homoleptic SO_2ClF complex. The weak coordination of the SO_2ClF molecules was demonstrated by ligand substitution reactions using nitrile bases RCN (R = CH_3, CH_2CH_3) which resulted in the corresponding homoleptic nitrile cation complexes which were also fully structurally characterized. The binding energies of the aforementioned complex cations were calculated and corroborate the SO_2ClF molecules are most weakly coordinated to Hg^{2+}. The $[Hg(SO_2ClF)_6][Sb(OTeF_5)_6]_2$ salt is expected to provide a precursor to explore the coordination chemistry of weak, unusual, and fundamentally important ligands, and the demonstrated methodology should be extended to other metals.

Another significant focus of this Thesis is the developement of the little studied chemistry of krypton by exploring the coordination chemistry of KrF_2. Initial efforts took advantage of the established Lewis acidity and oxidative resistance of $Hg(OTeF_5)_2$, which resulted in the isolation of the isostructural coordination complexes $Hg(OTeF_5)_2 \cdot 1.5NgF_2$ (Ng = Xe, Kr). At the time of publication, the KrF_2 complex provided only the second crystallographically characterized KrF_2 complex and the first example of bridge coordination by a KrF_2 molecule. In related efforts to advance the field, complex formation between KrF_2 and $Hg(AsF_6)_2$ was investigated in aHF which resulted in the first homoleptic coordination complex of KrF_2 as the HF-solvated complex

salt, $[Hg(KrF_2)_8][AsF_6]_2 \cdot 2HF$. This compound was fully characterized by low-temperature X-ray crystallography and Raman spectroscopy, showing that the weakly fluoro-basic $[AsF_6]^-$ anions can be displaced by KrF_2. This salt provides the highest KrF_2-to-metal molar ratio complex that is currently known, and the first crystallographically characterized examples in which KrF_2 is terminally coordinated to a transition metal element. Computational investigations of the cation provide important fundamental insights into the structure and bonding of NgF_2 complexes, suggesting that both electrostatic and orbital interactions of the $8\sigma_g$ (HOMO–4) and a $4\pi_u$ (HOMO) molecular orbital of KrF_2 are involved in bonding and rationalize the observed Hg–F–Kr coordination angles from an MO perspective. Further work explored low-temperature reactions with various molar ratios of KrF_2 and the salts $Hg(PnF_6)_2$ (Pn = As, Sb) and $FHg(AsF_6)$, resulting in the crystallographic characterization of a diverse series of eight Hg(II) coordination complexes in which the number of KrF_2 ligands coordinated to mercury ranges from one to five. Rare examples of both terminal and bridging coordination were isolated, and an unprecedented NgF_2 bonding modality in which a single fluorine atom of a terminally coordinated KrF_2 molecule bridges two Hg^{2+} cations was characterized. The molecular orbital bond description and origin of this bond modality was elucidated by use of quantum-chemical calculations, corroborating the involvement of both the $8\sigma_g$ and a $4\pi_u$ molecular orbitals of KrF_2 which interact predominately with both 6p and 6s valence orbitals of the Hg^{2+} cations. These studies extended and deepened our understanding of the nature of NgF_2-metal bonding and accounts for a major portion of what is known regarding KrF_2 coordination chemistry.

The final area of study in this Thesis advances noble-gas chemistry with the synthesis and characterization of only the second, and simplest, isolable Xe(II) oxide species as its CH_3CN adduct-cation salt, $[CH_3CN{-}{-}{-}XeOXe{-}{-}{-}NCCH_3][AsF_6]_2$. In addition to its X-ray crystal structure, the Raman spectrum was fully assigned with the aid of calculated vibrational frequencies and ^{18}O-enrichment studies. Insights into the nature of the Xe–O and Xe–N bonds were also explored computationally. This work not only represents a significant extension of noble-gas chemistry but also provides an important example of σ-hole bonding and its role in stabilizing highly reactive electrophiles.

10.2. Future Directions

10.2.1. F_5TeO-group and Related Chemistry

The first triply oxygen-bridge coordinated F_5TeO-group was characterized in this Thesis with the synthesis of the structurally interesting $Hg_3(OTeF_5)_6{\cdot}4N{\equiv}SF_3$ complex. More examples of this new coordination mode should be sought out, and one potential avenue involve macrocyclic multidentate Lewis acids or so-called “anticrowns”, such as $(o\text{-}C_6F_4Hg)_3$ (Figure 10.1).[1] This planar molecule has been shown to accept electron density at multiple mercury centers from a variety of neutral Lewis bases and anions,[2] due to the strong electron-withdrawing effects of the fluorine substituents and steric accessibility of the metal centers. Reactions of $(o\text{-}C_6F_4Hg)_3$ with $M[OTeF_5]$ (M = $[N(CH_3)_4]^+$, $[N(CH_2CH_3)_4]^+$, Cs^+) may afford salts having the desired coordination mode, e.g., $[M]_2[(o\text{-}C_6F_4Hg)_3(\mu_3\text{-}OTeF_5)_2]$.

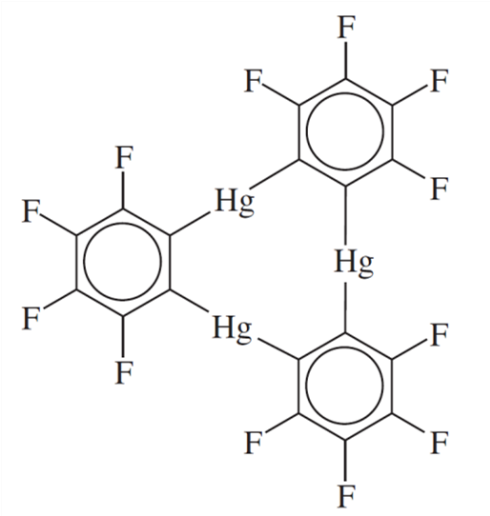

Figure 10.1. Drawing of the macrocyclic anticrown (*o*-$C_6F_4Hg)_3$

Given the limited number of F_5SeO-derivatives, it would be of interest to advance its chemistry and compare it with that of the F_5TeO-group. Furthermore, every group in the periodic table has F_5TeO–derivatives, except those of the alkaline earth and rare-earth metals. Teflate-substituted derivatives of these elements are also expected to be sterically unsaturated Lewis acids, and could provide interesting coordination chemistry. Analogous routes used to synthesize metal F_5TeO–derivatives, e.g., according to eq 10.1–10.2 should be evaluated for the group 2 and group 3 elements.

$$M^{n+}X_n + n\,HOChF_5 \longrightarrow M^{n+}(OChF_5)_n + n\,HX \quad (X = F \text{ or } Cl;\ n = 2 \text{ or } 3) \qquad (10.1)$$

$$M + {}^{n}/_{2}\,Xe(OChF_5)_2 \longrightarrow M(OChF_5)_n + {}^{n}/_{2}\,Xe_{(g)} \qquad (10.2)$$

Although currently unknown, the synthesis of $B(OSeF_5)_3$ would also provide a valuable

synthetic tool to transfer of the F_5SeO–group for the synthesis of new derivatives. Subsequently, the Lewis acid acceptor properties of these derivative should be further explored.

The related tetrafluorotellurates(VI) group has been isolated in pure stereospecific form as either *cis*- and *trans*-$(HO)_2TeF_4$,[3] but the chemistry of this interesting substituent has been limited to a few main-group derivatives such as $(XO)_2TeF_4$ (X = Cl, Br),[4] $[(CH_3)_3SiO]_2TeF_4$,[4] $Na_2O_2TeF_4$,[5] and preliminary evidence for the xenon(II) polymer $(XeO_2TeF_4)_\infty$.[6] The chemistry of this group should be extended to the transition metals and may provide interesting Lewis acidic derivatives.

10.2.2. Metal Cations of $[Sb(OTeF_5)_6]^-$

The synthetic approach developed in this Thesis which employed the preformed WCA, $[Sb(OTeF_5)_6]^-$, in SO_2ClF is expected to be applicable to other metal (M^{n+}) chloride salts in a range of oxidation states following the approach outlined in eq 10.3.

$$M^nCl_n + n\,[Xe(OTeF_5)][Sb(OTeF_5)_6] \xrightarrow{SO_2ClF} [M]^{n+}[Sb(OTeF_5)_6]_n + n\,ClOTeF_5 + n\,Xe \quad (10.3)$$

It would also be interesting to determine the limit of positive metal charge which could be stabilized in this fashion. Metal hexachlorides, such as $MoCl_6$, $ReCl_6$, and WCl_6, may provide sources of metals in the +6 formal oxidation state, although this seems unlikely. However, even partial oxidation of the chloride ligands would result in access to new cations, such as $[MCl_5]^+$, $[MCl_4]^{2+}$, $[MCl_3]^{3+}$, or related clusters which would be highly interesting.

The coordination chemistry of weak, unusual, and fundamentally important ligands should also be addressed by use of these very weakly coordinated $[M]^{n+}[Sb(OTeF_5)_6]_n$ species, including coordination of ligands such as CO, polychalcogenides $(Ch)_x$ (Ch = S, Se, Te), $Xe_{(g)}$, etc. Low-temperature reactions with the noble-gas fluorides NgF_2 (Ng = Kr, Xe), and even the weakest donor XeF_4 (eq 10.4), may also form a series of new, stable coordination complexes. The latter ligand is of particular interests because it is the weakest fluoride ion donor of the noble-gas fluorides and a strong oxidant. The $[Mg(XeF_2)(XeF_4)][AsF_6]_2$ complex is the only known example of XeF_4 functioning as a ligand.[7]

$$[M]^{n+}[Sb(OTeF_5)_6]_n + x\ XeF_4 \xrightarrow{SO_2ClF} [M(XeF_4)_x]^{n+}[Sb(OTeF_5)_6]_n \qquad (10.4)$$

A number of polyatomic mercury cations, e.g., Hg_2^{2+},[8,9] Hg_3^{2+},[8–10] and Hg_4^{2+},[8,11] have been synthesized as their $[PnF_6]^-$ salts by oxidation of elemental mercury. In all structurally characterized cases, the anions interact directly with the cations. With the pseudo gas-phase conditions provided by the WCA, it may be possible to stabilize unknown and larger polyatomic mercury cations according to eq 10.5.

$$[Hg][Sb(OTeF_5)_6]_2 + x\ Hg \xrightarrow{SO_2ClF} [Hg_x][Sb(OTeF_5)_6]_2 \qquad (10.5)$$

Polyatomic metal cations of other transition elements, such as the lighter group 12 elements, or even mixed metals could also be investigated by this approach. Reactions with allotropes of main-group elements, such as S_8, P_4, etc., could also lead to the formation of new and interesting polyatomic cations.

Other more convenient, room-temperature stable precursors for the introduction of the preformed $[Sb(OTeF_5)_6]^-$ anion to metal cations in weakly coordinating solvents should also be explored. Potential synthetically useful cations include $[NO]^+$ or $[NO_2]^+$, with the former having been recently been introduced to a number of other WCAs.[12] Modification of a synthetic approach recently used to generate the $[NR_4][Sb(OTeF_5)_6]$ salts,[13] as shown in eqs 10.6–10.8, may be promising routes to the synthesis of the $[NO_x][Sb(OTeF_5)_6]$ salts.

$$NO_xF + HOTeF_5 \xrightarrow{\text{Freon-114}} [NO_x][OTeF_5] + HF \quad (x = 1 \text{ or } 2) \qquad (10.6)$$

$$[NO_x][OTeF_5] + Sb(OTeF_5)_3 \xrightarrow[0^oC]{SO_2ClF} [NO_x][Sb(OTeF_5)_4] \qquad (10.7)$$

$$[NO_x][Sb(OTeF_5)_4] + Xe(OTeF_5)_2 \xrightarrow[0^oC]{SO_2ClF} [NO_x][Sb(OTeF_5)_6] + Xe \qquad (10.8)$$

The $[NO_x][Sb(OTeF_5)_6]$ salt salts could then be reacted with metal halides according to eq 10.9 with removal of volatile NO_xX at reasonably low-temperatures to provide clean routes to the metal salts.

$$M^{n+}X_n + n\,[NO_x][Sb(OTeF_5)_6] \xrightarrow{SO_2ClF} [M]^{n+}[Sb(OTeF_5)_6]_n + n\,NO_xX \qquad (10.9)$$

The salt $[NO][Sb(OTeF_5)_6]$ could also be valuable as an oxidant for the generation of other interesting cations, such as the polyphosphorus cations $[P]_x^+$, which have recently gained much attention using WCAs for their stabilization.[14]

10.2.3. XeF_2 and KrF_2 Coordination Complexes of Metal Centers

It was shown in Chapters 7 and 8 that a diverse series of KrF_2 coordination complexes are accessible using $Hg(PnF_6)_2$ salts. While this Thesis did not deal with the XeF_2 analogous, they should also be investigated and in the case of $FHg(PnF_6)$ systems are expected to provide examples of μ_3-FXeF ligands. The coordination chemistry of XeF_2 in related $M(PnF_6)_2$ salts has generally been explored throughout the periodic table, and should also be be extended to KrF_2. This is expected to provide a large number of new KrF_2 coordination complexes with metal cation centers (eq 10.10).

$$M^{n+}(PnF_6)_n + x\ NgF_2 \xrightarrow{HF} M^{n+}(XeF_2)_x(PnF_6)_n \qquad (10.10)$$

Furthermore, $M^{n+}(PnF_6)_n$ complexes of XeF_2 should also be thoroughly (re)investigated for some of these metal systems (see Table 1.3 of Chapter 1) because the present work has shown that careful control of the reaction stoichiometry and conditions can afford a diverse range of coordination complexes.

Other systems should also be investigated to provide further examples of the novel μ_3-FNgF coordination mode. The anticrown macrocycles $(o\text{-}C_6F_4Hg)_3$ (Figure 10.1),[1] mentioned above may be promising, however, it remains to be seen whether or not the perfluorinated aromatic substituents will be sufficiently oxidatively resistant towards NgF_2, in particular with KrF_2. It may be possible under low-temperature conditions to isolate μ_3-FNgF or demonstrate new ligand behaviour where one fluorine interacts with all three mercury centers, i.e., a "μ_4-FNgF" ligand.

10.2.4. Xenon(II) Oxides and Oxide Fluorides

It was shown in Chapter 9 that the adduct-cation $[CH_3CN{-}{-}{-}XeOXe{-}{-}{-}NCCH_3]^{2+}$ could be formed from $[FXeOXe{-}{-}{-}FXeF]^{+}$. Additional derivitization of the $[XeOXe]^{2+}$ cation should be explored, for example by the reaction with $CsOTeF_5$ to form the insoluble $Cs[AsF_6]$ salt and neutral teflate derivative (eq 10.11).

$$[CH_3CN{-}{-}{-}XeOXe{-}{-}{-}NCCH_3][AsF_6]_2 + 2\ CsOTeF_5 \longrightarrow O[Xe(OTeF_5)]_2 + 2\ Cs[AsF_6] + 2\ CH_3CN \qquad (10.11)$$

Previous work in our group provided preliminary Raman evidence for the displacement of XeF_2 from $[FXeOXe{-}{-}{-}FXeF]^{+}$ by NSF_3.[15] The reaction of oxidatively resistant CH_3CN (m.p., –45 °C; IP, 12.194 eV[16]) in an appropriate solvent other than aHF may enable the displacement of XeF_2 and subsequent crystallization of the nitrile stabilized $[FXeOXe{-}{-}{-}NCCH_3]^{+}$ cation which was proposed as an intermediate in the formation of $[CH_3CN{-}{-}{-}XeOXe{-}{-}{-}NCCH_3]^{2+}$. Although trifluoroacetonitrile expected to be a weaker base, it has a much lower liquid range (b.p., –64°C) and much higher first adiabatic ionization potential (IP, 13.9 eV[17]), which may allow the isolation of the aforementioned adduct-cation at low-temperature using a mixture of the two solvents following an approach similar to that outlined in this Thesis (eq 10.12). Similar reactions with the other known xenon(II) oxide

$$[FXeOXe{-}{-}{-}FXeF][AsF_6] + NCCH_3 \xrightarrow[-65\ ^oC]{NCCF_3} [FXeOXe{-}{-}{-}NCCH_3]^{+} + XeF_2 \qquad (10.12)$$

salt, $[XeOXeOXe][\mu\text{-}F\text{-}(ReO_2F_3)_2]_2$,[18] may also provide a route to the base stabilized $[XeOXeOXe]^{2+}$ cation.

Reactions of $[FXeOXe---FXeF]^+$ with AsF_5 were attempted to form $[FXeOXe][AsF_6]$, however, only $[XeF][AsF_6]$ or $[Xe_2F_3][AsF_6]$ were detected. A more promising route to this cation may be the reaction of $[FXeOXe---FXeF][AsF_6]$ with $[RCNH][AsF_6]$ in HF, which may afford the base-stabilized $[FXeOXe---NCR]^+$ cation (10.13) or potentially the unadducted cation according to eq 10.14.

$$[FXeOXe---FXeF][AsF_6] + [RCNH][AsF_6] \xrightarrow{HF} [FXeOXe---NCR][AsF_6] + [XeF][AsF_6] + HF \qquad (10.13)$$

$$[FXeOXe---FXeF][AsF_6] + [RCNH][AsF_6] \xrightarrow{HF} [FXeOXe][AsF_6] + [RCN---XeF][AsF_6] + HF \qquad (10.14)$$

10.3. References

(1) Ball, M. C.; Brown, D. S.; Massey, A. G.; Wickens, D. A. *J. Organomet. Chem.* **1981**, *206*, 265–277.

(2) a) Taylor, T. J.; Burress, C. N.; Gabbai, F. P. *Organometallics* **2007**, *26*, 5252–5263; b) Tikhonova, I. A. *et al. Organometallics*, **2009**, *28*, 6567–6573; c) Tugashov, K. *et al. J. Organomet. Chem.* **2013**, *747*, 167–173; d) Tugashov, K. I. *et al. Organometallics*, **2016**, *35*, 2197–2206; e) Fleischmann, M.; Jones, J. S.; Balázs, G.; Gabbai, F. P.; Scheer, M. *Dalton Trans.* **2016**, *45*, 13742–13749.

(3) Sladky, F.; Tötsch, W. *Chem. Ber.* **1982**, *115*, 1019–1027.

(4) Pötter, B.; Lentz, D.; Pritzkow, H.; Seppelt, K. *Angew. Chem. Int. Ed.* **1981**, *20*, 1036–1037.

(5) Seppelt, K. *Z. Anorg. Allg. Chem.* **1974**, *406*, 287–298.

(6) Turowsky, L.; Seppelt, K. *Inorg. Chem.* **1990**, *29*, 3226–3228.

(7) Tavčar, G.; Žemva, B. *Angew. Chem. Int. Ed.* **2009**, *48*, 1432–1434.

(8) Gillespie, R. J.; Granger, P.; Morgan, K. R.; Schrobilgen, G. J. *Inorg. Chem.* **1984**, *23*, 887–891.

(9) Cutforth, B. D.; Davies, C. G.; Gillespie, D. R. J.; Ireland, P. R.; Ummat, P. K. *Inorg. Chem.* **1973**, *12*, 1343–1347.

(10) a) Torsi, G.; Fung, K. W.; Begun, G. M.; Mamantov, G. *Inorg. Chem.* **1971**, *10*, 2285–2290; b) Ellison, R. D.; Levy, H. A.; Fung, K. W. *Inorg. Chem.* **1972**, *11*, 833–836.

(11) Cutforth, B. D.; Gillespie, D. R. J.; Ireland, P. R.; Sawyer, H. F.; Ummat, P. K. *Inorg. Chem.* **1983**, *22*, 1344–1347.

(12) a) Bernhardt, E.; Finze, M.; Willner, H. *Z. Anorg. Allg. Chem.* **2006**, *632*, 248–250; b) Decken, A.; Jenkins, H. D. B.; Nikiforov, G. B.; Passmore, J. *Dalton Trans.* **2004**, 2496–2504; c) Boli, C.; Koeschner, T.; Knapp, C. *Z. Anorg. Allg. Chem.* **2012**, *638*, 559–564. d) Köchner, T. *et al. Angew. Chem. Int. Ed.* **2010**, *49*, 8139–8143

(13) Mercier, H. P. A.; Sanders, J. C. P.; Schrobilgen, G. J. *J. Am. Chem. Soc.* **1994**, *116*, 2921–2937.

(14) Köchner, T.; Engesser, T. A.; Scherer, H.; Plattner, D. A.; Steffani, A.; Krossing, I. *Angew. Chem. Int. Ed.* **2012**, *51*, 6529–6531.

(15) Smith, G. L. Ph. D. Thesis, McMaster University, Hamilton, ON, Canada, **2010**.

(16) Rider, D. M.; Ray, G. W.; Darland, E. J.; Leroi, G. E. *J. Chem. Phys.* **1981**, *74*, 1652–1660.

(17) Bock, H.; Dammel, R.; Lentz, D. *Inorg. Chem.* **1984**, *23*, 1535–1540.

(18) Ivanova, M. V.; Mercier, H. P. A.; Schrobilgen, G. J. *J. Am. Chem. Soc.* **2015**, *137*, 13398−13413.

APPENDIX A

Chapter 3 Supporting Information

Thiazyl Trifluoride (NSF_3) Adducts and Imidodifluorosulfate (F_2OSN-) Derivatives of $Hg(OTeF_5)_2$

Adapted with permission from: DeBackere, J.R., Mercier, H.P.A., and Schrobilgen, G.J. *Inorganic Chemistry*, **2015**, *54*, 9989–1000.

LIST OF FIGURES

page

LIST OF TABLES

page

Table S3.1. Experimental Geometrical Parameters for $[Hg(OTeF_5)_2 \cdot N{\equiv}SF_3]_\infty$

Bond Lengths (Å)			
$Hg_1–O_1$	2.241(4)	$Te_1–O_1$	1.812(4)
$Hg_1–O_2$	2.227(5)	$Te_2–O_2$	1.811(5)
$Hg_1–O_{1A}$	2.502(4)		
$Hg_1–O_{2B}$	2.470(4)	Te–F	1.823(6)–1.871(5)
$Hg_1–N_1$	2.112(5)		
$Hg_1{-}{-}{-}F_4$ [b]	3.338(6)		
$Hg_1{-}{-}{-}F_{4A}$ [b]	2.996(6)		
$Hg_1{-}{-}{-}F_8$ [b]	3.060(6)	$S_1–F_{11A}$ [c]	1.489(7)
$Hg_1{-}{-}{-}F_{8B}$ [b]	3.063(20)	$S_1–F_{12A}$ [c]	1.516(8)
		$S_1–F_{13A}$ [c]	1.493(6)
$N_1–S_1$	1.398(5)		
$S_1–F_{11}$	1.489(6)	$S_1–F_{11B}$ [c]	1.490(7)
$S_1–F_{12}$	1.516(7)	$S_1–F_{12B}$ [c]	1.516(8)
$S_1–F_{13}$	1.493(5)	$S_1–F_{13B}$ [c]	1.493(6)
Bond Angles (deg)			
$O_1–Hg_1–O_2$	84.5(2)	$N_1–S_1–F_{11}$	121.5(5)
$O_1–Hg_1–O_{1A}$	76.5(2)	$N_1–S_1–F_{12}$	121.8(6)
$O_1–Hg_1–O_{2B}$	108.0(2)	$N_1–S_1–F_{13}$	119.3(6)
$O_2–Hg_1–O_{1A}$	99.6(2)		
$O_2–Hg_1–O_{2B}$	75.4(2)	$N_1–S_{1A}–F_{11A}$ [c]	123(2)
$O_{1A}–Hg_1–O_{2B}$	172.6(2)	$N_1–S_{1A}–F_{12A}$ [c]	116(2)
$N_1–Hg_1–O_1$	134.5(2)	$N_1–S_{1A}–F_{13A}$ [c]	124(2)
$N_1–Hg_1–O_2$	140.9(2)		
$N_1–Hg_1–O_{1A}$	92.1(2)	$N_1–S_{1B}–F_{11B}$ [c]	106(2)
$N_1–Hg_1–O_{2B}$	88.7(2)	$N_1–S_{1B}–F_{12B}$ [c]	126(3)
$Hg_1–O_1–Hg_{1A}$	52.8(1)	$N_1–S_{1B}–F_{13B}$ [c]	128(3)
$Hg_1–O_2–Hg_{1B}$	56.9(2)		
$Te_1–O_1–Hg_1$	127.5(2)	$F_{11}–S_1–F_{13}$	96.5(4)
$Te_1–O_1–Hg_{1A}$	79.0(2)	$F_{12}–S_1–F_{13}$	96.0(4)
$Te_2–O_2–Hg_1$	128.0(2)		
$Te_2–O_2–Hg_{1B}$	85.1(2)	$F_{11A}–S_{1A}–F_{12A}$ [c]	95.5(8)
		$F_{11A}–S_{1A}–F_{13A}$ [c]	96.5(7)
$Hg_1–N_1–S_1$	160.5(4)	$F_{12A}–S_{1A}–F_{13A}$ [c]	96.0(7)
		$F_{11B}–S_{1B}–F_{12B}$ [c]	95.4(8)
		$F_{11B}–S_{1B}–F_{13B}$ [c]	96.5(7)
		$F_{12B}–S_{1B}–F_{13B}$ [c]	96.0(7)

[a] The atom labeling scheme corresponds to that used in Figure 3.1. [b] The F_5TeO-group is twofold disordered. [c] The NSF_3 ligand is threefold disordered.

Table S3.2. Experimental Geometrical Parameters for $[Hg(OTeF_5)_2 \cdot 2N{\equiv}SF_3]_2$

Bond Lengths (Å)			
$Hg_1{-}O_1$	2.154(8)	$Te_1{-}O_1$	1.820(8)
$Hg_1{-}O_2$	2.348(7)	$Te_2{-}O_2$	1.798(7)
$Hg_1{-}O_{2A}$	2.467(8)		
$Hg_1{-}N_1$	2.164(10)	Te−F	1.820(8)–1.858(7)
$Hg_1{-}N_2$	2.377(10)		
$N_1{-}S_1$	1.388(10)	$N_2{-}S_2$	1.394(10)
$S_1{-}F_{11}$	1.544(7)	$S_2{-}F_{14}$	1.525(8)
$S_1{-}F_{12}$	1.520(7)	$S_2{-}F_{15}$	1.518(7)
$S_1{-}F_{13}$	1.498(7)	$S_2{-}F_{16}$	1.523(8)
Bond Angles (deg)			
$O_1{-}Hg_1{-}O_2$	94.0(3)	$Hg_1{-}O_2{-}Hg_{1A}$	100.8(3)
$O_1{-}Hg_1{-}O_{2A}$	86.4(3)	$Hg_1{-}N_1{-}S_1$	154.7(7)
$O_1{-}Hg_1{-}N_1$	169.3(4)	$Hg_1{-}N_2{-}S_2$	150.8(6)
$O_1{-}Hg_1{-}N_2$	94.4(3)	$Hg_1{-}O_1{-}Te_1$	121.3(4)
$O_2{-}Hg_1{-}O_{2A}$	79.2(3)	$Hg_1{-}O_2{-}Te_2$	133.4(4)
$O_2{-}Hg_1{-}N_1$	91.2(3)	$Hg_1{-}O_{2A}{-}Te_{2A}$	124.2(4)
$O_2{-}Hg_1{-}N_2$	105.9(3)		
$N_1{-}Hg_1{-}N_2$	93.3(4)		
$N_1{-}Hg_1{-}O_{2A}$	85.4(3)		
$N_2{-}Hg_1{-}O_{2A}$	174.8(3)		
$N_1{-}S_1{-}F_{11}$	120.1(5)	$N_2{-}S_2{-}F_{14}$	122.4(6)
$N_1{-}S_1{-}F_{12}$	123.1(6)	$N_2{-}S_2{-}F_{15}$	123.0(5)
$N_1{-}S_1{-}F_{13}$	119.3(6)	$N_2{-}S_2{-}F_{16}$	120.0(6)
$F_{11}{-}S_1{-}F_{12}$	96.6(4)	$F_{14}{-}S_2{-}F_{15}$	94.7(5)
$F_{11}{-}S_1{-}F_{13}$	96.1(4)	$F_{14}{-}S_2{-}F_{16}$	95.4(5)
$F_{12}{-}S_1{-}F_{13}$	95.7(4)	$F_{15}{-}S_2{-}F_{16}$	94.3(4)

[a] The atom labeling scheme corresponds to that used in Figure 3.2.

Table S3.3. Experimental Geometrical Parameters for $[Hg_3(OTeF_5)_6 \cdot 4N{\equiv}SF_3]$

Bond Lengths (Å)			
$Hg_1{-}O_1$	2.327(8)	$Te_1{-}O_1$	1.836(7)
$Hg_1{---}O_2$	2.781(11)	$Te_2{-}O_2$	1.823(8)
$Hg_1{-}O_5$	2.307(10)	$Te_3{-}O_3$	1.806(9)
$Hg_1{-}O_4$	2.301(8)	$Te_4{-}O_4$	1.818(8)
$Hg_1{-}N_1$	2.265(11)	$Te_5{-}O_5$	1.787(8)
$Hg_1{-}N_4$	2.223(10)	$Te_6{-}O_6$	1.811(10)
$Hg_2{-}O_1$	2.501(8)	Te−F	1.806(10)−1.860(10)
$Hg_2{-}O_2$	2.143(7)		
$Hg_2{-}O_3$	2.501(8)	$N_3{-}S_3$	1.398(16)
$Hg_2{-}O_5$	2.557(9)	$S_3{-}F_{37}$	1.518(8)
$Hg_2{-}O_6$	2.051(9)	$S_3{-}F_{38}$	1.517(9)
$Hg_2{---}F_9$	2.940(13)	$S_3{-}F_{39}$	1.506(8)
$Hg_3{-}O_1$	2.644(7)		
$Hg_3{---}O_2$	2.723(11)	$N_2{-}S_2$	1.371(16)
$Hg_3{-}O_3$	2.192(9)	$S_2{-}F_{34}$	1.515(9)
$Hg_3{-}O_4$	2.292(8)	$S_2{-}F_{35}$	1.525(10)
$Hg_3{-}N_2$	2.234(11)	$S_2{-}F_{36}$	1.509(9)
$Hg_3{-}N_3$	2.240(11)	$S_2{-}F_{34A}$	1.517(9)
		$S_2{-}F_{35A}$	1.518(10)
$N_1{-}S_1$	1.390(20)	$S_2{-}F_{36A}$	1.507(9)
$S_1{-}F_{31}$	1.517(9)		
$S_1{-}F_{32}$	1.519(10)	$N_4{-}S_4$	1.371(17)
$S_1{-}F_{33}$	1.508(9)	$S_4{-}F_{40}$	1.516(9)
$S_1{-}F_{31A}$	1.516(9)	$S_4{-}F_{41}$	1.536(10)
$S_1{-}F_{32A}$	1.522(10)	$S_4{-}F_{42}$	1.506(9)
$S_1{-}F_{33A}$	1.507(9)	$S_4{-}F_{40A}$	1.519(9)
		$S_4{-}F_{41A}$	1.519(10)
		$S_4{-}F_{42A}$	1.522(10)
Bond Angles (deg)			
$Hg_1{-}O_1{-}Hg_2$	96.2(4)	$Te_1{-}O_1{-}Hg_1$	122.8(5)
$Hg_1{-}O_1{-}Hg_3$	95.7(4)	$Te_1{-}O_1{-}Hg_2$	119.3(6)
$Hg_2{-}O_1{-}Hg_3$	90.0(3)	$Te_1{-}O_1{-}Hg_3$	124.9(5)
$Hg_1{-}O_2{-}Hg_2$	92.9(4)	$Te_2{-}O_2{---}Hg_1$	127.1(5)
$Hg_1{-}O_2{-}Hg_3$	84.2(3)	$Te_2{-}O_2{-}Hg_2$	119.3(5)
$Hg_2{-}O_2{-}Hg_3$	96.0(4)	$Te_2{-}O_2{---}Hg_3$	127.4(5)
$Hg_1{-}O_4{-}Hg_3$	107.0(4)	$Te_3{-}O_3{-}Hg_2$	133.1(7)
$Hg_3{-}O_3{-}Hg_2$	101.4(5)	$Te_3{-}O_3{-}Hg_3$	125.3(6)
$Hg_2{-}O_5{-}Hg_1$	95.1(4)	$Te_4{-}O_4{-}Hg_1$	126.1(6)

Table S3.3. continued…

		$Te_4–O_4–Hg_3$	126.3(6)
$N_1–Hg_1–N_4$	94.3(7)	$Te_5–O_5–Hg_1$	126.9(7)
$N_1–Hg_1–O_5$	104.1(5)	$Te_5–O_5–Hg_2$	137.9(7)
$N_1–Hg_1–O_1$	109.6(6)		
$N_1–Hg_1–O_2$	171.7(5)	$N_2–Hg_3–N_3$	108.7(6)
$N_1–Hg_1–O_4$	113.8(5)	$N_2–Hg_3–O_2$	159.8(5)
$N_4–Hg_1–O_5$	102.4(6)	$N_2–Hg_3–O_3$	112.8(5)
$N_4–Hg_1–O_1$	155.5(6)	$N_2–Hg_3–O_4$	93.9(5)
$N_4–Hg_1–O_2$	91.7(6)	$N_2–Hg_3–O_1$	98.9(5)
$N_4–Hg_1–O_4$	89.1(5)	$N_3–Hg_3–O_2$	88.8(5)
$O_5–Hg_1–O_1$	77.8(4)	$N_3–Hg_3–O_3$	104.7(5)
$O_5–Hg_1–O_2$	69.0(4)	$N_3–Hg_3–O_4$	97.5(5)
$O_5–Hg_1–O_4$	139.4(4)	$N_3–Hg_3–O_1$	150.7(4)
$O_1–Hg_1–O_2$	65.2(3)	$O_2–Hg_3–O_3$	70.6(4)
$O_1–Hg_1–O_4$	76.3(4)	$O_2–Hg_3–O_4$	73.2(4)
$O_2–Hg_1–O_4$	71.9(3)	$O_2–Hg_3–O_1$	62.4(3)
		$O_3–Hg_3–O_4$	136.6(4)
$O_6–Hg_2–O_5$	107.2(5)	$O_3–Hg_3–O_1$	72.1(4)
$O_6–Hg_2–O_3$	108.2(5)	$O_4–Hg_3–O_1$	70.4(4)
$O_6–Hg_2–O_1$	120.6(5)		
$O_6–Hg_2–O_2$	166.3(5)	$Hg_1–N_1–S_1$	151(1)
$O_5–Hg_2–O_3$	136.3(4)	$Hg_1–N_4–S_4$	176(1)
$O_5–Hg_2–O_1$	70.2(4)		
$O_5–Hg_2–O_2$	75.8(4)	$Hg_3–N_3–S_3$	166(1)
$O_3–Hg_2–O_1$	70.0(4)	$Hg_3–N_2–S_2$	161(1)
$O_3–Hg_2–O_2$	76.0(4)		
$O_1–Hg_2–O_2$	73.1(4)		
$N_1–S_1–F_{31}$	123.1(12)	$F_{31}–S_1–F_{32}$	95.9(8)
$N_1–S_1–F_{32}$	119.0(11)	$F_{31}–S_1–F_{33}$	97.5(8)
$N_1–S_1–F_{33}$	119.1(12)	$F_{32}–S_1–F_{33}$	95.3(8)
$N_1–S_1–F_{31A}$	116.3(12)	$F_{31A}–S_1–F_{32A}$	95.9(8)
$N_1–S_1–F_{32A}$	119.9(12)	$F_{31A}–S_1–F_{33A}$	97.9(8)
$N_1–S_1–F_{33A}$	125.7(12)	$F_{32A}–S_1–F_{33A}$	95.0(8)
$N_2–S_2–F_{34}$	126.4(12)	$F_{34}–S_2–F_{35}$	95.9(8)
$N_2–S_2–F_{35}$	119.6(11)	$F_{34}–S_2–F_{36}$	97.4(8)
$N_2–S_2–F_{36}$	116.4(11)	$F_{35}–S_2–F_{36}$	94.7(8)
$N_2–S_2–F_{34A}$	114.2(12)	$F_{34A}–S_2–F_{35A}$	96.3(9)
$N_2–S_2–F_{35A}$	121.9(11)	$F_{34A}–S_2–F_{36A}$	98.0(8)
$N_2–S_2–F_{36A}$	125.4(12)	$F_{35A}–S_2–F_{36A}$	95.1(8)
$N_3–S_3–F_{37}$	121.1(8)	$F_{37}–S_3–F_{38}$	96.1(6)
$N_3–S_3–F_{38}$	121.3(8)	$F_{37}–S_3–F_{39}$	96.8(6)
$N_3–S_3–F_{39}$	119.8(8)	$F_{38}–S_3–F_{39}$	95.7(6)

Table S3.3. continued…

$N_4–S_4–F_{40}$	122.6(13)	$F_{40}–S_4–F_{41}$	95.8(8)
$N_4–S_4–F_{41}$	106.7(13)	$F_{40}–S_4–F_{42}$	97.8(9)
$N_4–S_4–F_{42}$	131.3(14)	$F_{41}–S_4–F_{42}$	93.5(8)
$N_4–S_4–F_{40A}$	122.1(14)	$F_{40A}–S_4–F_{41A}$	96.3(9)
$N_4–S_4–F_{41A}$	132.4(13)	$F_{40A}–S_4–F_{42A}$	96.6(9)
$N_4–S_4–F_{42A}$	107.3(14)	$F_{41A}–S_4–F_{42A}$	93.7(9)
Dihedral Angles (deg)			
$Te_6–O_6–Hg_2–O_2–Te_2$	5.8 (8)		

[a] The atom labeling scheme corresponds to that used in Figure 3.3.

Table S3.4. Experimental Geometrical Parameters for $[Hg(OTeF_5)(N{=}SOF_2)\text{-}\cdot N{\equiv}SF_3]_\infty$

Bond Lengths (Å)			
$Hg_1{-}O_1$	2.537(2)	**F_2OSN-group**	
$Hg_1{-}O_{3A}$	2.408(2)	$N_1{-}S_1$	1.487(2)
$Hg_1{-}N_1$	2.130(2)	$S_1{-}O_4$	1.407(2)
$Hg_1{-}N_{5A}$	2.146(2)	$S_1{-}F_{16}$	1.540(2)
$Hg_1{-}N_2$	2.496(3)	$S_1{-}F_{17}$	1.533(2)
$Hg_1{---}F_7$	3.082(2)		
		$N_4{-}S_4$	1.488(3)
$Hg_2{-}O_1$	2.415(2)	$S_4{-}O_5$	1.403(3)
$Hg_2{-}N_1$	2.127(2)	$S_4{-}F_{24}$	1.529(2)
$Hg_2{-}O_2$	2.506(2)	$S_4{-}F_{25}$	1.535(2)
$Hg_2{-}N_4$	2.109(2)		
$Hg_2{---}N_3$	2.573(3)	$N_5{-}S_5$	1.484(2)
$Hg_2{---}F_{11}$	2.958(2)	$S_5{-}O_6$	1.407(2)
		$S_5{-}F_{26}$	1.525(2)
$Hg_3{-}O_3$	2.483(2)	$S_5{-}F_{27}$	1.532(2)
$Hg_3{---}F_1$	2.940(2)		
$Hg_3{-}O_2$	2.425(2)	**NSF_3 group**	
$Hg_3{-}N_5$	2.130(2)	$N_3{-}S_3$	1.407(3)
$Hg_3{-}N_4$	2.156(2)	$S_3{-}F_{21}$	1.528(2)
$Hg_3{---}N_6$	2.538(3)	$S_3{-}F_{22}$	1.526(2)
		$S_3{-}F_{23}$	1.527(2)
$Te_1{-}O_1$	1.798(2)		
$Te_2{-}O_2$	1.798(2)	$N_6{-}S_6$	1.399(3)
$Te_3{-}O_3$	1.802(2)	$S_6{-}F_{28}$	1.533(2)
		$S_6{-}F_{29}$	1.531(3)
Te–F	1.838(2)–1.864(2)	$S_6{-}F_{30}$	1.519(3)
		$N_2{-}S_2$	1.401(3)
		$S_2{-}F_{18}$	1.520(2)
		$S_2{-}F_{19}$	1.526(3)
		$S_2{-}F_{20}$	1.525(3)
Bond Angles (deg)			
$Hg_1{-}O_1{-}Hg_2$	91.8(1)	$N_1{-}Hg_2{-}O_2$	93.5(1)
$Hg_1{-}N_1{-}Hg_2$	113.4(1)	$N_1{-}Hg_2{-}N_4$	168.7(1)
$Hg_2{-}O_2{-}Hg_3$	91.6(1)	$N_1{-}Hg_2{-}O_1$	78.5(1)
$Hg_2{-}N_4{-}Hg_3$	111.9(1)	$N_1{-}Hg_2{---}N_3$	89.4(1)
$Hg_3{-}O_3{-}Hg_{1A}$	92.8(1)	$O_1{-}Hg_2{-}O_2$	100.2(1)
$Hg_3{-}N_5{-}Hg_{1A}$	111.9(1)	$O_1{-}Hg_2{---}N_3$	92.8(1)

Table S3.4. continued…

		O_1–Hg_2–N_4	109.9(1)
N_1–Hg_1–N_2	100.0(1)	O_2–Hg_2–N_4	77.8(1)
N_1–Hg_1–O_1	75.7(1)	O_2–Hg_2---N_3	167.0(1)
N_1–Hg_1–N_{5A}	166.8(1)	N_3–Hg_2–N_4	97.5(1)
N_1–Hg_1–O_{3A}	105.9(1)		
O_1–Hg_1–N_2	149.5(1)		
O_1–Hg_1–N_{5A}	91.1(1)	S_1–N_1–Hg_1	122.2(1)
O_1–Hg_1–O_{3A}	108.3(1)	S_1–N_1–Hg_2	124.4(1)
N_2–Hg_1–N_{5A}	91.7(1)	S_2–N_2–Hg_1	152.8(2)
N_2–Hg_1–O_{3A}	102.0(1)	S_3–N_3---Hg_2	141.5(2)
N_{5A}–Hg_1–O_{3A}	77.4(1)	S_4–N_4–Hg_2	126.8(1)
		S_4–N_4–Hg_3	121.3(1)
		S_5–N_5–Hg_3	124.5(1)
N_4–Hg_3–O_2	78.7(1)	S_5–N_5–Hg_{1A}	123.6(1)
N_4–Hg_3---N_6	88.1(1)	S_6–N_6---Hg_3	142.5(2)
N_4–Hg_3–N_5	168.2(1)		
N_4–Hg_3–O_3	92.7(1)	Te_1–O_1–Hg_1	129.8(1)
O_2–Hg_3---N_6	105.1(1)	Te_1–O_1–Hg_2	132.7(1)
O_2–Hg_3–N_5	105.7(1)	Te_2–O_2–Hg_2	130.9(1)
O_2–Hg_3–O_3	96.6(1)	Te_2–O_2–Hg_3	133.4(1)
N_6---Hg_3–N_5	101.1(1)	Te_3–O_3–Hg_3	131.8(1)
N_6---Hg_3–O_3	158.0(1)	Te_3–O_3–Hg_{1A}	133.9(1)
N_5–Hg_3–O_3	76.1(1)		

F_2OSN-group		**NSF_3 group**	
N_1–S_1–O_4	122.8(1)	N_2–S_2–F_{18}	120.9(2)
N_1–S_1–F_{16}	109.2(1)	N_2–S_2–F_{19}	120.6(2)
N_1–S_1–F_{17}	109.7(1)	N_2–S_2–F_{20}	122.8(2)
O_4–S_1–F_{16}	108.5(1)	F_{18}–S_2–F_{19}	95.2(2)
O_4–S_1–F_{17}	109.0(1)	F_{18}–S_2–F_{20}	95.3(2)
F_{16}–S_1–F_{17}	93.7(1)	F_{19}–S_2–F_{20}	95.4(2)
N_4–S_4–O_5	122.1(2)	N_3–S_3–F_{21}	120.0(2)
N_4–S_4–F_{24}	110.6(1)	N_3–S_3–F_{22}	121.7(2)
N_4–S_4–F_{25}	109.8(1)	N_3–S_3–F_{23}	122.3(2)
O_5–S_4–F_{24}	108.5(2)	F_{21}–S_3–F_{22}	95.4(1)
O_5–S_4–F_{25}	108.3(2)	F_{21}–S_3–F_{23}	95.9(1)
F_{24}–S_4–F_{25}	93.9(1)	F_{22}–S_3–F_{23}	95.1(1)
N_5–S_5–O_6	123.2(1)	N_6–S_6–F_{28}	120.6(2)
N_5–S_5–F_{26}	108.5(1)	N_6–S_6–F_{29}	122.2(2)
N_5–S_5–F_{27}	110.5(1)	N_6–S_6–F_{30}	122.3(2)
O_6–S_5–F_{26}	109.1(1)	F_{28}–S_6–F_{29}	94.9(1)
O_6–S_5–F_{27}	107.1(2)	F_{28}–S_6–F_{30}	95.1(2)
F_{26}–S_5–F_{27}	94.7(1)	F_{29}–S_6–F_{30}	94.9(2)

[a] The atom labeling scheme corresponds to that used in Figure 3.4.

Table S3.5. Experimental Geometrical Parameters for $[Hg_3(OTeF_5)_5(N{=}SOF_2)\cdot 2N{\equiv}SF_3]_2$

Bond Lengths (Å)			
$Hg_1{-}O_1$	2.053(6)	**F_2OSN-group**	
$Hg_1{-}{-}{-}O_{1A}$	2.658(7)	$N_1{-}S_1$	1.483(8)
$Hg_1{-}O_2$	2.462(7)	$S_1{-}O_6$	1.415(8)
$Hg_1{-}{-}{-}O_3$	2.711(7)	$S_1{-}F_{26}$	1.526(8)
$Hg_1{-}N_1$	2.065(7)	$S_1{-}F_{27}$	1.516(8)
$Hg_2{-}O_3$	2.077(6)		
$Hg_2{-}O_4$	2.027(8)	**NSF_3 group**	
$Hg_2{-}O_2$	2.506(7)	$N_3{-}S_3$	1.399(8)
$Hg_2{-}O_5$	2.501(7)	$S_3{-}F_{28}$	1.505(6)
$Hg_3{-}N_1$	2.185(8)	$S_3{-}F_{29}$	1.500(6)
$Hg_3{-}N_2$	2.340(12)	$S_3{-}F_{30}$	1.505(6)
$Hg_3{-}N_{2A}$	2.260(8)		
$Hg_3{-}N_{2B}$	2.326(12)	$N_2{-}S_2$	1.399(8)
$Hg_3{-}N_3$	2.284(8)	$N_{2A}{-}S_{2A}$	1.398(8)
$Hg_3{-}O_5$	2.126(7)	$N_{2B}{-}S_{2B}$	1.398(8)
		$S_2{-}F_{31}$	1.497(7)
$Te_1{-}O_1$	1.840(7)	$S_{2A}{-}F_{31A}$	1.495(7)
$Te_2{-}O_2$	1.814(7)	$S_{2B}{-}F_{31B}$	1.495(7)
$Te_3{-}O_3$	1.830(7)	$S_2{-}F_{32}$	1.509(7)
$Te_4{-}O_4$	1.806(8)	$S_{2A}{-}F_{32A}$	1.509(7)
$Te_5{-}O_5$	1.823(7)	$S_{2B}{-}F_{32B}$	1.511(7)
		$S_2{-}F_{33}$	1.505(7)
Te–F	1.838(2)−1.864(2)	$S_{2A}{-}F_{33A}$	1.508(7)
		$S_{2B}{-}F_{33B}$	1.505(7)
Bond Angles (deg)			
$Hg_1{-}O_2{-}Hg_2$	104.7(3)	$O_5{-}Hg_3{-}N_1$	132.1(3)
$Hg_2{-}O_5{-}Hg_3$	109.8(3)	$O_5{-}Hg_3{-}N_2$	26.2(4)
$Hg_3{-}N_1{-}Hg_1$	112.5(3)	$O_5{-}Hg_3{-}N_2$ [b]	27.4(3)
$Hg_1{-}{-}{-}O_3{-}Hg_2$	109.8(3)	$O_5{-}Hg_3{-}N_{2B}$ [b]	28.4(3)
$O_1{-}Hg_1{-}O_2$	92.2(3)	$O_5{-}Hg_3{-}N_3$	110.7(3)
$O_1{-}Hg_1{-}{-}{-}O_3$	105.4(2)	$N_3{-}Hg_3{-}N_2$	88.9(6)
$O_2{-}Hg_1{-}{-}{-}O_3$	64.8(2)	$N_3{-}Hg_3{-}N_{2A}$ [b]	96.4(7)
$N_1{-}Hg_1{-}O_2$	89.6(3)	$N_3{-}Hg_3{-}N_{2B}$ [b]	93.0(6)
$N_1{-}Hg_1{-}O_1$	176.9(3)	$N_3{-}Hg_3{-}N_1$	103.7(3)
$N_1{-}Hg_1{-}{-}{-}O_3$	77.7(3)	$N_1{-}Hg_3{-}N_2$	39.6(3)
$N_1{-}Hg_1{-}{-}{-}O_{1A}$	102.0(3)	$N_1{-}Hg_3{-}N_{2A}$ [b]	40.3(2)
$O_{1A}{-}{-}{-}Hg_1{-}O_3$	169.3(2)	$N_1{-}Hg_3{-}N_{2B}$ [b]	38.3(3)
$O_{1A}{-}{-}{-}Hg_1{-}O_2$	104.6(2)		
$O_3{-}Hg_2{-}O_2$	54.3(2)	$O_3{-}Hg_2{-}O_5$	81.0(3)
$O_2{-}Hg_2{-}O_4$	113.3(3)	$O_3{-}Hg_2{-}O_4$	169.3(3)

Table S3.5. continued…

O_2–Hg_2–O_5	72.7(3)
Hg_2–N_3–S_3	152.0(6)
Hg_2–N_2–S_2	155(1)
Hg_2–N_{2A}–S_{2A} [b]	174(1)
Hg_2–N_{2B}–S_{2B} [b]	157(2)
NSF_3 group	
N_3–S_3–F_{28}	122.3(5)
N_3–S_3–F_{29}	122.4(5)
N_3–S_3–F_{30}	119.2(4)
F_{28}–S_3–F_{29}	95.3(4)
F_{28}–S_3–F_{30}	93.9(4)
F_{29}–S_3–F_{30}	97.1(4)
N_2–S_2–F_{31}	123.0(7)
N_2–S_2–F_{32}	122.0(7)
N_2–S_2–F_{33}	118.9(6)
F_{31}–S_2–F_{32}	95.2(5)
F_{31}–S_2–F_{33}	97.7(6)
F_{32}–S_2–F_{33}	93.2(6)
N_{2A}–S_{2A}–F_{31A} [b]	123.4(7)
N_{2A}–S_{2A}–F_{32A} [b]	122.0(7)
N_{2A}–S_{2A}–F_{33A} [b]	118.9(7)
F_{31A}–S_{2A}–F_{32A} [b]	95.4(5)
F_{31A}–S_{2A}–F_{33A} [b]	97.7(6)
F_{32A}–S_{2A}–F_{33A} [b]	92.7(6)
N_{2B}–S_{2B}–F_{31B} [b]	123.2(7)
N_{2B}–S_{2B}–F_{32B} [b]	121.9(7)
N_{2B}–S_{2B}–F_{33B} [b]	119.0(6)
F_{31B}–S_{2B}–F_{32B} [b]	95.2(5)
F_{31B}–S_{2B}–F_{33B} [b]	98.1(6)
F_{32B}–S_{2B}–F_{33B} [b]	92.6(6)
Dihedral Angles (deg)	
Te_4–O_4–Hg_2–O_3–Te_3	40.7(6)
O_5–Hg_2–O_4	108.4(3)
O_5–Hg_2–O_2	69.1(3)
Te_1–O_1–Hg_1	121.5(4)
Te_2–O_2–Hg_1	126.8(3)
Te_2–O_2–Hg_3	132.6(3)
Te_2–O_2---Hg_2	115.0(3)
Te_3–O_3---Hg_1	129.6(3)
Te_3–O_3–Hg_2	120.2(3)
Te_4–O_4–Hg_2	120.2(4)
Te_5–O_5–Hg_3	127.1(4)
Te_5–O_5–Hg_2	123.1(4)
S_1–N_1–Hg_1	119.8(5)
S_1–N_1–Hg_3	127.2(4)
Hg_1–O_1---Hg_{1A}	104.8(3)
O_1–Hg_1---O_{1A}	75.2(3)
F_2OSN-group	
N_1–S_1–O_6	122.9(4)
N_1–S_1–F_{26}	109.0(5)
N_1–S_1–F_{27}	108.6(4)
O_6–S_1–F_{26}	109.1(4)
O_6–S_1–F_{27}	109.0(5)
F_{26}–S_1–F_{27}	94.3(5)

[a] The atom labeling scheme corresponds to that used in Figure 3.5. [b] The NSF_3 ligand is twofold disordered.

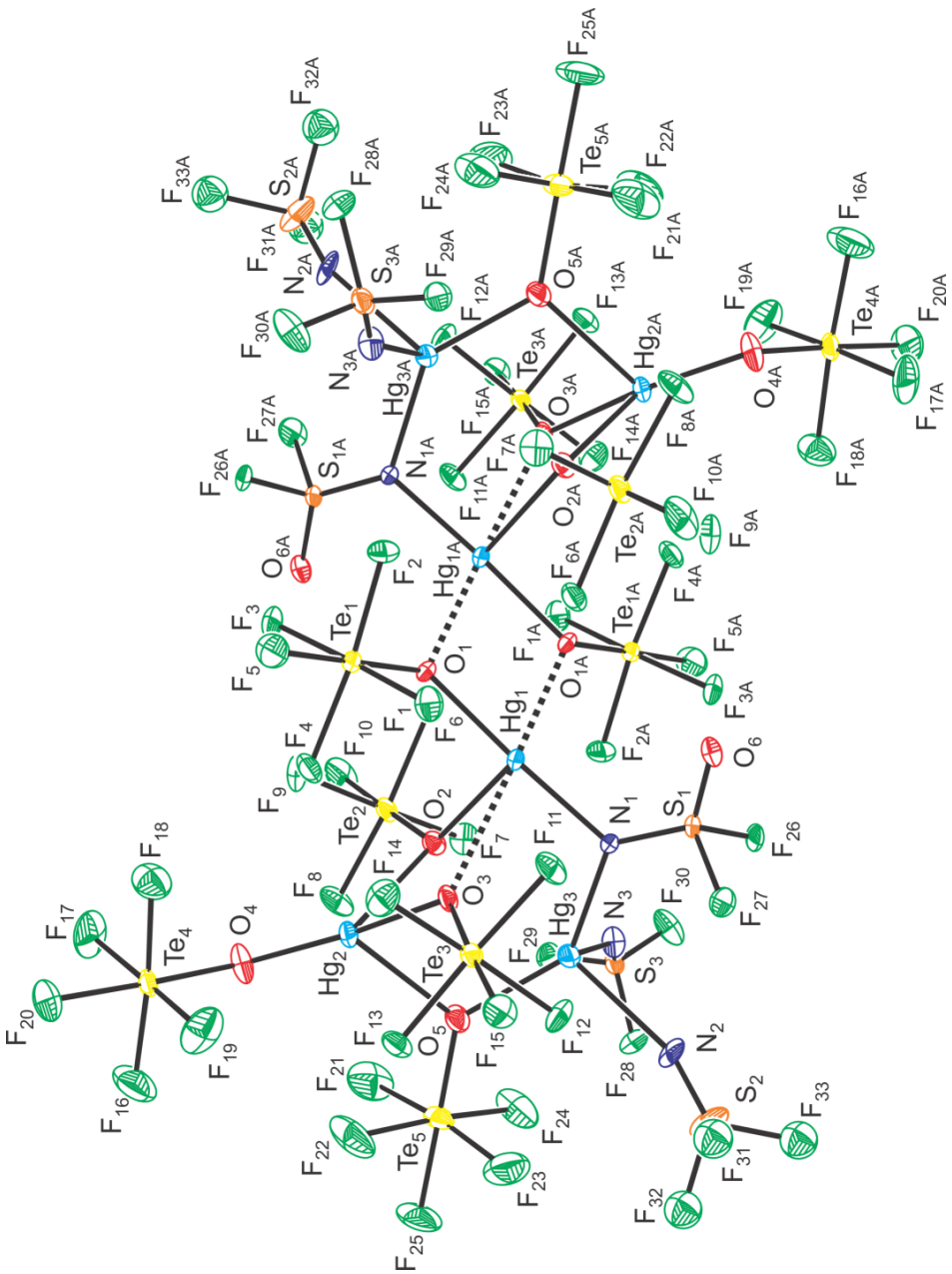

Figure S3.1. The X-ray crystal structure of dimeric $[Hg_3(OTeF_5)_5(N{=}SOF_2)\cdot 2N{\equiv}SF_3]_2$. Thermal ellipsoids are shown at the 30% probability level.

Table S3.6. Experimental and Calculated[a] Geometrical Parameters for $[Hg_3(OTeF_5)_6 \cdot 4N{\equiv}SF_3]$

	exptl	calcd
Bond Lengths (Å)		
$Hg_1{-}O_1$	2.327(8)	2.359
$Hg_1{---}O_2$	2.781(11)	2.864
$Hg_1{-}O_5$	2.307(10)	2.239
$Hg_1{-}O_4$	2.301(8)	2.336
$Hg_1{-}N_1$	2.265(11)	2.354
$Hg_1{-}N_4$	2.223(10)	2.306
$Hg_2{-}O_1$	2.501(8)	2.582
$Hg_2{-}O_2$	2.143(7)	2.195
$Hg_2{-}O_3$	2.501(8)	2.520
$Hg_2{-}O_5$	2.557(9)	2.522
$Hg_2{-}O_6$	2.051(9)	2.058
$Hg_3{---}O_1$	2.644(7)	2.614
$Hg_3{---}O_2$	2.723(11)	2.516
$Hg_3{-}O_3$	2.192(9)	2.217
$Hg_3{-}O_4$	2.292(8)	2.286
$Hg_3{-}N_2$	2.234(11)	2.328
$Hg_3{-}N_3$	2.240(11)	2.374
$Te_1{-}O_1$	1.836(7)	1.868
$Te_2{-}O_2$	1.823(8)	1.878
$Te_3{-}O_3$	1.806(9)	1.868
$Te_4{-}O_4$	1.818(8)	1.874
$Te_5{-}O_5$	1.787(8)	1.868
$Te_6{-}O_6$	1.811(10)	1.883
$Te{-}F_a$	1.808(7)−1.845(7)	1.882–1.885
$Te{-}F_e$	1.806(10)−1.860(10)	1.885–1.915
N−S	1.371(11)−1.398(11)	1.417–1.419
S−F	1.506(5)−1.536(7)	1.561–1.572
Bond Angles (deg)		
$Hg_1{-}O_1{-}Hg_2$	96.2(4)	96.1
$Hg_1{-}O_1{-}Hg_3$	95.7(4)	96.1
$Hg_2{-}O_1{-}Hg_3$	90.0(3)	88.3
$Hg_1{-}O_2{-}Hg_2$	92.9(4)	92.3
$Hg_1{-}O_2{-}Hg_3$	84.2(3)	86.7
$Hg_2{-}O_2{-}Hg_3$	96.0(4)	100.1
$Hg_1{-}O_4{-}Hg_3$	107.0(4)	106.4
$Hg_3{-}O_3{-}Hg_2$	101.4(5)	99.4
$Hg_2{-}O_5{-}Hg_1$	95.1(4)	101.0
$O_4{-}Hg_3{-}O_3$	136.6(4)	139.3

Table S3.6 continued…

O_3–Hg_2–O_5	136.3(4)	133.3
O_5–Hg_1–O_4	139.4(4)	135.1
N_1–Hg_1–N_4	94.3(7)	91.9
N_2–Hg_3–N_3	108.7(6)	91.2
Te_1–O_1–Hg_1	122.8(5)	126.3
Te_1–O_1–Hg_2	119.3(6)	123.1
Te_1–O_1---Hg_3	124.9(5)	118.0
Te_2–O_2---Hg_1	127.1(5)	117.3
Te_2–O_2–Hg_2	119.3(5)	122.1
Te_2–O_2---Hg_3	127.4(5)	128.1
Te_3–O_3–Hg_2	133.1(7)	134.6
Te_3–O_3–Hg_3	125.3(6)	125.9
Te_4–O_4–Hg_1	126.1(6)	126.0
Te_4–O_4–Hg_3	126.3(6)	127.0
Te_5–O_5–Hg_1	126.9(7)	125.8
Te_5–O_5–Hg_2	137.9(7)	132.0
N_2–Hg_3–O_2	159.8(5)	169.8
N_2–Hg_3–O_3	112.8(5)	115.6
N_2–Hg_3–O_4	93.9(5)	93.7
N_2–Hg_3–O_1	98.9(5)	111.3
N_3–Hg_3–O_4	97.5(5)	113.2
N_3–Hg_3–O_1	150.7(4)	157.2
N_3–Hg_3–O_2	88.8(5)	93.4
N_3–Hg_3–O_3	104.7(5)	94.8
O_6–Hg_2–O_5	107.2(5)	108.7
O_6–Hg_2–O_3	108.2(5)	108.7
O_6–Hg_2–O_1	120.6(5)	120.1
O_6–Hg_2–O_2	166.3(5)	169.8
O_5–Hg_2–O_1	70.2(4)	68.7
O_5–Hg_2–O_2	75.8(4)	74.9
O_3–Hg_2–O_1	70.0(4)	68.8
O_3–Hg_2–O_2	76.0(4)	73.3
O_1–Hg_2–O_2	73.1(4)	70.0
N_1–Hg_1–O_5	104.1(5)	99.0
N_1–Hg_1–O_1	109.6(6)	101.2
N_1–Hg_1–O_2	171.7(5)	160.3
N_1–Hg_1–O_4	113.8(5)	120.4
N_4–Hg_1–O_5	102.4(6)	111.9
N_4–Hg_1–O_1	155.5(6)	162.6
N_4–Hg_1–O_2	91.7(6)	106.2
N_4–Hg_1–O_4	89.1(5)	89.2
Hg_3–N_3–S_3	166(1)	153.4
Hg_3–N_2–S_2	161(1)	142.3
Hg_1–N_1–S_1	151(1)	150.6
Hg_1–N_4–S_4	176(1)	147.6
N–S–F	116.3(12)–126.4(12)	118.6–125.0
F–S–F	93.5(8)–98.0(8)	94.3–95.1

[a] Calculated at the PBE0/def2-SVP level of theory.

Table S3.7. NBO Valencies, Charges (NPA), and Bond Orders for $[Hg_3(OTeF_5)_6 \cdot 4N{\equiv}SF_3]$

Atom	Charge	Valencies	Atom	Charge	Valencies
Hg_1	1.565	0.780	F_{21}	-0.600	0.413
Hg_2	1.480	0.736	F_{22}	-0.609	0.409
Hg_3	1.563	0.791	F_{23}	-0.568	0.424
O_1	-1.202	0.826	F_{24}	-0.565	0.425
Te_1	3.270	2.858	F_{25}	-0.560	0.420
F_1	-0.561	0.434	O_6	-1.110	0.815
F_2	-0.589	0.419	Te_6	3.259	2.833
F_3	-0.604	0.427	F_{26}	-0.567	0.418
F_4	-0.585	0.416	F_{27}	-0.567	0.420
F_5	-0.556	0.422	F_{28}	-0.597	0.414
O_2	-1.191	0.845	F_{29}	-0.580	0.416
Te_2	3.276	2.851	F_{30}	-0.562	0.419
F_6	-0.596	0.428	N_1	-1.054	1.560
F_7	-0.577	0.422	S_1	2.379	3.339
F_8	-0.581	0.421	F_{31}	-0.434	0.520
F_9	-0.563	0.437	F_{32}	-0.428	0.526
F_{10}	-0.554	0.424	F_{33}	-0.414	0.541
O_3	-1.214	0.799	N_2	-1.052	1.573
Te_3	3.278	2.838	S_2	2.383	3.338
F_{11}	-0.567	0.423	F_{34}	-0.420	0.537
F_{12}	-0.606	0.409	F_{35}	-0.431	0.523
F_{13}	-0.600	0.414	F_{36}	-0.420	0.533
F_{14}	-0.565	0.428	S_3	2.373	3.337
F_{15}	-0.559	0.420	N_3	-1.047	1.562
O_4	-1.215	0.796	F_{37}	-0.435	0.518
Te_4	3.283	2.835	F_{38}	-0.428	0.526
F_{16}	-0.589	0.414	F_{39}	-0.415	0.539
F_{17}	-0.576	0.424	S_4	2.391	3.343
F_{18}	-0.578	0.424	N_4	-1.059	1.579
F_{19}	-0.588	0.415	F_{40}	-0.420	0.538
F_{20}	-0.558	0.421	F_{41}	-0.419	0.535
O_5	-1.212	0.796	F_{42}	-0.430	0.525
Te_5	3.275	2.841			

Table S3.7. continued…

Bond	Bond order	Bond	Bond order
Hg_1–O_1	0.099	Te_4–O_4	0.617
Hg_1–O_2	0.042	Te_4–F_{16}	0.432
Hg_1–O_4	0.100	Te_4–F_{17}	0.438
Hg_1–O_5	0.125	Te_4–F_{18}	0.435
Hg_1–N_1	0.135	Te_4–F_{19}	0.433
Hg_1–N_4	0.154	Te_4–F_{20}	0.451
Hg_2–O_1	0.060	Te_5–O_5	0.632
Hg_2–O_2	0.153	Te_5–F_{21}	0.421
Hg_2–O_3	0.076	Te_5–F_{22}	0.415
Hg_2–O_5	0.072	Te_5–F_{23}	0.446
Hg_2–O_6	0.240	Te_5–F_{24}	0.448
Hg_3–O_1	0.066	Te_5–F_{25}	0.450
Hg_3–O_2	0.070	Te_6–O_6	0.618
Hg_3–O_3	0.131	Te_6–F_{26}	0.447
Hg_3–O_4	0.111	Te_6–F_{27}	0.448
Hg_3–N_2	0.149	Te_6–F_{28}	0.414
Hg_3–N_3	0.133	Te_6–F_{29}	0.434
Te_1–O_1	0.634	Te_6–F_{30}	0.448
Te_1–F_1	0.447	S_1-N_1	1.517
Te_1–F_2	0.433	S_1–F_{31}	0.595
Te_1–F_3	0.414	S_1–F_{32}	0.598
Te_1–F_4	0.433	S_1–F_{33}	0.609
Te_1–F_5	0.452	S_2–N_2	1.511
Te_2–O_2	0.614	S_2–F_{34}	0.603
Te_2–F_6	0.420	S_2–F_{35}	0.598
Te_2–F_7	0.438	S_2–F_{36}	0.604
Te_2–F_8	0.438	S_3–N_3	1.519
Te_2–F_9	0.443	S_3–F_{37}	0.593
Te_2–F_{10}	0.454	S_3–F_{38}	0.597
Te_3–O_3	0.629	S_3–F_{39}	0.607
Te_3–F_{11}	0.447	S_4–N_4	1.511
Te_3–F_{12}	0.417	S_4–F_{40}	0.604
Te_3–F_{13}	0.420	S_4–F_{41}	0.605
Te_3–F_{14}	0.447	S_4–F_{42}	0.600
Te_3–F_{15}	0.450		

[a] Calculated at the PBE0/def2-SVP level of theory.

APPENDIX B

Chapter 4 Supporting Information

Pentafluoro-oxotellurate(VI) Anions of Mercury(II); the Syntheses and Structures of $[Hg(OTeF_5)_4]^{2-}$, $[Hg(OTeF_5)_5]^{3-}$, $[Hg_2(OTeF_5)_6]^{2-}$, $[Hg(OTeF_5)_4]^{2-}\cdot Hg(OTeF_5)_2$, and $[Hg_2(OTeF_5)_7]^{3-}\cdot Hg(OTeF_5)_2$

Adapted with permission from: DeBackere, J.R., Mercier, H.P.A., and Schrobilgen, G.J. *Inorganic Chemistry*, **2015**, *54*, 1606–1626.

LIST OF FIGURES

page

LIST OF TABLES

page

Table S4.1. Complete List of Experimental Geometrical Parameters for $[N(CH_2CH_3)_4]_2[Hg(OTeF_5)_4]$ [a]

Bond Lengths (Å) [b]			
$Hg_{(1)}–O_{(1)}$	2.214(6)	$N_{(1)}–C_{(1)}$	1.530 (12)
$Hg_{(1)}–O_{(2)}$	2.229(7)	$N_{(1)}–C_{(3)}$	1.521(11)
$Hg_{(1)}–O_{(3)}$	2.275(7)	$N_{(1)}–C_{(5)}$	1.529(12)
$Hg_{(1)}–O_{(4)}$	2.146(7)	$N_{(1)}–C_{(7)}$	1.521(12)
$Te_{(1)}–O_{(1)}$	1.788(6)	$C_{(1)}–C_{(2)}$	1.509(15)
$Te_{(2)}–O_{(2)}$	1.803(6)	$C_{(3)}–C_{(4)}$	1.523(13)
$Te_{(3)}–O_{(3)}$	1.798(6)	$C_{(5)}–C_{(6)}$	1.505(13)
$Te_{(4)}–O_{(4)}$	1.805(7)	$C_{(7)}–C_{(8)}$	1.511(14)
$Te_{(1)}–F_{(1)}$	1.832(6)	$N_{(2)}–C_{(9)}$	1.526(12)
$Te_{(1)}–F_{(2)}$	1.842(7)	$N_{(2)}–C_{(11)}$	1.533(12)
$Te_{(1)}–F_{(3)}$	1.850(6)	$N_{(2)}–C_{(13)}$	1.524(12)
$Te_{(1)}–F_{(4)}$	1.847(6)	$N_{(2)}–C_{(15)}$	1.522(12)
$Te_{(1)}–F_{(5)}$	1.816(6)	$C_{(9)}–C_{(10)}$	1.491(14)
$Te_{(2)}–F_{(6)}$	1.852(6)	$C_{(11)}–C_{(12)}$	1.495(13)
$Te_{(2)}–F_{(7)}$	1.857(5)	$C_{(13)}–C_{(14)}$	1.499(15)
$Te_{(2)}–F_{(8)}$	1.838(6)	$C_{(15)}–C_{(16)}$	1.533(15)
$Te_{(2)}–F_{(9)}$	1.851(5)	$C_{(6A)}H_3---F_{(1)}$	3.311(12)
$Te_{(2)}–F_{(10)}$	1.841(6)	$C_{(8)}H_3---F_{(11)}$	3.315(12)
$Te_{(3)}–F_{(11)}$	1.832(6)	$C_{(1A)}H_3---F_{(13)}$	3.335(12)
$Te_{(3)}–F_{(12)}$	1.849(5)	$C_{(4A)}H_3---F_{(14)}$	3.239(12)
$Te_{(3)}–F_{(13)}$	1.861(6)	$C_{(5)}H_3---F_{(16)}$	3.377(12)
$Te_{(3)}–F_{(14)}$	1.855(5)	$C_{(5)}H_3---F_{(19)}$	3.309(11)
$Te_{(3)}–F_{(15)}$	1.841(6)	$C_{(7A)}H_3---F_{(10)}$	3.382(12)
$Te_{(4)}–F_{(16)}$	1.842(6)	$C_{(8A)}H_3---F_{(9)}$	3.336(12)
$Te_{(4)}–F_{(17)}$	1.839(6)	$C_{(8A)}H_3---F_{(17)}$	3.202(12)
$Te_{(4)}–F_{(18)}$	1.836(6)	$C_{(9)}H_3---F_{(7)}$	3.398(11)
$Te_{(4)}–F_{(19)}$	1.861(6)	$C_{(10A)}H_3---F_{(2)}$	3.350(12)
$Te_{(4)}–F_{(20)}$	1.832(6)	$C_{(10A)}H_3---F_{(4)}$	3.339(12)
		$C_{(10A)}H_3---F_{(13)}$	3.178(12)
		$C_{(11A)}H_3---F_{(4)}$	3.269(12)
		$C_{(11A)}H_3---F_{(3)}$	3.186(12)
		$C_{(12A)}H_3---F_{(18)}$	3.376(12)
		$C_{(15A)}H_3---F_{(10)}$	3.247(12)
		$C_{(15A)}H_3---F_{(7)}$	3.267(12)
Bond Angles (deg)			
$O_{(1)}–Hg_{(1)}–O_{(2)}$	96.8(3)	$O_{(2)}–Te_{(2)}–F_{(6)}$	95.1 (3)
$O_{(1)}–Hg_{(1)}–O_{(3)}$	96.6(2)	$O_{(2)}–Te_{(2)}–F_{(7)}$	95.0 (3)
$O_{(1)}–Hg_{(1)}–O_{(4)}$	120.1(3)	$O_{(2)}–Te_{(2)}–F_{(8)}$	93.3 (3)
$O_{(2)}–Hg_{(1)}–O_{(3)}$	86.3(2)	$O_{(2)}–Te_{(2)}–F_{(9)}$	94.6 (3)
$O_{(2)}–Hg_{(1)}–O_{(4)}$	125.9(3)	$O_{(2)}–Te_{(2)}–F_{(10)}$	179.4 (3)
$O_{(3)}–Hg_{(1)}–O_{(4)}$	122.8(3)	$F_{(10)}–Te_{(2)}–F_{(6)}$	84.4(3)

Table S4.1. continued…

$Hg_{(1)}–O_{(1)}–Te_{(1)}$	124.1(3)	$F_{(10)}–Te_{(2)}–F_{(7)}$	85.2(3)
$Hg_{(1)}–O_{(2)}–Te_{(2)}$	122.4(4)	$F_{(10)}–Te_{(2)}–F_{(8)}$	87.2(3)
$Hg_{(1)}–O_{(3)}–Te_{(3)}$	118.2(3)	$F_{(10)}–Te_{(2)}–F_{(9)}$	85.2(3)
$Hg_{(1)}–O_{(4)}–Te_{(4)}$	120.6(4)	$F_{(6)}–Te_{(2)}–F_{(7)}$	89.1(3)
$O_{(1)}–Te_{(1)}–F_{(1)}$	93.0(3)	$F_{(6)}–Te_{(2)}–F_{(8)}$	171.6(3)
$O_{(1)}–Te_{(1)}–F_{(2)}$	93.9(3)	$F_{(7)}–Te_{(2)}–F_{(9)}$	170.4(3)
$O_{(1)}–Te_{(1)}–F_{(3)}$	94.9(3)	$F_{(6)}–Te_{(2)}–F_{(9)}$	90.2(3)
$O_{(1)}–Te_{(1)}–F_{(4)}$	95.0(3)	$F_{(7)}–Te_{(2)}–F_{(8)}$	90.1(3)
$O_{(1)}–Te_{(1)}–F_{(5)}$	179.4(3)	$F_{(8)}–Te_{(2)}–F_{(9)}$	89.3(3)
$F_{(5)}–Te_{(1)}–F_{(1)}$	86.4(3)	$O_{(4)}–Te_{(4)}–F_{(16)}$	95.0(3)
$F_{(5)}–Te_{(1)}–F_{(2)}$	86.1(4)	$O_{(4)}–Te_{(4)}–F_{(17)}$	93.3(3)
$F_{(5)}–Te_{(1)}–F_{(3)}$	85.6(3)	$O_{(4)}–Te_{(4)}–F_{(18)}$	93.6(3)
$F_{(5)}–Te_{(1)}–F_{(4)}$	85.0(3)	$O_{(4)}–Te_{(4)}–F_{(19)}$	94.6(3)
$F_{(1)}–Te_{(1)}–F_{(2)}$	88.6(3)	$O_{(4)}–Te_{(4)}–F_{(20)}$	178.8(3)
$F_{(1)}–Te_{(1)}–F_{(3)}$	172.1(3)	$F_{(20)}–Te_{(4)}–F_{(16)}$	85.8(3)
$F_{(2)}–Te_{(1)}–F_{(4)}$	171.1(3)	$F_{(20)}–Te_{(4)}–F_{(17)}$	85.8(3)
$F_{(1)}–Te_{(1)}–F_{(4)}$	90.2(3)	$F_{(20)}–Te_{(4)}–F_{(18)}$	85.6(3)
$F_{(2)}–Te_{(1)}–F_{(3)}$	91.1(4)	$F_{(20)}–Te_{(4)}–F_{(19)}$	86.3(3)
$F_{(3)}–Te_{(1)}–F_{(4)}$	88.8(3)	$F_{(16)}–Te_{(4)}–F_{(17)}$	90.7(3)
$O_{(3)}–Te_{(3)}–F_{(11)}$	94.8(3)	$F_{(16)}–Te_{(4)}–F_{(18)}$	171.4(3)
$O_{(3)}–Te_{(3)}–F_{(12)}$	95.2(3)	$F_{(17)}–Te_{(4)}–F_{(19)}$	172.1(3)
$O_{(3)}–Te_{(3)}–F_{(13)}$	93.7(3)	$F_{(16)}–Te_{(4)}–F_{(19)}$	89.7(3)
$O_{(3)}–Te_{(3)}–F_{(14)}$	94.7(3)	$F_{(17)}–Te_{(4)}–F_{(18)}$	88.9(3)
$O_{(3)}–Te_{(3)}–F_{(15)}$	177.9(3)	$F_{(18)}–Te_{(4)}–F_{(19)}$	89.6(3)
$F_{(15)}–Te_{(3)}–F_{(11)}$	87.3(3)		
$F_{(15)}–Te_{(3)}–F_{(12)}$	85.0(3)		
$F_{(15)}–Te_{(3)}–F_{(13)}$	84.2(3)		
$F_{(15)}–Te_{(3)}–F_{(14)}$	85.1(3)		
$F_{(11)}–Te_{(3)}–F_{(12)}$	89.4(3)		
$F_{(11)}–Te_{(3)}–F_{(13)}$	171.5(3)		
$F_{(12)}–Te_{(3)}–F_{(14)}$	170.1(3)	$C_{(1)}–N_{(1)}–C_{(3)}$	110.5(7)
$F_{(11)}–Te_{(3)}–F_{(14)}$	89.9(3)	$C_{(1)}–N_{(1)}–C_{(5)}$	111.2(7)
$F_{(12)}–Te_{(3)}–F_{(13)}$	90.7(3)	$C_{(1)}–N_{(1)}–C_{(7)}$	106.9(7)
$F_{(13)}–Te_{(3)}–F_{(14)}$	88.5(3)	$C_{(3)}–N_{(1)}–C_{(5)}$	106.5(6)
		$C_{(3)}–N_{(1)}–C_{(7)}$	111.2(7)
$N_{(1)}–C_{(1)}–C_{(2)}$	116.1(8)	$C_{(5)}–N_{(1)}–C_{(7)}$	110.6(7)
$N_{(1)}–C_{(3)}–C_{(4)}$	115.1(7)		
$N_{(1)}–C_{(5)}–C_{(6)}$	115.9(8)	$C_{(9)}–N_{(2)}–C_{(11)}$	110.3(7)
$N_{(1)}–C_{(7)}–C_{(8)}$	114.5(8)	$C_{(9)}–N_{(2)}–C_{(13)}$	106.9 (7)
$N_{(1)}–C_{(9)}–C_{(10)}$	115.0(8)	$C_{(9)}–N_{(2)}–C_{(15)}$	111.1 (7)
$N_{(1)}–C_{(11)}–C_{(12)}$	115.6(8)	$C_{(11)}–N_{(2)}–C_{(13)}$	111.0 (7)
$N_{(1)}–C_{(13)}–C_{(14)}$	115.9(9)	$C_{(11)}–N_{(2)}–C_{(15)}$	106.2 (7)
$N_{(1)}–C_{(15)}–C_{(16)}$	114.2(8)	$C_{(13)}–N_{(2)}–C_{(15)}$	111.4(8)

[a] The atom numbers are subscripted in parentheses, and the labeling scheme corresponds to that used in Figure 4.1 and Figure S4.2. [b] The subscripted letters refer to another asymmetric unit.

Table S4.2. Complete List of Experimental Geometrical Parameters for $[N(CH_3)_4]_3[Hg(OTeF_5)_5]$ [a]

Bond Lengths (Å) [b]			
$Hg_{(1)}–O_{(1)}$	2.318(5)	$N_{(1)}–C_{(1)}$	1.482(9)
$Hg_{(1)}–O_{(2)}$	2.227(5)	$N_{(1)}–C_{(2)}$	1.485(9)
$Hg_{(1)}–O_{(3)}$	2.301(5)	$N_{(1)}–C_{(3)}$	1.506(8)
$Hg_{(1)}–O_{(4)}$	2.323(4)	$N_{(1)}–C_{(4)}$	1.492(8)
$Hg_{(1)}–O_{(5)}$	2.230(5)	$N_{(2)}–C_{(5)}$	1.502(9)
$Hg_{(1)}---F_{(17)}$	3.008(4)	$N_{(2)}–C_{(6)}$	1.479(9)
$Te_{(1)}–O_{(1)}$	1.789(5)	$N_{(2)}–C_{(7)}$	1.482(9)
$Te_{(2)}–O_{(2)}$	1.772(5)	$N_{(2)}–C_{(8)}$	1.494(9)
$Te_{(3)}–O_{(3)}$	1.783(5)	$N_{(3)}–C_{(9)}$	1.519(9)
$Te_{(4)}–O_{(4)}$	1.801(4)	$N_{(3)}–C_{(10)}$	1.502(9)
$Te_{(5)}–O_{(5)}$	1.784(5)	$N_{(3)}–C_{(11)}$	1.476(10)
$Te_{(1)}–F_{(1)}$	1.847(4)	$N_{(3)}–C_{(12)}$	1.497(6)
$Te_{(1)}–F_{(2)}$	1.842(6)	$C_{(5A)}H_3---F_{(14)}$	3.117(9)
$Te_{(1)}–F_{(3)}$	1.853(4)	$C_{(1A)}H_3---F_{(2)}$	3.211(8)
$Te_{(1)}–F_{(4)}$	1.841(5)	$C_{(1A)}H_3---F_{(22)}$	3.389(9)
$Te_{(1)}–F_{(5)}$	1.854(5)	$C_{(1A)}H_3---F_{(11)}$	3.312(8)
$Te_{(2)}–F_{(6)}$	1.861(4)	$C_{(2)}H_3---F_{(24)}$	3.273(9)
$Te_{(2)}–F_{(7)}$	1.850(4)	$C_{(2)}H_3---F_{(18)}$	3.352(8)
$Te_{(2)}–F_{(8)}$	1.844(5)	$C_{(12A)}H_3---F_{(19)}$	3.360(9)
$Te_{(2)}–F_{(9)}$	1.843(5)	$C_{(12A)}H_3---F_{(5)}$	3.406(9)
$Te_{(2)}–F_{(10)}$	1.837(5)	$C_{(12A)}H_3---F_{(20)}$	3.119(9)
$Te_{(3)}–F_{(11)}$	1.861(4)	$C_{(12A)}H_3---F_{(15)}$	3.250(8)
$Te_{(3)}–F_{(12)}$	1.859 (4)	$C_{(3A)}H_3---F_{(9)}$	3.334(8)
$Te_{(3)}–F_{(13)}$	1.847(4)	$C_{(3A)}H_3---F_{(24)}$	3.399(9)
$Te_{(3)}–F_{(14)}$	1.840(5)	$C_{(6A)}H_3---F_{(24)}$	3.268(8)
$Te_{(3)}–F_{(15)}$	1.849(4)	$C_{(6A)}H_3---F_{(16)}$	3.386(9)
$Te_{(4)}–F_{(16)}$	1.853(4)	$C_{(7A)}H_3---F_{(8)}$	3.358(9)
$Te_{(4)}–F_{(17)}$	1.863(4)	$C_{(7A)}H_3---F_{(15)}$	3.207(9)
$Te_{(4)}–F_{(18)}$	1.854 (5)	$C_{(7A)}H_3---F_{(11)}$	3.340(8)
$Te_{(4)}–F_{(19)}$	1.843 (4)	$C_{(7A)}H_3---F_{(3)}$	3.310(9)
$Te_{(4)}–F_{(20)}$	1.845 (4)	$C_{(4A)}H_3---F_{(13)}$	3.035(9)
$Te_{(5)}–F_{(21)}$	1.860 (4)	$C_{(4)}H_3---F_{(17)}$	3.358(8)
$Te_{(5)}–F_{(22)}$	1.857 (5)	$C_{(11A)}H_3---F_{(23)}$	3.094(9)
$Te_{(5)}–F_{(23)}$	1.850(4)	$C_{(11)}H_3---F_{(6)}$	3.110(8)
$Te_{(5)}–F_{(24)}$	1.849 (4)	$C_{(8)}H_3---F_{(1)}$	3.369(9)
$Te_{(5)}–F_{(25)}$	1.846 (5)	$C_{(8A)}H_3---F_{(19)}$	3.333(8)
		$C_{(10A)}H_3---F_{(2)}$	3.317(9)
		$C_{(10A)}H_3---F_{(21)}$	3.334(9)
Bond Angles (deg)			
$O_{(1)}–Hg_{(1)}–O_{(2)}$	95.7(2)	$O_{(1)}–Te_{(1)}–F_{(1)}$	96.3(2)
$O_{(1)}–Hg_{(1)}–O_{(3)}$	96.4(1)	$O_{(1)}–Te_{(1)}–F_{(2)}$	95.8(3)

Table S4.2. continued…

$O_{(1)}$–$Hg_{(1)}$–$O_{(4)}$	156.3(2)	$O_{(1)}$–$Te_{(1)}$–$F_{(3)}$	94.9(2)
$O_{(1)}$–$Hg_{(1)}$–$O_{(5)}$	84.3(2)	$O_{(1)}$–$Te_{(1)}$–$F_{(4)}$	97.5(3)
$O_{(2)}$–$Hg_{(1)}$–$O_{(3)}$	94.8(2)	$O_{(1)}$–$Te_{(1)}$–$F_{(5)}$	178.7(2)
$O_{(2)}$–$Hg_{(1)}$–$O_{(4)}$	83.5(2)	$O_{(2)}$–$Te_{(2)}$–$F_{(6)}$	93.1(2)
$O_{(2)}$–$Hg_{(1)}$–$O_{(5)}$	161.6(2)	$O_{(2)}$–$Te_{(2)}$–$F_{(7)}$	95.2(3)
$O_{(3)}$–$Hg_{(1)}$–$O_{(4)}$	107.3(2)	$O_{(2)}$–$Te_{(2)}$–$F_{(8)}$	97.7(3)
$O_{(3)}$–$Hg_{(1)}$–$O_{(5)}$	103.5(2)	$O_{(2)}$–$Te_{(2)}$–$F_{(9)}$	95.9(3)
$O_{(4)}$–$Hg_{(1)}$–$O_{(5)}$	89.2(2)	$O_{(2)}$–$Te_{(2)}$–$F_{(10)}$	177.3(3)
$Hg_{(1)}$–$O_{(1)}$–$Te_{(1)}$	130.9(3)	$O_{(3)}$–$Te_{(3)}$–$F_{(11)}$	95.1(2)
$Hg_{(1)}$–$O_{(2)}$–$Te_{(2)}$	134.0(3)	$O_{(3)}$–$Te_{(3)}$–$F_{(12)}$	96.5(3)
$Hg_{(1)}$–$O_{(3)}$–$Te_{(3)}$	125.7(3)	$O_{(3)}$–$Te_{(3)}$–$F_{(13)}$	96.9(2)
$Hg_{(1)}$–$O_{(4)}$–$Te_{(4)}$	116.3(2)	$O_{(3)}$–$Te_{(3)}$–$F_{(14)}$	95.8(3)
$Hg_{(1)}$–$O_{(5)}$–$Te_{(5)}$	129.8(3)	$O_{(3)}$–$Te_{(3)}$–$F_{(15)}$	178.5(2)
		$O_{(4)}$–$Te_{(4)}$–$F_{(16)}$	95.6(2)
$F_{(5)}$–$Te_{(1)}$–$F_{(1)}$	85.0(2)	$O_{(4)}$–$Te_{(4)}$–$F_{(17)}$	95.1(2)
$F_{(5)}$–$Te_{(1)}$–$F_{(2)}$	83.8(2)	$O_{(4)}$–$Te_{(4)}$–$F_{(18)}$	94.7(2)
$F_{(5)}$–$Te_{(1)}$–$F_{(3)}$	83.9(2)	$O_{(4)}$–$Te_{(4)}$–$F_{(19)}$	95.1(2)
$F_{(5)}$–$Te_{(1)}$–$F_{(4)}$	82.8(2)	$O_{(4)}$–$Te_{(4)}$–$F_{(20)}$	179.2(2)
$F_{(1)}$–$Te_{(1)}$–$F_{(2)}$	90.2(3)	$O_{(5)}$–$Te_{(5)}$–$F_{(21)}$	94.0(2)
$F_{(1)}$–$Te_{(1)}$–$F_{(3)}$	168.8(2)	$O_{(5)}$–$Te_{(5)}$–$F_{(22)}$	96.0(2)
$F_{(2)}$–$Te_{(1)}$–$F_{(4)}$	166.5(2)	$O_{(5)}$–$Te_{(5)}$–$F_{(23)}$	97.3(2)
$F_{(1)}$–$Te_{(1)}$–$F_{(4)}$	90.6(3)	$O_{(5)}$–$Te_{(5)}$–$F_{(24)}$	95.0(2)
$F_{(2)}$–$Te_{(1)}$–$F_{(3)}$	88.6(3)	$O_{(5)}$–$Te_{(5)}$–$F_{(25)}$	177.3(2)
$F_{(3)}$–$Te_{(1)}$–$F_{(4)}$	88.0(3)		
$F_{(10)}$–$Te_{(2)}$–$F_{(6)}$	84.2(2)	$F_{(20)}$–$Te_{(4)}$–$F_{(16)}$	84.7(2)
$F_{(10)}$–$Te_{(2)}$–$F_{(7)}$	84.6(3)	$F_{(20)}$–$Te_{(4)}$–$F_{(17)}$	84.1(2)
$F_{(10)}$–$Te_{(2)}$–$F_{(8)}$	85.1(3)	$F_{(20)}$–$Te_{(4)}$–$F_{(18)}$	85.0(2)
$F_{(10)}$–$Te_{(2)}$–$F_{(9)}$	84.3(3)	$F_{(20)}$–$Te_{(4)}$–$F_{(19)}$	85.7(2)
$F_{(6)}$–$Te_{(2)}$–$F_{(7)}$	88.8(2)	$F_{(16)}$–$Te_{(4)}$–$F_{(17)}$	90.3(2)
$F_{(6)}$–$Te_{(2)}$–$F_{(8)}$	169.2(3)	$F_{(16)}$–$Te_{(4)}$–$F_{(18)}$	169.6(2)
$F_{(7)}$–$Te_{(2)}$–$F_{(9)}$	168.7(3)	$F_{(17)}$–$Te_{(4)}$–$F_{(19)}$	169.8(2)
$F_{(6)}$–$Te_{(2)}$–$F_{(9)}$	88.1(2)	$F_{(16)}$–$Te_{(4)}$–$F_{(19)}$	88.4(2)
$F_{(7)}$–$Te_{(2)}$–$F_{(8)}$	90.5(2)	$F_{(17)}$–$Te_{(4)}$–$F_{(18)}$	90.2(2)
$F_{(8)}$–$Te_{(2)}$–$F_{(9)}$	90.5(2)	$F_{(18)}$–$Te_{(4)}$–$F_{(19)}$	89.4(2)
$F_{(15)}$–$Te_{(3)}$–$F_{(11)}$	83.5(2)	$F_{(25)}$–$Te_{(5)}$–$F_{(21)}$	83.3(2)
$F_{(15)}$–$Te_{(3)}$–$F_{(12)}$	83.9(2)	$F_{(25)}$–$Te_{(5)}$–$F_{(22)}$	84.0(3)
$F_{(15)}$–$Te_{(3)}$–$F_{(13)}$	84.6(2)	$F_{(25)}$–$Te_{(5)}$–$F_{(23)}$	85.4(2)
$F_{(15)}$–$Te_{(3)}$–$F_{(14)}$	83.8(2)	$F_{(25)}$–$Te_{(5)}$–$F_{(24)}$	84.9(2)
$F_{(11)}$–$Te_{(3)}$–$F_{(12)}$	87.7(2)	$F_{(21)}$–$Te_{(5)}$–$F_{(22)}$	89.0(2)
$F_{(11)}$–$Te_{(3)}$–$F_{(13)}$	167.9(2)	$F_{(21)}$–$Te_{(5)}$–$F_{(23)}$	168.7(2)
$F_{(12)}$–$Te_{(3)}$–$F_{(14)}$	167.6(2)	$F_{(22)}$–$Te_{(5)}$–$F_{(24)}$	168.9(2)
$F_{(11)}$–$Te_{(3)}$–$F_{(14)}$	89.6(2)	$F_{(21)}$–$Te_{(5)}$–$F_{(24)}$	88.7(2)
$F_{(12)}$–$Te_{(3)}$–$F_{(13)}$	89.1(2)	$F_{(22)}$–$Te_{(5)}$–$F_{(23)}$	89.3(2)
$F_{(13)}$–$Te_{(3)}$–$F_{(14)}$	91.0(2)	$F_{(23)}$–$Te_{(5)}$–$F_{(24)}$	90.9(2)
$C_{(1)}$–$N_{(1)}$–$C_{(2)}$	110.2(6)	$C_{(9)}$–$N_{(1)}$–$C_{(10)}$	107.4(6)

Table S4.2. continued…

$C_{(1)}–N_{(1)}–C_{(3)}$	109.2(5)	$C_{(9)}–N_{(1)}–C_{(11)}$	109.8(5)
$C_{(1)}–N_{(1)}–C_{(4)}$	108.7(5)	$C_{(9)}–N_{(1)}–C_{(12)}$	109.8(5)
$C_{(2)}–N_{(1)}–C_{(3)}$	109.0(5)	$C_{(10)}–N_{(1)}–C_{(11)}$	109.4(5)
$C_{(2)}–N_{(1)}–C_{(4)}$	110.7(5)	$C_{(10)}–N_{(1)}–C_{(12)}$	109.0(5)
$C_{(3)}–N_{(1)}–C_{(4)}$	109.1(5)	$C_{(11)}–N_{(1)}–C_{(12)}$	111.5(6)
$C_{(5)}–N_{(1)}–C_{(6)}$	109.1(6)		
$C_{(5)}–N_{(1)}–C_{(7)}$	109.7(5)		
$C_{(5)}–N_{(1)}–C_{(8)}$	109.8(6)		
$C_{(6)}–N_{(1)}–C_{(7)}$	110.4(6)		
$C_{(6)}–N_{(1)}–C_{(8)}$	108.4(6)		
$C_{(7)}–N_{(1)}–C_{(8)}$	109.5(6)		

[a] The atom numbers are subscripted in parentheses, and the labeling scheme corresponds to that used in Figure 4.2 and Figure S4.3. [b] The subscripted letters refer to another asymmetric unit.

Table S4.3. Complete List of Experimental Geometrical Parameters for $[N(CH_3)_4]_2[Hg_2(OTeF_5)_6]$ [a]

Bond Lengths (Å)			
$Hg_{(1)}–O_{(4)}$	2.040(4)	$Hg_{(2)}–O_{(1)}$	2.075(4)
$Hg_{(1)}–O_{(3)}$	2.062(4)	$Hg_{(2)}–O_{(6)}$	2.104(5)
$Hg_{(1)}–O_{(5)}$	2.486(4)	$Hg_{(2)}–O_{(5)}$	2.350(4)
$Hg_{(1)}–O_{(2)}$	2.508(4)	$Hg_{(2)}–O_{(2)}$	2.416(4)
$Hg_{(1)}---F_{(4A)}$ [b]	2.850(3)	$Hg_{(2)}---F_{(18B)}$ [b]	2.813(4)
$Hg_{(1)}---F_{(11)}$	3.093(4)	$Hg_{(2)}---F_{(3)}$	3.214(4)
$Te_{(1)}–O_{(1)}$	1.816(4)	$Te_{(2)}–O_{(2)}$	1.790(4)
$Te_{(1)}–F_{(1)}$	1.848(4)	$Te_{(2)}–F_{(6)}$	1.845(3)
$Te_{(1)}–F_{(2)}$	1.842(3)	$Te_{(2)}–F_{(7)}$	1.855(4)
$Te_{(1)}–F_{(3)}$	1.848(4)	$Te_{(2)}–F_{(8)}$	1.848(3)
$Te_{(1)}–F_{(4)}$	1.854(3)	$Te_{(2)}–F_{(9)}$	1.858(3)
$Te_{(1)}–F_{(5)}$	1.836(3)	$Te_{(2)}–F_{(10)}$	1.834(4)
$Te_{(3)}–O_{(3)}$	1.821(4)	$Te_{(5)}–O_{(5)}$	1.802(4)
$Te_{(3)}–F_{(11)}$	1.849(4)	$Te_{(5)}–F_{(21)}$	1.844(4)
$Te_{(3)}–F_{(12)}$	1.833(4)	$Te_{(5)}–F_{(22)}$	1.846(4)
$Te_{(3)}–F_{(13)}$	1.828(3)	$Te_{(5)}–F_{(23)}$	1.836(4)
$Te_{(3)}–F_{(14)}$	1.834(4)	$Te_{(5)}–F_{(24)}$	1.841(4)
$Te_{(3)}–F_{(15)}$	1.834(4)	$Te_{(5)}–F_{(25)}$	1.838(4)
$Te_{(4)}–O_{(4)}$	1.812(4)	$Te_{(6)}–O_{(6)}$	1.809(5)
$Te_{(4)}–F_{(16)}$	1.836(3)	$Te_{(6)}–F_{(26A)}$	1.856(6)
$Te_{(4)}–F_{(17)}$	1.847(3)	$Te_{(6)}–F_{(27A)}$	1.872(6)
$Te_{(4)}–F_{(18)}$	1.842(4)	$Te_{(6)}–F_{(28A)}$	1.832(7)
$Te_{(4)}–F_{(19)}$	1.825(3)	$Te_{(6)}–F_{(29A)}$	1.815(6)
$Te_{(4)}–F_{(20)}$	1.831(4)	$Te_{(6)}–F_{(26B)}$	1.801(7)
		$Te_{(6)}–F_{(27B)}$	1.827(6)
		$Te_{(6)}–F_{(28B)}$	1.878(7)
		$Te_{(6)}–F_{(29B)}$	1.840(6)
$N_{(1)}–C_{(1)}$	1.496(8)	$Te_{(6)}–F_{(30)}$	1.830(4)
$N_{(1)}–C_{(2)}$	1.5030(8)		
$N_{(1)}–C_{(3)}$	1.499(8)	$C_{(1)}H_3---F_{(3)}$	3.375(8)
$N_{(1)}–C_{(4)}$	1.502(8)	$C_{(3)}H_3---F_{(7)}$	3.169(8)
$N_{(2)}–C_{(5)}$	1.494(8)	$C_{(3)}H_3---F_{(1)}$	3.248(7)
$N_{(2)}–C_{(6A)}$	1.451(11)	$C_{(3)}H_3---F_{(10)}$	3.332(7)
$N_{(2)}–C_{(7A)}$	1.496(11)	$C_{(3)}H_3---F_{(5)}$	3.389(8)
$N_{(2)}–C_{(8A)}$	1.536(11)	$C_{(5)}H_3---F_{(22)}$	3.089(7)
$N_{(2)}–C_{(6B)}$	1.483(11)	$C_{(2)}H_3---F_{(11)}$	2.949(8)
$N_{(2)}–C_{(7B)}$	1.453(11)	$C_{(4)}H_3---F_{(2)}$	3.249(7)
$N_{(2)}–C_{(8B)}$	1.522(10)	$C_{(4)}H_3---F_{(1)}$	3.359(7)

Table S4.3. continued…

Bond Angles (deg)			
$O_{(2)}$–$Hg_{(1)}$–$O_{(5)}$	70.0(1)	$O_{(2)}$–$Hg_{(2)}$–$O_{(5)}$	73.9(1)
$Hg_{(1)}$–$O_{(2)}$–$Hg_{(2)}$	102.1(1)	$Hg_{(1)}$–$O_{(5)}$–$Hg_{(2)}$	104.7(2)
$O_{(3)}$–$Hg_{(1)}$–$O_{(4)}$	174.1(2)	$O_{(1)}$–$Hg_{(2)}$–$O_{(6)}$	157.0(2)
$O_{(3)}$–$Hg_{(1)}$–$O_{(2)}$	85.4(2)	$O_{(1)}$–$Hg_{(2)}$–$O_{(2)}$	99.2(2)
$O_{(3)}$–$Hg_{(1)}$–$O_{(5)}$	87.2(2)	$O_{(1)}$–$Hg_{(2)}$–$O_{(5)}$	108.6(2)
$O_{(4)}$–$Hg_{(1)}$–$O_{(2)}$	98.3(2)	$O_{(6)}$–$Hg_{(2)}$–$O_{(2)}$	93.7(2)
$O_{(4)}$–$Hg_{(1)}$–$O_{(5)}$	98.4(2)	$O_{(6)}$–$Hg_{(2)}$–$O_{(5)}$	93.2(2)
$Hg_{(1)}$–$O_{(2)}$–$Te_{(2)}$	121.0(2)	$Hg_{(2)}$–$O_{(1)}$–$Te_{(1)}$	121.2(2)
$Hg_{(1)}$–$O_{(3)}$–$Te_{(3)}$	122.9(2)	$Hg_{(2)}$–$O_{(2)}$–$Te_{(2)}$	128.1(2)
$Hg_{(1)}$–$O_{(4)}$–$Te_{(4)}$	128.1(2)	$Hg_{(2)}$–$O_{(5)}$–$Te_{(5)}$	129.7(2)
$Hg_{(1)}$–$O_{(5)}$–$Te_{(5)}$	121.9(2)	$Hg_{(2)}$–$O_{(6)}$–$Te_{(6)}$	122.8(2)
$O_{(3)}$–$Te_{(3)}$–$F_{(11)}$	94.6(2)	$O_{(1)}$–$Te_{(1)}$–$F_{(1)}$	92.8(2)
$O_{(3)}$–$Te_{(3)}$–$F_{(12)}$	93.9(2)	$O_{(1)}$–$Te_{(1)}$–$F_{(2)}$	93.6(2)
$O_{(3)}$–$Te_{(3)}$–$F_{(13)}$	92.1(2)	$O_{(1)}$–$Te_{(1)}$–$F_{(3)}$	94.9(2)
$O_{(3)}$–$Te_{(3)}$–$F_{(14)}$	95.6(2)	$O_{(1)}$–$Te_{(1)}$–$F_{(4)}$	94.6(2)
$O_{(3)}$–$Te_{(3)}$–$F_{(15)}$	178.7(2)	$O_{(1)}$–$Te_{(1)}$–$F_{(5)}$	179.1(2)
$F_{(15)}$–$Te_{(3)}$–$F_{(11)}$	86.5(2)	$F_{(5)}$–$Te_{(1)}$–$F_{(1)}$	86.3(2)
$F_{(15)}$–$Te_{(3)}$–$F_{(12)}$	85.5(2)	$F_{(5)}$–$Te_{(1)}$–$F_{(2)}$	86.3(2)
$F_{(15)}$–$Te_{(3)}$–$F_{(13)}$	86.7(2)	$F_{(5)}$–$Te_{(1)}$–$F_{(3)}$	86.0(2)
$F_{(15)}$–$Te_{(3)}$–$F_{(14)}$	85.0(2)	$F_{(5)}$–$Te_{(1)}$–$F_{(4)}$	85.6(2)
$F_{(11)}$–$Te_{(3)}$–$F_{(12)}$	90.1(2)	$F_{(1)}$–$Te_{(1)}$–$F_{(2)}$	90.2(2)
$F_{(11)}$–$Te_{(3)}$–$F_{(13)}$	173.2(2)	$F_{(1)}$–$Te_{(1)}$–$F_{(3)}$	172.1(2)
$F_{(12)}$–$Te_{(3)}$–$F_{(14)}$	170.5(2)	$F_{(2)}$–$Te_{(1)}$–$F_{(4)}$	171.9(2)
$F_{(11)}$–$Te_{(3)}$–$F_{(14)}$	89.2(2)	$F_{(1)}$–$Te_{(1)}$–$F_{(4)}$	89.0(2)
$F_{(12)}$–$Te_{(3)}$–$F_{(13)}$	90.1(2)	$F_{(2)}$–$Te_{(1)}$–$F_{(3)}$	91.0(2)
$F_{(13)}$–$Te_{(3)}$–$F_{(14)}$	89.5(2)	$F_{(3)}$–$Te_{(1)}$–$F_{(4)}$	88.7(2)
$O_{(4)}$–$Te_{(4)}$–$F_{(16)}$	93.5(2)	$O_{(6)}$–$Te_{(6)}$–$F_{(26A)}$	98.4(3)
$O_{(4)}$–$Te_{(4)}$–$F_{(17)}$	94.8(2)	$O_{(6)}$–$Te_{(6)}$–$F_{(27A)}$	96.5(3)
$O_{(4)}$–$Te_{(4)}$–$F_{(18)}$	95.0(2)	$O_{(6)}$–$Te_{(6)}$–$F_{(28A)}$	97.6(3)
$O_{(4)}$–$Te_{(4)}$–$F_{(19)}$	92.3(2)	$O_{(6)}$–$Te_{(6)}$–$F_{(29A)}$	98.1(3)
$O_{(4)}$–$Te_{(4)}$–$F_{(20)}$	179.0(2)	$O_{(6)}$–$Te_{(6)}$–$F_{(30)}$	178.3(2)
$F_{(20)}$–$Te_{(4)}$–$F_{(16)}$	85.6(2)	$F_{(30)}$–$Te_{(6)}$–$F_{(26A)}$	82.0(3)
$F_{(20)}$–$Te_{(4)}$–$F_{(17)}$	85.4(2)	$F_{(30)}$–$Te_{(6)}$–$F_{(27A)}$	81.8(3)
$F_{(20)}$–$Te_{(4)}$–$F_{(18)}$	85.9(2)	$F_{(30)}$–$Te_{(6)}$–$F_{(28A)}$	81.8(3)
$F_{(20)}$–$Te_{(4)}$–$F_{(19)}$	87.6(2)	$F_{(30)}$–$Te_{(6)}$–$F_{(29A)}$	83.6(3)
$F_{(16)}$–$Te_{(4)}$–$F_{(17)}$	89.9(2)	$F_{(26A)}$–$Te_{(6)}$–$F_{(27A)}$	85.8(4)
$F_{(16)}$–$Te_{(4)}$–$F_{(18)}$	171.5(2)	$F_{(26A)}$–$Te_{(6)}$–$F_{(28A)}$	163.0(4)
$F_{(17)}$–$Te_{(4)}$–$F_{(19)}$	172.9(2)	$F_{(27A)}$–$Te_{(6)}$–$F_{(29A)}$	165.4(4)
$F_{(16)}$–$Te_{(4)}$–$F_{(19)}$	90.4(2)	$F_{(26A)}$–$Te_{(6)}$–$F_{(29A)}$	90.9(5)
$F_{(17)}$–$Te_{(4)}$–$F_{(18)}$	88.7(2)	$F_{(27A)}$–$Te_{(6)}$–$F_{(28A)}$	86.8(4)
$F_{(18)}$–$Te_{(4)}$–$F_{(19)}$	89.9(2)	$F_{(28A)}$–$Te_{(6)}$–$F_{(29A)}$	86.8(4)
$O_{(2)}$–$Te_{(2)}$–$F_{(6)}$	94.4(2)	$O_{(6)}$–$Te_{(6)}$–$F_{(26B)}$	89.4(4)
$O_{(2)}$–$Te_{(2)}$–$F_{(7)}$	94.6(2)	$O_{(6)}$–$Te_{(6)}$–$F_{(27B)}$	88.5(3)
$O_{(2)}$–$Te_{(2)}$–$F_{(8)}$	96.0(2)	$O_{(6)}$–$Te_{(6)}$–$F_{(28B)}$	93.4(3)

Table S4.3. continued…

$O_{(2)}$–$Te_{(2)}$–$F_{(9)}$	93.9(2)	$O_{(6)}$–$Te_{(6)}$–$F_{(29B)}$	92.1(3)
$O_{(2)}$–$Te_{(2)}$–$F_{(10)}$	178.9(2)	$O_{(6)}$–$Te_{(6)}$–$F_{(30)}$	178.3(2)
$F_{(10)}$–$Te_{(2)}$–$F_{(6)}$	84.5(2)	$F_{(30)}$–$Te_{(6)}$–$F_{(26B)}$	90.1(3)
$F_{(10)}$–$Te_{(2)}$–$F_{(7)}$	85.7(2)	$F_{(30)}$–$Te_{(6)}$–$F_{(27B)}$	89.9(3)
$F_{(10)}$–$Te_{(2)}$–$F_{(8)}$	85.1(2)	$F_{(30)}$–$Te_{(6)}$–$F_{(28B)}$	87.2(3)
$F_{(10)}$–$Te_{(2)}$–$F_{(9)}$	85.8(2)	$F_{(30)}$–$Te_{(6)}$–$F_{(29B)}$	89.6(3)
$F_{(6)}$–$Te_{(2)}$–$F_{(7)}$	90.8(2)	$F_{(26B)}$–$Te_{(6)}$–$F_{(27B)}$	91.9(4)
$F_{(6)}$–$Te_{(2)}$–$F_{(8)}$	169.6(2)	$F_{(26B)}$–$Te_{(6)}$–$F_{(28B)}$	177.1(4)
$F_{(7)}$–$Te_{(2)}$–$F_{(9)}$	171.5(2)	$F_{(27B)}$–$Te_{(6)}$–$F_{(29B)}$	174.5(5)
$F_{(6)}$–$Te_{(2)}$–$F_{(9)}$	89.8(2)	$F_{(26B)}$–$Te_{(6)}$–$F_{(29B)}$	93.6(5)
$F_{(7)}$–$Te_{(2)}$–$F_{(8)}$	88.9(2)	$F_{(27B)}$–$Te_{(6)}$–$F_{(28B)}$	87.3(4)
$F_{(8)}$–$Te_{(2)}$–$F_{(9)}$	89.0(2)	$F_{(28B)}$–$Te_{(6)}$–$F_{(29B)}$	87.2(4)
$O_{(2)}$–$Hg_{(1)}$---$F_{(4)}$	124.0(1)	$O_{(5)}$–$Te_{(5)}$–$F_{(21)}$	92.9(2)
$O_{(5)}$–$Hg_{(1)}$---$F_{(4)}$	158.0(1)	$O_{(5)}$–$Te_{(5)}$–$F_{(22)}$	94.6(2)
$O_{(3)}$–$Hg_{(1)}$---$F_{(4)}$	78.1(1)	$O_{(5)}$–$Te_{(5)}$–$F_{(23)}$	95.7(2)
$O_{(4)}$–$Hg_{(1)}$---$F_{(4)}$	96.0(1)	$O_{(5)}$–$Te_{(5)}$–$F_{(24)}$	94.9(2)
$O_{(2)}$–$Hg_{(1)}$---$F_{(11)}$	130.6(1)	$O_{(5)}$–$Te_{(5)}$–$F_{(25)}$	178.2(2)
$O_{(5)}$–$Hg_{(1)}$---$F_{(11)}$	74.6(1)	$F_{(25)}$–$Te_{(5)}$–$F_{(21)}$	85.2(2)
$O_{(3)}$–$Hg_{(1)}$---$F_{(11)}$	59.2(1)	$F_{(25)}$–$Te_{(5)}$–$F_{(22)}$	85.4(2)
$O_{(4)}$–$Hg_{(1)}$---$F_{(11)}$	120.4(2)	$F_{(25)}$–$Te_{(5)}$–$F_{(23)}$	86.2(2)
$O_{(2)}$–$Hg_{(2)}$---$F_{(18)}$	64.7(1)	$F_{(25)}$–$Te_{(5)}$–$F_{(24)}$	85.1(2)
$O_{(5)}$–$Hg_{(2)}$---$F_{(18)}$	21.8(1)	$F_{(21)}$–$Te_{(5)}$–$F_{(22)}$	89.4(2)
$O_{(1)}$–$Hg_{(2)}$---$F_{(18)}$	33.4(1)	$F_{(21)}$–$Te_{(5)}$–$F_{(23)}$	171.3(2)
$O_{(6)}$–$Hg_{(2)}$---$F_{(18)}$	40.7(1)	$F_{(22)}$–$Te_{(5)}$–$F_{(24)}$	170.5(2)
$C_{(1)}$–$N_{(1)}$–$C_{(2)}$	110.0(5)	$F_{(21)}$–$Te_{(5)}$–$F_{(24)}$	89.6(2)
$C_{(1)}$–$N_{(1)}$–$C_{(3)}$	109.3(5)	$F_{(22)}$–$Te_{(5)}$–$F_{(23)}$	88.9(2)
$C_{(1)}$–$N_{(1)}$–$C_{(4)}$	109.2(5)	$F_{(23)}$–$Te_{(5)}$–$F_{(24)}$	90.8(2)
$C_{(2)}$–$N_{(1)}$–$C_{(3)}$	110.0(5)	$C_{(5)}$–$N_{(2)}$–$C_{(6B)}$	106.2(7)
$C_{(2)}$–$N_{(1)}$–$C_{(4)}$	109.2(5)	$C_{(5)}$–$N_{(2)}$–$C_{(7B)}$	110.6(7)
$C_{(3)}$–$N_{(1)}$–$C_{(4)}$	109.1(5)	$C_{(5)}$–$N_{(2)}$–$C_{(8B)}$	110.4(7)
$C_{(5)}$–$N_{(2)}$–$C_{(6A)}$	114.5(7)	$C_{(6B)}$–$N_{(2)}$–$C_{(7B)}$	111.9(9)
$C_{(5)}$–$N_{(2)}$–$C_{(7A)}$	111.6(7)	$C_{(6B)}$–$N_{(2)}$–$C_{(8B)}$	105.6(8)
$C_{(5)}$–$N_{(2)}$–$C_{(8A)}$	106.3(7)	$C_{(7B)}$–$N_{(2)}$–$C_{(8B)}$	111.9(8)
$C_{(6A)}$–$N_{(2)}$–$C_{(7A)}$	111.4(8)		
$C_{(6A)}$–$N_{(2)}$–$C_{(8A)}$	108.4(8)		
$C_{(7A)}$–$N_{(2)}$–$C_{(8A)}$	104.0(8)		
Dihedral Angles (deg)			
$Te_{(3)}$–$O_{(3)}$–$Hg_{(1)}$–$O_{(4)}$–$Te_{(4)}$	122.3(3)	$Te_{(1)}$–$O_{(1)}$–$Hg_{(2)}$–$O_{(6)}$–$Te_{(6)}$	34.7(5)

[a] The atom numbers are subscripted in parentheses, and the labeling scheme corresponds to that used in Figure 4.3. [b] The subscripted letters refer to another asymmetric unit. Cs–F contacts involving disordered atoms are not included.

Table S4.4. Complete List of Experimental Geometrical Parameters for $Cs_2[Hg(OTeF_5)_4]\cdot Hg(OTeF_5)_2$ [a]

Bond Lengths (Å)			
$Hg_{(1)}–O_{(2)}$	2.058(2)	$Te_{(1)}–F_{(1)}$	1.846(1)
$Hg_{(1)}---O_{(3)}$	2.555(1)	$Te_{(1)}–F_{(2)}$	1.841(1)
$Hg_{(1)}---O_{(1)}$	2.737(1)	$Te_{(1)}–F_{(3)}$	1.846(1)
$Hg_{(2)}–O_{(1)}$	2.186(1)	$Te_{(1)}–F_{(4)}$	1.865(1)
$Hg_{(2)}–O_{(3)}$	2.287(1)	$Te_{(1)}–F_{(5)}$	1.842(1)
$Hg_{(2)}---F_{(6)}$	2.731(1)	$Te_{(2)}–F_{(6)}$	1.856(1)
$Te_{(1)}–O_{(1)}$	1.816(1)	$Te_{(2)}–F_{(7)}$	1.844(1)
$Te_{(2)}–O_{(2)}$	1.808(2)	$Te_{(2)}–F_{(8)}$	1.843(1)
$Te_{(3)}–O_{(3)}$	1.798(1)	$Te_{(2)}–F_{(9)}$	1.845(1)
		$Te_{(2)}–F_{(10)}$	1.838(1)
$Cs_{(1)}---F_{(4)}$	3.316(1)	$Te_{(3)}–F_{(11)}$	1.842(1)
$Cs_{(1)}---F_{(15)}$	3.174(1)	$Te_{(3)}–F_{(12)}$	1.853(1)
$Cs_{(1)}---F_{(5)}$	3.213(1)	$Te_{(3)}–F_{(13)}$	1.863(1)
$Cs_{(1)}---F_{(13)}$	3.340(1)	$Te_{(3)}–F_{(14)}$	1.845(1)
$Cs_{(1A)}---F_{(12)}$	3.076(1)	$Te_{(3)}–F_{(15)}$	1.843(1)
$Cs_{(1A)}---F_{(10)}$	3.128(1)		
$Cs_{(1A)}---F_{(8)}$	3.329(1)		
$Cs_{(1A)}---F_{(7)}$	3.347(1)		
$Cs_{(1A)}---F_{(3)}$	3.360(1)		
Bond Angles (deg)			
$O_{(1)}---Hg_{(1)}---O_{(1A)}$	180.0(1)	$O_{(1)}–Hg_{(2)}–O_{(3)}$	110.4(1)
$O_{(2)}–Hg_{(1)}–O_{(2A)}$	180.0(1)	$O_{(1)}–Hg_{(2)}–O_{(3A)}$	81.4(1)
$O_{(3)}---Hg_{(1)}---O_{(3A)}$	180.0	$O_{(1)}–Hg_{(2)}–O_{(1A)}$	147.8(1)
$O_{(3)}---Hg_{(1)}---O_{(1A)}$	66.8(1)	$O_{(3A)}–Hg_{(2)}–O_{(3)}$	137.9(1)
$O_{(3)}---Hg_{(1)}---O_{(1)}$	113.2(1)	$F_{(6)}---Hg_{(2)}–O_{(3)}$	74.0(1)
$O_{(2)}–Hg_{(1)}---O_{(3)}$	86.7(1)	$F_{(6)}---Hg_{(2)}–O_{(1A)}$	137.6(1)
$O_{(2)}–Hg_{(1)}---O_{(3A)}$	93.2(1)	$F_{(6)}---Hg_{(2)}–O_{(1)}$	74.3(1)
$O_{(2)}–Hg_{(1)}---O_{(1)}$	106.6(1)	$F_{(6)}---Hg_{(2)}–O_{(3A)}$	70.7(1)
$O_{(2)}–Hg_{(1)}---O_{(1A)}$	73.4(1)	$F_{(6)}---Hg_{(2)}---F_{(6A)}$	65.2(1)
$Hg_{(1)}–O_{(2)}–Te_{(2)}$	131.2(1)	$Hg_{(2)}–O_{(3)}–Te_{(3)}$	31.1(1)
$Hg_{(1)}---O_{(3)}–Te_{(3)}$	116.7(1)	$Hg_{(2)}–O_{(1)}–Te_{(1)}$	116.7(1)
$Hg_{(1)}---O_{(1)}–Te_{(1)}$	133.7(1)	$Hg_{(2)}---F_{(6)}–Te_{(2)}$	62.1(1)
$Hg_{(1)}---O_{(1)}–Hg_{(2)}$	103.3(1)	$Hg_{(2)}---F_{(6A)}–Te_{(2A)}$	154.4(1)
$Hg_{(1)}---O_{(3)}–Hg_{(2)}$	106.3(1)		
$O_{(1)}–Te_{(1)}–F_{(1)}$	95.3(1)	$O_{(2)}–Te_{(2)}–F_{(6)}$	96.4(1)
$O_{(1)}–Te_{(1)}–F_{(2)}$	96.9(1)	$O_{(2)}–Te_{(2)}–F_{(7)}$	94.8(1)
$O_{(1)}–Te_{(1)}–F_{(3)}$	93.9(1)	$O_{(2)}–Te_{(2)}–F_{(8)}$	91.2(1)
$O_{(1)}–Te_{(1)}–F_{(4)}$	92.6(1)	$O_{(2)}–Te_{(2)}–F_{(9)}$	94.4(1)
$O_{(1)}–Te_{(1)}–F_{(5)}$	176.2(1)	$O_{(2)}–Te_{(2)}–F_{(10)}$	178.2(1)
$O_{(3)}–Te_{(3)}–F_{(11)}$	97.2(1)	$F_{(10)}–Te_{(2)}–F_{(6)}$	85.4(1)
$O_{(3)}–Te_{(3)}–F_{(12)}$	94.3(1)	$F_{(10)}–Te_{(2)}–F_{(7)}$	85.6(1)
$O_{(3)}–Te_{(3)}–F_{(13)}$	91.8(1)	$F_{(10)}–Te_{(2)}–F_{(8)}$	87.0(1)

Table S4.4. continued…

$O_{(3)}$–$Te_{(3)}$–$F_{(14)}$	96.7(1)	$F_{(10)}$–$Te_{(2)}$–$F_{(9)}$	85.3(1)
$O_{(3)}$–$Te_{(3)}$–$F_{(15)}$	175.4(1)	$F_{(6)}$–$Te_{(2)}$–$F_{(7)}$	89.4(1)
$F_{(5)}$–$Te_{(1)}$–$F_{(1)}$	85.7(1)	$F_{(6)}$–$Te_{(2)}$–$F_{(8)}$	172.4(1)
$F_{(5)}$–$Te_{(1)}$–$F_{(2)}$	86.8(1)	$F_{(7)}$–$Te_{(2)}$–$F_{(9)}$	170.8(1)
$F_{(5)}$–$Te_{(1)}$–$F_{(3)}$	85.1(1)	$F_{(6)}$–$Te_{(2)}$–$F_{(9)}$	88.8(1))
$F_{(5)}$–$Te_{(1)}$–$F_{(4)}$	83.8(1)	$F_{(7)}$–$Te_{(2)}$–$F_{(8)}$	89.3(1)
$F_{(1)}$–$Te_{(1)}$–$F_{(2)}$	89.5(1)	$F_{(8)}$–$Te_{(2)}$–$F_{(9)}$	91.3(1)
$F_{(1)}$–$Te_{(1)}$–$F_{(3)}$	170.8(1)	$F_{(15)}$–$Te_{(3)}$–$F_{(11)}$	87.3(1)
$F_{(2)}$–$Te_{(1)}$–$F_{(4)}$	170.4(1)	$F_{(15)}$–$Te_{(3)}$–$F_{(12)}$	84.4(1)
$F_{(1)}$–$Te_{(1)}$–$F_{(4)}$	88.4(1)	$F_{(15)}$–$Te_{(3)}$–$F_{(13)}$	83.8(1)
$F_{(2)}$–$Te_{(1)}$–$F_{(3)}$	89.7(1)	$F_{(15)}$–$Te_{(3)}$–$F_{(14)}$	84.5(1)
$F_{(3)}$–$Te_{(1)}$–$F_{(4)}$	90.9(1)	$F_{(11)}$–$Te_{(3)}$–$F_{(12)}$	89.3(1)
		$F_{(11)}$–$Te_{(3)}$–$F_{(13)}$	171.1(1)
		$F_{(12)}$–$Te_{(3)}$–$F_{(14)}$	169.0(1)
		$F_{(11)}$–$Te_{(3)}$–$F_{(14)}$	90.5(1)
		$F_{(12)}$–$Te_{(3)}$–$F_{(13)}$	90.3(1)
		$F_{(13)}$–$Te_{(3)}$–$F_{(14)}$	88.2(1)
Dihedral Angles (deg)			
$Te_{(2)}$–$O_{(2)}$–$Hg_{(1)}$–$O_{(2A)}$–$Te_{(2A)}$	180.0	$Te_{(1)}$–$O_{(1)}$–$Hg_{(2)}$–$O_{(3)}$–$Te_{(3)}$	65.0(1)
$Te_{(3)}$–$O_{(3)}$---$Hg_{(1)}$---$O_{(3A)}$–$Te_{(3A)}$	180.0		
$Te_{(1)}$–$O_{(1)}$---$Hg_{(1)}$---$O_{(1A)}$–$Te_{(1A)}$	180.0		

[a] The atom numbers are subscripted in parentheses, and the labeling scheme corresponds to that used in Figure 4.4.

Table S4.5. Complete List of Experimental Geometrical Parameters for $\{Cs_3[Hg_2(OTeF_5)_7]\cdot Hg(OTeF_5)_2\}\cdot 4SO_2ClF$ [a]

Bond Lengths (Å) [b]			
$Hg_{(1)}-O_{(4)}$	2.059(5)	$Te_{(2)}-F_{(6)}$	1.852(5)
$Hg_{(1)}-O_{(5)}$	2.073(5)	$Te_{(2)}-F_{(7)}$	1.836(5)
$Hg_{(1)}\cdots O_{(6)}$	2.605(5)	$Te_{(2)}-F_{(8)}$	1.846(5)
$Hg_{(1)}\cdots O_{(7)}$	2.529(5)	$Te_{(2)}-F_{(9)}$	1.837(5)
$Hg_{(1)}\cdots O_{(8)}$	2.653(5)	$Te_{(2)}-F_{(10)}$	1.840(5)
$Hg_{(1)}\cdots O_{(2)}$	2.737(5)	$Te_{(3)}-F_{(11)}$	1.842(4)
		$Te_{(3)}-F_{(12)}$	1.848(5)
$Hg_{(2)}-O_{(1)}$	2.169(5)	$Te_{(3)}-F_{(13)}$	1.852(5)
$Hg_{(2)}-O_{(2)}$	2.156(5)	$Te_{(3)}-F_{(14)}$	1.840(5)
$Hg_{(2)}-O_{(3)}$	2.356(5)	$Te_{(3)}-F_{(15)}$	1.834(5)
$Hg_{(2)}-O_{(7)}$	2.359(5)	$Te_{(4)}-F_{(16)}$	1.860(5)
$Hg_{(2)}\cdots O_{(9)}$	2.680(5)	$Te_{(4)}-F_{(17)}$	1.838(5)
$Hg_{(2)}\cdots F_{(16)}$	2.668(5)	$Te_{(4)}-F_{(18)}$	1.828(5)
		$Te_{(4)}-F_{(19)}$	1.837(5)
$Hg_{(3)}-O_{(9)}$	2.211(5)	$Te_{(4)}-F_{(20)}$	1.832(5)
$Hg_{(3)}-O_{(8)}$	2.234(5)	$Te_{(5)}-F_{(21)}$	1.859(5)
$Hg_{(3)}-O_{(6)}$	2.266(5)	$Te_{(5)}-F_{(22)}$	1.830(5)
$Hg_{(3)}-O_{(3)}$	2.369(5)	$Te_{(5)}-F_{(23)}$	1.851(5)
$Hg_{(3)}\cdots O_{(1)}$	2.631(5)	$Te_{(5)}-F_{(24)}$	1.844(6)
$Hg_{(3)}\cdots F_{(21)}$	2.675(5)	$Te_{(5)}-F_{(25)}$	1.841(5)
		$Te_{(6)}-F_{(26)}$	1.836(5)
$Te_{(1)}-O_{(1)}$	1.816(5)	$Te_{(6)}-F_{(27)}$	1.840(5)
$Te_{(2)}-O_{(2)}$	1.816(5)	$Te_{(6)}-F_{(28)}$	1.849(5)
$Te_{(3)}-O_{(3)}$	1.815(5)	$Te_{(6)}-F_{(29)}$	1.857(5)
$Te_{(4)}-O_{(4)}$	1.802(5)	$Te_{(6)}-F_{(30)}$	1.843(5)
$Te_{(5)}-O_{(5)}$	1.801(5)	$Te_{(7)}-F_{(31)}$	1.856(4)
$Te_{(6)}-O_{(6)}$	1.813(5)	$Te_{(7)}-F_{(32)}$	1.852(5)
$Te_{(7)}-O_{(7)}$	1.811(5)	$Te_{(7)}-F_{(33)}$	1.844(5)
$Te_{(8)}-O_{(8)}$	1.804(5)	$Te_{(7)}-F_{(34)}$	1.844(5)
$Te_{(9)}-O_{(9)}$	1.802(5)	$Te_{(7)}-F_{(35)}$	1.8530(5)
		$Te_{(8)}-F_{(36)}$	1.852(5)
$Te_{(1)}-F_{(1)}$	1.857(5)	$Te_{(8)}-F_{(37)}$	1.848(5)
$Te_{(1)}-F_{(2)}$	1.837(5)	$Te_{(8)}-F_{(38)}$	1.851(5)
$Te_{(1)}-F_{(3)}$	1.840(5)	$Te_{(8)}-F_{(38)}$	1.828(6)
$Te_{(1)}-F_{(4)}$	1.836(5)	$Te_{(8)}-F_{(40)}$	1.847(5)
$Te_{(1)}-F_{(5)}$	1.837(5)	$Te_{(9)}-F_{(41)}$	1.842(5)
		$Te_{(9)}-F_{(42)}$	1.845(5)
S−O	1.367(7)− 1.408(7)	$Te_{(9)}-F_{(43)}$	1.839(5)
S−Cl	1.929(4) − 1.956(7)	$Te_{(9)}-F_{(44)}$	1.847(6)
S−F	1.546(7)−1.625(7)	$Te_{(9)}-F_{(45)}$	1.838(5)

Table S4.5. continued…

$Cl_{(1)}$---$F_{(14)}$	3.170(9)		
$Cl_{(1)}$---$F_{(10)}$	3.120(6)	$Cl_{(12)}$---$F_{(8)}$	3.170(6)
$Cl_{(14)}$---$F_{(34)}$	3.032(6)	$Cl_{(12)}$---$F_{(10)}$	3.120(6)
$Cl_{(14)}$---$F_{(2)}$	3.186(7)	$Cl_{(12)}$---$F_{(43)}$	3.157(6)
$Cs_{(1)}$---$F_{(31)}$	3.280(5)	$Cs_{(2)}$---$F_{(36)}$	3.251(5)
$Cs_{(1)}$---$F_{(35)}$	3.283(5)	$Cs_{(2)}$---$F_{(17)}$	3.070(5)
$Cs_{(1)}$---$F_{(28)}$	3.002(5)	$Cs_{(2)}$---$F_{(9)}$	3.265(5)
$Cs_{(1)}$---$O_{(10)}$	3.234(7)	$Cs_{(2)}$---$F_{(41)}$	3.134(5)
$Cs_{(1)}$---$O_{(11)}$	3.073(8)	$Cs_{(2)}$---$F_{(40)}$	3.323(5)
$Cs_{(1A)}$---$F_{(12)}$	3.068(5)	$Cs_{(2A)}$---$F_{(42)}$	3.318(5)
$Cs_{(1A)}$---$F_{(33)}$	3.189(5)	$Cs_{(2B)}$---$F_{(29)}$	3.085(5)
$Cs_{(1A)}$---$F_{(3)}$	3.212(5)	$Cs_{(2B)}$---$F_{(18)}$	3.112(5)
$Cs_{(1B)}$---$F_{(11)}$	3.393(5)	$Cs_{(2B)}$---$O_{(13)}$	3.151(8)
$Cs_{(1C)}$---$F_{(25)}$	3.034(5)	$Cs_{(2B)}$---$O_{(17)}$	3.073(9)
$Cs_{(1C)}$---$O_{(14)}$	3.100(6)		
$Cs_{(3)}$---$F_{(38)}$	3.108(5)	$Cs_{(4)}$---$F_{(6)}$	3.146(5)
$Cs_{(3)}$---$O_{(12)}$	3.168(8)	$Cs_{(4)}$---$F_{(32)}$	3.227(5)
$Cs_{(3A)}$---$F_{(38)}$	3.108(5)	$Cs_{(4)}$---$F_{(13)}$	3.394(5)
$Cs_{(3A)}$---$O_{(12)}$	3.168(8)	$Cs_{(4)}$---$F_{(23)}$	3.014(5)
$Cs_{(3B)}$---$F_{(1)}$	3.134(5)	$Cs_{(4)}$---$O_{(15)}$	3.126(7)
$Cs_{(3B)}$---$F_{(20)}$	3.212(5)	$Cs_{(4A)}$---$F_{(32)}$	3.227(5)
$Cs_{(3B)}$---$F_{(44)}$	3.247(5)	$Cs_{(4A)}$---$F_{(6)}$	3.146(5)
$Cs_{(3C)}$---$F_{(1)}$	3.134(5)	$Cs_{(4A)}$---$F_{(13)}$	3.394(5)
$Cs_{(3C)}$---$F_{(44)}$	3.247(5)	$Cs_{(4A)}$---$F_{(23)}$	3.014(5)
$Cs_{(3C)}$---$F_{(20)}$	3.212(5)	$Cs_{(4A)}$---$O_{(15)}$	3.126(7)
Bond Angles (deg)			
$O_{(4)}$–$Hg_{(1)}$–$O_{(5)}$	174.7(2)	$O_{(1)}$–$Hg_{(2)}$–$O_{(2)}$	156.4(2)
$O_{(4)}$–$Hg_{(1)}$---$O_{(2)}$	96.7(2)	$O_{(1)}$–$Hg_{(2)}$–$O_{(3)}$	75.0(2)
$O_{(4)}$–$Hg_{(1)}$---$O_{(6)}$	76.2(2)	$O_{(1)}$–$Hg_{(2)}$–$O_{(7)}$	108.4(2)
$O_{(4)}$–$Hg_{(1)}$---$O_{(7)}$	102.2(2)	$O_{(1)}$–$Hg_{(2)}$---$O_{(9)}$	71.5(2)
$O_{(4)}$–$Hg_{(1)}$---$O_{(8)}$	84.9(2)	$O_{(1)}$–$Hg_{(2)}$---$F_{(16)}$	82.6(2)
$O_{(5)}$–$Hg_{(1)}$---$O_{(2)}$	81.9(2)	$O_{(2)}$–$Hg_{(2)}$–$O_{(3)}$	117.4(2)
$O_{(5)}$–$Hg_{(1)}$---$O_{(6)}$	105.9(2)	$O_{(2)}$–$Hg_{(2)}$–$O_{(7)}$	79.4(2)
$O_{(5)}$–$Hg_{(1)}$---$O_{(7)}$	81.9(2)	$O_{(2)}$–$Hg_{(2)}$---$O_{(9)}$	93.1(2)
$O_{(5)}$–$Hg_{(1)}$---$O_{(8)}$	91.4(2)	$O_{(2)}$–$Hg_{(2)}$---$F_{(16)}$	75.6(2)
$O_{(2)}$---$Hg_{(1)}$---$O_{(6)}$	169.9(2)	$O_{(3)}$–$Hg_{(2)}$–$O_{(7)}$	130.8(2)
$O_{(2)}$---$Hg_{(1)}$---$O_{(7)}$	66.4(2)	$O_{(3)}$–$Hg_{(2)}$---$O_{(9)}$	70.5(2)
$O_{(2)}$---$Hg_{(1)}$---$O_{(8)}$	119.3(2)	$O_{(3)}$–$Hg_{(2)}$---$F_{(16)}$	141.0(2)
$O_{(6)}$---$Hg_{(1)}$---$O_{(7)}$	107.8(2)	$O_{(7)}$–$Hg_{(2)}$---$O_{(9)}$	158.6(2)
$O_{(6)}$---$Hg_{(1)}$---$O_{(8)}$	67.7(2)	$O_{(7)}$–$Hg_{(2)}$---$F_{(16)}$	86.3(2)
$O_{(7)}$---$Hg_{(1)}$---$O_{(8)}$	170.7(2)	$O_{(9)}$---$Hg_{(2)}$---$F_{(16)}$	72.3(2)

Table S4.5. continued…

$O_{(9)}$–$Hg_{(3)}$–$O_{(8)}$	127.2(2)	$Hg_{(1)}$---$O_{(7)}$–$Hg_{(2)}$	103.6(2)
$O_{(9)}$–$Hg_{(3)}$–$O_{(6)}$	127.2(2)	$Hg_{(1)}$---$O_{(2)}$–$Hg_{(2)}$	102.9(2)
$O_{(9)}$–$Hg_{(3)}$–$O_{(3)}$	79.1(2)	$Hg_{(1)}$---$O_{(6)}$–$Hg_{(3)}$	104.8(2)
$O_{(9)}$–$Hg_{(3)}$---$O_{(1)}$	71.9(2)	$Hg_{(1)}$---$O_{(8)}$–$Hg_{(3)}$	104.2(2)
$O_{(9)}$–$Hg_{(3)}$---$F_{(21)}$	148.3(2)	$Hg_{(2)}$–$O_{(1)}$---$Hg_{(3)}$	134.0(2)
$O_{(8)}$)–$Hg_{(3)}$–$O_{(6)}$	81.2(2)	$Hg_{(2)}$---$O_{(9)}$–$Hg_{(3)}$	91.7(2)
$O_{(8)}$–$Hg_{(3)}$–$O_{(3)}$	149.2(2)	$Hg_{(2)}$–$O_{(3)}$–$Hg_{(3)}$	96.(2)
$O_{(8)}$–$Hg_{(3)}$---$O_{(1)}$	103.2(2)	$Hg_{(2)}$–$F_{(29)}$–$Te_{(6)}$	74.5(2)
$O_{(8)}$–$Hg_{(3)}$---$F_{(21)}$	69.1(2)	$Hg_{(3)}$–$F_{(21)}$–$Te_{(5)}$	148.7(2)
$O_{(6)}$–$Hg_{(3)}$–$O_{(3)}$	95.3(2)		
$O_{(6)}$–$Hg_{(3)}$---$O_{(1)}$	152.4(2)	$O_{(1)}$–$Te_{(1)}$–$F_{(1)}$	94.8(3)
$O_{(6)}$–$Hg_{(3)}$---$F_{(21)}$	78.3(2)	$O_{(1)}$–$Te_{(1)}$–$F_{(2)}$	95.1(2)
$O_{(3)}$–$Hg_{(3)}$---$O_{(1)}$	66.8(2)	$O_{(1)}$–$Te_{(1)}$–$F_{(3)}$	94.3(3)
$O_{(3)}$–$Hg_{(3)}$---$F_{(21)}$	80.2(2)	$O_{(1)}$–$Te_{(1)}$–$F_{(4)}$	92.6(2)
$O_{(1)}$---$Hg_{(3)}$---$F_{(21)}$	78.0(2)	$O_{(1)}$–$Te_{(1)}$–$F_{(5)}$	178.5(2)
		$O_{(2)}$–$Te_{(2)}$–$F_{(6)}$	94.7(2)
$Hg_{(1)}$---$O_{(2)}$–$Te_{(2)}$		$O_{(2)}$–$Te_{(2)}$–$F_{(7)}$	94.3(2)
$Hg_{(1)}$–$O_{(4)}$–$Te_{(4)}$	138.8(3)	$O_{(2)}$–$Te_{(2)}$–$F_{(8)}$	94.5(2)
$Hg_{(1)}$–$O_{(5)}$–$Te_{(5)}$	131.4(3)	$O_{(2)}$–$Te_{(2)}$–$F_{(9)}$	94.4(2)
$Hg_{(1)}$---$O_{(6)}$–$Te_{(6)}$	125.3(2)	$O_{(2)}$–$Te_{(2)}$–$F_{(10)}$	179.8(2)
$Hg_{(1)}$---$O_{(7)}$–$Te_{(7)}$	120.1(3)	$O_{(3)}$–$Te_{(3)}$–$F_{(11)}$	96.2(2)
$Hg_{(1)}$---$O_{(8)}$–$Te_{(8)}$	115.7(2)	$O_{(3)}$–$Te_{(3)}$–$F_{(12)}$	94.1(2)
		$O_{(3)}$–$Te_{(3)}$–$F_{(13)}$	92.1(2)
$Hg_{(2)}$–$O_{(1)}$–$Te_{(1)}$	128.(3)	$O_{(3)}$–$Te_{(3)}$–$F_{(14)}$	95.7(3)
$Hg_{(2)}$–$O_{(2)}$–$Te_{(2)}$	123.2(3)	$O_{(3)}$–$Te_{(3)}$–$F_{(15)}$	177.4(3)
$Hg_{(2)}$–$O_{(3)}$–$Te_{(3)}$	121.3(3)	$O_{(4)}$–$Te_{(4)}$–$F_{(16)}$	95.7(2)
$Hg_{(2)}$–$O_{(7)}$–$Te_{(7)}$	132.0(3)	$O_{(4)}$–$Te_{(4)}$–$F_{(17)}$	95.2(3)
$Hg_{(2)}$---$O_{(9)}$–$Te_{(9)}$		$O_{(4)}$–$Te_{(4)}$–$F_{(18)}$	91.8(2)
		$O_{(4)}$–$Te_{(4)}$–$F_{(19)}$	94.7(3)
$Hg_{(3)}$–$O_{(9)}$–$Te_{(9)}$	122.8(3)	$O_{(4)}$–$Te_{(4)}$–$F_{(20)}$	179.0(3)
$Hg_{(3)}$–$O_{(8)}$–$Te_{(8)}$	131.3(3)	$O_{(5)}$–$Te_{(5)}$–$F_{(21)}$	96.8(2)
$Hg_{(3)}$–$O_{(6)}$–$Te_{(6)}$	123.3(3)	$O_{(5)}$–$Te_{(5)}$–$F_{(22)}$	96.3(2)
$Hg_{(3)}$–$O_{(3)}$–$Te_{(3)}$	134.2(3)	$O_{(5)}$–$Te_{(5)}$–$F_{(23)}$	91.5(2)
$Hg_{(3)}$---$O_{(1)}$–$Te_{(1)}$	136.2(3)	$O_{(5)}$–$Te_{(5)}$–$F_{(24)}$	93.2(3)
		$O_{(5)}$–$Te_{(5)}$–$F_{(25)}$	177.6(3)
$F_{(5)}$–$Te_{(1)}$–$F_{(1)}$	85.6(3)	$O_{(6)}$–$Te_{(6)}$–$F_{(26)}$	93.4(2)
$F_{(5)}$–$Te_{(1)}$–$F_{(2)}$	86.4(2)	$O_{(6)}$–$Te_{(6)}$–$F_{(27)}$	93.8(2)
$F_{(5)}$–$Te_{(1)}$–$F_{(3)}$	85.4(3)	$O_{(6)}$–$Te_{(6)}$–$F_{(28)}$	94.5(2)
$F_{(5)}$–$Te_{(1)}$–$F_{(4)}$	85.9(3)	$O_{(6)}$–$Te_{(6)}$–$F_{(29)}$	95.7(2)
$F_{(1)}$–$Te_{(1)}$–$F_{(2)}$	89.4(2)	$O_{(6)}$–$Te_{(6)}$–$F_{(30)}$	179.7(3)
$F_{(1)}$–$Te_{(1)}$–$F_{(3)}$	170.9(3)	$O_{(7)}$–$Te_{(7)}$–$F_{(31)}$	94.4(2)
$F_{(2)}$–$Te_{(1)}$–$F_{(4)}$	172.3(2)	$O_{(7)}$–$Te_{(7)}$–$F_{(32)}$	95.6(2)
$F_{(1)}$–$Te_{(1)}$–$F_{(4)}$	90.1(3)	$O_{(7)}$–$Te_{(7)}$–$F_{(33)}$	94.6(2)
$F_{(2)}$–$Te_{(1)}$–$F_{(3)}$	89.0(3)	$O_{(7)}$–$Te_{(7)}$–$F_{(34)}$	96.4(3)
$F_{(3)}$–$Te_{(1)}$–$F_{(4)}$	90.3(3)	$O_{(7)}$–$Te_{(7)}$–$F_{(35)}$	179.4(3)
$F_{(10)}$–$Te_{(2)}$–$F_{(6)}$	85.4(2)	$O_{(8)}$–$Te_{(8)}$–$F_{(36)}$	93.0(2)
$F_{(10)}$–$Te_{(2)}$–$F_{(7)}$	85.9(2)	$O_{(8)}$–$Te_{(8)}$–$F_{(37)}$	95.7(2)

Table S4.5. continued…

$F_{(10)}$–$Te_{(2)}$–$F_{(8)}$	85.4(2)	$O_{(8)}$–$Te_{(8)}$–$F_{(38)}$	94.9(2)
$F_{(10)}$–$Te_{(2)}$–$F_{(9)}$	85.5(2)	$O_{(8)}$–$Te_{(8)}$–$F_{(38)}$	96.0(3)
$F_{(6)}$–$Te_{(2)}$–$F_{(7)}$	90.8(3)	$O_{(8)}$–$Te_{(8)}$–$F_{(40)}$	178.1(3)
$F_{(6)}$–$Te_{(2)}$–$F_{(8)}$	89.0(3)	$O_{(9)}$–$Te_{(9)}$–$F_{(41)}$	94.5(3)
$F_{(7)}$–$Te_{(2)}$–$F_{(9)}$	88.9(3)	$O_{(9)}$–$Te_{(9)}$–$F_{(42)}$	94.2(2)
$F_{(6)}$–$Te_{(2)}$–$F_{(9)}$	170.9(2)	$O_{(9)}$–$Te_{(9)}$–$F_{(43)}$	96.1(3)
$F_{(7)}$–$Te_{(2)}$–$F_{(8)}$	171.3(2)	$O_{(9)}$–$Te_{(9)}$–$F_{(44)}$	94.6(3)
$F_{(8)}$–$Te_{(2)}$–$F_{(9)}$	89.9(3)	$O_{(9)}$–$Te_{(9)}$–$F_{(45)}$	178.9(3)
$F_{(15)}$–$Te_{(3)}$–$F_{(11)}$	86.1(2)		
$F_{(15)}$–$Te_{(3)}$–$F_{(12)}$	84.6(3)		
$F_{(15)}$–$Te_{(3)}$–$F_{(13)}$	85.6(3)		
$F_{(15)}$–$Te_{(3)}$–$F_{(14)}$	85.6(3)		
$F_{(11)}$–$Te_{(3)}$–$F_{(12)}$	90.1(2)		
$F_{(11)}$–$Te_{(3)}$–$F_{(13)}$	171.6(2)	$F_{(35)}$–$Te_{(7)}$–$F_{(31)}$	85.2(2)
$F_{(12)}$–$Te_{(3)}$–$F_{(14)}$	170.2(3)	$F_{(35)}$–$Te_{(7)}$–$F_{(32)}$	84.0(2)
$F_{(11)}$–$Te_{(3)}$–$F_{(14)}$	89.3(2)	$F_{(35)}$–$Te_{(7)}$–$F_{(33)}$	85.8(2)
$F_{(12)}$–$Te_{(3)}$–$F_{(13)}$	90.3(2)	$F_{(35)}$–$Te_{(7)}$–$F_{(34)}$	84.1(3)
$F_{(13)}$–$Te_{(3)}$–$F_{(14)}$	88.9(2)	$F_{(31)}$–$Te_{(7)}$–$F_{(32)}$	90.2(2)
$F_{(20)}$–$Te_{(4)}$–$F_{(16)}$	85.3(2)	$F_{(31)}$–$Te_{(7)}$–$F_{(33)}$	170.8(2)
$F_{(20)}$–$Te_{(4)}$–$F_{(17)}$	85.1(2)	$F_{(32)}$–$Te_{(7)}$–$F_{(34)}$	168.0(2)
$F_{(20)}$–$Te_{(4)}$–$F_{(18)}$	87.3(2)	$F_{(31)}$–$Te_{(7)}$–$F_{(34)}$	88.1(2)
$F_{(20)}$–$Te_{(4)}$–$F_{(19)}$	85.0(3)	$F_{(32)}$–$Te_{(7)}$–$F_{(33)}$	90.7(2)
$F_{(16)}$–$Te_{(4)}$–$F_{(17)}$	89.7(2)	$F_{(33)}$–$Te_{(7)}$–$F_{(34)}$	89.1(2)
$F_{(16)}$–$Te_{(4)}$–$F_{(18)}$	172.6(2)	$F_{(40)}$–$Te_{(8)}$–$F_{(36)}$	85.3(3)
$F_{(17)}$–$Te_{(4)}$–$F_{(19)}$	170.1(2)	$F_{(40)}$–$Te_{(8)}$–$F_{(37)}$	83.3(3)
$F_{(16)}$–$Te_{(4)}$–$F_{(19)}$	89.9(3)	$F_{(40)}$–$Te_{(8)}$–$F_{(38)}$	86.8(3)
$F_{(17)}$–$Te_{(4)}$–$F_{(18)}$	89.9(3)	$F_{(40)}$–$Te_{(8)}$–$F_{(39)}$	84.9(3)
$F_{(18)}$–$Te_{(4)}$–$F_{(19)}$	89.3(3)	$F_{(36)}$–$Te_{(8)}$–$F_{(37)}$	88.7(2)
$F_{(25)}$–$Te_{(5)}$–$F_{(21)}$	85.2(2)	$F_{(36)}$–$Te_{(8)}$–$F_{(38)}$	172.1(3)
$F_{(25)}$–$Te_{(5)}$–$F_{(22)}$	85.1(3)	$F_{(37)}$–$Te_{(8)}$–$F_{(39)}$	168.2(3)
$F_{(25)}$–$Te_{(5)}$–$F_{(23)}$	86.6(2)	$F_{(36)}$–$Te_{(8)}$–$F_{(39)}$	89.0(3)
$F_{(25)}$–$Te_{(5)}$–$F_{(24)}$	85.3(3)	$F_{(37)}$–$Te_{(8)}$–$F_{(38)}$	90.1(3)
$F_{(21)}$–$Te_{(5)}$–$F_{(22)}$	90.6(2)	$F_{(38)}$–$Te_{(8)}$–$F_{(39)}$	90.6(3)
$F_{(21)}$–$Te_{(5)}$–$F_{(23)}$	171.7(2)	$F_{(45)}$–$Te_{(9)}$–$F_{(41)}$	86.6(3)
$F_{(22)}$–$Te_{(5)}$–$F_{(24)}$	170.2(3)	$F_{(45)}$–$Te_{(9)}$–$F_{(42)}$	84.8(3)
$F_{(21)}$–$Te_{(5)}$–$F_{(24)}$	90.5(3)	$F_{(45)}$–$Te_{(9)}$–$F_{(43)}$	84.2(3)
$F_{(22)}$–$Te_{(5)}$–$F_{(23)}$	89.4(3)	$F_{(45)}$–$Te_{(9)}$–$F_{(44)}$	85.1(3)
$F_{(23)}$–$Te_{(5)}$–$F_{(24}$	88.2(3)	$F_{(41)}$–$Te_{(9)}$–$F_{(42)}$	171.3(3)
$F_{(30)}$–$Te_{(6)}$–$F_{(26)}$	86.8(3)	$F_{(41)}$–$Te_{(9)}$–$F_{(43)}$	90.0(3)
$F_{(30)}$–$Te_{(6)}$–$F_{(27)}$	86.0(3)	$F_{(42)}$–$Te_{(9)}$–$F_{(44)}$	90.5(3)
$F_{(30)}$–$Te_{(6)}$–$F_{(28)}$	85.2(3)	$F_{(41)}$–$Te_{(9)}$–$F_{(44)}$	89.7(3)
$F_{(30)}$–$Te_{(6)}$–$F_{(29)}$	84.6(3)	$F_{(42)}$–$Te_{(9)}$–$F_{(43)}$	88.1(3)
$F_{(26)}$–$Te_{(6)}$–$F_{(27)}$	172.8(3)	$F_{(43)}$–$Te_{(9)}$–$F_{(44)}$	169.3(3)
$F_{(26)}$–$Te_{(6)}$–$F_{(28)}$	88.8(3)	O–S–O	122.3(6)–125.2(6)
$F_{(27)}$–$Te_{(6)}$–$F_{(29)}$	88.4(3)	O–S–F	105.3(5)–108.5(4)
$F_{(26)}$–$Te_{(6)}$–$F_{(29)}$	91.2(3)	O–S–Cl	106.5(4)–110.4(4)
$F_{(27)}$–$Te_{(6)}$–$F_{(28)}$	90.3(3)	F–S–Cl	97.3(3)–102.9(5)
$F_{(28)}$–$Te_{(6)}$–$F_{(29)}$	169.8(2)		

Table S4.5. continued…

Dihedral Angles (deg)	
$Te_{(4)}–O_{(4)}–Hg_{(1)}–O_{(5)}–Te_{(5)}$	150.9 (4)

[a] The atom numbers are subscripted in parentheses, and the labeling scheme corresponds to those used in Figures 4.5. [b] The subscripted letters refer to another asymmetric unit. The bond lengths of the disordered SO_2ClF molecules and its contact distances are not included in the above table.

Table S4.6. Complete List of Experimental Geometrical Parameters for $[N(CH_2H_3)_4]_3[Hg(OTeF_5)_5]$ [a]

Bond Lengths (Å)			
$Hg_{(1)}–O_{(1)}$	2.265(3)	$Hg_{(2)}–O_{(6)}$	2.297(3)
$Hg_{(1)}–O_{(2)}$	2.317(3)	$Hg_{(2)}–O_{(7)}$	2.262(3)
$Hg_{(1)}–O_{(3)}$	2.313(3)	$Hg_{(2)}–O_{(8)}$	2.266(3)
$Hg_{(1)}–O_{(4)}$	2.259(3)	$Hg_{(2)}–O_{(9)}$	2.319(3)
$Hg_{(1)}–O_{(5)}$	2.276(3)	$Hg_{(2)}–O_{(10)}$	2.290(3)
$Hg_{(1)}---F_{(17)}$	3.141(3)	$Hg_{(2)}---F_{(46)}$	3.133(3)
$Te_{(1)}–O_{(1)}$	1.782(3)	$Te_{(6)}–O_{(6)}$	1.783(3)
$Te_{(2)}–O_{(2)}$	1.786(3)	$Te_{(7)}–O_{(7)}$	1.787(3)
$Te_{(3)}–O_{(3)}$	1.787(3)	$Te_{(8)}–O_{(8)}$	1.786(3)
$Te_{(4)}–O_{(4)}$	1.795(3)	$Te_{(9)}–O_{(9)}$	1.777(3)
$Te_{(5)}–O_{(5)}$	1.790(3)	$Te_{(10)}–O_{(10)}$	1.795(3)
$Te_{(1)}–F_{(1)}$	1.854(3)	$Te_{(6)}–F_{(26)}$	1.852(3)
$Te_{(1)}–F_{(2)}$	1.859(3)	$Te_{(6)}–F_{(27)}$	1.858(2)
$Te_{(1)}–F_{(3)}$	1.853(3)	$Te_{(6)}–F_{(28)}$	1.861(3)
$Te_{(1)}–F_{(4)}$	1.857(3)	$Te_{(6)}–F_{(29)}$	1.847(3)
$Te_{(1)}–F_{(5)}$	1.851(3)	$Te_{(6)}–F_{(30)}$	1.854(2)
$Te_{(2)}–F_{(6)}$	1.857(3)	$Te_{(7)}–F_{(31)}$	1.853(3)
$Te_{(2)}–F_{(7)}$	1.854(3)	$Te_{(7)}–F_{(32)}$	1.854(3)
$Te_{(2)}–F_{(8)}$	1.856(3)	$Te_{(7)}–F_{(33)}$	1.865(3)
$Te_{(2)}–F_{(9)}$	1.851(3)	$Te_{(7)}–F_{(34)}$	1.848(3)
$Te_{(2)}–F_{(10)}$	1.849(3)	$Te_{(7)}–F_{(35)}$	1.850(3)
$Te_{(3)}–F_{(11)}$	1.846(2)	$Te_{(8)}–F_{(36)}$	1.853(3)
$Te_{(3)}–F_{(12)}$	1.853(3)	$Te_{(8)}–F_{(37)}$	1.855(3)
$Te_{(3)}–F_{(13)}$	1.860(3)	$Te_{(8)}–F_{(38)}$	1.855(3)
$Te_{(3)}–F_{(14)}$	1.859(3)	$Te_{(8)}–F_{(39)}$	1.855(3)
$Te_{(3)}–F_{(15)}$	1.852(2)	$Te_{(8)}–F_{(40)}$	1.852(3)
$Te_{(4)}–F_{(16)}$	1.850(3)	$Te_{(9)}–F_{(41)}$	1.856(3)
$Te_{(4)}–F_{(17)}$	1.860(3)	$Te_{(9)}–F_{(42)}$	1.853(3)
$Te_{(4)}–F_{(18)}$	1.855(2)	$Te_{(9)}–F_{(43)}$	1.850(3)
$Te_{(4)}–F_{(19)}$	1.858(3)	$Te_{(9)}–F_{(44)}$	1.855(3)
$Te_{(4)}–F_{(20)}$	1.856(3)	$Te_{(9)}–F_{(45)}$	1.856(3)
$Te_{(5)}–F_{(21)}$	1.857(3)	$Te_{(10)}–F_{(46)}$	1.839(3)
$Te_{(5)}–F_{(22)}$	1.844(3)	$Te_{(10)}–F_{(47)}$	1.848(3)
$Te_{(5)}–F_{(23)}$	1.858(3)	$Te_{(10)}–F_{(48)}$	1.832(4)
$Te_{(5)}–F_{(24)}$	1.856(3)	$Te_{(10)}–F_{(49)}$	1.859(3)
$Te_{(5)}–F_{(25)}$	1.846(3)	$Te_{(10)}–F_{(50)}$	1.858(3)
$N_{(1)}–C_{(1)}$	1.510(5)	$N_{(4)}–C_{(25)}$	1.520(6)
$N_{(1)}–C_{(3)}$	1.525(5)	$N_{(4)}–C_{(27)}$	1.519(5)

Table S4.6. continued…

$N_{(1)}$–$C_{(5)}$	1.513(5)	$N_{(4)}$–$C_{(29)}$	1.519(5)
$N_{(1)}$–$C_{(7)}$	1.519(5)	$N_{(4)}$–$C_{(31)}$	1.518(5)
$N_{(2)}$–$C_{(9)}$	1.524(5)	$N_{(5)}$–$C_{(33)}$	1.520(6)
$N_{(2)}$–$C_{(11)}$	1.510(6)	$N_{(5)}$–$C_{(35)}$	1.514(5)
$N_{(2)}$–$C_{(13)}$	1.520(5)	$N_{(5)}$–$C_{(37)}$	1.516(5)
$N_{(2)}$–$C_{(15)}$	1.515(5)	$N_{(5)}$–$C_{(39)}$	1.512(5)
$N_{(3)}$–$C_{(17)}$	1.521(5)	$N_{(6)}$–$C_{(41)}$	1.523(5)
$N_{(3)}$–$C_{(19)}$	1.519(5)	$N_{(6)}$–$C_{(43)}$	1.518(5)
$N_{(3)}$–$C_{(21)}$	1.522(5)	$N_{(6)}$–$C_{(45)}$	1.5150(5)
$N_{(2)}$–$C_{(23)}$	1.523(5)	$N_{(6)}$–$C_{(47)}$	1.510(6)
$C_{(1)}$–$C_{(2)}$	1.527(7)	$C_{(25)}$–$C_{(26)}$	1.516(7)
$C_{(3)}$–$C_{(4)}$	1.521(6)	$C_{(27)}$–$C_{(28)}$	1.508(7)
$C_{(5)}$–$C_{(6)}$	1.512(6)	$C_{(29)}$–$C_{(30)}$	1.515(6)
$C_{(7)}$–$C_{(8)}$	1.513(6)	$C_{(31)}$–$C_{(32)}$	1.513(6)
$C_{(9)}$–$C_{(10)}$	1.512(6)	$C_{(33)}$–$C_{(34)}$	1.512(6)
$C_{(11)}$–$C_{(12)}$	1.506(6)	$C_{(35)}$–$C_{(36)}$	1.501(7)
$C_{(13)}$–$C_{(14)}$	1.515(7)	$C_{(37)}$–$C_{(38)}$	1.513(6)
$C_{(15)}$–$C_{(16)}$	1.514(7)	$C_{(39)}$–$C_{(40)}$	1.512(6)
$C_{(17)}$–$C_{(18)}$	1.512(6)	$C_{(41)}$–$C_{(42)}$	1.514(6)
$C_{(19)}$–$C_{(20)}$	1.528(6)	$C_{(43)}$–$C_{(44)}$	1.520(6)
$C_{(21)}$–$C_{(22)}$	1.520(7)	$C_{(45)}$–$C_{(46)}$	1.513(7)
$C_{(23)}$–$C_{(24)}$	1.512(6)	$C_{(47)}$–$C_{(48)}$	1.501(7)
CH_3---F [b]	2.954(6)-3.464(6)		
Bond Angles (deg)			
$O_{(1)}$–$Hg_{(1)}$–$O_{(2)}$	116.4(1)	$O_{(6)}$–$Hg_{(2)}$–$O_{(7)}$	86.5(1)
$O_{(1)}$–$Hg_{(1)}$–$O_{(3)}$	104.6(1)	$O_{(6)}$–$Hg_{(2)}$–$O_{(8)}$	108.9(1)
$O_{(1)}$–$Hg_{(1)}$–$O_{(4)}$	102.3(1)	$O_{(6)}$–$Hg_{(2)}$–$O_{(9)}$	145.9(1)
$O_{(1)}$–$Hg_{(1)}$–$O_{(5)}$	88.1(1)	$O_{(6)}$–$Hg_{(2)}$–$O_{(10)}$	87.6(1)
$O_{(2)}$–$Hg_{(1)}$–$O_{(3)}$	138.6(1)	$O_{(7)}$–$Hg_{(2)}$–$O_{(8)}$	107.5(1)
$O_{(2)}$–$Hg_{(1)}$–$O_{(4)}$	88.3(1)	$O_{(7)}$–$Hg_{(2)}$–$O_{(9)}$	87.8(1)
$O_{(2)}$–$Hg_{(1)}$–$O_{(5)}$	88.0(1)	$O_{(7)}$–$Hg_{(2)}$–$O_{(10)}$	161.5(1)
$O_{(3)}$–$Hg_{(1)}$–$O_{(4)}$	88.3(1)	$O_{(8)}$–$Hg_{(2)}$–$O_{(9)}$	104.9(1)
$O_{(3)}$–$Hg_{(1)}$–$O_{(5)}$	88.1(1)	$O_{(8)}$–$Hg_{(2)}$–$O_{(10)}$	91.0(1)
$O_{(4)}$–$Hg_{(1)}$–$O_{(5)}$	169.5(1)	$O_{(9)}$–$Hg_{(2)}$–$O_{(10)}$	87.4(1)
$Hg_{(1)}$–$O_{(1)}$–$Te_{(1)}$	131.2(2)	$Hg_{(2)}$–$O_{(6)}$–$Te_{(6)}$	128.4(2)
$Hg_{(1)}$–$O_{(2)}$–$Te_{(2)}$	126.8(2)	$Hg_{(2)}$–$O_{(7)}$–$Te_{(7)}$	125.1(2)
$Hg_{(1)}$–$O_{(3)}$–$Te_{(3)}$	124.6(2)	$Hg_{(2)}$–$O_{(8)}$–$Te_{(8)}$	130.1(2)
$Hg_{(1)}$–$O_{(4)}$–$Te_{(4)}$	120.5(2)	$Hg_{(2)}$–$O_{(9)}$–$Te_{(9)}$	132.8(2)
$Hg_{(1)}$–$O_{(5)}$–$Te_{(5)}$	124.3(2)	$Hg_{(2)}$–$O_{(10)}$–$Te_{(10)}$	120.1(2)

Table S4.6. continued…

$O_{(1)}–Te_{(1)}–F_{(1)}$	94.6(2)	$O_{(6)}–Te_{(6)}–F_{(26)}$	94.5(1)
$O_{(1)}–Te_{(1)}–F_{(2)}$	94.6(1)	$O_{(6)}–Te_{(6)}–F_{(27)}$	95.2(1)
$O_{(1)}–Te_{(1)}–F_{(3)}$	97.3(2)	$O_{(6)}–Te_{(6)}–F_{(28)}$	96.8(1)
$O_{(1)}–Te_{(1)}–F_{(4)}$	96.6(1)	$O_{(6)}–Te_{(6)}–F_{(29)}$	96.6(1)
$O_{(1)}–Te_{(1)}–F_{(5)}$	178.2(2)	$O_{(6)}–Te_{(6)}–F_{(30)}$	178.7(1)
$O_{(2)}–Te_{(2)}–F_{(6)}$	94.4(1)	$O_{(7)}–Te_{(7)}–F_{(31)}$	96.8(1)
$O_{(2)}–Te_{(2)}–F_{(7)}$	96.3(2)	$O_{(7)}–Te_{(7)}–F_{(32)}$	94.5(1)
$O_{(2)}–Te_{(2)}–F_{(8)}$	96.5(1)	$O_{(7)}–Te_{(7)}–F_{(33)}$	94.2(1)
$O_{(2)}–Te_{(2)}–F_{(9)}$	96.6(2)	$O_{(7)}–Te_{(7)}–F_{(34)}$	97.0(1)
$O_{(2)}–Te_{(2)}–F_{(10)}$	179.2(1)	$O_{(7)}–Te_{(7)}–F_{(35)}$	177.9(1)
$O_{(3)}–Te_{(3)}–F_{(11)}$	97.1(1)	$O_{(8)}–Te_{(8)}–F_{(36)}$	94.4(2)
$O_{(3)}–Te_{(3)}–F_{(12)}$	94.9(1)	$O_{(8)}–Te_{(8)}–F_{(37)}$	94.6(2)
$O_{(3)}–Te_{(3)}–F_{(13)}$	94.3(1)	$O_{(8)}–Te_{(8)}–F_{(38)}$	96.4(2)
$O_{(3)}–Te_{(3)}–F_{(14)}$	96.8(1)	$O_{(8)}–Te_{(8)}–F_{(39)}$	96.8(2)
$O_{(3)}–Te_{(3)}–F_{(15)}$	178.3(1)	$O_{(8)}–Te_{(8)}–F_{(40)}$	178.6(2)
$O_{(4)}–Te_{(4)}–F_{(16)}$	96.4(1)	$O_{(9)}–Te_{(9)}–F_{(41)}$	94.3(1)
$O_{(4)}–Te_{(4)}–F_{(17)}$	96.1(1)	$O_{(9)}–Te_{(9)}–F_{(42)}$	95.5(2)
$O_{(4)}–Te_{(4)}–F_{(18)}$	95.4(1)	$O_{(9)}–Te_{(9)}–F_{(43)}$	97.7(2)
$O_{(4)}–Te_{(4)}–F_{(19)}$	94.6(1)	$O_{(9)}–Te_{(9)}–F_{(44)}$	98.1(2)
$O_{(4)}–Te_{(4)}–F_{(20)}$	178.9(1)	$O_{(9}–Te_{(9)}–F_{(45)}$	178.1(1)
$O_{(5)}–Te_{(5)}–F_{(21)}$	96.2(1)	$O_{(10)}–Te_{(10)}–F_{(46)}$	95.7(1)
$O_{(5)}–Te_{(5)}–F_{(22)}$	95.0(2)	$O_{(10)}–Te_{(10)}–F_{(47)}$	96.2(2)
$O_{(5)}–Te_{(5)}–F_{(23)}$	94.4(2)	$O_{(10)}–Te_{(10)}–F_{(48)}$	94.9(2)
$O_{(5)}–Te_{(5)}–F_{(24)}$	97.3(2)	$O_{(10)}–Te_{(10)}–F_{(49)}$	97.1(2)
$O_{(5)}–Te_{(5)}–F_{(25)}$	178.9(2)	$O_{(10)}–Te_{(10)}–F_{(50)}$	179.7(2)
$F_{(5)}–Te_{(1)}–F_{(1)}$	83.9(2)	$F_{(30)}–Te_{(6)}–F_{(26)}$	84.4(1)
$F_{(5)}–Te_{(1)}–F_{(2)}$	84.6(1)	$F_{(30)}–Te_{(6)}–F_{(27)}$	84.1(1)
$F_{(5)}–Te_{(1)}–F_{(3)}$	84.3(1)	$F_{(30)}–Te_{(6)}–F_{(28)}$	84.2(1)
$F_{(5)}–Te_{(1)}–F_{(4)}$	84.3(1)	$F_{(30)}–Te_{(6)}–F_{(29)}$	84.1(1)
$F_{(1)}–Te_{(1)}–F_{(2)}$	89.6(2)	$F_{(26)}–Te_{(6)}–F_{(27)}$	87.9(2)
$F_{(1)}–Te_{(1)}–F_{(3)}$	168.1(1)	$F_{(26)}–Te_{(6)}–F_{(28)}$	168.5(1)
$F_{(2)}–Te_{(1)}–F_{(4)}$	168.8(1)	$F_{(27)}–Te_{(6)}–F_{(29)}$	168.2(1)
$F_{(1)}–Te_{(1)}–F_{(4)}$	90.2(1)	$F_{(26)}–Te_{(6)}–F_{(29)}$	90.7(1)
$F_{(2)}–Te_{(1)}–F_{(3)}$	89.5(1)	$F_{(27)}–Te_{(6)}–F_{(28)}$	89.2(1)
$F_{(3)}–Te_{(1)}–F_{(4)}$	88.4(1)	$F_{(28)}–Te_{(6)}–F_{(29)}$	90.0(2)
$F_{(10)}–Te_{(2)}–F_{(6)}$	84.9(1)	$F_{(35)}–Te_{(7)}–F_{(31)}$	84.8(1)
$F_{(10)}–Te_{(2)}–F_{(7)}$	83.1(1)	$F_{(35)}–Te_{(7)}–F_{(32)}$	84.1(1)
$F_{(10)}–Te_{(2)}–F_{(8)}$	84.2(1)	$F_{(35)}–Te_{(7)}–F_{(33)}$	84.1(1)
$F_{(10)}–Te_{(2)}–F_{(9)}$	83.9(1)	$F_{(35)}–Te_{(7)}–F_{(34)}$	84.3(1)
$F_{(6}–Te_{(2)}–F_{(7)}$	88.8(1)	$F_{(31)}–Te_{(7)}–F_{(32)}$	89.8(1)
$F_{(6)}–Te_{(2)}–F_{(8)}$	169.1(1)	$F_{(31)}–Te_{(7)}–F_{(33)}$	168.9(1)
$F_{(7)}–Te_{(2)}–F_{(9)}$	167.0(1)	$F_{(32)}–Te_{(7)}–F_{(34)}$	168.3(1)
$F_{(6)}–Te_{(2)}–F_{(9)}$	88.7(1)	$F_{(31)}–Te_{(7)}–F_{(34)}$	90.5(1)
$F_{(7)}–Te_{(2)}–F_{(8)}$	89.5(1)	$F_{(32)}–Te_{(7)}–F_{(33)}$	88.5(1)
$F_{(8)}–Te_{(2)}–F_{(9)}$	90.6(1)	$F_{(33)}–Te_{(7)}–F_{(34)}$	88.5(1)
$F_{(15)}–Te_{(3)}–F_{(11)}$	84.3(1)	$F_{(40)}–Te_{(8)}–F_{(36)}$	84.4(2)

Table S4.6. continued…

$F_{(15)}$–$Te_{(3)}$–$F_{(12)}$	84.1(1)	$F_{(40)}$–$Te_{(8)}$–$F_{(37)}$	84.6(2)
$F_{(15)}$–$Te_{(3)}$–$F_{(13)}$	84.3(1)	$F_{(40)}$–$Te_{(8)}$–$F_{(38)}$	84.8(2)
$F_{(15)}$–$Te_{(3)}$–$F_{(14)}$	84.2(1)	$F_{(40)}$–$Te_{(8)}$–$F_{(39)}$	84.0(1)
$F_{(11)}$–$Te_{(3)}$–$F_{(12)}$	90.5(1)	$F_{(36)}$–$Te_{(8)}$–$F_{(37)}$	89.9(2)
$F_{(11)}$–$Te_{(3)}$–$F_{(13)}$	168.7(1)	$F_{(36)}$–$Te_{(8)}$–$F_{(38)}$	169.1(2)
$F_{(12)}$–$Te_{(3)}$–$F_{(14)}$	168.2(1)	$F_{(37)}$–$Te_{(8)}$–$F_{(39)}$	168.6(1)
$F_{(11)}$–$Te_{(3)}$–$F_{(14)}$	90.0(1)	$F_{(36)}$–$Te_{(8)}$–$F_{(39)}$	88.7(1)
$F_{(12)}$–$Te_{(3)}$–$F_{(13)}$	88.7(1)	$F_{(37)}$–$Te_{(8)}$–$F_{(38)}$	90.5(2)
$F_{(13)}$–$Te_{(3)}$–$F_{(14)}$	88.5(1)	$F_{(38)}$–$Te_{(8)}$–$F_{(39)}$	88.8(1)
$F_{(20)}$–$Te_{(4)}$–$F_{(16)}$	83.9(1)	$F_{(45)}$–$Te_{(9)}$–$F_{(41)}$	84.2(1)
$F_{(20)}$–$Te_{(4)}$–$F_{(17)}$	84.9(1)	$F_{(45)}$–$Te_{(9)}$–$F_{(42)}$	83.4(1)
$F_{(20)}$–$Te_{(4)}$–$F_{(18)}$	84.3(1)	$F_{(45)}$–$Te_{(9)}$–$F_{(43)}$	83.9(1)
$F_{(20)}$–$Te_{(4)}$–$F_{(19)}$	84.4(1)	$F_{(45)}$–$Te_{(9)}$–$F_{(44)}$	83.0(1)
$F_{(16)}$–$Te_{(4)}$–$F_{(17)}$	89.7(1)	$F_{(41)}$–$Te_{(9)}$–$F_{(42)}$	89.1(2)
$F_{(16)}$–$Te_{(4)}$–$F_{(18)}$	168.1(1)	$F_{(41)}$–$Te_{(9)}$–$F_{(43)}$	168.0(1)
$F_{(17)}$–$Te_{(4)}$–$F_{(19)}$	169.3(1)	$F_{(42)}$–$Te_{(9)}$–$F_{(44)}$	166.4(2)
$F_{(16)}$–$Te_{(4)}$–$F_{(19)}$	89.0(1)	$F_{(41)}$–$Te_{(9)}$–$F_{(44)}$	89.0(2)
$F_{(17)}$–$Te_{(4)}$–$F_{(18)}$	90.1(1)	$F_{(42)}$–$Te_{(9)}$–$F_{(43)}$	90.5(2)
$F_{(18)}$–$Te_{(4)}$–$F_{(19)}$	89.0(1)	$F_{(43)}$–$Te_{(9)}$–$F_{(44)}$	88.6(2)
$F_{(25)}$–$Te_{(5)}$–$F_{(21)}$	84.6(2)	$F_{(50)}$–$Te_{(10)}$–$F_{(46)}$	84.5(2)
$F_{(25)}$–$Te_{(5)}$–$F_{(22)}$	84.2(2)	$F_{(50)}$–$Te_{(10)}$–$F_{(47)}$	83.7(2)
$F_{(25)}$–$Te_{(5)}$–$F_{(23)}$	84.8(2)	$F_{(50)}$–$Te_{(10)}$–$F_{(48)}$	84.9(2)
$F_{(25)}$–$Te_{(5)}$–$F_{(24)}$	83.5(2)	$F_{(50)}$–$Te_{(10)}$–$F_{(49)}$	83.0(2)
$F_{(21)}$–$Te_{(5)}$–$F_{(22)}$	90.5(1)	$F_{(46)}$–$Te_{(10)}$–$F_{(47)}$	90.7(2)
$F_{(21)}$–$Te_{(5)}$–$F_{(23)}$	169.4(1)	$F_{(46)}$–$Te_{(10)}$–$F_{(48)}$	169.2(2)
$F_{(22)}$–$Te_{(5)}$–$F_{(24)}$	167.5(1)	$F_{(47)}$–$Te_{(10)}$–$F_{(49)}$	166.6(2)
$F_{(21)}$–$Te_{(5)}$–$F_{(24)}$	90.5(1)	$F_{(46)}$–$Te_{(10)}$–$F_{(49)}$	87.1(1)
$F_{(22)}$–$Te_{(5)}$–$F_{(23)}$	88.4(1)	$F_{(47)}$–$Te_{(10)}$–$F_{(48)}$	90.3(2)
$F_{(23)}$–$Te_{(5)}$–$F_{(24)}$	88.3(1)	$F_{(48)}$–$Te_{(10)}$–$F_{(49)}$	89.6(2)
$C_{(1)}$–$N_{(1)}$–$C_{(3)}$	108.5(3)	$C_{(25)}$–$N_{(4)}$–$C_{(27)}$	111.7(3)
$C_{(1)}$–$N_{(1)}$–$C_{(5)}$	109.9(3)	$C_{(25)}$–$N_{(4)}$–$C_{(29)}$	106.1(3)
$C_{(1)}$–$N_{(1)}$–$C_{(7)}$	111.5(3)	$C_{(25)}$–$N_{(4)}$–$C_{(31)}$	111.0(3)
$C_{(3)}$–$N_{(1)}$–$C_{(5)}$	110.5(3)	$C_{(27)}$–$N_{(4)}$–$C_{(29)}$	110.7(3)
$C_{(3)}$–$N_{(1)}$–$C_{(7)}$	108.5(3)	$C_{(27)}$–$N_{(4)}$–$C_{(31)}$	105.4(3)
$C_{(5)}$–$N_{(1)}$–$C_{(7)}$	108.0(3)	$C_{(29)}$–$N_{(4)}$–$C_{(31)}$	112.1(3)
$C_{(9)}$–$N_{(2)}$–$C_{(11)}$	111.0(3)	$C_{(33)}$–$N_{(5)}$–$C_{(35)}$	111.3(3)
$C_{(9)}$–$N_{(2)}$–$C_{(13)}$	105.8(3)	$C_{(33)}$–$N_{(5)}$–$C_{(37)}$	106.1(3)
$C_{(9)}$–$N_{(2)}$–$C_{(15)}$	111.5(3)	$C_{(33)}$–$N_{(5)}$–$C_{(39)}$	111.5(3)
$C_{(11)}$–$N_{(2)}$–$C_{(13)}$	111.4(4)	$C_{(35)}$–$N_{(5)}$–$C_{(37)}$	110.9(3)
$C_{(11)}$–$N_{(2)}$–$C_{(15)}$	106.2(3)	$C_{(35)}$–$N_{(5)}$–$C_{(39)}$	105.4(3)
$C_{(13)}$–$N_{(2)}$–$C_{(15)}$	111.1(3)	$C_{(37)}$–$N_{(5)}$–$C_{(39)}$	111.7(3)
$C_{(17)}$–$N_{(3)}$–$C_{(19)}$	111.4(3)	$C_{(41)}$–$N_{(6)}$–$C_{(43)}$	105.6(3)
$C_{(17)}$–$N_{(3)}$–$C_{(21)}$	108.5(3)	$C_{(41)}$–$N_{(6)}$–$C_{(45)}$	111.0(3)
$C_{(17)}$–$N_{(3)}$–$C_{(23)}$	108.8(3)	$C_{(41)}$–$N_{(6)}$–$C_{(47)}$	111.3(3)
$C_{(19)}$–$N_{(3)}$–$C_{(21)}$	109.3(3)	$C_{(43)}$–$N_{(6)}$–$C_{(45)}$	110.5(3)
$C_{(19)}$–$N_{(3)}$–$C_{(23)}$	107.7(3)	$C_{(43)}$–$N_{(6)}$–$C_{(47)}$	111.3(3)
$C_{(21)}$–$N_{(3)}$–$C_{(23)}$	111.2(3)	$C_{(45)}$–$N_{(6)}$–$C_{(47)}$	107.3(3)

Table S4.6. continued…

$N_{(1)}–C_{(1)}–C_{(2)}$	114.8(4)	$N_{(4)}–C_{(25)}–C_{(26)}$	114.6(4)
$N_{(1)}–C_{(3)}–C_{(4)}$	115.2(4)	$N_{(4)}–C_{(27)}–C_{(28)}$	114.6(4)
$N_{(1)}–C_{(5)}–C_{(6)}$	115.6(4)	$N_{(4)}–C_{(29)}–C_{(30)}$	115.3(4)
$N_{(1)}–C_{(7)}–C_{(8)}$	115.0(4)	$N_{(4)}–C_{(31)}–C_{(32)}$	114.6(4)
$N_{(2)}–C_{(9)}–C_{(10)}$	115.3(4)	$N_{(5)}–C_{(33)}–C_{(34)}$	114.6(4)
$N_{(2)}–C_{(11)}–C_{(12)}$	115.5(4)	$N_{(5)}–C_{(35)}–C_{(36)}$	115.1(4)
$N_{(2)}–C_{(13)}–C_{(14)}$	115.7(4)	$N_{(5)}–C_{(37)}–C_{(38)}$	115.8(4)
$N_{(2)}–C_{(15)}–C_{(16)}$	115.5(4)	$N_{(5)}–C_{(39)}–C_{(40)}$	114.9(4)
$N_{(3)}–C_{(17)}–C_{(18)}$	115.3(4)	$N_{(6)}–C_{(41)}–C_{(42)}$	115.3(4)
$N_{(3)}–C_{(19)}–C_{(20)}$	114.6(4)	$N_{(6)}–C_{(43)}–C_{(44)}$	115.5(4)
$N_{(3)}–C_{(21)}–C_{(22)}$	114.9(4)	$N_{(6)}–C_{(45)}–C_{(46)}$	115.8(4)
$N_{(3)}–C_{(23)}–C_{(24)}$	114.4(4)	$N_{(6)}–C_{(47)}–C_{(48)}$	115.4(4)

[a] The atom numbers are subscripted in parentheses, and the labeling scheme corresponds to those used in Figure S4.1. [b] Contacts being less than the sum of the F[37] and CH_3[38] van der Waals radii (3.47 Å).

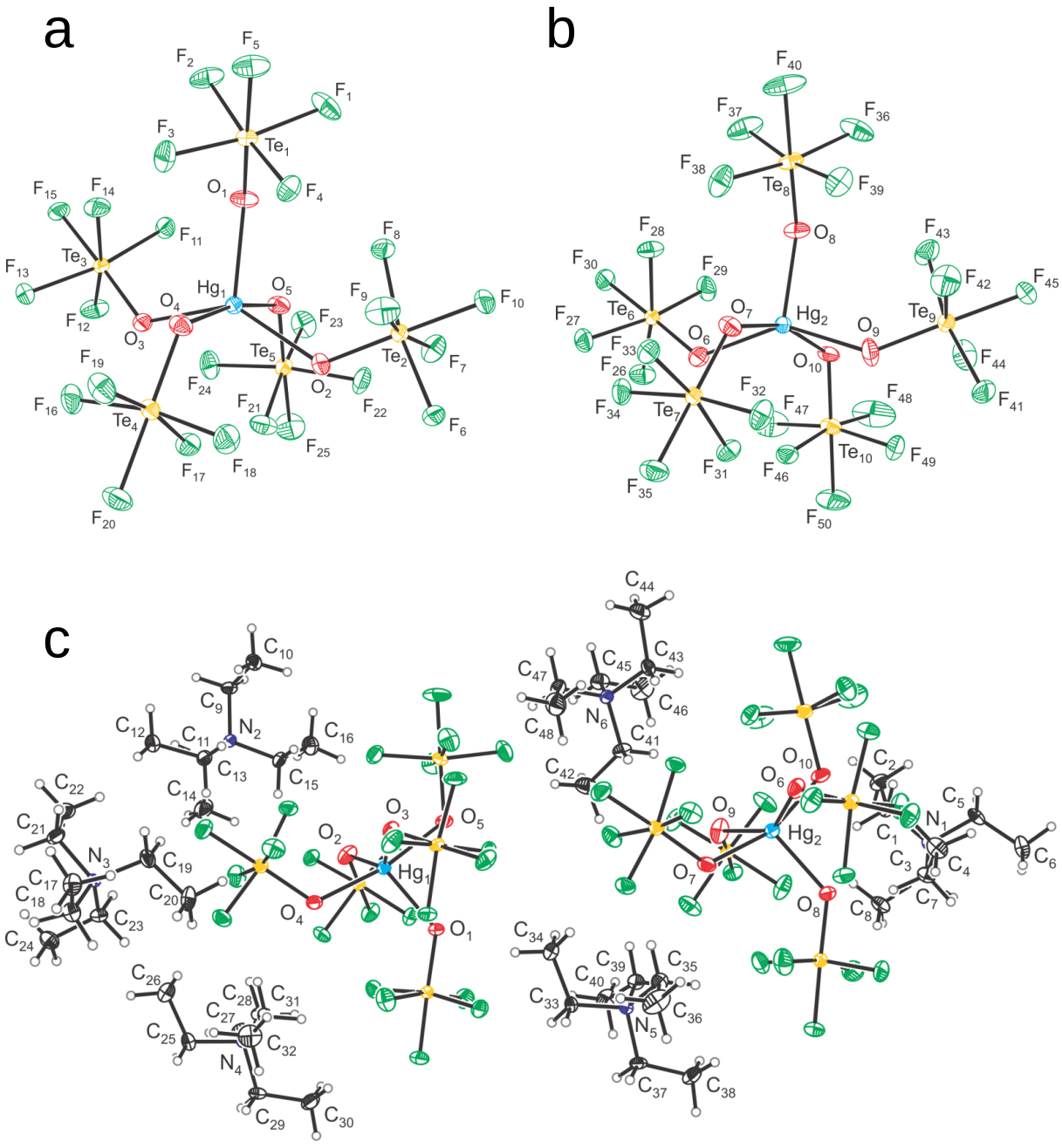

Figure S4.1. The X-ray crystal structure of $[N(CH_2CH_3)_4]_3[Hg(OTeF_5)_5]$ showing: (**a**) the $[Hg_{(1)}(OTeF_5)_5]^{3-}$ anion; (**b**) the $[Hg_{(2)}(OTeF_5)_5]^{3-}$ anion; and (**c**) the asymmetric unit of $[N(CH_2CH_3)_4]_3[Hg(OTeF_5)_5]$. Thermal ellipsoids drawn at the 50% probability level.

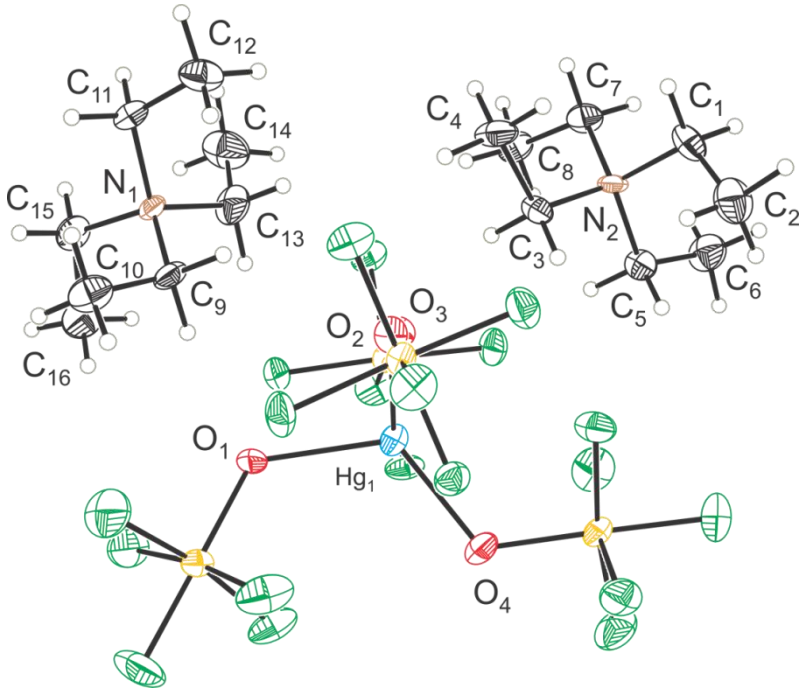

Figure S4.2. The asymmetric unit of $[N(CH_2CH_3)_4]_2[Hg(OTeF_5)_4]$ with thermal ellipsoids drawn at the 50% probability level.

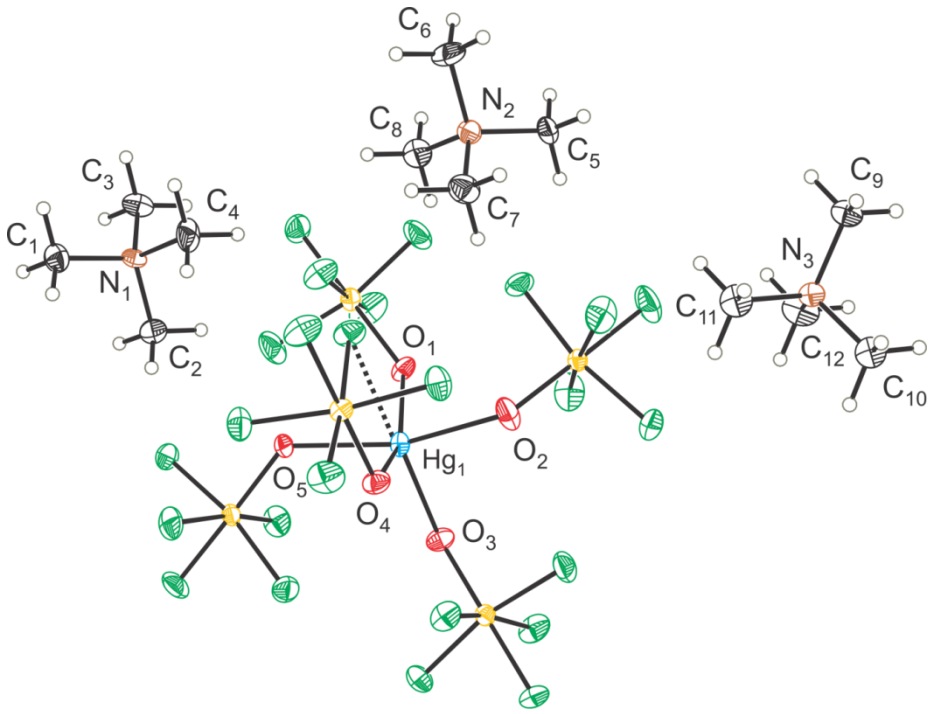

Figure S4.3. The asymmetric unit of $[N(CH_3)_4]_3[Hg(OTeF_5)_5]$ with thermal ellipsoids drawn at the 50% probability level.

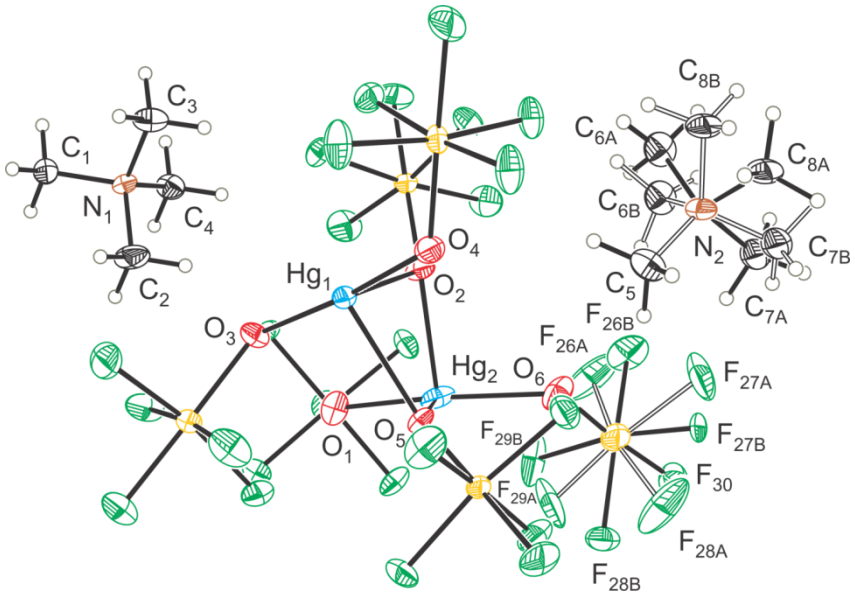

Figure S4.4. The assymetric unit of $[N(CH_3)_4]_2[Hg_2(OTeF_5)_6]$ with thermal ellipsoids drawn at the 50% probability level. The two orientations for the positionally disordered $[N(CH_3)_4]^+$ cation and F_5TeO-group are shown.

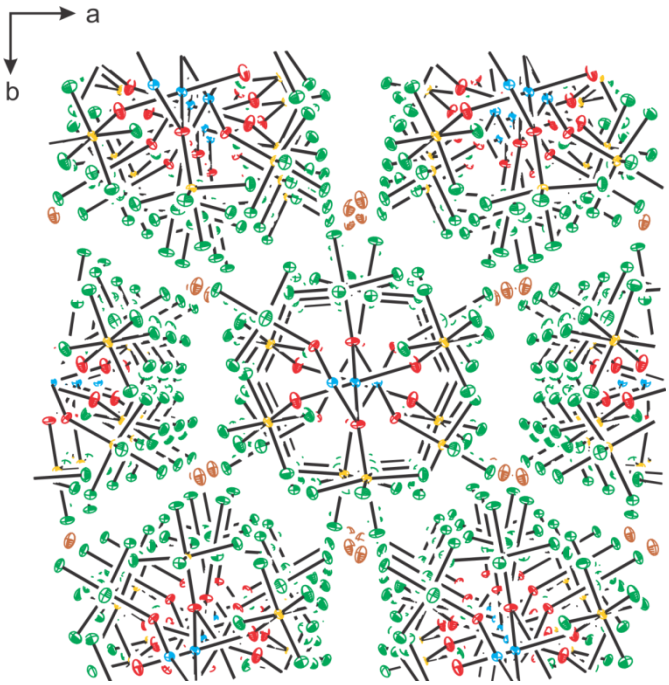

Figure S4.5. The crystallographic packing of $Cs_2[Hg(OTeF_5)_4]\cdot Hg(OTeF_5)_2$ viewed along the *c*-axis showing the packing of the Cs^+ around the chains that run parallel to the *c*-axis; thermal ellipsoids are shown at 50% probability level.

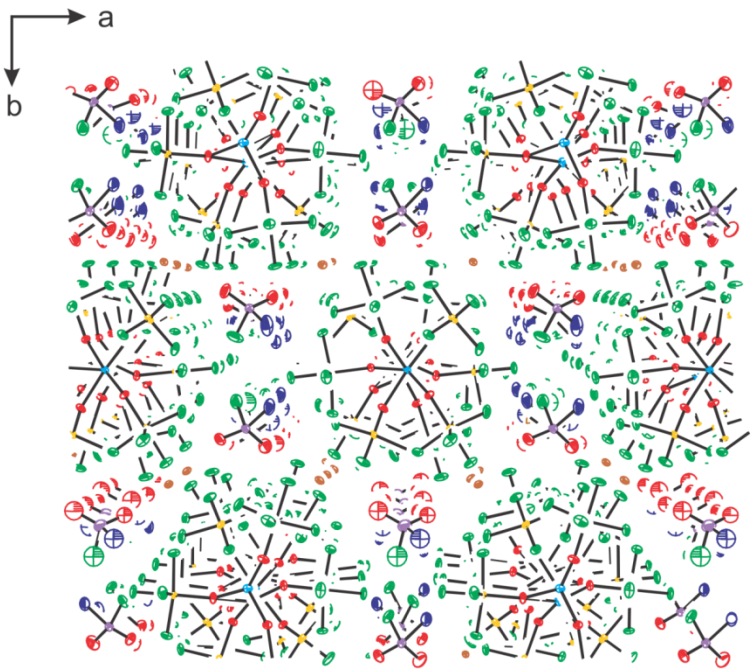

Figure S4.6. The crystallographic packing of $\{Cs_3[Hg_2(OTeF_5)_7]\cdot Hg(OTeF_5)_2\}\cdot 4SO_2ClF$ viewed along the *c*-axis; only one orientation for the disordered SO_2ClF molecules is shown. Thermal ellipsoids are shown at 50% probability level.

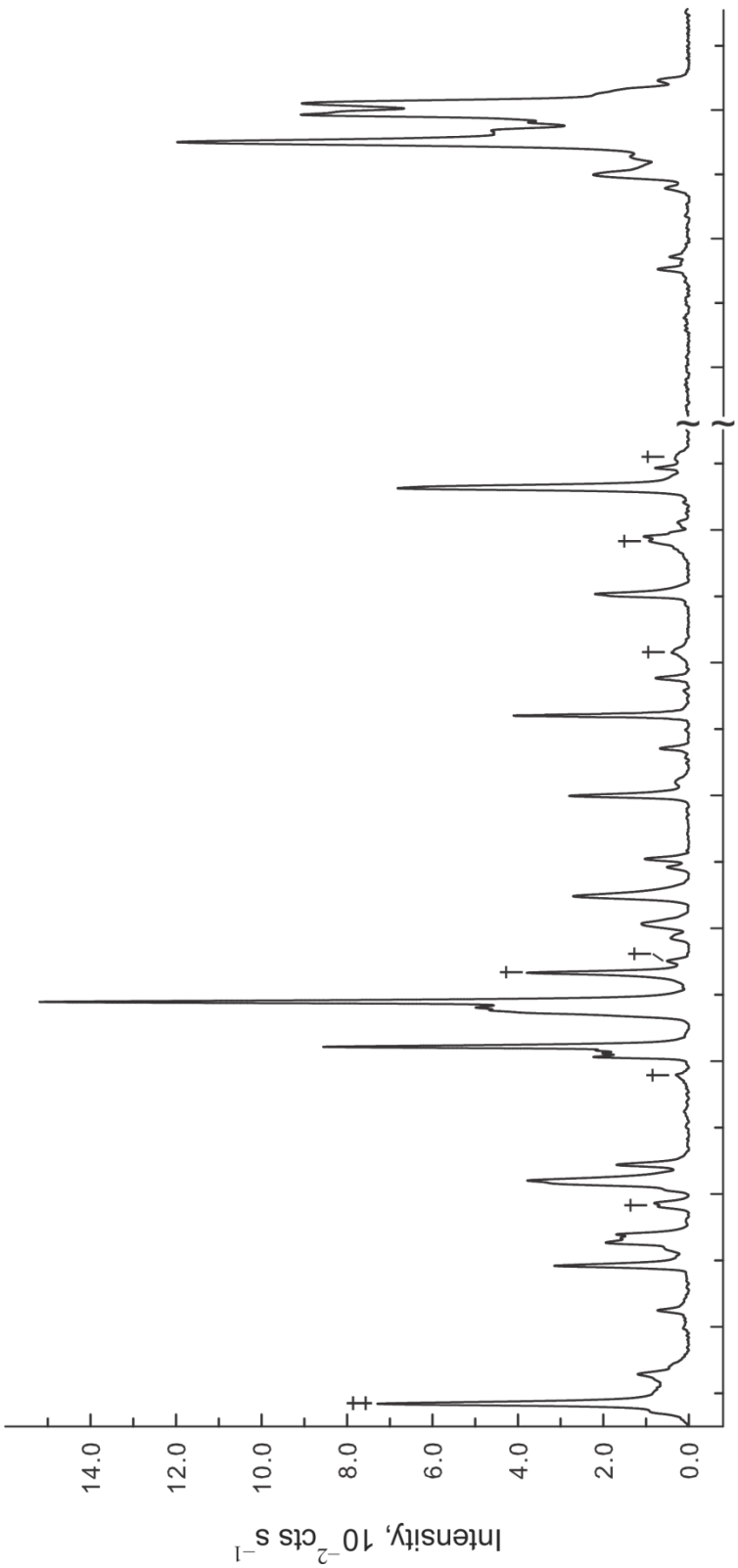

Figure S4.7. The complete Raman spectrum of $[N(CH_2H_3)_4]_2[Hg(OTeF_5)_4]$ recorded at −155 °C using 1064-nm excitation. Symbols denote purely FEP (†) bands, an instrumental artifact (‡).

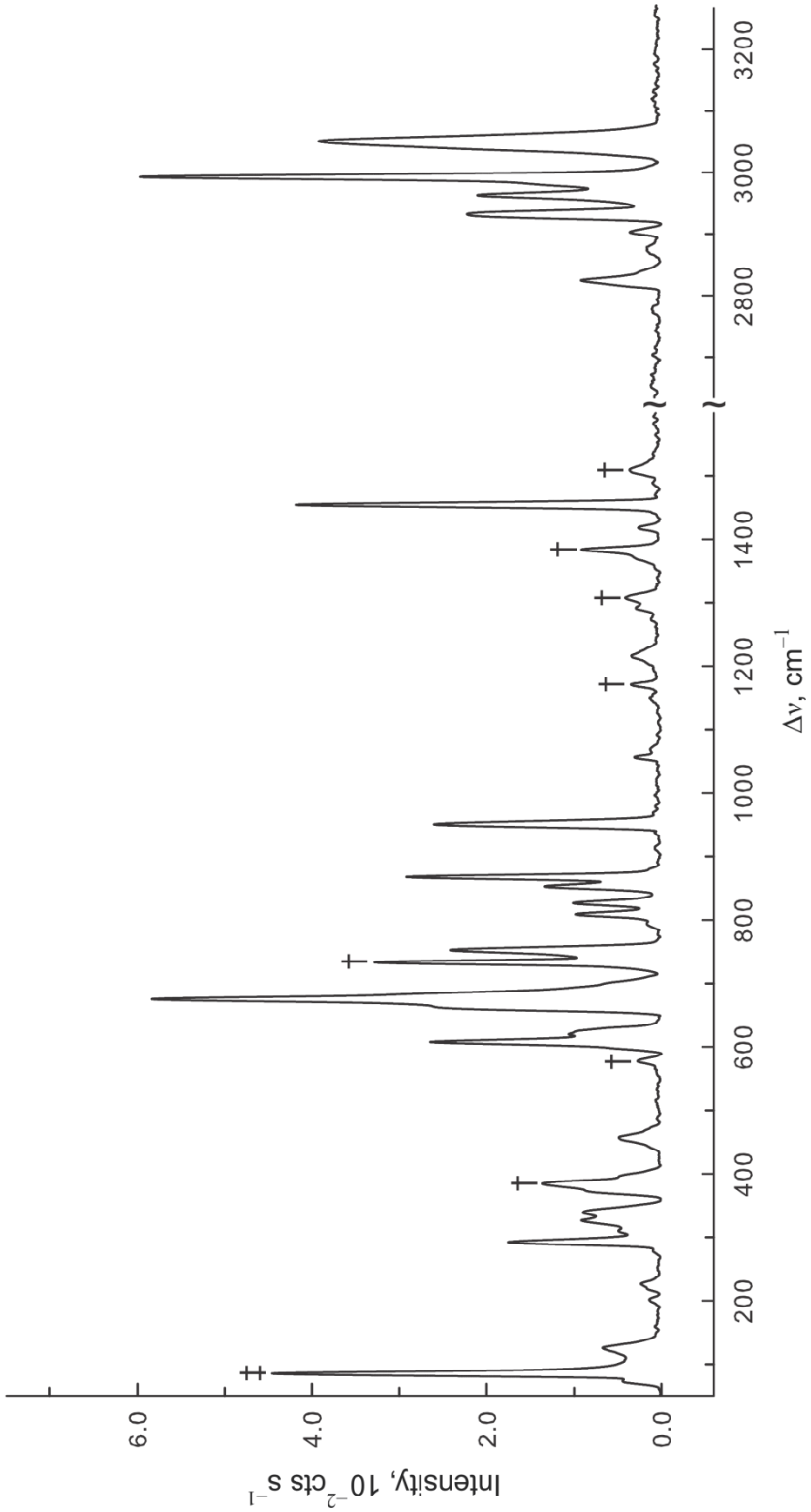

Figure S4.8. The complete Raman spectrum of $[N(CH_3)_4]_3[Hg(OTeF_5)_5]$ recorded at −155 °C using 1064-nm excitation. Symbols denote purely FEP (†) bands, an instrumental artifact (‡).

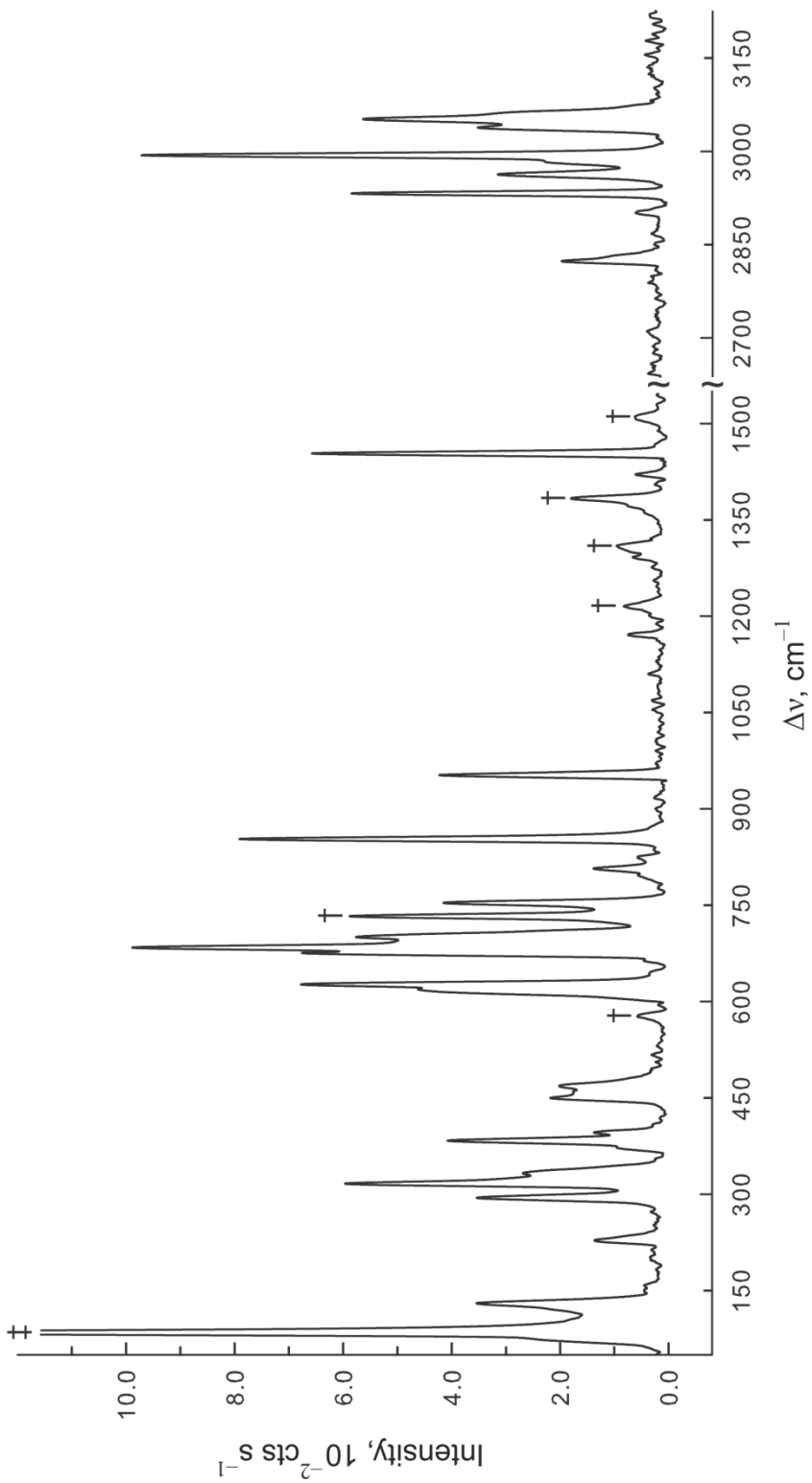

Figure S4.9. The complete Raman spectrum of $[N(CH_3)_4]_2[Hg_2(OTeF_5)_6]$ recorded at −155 °C using 1064-nm excitation. Symbols denote purely FEP (†) bands, an instrumental artifact (‡).

Table S4.7. Experimental Raman Frequencies and Intensities for $[Hg(OTeF_5)_4]^{2-}$ in $[N(CH_2CH_3)_4]_2[Hg(OTeF_5)_4]$ and Calculated Vibrational Frequencies and Intensities for $[Hg(OTeF_5)_4]^{2-}$ with Complete Mode Assignments

exptl $[Hg(OTeF_5)_4]^{2-}$ in $[N(CH_2CH_3)_4]_2[Hg(OTeF_5)_4]$ [a,b,c]	calcd $[Hg(OTeF_5)_4]^{2-}$ (S_4) [a,d]	
		assgnts [e]
848(18)	879(98)[0]	$[\nu(Hg_1\text{-}O_8) + \nu(Hg_1\text{-}O_{14}) + \nu(Hg_1\text{-}O_{18}) + \nu(Hg_1\text{-}O_{28})] - [\nu(Te_5\text{-}O_8) + \nu(Te_4\text{-}O_{14}) + \nu(Te_2\text{-}O_{18}) + \nu(Te_3\text{-}O_{28})]$
807(7)	839(36)[375]	$[\nu(Hg_1\text{-}O_{28}) + \nu(Te_5\text{-}O_{14})] - [\nu(Hg_1\text{-}O_{14}) + \nu(Te_3\text{-}O_{28})]$
	839(36)[375]	$[\nu(Hg_1\text{-}O_8) + \nu(Te_2\text{-}O_{18})] - [\nu(Hg_1\text{-}O_{18}) + \nu(Te_5\text{-}O_8)]$
	839(27)[439]	$[\nu(Hg_1\text{-}O_8) + \nu(Hg_1\text{-}O_{18}) + \nu(Te_3\text{-}O_{28}) + \nu(Te_4\text{-}O_{14})] - [\nu(Hg_1\text{-}O_{14}) + \nu(Hg_1\text{-}O_{28}) + \nu(Te_2\text{-}O_{18}) + \nu(Te_5\text{-}O_8)]$
681(33) 677(31) [f]	683(2)[372]	$[\nu(Te_2\text{-}F_{10}) + \nu(Te_3\text{-}F_{27}) + \nu(Te_4\text{-}F_{17}) + \nu(Te_5\text{-}F_6)] - [\nu(Te_2\text{-}F_{20}) + \nu(Te_3\text{-}F_{24}) + \nu(Te_4\text{-}F_{21}) + \nu(Te_5\text{-}F_{15})]$
	681(2)[404]	$[\nu(Te_2\text{-}F_{10}) + \nu(Te_3\text{-}F_{26}) + \nu(Te_4\text{-}F_{19}) + \nu(Te_5\text{-}F_{15})] - [\nu(Te_2\text{-}F_{20}) + \nu(Te_3\text{-}F_{25}) + \nu(Te_4\text{-}F_{22}) + \nu(Te_5\text{-}F_6)]$
	681(2)[404]	$[\nu(Te_2\text{-}F_{11}) + \nu(Te_3\text{-}F_{27}) + \nu(Te_4\text{-}F_{21}) + \nu(Te_5\text{-}F_9)] - [\nu(Te_2\text{-}F_{13}) + \nu(Te_3\text{-}F_{24}) + \nu(Te_4\text{-}F_{17}) + \nu(Te_5\text{-}F_{12})]$
	680(5)[0]	$[\nu(Te_2\text{-}F_{10}) + \nu(Te_3\text{-}F_{24}) + \nu(Te_4\text{-}F_{21}) + \nu(Te_5\text{-}F_6)] - [\nu(Te_2\text{-}F_{20}) + \nu(Te_3\text{-}F_{27}) + \nu(Te_4\text{-}F_{17}) + \nu(Te_5\text{-}F_{15})]$
	677(6)[59]	$[\nu(Te_2\text{-}F_{11}) + \nu(Te_3\text{-}F_{25}) + \nu(Te_4\text{-}F_{19}) + \nu(Te_5\text{-}F_{12})] - [\nu(Te_2\text{-}F_{13}) + \nu(Te_3\text{-}F_{26}) + \nu(Te_4\text{-}F_{22}) + \nu(Te_5\text{-}F_9)]$
	675(19)[0]	$[\nu(Te_2\text{-}F_{11}) + \nu(Te_3\text{-}F_{26}) + \nu(Te_4\text{-}F_{22}) + \nu(Te_5\text{-}F_{12})] - [\nu(Te_2\text{-}F_{13}) + \nu(Te_3\text{-}F_{25}) + \nu(Te_4\text{-}F_{19}) + \nu(Te_5\text{-}F_9)]$
	673(<1)[17]	$[\nu(Te_2\text{-}F_{10}) + \nu(Te_3\text{-}F_{25}) + \nu(Te_3\text{-}F_{24}) + \nu(Te_4\text{-}F_{22}) + \nu(Te_4\text{-}F_{17}) + \nu(Te_5\text{-}F_{15})] - [\nu(Te_2\text{-}F_{20}) + \nu(Te_3\text{-}F_{26}) + \nu(Te_3\text{-}F_{27}) + \nu(Te_4\text{-}F_{19}) + \nu(Te_4\text{-}F_{21}) + \nu(Te_5\text{-}F_6)]$
	673(<1)[17]	$[\nu(Te_2\text{-}F_{10}) + \nu(Te_2\text{-}F_{13}) + \nu(Te_3\text{-}F_{27}) + \nu(Te_4\text{-}F_{21}) + \nu(Te_5\text{-}F_{12}) + \nu(Te_5\text{-}F_{15})] - [\nu(Te_2\text{-}F_{20}) + \nu(Te_2\text{-}F_{11}) + \nu(Te_3\text{-}F_{24}) + \nu(Te_4\text{-}F_{17}) + \nu(Te_5\text{-}F_6) + \nu(Te_5\text{-}F_9)]$
689(100)	660(117)[0]	$[\nu(F_aF_{4e}Te_2) + \nu(F_aF_{4e}Te_3) + \nu(F_aF_{4e}Te_4) + \nu(F_aF_{4e}Te_5)]$
	656(5)[122]	$[\nu(F_aF_{4e}Te_2) + \nu(F_aF_{4e}Te_4)] - [\nu(F_aF_{4e}Te_3) + \nu(F_aF_{4e}Te_5)]$
	656(5)[122]	$[\nu(F_aF_{4e}Te_2) + \nu(F_aF_{4e}Te_3)] - [\nu(F_aF_{4e}Te_4) + \nu(F_aF_{4e}Te_5)]$
	656(5)[132]	$[\nu(F_aF_{4e}Te_2) + \nu(F_aF_{4e}Te_5)] - [\nu(F_aF_{4e}Te_3) + \nu(F_aF_{4e}Te_4)]$
622(57) 616(14) 612(13) 606(14)	609(5)[<0.1]	$[\nu(Te_2\text{-}F_{10}) + \nu(Te_2\text{-}F_{20})] - [\nu(Te_2\text{-}F_{11}) + \nu(Te_2\text{-}F_{13})] + [\nu(Te_3\text{-}F_{25}) + \nu(Te_3\text{-}F_{26})] - [\nu(Te_3\text{-}F_{24}) + \nu(Te_3\text{-}F_{27})] + [\nu(Te_4\text{-}F_{19}) + \nu(Te_4\text{-}F_{22})] - [\nu(Te_4\text{-}F_{17}) + \nu(Te_4\text{-}F_{21})] + [\nu(Te_5\text{-}F_6) + \nu(Te_5\text{-}F_{15})] - [\nu(Te_5\text{-}F_9) + \nu(Te_5\text{-}F_{12})]$
	608(2)[2]	$[\nu(Te_2\text{-}F_{10}) + \nu(Te_2\text{-}F_{20})] - [\nu(Te_2\text{-}F_{11}) + \nu(Te_2\text{-}F_{13})] + [\nu(Te_5\text{-}F_9) + \nu(Te_5\text{-}F_{12})] - [\nu(Te_5\text{-}F_6) + \nu(Te_5\text{-}F_{15})]$
	608(2)[2]	$[\nu(Te_3\text{-}F_{25}) + \nu(Te_3\text{-}F_{26})] - [\nu(Te_3\text{-}F_{24}) + \nu(Te_3\text{-}F_{27})] + [\nu(Te_4\text{-}F_{17}) + \nu(Te_4\text{-}F_{21})] - [\nu(Te_4\text{-}F_{19}) + \nu(Te_4\text{-}F_{22})]$
	608(4)[0]	$[\nu(Te_2\text{-}F_{10}) + \nu(Te_2\text{-}F_{20})] - [\nu(Te_2\text{-}F_{11}) + \nu(Te_2\text{-}F_{13})] + [\nu(Te_3\text{-}F_{24}) + \nu(Te_3\text{-}F_{27})] - [\nu(Te_3\text{-}F_{25}) + \nu(Te_3\text{-}F_{26})] + [\nu(Te_4\text{-}F_{17}) + \nu(Te_4\text{-}F_{21})] - [\nu(Te_4\text{-}F_{19}) + \nu(Te_4\text{-}F_{22})] + [\nu(Te_5\text{-}F_6) + \nu(Te_5\text{-}F_{15})] - [\nu(Te_5\text{-}F_9) + \nu(Te_5\text{-}F_{12})]$
	604(14)[0]	$[\nu(Te_2\text{-}F_{16}) + \nu(Te_3\text{-}F_{29}) + \nu(Te_4\text{-}F_{23}) + \nu(Te_5\text{-}F_7)] - [\nu(Te_2F_{4e}) + \nu(Te_3F_{4e}) + \nu(Te_4F_{4e}) + \nu(Te_5F_{4e})]_{small}$
	600(2)[<1]	$[\nu(Te_2\text{-}F_{16}) + \nu(Te_5\text{-}F_7) + \nu(Te_3F_{4e})_{small} + \nu(Te_4F_{4e})_{small}] - [\nu(Te_3\text{-}F_{29}) + \nu(Te_4\text{-}F_{23}) + \nu(Te_2F_{4e})_{small} + \nu(Te_5F_{4e})_{small}]$
	599(1)[6]	$[\nu(Te_2\text{-}F_{16}) + \nu(Te_5F_{4e})] - [\nu(Te_5\text{-}F_7) + \nu(Te_2F_{4e})]$
	599(1)[6]	$[\nu(Te_3\text{-}F_{29}) + \nu(Te_4\text{-}F_{23})] - [\nu(Te_4F_{4e}) + \nu(Te_3F_{4e})]$

Table S4.7. continued…

420(25)[f]	390(<1)[90]	$[\nu(Hg_1\text{-}O_{14}) + \nu(Te_4\text{-}O_{14})] - [\nu(Hg_1\text{-}O_{28}) + \nu(Te_3\text{-}O_{28})]$
417, sh	390(<1)[90]	$[\nu(Hg_1\text{-}O_8) + \nu(Te_5\text{-}O_8)] - [\nu(Hg_1\text{-}O_{18}) + \nu(Te_2\text{-}O_{18})]$
406, sh	390(3)[7]	$[\nu(Hg_1\text{-}O_{14}) + \nu(Hg_1\text{-}O_{28}) + \nu(Te_4\text{-}O_{14}) + \nu(Te_3\text{-}O_{28})] - [\nu(Hg_1\text{-}O_8) + \nu(Hg_1\text{-}O_{18}) + \nu(Te_5\text{-}O_8) + \nu(Te_2\text{-}O_{18})]$
	388(4)[0]	$[\nu(Hg_1\text{-}O_{14}) + \nu(Hg_1\text{-}O_8) + \nu(Te_4\text{-}O_{14}) + \nu(Te_5\text{-}O_8)] + [\nu(Hg_1\text{-}O_{28}) + \nu(Hg_1\text{-}O_{18}) + \nu(Te_3\text{-}O_{28}) + \nu(Te_2\text{-}O_{18})]$
339(11) 334(11) 327(13)	340(<1)[0]	$[\nu(Te_2F_{4e})_{umb} + \nu(Te_3F_{4e})_{umb} + \nu(Te_4F_{4e})_{umb} + \nu(Te_5F_{4e})_{umb}]$
	338(<1)[75]	$[\delta(F_{20}\text{-}Te_2\text{-}F_{16}) - \delta(F_{10}\text{-}Te_2\text{-}F_{16})] + [\delta(F_{27}\text{-}Te_3\text{-}F_{29}) - \delta(F_{24}\text{-}Te_3\text{-}F_{29})] + [\delta(F_{21}\text{-}Te_4\text{-}F_{23}) - \delta(F_{17}\text{-}Te_4\text{-}F_{23})] + [\delta(F_{15}\text{-}Te_5\text{-}F_7) - \delta(F_6\text{-}Te_5\text{-}F_7)]$
	338(2)[0]	$[\delta(F_{20}\text{-}Te_2\text{-}F_{16}) - \delta(F_{10}\text{-}Te_2\text{-}F_{16})] + [\delta(F_{27}\text{-}Te_3\text{-}F_{29}) - \delta(F_{24}\text{-}Te_3\text{-}F_{29})] + [\delta(F_{17}\text{-}Te_4\text{-}F_{23}) - \delta(F_{21}\text{-}Te_4\text{-}F_{23})] + [\delta(F_{15}\text{-}Te_5\text{-}F_7) - \delta(F_6\text{-}Te_5\text{-}F_7)]$
	337(<1)[14]	$[\delta(F_{20}\text{-}Te_2\text{-}F_{16}) - \delta(F_{10}\text{-}Te_2\text{-}F_{16})] + [\delta(F_{24}\text{-}Te_3\text{-}F_{29}) - \delta(F_{27}\text{-}Te_3\text{-}F_{29})] + [\delta(F_{17}\text{-}Te_4\text{-}F_{23}) - \delta(F_{21}\text{-}Te_4\text{-}F_{23})] + [\delta(F_6\text{-}Te_5\text{-}F_7) - \delta(F_{15}\text{-}Te_5\text{-}F_7)]$
	337(<1)[14]	$[\delta(F_{20}\text{-}Te_2\text{-}F_{16}) - \delta(F_{10}\text{-}Te_2\text{-}F_{16})] + [\delta(F_{27}\text{-}Te_3\text{-}F_{29}) - \delta(F_{24}\text{-}Te_3\text{-}F_{29})] + [\delta(F_{21}\text{-}Te_4\text{-}F_{23}) - \delta(F_{17}\text{-}Te_4\text{-}F_{23})] + [\delta(F_6\text{-}Te_5\text{-}F_7) - \delta(F_{15}\text{-}Te_5\text{-}F_7)]$
	335(<1)[20]	$[\delta(F_{11}\text{-}Te_2\text{-}F_{16}) - \delta(F_{13}\text{-}Te_2\text{-}F_{16})] + [\delta(F_{25}\text{-}Te_3\text{-}F_{29}) - \delta(F_{26}\text{-}Te_3\text{-}F_{29})] + [\delta(F_{19}\text{-}Te_4\text{-}F_{23}) - \delta(F_{22}\text{-}Te_4\text{-}F_{23})] + [\delta(F_{12}\text{-}Te_5\text{-}F_7) - \delta(F_9\text{-}Te_5\text{-}F_7)]$
	334(<1)[58]	$[\delta(F_{11}\text{-}Te_2\text{-}F_{16}) - \delta(F_{13}\text{-}Te_2\text{-}F_{16})] + [\delta(F_{26}\text{-}Te_3\text{-}F_{29}) - \delta(F_{25}\text{-}Te_3\text{-}F_{29})] + [\delta(F_{19}\text{-}Te_4\text{-}F_{23}) - \delta(F_{22}\text{-}Te_4\text{-}F_{23})] + [\delta(F_9\text{-}Te_5\text{-}F_7) - \delta(F_{12}\text{-}Te_5\text{-}F_7)]$
	334(<1)[58]	$[\delta(F_{11}\text{-}Te_2\text{-}F_{16}) - \delta(F_{13}\text{-}Te_2\text{-}F_{16})] + [\delta(F_{26}\text{-}Te_3\text{-}F_{29}) - \delta(F_{25}\text{-}Te_3\text{-}F_{29})] + [\delta(F_{22}\text{-}Te_4\text{-}F_{23}) - \delta(F_{19}\text{-}Te_4\text{-}F_{23})] + [\delta(F_{12}\text{-}Te_5\text{-}F_7) - \delta(F_9\text{-}Te_5\text{-}F_7)]$
	332(<0.1)[0]	$[\delta(F_{11}\text{-}Te_2\text{-}F_{16}) + \delta(F_{26}\text{-}Te_3\text{-}F_{29}) + \delta(F_{22}\text{-}Te_4\text{-}F_{23}) + \delta(F_7\text{-}Te_5\text{-}F_{12})] - [\delta(F_{13}\text{-}Te_2\text{-}F_{16}) + \delta(F_{25}\text{-}Te_3\text{-}F_{29}) + \delta(F_{19}\text{-}Te_4\text{-}F_{23}) + \delta(F_9\text{-}Te_5\text{-}F_7)]$
	329(3)[65]	$[\nu(Te_4F_{4e})_{umb} + \nu(Te_3F_{4e})_{umb}] - [\nu(Te_2F_{4e})_{umb} + \nu(Te_5F_{4e})_{umb}]$
	328(<1)[90]	$[\nu(Te_4F_{4e})_{umb} + \nu(Te_5F_{4e})_{umb}] - [\nu(Te_2F_{4e})_{umb} + \nu(Te_3F_{4e})_{umb}]$
	328(<1)[90]	$[\nu(Te_4F_{4e})_{umb} + \nu(Te_2F_{4e})_{umb}] - [\nu(Te_3F_{4e})_{umb} + \nu(Te_5F_{4e})_{umb}]$
317, sh, br	320(1)[109]	$[\delta(O_{14}\text{-}Hg_1\text{-}O_{28}) - \delta(O_8\text{-}Hg_1\text{-}O_{18})]$
	318(4)[0]	$[\delta(O_{14}\text{-}Hg_1\text{-}O_{28}) + \delta(O_8\text{-}Hg_1\text{-}O_{18})]$
	313(<1)[25]	$[\rho_t(O_8\text{-}Hg_1\text{-}O_{14}) + \rho_t(O_{18}\text{-}Hg_1\text{-}O_{28})]$
	313(<1)[25]	$[\rho_t(O_8\text{-}Hg_1\text{-}O_{28}) + \rho_t(O_{18}\text{-}Hg_1\text{-}O_{14})]$
292(15)	286(2)[<0.1]	$[\delta(F_{10}\text{-}Te_2\text{-}F_{11}) + \delta(F_{13}\text{-}Te_2\text{-}F_{20})] + [\delta(F_{24}\text{-}Te_3\text{-}F_{25}) + \delta(F_{26}\text{-}Te_3\text{-}F_{27})] + [\delta(F_{17}\text{-}Te_4\text{-}F_{22}) + \delta(F_{19}\text{-}Te_4\text{-}F_{21})] + [\delta(F_6\text{-}Te_5\text{-}F_{12}) + \delta(F_9\text{-}Te_5\text{-}F_{15})]$
	286(2)[<0.1]	$[\delta(F_{24}\text{-}Te_3\text{-}F_{25}) + \delta(F_{26}\text{-}Te_3\text{-}F_{27})] + [\delta(F_{17}\text{-}Te_4\text{-}F_{19}) + \delta(F_{21}\text{-}Te_4\text{-}F_{22})]$
	286(2)[<0.1]	$[\delta(F_{10}\text{-}Te_2\text{-}F_{11}) + \delta(F_{13}\text{-}Te_2\text{-}F_{20})] + [\delta(F_6\text{-}Te_5\text{-}F_9) + \delta(F_{12}\text{-}Te_5\text{-}F_{15})]$
	286(<0.1)[0]	$[\delta(F_{10}\text{-}Te_2\text{-}F_{13}) + \delta(F_{11}\text{-}Te_2\text{-}F_{20})] + [\delta(F_{24}\text{-}Te_3\text{-}F_{25}) + \delta(F_{26}\text{-}Te_3\text{-}F_{27})] + [\delta(F_{17}\text{-}Te_4\text{-}F_{22}) + \delta(F_{19}\text{-}Te_4\text{-}F_{21})] + [\delta(F_6\text{-}Te_5\text{-}F_9) + \delta(F_{12}\text{-}Te_5\text{-}F_{15})]$

Table S4.7. continued…

225(5)	216(1)[0]	$[\rho_w(F_{10}\text{-}Te_2\text{-}F_{20}) + \rho_w(F_{24}\text{-}Te_3\text{-}F_{27}) + \rho_w(F_{17}\text{-}Te_4\text{-}F_{21}) + \rho_w(F_6\text{-}Te_5\text{-}F_{15})]$	
	215(<0.1)[<1]	$[\rho_w(F_{10}\text{-}Te_2\text{-}F_{20}) + \rho_w(F_{25}\text{-}Te_3\text{-}F_{26}) + \rho_w(F_{19}\text{-}Te_4\text{-}F_{22}) + \rho_w(F_6\text{-}Te_5\text{-}F_{15})]$ $-[\rho_w(F_{11}\text{-}Te_2\text{-}F_{13}) + \rho_w(F_{24}\text{-}Te_3\text{-}F_{27}) + \rho_w(F_{17}\text{-}Te_4\text{-}F_{21}) + \rho_w(F_9\text{-}Te_5\text{-}F_{12})]$	
	214(<0.1)[<1]	$[\rho_w(F_{25}\text{-}Te_3\text{-}F_{26}) + \rho_w(F_{17}\text{-}Te_4\text{-}F_{21})] - [\rho_w(F_{24}\text{-}Te_3\text{-}F_{27}) + \rho_w(F_{19}\text{-}Te_4\text{-}F_{22})]$	
	214(<0.1)[<1]	$[\rho_w(F_{10}\text{-}Te_2\text{-}F_{20}) + \rho_w(F_9\text{-}Te_5\text{-}F_{12})] - [\rho_w(F_{11}\text{-}Te_2\text{-}F_{13}) + \rho_w(F_6\text{-}Te_5\text{-}F_{15})]$	
	213(<1)[0]	$[\rho_w(F_{10}\text{-}Te_2\text{-}F_{20}) + \rho_w(F_{24}\text{-}Te_3\text{-}F_{27}) + \rho_w(F_{17}\text{-}Te_4\text{-}F_{21}) + \rho_w(F_6\text{-}Te_5\text{-}F_{15})]$ $-[\rho_w(F_{11}\text{-}Te_2\text{-}F_{13}) + \rho_w(F_{25}\text{-}Te_3\text{-}F_{26}) + \rho_w(F_{19}\text{-}Te_4\text{-}F_{22}) + \rho_w(F_9\text{-}Te_5\text{-}F_{12})]$	
	211(<1)[7]	$[\rho_w(O_{28}\text{-}Te_3\text{-}F_{29}) + \rho_w(O_{14}\text{-}Te_4\text{-}F_{23})] - [\rho_w(F_{24}\text{-}Te_3\text{-}F_{27}) + \rho_w(F_{17}\text{-}Te_4\text{-}F_{21})]$	
	211(<1)[7]	$[\rho_w(O_{18}\text{-}Te_2\text{-}F_{16}) + \rho_w(O_8\text{-}Te_5\text{-}F_7)] - [\rho_w(F_{10}\text{-}Te_2\text{-}F_{20}) + \rho_w(F_6\text{-}Te_5\text{-}F_{15})]$	
	211(<1)[5]	$[\rho_w(F_{10}\text{-}Te_2\text{-}F_{20}) + \rho_w(F_{24}\text{-}Te_3\text{-}F_{27}) + \rho_w(F_{17}\text{-}Te_4\text{-}F_{21}) + \rho_w(F_6\text{-}Te_5\text{-}F_{15})]$	
n.o.	191(<0.1)[<0.1]	$[\rho_w(O_{18}\text{-}Te_2\text{-}F_{16}) + \rho_w(O_{28}\text{-}Te_3\text{-}F_{29}) + \rho_w(O_{14}\text{-}Te_4\text{-}F_{23}) + \rho_w(O_8\text{-}Te_5\text{-}F_7)]$ $-[\rho_w(F_{11}\text{-}Te_2\text{-}F_{13}) + \rho_w(F_{25}\text{-}Te_3\text{-}F_{26}) + \rho_w(F_{19}\text{-}Te_4\text{-}F_{22}) + \rho_w(F_9\text{-}Te_5\text{-}F_{12})]$	
	191(<0.1)[<0.1]	$[\rho_w(O_{18}\text{-}Te_2\text{-}F_{16}) + \rho_w(O_{14}\text{-}Te_4\text{-}F_{23}) + \rho_w(F_{25}\text{-}Te_3\text{-}F_{26}) + \rho_w(F_9\text{-}Te_5\text{-}F_{12})]$ $-[\rho_w(O_{28}\text{-}Te_3\text{-}F_{29}) + \rho_w(O_8\text{-}Te_5\text{-}F_7) + \rho_w(F_{11}\text{-}Te_2\text{-}F_{13}) + \rho_w(F_{19}\text{-}Te_4\text{-}F_{22})]$	
	191(<0.1)[<0.1]	$[\rho_w(O_{18}\text{-}Te_2\text{-}F_{16}) + \rho_w(O_{28}\text{-}Te_3\text{-}F_{29}) + \rho_w(F_{19}\text{-}Te_4\text{-}F_{22}) + \rho_w(F_9\text{-}Te_5\text{-}F_{12})]$ $-[\rho_w(O_{14}\text{-}Te_4\text{-}F_{23}) + \rho_w(O_8\text{-}Te_5\text{-}F_7) + \rho_w(F_{11}\text{-}Te_2\text{-}F_{13}) + \rho_w(F_{25}\text{-}Te_3\text{-}F_{26})]$	
	190(<0.1)[0]	$[\rho_w(O_{28}\text{-}Te_3\text{-}F_{29}) + \rho_w(O_{14}\text{-}Te_4\text{-}F_{23}) + \rho_w(F_{11}\text{-}Te_2\text{-}F_{13}) + \rho_w(F_9\text{-}Te_5\text{-}F_{12})]$ $-[\rho_w(O_{18}\text{-}Te_2\text{-}F_{16}) + \rho_w(O_8\text{-}Te_5\text{-}F_7) + \rho_w(F_{25}\text{-}Te_3\text{-}F_{26}) + \rho_w(F_{19}\text{-}Te_4\text{-}F_{22})]$	
	119(<0.1)[20]	$[\rho_f(F_aF_{4e}Te_3) + \rho_f(F_aF_{4e}Te_4)]$	
	119(<0.1)[20]	$[\rho_f(F_aF_{4e}Te_2) + \rho_f(F_aF_{4e}Te_5)]$	
	119(<1)[23]	$[\rho_f(F_aF_{4e}Te_2) + \rho_f(F_aF_{4e}Te_5)] - [\rho_f(F_aF_{4e}Te_3) + \rho_f(F_aF_{4e}Te_4)]$	
129(8)	113(2)[0]	$[\rho_f(F_aF_{4e}Te_2) + \rho_f(F_aF_{4e}Te_5) + \rho_f(F_aF_{4e}Te_3) + \rho_f(F_aF_{4e}Te_4)]$	
n.o.	47(<1)[7]	coupled deformation and torsion modes of $[Hg(OTeF_5)_4]^{2-}$	
	47(<1)[7]		
	44(<0.1)[11]		
	37(<1)[0]		
	36(<1)[4]		
	28(<1)[0]		
	26(<1)[1]		
	26(<1)[1]		
	13(<0.1)[<0.1]		
	13(<0.1)[<0.1]		
	13(<0.1)[<0.1]		
	10(<0.1)[0]		

Table S4.7. continued…

n.o.	10(<0.1)[<0.1]	coupled deformation and torsion modes of $[Hg(OTeF_5)_4]^{2-}$

[a] Frequencies are given in cm^{-1}. [b] Values in parentheses denote relative Raman intensities. The Raman spectrum was recorded in an FEP sample tube at −150 °C using 1064-nm excitation. [c] The abbreviations denote shoulder (sh), and broad (br), and not observed (n.o.). [d] Values in parentheses denote calculated Raman intensities ($Å^4$ amu^{-1}) and values in square brackets denote calculated infrared intensities (km mol^{-1}). [e] Assignments are for the energy-minimized geometry calculated at the PBE0/def2-TZVPP level with. The atom numbering scheme corresponds to that used in Figure 4.10. The abbreviations denote umbrella (umb), stretch (ν), bend (δ), twist (ρ_t), wag (ρ_w), and rock (ρ_r). [f] Overlap with a cation mode. The notation $Te_nF_{4e}F_a$, where *n* is the tellurium atom label, corresponds to the symmetric stretches of the axial fluorine (F_a) and the equatorial fluorines (F_{4e}) of the F_5Te_nO- group.

Table S4.8. Experimental Raman Frequencies and Intensities for $[Hg(OTeF_5)_5]^{3-}$ in $[N(CH_3)_4]_3[Hg(OTeF_5)_5]$ and Calculated Vibrational Frequencies and Intensities for $[Hg(OTeF_5)_5]^{3-}$ with Complete Mode Descriptions

exptl $[Hg(OTeF_5)_5]^{3-}$ in $[N(CH_3)_4]_3[Hg(OTeF_5)_5]$ [a,b,c]	calcd $[Hg(OTeF_5)_5]^{3-}$ (C_1) [a,d]	assgnts [e]
867(52)	893(222)[10]	$[\nu(Hg_1\text{-}O_8) + \nu(Hg_1\text{-}O_{12}) + \nu(Hg_1\text{-}O_{22}) + \nu(Hg_1\text{-}O_{25}) + \nu(Hg_1\text{-}O_{34}) - \nu(Te_3\text{-}O_8) + \nu(Te_2\text{-}O_{12}) + \nu(Te_6\text{-}O_{22}) + \nu(Te_4\text{-}O_{25}) + \nu(Te_4\text{-}O_{25})]$
853(22)	877(54)[315]	$[\nu(Hg_1\text{-}O_8) - \nu(Te_3\text{-}O_8)] + [\nu(Hg_1\text{-}O_{25}) - \nu(Te_4\text{-}O_{25})] - [\nu(Hg_1\text{-}O_{12}) - \nu(Te_2\text{-}O_{12})]$
	872(71)[322]	$\nu(Hg_1\text{-}O_8) - \nu(Te_3\text{-}O_8)] - [\nu(Hg_1\text{-}O_{25}) - \nu(Te_4\text{-}O_{25})]$
827(16)	849(4)[528]	$[\nu(Hg_1\text{-}O_{22}) - \nu(Te_6\text{-}O_{22})] - [\nu(Hg_1\text{-}O_{34}) - \nu(Te_5\text{-}O_{34})]$
809(16)	832(46)[25]	$[\nu(Hg_1\text{-}O_{22}) - \nu(Tc_6\text{-}O_{22})] + [\nu(Hg_1\text{-}O_{34}) - \nu(Tc_5\text{-}O_{34})]$
	688(<1)[357]	$[\nu(Te_5\text{-}F_{20}) + \nu(Te_5\text{-}F_{15}) + \nu(Te_6\text{-}F_9) + \nu(Te_6\text{-}F_{11})] - [\nu(Te_5\text{-}F_{13}) + \nu(Te_5\text{-}F_{32}) + \nu(Te_6\text{-}F_{17}) + \nu(Te_6\text{-}F_{26})]$
690, sh	688(<1)[336]	$[\nu(Te_5\text{-}F_{13}) + \nu(Te_5\text{-}F_{20}) + \nu(Te_6\text{-}F_9) + \nu(Te_6\text{-}F_{17})] - [\nu(Te_5\text{-}F_{15}) + \nu(Te_5\text{-}F_{32}) + \nu(Te_6\text{-}F_{11}) + \nu(Te_6\text{-}F_{26})]$
682, sh	687(3)[22]	$[\nu(Te_5\text{-}F_{13}) + \nu(Te_5\text{-}F_{20}) + \nu(Te_6\text{-}F_{11}) + \nu(Te_6\text{-}F_{26})] - [\nu(Te_5\text{-}F_{15}) + \nu(Te_5\text{-}F_{32}) + \nu(Te_6\text{-}F_9) + \nu(Te_6\text{-}F_{17})]$
	686(4)[1]	$[\nu(Te_5\text{-}F_{20}) + \nu(Te_5\text{-}F_{15}) + \nu(Te_6\text{-}F_{17}) + \nu(Te_6\text{-}F_{26})] - [\nu(Te_5\text{-}F_{13}) + \nu(Te_5\text{-}F_{32}) + \nu(Te_6\text{-}F_9) + \nu(Te_6\text{-}F_{11})]$
675(100)	657(112)[13]	$[\nu(F_aF_{4e}Te_5) + \nu(F_aF_{4e}Te_6)]$
	657(<1)[560]	$[\nu(Te_2\text{-}F_{36}) + \nu(Te_3\text{-}F_{35}) + \nu(Te_4\text{-}F_{30})] - [\nu(Te_2\text{-}F_{21}) + \nu(Te_3\text{-}F_{18}) + \nu(Te_4\text{-}F_{14})]$
670, sh	655(6)[173]	$[\nu(Te_4\text{-}F_{14}) + \nu(Te_4\text{-}F_{19}) + \nu(Te_3\text{-}F_{33}) + \nu(Te_3\text{-}F_{35})] - [\nu(Te_4\text{-}F_{30}) + \nu(Te_4\text{-}F_{31}) + \nu(Te_3\text{-}F_7) + \nu(Te_3\text{-}F_{18})]$
	654(2)[125]	$[\nu(Te_2\text{-}F_{36}) + \nu(Te_2\text{-}F_{28}) + \nu(Te_3\text{-}F_{33}) + \nu(Te_4\text{-}F_{31})] - [\nu(Te_2\text{-}F_{10}) + \nu(Te_2\text{-}F_{21}) + \nu(Te_3\text{-}F_7) + \nu(Te_4\text{-}F_{19})]$
	653(2)[60]	$[\nu(Te_2\text{-}F_{10}) + \nu(Te_3\text{-}F_{18}) + \nu(Te_4\text{-}F_{14})] - [\nu(Te_2\text{-}F_{28}) + \nu(Te_3\text{-}F_{35}) + \nu(Te_4\text{-}F_{30})] + [\nu(F_aF_{4e}Te_5) - \nu(F_aF_{4e}Te_6)]$
661(42)	652(10)[10]	$[\nu(Te_3\text{-}F_{18}) + \nu(Te_3\text{-}F_{33}) + \nu(Te_4\text{-}F_{19}) + \nu(Te_4\text{-}F_{30})] - [\nu(Te_3\text{-}F_7) + \nu(Te_3\text{-}F_{35}) + \nu(Te_4\text{-}F_{14}) + \nu(Te_4\text{-}F_{31})]$
	652(<1)[<1]	$[\nu(Te_2\text{-}F_{21}) + \nu(Te_3\text{-}F_{18}) + \nu(Te_4\text{-}F_{30}) + \nu(Te_4\text{-}F_{31})] - [\nu(Te_2\text{-}F_{36}) + \nu(Te_3\text{-}F_{35}) + \nu(Te_4\text{-}F_{14}) + \nu(Te_4\text{-}F_{19})]$
	649(1)[9]	$[\nu(Te_2\text{-}F_{21}) + \nu(Te_2\text{-}F_{28}) + \nu(Te_3\text{-}F_7) + \nu(Te_4\text{-}F_{19})] - [\nu(Te_2\text{-}F_{10}) + \nu(Te_2\text{-}F_{36}) + \nu(Te_3\text{-}F_{33}) + \nu(Te_4\text{-}F_{31})]$
	637(74)[16]	$[\nu(F_aF_{4e}Te_2) + \nu(F_aF_{4e}Te_3) + \nu(F_aF_{4e}Te_4)]$
627(15)	635(7)[152]	$[\nu(F_aF_{4e}Te_3) - \nu(F_aF_{4e}Te_4)]$
622(18)	634(9)[152]	$[\nu(F_aF_{4e}Te_2)]$
619(15)	613(3)[3]	$[\nu(Te_5\text{-}F_{13}) + \nu(Te_5\text{-}F_{15}) + \nu(Te_6\text{-}F_9) + \nu(Te_6\text{-}F_{26})] - [\nu(Te_5\text{-}F_{20}) + \nu(Te_5\text{-}F_{32}) + \nu(Te_6\text{-}F_{11}) + \nu(Te_6\text{-}F_{17})]$
	613(3)[15]	$[\nu(Te_5\text{-}F_{13}) + \nu(Te_5\text{-}F_{15}) + \nu(Te_6\text{-}F_{11}) + \nu(Te_6\text{-}F_{17})] - [\nu(Te_5\text{-}F_{20}) + \nu(Te_5\text{-}F_{32}) + \nu(Te_6\text{-}F_9) + \nu(Te_6\text{-}F_{26})]$
608(42)	597(1)[19]	$[\nu(Te_5\text{-}F_{29}) - \nu(Te_5F_{4e})] - [\nu(Te_6\text{-}F_{27}) - \nu(Te_6F_{4e})]$
	597(4)[7]	$[\nu(Te_5\text{-}F_{29}) - \nu(Te_5F_{4e})] + [\nu(Te_6\text{-}F_{27}) - \nu(Te_6F_{4e})]$
600, sh	587(4)[<1]	$[\nu(Te_4\text{-}F_{14}) + \nu(Te_4\text{-}F_{30}) + \nu(Te_3\text{-}F_7) + \nu(Te_3\text{-}F_{33})] - [\nu(Te_4\text{-}F_{19}) + \nu(Te_4\text{-}F_{31}) + \nu(Te_3\text{-}F_{18}) + \nu(Te_3\text{-}F_{35})]$
	586(5)[1]	$[\nu(Te_4\text{-}F_{14}) + \nu(Te_4\text{-}F_{30}) + \nu(Te_3\text{-}F_{18}) + \nu(Te_3\text{-}F_{35}) + \nu(Te_2\text{-}F_{21}) + \nu(Te_2\text{-}F_{36})] - [\nu(Te_4\text{-}F_{19}) + \nu(Te_4\text{-}F_{31}) + \nu(Te_3\text{-}F_7) + \nu(Te_3\text{-}F_{33}) + \nu(Te_2\text{-}F_{10}) + \nu(Te_2\text{-}F_{28})]$
	586(1)[1]	$[\nu(Te_4\text{-}F_{14}) + \nu(Te_4\text{-}F_{30})\ \nu(Te_2\text{-}F_{10}) + \nu(Te_2\text{-}F_{28}) + \nu(Te_3\text{-}F_{18}) + \nu(Te_3\text{-}F_{35})] - [\nu(Te_4\text{-}F_{19}) + \nu(Te_4\text{-}F_{31}) + \nu(Te_3\text{-}F_7) + \nu(Te_2\text{-}F_{21}) + \nu(Te_2\text{-}F_{36}) + \nu(Te_3\text{-}F_7) + \nu(Te_3\text{-}F_{33})\ ]$
	570(3)[1]	$[\nu(Te_3\text{-}F_{24}) - \nu(Te_3F_{4e})] + [\nu(Te_4\text{-}F_{16}) - \nu(Te_4F_{4e})]$
578(3)	569(1)[10]	$[\nu(Te_3\text{-}F_{24}) - \nu(Te_3F_{4e})] - [\nu(Te_4\text{-}F_{16}) - \nu(Te_4F_{4e})]$
	568(2)[8]	$[\nu(Te_2\text{-}F_{23}) - \nu(Te_2F_{4e})]$
396(7)	428(<1)[60]	$[\nu(Hg_1\text{-}O_{22}) + \nu(Te_6\text{-}O_{22})] - [\nu(Hg_1\text{-}O_{34}) + \nu(Te_5\text{-}O_{34})]$
	401(10)[10]	$[\nu(Hg_1\text{-}O_{22}) + \nu(Te_6\text{-}O_{22})] + [\nu(Hg_1\text{-}O_{34}) + \nu(Te_5\text{-}O_{34})]$

Table S4.8. continued…

	344(1)[42]		[δ(F$_{21}$-Te$_2$-F$_{23}$) – δ(F$_{23}$-Te$_2$-F$_{36}$)] / ρ$_w$(F$_{10}$-Te$_2$-F$_{28}$)]
	344(1)[35]		[δ(F$_{18}$-Te$_3$-F$_{24}$) – δ(F$_{24}$-Te$_3$-F$_{35}$)] / ρ$_w$(F$_7$-Te$_3$-F$_{33}$)]
341(13)	343(1)[28]		[δ(F$_{14}$-Te$_4$-F$_{16}$) – δ(F$_{16}$-Te$_4$-F$_{30}$)] / ρ$_w$(F$_{19}$-Te$_4$-F$_{31}$)
339(13)	343(1)[13]		[δ(F$_{10}$-Te$_2$-F$_{23}$) + δ(F$_{14}$-Te$_4$-F$_{16}$) + δ(F$_{24}$-Te$_3$-F$_7$) + δ(F$_{24}$-Te$_3$-F$_{33}$)] / [ρ$_w$(F$_{19}$-Te$_4$-F$_{31}$)]
337(13)	343(<1)[53]		[δ(F$_{28}$-Te$_2$-F$_{23}$) + δ(F$_{31}$-Te$_4$-F$_{16}$)] / [ρ$_w$(F$_{21}$-Te$_2$-F$_{23}$) + ρ$_w$(F$_{14}$-Te$_4$-F$_{16}$)]
	342(<1)[2]		[δ(F$_{19}$-Te$_4$-F$_{16}$) + δ(F$_{28}$-Te$_2$-F$_{23}$) + δ(F$_{33}$-Te$_3$-F$_{24}$)] – [δ(F$_{31}$-Te$_4$-F$_{16}$) + δ(F$_{10}$-Te$_2$-F$_{23}$) + δ(F$_7$-Te$_3$-F$_{24}$)]
	342(<1)[7]		[δ(F$_{19}$-Te$_4$-F$_{16}$) + δ(F$_{30}$-Te$_4$-F$_{16}$) + δ(F$_{33}$-Te$_3$-F$_{24}$) + δ(F$_{18}$-Te$_3$-F$_{24}$)]
	340(<1)[2]		[δ(F$_{13}$-Te$_5$-F$_{29}$) + δ(F$_9$-Te$_6$-F$_{27}$)] – [δ(F$_{15}$-Te$_5$-F$_{29}$) + δ(F$_{26}$-Te$_6$-F$_{27}$)] / ρ$_w$(F$_{20}$-Te$_5$-F$_{20}$)] + ρ$_w$(F$_{11}$-Te$_6$-F$_{17}$)]
328(15)	340(<1)[9]		[δ(F$_{26}$-Te$_6$-F$_{27}$) + δ(F$_{13}$-Te$_5$-F$_{29}$)] – [δ(F$_9$-Te$_6$-F$_{27}$)] / ρ$_w$(F$_{11}$-Te$_6$-F$_{17}$)]
	338(1)[27]		[δ(F$_{15}$-Te$_5$-F$_{29}$) + δ(F$_{32}$-Te$_5$-F$_{29}$)] – [δ(F$_{11}$-Te$_6$-F$_{27}$) + δ(F$_{26}$-Te$_6$-F$_{27}$)]
	336(1)[96]		[δ(Te$_2$F$_{4e}$)$_{umb}$ + δ(F$_9$-Te$_6$-F$_{27}$)] – [δ(Te$_2$F$_{4e}$)$_{umb}$ + δ(Te$_4$F$_{4e}$)$_{umb}$ + δ(F$_{26}$-Te$_6$-F$_{27}$)]
326(13)	335(<1)[140]	{	[δ(F$_{32}$-Te$_5$-F$_{29}$) + δ(F$_{17}$-Te$_6$-F$_{27}$)] – [δ(F$_{27}$-Te$_6$-F$_{11}$) + δ(F$_{20}$-Te$_5$-F$_{29}$)] / ρ$_w$(F$_{13}$-Te$_5$-F$_{15}$) – ρ$_w$(F$_{26}$-Te$_6$-F$_9$) / [ν(Te$_3$F$_{4e}$)$_{umb}$ – ν(Te$_4$F$_{4e}$)$_{umb}$]$_{small}$
	333(1)[13]		[δ(F$_{32}$-Te$_5$-F$_{29}$) + δ(F$_{27}$-Te$_6$-F$_{11}$)] – [δ(F$_{17}$-Te$_6$-F$_{27}$)] + δ(F$_{20}$-Te$_5$-F$_{29}$)] / ρ$_w$(F$_{13}$-Te$_5$-F$_{15}$) + ρ$_w$(F$_{26}$-Te$_6$-F$_9$)
324(13)	328(<0.1)[1]	{	δ(F$_{20}$-Te$_5$-O$_{34}$) + δ(F$_{17}$-Te$_6$-O$_{22}$)] – [δ(F$_{20}$-Te$_5$-F$_{29}$) + δ(F$_{17}$-Te$_6$-F$_{27}$)] / ρ$_w$(F$_{13}$-Te$_5$-F$_{15}$) + ρ$_w$(F$_{26}$-Te$_6$-F$_9$) / [ν(Te$_5$F$_{4e}$)$_{umb}$ + ν(Te$_6$F$_{4e}$)$_{umb}$]$_{small}$
	327(<0.1)[49]		[δ(F$_{20}$-Te$_5$-O$_{34}$) + δ(F$_{17}$-Te$_6$-F$_{27}$)] – [δ(F$_{17}$-Te$_6$-O$_{22}$) + δ(F$_{20}$-Te$_5$-F$_{29}$)] / ρ$_w$(F$_{13}$-Te$_5$-F$_{15}$) – ρ$_w$(F$_{26}$-Te$_6$-F$_9$)
320(10)	324(3)[121]	{	[δ(F$_{19}$-Te$_4$-O$_{25}$) + δ(F$_{30}$-Te$_4$-O$_{25}$) + δ(F$_{19}$-Te$_4$-F$_{19}$)] – [δ(F$_{18}$-Te$_3$-O$_8$) + δ(F$_{33}$-Te$_3$-O$_8$) + δ(F$_{18}$-Te$_3$-F$_{33}$)]
	322(6)[35]		[δ(F$_{19}$-Te$_4$-O$_{25}$) + δ(F$_{30}$-Te$_4$-O$_{25}$) + δ(F$_{19}$-Te$_4$-F$_{19}$) + δ(F$_{18}$-Te$_3$-O$_8$) + δ(F$_{33}$-Te$_3$-O$_8$) + δ(F$_{18}$-Te$_3$-F$_{33}$)]
316(7)	319(3)[50]	{	[δ(O$_{12}$-Hg$_1$-O$_{34}$) – δ(O$_{12}$-Hg$_1$-O$_{22}$)]
	319(1)[83]		[δ(O$_{25}$-Hg$_1$-O$_8$)]
	316(2)[30]		[δ(O$_{12}$-Hg$_1$-O$_{25}$) – δ(O$_{12}$-Hg$_1$-O$_8$)]
312(7)	312(<1)[<1]	{	[ρ$_t$(Hg$_1$-O$_8$O$_{12}$O$_{25}$)]
308(7)	311(2)[21]		[ρ$_w$(O$_{22}$-Hg$_1$-O$_{34}$)]
	303(<1)[12]		[ρ$_t$(Hg$_1$-O$_{12}$O$_{22}$O$_{34}$)]
292(15)	290(1)[3]	{	[δ(F$_9$-Te$_6$-F$_{11}$) + δ(F$_{17}$-Te$_6$-F$_{26}$) + δ(F$_{15}$-Te$_5$-F$_{20}$) + δ(F$_{13}$-Te$_5$-F$_{32}$)]
	288(1)[2]		[δ(F$_9$-Te$_6$-F$_{11}$) + δ(F$_{17}$-Te$_6$-F$_{26}$)] – [δ(F$_{15}$-Te$_5$-F$_{20}$) + δ(F$_{13}$-Te$_5$-F$_{32}$)]
	281(3)[<0.1]		[δ(F$_{10}$-Te$_2$-F$_{21}$) + δ(F$_{28}$-Te$_2$-F$_{36}$) + δ(F$_{33}$-Te$_3$-F$_{35}$) + δ(F$_7$-Te$_3$-F$_{18}$) + δ(F$_{14}$-Te$_4$-F$_{19}$) + δ(F$_{30}$-Te$_4$-F$_{31}$)]
	280(<1)[<1]		[δ(F$_{10}$-Te$_2$-F$_{21}$) + δ(F$_{28}$-Te$_2$-F$_{36}$)] – [δ(F$_{33}$-Te$_3$-F$_{35}$) + δ(F$_7$-Te$_3$-F$_{18}$)]
	280(1)[<1]		[δ(F$_{14}$-Te$_4$-F$_{19}$) + δ(F$_{30}$-Te$_4$-F$_{31}$)]
n.o.	229(<0.1)[9]		[δ(F$_{29}$-Te$_5$-F$_{32}$) – δ(F$_{11}$-Te$_6$-F$_{27}$)] / [ρ$_w$(F$_{13}$-Te$_5$-F$_{15}$) – ρ$_w$(F$_9$-Te$_6$-F$_{26}$)]
226(4)	219(<1)[<0.1]	{	[ρ$_w$(F$_{10}$-Te$_2$-F$_{28}$) – ρ$_w$(F$_{21}$-Te$_2$-F$_{36}$)]
	218(<0.1)[<0.1]		[ρ$_w$(F$_7$-Te$_3$-F$_{33}$) – ρ$_w$(F$_{18}$-Te$_3$-F$_{35}$)]
	218(<0.1)[<0.1]		[ρ$_w$(F$_{14}$-Te$_4$-F$_{30}$) – ρ$_w$(F$_{19}$-Te$_4$-F$_{31}$)]
	217(1)[<1]		[ρ$_w$(F$_9$-Te$_6$-F$_{26}$) + ρ$_w$(F$_{27}$-Te$_6$-O$_{22}$) + ρ$_w$(F$_{15}$-Te$_5$-F$_{13}$) + ρ$_w$(F$_{29}$-Te$_5$-O$_{34}$)]
	213(<0.1)[<0.1]		[ρ$_w$(F$_{13}$-Te$_5$-F$_{15}$) + ρ$_w$(F$_{11}$-Te$_6$-F$_{17}$)] – [ρ$_w$(F$_{20}$-Te$_5$-F$_{32}$) + ρ$_w$(F$_9$-Te$_6$-F$_{26}$)]
	213(<0.1)[<0.1]		[ρ$_w$(F$_{13}$-Te$_5$-F$_{15}$) + ρ$_w$(F$_9$-Te$_6$-F$_{26}$)] – [ρ$_w$(F$_{20}$-Te$_5$-F$_{32}$) + ρ$_w$(F$_{11}$-Te$_6$-F$_{17}$)]
	198(<0.1)[<0.1]		[ρ$_w$(F$_{29}$-Te$_5$-O$_{34}$) + ρ$_w$(F$_{11}$-Te$_6$-F$_{17}$)] – [ρ$_w$(F$_{27}$-Te$_6$-O$_{27}$) + ρ$_w$(F$_{20}$-Te$_5$-F$_{32}$)]
	196(<0.1)[<0.1]		[ρ$_w$(F$_{29}$-Te$_5$-O$_{34}$) + ρ$_w$(F$_{20}$-Te$_5$-F$_{32}$)] – [ρ$_w$(F$_{11}$-Te$_6$-F$_{17}$) + ρ$_w$(F$_{27}$-Te$_6$-O$_{27}$)]
	192(<1)[<1]		[δ(F$_{19}$-Te$_4$-F$_{30}$) + δ(F$_7$-Te$_3$-F$_{35}$)] – [δ(F$_{14}$-Te$_4$-F$_{31}$) + δ(F$_{18}$-Te$_3$-F$_{33}$)] / [ρ$_w$(F$_{16}$-Te$_4$-O$_{25}$) + ρ$_w$(F$_{24}$-Te$_3$-O$_8$)]
201(3)	191(<1)[<1]	{	[δ(F$_{19}$-Te$_4$-F$_{30}$) + δ(F$_{18}$-Te$_3$-F$_{33}$)] – [δ(F$_7$-Te$_3$-F$_{35}$) + δ(F$_{14}$-Te$_4$-F$_{31}$)] / [ρ$_w$(F$_{16}$-Te$_4$-O$_{25}$) – ρ$_w$(F$_{24}$-Te$_3$-O$_8$)]
	189(<0.1)[<1]		[δ(F$_{10}$-Te$_2$-F$_{21}$) – δ(F$_{28}$-Te$_2$-F$_{36}$) /ρ$_w$(F$_{23}$-Te$_2$-O$_{12}$)]
	189(<0.1)[<1]		[δ(F$_7$-Te$_3$-F$_{18}$) – δ(F$_{33}$-Te$_3$-F$_{35}$)/ ρ$_w$(F$_{24}$-Te$_3$-O$_8$)]
	188(<0.1)[<0.1]		[δ(F$_{19}$-Te$_4$-F$_{14}$) – δ(F$_{30}$-Te$_4$-F$_{31}$) / ρ$_w$(F$_{16}$-Te$_4$-O$_{25}$)]
	186(<0.1)[<1]		[δ(F$_{21}$-Te$_2$-F$_{28}$) – δ(F$_{10}$-Te-F$_{36}$) / ρ$_w$(F$_{23}$-Te$_2$-O$_{12}$)]

Table S4.8. continued…

n.o.	153(<0.1)[19]	$[\rho_t(Te_5\text{-}O_{34}\text{-}F_{20}\text{-}F_{29}\text{-}F_{32}) + \rho_t(Te_6\text{-}O_{22}\text{-}F_{11}\text{-}F_{27}\text{-}F_{17})] / [\rho_w(F_{13}\text{-}Te_5\text{-}F_{15}) - \rho_w(F_9\text{-}Te_6\text{-}F_{26})]$
124(10)	112(2)[<0.1]	$[\rho_t(Te_5\text{-}O_{34}\text{-}F_{20}\text{-}F_{29}\text{-}F_{32}) - \rho_t(Te_6\text{-}O_{22}\text{-}F_{11}\text{-}F_{27}\text{-}F_{17})] / [\rho_w(F_{13}\text{-}Te_5\text{-}F_{15}) + \rho_w(F_9\text{-}Te_6\text{-}F_{26})]$
n.o.	81(1)[23] 73(1)[24] 68(<1)[5] 66(<1)[4] 54(<1)[4] 52(<1)[2] 47(<1)[7] 42(<1)[2] 32(<0.1)[<1] 32(<0.1)[<1] 30(<0.1)[<0.1] 28(<1)[<1] 24(<0.1)[<1] 23(<0.1)[<1] 18(<0.1)[<0.1] 17(<0.1)[<0.1] 15(<0.1)[<1] 15(<0.1)[<1] 13(<0.1)[<0.1] 12(<0.1)[<0.1] 11(<0.1)[<0.1] 9(<1)[<0.1] 8(<1)[<0.1] 6(<0.1)[<0.1] 4(<0.1)[<0.1]	coupled deformation and torsion modes of $[Hg(OTeF_5)_5]^{3-}$

[a] Frequencies are given in cm^{-1}. [b] Values in parentheses denote relative Raman intensities. The Raman spectrum was recorded in an FEP sample tube at −150 °C using 1064-nm excitation. [c] The abbreviations denote shoulder (sh), broad (br), and not observed (n.o.). [d] Values in parentheses denote calculated Raman intensities ($Å^4$ amu^{-1}) and values in square brackets denote calculated infrared intensities (km mol^{-1}). [e] Assignments are for the energy-minimized geometry calculated at the PBE0/def2-TZVPP level. The atom numbering scheme corresponds to that used in Figure 4.11. The abbreviations denote umbrella (umb), stretch (ν), bend (δ), twist (ρ_t), wag (ρ_w), and rock (ρ_r). The notation $Te_nF_{4e}F_a$, where *n* is the tellurium atom label, corresponds to the symmetric stretches of the axial fluorine (F_a) and the equatorial fluorines (F_{4e}) of the F_5Te_nO- group.

Table S4.9. Experimental Raman Frequencies and Intensities for $[Hg_2(OTeF_5)_6]^{2-}$ in $[N(CH_3)_4]_2[Hg_2(OTeF_5)_6]$ and Calculated Vibrational Frequencies and Intensities for $[Hg_2(OTeF_5)_6]^{2-}$ with Complete Mode Descriptions

exptl $[Hg_2(OTeF_5)_6]^{2-}$ in $[N(CH_3)_4]_2[Hg_2(OTeF_5)_6]$ [a,b,c]	calcd $[Hg_2(OTeF_5)_6]^{2-}$ (D_2) [a,d]	assgnts [e]
853(77)	856(127)[0]	$[\nu(Hg_1\text{-}O_{22}) + \nu(Hg_1\text{-}O_{37}) + \nu(Hg_1\text{-}O_{24}) + \nu(Hg_1\text{-}O_{34}) + \nu(Hg_2\text{-}O_{36}) + \nu(Hg_2\text{-}O_{39}) + \nu(Hg_2\text{-}O_{24}) + \nu(Hg_2\text{-}O_{34})] - [\nu(Te_6\text{-}O_{22}) + \nu(Tc_4\text{-}O_{37}) + \nu(Tc_5\text{-}O_{24}) + \nu(Tc_7\text{-}O_{34}) + \nu(Tc_3\text{-}O_{36}) + \nu(Tc_8\text{-}O_{39})]$
826(5), br	823(<1)[665]	$[\nu(Hg_1\text{-}O_{37}) + \nu(Hg_2\text{-}O_{39}) + \nu(Te_6\text{-}O_{22}) + \nu(Te_3\text{-}O_{36})] - [\nu(Hg_1\text{-}O_{22}) + \nu(Hg_2\text{-}O_{36}) + \nu(Te_4\text{-}O_{37}) + \nu(Te_8\text{-}O_{39})]$
	822(47)[6]	$[\nu(Hg_1\text{-}O_{37}) + \nu(Hg_2\text{-}O_{36}) + \nu(Te_6\text{-}O_{22}) + \nu(Te_8\text{-}O_{39})] - [\nu(Hg_1\text{-}O_{22}) + \nu(Hg_2\text{-}O_{39}) + \nu(Te_3\text{-}O_{36}) + \nu(Te_4\text{-}O_{37})]$
808(12)	819(<1)[593]	$[\nu(Hg_1\text{-}O_{22}) + \nu(Hg_1\text{-}O_{37}) + \nu(Te_3\text{-}O_{36}) + \nu(Te_8\text{-}O_{39})] - [\nu(Hg_2\text{-}O_{36}) + \nu(Hg_2\text{-}O_{39}) + \nu(Te_6\text{-}O_{22}) + \nu(Te_4\text{-}O_{37})]$
	812(<0.1)[543]	$[\nu(Hg_1\text{-}O_{24}) + \nu(Hg_2\text{-}O_{24}) + \nu(Te_7\text{-}O_{34})\ ] - [\nu(Hg_1\text{-}O_{34}) + \nu(Hg_2\text{-}O_{34}) + \nu(Te_5\text{-}O_{24})]$
805(12), br	806(18)[0]	$[\nu(Hg_1\text{-}O_{22}) + \nu(Hg_1\text{-}O_{37}) + \nu(Hg_2\text{-}O_{36}) + \nu(Hg_2\text{-}O_{39}) + \nu(Te_5\text{-}O_{24}) + \nu(Te_7\text{-}O_{34})] - [\nu(Hg_1\text{-}O_{24}) + \nu(Hg_1\text{-}O_{34}) + \nu(Hg_2\text{-}O_{24}) + \nu(Hg_2\text{-}O_{34}) + \nu(Te_6\text{-}O_{22}) + \nu(Te_4\text{-}O_{37}) + \nu(Te_3\text{-}O_{36}) + \nu(Te_8\text{-}O_{39})]$
707(30)	699(1)[138]	$[\nu(Te_3\text{-}F_{10}) + \nu(Te_3\text{-}F_{31}) + \nu(Te_4\text{-}F_{14}) + \nu(Te_4\text{-}F_{16}) + \nu(Te_6\text{-}F_{20}) + \nu(Te_6\text{-}F_{21}) + \nu(Te_8\text{-}F_{41}) + \nu(Te_8\text{-}F_{44})] - [\nu(Te_3\text{-}F_{12}) + \nu(Te_3\text{-}F_{30}) + \nu(Te_4\text{-}F_9) + \nu(Te_4\text{-}F_{28}) + \nu(Te_6\text{-}F_{32}) + \nu(Te_6\text{-}F_{35}) + \nu(Te_8\text{-}F_{42}) + \nu(Te_8\text{-}F_{43})]$
	699(21)[0]	$[\nu(Te_3\text{-}F_{10}) + \nu(Te_3\text{-}F_{31}) + \nu(Te_4\text{-}F_9) + \nu(Te_4\text{-}F_{28}) + \nu(Te_6\text{-}F_{32}) + \nu(Te_6\text{-}F_{35}) + \nu(Te_8\text{-}F_{41}) + \nu(Te_8\text{-}F_{44})] - [\nu(Te_3\text{-}F_{12}) + \nu(Te_3\text{-}F_{30}) + \nu(Te_4\text{-}F_{14}) + \nu(Te_4\text{-}F_{16}) + \nu(Te_6\text{-}F_{20}) + \nu(Te_6\text{-}F_{21}) + \nu(Te_8\text{-}F_{42}) + \nu(Te_8\text{-}F_{43})]$
	698(4)[164]	$[\nu(Te_3\text{-}F_{12}) + \nu(Te_4\text{-}F_{28}) + \nu(Te_6\text{-}F_{21}) + \nu(Te_8\text{-}F_{44})] - [\nu(Te_3\text{-}F_{31}) + \nu(Te_6\text{-}F_{35}) + \nu(Te_4\text{-}F_{19}) + \nu(Te_8\text{-}F_{43})$
	698(<0.1)[525]	$[\nu(Te_3\text{-}F_{12}) + \nu(Te_4\text{-}F_{14}) + \nu(Te_6\text{-}F_{35}) + \nu(Te_8\text{-}F_{44})] - [\nu(Te_3\text{-}F_{31}) + \nu(Te_4\text{-}F_{28}) + \nu(Te_6\text{-}F_{21}) + \nu(Te_8\text{-}F_{43})]$
703(52) 699(47) 689(49)	696(1)[539]	$[\nu(Te_3\text{-}F_{10}) + \nu(Te_4\text{-}F_{16}) + \nu(Te_5\text{-}F_{15}) + \nu(Te_6\text{-}F_{32}) + \nu(Te_7\text{-}F_{19}) + \nu(Te_8\text{-}F_{42})] - [\nu(Te_3\text{-}F_{30}) + \nu(Te_4\text{-}F_9) + \nu(Te_5\text{-}F_{11}) + \nu(Te_6\text{-}F_{20}) + \nu(Te_7\text{-}F_{38}) + \nu(Te_8\text{-}F_{41})]$
	695(5)[17]	$[\nu(Te_3\text{-}F_{10}) + \nu(Te_4\text{-}F_{16}) + \nu(Te_5\text{-}F_{11}) + \nu(Te_6\text{-}F_{20}) + \nu(Te_7\text{-}F_{19}) + \nu(Te_8\text{-}F_{41})] - [\nu(Te_3\text{-}F_{30}) + \nu(Te_4\text{-}F_9) + \nu(Te_5\text{-}F_{15}) + \nu(Te_6\text{-}F_{32}) + \nu(Te_7\text{-}F_{38}) + \nu(Te_8\text{-}F_{42})]$
	691(3)[0]	$[\nu(Te_3\text{-}F_{10}) + \nu(Te_3\text{-}F_{12}) + \nu(Te_4\text{-}F_9) + \nu(Te_4\text{-}F_{14}) + \nu(Te_6\text{-}F_{21}) + \nu(Te_6\text{-}F_{32}) + \nu(Te_8\text{-}F_{41}) + \nu(Te_8\text{-}F_{43})] - [\nu(Te_3\text{-}F_{30}) + \nu(Te_3\text{-}F_{31}) + \nu(Te_4\text{-}F_{16}) + \nu(Te_4\text{-}F_{28}) + \nu(Te_6\text{-}F_{20}) + \nu(Te_6\text{-}F_{35}) + \nu(Te_8\text{-}F_{42}) + \nu(Te_8\text{-}F_{44})]$
	689(3)[5]	$[\nu(Te_3\text{-}F_{10}) + \nu(Te_4\text{-}F_9) + \nu(Te_6\text{-}F_{20}) + \nu(Te_8\text{-}F_{42})] - [\nu(Te_3\text{-}F_{30}) + \nu(Te_4\text{-}F_{16}) + \nu(Te_6\text{-}F_{32}) + \nu(Te_8\text{-}F_{41})]$
	688(<0.1)[59]	$[\nu(Te_3\text{-}F_{10}) + \nu(Te_4\text{-}F_{16}) + \nu(Te_5\text{-}F_{11}) + \nu(Te_6\text{-}F_{32}) + \nu(Te_7\text{-}F_{38}) + \nu(Te_8\text{-}F_{42})] - [\nu(Te_3\text{-}F_{30}) + \nu(Te_4\text{-}F_9) + \nu(Te_5\text{-}F_{15})\ + \nu(Te_6\text{-}F_{20}) + \nu(Te_7\text{-}F_{19}) + \nu(Te_8\text{-}F_{41})]$
	687(<0.1)[1]	$[\nu(Te_5\text{-}F_{11}) + \nu(Te_7\text{-}F_{19})] - [\nu(Te_5\text{-}F_{15}) + \nu(Te_7\text{-}F_{38})]$
	679(<0.1)[216]	$[\nu(Te_5\text{-}F_{27}) + \nu(Te_7\text{-}F_{25})] - [\nu(Te_5\text{-}F_{13}) + \nu(Te_7\text{-}F_{33})]$
	675(2)[2]	$[\nu(Te_5\text{-}F_{27}) + \nu(Te_7\text{-}F_{33})] - [\nu(Te_5\text{-}F_{13}) + \nu(Te_7\text{-}F_{25})]$
684(100)	673(155)[0]	$[\nu(F_aF_{4e}Te_3) + \nu(F_aF_{4e}Te_4) + \nu(F_aF_{4e}Te_5) + \nu(F_aF_{4e}Te_6) + \nu(F_aF_{4e}Te_7) + \nu(F_aF_{4e}Te_8)]$
678(51) 674(62)	670(<1)[309]	$[\nu(Te_3\text{-}F_{18}) + \nu(Te_8\text{-}F_{40})] - [\nu(Te_4\text{-}F_{17}) + \nu(Te_6\text{-}F_{23})]$
	669(<0.1)[51]	$[\nu(Te_3\text{-}F_{18}) + \nu(Te_6\text{-}F_{23})] - [\nu(Te_4\text{-}F_{17}) + \nu(Te_8\text{-}F_{40})]$
	669(11)[3]	$[\nu(Te_3\text{-}F_{18}) + \nu(Te_4\text{-}F_{17})] - [\nu(Te_6\text{-}F_{23}) + \nu(Te_8\text{-}F_{40})]$
	666(15)[0]	$[\nu(F_aF_{4e}Te_5) + \nu(F_aF_{4e}Te_7)]$
	665(<0.1)[136]	$[\nu(F_aF_{4e}Te_5) - \nu(F_aF_{4e}Te_7)]$

Table S4.9. continued…

	624(<1)[<1]	$[\nu(Te_3\text{-}F_{10}) + \nu(Te_3\text{-}F_{30}) + \nu(Te_4\text{-}F_9) + \nu(Te_4\text{-}F_{16}) + \nu(Te_6\text{-}F_{21}) + \nu(Te_6\text{-}F_{35}) + \nu(Te_8\text{-}F_{43}) + \nu(Te_8\text{-}F_{44})] - [\nu(Te_3\text{-}F_{12}) + \nu(Te_3\text{-}F_{31})$ $+ \nu(Te_4\text{-}F_{14}) + \nu(Te_4\text{-}F_{28}) + \nu(Te_6\text{-}F_{20}) + \nu(Te_6\text{-}F_{32}) + \nu(Te_8\text{-}F_{41}) + \nu(Te_8\text{-}F_{42})]$
	623(2)[<1]	$[\nu(Te_3\text{-}F_{10}) + \nu(Te_3\text{-}F_{30}) + \nu(Te_4\text{-}F_{14}) + \nu(Te_4\text{-}F_{28}) + \nu(Te_6\text{-}F_{20}) + \nu(Te_6\text{-}F_{32}) + \nu(Te_8\text{-}F_{43}) + \nu(Te_8\text{-}F_{44})]$ $- [\nu(Te_3\text{-}F_{12}) + \nu(Te_3\text{-}F_{31}) + \nu(Te_4\text{-}F_9) + \nu(Te_4\text{-}F_{16}) + \nu(Te_6\text{-}F_{21}) + \nu(Te_6\text{-}F_{35}) + \nu(Te_8\text{-}F_{41}) + \nu(Te_8\text{-}F_{42})]$
	622(17)[0]	$[\nu(Te_3\text{-}F_{12}) + \nu(Te_3\text{-}F_{31}) + \nu(Te_4\text{-}F_{14}) + \nu(Te_4\text{-}F_{28}) + \nu(Te_6\text{-}F_{21}) + \nu(Te_6\text{-}F_{35}) + \nu(Te_8\text{-}F_{43}) + \nu(Te_8\text{-}F_{44})]$ $- [\nu(Te_3\text{-}F_{18}) + \nu(Te_4\text{-}F_{17}) + \nu(Te_5\text{-}F_{29}) + \nu(Te_6\text{-}F_{23}) + \nu(Te_7\text{-}F_{26}) + \nu(Te_8\text{-}F_{40})]$
	621(4)[2]	$[\nu(Te_3\text{-}F_{10}) + \nu(Te_3\text{-}F_{30}) + \nu(Te_4\text{-}F_{14}) + \nu(Te_4\text{-}F_{28}) + \nu(Te_6\text{-}F_{21}) + \nu(Te_6\text{-}F_{35}) + \nu(Te_8\text{-}F_{41}) + \nu(Te_8\text{-}F_{42})]$ $- [\nu(Te_3\text{-}F_{12}) + \nu(Te_3\text{-}F_{31}) + \nu(Te_4\text{-}F_9) + \nu(Te_4\text{-}F_{16}) + \nu(Te_6\text{-}F_{20}) + \nu(Te_6\text{-}F_{32}) + \nu(Te_8\text{-}F_{43}) + \nu(Te_8\text{-}F_{44})]_{small}$
627(72)	621(12)[0]	$[\nu(Te_3\text{-}F_{10}) + \nu(Te_3\text{-}F_{30}) + \nu(Te_4\text{-}F_9) + \nu(Te_4\text{-}F_{16}) + \nu(Te_6\text{-}F_{20}) + \nu(Te_6\text{-}F_{32}) + \nu(Te_8\text{-}F_{41}) + \nu(Te_8\text{-}F_{42})]$ $- [\nu(Te_3\text{-}F_{12}) + \nu(Te_3\text{-}F_{31}) + \nu(Te_4\text{-}F_{14}) + \nu(Te_4\text{-}F_{28}) + \nu(Te_6\text{-}F_{21}) + \nu(Te_6\text{-}F_{35}) + \nu(Te_8\text{-}F_{43}) + \nu(Te_8\text{-}F_{44})]_{small}$
621(41)	619(<1)[5]	$[\nu(Te_3\text{-}F_{18}) + \nu(Te_6\text{-}F_{40}) + \nu(Te_4\text{-}F_{14}) + \nu(Te_4\text{-}F_{28}) + \nu(Te_4\text{-}F_9) + \nu(Te_4\text{-}F_{16}) + \nu(Te_6\text{-}F_{21}) + \nu(Te_6\text{-}F_{35})$
618(41)		$+ \nu(Te_6\text{-}F_{20}) + \nu(Te_6\text{-}F_{32})] - [\nu(Te_4\text{-}F_{17}) + \nu(Te_5\text{-}F_{23}) + \nu(Te_3\text{-}F_{10}) + \nu(Te_3\text{-}F_{30}) + \nu(Te_3\text{-}F_{12}) + \nu(Te_3\text{-}F_{31})$
613(34)		$+ \nu(Te_8\text{-}F_{43}) + \nu(Te_8\text{-}F_{44}) + \nu(Te_8\text{-}F_{41}) + \nu(Te_8\text{-}F_{42})]$
604(12)	617(5)[0]	$[\nu(Te_5\text{-}F_{29}) + \nu(Te_5\text{-}F_{13}) + \nu(Te_5\text{-}F_{27}) + \nu(Te_7\text{-}F_{26}) + \nu(Te_7\text{-}F_{25}) + \nu(Te_7\text{-}F_{33})] - [\nu(Te_5\text{-}F_{11}) + \nu(Te_5\text{-}F_{15}) + \nu(Te_7\text{-}F_{19})$ $+ \nu(Te_7\text{-}F_{38})]$
	617(<0.1)[<0.1]	$[\nu(Te_5\text{-}F_{11}) + \nu(Te_5\text{-}F_{15})] - [\nu(Te_7\text{-}F_{19}) + \nu(Te_7\text{-}F_{38})] - [\nu(Te_5\text{-}F_{13}) + \nu(Te_5\text{-}F_{27})] + [\nu(Te_7\text{-}F_{33}) + \nu(Te_7\text{-}F_{25})]$
	617(<0.1)[<1]	$[\nu(Te_3\text{-}F_{18}) + \nu(Te_6\text{-}F_{23}) + \nu(Te_4\text{-}F_{14}) + \nu(Te_4\text{-}F_{28}) + \nu(Te_4\text{-}F_9) + \nu(Te_4\text{-}F_{16}) + \nu(Te_8\text{-}F_{43}) + \nu(Te_8\text{-}F_{44}) + \nu(Te_8\text{-}F_{41})$ $+ \nu(Te_8\text{-}F_{42})] - [\nu(Te_4\text{-}F_{17}) + \nu(Te_6\text{-}F_{40}) + \nu(Te_3\text{-}F_{10}) + \nu(Te_3\text{-}F_{30}) + \nu(Te_3\text{-}F_{12}) + \nu(Te_3\text{-}F_{31}) + \nu(Te_6\text{-}F_{21})$ $+ \nu(Te_6\text{-}F_{35}) + \nu(Te_6\text{-}F_{20}) + \nu(Te_6\text{-}F_{32})]$
	616(<1)[<1]	$[\nu(Te_3\text{-}F_{18}) + \nu(Te_4\text{-}F_{17}) + \nu(Te_5\text{-}F_{29}) + \nu(Te_6\text{-}F_{20}) + \nu(Te_6\text{-}F_{32}) + \nu(Te_7\text{-}F_{19}) + \nu(Te_7\text{-}F_{38}) + \nu(Te_8\text{-}F_{41}) + \nu(Te_8\text{-}F_{42})]$ $- [\nu(Te_6\text{-}F_{23}) + \nu(Te_7\text{-}F_{26}) + \nu(Te_8\text{-}F_{40}) + \nu(Te_3\text{-}F_{10}) + \nu(Te_3\text{-}F_{30}) + \nu(Te_4\text{-}F_9) + \nu(Te_4\text{-}F_{16}) + \nu(Te_5\text{-}F_{11}) + \nu(Te_5\text{-}F_{15})]$
	610(2)[0]	$[\nu(Te_5\text{-}F_{29}) + \nu(Te_7\text{-}F_{26}) + \nu(Te_5\text{-}O_{24}) + \nu(Te_7\text{-}O_{34})] - [\nu(Te_5\text{-}F_{13}) + \nu(Te_5\text{-}F_{27}) + \nu(Te_7\text{-}F_{25}) + \nu(Te_7\text{-}F_{33})]$
	609(<0.1)[<1]	$[\nu(Te_5\text{-}F_{29}) + \nu(Te_5\text{-}O_{24}) + \nu(Te_7\text{-}F_{25}) + \nu(Te_7\text{-}F_{33})] - [+ \nu(Te_7\text{-}F_{26}) + \nu(Te_7\text{-}O_{34}) + \nu(Te_5\text{-}F_{13}) + \nu(Te_5\text{-}F_{27})]$
	469(<0.1)[116]	$[\nu(Hg_1\text{-}O_{22}) + \nu(Te_6\text{-}O_{22}) + \nu(Hg_2\text{-}O_{36}) + \nu(Te_3\text{-}O_{36})] - [\nu(Hg_1\text{-}O_{37}) + \nu(Te_4\text{-}O_{37}) + \nu(Hg\text{-}O_{39}) + \nu(Te_8\text{-}O_{39})]$
479(8)	465(<0.1)[<1]	$[\nu(Hg_1\text{-}O_{22}) + \nu(Te_6\text{-}O_{22}) + \nu(Hg\text{-}O_{39}) + \nu(Te_8\text{-}O_{39})] - [\nu(Hg_1\text{-}O_{37}) + \nu(Te_4\text{-}O_{37}) + \nu(Hg_2\text{-}O_{36}) + \nu(Te_3\text{-}O_{36})]$
470(17)	464(<0.1)[45]	$[\nu(Hg_1\text{-}O_{22}) + \nu(Te_6\text{-}O_{22}) + \nu(Hg_1\text{-}O_{37}) + \nu(Te_4\text{-}O_{37})] - [\nu(Hg_2\text{-}O_{36}) + \nu(Te_3\text{-}O_{36}) + \nu(Hg\text{-}O_{39}) + \nu(Te_8\text{-}O_{39})]$
	463(24)[0]	$[\nu(Hg_1\text{-}O_{22}) + \nu(Te_6\text{-}O_{22}) + \nu(Hg_1\text{-}O_{37}) + \nu(Te_4\text{-}O_{37}) + \nu(Hg_2\text{-}O_{36}) + \nu(Te_3\text{-}O_{36}) + \nu(Hg\text{-}O_{39}) + \nu(Te_8\text{-}O_{39})]$
397(13)	407(<0.1)[183]	$[\nu(Hg_1\text{-}O_{24}) + \nu(Hg_1\text{-}O_{34})] - [\nu(Hg_2\text{-}O_{24}) + \nu(Hg_2\text{-}O_{34})]$
	392(17)[<0.1]	$[\nu(Hg_1\text{-}O_{24}) + \nu(Hg_2\text{-}O_{24}) + \nu(Hg_1\text{-}O_{34})]$
	343(<1)[0]	$[\delta(Te_3F_{4e})_{umb} + \delta(Te_4F_{4e})_{umb} + \delta(Te_6F_{4e})_{umb} + \delta(Te_7F_{4e})_{umb} + \delta(Te_8F_{4e})_{umb}]$
	337(1)[<0.1]	$[\delta(F_{11}\text{-}Te_5\text{-}F_{29}) + \delta(F_{19}\text{-}Te_7\text{-}F_{26})] - [\delta(F_{15}\text{-}Te_5\text{-}F_{29}) + \delta(F_{38}\text{-}Te_7\text{-}F_{26})] / [\rho_w(F_{25}\text{-}Te_7\text{-}F_{33}) - \rho_w(F_{13}\text{-}Te_5\text{-}F_{27})]$
	337(<0.1)[53]	$[\delta(F_{11}\text{-}Te_5\text{-}F_{29}) + \delta(F_{38}\text{-}Te_7\text{-}F_{26})] - [\delta(F_{15}\text{-}Te_5\text{-}F_{29}) + \delta(F_{19}\text{-}Te_7\text{-}F_{26})] / [\rho_w(F_{25}\text{-}Te_7\text{-}F_{33}) + \rho_w(F_{13}\text{-}Te_5\text{-}F_{27})]$
	334(<0.1)[203]	$[\delta(F_{31}\text{-}Te_3\text{-}F_{18}) + \delta(F_{28}\text{-}Te_4\text{-}F_{17}) + \delta(F_{21}\text{-}Te_6\text{-}F_{23}) + \delta(F_{43}\text{-}Te_8\text{-}F_{40})] - [\delta(F_{12}\text{-}Te_3\text{-}F_{18}) + \delta(F_{14}\text{-}Te_4\text{-}F_{17}) + \delta(F_{35}\text{-}Te_6\text{-}F_{23})$ $+ \delta(F_{44}\text{-}Te_8\text{-}F_{40})] / [\rho_w(F_{10}\text{-}Te_3\text{-}F_{30}) + \rho_w(F_9\text{-}Te_4\text{-}F_{16}) + \rho_w(F_{20}\text{-}Te_6\text{-}F_{32}) + \rho_w(F_{41}\text{-}Te_8\text{-}F_{42})] / [\delta(Te_3F_{4e})_{umb} - \delta(Te_7F_{4e})_{umb}]$
334(23)		$[\delta(F_{31}\text{-}Te_3\text{-}F_{18}) + \delta(F_{43}\text{-}Te_8\text{-}F_{40})] - [\delta(F_{14}\text{-}Te_4\text{-}F_{17}) + \delta(F_{21}\text{-}Te_6\text{-}F_{23})] / [\rho_w(F_{10}\text{-}Te_3\text{-}F_{30}) + \rho_w(F_{41}\text{-}Te_8\text{-}F_{42})]$
330(22)	334(<0.1)[53]	$- [\rho_w(F_9\text{-}Te_4\text{-}F_{16}) + \rho_w(F_{20}\text{-}Te_6\text{-}F_{32})]$
	334(1)[0]	$[\delta(F_{12}\text{-}Te_3\text{-}F_{18}) + \delta(F_{14}\text{-}Te_4\text{-}F_{17}) + \delta(F_{21}\text{-}Te_6\text{-}F_{23}) + \delta(F_{43}\text{-}Te_8\text{-}F_{40})] - [\delta(F_{31}\text{-}Te_3\text{-}F_{18}) + \delta(F_{28}\text{-}Te_4\text{-}F_{17})$ $+ \delta(F_{35}\text{-}Te_6\text{-}F_{23}) + \delta(F_{44}\text{-}Te_8\text{-}F_{40})]$
	334(2)[32]	$[\delta(F_{12}\text{-}Te_3\text{-}F_{18}) + \delta(F_{28}\text{-}Te_4\text{-}F_{17}) + \delta(F_{21}\text{-}Te_6\text{-}F_{23}) + \delta(F_{44}\text{-}Te_8\text{-}F_{40})] - [\delta(F_{31}\text{-}Te_3\text{-}F_{18}) + \delta(F_{14}\text{-}Te_4\text{-}F_{17})$ $+ \delta(F_{35}\text{-}Te_6\text{-}F_{23}) + \delta(F_{43}\text{-}Te_8\text{-}F_{40})]$
	333(<0.1)[205]	$[\delta(F_{31}\text{-}Te_3\text{-}F_{18}) + \delta(F_{44}\text{-}Te_8\text{-}F_{40})] - [\delta(F_{28}\text{-}Te_4\text{-}F_{17}) + \delta(F_{35}\text{-}Te_6\text{-}F_{23})] / [\rho_w(F_{10}\text{-}Te_3\text{-}F_{30}) + \rho_w(F_{41}\text{-}Te_8\text{-}F_{42})]$
		$- [\rho_w(F_9\text{-}Te_4\text{-}F_{16}) + \rho_w(F_{20}\text{-}Te_6\text{-}F_{32})]$

Table S4.9. continued…

327(22)	332(<0.1)[28]	$[\delta(Te_5F_{4e})_{umb} - \delta(Te_7F_{4e})_{umb}] / [\delta(F_{12}\text{-}Te_3\text{-}F_{18}) + \delta(F_{14}\text{-}Te_4\text{-}F_{17}) + \delta(F_{35}\text{-}Te_6\text{-}F_{23}) + \delta(F_{40}\text{-}Te_8\text{-}F_{44})]_{small}$
	331(<1)[0]	$[\delta(Te_5F_{4e})_{umb} + \delta(Te_7F_{4e})_{umb}] - [\delta(Te_3F_{4e})_{umb} + \delta(Te_4F_{4e})_{umb} + \delta(Te_6F_{4e})_{umb} + \delta(Te_8F_{4e})_{umb}]_{small}$
	331(<0.1)[41]	$[\delta(F_{19}\text{-}Te_7\text{-}O_{34}) - \delta(F_{38}\text{-}Te_7\text{-}O_{34})] + [\delta(F_{15}\text{-}Te_5\text{-}O_{24}) - \delta(F_{11}\text{-}Te_5\text{-}O_{24})]$
	329(<1)[26]	$[\delta(F_{10}\text{-}Te_3\text{-}F_{18}) + \delta(F_{41}\text{-}Te_8\text{-}F_{40})] - [\delta(F_9\text{-}Te_4\text{-}F_{17}) + \delta(F_{32}\text{-}Te_6\text{-}F_{23})] / [\delta(F_{19}\text{-}Te_7\text{-}O_{34}) - \delta(F_{38}\text{-}Te_7\text{-}O_{34})] + [\delta(F_{15}\text{-}Te_5\text{-}O_{24}) - \delta(F_{11}\text{-}Te_5\text{-}O_{24})]_{small}$
	329(11)[111]	$[\delta(F_{19}\text{-}Te_7\text{-}O_{34}) - \delta(F_{38}\text{-}Te_7\text{-}O_{34})] + [\delta(F_{15}\text{-}Te_5\text{-}O_{24}) - \delta(F_{11}\text{-}Te_5\text{-}O_{24})] / [\delta(F_{10}\text{-}Te_3\text{-}F_{18}) + \delta(F_{20}\text{-}Te_6\text{-}F_{23})] - [\delta(F_{16}\text{-}Te_4\text{-}F_{17}) + \delta(F_{42}\text{-}Te_8\text{-}F_{40})]$
	329(<1)[17]	$[\delta(F_{30}\text{-}Te_3\text{-}F_{18}) + \delta(F_{16}\text{-}Te_4\text{-}F_{17})] - [\delta(F_{20}\text{-}Te_6\text{-}F_{23}) + \delta(F_{42}\text{-}Te_8\text{-}F_{40})] / [\rho_w(F_{12}\text{-}Te_3\text{-}F_{31}) + \rho_w(F_{14}\text{-}Te_4\text{-}F_{28})]_{small} - [\rho_w(F_{21}\text{-}Te_6\text{-}F_{35}) + \rho_w(F_{43}\text{-}Te_8\text{-}F_{44})]_{small}$
	329(1)[0]	$[\delta(F_{10}\text{-}Te_3\text{-}F_{18}) + \delta(F_9\text{-}Te_4\text{-}F_{17}) + \delta(F_{32}\text{-}Te_6\text{-}F_{23}) + \delta(F_{41}\text{-}Te_8\text{-}F_{40})]$
332(32)	327(4)[4]	$[\delta(F_{19}\text{-}Te_7\text{-}O_{34}) - \delta(F_{38}\text{-}Te_7\text{-}O_{34})] + [\delta(F_{11}\text{-}Te_5\text{-}O_{24}) - \delta(F_{15}\text{-}Te_5\text{-}O_{24})]$
	326(1)[9]	$[\delta(F_{10}\text{-}Te_3\text{-}F_{18}) + \delta(F_9\text{-}Te_4\text{-}F_{17})] - [\delta(F_{32}\text{-}Te_6\text{-}F_{23}) + \delta(F_{41}\text{-}Te_8\text{-}F_{40})] / [\rho_w(F_{12}\text{-}Te_3\text{-}F_{31}) + \rho_w(F_{14}\text{-}Te_4\text{-}F_{28})]_{small} - [\rho_w(F_{21}\text{-}Te_6\text{-}F_{35}) + \rho_w(F_{43}\text{-}Te_8\text{-}F_{44})]_{small}$
	326(<1)[38]	$[\delta(F_{27}\text{-}Te_5\text{-}F_{29}) + \delta(F_{33}\text{-}Te_7\text{-}F_{26})] - [\delta(F_{13}\text{-}Te_5\text{-}F_{29}) + \delta(F_{25}\text{-}Te_7\text{-}F_{26})] / [\rho_w(F_{11}\text{-}Te_5\text{-}F_{15}) - \rho_w(F_{19}\text{-}Te_7\text{-}F_{38})]$
	325(<0.1)[27]	$[\delta(F_{27}\text{-}Te_5\text{-}F_{29}) + \delta(F_{25}\text{-}Te_7\text{-}F_{26})] - [\delta(F_{13}\text{-}Te_5\text{-}F_{29}) + \delta(F_{33}\text{-}Te_7\text{-}F_{26})] / [\rho_w(F_{11}\text{-}Te_5\text{-}F_{15}) + \rho_w(F_{19}\text{-}Te_7\text{-}F_{38})]$
	324(<0.1)[71]	$[\delta(F_{10}\text{-}Te_3\text{-}F_{18}) + \delta(F_{32}\text{-}Te_6\text{-}F_{23})] - [\delta(F_9\text{-}Te_4\text{-}F_{17}) + \delta(F_{40}\text{-}Te_8\text{-}F_{41})]$
316(57)	320(<0.1)[80]	$[\delta(O_{22}\text{-}Hg_1\text{-}O_{37}) + \delta(O_{36}\text{-}Hg_2\text{-}O_{39})]_{o.o.p.}$
	316(3)[<0.1]	$[\delta(O_{22}\text{-}Hg_1\text{-}O_{37}) - \delta(O_{36}\text{-}Hg_2\text{-}O_{39})]_{o.o.p.}$
	312(<1)[0]	$[\delta(O_{22}\text{-}Hg_1\text{-}O_{37}) + \delta(O_{36}\text{-}Hg_2\text{-}O_{39})]$
	309(<1)[3]	$\delta(O_{22}\text{-}Hg_1\text{-}O_{37}) - \delta(O_{36}\text{-}Hg_2\text{-}O_{39})]$
396(31)	290(3)[0]	$[\delta(F_{10}\text{-}Te_3\text{-}F_{31}) + \delta(F_{12}\text{-}Te_3\text{-}F_{30})] + [\delta(F_9\text{-}Te_4\text{-}F_{28}) + \delta(F_{14}\text{-}Te_4\text{-}F_{16})] + [\delta(F_{20}\text{-}Te_6\text{-}F_{21}) + \delta(F_{32}\text{-}Te_6\text{-}F_{35})] + [\delta(F_{41}\text{-}Te_8\text{-}F_{44}) + \delta(F_{42}\text{-}Te_8\text{-}F_{43})]$
	290(2)[<0.1]	$[\delta(F_{10}\text{-}Te_3\text{-}F_{31}) + \delta(F_{12}\text{-}Te_3\text{-}F_{30})] + [\delta(F_9\text{-}Te_4\text{-}F_{14}) + \delta(F_{16}\text{-}Te_4\text{-}F_{28})] + [\delta(F_{20}\text{-}Te_6\text{-}F_{35}) + \delta(F_{21}\text{-}Te_6\text{-}F_{32})] + [\delta(F_{41}\text{-}Te_8\text{-}F_{44}) + \delta(F_{42}\text{-}Te_8\text{-}F_{43})]$
	289(1)[<1]	$[\delta(F_{10}\text{-}Te_3\text{-}F_{12}) + \delta(F_{30}\text{-}Te_3\text{-}F_{31})] + [\delta(F_9\text{-}Te_4\text{-}F_{14}) + \delta(F_{16}\text{-}Te_4\text{-}F_{28})] + [\delta(F_{32}\text{-}Te_6\text{-}F_{35}) + \delta(F_{21}\text{-}Te_6\text{-}F_{20})] + [\delta(F_{41}\text{-}Te_8\text{-}F_{44}) + \delta(F_{42}\text{-}Te_8\text{-}F_{43})]$
	289(<1)[<1]	$[\delta(F_{10}\text{-}Te_3\text{-}F_{12}) + \delta(F_{30}\text{-}Te_3\text{-}F_{31})] + [\delta(F_9\text{-}Te_4\text{-}F_{28}) + \delta(F_{16}\text{-}Te_4\text{-}F_{14})] + [\delta(F_{20}\text{-}Te_6\text{-}F_{35}) + \delta(F_{21}\text{-}Te_6\text{-}F_{32})] + [\delta(F_{41}\text{-}Te_8\text{-}F_{44}) + \delta(F_{42}\text{-}Te_8\text{-}F_{43})]$
	286(2)[<0.1]	$[\delta(F_{11}\text{-}Te_5\text{-}F_{27}) + \delta(F_{13}\text{-}Te_5\text{-}F_{15})] + [\delta(F_{19}\text{-}Te_7\text{-}F_{33}) + \delta(F_{25}\text{-}Te_7\text{-}F_{38})]$
	286(<0.1)[0]	$[\delta(F_{11}\text{-}Te_5\text{-}F_{13}) + \delta(F_{15}\text{-}Te_5\text{-}F_{27})] + [\delta(F_{19}\text{-}Te_7\text{-}F_{33}) + \delta(F_{25}\text{-}Te_7\text{-}F_{38})]$
233(9)	233(<0.1)[<1]	$[\rho_w(F_{12}\text{-}Te_3\text{-}F_{31}) + \rho_w(F_{21}\text{-}Te_6\text{-}F_{35})] - [\rho_w(F_{14}\text{-}Te_4\text{-}F_{28}) + \rho_w(F_{43}\text{-}Te_8\text{-}F_{44})] / [\delta(F_{18}\text{-}Te_3\text{-}F_{30}) + \delta(F_{17}\text{-}Te_4\text{-}F_{16})] - [\delta(F_{20}\text{-}Te_6\text{-}F_{23}) + \delta(F_{40}\text{-}Te_8\text{-}F_{42})]$
	233(1)[<1]	$[\rho_w(F_{12}\text{-}Te_3\text{-}F_{31}) + \rho_w(F_{43}\text{-}Te_8\text{-}F_{44})] - [\rho_w(F_{14}\text{-}Te_4\text{-}F_{28}) + \rho_w(F_{21}\text{-}Te_6\text{-}F_{35})] / [\delta(F_{18}\text{-}Te_3\text{-}F_{30}) + \delta(F_{40}\text{-}Te_8\text{-}F_{42})] - [\delta(F_{17}\text{-}Te_4\text{-}F_{16}) + \delta(F_{20}\text{-}Te_6\text{-}F_{23})]$
	228(<0.1)[12]	$[\rho_w(F_{12}\text{-}Te_3\text{-}F_{31}) + \rho_w(F_{43}\text{-}Te_8\text{-}F_{44})] - [\rho_w(F_{14}\text{-}Te_4\text{-}F_{28}) + \rho_w(F_{21}\text{-}Te_5\text{-}F_{35})]$
	228(4)[0]	$[\rho_w(F_{12}\text{-}Te_3\text{-}F_{31}) + \rho_w(F_{43}\text{-}Te_8\text{-}F_{44}) + \rho_w(F_{14}\text{-}Te_4\text{-}F_{28}) + \rho_w(F_{21}\text{-}Te_5\text{-}F_{35})]$

Table S4.9. continued…

226(12)	212(<0.1)[<1]	$[\rho_w(F_{10}\text{-}Te_3\text{-}F_{30}) + \rho_w(F_9\text{-}Te_4\text{-}F_{16}) + \rho_w(F_{13}\text{-}Te_5\text{-}F_{27}) + \rho_w(F_{21}\text{-}Te_6\text{-}F_{35}) + \rho_w(F_{19}\text{-}Te_7\text{-}F_{30}) + \rho_w(F_{43}\text{-}Te_8\text{-}F_{44})] - [\rho_w(F_{12}\text{-}Te_3\text{-}F_{31}) + \rho_w(F_{14}\text{-}Te_4\text{-}F_{28}) + \rho_w(F_{11}\text{-}Te_5\text{-}F_{15}) + \rho_w(F_{20}\text{-}Te_6\text{-}F_{32}) + \rho_w(F_{25}\text{-}Te_7\text{-}F_{33}) + \rho_w(F_{41}\text{-}Te_8\text{-}F_{42})]$
	212(<0.1)[0]	$[\rho_w(F_{13}\text{-}Te_5\text{-}F_{27}) + \rho_w(F_{25}\text{-}Te_7\text{-}F_{33})] - [\rho_w(F_{11}\text{-}Te_5\text{-}F_{15}) + \rho_w(F_{19}\text{-}Te_7\text{-}F_{30})] + [\rho_w(F_{10}\text{-}Te_3\text{-}F_{30}) + \rho_w(F_9\text{-}Te_4\text{-}F_{16}) + \rho_w(F_{20}\text{-}Te_6\text{-}F_{32}) + \rho_w(F_{41}\text{-}Te_8\text{-}F_{42})] - [\rho_w(F_{12}\text{-}Te_3\text{-}F_{31}) + \rho_w(F_{21}\text{-}Te_6\text{-}F_{35}) + \rho_w(F_{43}\text{-}Te_8\text{-}F_{44})]$
	212(<0.1)[<0.1]	$\left\{\begin{array}{l}[\rho_w(F_{10}\text{-}Te_3\text{-}F_{30}) + \rho_w(F_{14}\text{-}Te_4\text{-}F_{28}) + \rho_w(F_{21}\text{-}Te_6\text{-}F_{35}) + \rho_w(F_{41}\text{-}Te_8\text{-}F_{42})] - [\rho_w(F_{12}\text{-}Te_3\text{-}F_{31}) + \rho_w(F_9\text{-}Te_4\text{-}F_{16}) + \rho_w(F_{20}\text{-}Te_6\text{-}F_{32}) + \rho_w(F_{43}\text{-}Te_8\text{-}F_{44})] \\ [\rho_w(F_{43}\text{-}Te_8\text{-}F_{44})]\end{array}\right.$
	212(<0.1)[<0.1]	$\left\{\begin{array}{l}[\rho_w(F_{10}\text{-}Te_3\text{-}F_{30}) + \rho_w(F_{14}\text{-}Te_4\text{-}F_{28}) + \rho_w(F_{20}\text{-}Te_6\text{-}F_{32}) + \rho_w(F_{43}\text{-}Te_8\text{-}F_{44})] - [\rho_w(F_{12}\text{-}Te_3\text{-}F_{31}) + \rho_w(F_9\text{-}Te_4\text{-}F_{16}) + \rho_w(F_{21}\text{-}Te_6\text{-}F_{35}) + \rho_w(F_{41}\text{-}Te_8\text{-}F_{42})] \\ [\rho_w(F_{41}\text{-}Te_8\text{-}F_{42})]\end{array}\right.$
	212(<0.1)[0]	$\left\{\begin{array}{l}[\rho_w(F_{10}\text{-}Te_3\text{-}F_{30}) + \rho_w(F_9\text{-}Te_4\text{-}F_{16}) + \rho_w(F_{11}\text{-}Te_5\text{-}F_{15}) + \rho_w(F_{20}\text{-}Te_6\text{-}F_{32}) + \rho_w(F_{19}\text{-}Te_7\text{-}F_{30}) + \rho_w(F_{41}\text{-}Te_8\text{-}F_{42})] - [\rho_w(F_{12}\text{-}Te_3\text{-}F_{31}) + \rho_w(F_{14}\text{-}Te_4\text{-}F_{28}) + \rho_w(F_{13}\text{-}Te_5\text{-}F_{27}) + \rho_w(F_{21}\text{-}Te_6\text{-}F_{35}) + \rho_w(F_{25}\text{-}Te_7\text{-}F_{33}) + \rho_w(F_{43}\text{-}Te_8\text{-}F_{44})] \\ [\rho_w(F_{11}\text{-}Te_5\text{-}F_{15}) + \rho_w(F_{25}\text{-}Te_7\text{-}F_{33})] - [\rho_w(F_{13}\text{-}Te_5\text{-}F_{27}) + \rho_w(F_{19}\text{-}Te_7\text{-}F_{30})] + [\rho_w(F_{10}\text{-}Te_3\text{-}F_{30}) + \rho_w(F_9\text{-}Te_4\text{-}F_{16}) + \rho_w(F_{21}\text{-}Te_6\text{-}F_{35}) + \rho_w(F_{43}\text{-}Te_8\text{-}F_{44})] - [\rho_w(F_{12}\text{-}Te_3\text{-}F_{31}) + \rho_w(F_{14}\text{-}Te_4\text{-}F_{28}) + \rho_w(F_{20}\text{-}Te_6\text{-}F_{32}) + \rho_w(F_{41}\text{-}Te_8\text{-}F_{42})]\end{array}\right.$
n.o.	211(<0.1)[<1]	
	206(<0.1)[4]	$[\rho_w(O_{24}\text{-}Te_5\text{-}F_{29}) + \rho_w(O_{34}\text{-}Te_7\text{-}F_{26})] - [\rho_w(F_{11}\text{-}Te_5\text{-}F_{15}) + \rho_w(F_{19}\text{-}Te_7\text{-}F_{30})]$
	205(<1)[<0.1]	$[\rho_w(O_{24}\text{-}Te_5\text{-}F_{29}) + \rho_w(F_{19}\text{-}Te_7\text{-}F_{30})] - [\rho_w(O_{34}\text{-}Te_7\text{-}F_{26}) + \rho_w(F_{11}\text{-}Te_5\text{-}F_{15})]$
	198(<0.1)[<0.1]	$[\rho_w(O_{24}\text{-}Te_5\text{-}F_{29}) + \rho_w(O_{34}\text{-}Te_7\text{-}F_{26})] - [\rho_w(F_{13}\text{-}Te_5\text{-}F_{27}) + \rho_w(F_{25}\text{-}Te_7\text{-}F_{33})]$
	197(<0.1)[<0.1]	$[\rho_w(O_{24}\text{-}Te_5\text{-}F_{29}) + \rho_w(F_{25}\text{-}Te_7\text{-}F_{33})] - [\rho_w(O_{34}\text{-}Te_7\text{-}F_{26}) + \rho_w(F_{13}\text{-}Te_5\text{-}F_{27})]$
	194(<0.1)[<0.1]	$[\delta(O_{37}\text{-}Hg_1\text{-}O_{22}) + \delta(O_{39}\text{-}Hg_2\text{-}O_{36})] + [\delta(F_{32}\text{-}Te_6\text{-}F_{20}) + \delta(F_{16}\text{-}Te_4\text{-}F_9) + \delta(F_{10}\text{-}Te_3\text{-}F_{30}) + \delta(F_{40}\text{-}Te_8\text{-}F_{41})]$
	193(<1)[<0.1]	$[\delta(O_{37}\text{-}Hg_1\text{-}O_{22}) - \delta(O_{39}\text{-}Hg_2\text{-}O_{36})] - [\delta(F_{32}\text{-}Te_6\text{-}F_{20}) + \delta(F_{16}\text{-}Te_4\text{-}F_9) - \delta(F_{10}\text{-}Te_3\text{-}F_{30}) - \delta(F_{40}\text{-}Te_8\text{-}F_{41})]$
	190(<0.1)[0]	$[\delta(O_{37}\text{-}Hg_1\text{-}O_{22}) + \delta(O_{39}\text{-}Hg_2\text{-}O_{36})] + [\delta(F_{32}\text{-}Te_6\text{-}F_{20}) - \delta(F_{16}\text{-}Te_4\text{-}F_9) - \delta(F_{10}\text{-}Te_3\text{-}F_{30}) + \delta(F_{40}\text{-}Te_8\text{-}F_{41})]$
	190(<0.1)[<1]	$[\delta(O_{37}\text{-}Hg_1\text{-}O_{22}) - \delta(O_{39}\text{-}Hg_2\text{-}O_{36})] - [\delta(F_{32}\text{-}Te_6\text{-}F_{20}) - \delta(F_{16}\text{-}Te_4\text{-}F_9) + \delta(F_{10}\text{-}Te_3\text{-}F_{30}) - \delta(F_{40}\text{-}Te_8\text{-}F_{41})]$
	152(<0.1)[12]	$[\rho_t(Te_5\text{-}F_{18},F_{30}) + \rho_t(Te_6\text{-}F_{20},F_{23})] - [\rho_t(Te_4\text{-}F_{16},F_{17}) + \rho_t(Te_8\text{-}F_{40},F_{42})] / [\rho_w(F_{12}\text{-}Te_3\text{-}F_{31}) + \rho_w(F_{21}\text{-}Te_6\text{-}F_{35})] - [\rho_w(F_{14}\text{-}Te_4\text{-}F_{28}) + \rho_w(F_{43}\text{-}Te_8\text{-}F_{44})]$
	152(<1)[<0.1]	$[\rho_t(Te_5\text{-}F_{18},F_{30}) + \rho_t(Te_4\text{-}F_{16},F_{17})] - [\rho_t(Te_6\text{-}F_{20},F_{23}) + \rho_t(Te_8\text{-}F_{40},F_{42})] / [\rho_w(F_{12}\text{-}Te_3\text{-}F_{31}) + \rho_w(F_{14}\text{-}Te_4\text{-}F_{28})] - [\rho_w(F_{21}\text{-}Te_6\text{-}F_{35}) + \rho_w(F_{43}\text{-}Te_8\text{-}F_{44})]$
	121(<0.1)[2]	$[\rho_t(Te_3\text{-}F_{10},F_{18},F_{30}) + \rho_t(Te_8\text{-}F_{40},F_{41},F_{42})] - [\rho_t(Te_4\text{-}F_9,F_{16},F_{17}) + \rho_t(Te_6\text{-}F_{20},F_{23},F_{32})]$
130(31)	121(3)[0]	$[\rho_t(Te_3\text{-}F_{10},F_{18},F_{30}) + \rho_t(Te_4\text{-}F_9,F_{16},F_{17}) + \rho_t(Te_6\text{-}F_{20},F_{23},F_{32}) + \rho_t(Te_8\text{-}F_{40},F_{41},F_{42})]$

Table S4.9. continued…

n.o.	95(<0.1)[25] 90(<1)[0] 87(<0.1)[33] 87(<0.1)[0] 67(1)[0] 65(2)[<1] 63(<0.1)[39] 58(<0.1)[2] 57(<0.1)[1] 54(<0.1)[3] 53(<0.1)[<1] 49(<1)[<0.1] 36(<1)[0] 28(<0.1)[<0.1] 24(<0.1)[0]	coupled deformation and torsion modes of $[Hg_2(OTeF_5)_6]^{2-}$
	24(<0.1)[3] 21(<1)[<0.1] 19(<1)[0] 17(<0.1)[<1] 17(<0.1)[0] 16(<0.1)[0] 15(<0.1)[<0.1] 14(<0.1)[<1] 14(<1)[0] 12(<1)[<0.1] 11(<0.1)[<1] 11(<0.1)[<0.1] 9(<0.1)[0] 9(0)[<0.1] 6(<1)[<0.1] 5(<0.1)[0] 5(<0.1)[<0.1]	

[a] Frequencies are given in cm^{-1}. [b] Values in parentheses denote relative Raman intensities. The Raman spectrum was recorded in an FEP sample tube at −150 °C using 1064-nm excitation. [c] The abbreviations denote shoulder (sh), broad (br), and not observed (n.o.). [d] Values in parentheses denote calculated Raman intensities ($Å^4$ amu^{-1}) and values in square brackets denote calculated infrared intensities (km mol^{-1}). [e] Assignments are for the energy-minimized geometry calculated at the PBE0/def2-TZVPP level with. The atom numbering scheme corresponds to that used in Figure 4.12. The abbreviations denote umbrella (umb), stretch (ν), bend (δ), twist (ρ_t), wag (ρ_w), and rock (ρ_r). [f] Overlap with a cation mode. The notation $Te_nF_{4e}F_a$, where *n* is the tellurium atom label, corresponds to the symmetric stretches of the axial fluorine (F_a) and the equatorial fluorines (F_{4e}) of the F_5Te_nO- group.

Table S4.10. Experimental Raman Frequencies and Intensities for $Cs_2[Hg(OTeF_5)_4]\cdot Hg(OTeF_5)_2$ and Calculated Vibrational Frequencies and Intensities for $[Hg_3(OTeF_5)_8]^{2-}$

exptl [a,b,c] $Cs_2[Hg(OTeF_5)_4]\cdot Hg(OTeF_5)_2$	calcd [a,d] $[Hg_3(OTeF_5)_8]^{3-}$ (C_1)	assgnts [e]
866(40)	853(120)[8]	$[\nu(Hg_1\text{-}O_{16}) - \nu(Te_4\text{-}O_{16})] + [\nu(Hg_1\text{-}O_{17}) - \nu(Te_3\text{-}O_{17})] + [\nu(Hg_1\text{-}O_{31}) - \nu(Te_{33}\text{-}O_{31})] + [\nu(Hg_1\text{-}O_{32}) - \nu(Te_{39}\text{-}O_{32})] + [\nu(Hg_2\text{-}O_{23}) - \nu(Te_5\text{-}O_{23})] + [\nu(Hg_2\text{-}O_{24}) - \nu(Te_{25}\text{-}O_{24})] + [\nu(Hg_{45}\text{-}O_{46}) - \nu(Te_{48}\text{-}O_{46})] + [\nu(Hg_{45}\text{-}O_{47}) - \nu(Te_{49}\text{-}O_{47})] + \nu(Hg_2\text{-}O_{17}) + \nu(Hg_2\text{-}O_{31}) + \nu(Hg_{45}\text{-}O_{16}) + \nu(Hg_{45}\text{-}O_{32})$
826(10), br	834(8)[382]	$[\nu(Hg_1\text{-}O_{16}) - \nu(Te_4\text{-}O_{16})] + [\nu(Hg_1\text{-}O_{32}) - \nu(Te_{39}\text{-}O_{32})] - [\nu(Hg_1\text{-}O_{17}) - \nu(Te_3\text{-}O_{17})] - [\nu(Hg_1\text{-}O_{31}) - \nu(Te_{33}\text{-}O_{31})] + [\nu(Hg_{45}\text{-}O_{46}) - \nu(Te_{48}\text{-}O_{46})] + [\nu(Hg_{45}\text{-}O_{16}) + \nu(Hg_{45}\text{-}O_{32})] - [\nu(Hg_2\text{-}O_{24}) - \nu(Te_{25}\text{-}O_{24})] - [\nu(Hg_2\text{-}O_{17}) + \nu(Hg_2\text{-}O_{31})]$
	826(14)[398]	$[\nu(Hg_1\text{-}O_{16}) - \nu(Te_4\text{-}O_{16})] + [\nu(Hg_1\text{-}O_{32}) - \nu(Te_{39}\text{-}O_{32})]_{small} + [\nu(Hg_{45}\text{-}O_{47}) - \nu(Te_{49}\text{-}O_{47})] + [\nu(Hg_{45}\text{-}O_{16}) + \nu(Hg_{45}\text{-}O_{32})] - [\nu(Hg_{45}\text{-}O_{46}) - \nu(Te_{48}\text{-}O_{46})] - [\nu(Hg_2\text{-}O_{24}) - \nu(Te_{25}\text{-}O_{24})]$
	823(20)[310]	$[\nu(Hg_1\text{-}O_{16}) - \nu(Te_4\text{-}O_{16})] + [\nu(Hg_1\text{-}O_{32}) - \nu(Te_{39}\text{-}O_{32})]_{small} - [\nu(Hg_1\text{-}O_{17}) - \nu(Te_3\text{-}O_{17})] - [\nu(Hg_1\text{-}O_{31}) - \nu(Te_{33}\text{-}O_{31})]_{small} + [\nu(Hg_{45}\text{-}O_{47}) - \nu(Te_{49}\text{-}O_{47})] + [\nu(Hg_{45}\text{-}O_{16}) + \nu(Hg_{45}\text{-}O_{32})] - [\nu(Hg_{45}\text{-}O_{46}) - \nu(Te_{48}\text{-}O_{46})] - [\nu(Hg_2\text{-}O_{23}) - \nu(Te_5\text{-}O_{23})] - [\nu(Hg_2\text{-}O_{24}) - \nu(Te_{25}\text{-}O_{24})]$
816(3)	814(5)[69]	$[\nu(Hg_1\text{-}O_{16}) - \nu(Te_4\text{-}O_{16})]_{small} + [\nu(Hg_1\text{-}O_{17}) - \nu(Te_3\text{-}O_{17})]_{small} + [\nu(Hg_1\text{-}O_{31}) - \nu(Te_{33}\text{-}O_{31})]_{small} + [\nu(Hg_1\text{-}O_{32}) - \nu(Te_{39}\text{-}O_{32})]_{small} + [\nu(Hg_2\text{-}O_{17}) + \nu(Hg_2\text{-}O_{31}) + \nu(Hg_{45}\text{-}O_{16}) + \nu(Hg_{45}\text{-}O_{32})]_{small} - [\nu(Hg_{45}\text{-}O_{47}) - \nu(Te_{49}\text{-}O_{47})] - [\nu(Hg_2\text{-}O_{23}) - \nu(Te_5\text{-}O_{23})]$
	812(18)[205]	$[\nu(Hg_1\text{-}O_{16}) - \nu(Te_4\text{-}O_{16})] + [\nu(Hg_1\text{-}O_{32}) - \nu(Te_{39}\text{-}O_{32})] - [\nu(Hg_1\text{-}O_{17}) - \nu(Te_3\text{-}O_{17})] - [\nu(Hg_1\text{-}O_{31}) - \nu(Te_{33}\text{-}O_{31})] + [\nu(Hg_{45}\text{-}O_{16}) + \nu(Hg_{45}\text{-}O_{32})] + [\nu(Hg_2\text{-}O_{23}) - \nu(Te_5\text{-}O_{23})] + [\nu(Hg_2\text{-}O_{24}) - \nu(Te_{25}\text{-}O_{24})] - [\nu(Hg_2\text{-}O_{17}) + \nu(Hg_2\text{-}O_{31})] - [\nu(Hg_{45}\text{-}O_{46}) - \nu(Te_{48}\text{-}O_{46})] - [\nu(Hg_{45}\text{-}O_{47}) - \nu(Te_{49}\text{-}O_{47})]$
795(sh)		
790(6)	792(1)[583]	$[\nu(Hg_1\text{-}O_{16}) - \nu(Te_4\text{-}O_{16})] + [\nu(Hg_1\text{-}O_{17}) - \nu(Te_3\text{-}O_{17})] - [\nu(Hg_1\text{-}O_{31}) - \nu(Te_{33}\text{-}O_{31})] - [\nu(Hg_1\text{-}O_{32}) - \nu(Te_{39}\text{-}O_{32})]$
780(2)	791(1)[558]	$[\nu(Hg_1\text{-}O_{16}) - \nu(Te_4\text{-}O_{16})] + [\nu(Hg_1\text{-}O_{31}) - \nu(Te_{33}\text{-}O_{31})] - [\nu(Hg_1\text{-}O_{17}) - \nu(Te_3\text{-}O_{17})] - [\nu(Hg_1\text{-}O_{32}) - \nu(Te_{39}\text{-}O_{32})]$
776(2)		
721(15)	707(13)[37] 706(3)[202] 702(2)[10] 697(<1)[82]	*f*
715(19)	708(7)[107]	$[\nu(Te_4\text{-}F_7) - \nu(Te_4\text{-}F_{10})] + [\nu(Te_3\text{-}F_{12}) - \nu(Te_3\text{-}F_{13})] + [\nu(Te_{33}\text{-}F_{34}) - \nu(Te_{33}\text{-}F_{36})] + [\nu(Te_{39}\text{-}F_{42}) - \nu(Te_{39}\text{-}F_{43})] + [\nu(Te_{48}\text{-}F_{57}) - \nu(Te_{48}\text{-}F_{59})] + [\nu(Te_5\text{-}F_{19}) - \nu(Te_5\text{-}F_{18})] + [\nu(Te_5\text{-}F_{22}) - \nu(Te_5\text{-}F_{20})] + [\nu(Te_{25}\text{-}F_{30}) - \nu(Te_{25}\text{-}F_{28})] + [\nu(Te_{25}\text{-}F_{27}) - \nu(Te_{25}\text{-}F_{26})]$
713(19)	706(4)[155]	$[\nu(Te_4\text{-}F_7) - \nu(Te_4\text{-}F_{10})] + [\nu(Te_{39}\text{-}F_{43}) - \nu(Te_{39}\text{-}F_{42})] + [\nu(Te_{49}\text{-}F_{51}) - \nu(Te_{49}\text{-}F_{50})] + [\nu(Te_{48}\text{-}F_{57}) - \nu(Te_{48}\text{-}F_{59})]$
710(23)	705(1)[363]	$[\nu(Te_3\text{-}F_{12}) - \nu(Te_3\text{-}F_{13})] + [\nu(Te_{33}\text{-}F_{36}) - \nu(Te_{33}\text{-}F_{34})] + [\nu(Te_{25}\text{-}F_{26}) - \nu(Te_{25}\text{-}F_{27})]$
	705(6)[151]	$[\nu(Te_3\text{-}F_{12}) - \nu(Te_3\text{-}F_{13})] + [\nu(Te_{33}\text{-}F_{34}) - \nu(Te_{33}\text{-}F_{36})] + [\nu(Te_5\text{-}F_{20}) - \nu(Te_5\text{-}F_{22})] + [\nu(Te_{49}\text{-}F_{52}) - \nu(Te_{49}\text{-}F_{54})] + [\nu(Te_{48}\text{-}F_{59}) + \nu(Te_{48}\text{-}F_{55}) - \nu(Te_{48}\text{-}F_{56}) - \nu(Te_{48}\text{-}F_{57})]$
	704(1)[424]	$[\nu(Te_4\text{-}F_7) - \nu(Te_4\text{-}F_{10})] + [\nu(Te_{39}\text{-}F_{42}) - \nu(Te_{39}\text{-}F_{43})] + [\nu(Te_{48}\text{-}F_{59}) + \nu(Te_{48}\text{-}F_{56}) - \nu(Te_{48}\text{-}F_{55}) - \nu(Te_{48}\text{-}F_{57})] + [\nu(Te_{49}\text{-}F_{52}) + \nu(Te_{49}\text{-}F_{50}) - \nu(Te_{49}\text{-}F_{54}) - \nu(Te_{49}\text{-}F_{51})]$
696(100)	681(167)[<1]	$\nu(Te_3\text{-}F_8) + \nu(Te_4\text{-}F_{11}) + \nu(Te_{33}\text{-}F_{37}) + \nu(Te_{39}\text{-}F_{41}) + \nu(Te_5\text{-}F_{21}) + \nu(Te_{48}\text{-}F_{58}) + \nu(Te_{49}\text{-}F_{53}) + \nu(Te_{25}\text{-}F_{29})$

Table S4.10. continued…

691(sh)	699(<1)[29]	$[\nu(Te_3\text{-}F_{12}) - \nu(Te_3\text{-}F_{13})] + [\nu(Te_{33}\text{-}F_{36}) - \nu(Te_{33}\text{-}F_{34})] + [\nu(Te_{25}\text{-}F_{27}) - \nu(Te_{25}\text{-}F_{26})] + [\nu(Te_5\text{-}F_{19}) + \nu(Te_5\text{-}F_{22}) - \nu(Te_5\text{-}F_{20})]$
	699(1)[21]	$[\nu(Te_5\text{-}F_{18}) + \nu(Te_5\text{-}F_{19})] + [\nu(Te_{25}\text{-}F_{30}) - \nu(Te_{25}\text{-}F_{28})] + [\nu(Te_{48}\text{-}F_{59}) - \nu(Te_{48}\text{-}F_{57})] + [\nu(Te_{49}\text{-}F_{51}) - \nu(Te_{49}\text{-}F_{50})]$
	696(<1)[387]	$[\nu(Te_3\text{-}F_6) - \nu(Te_3\text{-}F_{14})] + [\nu(Te_{33}\text{-}F_{35}) - \nu(Te_{33}\text{-}F_{38})] + [\nu(Te_4\text{-}F_{15}) - \nu(Te_4\text{-}F_9)] + [\nu(Te_{39}\text{-}F_{44}) - \nu(Te_{39}\text{-}F_{40})] + [\nu(Te_5\text{-}F_{22}) + \nu(Te_5\text{-}F_{20})]_{small}$
	695(1)[45]	$[\nu(Te_3\text{-}F_{12}) + \nu(Te_3\text{-}F_{14}) - \nu(Te_3\text{-}F_{13}) - \nu(Te_3\text{-}F_6)] + [\nu(Te_{33}\text{-}F_{34}) + \nu(Te_{33}\text{-}F_{38}) - \nu(Te_{33}\text{-}F_{35}) - \nu(Te_{33}\text{-}F_{36})] + [\nu(Te_{39}\text{-}F_{43}) - \nu(Te_{39}\text{-}F_{42})] + [\nu(Te_4\text{-}F_{10}) - \nu(Te_4\text{-}F_7)] + [\nu(Te_{48}\text{-}F_{59}) - \nu(Te_{48}\text{-}F_{57})]_{small}$
688(sh)	692(9)[3]	$[\nu(Te_3\text{-}F_6) - \nu(Te_3\text{-}F_{14})] + [\nu(Te_{33}\text{-}F_{35}) - \nu(Te_{33}\text{-}F_{38})] + [\nu(Te_4\text{-}F_9) - \nu(Te_4\text{-}F_{15})] + [\nu(Te_{39}\text{-}F_{40}) - \nu(Te_{39}\text{-}F_{44})]$
	689(1)[4]	$[\nu(Te_3\text{-}F_6) - \nu(Te_3\text{-}F_{14})] + [\nu(Te_4\text{-}F_9) - \nu(Te_4\text{-}F_{15})] + [\nu(Te_{39}\text{-}F_{44}) - \nu(Te_{39}\text{-}F_{40})] + [\nu(Te_{33}\text{-}F_{38}) - \nu(Te_{33}\text{-}F_{35})]$
	688(1)[5]	$[\nu(Te_3\text{-}F_6) - \nu(Te_3\text{-}F_{14})] + [\nu(Te_4\text{-}F_{15}) - \nu(Te_4\text{-}F_9)] + [\nu(Te_{39}\text{-}F_{40}) - \nu(Te_{39}\text{-}F_{44})] + [\nu(Te_{33}\text{-}F_{38}) - \nu(Te_{33}\text{-}F_{35})]$
676(21) 671(sh)	678(3)[245]	$[\nu(Te_3\text{-}F_8) + \nu(Te_{33}\text{-}F_{37})] - [\nu(Te_4\text{-}F_{11}) + \nu(Te_{39}\text{-}F_{41})] - [\nu(Te_5\text{-}F_{18}) + \nu(Te_5\text{-}F_{21})] - [\nu(Te_{48}\text{-}F_{58}) + \nu(Te_{49}\text{-}F_{53})]$
	678(8)[9]	$[\nu(Te_3\text{-}F_8) + \nu(Te_{33}\text{-}F_{37})] - [\nu(Te_5\text{-}F_{21}) + \nu(Te_{48}\text{-}F_{58}) + \nu(Te_{49}\text{-}F_{53})]$
	677(5)[61]	$[\nu(Te_4\text{-}F_{11}) - [\nu(Te_{33}\text{-}F_{37}) + \nu(Te_{49}\text{-}F_{53})]$
	677(2)[73]	$[\nu(Te_3\text{-}F_8) + \nu(Te_{39}\text{-}F_{41})] - [\nu(Te_4\text{-}F_{11}) + \nu(Te_{33}\text{-}F_{37})] + \nu(Te_{48}\text{-}F_{58})_{small} - \nu(Te_{49}\text{-}F_{53})$
	677(2)[121]	$[\nu(Te_3\text{-}F_8) + \nu(Te_4\text{-}F_{11})] - [\nu(Te_{33}\text{-}F_{37}) + \nu(Te_{39}\text{-}F_{41})] + \nu(Te_{49}\text{-}F_{53})_{small} - \nu(Te_{48}\text{-}F_{58})$
	676(7)[80]	$\nu(Te_3\text{-}F_8) - \nu(Te_{39}\text{-}F_{41}) + \nu(Te_{48}\text{-}F_{58})$
653(6)	674(10)[102]	*f*
644(6)	631(<0.1)[1] 630(1)[2] 629(2)[1] 629(3)[<1]	*f*
628(35)	633(34)[<0.1]	$\nu(Te_3\text{-}F_8) + \nu(Te_{33}\text{-}F_{37})] + \nu(Te_4\text{-}F_{11}) + \nu(Te_{39}\text{-}F_{41}) + [\nu(Te_5\text{-}F_{21}) + \nu(Te_{48}\text{-}F_{58}) + \nu(Te_{49}\text{-}F_{53}) + \nu(Te_{25}\text{-}F_{29})]_{small}$
	628(4)[<1]	$[\nu(Te_4\text{-}F_7) + \nu(Te_4\text{-}F_{10})] + [\nu(Te_{39}\text{-}F_{42}) + \nu(Te_{39}\text{-}F_{43})] + [\nu(Te_5\text{-}F_{21}) + \nu(Te_{48}\text{-}F_{58}) + \nu(Te_{49}\text{-}F_{53}) + \nu(Te_{25}\text{-}F_{29})] - [\nu(Te_{48}\text{-}F_{57}) + \nu(Te_{48}\text{-}F_{59}) + \nu(Te_{49}\text{-}F_{50}) + \nu(Te_{49}\text{-}F_{51}) + \nu(Te_5\text{-}F_{18}) + \nu(Te_5\text{-}F_{19}) + \nu(Te_5\text{-}F_{20}) + \nu(Te_5\text{-}F_{22}) + \nu(Te_{25}\text{-}F_{26}) + \nu(Te_{25}\text{-}F_{27}) + \nu(Te_{25}\text{-}F_{28}) + \nu(Te_{25}\text{-}F_{30})]$
621(19)	627(6)[<1]	$[\nu(Te_3\text{-}F_{12}) + \nu(Te_3\text{-}F_{13})] + [\nu(Te_{33}\text{-}F_{34}) + \nu(Te_{33}\text{-}F_{36})] - [\nu(Te_4\text{-}F_7) + \nu(Te_4\text{-}F_{10})] - [\nu(Te_{39}\text{-}F_{42}) + \nu(Te_{39}\text{-}F_{43})] + \nu(Te_{48}\text{-}F_{57}) + \nu(Te_{48}\text{-}F_{59})$
613(16)	627(<1)[<1]	$[\nu(Te_4\text{-}F_7) + \nu(Te_4\text{-}F_{10})] - [\nu(Te_{39}\text{-}F_{42}) + \nu(Te_{39}\text{-}F_{43})]$
	626(8)[2]	$[\nu(Te_4\text{-}F_9) + \nu(Te_4\text{-}F_{15})] + [\nu(Te_{39}\text{-}F_{40}) + \nu(Te_{39}\text{-}F_{44})]_{small} + [\nu(Te_{48}\text{-}F_{55}) + \nu(Te_{48}\text{-}F_{56})] + [\nu(Te_{49}\text{-}F_{52}) + \nu(Te_{49}\text{-}F_{54})]$
610(19) 604(sh)	624(3)[4]	$[\nu(Te_3\text{-}F_6) + \nu(Te_3\text{-}F_{14})] + [\nu(Te_{33}\text{-}F_{35}) + \nu(Te_{33}\text{-}F_{38})]$
	623(8)[<1]	$[\nu(Te_4\text{-}F_9) + \nu(Te_4\text{-}F_{15})] + [\nu(Te_{39}\text{-}F_{40}) + \nu(Te_{39}\text{-}F_{44})] + [\nu(Te_3\text{-}F_6) + \nu(Te_3\text{-}F_{14})]_{small} + [\nu(Te_{33}\text{-}F_{35}) + \nu(Te_{33}\text{-}F_{38})]_{small} - [\nu(Te_{48}\text{-}F_{55}) + \nu(Te_{48}\text{-}F_{56})]$
n.o.	624(1)[1] 623(<1)[1]	*f*
n.o.	620(<1)[<1]	$[\nu(Te_3\text{-}F_6) + \nu(Te_3\text{-}F_{14})] - [\nu(Te_{33}\text{-}F_{35}) + \nu(Te_{33}\text{-}F_{38})]$
	620(<1)[<1]	$[\nu(Te_4\text{-}F_9) + \nu(Te_4\text{-}F_{15})] + \nu(Te_{39}\text{-}F_{41}) - [\nu(Te_{39}\text{-}F_{40}) + \nu(Te_{39}\text{-}F_{44})] - \nu(Te_4\text{-}F_{11}) + [\nu(Te_{49}\text{-}F_{52}) + \nu(Te_{49}\text{-}F_{54})]_{small}$

Table S4.10. continued…

492(sh)	499(<1)[40] 498(<1)[40]	*f*
488(6)	488(18)[24]	*f*
483(6)	487(14)[32]	*f*
448(8)	444(24)[<1]	$[\nu(Hg_1\text{-}O_{16}) + \nu(Hg_1\text{-}O_{17}) + \nu(Hg_1\text{-}O_{31}) + \nu(Hg_1\text{-}O_{32})] - [\nu(Hg_2\text{-}O_{17}) + \nu(Hg_2\text{-}O_{31}) + \nu(Hg_{45}\text{-}O_{16}) + \nu(Hg_{45}\text{-}O_{32})]$
	435(<1)[393]	$[\nu(Hg_1\text{-}O_{16}) + \nu(Hg_1\text{-}O_{32})] - [\nu(Hg_1\text{-}O_{17}) + \nu(Hg_1\text{-}O_{31})] + [\nu(Hg_2\text{-}O_{17}) + \nu(Hg_2\text{-}O_{31})] - [\nu(Hg_{45}\text{-}O_{16}) + \nu(Hg_{45}\text{-}O_{32})]$
430(15)	419(9)[3]	$[\nu(Hg_1\text{-}O_{16}) + \nu(Hg_1\text{-}O_{17})] - [\nu(Hg_1\text{-}O_{31}) + \nu(Hg_1\text{-}O_{32})] + [\nu(Hg_2\text{-}O_{31}) + \nu(Hg_{45}\text{-}O_{32})] - [\nu(Hg_{45}\text{-}O_{16}) + \nu(Hg_2\text{-}O_{17})]$
	419(9)[<1]	$[\nu(Hg_1\text{-}O_{17}) + \nu(Hg_1\text{-}O_{32})] - [\nu(Hg_1\text{-}O_{16}) + \nu(Hg_1\text{-}O_{31})] + [\nu(Hg_{45}\text{-}O_{16}) + \nu(Hg_2\text{-}O_{31})] - [\nu(Hg_2\text{-}O_{17}) + \nu(Hg_{45}\text{-}O_{32})]$
353(10)	345(1)[<1]	$\delta(Te_3F_{4e})_{umb} + \delta(Te_4F_{4e})_{umb} + \delta(Te_{33}F_{4e})_{umb} + \delta(Te_{39}F_{4e})_{umb} + \delta(Te_5F_{4e})_{umb} + \delta(Te_{25}F_{4e})_{umb} + \delta(Te_{48}F_{4e})_{umb} + \delta(Te_{49}F_{4e})_{umb}$
349(10)	338(<1)[2]	$\delta(Te_3O_{17}F_6F_8F_{14})_{umb} - \delta(Te_{33}O_{31}F_{35}F_{37}F_{38})_{umb} / \delta(Te_4O_{16}F_9F_{11}F_{15})_{umb} - \delta(Te_{39}O_{32}F_{40}F_{41}F_{44})_{umb}$
	336(<0.1)[155]	$\delta(Te_3O_{17}F_6F_8F_{14})_{umb} + \delta(Te_{33}O_{31}F_{35}F_{37}F_{38})_{umb}$
	336(<1)[127]	$\delta(Te_4O_{16}F_9F_{11}F_{15})_{umb} + \delta(Te_{39}O_{32}F_{40}F_{41}F_{44})_{umb}$
n.o.	336(<1)[159]	$\delta(F_8\text{-}Te_3\text{-}F_{12}) + \delta(F_{36}\text{-}Te_{33}\text{-}F_{37})$
334(8)	334(<1)[156]	$\delta(Te_4O_{16}F_9F_{11}F_{15})_{umb} - \delta(Te_{39}O_{32}F_{40}F_{41}F_{44})_{umb} / \delta(F_{58}\text{-}Te_{48}\text{-}F_{59}) + \delta(F_{50}\text{-}Te_{49}\text{-}F_{53})$
	334(<0.1)[154]	$\delta(Te_3O_{17}F_6F_8F_{14})_{umb} - \delta(Te_{33}O_{31}F_{35}F_{37}F_{38})_{umb} / \delta(F_{19}\text{-}Te_5\text{-}F_{21}) + \delta(F_{29}\text{-}Te_{25}\text{-}F_{30})$
n.o.	334(<0.1)[41]	$[\delta(F_7\text{-}Te_4\text{-}F_{11}) + \delta(F_{36}\text{-}Te_{33}\text{-}F_{37}) + \delta(F_{41}\text{-}Te_{39}\text{-}F_{42})] - \delta(F_8\text{-}Te_3\text{-}F_{12}) - [\delta(F_{28}\text{-}Te_{25}\text{-}F_{29}) + \delta(F_{22}\text{-}Te_{49}\text{-}F_{53}) / \rho_w(F_{35}\text{-}Te_{33}\text{-}F_{38})$
	334(<1)[27]	$\delta(F_8\text{-}Te_3\text{-}F_{12}) + \delta(F_{34}\text{-}Te_{33}\text{-}F_{37}) + \delta(F_{10}\text{-}Te_4\text{-}F_{11}) - \delta(F_{41}\text{-}Te_{39}\text{-}F_{42}) - [\delta(F_{21}\text{-}Te_5\text{-}F_{22}) + \delta(F_{52}\text{-}Te_{49}\text{-}F_{53}) + \delta(F_{58}\text{-}Te_{48}\text{-}F_{57}) / \rho_w(F_9\text{-}Te_4\text{-}F_{15}) + \rho_w(F_{35}\text{-}Te_{33}\text{-}F_{38})$
330(10)	333(<1)[24] 333(<1)[8]	*f*
327(11)	332(1)[5]	$\delta(O_{17}\text{-}Te_3\text{-}F_{13}) + \delta(F_{51}\text{-}Te_{49}\text{-}F_{53}) - [\delta(F_{50}\text{-}Te_{49}\text{-}F_{53}) + \delta(F_{58}\text{-}Te_{48}\text{-}F_{59})]$
321(6)	332(<1)[1] 332(<1)[13] 331(<1)[24] 330(<1)[25]	*f*
317(5)	329(1)[12]	$\delta(O_{31}\text{-}Te_{33}\text{-}F_{34}) + \delta(F_{36}\text{-}Te_{33}\text{-}F_{37}) - \delta(O_{17}\text{-}Te_3\text{-}F_{12}) + [\delta(F_{29}\text{-}Te_{25}\text{-}F_{30}) + \delta(F_{29}\text{-}Te_{25}\text{-}F_{26})] / \delta(Te_5F_{4e})_{umb}$
	328(2)[21]	$\delta(O_{16}\text{-}Te_4\text{-}F_{10}) + \delta(F_7\text{-}Te_4\text{-}F_{11}) + [\delta(O_{17}\text{-}Te_3\text{-}F_{13}) + \delta(O_{32}\text{-}Te_{39}\text{-}F_{42})]_{small} + \delta(F_{54}\text{-}Te_{49}\text{-}F_{53}) / \rho_w(F_{50}\text{-}Te_{49}\text{-}F_{51})$
	328(3)[65]	$\delta(O_{32}\text{-}Te_{39}\text{-}F_{43}) + \delta(F_{41}\text{-}Te_{39}\text{-}F_{42}) + \delta(O_{31}\text{-}Te_{33}\text{-}F_{36}) + \delta(F_{34}\text{-}Te_{33}\text{-}F_{37}) + \delta(F_{29}\text{-}Te_{25}\text{-}F_{26})$
	327(1)[63]	*f*
	327(3)[42]	$\delta(O_{17}\text{-}Te_3\text{-}F_{12}) + \delta(O_{32}\text{-}Te_{39}\text{-}F_{42}) + \delta(F_{29}\text{-}Te_{25}\text{-}F_{26}) + \delta(F_{58}\text{-}Te_{48}\text{-}F_{56})$
	326(<1)[32]	*f*
	325(<1)[18]	*f*
	323(<1)[11]	$\delta(O_{31}\text{-}Te_{33}\text{-}F_{36}) + \delta(O_{32}\text{-}Te_{39}\text{-}F_{42}) + \delta(F_{29}\text{-}Te_{25}\text{-}F_{27}) - \delta(O_{46}\text{-}Te_{48}\text{-}F_{59})$

Table S4.10. continued…

n.o.	323(<1)[10]	$\rho_w(O_{23}\text{-}Hg_2\text{-}O_{24}) + \rho_w(O_{47}\text{-}Hg_{45}\text{-}O_{46}) / [\delta(F_8\text{-}Te_3\text{-}F_{14}) + \delta(F_{35}\text{-}Te_{33}\text{-}F_{37})]_{small}$
	322(<0.1)[12]	$\rho_t(O_{17}\text{-}Hg_1\text{-}O_{31}) + \rho_t(O_{16}\text{-}Hg_1\text{-}O_{32}) / \delta(O_{47}\text{-}Te_{49}\text{-}F_{51}) + \delta(O_{47}\text{-}Te_{49}\text{-}F_{54})$
n.o.	323(<1)[10]	$\rho_w(O_{23}\text{-}Hg_2\text{-}O_{24}) + \rho_w(O_{47}\text{-}Hg_{45}\text{-}O_{46}) / [\delta(F_8\text{-}Te_3\text{-}F_{14}) + \delta(F_{35}\text{-}Te_{33}\text{-}F_{37})]_{small}$
	322(<0.1)[12]	$\rho_t(O_{17}\text{-}Hg_1\text{-}O_{31}) + \rho_t(O_{16}\text{-}Hg_1\text{-}O_{32}) / \delta(O_{47}\text{-}Te_{49}\text{-}F_{51}) + \delta(O_{47}\text{-}Te_{49}\text{-}F_{54})$
n.o.	321(<0.1)[76]	$[\delta(F_6\text{-}Te_3\text{-}F_8) + \delta(F_{35}\text{-}Te_{33}\text{-}F_{37})] - [\delta(F_{14}\text{-}Te_3\text{-}F_8) + \delta(F_{38}\text{-}Te_{33}\text{-}F_{37})]$
	319(2)[3]	$[\delta(F_6\text{-}Te_3\text{-}F_8) + \delta(F_{38}\text{-}Te_{33}\text{-}F_{37})] - [\delta(F_{14}\text{-}Te_3\text{-}F_8) + \delta(F_{35}\text{-}Te_{33}\text{-}F_{37})] / \rho_w(O_{23}\text{-}Hg_2\text{-}O_{24})$
	319(2)[4]	$[\delta(F_{15}\text{-}Te_4\text{-}F_{11}) + \delta(F_{40}\text{-}Te_{39}\text{-}F_{41})] - [\delta(F_9\text{-}Te_4\text{-}F_{11}) + \delta(F_{44}\text{-}Te_{39}\text{-}F_{41})] / \rho_w(O_{46}\text{-}Hg_{45}\text{-}O_{47})$
305(sh)	313(<1)[6]	*f*
	312(<0.1)[2]	
	293(1)[<1]	
	293(1)[<1]	
	292(1)[<1]	
	291(1)[<1]	
298(19)	321(<0.1)[9]	$[\delta(F_{15}\text{-}Te_4\text{-}F_{11}) + \delta(F_{44}\text{-}Te_{39}\text{-}F_{41})] - [\delta(F_9\text{-}Te_4\text{-}F_{11}) + \delta(F_{40}\text{-}Te_{39}\text{-}F_{41})] + \delta(F_{14}\text{-}Te_3\text{-}F_8)_{small}$
	290(<1)[<1]	$[\delta(F_6\text{-}Te_3\text{-}F_{12}) + \delta(F_{13}\text{-}Te_3\text{-}F_{14})] + [\delta(F_7\text{-}Te_4\text{-}F_9) + \delta(F_{10}\text{-}Te_4\text{-}F_{15})] + [\delta(F_{34}\text{-}Te_{33}\text{-}F_{35}) + \delta(F_{36}\text{-}Te_{33}\text{-}F_{38})] + [\delta(F_{40}\text{-}Te_{39}\text{-}F_{42}) + \delta(F_{43}\text{-}Te_{39}\text{-}F_{44})]$
	290(2)[<0.1]	$[\delta(F_6\text{-}Te_3\text{-}F_{12}) + \delta(F_{13}\text{-}Te_3\text{-}F_{14})] + [\delta(F_7\text{-}Te_4\text{-}F_9) + \delta(F_{10}\text{-}Te_4\text{-}F_{15})] + [\delta(F_{34}\text{-}Te_{33}\text{-}F_{38}) + \delta(F_{35}\text{-}Te_{33}\text{-}F_{36})] + [\delta(F_{40}\text{-}Te_{39}\text{-}F_{43}) + \delta(F_{42}\text{-}Te_{39}\text{-}F_{44})]$
	290(2)[<0.1]	$[\delta(F_6\text{-}Te_3\text{-}F_{12}) + \delta(F_{13}\text{-}Te_3\text{-}F_{14})] + [\delta(F_7\text{-}Te_4\text{-}F_{15}) + \delta(F_9\text{-}Te_4\text{-}F_{10})] + [\delta(F_{34}\text{-}Te_{33}\text{-}F_{38}) + \delta(F_{35}\text{-}Te_{33}\text{-}F_{36})]_{small} + [\delta(F_{40}\text{-}Te_{39}\text{-}F_{42}) + \delta(F_{43}\text{-}Te_{39}\text{-}F_{44})]$
	289(<0.1)[<0.1]	$[\delta(F_6\text{-}Te_3\text{-}F_{12}) + \delta(F_{13}\text{-}Te_3\text{-}F_{14})] + [\delta(F_7\text{-}Te_4\text{-}F_{15}) + \delta(F_9\text{-}Te_4\text{-}F_{10})] + [\delta(F_{34}\text{-}Te_{33}\text{-}F_{35}) + \delta(F_{36}\text{-}Te_{33}\text{-}F_{38})] + [\delta(F_{40}\text{-}Te_{39}\text{-}F_{43}) + \delta(F_{42}\text{-}Te_{39}\text{-}F_{44})]$
235(6)	242(<1)[<0.1]	*f*
	241(<1)[<1]	
	233(2)[6]	
	231(2)[6]	
204(2)	216(2)[<0.1]	$\delta(F_6\text{-}Te_3\text{-}F_8) + \delta(F_9\text{-}Te_4\text{-}F_{11}) + \delta(F_{35}\text{-}Te_{33}\text{-}F_{37}) + \delta(F_{40}\text{-}Te_{39}\text{-}F_{41}) / \rho_w(F_{12}\text{-}Te_3\text{-}F_{13}) + \rho_w(F_7\text{-}Te_4\text{-}F_{10}) + \rho_w(F_{34}\text{-}Te_{33}\text{-}F_{36}) + \rho_w(F_{42}\text{-}Te_{39}\text{-}F_{43})$
	214(<0.1)[1]	$[\rho_w(F_{12}\text{-}Te_3\text{-}F_{13}) + \rho_w(F_{34}\text{-}Te_{33}\text{-}F_{36})] - [\rho_w(F_7\text{-}Te_4\text{-}F_{10}) + \rho_w(F_{42}\text{-}Te_{39}\text{-}F_{43})] / [\rho_w(F_{35}\text{-}Te_{33}\text{-}F_{37}) - \rho_w(F_9\text{-}Te_4\text{-}F_{11})]_{small}$
	213(<0.1)[<0.1]	*f*
	212(<0.1)[<1]	$[\rho_w(F_{40}\text{-}Te_{39}\text{-}F_{44}) - \rho_w(F_{42}\text{-}Te_{39}\text{-}F_{43})] + [\rho_w(F_{52}\text{-}Te_{49}\text{-}F_{54}) - \rho_w(F_{50}\text{-}Te_{49}\text{-}F_{51})]$
	212(<0.1)[<1]	$[\rho_w(F_7\text{-}Te_4\text{-}F_{10}) - \rho_w(F_9\text{-}Te_4\text{-}F_{15})] + [\rho_w(F_{26}\text{-}Te_{25}\text{-}F_{27}) - \rho_w(F_{28}\text{-}Te_{25}\text{-}F_{30})]$
	212(<0.1)[<1]	$[\rho_w(F_6\text{-}Te_3\text{-}F_{14}) - \rho_w(F_{12}\text{-}Te_3\text{-}F_{13})] + [\rho_w(F_{42}\text{-}Te_{39}\text{-}F_{43}) - \rho_w(F_{40}\text{-}Te_{39}\text{-}F_{44})] + [\rho_w(F_{26}\text{-}Te_{25}\text{-}F_{27}) - \rho_w(F_{28}\text{-}Te_{25}\text{-}F_{30})]$
	212(<0.1)[<1]	$[\rho_w(F_6\text{-}Te_3\text{-}F_{14}) - \rho_w(F_{12}\text{-}Te_3\text{-}F_{13})] + [\rho_w(F_7\text{-}Te_4\text{-}F_{10}) - \rho_w(F_9\text{-}Te_4\text{-}F_{15})]$
	212(<0.1)[<1]	$[\rho_w(F_{34}\text{-}Te_{33}\text{-}F_{36}) - \rho_w(F_{35}\text{-}Te_{33}\text{-}F_{38})] + [\rho_w(F_{40}\text{-}Te_{39}\text{-}F_{44}) - \rho_w(F_{42}\text{-}Te_{39}\text{-}F_{43})] + [\rho_w(F_9\text{-}Te_4\text{-}F_{15}) - \rho_w(F_7\text{-}Te_4\text{-}F_{10})]_{small}$
	211(<1)[<0.1]	$[\rho_w(F_6\text{-}Te_3\text{-}F_{14}) - \rho_w(F_{12}\text{-}Te_3\text{-}F_{13})] + [\rho_w(F_9\text{-}Te_4\text{-}F_{15}) - \rho_w(F_7\text{-}Te_4\text{-}F_{10})] + [\rho_w(F_{35}\text{-}Te_{33}\text{-}F_{38}) + \rho_w(F_{34}\text{-}Te_{33}\text{-}F_{36})] + [\rho_w(F_{40}\text{-}Te_{39}\text{-}F_{44}) - \rho_w(F_{42}\text{-}Te_{39}\text{-}F_{43})] + [\rho_w(F_{55}\text{-}Te_{48}\text{-}F_{56}) - \rho_w(F_{57}\text{-}Te_{48}\text{-}F_{59})]$
	211(<0.1)[<0.1]	*f*

Table S4.10. continued…

n.o.	209(<0.1)[1]	$[\rho_w(O_{16}\text{-}Te_4\text{-}F_{11}) - \rho_w(F_7\text{-}Te_4\text{-}F_{10})] - [\rho_w(O_{32}\text{-}Te_{39}\text{-}F_{41}) - \rho_w(F_{42}\text{-}Te_{39}\text{-}F_{43})]$
	209(<0.1)[1]	$[\rho_w(O_{17}\text{-}Te_3\text{-}F_8) - \rho_w(F_{12}\text{-}Te_3\text{-}F_{13})] - [\rho_w(O_{31}\text{-}Te_{33}\text{-}F_{37}) - \rho_w(F_{36}\text{-}Te_{33}\text{-}F_{34})]$
	202(<0.1)[<1]	$[\rho_w(O_{17}\text{-}Te_3\text{-}F_8) - \rho_w(F_6\text{-}Te_3\text{-}F_{14})] + [\rho_w(O_{31}\text{-}Te_{33}\text{-}F_{37}) - \rho_w(F_{35}\text{-}Te_{33}\text{-}F_{38})]$
	202(<0.1)[<1]	$[\rho_w(O_{16}\text{-}Te_4\text{-}F_{11}) - \rho_w(F_9\text{-}Te_4\text{-}F_{15})] + [\rho_w(O_{32}\text{-}Te_{39}\text{-}F_{41}) - \rho_w(F_{40}\text{-}Te_{39}\text{-}F_{44})]$
	202(<0.1)[<0.1	$[\rho_w(O_{17}\text{-}Te_3\text{-}F_8) - \rho_w(F_6\text{-}Te_3\text{-}F_{14})] - [\rho_w(O_{31}\text{-}Te_{33}\text{-}F_{37}) - \rho_w(F_{35}\text{-}Te_{33}\text{-}F_{38})] / [\rho_w(O_{16}\text{-}Te_4\text{-}F_{11}) - \rho_w(F_9\text{-}Te_4\text{-}F_{15})]_{small} - [\rho_w(O_{32}\text{-}Te_{39}\text{-}F_{41}) - \rho_w(F_{40}\text{-}Te_{39}\text{-}F_{44})]_{small}$
	201(<0.1)[<0.1	$[\rho_w(O_{16}\text{-}Te_4\text{-}F_{11}) - \rho_w(F_9\text{-}Te_4\text{-}F_{15})] - [\rho_w(O_{32}\text{-}Te_{39}\text{-}F_{41}) - \rho_w(F_{40}\text{-}Te_{39}\text{-}F_{44})] / [\rho_w(O_{17}\text{-}Te_3\text{-}F_8) - \rho_w(F_6\text{-}Te_3\text{-}F_{14})] - [\rho_w(O_{31}\text{-}Te_{33}\text{-}F_{37}) - \rho_w(F_{35}\text{-}Te_{33}\text{-}F_{38})]$
n.o.	201(<0.1)[<0.1]	*f*
	200(<1)[<1]	
	193(<0.1)[<1]	
	190(<0.1)[<0.1]	
150(6)	159(<1)[5]	*f*
	158(<1)[5]	
n.o.	142(<0.1)[4]	$\rho_r(Te_3\text{-}F_6,F_8) + \rho_r(Te_{33}\text{-}F_{35},F_{37}) + \rho_r(Te_4\text{-}F_9,F_{11}) + \rho_r(Te_{39}\text{-}F_{40},F_{41}) / \rho_w(F_{12}\text{-}Te_3\text{-}F_{13}) + \rho_w(F_{34}\text{-}Te_{33}\text{-}F_{36}) + \rho_w(F_7\text{-}Te_4\text{-}F_{10}) + \rho_w(F_{42}\text{-}Te_{39}\text{-}F_{43})$
128(16)	126(2)[<1]	*f*
	126(<1)[3]	
n.o.	114(2)[<0.1]	$\rho_r(Te_3\text{-}F_6,F_8,F_{14}) + \rho_r(Te_{33}\text{-}F_{35},F_{37},F_{38}) + \rho_r(Te_4\text{-}F_9,F_{11},F_{15}) + \rho_r(Te_{39}\text{-}F_{40},F_{41},F_{44})$
n.o.	106(<0.1)[13]	$[\rho_r(Te_3\text{-}F_6,F_8,F_{14}) + \rho_r(Te_4\text{-}F_9,F_{11},F_{15})] - [\rho_r(Te_{33}\text{-}F_{35},F_{37},F_{38}) + \rho_r(Te_{39}\text{-}F_{40},F_{41},F_{44})]$
	105(<0.1)[13]	$[\rho_r(Te_3\text{-}F_6,F_8,F_{14}) + \rho_r(Te_{39}\text{-}F_{40},F_{41},F_{44})] - [\rho_r(Te_4\text{-}F_9,F_{11},F_{15}) + \rho_r(Te_{33}\text{-}F_{35},F_{37},F_{38})]$
n.o.	87(<1)[10]	coupled deformation and torsion modes
	87(<1)[10]	
	85(2)[3]	
	84(<1)[48]	
	76(<0.1)[<1]	
	72(1)[<0.1]	
	70(<0.1)[14]	
	69(<0.1)[10]	
	52(<0.1)[2]	
	51(<0.1)[3]	
	56(.1)[1]	
	56(.1)[2]	
	51(.1)[1]	
	50(.1)[<1]	
	48(<0.1)[<0.1]	
	41(<0.1)[<1]	
	40(<0.1)[<0.1]	
	36(<0.1)[<0.1]	

Table S4.10. continued…

n.o.	35(<0.1)[<0.1] 34(<0.1)[<1] 33(<0.1)[<0.1] 32(<0.1)[4] 31(<0.1)[<1] 30(<0.1)[<1] 30(<0.1)[<1] 29(<0.1)[<1] 28(<0.1)[<1] 28(<0.1)[<1] 23(<0.1)[<0.1] 19(<0.1)[<1] 18(<0.1)[<0.1] 17(<0.1)[<0.1] 17(<0.1)[<1] 16(.1)[<1] 16(.1)[<0.1] 15(.1)[<0.1] 12(.1)[<0.1] 11(.1)[<1] 11(.1)[<1] 10(.1)[<1] 8(<0.1)[<0.1] 5(<0.1)[<0.1] 5(<0.1)[<0.1]	coupled deformation and torsion modes

[a] Frequencies are given in cm^{-1}. [b] Values in parentheses denote relative Raman intensities. The Raman spectrum was recorded in an FEP sample tube at −150 °C using 1064-nm excitation. [c] The abbreviations denote shoulder (sh), broad (br), and not observed (n.o.). [d] Values in parentheses denote calculated Raman intensities ($Å^4$ amu^{-1}) and values in square brackets denote calculated infrared intensities (km mol^{-1}). [e] Assignments are for the energy-minimized geometry calculated at the PBE0/def2-TZVPP level with. The atom numbering scheme corresponds to that used in Figure 4.13. The abbreviations denote umbrella (umb), stretch (ν), bend (δ), twist (ρ_t), wag (ρ_w), and rock (ρ_r). [f] Overlap with a cation mode. The notation $Te_nF_{4e}F_a$, where *n* is the tellurium atom label, corresponds to the symmetric stretches of the axial fluorine (F_a) and the equatorial fluorines (F_{4e}) of the F_5Te_nO- group.

Table S4.11. Experimental Raman Frequencies and Intensities for $[OTeF_5]^-$ in $[N(CH_2CH_3)_4][OTeF_5]$, $[N(CH_3)_4][OTeF_5]$, and $Cs[OTeF_5]$ and Calculated Vibrational Frequencies and Intensities for the $[OTeF_5]^-$ Anion

exptl $OTeF_5^-$ [a,b,c]			calcd (C_{4v}) [a,d]	
$[N(CH_2CH_3)_4]^+$	$[N(CH_3)_4]^+$	Cs^+		assgnts [e]
866(36)	854(45)	873(100)	891(94)[13]	ν(Te-O)
		657(7)		
643(100)	650(100)	654(72)	638(65)[23]	$\nu(F_aF_{4e}Te)$
		649(97)		
		631(91)		
n.o.	n.o.	n.o.	634(214)[<1]	$\nu(Te\text{-}F_1) - \nu(Te\text{-}F_3)$
588(18)	592(22)	585(35)	570(0)[4]	$[\nu(Te\text{-}F_1) + \nu(Te\text{-}F_3)] - [\nu(Te\text{-}F_2) + \nu(Te\text{-}F_4)]$
579(16)	590(15)	580(61)	570(3)[5]	$\delta(F_1\text{-}Te\text{-}F_5) - \delta(F_5\text{-}Te\text{-}F_3)$
347(10)	347(12)	348(23)	343(29)[<1]	$\nu(Te\text{-}F_a) - \nu(TeF_{4e})$
344(9)	n.o.	335(46)	332(58)[<1]	$\delta(TeF_{4e})_{umb}$
		315(13)		
324(22)	329(47)	311(14)	326(34)[4]	$\delta(F_1\text{-}Te\text{-}O) - \delta(F_3\text{-}Te\text{-}O)$
281(12)	284(7)	288(19)	273(0)[2]	$\delta(F_1\text{-}Te\text{-}F_4) + \delta(F_2\text{-}Te\text{-}F_3)$
n.o.	n.o.	204(3)	219(0)[<0.1]	$\rho_w(F_1\text{-}Te\text{-}F_3) - \rho_w(F_2\text{-}Te\text{-}F_4)$
197(2)	195(2)	192(1)	183(<0.1)]<0.1]	$\rho_w(F_5\text{-}Te\text{-}O) - \rho_w(F_1\text{-}Te\text{-}F_3)$
n.o.	123(2)	141(1)		lattice modes
n.o.	n.o.	121(3)		

[a] Frequencies are given in cm^{-1}. [b] Values in parentheses denote relative Raman intensities. The Raman spectrum was recorded in an FEP sample tube at −150 °C using 1064-nm excitation. [c] The abbreviation denotes not observed (n.o.). [d] Values in parentheses denote calculated Raman intensities ($Å^4$ amu^{-1}) and values in square brackets denote calculated infrared intensities (km mol^{-1}). [e] Assignments are for the energy-minimized geometry calculated at the PBE0/def2-TZVPP level and the atom numbering scheme corresponds to that used in Figure S4.10. The abbreviations denote umbrella (umb), stretch (ν), bend (δ), and wag (ρ_w). The notation $Te_nF_{4e}F_a$, where *n* is the tellurium atom label, corresponds to the symmetric stretches of the axial fluorine (F_a) and the equatorial fluorines (F_{4e}) of the F_5Te_nO- group.

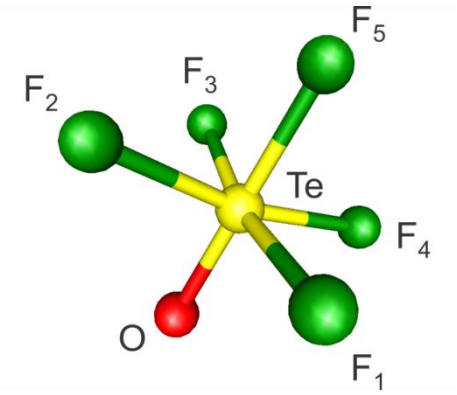

Figure S4.10. The gas-phase, energy-minimized geometry of $[OTeF_5]^-$ (C_{4v}) calculated at the PBE0/def2-TZVPP level of theory.

Table S4.12. Calculated Geometrical Parameters for $[OTeF_5]^-$ (C_{4v})

Bond Lengths (Å)			
Te–O	1.770	Te–F_3	1.889
Te–F_1	1.889	Te–F_4	1.889
Te–F_2	1.889	Te–F_5	1.881
Bond Angles (deg)			
O–Te–F_1	97.2	F_1–Te–F_5	82.8
O–Te–F_2	97.2	F_2–Te–F_3	89.1
O–Te–F_3	97.2	F_2–Te–F_4	165.6
O–Te–F_4	97.2	F_2–Te–F_5	82.8
O–Te–F_5	180.0	F_3–Te–F_4	89.1
F_1–Te–F_2	89.1	F_3–Te–F_5	82.8
F_1–Te–F_3	165.6	F_4–Te–F_5	82.8
F_1–Te–F_4	89.1		

[a] Calculated at the PBE0/def2-TVZPP level of theory. The atom labeling scheme corresponds to that used in Figure S4.10.

Table S4.13. Calculated Geometrical Parameters for $[Hg(OTeF_5)_4]^{2-}$ (S_4) [a]

Bond Lengths (Å)			
$Hg_1–O_8$	2.226	$Te_2–F_{11}$	1.865
$Hg_1–O_{14}$	2.226	$Te_2–F_{10}$	1.864
$Hg_1–O_{18}$	2.226	$Te_2–F_{13}$	1.867
$Hg_1–O_{28}$	2.226	$Te_2–F_{20}$	1.865
$Te_5–O_8$	1.799	$Te_2–F_{16}$	1.871
$Te_4–O_{14}$	1.799	$Te_3–F_{24}$	1.864
$Te_2–O_{18}$	1.799	$Te_3–F_{26}$	1.865
$Te_3–O_{28}$	1.799	$Te_3–F_{27}$	1.865
$Te_5–F_6$	1.864	$Te_3–F_{25}$	1.867
$Te_5–F_9$	1.867	$Te_3–F_{29}$	1.871
$Te_5–F_{15}$	1.865		
$Te_5–F_{12}$	1.865		
$Te_5–F_7$	1.870		
$Te_4–F_{17}$	1.865		
$Te_4–F_{19}$	1.867		
$Te_4–F_{21}$	1.864		
$Te_4–F_{22}$	1.865		
$Te_4–F_{23}$	1.871		
Bond Angles (deg)			
$O_8–Hg_1–O_{14}$	108.0	$O_{14}–Te_4–F_{17}$	95.4
$O_8–Hg_1–O_{18}$	112.4	$O_{14}–Te_4–F_{19}$	93.9
$O_8–Hg_1–O_{28}$	108.0	$O_{14}–Te_4–F_{21}$	96.0
$O_{14}–Hg_1–O_{18}$	108.0	$O_{14}–Te_4–F_{22}$	96.4
$O_{14}–Hg_1–O_{28}$	112.4	$O_{14}–Te_4–F_{23}$	178.6
$O_{18}–Hg_1–O_{28}$	108.0	$F_{23}–Te_4–F_{17}$	84.3
$Hg_1–O_8–Te_5$	132.4	$F_{23}–Te_4–F_{19}$	84.7
$Hg_1–O_{14}–Te_4$	132.4	$F_{23}–Te_4–F_{21}$	84.3
$Hg_1–O_{18}–Te_2$	132.4	$F_{23}–Te_4–F_{22}$	84.9
$Hg_1–O_{28}–Te_3$	132.4	$F_{17}–Te_4–F_{19}$	88.9
$O_8–Te_5–F_6$	96.0	$F_{17}–Te_4–F_{21}$	168.6
$O_8–Te_5–F_9$	93.9	$F_{17}–Te_4–F_{22}$	89.8
$O_8–Te_5–F_{15}$	95.4	$F_{19}–Te_4–F_{21}$	89.2
$O_8–Te_5–F_{12}$	96.4	$F_{19}–Te_4–F_{22}$	169.6
$O_8–Te_5–F_7$	178.5	$F_{21}–Te_4–F_{22}$	90.0
$F_7–Te_5–F_6$	84.3	$O_{28}–Te_3–F_{24}$	96.0
$F_7–Te_5–F_9$	84.7	$O_{28}–Te_3–F_{26}$	96.4
$F_7–Te_5–F_{15}$	84.5	$O_{28}–Te_3–F_{27}$	95.4
$F_7–Te_5–F_{12}$	84.9	$O_{28}–Te_3–F_{25}$	93.9
$F_6–Te_5–F_9$	89.4	$O_{28}–Te_3–F_{29}$	178.6
$F_6–Te_5–F_{15}$	168.6	$F_{29}–Te_3–F_{24}$	84.3
$F_6–Te_5–F_{12}$	90.0	$F_{29}–Te_3–F_{26}$	84.9
$F_9–Te_5–F_{15}$	88.9	$F_{29}–Te_3–F_{27}$	84.6

Table S4.13. continued…

F_9–Te_5–F_{12}	169.6	F_{29}–Te_3–F_{25}	84.7
F_{15}–Te_5–F_{12}	89.8	F_{24}–Te_3–F_{26}	90.0
O_{18}–Te_2–F_{10}	96.0	F_{24}–Te_3–F_{27}	168.6
O_{18}–Te_2–F_{13}	93.9	F_{24}–Te_3–F_{25}	89.2
O_{18}–Te_2–F_{20}	95.4	F_{26}–Te_3–F_{27}	89.8
O_{18}–Te_2–F_{11}	96.4	F_{26}–Te_3–F_{25}	169.6
O_{18}–Te_2–F_{16}	178.6	F_{27}–Te_3–F_{25}	88.9
F_{16}–Te_2–F_{10}	84.3		
F_{16}–Te_2–F_{11}	84.9		
F_{16}–Te_2–F_{20}	84.3		
F_{16}–Te_2–F_{13}	84.7		
F_{10}–Te_2–F_{13}	89.2		
F_{10}–Te_2–F_{20}	168.6		
F_{10}–Te_2–F_{11}	90.0		
F_{13}–Te_2–F_{20}	88.9		
F_{13}–Te_2–F_{11}	169.6		
F_{20}–Te_2–F_{11}	89.8		

[a] Calculated at the PBE0/def2-TVZPP level of theory. The atom labeling scheme corresponds to that used in Figure 4.10.

Table S4.14. Calculated Geometrical Parameters for $[Hg(OTeF_5)_5]^{3-}$ (C_1) [a]

Bond Lengths (Å)			
$Hg_1–O_8$	2.481	$Te_6–F_{17}$	1.854
$Hg_1–O_{12}$	2.510	$Te_6–F_9$	1.859
$Hg_1–O_{22}$	2.110	$Te_6–F_{11}$	1.868
$Hg_1–O_{25}$	2.482	$Te_6–F_{26}$	1.860
$Hg_1–O_{34}$	2.111	$Te_6–F_{27}$	1.878
$Te_3–O_8$	1.778	$Te_4–F_{14}$	1.879
$Te_2–O_{12}$	1.777	$Te_4–F_{19}$	1.875
$Te_6–O_{22}$	1.808	$Te_4–F_{30}$	1.875
$Te_4–O_{25}$	1.779	$Te_4–F_{31}$	1.880
$Te_5–O_{34}$	1.806	$Te_4–F_{16}$	1.890
$Te_3–F_7$	1.881	$Te_5–F_{13}$	1.859
$Te_3–F_{18}$	1.875	$Te_5–F_{15}$	1.860
$Te_3–F_{35}$	1.880	$Te_5–F_{20}$	1.855
$Te_3–F_{33}$	1.8764	$Te_5–F_{32}$	1.868
$Te_3–F_{24}$	1.890	$Te_5–F_{29}$	1.878
$Te_2–F_{10}$	1.879		
$Te_2–F_{21}$	1.877		
$Te_2–F_{28}$	1.879		
$Te_2–F_{36}$	1.877		
$Te_2–F_{23}$	1.891		
Bond Angles (deg)			
$O_8–Hg_1–O_{12}$	122.1	$O_8–Te_3–F_{24}$	178.9
$O_8–Hg_1–O_{22}$	88.2	$O_8–Te_3–F_7$	96.4
$O_8–Hg_1–O_{25}$	115.8	$O_8–Te_3–F_{18}$	97.8
$O_8–Hg_1–O_{34}$	89.9	$O_8–Te_3–F_{33}$	97.8
$O_{12}–Hg_1–O_{22}$	91.8	$O_8–Te_3–F_{35}$	96.5
$O_{12}–Hg_1–O_{25}$	122.1	$O_{12}–Te_2–F_{23}$	180.0
$O_{12}–Hg_1–O_{34}$	91.8	$O_{12}–Te_2–F_{10}$	97.2
$O_{22}–Hg_1–O_{25}$	89.9	$O_{12}–Te_2–F_{36}$	97.2
$O_{22}–Hg_1–O_{34}$	176.4	$O_{12}–Te_2–F_{28}$	97.2
$O_{25}–Hg_1–O_{34}$	88.3	$O_{12}–Te_2–F_{21}$	97.2
$Hg_1–O_8–Te_3$	154.7	$O_{22}–Te_6–F_{27}$	176.9
$Hg_1–O_{12}–Te_2$	180.0	$O_{22}–Te_6–F_9$	95.6
$Hg_1–O_{22}–Te_6$	133.3	$O_{22}–Te_6–F_{11}$	92.5
$Hg_1–O_{25}–Te_4$	154.8	$O_{22}–Te_6–F_{26}$	96.1
$Hg_1–O_{34}–Te_5$	133.4	$O_{22}–Te_6–F_{17}$	98.0
		$O_{25}–Te_4–F_{16}$	178.9
$F_{24}–Te_3–F_7$	82.8	$O_{25}–Te_4–F_{14}$	96.5
$F_{24}–Te_3–F_{18}$	83.0	$O_{25}–Te_4–F_{19}$	97.8
$F_{24}–Te_3–F_{33}$	83.0	$O_{25}–Te_4–F_{30}$	97.8
$F_{24}–Te_3–F_{35}$	82.8	$O_{25}–Te_4–F_{31}$	96.4
$F_7–Te_3–F_{18}$	88.9	$O_{34}–Te_5–F_{29}$	176.9

Table S4.14. continued…

F_7–Te_3–F_{33}	165.8	O_{34}–Te_5–F_{13}	95.7
F_7–Te_3–F_{35}	88.8	O_{34}–Te_5–F_{32}	92.5
F_{18}–Te_3–F_{33}	89.8	O_{34}–Te_5–F_{15}	96.0
F_{18}–Te_3–F_{35}	165.7	O_{34}–Te_5–F_{20}	98.0
F_{33}–Te_3–F_{35}	89.0	F_{16}–Te_4–F_{14}	82.8
F_{23}–Te_2–F_{10}	82.8	F_{16}–Te_4–F_{31}	82.8
F_{23}–Te_2–F_{36}	82.8	F_{16}–Te_4–F_{30}	83.0
F_{23}–Te_2–F_{28}	82.8	F_{16}–Te_4–F_{19}	83.0
F_{23}–Te_2–F_{21}	82.8	F_{14}–Te_4–F_{31}	88.8
F_{10}–Te_2–F_{36}	89.3	F_{14}–Te_4–F_{30}	165.7
F_{10}–Te_2–F_{28}	165.6	F_{14}–Te_4–F_{19}	89.0
F_{10}–Te_2–F_{21}	88.8	F_{31}–Te_4–F_{30}	88.9
F_{36}–Te_2–F_{28}	88.8	F_{31}–Te_4–F_{19}	165.8
F_{36}–Te_2–F_{21}	165.5	F_{30}–Te_4–F_{19}	89.8
F_{28}–Te_2–F_{21}	89.4	F_{29}–Te_5–F_{13}	84.1
F_{27}–Te_6–F_9	84.1	F_{29}–Te_5–F_{32}	84.4
F_{27}–Te_6–F_{11}	84.4	F_{29}–Te_5–F_{15}	84.0
F_{27}–Te_6–F_{26}	84.0	F_{29}–Te_5–F_{20}	85.1
F_{27}–Te_6–F_{17}	85.1	F_{13}–Te_5–F_{32}	88.4
F_9–Te_6–F_{11}	88.4	F_{13}–Te_5–F_{15}	167.9
F_9–Te_6–F_{26}	168.0	F_{13}–Te_5–F_{20}	90.6
F_9–Te_6–F_{17}	90.6	F_{32}–Te_5–F_{15}	88.3
F_{11}–Te_6–F_{26}	88.3	F_{32}–Te_5–F_{20}	169.6
F_{11}–Te_6–F_{17}	169.6	F_{15}–Te_5–F_{20}	90.6
F_{26}–Te_6–F_{17}	90.6		
Dihedral Angles (deg)			
Te_5–O_{34}–Hg_1–O_{22}–Te_6	132.3		

[a] The atom labeling scheme corresponds to that used in Figure 4.11. Calculated at the PBE0/def6-TVZPP level of theory.

Table S4.15. Calculated Geometrical Parameters for $[Hg_2(OTeF_5)_6]^{2-}$ (D_2) [a]

Bond Lengths (Å)			
$Hg_1–O_{22}$	2.081	$Hg_2–O_{36}$	2.081
$Hg_1–O_{37}$	2.081	$Hg_2–O_{39}$	2.081
$Hg_1–O_{24}$	2.441	$Hg_2–O_{24}$	2.441
$Hg_1–O_{34}$	2.441	$Hg_2–O_{34}$	2.441
$Te_6–O_{22}$	1.821	$Te_3–O_{36}$	1.821
$Te_4–O_{37}$	1.821	$Te_8–O_{39}$	1.821
$Te_5–O_{24}$	1.810	$Te_3–F_{10}$	1.863
$Te_7–O_{34}$	1.810	$Te_3–F_{12}$	1.854
$Te_6–F_{20}$	1.853	$Te_3–F_{30}$	1.853
$Te_6–F_{21}$	1.854	$Te_3–F_{31}$	1.858
$Te_6–F_{32}$	1.863	$Te_3–F_{18}$	1.860
$Te_6–F_{35}$	1.858	$Te_8–F_{41}$	1.863
$Te_6–F_{23}$	1.860	$Te_8–F_{44}$	1.858
$Te_4–F_9$	1.863	$Te_8–F_{42}$	1.855
$Te_4–F_{14}$	1.854	$Te_8–F_{43}$	1.854
$Te_4–F_{16}$	1.853	$Te_8–F_{40}$	1.860
$Te_4–F_{28}$	1.858	$Te_7–F_{19}$	1.858
$Te_4–F_{17}$	1.860	$Te_7–F_{25}$	1.865
$Te_5–F_{11}$	1.858	$Te_7–F_{38}$	1.858
$Te_5–F_{27}$	1.865	$Te_7–F_{33}$	1.865
$Te_5–F_{15}$	1.858	$Te_7–F_{26}$	1.861
$Te_5–F_{13}$	1.865		
$Te_5–F_{29}$	1.861		
Bond Angles (deg)			
$O_{22}–Hg_1–O_{37}$	162.5	$O_{36}–Hg_2–O_{39}$	162.5
$O_{22}–Hg_1–O_{34}$	97.6	$O_{36}–Hg_2–O_{34}$	96.5
$O_{22}–Hg_1–O_{24}$	96.5	$O_{36}–Hg_2–O_{24}$	97.6
$O_{37}–Hg_1–O_{34}$	96.5	$O_{39}–Hg_2–O_{34}$	97.6
$O_{37}–Hg_1–O_{24}$	97.6	$O_{39}–Hg_2–O_{24}$	96.5
$O_{24}–Hg_1–O_{34}$	72.8	$O_{34}–Hg_2–O_{24}$	72.80
$Hg_1–O_{24}–Hg_2$	107.2	$Hg_1–O_{34}–Hg_2$	107.2
$Hg_1–O_{22}–Te_6$	124.9	$Hg_2–O_{36}–Te_3$	124.9
$Hg_1–O_{37}–Te_4$	124.9	$Hg_2–O_{39}–Te_8$	124.9
$Hg_1–O_{24}–Te_5$	126.4	$Hg_2–O_{24}–Te_5$	126.4
$Hg_1–O_{34}–Te_7$	126.4	$Hg_2–O_{34}–Te_7$	126.4
$O_{22}–Te_6–F_{20}$	92.9	$O_{36}–Te_3–F_{10}$	95.1
$O_{22}–Te_6–F_{21}$	94.3	$O_{36}–Te_3–F_{12}$	94.3
$O_{22}–Te_6–F_{32}$	95.1	$O_{36}–Te_3–F_{30}$	92.9
$O_{22}–Te_6–F_{35}$	95.0	$O_{36}–Te_3–F_{31}$	95.0
$O_{22}–Te_6–F_{23}$	178.9	$O_{36}–Te_3–F_{18}$	178.9
$O_{37}–Te_4–F_9$	95.1	$O_{39}–Te_8–F_{41}$	95.1
$O_{37}–Te_4–F_{14}$	94.3	$O_{39}–Te_8–F_{43}$	94.3
$O_{37}–Te_4–F_{16}$	92.9	$O_{39}–Te_8–F_{42}$	92.9

Table S4.15. continued…

O_{37}–Te_4–F_{28}	95.0	O_{39}–Te_8–F_{44}	95.0
O_{37}–Te_4–F_{17}	178.9	O_{39}–Te_8–F_{40}	178.9
O_{24}–Te_5–F_{11}	95.2	O_{34}–Te_7–F_{19}	95.2
O_{24}–Te_5–F_{27}	93.8	O_{34}–Te_7–F_{25}	93.8
O_{24}–Te_5–F_{15}	95.2	O_{34}–Te_7–F_{38}	95.2
O_{24}–Te_5–F_{13}	93.8	O_{34}–Te_7–F_{33}	93.8
O_{24}–Te_5–F_{29}	180.0	O_{34}–Te_7–F_{26}	180.0
F_{23}–Te_6–F_{20}	86.1	F_{18}–Te_3–F_{10}	86.0
F_{23}–Te_6–F_{35}	85.4	F_{18}–Te_3–F_{12}	85.4
F_{23}–Te_6–F_{32}	86.0	F_{18}–Te_3–F_{30}	86.1
F_{23}–Te_6–F_{21}	85.4	F_{18}–Te_3–F_{31}	85.4
F_{20}–Te_6–F_{35}	89.9	F_{10}–Te_3–F_{12}	89.9
F_{20}–Te_6–F_{32}	172.0	F_{10}–Te_3–F_{30}	172.0
F_{20}–Te_6–F_{21}	89.4	F_{10}–Te_3–F_{31}	89.5
F_{35}–Te_6–F_{32}	89.5	F_{12}–Te_3–F_{30}	89.4
F_{35}–Te_6–F_{21}	170.8	F_{12}–Te_3–F_{31}	170.8
F_{32}–Te_6–F_{21}	89.9	F_{30}–Te_3–F_{31}	89.9
F_{17}–Te_4–F_9	86.0	F_{40}–Te_8–F_{41}	86.0
F_{17}–Te_4–F_{14}	85.4	F_{40}–Te_8–F_{43}	85.4
F_{17}–Te_4–F_{16}	86.1	F_{40}–Te_8–F_{42}	86.1
F_{17}–Te_4–F_{28}	85.4	F_{40}–Te_8–F_{44}	85.4
F_9–Te_4–F_{14}	89.9	F_{41}–Te_8–F_{43}	89.9
F_9–Te_4–F_{16}	172.0	F_{41}–Te_8–F_{42}	172.0
F_9–Te_4–F_{28}	89.5	F_{41}–Te_8–F_{44}	89.5
F_{14}–Te_4–F_{16}	89.4	F_{43}–Te_8–F_{42}	89.4
F_{14}–Te_4–F_{28}	170.8	F_{43}–Te_8–F_{44}	170.8
F_{16}–Te_4–F_{28}	89.9	F_{42}–Te_8–F_{44}	89.9
F_{29}–Te_5–F_{11}	84.8	F_{26}–Te_7–F_{19}	84.8
F_{29}–Te_5–F_{13}	86.2	F_{26}–Te_7–F_{25}	86.2
F_{29}–Te_5–F_{15}	84.8	F_{26}–Te_7–F_{38}	84.8
F_{29}–Te_5–F_{27}	86.2	F_{26}–Te_7–F_{33}	86.2
F_{11}–Te_5–F_{13}	89.6	F_{19}–Te_7–F_{25}	89.7
F_{11}–Te_5–F_{15}	169.5	F_{19}–Te_7–F_{38}	169.5
F_{11}–Te_5–F_{27}	89.7	F_{19}–Te_7–F_{33}	89.6
F_{13}–Te_5–F_{15}	89.7	F_{25}–Te_7–F_{38}	89.6
F_{13}–Te_5–F_{27}	172.4	F_{25}–Te_7–F_{33}	172.4
F_{15}–Te_5–F_{27}	89.6	F_{38}–Te_7–F_{33}	89.7
Dihedral Angles (deg)			
Te_6–O_{22}–Hg_1–O_{37}–Te_4	12.1	Te_3–O_{36}–Hg_2–O_{39}–Te_8	12.1

[a] The atom labeling scheme corresponds to that used in Figure 4.12. Calculated at the PBE0/def2-TVZPP level of theory.

Table S4.16. Calculated Geometrical Parameters for the central mercury environment in $[Hg_3(OTeF_5)_8]^{2-}$ (C_1) [a]

Bond Lengths (Å)			
Central $[Hg(OTeF_5)_4]^{2-}$ Unit			
Hg_1–O_{16}	2.228	Te_4–O_{16}	1.824
Hg_1–O_{17}	2.238	Te_3–O_{17}	1.823
Hg_1–O_{31}	2.231	Te_{33}–O_{31}	1.824
Hg_1–O_{32}	2.241	Te_{39}–O_{32}	1.823
Hg_2---O_{31}	2.560	Te_{33}–F_{34}	1.852
Hg_2---O_{17}	2.558	Te_{33}–F_{35}	1.862
Hg_{45}---O_{31}	2.564	Te_{33}–F_{36}	1.853
Hg_{45}---O_{32}	2.554	Te_{33}–F_{38}	1.856
Te_4–F_7	1.853	Te_{33}–F_{37}	1.853
Te_4–F_9	1.866	Te_{39}–F_{40}	1.862
Te_4–F_{10}	1.852	Te_{39}–F_{42}	1.854
Te_4–F_{15}	1.856	Te_{39}–F_{44}	1.857
Te_4–F_{11}	1.853	Te_{39}–F_{43}	1.852
Te_3–F_6	1.862	Te_{39}–F_{41}	1.853
Te_3–F_{12}	1.852		
Te_3–F_{14}	1.857		
Te_3–F_{13}	1.854		
Te_3–F_8	1.853		
Terminal $Hg(OTeF_5)_2$ Units			
Hg_2–O_{24}	2.040	Hg_{45}–O_{47}	2.041
Hg_2---O_{31}	2.560	Hg_{45}---O_{32}	2.554
Te_{25}–O_{24}	1.829	Te_{49}–O_{47}	1.829
Te_{25}–F_{26}	1.846	Te_{49}–F_{50}	1.857
Te_{25}–F_{27}	1.864	Te_{49}–F_{51}	1.850
Te_{25}–F_{28}	1.852	Te_{49}–F_{52}	1.848
Te_{25}–F_{29}	1.855	Te_{49}–F_{53}	1.855
Te_{25}–F_{30}	1.854	Te_{49}–F_{54}	1.863
Hg_2–O_{23}	2.040	Hg_{45}–O_{46}	2.040
Hg_2---O_{17}	2.558	Hg_2---O_{16}	2.564
Te_5–O_{23}	1.830	Te_{48}–O_{46}	1.829
Te_5–F_{18}	1.859	Te_{48}–F_{55}	1.847
Te_5–F_{19}	1.849	Te_{48}–F_{56}	1.864
Te_5–F_{20}	1.860	Te_{48}–F_{57}	1.856
Te_5–F_{21}	1.855	Te_{48}–F_{58}	1.855
Te_5–F_{22}	1.849	Te_{48}–F_{59}	1.850
Bond Angles (deg)			
Central $[Hg(OTeF_5)_4]^{2-}$ Unit			
O_{16}–Hg_1–O_{17}	126.8	Hg_1–O_{16}–Te_4	127.6
O_{16}–Hg_1–O_{31}	128.7	Hg_1–O_{17}–Te_3	127.8

Table S4.16. continued…

O_{16}–Hg_1–O_{32}	77.8	Hg_1–O_{31}–Te_{33}	127.8
O_{17}–Hg_1–O_{31}	77.8	Hg_1–O_{32}–Te_{39}	128.0
O_{17}–Hg_1–O_{32}	127.0	O_{31}–Te_{33}–F_{34}	94.3
O_{31}–Hg_1–O_{32}	126.6	O_{31}–Te_{33}–F_{35}	91.6
O_{16}–Te_4–F_7	94.2	O_{31}–Te_{33}–F_{36}	94.2
O_{16}–Te_4–F_9	91.6	O_{31}–Te_{33}–F_{38}	93.8
O_{16}–Te_4–F_{10}	94.3	O_{31}–Te_{33}–F_{37}	178.7
O_{16}–Te_4–F_{15}	93.8	O_{32}–Te_{39}–F_{40}	91.7
O_{16}–Te_4–F_{11}	178.6	O_{32}–Te_{39}–F_{42}	94.3
O_{17}–Te_3–F_6	91.7	O_{32}–Te_{39}–F_{44}	93.8
O_{17}–Te_3–F_{12}	94.4	O_{32}–Te_{39}–F_{43}	94.4
O_{17}–Te_3–F_{14}	93.8	O_{32}–Te_{39}–F_{41}	178.7
O_{17}–Te_3–F_{13}	94.2	F_{37}–Te_{33}–F_{34}	85.8
O_{17}–Te_3–F_8	178.7	F_{37}–Te_{33}–F_{35}	87.0
F_{11}–Te_4–F_7	85.7	F_{37}–Te_{33}–F_{36}	85.7
F_{11}–Te_4–F_9	87.0	F_{37}–Te_{33}–F_{38}	87.5
F_{11}–Te_4–F_{10}	85.8	F_{34}–Te_{33}–F_{35}	89.7
F_{11}–Te_4–F_{15}	87.6	F_{34}–Te_{33}–F_{36}	171.5
F_7–Te_4–F_9	89.5	F_{34}–Te_{33}–F_{38}	89.9
F_7–Te_4–F_{10}	171.5	F_{35}–Te_{33}–F_{36}	89.6
F_7–Te_4–F_{15}	90.0	F_{35}–Te_{33}–F_{38}	174.5
F_9–Te_4–F_{10}	89.9	F_{36}–Te_{33}–F_{38}	89.9
F_9–Te_4–F_{15}	174.6	F_{41}–Te_{39}–F_{40}	87.0
F_{10}–Te_4–F_{15}	89.8	F_{41}–Te_{39}–F_{42}	85.6
F_8–Te_3–F_6	87.0	F_{41}–Te_{39}–F_{44}	87.5
F_8–Te_3–F_{12}	85.7	F_{41}–Te_{39}–F_{43}	85.7
F_8–Te_3–F_{14}	87.5	F_{40}–Te_{39}–F_{42}	89.5
F_8–Te_3–F_{13}	85.7	F_{40}–Te_{39}–F_{44}	174.4
F_6–Te_3–F_{12}	89.8	F_{40}–Te_{39}–F_{43}	89.8
F_6–Te_3–F_{14}	174.5	F_{42}–Te_{39}–F_{44}	89.9
F_6–Te_3–F_{13}	89.5	F_{42}–Te_{39}–F_{43}	171.4
F_{12}–Te_3–F_{14}	89.9	F_{44}–Te_{39}–F_{43}	89.9
F_{12}–Te_3–F_{13}	171.4		
F_{14}–Te_3–F_{13}	89.9		
	Terminal $Hg(OTeF_5)_2$ Units		
O_{23}–Hg_2–O_{24}	172.2	O_{46}–Hg_{45}–O_{47}	172.0
O_{23}–Hg_2---O_{31}	92.4	O_{46}–Hg_{45}---O_{16}	90.6
O_{23}–Hg_2---O_{17}	96.3	O_{46}–Hg_{45}---O_{32}	93.9
O_{24}–Hg_2---O_{31}	94.2	O_{47}–Hg_{45}---O_{16}	96.1
O_{24}–Hg_2---O_{17}	90.1	O_{47}–Hg_{45}---O_{32}	92.5
O_{17}---Hg_2---O_{31}	66.5	O_{16}---Hg_{45}---O_{32}	66.5
O_{24}–Te_{25}–F_{26}	92.2	O_{47}–Te_{49}–F_{50}	94.2
O_{24}–Te_{25}–F_{27}	94.5	O_{47}–Te_{49}–F_{51}	93.8
O_{24}–Te_{25}–F_{28}	94.1	O_{47}–Te_{49}–F_{52}	92.6

Table S4.16. continued…

O_{24}–Te_{25}–F_{29}	179.0	O_{47}–Te_{49}–F_{53}	179.3
O_{24}–Te_{25}–F_{30}	94.3	O_{47}–Te_{49}–F_{54}	94.4
F_{26}–Te_{25}–F_{27}	173.3	F_{50}–Te_{49}–F_{51}	171.9
F_{26}–Te_{25}–F_{28}	90.0	F_{50}–Te_{49}–F_{52}	90.3
F_{26}–Te_{25}–F_{29}	86.8	F_{50}–Te_{49}–F_{53}	85.8
F_{26}–Te_{25}–F_{30}	90.2	F_{50}–Te_{49}–F_{54}	89.2
F_{27}–Te_{25}–F_{28}	89.5	F_{51}–Te_{49}–F_{52}	89.6
F_{27}–Te_{25}–F_{29}	86.5	F_{51}–Te_{49}–F_{53}	86.1
F_{27}–Te_{25}–F_{30}	89.3	F_{51}–Te_{49}–F_{54}	89.9
F_{28}–Te_{25}–F_{29}	85.9	F_{52}–Te_{49}–F_{53}	86.7
F_{28}–Te_{25}–F_{30}	171.6	F_{52}–Te_{49}–F_{54}	173.0
F_{29}–Te_{25}–F_{30}	85.7	F_{53}–Te_{49}–F_{54}	86.3
O_{23}–Te_{25}–F_{18}	94.2	O_{46}–Te_{48}–F_{55}	92.0
O_{23}–Te_{25}–F_{19}	93.2	O_{46}–Te_{48}–F_{56}	94.6
O_{23}–Te_{25}–F_{20}	94.3	O_{46}–Te_{48}–F_{57}	94.3
O_{23}–Te_{25}–F_{21}	179.4	O_{46}–Te_{48}–F_{58}	178.9
O_{23}–Te_{25}–F_{22}	93.0	O_{46}–Te_{48}–F_{59}	94.2
F_{18}–Te_{25}–F_{19}	172.6	F_{55}–Te_{48}–F_{56}	173.4
F_{18}–Te_{25}–F_{20}	89.3	F_{55}–Te_{48}–F_{57}	89.9
F_{18}–Te_{25}–F_{21}	86.2	F_{55}–Te_{48}–F_{58}	86.9
F_{18}–Te_{25}–F_{22}	90.2	F_{55}–Te_{48}–F_{59}	90.1
F_{19}–Te_{25}–F_{20}	90.3	F_{56}–Te_{48}–F_{57}	89.2
F_{19}–Te_{25}–F_{21}	86.4	F_{56}–Te_{48}–F_{58}	86.5
F_{19}–Te_{25}–F_{22}	89.4	F_{56}–Te_{48}–F_{59}	89.7
F_{20}–Te_{25}–F_{21}	86.2	F_{57}–Te_{48}–F_{58}	85.7
F_{20}–Te_{25}–F_{22}	172.8	F_{57}–Te_{48}–F_{59}	171.5
F_{21}–Te_{25}–F_{22}	86.5	F_{58}–Te_{48}–F_{59}	85.9
Dihedral Angles (deg)			
Te_5–O_{23}–Hg_2–O_{24}–Te_{25}	2.2	Te_{48}–O_{46}–Hg_{45}–O_{47}–Te_{49}	15.0

[a] The atom labeling scheme corresponds to that used in Figure 4.13. Calculated at the PBE0/def2-TVZPP level of theory.

Table S4.17. Calculated Natural Atomic Charges, Mayer Bond Orders, and Mayer Natural Atomic Orbital Valencies (PBE0/def2-TZVPP) for $[Hg(OTeF_5)_4]^{2-}$ [a]

Atom	Charges	Valence	Bond	Bond Order
Hg_1	1.6889	0.4554	Hg_1–O_8	0.1153
			Hg_1–O_{14}	0.1153
O_8	–1.23456	0.8057	Hg_1–O_{18}	0.1153
Te_5	3.41887	3.1684	Hg_1–O_{28}	0.1153
F_6	–0.62023	0.4179		
F_9	–0.62411	0.4132	Te_5–O_8	0.7838
F_{15}	–0.62147	0.4164	Te_4–O_{14}	0.7838
F_{12}	–0.61941	0.4215	Te_2–O_{18}	0.7838
F_7	–0.62131	0.4070	Te_3–O_{28}	0.7838
O_{14}	–1.23456	0.8057	Te_5–F_6	0.4805
Te_4	3.41887	3.1684	Te_5–F_9	0.4773
F_{17}	–0.62147	0.4164	Te_5–F_{15}	0.4793
F_{19}	–0.62411	0.4132	Te_5–F_{12}	0.4805
F_{21}	–0.62023	0.4179	Te_5–F_7	0.4727
F_{22}	–0.61941	0.4215		
F_{23}	–0.62131	0.4070	Te_4–F_{17}	0.4793
			Te_4–F_{19}	0.4773
O_{18}	–1.23456	0.8057	Te_4–F_{21}	0.4805
Te_2	3.41887	3.1684	Te_4–F_{22}	0.4805
F_{10}	–0.62023	0.4179	Te_4–F_{23}	0.4727
F_{11}	–0.61941	0.4215		
F_{13}	–0.62411	0.4132	Te_2–F_{10}	0.4805
F_{20}	–0.62147	0.4164	Te_2–F_{11}	0.4805
F_{16}	–0.62131	0.4070	Te_2–F_{13}	0.4773
			Te_2–F_{20}	0.4793
O_{28}	–1.23456	0.8057	Te_2–F_{16}	0.4727
Te_3	3.41887	3.1684		
F_{24}	–0.62023	0.4179	Te_3–F_{24}	0.4805
F_{25}	–0.62411	0.4132	Te_3–F_{25}	0.4773
F_{26}	–0.61941	0.4215	Te_3–F_{26}	0.4805
F_{27}	–0.62147	0.4164	Te_3–F_{27}	0.4793
F_{29}	–0.62131	0.4070	Te_3–F_{29}	0.4727

[a] The atom labeling scheme corresponds to that used in Figure 4.10. Calculated at the PBE0/def2-TVZPP level of theory.

Table S4.18. Calculated Natural Atomic Charges, Mayer Bond Orders, and Mayer Natural Atomic Orbital Valencies (PBE0/def2-TZVPP) for $[Hg(OTeF_5)_5]^{3-}$ [a]

Atom	Charges	Valence	Bond	Bond Order
Hg_1	1.67488	0.4440	Hg_1–O_8	0.0360
			Hg_1–O_{12}	0.0343
O_8	–1.20286	0.7852	Hg_1–O_{22}	0.1704
Te_3	3.39793	3.1594	Hg_1–O_{25}	0.0360
F_7	–0.63756	0.4017	Hg_1–O_{34}	0.1701
F_{18}	–0.63104	0.4084		
F_{33}	–0.63159	0.4081	Te_3–O_8	0.8411
F_{35}	–0.63640	0.4026	Te_2–O_{12}	0.8458
F_{24}	–0.63897	0.3861	Te_6–O_{22}	0.7655
			Te_4–O_{25}	0.8409
O_{12}	–1.21006	0.7918	Te_5–O_{34}	0.7666
Te_2	3.39880	3.1599		
F_{10}	–0.63503	0.4046	Te_3–F_7	0.4636
F_{21}	–0.63327	0.4066	Te_3–F_{18}	0.4693
F_{28}	–0.63502	0.4047	Te_3–F_{33}	0.4689
F_{36}	–0.63326	0.4065	Te_3–F_{35}	0.4645
F_{23}	–0.64030	0.3849	Te_3–F_{24}	0.4527
O_{22}	–1.20179	0.8434	Te_2–F_{10}	0.4652
Te_6	3.42940	3.1599	Te_2–F_{21}	0.4667
F_9	–0.61351	0.4225	Te_2–F_{28}	0.4652
F_{11}	–0.62638	0.4109	Te_2–F_{36}	0.4668
F_{26}	–0.61447	0.4207	Te_2–F_{23}	0.4504
F_{17}	–0.60585	0.4329		
F_{27}	–0.63012	0.3994	Te_6–F_9	0.4857
			Te_6–F_{11}	0.4748
O_{25}	–1.20286	0.7852	Te_6–F_{26}	0.4845
Te_4	3.39791	3.159	Te_6–F_{17}	0.4920
F_{14}	–0.63639	0.4025	Te_6–F_{27}	0.4652
F_{19}	–0.63158	0.4085		
F_{30}	–0.63109	0.4081	Te_4–F_{14}	0.4645
F_{31}	–0.63752	0.4018	Te_4–F_{19}	0.4690
F_{16}	–0.63903	0.386	Te_4–F_{30}	0.4692
			Te_4–F_{31}	0.4635
O_{34}	–1.20218	0.8439	Te_4–F_{16}	0.4527
Te_5	3.42994	3.1612		
F_{13}	–0.61353	0.4226	Te_5–F_{13}	0.4859
F_{20}	–0.60589	0.4329	Te_5–F_{20}	0.4919
F_{15}	–0.61466	0.4208	Te_5–F_{15}	0.4846
F_{32}	–0.62652	0.4108	Te_5–F_{32}	0.4747
F_{29}	–0.63013	0.3993	Te_5–F_{29}	0.4654

[a] The atom labeling scheme corresponds to that used in Figure 4.11. Calculated at the PBE0/def2-TVZPP level of theory.

Table S4.19. Calculated Natural Atomic Charges, Mayer Bond Orders, and Mayer Natural Atomic Orbital Valencies (PBE0/def2-TZVPP) for $[Hg_2(OTeF_5)_6]^{2-}$ [a]

Atom	Charges	Valence	Bond	Bond Order
Hg_1	1.59074	0.4098	Hg_1–O_{22}	0.1830
Hg_2	1.59074	0.4098	Hg_1–O_{37}	0.1830
			Hg_1–O_{24}	0.0200
O_{24}	–1.29717	0.6921	Hg_1–O_{34}	0.0200
Te_5	3.43656	3.1667		
F_{11}	–0.61167	0.4256	Hg_2–O_{36}	0.1830
F_{13}	–0.62116	0.4243	Hg_2–O_{39}	0.1830
F_{15}	–0.61167	0.4256	Hg_2–O_{24}	0.0200
F_{27}	–0.62116	0.4243	Hg_2–O_{34}	0.0200
F_{29}	–0.61067	0.4190		
			Te_5–O_{24}	0.7542
O_{34}	–1.29717	0.6921	Te_5–F_{11}	0.4885
Te_7	3.43656	3.1667	Te_5–F_{13}	0.4806
F_{19}	–0.61167	0.4256	Te_5–F_{15}	0.4885
F_{25}	–0.62116	0.4243	Te_5–F_{27}	0.4806
F_{38}	–0.61167	0.4256	Te_5–F_{29}	0.4829
F_{33}	–0.62116	0.4243		
F_{26}	–0.61067	0.4190	Te_7–O_{34}	0.7542
			Te_7–F_{19}	0.4885
O_{22}	–1.19695	0.8232	Te_7–F_{25}	0.4806
Te_6	3.42594	3.1671	Te_7–F_{38}	0.4885
F_{20}	–0.60800	0.4275	Te_7–F_{33}	0.4806
F_{21}	–0.60819	0.4259	Te_7–F_{26}	0.4829
F_{32}	–0.61694	0.4232		
F_{35}	–0.61224	0.4230	Te_6–O_{22}	0.7405
F_{23}	–0.61052	0.4178	Te_6–F_{20}	0.4912
			Te_6–F_{21}	0.4905
O_{37}	–1.19695	0.8232	Te_6–F_{32}	0.4823
Te_4	3.42594	3.1671	Te_6–F_{35}	0.4869
F_9	–0.61694	0.4232	Te_6–F_{23}	0.4838
F_{14}	–0.60819	0.4259		
F_{16}	–0.60800	0.4275	Te_4–O_{37}	0.7405
F_{28}	–0.61224	0.4230	Te_4–F_9	0.4823
F_{17}	–0.61052	0.4178	Te_4–F_{14}	0.4905
			Te_4–F_{16}	0.4912
O_{36}	–1.19695	0.8232	Te_4–F_{28}	0.4869
Te_3	3.42594	3.1671	Te_4–F_{17}	0.4838
F_{10}	–0.61694	0.4232		
F_{12}	–0.60819	0.4259	Te_3–O_{36}	0.7405
F_{30}	–0.60800	0.4275	Te_3–F_{10}	0.4823
F_{31}	–0.61224	0.4230	Te_3–F_{12}	0.4905
F_{18}	–0.61052	0.4178	Te_3–F_{30}	0.4912
			Te_3–F_{31}	0.4869
O_{39}	–1.19695	0.8232	Te_3–F_{18}	0.4838
Te_8	3.42594	3.1671		
F_{41}	–0.61694	0.4232	Te_8–O_{39}	0.7405
F_{42}	–0.60800	0.4275	Te_8–F_{41}	0.4838

Table S4.19. continued…

F_{43}	–0.60819	0.4259	Te_8–F_{42}	0.4823
F_{44}	–0.61224	0.4230	Te_8–F_{43}	0.4912
F_{40}	–0.61052	0.4178	Te_8–F_{44}	0.4905
			Te_8–F_{40}	0.4869

[a] The atom labeling scheme corresponds to that used in Figure 4.12. Calculated at the PBE0/def2-TVZPP level of theory.

Table S4.20. Calculated Natural Atomic Charges, Mayer Bond Orders, and Mayer Natural Atomic Orbital Valencies (PBE0/def2-TZVPP) for $Hg(OTeF_5)_2$ [a]

Atom	Charges	Valence	Bond	Bond Order
Hg_1	1.42218	0.6020	Hg_1–O_2	0.2909
O_2	–1.17587	0.8634	Hg_1–O_9	0.2909
Te_3	3.43706	3.1786	Te_3–O_2	0.6724
F_5	–0.58304	0.4482	Te_{10}–O_9	0.6724
F_6	–0.62141	0.4256	Te_3–F_5	0.5122
F_7	–0.59601	0.4332	Te_3–F_6	0.4785
F_8	–0.59332	0.4351	Te_3–F_7	0.5011
F_4	–0.57849	0.4487	Te_3–F_8	0.5031
			Te_3–F_4	0.5133
O_9	–1.17587	0.8634	Te_{10}–F_{12}	0.5133
Te_{10}	3.43706	3.1786	Te_{10}–F_{13}	0.4785
F_{12}	–0.57849	0.4487	Te_{10}–F_{14}	0.5011
F_{13}	–0.62141	0.4256	Te_{10}–F_{15}	0.5031
F_{14}	–0.59601	0.4332	Te_{10}–F_{11}	0.5122
F_{15}	–0.59332	0.4351		
F_{11}	–0.58304	0.4482		

[a] See Chapter 4, reference 26.

Table S4.21. Calculated Natural Atomic Charges, Mayer Bond Orders, and Mayer Natural Atomic Orbital Valencies (PBE0/def2-TZVPP) for $[OTeF_5]^-$ [a]

Atom	Charges	Valence	Bond	Bond Order
Te	3.34408	3.1341	Te–O	0.8656
O	–1.12737	0.7814	Te–F_1	0.4587
F_1	–0.62902	0.3930	Te–F_2	0.4525
F_2	–0.64692	0.3954	Te–F_3	0.4525
F_3	–0.64692	0.3954	Te–F_4	0.4525
F_4	–0.64692	0.3954	Te–F_5	0.4525
F_5	–0.64692	0.3954		

[a] The atom labeling scheme corresponds to that used in Figure S4.10. Calculated at the PBE0/def2-TVZPP level of theory.

APPENDIX C

Chapter 5 Supporting Information

Syntheses and Characterization of Homoleptic Solvent Complexes of Mercury using the Weakly Coordinating $[Sb(OTeF_5)_6]^-$ Anion

LIST OF FIGURES

LIST OF TABLES

Table S5.1. Experimental Geometrical Parameters of the $[Sb(OTeF_5)_6]^-$ Anions in $[Hg(SO_2ClF)_6][Sb(OTeF_5)_6]_2$ [a]

Bond Lengths (Å)			
$Sb_1–O_3$	1.956(3)	$Sb_1–O_4$	1.955(3)
$O_3–Te_1$	1.846(3)	$O_4–Te_2$	1.847(3)
$Te_1–F_2$	1.833(3)	$Te_2–F_7$	1.833(3)
$Te_1–F_3$	1.835(3)	$Te_2–F_8$	1.825(3)
$Te_1–F_4$	1.823(3)	$Te_2–F_9$	1.824(3)
$Te_1–F_5$	1.829(3)	$Te_2–F_{10}$	1.826(3)
$Te_1–F_6$	1.838(3)	$Te_2–F_{11}$	1.840(3)
Cl_1---F_{2C}	3.017(4)	O_2---F_{5E}	2.953(5)
Cl_1---F_{3C}	3.190(3)	O_2---F_{7E}	2.937(7)
Cl_1---F_{11D}	2.901(4)	F_1---F_{8E}	2.907(5)
		F_1---F_{5E}	2.883(6)
Bond Angles (deg)			
$O_3–Sb_1–O_4$	89.5(1)	$O_3–Sb_1–O_{3B}$	90.6(1)
$O_3–Sb_1–O_{4A}$	89.5(1)	$O_4–Sb_1–O_{4A}$	90.5(1)
$O_3–Sb_1–O_{4B}$	179.9(2)	$O_4–Sb_1–O_{4B}$	90.5(1)
$O_3–Sb_1–O_{3A}$	90.6(1)		
$Sb_1–O_3–Te_1$	138.1(2)	$Sb_1–O_4–Te_2$	137.9(2)
$F_2–Te_1–O_3$	90.5(1)	$F_7–Te_2–O_4$	94.3(1)
$F_3–Te_1–O_3$	93.5(1)	$F_8–Te_2–O_4$	90.6(2)
$F_4–Te_1–O_3$	94.1(1)	$F_9–Te_2–O_4$	91.3(1)
$F_5–Te_1–O_3$	92.1(1)	$F_{10}–Te_2–O_4$	93.8(1)
$F_6–Te_1–O_3$	178.2(1)	$F_{11}–Te_2–O_4$	178.2(1)
$F_2–Te_1–F_6$	87.8(1)	$F_7–Te_2–F_{10}$	89.6(2)
$F_2–Te_1–F_5$	88.7(1)	$F_7–Te_2–F_{11}$	87.3(1)
$F_2–Te_1–F_3$	89.4(1)	$F_7–Te_2–F_9$	91.0(2)
$F_3–Te_1–F_6$	87.1(1)	$F_7–Te_2–F_8$	175.0(1)
$F_3–Te_1–F_5$	174.2(1)	$F_8–Te_2–F_9$	88.6(1)
$F_4–Te_1–F_2$	175.3(1)	$F_8–Te_2–F_{10}$	90.2(1)
$F_4–Te_1–F_6$	87.6(1)	$F_8–Te_2–F_{11}$	87.8(1)
$F_4–Te_1–F_5$	90.5(1)	$F_9–Te_2–F_{11}$	87.8(1)
$F_4–Te_1–F_3$	90.8(1)	$F_9–Te_2–F_{10}$	174.8(1)
$F_5–Te_1–F_6$	87.3(1)	$F_{10}–Te_2–F_{11}$	87.1(1)

[a] The atom labeling scheme corresponds to that used in Figure S5.1.

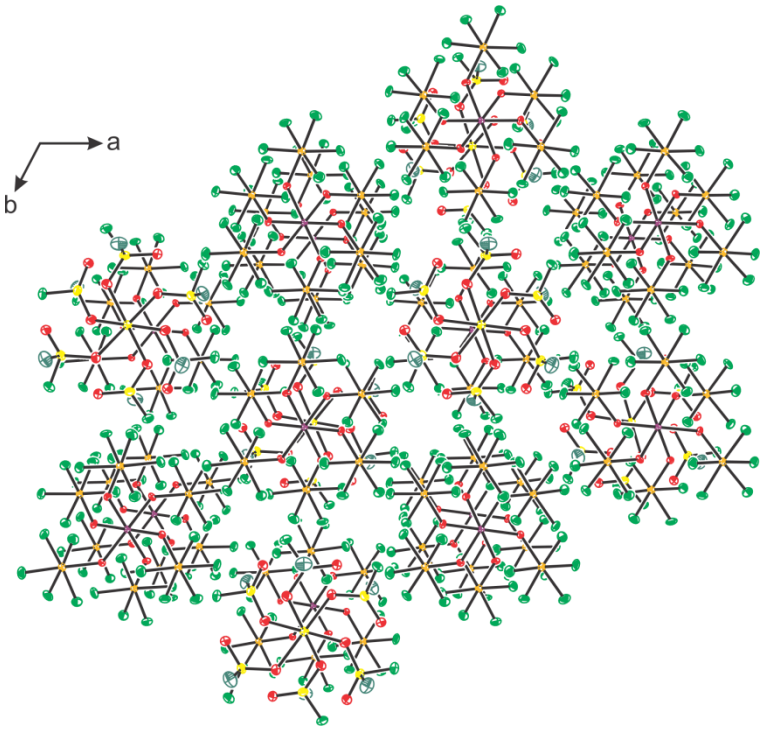

Figure S5.1. Crystal packing diagram for $[Hg(SO_2ClF)_6][Sb(OTeF_5)_6]_2$ viewed down the c-axis.

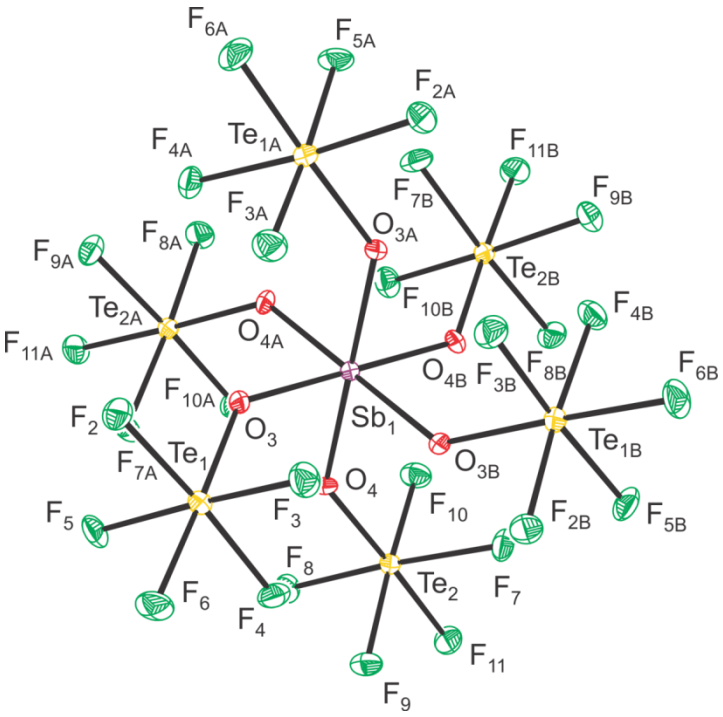

Figure S5.2. The $[Sb(OTeF_5)_6]^-$ anion in the single-crystal X-ray structure of $[Hg(SO_2ClF)_6][Sb(OTeF_5)_6]_2$ with thermal ellipsoids shown at the 50% probability level.

Table S5.2. Experimental Geometrical Parameters of the $[Sb(OTeF_5)_6]^-$ Anions and Co-crystallized SO_2ClF molecules in $[Hg(NCCH_2CH_3)_5][Sb(OTeF_5)_6]_2 \cdot 2SO_2ClF$

Bond Lengths (Å)			
$(NCCH_2CH_3)$---(SO_2ClF)		**(SO_2ClF)---$[Sb(OTeF_{5)6}]^-$**	
C_5---O_{16B}	2.969(6)	F_{61}---F_{52}	2.916(6)
C_4---O_{16B}	3.008(6)	F_{61}---F_{57}	2.818(6)
C_5---O_{15}	3.070(6)	Cl_1---F_{30}	2.897(4)
C---O_{15B}	2.966(6)	Cl_2---F_{56}	2.580(6)
		O_{13}---F_{47}	2.950(7)
$(NCCH_2CH_3)$---$[Sb(OTeF_{5)6}]^-$			
C---F	≥ 2.964(5)		
C(H)---F	≥ 3.165(6)		
$C(H_3)$---F	≥ 3.081(9)		
		$[Sb(OTeF_5)_6]^-$	
Sb_1–O_1	1.959(3)	Te_1–F_1	1.835(2)
Sb_1–O_2	1.957(3)	Te_1–F_2	1.830(3)
Sb_1–O_3	1.961(3)	Te_1–F_3	1.832(3)
Sb_1–O_4	1.958(3)	Te_1–F_4	1.839(3)
Sb_1–O_5	1.955(3)	Te_1–F_5	1.819(3)
Sb_1–O_6	1.956(3)		
		Te_2–F_6	1.835(3)
Sb_2–O_7	1.964(3)	Te_2–F_7	1.830(2)
Sb_2–O_8	1.958(3)	Te_2–F_8	1.836(3)
Sb_2–O_9	1.960(3)	Te_2–F_9	1.827(3)
		Te_2–F_{10}	1.832(2)
O_1–Te_1	1.841(2)		
O_2–Te_2	1.849(3)	Te_3–F_{11}	1.835(3)
O_3–Te_3	1.843(3)	Te_3–F_{12}	1.828(4)
O_4–Te_4	1.844(3)	Te_3–F_{13}	1.832(3)
O_5–Te_5	1.851(2)	Te_3–F_{14}	1.819(3)
O_6–Te_6	1.849(3)	Te_3–F_{15}	1.831(4)
O_7–Te_7	1.844(3)		
O_8–Te_8	1.847(3)	Te_4–F_{16}	1.833(2)
O_9–Te_9	1.846(2)	Te_4–F_{17}	1.827(2)
$O_{10}Te_{10}$	1.843(3)	Te_4–F_{18}	1.833(3)
O_{11}–Te_{11}	1.870(6)	Te_4–F_{19}	1.831(3)
O_{12}–Te_{12}	1.840(6)	Te_4–F_{20}	1.832(3)

Table S5.2. continued…

Te_5–F_{21}	1.823(3)	Te_7–F_{31}	1.832(3)
Te_5–F_{22}	1.836(2)	Te_7–F_{32}	1.835(3)
Te_5–F_{23}	1.830(3)	Te_7–F_{33}	1.835(2)
Te_5–F_{24}	1.833(3)	Te_7–F_{34}	1.830(3)
Te_5–F_{25}	1.829(3)	Te_7–F_{35}	1.830(2)
Te_6–F_{26}	1.825(3)	Te_8–F_{36}	1.826(2)
Te_6–F_{27}	1.826(3)	Te_8–F_{37}	1.831(3)
Te_6–F_{28}	1.830(3)	Te_8–F_{38}	1.827(3)
Te_6–F_{29}	1.827(4)	Te_8–F_{39}	1.837(3)
Te_6–F_{30}	1.838(4)	Te_8–F_{40}	1.831(2)
		Te_9–F_{41}	1.831(3)
		Te_9–F_{42}	1.832(3)
		Te_9–F_{43}	1.833(2)
		Te_9–F_{44}	1.836(2)
		Te_9–F_{45}	1.831(3)
	Positionally Disordered Anion		
Sb_3–O_{10}	1.960(3)	Te_{10}–F_{47B}	1.671(12)
Sb_3–O_{11}	1.956(3)	Te_{10}–F_{48}	1.809(6)
Sb_3–O_{11B}	1.941(3)	Te_{10}–F_{48B}	2.074(11)
Sb_3–O_{12}	1.956(3)	Te_{10}–F_{49}	1.720(6)
Sb_3–O_{12B}	1.949(3)	Te_{10}–F_{49B}	2.018(12)
		Te_{10}–F_{50}	1.858(5)
Te_{11}–F_{51}	1.784(4)	Te_{10}–F_{50B}	1.833(12)
Te_{11}–F_{51B}	1.939(10)		
Te_{11}–F_{52}	1.877(4)	Te_{12}–F_{56}	1.867(5)
Te_{11}–F_{52B}	1.734(10)	Te_{12}–F_{56B}	1.761(10)
Te_{11}–F_{53}	1.834(7)	Te_{12}–F_{57}	1.793(5)
Te_{11}–F_{53B}	1.826(17)	Te_{12}–F_{57B}	1.914(10)
Te_{11}–F_{54}	1.833(7)	Te_{12}–F_{58}	1.880(7)
Te_{11}–F_{54B}	1.829(14)	Te_{12}–F_{58B}	1.747(13)
Te_{11}–F_{55}	1.825(5)	Te_{12}–F_{59}	1.805(9)
Te_{11}–F_{55B}	1.846(11)	Te_{12}–F_{59B}	1.896(18)
Te_{10}–F_{46}	1.930(6)	Te_{12}–F_{60}	1.840(4)
Te_{10}–F_{46B}	1.637(11)	Te_{12}–F_{60B}	1.798(10)
Te_{10}–F_{47}	1.866(6)		

Table S5.2. continued…

		SO_2ClF	
$S_1–O_{13}$	1.403(4)	$S_1–Cl_1$	1.956(2)
$S_1–O_{14}$	1.387(5)	$S_1–F_{61}$	1.544(4)
		Positionally Disordered SO_2ClF	
$S_2–O_{15}$	1.473(13)	$S_2–O_{15B}$	1.49(4)
$S_2–O_{16}$	1.515(17)	$S_2–O_{16B}$	1.38(3)
$S_2–Cl_2$	1.780(14)	$S_2–Cl_{2B}$	1.86(2)
$S_2–F_{62}$	1.593(12)	$S_2–F_{62B}$	1.58(3)
Bond Angles (deg)			
		$[Sb(OTeF_5)_6]^-$	
$O_1–Sb_1–O_2$	87.9(1)	$O_7–Sb_2–O_8$	90.9(1)
$O_1–Sb_1–O_3$	90.5(1)	$O_7–Sb_2–O_9$	89.3(1)
$O_1–Sb_1–O_4$	89.8(1)	$O_7–Sb_2–O_7$	180.0
$O_1–Sb_1–O_5$	179.3(1)	$O_7–Sb_2–O_8$	89.1(1)
$O_1–Sb_1–O_6$	90.3(1)	$O_7–Sb_2–O_9$	90.7(1)
$O_2–Sb_1–O_3$	178.3(1)	$O_8–Sb_2–O_9$	88.3(1)
$O_2–Sb_1–O_4$	91.3(1)	$O_8–Sb_2–O_7$	89.1(1)
$O_2–Sb_1–O_5$	92.2(1)	$O_8–Sb_2–O_8$	180(1)
$O_2–Sb_1–O_6$	89.6(1)	$O_8–Sb_2–O_9$	91.7(1)
$O_3–Sb_1–O_4$	88.0(1)	$O_9–Sb_2–O_7$	90.7(1)
$O_3–Sb_1–O_5$	89.5(1)	$O_9–Sb_2–O_8$	91.7(1)
$O_3–Sb_1–O_6$	91.0(1)	$O_9–Sb_2–O_9$	180.0
$O_4–Sb_1–O_5$	90.9(1)		
$O_4–Sb_1–O_6$	179.0(1)		
$O_5–Sb_1–O_6$	89.0(1)		
$Sb_1–O_1–Te_1$	138.2(2)	$Sb_2–O_7–Te_7$	138.8(1)
$Sb_1–O_2–Te_2$	139.6(2)	$Sb_2–O_8–Te_8$	139.0(1)
$Sb_1–O_3–Te_3$	139.8(2)	$Sb_2–O_9–Te_9$	137.5(1)
$Sb_1–O_4–Te_4$	138.9(2)		
$Sb_1–O_5–Te_5$	138.2(2)		
$Sb_1–O_6–Te_6$	137.6(2)		
$O_1–Te_1–F_1$	176.0(1)	$O_6–Te_6–F_{26}$	178.1(1)
$O_1–Te_1–F_2$	96.0(1)	$O_6–Te_6–F_{27}$	90.7(1)
$O_1–Te_1–F_3$	88.9(1)	$O_6–Te_6–F_{28}$	93.2(1)
$O_1–Te_1–F_4$	92.5(1)	$O_6–Te_6–F_{29}$	90.4(1)
$O_1–Te_1–F_5$	92.6(1)	$O_6–Te_6–F_{30}$	94.2(1)
$F_1–Te_1–F_2$	87.9(1)	$F_{26}–Te_6–F_{27}$	88.3(2)

Table S5.2. continued…

F_1–Te_1–F_3	87.2(1)	F_{26}–Te_6–F_{28}	87.8(1)
F_1–Te_1–F_4	86.9(1)	F_{26}–Te_6–F_{29}	88.0(1)
F_1–Te_1–F_5	88.0(1)	F_{26}–Te_6–F_{30}	87.4(2)
F_2–Te_1–F_3	175.1(1)	F_{27}–Te_6–F_{28}	176.0(1)
F_2–Te_1–F_4	89.4(1)	F_{27}–Te_6–F_{29}	90.3(1)
F_2–Te_1–F_5	90.3(1)	F_{27}–Te_6–F_{30}	90.4(2)
F_3–Te_1–F_4	89.7(1)	F_{28}–Te_6–F_{29}	89.0(1)
F_3–Te_1–F_5	90.2(2)	F_{28}–Te_6–F_{30}	89.9(1)
F_4–Te_1–F_5	174.9(2)	F_{29}–Te_6–F_{30}	175.3(2)
O_2–Te_2–F_6	178.1(1)	O_7–Te_7–F_{31}	91.4(1)
O_2–Te_2–F_7	93.4(1)	O_7–Te_7–F_{32}	178.1(1)
O_2–Te_2–F_8	93.8(1)	O_7–Te_7–F_{33}	90.3(1)
O_2–Te_2–F_9	90.5(1)	O_7–Te_7–F_{34}	93.8(1)
O_2–Te_2–F_{10}	91.1(1)	O_7–Te_7–F_{35}	94.4(1)
F_6–Te_2–F_7	87.9(1)	F_{31}–Te_7–F_{32}	87.6(1)
F_6–Te_2–F_8	87.6(1)	F_{31}–Te_7–F_{33}	89.2(1)
F_6–Te_2–F_9	88.1(1)	F_{31}–Te_7–F_{34}	174.8(1)
F_6–Te_2–F_{10}	87.6(1)	F_{31}–Te_7–F_{35}	89.9(1)
F_7–Te_2–F_8	89.9(1)	F_{32}–Te_7–F_{33}	88.1(1)
F_7–Te_2–F_9	91.3(1)	F_{32}–Te_7–F_{34}	87.2(1)
F_7–Te_2–F_{10}	175.5(1)	F_{32}–Te_7–F_{35}	87.3(1)
F_8–Te_2–F_9	175.5(1)	F_{33}–Te_7–F_{34}	90.2(1)
F_8–Te_2–F_{10}	89.4(1)	F_{33}–Te_7–F_{35}	175.3(1)
F_9–Te_2–F_{10}	89.1(1)	F_{34}–Te_7–F_{35}	90.2(1)
O_3–Te_3–F_{11}	177.8(1)	O_8–Te_8–F_{36}	91.6(1)
O_3–Te_3–F_{12}	91.9(1)	O_8–Te_8–F_{37}	178.5(1)
O_3–Te_3–F_{13}	94.7(1)	O_8–Te_8–F_{38}	90.1(1)
O_3–Te_3–F_{14}	89.9(2)	O_8–Te_8–F_{39}	93.8(1)
O_3–Te_3–F_{15}	93.6(1)	O_8–Te_8–F_{40}	93.1(1)
F_{11}–Te_3–F_{12}	87.2(2)	F_{36}–Te_8–F_{37}	87.8(1)
F_{11}–Te_3–F_{13}	87.3(1)	F_{36}–Te_8–F_{38}	89.1(1)
F_{11}–Te_3–F_{14}	88.1(2)	F_{36}–Te_8–F_{39}	89.5(1)
F_{11}–Te_3–F_{15}	87.4(1)	F_{36}–Te_8–F_{40}	175.3(1)
F_{12}–Te_3–F_{13}	89.6(1)	F_{37}–Te_8–F_{38}	88.5(1)
F_{12}–Te_3–F_{14}	90.4(2)	F_{37}–Te_8–F_{39}	87.6(1)
F_{12}–Te_3–F_{15}	174.4(2)	F_{37}–Te_8–F_{40}	87.5(1)
F_{13}–Te_3–F_{14}	175.4(2)	F_{38}–Te_8–F_{39}	175.9(1)
F_{13}–Te_3–F_{15}	89.0(1)	F_{38}–Te_8–F_{40}	91.2(1)
F_{14}–Te_3–F_{15}	90.5(2)	F_{39}–Te_8–F_{40}	89.9(1)

Table S5.2. continued…

O_4–Te_4–F_{16}	94.1(1)	O_9–Te_9–F_{41}	91.7(1)
O_4–Te_4–F_{17}	90.1(1)	O_9–Te_9–F_{42}	92.9(1)
O_4–Te_4–F_{18}	90.7(1)	O_9–Te_9–F_{43}	95.6(1)
O_4–Te_4–F_{19}	177.7(1)	O_9–Te_9–F_{44}	176.8(1)
O_4–Te_4–F_{20}	94.2(1)	O_9–Te_9–F_{45}	89.7(1)
F_{16}–Te_4–F_{17}	175.7(1)	F_{41}–Te_9–F_{42}	175.4(1)
F_{16}–Te_4–F_{18}	90.5(1)	F_{41}–Te_9–F_{43}	89.8(1)
F_{16}–Te_4–F_{19}	87.3(1)	F_{41}–Te_9–F_{44}	87.5(1)
F_{16}–Te_4–F_{20}	90.7(1)	F_{41}–Te_9–F_{45}	89.6(1)
F_{17}–Te_4–F_{18}	88.8(1)	F_{42}–Te_9–F_{43}	89.8(1)
F_{17}–Te_4–F_{19}	88.5(1)	F_{42}–Te_9–F_{44}	87.9(1)
F_{17}–Te_4–F_{20}	89.6(1)	F_{42}–Te_9–F_{45}	90.4(1)
F_{18}–Te_4–F_{19}	87.4(1)	F_{43}–Te_9–F_{44}	87.5(1)
F_{18}–Te_4–F_{20}	174.9(1)	F_{43}–Te_9–F_{45}	174.7(1)
F_{19}–Te_4–F_{20}	87.7(1)	F_{44}–Te_9–F_{45}	87.2(1)
O_5–Te_5–F_{21}	91.2(1)	F_{21}–Te_5–F_{24}	89.5(1)
O_5–Te_5–F_{22}	177.0(1)	F_{21}–Te_5–F_{25}	175.5(1)
O_5–Te_5–F_{23}	90.0(1)	F_{22}–Te_5–F_{23}	87.3(1)
O_5–Te_5–F_{24}	95.0(1)	F_{22}–Te_5–F_{24}	87.7(1)
O_5–Te_5–F_{25}	93.2(1)	F_{22}–Te_5–F_{25}	88.0(1)
F_{21}–Te_5–F_{22}	87.5(1)	F_{23}–Te_5–F_{24}	175.0(1)
F_{21}–Te_5–F_{23}	90.0(1)	F_{23}–Te_5–F_{25}	90.4(1)
		F_{24}–Te_5–F_{25}	89.7(1)
	Positionally Disordered Anion		
Sb_3–O_{10}–Te_{10}	139.3(2)	O_{11}–Te_{11}–F_{55}	173.7(2)
Sb_3–O_{11}–Te_{11}	136.8(3)	O_{11B}–Te_{11}–F_{55B}	170.3(5)
Sb_3–O_{11B}–Te_{11B}	137.7(7)	O_{11}–Te_{11}–F_{52}	89.4(2)
Sb_3–O_{12}–Te_{12}	139.3(3)	O_{11B}–Te_{11}–F_{52B}	97.7(5)
Sb_3–O_{12B}–Te_{12B}	133.5(7)	O_{11}–Te_{11}–F_{51}	94.1(2)
O_{12}–Sb_3–O_{11}	89.5(2)	O_{11B}–Te_{11}–F_{51B}	86.2(5)
O_{12B}–Sb_3–O_{11B}	89.2(5)	O_{11}–Te_{11}–F_{53}	88.2(3)
O_{12}–Sb_3–O_{10}	86.9(2)	O_{11B}–Te_{11}–F_{53B}	92.7(5)
O_{12B}–Sb_3–O_{10}	92.6(4)	O_{11}–Te_{11}–F_{54}	95.7(3)
O_{12}–Sb_3–O_{12}	180.0	O_{11B}–Te_{11}–F_{54B}	89.1(5)
O_{12B}–Sb_3–O_{12B}	180.0(5)	F_{55}–Te_{11}–F_{52}	86.7(2)
O_{11}–Sb_3–O_{10}	92.2(2)	F_{55B}–Te_{11}–F_{52B}	91.1(5)
O_{11B}–Sb_3–O_{10}	84.1(4)	F_{55}–Te_{11}–F_{51}	89.6(2)
O_{11}–Sb_3–O_{11}	180.0	F_{55B}–Te_{11}–F_{51B}	84.9(5)
O_{11B}–Sb_3–O_{11B}	180.0(2)	F_{55}–Te_{11}–F_{53}	86.7(3)
O_{10}–Sb_3–O_{10}	180.0	F_{55B}–Te_{11}–F_{53B}	90.7(5)

Table S5.2. continued…

O_{10}–Te_{10}–F_{50}	175.4(2)	F_{55}–Te_{11}–F_{54}	89.2(2)
O_{10}–Te_{10}–F_{50B}	166.3(4)	F_{55B}–Te_{11}–F_{54B}	86.0(5)
O_{10}–Te_{10}–F_{47}	90.7(2)	F_{52}–Te_{11}–F_{51}	176.0(2)
O_{10}–Te_{10}–F_{47B}	94.4(4)	F_{52B}–Te_{11}–F_{51B}	175.6(5)
O_{10}–Te_{10}–F_{46}	92.9(2)	F_{52}–Te_{11}–F_{53}	87.8(3)
O_{10}–Te_{10}–F_{46B}	97.3(4)	F_{52B}–Te_{11}–F_{53B}	94.8(6)
O_{10}–Te_{10}–F_{48}	95.1(2)	F_{52}–Te_{11}–F_{54}	88.5(2)
O_{10}–Te_{10}–F_{48B}	95.1(2)	F_{52B}–Te_{11}–F_{54B}	95.0(5)
O_{10}–Te_{10}–F_{49}	93.4(2)	F_{51}–Te_{11}–F_{53}	90.2(3)
O_{10}–Te_{10}–F_{49B}	93.4(2)	F_{51B}–Te_{11}–F_{53B}	87.1(6)
F_{50}–Te_{10}–F_{47}	86.1(2)	F_{51}–Te_{11}–F_{54}	93.2(2)
F_{50B}–Te_{10}–F_{47B}	91.8(5)	F_{51B}–Te_{11}–F_{54B}	83.0(5)
F_{50}–Te_{10}–F_{46}	83.6(2)	F_{53}–Te_{11}–F_{54}	174.6(3)
F_{50B}–Te_{10}–F_{46B}	92.0(5)	F_{53B}–Te_{11}–F_{54B}	169.8(6)
F_{50}–Te_{10}–F_{48}	87.7(2)		
F_{50B}–Te_{10}–F_{48B}	84.6(4)	O_{12B}–Te_{12}–F_{56B}	93.8(5)
F_{50}–Te_{10}–F_{49}	90.0(2)	O_{12}–Te_{12}–F_{57}	95.7(2)
F_{50B}–Te_{10}–F_{49B}	73.0(4)	O_{12B}–Te_{12}–F_{57B}	86.4(5)
F_{47}–Te_{10}–F_{46}	86.8(2)	F_{59}–Te_{12}–F_{56}	91.2(3)
F_{47B}–Te_{10}–F_{46B}	110.4(6)	F_{59B}–Te_{12}–F_{56B}	82.3(5)
F_{47}–Te_{10}–F_{48}	171.7(2)	F_{59}–Te_{12}–F_{57}	92.0(3)
F_{47B}–Te_{10}–F_{48B}	162.6(5)	F_{59B}–Te_{12}–F_{57B}	87.2(5)
F_{47}–Te_{10}–F_{49}	91.7(2)	F_{58}–Te_{12}–F_{60}	85.1(2)
F_{47B}–Te_{10}–F_{49B}	87.2(5)	F_{58B}–Te_{12}–F_{60B}	93.7(5)
F_{46}–Te_{10}–F_{48}	87.1(2)	F_{58}–Te_{12}–F_{56}	85.8(2)
F_{46B}–Te_{10}–F_{48B}	85.9(5)	F_{58B}–Te_{12}–F_{56B}	98.7(5)
F_{46}–Te_{10}–F_{49}	173.5(2)	F_{58}–Te_{12}–F_{57}	90.5(2)
F_{46B}–Te_{10}–F_{49B}	161.2(5)	F_{58B}–Te_{12}–F_{57B}	91.9(5)
F_{48}–Te_{10}–F_{49}	93.8(3)	F_{60}–Te_{12}–F_{56}	86.8(2)
F_{48B}–Te_{10}–F_{49B}	76.0(5)	F_{60B}–Te_{12}–F_{56B}	91.5(5)
		F_{60}–Te_{12}–F_{57}	88.6(2)
O_{12}–Te_{12}–F_{59}	95.1(3)	F_{60B}–Te_{12}–F_{57B}	86.5(4)
O_{12B}–Te_{12}–F_{59B}	83.6(5)	F_{56}–Te_{12}–F_{57}	174.3(2)
O_{12}–Te_{12}–F_{58}	91.3(2)	F_{56B}–Te_{12}–F_{57B}	169.4(4)
O_{12B}–Te_{12}–F_{58B}	95.9(5)	F_{59}–Te_{12}–F_{58}	172.8(3)
O_{12}–Te_{12}–F_{60}	174.5(2)	F_{59B}–Te_{12}–F_{58B}	179.0(5)
O_{12B}–Te_{12}–F_{60B}	168.2(5)	F_{59}–Te_{12}–F_{60}	88.2(3)
O_{12}–Te_{12}–F_{56}	88.8(2)	F_{59B}–Te_{12}–F_{60B}	86.7(6)

Table S5.2. continued…

		SO_2ClF	
$Cl_1–S_1–F_{61}$	97.3(2)	$F_{61}–S_1–O_{13}$	107.6(2)
$Cl_1–S_1–O_{13}$	108.9(2)	$F_{61}–S_1–O_{14}$	107.0(3)
$Cl_1–S_1–O_{14}$	110.2(2)	$O_{13}–S_1–O_{14}$	122.7(3)
		Positionally Disordered SO_2ClF	
$Cl_2–S_2–F_{62}$	94.7(7)	$Cl_{2B}–S_2–F_{62B}$	105(2)
$Cl_2–S_2–O_{16}$	105.7(8)	$Cl_{2B}–S_2–O_{16B}$	107(2)
$Cl_2–S_2–O_{15}$	109.8(8)	$Cl_{2B}–S_2–O_{15B}$	105(2)
$F_{62}–S_2–O_{16}$	115.0(9)	$F_{62B}–S_2–O_{16B}$	118(2)
$F_{62}–S_2–O_{15}$	117.8(9)	$F_{62B}–S_2–O_{15B}$	88(2)
$O_{16}–S_2–O_{15}$	111.8(9)	$O_{16B}–S_2–O_{15B}$	132(2)

[a] The atom labeling scheme corresponds to that used in Figure S5.2.

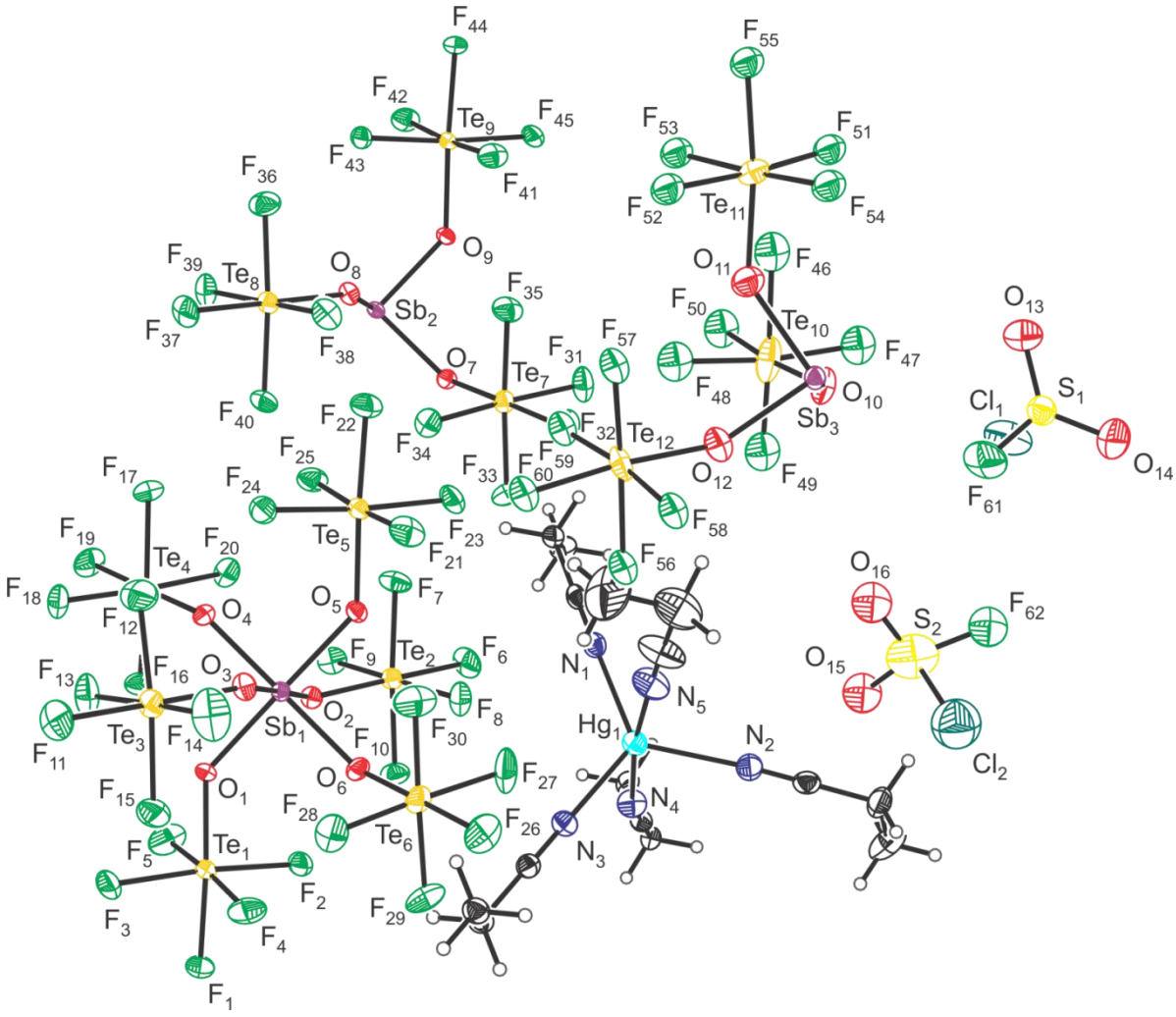

Figure S5.3. The asymmetric unit in the single-crystal X-ray structure of $[Hg(NCCH_2CH_3)_5][Sb(OTeF_5)_6]_2 \cdot 2SO_2ClF$ showing the $[Sb(OTeF_5)_6]^-$ anion and co-crystallized SO_2ClF molecules; thermal ellipsoids shown at the 50% probability level. The symmetry generated F_5TeO-groups of $Sb_{(2)}$ and $Sb_{(3)}$ are not shown. Only one orientation of the all the positionally disordered F_5TeO-groups of $Sb_{(3)}$, and disordered SO_2ClF molecule of $S_{(2)}$are shown for clarity. The carbon (black) and hydrogen (grey) atoms are not labelled for clarity.

Table S5.3. Experimental and Calculated Raman Frequencies and Intensities for of the $[Sb(OTeF_5)_6]^-$ anions in the $[Hg(SO_2ClF)_6]^+$ (**1**), $[Hg(NCCH_3)_5]^{2+}$ (**2**) and $[Hg(NCCH_2CH_3)_5]^{2+}$ (**3**) salts.

$[Sb(OTeF_5)_6]^-$				
(1) exptl. [a]	**(2) exptl.** [a]	**(3) exptl.** [a]	**calcd. (S_6)** [b]	**assign** [c]
			944(4)[0]	
			863(0)[892]	[ν(Te–O) – ν(Sb–O)]
817(6)	816(sh)		829(16)[0]	
			730(2)[0]	
725(sh)			728(0)[282]	
722(18)			727(6)[0]	
	718(31)	720(27)	727(0)[790]	ν(Te–F_{eq})
			718(0)[99]	
715(sh)			716(0)[72]	
712(17)			715(9)[0]	
			710(<1)[0]	
701(100)	703(100)	703(95)	693(123)[0]	
693(30)			689(0)[358]	ν(Te–F_{ax})
687(7)	694(sh)		689(0)[200]	
			686(14)[0]	
668(31)	662(87), br	662(100)	653(43)[0]	[ν(Te–F_{ax}) – ν(Te–F_{eq})]
662(43)			647(0)[22]	
			649(0)[3]	
			647(6)[0]	
648(22) [d]	647(30)	647(30)	646(0)[3]	ν(Te–F_{eq})
645(21) [d]	632(sh), br		643(<1)[0]	
			642(0)[<1]	
			641(10)[0]	
			478(0)[246]	
415(26)	415(sh)		460(2)[0]	[ν(Te–O) + ν(Sb–O)]
			456(0)[1]	
			414(36)[0]	
366(6)	369(9)	368(10)	368(0)[34]	δ(O–Sb–O)
			362(4)[0]	
344(4)			337(<1)[0]	$\delta_{umb}(TeF_4)$
337(18)	335(22)	340(sh)	337(0)[106]	ρ_w(O–Sb–O)
333(20)		334(24)	328(0)[244]	
330(sh)			326(3)[0]	
			326(4)[0]	
			324(0)[224]	
			324(2)[0]	δ(F–Te–F)
			322(0)[78]	
			321(0)[6]	
			320(<1)[0]	
323(14)	323(sh)	322(sh)	320(<1)[0]	
320(sh)			318(0)[60]	
			318(0)[306]	ρ_w(O–Sb–O)

Table S5.3. continued…

			318(0)[306]	ρ_w(O–Sb–O)
			303(4)[0]	ρ_r(O–Sb–O)
			297(0)[10]	δ(F–Te–F)
			297(1)[0]	
			297(0)[1]	
			296(1)[0]	
257(1)				
252(2)	242(15)	241(17) [d]	255(0)[53]	
245(9)			254(0)[58]	
241(9)				
231(4)	228(6)	228(7) [d]	236(3)[0]	ρ_w(F–Te–F)
			234(2)[0]	
215(1)	213(2)	214(sh) [d]	224(0)[21]	
			221(1)[0]	
			214(0)[13]	ρ_w(F–Te–F) / ρ_w(F–Te–O)
			213(0)[<1]	ρ_w(F–Te–F)
			209(<1)[0]	
			207(<1)[0]	
			205(0)[9]	
			204(<1)[0]	ρ_w(F–Te–F) / ρ_w(F–Te–O)
			199(0)[14]	
			197(0)[31]	
145(20)	143(20)	143(20)	135(4)[0]	$\rho_r(F_aF_{4e}Te)$
135(12)	134(11)	133(12)	127(1)[0]	
122(14)	122(11)	120(11)	118(0)[4]	
			113(0)[6]	
			111(<1)[0]	
115(13)	112(13)	112(11)	105(0)[<0.1]	
			105(1)[0]	
			92(0)[<1]	
			< 82(1)[0]	deformation modes

[a] The Raman spectrum was obtained at −150 °C on the crystalline samples contained in an FEP sample tube using 1064-nm excitation. Values in parentheses denote relative experimental Raman intensities. [b] Calculated using the PBE0-TZVPD(GD3BJ) basis set. Values in parentheses denote calculated Raman intensities (Å amu^{-1}). Values in square brackets denote calculated infrared intensities (km mol^{-1}). Assignments were made by visual inspection of the vibrational displacements obtained at the PBE0 level of theory. [c] Bond elongations and angle openings are denoted by plus (+) signs and bond contractions and angle compressions are denoted by minus (–) signs. Symbols/abbreviations denote stretch (ν), bend (δ), rock (ρ_r), wag (ρ_w), equatorial (4e, where the four Fe atoms are in-phase), axial (a), shoulder (sh), broad (br), and not observed (n.o.). [d] Possible overlap or contributions from cation.

Table S5.4. Experimental and Calculated Geometrical Parameters for the $[Hg(SO_2ClF)_6]^{2+}$ Dication in the Crystal Structure of $[Hg(SO_2ClF)_6]$-$[Sb(OTeF_5)_6]_2$ (S_6) and the Gas-phase (S_6) [a]

	exptl	calcd		
		B3LYP	**PBE0 (GD3BJ)**	**APFD**
Bond Lengths (Å)				
$Hg_1{-}O_1$	2.342(4)	2.375	2.363	2.302
$S_1{-}O_1$	1.442(4)	1.444	1.444	1.446
$S_1{-}O_2$	1.409(4)	1.406	1.406	1.408
$S_1{-}F_1$	1.524(3)	1.530	1.529	1.533
$S_1{-}Cl_1$	1.917(2)	1.948	1.947	1.950
Bond Angles (deg)				
$O_1{-}Hg_1{-}O_{1A}$	180.0	180.0	180.0	180.0
$O_1{-}Hg_1{-}O_{1B}$	82.9(2)	89.6	89.3	85.0
$O_1{-}Hg_1{-}O_{1C}$	97.1(2)	90.4	90.7	95.0
$O_1{-}Hg_1{-}O_{1D}$	82.9(2)	89.6	89.3	85.0
$O_1{-}Hg_1{-}O_{1E}$	97.1(2)	90.4	90.7	95.0
$Hg_1{-}O_1{-}S_1$	122.7(2)	133.0	128.9	124.7
$F_1{-}S_1{-}O_1$	105.1(3)	105.3	105.4	105.5
$F_1{-}S_1{-}O_2$	109.1(3)	109.2	109.2	109.0
$Cl_1{-}S_1{-}O_1$	109.0(2)	108.0	107.9	108.0
$Cl_1{-}S_1{-}O_2$	112.3(2)	112.3	112.4	112.6
$Cl_1{-}S_1{-}F_1$	100.6(2)	100.1	100.2	100.3
$O_2{-}S_1{-}O_1$	119.0(3)	119.9	119.8	119.5

[a] The atom labeling scheme corresponds to that used in Figures 5.1.

Table S5.5. Experimental and Calculated Geometrical Parameters for the $[Hg(NCCH_3)_5]^{2+}$ Dication in the Crystal Structure of $[Hg(NCCH_3)_5][Sb(OTeF_5)_6]_2 \cdot 2SO_2ClF$. ($C_1$) and the Gas-phase ($C_3$).[a]

	exptl	calcd		
		B3LYP	**PBE0 (GD3BJ)**	**APFD**
Bond Lengths (Å)				
$Hg_1–N_1$	2.217(9)	2.285	2.251	2.227
$Hg_1–N_2$	2.231(10)	2.285	2.251	2.227
$Hg_1–N_3$	2.235(8)	2.285	2.251	2.227
$Hg_1–N_4$	2.381(11)	2.435	2.401	2.348
$Hg_1–N_5$	2.455(10)	2.435	2.401	2.348
$N_1–C_1$	1.125(13)	1.146	1.145	1.146
$N_2–C_3$	1.129(16)	1.146	1.145	1.146
$N_3–C_5$	1.123(18)	1.146	1.145	1.146
$N_4–C_7$	1.147(16)	1.148	1.147	1.147
$N_5–C_9$	1.138(15)	1.148	1.147	1.147
$C_1–C_2$	1.465(14)	1.448	1.440	1.443
$C_3–C_4$	1.447(22)	1.448	1.440	1.443
$C_5–C_6$	1.455(14)	1.448	1.440	1.443
$C_7–C_8$	1.444(20)	1.449	1.442	1.445
$C_9–C_{10}$	1.141(17)	1.449	1.442	1.445
Bond Angles (deg)				
$N_1–Hg_1–N_2$	127.6(4)	120.0	120.0	120.0
$N_1–Hg_1–N_3$	116.4(3)	120.0	120.0	120.0
$N_2–Hg_1–N_3$	115.5(3)	120.0	120.0	120.0
$N_1–Hg_1–N_4$	90.7(3)	90.0	90.1	90.0
$N_1–Hg_1–N_5$	91.4(3)	90.0	89.9	90.0
$N_2–Hg_1–N_4$	90.8(5)	90.0	90.1	90.0
$N_2–Hg_1–N_5$	88.5(4)	90.0	89.9	90.0
$N_3–Hg_1–N_4$	96.2(4)	90.0	90.1	90.0
$N_3–Hg_1–N_5$	82.3(3)	90.0	89.9	90.0
$N_4–Hg_1–N_5$	178.84)	180.0	180.0	180.0
$Hg_1–N_1–C_1$		180.0	179.9	179.9
$Hg_1–N_2–C_3$	178.4(9)	180.0	179.9	179.9
$Hg_1–N_3–C_5$	167.7(14)	180.0	179.9	179.9
$Hg_1–N_4–C_7$	172.7(9)	180.0	180.0	180.0
$Hg_1–N_5–C_9$	164.4(10)	180.0	180.0	180.0
$N_1–C_1–C_2$	178.8(13)	180.0	180.0	180.0
$N_2–C_3–C_4$	178.8(11)	180.0	180.0	180.0

Table S5.5. continued…

N_3–C_5–C_6	179.2(16)	180.0	180.0	180.0
N_4–C_7–C_8	179.3(12)	180.0	180.0	180.0
N_5–C_9–C_{10}	179.4(15)	180.0	180.0	180.0

[a] The atom labeling scheme corresponds to that used in Figures 5.2.

Table S5.6. Experimental and Calculated Geometrical Parameters for the $[Hg(NCCH_2CH_3)_5]^{2+}$ dication in the crystal structure of $[Hg(NCCH_2CH_3)_5][Sb(OTeF_5)_6]_2 \cdot 2SO_2ClF$ (C_1) and the gas-phase (C_1) [a]

	exptl	calcd		
		B3LYP	**PBE0 (GD3BJ)**	**APFD**
Bond Lengths (Å)				
$Hg_1–N_1$	2.216(4)	2.282	2.248	2.225
$Hg_1–N_2$	2.240(4)	2.282	2.248	2.225
$Hg_1–N_3$	2.220(5)	2.282	2.248	2.225
$Hg_1–N_4$	2.402(5)	2.436	2.403	2.347
$Hg_1–N_5$	2.393(5)	2.438	2.403	2.348
$N_1–C_1$	1.136(6)	1.147	1.146	1.147
$N_2–C_4$	1.138(6)	1.147	1.146	1.147
$N_3–C_7$	1.132(6)	1.147	1.146	1.147
$N_4–C_{10}$	1.143(6)	1.149	1.148	1.148
$N_5–C_{13}$	1.087(8)	1.148	1.147	1.148
$C_1–C_2$	1.472(6)	1.454	1.447	1.450
$C_4–C_5$	1.451(7)	1.454	1.447	1.450
$C_7–C_8$	1.466(6)	1.454	1.447	1.450
$C_{10}–C_{11}$	1.465(6)	1.456	1.449	1.451
$C_{13}–C_{14}$	1.480(9)	1.456	1.449	1.451
$C_2–C_3$	1.534(7)	1.539	1.529	1.533
$C_5–C_6$	1.561(9)	1.539	1.529	1.533
$C_8–C_9$	1.534(6)	1.539	1.529	1.533
$C_{11}–C_{12}$	1.527(6)	1.538	1.529	1.532
$C_{14}–C_{15}$	1.479(10)	1.538	1.529	1.532
Bond Angles (deg)				
$N_1–Hg_1–N_2$	120.8(2)	120.1	119.9	119.9
$N_1–Hg_1–N_3$	122.7(2)	120.1	120.2	120.3
$N_2–Hg_1–N_3$	116.5(2)	90.2	90.0	90.0
$N_1–Hg_1–N_5$	89.4(2)	89.9	89.9	89.8
$N_1–Hg_1–N_4$	94.8(2)	119.8	119.9	119.8
$N_2–Hg_1–N_4$	84.6(2)	89.9	90.2	90.3
$N_2–Hg_1–N_5$	89.0(2)	90.1	90.0	90.0
$N_3–Hg_1–N_4$	91.4(2)	89.5	89.9	89.9
$N_3–Hg_1–N_5$	90.4(2)	90.3	89.9	90.0
$N_4–Hg_1–N_5$	173.5(2)	179.8	179.7	179.8
$Hg_1–N_1–C_1$	177.2(4)	178.3	179.0	178.7

Table S5.6. Continued…

$Hg_1–N_2–C_4$	175.7(4)	178.2	178.8	178.5
$Hg_1–N_3–C_7$	179.6(4)	177.9	179.3	178.9
$Hg_1–N_4–C_{10}$	164.9(4)	177.8	178.9	178.5
$Hg_1–N_5–C_{13}$	174.7(5)	178.2	178.6	178.2
$N_1–C_1–C_2$	177.5(5)	179.4	179.1	179.0
$N_2–C_4–C_5$	179.2(5)	179.4	179.1	179.0
$N_3–C_7–C_8$	178.0(5)	179.4	179.1	179.0
$N_4–C_{10}–C_{11}$	176.2(5)	179.4	179.1	179.0
$N_5–C_{13}–C_{14}$	178.1(8)	179.4	179.1	179.0
$C_1–C_2–C_3$	110.7(4)	112.9	112.4	112.2
$C_4–C_5–C_6$	110.8(5)	112.9	112.4	112.2
$C_7–C_8–C_9$	110.2(4)	112.9	112.4	112.2
$C_{10}–C_{11}–C_{12}$	110.2(4)	113.0	112.5	112.2
$C_{13}–C_{14}–C_{15}$	111.5(7)	113.0	112.5	112.2

[a] The atom labeling scheme corresponds to that used in Figures 5.3.

Table S5.7. Calculated Geometrical Parameters for SO_2ClF (C_s).[a]

Bond Lengths (Å)			
S–$O_{1,2}$	1.410	S−F	1.552
S−Cl	1.990		
Bond Angles (deg)			
O_2–S–O_1	123.8	Cl–S–$O_{1,2}$	109.0
F–S–$O_{1,2}$	107.1	Cl–S–F	97.8

[a] The atom labeling scheme corresponds to that used in Figure S5.4. Calculated at the PBE0/def2-TZVPD(GD3BJ) level of theory.

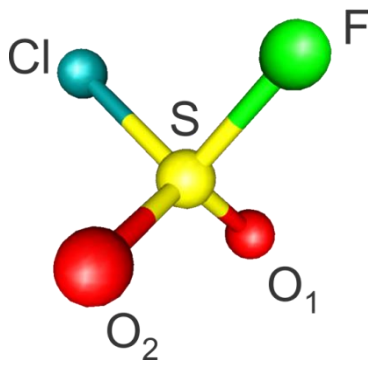

Figure S5.4. The calculated SO_2ClF (C_s) molecule at the PBE0/def2-TZVPD(GD3BJ) level of theory.

Table S5.8. Calculated Geometrical Parameters for $NCCH_3$ (C_{3v}) [a]

Bond Lengths (Å)			
N–C_1	1.149	C_2–$H_{1\text{-}3}$	1.091
C_1–C_2	1.450		
Bond Angles (deg)			
N–C_1–C_2	180.0	C_1–C_2–$H_{1\text{-}3}$	110.1

[a] The atom labeling scheme corresponds to that used in Figure S5.5. Calculated at the PBE0/def2-TZVPD(GD3BJ) level of theory.

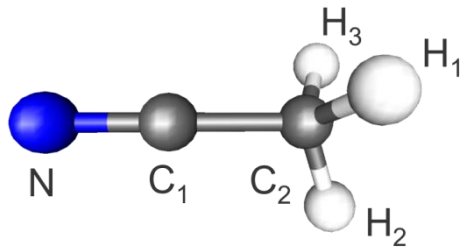

Figure S5.5. The calculated $NCCH_3$ (C_{3v}) molecule at the PBE0/def2-TZVPD(GD3BJ) level of theory.

Table S5.9. Calculated Geometrical Parameters for CH_3CH_2CN (C_s) [a]

Bond Lengths (Å)			
N–C_1	1.150	C_2–$H_{1/2}$	1.094
C_1–C_2	1.455	C_3–$H_{3\text{-}5}$	1.091
C_2–C_3	1.526		
Bond Angles (deg)			
N–C_1–C_2	179.0	C_1–C_2–$H_{1/2}$	108.0
C_1–C_2–C_3	112.4	C_3–C_2–$H_{1/2}$	110.8
		C_2–C_3–$H_{3\text{-}5}$	110.9

[a] The atom labeling scheme corresponds to that used in Figures 5.6. Calculated at the PBE0/def2-TZVPD(GD3BJ) level of theory.

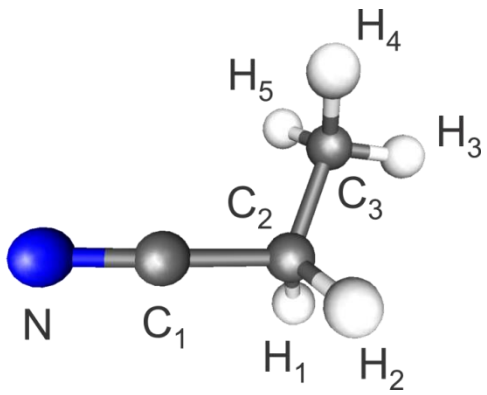

Figure S5.6. The calculated CH_3CH_2CN (C_s) molecule at the PBE0/def2 TZVPD(GD3BJ) level of theory.

Table S5.10. Calculated Valences, Charges (NPA), and Wiberg Bond Orders for $[Hg(SO_2ClF)_6]^{2+}$ using NBO Version 3.1 [Version 6.0]

Atom	Charge	Valences	Bond	Bond Order
Hg	1.346 [1.659]	1.270 [0.678]	$Hg–O_b$	0.166 [0.089]
S	2.300 [2.294]	4.353 [4.358]	$S–O_b$	1.200 [1.204]
O_b	–0.937 [–0.977]	1.711 [1.635]	$S–O_t$	1.448 [1.451]
O_t	–0.815 [–0.821]	1.834 [1.824]	S–F	0.730 [0.732]
F	–0.413 [–0.413]	0.972 [0.968]	S–Cl	0.953 [0.955]
Cl	–0.027 [–0.027]	1.270 [1.267]		
$\sum SO_2ClF$	**0.109 [0.057]**			
$\sum Hg(SO_2ClF)_6$	**2.000 [2.000]**			

Table S5.11. Calculated Valences, Charges (NPA), and Wiberg Bond Orders for SO_2ClF (C_s) using NBO Version 3.1 [Version 6.0][a]

Atom	Charge	Valences	Bond	Bond Order
S	2.289 [2.293]	4.371 [4.365]	$S–O_1$	1.422 [1.421]
O_1	–0.842 [–0.842]	1.799 [1.797]	$S–O_2$	1.422 [1.421]
O_2	–0.842 [–0.842]	1.799 [1.797]	$S–F_1$	0.683 [0.682]
F_1	–0.452 [–0.452]	0.914 [0.913]	$S–Cl_1$	0.844 [0.840]
Cl_1	–0.152 [–0.158]	1.152 [1.147]		
$\sum SO_2ClF$	**0.000 [0.000]**			

[a] The atom labeling scheme corresponds to that used in Figures S5.4.

Table S5.12. Calculated Valences, Charges (NPA), and Wiberg Bond Orders for $[Hg(NCCH_3)_5]^{2+}$ using NBO Version 3.1 [Version 6.0] [a]

Atom	Charge	Valences	Bond	Bond Order
Hg	1.204 [1.649]	1.594 [0.797]		
		Axial Ligands		
N_4	–0.444 [–0.507]	3.197 [3.075]	Hg–N_4	0.247 [0.114]
C_9	0.465 [0.452]	3.938 [3.944]	N_4–C_9	2.790 [2.795]
C_{10}	–0.751 [–0.751]	3.806 [3.806]	C_9–C_{10}	1.109 [1.112]
H_{13}	0.289 [0.289]	0.918 [0.917]	C_{10}–H_{13}	0.882 [0.882]
H_{14}	0.289 [0.289]	0.918 [0.917]	C_{10}–H_{14}	0.882 [0.882]
H_{15}	0.289 [0.289]	0.918 [0.917]	C_{10}–H_{15}	0.882 [0.882]
∑ CH_3CN	**0.137 [0.061]**			
N_5	–0.445 [–0.509]	3.198 [3.075]	Hg–N_5	0.248 [0.115]
C_7	0.467 [0.453]	3.937 [3.943]	N_5–C_7	2.789 [2.794]
C_8	–0.751 [–0.751]	3.805 [3.806]	C_7–C_8	1.110 [1.112]
H_{10}	0.289 [0.289]	0.918 [0.917]	C_8–H_{10}	0.881 [0.882]
H_{11}	0.289 [0.289]	0.918 [0.917]	C_8–H_{11}	0.881 [0.882]
H_{12}	0.289 [0.289]	0.918 [0.917]	C_8–H_{12}	0.881 [0.882]
∑ CH_3CN	**0.138 [0.062]**			
		Equatorial Ligands		
N_1	–0.460 [–0.542]	3.234 [3.090]	Hg–N_1	0.323 [0.156]
C_1	0.504 [0.489]	3.919 [3.923]	N_1–C_2	2.756 [2.763]
C_2	–0.753 [–0.753]	3.801 [3.802]	C_2–C_3	1.115 [1.117]
H_1	0.294 [0.293]	0.915 [0.915]	C_3–H_1	0.878 [0.878]
H_2	0.294 [0.293]	0.915 [0.914]	C_3–H_2	0.878 [0.878]
H_3	0.294 [0.293]	0.915 [0.915]	C_3–H_3	0.878 [0.878]
∑ CH_3CN	**0.173 [0.076]**			
N_2	–0.460 [–0.543]	3.234 [3.091]	Hg–N_2	0.323 [0.156]
C_3	0.504 [0.492]	3.919 [3.927]	N_2–C_3	2.756 [2.763]
C_4	–0.753 [–0.754]	3.801 [3.802]	C_3–C_4	1.115 [1.117]
H_4	0.294 [0.293]	0.915 [0.915]	C_4–H_4	0.878 [0.878]
H_5	0.294 [0.294]	0.915 [0.914]	C_4–H_5	0.878 [0.878]
H_6	0.294 [0.294]	0.915 [0.914]	C_4–H_6	0.878 [0.878]
∑ CH_3CN	**0.173 [0.076]**			
N_3	–0.460 [–0.544]	3.234 [3.091]	Hg–N_3	0.323 [0.156]
C_5	0.504 [0.492]	3.919 [3.927]	N_3–C_5	2.756 [2.763]
C_6	–0.753 [–0.754]	3.801 [3.802]	C_5–C_6	1.115 [1.117]
H_7	0.294 [0.293]	0.915 [0.914]	C_6–H_7	0.878 [0.878]
H_8	0.294 [0.294]	0.915 [0.914]	C_6–H_8	0.878 [0.878]
H_9	0.294 [0.294]	0.915 [0.914]	C_6–H_9	0.878 [0.878]
∑ CH_3CN	**0.173 [0.076]**			
∑$Hg(NCCH_3)_5$	**2.000 [2.000]**			

[a] The atom labeling scheme corresponds to that used in Figures 5.2b.

Table S5.13. Calculated Valences, Charges (NPA), and Wiberg Bond Orders for CH_3CN (C_3) using NBO Version 3.1 [Version 6.0] [a]

Atom	Charge	Valences	Bond	Bond Order
N	–0.320 [–0.318]	3.033 [3.029]		
C_1	0.278 [0.275]	4.005 [4.003]	N–C_1	2.908 [2.907]
C_2	–0.731 [–0.730]	3.836 [3.834]	C_1–C_2	1.086 [1.086]
H_1	0.258 [0.258]	0.936 [0.935]	C_2–H_1	0.903 [0.903]
H_2	0.258 [0.258]	0.936 [0.935]	C_2–H_2	0.903 [0.903]
H_3	0.258 [0.258]	0.936 [0.935]	C_2–H_3	0.903 [0.903]
$\sum$ CH_3CN	**0.000 [0.000]**			

[a] The atom labeling scheme corresponds to that used in Figures S5.5.

Table S5.14. Calculated Valences, Charges (NPA), and Wiberg Bond Orders for $[Hg(NCCH_2CH_3)_5]^{2+}$ using NBO Version 3.1 [Version 6.0] [a]

Atom	Charge	Valences	Bond	Bond Order
Hg_1	1.205 [1.648]	1.596 [0.802]		
		Equatorial Ligands		
N_1	–0.470 [–0.551]	3.240 [3.093]	Hg_1–N_1	0.322 [0.156]
C_1	0.509 [0.497]	3.919 [3.929]	N_1–C_1	2.757 [2.765]
C_2	–0.540 [–0.540]	3.880 [3.879]	C_1–C_2	1.089 [1.091]
H_1	0.282 [0.281]	0.922 [0.922]	C_2–H_1	0.869 [0.869]
H_2	0.282 [0.281]	0.922 [0.922]	C_2–H_2	0.869 [0.869]
C_3	–0.597 [–0.596]	3.839 [3.839]	C_2–C_3	1.000 [1.000]
H_3	0.251 [0.250]	0.938 [0.938]	C_3–H_3	0.918 [0.919]
H_4	0.228 [0.227]	0.950 [0.949]	C_3–H_4	0.934 [0.934]
H_5	0.227 [0.227]	0.950 [0.950]	C_3–H_5	0.934 [0.934]
∑ CH_3CH_2CN	**0.173 [0.076]**			
N_2	–0.471 [–0.550]	3.240 [3.092]	Hg_1–N_2	0.322 [0.157]
C_4	0.510 [0.495]	3.919 [3.929]	N_2–C_4	2.757 [2.764]
C_5	–0.540 [–0.539]	3.880 [3.880]	C_4–C_5	1.089 [1.091]
H_6	0.282 [0.281]	0.922 [0.922]	C_5–H_6	0.869 [0.869]
H_7	0.282 [0.281]	0.922 [0.922]	C_5–H_7	0.869 [0.869]
C_6	–0.597 [–0.596]	3.839 [3.839]	C_5–C_6	1.000 [1.000]
H_8	0.251 [0.250]	0.938 [0.938]	C_6–H_8	0.918 [0.919]
H_9	0.228 [0.228]	0.950 [0.949]	C_6–H_9	0.934 [0.934]
H_{10}	0.228 [0.228]	0.950 [0.949]	C_6–H_{10}	0.934 [0.934]
∑ CH_3CH_2CN	**0.173 [0.076]**			
N_3	–0.470 [–0.550]	3.240 [3.092]	Hg_1–N_3	0.322 [0.156]
C_7	0.509 [0.495]	3.919 [3.929]	N_3–C_7	2.757 [2.765]
C_8	–0.539 [–0.539]	3.880 [3.879]	C_7–C_8	1.089 [1.091]
H_{11}	0.282 [0.281]	0.922 [0.922]	C_8–H_{11}	0.869 [0.869]
H_{12}	0.282 [0.281]	0.922 [0.922]	C_8–H_{12}	0.869 [0.869]
C_9	–0.597 [–0.596]	3.839 [3.839]	C_8–C_9	1.000 [1.000]
H_{13}	0.251 [0.250]	0.938 [0.938]	C_9–H_{13}	0.918 [0.919]
H_{14}	0.228 [0.227]	0.950 [0.949]	C_9–H_{14}	0.934 [0.934]
H_{15}	0.227 [0.227]	0.950 [0.950]	C_9–H_{15}	0.934 [0.934]
∑ CH_3CH_2CN	**0.173 [0.076]**			

Table S5.14. continued…

		Axial Ligands		
N_4	–0.450 [–0.514]	3.202 [3.077]	$Hg_1–N_4$	0.246 [0.114]
C_{10}	0.469 [0.457]	3.940 [3.946]	$N_4–C_{10}$	2.794 [2.799]
C_{11}	–0.537 [–0.536]	3.884 [3.883]	$C_{10}–C_{11}$	1.084 [1.086]
H_{16}	0.277 [0.276]	0.925 [0.925]	$C_{11}–H_{16}$	0.872 [0.873]
H_{17}	0.276 [0.276]	0.925 [0.925]	$C_{11}–H_{17}$	0.872 [0.873]
C_{12}	–0.597 [–0.596]	3.843 [3.842]	$C_{11}–C_{12}$	1.003 [1.002]
H_{18}	0.249 [0.248]	0.940 [0.939]	$C_{12}–H_{18}$	0.920 [0.920]
H_{19}	0.225 [0.225]	0.951 [0.950]	$C_{12}–H_{19}$	0.934 [0.934]
H_{20}	0.226 [0.226]	0.951 [0.950]	$C_{12}–H_{20}$	0.934 [0.935]
$\sum CH_3CH_2CN$	**0.138 [0.062]**			
N_5	–0.450 [–0.514]	3.201 [3.077]	$Hg_1–N_5$	0.246 [0.114]
C_{13}	0.469 [0.458]	3.940 [3.946]	$N–C_{13}$	2.794 [2.798]
C_{14}	–0.537 [–0.536]	3.884 [3.883]	$C_{13}–C_{14}$	1.084 [1.087]
H_{21}	0.277 [0.276]	0.925 [0.925]	$C_{14}–H_{21}$	0.872 [0.873]
H_{22}	0.277 [0.276]	0.925 [0.925]	$C_{14}–H_{22}$	0.872 [0.873]
C_{15}	–0.597 [–0.596]	3.843 [3.842]	$C_{14}–C_{15}$	1.003 [1.002]
H_{23}	0.249 [0.248]	0.940 [0.939]	$C_{15}–H_{23}$	0.920 [0.920]
H_{24}	0.226 [0.225]	0.951 [0.950]	$C_{15}–H_{24}$	0.934 [0.935]
H_{25}	0.226 [0.226]	0.951 [0.950]	$C_{15}–H_{25}$	0.934 [0.935]
$\sum CH_3CH_2CN$	**0.138 [0.062]**			
$\sum Hg(NCCH_3)_5$	**2.000 [2.000]**			

[a] The atom labeling scheme corresponds to that used in Figures 5.3b.

Table S5.15. Calculated Valences, Charges (NPA), and Wiberg Bond Orders for CH_3CH_2CN (C_s) using NBO Version 3.1 [Version 6.0][a]

Atom	Charge	Valences	Bond	Bond Order
N	–0.324 [–0.323]	3.034 [3.032]		
C_1	0.281 [0.279]	4.008 [4.007]	N–C_1	2.912 [2.912]
C_2	–0.521 [–0.517]	3.902 [3.900]	C_1–C_2	1.064 [1.064]
H_1	0.249 [0.249]	0.940 [0.940]	C_2–H_1	0.891 [0.891]
H_2	0.249 [0.249]	0.940 [0.940]	C_2–H_2	0.891 [0.891]
C_3	–0.597 [–0.595]	3.861 [3.861]	C_2–C_3	1.013 [1.012]
H_3	0.219 [0.218]	0.953 [0.593]	C_3–H_3	0.935 [0.935]
H_4	0.221 [0.221]	0.954 [0.593]	C_3–H_4	0.935 [0.936]
H_5	0.221 [0.221]	0.954 [0.593]	C_3–H_5	0.935 [0.936]
$\sum CH_3CH_2CN$	**0.000 [0.000]**			

[a] The atom labeling scheme corresponds to that used in Figures S5.6.

APPENDIX D

Chapter 6 Supporting Information

Noble-Gas Difluoride Complexes of Mercury(II); the Syntheses and Structures of $Hg(OTeF_5)_2 \cdot 1.5NgF_2$ (Ng = Xe, Kr) and $Hg(OTeF_5)_2$

Adapted with permission from: DeBackere, J.R., Mercier, H.P.A., and Schrobilgen, G.J. *Journal of the American Chemical Society*, **2014**, *136*, 3888–3903.

LIST OF FIGURES

LIST OF TABLES

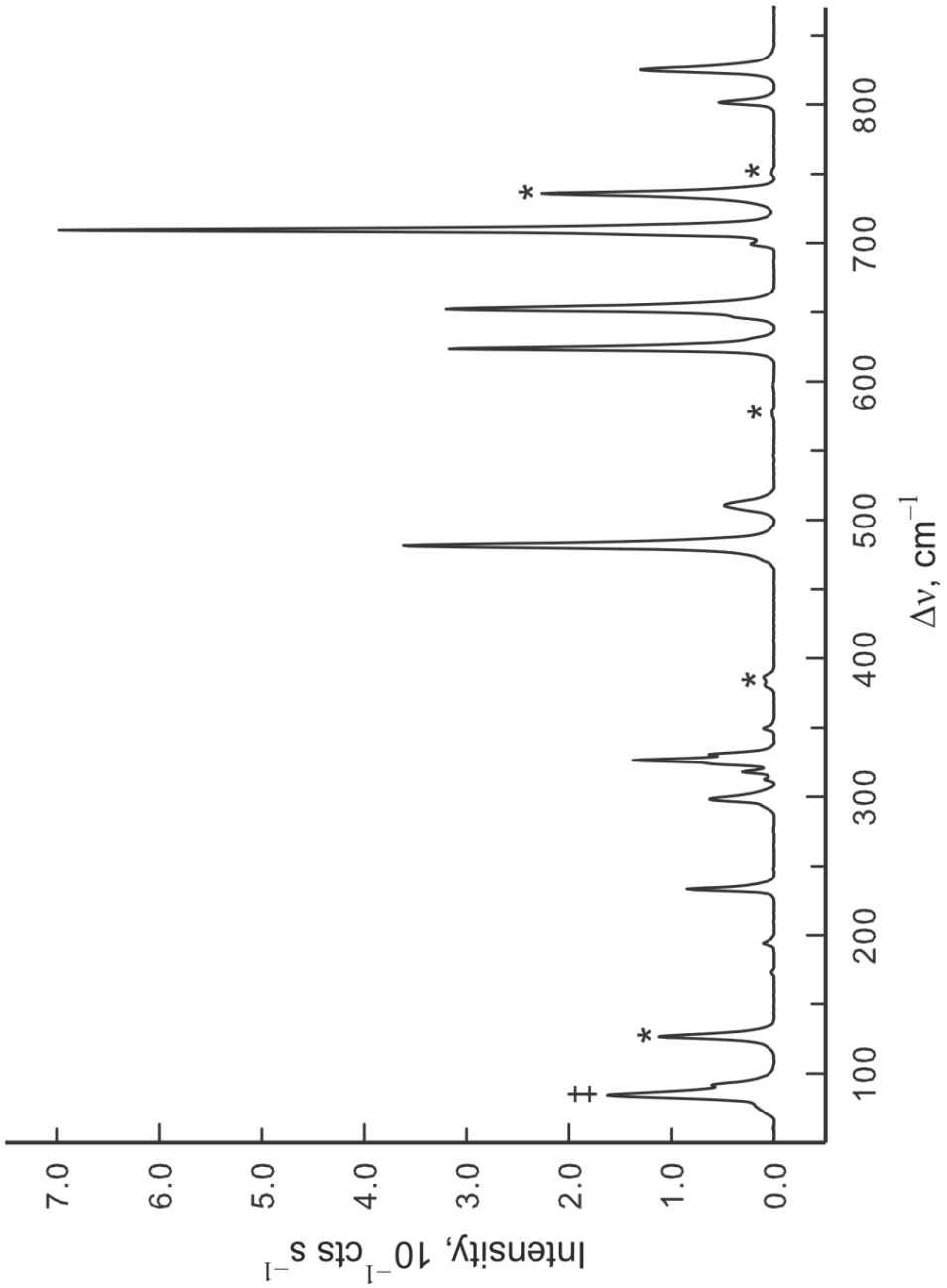

Figure S6.1. The Raman spectrum of pure $Hg(OTeF_5)_2$ recorded in a FEP sample tube at −150 °C using 1064-nm excitation. Symbols denote FEP sample tube lines (*) and an instrumental artifact (‡).

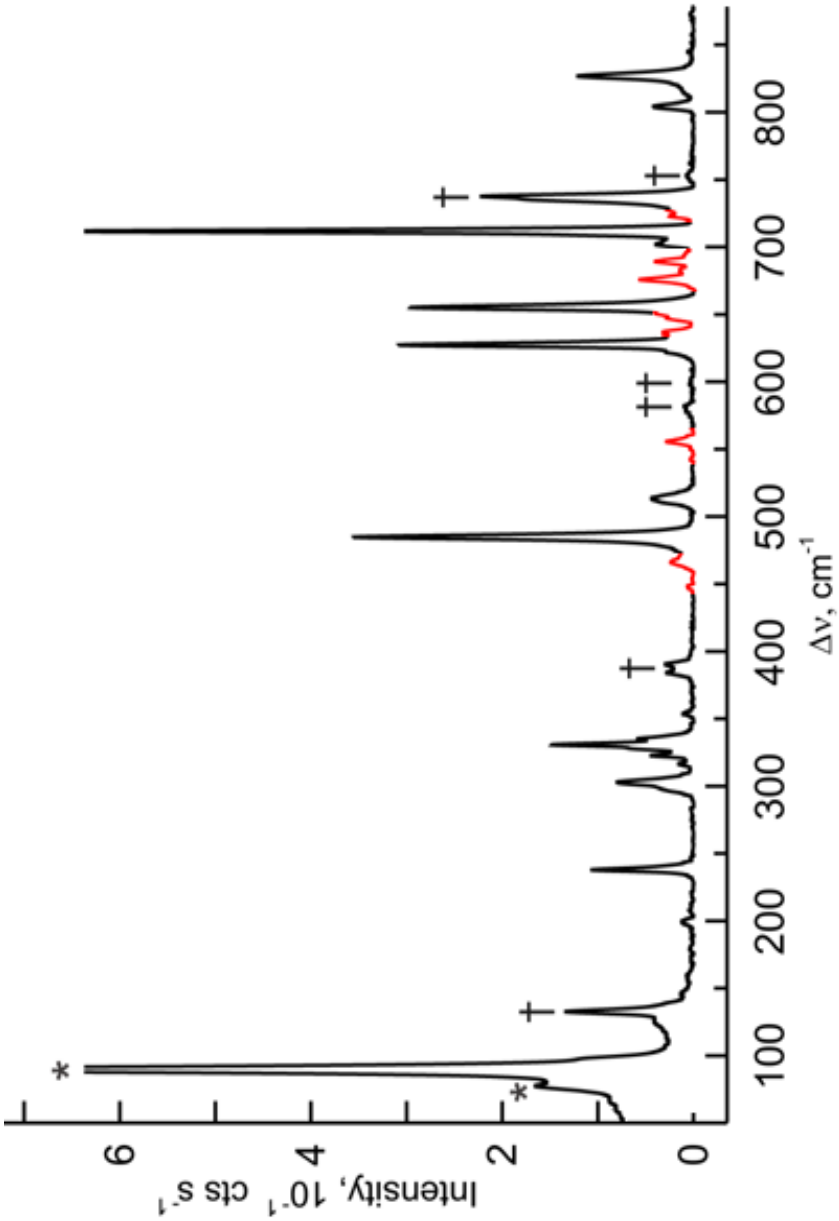

Figure S6.2. The Raman spectrum of $Hg(OTeF_5)_2$ sublimed at 135–165 °C recorded at −150 °C using 1064-nm excitation. Symbols denote FEP sample tube lines (†) and an instrumental artifact (*). Additional bands in red at 444(2), 462(4), 554(4), 576(2), 580(2), 634(6), 675(7), 682(2), 689(6), 693(2), 701(6), 721(4), 727(4) and at 1132(2), 2947(2), and 2990(2) cm^{-1} (not shown) are attributed to decomposition products that form upon sublimation.

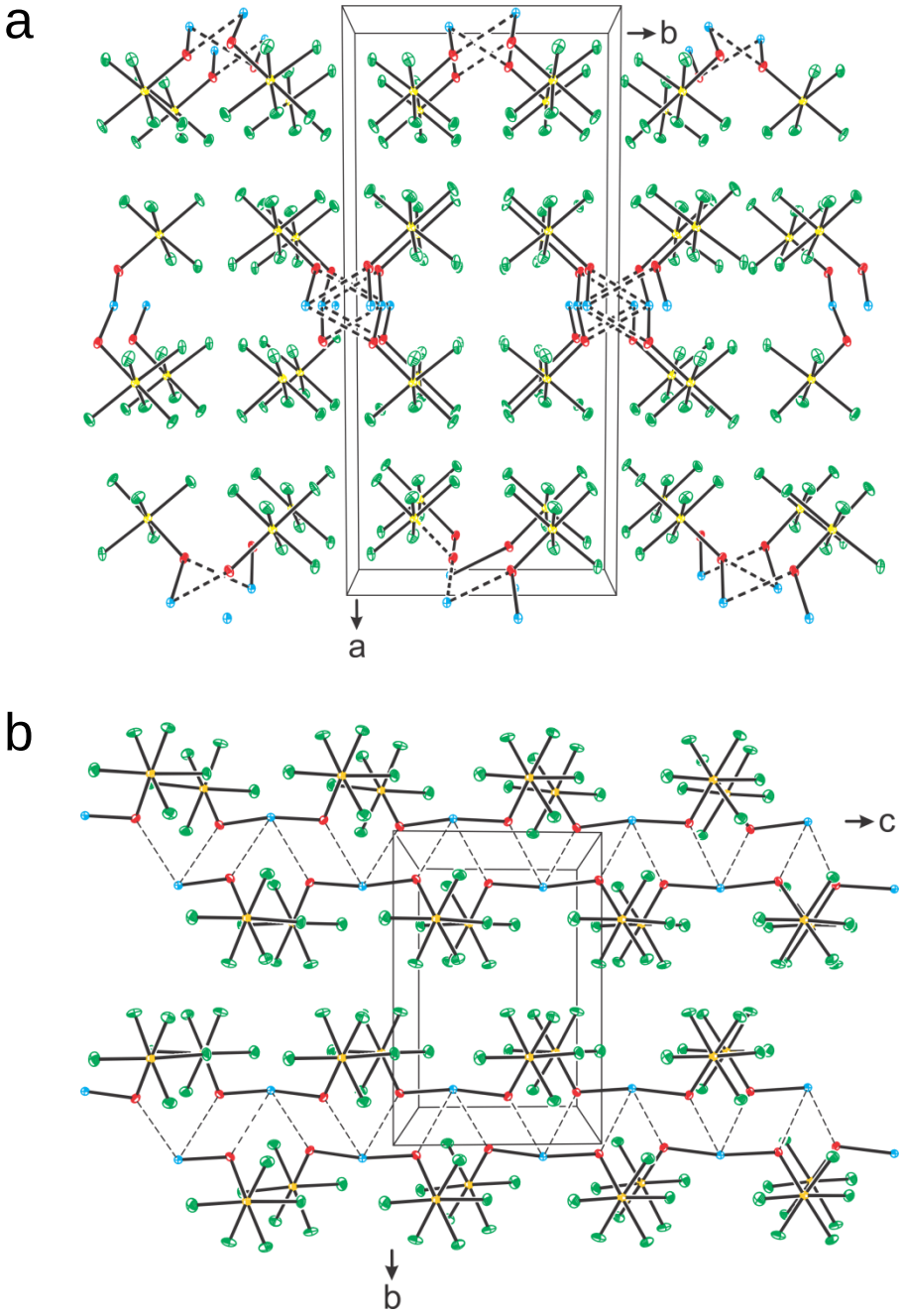

Figure S6.3. The crystallographic unit cell of $Hg(OTeF_5)_2$ showing the chains running parallel to the *c*-axis and viewed along (a) the *c*-axis and (b) the *a*-axis; thermal ellipsoids are shown at 50% probability level. Secondary bonding interactions are indicated by dashed lines drawn from the F and O atoms of adjacent $Hg(OTeF_5)_2$ units to the Hg(II) atoms.

Table S6.1. Experimental Raman Frequencies and Intensities of $Hg(OTeF_5)_2$ and Calculated (C_2) Vibrational Frequencies and Intensities of Monomeric $Hg(OTeF_5)_2$

exptl[a]	calcd[b] monomeric $Hg(OTeF_5)_2$				assgnts monomeric $Hg(OTeF_5)_2$[c] (C_2)
	B3LYP		PBE1PBE		
	def2-TZVPP	aug-cc-pVTZ	def2-TZVPP	aug-cc-pVTZ	
825(19)	788(12)[3]	776(14)[9]	824(11)[13]	813(13)[10]	$[\nu(Hg\text{-}O_2) + \nu(Hg\text{-}O_9)] - [\nu(Te_{10}\text{-}O_9) + \nu(Te_3\text{-}O_2)]$
801(8)	779(<1)[631]	769(<1)[588]	814(<1)[632]	805(<1)[599]	$[\nu(Hg\text{-}O_2) + \nu(Te_{10}\text{-}O_9)] - [\nu(Hg\text{-}O_9) + \nu(Te_3\text{-}O_2)]$
n.o.	692(4)[248]	684(2)[242]	720(2)[252]	713(<1)[250]	$[\nu(Te_3\text{-}F_8) + \nu(Te_{10}\text{-}F_{15})] - [\nu(Te_3\text{-}F_7) + \nu(Te_{10}\text{-}F_{14})]$
	691(<0.1)[266]	683(<1)[202]	719(<1)[192]	711(1)[150]	$[\nu(Te_3\text{-}F_5) + \nu(Te_{10}\text{-}F_{11})] - [\nu(Te_3\text{-}F_6) + \nu(Te_{10}\text{-}F_{13})]_{small}$
735(25)	691(20)[27]	683(24)[3]	719(18)[6]	711(21)[<1]	$[\nu(Te_3\text{-}F_5) + \nu(Te_{10}\text{-}F_{13})] - [\nu(Te_3\text{-}F_6) + \nu(Te_{10}\text{-}F_{11})]$
	690(3)[11]	682(2)[82]	717(1)[124]	710(1)[142]	$[\nu(Te_3\text{-}F_7) + \nu(Te_{10}\text{-}F_{15})] - [\nu(Te_3\text{-}F_8) + \nu(Te_{10}\text{-}F_{14})]$
699(3)	678(<1)[146]	671(<1)[120]	705(<1)[136]	698(<1)[123]	$\nu(Te_3\text{-}F_4) - \nu(Te_{10}\text{-}F_{12})$
709(100)	676(24)[3]	668(30)[10]	703(21)[14]	695(26)[10]	$\nu(Te_3\text{-}F_4) + \nu(Te_{10}\text{-}F_{12})$
652(46)	626(24)[<0.1]	618(29)[<0.1]	650(19)[<0.1]	641(24)[<0.1]	$[\nu(Te_3\text{-}F_7) + \nu(Te_3\text{-}F_8)] + [\nu(Te_{10}\text{-}F_{14}) + \nu(Te_{10}\text{-}F_{15})]$
647, sh	623(<1)[17]	615(2)[17]	647(2)[13]	638(2)[13]	$[\nu(Te_3\text{-}F_7) + \nu(Te_3\text{-}F_8)] - [\nu(Te_{10}\text{-}F_{14}) + \nu(Te_{10}\text{-}F_{15})]$
624(46)	607(14)[<1]	599(15)[2]	629(9)[2]	621(11)[2]	$[\nu(Te_3\text{-}F_6) + \nu(Te_{10}\text{-}F_{13})] + [\nu(Te_3\text{-}F_5) + \nu(Te_{10}\text{-}F_{11})]_{small}$
630, sh	607(<1)[20]	599(1)[15]	629(1)[14]	622(1)[12]	$[\nu(Te_3\text{-}F_6) + \nu(Te_3\text{-}F_5)] - [\nu(Te_{10}\text{-}F_{13}) + \nu(Te_{10}\text{-}F_{11})]$
511(7)	530(<1)[42]	531(<1)[39]	550(<1)[44]	553(<1)[45]	$[\nu(Hg\text{-}O_2) + \nu(Te_3\text{-}O_2)] - [\nu(Hg\text{-}O_9) + \nu(Te_{10}\text{-}O_9)]$
481(52) 472, sh	481(43)[1]	484(43)[4]	502(35)[6]	504(35)[4]	$[\nu(Hg\text{-}O_2) + \nu(Te_3\text{-}O_2)] + [\nu(Hg\text{-}O_9) + \nu(Te_{10}\text{-}O_9)]$
349(3)	327(<1)[<1]	321(<1)[3]	336(<1)[3]	330(<1)[2]	$\delta(Te_{10}\text{-}F_{4e})_{umb} + \delta(Te_3\text{-}F_{4e'})_{umb}$
	321(<0.1)[207]	315(<0.1)[190]	329(<0.1)[188]	323(<0.1)[189]	$\delta(O_2\text{-}Hg\text{-}O_9)_{o.o.p.}$
	321(<1)[66]	314(<1)[74]	330(<1)[64]	324(<1)[74]	$\delta(Te_{10}\text{-}F_{4e})_{umb} - \delta(Te_3\text{-}F_{4e'})_{umb}$
331(11)	316(1)[2]	309(<1)[12]	324(<1)[29]	317(<1)[14]	$[\delta(F_{12}\text{-}Te_{10}\text{-}F_{14}) + \delta(F_4\text{-}Te_3\text{-}F_8)] - [\delta(F_{12}\text{-}Te_{10}\text{-}F_{15}) + \delta(F_4\text{-}Te_3\text{-}F_7)] / \rho_w(F_{11}\text{-}Te_{10}\text{-}F_{13}) - \rho_w(F_5\text{-}Te_3\text{-}F_6)$
327(20)	316(<1)[29]	308(<1)[9]	324(<1)[10]	316(<1)[16]	$[\delta(F_{12}\text{-}Te_{10}\text{-}F_{14}) + \delta(F_4\text{-}Te_3\text{-}F_7)] - [\delta(F_{12}\text{-}Te_{10}\text{-}F_{15}) + \delta(F_4\text{-}Te_3\text{-}F_8)] / \rho_w(F_{11}\text{-}Te_{10}\text{-}F_{13}) + \rho_w(F_5\text{-}Te_3\text{-}F_6)$
324, sh	310(1)[33]	303(<1)[37]	318(<1)[42]	311(<1)[41]	$[\delta(F_{12}\text{-}Te_{10}\text{-}F_{13}) + \delta(F_4\text{-}Te_3\text{-}F_5)] - [\delta(F_{12}\text{-}Te_{10}\text{-}F_{11}) + \delta(F_4\text{-}Te_3\text{-}F_6)] / \rho_w(F_{14}\text{-}Te_{10}\text{-}F_{15}) + \rho_w(F_7\text{-}Te_3\text{-}F_8)$ + Torsion of $O_2\text{-}Hg\text{-}O_9$ around Hg
318(5)	309(2)[<1]	302(1)[2]	317(2)[2]	311(1)[2]	$[\delta(F_{12}\text{-}Te_{10}\text{-}F_{13}) + \delta(F_4\text{-}Te_3\text{-}F_6)] - [\delta(F_{12}\text{-}Te_{10}\text{-}F_{11}) + \delta(F_4\text{-}Te_3\text{-}F_5)] / \rho_w(F_{14}\text{-}Te_{10}\text{-}F_{15}) - \rho_w(F_7\text{-}Te_3\text{-}F_8)$ + Torsion of $O_2\text{-}Hg\text{-}O_9$ around Hg
312(1)	309(1)[14]	302(2)[9]	320(2)[2]	311(2)[10]	$[\delta(O_9\text{-}Te_{10}\text{-}F_{14}) + \delta(O_2\text{-}Te_3\text{-}F_8)] - \delta(F_{15}\text{-}Te_{10}\text{-}F_{12}) + \delta(F_4\text{-}Te_3\text{-}F_7)] / [\rho_w(F_{14}\text{-}Te_{10}\text{-}F_{15}) + \rho_w(F_7\text{-}Te_3\text{-}F_8)]_{small}$

Table S6.1. continued…

298(9)	286(<1)[<1]	277(<1)[<1]	294(1)[<1]	284(<1)[<1]	$[\delta(F_{11}\text{-}Te_{10}\text{-}F_{14}) + \delta(F_{13}\text{-}Te_{10}\text{-}F_{15})] + [\delta(F_6\text{-}Te_3\text{-}F_7) + \delta(F_5\text{-}Te_3\text{-}F_8)]$
	286(4)[<0.1]	277(2)[<0.1]	294(2)[<1]	284(2)[<0.1]	$[\delta(F_{11}\text{-}Te_{10}\text{-}F_{14}) + \delta(F_{13}\text{-}Te_{10}\text{-}F_{15})] - [\delta(F_6\text{-}Te_3\text{-}F_7) + \delta(F_5\text{-}Te_3\text{-}F_8)]$
n.o.	238(<0.1)[15]	233(<0.1)[13]	245(<0.1)[13]	240(<0.1)[13]	$\delta(F_4\text{-}Te_3\text{-}F_5) - \delta(F_{11}\text{-}Te_{10}\text{-}F_{12}) / \rho_w(F_{14}\text{-}Te_{10}\text{-}F_{15}) - \rho_w(F_7\text{-}Te_3\text{-}F_8)$
233(12)	224(4)[<1]	219(4)[<1]	231(3)[<1]	223(3)[<1]	$\delta(F_4\text{-}Te_3\text{-}F_5) + \delta(F_{11}\text{-}Te_{10}\text{-}F_{12}) / \rho_w(F_{14}\text{-}Te_{10}\text{-}F_{15}) + \rho_w(F_7\text{-}Te_3\text{-}F_8)$
194(2)	202(<0.1)[<1]	198(<0.1)[<1]	208(<0.1)[<0.1]	204(<0.1)[<1]	$[\rho_w(F_{11}\text{-}Te_{10}\text{-}F_{13}) + \rho_w(F_5\text{-}Te_3\text{-}F_6)] - [\rho_w(F_{12}\text{-}Te_{10}\text{-}O_9) + \rho_w(F_4\text{-}Te_3\text{-}O_2)]$
	201(<0.1)[<1]	197(<0.1)[<1]	207(<0.1)[<1]	203(<0.1)[<1]	$[\rho_t(F_5\text{-}Te_3\text{-}F_8) - \rho_t(F_7\text{-}Te_3\text{-}F_6)] + [\rho_t(F_{13}\text{-}Te_{10}\text{-}F_{15}) - \rho_t(F_{11}\text{-}Te_3\text{-}F_{14})]$
	201(<0.1)[<1]	196(<1)[<1]	206(<0.1)[<1]	201(<0.1)[<1]	$[\rho_t(F_5\text{-}Te_3\text{-}F_8) - \rho_t(F_7\text{-}Te_3\text{-}F_6)] - [\rho_t(F_{13}\text{-}Te_{10}\text{-}F_{15}) - \rho_t(F_{11}\text{-}Te_{10}\text{-}F_{14})]$
	192(<0.1)[<0.1]	189(<1)[<1]	199(<0.1)[<1]	193(<0.1)[<1]	$[\rho_t(O_2\text{-}Te_3\text{-}F_5) - \rho_t(F_4\text{-}Te_3\text{-}F_6)] + [\rho_t(O_9\text{-}Te_{10}\text{-}F_{11}) - \rho_t(F_{12}\text{-}Te_{10}\text{-}F_{13})]$
173(<1)	161(<0.1)[11]	157(<0.1)[9]	163(<0.1)[9]	160(<0.1)[9]	$[\rho_t(O_2\text{-}Te_3\text{-}F_7) - \rho_t(F_8\text{-}Te_3\text{-}F_4)] - [\rho_t(O_9\text{-}Te_{10}\text{-}F_{15}) - \rho_t(F_{12}\text{-}Te_{10}\text{-}F_{14})]$
	124(2)[<0.1]	123(2)[<0.1]	129(2)[<0.1]	126(2)[<0.1]	$[\rho_r(Te_3\text{-}F_4F_5F_6) + \rho_r(Te_{10}\text{-}F_{11}F_{12}F_{13})] / \rho_w(F_7\text{-}Te_3\text{-}F_8) + \rho_w(F_{14}\text{-}Te_{10}\text{-}F_{15})$
	100(<0.1)[4]	99(<0.1)[4]	103(<0.1)[4]	103(<0.1)[4]	$\delta(Hg\text{-}O_2\text{-}Te_3) - \delta(Hg\text{-}O_9\text{-}Te_{10})$
	89(<0.1)[1]	90(<0.1)[<1]	94(<0.1)[<1]	93(<0.1)[<1]	$\rho_w(O_2\text{-}Hg\text{-}O_9)$
	55(<1)[<0.1]	53(<1)[<0.1]	54(<1)[<0.1]	55(<1)[<0.1]	$\delta(Hg\text{-}O_2\text{-}Te_3) + \delta(Hg\text{-}O_9\text{-}Te_{10})$
	30(<0.1)[1]	38(<1)[1]	40(<1)[1]	39(<1)[1]	$\rho_r(Te_3\text{-}F_4F_5F_6O_2) - \rho_r(Te_{10}\text{-}F_{11}F_{12}F_{13}O_9)$
	9(<0.1)[<0.1]	18(<0.1)[<0.1]	17(<0.1)[<0.1]	18(<0.1)[<0.1]	$\rho_t(O_2\text{-}Hg\text{-}O_9)$
	16(<1)[<1]	17(<1)[<1]	14(<1)[<1]	16(<1)[<1]	$\rho_r(Te_3\text{-}F_4F_7F_8O_2) + \rho_r(Te_{10}\text{-}F_{12}F_{14}F_{15}O_9)$
n.o.	1(<0.1)[1]	6(<0.1)[<1]	6(<0.1)[<1]	6(<0.1)[<1]	$\rho_r(Te_3\text{-}F_4F_7F_8O_2) - \rho_r(Te_{10}\text{-}F_{12}F_{14}F_{15}O_9)$
127(16) 92(9)					lattice modes

[a] All Frequencies are given in cm^{-1}. Values in parentheses denote relative Raman intensities. The Raman spectrum was recorded in an FEP sample tube at −150 °C using 1064-nm excitation. The abbreviations denote shoulder (sh) and not observed (n.o.). [b] Values in parentheses are Raman intensities ($Å^4$ amu^{-1}) and values in square brackets are infrared intensities (km mol^{-1}). [c] The atom numbering corresponds to that used in Figure 6a and abbreviations denote out-of-plane (o.o.p.), equatorial (4e and 4e'), umbrella (umb), stretch (ν), bend (δ), twist (ρ_t), wag (ρ_w) and rock (ρ_r) vibrational modes. The subscript, "small", denotes a small contribution of the bracketed vibrational mode relative to the other coupled vibrational modes. For the atom labelling scheme, see Figure 6.6a.

Table S6.2. Experimental Raman Frequencies and Intensities of $Hg(OTeF_5)_2$ and the Calculated Vibrational Frequencies and Intensities of $[Hg(OTeF_5)_2]_3$

exptl [a,b,c] $Hg(OTeF_5)_2$	calcd [a,c,d] $[Hg(OTeF_5)_2]_3$	assgnts [e]
825(19)	824(27)[76]	$[\nu(Hg_{16}\text{-}O_{22}) - \nu(Te_{17}\text{-}O_{22})] + [\nu(Hg_{16}\text{-}O_{37}) - \nu(Te_{32}\text{-}O_{37})] + [\nu(Hg_1\text{-}O_{14}) - \nu(Te_9\text{-}O_{14})] + [\nu(Hg_1\text{-}O_7) - \nu(Te_2\text{-}O_7)] + [\nu(Hg_{25}\text{-}O_{30}) - \nu(Te_{24}\text{-}O_{30})] + [\nu(Hg_{25}\text{-}O_{44}) - \nu(Te_{39}\text{-}O_{44})]$
	816(2)[84]	*f*
	808(7)[695]	
n.o.	806(4)[112]	$[\nu(Hg_{16}\text{-}O_{22}) - \nu(Te_{17}\text{-}O_{22})] + [\nu(Hg_{16}\text{-}O_{37}) - \nu(Te_{32}\text{-}O_{37})] + [\nu(Hg_1\text{-}O_{14}) - \nu(Te_9\text{-}O_{14})] - [\nu(Hg_1\text{-}O_7) - \nu(Te_2\text{-}O_7)] + [\nu(Hg_{25}\text{-}O_{30}) - \nu(Te_{24}\text{-}O_{30})] - [\nu(Hg_{25}\text{-}O_{44}) - \nu(Te_{39}\text{-}O_{44})]$
801(8)	793(3)[663]	$[\nu(Hg_{16}\text{-}O_{22}) - \nu(Te_{17}\text{-}O_{22})] - [\nu(Hg_{16}\text{-}O_{37}) - \nu(Te_{32}\text{-}O_{37})]$
	787(1)[314]	$[\nu(Hg_{16}\text{-}O_{22}) - \nu(Te_{17}\text{-}O_{22})] + [\nu(Hg_{16}\text{-}O_{37}) - \nu(Te_{32}\text{-}O_{37})] - [\nu(Hg_1\text{-}O_{14}) - \nu(Te_9\text{-}O_{14})] - [\nu(Hg_{25}\text{-}O_{30}) - \nu\,(Te_{24}\text{-}O_{30})]$
735(25)	726(11)[2]	$[\nu(Te_{17}\text{-}F_{23}) + \nu(Te_{32}\text{-}F_{38})] - [\nu(Te_{17}\text{-}F_{19}) + \nu(Te_{32}\text{-}F_{34})] + [\nu(Te_{24}\text{-}F_{31}) - \nu(Te_{32}\text{-}F_{27})] + [\nu(Te_9\text{-}F_{15}) - \nu(Te_9\text{-}F_{11})]$
	725(<0.1)[218]	$[\nu(Te_{17}\text{-}F_{23}) + \nu(Te_{32}\text{-}F_{34})] - [\nu(Te_{17}\text{-}F_{19}) + \nu(Te_{32}\text{-}F_{38})] + [\nu(Te_{24}\text{-}F_{31}) - \nu(Te_{32}\text{-}F_{27})] + [\nu(Te_9\text{-}F_{11}) - \nu(Te_9\text{-}F_{15})]$
	724(<0.1)[235]	$[\nu(Te_{32}\text{-}F_{38}) + \nu(Te_{32}\text{-}F_{35}) + \nu(Te_{17}\text{-}F_{20}) + \nu(Te_{17}\text{-}F_{23})] - [\nu(Te_{32}\text{-}F_{34}) + \nu(Te_{32}\text{-}F_{36}) + \nu(Te_{17}\text{-}F_{19}) + \nu(Te_{17}\text{-}F_{21})] + [\nu(Te_{32}\text{-}F_{27}) - \nu\,(Te_{24}\text{-}F_{31})] + [\nu(Te_9\text{-}F_{11}) - \nu(Te_9\text{-}F_{15})]$
	721(<1)[191]	*f*
	718(13)[1]	
	711(30)[40]	
	710(3)[49]	
709(100)	709(6)[45]	$[\nu(Te_{32}\text{-}F_{33})_a - \nu(Te_{17}\text{-}F_{18})_a]$
	707(28)[61]	$[\nu(Te_{32}\text{-}F_{33})_a + \nu(Te_{17}\text{-}F_{18})_a]$
699(3)	719(15)[<1]	$[\nu(Te_{32}\text{-}F_{35}) + \nu(Te_{17}\text{-}F_{20})] - [\nu(Te_{32}\text{-}F_{36}) + \nu(Te_{17}\text{-}F_{21})] + [\nu(Te_{39}\text{-}F_{45}) + \nu(Te_{39}\text{-}F_{42}) + \nu(Te_2\text{-}F_5) + \nu(Te_2\text{-}F_8)] - [\nu(Te_{39}\text{-}F_{41}) + \nu(Te_{39}\text{-}F_{43}) + \nu(Te_2\text{-}F_4) + \nu(Te_2\text{-}F_6)]$
	719(<1)[392]	$[\nu(Te_{32}\text{-}F_{38}) + \nu(Te_{32}\text{-}F_{35}) + \nu(Te_{17}\text{-}F_{19}) + \nu(Te_{17}\text{-}F_{21})] - [\nu(Te_{32}\text{-}F_{34}) + \nu(Te_{32}\text{-}F_{36}) + \nu(Te_{17}\text{-}F_{20}) + \nu(Te_{17}\text{-}F_{23})] + [\nu(Te_2\text{-}F_4) + \nu(Te_2\text{-}F_6) + \nu(Te_{39}\text{-}F_{45}) + \nu(Te_{39}\text{-}F_{42})] - [\nu(Te_{39}\text{-}F_{41}) + \nu(Te_{39}\text{-}F_{43}) + \nu(Te_2\text{-}F_5) + \nu(Te_2\text{-}F_8)]$
	717(<1)[17]	$[\nu(Te_{32}\text{-}F_{36}) + \nu(Te_{17}\text{-}F_{20})] - [\nu(Te_{32}\text{-}F_{35}) + \nu(Te_{17}\text{-}F_{21})] + \nu(Te_2\text{-}F_4) - \nu(Te_{39}\text{-}F_{41})$
	716(<1)[249]	$[\nu(Te_{32}\text{-}F_{36}) + \nu(Te_{32}\text{-}F_{38}) + \nu(Te_{17}\text{-}F_{19}) + \nu(Te_{17}\text{-}F_{20})] - [\nu(Te_{32}\text{-}F_{34}) + \nu(Te_{32}\text{-}F_{35}) + \nu(Te_{17}\text{-}F_{21}) + \nu(Te_{17}\text{-}F_{23})] + [\nu(Te_9\text{-}F_{11}) + \nu(Te_{24}\text{-}F_{31}) + \nu(Te_{39}\text{-}F_{41})] - [\nu(Te_2\text{-}F_4) + \nu(Te_{24}\text{-}F_{27}) + \nu(Te_9\text{-}F_{15})]$
	714(2)[18]	$[\nu(Te_{32}\text{-}F_{36}) + \nu(Te_{17}\text{-}F_{21})] - [\nu(Te_{32}\text{-}F_{35}) + \nu(Te_{17}\text{-}F_{20})] + [\nu(Te_9\text{-}F_{10}) + \nu(Te_9\text{-}F_{11}) + \nu(Te_{24}\text{-}F_{26}) + \nu(Te_{24}\text{-}F_{27})] - [\nu(Te_2\text{-}F_4) + \nu(Te_{24}\text{-}F_{31}) + \nu(Te_{39}\text{-}F_{41}) + \nu(Te_9\text{-}F_{15})]$
	703(11)[153]	*f*
	703(2)[81]	
	703(2)[165]	
	702(3)[3]	
652(46)	654(50)[1]	$[\nu(Te_{32}\text{-}F_{4e'}) - \nu(Te_{17}\text{-}F_{18})] + [\nu(Te_{17}\text{-}F_{4e}) - \nu(Te_{32}\text{-}F_{33})] + [\nu(Te_{24}\text{-}F_{27}) + \nu(Te_{24}\text{-}F_{31}) + \nu(Te_9\text{-}F_{15}) + \nu(Te_9\text{-}F_{11})]$
647, sh	652(1)[4]	$[\nu(Te_{32}\text{-}F_{34}) + \nu(Te_{32}\text{-}F_{38})] + [\nu(Te_{17}\text{-}F_{19}) + \nu(Te_{17}\text{-}F_{23})] - [\nu(Te_{24}\text{-}F_{27}) + \nu(Te_{24}\text{-}F_{31}) + \nu(Te_9\text{-}F_{15}) + \nu(Te_9\text{-}F_{11})]$
	649(1)[10]	$[\nu(Te_{32}\text{-}F_{34}) + \nu(Te_{32}\text{-}F_{38})] - [\nu(Te_{17}\text{-}F_{19}) + \nu(Te_{17}\text{-}F_{23})] - [\nu(Te_{24}\text{-}F_{27}) + \nu(Te_{24}\text{-}F_{31})] + [\nu(Te_9\text{-}F_{15}) + \nu(Te_9\text{-}F_{11})]$
	649(<1)[10]	$[\nu(Te_{32}\text{-}F_{4e'}) - \nu(Te_{17}\text{-}F_{18})] + [\nu(Te_{17}\text{-}F_{4e}) - \nu(Te_{32}\text{-}F_{33})] + [\nu(Te_{24}\text{-}F_{27}) + \nu(Te_{24}\text{-}F_{31}) + \nu(Te_9\text{-}F_{15}) + \nu(Te_9\text{-}F_{11})]$
	647(7)[<1]	*f*
	647(<1)[11]	

Table S6.2. continued…

630, sh	641(2)[8]	$[\nu(Te_{32}\text{-}F_{35}) + \nu(Te_{32}\text{-}F_{36})] - [\nu(Te_{17}\text{-}F_{20}) + \nu(Te_{17}\text{-}F_{21})]$
624(45)	640(6)[<1]	$[\nu(Te_{32}\text{-}F_{35}) + \nu(Te_{32}\text{-}F_{36})] + [\nu(Te_{17}\text{-}F_{20}) + \nu(Te_{17}\text{-}F_{21})]$
	633(<1)[33]	
	631(10)[4]	
	630(<1)[15]	*f*
	628(15)[<1]	
	530(11)[7]	
511(7)	530(2)[81]	$[\nu(Hg_{16}\text{-}O_{22}) + \nu(Te_{17}\text{-}O_{22})] - [\nu(Hg_{16}\text{-}O_{37}) + \nu(Te_{32}\text{-}O_{37})] + [\nu(Hg_{1}\text{-}O_{7}) + \nu(Te_{2}\text{-}O_{7})] - [\nu(Hg_{1}\text{-}O_{14}) + \nu(Te_{9}\text{-}O_{14})] + [\nu(Hg_{25}\text{-}O_{30}) + \nu(Te_{24}\text{-}O_{30})]_{small} - [\nu(Hg_{25}\text{-}O_{44}) + \nu(Te_{39}\text{-}O_{44})]_{small}$
	528(6)[11]	$[\nu(Hg_{16}\text{-}O_{22}) + \nu(Te_{17}\text{-}O_{22})] - [\nu(Hg_{16}\text{-}O_{37}) + \nu(Te_{32}\text{-}O_{37})]_{small} - [\nu(Hg_{1}\text{-}O_{7}) + \nu(Te_{2}\text{-}O_{7})] + [\nu(Hg_{1}\text{-}O_{14}) + \nu(Te_{9}\text{-}O_{14})] - [\nu(Hg_{25}\text{-}O_{30}) + \nu(Te_{24}\text{-}O_{30})] + [\nu(Hg_{25}\text{-}O_{44}) + \nu(Te_{39}\text{-}O_{44})]$
	507(7)[27]	*f*
481(52)	506(75)[3]	$[\nu(Hg_{16}\text{-}O_{22}) + \nu(Te_{17}\text{-}O_{22})] + [\nu(Hg_{16}\text{-}O_{37}) + \nu(Te_{32}\text{-}O_{37})] + [\nu(Hg_{1}\text{-}O_{7}) + \nu(Te_{2}\text{-}O_{7})] + [\nu(Hg_{1}\text{-}O_{14}) + \nu(Te_{9}\text{-}O_{14})] + [\nu(Hg_{25}\text{-}O_{30}) + \nu(Te_{24}\text{-}O_{30})] + [\nu(Hg_{25}\text{-}O_{44}) + \nu(Te_{39}\text{-}O_{44})]$
472, sh	516(3)[138]	$[\nu(Hg_{16}\text{-}O_{22}) + \nu(Te_{17}\text{-}O_{22})] + [\nu(Hg_{16}\text{-}O_{37}) + \nu(Te_{32}\text{-}O_{37})] - [\nu(Hg_{1}\text{-}O_{7}) + \nu(Te_{2}\text{-}O_{7})] - [\nu(Hg_{1}\text{-}O_{14}) + \nu(Te_{9}\text{-}O_{14})] - [\nu(Hg_{25}\text{-}O_{30}) + \nu(Te_{24}\text{-}O_{30})] - [\nu(Hg_{25}\text{-}O_{44}) + \nu(Te_{39}\text{-}O_{44})]$
349(2)	341(<1)[5]	$\delta(Te_{17}F_{4e})_{umb} + \delta(Te_{32}F_{4e'})_{umb} + [\delta(Te_{9}F_{4e})_{umb} + \delta(Te_{2}F_{4e'})_{umb} + \delta(Te_{24}F_{4e})_{umb} + \delta(Te_{39}F_{4e'})_{umb}]$
	334(<1)[1]	
	334(<0.1)[2]	*f*
331(9)	332(<0.1)[137]	$\delta(O_{22}\text{-}Hg_{16}\text{-}O_{37})_{o.o.p.} + [\delta(O_{7}\text{-}Hg_{1}\text{-}O_{14})_{o.o.p} + \delta(O_{30}\text{-}Hg_{25}\text{-}O_{44})_{o.o.p}]_{small}$
	331(<0.1)[219]	$\delta(Te_{17}F_{4e})_{umb} + \delta(Te_{32}F_{4e'})_{umb} - [\delta(Te_{9}F_{4e})_{umb} + \square\delta(Te_{2}F_{4e'})_{umb} + \delta(Te_{24}F_{4e})_{umb} + \delta(Te_{39}F_{4e'})_{umb}]$
327(20)	328(<0.1)[364]	$\delta(Te_{17}F_{4e})_{umb} - \delta(Te_{32}F_{4e'})_{umb} + [\delta(Te_{2}F_{4e'})_{umb} + \delta(Te_{24}F_{4e})_{umb}] - [\delta(Te_{9}F_{4e})_{umb} + \delta(Te_{39}F_{4e'})_{umb}]$
	327(<1)[22]	$\delta(Te_{17}F_{4e})_{umb} - \delta(Te_{32}F_{4e'})_{umb} + [\delta(Te_{9}F_{4e})_{umb} + \square\ \delta(Te_{39}F_{4e'})_{umb}] - [\delta(Te_{2}F_{4e'})_{umb} + \delta(Te_{24}F_{4e})_{umb}]$
	327(<0.1)[364]	
	327(<1)[18]	*f*
	324(<1)[<1]	
324, sh	324(<0.1)[52]	$\delta(O_{22}\text{-}Hg_{16}\text{-}O_{37})_{o.o.p} + \delta(O_{22}\text{-}Te_{17}\text{-}F_{23}) - \delta(O_{37}\text{-}Te_{32}\text{-}F_{38})_{.} + [\delta(O_{30}\text{-}Hg_{25}\text{-}O_{44})_{o.o.p.} - \delta(O_{9}\text{-}Hg_{1}\text{-}O_{14})_{o.o.p.} / [\rho_{w}(F_{40}\text{-}Te_{39}\text{-}O_{44}) + \rho_{w}(F_{41}\text{-}Te_{39}\text{-}F_{45})] - [\rho_{w}(F_{3}\text{-}Te_{2}\text{-}O_{7}) + \rho_{w}(F_{4}\text{-}Te_{2}\text{-}F_{8})]$
	323(<1)[15]	$\rho_{t}(O_{22}\text{-}Hg_{16}\text{-}O_{37})$
	323(2)[7]	*f*
318(5)	320(2)[17]	$[\delta(F_{33}\text{-}Te_{32}\text{-}F_{38}) + \delta(F_{34}\text{-}Te_{32}\text{-}O_{37})] + [\delta(F_{18}\text{-}Te_{17}\text{-}F_{23}) + \delta(F_{19}\text{-}Te_{17}\text{-}O_{22})]$
	320(<0.1)[11]	$[\delta(F_{33}\text{-}Te_{32}\text{-}F_{38}) + \delta(F_{34}\text{-}Te_{32}\text{-}O_{37})] - [\delta(F_{18}\text{-}Te_{17}\text{-}F_{23}) + \delta(F_{19}\text{-}Te_{17}\text{-}O_{22})]$
	319(<1)[46]	
	319(<1)[29]	
	318(1)[<1]	
	317(<1)[48]	*f*
	317(<1)[2]	
	316(<1)[28]	
	316(2)[1]	

Table S6.2. continued…

312(1)	315(6)[1]	$[\delta(F_{18}\text{-}Te_{17}\text{-}F_{20}) + \delta(F_{33}\text{-}Te_{32}\text{-}F_{35})] - [\delta(F_{18}\text{-}Te_{17}\text{-}F_{21}) + \delta(F_{33}\text{-}Te_{32}\text{-}F_{36})] / [\rho_w(F_{34}\text{-}Te_{32}\text{-}F_{38}) + \rho_w(F_{19}\text{-}Te_{17}\text{-}F_{23})] + [\rho_w(F_{26}\text{-}Te_{24}\text{-}O_{30}) + \rho_w(F_{10}\text{-}Te_9\text{-}O_{14})]$
	315(<1)[<0.1]	$[\delta(F_{18}\text{-}Te_{17}\text{-}F_{20}) + \delta(F_{33}\text{-}Te_{32}\text{-}F_{35})] - [\delta(F_{18}\text{-}Te_{17}\text{-}F_{21}) + \delta(F_{33}\text{-}Te_{32}\text{-}F_{36})] / [\rho_w(F_{34}\text{-}Te_{32}\text{-}F_{38}) + \rho_w(F_{19}\text{-}Te_{17}\text{-}F_{23})]$
	314(<1)[12]	*f*
298(9)	295(2)[<1]	$[\delta(F_{34}\text{-}Te_{32}\text{-}F_{35}) + \delta(F_{36}\text{-}Te_{32}\text{-}F_{38})] + [\delta(F_{19}\text{-}Te_{17}\text{-}F_{20}) + \delta(F_{21}\text{-}Te_{17}\text{-}F_{23})]$
	295(1) [<0.1]	$[\delta(F_{34}\text{-}Te_{32}\text{-}F_{35}) + \delta(F_{36}\text{-}Te_{32}\text{-}F_{38})] - [\delta(F_{19}\text{-}Te_{17}\text{-}F_{20}) + \delta(F_{21}\text{-}Te_{17}\text{-}F_{23})]$
	294(2)[<0.1]	*f*
	294(<1)[<1]	
	293(1)[<0.1]	
	292(1)[<1]	
	244(<0.1)[3]	
n.o.	245(<1)[<1]	$[\rho_w(F_{19}\text{-}Te_{17}\text{-}F_{23}) + \rho_w(F_{35}\text{-}Te_{32}\text{-}F_{36})] - [\rho_w(F_{34}\text{-}Te_{32}\text{-}F_{38}) + \rho_w(F_{20}\text{-}Te_{17}\text{-}F_{21})] + \rho_w(F_{42}\text{-}Te_{39}\text{-}F_{43}) - \rho_w(F_5\text{-}Te_2\text{-}F_6) + \rho_w(F_{12}\text{-}Te_9\text{-}F_{13}) + \rho_w(F_{28}\text{-}Te_{24}\text{-}F_{29})$
	244(<0.1)[4]	$[\rho_w(F_{34}\text{-}Te_{32}\text{-}F_{38}) + \rho_w(F_{35}\text{-}Te_{32}\text{-}F_{36})] - [\rho_w(F_{20}\text{-}Te_{17}\text{-}F_{21}) + \rho_w(F_{19}\text{-}Te_{17}\text{-}F_{23})] + [\rho_w(F_{42}\text{-}Te_{39}\text{-}F_{43}) - \rho_w(F_5\text{-}Te_2\text{-}F_6)] + [\rho_w(F_{12}\text{-}Te_9\text{-}F_{13}) - \rho_w(F_{28}\text{-}Te_{24}\text{-}F_{29})]$
	234(<0.1)[7]	$[\delta(F_{34}\text{-}Te_{32}\text{-}F_{36}) - \delta(F_{35}\text{-}Te_{32}\text{-}F_{38}) - \rho_w(F_{33}\text{-}Te_{32}\text{-}O_{37})] + [\delta(F_{19}\text{-}Te_{17}\text{-}F_{21}) - \delta(F_{20}\text{-}Te_{17}\text{-}F_{23}) - \rho_w(F_{18}\text{-}Te_{17}\text{-}O_{22})]$
	232(<1)[1]	*f*
233(12)	232(6)[1]	$[\delta(F_{34}\text{-}Te_{32}\text{-}F_{36}) - \delta(F_{35}\text{-}Te_{32}\text{-}F_{38})] - [\delta(F_{20}\text{-}Te_{17}\text{-}F_{23}) + \delta(F_{19}\text{-}Te_{17}\text{-}F_{21})] + [\rho_w(F_{42}\text{-}Te_{39}\text{-}F_{43}) + \rho_w(F_{28}\text{-}Te_{24}\text{-}F_{29}) + \rho_w(F_{27}\text{-}Te_{24}\text{-}F_{31}) + \rho_w(F_{12}\text{-}Te_9\text{-}F_{13}) + \rho_w(F_{11}\text{-}Te_9\text{-}F_{15}) + \rho_w(F_5\text{-}Te_2\text{-}F_6)$
	209(<0.1)[<1]	*f*
	208(<0.1)[<1]	
	207(<0.1)[<1]	
	207(<0.1)[<0.1]	
n.o.	207(<0.1)[<1]	$[\rho_w(F_{35}\text{-}Te_{32}\text{-}F_{36}) + \rho_w(F_{19}\text{-}Te_{17}\text{-}F_{23})] - [\rho_w(F_{34}\text{-}Te_{32}\text{-}F_{38}) + \rho_w(F_{20}\text{-}Te_{17}\text{-}F_{21})]$
	206(<0.1)[<0.1]	$[\rho_w(F_{35}\text{-}Te_{32}\text{-}F_{36}) + \rho_w(F_{20}\text{-}Te_{17}\text{-}F_{21})] - [\rho_w(F_{34}\text{-}Te_{32}\text{-}F_{38}) + \rho_w(F_{19}\text{-}Te_{17}\text{-}F_{23})]$
	195(<0.1)[<0.1]	$[\rho_w(F_{35}\text{-}Te_{32}\text{-}F_{36}) + \rho_w(F_{19}\text{-}Te_{17}\text{-}F_{23})] - [\rho_w(F_{20}\text{-}Te_{17}\text{-}F_{21}) + \rho_w(F_{34}\text{-}Te_{32}\text{-}F_{38})] / \delta(O_{22}\text{-}Hg_{16}\text{-}O_{37})_{o.o.p.}$
	201(<1)[<0.1]	*f*
	201(<0.1)[<0.1]	
194(2)	191(<0.1)[<0.1]	$[\rho_w(F_{35}\text{-}Te_{32}\text{-}F_{36}) + \rho_w(F_{20}\text{-}Te_{17}\text{-}F_{21})] - [\rho_w(F_{34}\text{-}Te_{32}\text{-}F_{38}) + \rho_w(F_{19}\text{-}Te_{17}\text{-}F_{23})] / \rho_t(O_{22}\text{-}Hg_{16}\text{-}O_{37}) + [\rho_w(O_{14}\text{-}Te_9\text{-}F_{10}) + \rho_w(F_{15}\text{-}Te_9\text{-}F_{11}) + \rho_w(O_{30}\text{-}Te_{24}\text{-}F_{26}) + \rho_w(F_{27}\text{-}Te_{24}\text{-}F_{31}) + \rho_w(F_{12}\text{-}Te_9\text{-}F_{13}) + \rho_w(F_{28}\text{-}Te_{24}\text{-}F_{29})]$
	190(<1)[<0.1]	$[\rho_w(F_{35}\text{-}Te_{32}\text{-}F_{36}) + \rho_w(F_{20}\text{-}Te_{17}\text{-}F_{21})] - [\rho_w(F_{34}\text{-}Te_{32}\text{-}F_{38}) + \rho_w(F_{19}\text{-}Te_{17}\text{-}F_{23})] / \rho_t(O_{22}\text{-}Hg_{16}\text{-}O_{37}) - [\rho_w(O_{14}\text{-}Te_9\text{-}F_{10}) + \rho_w(F_{15}\text{-}Te_9\text{-}F_{11}) + \rho_w(F_{12}\text{-}Te_9\text{-}F_{13}) + \rho_w(O_{30}\text{-}Te_{24}\text{-}F_{26}) + \rho_w(F_{27}\text{-}Te_{24}\text{-}F_{31}) + \rho_w(F_{28}\text{-}Te_{24}\text{-}F_{29})]$
	189(<0.1)[<0.1]	*f*
173(<1)	167(<0.1)[<1]	$[\rho_w(F_{18}\text{-}Te_{17}\text{-}O_{22}) - \rho_w(F_{33}\text{-}Te_{32}\text{-}O_{37})] / [\rho_w(F_{35}\text{-}Te_{32}\text{-}F_{36}) - \rho_w(F_{19}\text{-}Te_{17}\text{-}F_{21})]$
	163(<0.1)[14]	*f*
	163(<0.1)[<1]	
	128(<1)[<1]	

Table S6.2. continued…

127(16)	129(<1)[2]	$[\rho_r(Te_{17}F_{4e}F_a) + \rho_r(Te_{32}F_{4e'}F_{a'})] - [\rho_r(Te_2F_{4e'}F_{a'}) + \rho_r(Te_9F_{4e}F_a)] - [\rho_r(T_{24}F_{4e}F_a) + \rho_r(Te_{39}F_{4e'}F_{a'})]$
	127(4) [<0.1]	$[\rho_r(Te_{17}F_{4e}F_a) + \rho_r(Te_{32}F_{4e'}F_{a'})] + [\rho_r(Te_2F_{4e'}F_{a'}) + \rho_r(Te_9F_{4e}F_a)] + [\rho_r(T_{24}F_{4e}F_a) + \rho_r(Te_{39}F_{4e'}F_{a'})]$
	97(<1)[17]	$\delta(O_{37}\text{-}Hg_{16}\text{-}O_{22})_{i.p.} - [\delta(O_{14}\text{-}Hg_1\text{-}O_7]_{i.p.} + \delta(O_{30}\text{-}Hg_{25}\text{-}O_{44}]_{i.p.}]$
92(9)	94(<0.1)[3]	$\delta(O_{37}\text{-}Hg_{16}\text{-}O_{22})_{o.o.p.} + [\delta((O_{14}\text{-}Hg_1\text{-}O_7)_{o.o.p.} + \delta(O_{30}\text{-}Hg_{25}\text{-}O_{44}]_{o.o.p.}]$
	93(2)[1]	$\delta(O_{37}\text{-}Hg_{16}\text{-}O_{22})_{i.p.}$
	95(<1)[5]	coupled deformation and torsion modes of $[Hg(OTeF_5)_2]_3$
	90(<1)[<1]	
	90(<1)[<0.1]	
	68(<1)[<0.1]	
	67(<1)[2]	
	62(<1)[3]	
	47(<1)[<1]	
	41(<1)[<0.1]	
	40(<1)[2]	
	37(<1)[<0.1]	
	35(<1)[<1]	
	34(<1)[1]	
	30(<1)[<1]	
	26(<0.1)[1]	
	25(<0.1)[<1]	
	22(<0.1)[<1]	
	22(<0.1)[<0.1]	
	16(<1)[<1]	
	16(<0.1)[<0.1]	
	16(<0.1)[<0.1]	
	15(<0.1)[<0.1]	
	14(<0.1)[<0.1]	
	12(<0.1)[<1]	
	11(<0.1)[<0.1]	
	11(<0.1)[<0.1]	
	10(<0.1)[<0.1]	
	10(<0.1)[<0.1]	
	7(<0.1)[<0.1]	
	5(<0.1)[<1]	
	5(<0.1)[<0.1]	

Table S6.2. continued…

[a] Frequencies are given in cm^{-1}. [b] Values in parentheses denote relative Raman intensities. The Raman spectrum was recorded in an FEP sample tube at −155 °C using 1064-nm excitation. The abbreviations denote shoulder (sh) and not observed (n.o.). [c] The abbreviations denote out-of-plane (o.o.p.) and in-plane (i.p.) where the planes contain the (Te-O–Hg–O-Te) group, umbrella (umb), equatorial (4e and 4e´), axial (a and a´), stretch (ν), bend (δ), twist (ρ_t), wag (ρ_w) and rock (ρ_r) modes. [d] Values in parentheses denote calculated Raman intensities ($Å^4$ amu^{-1}) while values in square brackets denote calculated infrared intensities (km mol^{-1}). [e] Assignments are for the energy-minimized geometry using the PBE0/def2-TVZPP; only the mode assignments that involve the central $Hg(OTeF_5)_2$ unit are provided. For the atom labelling scheme, see Figure 6.6b. [f] Modes belonging to the terminal $Hg(OTeF_5)_2$ units of the $[Hg(OTeF_5)_2]_3$ trimer.

Table S6.3. Experimental Raman Frequencies and Intensities of $Hg(OTeF_5)_2 \cdot 1.5XeF_2$ and the Calculated Vibrational Frequencies and Intensities of $[Hg(OTeF_5)_2]_3 \cdot 2XeF_2$

exptl[a,b,c] $Hg(OTeF_5)_2 \cdot 1.5XeF_2$	calcd[a,d] $[Hg(OTeF_5)_2]_3 \cdot 2XeF_2$	*Assgnts*[e]
	834(5)[143] 833(21)[47]	*f*
853(5)	828(9)[155]	$[\nu(Hg_{12}\text{-}O_{28}) - \nu(Te_{14}\text{-}O_{28})] + [\nu(Hg_{12}\text{-}O_{31}) - \nu(Te_{15}\text{-}O_{31})]$
	822(3)[522]	
825(7)	817(2)[547]	$[\nu(Hg_{12}\text{-}O_{28}) - \nu(Te_{14}\text{-}O_{28})] - [\nu(Hg_{12}\text{-}O_{31}) - \nu(Te_{15}\text{-}O_{31})] + [\nu(Hg_{32}\text{-}O_{48}) - \nu(Te_{35}\text{-}O_{48})] - [\nu(Hg_{32}\text{-}O_{45}) - \nu(Te_{34}\text{-}O_{45})]$
	815(2)[346]	$[\nu(Hg_{12}\text{-}O_{28}) - \nu(Te_{14}\text{-}O_{28})] - [\nu(Hg_{12}\text{-}O_{31}) - \nu(Te_{15}\text{-}O_{31})] - [\nu(Hg_{32}\text{-}O_{48}) - \nu(Te_{35}\text{-}O_{48})] + [\nu(Hg_{32}\text{-}O_{45}) - \nu(Te_{34}\text{-}O_{45})]$
$753(<1)_{broad}$	721(16)[10]	$[\nu(Te_{14}\text{-}F_{21}) - \nu(Te_{14}\text{-}F_{22})] + [\nu(Te_{35}\text{-}F_{42}) + \nu(Te_{33}\text{-}F_2)] - [\nu(Te_{35}\text{-}F_{43}) + \nu(Te_{33}\text{-}F_1)]$
	720(10)[195] 718(3)[149]	*f*
722(2) 711(<1)	717(4)[102]	$[\nu(Te_{15}\text{-}F_{25}) - \nu(Te_{15}\text{-}F_{26})]_{small} + [\nu(Te_6\text{-}F_{10}) + \nu(Te_6\text{-}F_9)]$
	716(5)[291]	$[\nu(Te_{14}\text{-}F_{21}) + \nu(Te_{15}\text{-}F_{25}) - [\nu(Te_{14}\text{-}F_{22}) + \nu(Te_{15}\text{-}F_{26})] + [\nu(Te_{35}\text{-}F_{43}) + \nu(Te_{34}\text{-}F_{36})] - [\nu(Te_{35}\text{-}F_{42}) + \nu(Te_{34}\text{-}F_{37}) + \nu(Te_{33}\text{-}F_4)]$
	715(9)[278]	$[\nu(Te_{14}\text{-}F_{21}) + \nu(Te_{15}\text{-}F_{26}) - [\nu(Te_{14}\text{-}F_{22}) + \nu(Te_{15}\text{-}F_{25})] + [\nu(Te_{34}\text{-}F_{38}) + \nu(Te_{35}\text{-}F_{46})] - [\nu(Te_{34}\text{-}F_{39}) + \nu(Te_{35}\text{-}F_{44}) + \nu(Te_{33}\text{-}F_4) + \nu(Te_6\text{-}F_9)]$
	714(2)[135]	$[\nu(Te_{14}\text{-}F_{21}) + \nu(Te_{15}\text{-}F_{26})] - [\nu(Te_{14}\text{-}F_{22}) + \nu(Te_{15}\text{-}F_{25})] + [\nu(Te_{34}\text{-}F_{39}) + \nu(Te_{35}\text{-}F_{43})] - [\nu(Te_{35}\text{-}F_{42}) + \nu(Te_{34}\text{-}F_{38}) + \nu(Te_6\text{-}F_9)]$
	713(2)[13]	$[\nu(Te_{15}\text{-}F_{29}) - \nu(Te_{15}\text{-}F_{27})] + [\nu(Te_{35}\text{-}F_{43}) + \nu(Te_{35}\text{-}F_{44}) + \nu(Te_{34}\text{-}F_{37})] - [\nu(Te_{35}\text{-}F_{42}) + \nu(Te_{34}\text{-}F_{36})]$
	713(2)[243]	$[\nu(Te_{15}\text{-}F_{29}) + \nu(Te_{14}\text{-}F_{21})] - [\nu(Te_{15}\text{-}F_{27})] + [\nu(Te_{35}\text{-}F_{44}) + \nu(Te_{34}\text{-}F_{36}) - [\nu(Te_{34}\text{-}F_{37}) + \nu(Te_{35}\text{-}F_6)]$
	711(<1)[21]	$[\nu(Te_{14}\text{-}F_{21}) + \nu(Te_{15}\text{-}F_{27}) + \nu(Te_{15}\text{-}F_{25})] - [\nu(Te_{14}\text{-}F_{22}) + \nu(Te_{15}\text{-}F_{29})]_{small} + [\nu(Te_{35}\text{-}F_{44}) + \nu(Te_{34}\text{-}F_{37})] - [\nu(Te_{35}\text{-}F_{46}) + \nu(Te_{34}\text{-}F_{37}) + \nu(Te_{34}\text{-}F_{39}) + \nu(Te_{34}\text{-}F_{36}) + \nu(Te_{34}\text{-}F_{39})]$
	710(2)[152]	*f*
702(3)	695(<1)[205]	$\nu(Te_{14}\text{-}F_{18}) - \nu(Te_{14}\text{-}F_{19})$
	701(4)[29] 701(11)[64]	*f*
685(29)	705(13)[8]	$[\nu(Te_{14}\text{-}F_{24})_a + \nu(Te_{35}\text{-}F_{47})_a]$
	699(18)[18]	$\nu(Te_{15}\text{-}F_{30})_a$
	699(4)[187] 690(19)[71] 647(<1)[1]	*f*
640(10) 635(2)	644(38)[4]	$[\nu(Te_{14}\text{-}F_{18}) + \nu(Te_{14}\text{-}F_{19}) + \nu(Te_{14}\text{-}F_{21}) + \nu(Te_{14}\text{-}F_{22}) + \nu(Te_{15}\text{-}F_{25}) + \nu(Te_{15}\text{-}F_{26}) + \nu(Te_{15}\text{-}F_{27}) + \nu(Te_{15}\text{-}F_{29})] - [\nu(Te_{14}\text{-}F_{24})_a + \nu(Te_{15}\text{-}F_{30})] + [\nu(Te_{33}\text{-}F_1) + \nu(Te_{33}\text{-}F_2) + \nu(Te_{35}\text{-}F_{42}) + \nu(Te_{35}\text{-}F_{43}) + \nu(Te_{35}\text{-}F_{44}) + \nu(Te_{35}\text{-}F_{45}) + \nu(Te_{34}\text{-}F_{36}) + \nu(Te_{34}\text{-}F_{37}) + \nu(Te_{34}\text{-}F_{38})] - [\nu(Te_{33}\text{-}F_5) + \nu(Te_{35}\text{-}F_{47})]$
	643(2)[11]	$[\nu(Te_{14}\text{-}F_{18}) + \nu(Te_{14}\text{-}F_{19}) + \nu(Te_{14}\text{-}F_{21}) + \nu(Te_{14}\text{-}F_{22}) + \nu(Te_{15}\text{-}F_{25}) + \nu(Te_{15}\text{-}F_{26}) + \nu(Te_{15}\text{-}F_{27}) + \nu(Te_{15}\text{-}F_{29})] - [\nu(Te_{14}\text{-}F_{24})_a + \nu(Te_{15}\text{-}F_{30})] + [\nu(Te_{34}\text{-}F_{37}) + \nu(Te_{34}\text{-}F_{36}) + \nu(Te_{34}\text{-}F_{38}) + \nu(Te_{34}\text{-}F_{39}) + \nu(Te_{35}\text{-}F_{44}) + \nu(Te_{35}\text{-}F_{45}) + \nu(Te_{35}\text{-}F_{42}) + \nu(Te_{43}\text{-}F_{43})]$
	640(3)[8]	$\nu(Te_{15}\text{-}F_{27}) + \nu(Te_{15}\text{-}F_{29}) - \nu(Te_{35}\text{-}F_{44}) + \nu(Te_{35}\text{-}F_{46}) + \nu(Te_{34}\text{-}F_{36}) + \nu(Te_{34}\text{-}F_{37}) + \nu(Te_6\text{-}F_7) + \nu(Te_6\text{-}F_8)$
	639(3)[7]	$[\nu(Te_{15}\text{-}F_{29}) + \nu(Te_{14}\text{-}F_{27})] - [\nu(Te_{14}\text{-}F_{22}) + \nu(Te_{14}\text{-}F_{21}] - [\nu(Te_{34}\text{-}F_{36}) + \nu(Te_{34}\text{-}F_{37}) + \nu(Te_6\text{-}F_8) + \nu(Te_6\text{-}F_7)] + [\nu(Te_{35}\text{-}F_{44}) + \nu(Te_{35}\text{-}F_{45})]$

Table S6.3. continued…

	640(6)[6]	}
	633(6)[10]	
	632(2)[5]	} *f*
	629(3)[6]	
	628(9)[14]	$[\nu(Te_{14}\text{-}F_{18}) + \nu(Te_{14}\text{-}F_{19})] - [\nu(Te_{14}\text{-}F_{21}) + \nu(Te_{14}\text{-}F_{22})]$
623(4)	622(3)[14]	$[\nu(Te_{15}\text{-}F_{25}) + \nu(Te_{15}\text{-}F_{26})]$
	620(4)[21]	*f*
	534(3)[178]	$[\nu(Xe_{13}\text{-}F_{17}) - \nu(Xe_{13}\text{-}F_{20})] + [\nu(Hg_{49}\text{-}O_{51}) + \nu(Te_{6}\text{-}O_{51})] - [\nu(Hg_{49}\text{-}O_{50}) + \nu(Te_{33}\text{-}O_{50})]$
518(10)	528(5)[167]	$[\nu(Xe_{13}\text{-}F_{17}) - \nu(Xe_{13}\text{-}F_{20})] + [\nu(Xe_{16}\text{-}F_{23}) - \nu(Xe_{16}\text{-}F_{40})] + [\nu(Hg_{49}\text{-}O_{50}) + \nu(Te_{33}\text{-}O_{50})] - [\nu(Hg_{49}\text{-}O_{51}) + \nu(Te_{6}\text{-}O_{51})]$
	527(2)[33]	*f*
	524(9)[67]	$[\nu(Hg_{12}\text{-}O_{28}) + \nu(Te_{14}\text{-}O_{28})] - [\nu(Hg_{12}\text{-}O_{31}) + \nu(Te_{15}\text{-}O_{31})]$
508(100)	521(54)[90]	$\nu(Xe_{13}\text{-}F_{20}) - \nu(Xe_{16}\text{-}F_{40})$
501(56)	516(38)[11]	$[\nu(Xe_{13}\text{-}F_{17}) + \nu(Xe_{13}\text{-}F_{20})] + [\nu(Xe_{16}\text{-}F_{23}) + \nu(Xe_{16}\text{-}F_{40})]_{small}$
489(10)	510(35)[80]	$\nu(Xe_{13}\text{-}F_{17}) - \nu(Xe_{16}\text{-}F_{23})$
478(3)		
474, sh	502(73)[3]	$[\nu(Hg_{12}\text{-}O_{28}) + \nu(Te_{14}\text{-}O_{28})] + [\nu(Hg_{12}\text{-}O_{31}) + \nu(Te_{15}\text{-}O_{31})] + [\nu(Hg_{32}\text{-}O_{48} + \nu(Te_{14}\text{-}O_{28})] + [\nu(Hg_{32}\text{-}O_{45}) + \nu(Te_{34}\text{-}O_{45})]$
445(11)	499(6)[230]	$[\nu(Hg_{12}\text{-}O_{28}) + \nu(Te_{14}\text{-}O_{28}) + [\nu(Hg_{12}\text{-}O_{31}) + \nu(Te_{15}\text{-}O_{31})] - [\nu(Hg_{32}\text{-}O_{48} + \nu(Te_{14}\text{-}O_{28})] - [\nu(Hg_{32}\text{-}O_{45}) + \nu(Te_{34}\text{-}O_{45})]$ / / $\nu(Xe_{16}\text{-}F_{23})$
	487(31)[32]	*f*
	337(<1)[34]	$[\delta(Te_{14}F_{4e})_{umb} + \delta(Te_{15}F_{4e'})_{umb}] + [\delta(Te_{34}F_{4e})_{umb} + \delta(Te_{35}F_{4e'})_{umb}]$
334, sh	334(<1)[10]	$\delta(Te_{15}F_{4e'})_{umb} + [\delta(Te_{6}F_{4e})_{umb} + \delta(Te_{33}F_{4e'})_{umb}]$
	334(<1)[99]	$[\delta(Te_{14}F_{4e})_{umb} + \delta(Te_{15}F_{4e'})_{umb}] - [\delta(Te_{34}F_{4e})_{umb} + \delta(Te_{6}F_{4e})_{umb} + \delta(Te_{33}F_{4e'})_{umb}]$
	331(<1)[95]	$\delta(O_{28}\text{-}Hg_{12}\text{-}O_{31})_{o.o.p} + \delta(O_{48}\text{-}Hg_{32}\text{-}O_{45})_{o.o.p} + [\delta(Te_{6}F_{4e})_{umb} - \delta(Te_{33}F_{4e'})_{umb}]$
332(3)	330(<1)[83]	$\delta(Te_{15}F_{4e'})_{umb} + [\rho_w(O_{28}\text{-}Te_{14}\text{-}F_{24}) + [\rho_w(F_{18}\text{-}Te_{14}\text{-}F_{19})] + \delta(Te_{6}F_{4e})_{umb} + [\delta(Te_{35}F_{4e'})_{umb} - \delta(Te_{34}F_{4e})_{umb}] / [\rho_w(F_3\text{-}Te_{33}\text{-}F_4) + \rho_w(O_{50}\text{-}Te_{33}\text{-}F_5)]$
	328(<1)[98]	*f*
329(3)	328(1)[145]	$[\delta(O_{28}\text{-}Te_{14}\text{-}F_{22}) + \delta(F_{21}\text{-}Te_{14}\text{-}F_{24})] + \delta(O_{31}\text{-}Te_{15}\text{-}F_{27}) + \delta(O_{50}\text{-}Te_{33}\text{-}F_1) + \delta(F_5\text{-}Te_{33}\text{-}F_2) + \delta(O_{50}\text{-}Te_{33}\text{-}F_3) - \delta(F_{44}\text{-}Te_{35}\text{-}F_{47}) / \rho_w(F_{42}\text{-}Te_{35}\text{-}F_{43})$
	326(<1)[54]	$[\delta(O_{31}\text{-}Te_{15}\text{-}F_{27}) + \delta(F_{29}\text{-}Te_{15}\text{-}F_{30})] / \rho_w(F_{25}\text{-}Te_{15}\text{-}F_{26})$
326, sh	326(<1)[34]	$\delta(O_{28}\text{-}Hg_{12}\text{-}O_{31})_{o.o.p} + \delta(O_{45}\text{-}Te_{34}\text{-}F_{37}) + \delta(F_{36}\text{-}Te_{34}\text{-}F_{41}) + \delta(O_{48}\text{-}Te_{35}\text{-}F_{46}) + \delta(F_{44}\text{-}Te_{35}\text{-}F_{47}) / \rho_w(O_{51}\text{-}Te_{6}\text{-}F_{11}) + \rho_w(F_9\text{-}Te_{6}\text{-}F_{10}) + \rho_w(O_{50}\text{-}Te_{33}\text{-}F_5)$
	326(1)[21]	$\delta(F_{29}\text{-}Te_{15}\text{-}F_{30}) + \rho_w(F_{25}\text{-}Te_{15}\text{-}F_{26}) + \delta(F_1\text{-}Te_{33}\text{-}F_5) + \delta(F_{37}\text{-}Te_{34}\text{-}F_{41}) - \delta(F_{47}\text{-}Te_{35}\text{-}F_{44})$
	325(<1)[63]	}
	325(2)[24]	} *f*
324(2)	324(<1)[13]	$\rho_w(O_{28}\text{-}Te_{14}\text{-}F_{24}) + \rho_w(F_{18}\text{-}Te_{14}\text{-}F_{19}) + \rho_w(F_{21}\text{-}Te_{14}\text{-}F_{22}) + \delta(O_{31}\text{-}Te_{15}\text{-}F_{29}) - [\delta(F_{36}\text{-}Te_{34}\text{-}F_{41}) + \delta(F_{47}\text{-}Te_{35}\text{-}F_{46})]$
	323(1)[24]	*f*

Table S6.3. continued…

	322(<1)[28]	$\delta(F_{22}\text{-}Te_{14}\text{-}F_{24}) + \delta(O_{28}\text{-}Te_{14}\text{-}F_{19}) + \delta(F_5\text{-}Te_{33}\text{-}F_3) + \delta(F_{44}\text{-}Te_{53}\text{-}F_{47}) + \delta(O_{51}\text{-}Te_6\text{-}F_7) / \rho_w(F_1\text{-}Te_{33}\text{-}F_2)$
321(1)	321(<1)[8]	$\delta(F_{22}\text{-}Te_{14}\text{-}F_{24}) + \rho_w(F_{18}\text{-}Te_{14}\text{-}F_{19}) + [\delta(F_5\text{-}Te_{33}\text{-}F_3) + \delta(F_{39}\text{-}Te_{34}\text{-}F_{41})] - [\delta(F_5\text{-}Te_{33}\text{-}F_4) + \delta(F_{42}\text{-}Te_{35}\text{-}F_{47})] / \rho_w(F_1\text{-}Te_{33}\text{-}F_2) + \rho_w(F_{35}\text{-}Te_{34}\text{-}F_{37}) - \rho_w(F_{44}\text{-}Te_{35}\text{-}F_{46})$
	320(<1)[26]	$\delta(F_{25}\text{-}Te_{15}\text{-}F_{30}) - \delta(F_{26}\text{-}Te_{15}\text{-}F_{30}) / \rho_w(F_{27}\text{-}Te_{15}\text{-}F_{29})$
	320(2)[15]	*f*
	319(<1)[9]	
	318(<1)[7]	
	317(<1)[58]	
	317(<1)[12]	$\delta(F_{18}\text{-}Te_{14}\text{-}F_{24}) + \rho_w(F_{21}\text{-}Te_{14}\text{-}F_{22}) + \rho_t(O_{28}\text{-}Hg_{12}\text{-}O_{31}) + \rho_t(O_{48}\text{-}Hg_{32}\text{-}O_{45}) + \rho_t(O_{50}\text{-}Hg_{49}\text{-}O_{51})$
311(2)	316(1)[16]	$\rho_t(O_{28}\text{-}Hg_{12}\text{-}O_{31}) + \delta(F_{18}\text{-}Te_{14}\text{-}O_{28}) + \delta(F_{29}\text{-}Te_{15}\text{-}O_{31}) + \delta(F_{38}\text{-}Te_{34}\text{-}F_{41})$
	316(<1)[15]	$\delta(F_{18}\text{-}Te_{14}\text{-}F_{24}) - \delta(F_{19}\text{-}Te_{14}\text{-}F_{24}) + \rho_w(F_{21}\text{-}Te_{14}\text{-}F_{22}) + \delta(F_{41}\text{-}Te_{34}\text{-}F_{38}) / \rho_w(F_{36}\text{-}Te_{34}\text{-}F_{37}) + \rho_t(O_{48}\text{-}Hg_{32}\text{-}O_{45})$
	294(1)[<1]	*f*
	294(3)[<1]	
	293(2)[<1]	
	293(2)[<1]	
303(3)	293(2)[<1]	$\delta(F_{25}\text{-}Te_{15}\text{-}F_{29}) + \delta(F_{26}\text{-}Te_{15}\text{-}F_{27})$
	291(1)[<1]	$\delta(F_{18}\text{-}Te_{14}\text{-}F_{22}) + \delta(F_{19}\text{-}Te_{14}\text{-}F_{21})$
	245(<1)[18]	*f*
	245(<0.1)[2]	
248, sh	244(<1)[<1]	$\delta(F_{25}\text{-}Te_{15}\text{-}O_{31}) / \rho_w(F_{21}\text{-}Te_{14}\text{-}F_{22}) + \rho_w(F_{18}\text{-}Te_{14}\text{-}F_{19}) - \rho_w(F_{27}\text{-}Te_{15}\text{-}F_{29})$
241(1)	236(<1)[22]	$\delta(F_{17}\text{-}Xe_{13}\text{-}F_{20})_{o.o.p.}$
	231(3)[14]	*f*
236(1)	231(3)[3]	$\rho_w(F_{21}\text{-}Te_{14}\text{-}F_{22}) + \rho_w(F_{18}\text{-}Te_{14}\text{-}F_{19}) + \rho_w(F_{27}\text{-}Te_{15}\text{-}F_{29}) + \delta(F_{25}\text{-}Te_{15}\text{-}O_{31}) + \delta(F_{39}\text{-}Te_{34}\text{-}O_{45}) / \rho_w(F_{44}\text{-}Te_{35}\text{-}F_{46}) + \rho_w(F_{36}\text{-}Te_{34}\text{-}F_{37})$
	230(2)[2]	*f*
223(2)	221(<1)[21]	$[\delta(F_{17}\text{-}Xe_{13}\text{-}F_{20})_{i.p}]_{small} + \delta(F_{23}\text{-}Xe_{16}\text{-}F_{40})_{o.o.p}$
	219(<1)[21]	$\delta(F_{23}\text{-}Xe_{16}\text{-}F_{40})_{i.p.}$
	218(<0.1)[12]	$\delta(F_{17}\text{-}Xe_{13}\text{-}F_{20})_{i.p.} + [\delta(F_{23}\text{-}Xe_{16}\text{-}F_{40})_{o.o.p.}]_{small}$
	209(<0.1)[<1]	*f*
	208(<0.1)[<1]	
	208(<0.1)[<1]	
	208(<0.1)[<1]	
	205(<0.1)[<1]	
	204(<0.1)[<1]	
	199(<0.1)[<0.1]	
	196(<0.1)[<0.1]	

Table S6.3. continued…

n.o.		
	210(<0.1)[<1]	$\rho_w(F_{18}\text{-}Te_{14}\text{-}F_{19}) - \rho_w(F_{21}\text{-}Te_{14}\text{-}F_{22})$
	209(<0.1)[<1]	$\rho_w(F_{25}\text{-}Te_{15}\text{-}F_{26}) - \rho_w(F_{27}\text{-}Te_{15}\text{-}F_{29}) / [\rho_w(F_{38}\text{-}Te_{34}\text{-}F_{39}) - \rho_w(F_{36}\text{-}Te_{34}\text{-}F_{37})]_{small}$
	202(<0.1)[<1]	$\rho_w(O_{31}\text{-}Te_{15}\text{-}F_{30}) - \rho_w(F_{25}\text{-}Te_{15}\text{-}F_{26}) / [\rho_w(F_{18}\text{-}Te_{14}\text{-}F_{19}) - \rho_w(F_{21}\text{-}Te_{14}\text{-}F_{22})]_{small}$
	191(<0.1)[<0.1]	$\rho_w(O_{28}\text{-}Te_{14}\text{-}F_{24}) - \rho_w(F_{18}\text{-}Te_{14}\text{-}F_{19}) + \rho_w(F_{21}\text{-}Te_{14}\text{-}F_{22}) / [\rho_w(O_{31}\text{-}Te_{15}\text{-}F_{30}) - \rho_w(F_{25}\text{-}Te_{15}\text{-}F_{26})]_{small}$
	162(<0.1)[6]	$\rho_t(F_{19}\text{-}Te_{14}\text{-}F_{24}) - \rho_t(F_{25}\text{-}Te_{15}\text{-}F_{29}) / \rho_w(F_{27}\text{-}Te_{15}\text{-}F_{29}) - \rho_w(F_{21}\text{-}Te_{14}\text{-}F_{22})$
	163(<0.1)[9]	*f*
	161(<0.1)[5]	*f*
	129(1)[<1]	$\rho_t(Te_{14}\text{-}F_{18},F_{19},F_{24}) + \rho_t(Te_{15}\text{-}F_{25},F_{26},F_{30}) - [\rho_t(Te_6\text{-}F_9,F_{10},F_{11}) + \rho_t(Te_{33}\text{-}F_3,F_4,F_5)]$
137(5)	129(1)[<1]	$\rho_t(Te_{14}\text{-}F_{18}F_{19}F_{24}) + \rho_t(Te_{15}\text{-}F_{25}F_{26}F_{30}) + \rho_t(Te_{33}\text{-}F_3F_4F_5) + \rho_t(Te_6\text{-}F_9F_{10}F_{11})$
131(7)	128(2)[<1]	$\rho_t(F_{17}\text{-}Xe_{13}\text{-}F_{20})$
	106(4)[9]	$\rho_t(F_{17}\text{-}Xe_{13}\text{-}F_{20}) / \delta(O_{50}\text{-}Hg_{49}\text{-}O_{51})_{i.p.}$
124(8)	100(<1)[3]	*f*
	97(<1)[5]	$\delta(O_{28}\text{-}Hg_{12}\text{-}O_{31})_{i.n.} / \rho_t(F_{20}\text{-}Xe_{13}\text{-}F_{17})_{small}$
	96(1)[3]	$\delta(O_{28}\text{-}Hg_{12}\text{-}O_{31})_{o.o.p.} / \rho_t(F_{20}\text{-}Xe_{13}\text{-}F_{17})_{small}$
99(3)	91(<1)[5]	$\rho_t(F_{40}\text{-}Xe_{16}\text{-}F_{23})$
	83(2)[<1]	$\rho_t(F_{40}\text{-}Xe_{16}\text{-}F_{23})$
	78(3)[<1]	$\rho_t(F_{17}\text{-}Xe_{13}\text{-}F_{20})$
	72(2)[<1]	coupled deformation and torsion modes of $3Hg(OTeF_5)_2{\cdot}2XeF_2$
	94(<1)[2]	
	92(<1)[2]	
	67(<0.1)[2]	
	66(<1)[2]	
	57(<1)[2]	
	54(<1)[<1]	
	52(<1)[<1]	
	49(<0.1)[1]	
	44(<0.1)[<1]	
	39(<1)[<0.1]	
	36(<1)[<0.1]	
	36(<1)[<0.1]	
	33(<0.1)[<1]	
	32(<0.1)[<0.1]	
	31(<1)[<1]	
	30(<0.1)[<1]	
	28(<1)[<0.1]	
	24(<0.1)[<1]	
	24(<0.1)[<1]	

Table S6.3. continued…

22(<0.1)[<1] 21(<0.1)[<1] 21(<0.1)[<1] 18(<1)[<1] 16(<1)[<1] 15(<1)[<1] 13(<0.1)[<1] 11(<0.1)[<1] 10(<0.1)[<0.1] 10(<0.1)[<0.1] 9(<1)[<0.1] 9(<0.1)[<1] 7(<0.1)[<1] 6(<0.1)[<0.1] 3(<1)[<0.1] 3(<1)[<1]	coupled deformation and torsion modes of $3Hg(OTeF_5)_2 \cdot 2XeF_2$

[a] All frequencies are given in cm^{-1}. [b] The Raman spectrum was recorded in a quartz sample tube at −155 °C using 1064-nm excitation. A band at 496(27) cm^{-1} was also observed and assigned to excess XeF_2. [c] The abbreviations denote shoulder (sh), and not observed (n.o.). [d] Values in parentheses are Raman intensities ($Å^4$ amu^{-1}), and values in square brackets are infrared intensities (km mol^{-1}). [e] Abbreviations denote out-of-plane (o.o.p.) and in-plane (i.p.) where the plane contains both XeF_2 molecules or the Te-O–Hg–O-Te groups, umbrella (umb), equatorial (4e and 4e′), axial (a and a′), stretch (ν), bend (δ), twist (ρ_t), wag (ρ_w) and rock (ρ_r) vibrational modes. The subscript, "small", denotes a small contribution of the bracketed vibrational mode relative to the other coupled vibrational modes. Assignments are for the energy-minimized geometry (PBE0/def2-TVZPP); only the mode assignments that involve the central $Hg(OTeF_5)_2$ and the two XeF_2 units are provided. The atom numbering corresponds to that used in Figure 6.7a. [f] Modes belonging to the terminal $Hg(OTeF_5)_2$ units of $[Hg(OTeF_5)_2]_3 \cdot 2XeF_2$

Table S6.4. Experimental Raman Frequencies and Intensities of $Hg(OTeF_5)_2 \cdot 1.5KrF_2$ and the Calculated Vibrational Frequencies and Intensities of $[Hg(OTeF_5)_2]_3 \cdot 2KrF_2$

exptl[a,b,c] $Hg(OTeF_5)_2 \cdot 1.5KrF_2$	calcd[a,d] $[Hg(OTeF_5)_2]_3 \cdot 2KrF_2$	assgnts[e]
	833(5)[132]	*f*
	832(21)[29]	
844(2)	826(9)[165]	$[\nu(Hg_{12}\text{-}O_{28}) - \nu(Te_{14}\text{-}O_{28})] + [\nu(Hg_{12}\text{-}O_{31}) - \nu(Te_{15}\text{-}O_{31})]$
	822(2)[591]	*f*
	816(2)[510]	
821(2)	812(2)[358]	$[\nu(Hg_{12}\text{-}O_{28}) - \nu(Te_{14}\text{-}O_{28})] - [\nu(Hg_{12}\text{-}O_{31}) - \nu(Te_{15}\text{-}O_{31})] + [\nu(Hg_{32}\text{-}O_{48}) - \nu(Te_{35}\text{-}O_{48})]_{small} - [\nu(Hg_{32}\text{-}O_{45}) - \nu(Te_{34}\text{-}O_{45})]_{small}$
723(1)	723(16)[15]	$[\nu(Te_{14}\text{-}F_{21}) - \nu(Te_{14}\text{-}F_{22})] + [\nu(Te_{35}\text{-}F_{42}) + \nu(Te_{33}\text{-}F_2)] - [\nu(Te_{35}\text{-}F_{43}) + \nu(Te_{33}\text{-}F_1)]$
	721(6)[193]	*f*
	718(3)[151]	
	718(4)[92]	$[\nu(Te_{15}\text{-}F_{25}) - \nu(Te_{15}\text{-}F_{26})] + [\nu(Te_6\text{-}F_{10}) - \nu(Te_6\text{-}F_9)]$
	717(5)[294]	$[\nu(Te_{14}\text{-}F_{21}) + \nu(Te_{15}\text{-}F_{25}) - [\nu(Te_{14}\text{-}F_{22}) + \nu(Te_{15}\text{-}F_{26})] + [\nu(Te_{35}\text{-}F_{43}) + \nu(Te_{34}\text{-}F_{36})] - [\nu(Te_{35}\text{-}F_{42}) + \nu(Te_{34}\text{-}F_{37}) + \nu(Te_{33}\text{-}F_4)]$
	715(13)[215]	$[\nu(Te_{14}\text{-}F_{21}) + \nu(Te_{15}\text{-}F_{26}) - [\nu(Te_{14}\text{-}F_{22}) + \nu(Te_{15}\text{-}F_{25})] + [\nu(Te_{34}\text{-}F_{38}) + \nu(Te_{35}\text{-}F_{46})] - [\nu(Te_{34}\text{-}F_{39}) + \nu(Te_{35}\text{-}F_{44}) + \nu(Te_{33}\text{-}F_4) + \nu(Te_6\text{-}F_9)]$
717(<1)		
715(<1)	715(2)[186]	$[\nu(Te_{14}\text{-}F_{21}) + \nu(Te_{15}\text{-}F_{26}) + \nu(Te_{15}\text{-}F_{27})] - [\nu(Te_{14}\text{-}F_{22}) + \nu(Te_{15}\text{-}F_{25}) + \nu(Te_{15}\text{-}F_{29})] + [\nu(Te_{34}\text{-}F_{39}) + \nu(Te_{35}\text{-}F_{43}) + \nu(Te_{33}\text{-}F_4)] - [\nu(Te_{35}\text{-}F_{42}) + \nu(Te_{34}\text{-}F_{38}) + \nu(Te_6\text{-}F_9)]$
709(<1)		
704(1)	714(1)[32]	$[\nu(Te_{15}\text{-}F_{29}) - \nu(Te_{15}\text{-}F_{27})] + [\nu(Te_{35}\text{-}F_{43}) + \nu(Te_{35}\text{-}F_{44}) + \nu(Te_{34}\text{-}F_{37})] - [\nu(Te_{35}\text{-}F_{42}) + \nu(Te_{34}\text{-}F_{36}) + \nu(Te_{35}\text{-}F_{46})]$
	713(2)[195]	$[\nu(Te_{15}\text{-}F_{29}) + \nu(Te_{14}\text{-}F_{21})] - [\nu(Te_{15}\text{-}F_{27})] + [\nu(Te_{35}\text{-}F_{42}) + \nu(Te_{34}\text{-}F_{36}) + \nu(Te_{33}\text{-}F_1)] - [\nu(Te_{34}\text{-}F_{37}) + \nu(Te_{33}\text{-}F_2) + \nu(Te_{35}\text{-}F_{46})]$
	712(<1)[49]	$[\nu(Te_{14}\text{-}F_{21}) + \nu(Te_{15}\text{-}F_{27}) + \nu(Te_{15}\text{-}F_{25})] - [\nu(Te_{14}\text{-}F_{22}) + \nu(Te_{15}\text{-}F_{29})] + [\nu(Te_{35}\text{-}F_{44}) + \nu(Te_{34}\text{-}F_{37}) + \nu(Te_{33}\text{-}F_1) - [\nu(Te_{35}\text{-}F_{46}) + \nu(Te_{34}\text{-}F_{37}) + \nu(Te_6\text{-}F_9) + \nu(Te_{34}\text{-}F_{36}) + \nu(Te_{34}\text{-}F_{39}) + \nu(Te_{33}\text{-}F_2)]$
	693(1)[231]	$\nu(Te_{14}\text{-}F_{18}) - \nu(Te_{14}\text{-}F_{19}) + \nu(Te_{33}\text{-}F_5)$
	711(2)[150]	*f*
	701(4)[37]	
	701(9)[44]	
688(14)	706(12)[7]	$\nu(Te_{14}\text{-}F_{24})_a + \nu(Te_{35}\text{-}F_{47})_a$
683, sh	700(2)[223]	$\nu(Te_{15}\text{-}F_{30})_a + \nu(Te_{35}\text{-}F_{47})_a + \nu(Te_6\text{-}F_{11})_a$
	699(20)[4]	$\nu(Te_{15}\text{-}F_{30})_a + \nu(Te_{35}\text{-}F_{47})_a$
	693(1)[231]	*f*
	289(18)[51]	
	647(3)[1]	
	645(13)[5]	
	640(8)[4]	

Table S6.4. continued…

645(4) 642, sh 638(1) 624(2)	646(24)[12]	{	$[\nu(Te_{14}\text{-}F_{18}) + \nu(Te_{14}\text{-}F_{19}) + \nu(Te_{14}\text{-}F_{21}) + \nu(Te_{14}\text{-}F_{22}) + \nu(Te_{15}\text{-}F_{25}) + \nu(Te_{15}\text{-}F_{26}) + \nu(Te_{15}\text{-}F_{27}) + \nu(Te_{15}\text{-}F_{29})] - [\nu(Te_{14}\text{-}F_{24}) + \nu(Te_{15}\text{-}F_{30})] + \nu(Te_{33}\text{-}F_5) - [\nu(Te_{33}\text{-}F_1) + \nu(Te_{33}\text{-}F_2)]$
	642(3)[8]	{	$[\nu(Te_{15}\text{-}F_{29}) + \nu(Te_{14}\text{-}F_{27})] - [\nu(Te_{15}\text{-}F_{30}) + \nu(Te_{14}\text{-}F_{22}) + \nu(Te_{14}\text{-}F_{21}] + [\nu(Te_{34}\text{-}F_{36}) + \nu(Te_{34}\text{-}F_{37})] - [\nu(Te_{35}\text{-}F_{44}) + \nu(Te_{35}\text{-}F_{45})]$
	641(2)[9]	{	$[\nu(Te_{15}\text{-}F_{29}) + \nu(Te_{14}\text{-}F_{27})] - [\nu(Te_{15}\text{-}F_{30}) + \nu(Te_{14}\text{-}F_{22}) + \nu(Te_{14}\text{-}F_{21}] + [\nu(Te_{35}\text{-}F_{44}) + \nu(Te_{35}\text{-}F_{45})] - [\nu(Te_{34}\text{-}F_{36}) + \nu(Te_{34}\text{-}F_{37})]$
	627(11)[22]		$[\nu(Te_{14}\text{-}F_{18}) + \nu(Te_{14}\text{-}F_{19})] - [\nu(Te_{14}\text{-}F_{21}) + \nu(Te_{14}\text{-}F_{22})]$
	624(2)[32]		$[\nu(Te_{15}\text{-}F_{27}) + \nu(Te_{15}\text{-}F_{29})] - [\nu(Te_{15}\text{-}F_{25}) + \nu(Te_{15}\text{-}F_{26})] + [\nu(Te_{33}\text{-}F_4) + \nu(Te_{33}\text{-}F_3)]$
	623(4)[3]		$[\nu(Te_{15}\text{-}F_{25}) + \nu(Te_{15}\text{-}F_{26})] + [\nu(Te_{33}\text{-}F_4) + \nu(Te_{33}\text{-}F_3)]$
	633(6)[12] 632(2)[7] 629(2)[4]		*f*
558(1)	574(2)[342]		$[\nu(Kr_{13}\text{-}F_{17}) - \nu(Kr_{13}\text{-}F_{20})] + [\nu(Kr_{16}\text{-}F_{23}) - \nu(Kr_{16}\text{-}F_{40})]$
553(<1)	560(6)[339]		$[\nu(Kr_{13}\text{-}F_{17}) - \nu(Kr_{13}\text{-}F_{20})] - [\nu(Kr_{16}\text{-}F_{23}) - \nu(Kr_{16}\text{-}F_{40})]$
	533(1)[23] 528(2)[20]		*f*
484(3)	527(2)[34]		$[\nu(Hg_{12}\text{-}O_{28}) + \nu(Te_{14}\text{-}O_{28})] - [\nu(Hg_{12}\text{-}O_{31}) + \nu(Te_{15}\text{-}O_{31})]$
468(100)	513(61)[5]		$[\nu(Kr_{13}\text{-}F_{17}) + \nu(Kr_{13}\text{-}F_{20})] + [\nu(Kr_{16}\text{-}F_{23}) + \nu(Kr_{16}\text{-}F_{40})]$
	512(100)[5]		$[\nu(Kr_{13}\text{-}F_{17}) + \nu(Kr_{13}\text{-}F_{20})] - [\nu(Kr_{16}\text{-}F_{23}) + \nu(Kr_{16}\text{-}F_{40})]$
458(17)	505(69)[37]		$[\nu(Hg_{12}\text{-}O_{28}) + \nu(Te_{14}\text{-}O_{28})] + [\nu(Hg_{12}\text{-}O_{31} + \nu(Te_{15}\text{-}O_{31})]$
	503(33)[69] 489(32)[21]		*f*
334(1)	337(<1)[35]		$[\delta(Te_{14}F_{4e})_{umb} + \delta(Te_{15}F_{4e})_{umb}] + [\delta(Te_{34}F_{4e})_{umb} + \delta(Te_{35}F_{4e})_{umb}]$
	335(<1)[14]		$\delta(Te_{15}F_{4e})_{umb} + [\delta(Te_6F_{4e})_{umb} + \delta(Te_{33}F_{4e})_{umb}]$
	334(<1)[102]		$[\delta(Te_{14}F_{4e})_{umb} + \delta(Te_{15}F_{4e})_{umb}] - [\delta(Te_{34}F_{4e})_{umb} + \delta(Te_6F_{4e})_{umb} + \delta(Te_{33}F_{4e})_{umb}]$
329(1)	331(<1)[62]		$\delta(O_{28}\text{-}Hg_{12}\text{-}O_{31})_{o.o.p} + \delta(O_{48}\text{-}Hg_{32}\text{-}O_{45})_{o.o.p} + [\delta(Te_6F_{4e})_{umb} - \delta(Te_{33}F_{4e})_{umb}]$
	330(<1)[102]	{	$\delta(Te_{15}F_{4e})_{umb} + [\rho_w(O_{28}\text{-}Te_{14}\text{-}F_{24}) + [\rho_w(F_{18}\text{-}Te_{14}\text{-}F_{19})] + \delta(Te_6F_{4e})_{umb} + [\rho_w(F_3\text{-}Te_{33}\text{-}F_4) + \rho_w(O_{50}\text{-}Te_{33}\text{-}F_5)] + [\delta(Te_{35}F_{4e})_{umb} - \delta(Te_{34}F_{4e})_{umb} + \delta(O_{45}\text{-}Hg_{32}\text{-}O_{48})_{o.o.p}]$
	328(<1)[107]		*f*
324(1)	328(1)[133]	{	$[\delta(O_{28}\text{-}Te_{14}\text{-}F_{22}) + \delta(F_{21}\text{-}Te_{14}\text{-}F_{24})] + \delta(O_{31}\text{-}Te_{15}\text{-}F_{27})] + \delta(O_{50}\text{-}Te_{33}\text{-}F_1) + \delta(F_5\text{-}Te_{33}\text{-}F_2) + \delta(O_{50}\text{-}Te_{33}\text{-}F_3) - \delta(F_{44}\text{-}Te_{35}\text{-}F_{47}) + \rho_w(F_{42}\text{-}Te_{35}\text{-}F_{43})$
	326(<1)[70]		$[\delta(O_{31}\text{-}Te_{15}\text{-}F_{27}) + \delta(F_{29}\text{-}Te_{15}\text{-}F_{30})] + \rho_w(F_{25}\text{-}Te_{15}\text{-}F_{26}) + \rho_w(O_{45}\text{-}Hg_{37}\text{-}O_{48}) + \delta(F_5\text{-}Te_{33}\text{-}F_2) + \rho_w(F_{38}\text{-}Te_{34}\text{-}F_{39})$
	326(<1)[22]	{	$\delta(O_{28}\text{-}Hg_{12}\text{-}O_{31})_{o.o.p} + \delta(O_{45}\text{-}Te_{34}\text{-}F_{37}) + \delta(F_{36}\text{-}Te_{34}\text{-}F_{41}) + \delta(O_{48}\text{-}Te_{35}\text{-}F_{46}) + \delta(F_{44}\text{-}Te_{35}\text{-}F_{47}) + \rho_w(O_{51}\text{-}Te_6\text{-}F_{11}) + \rho_w(F_9\text{-}Te_6\text{-}F_{10}) + \rho_w(O_{50}\text{-}Te_{33}\text{-}F_5) + \rho_w(F_3\text{-}Te_{33}\text{-}F_4)$
	326(1)[62]		$\delta(F_{29}\text{-}Te_{15}\text{-}F_{30}) + \rho_w(F_{25}\text{-}Te_{15}\text{-}F_{26}) + \delta(O_{28}\text{-}Te_{14}\text{-}F_{22}) + \delta(F_1\text{-}Te_{33}\text{-}F_5) + \delta(F_{37}\text{-}Te_{34}\text{-}F_{41}) + \rho_w(F_{38}\text{-}Te_{34}\text{-}F_{39})$
	325(<1)[30] 324(1)[8] 324(1)[12] 323(1)[20]		*f*

Table S6.4. continued…

320(1)	322(<1)[25]	$\delta(O_{31}\text{-}Te_{15}\text{-}F_{27}) + \delta(F_{22}\text{-}Te_{14}\text{-}F_{24}) + \delta(O_{51}\text{-}Te_{6}\text{-}F_{7}) + \delta(F_{5}\text{-}Te_{33}\text{-}F_{3}) - \delta(F_{5}\text{-}Te_{33}\text{-}F_{4}) + \rho_w(F_{1}\text{-}Te_{33}\text{-}F_{2})$
	321(<1)[19]	$\delta(F_{22}\text{-}Te_{14}\text{-}F_{24}) + \rho_w(F_{18}\text{-}Te_{14}\text{-}F_{19}) + [\delta(F_{5}\text{-}Te_{33}\text{-}F_{3}) + \delta(F_{39}\text{-}Te_{34}\text{-}F_{41}) + \delta(F_{39}\text{-}Te_{34}\text{-}F_{41})] - [\delta(F_{5}\text{-}Te_{33}\text{-}F_{4}) + \delta(F_{42}\text{-}Te_{35}\text{-}F_{47})] + \rho_w(F_{1}\text{-}Te_{33}\text{-}F_{2}) + \rho_w(F_{35}\text{-}Te_{34}\text{-}F_{37}) - \rho_w(F_{44}\text{-}Te_{35}\text{-}F_{46})$
	320(<1)[22]	$\delta(F_{25}\text{-}Te_{15}\text{-}F_{30}) - \delta(F_{26}\text{-}Te_{15}\text{-}F_{30}) + \rho_w(F_{27}\text{-}Te_{15}\text{-}F_{29}) + \delta(O_{50}\text{-}Te_{33}\text{-}F_{1}) + \delta(F_{11}\text{-}Te_{6}\text{-}F_{10})$
	320(2)[21]	$\delta(F_{25}\text{-}Te_{15}\text{-}F_{30}) - \delta(F_{30}\text{-}Te_{15}\text{-}F_{26}) + \delta(F_{10}\text{-}Te_{6}\text{-}F_{11}) - \delta(O_{51}\text{-}Te_{6}\text{-}F_{9}) + \rho_w(F_{7}\text{-}Te_{6}\text{-}F_{8}) + \delta(F_{1}\text{-}Te_{33}\text{-}F_{5}) + \delta(F_{2}\text{-}Te_{33}\text{-}O_{50})$
	319(<1)[6]	*f*
	317(<1)[6]	
	317(<1)[58]	
	317(<1)[10]	
314(1)	316(1)[20]	$\rho_t(O_{28}\text{-}Hg_{12}\text{-}O_{31}) + \delta(F_{18}\text{-}Te_{14}\text{-}F_{24}) + \delta(F_{29}\text{-}Te_{15}\text{-}O_{31}) + \delta(F_{38}\text{-}Te_{34}\text{-}F_{41}) + \delta(F_{41}\text{-}Te_{34}\text{-}F_{39})$
311(1)	316(<1)[18]	$\delta(F_{18}\text{-}Te_{14}\text{-}F_{24}) - \delta(F_{19}\text{-}Te_{14}\text{-}F_{24}) + \rho_w(F_{21}\text{-}Te_{14}\text{-}F_{22}) + \delta(F_{41}\text{-}Te_{34}\text{-}F_{38}) + \rho_t(O_{48}\text{-}Hg_{32}\text{-}O_{45})$
	295(2)[<1]	*f*
	294(2)[<1]	
	294(2)[<1]	
	293(2)[<1]	
304(2)	293(2)[<1]	$\delta(F_{25}\text{-}Te_{15}\text{-}F_{29}) + \delta(F_{26}\text{-}Te_{15}\text{-}F_{27})$
291, sh	291(1)[<1]	$\delta(F_{18}\text{-}Te_{14}\text{-}F_{22}) + \delta(F_{19}\text{-}Te_{14}\text{-}F_{21})$
260(1)	266(<1)[25]	$\delta(F_{17}\text{-}Kr_{13}\text{-}F_{20})_{o.o.p.}$
236(<1)	254(<1)[18]	$\delta(F_{17}\text{-}Kr_{13}\text{-}F_{20})_{i.p.} + \delta(F_{23}\text{-}Kr_{16}\text{-}F_{40})_{o.o.p.}$
	252(1)[22]	$\delta(F_{17}\text{-}Kr_{13}\text{-}F_{20})_{i.p.} + \delta(F_{23}\text{-}Kr_{16}\text{-}F_{40})_{o.o.p.}$
	252(<1)[10]	$\delta(F_{17}\text{-}Kr_{13}\text{-}F_{20})_{i.p.} - \delta(F_{23}\text{-}Kr_{16}\text{-}F_{40})_{o.o.p}$
n.o.	244(<1)[5]	$\delta(F_{17}\text{-}Kr_{13}\text{-}F_{20})_{i.p.} + \delta(F_{9}\text{-}Te_{6}\text{-}F_{11}) - \delta(F_{11}\text{-}Te_{6}\text{-}F_{10}) + \rho_w(F_{7}\text{-}Te_{6}\text{-}F_{8}) + \delta(F_{3}\text{-}Te_{33}\text{-}F_{5}) - \delta(F_{5}\text{-}Te_{33}\text{-}F_{4}) + \rho_w(F_{1}\text{-}Te_{33}\text{-}F_{2}) + \delta(F_{42}\text{-}Te_{35}\text{-}F_{47}) + \rho_w(F_{44}\text{-}Te_{35}\text{-}F_{46}) + \delta(F_{39}\text{-}Te_{34}\text{-}F_{41}) - \delta(F_{41}\text{-}Te_{34}\text{-}F_{38}) + \rho_w(F_{36}\text{-}Te_{34}\text{-}F_{37})$
	243(<1)[3]	$\rho_t(F_{18}\text{-}Te_{14}\text{-}F_{29}) + \rho_r(F_{26}\text{-}Te_{15}\text{-}F_{25}) + \rho_w(F_{22}\text{-}Te_{14}\text{-}F_{21}) + \rho_w(F_{18}\text{-}Te_{14}\text{-}F_{19})$
	243(<1)[3]	*f*
225(1)	231(3)[4]	$\delta(F_{26}\text{-}Te_{15}\text{-}F_{30}) - \delta(F_{30}\text{-}Te_{15}\text{-}F_{25}) + \rho_w(F_{27}\text{-}Te_{15}\text{-}F_{29}) + \rho_w(F_{21}\text{-}Te_{14}\text{-}F_{22}) + \rho_w(F_{18}\text{-}Te_{14}\text{-}F_{19}) + \delta(F_{18}\text{-}Te_{14}\text{-}F_{24})$
	231(3)[4]	*f*
	230(2)[8]	
n.o.	211(<0.1)[<1]	$\rho_w(F_{18}\text{-}Te_{14}\text{-}F_{19}) - \rho_w(F_{21}\text{-}Te_{14}\text{-}F_{22})$
	209(<0.1)[<1]	$\rho_w(F_{25}\text{-}Te_{15}\text{-}F_{26}) - \rho_w(F_{27}\text{-}Te_{15}\text{-}F_{29})$
	209(<0.1)[<1]	*f*
	209(<0.1)[<0.1]	
	208(<0.1)[<1]	
	208(<0.1)[<1]	
	205(<0.1)[<1]	
	204(<0.1)[<0.1]	
n.o.	202(<0.1)[<1]	$\rho_w(O_{31}\text{-}Te_{15}\text{-}F_{30}) - \rho_w(F_{25}\text{-}Te_{15}\text{-}F_{26})$
	200(<0.1)[<1]	*f*
	197(<0.1)[<0.1]	
n.o.	192(<1)[<1]	$\rho_w(O_{28}\text{-}Te_{14}\text{-}F_{24}) - \rho_w(F_{18}\text{-}Te_{14}\text{-}F_{19})$
	161(<0.1)[6]	$\rho_r(F_{19}\text{-}Te_{14}\text{-}F_{24}) - \rho_r(F_{25}\text{-}Te_{15}\text{-}F_{29}) + \rho_w(F_{27}\text{-}Te_{15}\text{-}F_{29}) + \rho_w(F_{21}\text{-}Te_{14}\text{-}F_{22})$

Table S6.4. continued…

n.o.		
	161(<0.1)[6]	$\rho_t(F_{19},Te_{14},F_{24}) - \rho_t(F_{25},Te_{15},F_{29}) + \rho_w(F_{27}\text{-}Te_{15}\text{-}F_{29}) - \rho_w(F_{21}\text{-}Te_{14}\text{-}F_{22})$
	163(<0.1)[9]	} *f*
	161(<0.1)[4]	}
138, sh		
130, sh	129(2)[<1]	$\rho_t(Te_{14}\text{-}F_{18},F_{19},F_{24}) + \rho_t(Te_{15}\text{-}F_{25},F_{26},F_{30}) + \rho_w(F_{27}\text{-}Te_{15}\text{-}F_{29}) + \rho_w(F_{21}\text{-}Te_{14}\text{-}F_{22})$
		f
	129(1)[<1]	$\rho_t(F_{20}\text{-}Kr_{13}\text{-}F_{17}) + \rho_t(Te_{33}\text{-}F_3F_4F_5) - \rho_t(Te_6\text{-}F_9F_{10}F_{11})$
123(7)	102(2)[7]	$\rho_t(F_{20}\text{-}Kr_{13}\text{-}F_{17}) + \rho_t(Te_{14}\text{-}F_{18}F_{22}F_{24}) + \rho_t(Te_{15}\text{-}F_{30}F_{26}F_{25}) + \delta(O_{28}\text{-}Hg_{12}\text{-}O_{31})_{i.p.}$
	98(2)[3]	*f*
	97(<1)[4]	
101(3)	95(4)[4]	$\rho_t(F_{20}\text{-}Kr_{13}\text{-}F_{17}) + \rho_t(Te_{15}\text{-}F_{30}F_{26}F_{27})$
	94(1)[2]	$\rho_t(F_{20}\text{-}Kr_{13}\text{-}F_{17}) + \delta(O_{48}\text{-}Hg_{32}\text{-}O_{45})_{i.p.} + \rho_t(F_{23}\text{-}Kr_{16}\text{-}F_{40})$
	91(1)[5]	$\delta(O_{28}\text{-}Hg_{12}\text{-}O_{31})_{o.o.p.} + \rho_t(F_{20}\text{-}Kr_{13}\text{-}F_{17})_{small}$
		f
	92(<1)[1]	$\rho_t(F_{40}\text{-}Kr_{16}\text{-}F_{23})$
	78(3)[2]	$\rho_t(F_{40}\text{-}Kr_{16}\text{-}F_{23})$
	77(7)[<1]	$\rho_t(F_{17}\text{-}Kr_{13}\text{-}F_{20})$
	70(2)[1]	$\delta(Te_{15}\text{-}O_{31}\text{-}Hg_{12}) - \delta(Te_{14}\text{-}O_{28}\text{-}Hg_{12})$
	67(<1)[1]	} coupled deformation and torsion modes of $3Hg(OTeF_5)_2{\cdot}2KrF_2$
	66(<1)[1]	
	59(<1)[<1]	
	57(<1)[2]	
	52(<0.1)[<1]	
	49(<0.1)[<1]	
	45(<1)[<0.1]	
	43(<0.1)[<1]	
	37(<1)[<1]	
	37(<0.1)[<1]	
	35(<1)[<1]	
	34(<0.1)[<1]	
	31(<0.1)[<1]	
	31(<1)[<1]	
	29(<1)[<1]	
	27(<1)[<1]	
	24(<0.1)[<1]	
	22(<1)[<1]	
	22(<0.1)[<0.1]	
	20(<0.1)[<1]	
	18(<1)[<1]	
	16(<1)[<0.1]	
	16(<1)[<1]	
	14(<1)[<1]	

Table S6.4. continued…

n.o.	13(<0.1)[<1] 11(<0.1)[<0.1] 10(<1)[<0.1] 9(<1)[<1] 9(<0.1)[<1] 8(<1)[<1] 6(<1)[<1] 4(<1)[<0.1] 2(<1)[<0.1]	coupled deformation and torsion modes of $3Hg(OTeF_5)_2 \cdot 2KrF_2$

[a] All frequencies are given in cm^{-1}. [b] The Raman spectrum was recorded in a quartz sample tube at −155 °C using 1064-nm excitation. A band at 464(21) cm^{-1} was also observed and assigned to excess KrF_2. [c] The abbreviations denote shoulder (sh), and not observed (n.o.). [d] Values in parentheses are Raman intensities ($Å^4$ amu^{-1}), and values in square brackets are infrared intensities (km mol^{-1}). [e] Abbreviations denote out-of-plane (o.o.p.) and in-plane (i.p.) where the plane contains both XeF_2 molecules or the Te-O–Hg–O-Te groups, umbrella (umb), equatorial (4e and 4e′), axial (a and a′), stretch (ν), bend (δ), twist (ρ_t), wag (ρ_w) and rock (ρ_r) vibrational modes. The subscript, "small", denotes a small contribution of the bracketed vibrational mode relative to the other coupled vibrational modes. Assignments are for the energy-minimized geometry (PBE0/def2-TVZPP); only the mode assignments that involve the central $Hg(OTeF_5)_2$ and the two KrF_2 units are provided. The atom numbering corresponds to that used in Figure 6.7b. [f] Modes belonging to the terminal $Hg(OTeF_5)_2$ units of $[Hg(OTeF_5)_2]_3 \cdot 2KrF_2$.

Table S6.5. Experimental and Calculated Vibrational Frequencies[a] for XeF_2

exptl[b]	calcd[f]	assgnts[g]
555[c]	568(0)[254]	$\nu_3(\Sigma_u^+)$ $\nu_{as}(XeF_2)$
515,[d] 496[e]	530(38)[0]	$\nu_1(\Sigma_g^+)$ $\nu_s(XeF_2)$
213[c]	215(0)[17]	$\nu_2(\Pi_u)$ $\delta(XeF_2)$

[a] Frequencies are given in cm^{-1}. [b] From ref S1. [c] The values were determined for XeF_2 by gas-phase infrared spectroscopy and are reported as intense in ref S1. [d] The value was obtained from a weak $\nu_1 + \nu_3$ combination band in the gas-phase infrared spectrum of XeF_2 (ref S1). [e] The value was obtained by Raman spectroscopy from solid XeF_2 at −150 °C. [f] The PBE0/def2-TZVPP method was used. Values in parentheses denote Raman intensities ($Å^4\ u^{-1}$) and values in square brackets denote infrared intensities (km mol^{-1}). [g] The abbreviations denote symmetric (s), asymmetric (as), stretch (ν) and bend (δ).

Table S6.6. Experimental and Calculated Frequencies[a] for KrF_2

exptl	calcd[b]	assgnts[c]
580[d]	607(0)[281]	$\nu_3(\Sigma_u^+)$ $\nu_{as}(KrF_2)$
465.5[e] 469.5, 468.6[e]	519(46)[0]	$\nu_1(\Sigma_g^+)$ $\nu_s(KrF_2)$
236[d]	250(0)[15]	$\nu_2(\Pi_u)$ $\delta(KrF_2)$

[a] Frequencies are given in cm^{-1}. [b] The PBE0/def2-TZVPP method was used. Values in parentheses denote Raman intensities ($Å^4$ amu^{-1}) and values in square brackets denote infrared intensities (km mol^{-1}). [c] The abbreviations denote symmetric (s), asymmetric (as), stretch (ν) and bend (δ). [d] Infrared frequencies were obtained from matrix-isolated KrF_2 in ref S2. [e] Solid-state Raman frequencies for the α-phase of KrF_2 (−196 °C) are from ref S3 and those for the β-phase of KrF_2 (−80 °C) are from ref S3.

Table S6.7. Experimental and Calculated Bond Lengths and Bond Angles of Monomeric $Hg(OTeF_5)_2$

exptl $Hg(OTeF_5)_2$ (C_{2h})		calcd[a] monomeric $Hg(OTeF_5)_2$ (C_2)				
			B3LYP/ def2-TZVPP	**B3LYP/ aug-cc-pVTZ**	**PBE1PBE/ def2-TZVPP**	**PBE1PBE/ aug-cc-pVTZ**
Bond Lengths (Å)		**Bond Lengths (Å)**				
$Hg_1–O_1$	2.016(6)	$Hg_1–O_2$	1.997	1.998	1.976	1.978
$O_1–Te_1$	1.842(7)	$O_2–Te_3$	1.874	1.884	1.856	1.866
$Te_1–F_1$	1.819(6)	$Te_3–F_4$	1.851	1.862	1.835	1.846
$Te_1–F_2$	1.824(6)	$Te_3–F_5$	1.851	1.863	1.835	1.855
$Te_1–F_3$	1.830(6)	$Te_3–F_8$	1.862	1.872	1.844	1.878
$Te_1–F_4$	1.833(6)	$Te_3–F_7$	1.861	1.874	1.845	1.846
$Te_1–F_5$	1.839(6)	$Te_3–F_6$	1.883	1.895	1.866	1.857
Bond Angles (deg)		**Bond Angles (deg)**				
$O_1–Hg_1–O_2$	170.5(4)	$O_2–Hg_1–O_9$	178.4	176.8	176.8	177.0
$Hg_1–O_1–Te_1$	124.1(3)	$Hg_1–O_2–Te_3$	122.3	121.2	121.9	120.7
$O_1–Te_1–F_1$	178.3(3)	$O_2–Te_3–F_4$	179.8	179.9	179.9	179.9
$O_1–Te_1–F_2$	91.0(3)	$O_2–Te_3–F_5$	90.5	90.5	90.6	92.6
$O_1–Te_1–F_3$	92.9(3)	$O_2–Te_3–F_8$	92.5	92.6	92.5	91.8
$O_1–Te_1–F_4$	90.7(3)	$O_2–Te_3–F_7$	92.4	92.5	92.4	90.7
$O_1–Te_1–F_5$	91.8(3)	$O_2–Te_3–F_6$	91.8	91.8	91.8	92.5
$F_1–Te_1–F_2$	89.0(3)	$F_4–Te_3–F_5$	89.4	89.4	89.3	87.5
$F_1–Te_1–F_3$	88.8(3)	$F_4–Te_3–F_8$	87.5	87.5	87.6	89.4
$F_1–Te_1–F_4$	87.6(3)	$F_4–Te_3–F_7$	87.5	87.4	87.5	88.2
$F_1–Te_1–F_5$	88.2(3)	$F_4–Te_3–F_6$	88.4	88.3	88.3	87.4
$F_2–Te_1–F_4$	89.7(3)	$F_5–Te_3–F_7$	90.7	90.7	90.7	90.7
$F_4–Te_1–F_5$	89.1(3)	$F_7–Te_3–F_6$	89.3	89.1	89.1	90.7
$F_5–Te_1–F_3$	89.5(3)	$F_6–Te_3–F_8$	89.2	89.4	89.3	89.0
$F_3–Te_1–F_2$	91.5(3)	$F_8–Te_3–F_5$	90.7	90.7	90.7	89.3
$F_2–Te_1–F_5$	177.0(3)	$F_5–Te_3–F_6$	177.7	177.7	177.6	174.7
$F_3–Te_1–F_4$	176.2(3)	$F_8–Te_3–F_7$	174.9	174.8	174.9	177.6
$Te_1–O_1–Hg_1–O_2–Te_2$	53.7(3)	$Te_3–O_2–Hg_1–O_9–Te_{10}$	161.0	142.5	139.1	143.6

Table S6.8. NBO Valencies, Bond Orders, and Charges (NPA) for $Hg(OTeF_5)_2$, $[Hg(OTeF_5)_2]_3$, $[Hg(OTeF_5)_2]_3 \cdot 2NgF_2$ and NgF_2 (Ng = Xe, Kr)

Charges [Valencies]																			
$Hg(OTeF_5)_2$			**$[Hg(OTeF_5)_2]_3$**			**$[Hg(OTeF_5)_2]_3 \cdot 2XeF_2$**			**$[Hg(OTeF_5)_2]_3 \cdot 2KrF_2$**			**XeF_2**			**KrF_2**		
Hg_1	1.328	[0.984]	Hg_{16}	1.333	[1.313]	Hg_{12}	1.339	[1.168]	Hg_{12}	1.334	[1.164]						
O_2	–1.133	[1.014]	O_{22}	-1.208	[0.948]	O_{31}	-1.137	[1.023]	O_{31}	-1.137	[1.025]						
Te_3	3.443	[3.195]	Te_{17}	3.463	[3.225]	Te_{15}	3.443	[3.208]	Te_{15}	3.443	[3.207]						
F_4	-0.580	[0.449]	F_{18}	-0.575	[0.462]	F_{30}	-0.583	[0.446]	F_{30}	-0.583	[0.447]						
F_5	-0.585	[0.450]	F_{21}	-0.586	[0.469]	F_{29}	-0.594	[0.443]	F_{29}	-0.594	[0.443]						
F_6	-0.617	[0.440]	F_{20}	-0.600	[0.467]	F_{27}	-0.607	[0.435]	F_{27}	-0.606	[0.434]						
F_7	-0.598	[0.434]	F_{23}	-0.595	[0.463]	F_{25}	-0.586	[0.450]	F_{25}	-0.585	[0.450]						
F_8	-0.595	[0.437]	F_{19}	-0.583	[0.467]	F_{26}	-0.621	[0.447]	F_{26}	-0.620	[0.447]						
O_9	-1.133	[1.014]	O_{37}	-1.208	[0.948]	O_{28}	-1.163	[1.011]	O_{28}	-1.156	[1.015]						
Te_{10}	3.443	[3.195]	Te_{32}	3.463	[3.225]	Te_{14}	3.453	[3.211]	Te_{14}	3.452	[3.210]						
F_{11}	-0.585	[0.450]	F_{35}	-0.600	[0.467]	F_{19}	-0.612	[0.454]	F_{19}	-0.613	[0.457]						
F_{12}	-0.580	[0.449]	F_{33}	-0.575	[0.462]	F_{24}	-0.576	[0.452]	F_{24}	-0.575	[0.454]						
F_{13}	-0.617	[0.440]	F_{36}	-0.586	[0.469]	F_{18}	-0.604	[0.453]	F_{18}	-0.605	[0.454]						
F_{14}	-0.598	[0.434]	F_{38}	-0.595	[0.463]	F_{21}	-0.589	[0.449]	F_{21}	-0.589	[0.449]						
F_{15}	-0.595	[0.437]	F_{34}	-0.583	[0.467]	F_{22}	-0.609	[0.443]	F_{22}	-0.604	[0.446]						
$\sum_{Hg(OTeF_5)_2}$	**-0.002**			**-0.035**			**-0.046**			**-0.038**								
						Xe_{13}	1.256	[0.617]	Kr_{13}	1.060	[0.586]	Xe_1	1.196	[0.606]	Kr_1	1.013	[0.549]
						F_{17}	-0.602	[0.347]	F_{17}	-0.511	[0.340]	F_2	-0.598	[0.306]	F_2	-0.506	[0.280]
						F_{20}	-0.602	[0.344]	F_{20}	-0.504	[0.337]	F_3	-0.598	[0.306]	F_3	-0.506	[0.280]
$\sum_{NgF_2}$							**+0.052**			**+0.045**								
						Xe_{16}	1.259	[0.608]	Kr_{16}	1.066	[0.563]						
						F_{23}	-0.613	[0.353]	F_{23}	-0.520	[0.339]						
						F_{40}	-0.606	[0.356]	F_{40}	-0.513	[0.340]						
$\sum_{NgF_2}$							**+0.040**			**+0.033**								

Table S6.8. continued…

Bond orders											
$Hg(OTeF_5)_2$		**$[Hg(OTeF_5)_2]_3$**		**$[Hg(OTeF_5)_2]_3 \cdot 2XeF_2$**		**$[Hg(OTeF_5)_2]_3 \cdot 2KrF_2$**		**XeF_2**		**KrF_2**	
Hg_1-O_2	0.443	Hg_{16}-O_{22}	0.320	Hg_{12}-O_{28}	0.413	Hg_{12}-O_{28}	0.419				
O_2-Te_3	0.674	O_{22}-Te_{17}	0.654	O_{28}-Te_{14}	0.688	O_{28}-Te_{14}	0.686				
Te_3-F_4	0.513	Te_{17}-F_{18}	0.518	Te_{14}-F_{24}	0.515	Te_{14}-F_{24}	0.517				
Te_3-F_5	0.513	Te_{17}-F_{19}	0.511	Te_{14}-F_{18}	0.491	Te_{14}-F_{18}	0.489				
Te_3-F_6	0.476	Te_{17}-F_{20}	0.490	Te_{14}-F_{19}	0.490	Te_{14}-F_{19}	0.488				
Te_3-F_7	0.501	Te_{17}-F_{21}	0.508	Te_{14}-F_{21}	0.509	Te_{14}-F_{21}	0.509				
Te_3-F_8	0.503	Te_{17}-F_{23}	0.497	Te_{14}-F_{22}	0.491	Te_{14}-F_{22}	0.495				
Hg_1-O_9	0.443	Hg_{16}-O_{37}	0.320	Hg_{12}-O_{31}	0.434	Hg_{12}-O_{31}	0.439				
O_9-Te_{10}	0.674	O_{37}-Te_{32}	0.654	O_{31}-Te_{15}	0.689	O_{31}-Te_{15}	0.686				
Te_{10}-F_{12}	0.513	Te_{32}-F_{33}	0.518	Te_{15}-F_{30}	0.510	Te_{15}-F_{30}	0.510				
Te_{10}-F_{11}	0.513	Te_{10}-F_{34}	0.511	Te_{15}-F_{25}	0.513	Te_{15}-F_{25}	0.513				
Te_{10}-F_{13}	0.476	Te_{10}-F_{35}	0.490	Te_{15}-F_{26}	0.472	Te_{15}-F_{26}	0.473				
Te_{10}-F_{14}	0.501	Te_{10}-F_{36}	0.508	Te_{15}-F_{27}	0.492	Te_{15}-F_{27}	0.493				
Te_{10}-F_{15}	0.503	Te_{10}-F_{38}	0.497	Te_{15}-F_{29}	0.504	Te_{15}-F_{29}	0.504				
		Hg_{16}---O_{14}	0.051	Hg_{12}---F_{17}	0.063	Hg_{12}---F_{17}	0.061				
		Hg_{16}---O_{30}	0.051	Hg_{12}---F_{23}	0.062	Hg_{12}---F_{23}	0.061				
				Xe_{13}-F_{17}	0.281	Kr_{13}-F_{17}	0.274	Xe_1-F_2	0.303	Kr_1-F_2	0.275
				Xe_{13}-F_{20}	0.283	Kr_{13}-F_{20}	0.279	Xe_1-F_3	0.303	Kr_1-F_3	0.275
				Xe_{16}-F_{23}	0.285	Kr_{16}-F_{23}	0.271				
				Xe_{13}-F_{40}	0.293	Kr_{13}-F_{40}	0.275				

APPENDIX D References

(S1) Agron, P. A.; Begun, G. M.; Levy, H. A.; Mason, A. A.; Jones, C. G.; Smith, D. F. *Science*, **1963**, *139*, 842–844.

(S2) Turner, J. J.; Pimentel, G. C. *Science* **1963**, *140*, 974–975.

(S3) Al-Mukhtar, M.; Holloway, J. H.; Hope, E. G.; Schrobilgen, G. J. *J. Chem. Soc., Dalton Trans.* **1991,** 2831−2834.

APPENDIX E

Chapter 7 Supporting Information

A Homoleptic KrF_2 Complex, $[Hg(KrF_2)_8][AsF_6]_2 \cdot 2HF$

Adapted with permission from: DeBackere, J.R., and Schrobilgen, G.J. *Angew. Chem. Int. Ed.* **2018**, *57*, 13167–13171.

LIST OF FIGURES

page

LIST OF TABLES

page

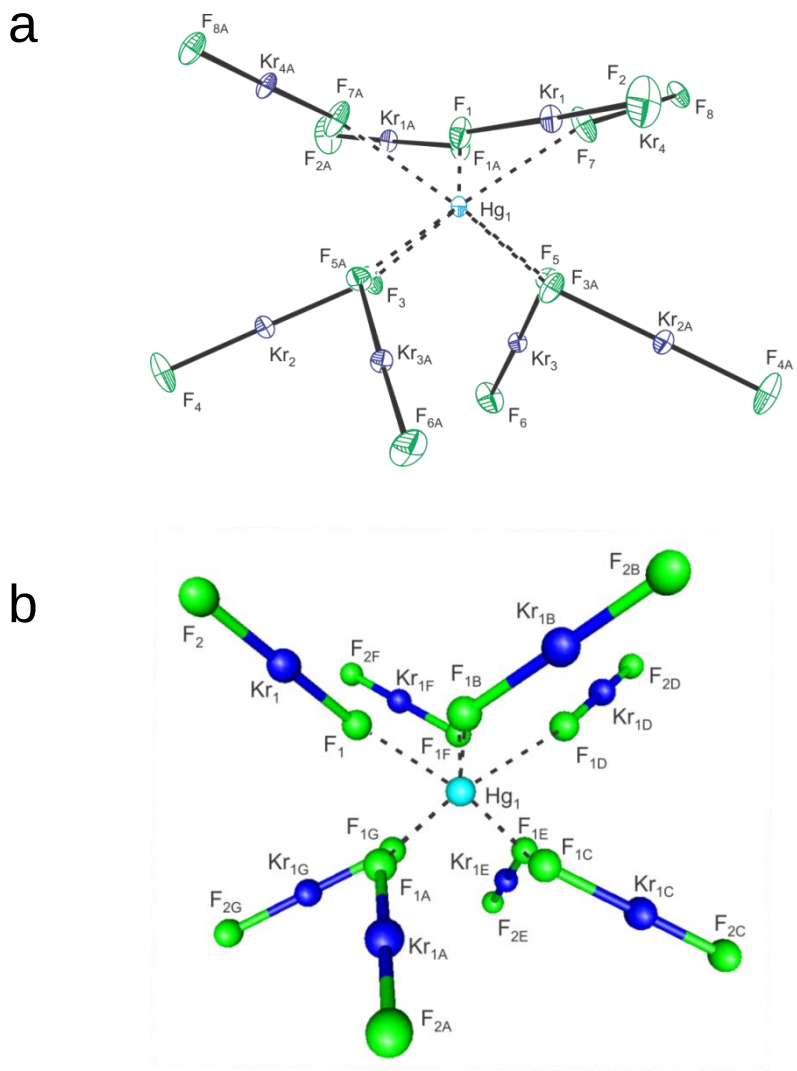

Figure S7.1. The slightly distorted square antiprismatic $[Hg(KrF_2)_8]^{2+}$ cation viewed perpendicular to its C_2-axis in **a**) the single-crystal X-ray structure of $[Hg(KrF_2)_8][AsF_6]_2 \cdot 2HF$ and **b**) the calculated gas-phase structure (S_8) at the B3LYP/def2-TZVPD level.

Figure S7.2. Factor-group analysis for $[Hg(KrF_2)_8]^{2+}$ in $[Hg(KrF_2)_8][AsF_6]_2 \cdot 2HF$[a]

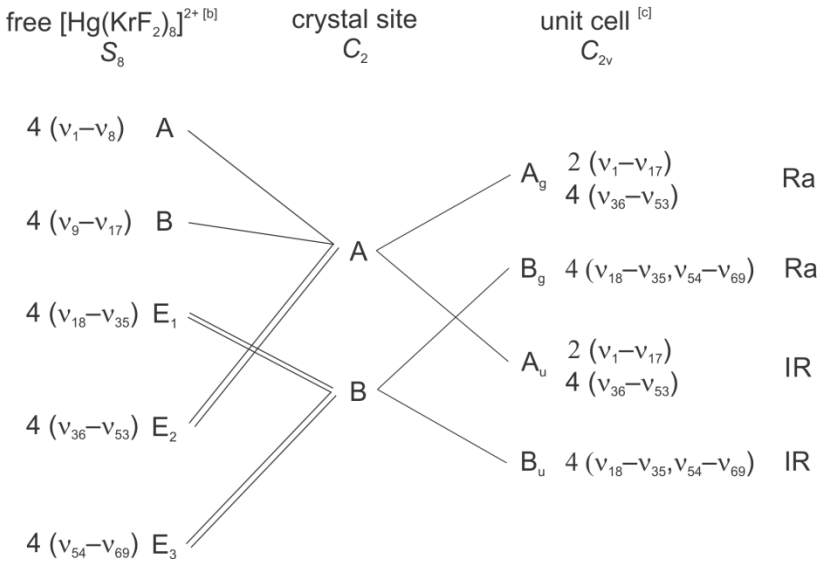

[a] The factor-group analysis for the external modes is not given. [b] The irreducible representation for the vibrations of gas phase $[Hg(KrF_2)_8]^{2+}$ is $\Gamma = 8A + 9B + 18E_1 + 18\ E_2 + 16\ E_3$. [c] Space group, *C*2/c; *Z* = 4.

Figure S7.3. Factor-group analysis for $[As_{(1)}F_6]^-$ in $[Hg(KrF_2)_8][AsF_6]_2 \cdot 2HF$ [a]

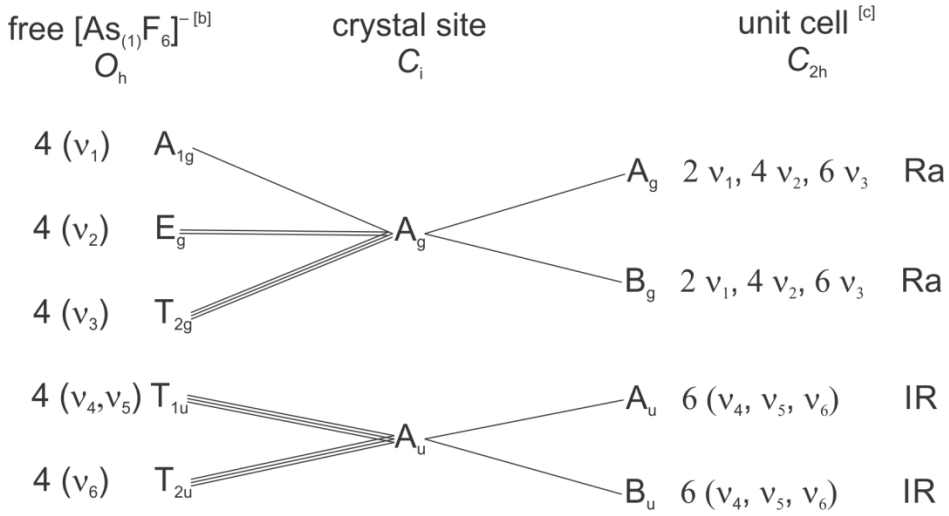

[a] The factor-group analysis for the external modes is not given. [b] The irreducible representation for the vibrations of gas-phase $[AsF_6]^-$ is $\Gamma = A_{1g} + E_g + T_{2g} + 2T_{1u} + T_{2u}$. [c] Space group, *C*2/c; *Z* = 4.

Figure S7.4. Factor-Group analysis for $[As_{(2)}F_6]^-$ in $[Hg(KrF_2)_8][AsF_6]_2 \cdot 2HF$ [a]

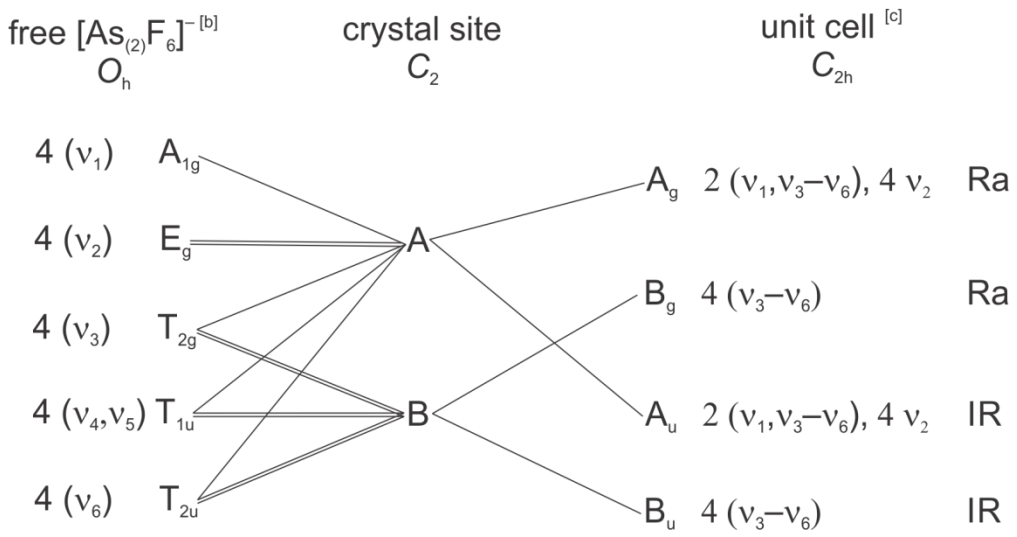

[a] The factor-group analysis for the external modes is not given. [b] The irreducible representation for the vibrations of gas-phase $[AsF_6]^-$ is $\Gamma = A_{1g} + E_g + T_{2g} + 2T_{1u} + T_{2u}$. [c] Space group, *C*2/c; *Z* = 4.

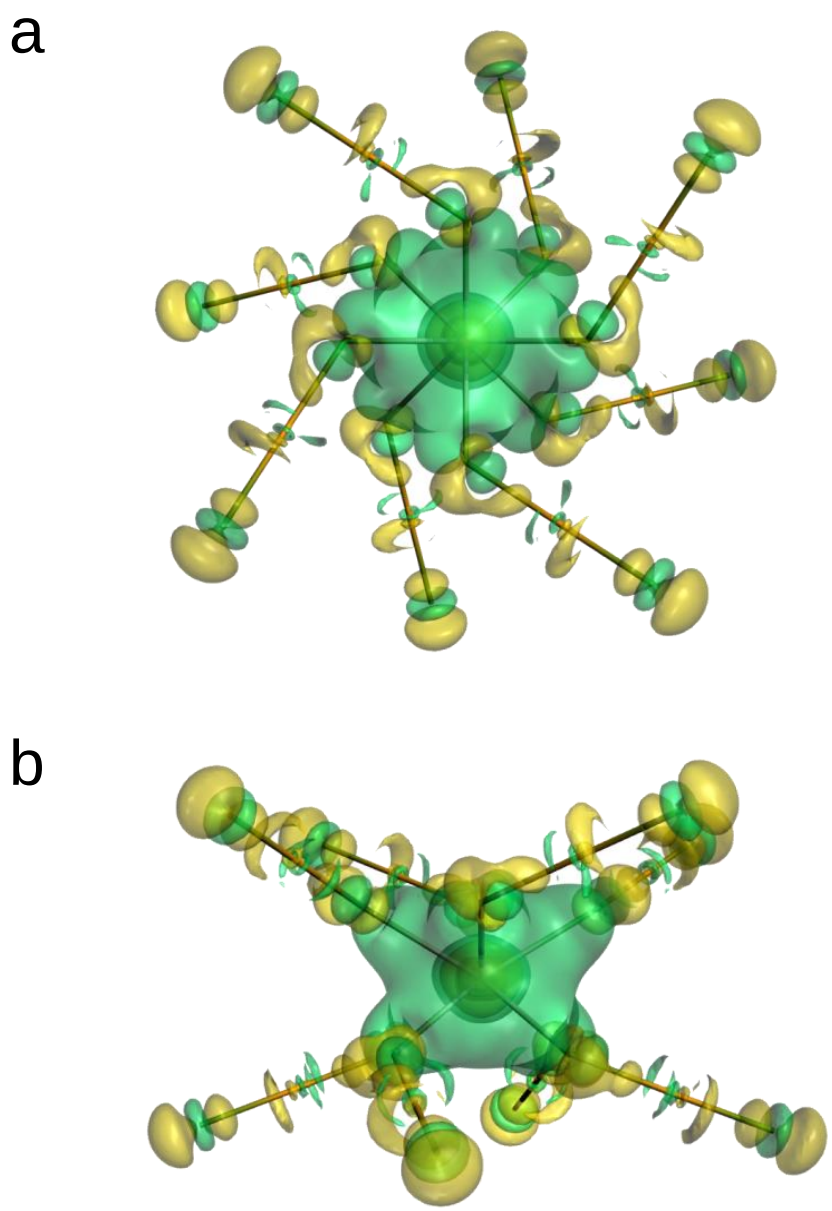

Figure S7.5. The SCF deformation density isosurface (0.003 a.u.) for $[Hg(KrF_2)_8]^{2+}$ showing the charge flow which results from interaction of the Hg^{2+} and $(KrF_2)_8$ fragments; colors indicate increased electron density (green) and decreased electron density (yellow) relative to the parent fragments. **a**) Top-on view looking down the C_2-axis and **b**) side-on view perpendicular to the C_2-axis. Calculated at the PBE/TZ2P level of theory.

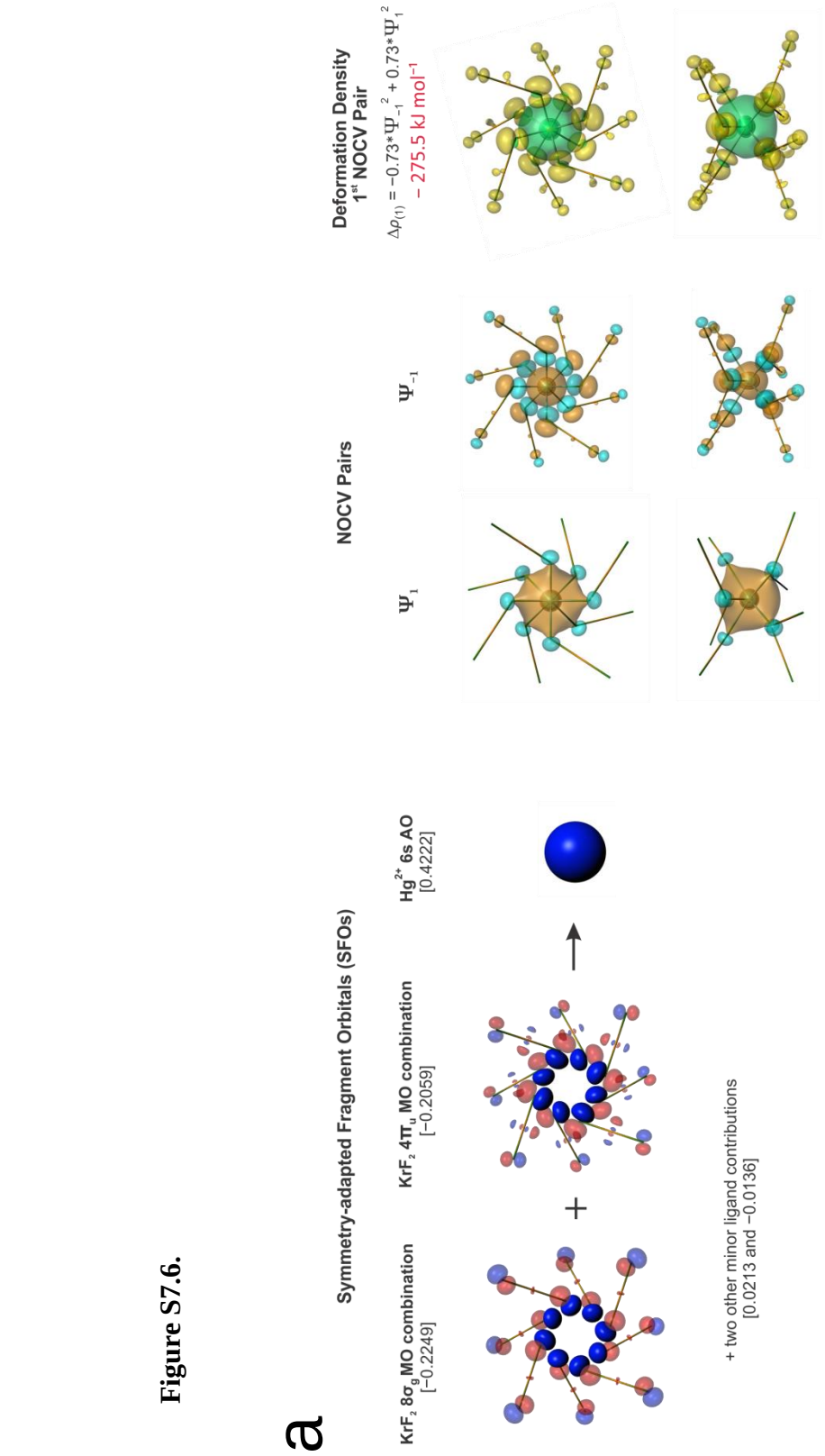
a
Symmetry-adapted Fragment Orbitals (SFOs)
KrF2 8σg MO combination
[−0.2249]
KrF2 4πu MO combination
[−0.2059]
Hg2+ 6s AO
[0.4222]
+ two other minor ligand contributions
[0.0213 and −0.0136]
NOCV Pairs
Ψ1
Ψ−1
Deformation Density
1st NOCV Pair
Δρ(1) = −0.73*Ψ−1 2 + 0.73*Ψ1 2
– 275.5 kJ mol−1

Figure S7.6.

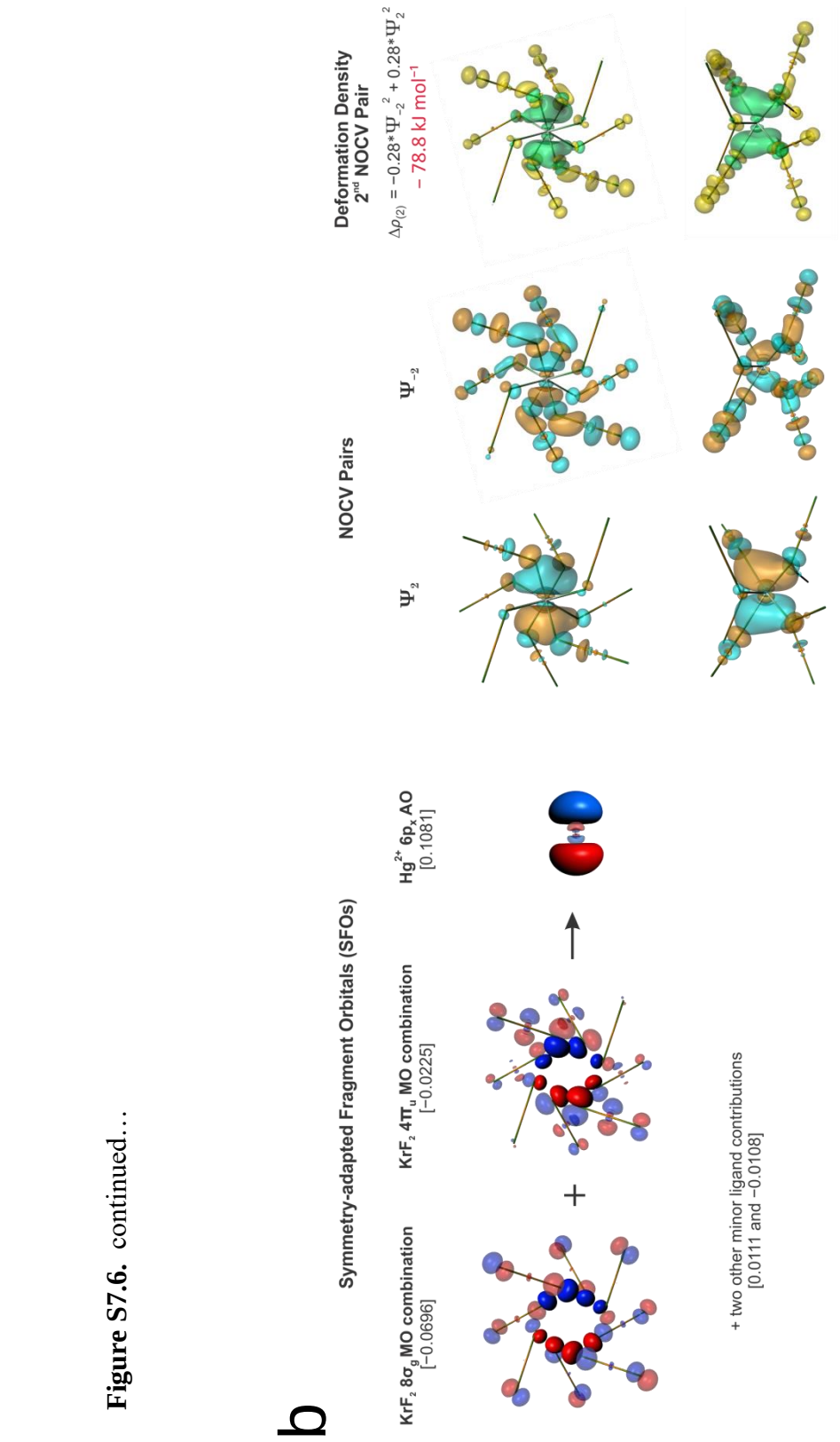

Figure S7.6. continued…

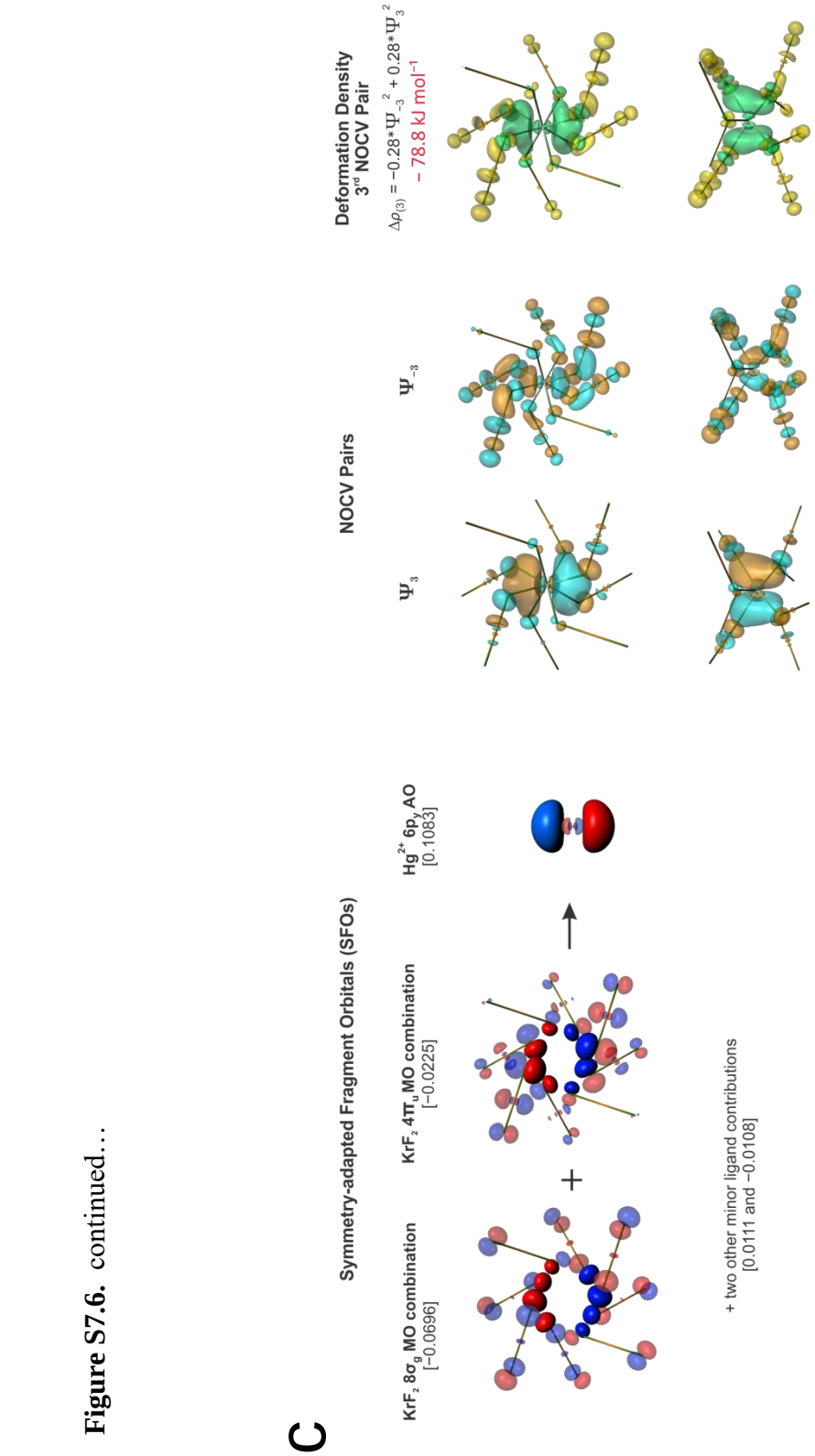

Figure S7.6. continued…

Figure S7.6. continued…

d

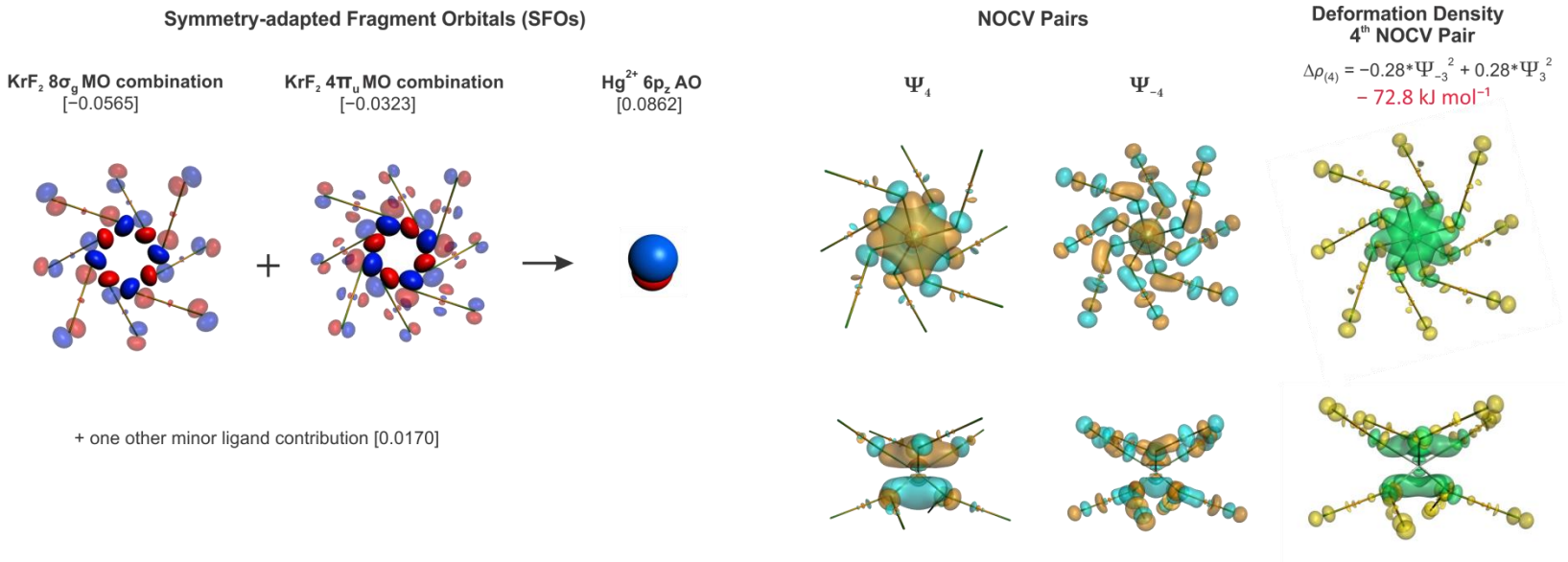

Figure S7.6. The ETS-NOCV analysis for Hg^{2+} and the $(KrF_2)_8$ ligand group of $[Hg(KrF_2)_8]^{2+}$ (S_4, PBE/TZ2P) showing combinations of the $8\sigma_g$ (HOMO–4) and $4\pi_u$ (HOMO) MOs on the KrF_2 ligands (Figure S6) which donate electron density to the empty Hg^{2+} **a)** 6s, **b)** $6p_x$, **c)** $6p_y$, and **d)** $6p_z$ orbitals. The isosurface values used for orbital depictions are: ligand fragment orbitals (0.03 a.u.), metal fragment orbitals (0.06 a.u.), NOCV pairs (0.03 a.u.), and deformation densities (0.001 a.u.). Fractional contributions of the Symmetry-adapted Fragment Orbitals (SFOs) to the NOCV pairs are given in square brackets. The relative phases of the NOCV pairs are indicated in turquoise and brown colors. The colors of the deformation densities indicate increased

Energy Decomposition Analysis (EDA)

The nature of a chemical bond is often discussed in terms of relative electrostatic (ionic) and covalent contributions. Arguments for each are frequently made based on atom electronegativities and calculated atomic partial charges; however, the latter can be misleading because the spatial charge distribution is not considered. The relative contributions of the electrostatic and covalent terms are therefore addressed by partitioning the interaction energy using the energy decomposition analysis (EDA) of Zeigler and Rauk.[S1]

The total instantaneous Kohn-Sham interaction energy (ΔE_{int}) is calculated as the energy difference between the molecule and its respective fragments in the frozen geometric states of the molecule/ion by use of density functional theory (DFT). The EDA divides ΔE_{int} into three contributions, the electrostatic, the exchange-repulsion, and the covalent bonding terms, as well as a ΔE_{disp} term when dispersion energy corrections are included (eq S7.1).

$$\Delta E_{int} = \Delta E_{Pauli} + \Delta E_{elstat} + \Delta E_{orb} + \Delta E_{disp} \qquad \text{(S7.1)}$$

The destabilizing Pauli interaction energy term (ΔE_{Pauli}) results from repulsive interactions of electrons having the same spin in the occupied orbitals of the interacting fragments. The ΔE_{elstat} term incorporates the quasiclassical electrostatic energy that occurs between the interacting fragments and is usually attractive. The orbital interaction energy (ΔE_{orb}) is also attractive, arising from charge transfer and mixing of the occupied and unoccupied orbitals of the fragments. Although ΔE_{orb} is used to estimate the degree of covalent bond character, the use of frozen charge distributions for the interacting fragments results in the inclusion of energy contributions arising from charge polarization. Stabilization of a complex requires that the sum of the attractive energy terms exceed the repulsive ΔE_{Pauli} term. The bond dissociation energy D_E (eq S7.2) is defined in terms of ΔE_{int} and the preparatory energy, ΔE_{prep}, which is the energy required to distort the equilibrium geometries and electronic states of all fragments to that of the molecule/ion.

$$D_E = -(\Delta E_{int} + \Delta E_{prep}) \qquad \text{(S7.2)}$$

Further details relating to EDA partitioning and its application to the analysis of chemical bonding may be found in the literature.[S2]

The bonding in $[Hg(KrF_2)_8]^{2+}$ was analyzed in terms of the interaction between a naked Hg^{2+} metal atom and a neutral $(KrF_2)_8$ ligand group (fragments were generated

from the TZ2P geometry-optimized structure of $[Hg(KrF_2)_8]^{2+}$ with their geometries frozen) with no targeted symmetry specified. The results of this analysis are provided in Table S7.1. The ΔE_{prep}-value for Hg^{2+} + $(KrF_2)_8$ was estimated using the energy difference between a geometry-optimized KrF_2 molecule ($D_{\infty h}$, "relaxed" fragment) and a single-point calculation using the coordinates of a KrF_2 molecule from the $(KrF_2)_8$ fragment ("prepared" fragment). This provided a preparation energy of 9.7 kJ mol^{-1} per KrF_2 ligand and an estimate of the total $(KrF_2)_8$ ligand group preparation energy, 8 × 9.7 = 77.6 kJ mol^{-1}. The resulting average bond energy calculated for each KrF_2 ligand is –151.1 kJ mol^{-1}. The ΔE_{orb} term for $[Hg(KrF_2)_8]^{2+}$ is greater than the corresponding ΔE_{elec} term, indicating the bonding is predominantly covalent; however, the ETS-NOCV analyses (vide infra) show that only ~53% of ΔE_{orb} comes from metal-ligand bonding.

For comparison, the EDA analysis for one KrF_2 ligand and a $[Hg(KrF_2)_7]^{2+}$ fragment was also carried out (Table S7.1). Although the preparation energy was not determined, the ΔE_{elec} term (–91.8 kJ mol^{-1}) is greater than the ΔE_{orb} term (–74.5 kJ mol^{-1}) which indicates the Hg–F(KrF) bond is predominantly electrostatic. In either case, these results indicate that both electrostatic and covalent interactions are important for the stabilization of $[Hg(KrF_2)_8]^{2+}$.

Table S7.1. Energy decomposition analyses for $[Hg(KrF_2)_8]^{2+}$ and $[Hg(KrF_2)_7]^{2+}$ (kJ mol^{-1}).[a]

	$Hg^{2+} + (KrF_2)_8$	$[Hg(KrF_2)_7]^{2+} + KrF_2$
ΔE_{int}	–1286.6	–79.4
ΔE_{orb}[b]	–940.1 (58.1%)	–74.5 (41.8%)
ΔE_{elstat}[b]	–651.0 (40.2%)	–91.8 (51.5%)
ΔE_{disp}[b]	–26.9 (1.7%)	–11.8 (6.6%)
ΔE_{Pauli}	331.4	98.7
Total ΔE_{prep}	77.6	
ΔE_{prep} for KrF_2	9.7	
$-D_E$	–1209.0	

[a] Calculated using the PBE density functional with a TZ2P all-electron basis set.
[b] Values in parentheses give the percentage of attractive interactions.

Extended Transition State and Natural Orbitals for Chemical Valence (ETS-NOCV)

Mitoraj and Michalak[S3] have combined the Extended Transition State and Natural Orbitals for Chemical Valence (ETS-NOCV) charge and energy partitioning scheme with EDA analyses, making it possible to divide the orbital interaction term, ΔE_{orb}, into pairwise energy contributions from fragment orbitals. This analysis results in a total differential density $\Delta\rho_{(r)}$ (corresponding to ΔE_{orb}) that is partitioned into deformation densities ($\Delta\rho_{(i)}$) which show the electron density flow. Each deformation density and its associated energy corresponds to the pair-wise donation and back donation of electron density between the fragments using NOCV pairs ($\Psi_{-i}/\ \Psi_i$) which are derived from the diagonal transition-state Kohn-Sham matrix elements. These NOCVs can be expressed in terms of the Kohn-Sham fragment orbitals which make significant contributions. Further details relating to the ETS-NOCV method and some recent applications are available in the literature.[S4]

There has been controversy relating to the inclusion of empty metal *n*p-AOs as true valence orbitals or as polarization functions for transition metals.[S5] The present ETS-NOCV analysis of Hg^{2+} + $(KrF_2)_8$ (Figure S7.6) suggests that contributions involving the Hg^{2+} 6p orbitals (–231 kJ mol^{-1}) are almost as important as those involving the Hg^{2+} 6s orbital (–275 kJ mol^{-1}) and therefore must be considered herein as valence functions. The most important metal-ligand orbital interactions in $[Hg(KrF_2)_8]^{2+}$ (–275.5 kJ mol^{-1}) predominately involve in-phase combinations of each KrF_2 ligands $8\sigma_g$ and $4\pi_u$ MOs (see Figure 7.4) with the empty 6s orbital of Hg^{2+} (Figure S7.6a). The next most significant orbital contributions (–78.8 kJ mol^{-1} and –78.8 kJ mol^{-1}) arise from the empty and degenerate $6p_x$ and $6p_y$ orbitals of Hg^{2+}, which mainly accept electron density from appropriately phased combinations of the $8\sigma_g$ and $4\pi_u$ MOs of KrF_2 (Figure S7.6b and S7.6c). The $8\sigma_g$ and $4\pi_u$ MOs of the KrF_2 ligands of the $(KrF_2)_8$ fragment do not all interact equivalently with the $6p_x$ and $6p_y$ orbitals of Hg^{2+}. Two of the eight KrF_2 molecules are effectively not involved in each case, as shown by visual inspection of the SFOs and by the absence of charge accumulation (green) between both of these KrF_2 molecules and the Hg^{2+} cation in the deformation densities (Figures S7.6b and S7.6c). The next most significant orbital contribution is similar and involves combinations of the $8\sigma_g$ and $4\pi_u$ MOs from all KrF_2 ligands that interact with the empty $6p_z$ orbital of Hg^{2+} (–72.8 kJ mol^{-1}, Figure S7.6d). The four metal-ligand interactions depicted in Figure S7.6 account for only ~53% of the ΔE_{orb} term. Although it is beyond the scope of the present work, several bonding contributions also arise from combinations of the occupied ligand $8\sigma_g$ and $4\pi_u$ MOs with the unoccupied $6\sigma_u$ (LUMOs) of neighboring KrF_2 ligands (–196.2

kJ mol^{-1}); this mixing of occupied and virtual orbitals within the same fragment is attributed to intra-fragment polarization which may be linked to the electronic bonding effects arising from chemical bond formation.[S6]

For comparison, the ETS-NOCV analysis was also carried out for the interaction of a KrF_2 ligand with $[Hg(KrF_2)_7]^{2+}$ (Table S7.1). There was only one significant contribution to the orbital interaction term (–39.9 kJ mol^{-1}) which resulted from electron donation by the $8\sigma_g$ and a $4\pi_u$ MOs of KrF_2 into two acceptor MOs of the $[Hg(KrF_2)_7]^{2+}$ fragment. The two $[Hg(KrF_2)_7]^{2+}$ acceptor MOs only have significant contributions (24.7% and 47.2%) from the 6s orbital of Hg^{2+}. The model corroborates involvement of the $8\sigma_g$ and a $4\pi_u$ MO of a KrF_2 ligand in bonding to Hg^{2+}. A major advantage of the Hg^{2+} + $(KrF_2)_8$ ligand-group model is that it directly shows the 6s and the 6p orbitals of Hg^{2+} are significant contributors to the metal-ligand group bonding of $[Hg(KrF_2)_8]^{2+}$.

APPENDIX E References

[S1] a) T. Ziegler, A. Rauk, *Theor. Chim. Acta* **1977**, *46*, 1; b) T. Ziegler, A. Rauk, *Inorg. Chem.* **1979**, *18*, 1755; c) T. Ziegler, A. Rauk, *Inorg. Chem.* **1979**, *18*, 1558.

[S2] a) A. Diefenbach, F. M. Bichelhaupt, G. Frenking, *J. Am. Chem. Soc.* **2000,** *122*, 6449; b) M. Mitoraj, A. Michalak, T. Zeigler, *J. Chem. Theory Comput*. **2009**, *5*, 962; c) M. Mitoraj, A. Michalak, T. Zeigler, *Organometallics*, **2009**, *28*, 3727; d) L. Zhao, M. von Hopffgarten, D. M. Andrada, G. Frenking. *WIREs Comput. Mol. Sci*. **2018**, *8*, e1345.

[S3] a) A. Michalak, M. Mitoraj, T. Zeigler, *J. Phys. Chem. A* **2008**, *112*, 1933; b) M. Mitoraj, A. Michalak, *Organometallics* **2007**, *26*, 6576; c) M. Mitoraj, A. Michalak, *J. Mol. Model.* **2007**, *13*, 347; e) M. P. Mitoraj, A. Michalak, T. Ziegler, *J. Chem. Theory Comput.* **2009**, *5*, 962.

[S4] a) M. Mitoraj, A. Michalak, *J. Mol. Model.* **2008**, *14*, 681; b) T. A. N. Nguyen, G. Frenking, *Chem. Eur. J.* **2012**, *18*, 12733; c) M. Mousavi, G. Frenking, *Organometallics*, **2013**, *32*, 1743; d) M. P. Mitoraj, A. Michalak, *J. Mol. Model.* **2013**, *19*, 4681; e) M. P. Mitoraj, M. Parafiniuk, M. Srebreo, M. Handzlik, A. Buczek, A. Michalak, *J. Mol. Model.* **2011**, *17*, 2337.

[S5] a) F. Maseras, K. Morokuma, *Chem. Phys. Lett.* **1992**, *195*, 500; b) C. A. Bayse, M. B. Hall, *J. Am. Chem. Soc.* **1999**, *121*, 1348; c) G. Frenking, N. Fröhlich, *Chem. Rev*. **2000**, *100*, 717; d) C. R. Landis, F. Weinhold, *J. Comput. Chem.* **2007**, *28*, 198; e) G. Frenking, in *The Chemical Bond: Chemical Bonding Across the Periodic Table* (Eds.: G. Frenking and S. Shaik), Wiley-VCH, Weinheim, **2014**, pp. 175–218.

[S6] M. P. Mitoraj, R. Kurczab, M. Boczar, A. Michalak, *J. Mol. Model*. **2010**, *16*, 1789.

APPENDIX F

Chapter 8 Supporting Information

Syntheses and Structures of a Series of Krypton Difluoride Coordination Complexes of $Hg(PnF_6)_2$ (Pn = As or Sb) and $FHg(AsF_6)$

LIST OF FIGURES

LIST OF TABLES

Table S8.1. Experimental and Calculated Geometrical Parameters of $Hg(KrF_2)_5(AsF_6)_2$ **(5)** and **(5′)**

	exptl [a]		**calcd** [b]
Bond Lengths (Å)			
$Hg_1–F_{1(Kr1)}$	2.317(4)	$Hg_1–F_{1(Kr1)}$	2.419
$Hg_1–F_{3(Kr2)}$	2.332(5)	$Hg_1–F_{3(Kr2)}$	2.366
$Hg_1–F_{5(Kr3)}$	2.307(5)	$Hg_1–F_{5(Kr3)}$	2.425
$Hg_1–F_{7(Kr4)}$	2.381(4)	$Hg_1–F_{7(Kr4)}$	2.468
$Hg_1–F_{9(Kr5)}$	2.324(5)	$Hg_1–F_{9(Kr5)}$	2.422
Hg_1--$F_{11(As1)}$	2.558(5)	Hg_1--$F_{11(As1)}$	2.438
Hg_1--$F_{13(As1)}$	2.591(5)	Hg_1--$F_{13(As1)}$	2.616
Hg_1--$F_{17(As2)}$	2.392(5)	Hg_1--$F_{17(As2)}$	2.316
$Kr_1–F_1$	1.948(4)	$Kr_1–F_1$	1.983
$Kr_2–F_3$	1.938(4)	$Kr_2–F_3$	1.984
$Kr_3–F_5$	1.932(5)	$Kr_3–F_5$	1.968
$Kr_4–F_7$	1.932(5)	$Kr_4–F_7$	1.953
$Kr_5–F_9$	1.948(5)	$Kr_5–F_9$	1.960
$Kr_1–F_2$	1.842(4)	$Kr_1–F_2$	1.846
$Kr_2–F_4$	1.850(5)	$Kr_2–F_4$	1.846
$Kr_3–F_6$	1.843(5)	$Kr_3–F_6$	1.851
$Kr_4–F_8$	1.851(5)	$Kr_4–F_8$	1.859
$Kr_5–F_{10}$	1.847(5)	$Kr_5–F_{10}$	1.856
$As_1–F_{17}$	1.757(4)	$As_1–F_{17}$	1.855
$As_1–F_{18}$	1.716(5)	$As_1–F_{18}$	1.747
$As_1–F_{19}$	1.717(5)	$As_1–F_{19}$	1.751
$As_1–F_{20}$	1.713(4)	$As_1–F_{20}$	1.731
$As_1–F_{21}$	1.697(5)	$As_1–F_{21}$	1.728
$As_1–F_{22}$	1.713(5)	$As_1–F_{22}$	1.711
$As_2–F_{11}$	1.752(4)	$As_2–F_{11}$	1.827
$As_2–F_{12}$	1.715(4)	$As_2–F_{12}$	1.745
$As_2–F_{13}$	1.759(4)	$As_2–F_{13}$	1.793
$As_2–F_{14}$	1.711(4)	$As_2–F_{14}$	1.733
$As_2–F_{15}$	1.709(4)	$As_2–F_{15}$	1.715
$As_2–F_{16}$	1.704(4)	$As_2–F_{16}$	1.711
Bond Angles (deg)			
$Kr_1–F_1–Hg_1$	128.9(2)	$Hg_1–F_1–Kr_1$	129.1
$Kr_2–F_3–Hg_1$	138.6(2)	$Hg_1–F_3–Kr_2$	131.2
$Kr_3–F_5–Hg_1$	133.5(2)	$Hg_1–F_5–Kr_3$	131.9

Table S8.1. continued….

Kr_4–F_7–Hg_1	139.1(2)	Hg_1–F_7–Kr_4	131.5
Kr_5–F_9–Hg_1	124.6(2)	Hg_1–F_9–Kr_5	124.4
F_1–Kr_1–F_2	179.1(2)	F_1–Kr_1–F_2	178.2
F_3–Kr_2–F_4	178.2(2)	F_3–Kr_2–F_4	177.9
F_5–Kr_3–F_6	178.9(2)	F_5–Kr_3–F_6	177.4
F_7–Kr_4–F_8	178.4(2)	F_7–Kr_4–F_8	178.2
F_9–Kr_5–F_{10}	177.6(2)	F_9–Kr_5–F_{10}	178.4
As_1–F_{17}--Hg_1	144.8(3)	As_1–F_{17}--Hg_1	138.4
As_2–F_{11}--Hg_1	109.2(2)	As_2–F_{11}--Hg_1	112.0
As_2–F_{13}--Hg_1	107.6(2)	As_2–F_{13}--Hg_1	105.8
F_1–Hg_1–F_3	135.4(2)	F_1–Hg_1–F_3	136.6
F_1–Hg_1–F_9	76.6(2)	F_1–Hg_1–F_9	71.5
F_1–Hg_1–F_5	125.9(2)	F_1–Hg_1–F_5	123.0
F_1–Hg_1--F_{11}	75.6(2)	F_1–Hg_1--F_{11}	80.3
F_1–Hg_1--F_{17}	70.9(2)	F_1–Hg_1--F_{17}	74.6
F_1–Hg_1--F_{13}	71.9(2)	F_1–Hg_1--F_{13}	71.4
F_1–Hg_1–F_7	142.7(2)	F_1–Hg_1–F_7	142.3
F_3–Hg_1–F_9	144.6(2)	F_3–Hg_1–F_9	150.9
F_3–Hg_1–F_5	80.0(2)	F_3–Hg_1–F_5	87.2
F_3–Hg_1--F_{11}	99.8(2)	F_3–Hg_1--F_{11}	99.3
F_3–Hg_1--F_{17}	84.2(2)	F_3–Hg_1--F_{17}	89.3
F_3–Hg_1–F_7	70.6(2)	F_3–Hg_1–F_7	73.4
F_3–Hg_1--F_{13}	69.5(2)	F_3–Hg_1--F_{13}	72.3
F_9–Hg_1–F_5	91.9(2)	F_9–Hg_1–F_5	78.7
F_9–Hg_1--F_{11}	70.4(1)	F_9–Hg_1--F_{11}	74.9
F_9–Hg_1--F_{17}	127.3(2)	F_9–Hg_1--F_{17}	109.8
F_9–Hg_1–F_7	74.0(2)	F_9–Hg_1–F_7	77.8
F_9–Hg_1--F_{13}	122.4(2)	F_9–Hg_1--F_{13}	122.9
F_5–Hg_1--F_{11}	149.2(2)	F_5–Hg_1--F_{11}	136.1
F_5–Hg_1--F_{17}	75.9(2)	F_5–Hg_1--F_{17}	71.5
F_5–Hg_1–F_7	77.8(2)	F_5–Hg_1–F_7	69.7
F_5–Hg_1–F_{13}	145.5(2)	F_5–Hg_1–F_{13}	158.3
F_7–Hg_1--F_{13}	105.7(2)	F_7–Hg_1--F_{13}	109.9
F_{11}--Hg_1--F_{17}	134.9(2)	F_{11}--Hg_1--F_{17}	150.9
F_{11}--Hg_1–F_7	73.2(2)	F_{11}--Hg_1–F_7	70.9
F_{11}--Hg_1--F_{13}	55.8(1)	F_{11}--Hg_1--F_{13}	57.4
F_{17}--Hg_1–F_7	146.3(2)	F_{17}--Hg_1–F_7	138.0
F_{17}--Hg_1--F_{13}	85.2(2)	F_{17}--Hg_1--F_{13}	100.2

Table S8.1. continued….

F_{21}–As_1–F_{22}	91.7(3)	F_{21}–As_1–F_{22}	94.2
F_{22}–As_1–F_{20}	91.6(2)	F_{22}–As_1–F_{20}	93.6
F_{22}–As_1–F_{18}	91.0(2)	F_{22}–As_1–F_{18}	92.9
F_{20}–As_1–F_{19}	90.1(2)	F_{20}–As_1–F_{19}	89.4
F_{21}–As_1–F_{17}	89.7(3)	F_{21}–As_1–F_{17}	86.5
F_{20}–As_1–F_{17}	88.5(2)	F_{20}–As_1–F_{17}	87.1
F_{19}–As_1–F_{17}	87.9(3)	F_{19}–As_1–F_{17}	86.1
F_{21}–As_1–F_{20}	90.3(2)	F_{21}–As_1–F_{20}	89.9
F_{21}–As_1–F_{18}	89.4(3)	F_{21}–As_1–F_{18}	89.9
F_{22}–As_1–F_{19}	90.7(3)	F_{22}–As_1–F_{19}	93.1
F_{18}–As_1–F_{19}	90.1(3)	F_{18}–As_1–F_{19}	88.7
F_{18}–As_1–F_{17}	88.9(2)	F_{18}–As_1–F_{17}	86.4
F_{20}–As_1–F_{18}	177.4(2)	F_{20}–As_1–F_{18}	173.3
F_{22}–As_1–F_{17}	178.6(3)	F_{22}–As_1–F_{17}	178.9
F_{21}–As_1–F_{19}	177.6(3)	F_{21}–As_1–F_{19}	172.6
F_{16}–As_2–F_{15}	92.6(2)	F_{16}–As_2–F_{15}	95.3
F_{15}–As_2–F_{14}	91.0(2)	F_{15}–As_2–F_{14}	92.0
F_{15}–As_2–F_{12}	91.2(2)	F_{15}–As_2–F_{12}	91.4
F_{14}–As_2–F_{11}	89.6(2)	F_{14}–As_2–F_{11}	87.8
F_{16}–As_2–F_{13}	90.8(2)	F_{16}–As_2–F_{13}	91.2
F_{14}–As_2–F_{13}	88.6(2)	F_{14}–As_2–F_{13}	88.5
F_{11}–As_2–F_{13}	86.6(2)	F_{11}–As_2–F_{13}	84.3
F_{16}–As_2–F_{14}	90.8(3)	F_{16}–As_2–F_{14}	92.7
F_{16}–As_2–F_{12}	91.1(3)	F_{16}–As_2–F_{12}	92.2
F_{15}–As_2–F_{11}	90.0(2)	F_{15}–As_2–F_{11}	89.2
F_{12}–As_2–F_{11}	88.4(2)	F_{12}–As_2–F_{11}	87.0
F_{12}–As_2–F_{13}	89.1(2)	F_{12}–As_2–F_{13}	87.5
F_{15}–As_2–F_{13}	176.6(2)	F_{15}–As_2–F_{13}	173.4
F_{14}–As_2–F_{12}	177.1(2)	F_{14}–As_2–F_{12}	173.7
F_{16}–As_2–F_{11}	177.4(3)	F_{16}–As_2–F_{11}	175.5

[a] The atom labeling scheme corresponds to that used in Figure 8.1a. [b] The atom labeling scheme corresponds to that used in Figure 8.1b. Calculated at the B3LYP/def2–TZVPP level of theory.

Table S8.2. Experimental Geometrical Parameters of $[Hg(KrF_2)_4(HF)_2(SbF_6)]_2[SbF_6]_2$ **(4)** and Calculated Geometrical Parameters of $[Hg_2(KrF_2)_8(HF)_4(SbF_6)_2]^{2+}$ (**4′**)

exptl [a]		**calcd** [b]	
Bond Lengths (Å)			
$Hg_1–F_{1(Kr1)}$	2.361(2)	$Hg_1–F_{1(Kr1)}$ $Hg_2–F_{9(Kr5)}$	2.325 2.325
$Hg_1–F_{3(Kr2)}$	2.345(2)	$Hg_1–F_{3(Kr2)}$ $Hg_2–F_{11(Kr6)}$	2.303 2.303
$Hg_1–F_{5(Kr3)}$	2.383(2)	$Hg_1–F_{5(Kr3)}$ $Hg_2–F_{13(Kr7)}$	2.351 2.351
$Hg_1–F_{7(Kr4)}$	2.309(2)	$Hg_1–F_{7(Kr4)}$ $Hg_2–F_{15(Kr8)}$	2.295 2.295
$Hg_1–F_{9(H)}$ $Hg_1–F_{10(H)}$	2.369(2) 2.400(2)	$Hg_1–F_{17(H)}$ $Hg_1–F_{18(H)}$ $Hg_2–F_{19(H)}$ $Hg_2–F_{20(H)}$	2.492 2.470 2.470 2.492
Hg_1--$F_{13A(Sb1A)}$	2.410(2)	Hg_1--$F_{28(Sb2)}$ Hg_2--$F_{22(Sb1)}$	2.466 2.467
Hg_1--$F_{11(Sb1)}$	2.384(2)	Hg_1--$F_{21(Sb1)}$ Hg_2--$F_{27(Sb2)}$	3.566 3.567
$Kr_1–F_1$	1.938(2)	$Kr_1–F_1$ $Kr_5–F_9$	2.007 2.007
$Kr_2–F_3$	1.932(2)	$Kr_2–F_3$ $Kr_6–F_{11}$	2.009 2.009
$Kr_3–F_5$	1.934(2)	$Kr_3–F_5$ $Kr_7–F_{13}$	2.012 2.012
$Kr_4–F_7$	1.945(1)	$Kr_4–F_7$ $Kr_8–F_{15}$	2.001 2.001
$Kr_1–F_2$	1.844(2)	$Kr_1–F_2$ $Kr_5–F_{10}$	1.830 1.829
$Kr_2–F_4$	1.843(2)	$Kr_2–F_4$ $Kr_6–F_{12}$	1.830 1.830
$Kr_3–F_6$	1.841(2)	$Kr_3–F_6$ $Kr_7–F_{14}$	1.828 1.828
$Kr_4–F_8$	1.840(2)	$Kr_4–F_8$ $Kr_8–F_{16}$	1.833 1.833

Table S8.2. continued….

		$Sb_1–F_{22}$	1.943
		$Sb_1–F_{23}$	1.920
$Sb_1–F_{11}$	1.908(2)	$Sb_1–F_{25}$	1.937
$Sb_1–F_{13}$	1.913(2)	$Sb_2–F_{28}$	1.943
		$Sb_2–F_{29}$	1.920
		$Sb_2–F_{31}$	1.937
		$Sb_1–F_{21}$	1.896
$Sb_1–F_{12}$	1.868(2)	$Sb_1–F_{24}$	1.876
$Sb_1–F_{14}$	1.858(2)	$Sb_1–F_{26}$	1.882
$Sb_1–F_{15}$	1.864(2)	$Sb_2–F_{27}$	1.896
$Sb_1–F_{16}$	1.867(2)	$Sb_2–F_{30}$	1.876
		$Sb_2–F_{32}$	1.882
$Sb_2–F_{17}$	1.869(2)		
$Sb_2–F_{18}$	1.871(2)		
$Sb_2–F_{19}$	1.864(2)		
$Sb_2–F_{20}$	1.899(2)		
$Sb_2–F_{21}$	1.874(2)		
$Sb_2–F_{22}$	1.896(2)		
		H_1--$F_{29(Sb2)}$	1.583
		H_2--$F_{25(Sb1)}$	1.515
		H_3--$F_{31(Sb1)}$	1.515
		H_4--$F_{23(Sb2)}$	1.583
		$F_{17(H)}$--$F_{29(Sb2)}$	2.523
$F_{9(H)}$--F_{20}	2.526(2)	$F_{18(H)}$--$F_{25(Sb1)}$	2.476
$F_{10(H)}$--F_{22A}	2.553(2)	$F_{19(H)}$--$F_{31(Sb1)}$	2.476
		$F_{20(H)}$--$F_{23(Sb2)}$	2.523
Bond Angles (deg)			
		$Kr_1–F_1–Hg_1$	136.7
		$Kr_2–F_3–Hg_1$	139.5
$Kr_1–F_1–Hg_1$	130.6(1)	$Kr_3–F_5–Hg_1$	140.3
$Kr_2–F_3–Hg_1$	135.6(1)	$Kr_4–F_7–Hg_1$	137.3
$Kr_3–F_5–Hg_1$	136.9(1)	$Kr_5–F_9–Hg_2$	136.7
$Kr_4–F_7–Hg_1$	127.3(1)	$Kr_6–F_{11}–Hg_2$	139.5
		$Kr_7–F_{13}–Hg_2$	140.3
		$Kr_8–F_{15}–Hg_2$	137.3

Table S8.2. continued….

$Sb_{1A}–F_{13A}$--Hg_1	150.8(1)	$Sb_2–F_{28}$--Hg_1	149.5
		$Sb_1–F_{22}$--Hg_2	149.5
$Sb_1–F_{11}$--Hg_1	158.4(1)	$Sb_1–F_{21}$--Hg_1	130.4
		$Sb_2–F_{27}$--Hg_2	130.4
		$F_1–Kr_1–F_2$	179.3
		$F_3–Kr_2–F_4$	179.4
		$F_5–Kr_3–F_6$	179.4
$F_1–Kr_1–F_2$	178.6(1)	$F_7–Kr_4–F_8$	179.1
$F_3–Kr_2–F_4$	179.5(1)	$F_9–Kr_5–F_{10}$	179.3
$F_5–Kr_3–F_6$	177.5(1)	$F_{11}–Kr_6–F_{12}$	179.4
$F_7–Kr_4–F_8$	179.6(1)	$F_{13}–Kr_7–F_{14}$	179.4
		$F_{15}–Kr_8–F_{16}$	179.1
		$F_7–Hg_1–F_3$	154.5
$F_7–Hg_1–F_3$	122.3(1)	$F_{15}–Hg_2–F_{11}$	154.5
$F_3–Hg_1–F_1$	73.1(1)	$F_3–Hg_1–F_1$	81.7
		$F_{11}–Hg_2–F_9$	81.7
$F_3–Hg_1–F_5$	72.7(1)	$F_3–Hg_1–F_5$	124.5
		$F_{11}–Hg_2–F_{13}$	124.5
$F_7–Hg_1–F_5$	74.7(1)	$F_7–Hg_1–F_5$	78.9
		$F_{15}–Hg_2–F_{13}$	78.9
$F_1–Hg_1–F_5$	74.0(1)	$F_1–Hg_1–F_5$	83.4
		$F_9–Hg_2–F_{13}$	83.4
$F_7–Hg_1–F_1$	137.9(1)	$F_7–Hg_1–F_1$	91.0
		$F_{15}–Hg_2–F_9$	91.0
$F_3–Hg_1–F_9$	74.0(1)	$F_3–Hg_1–F_{17}$	78.6
		$F_{11}–Hg_2–F_{20}$	78.6
$F_7–Hg_1–F_9$	144.7(1)	$F_7–Hg_1–F_{17}$	75.9
		$F_{15}–Hg_2–F_{20}$	75.9
$F_1–Hg_1–F_9$	74.4(1)	$F_1–Hg_1–F_{17}$	76.8
		$F_9–Hg_2–F_{20}$	76.8
$F_5–Hg_1–F_9$	139.2(1)	$F_5–Hg_1–F_{17}$	147.0
		$F_{13}–Hg_2–F_{20}$	147.0
$F_3–Hg_1–F_{10}$	140.6(1)	$F_3–Hg_1–F_{18}$	74.8
		$F_{11}–Hg_2–F_{19}$	74.8
$F_5–Hg_1–F_{10}$	78.6(1)	$F_5–Hg_1–F_{17}$	147.0
		$F_{13}–Hg_2–F_{29}$	147.0
$F_7–Hg_1–F_{10}$	73.4(1)	$F_7–Hg_1–F_{18}$	126.9
		$F_{15}–Hg_2–F_{19}$	126.9

Table S8.2. continued….

F_1–Hg_1–F_{10}	73.4(1)
F_7–Hg_1--F_{11}	76.0(1)
F_1–Hg_1--F_{11}	117.4(1)
F_3–Hg_1--F_{11}	142.3(1)
F_5–Hg_1--F_{11}	143.9(1)
F_3–Hg_1--F_{13A}	78.3(1)
F_5–Hg_1--F_{13A}	116.2(1)
F_7–Hg_1--F_{13A}	75.3(1)
F_1–Hg_1--F_{13A}	144.9(1)
F_{11}--Hg_1--F_{13A}	75.5(1)
F_9–Hg_1--F_{13A}	78.6(1)
F_9–Hg_1--F_{11}	74.8(1)
F_{10}–Hg_1--F_{11}	73.1(1)
F_{10}–Hg_1--F_{13A}	139.9(1)
F_9–Hg_1–F_{10}(H)	115.6(1)
F_1–Hg_1–F_{18}	129.1
F_9–Hg_2–F_{19}	129.1
F_7–Hg_1--F_{21}	59.7
F_{15}–Hg_2--F_{27}	59.6
F_1–Hg_1--F_{21}	141.1
F_9–Hg_2--F_{27}	141.1
F_3–Hg_1--F_{21}	135.7
F_{11}–Hg_2--F_{27}	135.7
F_5–Hg_1--F_{21}	67.1
F_{13}–Hg_2--F_{27}	67.1
F_3–Hg_1--F_{28}	87.7
F_{11}–Hg_2--F_{22}	87.7
F_5–Hg_1--F_{28}	123.2
F_{13}–Hg_2--F_{22}	123.2
F_7–Hg_1--F_{28}	87.6
F_{15}–Hg_2--F_{22}	87.6
F_1–Hg_1--F_{28}	152.3
F_9–Hg_2--F_{22}	152.3
F_{21}--Hg_1--F_{28}	58.6
F_{27}--Hg_2--F_{22}	58.6
F_{17}–Hg_1--F_{28}	76.0
F_{20}–Hg_2--F_{22}	76.0
F_{17}–Hg_1--F_{21}	115.0
F_{20}–Hg_2--F_{27}	115.0
F_{18}–Hg_1--F_{21}	67.9
F_{19}–Hg_2--F_{27}	67.9
F_{18}–Hg_1--F_{28}	71.3
F_{19}–Hg_2--F_{22}	71.3
F_{17}–Hg_1–F_{18}	138.2
F_{20}–Hg_2–F_{19}	138.2
F_{12}–Sb_1–F_{15}	90.6(1)
F_{12}–Sb_1–F_{16}	90.9(1)
F_{14}–Sb_1–F_{11}	89.6(1)
F_{15}–Sb_1–F_{11}	90.4(1)
F_{21}–Sb_1–F_{22}	89.6
F_{21}–Sb_1–F_{24}	91.5
F_{21}–Sb_1–F_{25}	88.1
F_{21}–Sb_1–F_{26}	92.2
F_{22}–Sb_1–F_{23}	86.3
F_{22}–Sb_1–F_{25}	87.0
F_{22}–Sb_1–F_{26}	88.2
F_{23}–Sb_1–F_{24}	92.4
F_{23}–Sb_1–F_{25}	88.3

Table S8.2. continued….

F_{14}–Sb_1–F_{13}	88.4(1)	F_{23}–Sb_1–F_{26}	91.0
F_{11}–Sb_1–F_{13}	87.2(1)	F_{24}–Sb_1–F_{25}	89.6
F_{14}–Sb_1–F_{15}	92.2(1)	F_{24}–Sb_1–F_{26}	95.2
F_{14}–Sb_1–F_{16}	91.9(1)	F_{27}–Sb_2–F_{28}	89.6
F_{15}–Sb_1–F_{16}	93.0(1)	F_{27}–Sb_2–F_{30}	91.5
F_{12}–Sb_1–F_{11}	87.5(1)	F_{27}–Sb_2–F_{31}	88.1
F_{12}–Sb_1–F_{13}	88.8(1)	F_{27}–Sb_2–F_{32}	92.2
F_{16}–Sb_1–F_{13}	89.4(1)	F_{28}–Sb_2–F_{29}	86.3
		F_{28}–Sb_2–F_{31}	87.0
		F_{28}–Sb_2–F_{32}	88.2
		F_{29}–Sb_2–F_{30}	92.4
		F_{29}–Sb_2–F_{31}	88.3
		F_{29}–Sb_2–F_{32}	91.0
		F_{30}–Sb_2–F_{31}	89.6
		F_{30}–Sb_2–F_{32}	95.2
		F_{21}–Sb_1–F_{23}	174.7
F_{16}–Sb_1–F_{11}	176.3(1)	F_{22}–Sb_1–F_{24}	176.4
F_{14}–Sb_1–F_{12}	176.0(1)	F_{25}–Sb_1–F_{26}	175.1
F_{15}–Sb_1–F_{13}	177.6(1)	F_{27}–Sb_2–F_{29}	174.7
		F_{28}–Sb_2–F_{30}	176.4
		F_{31}–Sb_2–F_{32}	175.1
F_{19}–Sb_2–F_{18}	91.5(1)		
F_{18}–Sb_2–F_{21}	90.1(1)		
F_{21}–Sb_2–F_{22}	89.3(1)		
F_{17}–Sb_2–F_{20}	88.7(1)		
F_{21}–Sb_2–F_{20}	88.2(1)		
F_{22}–Sb_2–F_{20}	89.7(1)		
F_{19}–Sb_2–F_{17}	91.7(1)		
F_{17}–Sb_2–F_{18}	91.8(1)		
F_{17}–Sb_2–F_{21}	90.5(1)		
F_{19}–Sb_2–F_{22}	88.5(1)		
F_{18}–Sb_2–F_{22}	89.8(1)		
F_{19}–Sb_2–F_{20}	90.2(1)		
F_{18}–Sb_2–F_{20}	178.3(1)		
F_{17}–Sb_2–F_{22}	178.4(1)		
F_{19}–Sb_2–F_{21}	177.3(1)		

[a] The atom labeling scheme corresponds to that used in Figure 8.2 and Figure S8.3. [b] The atom labeling scheme corresponds to that used in Figure 8.9a. Calculated at the B3LYP/def2–TZVPP level of theory.

Table S8.3. Experimental Geometrical Parameters of $Hg(KrF_2)_3(HF)(SbF_6)_2$ **(3)** and Calculated Geometrical Parameters of $Hg(KrF_2)_3(HF)(SbF_6)_2$ (**3′**)

exptl [a]		**calcd** [b]	
Bond Lengths (Å)			
$Hg_1–F_{1(Kr1)}$	2.289(3)	$Hg_1–F_{1(Kr1)}$	2.334
$Hg_1–F_{3(Kr2)}$	2.366(3)	$Hg_1–F_{3(Kr2)}$	2.371
$Hg_1–F_{5(Kr3)}$	2.317(3)	$Hg_1–F_{5(Kr3)}$	2.368
$Hg_1–F_{7(H)}$	2.366(3)	$Hg_1–F_{7(H)}$	2.349
$Hg_1\text{--}F_{8(Sb1)}$	2.388(3)	$Hg_1\text{--}F_{8(Sb1)}$	2.404
$Hg_1\text{--}F_{14(Sb2)}$	2.424(3)	$Hg_1\text{--}F_{9(Sb1)}$	2.416
$Hg_1\text{--}F_{10A(Sb1A)}$	2.404(3)	$Hg_1\text{--}F_{14(Sb2)}$	2.402
$Hg_1\text{--}F_{15B(Sb2A)}$	2.448(2)		
$Kr_1–F_1$	1.950(3)	$Kr_1–F_1$	1.990
$Kr_2–F_3$	1.956(3)	$Kr_2–F_3$	1.974
$Kr_3–F_5$	1.956(3)	$Kr_3–F_5$	1.981
$Kr_1–F_2$	1.835(3)	$Kr_1–F_2$	1.842
$Kr_2–F_4$	1.826(3)	$Kr_2–F_4$	1.846
$Kr_3–F_6$	1.828(4)	$Kr_3–F_6$	1.845
$Sb_1–F_8$	1.904(3)	$Sb_1–F_8$	1.970
$Sb_1–F_9$	1.863(3)	$Sb_1–F_9$	1.977
$Sb_1–F_{10}$	1.903(3)	$Sb_1–F_{10}$	1.872
$Sb_1–F_{11}$	1.874(3)	$Sb_1–F_{11}$	1.894
$Sb_1–F_{12}$	1.867(3)	$Sb_1–F_{12}$	1.892
$Sb_1–F_{13}$	1.862(3)	$Sb_1–F_{13}$	1.875
$Sb_2–F_{16}$	1.865(3)	$Sb_2–F_{14}$	1.978
$Sb_2–F_{14}$	1.897(3)	$Sb_2–F_{15}$	1.960
$Sb_2–F_{15}$	1.897(2)	$Sb_2–F_{16}$	1.892
		$Sb_2–F_{17}$	1.878
$Sb_3–F_{18}$	1.864(3)	$Sb_2–F_{18}$	1.872
$Sb_3–F_{19}$	1.866(3)	$Sb_2–F_{19}$	1.892
$Sb_3–F_{17}$	1.908(3)		
$F_{7(H)}\text{---}F_{17(Sb3)}$	2.487(4)	$F_{7(H)}\text{---}F_{15}$	2.416
		$H–F_7$	0.977
		$H\text{---}F_{15(Sb2)}$	1.444

Table S8.3. continued….

Bond Angles (deg)			
$Kr_1–F_1–Hg_1$	138.4(1)	$Hg_1–F_1–Kr_1$	133.9
$Kr_2–F_3–Hg_1$	137.8(2)	$Hg_1–F_3–Kr_2$	133.9
$Kr_3–F_5–Hg_1$	134.3(1)	$Hg_1–F_5–Kr_3$	128.7
$Sb_1–F_{10A}$--Hg_1	146.7(2)	Hg_1--$F_9–Sb_1$	107.2
$Sb_1–F_8$--Hg_1	153.8(2)	Hg_1--$F_8–Sb_1$	107.8
$Sb_2–F_{15B}$--Hg_1	146.2(1)	Hg_1--$F_{15}–Sb_2$	86.7
$Sb_2–F_{14}$--Hg_1	141.5(1)		
$F_1–Kr_1–F_2$	177.6(1)	$F_1–Kr_1–F_2$	178.6
$F_3–Kr_2–F_4$	179.3(2)	$F_3–Kr_2–F_4$	178.2
$F_5–Kr_3–F_6$	178.1(2)	$F_5–Kr_3–F_6$	178.5
$F_1–Hg_1–F_5$	125.7(1)	$F_1–Hg_1–F_5$	154.1
$F_5–Hg_1–F_3$	75.0(1)	$F_3–Hg_1–F_5$	79.6
$F_1–Hg_1–F_3$	140.8(1)	$F_1–Hg_1–F_3$	123.2
$F_1–Hg_1–F_7$	140.1(1)	$F_1–Hg_1–F_7$	83.3
$F_3–Hg_1–F_7$	71.3(1)	$F_3–Hg_1–F_7$	81.9
$F_5–Hg_1–F_7$	77.0(1)	$F_5–Hg_1–F_7$	88.8
$F_1–Hg_1$--F_8	73.6(1)	$F_1–Hg_1$--F_8	103.9
$F_3–Hg_1$--F_8	74.4(1)	$F_3–Hg_1$--F_8	106.1
$F_1–Hg_1$--F_{10A}	73.8(1)	$F_5–Hg_1$--F_8	78.0
$F_3–Hg_1$--F_{10A}	80.4(1)	$F_1–Hg_1$--F_9	76.8
F_8--Hg_1--F_{10A}	83.1(1)	$F_3–Hg_1$--F_9	74.8
$F_5–Hg_1$--F_{14}	70.9(1)	$F_5–Hg_1$--F_9	124.9
$F_5–Hg_1$--F_{15A}	134.0(1)	$F_1–Hg_1$--F_{14}	74.7
$F_5–Hg_1$--F_8	146.1(1)	$F_3–Hg_1$--F_{14}	117.8
$F_5–Hg_1$--F_{10A}	77.8(1)	$F_5–Hg_1$--F_{14}	83.9
$F_1–Hg_1$--F_{15B}	71.2(1)	$F_1–Hg_1$--F_{14}	77.8
$F_3–Hg_1$--F_{15B}	121.3(1)		
$F_1–Hg_1$--F_{14}	71.2(1)		
$F_3–Hg_1$--F_{14}	144.3(1)		
$F_7–Hg_1$--F_{14}	90.8(1)	$F_7–Hg_1$--F_{14}	82.2
$F_7–Hg_1$--F_{15B}	70.4(1)	$F_7–Hg_1$--F_8	162.8
$F_7–Hg_1$--F_8	106.3(1)	$F_7–Hg_1$--F_9	133.2
$F_7–Hg_1$--F_{10A}	146.0(1)		
F_{10A}--Hg_1--F_{14}	102.1(1)	F_8--Hg_1--F_9	64.1
F_{10A}--Hg_1--F_{15B}	142.8(1)	F_8--Hg_1--F_{14}	84.0

Table S8.3. continued….

F_8--Hg_1--F_{15B}	75.7(1)	F_9--Hg_1--F_{14}	151.1
F_{14}--Hg_1--F_{15B}	77.9(1)		
F_8--Hg_1--F_{14}	141.2(1)	Hg_1–F_7–H_1	109.5
F_{13}–Sb_1–F_{12}	91.8(2)	F_{12}–Sb_1–F_9	86.7
F_{13}–Sb_1–F_{11}	91.0(1)	F_{12}–Sb_1–F_8	87.0
F_{12}–Sb_1–F_{11}	91.0(1)	F_{12}–Sb_1–F_{10}	93.4
F_9–Sb_1–F_{10}	88.8(2)	F_{12}–Sb_1–F_{13}	92.3
F_{11}–Sb_1–F_{10}	88.4(1)	F_9–Sb_1–F_8	80.8
F_9–Sb_1–F_8	89.0(2)	F_9–Sb_1–F_{11}	85.9
F_{11}–Sb_1–F_8	88.0(1)	F_9–Sb_1–F_{13}	91.1
F_{13}–Sb_1–F_9	92.0(2)	F_8–Sb_1–F_{11}	87.5
F_9–Sb_1–F_{12}	92.0(2)	F_8–Sb_1–F_{10}	91.0
F_{13}–Sb_1–F_{10}	89.4(1)	F_{11}–Sb_1–F_{10}	93.3
F_{12}–Sb_1–F_8	89.4(1)	F_{11}–Sb_1–F_{13}	92.2
F_{10}–Sb_1–F_8	89.4(1)	F_{10}–Sb_1–F_{13}	97.1
F_9–Sb_1–F_{11}	175.9(2)	F_{12}–Sb_1–F_{11}	171.4
F_{12}–Sb_1–F_{10}	178.6(1)	F_8–Sb_1–F_{13}	171.9
F_{13}–Sb_1–F_8	178.5(2)	F_9–Sb_1–F_{10}	171.8
F_{16}–Sb_2–F_{14}	89.8(1)	F_{19}–Sb_2–F_{17}	92.0
F_{16}–Sb_2–F_{14}	90.2(1)	F_{19}–Sb_2–F_{14}	85.7
F_{16}–Sb_2–F_{15}	89.3(1)	F_{19}–Sb_2–F_{18}	93.9
F_{14}–Sb_2–F_{15}	89.6(1)	F_{19}–Sb_2–F_{15}	87.7
F_{16}–Sb_2–F_{15}	90.8(1)	F_{17}–Sb_2–F_{14}	89.1
F_{14}–Sb_2–F_{15}	90.4(1)	F_{17}–Sb_2–F_{18}	95.6
F_{15}–Sb_2–F_{15A}	180.0	F_{17}–Sb_2–F_{16}	91.9
F_{14}–Sb_2–F_{14A}	180.0	F_{14}–Sb_2–F_{15}	85.1
F_{16}–Sb_2–F_{16A}	180.0	F_{14}–Sb_2–F_{16}	86.4
		F_{18}–Sb_2–F_{15}	90.1
F_{18}–Sb_3–F_{19}	90.1(2)	F_{18}–Sb_2–F_{16}	93.7
F_{18}–Sb_3–F_{19}	89.9(2)	F_{15}–Sb_2–F_{16}	87.6
F_{18}–Sb_3–F_{17}	89.8(2)	F_{19}–Sb_2–F_{16}	171.1
F_{19}–Sb_3–F_{17}	90.1(1)	F_{17}–Sb_2–F_{15}	174.3
F_{18}–Sb_3–F_{17}	90.2(2)	F_{14}–Sb_2–F_{18}	175.2
F_{19}–Sb_3–F_{17}	89.9(1)		
F_{19}–Sb_3–F_{19A}	180.0		
F_{17}–Sb_3–F_{17A}	180.0		
F_{18}–Sb_3–F_{18A}	180.0		

[a] The atom labeling scheme corresponds to that used in Figure 8.3. [b] The atom labeling scheme corresponds to that used in Figure 8.9b. Calculated at the B3LYP/def2–TZVPP level of theory.

Table S8.4. Experimental Geometrical Parameters of $Hg(KrF_2)_2(AsF_6)_2$ **(2)** and Calculated Geometrical Parameters of $Hg(KrF_2)_2(AsF_6)_2$ **(2′)**

exptl [a]		calcd [b]	
Bond Lengths (Å)			
$Hg_1–F_{1(Kr1)}$	2.136(3)	$Hg_1–F_{1(Kr1)}$	2.355
$Hg_1–F_{3(Kr2)}$	2.141(3)	$Hg_1–F_{3(Kr2)}$	2.355
$Hg_1\text{--}F_{5(As1)}$	2.408(3)	$Hg_1\text{--}F_{5(As1)}$	2.388
$Hg_1\text{--}F_{11(As2)}$	2.423(3)	$Hg_1\text{--}F_{11(As2)}$	2.388
$Hg_1\text{--}F_{9A(As1A)}$	2.594(3)	$Hg_1\text{--}F_{6(As1)}$	2.255
$Hg_1\text{--}F_{8A(As1A)}$	2.679(3)	$Hg_1\text{--}F_{12(As2)}$	2.255
$Hg_1\text{--}F_{14A(As2A)}$	2.547(3)		
$Hg_1\text{--}F_{13A(As2A)}$	2.875(3)		
$Kr_1–F_1$	1.995(3)	$Kr_1–F_1$	1.978
$Kr_1–F_2$	1.805(3)	$Kr_1–F_2$	1.846
$Kr_2–F_3$	2.004(2)	$Kr_2–F_3$	1.978
$Kr_2–F_4$	1.811(3)	$Kr_2–F_4$	1.846
$As_1–F_5$	1.747(3)	$As_1–F_5$	1.825
$As_1–F_6$	1.699(3)	$As_1–F_6$	1.864
$As_1–F_7$	1.704(3)	$As_1–F_7$	1.706
$As_1–F_8$	1.734(3)	$As_1–F_8$	1.705
$As_1–F_9$	1.738(3)	$As_1–F_9$	1.722
$As_1–F_{10}$	1.709(3)	$As_1–F_{10}$	1.732
$As_2–F_{11}$	1.746(3)	$As_2–F_{11}$	1.825
$As_2–F_{12}$	1.710(3)	$As_2–F_{12}$	1.864
$As_2–F_{13}$	1.714(3)	$As_2–F_{13}$	1.706
$As_2–F_{14}$	1.740(3)	$As_2–F_{14}$	1.705
$As_2–F_{15}$	1.712(3)	$As_2–F_{15}$	1.732
$As_2–F_{16}$	1.694(3)	$As_2–F_{16}$	1.722
Bond Angles (deg)			
$Kr_1–F_1–Hg_1$	148.6(2)	$Hg_1–F_1–Kr_1$	136.0
$Kr_2–F_3–Hg_1$	135.1(1)	$Hg_1–F_3–Kr_2$	136.0
$F_1–Kr_1–F_2$	177.6(1)	$F_1–Kr_1–F_2$	178.6
$F_3–Kr_2–F_4$	177.8(1)	$F_3–Kr_2–F_4$	178.6
$F_1–Hg_1–F_3$	170.5(1)	$F_1–Hg_1–F_3$	168.6

Table S8.4. continued….

F_3–Hg_1--F_5	87.7(1)	F_3–Hg_1--F_5	83.3
F_3–Hg_1--F_{11}	106.1(1)	F_3–Hg_1--F_{11}	104.8
F_1–Hg_1--F_{14A}	98.1(1)	F_1–Hg_1--F_5	104.8
F_5--Hg_1--F_{14A}	76.1(1)	F_5--Hg_1--F_6	63.3
F_1–Hg_1--F_{9A}	71.0(1)	F_1–Hg_1--F_{11}	83.3
F_5--Hg_1--F_{9A}	94.9(1)	F_5--Hg_1--F_{11}	91.6
F_{14A}--Hg_1--F_{9A}	166.6(1)	F_6--Hg_1--F_{12}	145.1
F_1–Hg_1--F_5	85.6(1)	F_1–Hg_1--F_6	87.6
F_1–Hg_1--F_{11}	82.0(1)	F_1–Hg_1--F_{12}	89.0
F_5--Hg_1--F_{11}	161.1(1)	F_5--Hg_1--F_{12}	150.1
F_3–Hg_1--F_{14A}	73.8(1)	F_3–Hg_1--F_6	89.0
F_{11}--Hg_1--F_{14A}	119.7(1)	F_{11}--Hg_1--F_6	150.1
F_3–Hg_1--F_{9A}	116.3(1)	F_3–Hg_1--F_{12}	87.6
F_{11}--Hg_1--F_{9A}	67.5(1)	F_{11}--Hg_1--F_{12}	63.3
F_1–Hg_1--F_{13A}	71.1		
F_5--Hg_1--F_{13A}	116.3(1)		
F_{9A}--Hg_1—F_{13A}	127.8(1)		
F_3–Hg_1--F_{13A}	106.3(1)		
F_{11}--Hg_1--F_{13A}	72.9(1)		
F_{14A}--Hg_1--F_{13A}	51.5(9)		
As_{1A}–F_{8A}--Hg_1	108.3(1)		
As_{1A}–F_{9A}--Hg_1	111.9(1)	Hg_1--F_5–As_1	104.8
As_1–F_5--Hg_1	143.4(2)	Hg_1--F_{11}–As_2	104.8
As_{2A}–F_{14A}--Hg_1	117.5(2)	Hg_1--F_6–As_1	108.8
As_{2A}–F_{13A}--Hg_1	104.1(1)	Hg_1--F_{12}–As_2	108.8
As_2–F_{11}--Hg_1	119.2(1)		
F_6–As_1–F_{10}	91.3(2)	F_5–As_1–F_9	87.2
F_{10}–As_1–F_8	90.1(2)	F_5–As_1–F_8	91.1
F_8–As_1–F_9	85.7(1)	F_5–As_1–F_6	82.8
F_7–As_1–F_5	89.9(1)	F_5–As_1–F_{10}	86.8
F_8–As_1–F_5	87.9(2)	F_9–As_1–F_8	93.4
F_6–As_1–F_7	92.0(2)	F_9–As_1–F_7	92.9
F_7–As_1–F_{10}	91.3(1)	F_9–As_1–F_6	86.7
F_7–As_1–F_8	91.3(1)	F_8–As_1–F_7	96.7
F_6–As_1–F_9	91.0(2)	F_8–As_1–F_{10}	92.7
F_{10}–As_1–F_9	90.3(1)	F_7–As_1–F_6	89.4
F_6–As_1–F_5	90.7(2)	F_7–As_1–F_{10}	92.2
F_9–As_1–F_5	88.5(1)	F_6–As_1–F_{10}	86.5

Table S8.4. continued….

F_{10}–As_1–F_5	177.7(2)	F_5–As_1–F_7	172.2
F_7–As_1–F_9	176.6(1)	F_6–As_1–F_8	173.9
F_6–As_1–F_8	176.4(2)	F_9–As_1–F_{10}	171.5
F_{16}–As_2–F_{12}	91.0(1)	F_{15}–As_2–F_{11}	86.8
F_{12}–As_2–F_{15}	90.4(1)	F_{15}–As_2–F_{14}	92.7
F_{12}–As_2–F_{13}	92.1(2)	F_{15}–As_2–F_{12}	86.5
F_{16}–As_2–F_{14}	91.3(2)	F_{15}–As_2–F_{13}	92.2
F_{15}–As_2–F_{14}	90.5(1)	F_{11}–As_2–F_{14}	91.1
F_{15}–As_2–F_{11}	87.2(2)	F_{11}–As_2–F_{16}	87.2
F_{14}–As_2–F_{11}	88.8(1)	F_{11}–As_2–F_{12}	82.8
F_{16}–As_2–F_{15}	91.6(2)	F_{14}–As_2–F_{16}	93.4
F_{16}–As_2–F_{13}	91.8(2)	F_{14}–As_2–F_{13}	96.7
F_{13}–As_2–F_{14}	86.9(2)	F_{16}–As_2–F_{12}	86.7
F_{12}–As_2–F_{11}	88.9(1)	F_{16}–As_2–F_{13}	92.9
F_{13}–As_2–F_{11}	89.4(2)	F_{12}–As_2–F_{13}	89.4
F_{16}–As_2–F_{11}	178.8(2)	F_{15}–As_2–F_{16}	171.5
F_{15}–As_2–F_{13}	175.7(2)	F_{11}–As_2–F_{13}	172.2
F_{12}–As_2–F_{14}	177.5(2)	F_{12}–As_2–F_{14}	173.9

[a] The atom labeling scheme corresponds to that used in Figure 8.4. [b] The atom labeling scheme corresponds to that used in Figure 8.9c. Calculated at the B3LYP/def2–TZVPP level of theory.

Table S8.5. Experimental Geometrical Parameters of $Hg(KrF_2)(HF)(AsF_6)_2$ **(1)** and Calculated Geometrical Parameters of $Hg(KrF_2)(HF)(AsF_6)_2$ **(1′)**

exptl [a]		**calcd** [b]	
Bond Lengths (Å)			
$Hg_1–F_{1(Kr1)}$	2.205(5)	$Hg_1–F_{1(Kr1)}$	2.344
$Hg_1–F_{3(H)}$	2.285(4)	$Hg_1–F_{3(H)}$	2.391
$Kr_1–F_1$	1.956(5)	$Kr_1–F_1$	1.983
$Kr_1–F_2$	1.809(5)	$Kr_1–F_2$	1.843
$Hg_1\text{--}F_{4(As1)}$	2.482(4)	$Hg_1\text{--}F_{4(As1)}$	2.341
$Hg_1\text{--}F_{7A(As1A)}$	2.470(4)	$Hg_1\text{--}F_{10(As2)}$	2.393
$Hg_1\text{--}F_{8A(As1A)}$	2.610(4)	$Hg_1\text{--}F_{5(As1)}$	2.258
$Hg_1\text{--}F_{10(As2)}$	2.437(4)	$Hg_1\text{--}F_{11(As2)}$	2.326
$Hg_1\text{--}F_{11A(As2A)}$	2.428(4)		
$Hg_1\text{--}F_{15B(As2B)}$	2.376(4)		
$Hg_1\text{--}F_{14(As2)}$	2.838(4)		
$As_1–F_4$	1.737(4)	$As_1–F_4$	1.840
$As_1–F_5$	1.700(4)	$As_1–F_8$	1.716
$As_1–F_6$	1.689(4)	$As_1–F_7$	1.704
$As_1–F_7$	1.747(4)	$As_1–F_6$	1.704
$As_1–F_8$	1.740(4)	$As_1–F_5$	1.864
$As_1–F_9$	1.725(4)	$As_1–F_9$	1.734
$As_2–F_{10}$	1.742(4)	$As_2–F_{14}$	1.785
$As_2–F_{11}$	1.758(4)	$As_2–F_{10}$	1.816
$As_2–F_{12}$	1.691(4)	$As_2–F_{13}$	1.701
$As_2–F_{13}$	1.692(4)	$As_2–F_{15}$	1.711
$As_2–F_{14}$	1.714(4)	$As_2–F_{11}$	1.835
$As_2–F_{15}$	1.741(4)	$As_2–F_{12}$	1.702
$F_{3(H)}\text{---}F_{9B}$	2.512(4)	$F_{3(H)}\text{---}F_{14}$	2.485
		$F_3–H_1$	0.961
		$F_{14}\text{---}H_1$	1.550
Bond Angles (deg)			
$Hg_1–F_1–Kr_1$	168.5(3)	$Hg_1–F_1–Kr_1$	139.0
$F_1–Kr_1–F_2$	178.4(2)	$F_1–Kr_1–F_2$	178.4

Table S8.5. continued….

F_1–Hg_1–F_3	142.3(2)	F_1–Hg_1–F_3	159.7
F_1–Hg_1--F_{10}	73.7(2)	F_1–Hg_1--F_{10}	98.4
F_1–Hg_1--F_{7A}	77.4(2)	F_1–Hg_1--F_5	93.3
F_1–Hg_1--F_4	78.2(2)	F_1–Hg_1--F_{11}	83.6
F_1–Hg_1--F_{11A}	75.2(2)		
F_1–Hg_1--F_{15B}	139.1(2)		
F_1–Hg_1--F_{8A}	119.8(2)		
F_3–Hg_1--F_{15B}	78.2(2)		
F_3–Hg_1--F_{11A}	122.3(2)	F_3–Hg_1--F_4	115.9
F_3–Hg_1--F_{8A}	67.4(1)	F_3–Hg_1--F_{10}	78.9
F_3–Hg_1--F_4	69.7(1)	F_3–Hg_1--F_{11}	77.5
F_3–Hg_1--F_{7A}	79.4(2)	F_3–Hg_1--F_5	95.7
F_3–Hg_1--F_{10}	135.6(1)		
F_{11A}--Hg_1--F_4	89.2(1)		
F_{11A}--Hg_1--F_{7A}	152.5(2)		
F_{11A}--Hg_1--F_{10}	84.9(1)		
F_{11A}--Hg_1--F_{8A}	144.5(1)		
F_{15B}--Hg_1--F_{11A}	75.1(2)		
F_{15B}--Hg_1--F_{7A}	129.7(1)	F_4--Hg_1--F_{10}	100.1
F_{15B}--Hg_1--F_{10}	76.2(2)	F_4--Hg_1--F_5	64.1
F_{15B}--Hg_1--F_{8A}	74.2(1)	F_4--Hg_1--F_{11}	156.2
F_{15B}--Hg_1--F_4	128.6(1)	F_{10}--Hg_1--F_5	159.4
F_{7A}--Hg_1--F_{8A}	55.7(1)	F_{10}--Hg_1--F_{11}	61.6
F_{7A}--Hg_1--F_4	82.8(1)	F_5--Hg_1--F_{11}	137.1
F_{10}--Hg_1--F_{7A}	89.8(1)		
F_{10}--Hg_1--F_4	151.9(2)		
F_{10}--Hg_1--F_{8A}	71.0(1)		
F_4--Hg_1--F_{8A}	124.0(1)		
		Hg_1–F_3–H_1	104.3
Hg_1--F_{8A} –As_{1A}	106.3(2)		
Hg_1--F_{7A}–As_{1A}	112.0(2)	Hg_1–F_4–As_1	105.5
Hg_1--F_4–As_1	143.3(2)	Hg_1–F_{10}–As_2	106.5
Hg_1--F_{10}–As_2	154.3(2)	Hg_1–F_5–As_1	108.0
Hg_1--F_{11A}–As_{2A}	118.1(2)	Hg_1–F_{11}–As_2	108.5
Hg_1--F_{15B}–As_{2B}	162.3(2)		
F_6–As_1–F_5	93.0(2)	F_{14}–As_2–F_{10}	85.8
F_5–As_1–F_9	90.1(2)	F_{14}–As_2–F_{13}	90.7
F_5–As_1–F_4	90.4(2)	F_{14}–As_2–F_{11}	85.5

Table S8.5. continued….

F_9–As_1–F_8	90.3(2)	F_{14}–As_2–F_{12}	90.4
F_6–As_1–F_7	90.4(2)	F_{10}–As_2–F_{13}	90.8
F_9–As_1–F_7	89.8(2)	F_{10}–As_2–F_{15}	89.0
F_8–As_1–F_7	85.8(2)	F_{10}–As_2–F_{11}	82.9
F_6–As_1–F_9	90.8(2)	F_{13}–As_2–F_{15}	94.5
F_6–As_1–F_4	90.7(2)	F_{13}–As_2–F_{12}	96.3
F_5–As_1–F_8	90.8(2)	F_{15}–As_2–F_{11}	88.8
F_4–As_1–F_8	88.2(2)	F_{15}–As_2–F_{12}	94.1
F_4–As_1–F_7	89.6(2)	F_{11}–As_2–F_{12}	89.8
F_5–As_1–F_7	176.6(2)	F_{14}–As_2–F_{15}	172.7
F_9–As_1–F_4	178.4(2)	F_{10}–As_2–F_{12}	172.0
F_6–As_1–F_8	176.1(2)	F_{13}–As_2–F_{11}	172.8
F_{12}–As_2–F_{13}	92.6(2)	F_4–As_1–F_8	87.2
F_{13}–As_2–F_{14}	91.4(2)	F_4–As_1–F_7	90.7
F_{13}–As_2–F_{15}	90.9(2)	F_4–As_1–F_5	82.4
F_{12}–As_2–F_{10}	90.2(2)	F_4–As_1–F_9	86.2
F_{14}–As_2–F_{10}	89.9(2)	F_8–As_1–F_7	93.8
F_{12}–As_2–F_{11}	89.5(2)	F_8–As_1–F_6	93.4
F_{14}–As_2–F_{11}	86.5(2)	F_8–As_1–F_5	86.8
F_{10}–As_2–F_{11}	88.3(2)	F_7–As_1–F_6	97.1
F_{12}–As_2–F_{15}	90.1(2)	F_7–As_1–F_9	92.5
F_{14}–As_2–F_{15}	89.6(2)	F_6–As_1–F_5	89.7
F_{13}–As_2–F_{10}	91.8(2)	F_6–As_1–F_9	92.2
F_{15}–As_2–F_{11}	89.0(2)	F_5–As_1–F_9	86.1
F_{15}–As_2–F_{10}	177.3(2)	F_4–As_1–F_6	172.1
F_{13}–As_2–F_{11}	177.9(2)	F_8–As_1–F_9	171.0
F_{12}–As_2–F_{14}	176.0(2)	F_7–As_1–F_5	173.1

[a] The atom labeling scheme corresponds to that used in Figure 8.5. [b] The atom labeling scheme corresponds to that used in Figure 8.9d. Calculated at the B3LYP/def2–TZVPP level of theory.

Table S8.6. Experimental Geometrical Parameters of $Hg(KrF_2)_4(HF)_2(AsF_6)_2 \cdot HF$ **(6)** and Calculated Geometrical Parameters of $Hg(KrF_2)_4(HF)_2(AsF_6)_2 \cdot HF$ **(6′)**

exptl [a]		**calcd** [b]	
Bond Lengths (Å)			
$Hg_1–F_{1(Kr1)}$	2.574(3)	$Hg_1–F_{1(Kr1)}$	2.347
$Hg_1–F_{3(Kr2)}$	2.639(3)	$Hg_1–F_{3(Kr2)}$	2.412
$Hg_1–F_{5(Kr3)}$	2.529(3)	$Hg_1–F_{5(Kr3)}$	2.390
$Hg_1–F_{7(Kr4)}$	2.929(3)	$Hg_1–F_{7(Kr4)}$	2.762
$Hg_1–F_{9(H)}$	2.086(3)	$Hg_1–F_{9(H)}$	2.500
$Hg_1–F_{10(H)}$	2.079(3)	$Hg_1–F_{10(H)}$	2.430
$Hg_1\text{--}F_{11(As1)}$	2.626(3)	$Hg_1\text{--}F_{11(As1)}$	2.453
$Hg_1\text{--}F_{18(As2)}$	2.844(3)	$Hg_1\text{--}F_{12(As1)}$	2.356
		$Hg_1\text{--}F_{18(As2)}$	2.525
$Kr_1–F_1$	1.909(3)	$Kr_1–F_1$	1.971
$Kr_2–F_3$	1.927(3)	$Kr_2–F_3$	1.969
$Kr_3–F_5$	1.923(3)	$Kr_3–F_5$	1.963
$Kr_4–F_7$	1.895(3)	$Kr_4–F_7$	1.916
$Kr_1–F_2$	1.872(3)	$Kr_1–F_2$	1.849
$Kr_2–F_4$	1.858(3)	$Kr_2–F_4$	1.852
$Kr_3–F_6$	1.859(4)	$Kr_3–F_6$	1.855
$Kr_4–F_8$	1.871(3)	$Kr_4–F_8$	1.882
$As_1–F_{11}$	1.743(3)	$As_1–F_{11}$	1.816
$As_1–F_{12}$	1.716(2)	$As_1–F_{12}$	1.825
$As_1–F_{13}$	1.716(2)	$As_1–F_{13}$	1.737
$As_1–F_{14}$	1.711(2)	$As_1–F_{14}$	1.733
$As_1– F_{15}$	1.737(2)	$As_1– F_{15}$	1.711
$As_1–F_{16}$	1.730(3)	$As_1–F_{16}$	1.709
$As_2–F_{17}$	1.741(3)	$As_2–F_{17}$	1.775
$As_2–F_{18}$	1.733(2)	$As_2–F_{18}$	1.798
$As_2–F_{19}$	1.720(3)	$As_2–F_{19}$	1.730
$As_2–F_{20}$	1.713(2)	$As_2–F_{20}$	1.777
$As_2–F_{21}$	1.714(4)	$As_2–F_{21}$	1.727
$As_2–F_{22}$	1.709(4)	$As_2–F_{22}$	1.705
$F_{9(H)}\text{---}F_{16A(As1A)}$	2.682(5)	$F_{9(H)}\text{---}F_{20}$	2.528

Table S8.6. continued….

		F_9–H_1	0.954
		H_1---F_{20}	1.583
$F_{10(H)}$---F_{23}	2.655(5)	$F_{10(H)}$---F_{23}	2.480
		F_{10}–H_2	0.964
		H_2---F_{23}	1.517
$F_{23(H)}$---$F_{17A(H)}$	2.562(4)	$F_{23(H)}$---F_{17}	2.539
		F_{23}–H_3	0.953
		H_3---F_{17}	1.586
Bond Angles (deg)			
Hg_1–F_1–Kr_1	140.4(1)	Hg_1–F_1–Kr_1	132.1
Hg_1–F_3–Kr_2	128.4(1)	Hg_1–F_3–Kr_2	127.9
Hg_1–F_5–Kr_3	143.1(1)	Hg_1–F_5–Kr_3	131.7
Hg_1–F_7–Kr_4	145.9(2)	Hg_1–F_7–Kr_4	148.4
F_1–Kr_1–F_2	178.1(1)	F_1–Kr_1–F_2	178.6
F_3–Kr_2–F_4	179.0(1)	F_3–Kr_2–F_4	178.2
F_6–Kr_3–F_5	179.3(1)	F_6–Kr_3–F_5	178.6
F_8–Kr_4–F_7	178.8(1)	F_8–Kr_4–F_7	179.4
F_1–Hg_1–F_5	125.8(1)	F_1–Hg_1–F_5	143.3
F_1–Hg_1–F_9	86.9(1)	F_1–Hg_1– F_9	75.7
F_{10}–Hg_1–F_5	113.6(1)	F_{10}–Hg_1–F_5	110.2
F_{10}–Hg_1–F_9	169.6(1)	F_{10}–Hg_1–F_9	138.2
F_{10}–Hg_1–F_1	87.9(1)	F_{10}–Hg_1–F_1	78.6
F_3–Hg_1–F_1	137.6(1)	F_3–Hg_1–F_1	142.0
F_3–Hg_1–F_9	88.2(1)	F_3–Hg_1–F_9	141.9
F_3–Hg_1–F_{10}	89.6(1)	F_3–Hg_1–F_{10}	72.3
F_3–Hg_1–F_5	93.7(1)	F_3–Hg_1–F_5	71.5
F_9–Hg_1–F_5	76.7(1)	F_9–Hg_1–F_5	75.0
F_7–Hg_1–F_1	148.2(1)	F_7–Hg_1–F_1	106.9
F_7–Hg_1–F_3	62.3(1)	F_7–Hg_1–F_3	72.2
F_7–Hg_1–F_5	59.0(1)	F_7–Hg_1–F_5	62.6
F_7–Hg_1–F_9	122.4(1)	F_7–Hg_1–F_9	107.7
F_7–Hg_1–F_{10}	64.9(1)	F_7–Hg_1–F_{10}	50.3
F_{10}–Hg_1--F_{11}	87.8(1)	F_{10}–Hg_1--F_{11}	82.5
F_{11}--Hg_1–F_5	153.3(1)	F_{11}--Hg_1–F_5	138.6
F_{11}--Hg_1–F_1	67.9(1)	F_{11}--Hg_1–F_1	76.7
F_{11}--Hg_1–F_9	81.9(1)	F_{11}--Hg_1–F_9	122.0

Table S8.6. continued….

F_{11}--Hg_1–F_3	69.7(1)	F_3–Hg_1--F_{11}	75.8
F_{11}--Hg_1–F_7	123.6(1)	F_7–Hg_1--F_{11}	128.9
F_{18}--Hg_1–F_1	73.1(1)	F_{18}--Hg_1–F_1	78.6
F_{18}--Hg_1–F_3	145.1(1)	F_{18}--Hg_1–F_3	112.8
F_{18}--Hg_1–F_5	67.9(1)	F_{18}--Hg_1–F_5	71.8
F_{18}--Hg_1--F_{11}	136.8(1)	F_{18}--Hg_1--F_{11}	146.4
F_{18}--Hg_1–F_9	114.1(1)	F_{18}--Hg_1–F_9	72.3
F_{18}--Hg_1–F_{10}	72.8(1)	F_{18}--Hg_1–F_{10}	70.6
F_{18}--Hg_1---F_7	82.9(1)	F_{18}--Hg_1–F_7	41.0
		Hg_1–F_9–H_9	111.5
		Hg_1–F_{10}–H_{10}	119.9
Hg_1--F_{18}–As_2	117.0(1)	Hg_1--F_{18}–As_2	148.1
Hg_1--F_{11}–As_1	137.6(1)	Hg_1--F_{11}–As_1	105.6
		Hg_1--F_{12}–As_1	109.2
F_{11}–As_1–F_{13}	90.7(1)	F_{11}–As_1–F_{13}	87.4
F_{12}–As_1–F_{14}	178.8(1)	F_{12}–As_1–F_{14}	87.9
F_{12}–As_1–F_{16}	89.3(1)	F_{12}–As_1–F_{16}	90.2
F_{12}–As_1–F_{11}	89.4(1)	F_{12}–As_1–F_{11}	83.7
F_{12}–As_1–F_{15}	89.5(1)	F_{12}–As_1–F_{15}	174.2
F_{12}–As_1–F_{13}	90.7(1)	F_{12}–As_1–F_{13}	87.1
F_{14}–As_1–F_{11}	89.9(1)	F_{14}–As_1–F_{11}	87.3
F_{14}–As_1–F_{13}	90.3(1)	F_{14}–As_1–F_{13}	173.1
F_{14}–As_1–F_{16}	91.3(1)	F_{14}–As_1–F_{16}	92.4
F_{15}–As_1–F_{13}	179.2(1)	F_{15}–As_1–F_{13}	92.2
F_{15}–As_1–F_{11}	88.5(1)	F_{15}–As_1–F_{11}	90.5
F_{15}–As_1–F_{14}	89.5(1)	F_{15}–As_1–F_{14}	92.3
F_{15}–As_1–F_{16}	90.3(1)	F_{15}–As_1–F_{16}	95.6
F_{16}–As_1–F_{11}	178.3(1)	F_{16}–As_1–F_{11}	173.9
F_{16}–As_1–F_{13}	90.6(1)	F_{16}–As_1–F_{13}	92.3
F_{17}–As_2–F_{19}	179.0(1)	F_{17}–As_2–F_{19}	90.1
F_{17}–As_2–F_{21}	88.9(1)	F_{17}–As_2–F_{21}	90.1
F_{17}–As_2–F_{22}	89.0(1)	F_{17}–As_2–F_{22}	92.6
F_{17}–As_2–F_{20}	89.6(1)	F_{17}–As_2–F_{20}	174.5
F_{18}–As_2–F_{20}	179.5(1)	F_{18}–As_2–F_{20}	87.6
F_{18}–As_2–F_{19}	88.8(1)	F_{18}–As_2–F_{19}	87.5
F_{18}–As_2–F_{21}	89.4(1)	F_{18}–As_2–F_{21}	88.1

Table S8.6. continued….

F_{18}–As_2–F_{17}	90.2(1)	F_{18}–As_2–F_{17}	87.0
F_{18}–As_2–F_{22}	90.5(1)	F_{18}–As_2–F_{22}	179.3
F_{19}–As_2–F_{22}	91.0(1)	F_{19}–As_2–F_{22}	92.0
F_{20}–As_2–F_{22}	90.0(1)	F_{20}–As_2–F_{22}	92.8
F_{20}–As_2–F_{19}	91.4(1)	F_{20}–As_2–F_{19}	89.9
F_{21}–As_2–F_{22}	177.9(1)	F_{21}–As_2–F_{22}	92.4
F_{21}–As_2–F_{20}	90.1(1)	F_{21}–As_2–F_{20}	89.5
F_{21}–As_2–F_{19}	91.1(1)	F_{21}–As_2–F_{19}	175.6
$F_{10(H)}$---$F_{23(H)}$---F_{17A}	126.2(2)	$F_{10(H)}$---$F_{23(H)}$---F_{17A}	113.4

[a] The atom labeling scheme corresponds to that used in Figure 8.6. [b] The atom labeling scheme corresponds to that used in Figure 8.9e. Calculated at the B3LYP/def2–TZVPP level of theory.

Table S8.7. Experimental Geometrical Parameters of $FHg(\mu_3\text{-}FKrF)_{1.5}(KrF_2)_{0.5}(AsF_6)$ **(7)** and Calculated Geometrical Parameters of $[F(HgF)_2(\mu_3\text{–}FKrF)_2]^+$.

exptl [a]		**calcd $[F(HgF)_2(\mu_3\text{–}FKrF)_2]^+$** [b]	
Bond Lengths (Å)			
Hg_1–$F_{1(Kr1)}$	2.542(6)		
Hg_2–$F_{1(Kr1)}$	2.691(6)	Hg_1–$F_{1(Kr1)}$	2.699
Hg_1–$F_{3(Kr2)}$	2.757(6)		
Hg_2–$F_{3(Kr2)}$	2.635(6)		
Hg_1–F_5	2.458(5)		
Hg_1–F_7	2.290(6)		
Hg_2–F_{6A}	2.620(6)		
Hg_2–F_{7A}	2.907(5)		
Hg_1–F_9	2.155(5)	Hg_1–F_3	2.083
Hg_2–F_9	2.053(5)		
Hg_1–F_{10A}	2.203(5)	Hg_1–F_4	1.935
Hg_2–F_{10}	2.032(5)		
Hg_1--$F_{11(As1)}$	2.484(7)		
Hg_1--$F_{14(As2)}$	2.567(8)		
Hg_2--$F_{17(As3)}$	2.566(8)		
Hg_2--$F_{20(As4)}$	2.575(9)		
Kr_1–F_1	1.955(6)	Kr_1–F_1	2.027
Kr_2–F_3	1.969(6)		
Kr_3–F_5	1.912(6)		
Kr_4–F_7	1.999(6)		
Kr_1–F_2	1.836(9)	Kr_1–F_2	1.871
Kr_2–F_4	1.846(8)		
Kr_3–F_6	1.854(6)		
Kr_4–F_8	1.820(6)		
As_1–F_{11}	1.735(5)		
As_1–F_{12}	1.690(7)		
As_1–F_{13}	1.714(6)		
As_2–F_{14}	1.738(7)		
As_2–F_{15}	1.694(7)		
As_2–F_{16}	1.712(7)		

Table S8.7. continued….

$As_3–F_{18}$	1.719(6)
$As_3–F_{17}$	1.741(6)
$As_3–F_{19}$	1.707(6)
$As_4–F_{20}$	1.728(7)
$As_4–F_{21}$	1.702(7)
$As_4–F_{22}$	1.710(8)

Bond Angles (deg)

$Hg_1–F_1–Kr_1$	134.4(3)		
$Hg_2–F_1–Kr_1$	125.3(3)	$Hg_1–F_1–Kr_1$	138.9
$Hg_1–F_3–Kr_2$	128.6(3)		
$Hg_2–F_3–Kr_2$	124.8(3)		
$Hg_1–F_7–Kr_4$	135.4(3)		
$Hg_2–F_7–Kr_4$	127.8(2)		
$Hg_1–F_1–Hg_2$	86.5(2)	$Hg_1–F_1–Hg_{1A}$	82.0
$Hg_1–F_3–Hg_2$	83.3(2)		
$Hg_1–F_7–Hg_{2A}$	94.9(2)		
$Hg_1–F_9–Hg_2$	116.9(2)	$Hg_1–F_3–Hg_{1A}$	116.5
$Hg_{1A}–F_{10}–Hg_2$	130.7(3)		
$F_7–Kr_4–F_8$	178.9(3)		
$F_5–Kr_3–F_6$	179.3(3)		
$F_4–Kr_2–F_3$	178.8(3)		
$F_2–Kr_1–F_1$	178.5(3)		
$Hg_1–F_5–Kr_3$	136.6(3)		
$Hg_1–F_7–Kr_4$	135.4(3)		
$Hg_2–F_{6A}–Kr_{3A}$	168.4(3)		
$F_9–Hg_1–F_5$	78.3(2)		
$F_9–Hg_1–F_7$	147.0(2)		
$F_9–Hg_1–F_3$	69.0(2)		
$F_9–Hg_1–F_1$	70.9(2)		
$F_9–Hg_1$--F_{11}	85.3(2)		
$F_9–Hg_1–F_{14}$	108.5(2)		
$F_9–Hg_1–F_{10A}$	139.6(2)		

Table S8.7. continued….

F_5–Hg_1–F_7	69.6(2)		
F_5–Hg_1–F_3	128.4(2)		
F_5–Hg_1–F_1	133.6(2)		
F_5–Hg_1--F_{11}	73.4(2)		
F_5–Hg_1--F_{14}	82.7(2)		
F_5–Hg_1–F_{10A}	141.9(2)		
F_7–Hg_1–F_3	127.0(2)		
F_7–Hg_1–F_1	138.6(2)		
F_7–Hg_1--F_{11}	78.9(2)		
F_7–Hg_1--F_{14}	75.1(2)		
F_7–Hg_1–F_{10A}	72.3(2)		
F_3–Hg_1–F_1	70.5(2)		
F_3–Hg_1--F_{11}	65.3(2)		
F_3–Hg_1--F_{14}	144.8(2)		
F_3–Hg_1–F_{10A}	77.2(2)		
F_1–Hg_1--F_{11}	135.0(2)		
F_1–Hg_1--F_{14}	75.5(2)		
F_1–Hg_1–F_{10A}	77.5(2)		
F_{11}--Hg_1--F_{14}	149.4(2)		
F_{11}--Hg_1–F_{10A}	100.5(2)		
F_{14}–Hg_1–F_{10A}	86.6(2)		
F_9–Hg_2–F_3	73.0(2)		
F_9–Hg_2–F_{10}	177.5(2)	F_3–Hg_1–F_4	176.2
F_9–Hg_2–F_1	69.1(2)		
F_9–Hg_2--F_{17}	90.0(2)		
F_9–Hg_2--F_{20}	88.7(2)		
F_9–Hg_2–F_{6A}	70.6(2)		
F_3–Hg_2–F_{10}	107.5(2)		
F_3–Hg_2–F_1	70.2(2)		
F_3–Hg_2--F_{17}	72.4(2)		
F_3–Hg_2--F_{20}	139.3(2)		
F_3–Hg_2–F_{6A}	127.1(2)		
F_{10}– Hg_2–F_1	113.3(2)		
F_{10}–Hg_2--F_{17}	87.8(2)		
F_{10}–Hg_2--F_{20}	92.4(2)		
F_{10}–Hg_2–F_{6A}	107.4(2)		
F_1–Hg_2--F_{17}	141.1(2)		
F_1–Hg_2--F_{20}	69.3(2)		

Table S8.7. continued….

F_1–Hg_2–F_{6A}	126.7(2)
F_{17}--Hg_2--F_{20}	145.3(2)
F_{20}--Hg_2–F_{6A}	76.3(2)
F_{7A}–Hg_2–F_9	120.0(2)
F_{7A}–Hg_2–F_{10}	62.0(2)
F_{7A}–Hg_2–F_3	61.8(2)
F_{7A}–Hg_2–F_1	60.1(2)
F_{7A}–Hg_2–F_{6A}	169.1(2)
F_{7A}–Hg_2–F_{17}	109.9(2)
F_{7A}–Hg_2–F_{20}	100.6(2)
Hg_1–F_{11}–As_1	151.7(3)
Hg_1–F_{14}–As_2	127.9(2)
Hg_2–F_{17}–As_3	144.9(3)
Hg_2–F_{20}–As_4	140.6(3)
F_{11}–As_1–F_{13}	89.5(3)
F_{11}–As_1–F_{12}	91.7(4)
F_{11}–As_1–F_{11A}	180.0
F_{12}–As_1–F_{12A}	180.0
F_{13}–As_1–F_{13A}	180.0
F_{11}–As_1–F_{13A}	90.5(3)
F_{11}–As_1–$F_{12\ A}$	88.3(4)
F_{13}–As_1–F_{12}	89.3(4)
F_{13}–As_1–F_{12A}	90.7(4)
F_{14}–As_2–F_{15}	89.9(4)
F_{14}–As_2–F_{14A}	177.7(5)
F_{14}–As_2–F_{15A}	91.8(4)
F_{14}–As_2–F_{16A}	87.2(4)
F_{15}–As_2–F_{16}	178.8(4)
F_{15}–As_2–F_{15A}	90.0(7)
F_{15}–As_2–F_{16A}	90.6(4)
F_{16}–As_2–F_{16A}	88.9(4)
F_{14}–As_2–F_{16}	91.1(4)
F_{18}–As_3–F_{19}	89.7(3)
F_{18}–As_3–F_{17}	90.2(3)
F_{18}–As_3–F_{19A}	90.3(3)

Table S8.7. continued….

F_{18}–As_3–F_{17A}	89.8(3)
F_{19}–As_3–F_{17}	91.1(4)
F_{19}–As_3–F_{17A}	88.9(4)
F_{17}–As_3–F_{17A}	180.0
F_{18}–As_3–F_{18A}	180.0
F_{19}–As_3–F_{19A}	180.0
F_{21}–As_4–F_{22}	90.1(4)
F_{21}–As_4–F_{20}	88.7(4)
F_{21}–As_4–F_{21A}	178.6(5)
F_{21}–As_4–F_{22}	90.9(4)
F_{22}–As_4–F_{20A}	179.5(4)
F_{22}–As_4–F_{20}	90.0(5)
F_{22}–As_4–F_{22A}	90.2(7)
F_{20}–As_4–F_{22A}	179.5(4)
F_{21}–As_4–F_{20A}	90.3(4)
F_{20}–As_4–F_{20A}	89.7(6)

[a] The atom labeling scheme corresponds to that used in Figures 8.7 and 8.10a–8.10c. [b] The atom labeling scheme corresponds to that used in Figures 8.10d–8.10f. Calculated at the PBE/TZ2P level of theory.

Table S8.8. Experimental Geometrical Parameters of $FHg(\mu_3\text{-}FKrF)_{0.5}(KrF_2)_{1.5}(AsF_6)$ **(8)** [a]

Bond Lengths (Å)			
$Hg_1–F_{1(Kr1)}$	2.345(2)	$Hg_2–F_{5(Kr3)}$	2.445(4)
$Hg_1–F_{3(Kr2)}$	2.455(2)	$Hg_2–F_{7(Kr4)}$	2.421(4)
		$Hg_2–F_{3A(Kr2A)}$	2.883(3)
$Hg_1–F_9$	2.222(2)	$Hg_2–F_{10}$	2.167(3)
$Hg_1–F_{10B}$	2.229(2)	$Hg_2–F_9$	2.241(2)
$Hg_1–F_{10A}$	2.387(2)	$Hg_2–F_{9A}$	2.452(2)
$Hg_1\text{--}F_{11(As1)}$	2.419(3)	$Hg_2\text{--}F_{18(As2)}$	2.376(2)
$Hg_1\text{--}F_{17(As2)}$	2.450(2)	$Hg_2\text{--}F_{13B(As1B)}$	2.549(3)
$Hg_1\text{--}F_{12A(As1A)}$	2.605(3)		
$Kr_1–F_1$	1.937(2)	$Kr_1–F_2$	1.856(3)
$Kr_2–F_3$	1.958(2)	$Kr_2–F_4$	1.831(3)
$Kr_3–F_5$	1.932(3)	$Kr_3–F_6$	1.849(3)
$Kr_4–F_7$	1.952(3)	$Kr_4–F_8$	1.832(4)
$As_1–F_{11}$	1.756(3)	$As_2–F_{17}$	1.752(3)
$As_1–F_{12}$	1.748(2)	$As_2–F_{18}$	1.766(2)
$As_1–F_{13}$	1.752(2)	$As_2–F_{19}$	1.708(3)
$As_1–F_{14}$	1.697(2)	$As_2–F_{20}$	1.702(2)
$As_1–F_{15}$	1.707(3)	$As_2–F_{21}$	1.711(4)
$As_1–F_{16}$	1.704(4)	$As_2–F_{22}$	1.698(4)
Bond Angles (deg)			
$Hg_2–F_9–Hg_{2A}$	101.5(1)	$Hg_2–F_{10}–Hg_{1B}$	107.5(1)
$Hg_1–F_9–Hg_2$	103.5(1)	$Hg_1–F_{10A}–Hg_{1C}$	109.1(1)
$Hg_1–F_9–Hg_{2A}$	144.2(1)	$Hg_{2A}–F_{10A}–Hg_1$	130.2(1)
$Hg_1–F_{3A}–Hg_{2A}$	96.4(1)		
$Hg_2\text{--}F_{13B}–As_{1B}$	127.9(1)	$Hg_1\text{--}F_{17}–As_2$	146.9(1)
$Hg_2\text{--}F_{18}–As_2$	138.6(1)	$Hg_1\text{--}F_{12A}–As_1$	151.9(1)
$Hg_1\text{--}F_{11}–As_1$	142.6(1)		
$Hg_1–F_3–Kr_2$	130.5(1)	$Hg_2\text{---}F_{3A}–Kr_{2A}$	121.9(1)
$Hg_1–F_1–Kr_1$	125.7(1)	$Hg_2–F_5–Kr_3$	127.1(2)
		$Hg_2–F_7–Kr_4$	127.3(1)

Table S8.8. continued….

F_1–Kr_1–F_2	178.8(1)	F_6–Kr_3–F_5	179.3(1)
F_1–Kr_1–F_2	178.8(1)	F_6–Kr_3–F_5	179.3(1)
F_3–Kr_2–F_4	178.9(1)	F_7–Kr_4–F_8	178.3(1)
F_3–Hg_1–F_{10B}	68.7(1)	F_5–Hg_2–F_7	148.6(1)
F_1–Hg_1–F_{12A}	68.9(1)	F_5–Hg_2–F_{3A}	72.9(1)
F_{10B}–Hg_1–F_{10A}	70.9(1)	F_5–Hg_2–F_9	76.1(1)
F_{11}--Hg_1--F_{17}	71.0(1)	F_5–Hg_2–F_{9A}	108.7(1)
F_{10B}–Hg_1--F_{12A}	71.0(1)	F_5–Hg_2–F_{10}	76.4(1)
F_9–Hg_1–F_{10B}	72.9(1)	F_5–Hg_2--F_{18}	91.5(1)
F_1–Hg_1–F_3	73.8(1)	F_5–Hg_2--F_{13B}	134.9(1)
F_3–Hg_1--F_{17}	74.1(1)	F_7–Hg_2–F_{3A}	128.0(1)
F_9–Hg_1--F_{12A}	74.4(1)	F_7–Hg_2–F_9	74.5(1)
F_{11}--Hg_1–F_{10B}	75.8(1)	F_7–Hg_2–F_{9A}	75.8(1)
F_{11}--Hg_1–F_3	76.9(1)	F_7–Hg_2–F_{10}	132.4(1)
F_{10A}–Hg_1--F_{12A}	77.0(1)	F_7–Hg_2--F_{18}	77.8(1)
F_9–Hg_1--F_{17}	79.3(1)	F_7–Hg_2--F_{13B}	68.7(1)
F_1–Hg_1--F_{17}	81.6(1)	F_{3A}–Hg_2–F_9	142.0(1)
F_{11}--Hg_1–F_{10B}	85.2(1)	F_{3A}–Hg_2–F_{9A}	132.2(1)
F_1–Hg_1–F_9	93.4(1)	F_{3A}–Hg_2–F_{10}	61.3(1)
F_1–Hg_1–F_{10B}	102.5(1)	F_{3A}–Hg_2--F_{18}	69.9(1)
F_9–Hg_1--F_{11}	103.2(1)	F_{3A}–Hg_2--F_{13B}	62.4(1)
F_3–Hg_1--F_{12A}	121.2(1)	F_9–Hg_2–F_{9A}	78.5(1)
F_{17}--Hg_1–F_{10B}	129.9(1)	F_9–Hg_2–F_{10}	130.4(1)
F_3–Hg_1–F_{10B}	132.5(1)	F_9–Hg_2--F_{18}	89.9(1)
F_{17}--Hg_1--F_{12A}	138.6(1)	F_9–Hg_2--F_{13B}	140.6(1)
F_9–Hg_1–F_{10B}	139.4(1)	F_{9A}–Hg_2–F_{10}	72.5(1)
F_{17}--Hg_1–F_{10B}	139.4(1)	F_{9A}–Hg_2--F_{18}	153.1(1)
F_1–Hg_1–F_{10B}	139.8(1)	F_{9A}–Hg_2--F_{13B}	104.9(1)
F_1–Hg_1--F_{11}	144.3(1)	F_{10}–Hg_2--F_{18}	131.2(1)
F_{11}--Hg_1--F_{12A}	146.0(1)	F_{10}–Hg_2--F_{13B}	86.3(1)
F_9–Hg_1–F_3	151.9(1)	F_{18}--Hg_2--F_{13B}	69.4(1)
F_{18}–As_2–F_{19}	89.9(1)	F_{16}–As_1–F_{15}	93.7(2)
F_{17}–As_2–F_{20}	90.7(1)	F_{12}–As_1–F_{13}	86.8(1)
F_{21}–As_2–F_{19}	91.1(2)	F_{11}–As_1–F_{13}	87.4(1)
F_{22}–As_2–F_{20}	91.3(2)	F_{11}–As_1–F_{12}	88.4(1)
F_{22}–As_2–F_{19}	91.5(2)	F_{11}–As_1–F_{15}	88.6(1)
F_{20}–As_2–F_{21}	91.7(2)	F_{16}–As_1–F_{13}	90.3(1)

Table S8.8. continued….

F_{20}–As_2–F_{19}	91.8(2)	F_{14}–As_1–F_{13}	90.7(1)
F_{22}–As_2–F_{17}	88.6(1)	F_{16}–As_1–F_{14}	92.5(2)
F_{17}–As_2–F_{21}	88.7(1)	F_{14}–As_1–F_{15}	92.8(2)
F_{18}–As_2–F_{22}	88.8(1)	F_{11}–As_1–F_{14}	89.1(1)
F_{18}–As_2–F_{17}	87.6(1)	F_{12}–As_1–F_{15}	89.6(1)
F_{18}–As_2–F_{21}	88.1(1)	F_{16}–As_1–F_{12}	89.8(1)
F_{17}–As_2–F_{19}	177.5(1)	F_{15}–As_1–F_{13}	174.7(1)
F_{18}–As_2–F_{20}	178.3(1)	F_{14}–As_1–F_{12}	176.6(1)
F_{22}–As_2–F_{21}	176.0(2)	F_{11}–As_1–F_{16}	177.1(1)

[a] The atom labeling scheme corresponds to that used in Figure 8.8.

Table S8.9. Experimental Geometrical Parameters of $Hg_4F_5(AsF_6)_3 \cdot HF$ **(9)** [a]

Bond Lengths (Å)			
$Hg_1–F_1$	2.251(4)	$Hg_2–F_2$	2.114(4)
$Hg_1–F_2$	2.149(4)	$Hg_2–F_3$	2.041(4)
$Hg_1–F_{2A}$	2.707(4)	$Hg_2–F_5$	2.347(4)
$Hg_1–F_5$	2.228(4)		
$Hg_3–F_1$	2.246(3)	$Hg_4–F_1$	2.290(4)
$Hg_3–F_3$	2.132(4)	$Hg_4–F_4$	2.136(4)
$Hg_3–F_4$	2.234(4)	$Hg_4–F_{4A}$	2.523(4)
		$Hg_4–F_5$	2.192(4)
$Hg_1\text{--}F_{6(As1)}$	2.549(4)	$Hg_2\text{--}F_{7(As1)}$	2.584(5)
$Hg_1\text{--}F_{10(As1)}$	2.713(5)	$Hg_2\text{--}F_{8A(As1A)}$	2.649(6)
$Hg_1\text{--}F_{17(As2)}$	2.581(5)	$Hg_2\text{--}F_{11B(As1B)}$	2.607(4)
$Hg_1\text{--}F_{15A(As2A)}$	2.583(5)	$Hg_2\text{--}F_{14A(As2A)}$	2.651(6)
$Hg_3\text{--}F_{12(As2)}$	2.565(5)	$Hg_4–F_{24(H)}$	2.649(8)
$Hg_3\text{--}F_{18(As3)}$	2.498(5)		
$Hg_3\text{--}F_{21A(As3A)}$	2.642(5)	$Hg_4\text{--}F_{13(As2)}$	2.641(5)
$Hg_3\text{--}F_{9A(As1A)}$	2.629(5)	$Hg_4\text{--}F_{23A(As3A)}$	2.636(5)
$Hg_3\text{--}F_{22B(As3B)}$	2.681(6)	$Hg_4\text{--}F_{20B(As3B)}$	2.547(5)
$As_1–F_6$	1.758(5)	$As_3–F_{18}$	1.744(5)
$As_1–F_7$	1.720(4)	$As_3–F_{19}$	1.712(5)
$As_1–F_8$	1.718(5)	$As_3–F_{20}$	1.739(6)
$As_1–F_9$	1.740(4)	$As_3–F_{21}$	1.724(4)
$As_1–F_{10}$	1.727(4)	$As_3–F_{22}$	1.732(5)
$As_1–F_{11}$	1.719(4)	$As_3–F_{23}$	1.726(5)
$As_2–F_{12}$	1.727(5)		
$As_2–F_{13}$	1.729(5)		
$As_2–F_{14}$	1.722(5)		
$As_2–F_{15}$	1.735(5)		
$As_2–F_{16}$	1.727(4)		
$As_2–F_{17}$	1.726(4)		
Bond Angles (deg)			
$Hg_1–F_2–Hg_{1A}$	110.8(2)	$Hg_2–F_5–Hg_4$	135.6(2)
$Hg_1–F_2–Hg_2$	145.1(2)	$Hg_2–F_3–Hg_3$	155.3(2)

Table S8.9. continued….

Hg_1–F_1–Hg_3	136.7(2)	Hg_3–F_1–Hg_{4B}	111.1(2)
Hg_1–F_1–Hg_4	105.3(2)	Hg_3–F_4–Hg_4	149.4(2)
Hg_1–F_5–Hg_{2A}	113.1(2)	Hg_3–F_4–Hg_{4B}	103.5(2)
Hg_1–F_5–Hg_4	109.5(2)	Hg_4–F_4–Hg_{4A}	106.7(2)
Hg_1–F_2–Hg_2	104.0(2)		
F_2–Hg_1--F_{10}	85.7(1)	F_3–Hg_2–F_2	173.7(2)
F_2–Hg_1–F_1	151.4(2)	F_3–Hg_2--F_7	95.0(2)
F_2–Hg_1--F_6	80.2(2)	F_3–Hg_2--F_{11B}	88.7(2)
F_2–Hg_1–F_{2A}	69.2(1)	F_3–Hg_2–F_5	110.1(2)
F_2–Hg_1–F_5	134.7(2)	F_3–Hg_2--F_{14A}	96.8(2)
F_2–Hg_1--F_{17}	95.8(2)	F_3–Hg_2--F_{8A}	104.5(2)
F_2–Hg_1--F_{15A}	74.9(2)	F_2–Hg_2--F_7	82.5(2)
F_{10}--Hg_1–F_1	76.6(1)	F_2–Hg_2--$F_{11\ B}$	85.1(2)
F_{10}--Hg_1--F_6	54.6(1)	F_2–Hg_2–F_5	75.0(2)
F_{10}--Hg_1–F_2	132.5(1)	F_2–Hg_2--F_{14A}	80.8(2)
F_{10}--Hg_1–F_5	131.5(1)	F_2–Hg_2--F_{8A}	79.8(2)
F_{10}--Hg_1--F_{17}	135.7(1)	F_7--Hg_2--$F_{11\ B}$	73.7(1)
F_{10}--Hg_1--F_{15A}	66.9(1)	F_7--Hg_2–F_5	141.7(1)
F_1–Hg_1--F_6	71.3(1)	F_7--Hg_2–F_{14}	131.3(1)
F_1–Hg_1–F_2	138.7(1)	F_7--Hg_2--F_{8A}	66.1(1)
F_1–Hg_1–F_5	72.6(2)	F_{11B}--Hg_2–F_5	133.1(1)
F_1–Hg_1--F_{17}	82.1(1)	F_{11B}--Hg_2--F_{14A}	59.6(1)
F_1–Hg_1--F_{15A}	116.8(1)	F_{11B}--Hg_2--F_{8A}	138.4(1)
F_6--Hg_1–F_2	46.6(1)	F_5–Hg_2–F_{14A}	75.3(2)
F_6--Hg_1–F_5	139.4(2)	F_5–Hg_2--F_{8A}	79.6(1)
F_6--Hg_1--F_{17}	81.9(1)	F_{14A}--Hg_2--F_{8A}	151.5(1)
F_6--Hg_1--F_{15A}	117.4(1)		
F_{2A}–Hg_1–F_5	66.1(1)		
F_{2A}–Hg_1--F_{17}	87.9(1)		
F_{2A}–Hg_1--F_{15A}	67.9(1)		
F_5–Hg_1--F_{17}	75.4(1)		
F_5–Hg_1--F_{15A}	95.1(2)		
F_{17}–Hg_1--F_{15A}	155.8(1)		
F_3–Hg_3--F_{18}	75.2(2)	F_5–Hg_4–F_4	143.2(2)
F_3–Hg_3–F_4	148.8(2)	F_5–Hg_4–F_{24}	63.2(2)
F_3–Hg_3--F_{12}	72.4(2)	F_5–Hg_4–F_4	137.5(2)
F_3–Hg_3--F_{9A}	72.5(2)	F_5–Hg_4–F_1	72.5(2)

Table S8.9. continued….

F_3–Hg_3–F_1	131.4(2)	F_5–Hg_4–F_{23}	119.0(1)
F_3–Hg_3--F_{21A}	73.1(2)	F_5–Hg_4--F_{13}	83.1(2)
F_3–Hg_3--F_{22B}	122.4(2)	F_5–Hg_4--F_{20B}	76.7(2)
F_{18}--Hg_3–F_4	90.1(2)	F_4–Hg_4–F_{24}	80.5(2)
F_{18}--Hg_3--F_{12}	139.6(2)	F_4–Hg_4–F_{4A}	73.3(2)
F_{18}--Hg_3--F_{9A}	90.7(2)	F_4–Hg_4–F_1	142.4(2)
F_{18}--Hg_3–F_1	144.1(2)	F_4–Hg_4--F_{23A}	86.6(2)
F_{18}--Hg_3--F_{21A}	76.7(2)	F_4–Hg_4--F_{13}	98.7(2)
F_{18}--Hg_3--F_{22B}	72.9(2)	F_4–Hg_4--F_{20B}	84.6(2)
F_4–Hg_3--F_{12}	105.7(2)	F_{24}–Hg_4–F_{4A}	134.8(2)
F_4–Hg_3--F_{9A}	136.1(1)	F_{24}–Hg_4–F_1	129.2(2)
F_4–Hg_3–F_1	75.3(2)	F_{24}–Hg_4--F_{23A}	144.0(2)
F_4–Hg_3--F_{21A}	76.9(2)	F_{24}–Hg_4--F_{13}	82.4(2)
F_4–Hg_3--F_{22B}	77.0(1)	F_{24}–Hg_4--$_{20B}$	68.0(2)
F_{12}--Hg_3--F_{9A}	101.7(1)	F_{4A}–Hg_4–F_1	69.1(1)
F_{12}--Hg_3–F_1	76.3(1)	F_{4A}–Hg_4--F_{23A}	70.7(1)
F_{12}--Hg_3--F_{21A}	71.3(1)	F_{4A}–Hg_4--F_{13}	66.4(1)
F_{12}--Hg_3--F_{22B}	146.2(1)	F_{4A}–Hg_4--F_{20B}	141.9(2)
F_{9A}--Hg_3–F_1	78.7(1)	F_1–Hg_4--F_{23A}	79.2(1)
F_{9A}--Hg_3--F_{21A}	145.3(1)	F_1–Hg_4--F_{13}	68.4(1)
F_{9A}--Hg_3--F_{22B}	61.4(1)	F_1–Hg_4--F_{20B}	125.0(2)
F_1–Hg_3--F_{21A}	129.1(1)	F_{23A}--Hg_4--F_{13}	133.0(1)
F_1–Hg_3--F_{22B}	71.9(1)	F_{23A}--Hg_4--F_{20B}	77.5(2)
F_{21A} --Hg_3--F_{22B}	139.5(1)	F_{13}--Hg_4--F_{20B}	149.3(2)
Hg_1--F_6–As_1	111.4(2)	Hg_2--F_{11B}–As_{1B}	133.2(2)
Hg_1--F_{10}–As_1	105.6(2)	Hg_2--F_7–As_1	139.5(2)
Hg_1--F_{17}–As_2	133.8(2)	Hg_2--F_{8A}–As_{1A}	140.3(2)
Hg_1--F_{15A}–As_{2A}	112.1(2)	Hg_2--F_{14A}–As_{2A}	142.8(3)
Hg_3--F_{18}–As_3	140.6(3)	Hg_4--F_{23A}–As_{3A}	148.1(2)
Hg_3--F_{9A}–As_{1A}	124.9(2)	Hg_4--F_{13}–As_2	145.9(2)
Hg_3--F_{22B}–As_{3B}	144.0(2)	Hg_4--F_{20B}–As_{3B}	146.8(3)
Hg_3--F_{21A}–As_{3A}	149.5(2)		
Hg_3--F_{12}–As_2	126.2(2)		
F_{11}–As_1–F_9	89.6(2)	F_{14}–As_2–F_{17}	90.9(2)
F_{11}–As_1–F_{10}	177.4(2)	F_{14}–As_2–F_{13}	90.1(2)
F_{11}–As_1–F_7	89.6(2)	F_{14}–As_2–F_{15}	90.2(2)

Table S8.9. continued….

F_{11}–As_1–F_6	89.4(2)	F_{14}–As_2–F_{12}	179.1(2)
F_{11}–As_1–F_8	91.5(2)	F_{14}–As_2–F_{16}	90.0(2)
F_9–As_1–F_{10}	90.6(2)	F_{17}–As_2–F_{13}	90.3(2)
F_9–As_1–F_7	178.4(2)	F_{17}–As_2–F_{15}	90.2(2)
F_9–As_1–F_6	89.1(2)	F_{17}–As_2–F_{12}	89.7(2)
F_9–As_1–F_8	90.0(2)	F_{17}–As_2–F_{16}	178.7(2)
F_{10}–As_1–F_7	90.1(2)	F_{13}–As_2–F_{15}	179.3(2)
F_{10}–As_1–F_6	87.9(2)	F_{13}–As_2–F_{12}	89.2(2)
F_{10}–As_1–F_8	91.1(2)	F_{13}–As_2–F_{16}	90.6(2)
F_7–As_1–F_6	89.5(2)	F_{15}–As_2–F_{12}	90.5(2)
F_7–As_1–F_8	91.5(2)	F_{15}–As_2–F_{16}	88.8(2)
F_6–As_1–F_8	178.6(2)	F_{12}–As_2–F_{16}	89.5(2)
F_{18}–As_3–F_{21}	89.4(2)	F_{21}–As_3–F_{20}	89.4(2)
F_{18}–As_3–F_{22}	89.4(2)	F_{21}–As_3–F_{19}	178.2(2)
F_{18}–As_3–F_{23}	179.6(2)	F_{22}–As_3–F_{23}	90.3(2)
F_{18}–As_3–F_{20}	90.1(2)	F_{22}–As_3–F_{20}	179.4(2)
F_{18}–As_3–F_{19}	89.2(2)	F_{22}–As_3–F_{19}	90.2(2)
F_{21}–As_3–F_{22}	90.9(2)	F_{23}–As_3–F_{20}	90.1(2)
F_{21}–As_3–F_{23}	90.3(2)	F_{23}–As_3–F_{19}	91.1(2)
		F_{20}–As_3–F_{19}	89.5(3)

[a] The atom labeling scheme corresponds to that used in Figure S8.10.

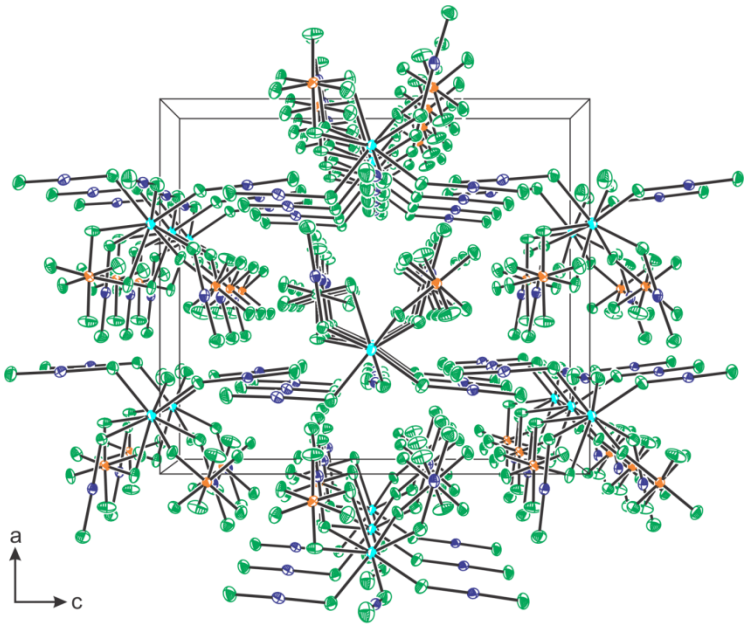

Figure S8.1. The crystallographic packing of $Hg(KrF_2)_5(AsF_6)_2$ **(5)** viewed along the *b*-axis; thermal ellipsoids are shown at the 50% probability level. Colors represent Hg (light blue), Kr (dark blue), As (orange), and F (green).

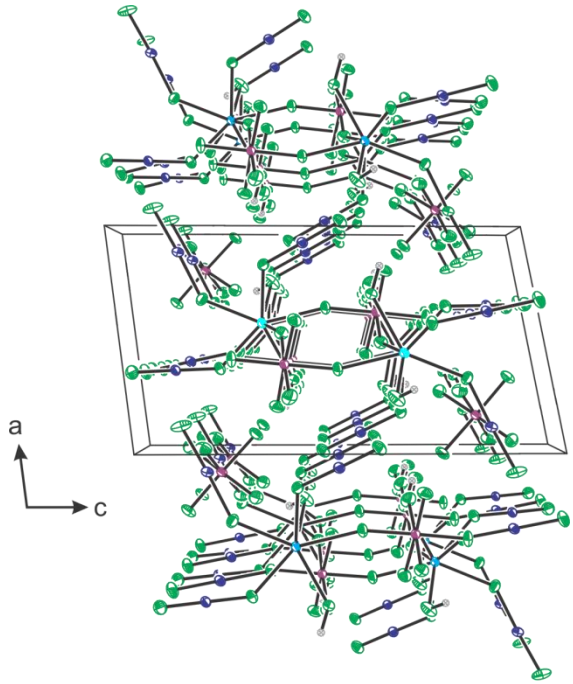

Figure S8.2. The crystallographic packing of $[Hg(KrF_2)_4(HF)_2(SbF_6)]_2[SbF_6]_2$ **(4)** viewed along the *b*-axis; thermal ellipsoids are shown at the 50% probability level. Colors represent Hg (light blue), Kr (dark blue), Sb (purple), F (green), and H (grey).

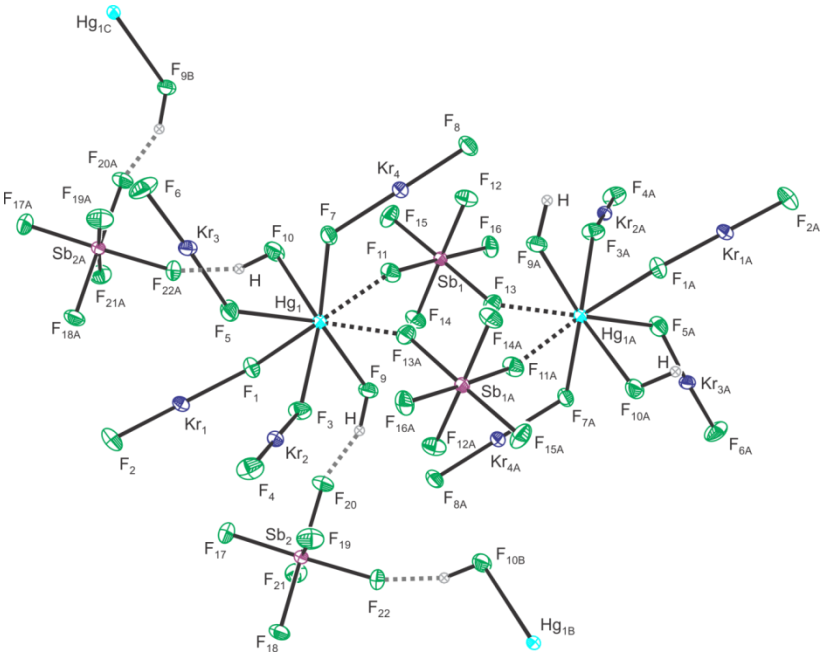

Figure S8.3. The crystal structure of $[Hg(KrF_2)_4(HF)_2(SbF_6)]_2[SbF_6]_2$ **(4)** showing hydrogen bonding (grey dotted lines) to the $[SbF_6]^-$ anions and neighboring cations; for clarity, interactions for only half of the dimer cation are shown. Thermal ellipsoids are shown at the 50% probability level.

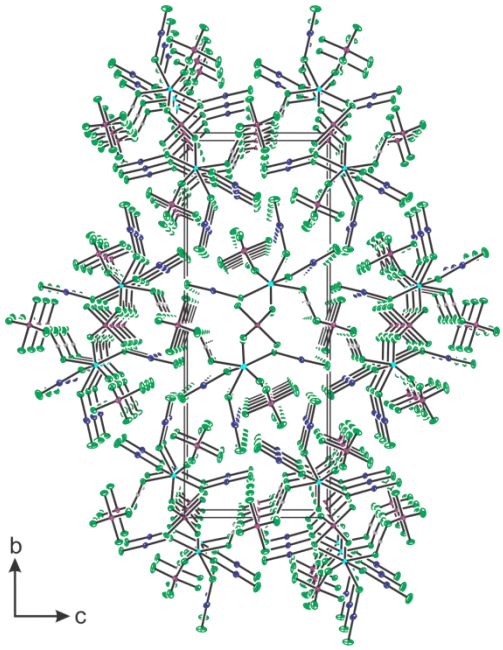

Figure S8.4. The crystallographic packing of $Hg(KrF_2)_3(HF)(SbF_6)_2$ **(3)** viewed along the *a*-axis; thermal ellipsoids are shown at the 50% probability level. Colors represent Hg (light blue), Kr (dark blue), Sb (purple), F (green), and H (grey).

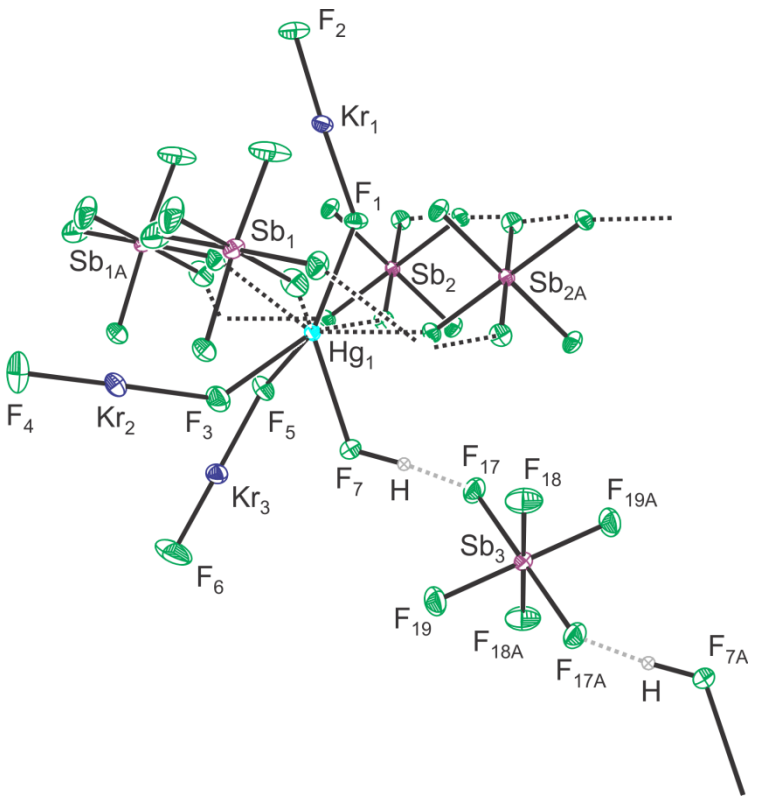

Figure S8.5. The partially labeled crystal structure of $Hg(KrF_2)_3(HF)(SbF_6)_2$ **(3)** showing hydrogen bonding (grey dotted lines) to the $[Sb_{(3)}F_6]^-$ anion; Thermal ellipsoids are shown at the 50% probability level.

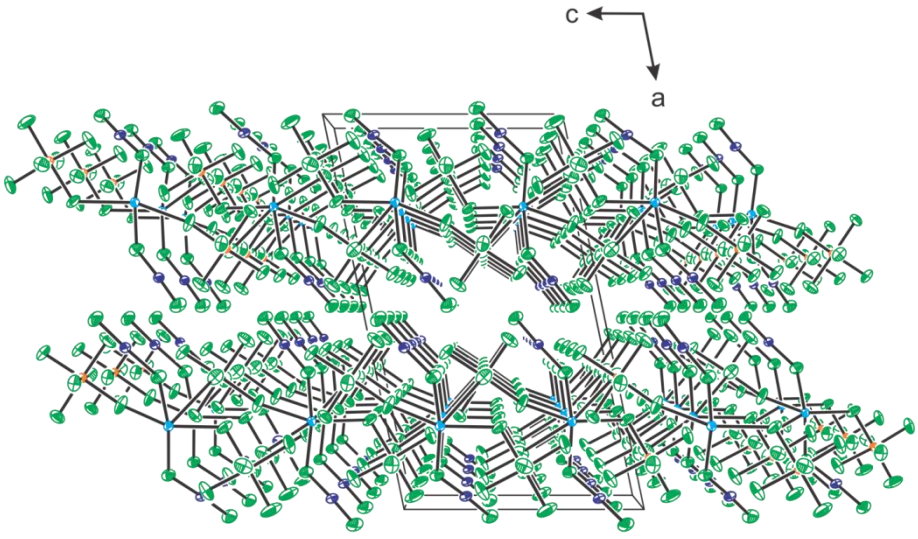

Figure S8.6. The crystallographic packing of $Hg(KrF_2)_2(AsF_6)_2$ **(2)** viewed along the *b*-axis; thermal ellipsoids are shown at the 50% probability level. Colors represent Hg (light blue), Kr (dark blue), As (orange), and F (green).

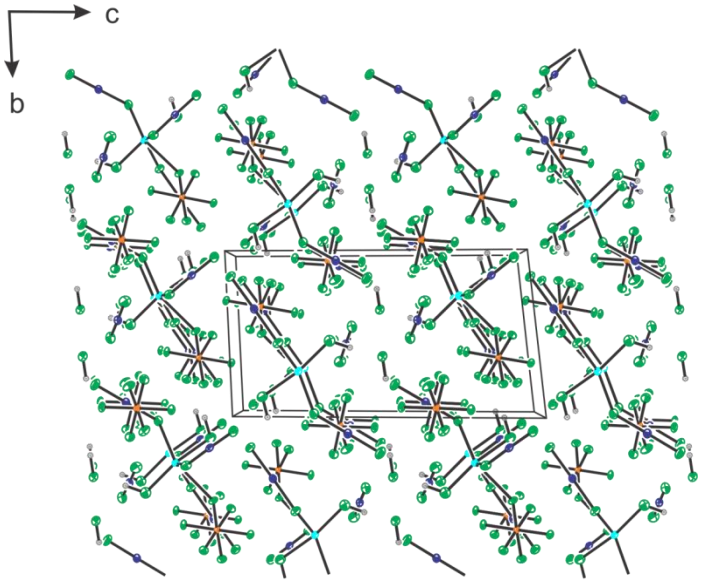

Figure S8.7. The crystallographic packing of $Hg(KrF_2)_4(HF)_2(AsF_6)_2 \cdot HF$ **(6)** viewed along the *a*-axis; thermal ellipsoids are shown at the 50% probability level. Colors represent Hg (light blue), Kr (dark blue), As (orange), F (green), and H (grey).

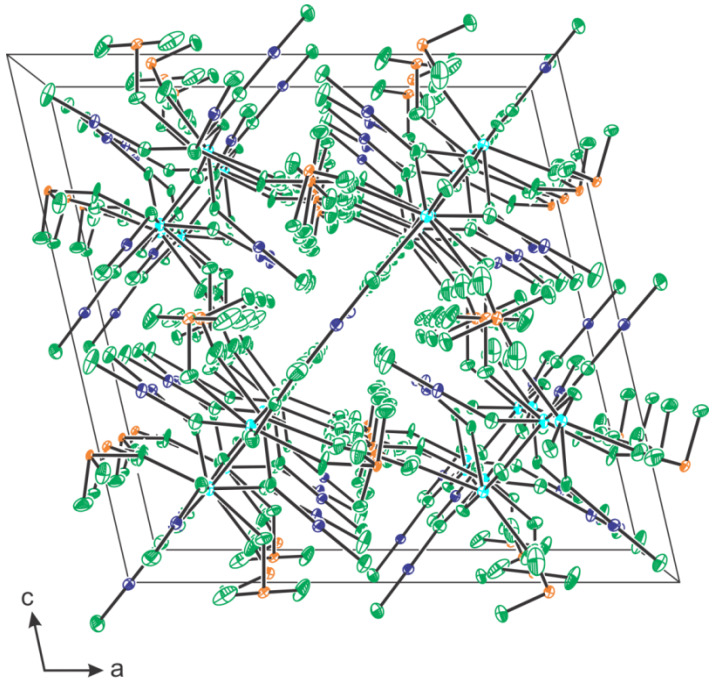

Figure S8.8. The crystallographic packing of $FHg(\mu_3\text{-}FKrF)_{1.5}(KrF_2)_{0.5}(AsF_6)$ **(7)** viewed along the *b*-axis; thermal ellipsoids are shown at the 50% probability level. Colors represent Hg (light blue), Kr (dark blue), As (orange), F (green), and H (grey).

a

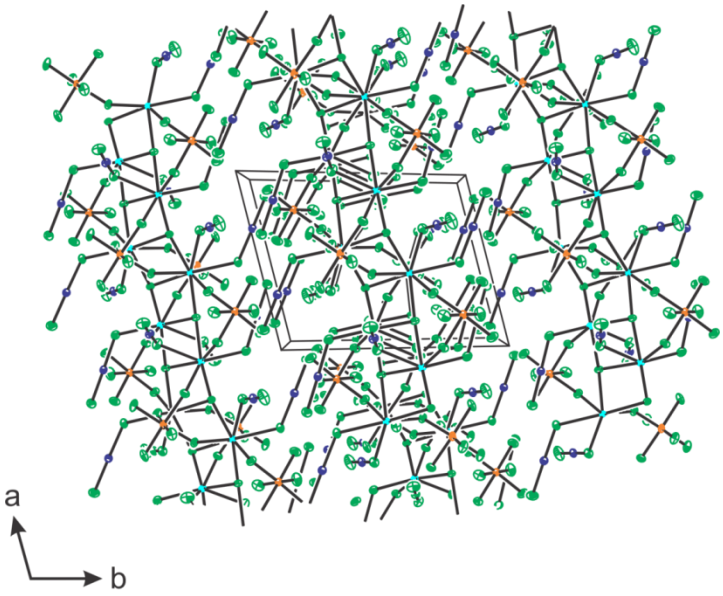

b

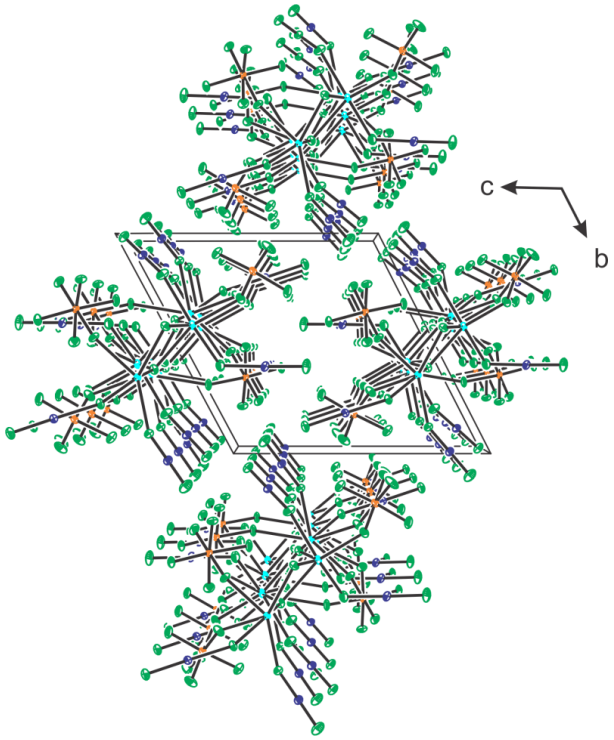

Figure S8.9. The crystallographic packing of $FHg(\mu_3\text{-}FKrF)_{0.5}(KrF_2)_{1.5}(AsF_6)$ **(8)** viewed **a)** along the *c*-axis and b) along the *a*-axis; thermal ellipsoids are shown at the 50% probability level. Colors represent Hg (light blue), Kr (dark blue), As (orange), F (green), and H (grey).

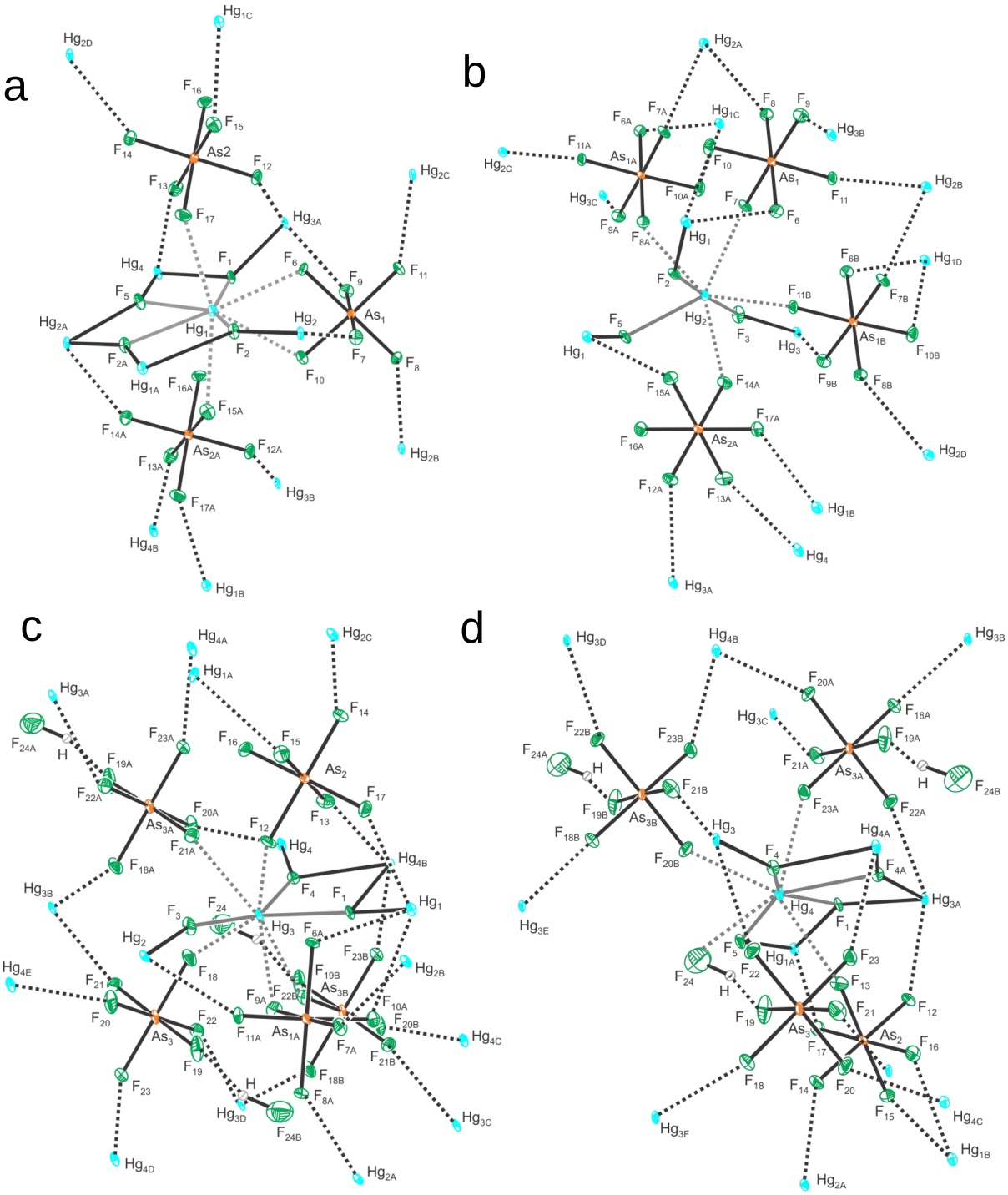

Figure S8.10. The crystal structure of $Hg_4F_5(AsF_6)_3$·HF showing the environment around atoms (**a**) Hg_1, (**b**) Hg_2, (**c**) Hg_3, and (**d**) Hg_4. Grey bond line color used for interactions with each respective mercury atom and dotted lines indicate interactions with the anions; thermal ellipsoids are shown at the 50% probability level.

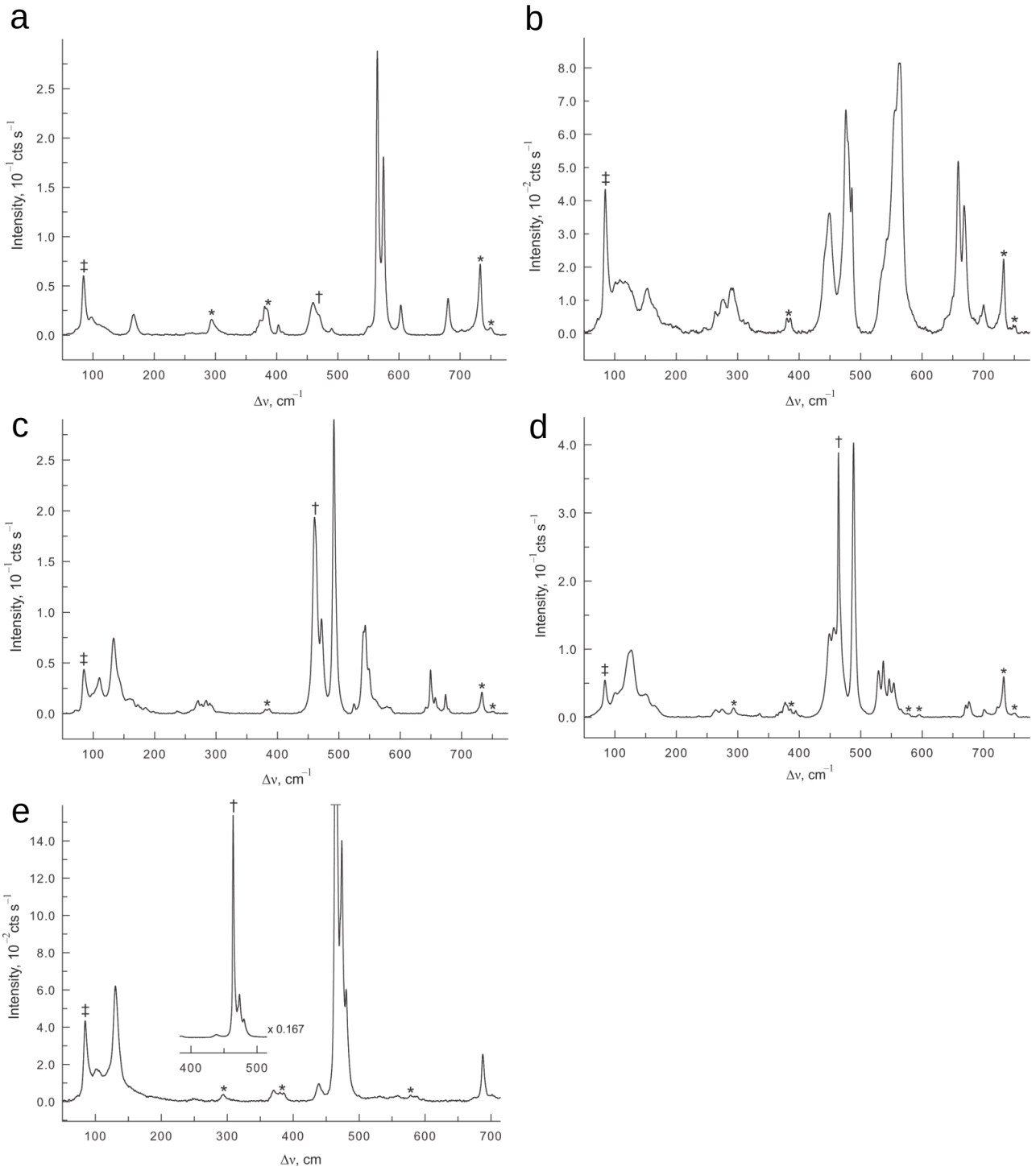

Figure S8.11. Raman spectrum of the crystalline reaction products predominantly containing the complex **a)** $Hg(KrF_2)(HF)(AsF_6)_2$ and $Hg(KrF_2)_2(AsF_6)_2$ **(2), b)** $Hg(KrF_2)_3(HF)(SbF_6)_2$, **c)** $[Hg(KrF_2)_4(HF)_2(SbF_6)]_2[SbF_6]_2$, **d)** $Hg(KrF_2)_5(AsF_6)_2$ and **e)** $Hg(KrF_2)_4(HF)_2(AsF_6)_2 \cdot HF$,; recorded at –150 °C using 1064-nm. Symbols denote FEP sample tube lines/overlap (*), instrumental artifact (‡), and unreacted/overlapping free KrF_2 (†).

Table S8.10. Experimental Raman Frequencies and Intensities for Reactions Predominantly giving (**1**)-(**6**) and for $[Hg(KrF_2)_8][AsF_6]_2 \cdot 2HF$, and Calculated Raman Frequencies and Intensities for (1′)-(6′) and $[Hg(KrF_2)_8]^{2+}$.[a]

exptl[b]	calcd[c]		exptl[b]	calcd[c]	exptl[b]	calcd[c]	exptl[b]	calcd[c]	exptl[b]	calcd[c]		[Hg(KrF$_2$)$_8$][AsF$_6$]$_2$·2HF[e]	
(1) + (2)	(1′)	(2′)	(3)	(3′)	(4)	(4′)	(5)	(5′)	(6)	(6′)	assgnts[d]	exptl	calcd [Hg(KrF$_2$)$_8$]$^{2+}$
n.o.	≥ 952(1)		n.o.	≥ 845(<1)	n.o.	≥ 699(<1)			n.o.	≥ 744(<1)	HF modes		
	752(2)						**722(4)**	726(9)		737(5)			
	745(<1)							724(5)		729(6)			
703(2)	743(13)	738(<0.1)	**700(11)**	676(11)			**701(3)**	722(1)	**702(1)**	725(4)	$\nu_3(T_{1u})$ [PnF$_6$]$^-$	**707(<1)**	
	739(4)	738(8)		676(3)				716(<1)		719(<0.1)			
	735(5)	735(1)	**695(6)**	670(7)				714(<1)	**687(3)**	718(<1)	$\nu_1(A_{1g})$ [PnF$_6$]$^-$	**685(12)**	
	729(2)	735(5)		668(<0.1)				711(<1)		681(<1)			
680(13)	729(2)	735(9)		665(3)	**679(2)**	669(<0.1)				656(14)			
	644(8)	731(<1)		664(<1)	**674(7)**	665(9)	**676(6)**			638(8)			
	602(7)	644(16)	**668(48)**	612(13)	**670(1)**	656(<0.1)	**671(4)**	652(10)		631(<1)			
		643(<1)	**659(64)**	607(7)	**657(6)**	656(10)		639(5)					
					649(15)	638(5)							
					642(2)								
						608(81)							
603(11)						604(<0.1)						**603(2)**	616(106)
		585(51)				596(<0.1)[x]			**588(<1)**	586(39)			593(0)
575(63)	581(48)				**578(2)**	594(145)[x]	**576(1)**[‡]	597(38)		573(15)			593(0)
565(100)		576(21)	**563(100)**	592(44)		589(<0.1)	**565(3)**[‡]	576(8)[x]		571(7)			590(0)
			556(83)	578(32)	**558(sh)**	588(71)	**554(12)**	574(12)[x]	**558(<1)**	566(22)	ν(Kr–F$_t$)	**554(6)**	586(54)
			543(36)	574(24)	**549(15)**	587(<0.1)	**546(14)**	572(34)		552(17)[x]			586(54)
					543(30)	586(115)		568(10)					586(49)
					540(28)	585(<0.1)		565(22)				**543(12)**	586(49)
						584(40)	**537(21)**[*]					**540(sh)**	
550(3)	513(8)	524(28)	**535(sh)**	529(39)	**524(3)**	533(<0.1)		544(8)	**531(<1)**	531(17)			
	504(3)	512(<1)		520(1)		532(3)	**529(17)**			506(10)	$\nu_2(E_g)$ [PnF$_6$]$^-$	**582(<1), br**	
				480(5)		509(24)		481(14)					

Table S8.10. continued…

(1) + (2)	(1′)	(2′)	(3)	(3′)	(4)	(4′)	(5)	(5′)	(6)	(6′)	assgnts [d]	exp. [e]	calc. [e] $[Hg(KrF_2)_8]^{2+}$
490(2)[‡]				469(22)[x]	**492(100)**		**488(100)**	493(102)				**508(sh),br**	469(240)
			486(54)	459(73)[x]		465(263)						**489(100)**	439(0)
468(sh)			**476(83)**			436(29)			**480(8)**	481(52)			439(0)
464, sh[†]	466(26)[x]	469(108)[x]			**472(32)**	420(130)			**474(19)**	475(31)[x]			429(0)
460(11),	456(17)[x]	450(16)			**460(67)**[†]	418(<0.1)	**464(97)**[†]	465(59)[x]	**464(100)**[†]	462(69)[x]		**477(3)**	421(39)
br						414(<0.1)		453(43)		453(29)	ν(Kr–F_b)	**464(49)**[†]	421(39)
						413(106)		444(54)		446(54)			416(66)
				441(36)			**456(33)**						416(66)
				434(34)[x]				439(41)				**456(sh)**	
			449(44)				**449(31)**	436(23)[x]	**439(1)**			**451(sh)**	
												449(38)	
409(1)	425(<1)	442(3)								405(<1)			
403(4)	422(6)	426(<1)		384(<1)			**403(<1)**	399(3)		404(6)			
	413(11)	419(<0.1)						393(<1)		400(<1)			
	401(<1)	408(10)					**394(2)**	390(2)		394(5)			
	398(7)	391(<0.1)					**390(2)**	389(2)		386(<1)			
380(4)	392(<1)	389(28)[x]					**379(sh)**	386(1)		382(<1)			
	380(<1)	382(<0.1)		330(6)			**377(5)**	377(<1)		372(<1)			
373(5)	374(<1)	379(2)		301(<1)			**375(sh)**	368(2)		371(2)		**375(sh)**	
	371(2)	375(<1)		292(<1)		347(<1)	**370(2)**	362(3)	**370(1)**	362(2)		**371(2)**	
	362(<1)	373(3)		291(<1)	**n.o.**	325(1)	**368(2)**	361(2)		359(2)	$\nu_5(T_{2g})$ $[PnF_6]^-$	**369(2)**	
363(1)	358(1)	360(<1)		286(<1)		291(<1)	**363(1)**	353(1)		351(1)		**362(<1)**	
	348(1)	359(3)	**317(4)**	278(<1)		270(<1)	**335(1)**	352(2)		345(<1)			
	343(1)	347(2)	**309(5)**	275(<1)		268(2)		344(<1)		340(1)			
	278(<1)	347(<1)		271(1)						281(<1)			
			292(17)		**290(3)**	263(<0.1)							256(0)
			289(17)			263(1)		268(1)		266(<1)			256(0)
					284(4)	261(3)[x]		265(3)		262(1)		**282(2)**	251(1)
			276(12)	270(2)[x]	**276(3)**	259(<0.1)[x]	**274(3)**	260(<1)		258(3)			249(0)
				269(<1)[x]	**271(4)**	258(2)[x]		256(3)	**n.o.**		$\delta(KrF_2)$		246(3)
260(1)	253(<1)	257(<0.1)	**263(9)**	269(<1)[x]		252(5)	**264(3)**	254(3)		240(<0.1)		**262(1)**	246(3)
		253(3)[x]				252(<0.1)		244(<1)[x]					245(4)
		244(4)[x]				250(<0.1)		240(<1)[x]				**238(<1)**	245(4)
						250(4)							232(<0.1)

Table S8.10. continued…

(1) + (2)	(1′)	(2′)	(3)	(3′)	(4)	(4′)	(5)	(5′)	(6)	(6′)	assgnts [d]	exp. [e]	calc. [e] $[Hg(KrF_2)_8]^{2+}$
	249(<1) 238(<0.1) 233(<0.1) 229(<0.1) 222(<1)[x] 221(<1)[x] 212(<0.1) 196(1)	252(<1) 235(<1) 233(<0.1) 231(<0.1) 226(<0.1) 223(<1) 221(<1)[x]	**249(2)**	268(2) 261(2) 260(2)[x] 245(2) 232(<1)[x] 231(<0.1) 228(<1)	**237(1)**	234(<0.1) 233(1) 222(1)[x] 221(<1) 220(<0.1) 220(1)[x] 218(<1) 217(<0.1) 217(<1)		240(<1) 240(<1) 239(<1) 237(<0.1) 233(<0.1) 231(<0.1)[x] 229(<0.1) 227(<0.1) 226(<0.1)[x] 225(<0.1)[x] 220(<0.1)		246(<1) 238(<0.1) 237(<0.1)[x] 235(<0.1) 232(<1) 231(<1) 229(<0.1) 228(<0.1) 223(<1)	$\delta(KrF_2)$ / $\delta(Pn–F)_{weak}$		228(0) 226(0) 226(0) 219(<1) 219(<1) 219(<1) 219(<1)
				197(3) 184(<1) 181(<1) 179(<0.1) 177(<0.1) 171(<1)	**198(1)** **185(2)** **173(3)**	179(4) 168(<1)				216(<1) 189(<1)	$\delta[PnF_6]^-$		
167(7)	147(<1) 134(3)	156(<1) 146(<1)	**154(17)**	156(<1) 151(2)	**160(5)** **142(sh)**	159(2) 157(<1) 153(<1)	**165(4)** **150(8)**	147(<1) 138(2) 136(3)		168(2) 156(<1) 148(<1)	$\delta(KrF_2)$	**141(13)**	137(0) 137(0) 135(1)
		128(6)[x]	**128(16)**	137(6) 124(5)	**133(26)**	146(2) 140(4)	**127(25)** **126(sh)** **122(sh)**	128(4)	**130(9)**	131(3) 120(4)			131(0)
			117(20)									**118(8)**	99(13) 99(13) 99(16)
			108(20)		**110(12)**	119(15)[x] 118(<0.1) 113(<0.1)							99(16) 99(13) 99(13)
97(6)	109(<1) 93(<1)	108(3)[x] 94(6)[x]	**104(19)** **101(20)**	100(3)[x] 90(1)[x] 86(3)	**98(sh)**	112(13) 103(1) 103(2)	**101(9)**	106(15) 100(5)[x] 96(5)[x] 90(4)[x]	**101(3)**	115(7) 105(2) 99(2)		**99(3)**	99(16) 99(16) 87(13) 86(0) 85(0)

Table S8.10. continued…

(1) + (2)	(1′)	(2′)	(3)	(3′)	(4)	(4′)	(5)	(5′)	(6)	(6′)	assgnts [d]	exp. [e]	calc. [e] $[Hg(KrF_2)_8]^{2+}$
n.o.	< 78(<1)	< 81(<1)	n.o.	< 77(1)	n.o.	< 88(<1)	n.o.	< 83(6)	n.o.	< 91(2)	Deformation Modes		< *76(2)*

[a] Frequencies are given in cm^{-1} and spectra correspond to those shown in Figure S8.11. Values in parentheses denote relative Raman intensities. [b] The Raman spectra were recorded in ¼-in. o.d. FEP sample tubes between –150 to –155 °C using 1064-nm excitation. Abbreviations denote shoulder (sh), bands from another complex (‡), possibly overlapping KrF_2 and $[PnF_6]^-$ (Pn = As or Sb) bands (*), and overlapping/ unreacted (ν_1, $\sum_g^+$) stretching mode of free KrF_2 (†). [c] The superscript symbol (^{x}) denotes weak coupling of KrF_2 modes with those of the $[PnF_6]^-$ anions. In (**1′**), (**3′**), (**4′**) and (**6′**), Calculated high-frequency HF modes and low-frequency deformation modes values were omitted for clarity since they were not observed experimentally. Calculations were carried out at the B3LYP/def2-TZVPP level of theory and correspond to those in Figure 8.9. [d] Symbols denote stretch (ν) and bend (δ). The $[PnF_6]^-$ anion bands were assigned under O_h symmetry by comparison with the literature values.[31,32] [e] From ref 23.

Discussion of Raman Spectroscopic Assignments for the $[PnF_6]^-$ Anions

Raman bands arising from the $[AsF_6]^-$ anions, and $[SbF_6]^-$ anions, (Table S8.10) were assigned by comparison with the literature values and by comparison with $[Hg(KrF_2)_8][AsF_6]_2 \cdot 2HF$. Lowering of the anion symmetry from O_h to the site symmetries, and vibrational mode coupling within the crystallographic unit cell, result in the observation of the formally Raman-inactive (infrared-active) $\nu_3(T_{1u})$ band, and splitting of the bands. In $Hg(KrF_2)_5(AsF_6)_2$ **(5),** the bands at 671 and 676 cm^{-1} are assigned to the $\nu_1(A_{1g})$ mode of $[AsF_6]^-$ under O_h symmetry. Bands arising from the formally infrared-active $\nu_3(T_{1u})$ mode were observed at 701 and 722 cm^{-1} (calcd, 711–726 cm^{-1}). The corresponding Raman bands of $[Hg(KrF_2)_8][AsF_6]_2 \cdot 2HF$ occur at 685 and 707 cm^{-1}, respectively. The analogous $[AsF_6]^-$ (exptl, 671–703 cm^{-1}; calcd, 639–738 cm^{-1}) and $[SbF_6]^-$ (exptl, 642–700 cm^{-1}; calcd, 607–681 cm^{-1}) bands are observed in the other complexes reported in this study. The remaining anion modes are expected to be much weaker in intensity. In **(5)**, the $\nu_2(E_g)$ mode is assigned to the band at 529(17) cm^{-1} (calcd, 544(8), 481(14) cm^{-1}), while for the other complexes the analogous modes are assigned to bands between 530–550 cm^{-1} for $[AsF_6]^-$ (calcd, 512–547 cm^{-1}) and between 524–535 cm^{-1} for $[SbF_6]^-$ (calcd., 520–564 cm^{-1}). In $Hg(KrF_2)_5(AsF_6)_2$ **(5)**, a number of weak bands are observed between 335–403 cm^{-1} (calcd., 344–399 cm^{-1}) and are assigned to ν_5 (T_{2g}) modes. In spectra of the other complexes, these bands are also very weak and occur in a similar range for $[AsF_6]^-$ (exptl., 363–409 cm^{-1}; calcd., 347–442 cm^{-1}) and in the case of for $[SbF_6]^-$ are for **(3)** at 309 and 317 cm^{-1} (calcd., 301 and 330 cm^{-1}). In $[Hg(KrF_2)_8][AsF_6]_2 \cdot 2HF$, four weak bands associated with ν_5 (T_{2g}) modes occur between at 362, 369, 371 and 375 cm^{-1}. Similar frequencies were also observed for the $[AsF_6]^-$ anion of $Mg(KrF_2)_4(AsF_6)_2$ (712, 687, 386, 383, 374, 364 cm^{-1}).

Table S8.11. Calculated Valences, Charges (NPA), and Wiberg Bond Orders for $Hg(KrF_2)_5(AsF_6)_2$ (5′) using NBO Version 3.1 [Version 6.0] [a]

Atom	Charge	Valences	Atom	Charge	Valences
Hg_1	1.448 [1.702]	1.087 [0.604]			
Kr_1	1.061 [1.053]	1.092 [1.090]	Kr_4	1.041 [1.033]	1.100 [1.099]
F_1	–0.578 [–0.605]	0.727 [0.669]	F_7	–0.542 [–0.567]	0.770 [0.716]
F_2	–0.415 [–0.413]	0.850 [0.847]	F_8	–0.437 [–0.434]	0.832 [0.829]
$\sum KrF_2$	**0.068 [0.035]**		**$\sum KrF_2$**	**0.062 [0.032]**	
Kr_2	1.062 [1.054]	1.092 [1.089]	Kr_5	1.045 [1.036]	1.101 [1.097]
F_3	–0.574 [–0.603]	0.736 [0.673]	F_9	–0.545 [–0.571]	0.770 [0.713]
F_4	–0.414 [–0.411]	0.851 [0.847]	F_{10}	–0.431 [–0.428]	0.837 [0.833]
$\sum KrF_2$	**0.074 [0.040]**		**$\sum KrF_2$**	**0.069 [0.037]**	
Kr_3	1.048 [1.039]	1.098 [1.096]			
F_5	–0.556 [–0.583]	0.755 [0.697]			
F_6	–0.423 [–0.420]	0.844 [0.840]			
$\sum KrF_2$	**0.069 [0.036]**				
As_1	2.832 [2.834]	3.166 [3.162]	As_2	2.834 [2.837]	3.162 [3.159]
F_{20}	–0.612 [–0.613]	0.674 [0.674]	F_{13}	–0.637 [–0.659]	0.651 [0.612]
F_{17}	–0.668 [–0.699]	0.612 [0.556]	F_{12}	–0.625 [–0.628]	0.655 [0.651]
F_{21}	–0.608 [–0.609]	0.681 [0.681]	F_{15}	–0.596 [–0.597]	0.700 [0.700]
F_{18}	–0.628 [–0.630]	0.651 [0.648]	F_{14}	–0.613 [–0.615]	0.673 [0.671]
F_{22}	–0.595 [–0.596]	0.701 [0.701]	F_{11}	–0.651 [–0.677]	0.636 [0.588]
F_{19}	–0.630 [–0.635]	0.649 [0.641]	F_{16}	–0.593 [–0.594]	0.705 [0.704]
$\sum[As_{(1)}F_6]$	**–0.881 [–0.936]**		**$\sum[As_{(2)}F_6]$**	**–0.909 [–0.948]**	
			$\sum Hg(KrF_2)_5(AsF_6)_2$	**0.000 [0.000]**	

Bond	Bond order	Bond	Bond order
Hg_1–F_1	0.121 [0.068]	Hg_1–F_5	0.119 [0.065]
Hg_1–F_3	0.134 [0.076]	Hg_1–F_7	0.108 [0.058]
Hg_1–F_9	0.117 [0.064]		
Hg_1--F_{13}	0.079 [0.039]	Hg_1--F_{17}	0.142 [0.084]
Hg_1--F_{11}	0.113 [0.064]		
Kr_1–F_1	0.410 [0.411]	Kr_4–F_8	0.628 [0.632]
Kr_1–F_2	0.658 [0.662]	Kr_4–F_7	0.451 [0.452]
Kr_3–F_5	0.430 [0.432]	Kr_5–F_{10}	0.635 [0.639]
Kr_3–F_6	0.644 [0.648]	Kr_5–F_9	0.443 [0.44]

Table S8.11. continued…

Kr_2–F_3	0.407 [0.407]		
Kr_2–F_4	0.660 [0.663]		
As_1–F_{20}	0.561 [0.560]	As_2–F_{13}	0.462 [0.4623]
As_1–F_{17}	0.369 [0.370]	As_2–F_{12}	0.539 [0.5387]
As_1–F_{21}	0.567 [0.566]	As_2–F_{15}	0.588 [0.5866]
As_1–F_{18}	0.535 [0.535]	As_2–F_{14}	0.5583[0.5578]
As_1–F_{22}	0.593 [0.592]	As_2–F_{11}	0.4149[0.4159]
As_1–F_{19}	0.527 [0.527]	As_2–F_{16}	0.5940[0.5926]

[a] Calculated at the B3LYP/def2–TZVPP level of theory.

Complementary Discussion of Energy Decomposition (EDA) and ETS-NOCV Analyses

The bonding in the hypothetical, gas-phase $[F(HgF)_2(\mu_3\text{-}FKrF)_2]^+$ cation was analyzed in terms of the interaction between $[F(HgF)_2]^+$ and two symmetry-related neutral KrF_2 ligands with C_{2v} symmetry specified (Table S8.8). The fragments were generated from the PBE/TZ2P geometry-optimized structure of $[F(HgF)_2(\mu_3\text{-}FKrF)_2]^+$ with their geometries frozen. The results of this analysis are discussed in Chapter 8. The ΔE_{prep}-value was calculated for the $[F(HgF)_2]^+$ fragment as the difference between a geometry-optimized (C_{2v}, "relaxed" fragment) energy and the single-point energy using the frozen coordinates of the $[F(HgF)_2(\mu_3\text{-}FKrF)_2]^+$ cation ("prepared" fragment). A similar calculation was carried out for each KrF_2 molecule using the energy of the geometry-optimized KrF_2 molecule ($D_{\infty h}$).

For comparison, the EDA analysis of $[F(HgF)_2]^+$ and one fragment comprised of two neutral FKrF ligands was also carried out using the same preparation energy with C_{2v} symmetry specified. Treatment of both KrF_2 ligands as a single fragment had a negligible effect on the overall energy (Table S8.12).

Table S8.12. Energy Decomposition Analysis for $[F(HgF)_2(\mu_3\text{-}FKrF)_2]^+$ (C_{2v}) [a]

	$[F(HgF)_2]^+ + (KrF_2)_2$	$[F(HgF)_2]^+ + 2\ KrF_2$
ΔE_{int}	–168.4	–166.5
ΔE_{orb} [b]	–132.2 (42.2%)	–125.8 (40.2%)
ΔE_{elstat} [b]	–168.5 (53.7%)	–173.4 (55.4%)
ΔE_{disp} [b]	–12.8 (4.1%)	–13.5 (4.3%)
ΔE_{Pauli}	145.1	146.2
Total ΔE_{prep}	29.6	29.6
ΔE_{prep} $[F(HgF)_2]^+$	11.6	11.6
ΔE_{prep} per KrF_2	9.0	9.0
$-D_E$	–138.8	–136.9

[a] Calculated using the PBE density functional with TZ2P all-electron basis set. Values in kJ mol^{-1}.
[b] Values in parentheses are the percentage of the ttractive interactions.

Contributions involving the Hg^{2+} 6p orbitals of $[Hg(KrF_2)_8][AsF_6]_2 \cdot 2HF$ were shown to be important and therefore should be included as valence functions for the systems described in the present study. The ETS-NOCV analyses for $[F(HgF)_2]^+$ and two symmetry-related neutral KrF_2 ligands is discussed in Chapter 8 and is depicted in Figure 8.10. The symmetry-adapted fragment orbitals (SFOs) under C_{2v} molecular symmetry are shown in Figure S8.13.

The ETS-NOCV analysis was also carried out for the interaction of $[F(HgF)_2]^+$ and one fragment comprised of two neutral KrF_2 ligands. The resulting bonding descriptions and relative energies were essentially identical to those used in the above approach. The only notable difference arose for the combination of the out-of-phase $8\sigma_g$ orbital with the LUMO+3 fragment orbital of $[F(HgF)_2]^+$, which also had a component that involved the unoccupied $6\sigma_u$ (LUMOs) of the KrF_2. Mixing of occupied and virtual orbitals within the same fragment is attributed to intrafragment polarization that is likely linked to electronic bonding effects arising from chemical bond formation. A similar situation pertains to the analysis of $[Hg(KrF_2)_8]^{2+}$ in $[Hg(KrF_2)_8][AsF_6]_2 \cdot 2HF$.

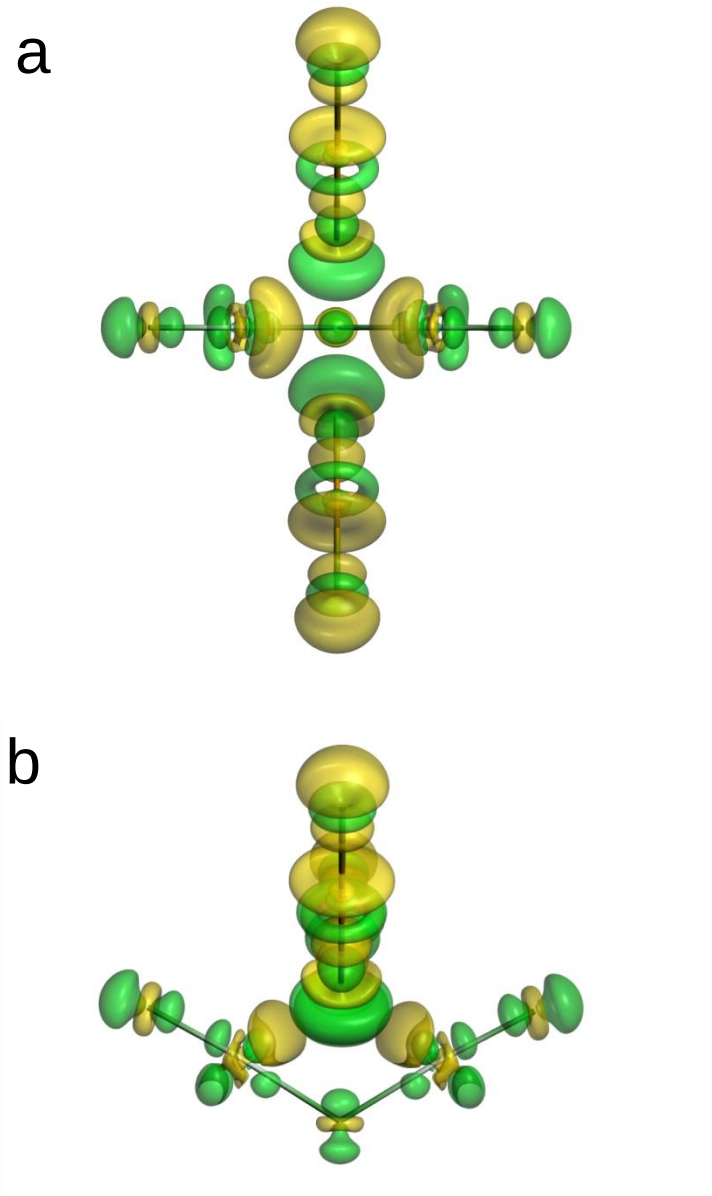

Figure S8.12. The SCF deformation density isosurfaces (0.0015 a.u.) of the hypothetical $[F(HgF)_2(\mu_3\text{-}FKrF)_2]^+$ cation showing the charge flow which results from the interaction of the $[F(HgF)_2]^+$ cation and two KrF_2 fragments; colors indicate increased electron density (green) and decreased electron density (yellow) relative to the parent fragments. **a**) Top-on view looking down the C_2-axis and **b**) side-on view perpendicular to the $\sigma_{(yz)}$-mirror plane. Calculated at the PBE/TZ2P level of theory.

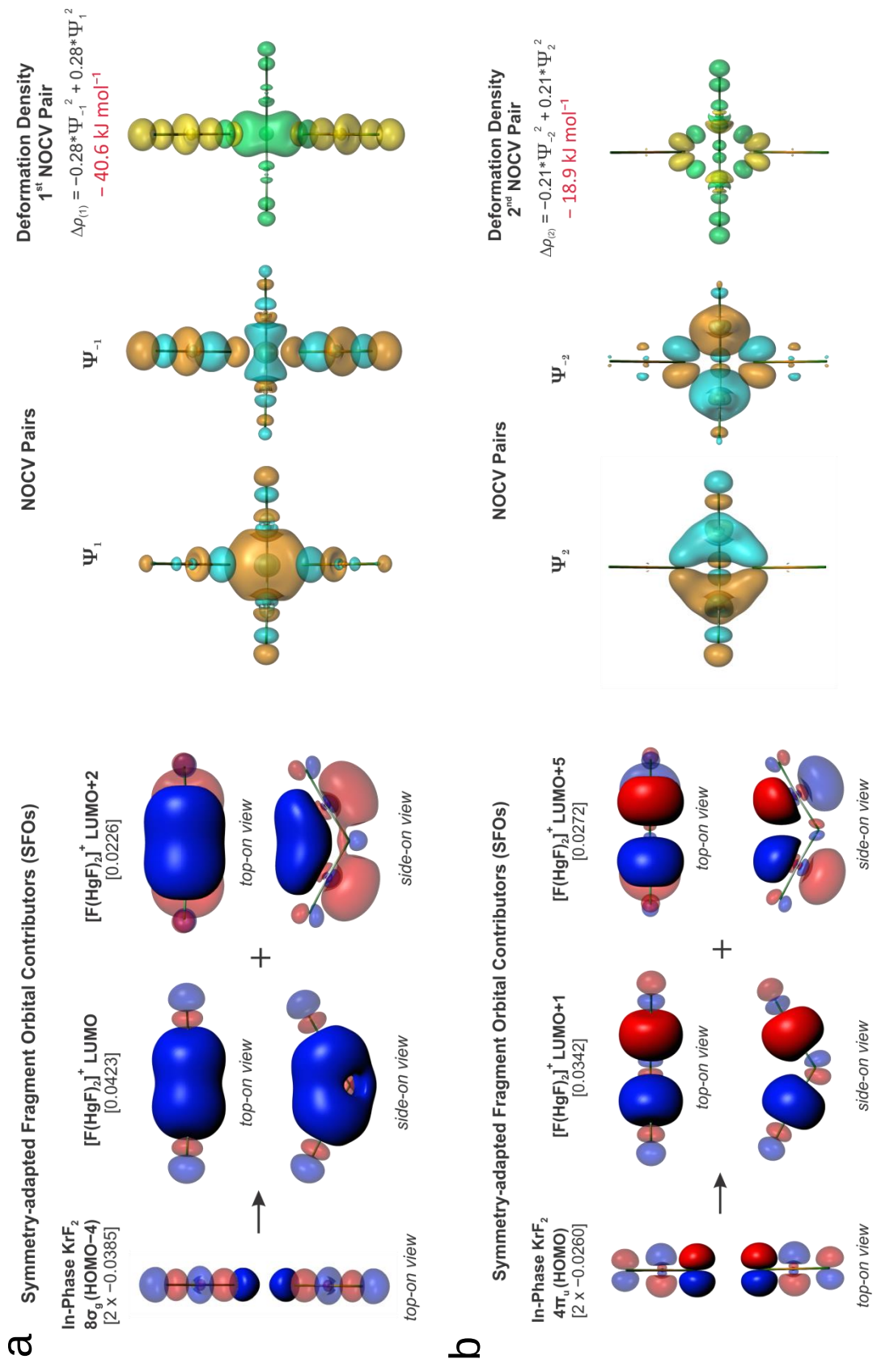
a
Symmetry-adapted Fragment Orbital Contributors (SFOs)
In-Phase KrF2
8σg (HOMO–4)
[2 x –0.0385]
[F(HgF)2]+ LUMO
[0.0423]
[F(HgF)2]+ LUMO+2
[0.0226]
top-on view
side-on view
NOCV Pairs
Ψ1
Ψ–1
Deformation Density
1st NOCV Pair
Δρ(1) = –0.28*Ψ–1 2 + 0.28*Ψ1 2
– 40.6 kJ mol–1
b
Symmetry-adapted Fragment Orbital Contributors (SFOs)
In-Phase KrF2
4πu (HOMO)
[2 x –0.0260]
[F(HgF)2]+ LUMO+1
[0.0342]
[F(HgF)2]+ LUMO+5
[0.0272]
top-on view
side-on view
NOCV Pairs
Ψ2
Ψ–2
Deformation Density
2nd NOCV Pair
Δρ(2) = –0.21*Ψ–2 2 + 0.21*Ψ2 2
– 18.9 kJ mol–1

Figure 8.13.

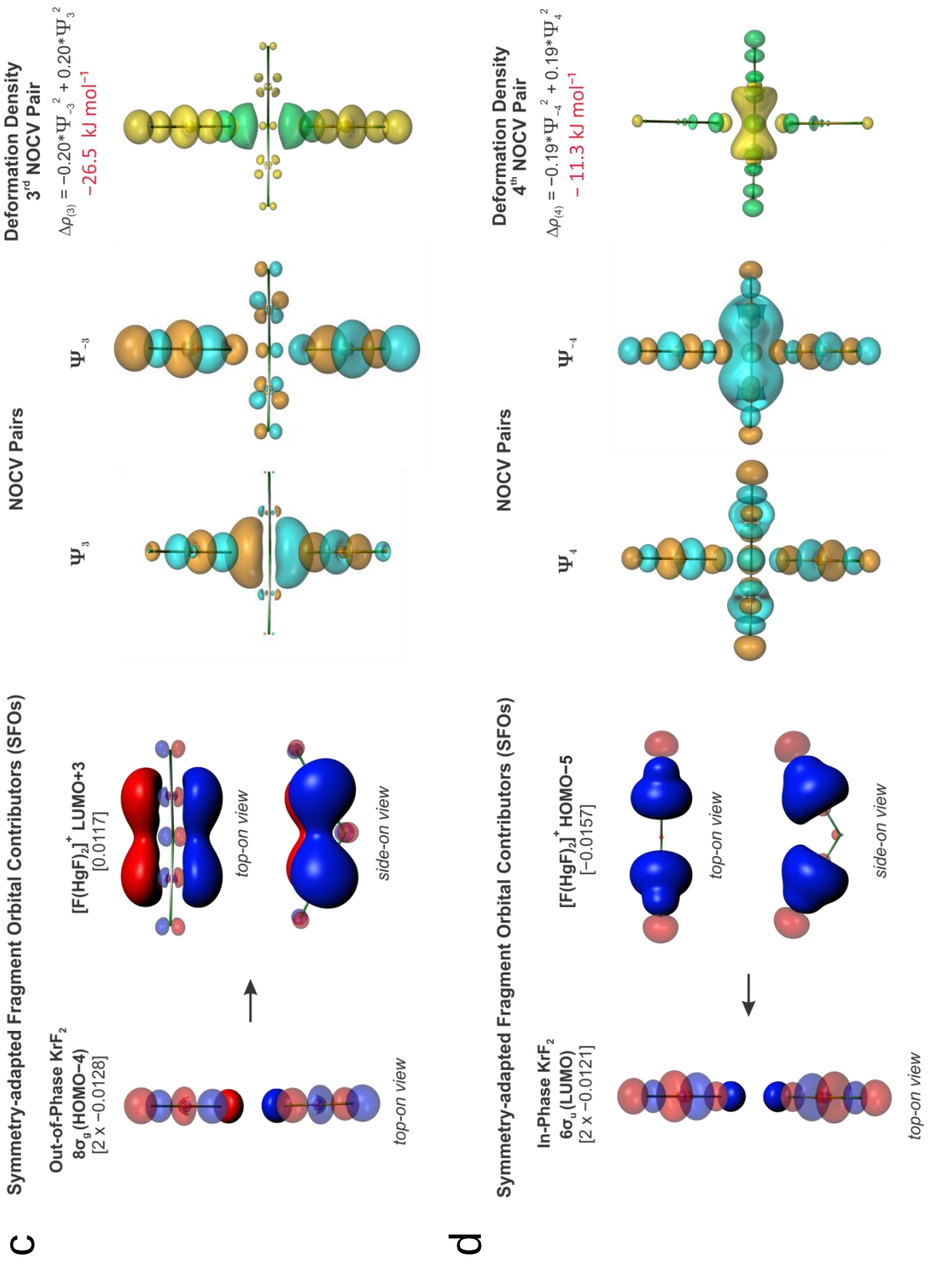

Figure 8.13. continued…

e

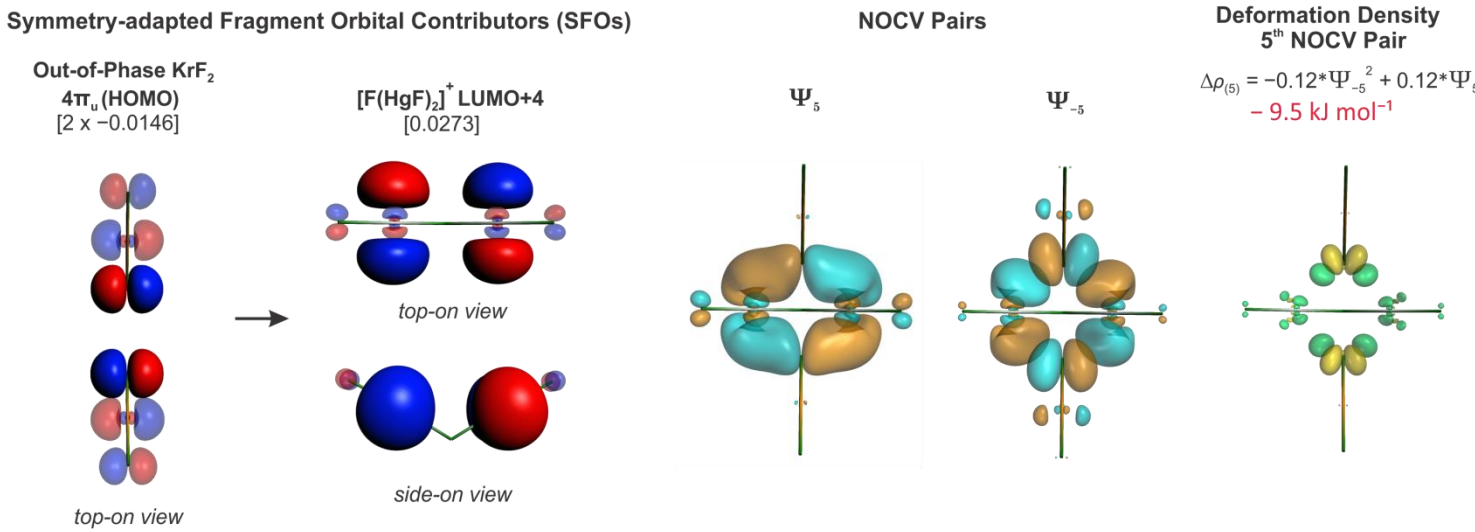

Figure S8.13. The ETS-NOCV analyses for $[F(HgF)_2]^+$ and two KrF_2 ligands in the hypothetical $[F(HgF)_2(\mu_3\text{-}FKrF)_2]^+$ cation ($C_{2v,}$ PBE/TZ2P) showing orbital combinations having **a**) A_1, **b**) B_1, **c**) B_2, **d**) A_1, and **e**) A_2 symmetries. The isosurface values used for orbital depictions are: KrF_2 fragment orbitals (0.03 a.u.), $[F(HgF)_2]^+$ MOs (0.06 a.u.), NOCV pairs (0.03 a.u.), and deformation densities (0.0015 a.u.). Fractional contributions to the Symmetry-adapted Fragment Orbitals (SFOs) to the NOCV pairs are given in square brackets, and descriptions of the two KrF_2 MOs are based on the parent $D_{\infty h}$ point group (see Chapter 7, Figure 7.4). The relative phases of the NOCV pairs are indicated in turquoise and brown colors. The colors of the deformation densities indicate increased electron density (green) and decreased electron density (yellow) relative to the parent fragments. Top-on view looking down the C_2-axis and side-on view perpendicular to the $\sigma_{(yz)}$-mirror plane.

APPENDIX G

Chapter 9 Supporting Information

A New Xenon(II) Oxide; Synthesis and Characterization of $[XeOXe]^{2+}$ in the Adduct-Cation Salt, $[CH_3CN{-}{-}{-}XeOXe{-}{-}{-}NCCH_3][AsF_6]_2$

Adapted with permission from: DeBackere, J.R., Bortolus, M.R., and Schrobilgen, G.J. *Angew. Chem. Int. Ed.* **2016**, *55*, 11917–11920.

LIST OF TABLES

Table S9.1. Experimental Geometrical Parameters of the $[AsF_6]^-$ Anions in $[H_3CCN{-}{-}{-}XeOXe{-}{-}{-}NCCH_3][AsF_6]_2$ [a]

Bond Lengths (Å)			Bond Angles (deg)		
$As_1–F_1$	1.726(1)	$F_1–As_1–F_2$	89.9(1)	$F_8–As_3–F_{13}$	178.6(1)
$As_1–F_2$	1.732(2)	$F_1–As_1–F_3$	179.3(1)	$F_9–As_3–F_{10}$	89.5(1)
$As_1–F_3$	1.716(2)	$F_2–As_1–F_3$	90.4(1)	$F_9–As_3–F_{11}$	178.5(1)
$As_2–F_4$	1.715(2)	$F_4–As_2–F_5$	89.9(1)	$F_9–As_3–F_{12}$	90.6(1)
$As_2–F_5$	1.723(3)	$F_4–As_2–F_6$	88.7(1)	$F_9–As_3–F_{13}$	90.8(1)
$As_2–F_6$	1.721(2)	$F_4–As_2–F_7$	90.1(1)	$F_{10}–As_3–F_{11}$	89.8(1)
$As_2–F_7$	1.711(3)	$F_5–As_2–F_6$	91.2 (1)	$F_{10}–As_3–F_{12}$	179.4(1)
$As_3–F_8$	1.729(2)	$F_5–As_2–F_7$	180.0	$F_{10}–As_3–F_{13}$	89.8(1)
$As_3–F_9$	1.725(2)	$F_6–As_2–F_7$	88.8(1)	$F_{11}–As_3–F_{12}$	90.1(1)
$As_3–F_{10}$	1.735(2)	$F_8–As_3–F_9$	89.4(1)	$F_{11}–As_3–F_{13}$	90.5(1)
$As_3–F_{11}$	1.722(2)	$F_8–As_3–F_{10}$	88.8(1)	$F_{12}–As_3–F_{13}$	90.8(1)
$As_3–F_{12}$	1.724(2)	$F_8–As_3–F_{11}$	89.4(1)		
$As_3–F_{13}$	1.714(2)	$F_8–As_3–F_{12}$	90.6(1)		

[a] The atom labels correspond to those given in Figure 9.1.

Table S9.2. Calculated Vibrational Frequencies of $[H_3CCN\text{---}XeOXe\text{---}NCCH_3]^{2+}$ (C_{2v}) [a]

Def2-SVPD (H,C,N,O) and aug-cc-pVDZ(-PP) (Xe)	Def2-TZVPD (H,C,N,O) and aug-cc-pVDZ(-PP) (Xe)	aug-cc-pVTZ (H,C,N,O) and aug-cc-pVTZ(-PP) (Xe)	Assgnts [b]
3129(79)[39]	3116(70)[29]	3114(74)[32]	B_1, $\nu_{as}(CH_3)_{A+B}$
3129(120)[0]	3116(151)[5]	3114(114)[0]	A_2, $\nu_{as}(CH_3)_{A-B}$
3128(66)[36]	3114(75)[32]	3113(60)[29]	A_1, $\nu_{as}(CH_3)_{A+B}$
3128(161)[5]	3114(115)[0]	3113(153)[4]	B_2, $\nu_{as}(CH_3)_{A-B}$
3032(984)[10]	3037(941)[9]	3036(924)[8]	A_1, $\nu_{s}(CH_3)_{A+B}$
3031(32)[147]	3037(31)[122]	3036(27)[122]	B_2, $\nu_{s}(CH_3)_{A-B}$
2394(1004)[80]	2371(1010)[72]	2368(984)[70]	A_1, $\nu(CN)_{A+B}$
2389(116)[1236]	2367(108)[1158]	2363(103)[1154]	B_2, $\nu(CN)_{A-B}$
1404(8)[33]	1438(7)[32]	1440(7)[32]	A_1, $\delta_{as}(CH_3)_{A+B}$
1403(8)[3]	1438(8)[2]	1440(8)[2]	B_2, $\delta_{as}(CH_3)_{A-B}$
1403(<1)[36]	1437(<1)[35]	1439(<1)[35]	B_1, $\delta_{as}(CH_3)_{A+B}$
1403(16)[0]	1437(15)[0]	1439(15)[0]	A_2, $\delta_{as}(CH_3)_{A-B}$
1365(51)[2]	1398(42)[1]	1398(42)[1]	A_1, $\delta_{s}(CH_3)_{A+B}$
1365(8)[8]	1398(6)[7]	1397(6)[7]	B_2, $\delta_{s}(CH_3)_{A-B}$
1020(<1)[19]	1046(<1)[16]	1046(<1)[16]	B_1, $\rho_{r}(CH_3)_{A+B}$
1020(6)[0]	1046(5)[0]	1046(5)[0]	A_2, $\rho_{r}(CH_3)_{A-B}$
1019(10)[16]	1045(13)[14]	1045(10)[14]	A_1, $\rho_{r}(CH_3)_{A+B}$
1019(3)[4]	1045(2)[4]	1045(3)[3]	B_2, $\rho_{r}(CH_3)_{A-B}$
958(2)[6]	945(2)[6]	944(2)[6]	A_1, $\nu(CC)_{A+B}$
955(<0.1)[110]	942(<0.1)[114]	941(<0.1)[111]	B_2, $\nu(CC)_{A-B}$
592(33)[346]	576(33)[329]	586(32)[377]	B_2, $\nu(Xe_1O) - \nu(Xe_2O)$
445(41)[17]	446(33)[17]	444(34)[17]	A_1, $\nu(Xe_1O) + \nu(Xe_2O) + [(\delta(CCN)_{A+B})_{ip}]_{small}$
402(<1)[4]	408(1)[<0.1]	411(3)[0]	A_2, $(\delta(CCN)_{A-B})_{oop}$
402(1)[<0.1]	408(<1)[4]	411(<1)[4]	B_1, $(\delta(CCN)_{A+B})_{oop}$
402(3)[0]	408(3)[0]	410(1)[<1]	B_2, $(\delta(CCN)_{A-B})_{ip}$
397(28)[<1]	403(36)[<0.1]	403(35)[<0.01]	A_1, $(\delta(CCN)_{A+B})_{ip} + [\nu(Xe_1O) + \nu(Xe_2O)]_{small}$
246(19)[4]	243(18)[5]	243(15)[5]	A_1, $\delta(Xe_1OXe_2)_{ip} - \nu(XeN)_{A+B}$
213(<1)[229]	208(<1)[230]	209(<1)[236]	B_2, $\nu(XeN)_{A-B}$
196(<1)[15]	196(<1)[14]	196(<1)[15]	B_1, $\delta(Xe_1OXe_2)_{oop} + (\delta(XeNC)_{A+B})_{oop}$
168(34)[4]	166(38)[4]	167(35)[4]	A_1, $(\delta(XeNC)_{A+B})_{ip}$
162(<1)[0]	160(<1)[0]	162(<1)[0]	A_2, $(\delta(XeNC)_{A-B})_{oop}$
157(<1)[<1]	155(<1)[<1]	156(<1)[<0.1]	B_2, $(\delta(XeNC)_{A-B})_{ip}$
89(8)[5]	87(7)[6]	87(7)[6]	A_1, $(\delta(XeNC)_{A+B})_{ip} - \delta(Xe_1OXe_2)_{ip}$
68(<0.1)[4]	63(<0.1)[4]	60(<0.1)[4]	B_1, $\delta(Xe_1OXe_2)_{oop} - (\delta(XeNC)_{A-B})_{oop}$

Table S9.2. continued…

46(<1)[1]	49(<0.1)[0]	45(<1)[1]	B_2, $\rho_t(CH_3)_{A-B}$
46(2)[0]	48(<0.1)[<1]	44(2)[0]	A_2, $\rho_r(Xe_1OXe_2)$ + $(\delta(XeNC)_{A+B})_{oop}$
25(6)[10]	45(<1)[1]	24(6)[10]	A_1, $\rho_w(NCC)_{A+B}$
12(<0.1)[0]	44(2)[0]	17(<0.1)[0]	A_2, $\rho_t(CH_3)_{A+B}$
12(<0.1)[<1]	25(6)[10]	16(<0.1)[<1]	B_1, $\rho_t(CH_3)_{A-B}$

[a] The B3LYP method was used. [b] See Table 9.3 footnote [d] for abbreviations. The atom labels correspond to those given in Figure 9.3.

Table S9.3. Calculated Geometrical Parameters of $[H_3CCN\text{---}XeOXe\text{---}NCCH_3]^{2+}$ (C_{2v}) [a]

	Def2-SVPD (H,C,N,O) and aug-cc-pVDZ(-PP) (Xe)	**Def2-TZVPD (H,C,N,O) and aug-cc-pVDZ(-PP) (Xe)**	**aug-cc-pVTZ (H,C,N,O) and aug-cc-pVTZ(-PP) (Xe)**
Bond Lengths (Å)			
$Xe_1–O_1$	2.075	2.072	2.049
$Xe_1\text{---}N_1$	2.319	2.317	2.310
$N_1–C_1$	1.156	1.148	1.148
$C_1–C_2$	1.446	1.442	1.442
$C_2–H$	1.101	1.092	1.091
Bond Angles (deg)			
$Xe_1–O_1–Xe_2$	125.10	124.49	125.26
$N_1–Xe_1–O_1$	174.32	174.30	174.23
$C_1–N_1–Xe_1$	176.66	175.55	175.80
$C_2–C_1–N_1$	179.85	179.67	179.75

[a] The B3LYP method was used. Only half of the atoms and their geometrical parameters listed; the remaining half are equivalent by symmetry (C_{2v}). The atom labeling scheme is given in Figure 9.3.

Table S9.4. Natural Population Analysis (NPA) Charges, Wiberg Valencies, and Wiberg Bond Indices for $[H_3CCN{-}{-}{-}XeOXe{-}{-}{-}NCCH_3]^{2+}$, $[XeOXe]^{2+}$, and CH_3CN

	$[H_3CCN{-}{-}{-}XeOXe{-}{-}{-}NCCH_3]^{2+}$ (C_{2v})	**$[XeOXe]^{2+}$ (C_{2v})**	**CH_3CN (C_{3v})**
Atom [a]	NPA Charges [Wiberg Valencies] [b]		
Xe_1	1.190 [1.091]	1.288 [1.0497]	
Xe_2	1.190 [1.091]	1.288 [1.0497]	
O_1	–0.865 [1.640]	–0.575 [1.8577]	
$\sum[XeOXe]^{2+}$	**+1.515**	**+2.000**	
N_1	–0.506 [3.282]		–0.326[3.023]
C_1	0.578 [3.879]		0.280[4.001]
C_2	–0.716 [3.808]		–0.687[3.852]
H_1	0.295 [0.915]		0.245[0.942]
H_2	0.295 [0.915]		0.245[0.942]
H_3	0.296 [0.914]		0.245[0.942]
$\sum[CH_3CN]_A$	**+0.242**		**+0.000**
N_2	–0.506 [3.282]		
C_3	0.578 [3.879]		
C_4	–0.716 [3.808]		
H_4	0.295 [0.915]		
H_5	0.295 [0.915]		
H_6	0.296 [0.914]		
$\sum[CH_3CN]_B$	**+0.242**		
$\sum[CH_3CN{-}{-}{-}XeOXe{-}{-}{-}NCCH_3]^{2+}$	**+2.000**		
Bond [a]	Wiberg Bond Indices [b]		
Xe_1–O_1	0.676	0.929	
Xe_2–O_1	0.676	0.929	
$Xe_1{-}{-}{-}Xe_2$	0.041	0.121	
$Xe_1{-}{-}{-}N_1$	0.330		
$Xe_2{-}{-}{-}N_2$	0.330		
N_1–C_1	2.678		2.901
C_1–C_2	1.135		1.088
C_2–H_1	0.873		0.909
C_2–H_2	0.873		0.909
C_2–H_3	0.873		0.909
N_2–C_3	2.678		
C_3–C_4	1.135		

Table S9.4. continued…

C_4–H_4	0.873
C_4–H_5	0.873
C_4–H_6	0.873

[a] The atom labeling scheme is given in Figures 9.3 and 9.4. [b] Calculations were carried out at the B3LYP/aug-cc-pVTZ(-PP) level of theory.